europhysics
conference
abstracts

12 th European Conference on

Controlled Fusion and Plasma Physics

Budapest, 2 - 6 September 1985

Editors L. Pócs, A. Montvai

Contributed Papers
Part I

Published by: European Physical Society

Series Editor: Prof. S. Methfessel, Bochum

Managing Editor: G. Thomas, Geneva

VOLUME
9 F
PART I

Max-Planck-Institut für Plasmaphysik
14. MAI 1986
Bibliothek

12 th European Conference on

Controlled Fusion and Plasma Physics

Budapest, 2 - 6 September 1985

Editors L. Pócs, A. Montvai

Contributed Papers
Part I

0306-86

EUROPHYSICS CONFERENCE ABSTRACTS is published by the
European Physical Society, © 1985
Reproduction rights reserved

This volume is published under the copyright of the European Physical Society. We want to inform the authors that the transfer of the copyright to EPS should not prevent an author to publish an article in a journal quoting the original first publication or to use the same abstract for another conference. This copyright is just to protect EPS against using the same material in similar publications.

ISBN 963 372 376 0 (összkiadás)

ISBN 963 372 377 9

Kiadja a Központi Fizikai Kutató Intézet
Felelős kiadó: Pócs Lajos
Példányszám: 800 Törzsszám: 85-420
Készült a KFKI sokszorosító üzemében
Felelős vezető: Töreki Béláné
Budapest, 1985. julius hó

PREFACE

The 12. European Conference of Controlled Fusion and Plasma Physics, was organized by the Roland Eotvos Physical Society and the Central Research Institute for Physics, Budapest, Hungary for the Plasma Physics Division of the European Physical Society (EPS).

The programmme of the Conference was arranged by the Programme Committee wich was elected by the Board of the Plasma Physics Division of the EPS during the Aachen conference, September 1983. This volumes contain all the accepted and by the Scientific Secretary in due time received contributed papers. Some papers received after the deadline but before the final proof, were added in a separate chapter as "late papers". The abstracts were reproduced photographically using the camera ready manuscripts submitted by the authors.

This Conference is a topical conference of the EPS. Therefore, the contributed papers are published as Europhysics Conference Abstracts. This fact determined the size and form of the books. The invited papers of the Conference will be published in a special issue of the journal "Plasma Physics and Nuclear Fusion", early 1986.

We wish to express our acknowledgements to all those people, first of all to Ms. Orsolya Pongracz and the Publishing Department of the Central Research Institute for Physics, who helped the printing of these books.

22. July, 1985

The Editors

PROGRAMME COMMITTEE

G. Grieger, MPIPP, Garching, FRG (Chairman)
L. Pocs, KFKI, Budapest, Hungary (Vice Chairman)
A. Fabre, Ecole Politechnique, Palaisseau, France
A. Gibson, JET
E. Hintz, KFA, Juelich, FRG
J. Jacquinot, JET
V.D. Shafranov, Kurchatov Institute, Moscow, USSR
D.R. Sweetman, Culham Laboratory, Abingdon, UK
H. Wolff, ZIE, Berlin, GDR

contents

In order to facilitate the orientation, each paper of the Conference a unique code was given. This code is to be found

- in the volumes of the contributed papers, in the table of contents and on the upper right corner of the first page of each abstract;
- on the top of the poster tables during poster sessions;
- in the conference programme booklet.

The code has the following structure:

- first character: the topic of the contribution, i.e.
  - A - tokamaks
  - B - stellarators
  - C - mirrors
  - D - compact tori and pinches
  - E - inertial confinement
  - F - plasma heating and current drive
  - G - basic theory
  - H - plasma edge physics
  - I - other related topics
  - J - late papers
- second character: the type of the contribution, i.e.
  - L - invited lecture
  - O - oral contribution
  - P - poster
- two letters: the day of event (Mo,Tu,We,Th or Fr)
- the next number is
  - = in the case of invited and oral lectures, the time of beginning (e.g. 1530 is 15 hours 30 min, i.e. PM 3.30)
  - = in the case of posters, the number of poster stand.
- volume and page number in the contributed papers volumes
- in the case of oral events (L and O) a letter (M or S) shows the lecture room.

Redundant information may be left out, for example the volume and page numbers in the codes used at the beginning of the papers.

Examples:

A O Mo 1640 1 379 M

is an oral contribution about tokamaks, which will be given on Monday in room M at 16 h 40 min. The paper is to be found in the first volume on page 379.

A P Fr 29 1 323

is a poster, which will be exposed on Friday on poster stand No 29. The paper is to be found in the first volume of the Proceedings on page 323.

VOLUME I

A - TOKAMAKS

DeBoo, J C; Groebner, R J; Doublet III Group
Energy confinement experiment on DOUBLET III with high power neutral beam heating A P Mo 1 1 2 2
Abe, M; Hirayama, T; Kitsunezaki, A; Kameari, A; Konoshima, S; ...
Ion energy confinement properties in high power beam heated plasmas in DOUBLET III A P Mo 2 1 6 6
Zurro, B; Pardo, C; Cabrera, J A; Cepero, J R; TJ-1 Group
Radiated power loss behaviour in the TJ-I tokamak A P Mo 3 1 10 10
Joye, B; Lister, J B; Marmillod, Ph; Moret, J-M; Nowak, S
The radiated power profile under wide-ranging Ohmic conditions in the TCA tokamak A P Mo 4 1 14 14
Gruber, O; Jilge, W; Bernhardi, K; Eberhagen, A; Fussmann, G; ...
Radial energy balance analysis of ASDEX H-mode discharges A P Mo 5 1 18 18
Taroni, A; Abels van-Maanen, A E P M; Core, W; Duechs, D F; ...
Transport calculations for JET discharges with ICRH A P Mo 6 1 22 22
Cordey, J G; Bartlett, D V; Bickerton, R J; Brusati, M; ...
Global energy confinement studies in Ohmically heated JET plasmas A 0 Mo 1430 1 26 M 26
Gottardi, N; Krause, H; Mast, F
Limits in evaluating energy loss profiles from bolometric measurements at JET A P Mo 7 1 30 30
Brusati, M; Cordey, J G
Transport analysis of JET discharges A P Mo 8 1 34 34
T-10 Group
Study of electron heat conductivity on T-10 by propagation of a heat pulse from ECRH A P Mo 9 1 38 38
T-10 Group
Energy confinement dependence on plasma current in T-10 under ECRH A P Mo 10 1 42 42
Kalmykov, S G; Lashkul, S I; Petrov, Yu V; Shprits, I D
Temperature dependence of electron heat conductivity in TUMAN-2A-the tokamak with magnetic compression A P Mo 11 1 46 46
Hofmann, F; Marcus, F B; Turnbull, A D
Positional stability of highly elongated tokamak plasma in a conducting shell A P Mo 12 1 50 50
Goedbloed, J P; Hogeweij, G M D; Kleibergen, R; Rem, J; ...
High-beta tokamak stability of toroidal plasmas with elliptical and D-shaped cross-sections A P Mo 13 1 54 54
Takahashi, H; Bol, K; Buchenauer, D; Couture, P; Fonck, R; ...
High beta-t studies in the PBX tokamak A 0 Mo 1450 1 58 M 58
Shoji, T; Hoshino, K; Kasai, S; Kawakami, T; Kawashima, H; ...
High beta and confinement studies in the JFT-2M tokamak A P Mo 14 1 62 62

VOLUME I

Gruber, O; Lackner, K; Lappus, G; Preis, H; Seidel, U; ...
Configuration control for ASDEX Upgrade
A P Mo 15 1 66 66

Tanga, A; Campbell, D J; Denne, B; Gibson, A; Gottardi, N; ...
The formation of a magnetic separatrix in JET
A O Mo 1510 1 70 M 70

Ming lun, Xue; Xiao, Li
Vaporization model of pellet under fusion plasma conditions
A P Mo 16 1 74 74

Vlases, G; Kaufmann, M; Gruber, O; Haas, G; Lang, R S; ...
Quasi stationary D-2 pellet injection into ASDEX divertor discharges
A O Mo 1720 1 78 M 78

Lengyel, L; Neuhauser, J
Ignition and fuelling scenarios based on the injection of pellets in thermonuclear plasmas A P Mo 17 1 82 82

Stringer, T E
A theory of marfes A P Tu 1 1 86 86

Goloborod'ko, V Ya; Kolesnichenko, Ya I; Yavorskij, V A
Stochastic motion and diffusion of alpha particles in tokamaks due to toroidal ripple A P Tu 2 1 90 90

Gott, Yu, V; Yurchenko, E I
To the theory of ion heat conduction in tokamak
A P Tu 3 1 94 94

Parail, V V; Yushmanov, P N
Stochastic motion of particles and anomalous heat conduction in tokamak A P Tu 4 1 98 98

Dnestrovskij, Yu N; Kostomarov, D P; Pedorenko, A V; Popov, A M
Non-linear development of helical modes and helical equilibrium in tokamak A P Tu 5 1 102 102

Degtyarev, L M; Drozdov, V V; Martynov, A A; Medvedev, S Yu
On scaling for the limiting beta values in tokamaks
A P Tu 6 1 106 106

De Menna, L; Miano, G; Rubinacci, G
Free boundary plasma equilibria in a non circular shell
A P Tu 7 1 110 110

Olivares, A G; Soler, Mario
Prediction of sawtooth oscillation parameters in tokamak discharges
A P Tu 8 1 114 114

Waidmann, G; Hrehuss, G
ECE-measurements on TEXTOR tokamak during Ohmic and ion cyclotron resonance heating experiments A P Tu 9 1 118 118

Goedheer, W J; Westerhof, E
Simulation of tokamak discharges with sawteeth
A P Tu 10 1 122 122

Duperrex, P A; Keller, R; Malacarne, M; Pochelon, A
Magnetic activity during internal disruptions in JET discharges
A P Tu 11 1 126 126

Campbell, D J; Bartlett, D V; Best, C; Brusati, M; Christiansen, J P; ...
Analysis of sawtooth instabilities in JET
A P Tu 12 1 130 130

VOLUME I

McGuire, K; Callen, J D; Colchin, R J; Efthimion, P C; ...
Compound sawteeth and heat pulse propagation in TFTR
A P Tu 13 1 134 134
Alladio, F; Mazzitelli, G; Tuccillo, A A; Vlad, G
Analysis of sawtooth relaxations in Ohmic and RF heated discharges of the FT tokamak A P Tu 14 1 138 138
Bobrovskii, G A; Esipchuk, Yu V; Notkin, G E; Portnov, D V; ...
Internal disruption study in T-10 plasmas
A P Tu 15 1 142 142
Montvai, A; Zoletnik, S
Topological invariant of the tokamak configuration, and its role in processes leading to fast redistribution of the plasma current
A P Tu 16 1 146 146
Wesson, J; Gowers, C; Han, W; Mast, F; Nave, F; ...
Density limit disrupions in JET A P Tu 17 1 147 147
Schueller, F C; Alladio, F; Campbell, D; Crisanti, F; de Kock, L; ...
Experimental observations of disruptions in JET
A P Tu 18 1 151 151
O'Rourke, J; Campbell, D; Denne, B; Gondhalekar, A; Gottardi, N; ...
Poloidally asymmetric edge phenomena in JET
A P Tu 19 1 155 155
Niedermeyer, H; Bartiromo, R; Becker, G; Bosch, H S; Brocken, H; ...
Investigations into the density limit of the tokamak with Ohmic and neutral beam heating A 0 Tu 1630 1 159 S 159
Braams, B J; Jilge, W; Martin, P
Fast determination of plasma parameters through function parametrization A P Tu 20 1 163 163
Braams, B J
MHD equilibrium determination A P Tu 21 1 167 167
Alladio, F; Crisanti, F; Marinucci, M
Analysis of axisymmetric MHD equilibria by toroidal multipolar expansion A P Tu 22 1 171 171
Spineanu, F; Vlad, M
Comparative studies for the numerical simulations of impurity transport in tokamak plasmas A P Tu 23 1 175 175
Shimizu, K; Shirai, H; Hirayama, T; Azumi, M; Takizuka, T; ...
Numerical simulation of MHD effects of tokamak plasma confinement
A P Tu 24 1 179 179
Heifetz, D B; Langer, W D; Ehrhardt, A B
Three-dimensional calculations of the transport of neutral hydrogen and molecular impurities in TFTR A P Tu 25 1 183 183
Boerner, P; Kaleck, A
CATI - a code for axisymmetric motions of plasma in tokamaks with iron-core transformer A P Tu 85 1 187 187
Saoutic, B; TFR Group
Laser-injected impurity transport in Ohmic and ICRF-heated TFR plasmas
A P Th 1 1 191 191
Fussmann, G; Bartiromo, R; Janeschitz, G; Kotze, P B; Mueller, E R; ...
Impurity behaviour for various auxiliary heating methods in ASDEX
A P Th 2 1 195 195

McCormick, K; Bartiromo, R; Bosch, H S; Brambilla, M; Derfler, H; ...
Measurement of the current distribution in ASDEX during lower hybrid current drive using the Li-beam/Zeeman-effect technique
A P Th 3 1 199 199

Duval, B P; Fielding, S J; Hawkes, N C; Hugill, J; Peacock, N J
Charge exchange spectroscopy on DITE
A P Th 4 1 203 203

Bagdasarov, A A; Bugarya, V I; Vasin, N L; Vershkov, V A; ...
Injected impurity transport study in the T-10 plasma by X-ray and VUV-spectroscopy
A O Th 1710 1 207 M 207

Bittoni, E; Fubini, A; Haegi, M; Pedretti, E; Pillon, M; ...
Preliminary measurement of the burn up of the fusion-produced tritons in FT
A P Fr 1 1 211 211

Tubbing, B J D; Barbian, E; Campbell, D J; Hugenholtz, C A J; ...
A twelve-channel grating polichromator for measurement of electron temperature in JET
A P Fr 2 1 215 215

Corti, S; Bracco, G; Brusati, M; Gondhalekar, A; Grosso, G; ...
Analysis of neutral particles in JET
A P Fr 3 1 219 219

Jarvis, O N; Gorini, G; Hone, M; Kaellne, J; Maerlo, V; ...
Ion temperature and density measurements in JET using neutron diagnostics
A P Fr 4 1 223 223

Costley, A E; Baker, E A M; Brusati, M; Bartlett, D V; Campbell, D J; ...
Electron temperature measurement on JET
A P Fr 5 1 227 227

Huebner, K; Baetzner, R; Hinsch, H; Rapp, H; Wurz, H; ...
Neutron production during deuterium injection in deuterium plasmas in ASDEX
A P Fr 6 1 231 231

Berezovsky, E L; Dnestrovsy, Yu N; Efremof, S L; Zaveryaev, V S; ...
Ion temperature measurements by charge exchange in the presence of convective ion transfer in tokamak
A P Fr 7 1 235 235

Barbotko, V M; Bychkov, S S; Ivanov, R S; Stotsky, G J
Method of local effective ion charge determination in tokamak by means of resonance fluorescence
A P Fr 8 1 239 239

Irisov, G S; Yushmanov, P N
Distortion of the Maxwellian distribution in inhomogeneous magnetized plasma
A P Fr 9 1 243 243

Bondarenko, S P; Kaminskij, A O; Kuznetsov, Yu K; Pyatov, V N; ...
Investigation of current profiles in the TUMAN-3 tokamak
A P Fr 10 1 247 247

Bertschinger, G; Reiter, D; Koenen, L
Determination of the flux of thermal neutral particles from the wall to a tokamak by pulsed gas injection
A P Fr 11 1 251 251

Hickok, R L; Saadatmand, K; Jennings, W C
Fluctuation measurements on the RENTOR tokamak
A P Fr 12 1 255 255

De Simone, P; Frigione, D; Orsitto, F
Density fluctuations measurement on FT tokamak by small angle CO-2 scattering
A P Fr 13 1 259 259

VOLUME I

Carolan, P G; Forrest, M J; Hawkes, N C; Peacock, N J
Studies of edge phenomena in JET with visible spectroscopy
A P Fr 14 1 263 263

Carolan, P G; Duval, B P; Field, A R; Fielding, S J; Hawkes, N C; ...
Charge exchange recombination spectroscopy of ASDEX
A P Fr 15 1 267 267

Bakos, J S; Sorlei, Zs
Optically pumped FIR lasers and tokamak interferometry
A P Fr 16 1 271 271

Valovic, M; Badalec, J; Jakubka, K; Kopecky, V; Stoeckel, J; ...
A start-up discharge phase in a CASTOR tokamak
A P Fr 17 1 275 275

Gruber, O; Lackner, K; Wunderlich, R
Transport analysis for current build-up in ASDEX and JET
A P Fr 18 1 279 279

Thomas, P R; Christiansen, J P; Ejima, S
Volt-seconds consumption of JET discharges
A P Fr 19 1 283 283

Schueller, F C; Thomas, P R; Kellman, A; Lazzaro, E; Lomas, P; ...
Plasma evolution and skin-effects in JET
A P Fr 20 1 287 287

Sawley, M L; Pochelon, A; Keller, R
Studies of broadband magnetic fluctuations int the TCA tokamak
A P Fr 21 1 291 291

TFR Group; Truc, A
Connection between low frequency turbulence and electron energy confinement in TFR A P Fr 22 1 295 295

Feneberg, W; Kornherr, M; Smeulders, P; Bartiromo, R; Becker, G; ...
Poloidal asymmetric impurity radiation in ASDEX in the presence of neutral ijection A P Fr 23 1 299 299

Budaev, V P; Ivanov, R S
Turbulence-induced plasma transport in tokamak TV-1
A P Fr 24 1 303 303

Borshchegovskij, A A; Popov, I A; Stepanenko, M M
MHD-mode m=2 suppression by ECRH heating in the tokamak T-10
A P Fr 25 1 307 307

Howling, A; Cote, A; Doyle, E J; Evans, D E; Robinson, D C
Fluctuations and losses in the TOSCA tokamak
A P Fr 26 1 311 311

Haynes, P S; Morris, A W; Robinson, D C
Observation of multiple helicity modes on JET
A P Fr 27 1 315 315

Alladio, F; Crisanti, F; Lazzaro, E
Identification of magnetic helical perturbation in a tokamak
A P Fr 28 1 319 319

Harbour, P J; Johnson, P C
Extrapolation of bundle divertor results to a reactor of INTOR/NET size A P Fr 29 1 323 323

Christiansen, J P; Campbell, D J; Cordey, J G; Ejima, S; Lazzaro, E
Resistivity and field diffusion in JET
A P Fr 30 1 327 327

VOLUME I

Gierke, G v.; Keilhacker, M; Bartiromo, R; Becker, G; Bosch, H S; ...
The transient behaviour of the beta limit in ASDEX
A P Fr 31 1 331 331

Wagner, F; Gruber, O; Bartiromo, R; Becker, G; Bosch, H S; ...
Confinement studies on ASDEX in the intermediate region from Ohmic to neutral injection scaling A P Fr 32 1 335 335

Strachan, J D; Boody, F P; Bush, C; Grek, B; Hawryluk, R J; ...
Formation of detached plasmas in TFTR
A P Fr 33 1 339 339

Medley, S S; Bitter, M; England, A C; Fredrickson, E; Goeler, S von; ...
Ion behaviour in TFTR during Ohmic and neutral beam operation
A P Fr 34 1 343 343

Degtyarev, L N; Medvedev, S Yu; Putvinskij, S V; Chuyanov, V A
On limit beta in a tokamak with strong field and with adiabatic plasma compression A P Fr 35 1 347 347

Vasin, N L
Electron density profile dependence on plasma parameters on T-10
A P Fr 36 1 351 351

Gulyaev, V A; Levkov, B S; Notkin, G E
Plasma current density shaping at the initial stage of discharge on T-10 A P Fr 37 1 355 355

Gladushchak, V I; Ipatov, V A; Kalmykov, S G; Lashkul, S I; ...
Local particle balance in a tokamak with magnetic compression - TUMAN-2A A P Fr 38 1 359 359

Askinasi, L G; Golant, V E; Goncharov, S G; Gryaznevich, M P; ...
Experiments on R-compression and ICR heating in the tokamak 'TUMAN-3'
A O Th 1510 1 363 M 363

Sestero, A; Nocentini, A
Difficulties with the establishing of "gas blankets" at the border of magnetically confined plasmas A P Fr 39 1 367 367

Axon, K B; Hawkes, N C; Hugill, J; Johnson, P C; Millar, W; ...
Effect of the non-axisymmetric field of the DITE bundle divertor on magnetic topology, mhd instabilities and rotation
A P Fr 40 1 371 371

Tsuji, S; Koide, Y; Yoshida, H; Yamada, K; Hirayama, T; ...
MHD characteristics of JT-60 plasmas
A O Mo 1640 1 375 M 375

Denne, B; Behringer, K H; Engelhardt, W; Gill, R D; Hawkes, N C; ...
Spectroscopic measurements of the impurity content of JET plasmas with Ohmic and RF heating A O Th 1630 1 379 M 379

B - STELLARATORS

Maassberg, H; W VII-A Team; NI Team; ECRH Group
Ambipolar electric fields and transport
B P Mo 18 1 384 384

Wilhelm, R; Erckmann, V; Janzen, G; Kasparek, W; Mueller, G A; ...
70 GHz ECRH experiments on the W VII-A stellarator
B O Mo 1640 1 385 S 385

W VII-A Team; NI Team; ECRH Group
Influence of the magnetic configuration on plasma behaviour in the WENDELSTEIN VII-A stellarator B P Mo 19 1 393 393

VOLUME I

Penningsfeld, F P; Ott, W; Speth, E
Computation of fast ion confinement by electric fields in the W VII A stellarator B P Mo 20 1 397 397
Uo, K; Iiyoshi, A; Obiki, T; Motojima, O; Morimoto, S; ...
NBI and ECR heating experiments of the HELIOTRON E device B O Mo 1700 1 401 S 401
Motojima, O; Zushi, H; Sudo, S; Kaneko, K; Sano, F; ...
Study of the transprt and energy balance of HELIOTRON E plasmas B P Mo 21 1 405 405
Herrnegger, F; Johnson, J L
Effect of wall stabilization on free boundary m=2 modes in toroidal l=2 stellarators with small shear B P Mo 22 1 408 409
Akulina, D K; Lasarev, V B; Lapshin, V I; Leonov, V N; ...
Measurements of electron cyclotron radiation spectrum (ECR) in the L-2 stellarator by fast-scanning Fourier spectrometer B P Mo 23 1 413 413
Fraiman, A A; Smolyakova, O B; Suvorov, E V
A numerical simulation of experiments on EC preionization and plasma heating at L-2 stellarator B P Mo 24 1 417 417
Andryukhina, E D; Batanov, G M; Berezhetskij, M S; Blokh, M A; ...
Comparison of experimental results and numerical simulations on ECR production and heating in currentless plasma in the L-2 stell. B O Mo 1720 1 421 S 421
Blokh, M A; Voronov, G S; Donskaya, N P; Kladov, S V; Larionova, N F; ...
Spectroscopic studies of impurities during ECR plasma heating in the L-2 stellarator B P Mo 25 1 424 424
Hamberger, S M; Sharp, L E; Shi, S X; Blackwell, B D
Plasma production and confinement in a toroidal heliac B P Mo 26 1 429 429
Perea, A; Alvarez Rivas, J L; Botija, J; Cepero, J R; Fabregas, J A; ...
Physics issues in the design of TJ-II B P Mo 27 1 433 433
Guasp, J; Fabregas, J A
HELICON, a new helical axis stellarator B P Mo 28 1 437 437
Guasp, J; Alvarez Rivas, J L; Fabregas, J A; Lopez Fraguas, J A; ...
Physics studies for the TJ-II device B P Mo 29 1 441 441
Nuehrenberg, J; Zille, R
Ballooning modes in 3D finite-beta stellarators B P Mo 30 1 445 445
Harmeyer, E; Kisslinger, J; Rau, F; Wobig, H
On conventional and modular heliacs B P Mo 31 1 449 449
Wobig, H; Kisslinger, J
Stellarator equilibrium by low-beta-expansion B P Mo 32 1 453 453
Nagao, S; Miyajima, S; Fujii, M; Saito, T; Katsumori, H
Improvement of magnetic surfaces of helical axis torsatron B P Mo 33 1 457 457

VOLUME I

Beidler, C D; Hitchon, W N G; Mynick, H E; Shohet, J L
Ripple transport at low collisionality in stellarators
B P Mo 34 1 461 461

Anderson, D T; Anderson, F S B; Doerner, R P; Probert, P H; ...
Magnetic field structure and ECR plasmas in IMS
B P Mo 35 1 465 465

Vasil'ev, M P; Kulaga, A E; Kuleshov, I E; Perepelkin, N F; ...
Collective phenomena in ECR wave-plasma interaction in SATURN stellarator
B P Mo 36 1 469 469

Grekov, D L; D'yakov, V E
Features of lower hybrid heating in stellarators
B P Mo 37 1 473 473

Fukuyama, A; Okazaki, N; Goto, A; Itoh, S-I; Itoh, K
Structure of ICRF waves in a plasma with helical symmetry
B P Mo 38 1 477 477

Andryukhina, E D; Danilkin, I S; Dyabilin, K S; Fedyanin, O I
Determination the plasma-pressure anisotropy in stellarators
B P Mo 39 1 481 481

Mond, M
Stability of high beta plasmas with helical magnetic axis
B P Mo 40 1 485 485

Berge, G; Choe, W H; Freidberg, J P
Ideal magnetohydrodynamic equilibrium and stability studies of a toroidal system with arbitrary helical fields
B P Mo 41 1 487 487

Shoji, T; Fujiwara, M; Hosokawa, M; Kamimura, T; Ikegami, H; ...
Effect of ECH and ICH on ambipolar potential formation in Nagoya BUMPY TORUS
B P Mo 42 1 491 491

C - MIRRORS

Kammash, T; Zavala, G
Streaming instabilities in tandem mirror thermal barriers
C P Fr 41 1 496 496

Phillips, M W; Todd, A M M
ICRF field solutions in axisymmetric mirror plasmas
C P Fr 42 1 500 500

Kumazawa, R; Adati, K; Aoki, T; Fujita, H; Hattori, K; ...
Slooshing ion distribution produced by ICRH in an axisymmetric mirror-cusp device, RFC-XX-M
C P Fr 43 1 504 504

Knyazev, B A; Chikunov, V V; Koidan, V S; Lebedev, S V; ...
Magnetic focusing of 80 kJ microsecond electron beam for plasma heating in solenoids
C P Fr 44 1 508 508

Mirnov, V V
Stability of a steady state in open traps with neutral injection
C P Fr 45 1 512 512

Botcharov, V N; Breizman, B N; Kiselev, A V; Konstantinov, S G; ...
MHD stable confinement of rotating plasma in an axisymmetrical open trap
C P Fr 46 1 516 516

Ren, Z; Chen, Sh; Huang, Ch; Fang, Y; Wang, Zh; ...
Investigation of low-frequency plasma fluctuation in the HER device
C P Fr 47 1 520 520

VOLUME I

Goto, A; Fukuyama, A; Furutani, Y
Propagation of ICRF waves in an axisymmetric mirror plasma
C P Fr 48 1 524 524

Mase, A; Adachi, S; Cho, T; Ichimura, M; Inutake, M; ...
Plasma confinement in the axisymmetrized tandem mirror GAMMA 1)
C O Fr 1210 1 528 M 528

Kies, W; Van Calker, C; Decker, G; Maelzig, M; Ziethen, G
300 kV plasma focus SPEED 2: first results from 3 MA-discharges
C P Mo 51 1 566 566

D - COMPACT TORI AND PINCHES

Sinman, A; Sinman, S
A fast dense plasma focus system employing REB technology
D P Mo 43 1 534 534

Sadowski, M; Jakubowski, L; Rydygier, E; Zebrowski, J
Space- and time-resolved studies of X-ray and ion emission from the PF-360 experiment D P Mo 44 1 538 538

Jaeger, U; Biermayer, W; Herold, H; Kaeppeler, H J; Schmidt, H; ...
Fusion reaction mechanisms in the plasma focus POSEIDON
D P Mo 45 1 542 542

Borowiecki, M; Czekaj, S; Denus, S; Koziarkiewicz, W; ...
Influence of insulator on plasma-focus discharge
D P Mo 46 1 546 546

Czekaj, S; Denus, S; Kasperczuk, A; Miklaszewski, R; Paduch, M; ...
The study of plasma dynamics in the PF-300 device by means of laser diagnostics D P Mo 47 1 550 550

Yokoyama, M; Yamada, Y; Yamamoto, Y; Kitagawa, Y; Yamanaka, M
Experimental studies in dense plasma focus
D P Mo 48 1 554 554

Ursu, I; Ivascu, M; Cotruta, D; Dimitrescu-Zoita, C; Ludu, A; ...
Experiments with a plasma focus device powered by magnetic flux-compression generators D P Mo 49 1 558 558

Salukvadze, R G; Khautiev, E Yu; Kraus, V I; Batenyuk, A A
Formation of electron and ion beams in a plasma focus
D P Mo 50 1 562 562

Weber, P G; Baker, D A; Buchenauer, C J; Burkhardt, L C; Cayton, T E; ...
Results from the Los Alamos RFP experiments
D O Fr 1150 1 570 M 570

Wahlberg, C
Conditions for confinement and positional stability of a z-pinch in high order multipole and cusp fields
D P Mo 52 1 574 574

Alper, A; Antoni, V; Bassan, N; Buffa, A; Costa, S; ...
RFP confinement studies in ETA-BETA II
D P Mo 53 1 578 578

Antoni, V; Ortolani, S
Large amplitude oscillations and relaxation phenomena in reversed field pinches D P Mo 54 1 582 582

Gabellieri, L; Ortolani, S; Puiatti, M E; Scarin, P; Tondello, G
Space-resolved impurity measurements on ETA-BETA II
D P Mo 55 1 586 586

VOLUME I

Siemon, R E; Armstrong, W T; Chrien, R E; Hugrass, W N; McKenna, K F; ...
Field-reversed configuration formation, translation, and confinement studies on the FRX-C/T experiment D P Mo 56 1 590 590

Bobeldijk, C; Hoekzema, J A; Lok, J; van der Meer, A F G; Oepts, D; ...
SPICA-II: A high-beta experiment with elongated plasma cross-section D P Mo 57 1 594 594

Nalesso, G F
Non linear boundary equations at a thin anisotropically conducting wall (liner) D P Mo 58 1 598 598

Toyama, H; Asakura, N; Hattori, K; Inoue, N; Ishida, S; ...
Effects of bias toroidal field and filling pressure on the performance of the reversed field pinch device REPUTE-1 D P Mo 59 1 602 602

Panarella, E; Guty, V
Application of the scaling laws to the REXIMPLO spherical pinch machine: experimental results D P Mo 60 1 606 606

Witalis, E A
Current and field self-reversals in toroidal pinches D P Mo 61 1 610 610

Evans, D E; Storey, D P; Wilcock, P D
Density studies in HBTX1A reversed field pinch D P Mo 62 1 614 614

Eriksson, G
Charged particle motion in a cylindrically symmetric z-pinch D P Mo 63 1 618 618

Liberman, M A; Velikovich, A L
Self-similar motions in a Z pinch dynamics D P Mo 64 1 622 622

Asakura, N; Inoue, N; Miyamoto, K; Nagayama, Y; Shinohara, S; ...
Equilibrium of reversed field pinch with iron core D P Mo 65 1 626 626

Briguglio, S; Romanelli, F; Vlad, G
Current driven drift waves in reversed field pinches D P Mo 66 1 630 630

Bunting, CC A; Carolan, P G; Field, A R
Ion behaviour in the HBTX1A reversed field pinch D P Mo 67 1 634 634

Martini, S; Ortolani, S
Soft X-ray measurements on ETA-BETA II D P Mo 68 1 638 638

Sinman, S; Sinman, A
A compact toroid formed by multi magnetized T-tubes D P Tu 26 1 642 642

Hoida, H W; Barnes, C W; Henins, I; Jarboe, T R; Buchenauer, C J; ...
Local drift parameter, j/ne and resistivity anomaly measurements in CTX spheromaks D P Tu 27 1 643 643

Jones, I R; Knight, A
A field reversed configuration generated by means of a rotating magnetic field D P Tu 28 1 647 647

VOLUME I

Jones, I R; Kirolous, H
Long duration rotamak experiments D P Tu 29 1 651 651
Bruhns, H; Allgeier, C; Raupp, G; Steiger, J; Weichelt, A
Generation of double toroids of the spheromak-type in the Heidelberg spheromak experiment D P Tu 30 1 655 655
Bruhns, H; Allgeier, C; Boeckle, G; Raupp, G; Steiger, J; ...
Studies of single toroids in the Heidelberg spheromak experiment D P Tu 31 1 659 659
Ag, A; Nemeth, G
Turbulent transfer rate of the magnetic field in a spheromak D P Tu 32 1 663 663

VOLUME II

E - INERTIAL CONFINEMENT

Denus, S; Arendzikowski, R; Fiedorowicz, H; Jeziak, K; ...
Experimental study of laser-driven implosion of spherical microtargets E O Th 1450 2 2 S 2
Denus, S; Fiedorowicz, H; Kostecki, J; Nagraba, S; Pawlowicz, W; ...
Spectral analysis of 2-omega-null and 3/2-omega-null harmonic emission from laser irradiated spherical microshells E P Th 5 2 6 6
Fabbro, R; Faral, B; Virmont, J; Cottet, F; Romain, J P; ...
Generation of very high pressures in planar geometry in o.26 mikrom wavelength laser experiments E P Th 6 2 10 10
Meyer, J; McIntosh, G; Houtman, H
Experimental investigation of the two plasmon decay and stimulated Raman scattering instabilities in a CO2 laser produced plasma E P Th 7 2 14 14
Golota, V I; Karas, V I
On the high-current ion beam instability in the Z-pinch plasma channel E P Th 8 2 18 18
Kawata, S; Niu, K
Target implosion in LIB ICF E P Th 9 2 22 22
Bakhst, R B; Datsko, I M; Kovsharov, N F; Loskutov, V V; ...
Study of the implosion of wire arrays at 1 MA current pulses E P Th 10 2 26 26
Kamelander, G
Effects of fusion product transport on burn characteristics of ICF-pellets E P Th 11 2 30 30

F - PLASMA HEATING AND CURRENT DRIVE

Hansen, F R; Lynov, J P; Maroli, C; Petrillo, V
Full-wawe calculation of the O-X mode conversion process F P Fr 49 2 36 36
Ejima, S; Jahns, G L; Lin, S H; Moeller, C P; Prater, R; ...
Heating and confinement in the DOUBLET III tokamak with electron cyclotron heating F O Fr 980 2 40 M 40
Zhang, Z X; Jiang, H Y
An ECRH ray-tracing study with multi-reflection and mode conversion F P Fr 50 2 44 44

VOLUME II

Faulconer, D W; Bral, L
Plasma-induced TM mode transparency of electrostatic shields used in RF heating F P Fr 51 2 48 48
Bornatici, M; Ruffina, U; Westerhof, E
Electron cyclotron absorption and emission in the presence of a small population of drifting superthermals F P Fr 52 2 52 52
Heikkinen, J A; Karttunen, S J
Scattering of the heating wave off ion wave in electron cyclotron resonance heating F P Fr 53 2 56 56
FOM-ECRH Team; TFR Group
First results of the electron cyclotron experiment on TFR F O Fr 920 2 60 M 60
Litwin, C; Hershkowitz, N; Callen, J D
Eigenmode structure, ICRF heating and stabilization of axially symmetric systems F P Fr 54 2 64 64
Vasin, N L
Electron density profile behaviour under ECRH on T-10 F P Fr 55 2 68 68
Fukuyama, A; Goto, A; Itoh, K; Itoh, S-I
Two-dimensional kinetic analysis of ICRF waves in a tokamak F P Fr 56 2 72 72
O'Brien, M R; Cox, M; Start, D F H
Numerical studies of high power ECRH in tokamaks F P Fr 57 2 76 76
Edlington, T; Ainsworth, N R; Alper, B; Atkinson, D; Blewett, S G F; ...
Fundamental and 2nd harmonic heating at the electron cyclotron resonance on cleo tokamak F P Fr 58 2 80 80
Airoldi, A; Cenacchi, G; Orefice, A; Ramponi, G
Electron cyclotron heating simulation in tokamaks by combined codes F P Fr 59 2 84 84
Pesic, S
Wave absorption near the second harmonic of the electron cyclotron frequency F P Fr 60 2 88 88
Consoli, T
Current drive and plasma heating by longitudinal ECR waves F P Fr 61 2 92 92
Giruzzi, G; Krivenski, V; Ziebell, L F
Electron cyclotron heating of a tokamak plasma at down shifted frequencies F P Fr 62 2 96 96
Soell, M; Noterdaeme, J-M
Optimisation of ICRH antennas based on coupling and absorption F P Tu 33 2 100 100
Itoh, S I; Itoh, K; Fukuyama, A; Nishikawa, K
Control of energy exchange rate by ICRF catalyst F P Tu 34 2 104 104
Adam, J; Equipe TFR
Comparison of two Kii antenna configurations for ICRH experiments in TFR F P Tu 35 2 108 108

VOLUME II

Saoutic, B; TFR Group
Influence of laser blow-off injected vanadium ions on the deuteron heating during ICRH in TFR F P Tu 36 2 112 112
Milovich, J L; Morales, G J; Fried, Burton
Effect of current drive in ICRF heating F P Tu 37 2 116 116
Hosea, J C; Bell, R; Bitter, M; Cavallo, A; Cohen, S; ...
Heating, confinement, and stability during high power ICRF experiments on PLT F O Tu 1450 2 120 M 120
Hellsten, T; Core, W; Hamnen, H; Appert, K; Succi, S
Effect of particle trapping in ICRF-Beam heated tokamak plasmas F P Tu 38 2 124 124
Grigor'eva, L I; Pashchenko, A V; Smerdov, B I; Checkin, V V
Simulation of plasma potential induction and particle transport during ICRF heating F P Tu 39 2 128 128
Longinov, A V; Pavlov, S S; Stepanov, K N
The use of heavy admixture ions for enhancing the ICRF plasma heating efficiency F P Tu 40 2 132
Shurygin, R V; Yushmanov, P N
Ion heat transfer under cyclotron heating in tokamak F P Tu 41 2 136 136
Cox, M; Dendy, R; Hamnen, H; Jacquinot, J; Lallia, P; ...
Fokker Planck calculations of ICRF current drive on JET F P Tu 42 2 140 140
Scharer, J; Jacquinot, J; Lallia, P; Sand, F
Fokker-Planck calculations for JET ICRF heating scenarios F P Tu 43 2 144 144
Bures, M; Evrard, M P; Jacquinot, J; Lallia, P P; Sand, F
Plasma-antenna coupling and the related scrape-off layer studies on JET F P Tu 44 2 148 148
Gambier, D J; Bartlett, D V; Bures, M; Campbell, D J; Cottrell, G A; ...
Electron power deposition profile durig ICRF heating on JET F P Tu 45 2 152 152
Alikaev, V V; Berezovskij, E L; Vasin, N A; Vdovin, V L; ...
ICRH experiments in T-10 tokamak F O Tu 1430 2 156 M 156
Alikaev, V V; Bagdasarov, A A; Berezovsky, E L; Buzankin, V V; ...
ICRF heating experiments on T-10 tokamak at the ion-ion hybrid resonance conditions F P Tu 46 2 160 160
Hoang, G T; Bottollier, H; Briand, P; Briffod, G; Chabert, P; ...
Bulk plasma heating with lower hybrid wawes in the PETULA-B tokamak F P Th 12 2 164 164
Girard, A; Melin, G; Agarici, G; Blanc, P; Bottollier, H; ...
Hot electron studies in PETULA-B discharges during LH wawe application F P Th 13 2 168 168
Parlange, F; Agarici, G; Blanc, P; Bottollier-Curtet, H; Briand, P; ...
Lower hybrid ion heating and current drive with one and two grills in PETULA B F O Th 1430 2 172 M 172
Wegrowe, J-G
On the RF current and the RF power absorption at finite levels of injected power in lower-hybrid current drive F P Th 14 2 176 176

Nocentini, A
Comparison between theory and experiments on lower hybrid current drive F P Th 15 2 180 180
Hoshino, K; Yamamoto, T; Suzuki, N; Uesugi, Y; Kawashima, H; ...
RF current drive (LHH+ECH) and electron heating experiments on JFT-2M tokamak F P Th 16 2 184 184
Pavlo, P; Klima, R
Computer simulation of lower hybrid current drive in T-7 tokamak F P Th 17 2 188 188
Stevens, J E; Bell, R; Bernabei, S; Cavallo, A; Chu, T K; ...
Lower hybrid experiments at 2.45 GHz on PLT F O Th 1450 2 192 M 192
Barbato, E; Bracco, G; Podda, S; Zanza, V
Simulation of neutral emission in the ion interaction regime during LH experiment in FT F P Th 18 2 196 196
Dnestrovskij, Yu N; Parail, V V; Kostomarov, D P; Luk'yanitsa, A A; ...
Toroidal and electrical field effects on current drive in tokamak by LH-waves and by ECR-waves F P Th 19 2 200 200
Stepanov, K N; Yegorenkov, V D
Current drive by nonuniform external forces F P Th 20 2 204 204
Belikov, V S; Kolesnichenko, Ya I; Plotnik, I S
Effect of the toroidal magnetic field on the current drive in tokamaks with travelling waves F P Th 21 2 208 208
Neudachin, S V; Parail, V V; Pereverzev, G V; Shurygin, R V
Influence of toroidal effects on the propagation of lower hybrid waves in plasma F P Th 22 2 212 212
Krasheninnikov, S I; Soboleva, T K
Current drive in tokamak-reactor due to RF-heating of alpha-particles F P Th 23 2 216 216
Cesario, R; Pericoli-Ridolfini, V
Parametric instabilties during the lower hybrid power injection in the high density regime of the FT tokamak F P Th 24 2 220 220
Yang, W H; Li, D F; Huo, Y P
Large angle scattering and LH current drive F P Th 25 2 224 224
Cardinali, A; Romanelli, F
Asymptotic analysis of lower hybrid waves propagation in tokamaks in the cold electrostatic approximation F P Th 26 2 228 228
Knowlton, S; McDermott, S; Porkolab, M; Takase, Y; Texter, S; ...
Lower hybrid current drive experiments on the MIT ALCATTOR C and VERSATOR II tokamaks F P Th 27 2 232 232
Gell, Y; Nakach, R
Ion tail formation by cascade trapping in lower-hybrid heating experiments F P Th 28 2 236 236
Leuterer, F; Eckhartt, D; Soeldner, F; Bartiromo, R; Becker, G; ...
Lower hybrid current drive in the ASDEX tokamak F P Th 29 2 240 240

VOLUME II

Soeldner, F; Eckhartt, D; Leuterer, F; Eberhagen, A; Guiliana, A; ...
Power absorption studies for lower hybrifd heating and current drive in ASDEX F O Tu 1520 2 244 M 244
Collins, G A; Joye, B; Lister, J B; Moret, J-M
A study of the density rise observed during AWH in TCA F P Tu 47 2 248 248
Huang, L; Qiu, X; Ding, N
Kinetic theory of Alfven wave heating in finite beta tokamak plasma F P Tu 48 2 252 252
Elfimov, A G
Double Alfven wave resonance - is the possible heating scheme of the large tokamak plasma F P Tu 49 2 256 256
Kirov, A G; Sidorov, V P; Lozovskij, S N; Elfimov, A G; Ruchko, L F; ...
RF power input in the tokamak reactor with Alfven heating F P Tu 50 2 260 260
de Chambrier, A; Collins, G A; Joye, B; Lietti, A; Lister, J B; ...
Strong electron and ion heating in clean connditions in TCA F O Fr 1130 2 264 M 264
Joye, B; Lister, J B; Marcus, F B; Nowak, S
Towards a better understanding of impurties in TCA F P Tu 51 2 268 268
de Kluiver, H; Yousef, N; de Groot, B; Barth, C J; van der Laan, H A; ...
Plasma heating in the TORTUR tokamak by low-frequency toroidal current pulses F P Tu 52 2 272 272
Cap, F F
Electromagnetic waves in toroidal anisotropic inhomogeneous plasmas F P Tu 53 2 276 276
Saito, K; Inaba, N; Osanai, Y; Nogi, Y; Shiina, S
Further heating of a high beta plasma by the compressional Alfven wawe F P Tu 54 2 280 280
Speth, E; Eberhagen, A; Gehre, O; Gernhardt, J; Janeschitz, G; ...
The effect of neutral beam deposition on heating and confinement in ASDEX F P Tu 55 2 284 284
Miley, G H; Sutton, W R; Sigmar, D J
Alpha-driven fast magnetosonic wave heating in tokamak plasmas F P Tu 56 2 288 288
Freisinger, J; Kaufmann, M; Kraus, W; Loeb, H W; Reuschling, R
The RF-neutral injector ion sources RIG F P Tu 57 2 292 292
Sund, R S; Scharer, J E; McVey, B D
Local power conservation for linear wave propagation in an inhomogeneus plasma F P Tu 58 2 296 296
Argenti, L; Cima, G; Cirant, S; De Luca, F; Jacchia, A; ...
Effects of ECW injection into the THOR tokamak plasma F P Tu 59 2 300 300
Katzenstein, J; Li, R; Rostoker, N
Injection and trapping of intense neutralized ion beams in closed magnetic configuration F P Tu 60 2 304 304
Hutter, T; Roubin, J P; TFR Group
Fast ions behaviour during N.B.I. in TFR from auxiliary modulated beam measurements F P Tu 61 2 308 308

VOLUME II

G - BASIC THEORY

Canobbio, E; Croci, R
The ponderomotive decay of LH waves as a means of filling the spectral gap and understanding the opacity of high-density...
G P Fr 63 2 314 314

Porcelli, F; Pegoraro, F
Asymptotic theory of fluid waves in relativistic plasmas
G P Fr 64 2 318 318

Pegoraro, F; Coppi, B; Detragiache, P
Magnetosonic normal modes in inhomogeneous toroidal plasmas
G P Fr 65 2 322 322

Shukla, P K; Spatschek, K H
Pseudo three-dimensional interchange-mode turbulence in magnetized plasmas
G P Fr 66 2 326 326

Nassri, A; Heindler, M
Analytical treatement of the absorption/emission coefficient for synchrotron radiation
G P Fr 67 2 330 330

Kraemer, M; Sollich, N; Dietrich, J
Mode conversion of lower hybrid waves
G P Fr 68 2 334 334

Sedlacek, Z; Jungwirth, K; Stavinoha, P; Breizman, B N
Strong Langmuir turbulence - computer simulations
G P Fr 69 2 338 338

Preinhaelter, J; Lacina, J; Omeltchenko, A Y
Initial stage of development of non-linear effects at oblique incidence of electromagnetic waves on an inhomogeneous plasma
G P Fr 70 2 342 342

Litvak, A G; Petrova, T A; Sergeev, A M; Yunakovsky, A D; ...
Self-interaction of plasma oscillations with anomalous dipersion
G P Fr 71 2 346 346

Petviashvili, V I
Alfven-drift mode vortices and transport in plasma after HF heating
G P Fr 72 2 350 350

Moroz, P E
On the cyclotron absorption of a fast-wave
G P Fr 73 2 351 351

Wang, Z
Stochastic instability in hot electron plasma
G P Fr 74 2 355 355

Furth, H P; Glasser, A H; Park, W; Rutherford, P; Selberg, H; ...
The q(0)<1 regime of the tokamak
G O Tu 1650 2 358 H 358

Thyagaraja, A; Haas, F A
Test-particle transport due to fluctuating magnetic fields in tokamaks
G P Tu 62 2 362 362

Schep, T J; Pegoraro, F
Linear theory and energy integral of resistive modes
G P Tu 63 2 366 366

Eggen, J B M M; Schuurman, W
Minimum energy principle for plasma relaxation to equlibria with pressure and temperature profiles
G P Tu 64 2 370 370

VOLUME II

Edenstrasser, J W; Schuurman, W
The F-theta-diagram and other characteristics of a variational principle for stationary, finite-beta plasma equilibria
6 P Tu 65 2 374 374

Minardi, E; Toschi, V
Metastable states in tokamaks 6 P Tu 66 2 378 378

van Houten, M A; Weenink, M P H; Schuurman, W
On the second variation of a minimum energy principle for a force free plasma with a free boundary 6 P Tu 67 2 382 382

Dubois, M; Samain, A
Ion kinetic energy production during fast reconnections
6 P Tu 68 2 386 386

Stacey, W M; Sigmar, D J
Toroidal momentum confinement of strongly rotating tokamak plasma
6 P Tu 69 2 390 390

Andersson, P; Weiland, J
Analytic theory of MHD ballooning modes
6 P Tu 70 2 394 394

Callen, J D; Qu, W X; Shaing, K C
Neoclassical MHD instabilities and transport in tokamaks
6 P Tu 71 2 397 397

Bishop, C M; Taylor, J B
A class of special toroidal MHD equilibria, including minimum-B
6 O Fr 1130 2 401 S 401

Karlson, E T
Constants of the motion for inhomogeneous plasma
6 P Tu 73 2 405 405

Parail, V V; Pogutse, O P; Voytsekhovich, I A
Departure of run-away electrons and the fan-like instability in tokamak 6 P Tu 74 2 409 409

Beklemishev, A D; Yurchenko, E I
Theory of dissipative ballooning modes in tokamak at a finite sound speed 6 P Tu 75 2 413 413

Besedin, N T; Pankratov, I M
On stability of runaway electrons 6 P Tu 76 2 417 417

Cheng, C Z; Chance, M S
A nonvariational MHD stability Code for Axysimmetric plasmas
6 P Tu 77 2 421 421

Boozer, A H
Canonical representation of magnetic fields
6 P Tu 78 2 425 425

Pan, C H; Ding, H C; Wu, L Q
Kinetic theory of ballooning-mode in collisional plasma
6 P Tu 79 2 429 429

Tsunematsu, T; Tokuda, S; Takeda, T
Stability of external kink mode of tokamak
6 P Tu 80 2 433 433

Tsypin, V S
Toroidal rotation effect on the collisional plasma transport in a tokamak 6 P Tu 81 2 437 437

Montvai, A
New representation of the plasma-magnetic field system in equilibrium
G P Tu 72 2 441 441

Arter, W; Edwards, D N
Dimensionality and MHD mode coupling studies of DITE
G.0 Fr 1210 2 442 S 442

Gee, S J; Taylor, J B
Dimension measurement of fluctuations in HBTX1A
G P Tu 82 2 446 446

Cote, A; Haynes, P; Howling, A; Morris, A W; Robinson, D C
Dimensionality of fluctuations in TOSCA and JET
G P Tu 83 2 450 450

Becker, G
Anomalous transport and unstable modes in neutral-beam-heated L and H plasmas of ASDEX G P Tu 84 2 454 454

H - PLASMA EDGE PHYSICS

Claassen, H A; Gerhauser, H
Impurity transport in the limiter shadow due to convection and cross-field diffusion H P Th 30 2 460 460

Gerhauser, H; Claassen, H A
A numerical study of plasma profiles in the limiter shadow region of a tokamak H P Th 31 2 464 464

Behnel, J
Plasma sheath transition in a magnetic field parallel to the wall
H P Th 32 2 468 468

Chodura, R
Electron energy flow in a collisional scrape-off plasma
H P Th 33 2 472 472

Neuhauser, J; Schneider, W; Wunderlich, R
Thermal instabilities on magnetic flux surfaces
H P Th 34 2 476 476

Braams, B J
Two-dimensional multispecies plasma transport modelling
H P Th 35 2 480 480

Simonini, R; Feneberg, W; Taroni, A
Two dimensional analytic and numerical models of the scrape-off layer of toroidal limiters H P Th 36 2 484 484

Igitkhanov, Yu L; Kukushkin, A S; Pistunovich, V I; Pozharov, V A
Improved hydrodynamic simulation of a divertor plasma under weak collisions H P Th 37 2 488 488

Nedospasov, A V; Petrov, V G
Thermal fluxes with plasma convection in the tokamak limiter scrape-off layer H P Th 38 2 492 492

Tokar', M Z
On izotope composition of plasma and gas in tokamak reactor divertor
H P Th 39 2 496 496

Krasheninnikov, S I; Kukushkin, A S; Pistunovich, V I; Pozharov, A V
Relaxational oscillations in the divertor plasma
H P Th 40 2 500 500

VOLUME II

Hugill, J
Effect of cross-field transport on the temperature in the scrape-off layer of a tokamak reactor - a critique of collisional...
H P Th 41 2 504 504

Johnson, P C; Edwards, D N; Fielding, S J; Harbour, P J; ...
Application to the DITE bundle divertor of models for plasma exhaust and neutral particles in the divertor
H P Th 42 2 508 508

Weiland, J; Mondt, J P
Nonlinear theory of thermal excitations in edge plasmas
H P Th 43 2 512 512

Alexander, K F; Hintze, W
Stationary particle balance in the edge region of a tokamak plasma: influence of a density dependent diffusion coefficient
H P Th 44 2 515 515

Nicolai, A; Reiter, D
Plasma transport and particle removal capability of the advanced pump limiter test facilities ALT I and ALT II
H P Th 45 2 519 519

Pospieszczyk, A; Bay, H L; Bogen, P; Rosbueldt, D; Samm, U; ...
Impurity fluxes in TEXTOR H P Th 46 2 523 523

Bogen, P; Hartwig, H; Hintz, E; Hothker, K; Lie, Y T; ...
Properties of the TEXTOR boundary layer
H P Th 47 2 527 527

Dippel, K H; Finken, K H; Thomas, G J; Pontau, A E; Campbell, G A; ...
Radial dependence and material effects with ALT-I pump limiter in TEXTOR H P Th 48 2 531 531

Morgan, P D; Corti, S; Ehrenberger, J; Forrest, M J; Gondhalekar, A; ...
Recycling, isotopic exchange and density behaviour in JET discharges
H P Th 49 2 535 535

Stamp, M F; Behringer, K H; Forrest, M J; Morgan, P D; Summers, H P
Impurity sources and impurity influxes in the JET tokamak
H P Th 50 2 539 539

Roth, J; Fussmann, G; Janeschitz, G; Verbeek, H; Wagner, F; ...
Impurity sources during Ohmic-heated discharges in ASDEX
H P Th 51 2 543 543

Bessenrodt-Weberpals, M; Hackmann, J; Uhlenbusch, J
On behaviour of beryllium impurities in the plasma edge region of the tokamak UNITOR H P Th 52 2 547 547

Laux, M; Grote, H; Herrmann, A; Hildebrandt, D; Pech, P; ...
Properties of the sol of T-10 investigated by a Langmuir double probe
H P Th 53 2 551 551

Ferro, C; Franconi, E; Maddaluno, G; Ciotti, M; Neri, A
Experimental observations on the FT limiters
H P Th 54 2 555 555

Lingertat, J; Alexander, K F; Grunow, Ch; Guenther, K; ...
Limiter termography and power balance studies in the T-10
H O Th 1730 2 559 M 559

Vertiporokh, A N; Evstigneev, S A; Ivanov, I V; Maksimov, Yu S; ...
Study of the plasma interaction with a limiter under Ohmic heating in T-10 H P Th 55 2 563 563

VOLUME II

Guenther, K; Grunow, C; Lingertat, J; Chicherov, V M; ...
Characteristics of scrape-off plasma interaction with the T-10 limiter studied by infrared thermography H P Th 56 2 567 567
Coad, J P; McCracken, G M; Erents, S K; Ehrenberg, J; de Kock, L; ...
Impurity fluxes in the boundary layer of JET H O Th 1650 2 571 H 571
Ehrenberg, J; Behrisch, R; Martinelli, P; Kukral, H; McCracken, G M; ...
Erosion and redeposition of wall and limiter material in JET H P Th 57 2 575 575
Stangeby, P C; Erents, S K; Tagle, J A; McCracken, G M; de Kock, L
Density, temperature and power measurements in the JET edge plasma using heat flux/Langmuir probes H P Th 58 2 579 579
ASDEX-team; Verbeek, H
Low energy neutral particle analysis in the ASDEX tokamak H P Th 59 2 583 583
Poschenrieder, W; Venus, G; Wang, Y G; Mueller, E R; Bartiromo, R; ...
Flux measurements with a Sniffer probe near the wall in ASDEX H P Th 75 2 587 587
Matthews, G F
Ion temperature measurements in DITE edge plasmas H P Th 60 2 591 591
Aumayr, F; Winter, H
Plasma edge diagnostics by means of lithium beam-activated charge exchange spectroscopy H P Th 61 2 595 595
Bychkov, S S; Ivanov, R S; Sergienko, G V; Stotsky, G J
Joint set-up of laser diagnostics for determination of plasma parameters H P Th 62 2 599 599
Vizkelethy, Gy; Mezey, G; Paszti, F; Manuaba, A; Fried, M; ...
Simultaneous deposition and erosion on special probes in T-10 tokamak H P Th 63 2 603 603
Hollenstein, Ch; Hofmann, F; Marcus, F B; Martin, Y; Simm, W
Wave studies in the scrape-off layer of TCA during Alfven wave heating H P Th 64 2 607 607
Sidorov, V P; Minenko, V P
Control of plasma impurities by means of external prces H P Th 65 2 611 611
Hildebrandt, D; Grote, H; Herrmann, A; Laux, M; Pech, P; ...
Edge plasma effects during RF heating in T-10 measured by active and passive probes H P Th 66 2 615 615
Hildebrandt, D; Grote, H; Herrmann, A; Laux, M; Pech, P; ...
Deposition probe measurements of impurities injected into a tokamak plasma H P Th 67 2 619 619
Martinelli, A P; Behrisch, R; Englert, W
Wall material deposition on the limiters of several European tokamaks H P Th 68 2 623 623
Schlueter, J; Graffmann, E; Koenen, L; Waelbroeck, F; Waidmann, G; ...
Influence of in-situ carbon deposition on the performance of TEXTOR H P Th 69 2 627 627
Berendeev, S A; Kagan, D N; Shpilrain, E E; Lebo, I G; Rozanov, V B; ...
Investigation of film protection ICF reactor first wall H P Th 70 2 631 631

VOLUME II

Pavlov, Yu D; Petrov, D P; Solnetsev, A M; Stefanovskij, A M; ...
The effective plasma charge in tokamak with the graphite wall and the graphite limiter (TM-G) H P Th 71 2 635 635

My, N T; Mezey, G; Pcgany, L; Manuaba, A; Kotai, E; ...
The effect of heavy ion bombardement induced damage on surface deformation and re-emission characteristics of aluminium..
H P Th 73 2 639 639

My, N T; Manuaba, A; Mezey, G; Paszti, F; Kotai, E; ...
Surface modification and gas re-emission behaviour on aluminium under quasi-simultaneous multiple energy helium bombardment
H P Th 74 2 642 642

I - OTHER RELATED TOPICS

Andersen, V
Injection of solid deuterium pellets as diagnostic tool
I P Mo 69 2 648 648

Sorensen, H; Andersen, S A; Nordskov Nielsen, A; Sass, B; ...
D-2 pellet injector work at Riso I P Mo 70 2 652 652

Chang, C T; Thomsen, K
Scaling law of the pellet ablation rate
I P Mo 71 2 656 656

Lalousis, P; Lengyel, L
Pellet ablation in high-temperature plasmas with allowance for magnetic confinement effects I P Mo 72 2 660 660

Lehner, T; Gresillon, D; Zou, X L; De Gentile, B
Plasma scattered light depolarization by magnetic field fluctuations
I P Mo 73 2 664 664

Sunka, P; Babicky, V; Bohacek, V; Clupek, M; Kolacek, K; ...
Controlled REB energy deposition in an inhomogeneous plasma
I P Mo 74 2 668 668

J - LATE PAPERS

Schmidt, G L; Milora, S L; Bell, M G; Bitter, M; Bush, C E; ...
Production of high density plasma by pellet injection in TFTR
J O Mo 1700 2 674 M 674

Eckhartt, D; Leuterer, F; Soeldner, F; Eberhagen, A; Guiliana, A; ...
Lower hybrid heating effects in the ASDEX tokamak
J P Th 76 2 678 678

Baratov, D G; Vasiliev, A A; Demyanenko, V N; Demyanenko, L E; ...
Peripheral plasma behaviour and limiter erosion studies in T-3M tokamak J P Th 77 2 682 682

Labaune, C; Fabre, E; Briand, F; Baldis, H
Experimental study of stimulated Raman scattering in laser-plasma interaction at 0.26 micrometer J P Th 78 2 686 686

De Angelis, R; Tonini, G
Behaviour of recycling and impurity radiation during LH heating in FT dischargess J P Th 79 2 690 690

Pavlenko, V N; Panchenko, V G; Revenchuk, S M
Turbulent conductivity of a magnetized plasma
J P Fr 75 2 694 694

Barbato, E; Giannella, R
Simulation of the plasma response to modulated power in lower hybrid electron heating experiments J P Th 80 2 698 698
Fujita, J; Watari, T; Toi, K; Amano, T; Ando, R; ...
High power ICRF heating in JIPP T-IIU tokamak J P Tu 86 2 702 702
Alabyad, A; Almagri, A; Letuchii, A; Mabruk, E; Nagornii, A; ...
Investigation of disruptive instability on tokamak LIBTOR J P Fr 76 2 706 706
Navarro, A P; Aguilar, M; Romero, E; TJ-I Group
Fluctuation studies in the TJ-I tokamak J P Fr 77 2 710 710
Bulanin, V V; Esipov, L A; Korneev, D O; Stepanov, A Yu; ...
Observation of small-scale turbulence in the "FT-2" tokamak via CO2 laser scattering J P Fr 78 2 714 714
Berk, H L; Friedberg, J P; Llobet, X; Morrison, P J; Rosenbluth, M N; ...
Toroidal equilibrium and stability for steep pressure profile stellarators J P Mo 75 2 718 718
Egorov, S M; Kuteev, B V; Sergeev, V Yu
Study of T-10 tokamak plasma by low-Z impurity pellet injection J P Th 81 2 721 721

Author index 725

A

tokamaks

ENERGY CONFINEMENT EXPERIMENTS ON DOUBLET III WITH HIGH POWER NEUTRAL BEAM HEATING†

J.C. DeBoo, R.J. Groebner,
Doublet III Physics, Operations, and Neutral Beam Groups

GA Technologies Inc.
P.O. Box 85608, San Diego, CA 92138, U.S.A.

Energy confinement experiments with up to 8 MW of both hydrogen and deuterium neutral beam power were performed in deuterium plasmas with limiter and expanded boundary divertor configurations. The results of NBI-dominated experiments indicated that total stored energy W_T and energy confinement time τ_E had little or no variation with electron density $\bar{n}_e$ and toroidal field B_T and scaled linearly with plasma current I_p. Previous studies in limiter discharges indicated a weak dependence on plasma elongation κ. The confinement time dependence on elongation was not determined for divertor discharges, but assuming a dependence similar to that for limiter discharges both limiter and divertor data were consistent with W_T and τ_E proportional to $I_p\sqrt{\kappa}$. The variation of plasma stored energy with neutral beam power was consistent with a linear relationship. The linear equation describing this relationship had a non-zero intercept which illustrated the fact that energy confinement time deteriorated with neutral beam power. The energy confinement time appears to be approaching an asymptotic value at high power, consistent with a linear functional form for stored energy. However, a power law functional form for stored energy and energy confinement time can not be ruled out. We found several magnetic configurations and conditions that exhibited improved energy confinement as compared to confinement in hydrogen beam heated discharges limited toward the outside of the vacuum vessel [1]. Operation in a divertor configuration yielded superior energy confinement as compared to a limiter configuration and deuterium beam heating resulted in better energy confinement than hydrogen beam heating. Also, discharges limited toward the inside exhibited an improvement of energy confinement relative to those limited toward the outside. These different cases can be arranged in order of highest to lowest normalized energy confinement time, $\tau_E^* \equiv \tau_E/I_p\sqrt{\kappa}$: (1) D° heated divertor; (2) D° heated inside limiter; (3) H° heated divertor; (4) D° heated outside limiter and H° heated inside limiter were comparable; (5) H° heated outside limiter; and the values of τ_E^* were in the approximate ratio 2.0:1.8:1.6:1.4:1.0, respectively, for beam powers of 6 – 7 MW.

The power dependence of τ_E^* is shown in Fig. 1 for H° beam heated discharges limited on the outside primary limiter and for divertor discharges. The trend of τ_E diminishing with additional heating power does not appear to be specifically related to neutral beam heating as 1 MW ECH heating experiments on DIII displayed a similar trend [2,3]. The power dependence of normalized plasma stored energy, $W_T^* \equiv W_T/\ I_p\sqrt{\kappa}$, is consistent with the functional form $W_T^* = a + bP_T$ (see Fig. 2). This implies $\tau_E^* = b + a/P_T$. A least squares fit of the limiter data in Fig. 1 to this functional form yields $a = 0.061 \pm 0.005$ and $b = 0.022$

†Supported by U.S. Department of Energy Contract DE-AT03-84ER51044.

$\pm$ 0.002 where τ_E (s), I_p (MA), and total absorbed ohmic plus beam power P_T (MW). Note that at $P_T = 6$ MW, the power dependent term is only one third of the total confinement value and becomes insignificant at higher powers, indicating that τ_E^* is approaching a new constant value characteristic of high power NBI heating. The normalized confinement time is about 60% larger for divertor discharges for $P_T = 6-7$ MW. Also shown in Fig. 1 is the curve obtained by performing a least squares fit of the divertor data to the functional form $\tau_E^* = b + a/P_T$ which gives $a = 0.059 \pm 0.011$ and $b = 0.044 \pm 0.003$. The fit value that τ_E^* approaches at sufficiently large power is twice as large in divertor discharges as compared to limiter discharges. A power law functional form, $\tau_E^* = cP_T^{-\alpha}$, will also fit the divertor and limiter data where $c = 0.097 \pm 0.006$ (0.074 ± 0.002) and $\alpha = 0.35 \pm 0.03$ (0.49 ± 0.02) for divertor (limiter) data.

Confinement experiments employing deuterium neutral beams, operated at the same energy as the hydrogen beams, have shown a 25% to 40% improvement in plasma heating efficiency in both limiter and divertor configurations. The slope of the D° data for outside limited discharges is about 70% larger than that for H°, indicating a significant improvement in the incremental heating $\Delta W_T^*/\Delta P_T$ with deuterium beams. These trends are illustrated by the outside limited discharge data displayed in Fig. 2a and 2b. The values of τ_E^* are 1.3 to 1.4 times larger at $P_T = 6-7$ MW for D° beam heated outside limited discharges. When scaling $\tau_E^* = b + a/P_T$ as discussed earlier, note that $\Delta W_T^*/\Delta P_T = b$, the value that τ_E^* approaches at sufficiently large power.

An improvement in normalized energy confinement is also observed for limiter discharges shifted radially inward and limited on three neutral beam armor plates located on the inner wall of the vacuum vessel. This movement requires a major radius shift of 5% or less ($\leq$ 7 cm), making it unlikely that the improvement in confinement is due to a dependence on major radius. A comparison of inside and outside limited discharges is shown in Fig. 2a for H° beam heating and in Fig. 2b for D° beam heating. The H° beam heating cases indicate an average improvement in W_T^* of about 40% at high power. A comparison of data trends from inside and outside limiter discharges indicates an improvement in incremental heating $\Delta W_T^*/\Delta P_T$ of about 40%. For D° beam heating the average improvement in τ_E^* is ~25% at high powers for inside as compared to outside limited discharges. Comparison of Fig. 2a and 2b indicates that W_T^* and τ_E^* in inside limited H° heated discharges are similar to values obtained in outside limited D° heated discharges. It is also interesting to note that at beam powers above 6 MW inside limited D° heated discharges exhibit τ_E^* values similar to those in H° heated divertor discharges, $\tau_E^* = 0.057$ and 0.051 respectively. A comparison of τ_E^* values for the different plasma configurations and neutral beam species employed in our confinement experiments is displayed in Table I for $P_T = 6-7$ MW.

Generally, the dominant power loss mechanism in our NBI-heated discharges was thermal conduction for both electrons and ions for $r/a \leq 0.8$. The fraction of beam power deposited in each species was conducted away by the same species, usually with little transfer of power between species. Spatially-resolved measurements of the ion temperature profile were coupled with transport analysis to obtain spatial profiles of the ion thermal conductivity κ_i^{exp} for a series of H° beam heated, expanded boundary divertor discharges [4]. The experimentally inferred values of κ_i^{exp} were compared with the neoclassical values of the ion thermal conductivity κ_i^{neo}, obtained from Chang-Hinton [5] with account taken of the noncircular plasma shapes and the presence of an oxygen impurity in

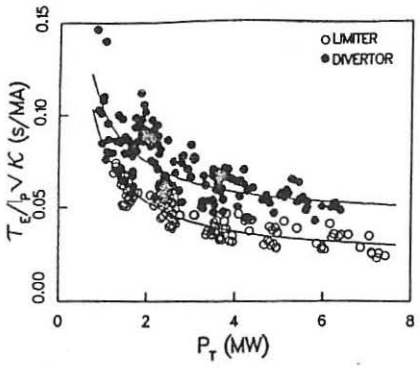

FIG. 1. Normalized energy confinement time variation with power for H° beam heated divertor and outside limiter discharges.

TABLE I
NORMALIZED CONFINEMENT TIMES τ_E^* (s/MA) FOR P_T = 6–7 MW

Beam Species	Outside Limiter	Inside Limiter	Divertor
H°	0.032	0.046	0.051
D°	0.046	0.057	0.065

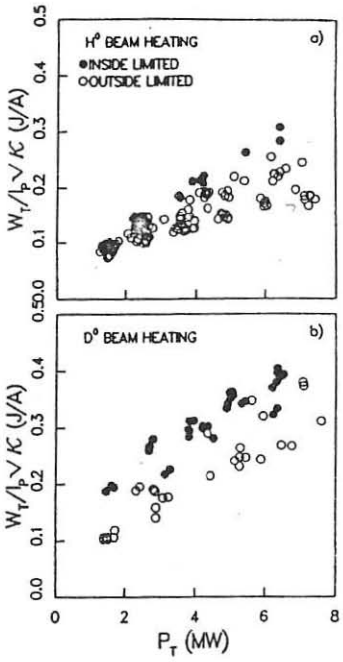

FIG. 2. Normalized stored energy for inside and outside limited discharges with (a) hydrogen and (b) deuterium beam heating.

the plasma. No modeling of sawtooth transport was incorporated into this analysis, but all of the discharges analyzed exhibited sufficiently long sawtooth periods that the plasma reached a nearly steady state before each sawtooth disruption. For the parameter range $B_T = 2.53$ T, $I_p = 350 - 900$ kA, vertical elongation 1.4 to 1.9, $\bar{n}_e = 3.7 - 7.9 \times 10^{19}\mathrm{m}^{-3}$, and $P_T = 3.5 - 6.6$ MW, the ion collisionality was in the banana-plateau transition regime, $\nu_{i^*} = 0.02 - 0.19$ for $0.2 \leq r/a \leq 0.7$. $T_i(r)$ profiles were obtained from Doppler broadening of the He II 4686 Å line, produced by charge transfer between the hydrogen atoms in one of the heating beams and fully ionized helium in the plasma. For densities above 5.7×10^{19} m^{-3}, T_i and T_e profiles were very similar.

A comparison of κ_i^{exp} and κ_i^{neo} is shown in Fig. 3 for one of the cases studied. The conclusions are the same for all cases examined: κ_i^{exp} is consistent with neoclassical theory near the plasma center but for $0.2 \leq r/a \leq 0.7$ the observed ion heat conduction losses are larger than can be explained by present neoclassical theory alone. We find after careful error analysis that the error bars on the measured and theoretical values for the ion thermal conductivity do not overlap.

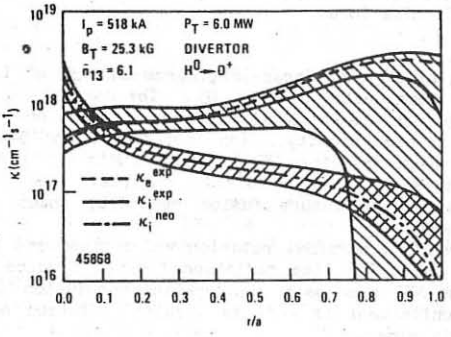

FIG. 3. Comparison of experimental and theoretical values of ion thermal conductivity. The cross-hatched areas show the error bands due to uncertainties in the experimental data. For clarity, the error band for κ_e is not shown.

REFERENCES

[1] DEBOO, J.C., et al., GA Technologies Report GA-A17805 (1985), submitted to Nuclear Fusion.

[2] EJIMA, et al., Bull. Am. Phys. Soc. **29**, (1984) 1427.

[3] BURRELL, K.H., et al., in Plasma Physics and Controlled Nuclear Fusion Research 1984 (Proceedings of the Tenth International Conference, London, 1984) Vol. I, IAEA, Vienna (1985) 131.

[4] GROEBNER, R.J., et al., GA Technologies Report GA-A17935 (1985), submitted to Nuclear Fusion.

[5] CHANG, C.J. and HINTON, F.L., Phys. Fluids **25** (1982) 1493.

Ion Energy Confinement Properties in High Power Beam Heated Plasmas in Doublet III

M.Abe*, T.Hirayama, A.Kitsunezaki, A.Kameari**, S.Konoshima, M.Nagami, M.Shimada, S.Sengoku, T.Yamamoto, M.Washizu***, Japan Atomic Energy Research Institute, Naka, Ibaraki, Japan, and T.Angel, K.Burrell, R.Groebner, D.Schissel, and the Doublet III Group, GA Technologies Inc., San Diego, CA, USA

* On leave from Hitachi, Ltd.,
** On leave from Mitsubishi Atomic Power Industries Inc.
*** On leave from Toshiba Corp.

1. INTRODUCTION

The last phase of a joint Japan-US program on Doublet III was intended for study of high power beam heated plasmas [1]. The one of the objectives for the JAERI team was to achieve a high pressure plasma or to achieve a high temperature plasma at high density. Ion temperatures of 5-6 keV were attained with 7.6MW neutral beam injected (NBI) plasmas with divertor configulation at the electron densities of $\bar{n}_e$=6-7 x $10^{19}m^{-3}$ [1] (ie. the H-mode [2]).These are the closest plasma to the future fusion reactors, which have been obtained experimentally to date.

Ion temperatures and toroidal rotation velocities were measured by Doppler spectroscopy using the OVIII line radiation (2976Å) produce by charge-exchange recombination on the NBI beam path with spatial resolution [3]. Based on these data, ion energy confinement as well as toroidal-rotation momentum confinement are discussed on this paper.

2. GENERAL OBSERVATIONS

Major plasma and device parameters of Doublet III are summarized in Table 1. Neutral beams(NB) were injected at an angle of 27 degrees on the magnetic axis in co-direction of plasma current. This results in the increase of the toroidal plasma rotation.

The plasma stored energy starts to increase with injection of the NB and saturates in 50-200ms, which depends on the energy confinement time of the plasma. The data which are used in this paper are sampled after this saturation or during the steady stage of the discharge

The toroidal rotation velocities V_ϕ of the plasma increase from the beginning of NBI, and saturates with H_α /D_α bursts. The increment of T_i slows down after the on-set of H_α /D_α bursts. The neutron yields F due to thermal fusion (D(d,n)He) rise with NBI in the same manner as the ion temperature. The maximum values of Ti,V_ϕ and F obtained are 6.0 keV, 2 x 10^5 m/s and 7.1 x 10^{13} n/s, respectively, at the density of $\bar{n}_e$=5.5-7 x 10^{19} m^{-3} with hydrogen(H^0) NB and deuterium plasma.

TABLE 1. PARAMETERS OF DOUBLET III

PARAMETER	VALUE
PLASMA CURRENT I_p	250-1000 kA
DENSITY $\bar{n}_e$	2-10x$10^{19}m^{-3}$
TOROIDAL FIELD B_t	1.0-2.7 T
WORKING GAS	D_2
MAJOR RADIUS	1.42 m
MINOR RADIUS a	0.42 m
NBI POWER	$\lesssim$7.6 MW
INJECTED NEUTRAL	H^0 and D^0
NBI BEAM VOLTAGE	$\sim$ 75 keV

3. EFFECT OF EDGE CONFINEMENT PROPERTY

Fig. 1 shows $T_i(0)$ and $V_\phi(0)$ vs. heating power P_{abs} at plasma current of I_p=700-840kA and $_{NB}$ density of $\bar{n}_e$=6.0-7.5 x 10^{13}, here P_{abs} is the absorbed power by plasma from NB. Both $T_i(0)$ and $V_\phi(0)$ increased in factor of about 2 in the H-mode discharges. T_i increases linearly with P_{abs} in the H-mode, and has much weaker dependence on P_{abs} in the L-mode [4]. $V_\phi(0)$ of both H and L-modes are proportional to P_{abs}^{NB}. The H-mode appears in the power region of about

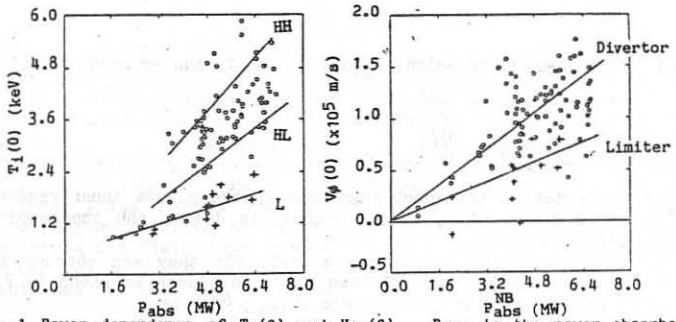

Fig. 1 Power dependence of $T_i(0)$ and $V\phi$ (0). P_{abs} is the power absorbed by plasma including ohmic heating power and P_{abs}^{NB} is the absorbed power from neutral beam. (a) $T_i(0)$ vs. P_{abs}, (b) $V\phi$ (0) vs. P_{abs}^{NB}. (o:divertor discharge, +:limiter discharge, B_t=2.1-2.7T, I_p=700-840 kA, $\bar{n}_e$=5.5- 7.5 x $10^{19}m^{-3}$)

$P_{abs} > 3.0$MW judging from $T_i(0)$, as ref [5]. $T_i(0)$ is in the range of 3 - 6keV and $V\phi$ is 8 x 10^4 -1.7 x 10^5 m/s at P_{abs}=5MW in divertor discharges. We disignate very high $T_i(0)$ H-mode discharges as HH-mode discharges and low $T_i(0)$ as HL-mode discharges, as shown in Fig. 1(a). The question is how the differences between the H and L-modes, and between the HH and HL-modes are generated.

Fig. 2 shows the radial distribution of T_i and $V\phi$ in the plasma for HH-,HL- and L-modes. The plasma center is R=1.42m and ψ_s is the separatrix position. These profile data are taken by a shot-by-shot process. The important point is that the H-mode have the rather higher edge values $T_i(a)$, $V\phi$ (a) and they are larger in better confined plasmas, where a is the plasma minor radius. This is the same tendency as the edge electron temperature [4,6]. The difference of $T_i(0)$ between HH- and HL-mode is due to the edge region. The difference of $T_i(0)$ is the same value as for the difference of T_i at R=1.72m. Comparing the HL-mode with the L-mode, the former has a high edge temperature and dT_i/dr is 50% larger. Since the central electron temperature of the L-and HL-mode in Fig.2 increases from 1.5keV to 3keV, the ion heating power from the NB is expected to increase about 50% in the HL-mode. The larger dT_i/dr in the H-mode is the result of the high ion heating power due to the high electron temperature. These argument indicate that the ion energy transport mechanism itself in the core plasma does not differ in these three discharge mode[7,8].

The toroidal rotation velocity shows the similer behavier to T_i. The well confined discharge has a high edge rotation velocity. $dV\phi/dr$ is almost same in these three modes.

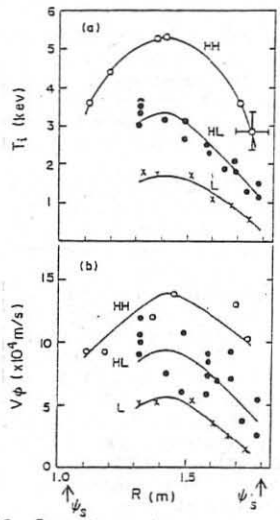

Fig. 2 Ion temperature and toroidal rotation velocity distribution along the minor radius, comparing good and poor confinment discharges. (a) Ion temperature, (b) toroidal rotation velocity. (I_p=770-820kA, B_t=2.6T Pinj=5.8-6.3MW, o:divertor, $\bar{n}_e$=5.2-5.8x$10^{19}m^{-3}$, ●:divertor, $\bar{n}_e$=6.5x$10^{19}m^{-3}$, x :limiter $\bar{n}_e$=6.5-6.7 x $10^{19}m^{-3}$)

Based on the above discussion, $T_i(0)$ and $V\phi$ (0) can be written as,

$$T_i(0) = \varepsilon_{1a} \left.\frac{dT_i}{dr}\right|_{r=0.5a} + T_i(a)$$

$$V\phi(0) = \varepsilon_{2a} \left.\frac{dV\phi}{dr}\right|_{r=0.5a} + V\phi(a) \qquad \ldots\ldots(1)$$

The first term is due to transport phenomena in the plasma inner region and the second term, which appears only in the H-mode, is due to the improvement of the edge plasma confinement.

$\bar{n}_e$ and I_p dependencies are also examined, but they are obscure in the H-mode. The H-mode discharge needs certain power to appear as shown in Fig. 1 [5]. The scaling we get in the high power range ($P_{abs} \geq 5MW$) is,

$$\begin{aligned} Ti(0) &\propto P_{abs} \cdot n_e^{\alpha} \cdot I_p^{\beta} \\ \tau\phi &\propto n_e^{\gamma}, \end{aligned} \qquad \ldots\ldots(2)$$

where $\tau\phi$ is the momentum confinement time defined as $V\phi(0) \cdot \bar{n}_e / P_{abs}^{NB}$, $\alpha = -1.0$ for the L-mode, -0.5 for the H-mode, $\beta = 0.5$-1.0 and $\gamma = -0.5$--1.0 for both modes. The $\bar{n}_e$ dependence of $\tau\phi$ obtained here disagrees with earlier reseach in other machines, which have the positive $\bar{n}_e$ dependence of $\gamma = 0$-1.0 [9, 10, 11].

Assuming T_i and $\tau\phi$ are the function of $\bar{n}_e$ and taking account of that $T_i(0)$ and $V\phi(0)$ in the H-mode is as twice as higher than those in the L-mode, $dT_i/d\bar{n}_e$ and $d\tau\phi/d\bar{n}_e$ in the H-mode are approximately the same as those in the L-mode. This suggest that the first term of the equation(1) is due to the inner plasma transport and has the $\bar{n}_e$ dependence, but the second term added to the H-mode might have no $\bar{n}_e$ dependence.

4. EFFECT OF $H\alpha/D\alpha$ BURST ON T_i and $V\phi$

$H\alpha/D\alpha$ bursts normally cause a $V\phi$ saturation. However in some shot rapid decrease of $V\phi(0)$ was observed. One such discharge is shown in Fig. 3, which shows temporal evolution of plasma current (I_p), stored energy (W_{st}), soft X-ray intensity from the plasma center and edge (SX_c, SX_e), edge recycling light intensity ($H\alpha/D\alpha$) T_i and $V\phi$. The measured points of T_i and $V\phi$ are R=1.59, 1.67, 1.74m in one shot [12]. The plasma parameters are I_p=785kA, $\bar{n}_e$= 5.8 x $10^{19}\,m^{-3}$, B_t=2.5T and P_{inj}=6.7MW, in which 2.4MW injection is for deuterium neutral beam.

The $H\alpha/D\alpha$ bursts start at 0.76s, and $V\phi$ at R=1.59m starts to decrease at 0.81s, while the $V\phi$ in the outer region of the plasma is still slowly increasing. $V\phi$ values of R=1.67, 1.74m start to decrease from 0.87s and 0.9s,

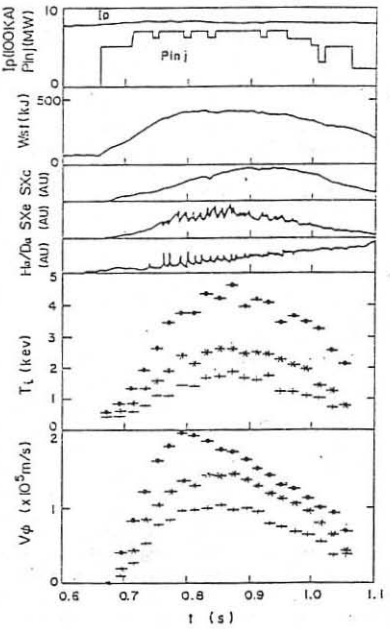

Fig. 3 Temporal evolution of T_i and $V\phi$. The plasma parameters of this discharge are $\bar{n}_e$=5.8 x $10^{19}m^{-3}$, I_p=785kA, B_t=2.5T, and one-third of the neutral beam power is due to the deuterium neutral beam. (◆:R=1.59m, ×:R=1.67m, +:R=1.74m)

respectively. The ion temperatures at these 3 points kept almost constant values from 0.8s to 0.9s and these are the same tendency as the $V\phi$ at plasma edge(R=1.74m). This suggests that the mechanisms of transport in the plasma for the the toroidal rotation momentum is different from the transport for the ion energy.

When the intensity of $H\alpha/D\alpha$ shows a gradual increase, at time of 0.8-0.9s, the SX_e stops increasing, and SX_c keeps rising. These facts suggest that the $H\alpha/D\alpha$ burst is a trigger to cool the plasma edge region relative to the center, which might enhance the momentum diffusion across the field line, however the start of the $V\phi$ decrease is delayed in the outer region (such as R=1.67, 1.74m) indicates that the edge momentum confinement does not deteriorate so much.

5. SUMMARY

Confinement properties of ion energy and plasma toroidal rotation momentum were discussed using the ion temperature and rotation velocity data obtained by the spacially resolved Doppler spectroscopy using the OVIII line radiation (2976Å) produced by charge transfer reaction between O^{8+} in the plasma and H^0 in the neutral beam. In the H-mode, the ion energy and momentum confinements are improved in the plasma edge region. Since the central ion temperature $T_i(0)$ and the central toroidal rotation speed $V\phi(0)$ are the functions of the edge value, which appears in the H-mode, and the inner transport term, the scaling of $T_i(0)$ and $V\phi(0)$ in the H-mode are different from that in the L-mode. However the transport mechanism in the core plasma for ion energy and toroidal rotation momentum of the H-mode discharge seems to be similer to those of the L-mode respectively.

ACKNOLEDGEMENT

The authors would like to thank Drs. S. Mori and M.Yoshikawa for their continuous encouragement throughout this work. The authors would also like to thank T.Ohkawa and the staffs of GA Thechnologies Inc. for their supports.

This work was performed under a cooperative agreement between the Japan Atomic Energy Resarch Institute and the united States Department of Energy under DOE Contract No. SE-AT03-80SF11512.

References

[1] KITSUNEZAKI,A., et al., in Plasma Physics and Controlled Nuclear Fusion Research (Proc. 10th Int. Conf. London, 1984), Vol. 1, IIAEA, Vienna (1985) 57.
[2] WAGNER,F., et al., in Plasma Physics and controlled Nuclear Fusion Research (Proc. 9th Int. Conf. Baltimore, 1982), Vol. 1, IAEA, Vienna (1983) 27.
[3] GROEBNER,R.J., et al., Appl. Phys. Lett. 43 (1983) 920
[4] NAGAMI,M., et al. Nucl. Fusion Vol. 24 (1984) 183.
[5] YOKOMIZO,H., et al. J.J.A.P. Vol. 23 (1984) L316.
[6] MCGUIRE,M., et al., in Plasma Physics and Controlled Nuclear Fusion Research (Proc. 10th Int. Conf. London, 1984), Volg. 1, IAEA, Vienna (1985) 117.
[7] KASAI,M., et al., to be published in Nucl. Fusion.
[8] ABE,M., et al., to be published in Nucl. Fusion.
[9] MURAKAMI,M., et al., in Plasma Physics and Controlled Nuclear Fusion Research (Proc. 10th Int. Conf. London, 1984), Vol. 1, IAEA, Vienna(1985) 87.
[10] BRAU,K., et al., Nucl. Fusion 23 (1983) 1643
[11] SUCHKEWER, S., et al., Nucl. Fusion 21 (1981) 1301.
[12] SERAYDARIAN,R., et al., GA-A 17953 (1985).

RADIATED POWER LOSS BEHAVIOUR IN THE TJ-1 TOKAMAK

B. Zurro, C. Pardo, J.A. Cabrera, J.R. Cepero and TJ-1 Group.
División de Fusión, Junta de Energía Nuclear, 28040 Madrid. Spain.

Empirical studies of radiation loss behaviour in ohmically heated discharges of the TJ-1 tokamak are presented. This small device (R = 30 cm, a = 10 cm) is operated at a toroidal field of 1T, plasma current lower than 65 KA and line average density below 4 x 10^{13} cm^{-3}.

Radiated power has been studied under different operational conditions. It has been compared with the time evolution within discharges of Z_{eff} deduced from Thomson scattering profiles and spectroscopic data. Time evolution of radiated power has been analyzed during a sudden perturbation produced by laser flash desorption from the wall.

Total radiated power is monitored in TJ-1 with a well collimated pyroelectric detector looking through a central chord and an uncollimated bolometer based on quartz radioluminescence(1). Both detectors show similar signatures in puffed and unpuffed discharges, Fig. 1. Excluding the start-up phase they respond with good proporcionality for a wide range of plasma conditions. Total radiated power is 40-50% of the ohmic heating power.

Radiated power per electron ($P_R/\bar{n}_e$) versus line averaged density, measured by a 2 mm microwave interferometer, is shown in Fig. 2. An improvement in cleanliness when density increases is evident from these data. Plotted points correspond to a fixed time in discharges with similar values of plasma currents (42 $\pm$ 3KA). A monotonous and slight increase in $P_R/\bar{n}_e$ along a sequence of reproducible discharges is seen during a day. Its comparison with line emission of impurities, followed by spectroscopic techniques, allows us to con-

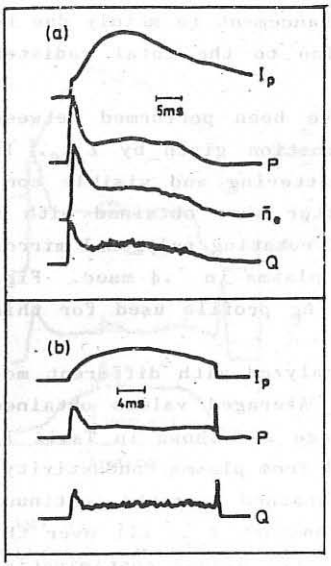

Fig. 1. Signatures of pyroelectric (P) and quartz (Q) bolometers in typical TJ-1 discharges without (a) and with (b) puffing.

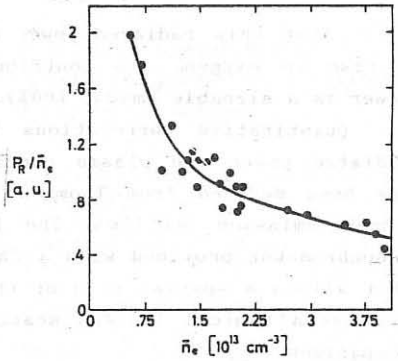

Fig. 2. Behaviour of radiated power per electron versus line averaged density.

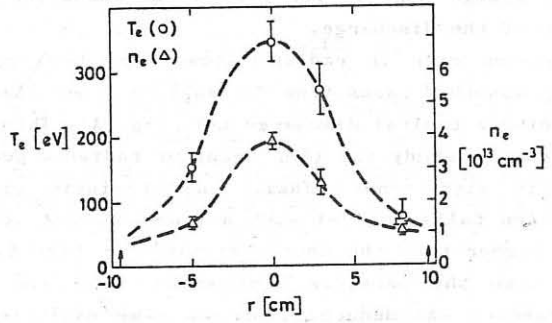

Fig. 3. Electron temperature and density profiles at 7 ms, measured by Thomson scattering.

clude that this radiated power enhancement is mainly due to a rise in oxygen. Its contribution to the total radiated power is a sizeable amount (60%).

Quantitative correlations have been performed between radiated power and plasma contamination given by Z_{eff}. It has been deduced from Thomson scattering and visible continuum emission profiles. The latter were obtained with a monochromator provided with a fast rotating polygonal mirror that allows a spatial scan of the plasma in .4 msec. Fig. 3 shows a typical Thomson scattering profile used for this comparison.

Experimental profiles were analyzed with different models to obtain Z_{eff} and $Z_{eff}(r)$. Averaged values obtained for several times along a discharge are shown in Table I. First and second rows were deduced from plasma conductivity, by choosing a radial dependence obtained from the continuum profile (Z_C^B) and by assuming a constant Z_{eff} all over tha plasma cross-section (Z_C^{TS}). A relative plasma contamination deduced from the total radiated power, proportional to $P_R/\tilde{n}_e$, is also included in this table. Good agreement is found among these results. From these comparisons we can conclude that, at least for the TJ-1 tokamak, $P_R/\tilde{n}_e$ is a good and simple monitor for plasma contamination along the hot phase of the discharge.

A sudden rise in radiated power has been produced by releasing adsorbed gases from the wall by laser flash desorption, during a typical discharge (see Fig. 4). This perturbation allows to study the time decay of radiated power and to compare it with other plasma characteristic times. This perturbation falls in TJ-1 with a time constant of .4 msec. that is higher that the energy confinement time (.2 ms) and smaller that the particle confinement time (.8 ms). This last parameter was deduced from the time evolution of a CV line during the perturbation which has been simulated with a transport code (2).

These studies were performed in hydrogen discharges but we will extend them to deuterium and helium.

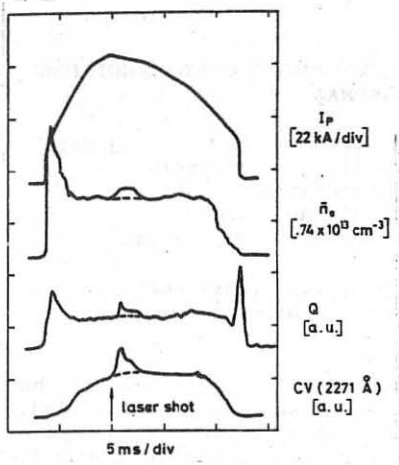

Fig. 4. Time evolution of different monitors during a laser desorption experiment. Dashed lines correspond to unperturbed discharge.

TABLE I. Comparison of Z_{eff} and radiated power per electron for a dirty discharge.

Zeff \ t(ms)	5	7	13
Z_C^B	4.4	3.9	2.3
Z_C^{TS}	4.6	4.5	1.5
$P_r/\bar{n}_e$	4.4	3.9	2

REFERENCES

(1) B. Zurro, C. Pardo, J.L. Alvarez-Rivas and TJ-1 group. Bull. Am. Phys. Soc. 29, 8, 1191 (1984).

(2) G. Navas and B. Zurro "Analysis tools for spectroscopic data in TJ-1 tokamak". Report JEN-519 (1982).

THE RADIATED POWER PROFILE UNDER WIDE-RANGING OHMIC CONDITIONS IN THE TCA TOKAMAK

B. Joye, J.B. Lister, Ph. Marmillod, J.-M. Moret, S. Nowak+
Centre de Recherches en Physique des Plasmas
Association Euratom - Confédération Suisse
Ecole Polytechnique Fédérale de Lausanne
21, Av. des Bains, CH-1007 Lausanne / Switzerland

+ University of Fribourg, Physics Departement
Pérolles, CH-1700 Fribourg / Switzerland

Introduction

A multichannel radiation bolometer with 16 detectors [1] has recently been commissioned on the TCA tokamak (R,a = .6,.18m).A pinhole camera design allows the simultaneous view of 16 spatial chords covering an entire vertical plasma cross-section. The radiated power profile of a tokamak pulse (100 ms flat-top) can be obtained with a time resolution of about 1 msec. The detection limit corresponds to about 10 mW/cm^3 after Abel-inversion.

A detailed study of the radiated power profile has been carried out for ohmically heated discharges. Experiments were performed using density and current programming with n_{eo} = (0.15 - 1.05)·10^{14} cm^{-3} and I_p = 20 - 125 kA at three different magnetic fields (0.78 T, 1.16 T, 1.51 T) thus covering the entire operation range of the TCA tokamak for q_a > 3. In all of the conditions the density was increased until the disruption limit was met. All of the parameters were measured at the time of the Thomson T_{eo} measurement. Combining the radiated power profile with the data from an 8-channel FIR-interferometer allowed an estimation of the impurity concentrations. Assuming coronal equilibrium an attempt was then made to model the radiation profile. Particular interest was also invested to a short period before a disruption occurred.

Another set of discharges was dedicated to the study of impurity injection of low-Z gases resulting in a large increase of the electron density. As in the previous case the evolution of the radiated power profile under these conditions was studied and the concentrations of these impurities were compared with calculations assuming coronal equilibrium.

Results

The total radiation loss is dependent mainly on density, being linear with density throughout the entire operation range. Both total and central radiated power roughly follow the density. There is a weak inverse dependence on plasma current as well but no evidence for a strong influence of the toroidal magnetic

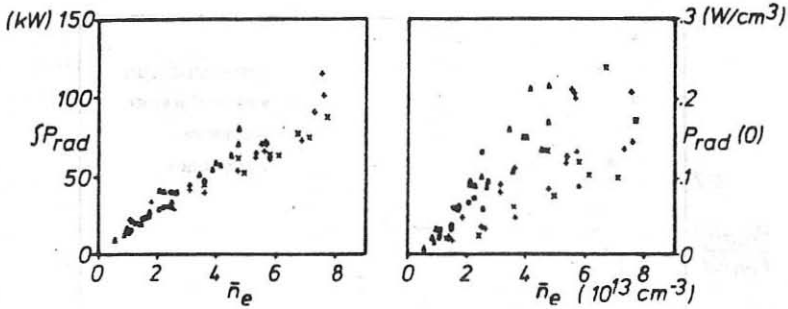

Fig.1 Total and central radiated power as function of electron density for ohmically heated discharges. The symbols correspond to different ranges of plasma current, • - 30 kA, ▲ - 60 kA, + - 100 kA, x - 125 kA.

field. If we consider the central radiated power the same tendencies can be observed with a larger scatter on the experimental data due to the errors introduced by Abel-inversion. These results are summarized in Fig. 1. Comparing the central radiated power with the central ohmic power for non-disruptive dischargews results in values of $P_{rad}(0)/P_{oh}(0)$ ranging from 1% to 15%, assuming $q(0) \approx 1$.

The radiated power profile in the low density, high current corner of the operation diagram is hollow with very little radiation from the plasma axis. As the density is increased no particular change in the shape of the radiation profile can be observed but the level increases linearly with density. For these low q conditions the radiation is probably dominated by low and intermediate Z impurities. As the current decreases the radiated power profile became flatter and eventually slightly peaked on axis. This is consistent with the image of a shrinking current channel together with a decreasing central electron temperature.

Making the usual assumption that P_{rad} is proportional to the product of electron and impurity density [2] with a cooling rate, the impurity concentration can be calculated by dividing the radiated power profile by the electron density profile. The limiter for these discharges was made of carbon with a coating of SiC. Consequently a large signal from Si-lines was observed spectroscopically. Assuming coronal equilibrium Si concentrations were estimated in order to match the central radiated power. Taking the density and temperature values into account the coronal model overestimates the total radiated power by far if only Si is considered. We therefore conclude that several impurities contribute substantially to the radiated power. A small fraction of high-Z impurities, Fe or Ti (both present in the vacuum chamber), accounts for a part of the observed core radiation. Si mostly contributes to the radiation from intermediate plasma

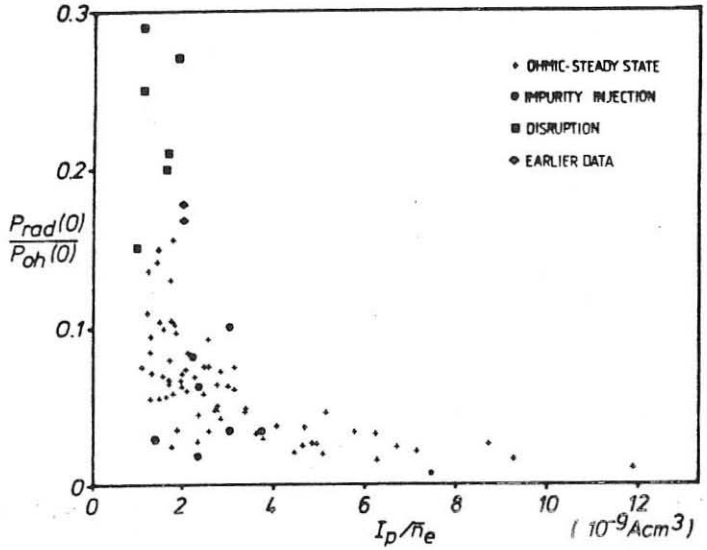

Fig.2 $P_{rad}(0)/P_{oh}(0)$ for different plasma conditions for $q_a > 3$ as function of the operational parameter I_p/n_e.

radii. In order to explain the observed value of Z_{eff} ranging from 1.5 to 3 up to two percent of low-Z impurities (O and C) have to be considered. Carrying out these modeling calculations for all of the conditions shows no large deviations from this picture of a mixture of impurities contributing to the radiated power. As a consequence one should rather concentrate on the impurity density than the concentration. Over all the conditions observed the impurity densities remain fairly unchanged. This again is consistent with the good linearity of the radiated power with electron density. Average impurity densities are $n_m \approx 0.3 \cdot 10^{11}$ cm^{-3}, $n_{Si} \approx 1.5 \cdot 10^{11}$ and $n_l \approx 2 \cdot 10^{11}$ cm^{-3}. The coronal model thus gives a consistent picture of the radiated power profile although the measured profile does not show all of the spatial details.

During these experiments the electron density was increased until a disruption occured. The radiated power profile was studied in detail for evidence of its possible influence on the disruption. Looking at the time evolution of the radiated power profile a few msec before a disruption showed no evidence of a precursor to the disruption. In particular no strong peaking or asymmetry of the bolometer profile was observed. We therefore conclude that there is no evidence for the radiation being the primary cause for the disruption even if the level of radiation is high before the disruption. Discharges were observed in ear-

lier experiments [3] where a similarly large radiated power was not followed by a disruption. This is again consistent with the fact that impurity densities remain fairly unchanged with changing plasma conditions so it seems that there is no particular accumulation of impurities which could invoke a radiation level large enough to destabilize thermally the plasma column. Once the disruption has occured the radiated power strongly peaks on axis due to the cooling and fast current narrowing. The total radiation loss observed cannot be explained by the content of the kinetic energy alone. A considerable amount of stored magnetic energy is lost through radiation as well, e.g. $W_{rad} \approx 2.0$ kJ, $W_{kin} \approx 1.3$ kJ and $W_{mag,int} \approx 4.4$ kJ.

Impurity puffing of various low-Z gases (He, Ne, N_2 and O_2) was carried out into hydrogen discharges resulting in an increase in density of up to 250%. The radiation profile for these experiments again followed the density, being hollow throughout the pulse, indicating that low-Z impurities account for the increase in total radiation. No increase in central radiated power was observed, therefore the concentration of heavy impurities does not change with low-Z impurity puffing. The coronal model which was applied to these experiments could well explain the increase in radiation by the incoming impurities. Before injection the radiation is likely to be dominated by Si-lines. During injection the radiation can be explained by the same Si-density and a reasonable concentration of the injected impurity. Thus the radiation profile can be described by a rather unchanged density of intrinsic impurities in combination with a certain amount of the injected impurity which is consistent with the case discussed above.

In Fig. 2 $P_{rad}(0)/P_{oh}(0)$ is plotted for the different experimental series covered by this paper. For this parameter values up to 0.5 were observed in earlier experiments not being followed by a disruption [3].

Conclusion

The modeling of the radiated power loss carried out for various ohmic conditions and impurity injection led to a consistent picture of the impurity composition of the TCA tokamak plasma. Impurities and the associated radiated power are not a severe problem in the present clean conditions.

Acknowlegements

We recognize the assistance of the whole TCA team in this work and the support of Prof. F. Troyon and A. Heym. The work was partly supported by the Fonds National Suisse.

References

[1] H. Jaeckel et al., Proc. DPG, Munich, 1978
[2] D. Post et al.,Atomic Data and Nucl.Data Tables 20(1977) 397
[3] F. Hofmann et al., Lausanne Report LRP 229/83

Radial Energy Balance Analysis of ASDEX H-Mode Discharges

O.Gruber, W.Jilge, K.Bernhardi, A.Eberhagen, G.Fußmann, O.Gehre, J.Gernhardt, G.v.Gierke, E.Glock, G.Haas, G.Janeschitz, F.Karger, M.Keilhacker, O.Klüber, M.Kornherr, K.Lackner, G.Lisitano, H.-M. Mayer, K.McCormick, D.Meisel, V.Mertens, E.R.Müller, H.Niedermeyer, W.Poschenrieder, H.Rapp, J.Roth, F.Ryter, F.Schneider, G.Siller, P.Smeulders, F.Söldner, E.Speth, A.Stäbler, K.Steuer, O.Vollmer, F.Wagner
Max-Planck-Institut für Plasmaphysik, EURATOM Association, D-8046 Garching, Fed. Rep. of Germany

Abstract
Radial transport and confinement properties of ELM dominated (H) and ELM free (H*) beam heated ASDEX-discharges are studied using the PPPL transport analysis code TRANSP. For similar plasma parameters the H* discharges have energy confinement times of about 1.5 as large as those in H discharges and correspondingly reduced electron heat diffusivities due to the absence of the ELM's. Electron conductive losses dominate the energy losses besides radiation cooling.

1. Introduction

In the beam-heated high confinement ASDEX discharges (H-mode) confinement times comparable to the ohmic values are found and usually edge localised modes (ELM's) are observed which are associated with burst-like releases of particles and energy from the outer half of the plasma /1/. Confinement depends on the frequency of the ELM's and the deduced transport coefficients should be upper limits for the values describing the underlying quasi-stationary transport. Moving the plasma column to the outer wall suppresses the ELM's (H*-mode), but high Z-impurities accumulate in the plasma center and produce together with the strongly rising plasma density a rapid increase of the total radiation losses and a peaking of the radiation power density at the magnetic axis /1/.
Radial transport of H-(# 8475) and H*-(#11447) discharges has been studied using the transport analysis code TRANSP (PPPL) /2/ and measured radial plasma profiles, namely the electron temperature, electron density and radiation losses. The measured shape of the plasma boundary vs. time can be specified as input data for TRANSP and the interior flux surface geometry is periodically updated. This is of importance for the analysis of the flux surface averaged transport of the plasmas investigated with β_p up to 2, where a

large toroidal shift of the magnetic axis (up to a/5) and of the plasma profiles exist. Compared with previous studies /3/ using a predictive transport code the present calculations differ through the mentioned geometrical effects, a more transparent propagation of the experimental errors and the applicability to discharges with strong radiation losses exceeding 50 % of the input power.

2. Radial transport in H and H* discharges

The two discharges described here differ only weakly in the time development of the line density and temperatures up to 100 ms after the neutral beam heating is turned on (t_{on} = 1.1 sec; t_{off} = 1.3 sec; 3.2 MW heating power, $H^0 \rightarrow D^+$, co-direction), but then the density in the H* discharge rises further. The plasma current I is different, namely 380 kA in the H- and 320 in the H*-discharge (B_t = 2.16 T). Energy transport during beam heating is dominated by electron heat conduction in all cases studied. During the L-phase after the beams are turned on the energy confinement time $\tau_E = W/(P_{cond} + P_{conv})$ decreases by a factor of more than two compared with the ohmic one, being close to the energy replacement time $\tau_E^* = W/(P_{heat} - dW/dt)$ (see Fig. 1). This shows that nearly the whole input power is lost by energy transport; radiation and CX losses are small. The electron thermal diffusivity χ_e is enhanced over a large part of the plasma column compared with the ohmic values (see Fig. 2). Whereas the ohmic χ_e is well described by a parameter dependence $\chi_e = \frac{3.4 \cdot 10^{15}\ B_t\ a/R}{n_e^{0.8}\ T_e\ q}$ [m²/s, T, m^{-3}, keV] for the q >1 region /4/, the confinement times during the L-phase are roughly given by $\tau_E(L) \propto P_{heat}^{-1/3} \cdot I$ which can be written as $\tau_E(L) \propto I^{3/2}/\langle n^{2/3}\ T^{1/2} \rangle$ /4/.

The H-mode is associated with an increase of the energy confinement and with a reduction of the still dominating electron thermal conduction over the entire plasma cross-section. The same holds for the H*-mode, but now the energy replacement time is decreasing over the time due to the increasing radiation losses (see Fig. 1,2). Taking the scaling of the H-mode confinement $\tau_E(H) \propto I$ /4/ the energy confinement of the H-discharge # 8475 should exceed that of the H* discharge # 11447 by a factor of 1.2. But with approximately the same density and temperature

profiles at 1.21 sec for both discharges τ_E(H) is only 75 ms at r = 35 cm whereas τ_E(H*) $>$ 120 ms is obtained (see Fig. 1). On the contrary the electron thermal diffusivities are reduced over a large part of the plasma area compared with those of the H-mode (see Fig. 2). This improvement of confinement for the H* mode can obviously be attributed to the absence of the energy loss channel by the ELM's.

The time dependences of τ_E and χ_e at all radii show that transition from OH → L behaviour is abrupt (see Fig. 1). There is no delay between the turn-on of the beams and the switching from the OH to the L-mode behaviour of χ_e. The transition from L → H mode is much slower, whereas the L → H* change over is again sharp for the range r $>$ 30 cm where the transition obviously starts. χ_e near the plasma axis is decreasing due to the increasing radiation losses in the center starting already in the L-phase.

The ion heat conduction is described by the neoclassical value in all discharge phases (OH,L,H,H*) yielding for the calculated T_i-profiles the measured neutron fluxes. In all cases the conductive ion losses are comparable to the convective ones (calculated by assuming a particle confinement time of 50 - 100 ms) and much smaller than the conductive electron losses.

3. Conclusions

Comparing the electron thermal conductivities of H and H* discharges, dominating the energy losses besides the strong radiation losses of the H* discharges, reduced χ_e(H*) values and correspondingly higher τ_E(H*) are found, which can be attributed to the lack of energy losses due to ELM's. Similar behaviour has been stated by /3/ for H-discharges with ELM free phases of less than 30 ms being much shorter than the energy confinement time of 120 ms. There seems to be no further increase of τ_E or decrease of χ_e up to the radiation collapse time at 1.27 sec (burst-free phase lasts from 1.16 s to 1.27 sec). A study of the properties of an insulating sheath near the separatrix /5/ needs more error handling. Indeed a blocking of the heat flux is found at the plasma edge and the T_e-profiles become flat there with high edge T_e- values. But high radiation losses in the later phases of the H*-discharges and

the uncertainties in the T_e-measurements increase the error for the calculated plasma energy losses due to the electrons and ions in this boundary region.

References

/1/ Keilhacker, M., et al., IAEA-CN-44/A-II-1, London (1984).
/2/ Hawryluk, R., Proceedings of "Physics of Plasmas Close to Thermonucl. Conditions", Varenna (1979), Vol. 1, p. 19.
/3/ Becker, G., et al., IPP III/99 (1984), internal report.
/4/ Gruber, O., Proc. Invited papers Int. Conf. on Plasma Physics, Lausanne (1984), Vol. I, p. 67.
/5/ Wagner, F., et al., Phys. Rev. Lett. 53, 1453 (1984).

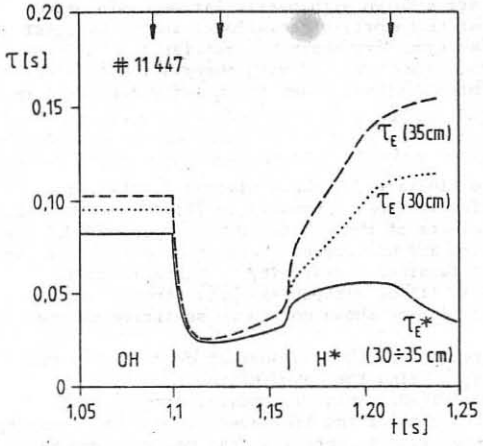

Fig. 1: Energy confinement (τ_E) and replacement (τ_E^*) time of a H* discharge. Arrows indicate the times where the radial χ_e profiles of Fig. 2 have been taken.

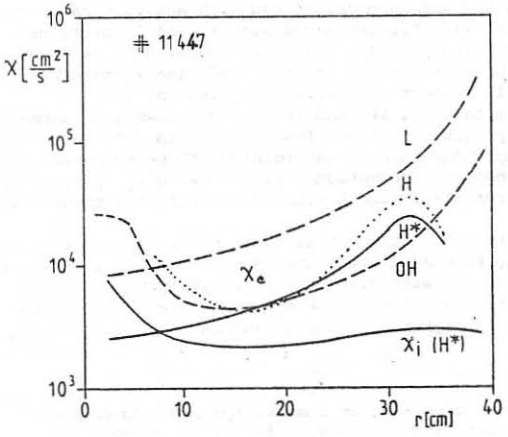

Fig. 2: Radial profiles of the electron thermal diffusivity χ_e for OH, L and H* mode in a H* discharge. For comparison the χ_e profile of a H-discharge (# 8475) with similar plasma parameters and the neoclassical ion heat diffusivity χ_i (H*) are also shown.

TRANSPORT CALCULATIONS FOR JET DISCHARGES WITH ICRH

A. Taroni, A.E.P.M. Abels van-Maanen*, W. Core, D.F. Düchs, T. Hellsten, D.G. Muir, P.M. Stubberfield, F. Tibone, M.L. Watkins.

JET Joint Undertaking, Abingdon, Oxon., OX14 3EA, UK
* On attachment from Mathematical Institute, University of Oxford, UK.

1. Introduction

In this paper we discuss the results of 1-D and 1½-D transport codes in simulating JET discharges and in predicting future JET performance.

In Section 2 ohmic plasmas are studied with particular emphasis on the possible importance of ion thermal transport, especially at the highest JET densities. In Section 3 the transition from ohmic to auxiliary heated discharges (ICRH) is simulated. Results are compared with observations in JET. Extrapolations to higher levels of additional power are briefly discussed in Section 4.

2. The Ohmic Phase

The transport models used to simulate JET ohmic plasmas (including target plasmas for ICRH) are basically those discussed in [1]. In particular, electron energy diffusion coefficients of the Alcator-Intor (χ_{eAI}) and of the Coppi-Mazzucato-Gruber (χ_{eCMG}) form are considered. Classical energy transfer between electrons and ions and neoclassical resistivity η_{neo} are assumed. Impurities are treated either as in [1] or without assuming coronal equilibrium. Results given in this section are shown not to be sensitive to the choice.

The dependence of computed results on the ion thermal conductivity has been studied taking $\chi_i = \alpha\chi_{iCH}$, χ_{iCH} being the Chang-Hinton neoclassical expression [2]. Results are illustrated in Fig. 1, showing observed and computed peak temperatures as a function of the line-averaged electron density $\bar{n}_e$ for various values of α. At the highest densities, the maximum temperature difference computed with $\alpha = 1$ and with a model of sawtooth activity based on Kadomtsev's reconnection scheme (with flattening of both T_e and T_i profiles) is $\Delta T \equiv T_{eo} - T_{io} \lesssim 400$eV. An anomaly factor $\alpha \gtrsim 10$ is required to produce $\Delta T \gtrsim 1$keV at intermediate and high densities. At the same time χ_e must be reduced by a factor up to 3 with respect to the values given in [1].

The need for large anomaly factors, if confirmed, would mean that anomalous ion thermal conductivity, possibly having a functional form different from neoclassical, could play an important role in determining JET performance. On the other hand, Fig. 1 shows that the conventional picture with $\chi_i \sim 3\chi_{iCH} < \chi_e$ produces results within the error bars, albeit with ΔT consistently towards the lower limits.

Another important result to be pointed out is that the high ohmic electron temperatures and values of Z_{eff} from Bremsstrahlung as observed now in JET are compatible with neoclassical but not with Spitzer's resistivity η_{Sp}. This result differs from that reported in [1] when lower temperature plasmas with higher values of Z_{eff} were available for simulation, and neither η_{neo} nor η_{Sp} could be excluded.

3. ICR Heated Plasmas

RF heating of JET plasmas is simulated by a model for additional power sources for the electrons and ions, and by allowing for an enhancement of

transport losses during RF pulses.

In order to determine the auxiliary power deposition profile, we derived a simplified model for use in transport codes and containing as much as possible of the information provided by 'stand-alone' codes treating different aspects of the RF heating problem for an assumed background plasma. This model can be summarised as follows:

- the additional power is uniformly deposited within a rectangular portion (the same for electrons and ions) of the poloidal plasma section;
- the absorption region is bounded by major radii corresponding to the position of the ion-ion hybrid and the ion cyclotron resonance for the minority species, and by a height Z determined by ray tracing calculations ($Z \sim 1.5$m);
- direct heating of the electrons by mode conversion using the Budden formulae, and minority ion heating by ion cyclotron damping are estimated [3];
- heating of the background plasma ions and of the electrons is then estimated using a steady-state solution to a Fokker-Planck equation for the energy distribution function of the minority species.

Confinement degradation during RF heating has been simulated through an enhancement of the ohmic electron thermal diffusivity by a power-dependent factor, along the lines suggested by the "Principle of Profile Consistency" [4].

These models must be tested against observations and can be used in a predictive way only for studies of sensitivity of results to the assumptions they involve. Both purposes have been pursued by undertaking an extensive series of computations. Our findings are summarised in the following.

Assuming that most of P_{rf} (the total RF-power coupled to the plasma) is deposited in the central region of the plasma, as suggested by theory, a degradation of energy confinement is required to produce variations in T_{eo}, T_{io} and $\langle T_e \rangle$ comparable to the experimental ones. Furthermore, numerical results are in better agreement with observations when the power globally coupled to the electrons, P_{rf}^{e}, is not less than that to the ions, P_{rf}^{i}. This is illustrated in Fig. 2 for the case of ^{3}He minority heating, under the following assumptions:

- strong ion transport ($\chi_i > \chi_e$) as described in Section 2, but no further degradation of χ_i during RF pulses;
- $\chi_e = C \cdot \chi_{eCMG}$, with $C \sim 1$ during the ohmic phase but $C > 1$ during RF heating (scaling roughly as $C \sim (P_{oh} + P_{rf})/P_{oh}$).

Similar results have been obtained for the case of H-minority heating, with substantially different target plasmas.

Enhanced particle (including impurities) influxes at the plasma boundary allow simulation of the experimentally observed increases in line-averaged $\bar{n}_e$ (up to 30% when $P_{rf} \sim 5$MW) and total radiated power (without significant changes in Z_{eff} and in P_{rad}/P_{input}).

Our main conclusions, namely the need for transport degradation during RF heating and $P_{rf}^{e} \gtrsim P_{rf}^{i}$, are stable against model variations as long as central power deposition is retained. If, however, a large fraction of the absorbed power ($\gtrsim$ 50% when $P_{rf} \sim 2$MW) is assumed to be deposited in the plasma external region, where radiation dominates, then both peak and average temperature increase can be simulated without degrading χ_e.

The evolution of the central electron temperature constrains the power to the electrons in the central region to a minimum of $\sim$ 50% P_{rf}, as mentioned above. In addition, the moderate saturation of T_{eo} during sawtooth rise

suggests that electron transport is strongly reduced towards the plasma centre, and even degradation does not play a significant role there.

4. Extrapolation to Higher Levels of RF Power

The picture emerging from the previous Sections indicates that it is only reasonable to predict ranges of possible performance that take into account variations of all important parameters in the model, and possibly of the model itself. It is practically impossible to follow such a procedure systematically. The only way to face the problem would consist of treating all of the parameters within a given model on the same basis, and changing them randomly within reasonable ranges and constraints.

A few preliminary results using different scalings of χ_e with additional power are shown in Fig. 3 for P_{rf} = 5, 10, 15MW. They refer to two sets of transport assumptions for two different target plasmas: the 'large' $\chi_i \geq 10\chi_{iCH}$ with $\chi_e \sim \chi_{eCMG}$ when $\Delta T \sim 1.5$keV and $Z_{eff} \sim 4.0$ (Fig. 3a) and the 'standard' $\chi_i \sim 4\chi_{iCH}$ with $\chi_e \sim \chi_{AI}$ when $\Delta T \sim 0.6$keV and $Z_{eff} \sim 2.5$ (Fig. 3b).

References

[1] Behringer, K.H. et al., in Plasma Physics and Controlled Nuclear Fusion Research (Proc. 10th Int. Conf., London, 1984) 1, IAEA, Vienna (1985) 291.

[2] Chang, C.S. and Hinton, F.L., Phys. Fluids, 25 (1982) 1493.

[3] Brambilla, M., Lallia, P.L. and Thomsen, K., Private communication (1985).

[4] Coppi, B., Comments Plasma Physics and Controlled Fusion, 7 (1982) 1.

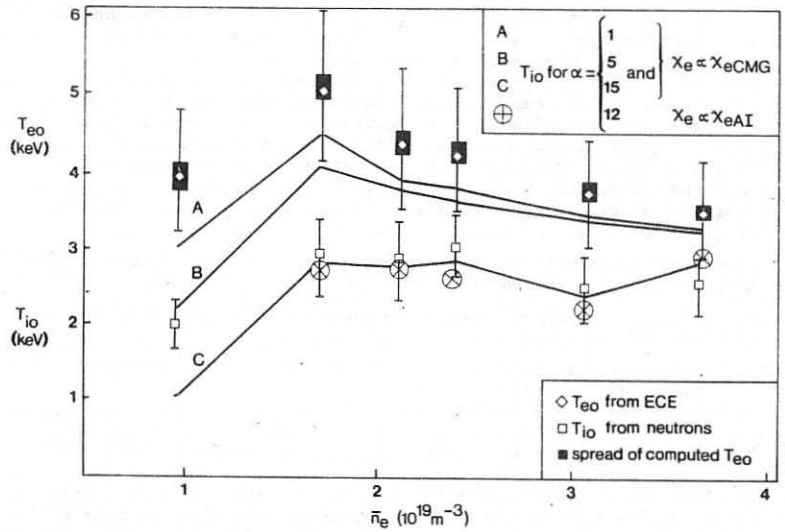

Fig 1: Observed and computed central (sawtooth averaged) temperatures. Results A, B, C were obtained with a 1-D code, ⊗ with a 1½-D code and non-coronal impurity radiation. B_t = 3.4T, I_p = 3.0MA except for the lowest density (I_p = 1MA) and the highest density (I_p = 3.6MA) case.

Fig 2: Computed and experimental peak temperatures for different levels of RF power with P_{rf}^{i}/P_{rf} = 25%(A,A'), 50%B,B'), 75%(C,C') and degraded(——) and undegraded (---) electron transport.

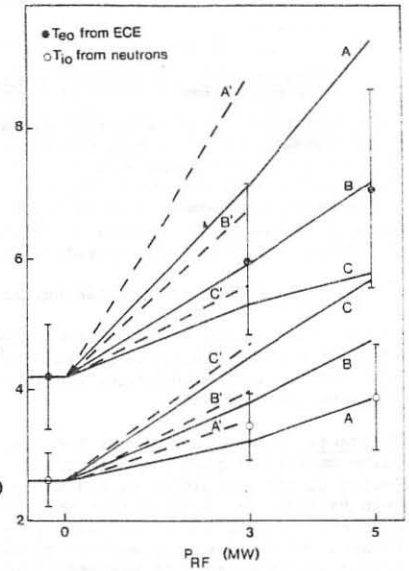

Fig 2

Fig 3: Predictions for P_{rf} up to 15MW based on plasmas with B_T=3.4T and

a) I_p=4MA, $\bar{n}_e \simeq 2.6.10^{19} m^{-3}$, $Z_{eff} \simeq 4$, $\chi_e = \chi_{eCMG} \cdot (P_\Omega + P_{rf})/P_\Omega$, α=12;

b) I_p=3.6MA, $\bar{n}_e \simeq 3.10^{19} m^{-3}$, $Z_{eff} \simeq 2.5$, $\chi_e = \chi_{eAI} \cdot \int_0^\rho P_{tot}^{e}(\rho)\,dV / \int_0^\rho P_\Omega(\rho)\,dV$, α=4.

A,B,C as in Fig 2. B' corresponds to P_{rf}^{i} = 50% P_{rf} and degradation saturated at 10MW.

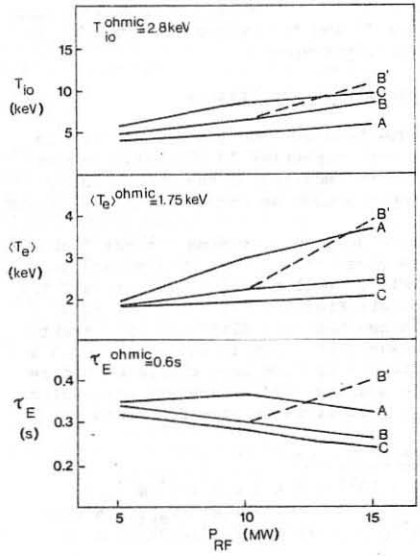

Fig 3a

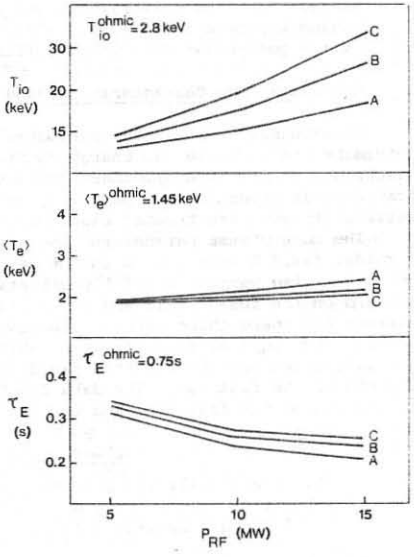

Fig 3b

GLOBAL ENERGY CONFINEMENT STUDIES IN OHMICALLY HEATED JET PLASMAS

J.G. Cordey, D.V. Bartlett, R.J. Bickerton, M. Brusati, D.J. Campbell, J.P. Christiansen, S. Corti, A.E. Costley, A. Edwards, S. Ejima#, J. Fessey, M. Gadeberg*, A. Gibson, R.D. Gill, N. Gottardi, A. Gondhalekar, C.W. Gowers, F. Hendriks, O.N. Jarvis, E. Källne, J. Källne, S. Kissel, L. de Kock, H. Krause+ E. Lazzaro, P.J. Lomas, F.K. Mast+, P.D. Morgan, P. Nielsen, R. Prentice, R.T. Ross, J. O'Rourke, G. Sadler, F. Schueller, M.F. Stamp, P.E. Stott, D.R. Summers A. Tanga, P.R. Thomas, G. Tonetti†, M.L. Watkins

JET Joint Undertaking, Abingdon, Oxon., OX14 3EA, UK

On attachment from: # G.A. Technologies, San Diego, USA; * EURATOM-Risø Association, Risø National Laboratory, Roskilde, Denmark; + EURATOM-IPP Association, IPP Garching, F.R. Germany; † EURATOM-Suisse Association, CRPP, Lausanne, Switzerland.

Abstract: Systematic scans of the plasma density n have been completed for a large variety of plasma conditions in JET. The toroidal field B, the safety factor q, the elongation K, the major radius R and the minor radius a have all been varied. It is shown that the resulting data set contains two important parametric constraints, one which is a direct consequence of the ohmic heating, relates the electron temperature T_e to the variables n, B, q, K and a further constraint which relates the effective plasma charge Z_{eff} to the same set of variables.

Subject to these constraints, the global energy confinement time τ_E is found to scale as $(nB)^{1/2}\,(q)^{1/3}\,R^{1.7}\,a^{1.3}$ and this empirical scaling is shown to be consistent with low β-collisional transport.

I General Plasma Characteristics and Parametric Constraints

An extensive series of experiments have been carried out during 1985 to determine the particle and energy confinement properties of ohmically heated discharges in JET, a preliminary account of the scaling of the global energy transport is given in this paper, other aspects such as local transport, plasma resistivity etc. are treated elsewhere [1-2].

The main plasma parameters line average density $\bar{n}$, plasma current I and toroidal field B were varied in the ranges given in Table I. The plasma geometry was also varied from fully elliptical to small circular plasmas (a=0.8m) limited on the inside wall and on the limiter; Fig. 1 shows the outer flux surface for these three cases. The discharges had long flat tops in current, density and temperature, 4-12 secs, which was sufficient in all but the 3.5 and 4MA discharges for the magnetic field diffusion to have been completed before the end of the flat top. The data for the scaling studies are extracted close to the end of the flat top, and the data set consists of some 200 shots.

Table I: Parameter Ranges

$$1.7 < B < 3.4T;\ 1 < I < 4MA;\ 0.5 \times 10^{19} < \bar{n} < 3.6 \times 10^{19}\ m^{-3}$$
$$1 < K(= b/a) < 1.7;\ 0.8 < a < 1.23m;\ 2.5 < R < 3.4m;\ 2 < Z_{eff} < 8$$
$$1.7 < q(= BA/\mu RI) < 12;\ 1.5 < \hat{T}_e < 6keV;\ 1 < \hat{T}_i < 3keV$$

All of the discharges exhibited strong sawtoothing behaviour on the flat top and the electron temperature profile which was measured by the ECE diag-

nostic, showed the characteristic flattening in the q < 1 region. Profiles for the three types of geometry are shown in Fig. 2. The calibration of the ECE system was checked with the single point Thomson scattering system [3]. The remainder of the data for the study was obtained from the following diagnostics, 2mm and far infra-red interferometers for the line average electron density, NPA and neutron yield for the ion temperature, visible Bremsstrahlung for the effective plasma charge Z_{eff}, VUV and visible spectroscopy for the carbon to oxygen density ratio and metal concentration. The range of variation of these parameters is also given in Table I.

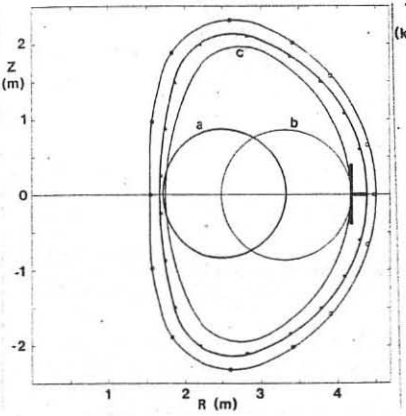

Fig 1: Outer flux surfaces for three extreme geometries a) R=2.5m, a=0.8m; b) R=3.4m, a=0.8m; c) R=2.95m, a=1.23m K=1.7.

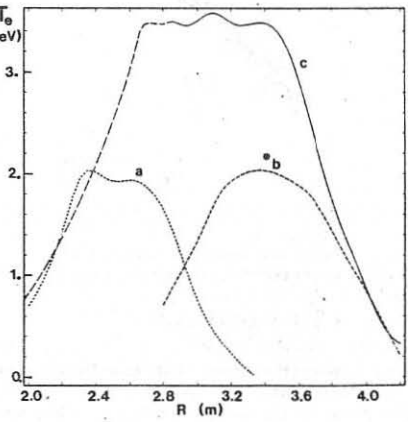

Fig 2: Typical electron temperature profiles for the geometries of Fig 1. The dotted portion of C is an extrapolation around the flux surfaces.

In any scaling study it is essential to first identify the independent variables and determine the parametric relationships that exist between these variables and the dependent variables. The independently controllable variables are $\bar{n}$, B, I, R, b, a; actually these are not fully independent since certain combinations violate stability limits. To enable comparisons to be easily made with the dimensional constraints [4] imposed by the various theoretical models the above set is replaced by $\bar{n}$, B, q_{cyl}, R, a, K.

Inspection of the data set shows that there is a strong relationship between the volume average electron temperature and the independent variables, which is a direct consequence of the ohmic heating. This ohmic heating scaling law for the JET data set is

$$\bar{T}_e \propto B^{1.8}\, \bar{n}^{-0.6}\, q^{-1.0}\, K^{0.8} \qquad \ldots (1)$$

and the fit is shown in Fig. 3. A similar scaling law was obtained by Pfeiffer and Waltz [5] in their study of confinement in small ohmically heated tokamaks, the main difference is the dependence on magnetic field which is much stronger in JET and apparently also in other large tokamaks [6,7].

There is also a further parametric relationship in the data set between the effective plasma charge Z_{eff} and the independent variables. This is

$$Z_{eff} \propto B\, \bar{n}^{-0.9}\, q^{-0.7}\, K^{0.5} \qquad \ldots (2)$$

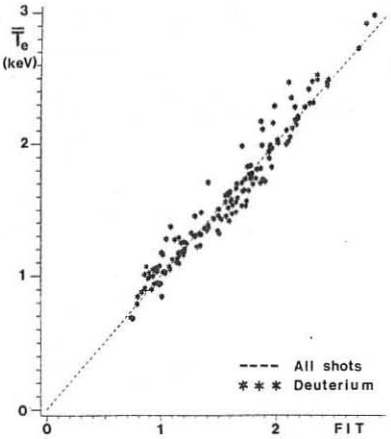

Fig 3: The ohmic heating constraint, average electron temperature versus the best fit:

$\bar{T}_e \propto B^{1.8}\ \bar{n}^{-0.6}\ q^{-1.0}\ K^{0.7}$

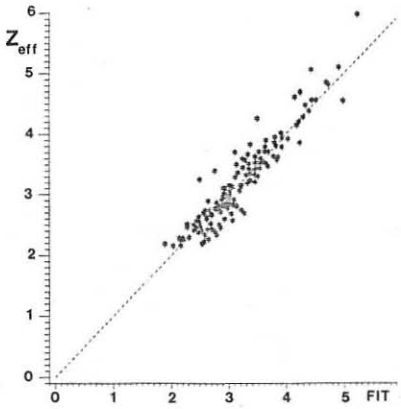

Fig 4: Effective plasma charge Z_{eff} versus the best fit:

$Z_{eff} \propto B\ n^{-0.86}\ q^{-0.7}\ K^{0.48}$

it is somewhat weaker than the ohmic constraint but nevertheless is statistically significant as the fit of Fig. 4 shows. This constraint can also be re-expressed in the form $Z_{eff} \propto P_\Omega / \bar{n}$ where P_Ω is the ohmic input power suggesting that the origin of this relationship is that the density of impurities in the plasma is related to the power flux on to the walls and limiter. It was not possible to obtain the dimensional scaling of either of these constraints due to the small range of R and a covered by the data set.

II The Scaling of the Global Energy Confinement Time

The global energy confinement time is defined as $\tau_\varepsilon = 3/2 \int n(T_e + T_i)\ dv/P_\Omega$ where the volume integral is taken over the magnetic surfaces. The variation of τ_ε with density is shown in Fig. 5 for a few of the scans with different magnetic field, current and plasma dimensions. For the range of density explored by JET the τ_ε is found to scale fairly weakly with density increasing as $\tau_\varepsilon \propto n^{1/2}$, and even this weak dependence comes mainly from the ions. This latter point is demonstrated in Fig. 6 which shows that the dependence of the electron energy confinement time $\tau_{\varepsilon e} (= 3/2 \int n T_e\ dv/P_\Omega)$ upon density is very weak indeed.

Applying regression analysis to the full data set gives

$$\tau_\varepsilon \propto (nB)^{1/2}\ (q)^{1/3}\ R^{1.7}\ a^{1.3} \qquad \ldots (3)$$

the fit is shown in Fig. 7. This scaling is similar to that found in TFTR [6], except the q dependence is weaker and the B dependence stronger. The cubic dimensional dependence is close to that found by Pfeiffer and Waltz [5], the main difference between that initial study and present studies in larger tokamaks [6,7] is the B and q scaling. Interestingly, expression (1) also satisfies the constraints imposed by low-β collisional theory $\tau_\varepsilon \equiv 1/B\ F(nL^2, B^4L^5)$. The other theoretical scalings considered by Connor and Taylor [4] give a significantly poorer fit.

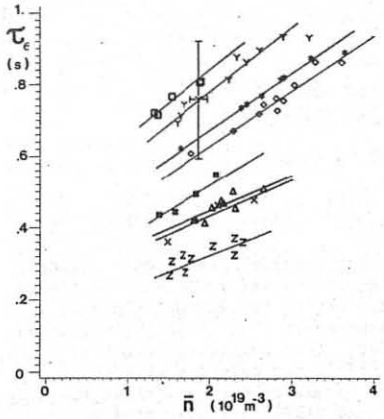

Fig 5: Global energy confinement time τ_ϵ versus line average electron density $\bar{n}$.

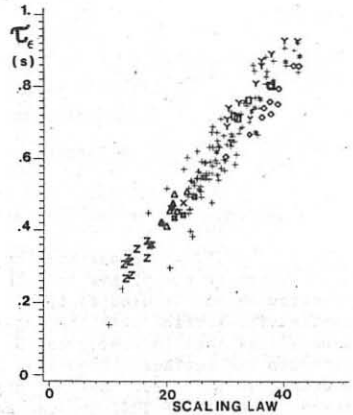

Fig 7: Global energy confinement time τ_ϵ versus best fit (symbols as Fig 5, other pulses +).

K=1.5, R=3.0m, a=1.2m, ◇ B=3.4T, I=4MA; ✱ B=3.4T, I=3.5MA; Y B=3.4T, I=3MA; ◻ B=3.4T, I=2MA; # B=2.5T, I=3MA; △ B=1.7T, I=2.5MA; K=1.0, ✕ B=2.5T, I=1MA, R=3.4m, a=0.8m; Z B=2.9T, I=1MA, R=2.5m, a=0.8m.

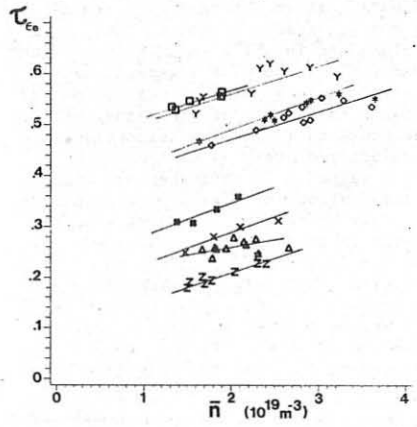

Fig 6: Electron energy confinement time versus density (symbols as Fig 5).

References

[1] Brusati, M. & Cordey, J.G., Transport analysis of JET discharges, EPS, Budapest (1985), paper 189.

[2] Christiansen, J.P. et al., Resistivity and field diffusion in JET, EPS, Budapest (1985), paper 177.

[3] Costley, A.E. et al., Electron temperature measurements in JET, EPS, Budapest (1985), paper 186.

[4] Connor, J.W. & Taylor, J.B., Nucl. Fusion, 17, 1047 (1977).

[5] Pfeiffer, W. & Waltz, R.E., Nucl. Fusion, 19, 51 (1979).

[6] Efthimion, P.C. et al., Plasma Physics and Controlled Nuclear Fusion, IAEA Conf., London, 1984, paper A-I-2.

[7] Ejima, S. et al., Nucl. Fusion, 22, 1627 (1982).

LIMITS IN EVALUATING ENERGY LOSS PROFILES FROM BOLOMETRIC MEASUREMENTS AT JET

N Gottardi, H Krause*, K F Mast*

JET Joint Undertaking, Abingdon, Oxon, OX14 3EA.
* On assignment from Max-Planck-Institut für Plasmaphysik, Garching, FRG.

ABSTRACT In JET three pin-hole type bolometer cameras observe one poloidal cross-section of the plasma from three different viewing positions. A simple projection method is used to test the consistency of the assumed shape of isoemissivity surface with the integral measurements. If consistency is found a generalized Abel inversion can be performed. In a considerable number of discharges the surfaces of constant emissivity do not coincide with the magnetic flux surfaces. Besides the obvious asymmetry due to limiter and R.F. antenna, a strong ($\tilde{>}$ 30%) up/down asymmetry and MARFEs are presented as examples. A neoclassical explanation for the up/down asymmetry is proposed.

Radiation losses play an essential role in the measurement of energy balance of tokamak plasmas. Bolometers measure the plasma emissivity only integrated along the lines of sight. Local emissivities, however, are wanted for the energy balance. A local emissivity can be obtained either by tomographic methods or through assumptions on the geometry of the isoemissivity surfaces. In JET, with the present arrangement (maximum 34 lines of sight from only three view points [1], tomographic methods yield an unsatisfactory spatial resolution. A resolution of 10 cm would require several hundred bolometer channels distributed rather homogeneously around the plasma cross-section. Assumption of the surface geometry reduces the two-dimensional to a one-dimensional problem, and in JET a resolution of about $\sim$ 10 cm is possible. This can be achieved with the help of a generalized 2-step inversion method [2] which can be applied to any set of nested contour lines. Usually the geometry has been assumed to be that of the magnetic flux surfaces derived at JET from magnetic measurements [3]. This assumption is not justified in general. We check the validity of this by utilizing the first step of the above mentioned inversion method. In this step all sight lines are projected to a common virtual observation point each line remaining always tangent to the same contour line. This procedure transforms also the integrated signals. If the assumed geometry is correct all transformed signals which are tangent to the same contour line must coincide. To illustrate this let us consider an observation plane (Fig. 2) with viewing lines (S_1-S_5) and selected isoemissivity surfaces (σ_0-σ_5) each of which is tangent to one of the viewing lines. The spaces between adjacent σ are the pixels in which the emissivity ε is considered constant. If the total length of viewing line S_i inside pixel ε_k is denoted by A_{ik} then the line integrated intensity I_i is given by

$$I_i = \Sigma A_{ik} \varepsilon_k \qquad (1)$$

Straightforward inversion of this linear system, where A is a lower-triangular matrix, would yield the emissivity ε from the measurements I but the resulting emission profile would be too discontinuous due to noise in the measurements and the pixel spacing too irregular.

A method of spatial smoothing and interpolation of the measured I is therefore needed. Since measurements result from cameras with different

points of view interpolation between data from different cameras are not directly possible. Following a suggestion [4] the data from all cameras is therefore projected first into the viewing frame of a virtual camera at an arbitrary position, eg the position of a real camera.

Let T_1-T_5 be a set of view lines emerging from the pin-hole P (cf. Fig.2) of a virtual camera, each T_i chosen to be tangent to the isoemissivity surface σ_i. The virtual intensities I' are then given by

$$I'_i = \Sigma B_{ik} \epsilon_k \qquad (2)$$

with the B_{ik} being the total length of T_i inside pixel ϵ_k. From Eq.1 and Eq.2 then follows the projection of real intensities into virtual ones

$$I' = B \cdot A^{-1} \cdot I \qquad (3)$$

In this way all measurements can be represented as a function of a single coordinate. Cubic splines and/or Chebyshev polynomials are used to fit a smooth curve through all the data. At this stage it can be checked if the assumed isoemissivity surfaces are adequate by inspection of the deviations of the I' from the fit curve. In many cases a consistent set of I' can be achieved by the elimination of single strongly affected channels (eg limiter effects). Inversion then proceeds by sampling the fit curve on a fine numerical grid and solving a matrix equation (as in Eq.1) for the samples.

Fig.3 illustrates this technique applied to an assumed hollow emissivity profile with the real camera geometry for a set of isoemissivity surfaces taken to be the magnetic flux surfaces of an actual pulse (cf. Fig.1). After projection of the (calculated) line averaged data on to the virtual camera the resulting inversion of the fit curve reproduces the initial profile very well.

Fig.4 shows the procedure using actually measured intensities. The pulse shows a typical level of data scatter between the different cameras after projection which still allows a satisfactory inversion result. Some evident deviation might be explained by the nearness of structures (limiter, RF antenna) to the observation plane.

For plasmas in the vicinity of the density limit MARFEs are frequently observed in JET. Details can be found in [5].

Differences of more than one order of magnitude are observed when the plasma is limited by the inside column of the torus rather than by the outside limiters. Those channels viewing the region where the plasma touches the wall both in the horizontal cameras and the vertical camera then show drastically enhanced signals.

A similar observation holds for discharges with an internal separatrix whose flux surface geometry is similar to the one in Fig.1. Here the plasma streaming along the separatrix to the top and bottom wall of the vessel causes drastic local radiation which shows on some vertical and horizontal channels at about five times the intensity of a normal central channel while not affecting the majority of channels.

Fig.5 gives a typical example of significant ($\sim\pm25\%$) up/down asymmetry. One possible explanation for this type of asymmetry is given by an analytical one-dimensional neoclassical two-fluid model [6,7]. It considers a radial electric field which gives rise to diamagnetic rotation of the bulk plasma and of the impurities with different velocities corresponding to their different electric charge Z.

The friction force between impurities and the bulk plasma then results in a pressure gradient of the impurities in poloidal direction due to finite aspect ratio effects. With the assumption of constant temperature on flux surfaces and negligible radial transport the relative variation of impurity density n_z/n_z on a flux surface can be derived. This variation is then expanded in a Fourier series with respect to the poloidal angle θ. There are two toroidally symmetric first order Fourier terms representing up/down asymmetry (first term) and inward/outward asymmetry (second term).

$$\frac{\tilde{n}_z}{n_z} = 2\frac{r}{R_o}\,\frac{\bar{\Omega}}{1+\Omega^2}\,\sin\Theta - 2\,\frac{r}{R_o}\,\frac{1}{1+\Omega^2}\cos\Theta \qquad (4)$$

The parameter Ω is given by

$$\Omega = \frac{\omega_H \tau_{HH}^{b/a}}{r\,Z^2}\,\frac{r^2}{q(r)R_o^2}\,\frac{P_H(r)}{dP_H/dr} \qquad (5)$$

with P_H pressure of H, ω_H H^+-gyrofrequency, τ_{HH} H^+-collision time, b/a axis ratio of ellipse.

Eq.4 shows that the up/down asymmetry changes sign with the toroidal magnetic field. The inward/outward asymmetry represents always an impurity accumulation at the torus inside plasma edge.

With Nickel and Carbon as typical JET impurities Ω is estimated to be in the range of 2 to 3. Eq.4 then predicts up/down asymmetries larger than inward/outward asymmetries which in JET could easily be masked by effects of localised plasma-wall interactions, eg by limiters. For up/down asymmetries Eq.4 gives a scaling law

$$\left(\frac{\tilde{n}_z}{n_z}\right)_{max} \approx \frac{2r}{R_o\Omega} \approx \frac{r^4}{T_e^{3/2}}\,\frac{B_T n_e}{I_p^2(r)\ b/a} \qquad (6)$$

Since absolute numbers for n_e and T_e are quite uncertain at the plasma edge the measured maximum up/down asymmetry in the emissivity $\tilde{\epsilon}/\epsilon$ which is expected to scale with $\tilde{n}_z/n_z$ is normalised to one for one time in a pulse and the subsequent development of density, temperature and current in this pulse is used to compare the normalised asymmetry with Eq.6. Fig.6 shows good agreement between the prediction and the experimental points.

For high densities and/or low T_e Eq.4 predicts small up/down and large inward/outward asymmetries. This could explain why MARFEs nearly always form at the torus inside plasma edge.

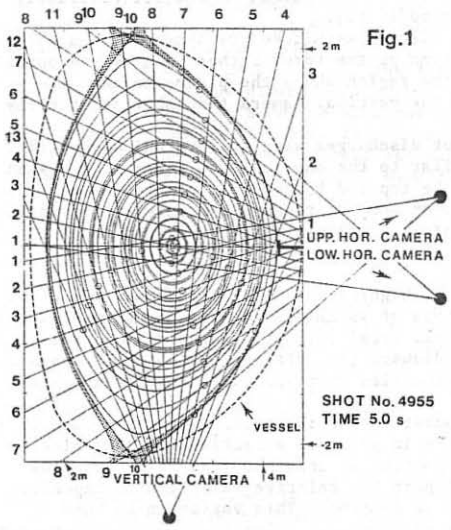

Fig.1

FIG.1 Arrangement of bolometer channels in JET.

REFERENCES

[1] K F Mast et al., Proc. of the 5th Top. Conf. on High Temp. Pl. Diagn., 1984 Tahoe City, USA.

[2] N Gottardi. Evaluation of local distributions from line Integrated Measurements, JET Report, in prep.

[3] J Blum et al., JET Contract No. JT3/9008; Jan. 1985.

[4] W Engelhardt, private communication.

[5] J O'Rourke et al., Poloidally Asymmetric Edge Phenomena in JET, this conference.

[6] K Feneberg et al., Radiation Asymmetries in JET, JET report, to be publ.

[7] K Feneberg et al., Poloidal Asymmetric Impurity Radiation in ASDEX in the Presence of Neutral Injection, this conference.

ACKNOWLEDGEMENT

The authors thank D F Düchs for many discussions and S Springmann for improving flux surface handling routines.

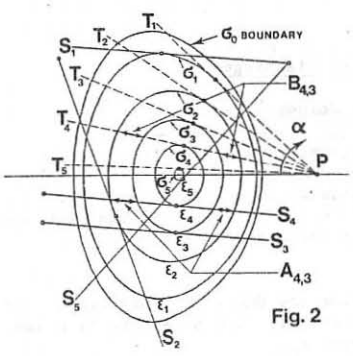

Fig. 2

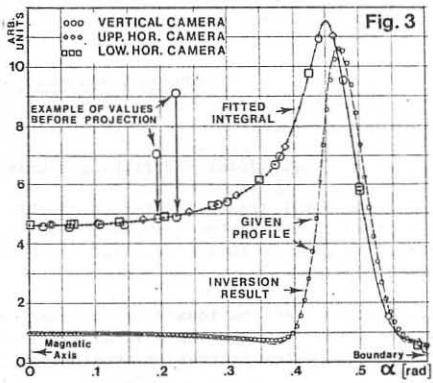

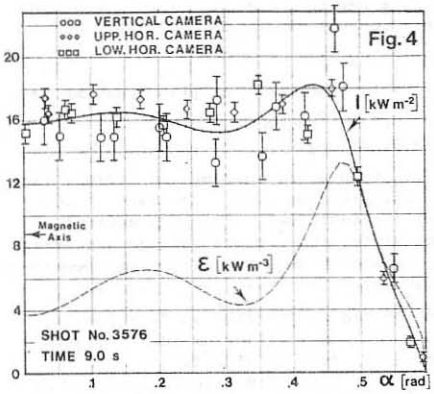

FIG.2 Isoemissivity lines and the projection of real view lines into a virtual camera.
FIG.3 Generalised Abel inversion for an assumed initial emissivity distribution; α as in Fig.2.
FIG.4 Measured data from three bolometer cameras projected into the viewing frame of a virtual camera in the equatorial plane outside the plasma and resulting local emissivity; α as in Fig.2.
FIG.5 Up/down asymmetry evident in data from the upper and lower horizontal camera; α as in Fig.2.
FIG.6 Normalised neoclassical prediction and normalised experimental data for the up/down asymmetry.

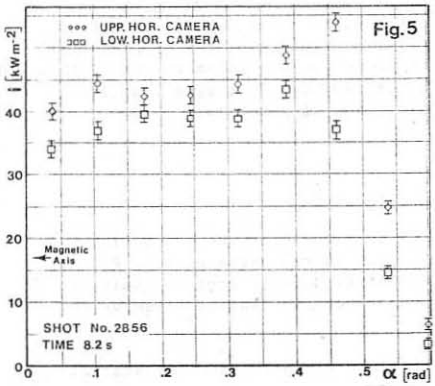

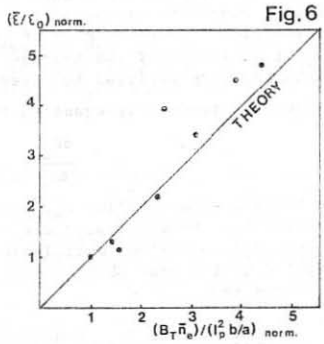

Transport Analysis of JET Discharges

M. Brusati, J.G. Cordey

JET Joint Undertaking, Abingdon, Oxon. OX14 3EA, UK.

Abstract: Local transport studies of JET ohmically heated plasmas show that ion losses in the region $r/a<2/3$ exceed electron losses when the local electron density is greater than a critical value which increases with the plasma current I_p.

Both ion and electron losses in the $1<q<2$ region are due to thermal conduction, the ion conductivity being several times neoclassical, the departure from the neoclassical value increasing monotonically with I_p.

The total energy confinement time τ_E of this region is up to 1.1sec; τ_E scales as $n_e^{0.6}$, and no clear dependence on plasma current is found.

I Local plasma energy balance

Ohmic plasmas have been obtained in JET over a wide range of plasma parameters:

$$1.7<B_t(T)<3.4;\ 1.0<I_p(MA)<4.0;\ 0.5\times10^{19}<\bar{n}_e(m^{-3})<3.6\times10^{19}$$
$$2.0<T_e(keV)<7.0;\ 1.5<T_i(keV)<3.0;\ 2<Z_{eff}<5$$

The plasma balance is calculated at several time points during the current flat top by the 1½D time dependent transport analysis code JICS. The current and mean density waveforms have a flat top of at least 5sec. The high current discharges ($I_p>3$MA) do not reach a steady state, the surface voltage exceeding the resistive voltage on axis means that inductive effects have to be taken into account when analysing the plasma equilibrium.

The ion and electron energy equations are solved in the flux surface geometry which is determined from the magnetic data and the equilibrium identification code IDENTB [1]. Other diagnostic information input to JICS include the electron T_e profile from ECE, density n_e from 2mm and FIR interferometry, ion temperature T_i from c-x and neutron yield, radiation losses from bolometry, effective ion charge Z_{eff} from visible bremsstrahlung; information on the average ion species is obtained from VUV and visible spectroscopy, and on particle recycling at the edge from H_α monitors. The results presented here are restricted to the region of the plasma where the radiation is small; this extends up to 2/3 of the average plasma minor radius. Thus more than 150 discharges were analysed to cover the above range of parameters.

In JICS the ion energy equation is given by:

$$\frac{dE_i}{dt} = P_{ei} + P_{cx} + P_{cv} + P_{cd}$$

The electron-ion coupling P_{ei} is assumed to be classical; the convection P_{cv} is determined from the particle balance and the charge exchange term P_{cx} relies on the self consistent calculation of the neutral density profile; this is computed by the code FRANTIC [2]; the boundary neutral flux is given by the H_α intensity.

conduction term P_{cd} is derived from multiple times of the neoclassical

conductivity; the results presented here have been obtained using the Chang-Hinton formulation of the conductivity [3]. Equation (1) is solved for T_i adjusting the multiplier until agreement is found between the calculated central ion temperature and the measured one.

Results of the analysis are shown in fig.1a for a I_p=4.0MA, B_t=3.4T plasma; ion losses are due mainly to conduction, P_{cv} and P_{cx} being negligible. To reproduce the measured central ion temperature it is necessary to use a large multiplier for the ion conductivity. The "anomalous" ion transport, including MHD driven ion losses [4] within the q=1 region, can be up to an order of magnitude higher than neoclassical, the departure from neoclassical increasing with plasma current.

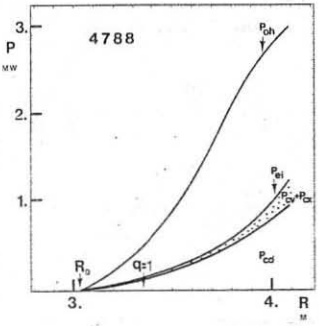

Fig.1a

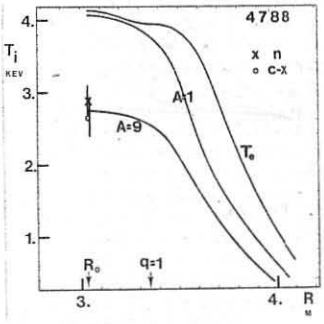

Fig.1b

This treatment of the ion heat diffusion does not allow any further conclusion on its nature but the relative importance of electrons and ions in plasma confinement can be investigated by comparing P_{ei} with the main electron losses.

The electron energy equation is:

$$\frac{dE_e}{dt} = P_{OH} + P_{RAD} + P_{ei} + P_{cv} + P^e_{CD} + P_{iz} \qquad (2)$$

P_{RAD} is the radiation loss, P_{cv} the convection, defined similarly to the ion term, P_{iz} the ionization term.

The ohmic term P_{OH} is computed from the local current density and electric field, derived from the time derivative of the poloidal flux [1]. In JET the resistive voltage is 0.5-0.8V on axis, increasing with poloidal flux to 1.-1.5V at the plasma edge, resulting in up to 3.2MW coupled to the electrons at I_p= 4.0MA with $Z_{eff} \sim 3.0$.

Equation (2) is solved for the electron heat diffusion term P^e_{CD}. The power balance is shown in fig.2a for the same discharge as in fig.1. The ohmic power is lost mainly by coupling to the ions and heat conduction.

The role of electrons and ions in plasma confinement is assessed by comparing electron heat losses P^e_{CD} with P_{ei}. This is shown in fig.3 where P^e_{CD}/P_{ei} is plotted for a large number of discharges against local electron density for various currents at B_t=2.5 and 3.4T. The scatter of the data reflects the uncertainty on the ion neoclassical term, most of which is due to experimental

errors in the region outside the plasma volume considered. The density at which $P^{e}_{CD}/P_{ei} \cong 1$ increases with I_p, from $\sim 1.5 \times 10^{19} m^{-3}$ at I_p=2MA to $\sim 3.\times 10^{19} m^{-3}$ at I_p=4MA, apparently saturating at high current. No toroidal field dependence can be resolved within the data scatter.

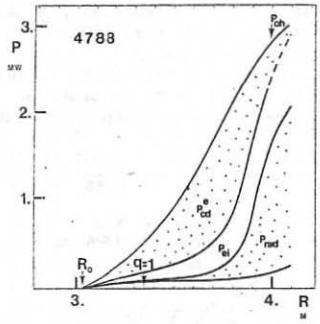

Fig.2a

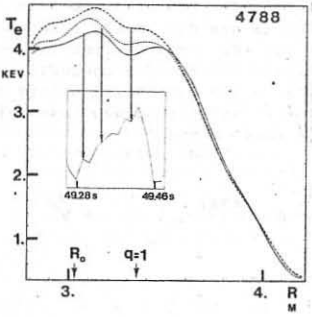

Fig.2b

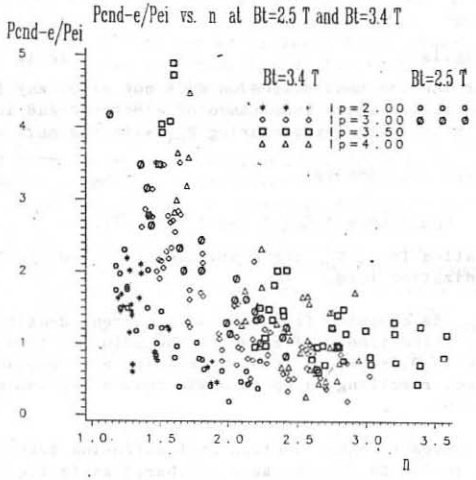

Fig.3

II Plasma Confinement Scaling

The plasma energy confinement in the inner volume V is:

$$\tau_E = \frac{\frac{3}{2}\int_V (n_e T_e + n_i T_i)\,dv}{P_{OH} - \frac{3}{2}\frac{d}{dt}\int_V (n_e T_e + n_i T_i)\,dv}$$

Density scans were performed on JET at different B_t and I_p values. No clear dependence was found for the confinement of the inner plasma on I_p, in contrast with previous results [5]. The scaling of τ_E with density is shown in fig.4; τ_E appears to scale as $n_e^{0.6}$; uncertainties at higher densities (~30%) are related to higher ion losses.

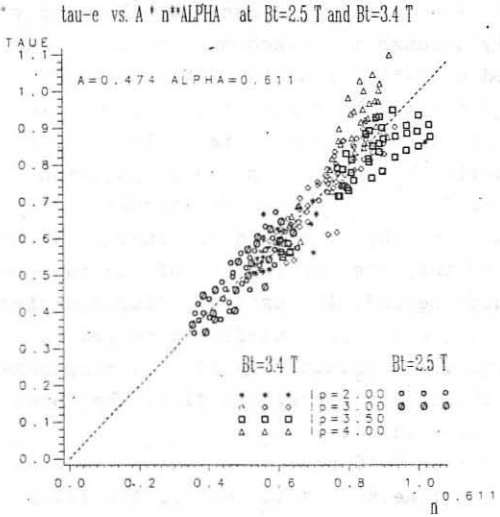

Fig.4

Summary

It is found that in JET ohmic plasmas, ion losses exceed neoclassical values and become dominant, at higher plasma currents, at lower electron densities than previously reported [6]. The total energy confinement time in the radiation free region of the plasma scales less than linearly with n_e, without saturation effects at higher densities. No clear dependence is observed as yet on plasma current and toroidal field.

References

[1] BRUSATI, M. et al. Comp. Phys. Report 1, (1981) 345 and references therein.

[2] TAMOR, S. Journal of Comp. Physics 1 (1981) 104.
GOLDSTON, R., TOWNER, H. Private communication.

[3] CHANG, C.S., HINTON, F.L. Phys. Fluids 25 (1985) 1493.

[4] CORDEY, G.G., STRINGER, T.E. To be published.

[5] EFTHIMION, P.C. et al. "Plasma Physics and Controlled Nuclear Fusion Research", London 1984, Vol.1, IAEA-CN-44/A-I-2 page 29.
EJIMA, S. Nucl. Fusion 22 (1982) 1627.

[6] GONDHALEKAR, A. et al. "Plasma Physics and Controlled Nuclear Fusion Research", Innsbruck 1978, Vol.1, IAEA-CN-37/C-4, page 199.

Study of Electron Heat Conductivity on T-10 by Propagation of a Heat Pulse from ECRH

T-10 Group
Kurchatov Institute of Atomic Energy, 123182, Moscow, USSR

Usual method of determination of the local K_e^B from the energy balance is valid only in low density plasmas when the energy flux is transported largely through the electron (not ion) channel. The K_e^p-value estimated on T-10 /1/ and on other tokamaks by propagation of cooling wave excited by pellet is, as a rule, a few times higher than K_e^B. Similar discrepancy is registered in some experiments when measuring K_e^{ST} by heat pulse propagation from an internal disruption. It is not clear yet whether those discrepancies are the results of the errors in the energy balance component measurements or they are the results of plasma perturbation by such a "dynamic" method. At last, the discrepancies may indicate a complex structure of the heat flux observed in the Ohmic phase: the outward heat conductivity flux is compensated to a great extent, by the inward convective flux. The "heat injection" could destroy this balance.

The K_e^{EC}-value is measured on T-10 also by a heat pulse propagation from ECRH. This technique allows to control the level of perturbation of initial plasma. If the HF-power is absorbed in a narrow region near the ECR-zone then out of it the K_e^{EC}-value averaged through the layer (r_2-r_1) can be found from:

$$K_e^{EC} = 2.3 \frac{(r_2-r_1)^2 \cdot n_e}{t_2-t_1} \cdot /\ln^{-2} \psi(t_2) - \ln^{-2} \psi(t_1)/, \quad (1)$$

where $\psi(t)=(r_2/r_1)^{0.6} \cdot \frac{\Delta T_e(r_2,t)}{\Delta T_e(r_1,t)}$. The T_e-increase, $\Delta T_e = T_e - T_{eOH}$, with ECRH was measured by the EC-radiometer at 4 radii simultaneously. The multidetector imaging system was also used. Additionally, both techniques were used to determine $K_e^{ST} = n_e(r_2-r_0)^2/8\Delta t$, ($r_0$ is the mixing radius, Δt is time of a heat pulse propagation from r_0 to r) /2/. Two regimes were chosen to study K_e^{EC}:

	I_p, kA	$\bar{n}_e$, cm^{-3}	B_t, T	q_L	K_e^B	K_e^{ST}	K_e^{EC}	
					10^{17} $cm^{-1}s^{-1}$ $(r<a_L/2)$			
A	270→290	2.10^{13}	3.15	4.3	2	0.8→1.8	2	OH
					$2\sqrt{T_e/T_{eOH}}$	-	$2\sqrt{T_e/T_{eOH}}$	ECRH
B	170→180	3.10^{13}	3.0	6.5	0.3→0.5	0.3→0.5	0.3	OH
					2	4→5	drastic rise	ECRH

In A-regime /3/ the K_e^B-value has been shown to be equal to 2.10^{17} $cm^{-1}s^{-1}$ in the Ohmic phase and to vary slightly with r. The results of measuring $\Delta T_e(r_j,t)/T_{eOH}(r_j)$ during ECRH with P_{HF}=360→380 kW are given in Fig.1 (curves 1, the data are averaged over 5 discharges). Fig.2 shows the relative T_e-increase $\Psi^*=\Delta T_e(r_j,t)/\Delta T_e(r_k,t)$ for different pairs of r_j, r_k. The Ψ^*-value does not tend to zero at $t\to 0$, what is the result of a wide absorption layer. As

$$\frac{\Delta T_e(r_j)}{\Delta T_e(r_k)}_{t\to 0} \approx \frac{Q(r_j)}{Q(r_k)} \cdot \frac{n_e(r_k)}{n_e(r_j)},$$

the profile of the specific HF-power, Q(r), can be determined from the data shown in Fig.2 and from the measurements of $dT_e/dt_{t\to 0}$ within the layer of the maximum deposit of HF-power (Fig.3). The Q-profile turns out to be too wide to allow the K_e^{EC}-calculation by (1), therefore the transport code was used to determine K_e^{EC}. The good agreement with the experimental results took place at $K_e^{EC}=2.10^{17}\sqrt{T_e/T_{eOH}}$ $cm^{-1}s^{-1}$ (Fig.1, curves 2). Thus, the "dynamic" method gives in A-regime the K_e^{EC}-value which is close to K_e^B. In this regime, the radius r_0 of a region affected immediatly by an internal disruption was shown to be 2→2.5 times larger than that predicted by heuristic theory of /4/. At larger radii a diffusive propagation of heat pulse takes place. However, too rough estimation of r_0 leads to an uncertainty in K_e^{ST}= (0.8 → 1.8).10^{17} $cm^{-1}s^{-1}$.

In B-regime specified in /5/ and in the Table, K_e^B is equal to (0.3→0.5)10^{17} $cm^{-1}s^{-1}$ in plasma interior, $0<r<16$ cm. The X-ray detector signals given in Fig.4[a] indicate that sawteeth can be well described by a diffusive propagation of heat within the region r=7→10 cm (r_s=2.5 cm) in the Ohmic phase of this regime. The perturbation due to internal disruption is small and allow

to measure K_e^{ST} which is shown to be equal to $(0.3 \div 0.5)10^{17}$ cm^{-1} s^{-1} ($r=7 \div 10$ cm). With ECRH the electron heat conductivity rises up to $(4 \div 8)10^{17}$ $cm^{-1}s^{-1}$ in a time not longer than 10 ms (Fig.4^a). The K_e^B-value close to K_e^{ST} was calculated at a steady state of ECRH. At ECRH start-up (Fig.4^b), an increase in a delay time and a rise in the slope of X-ray intensity signals with a distance from the ECR-zone were observed out of the power deposition zone. The simulation pointed out to possibility of appearance of the enhanced transport region which followed the wave front. The enhanced transport appears to be the result of a rise in ∇T_e (or ∇p_e).

Summary.

1. In the regime with high electron heat conductivity $K_e=2.10^{17}$ $cm^{-1}s^{-1}$, K_e^{EC} measured by a heat pulse propagation from ECRH coincides with K_e^B determined from the energy balance. That points to the diffusivity nature of the heat transport in this regime. An increase in K_e under ECRH can be described by the scaling $K_e \propto \sqrt{T_e}$.

2. In the low current regime with high n_e and low K_e /5/ ECRH leads to a steep rise of the electron heat transport. The enhanced transport is saved during the whole ECRH-pulse. The region of the enhanced transport follows the thermal wave front. A possible reason of the enhancement is an instability development due to a rise in ∇T_e (or in ∇p_e). Another reason can consist in that the heat flux directed toward the center can compensate, to a great extent, the heat conduction losses in the Ohmic phase, but this balance is broken when ∇T_e rises under ECRH.

3. Too large value of K_e^p determined by a cooling wave propagation from a pellet is, probably, explained by an extremely strong plasma perturbation by the injection.

References.

/1/. Andreev A.P. et al. Pis'ma JETPh. 10, 1199 (1984)
/2/. Soler M., Callen J.D. Nucl. Fusion. 19, 703 (1979)
/3/. Alikaev V.V. et al. In Plasma Phys. and Contr. Nucl. Fusion Res. 1984, IAEA, Vienna, 1985, v.1, p.419.
/4/. Kadomtsev B.B. Fizika Plasmy. 1, 710 (1975)
/5/. Alikaev V.V. et al. The paper presented to this Conference

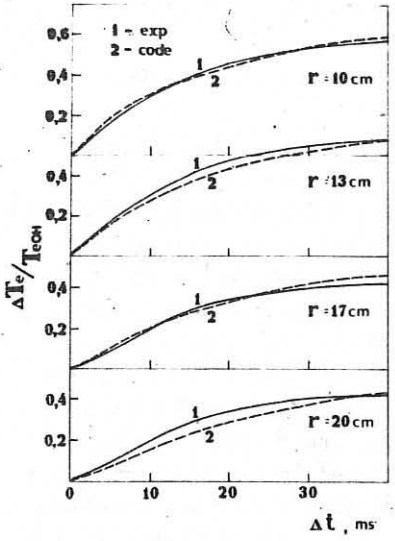

FIG. 1

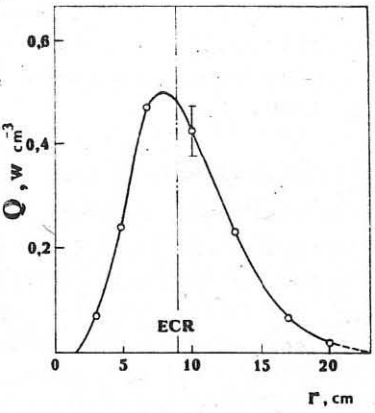

FIG. 3

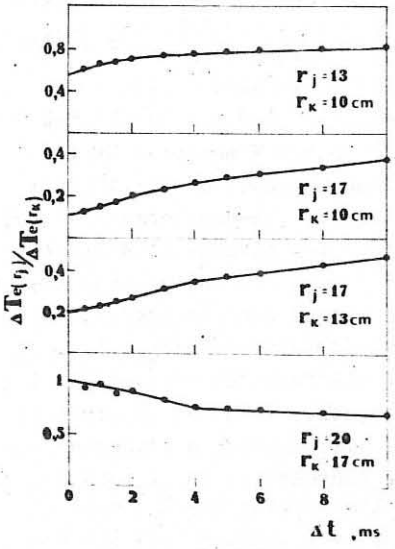

FIG. 2

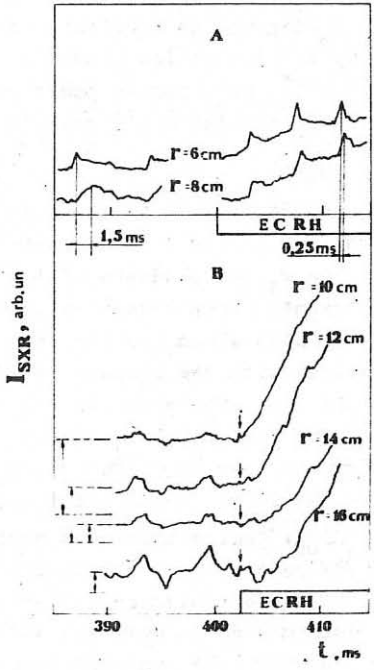

FIG. 4

Energy Confinement Dependence on Plasma Current in T-10 under ECRH

T-10 Group
Kurchatov Institute of Atomic Energy, 123182, Moscow, USSR

In some experiments with auxiliary heating (mainly, NBI) the τ_E-degradation with the P_{aux}-increase was stronger than that prescribed by the Ohmic scaling /1/. However, in the ECRH experiments on T-10 with $P_{aux}/P_{OH} \leq 2$ the degradation in τ_{Ee} and in K_e (electron energy confinement time and the local electron heat conductivity) was shown to follow the Ohmic scaling /2/ ($\tau_{Ee} \propto \langle T_e \rangle^{-0.5}$, $K_e \propto T_e^{0.5}$). The validity of this conclusion at higher values of P_{aux}/P_{OH} was studied in the recent T-10 experiments. The P_{aux}/P_{OH}-increase was achieved by the I_p-decrease. The I_p-dependence of plasma confinement with ECRH was simultaneously studied at low plasma current /2/. The total power $P_{tot} = P_{aux}^{abs} + P_{OH}^{*}$ (P_{OH}^{*} -Ohmic power under ECRH) more than 3 times exceeded the initial Ohmic power P_{OH} in the regime specified below:

	a_L, cm	I_p, kA	B_t, T	$\bar{n}_e$, cm^{-3}	τ_E, ms	$\tau_{Ee}(a_L)$, ms	τ_{Ei}, ms	P_{aux}^{max}, kW
OH	32÷34	170÷180	3.0	2.9×10^{13}	70÷75	120÷140	75	-
ECRH	-"-	-"-	-"-	3.2×10^{13}	45	110	20÷22	560

The P_{tot}-dependence of the plasma energy W measured by the diamagnetic loop under the central ECRH is shown in Fig.1 (B_t = 3.0 T, also shown are the data from the 270 kA-discharge /2/). Together with the results of /2/ concerning plasmas with I_p=270÷500 kA, the data shown in Fig.1 lead to the conclusion that there is no I_p-dependence either in the energy content increase ΔW (under the same P_{tot} and $\bar{n}_e$) or in the behavior of W/W_{OH}, τ_E/τ_{EOH} with the P_{tot}/P_{OH}-variation over the entire range of I_p and P_{tot}/P_{OH}. Taking this into account together with the conclusions of /2/ related to the behavior of electron energy confinement under ECRH one could conclude that the degradation in τ_{Ee} and in K_e during ECRH agrees with Ohmic scaling in the low I_p regime.

However, the energy balance analysis indicates that the be-

havior of τ_E with P_{tot}-variation does not characterize the peculiarities in the behavior of separate components of EC-heated plasma. In Fig.2 we report the measured $T_e(r)$, $T_i(r)$ and $n_e(r)$ along with the heat conductivity coefficients obtained from the energy balance:

$$K_e = \frac{Q_{OH}(r) - Q_{ei}(r) - Q_{rad}(r)}{4\pi^2 . R . r . dT_e/dr} , \qquad K_i = \frac{Q_{ei}}{4\pi^2 . R . r . dT_i/dr} .$$

These profiles, together with the data obtained on T-10 earlier /2/, demonstrate the general features of the profiles of the Ohmically heated plasma parameters at the transition to a high n_e (at which $Q_{ei} \approx Q_{OH}$). These features are: a) the K_e-decrease in the plasma core with relatively weak variation at the periphery; b) the T_e-profile peaking, which should lead to the j-profile peaking, i.e. to the current channel shrinkage. Additionally, the peaked n_e-profile and the neoclassical K_i-values in the plasma core are observed in the regime studied. At the periphery, K_i is rised in comparison with the neoclassical value, which is the formal result of charge exchange (and of diffusion). All these features lead to the high values of τ_{Ee} and τ_{Ei} at the Ohmic phase (see Table). A dramatic rise (8÷10 times) in $K_e(0)$ was observed under the central ECRH. The K_e-increase is remarkably weaker (2 times, Fig.2^c) in the plasma exterior ($r \approx 2/3 . a_L$) which is responsible for the global losses of electron energy. Therefore, $\tau_{Ee}(a_L)$ decreases slightly with ECRH, i.e. the electron losses are not responsible for the τ_E-degradation.

The heat transfer Q_{ei} between electrons and ions is more than doubled and the neoclassical K_i-value is conserved under ECRH. Nevertheless, the T_i-rise is weak, which may be caused by a re-distribution of $Q_{ei}(r)$ to larger radii ($r > a_L/2$) where confinement is much worse. The re-distribution is a result of the n_e-profile change (Fig.2^b). As a result, τ_{Ei} drastically drops and that largely determines the τ_E-degradation.

In the 180 kA-regime the low K_e is connected with the peaked j-profile. If $P_{HF}(r)$ is broader than $P_{OH}(r)$, then the j-profile will be broader. It should lead to a decrease in ΔW after the j(r) skin re-distribution. From this point of view we can explain the T-10 experiments with an outward shift of the ECR-zone

and with ECRH in a 100 kA-regime. The shift of ECR-zone up to a maximum of dj/dr does not change the energy content increase ΔW during the first 30÷40 ms after ECRH-initiation, ΔW being the same as under the central ECRH (Fig.3^a). After this period, a considerable degradation in confinement is observed (Fig.3^b). The same result, but with the central ECRH, is observed in the 100 kA-discharge, where the P_{aux} profile is broader than the P_{OH}-profile. After the ECRH-pulse, the energy content drops below the initial level and then restores for a skin time. The peaked j-profile can be achieved at different n_e dependent on vacuum conditions, i.e. on impurity influx from the walls. Considerably lower values of W obtained previously in the regime with I_p=180 kA, $\bar{n}_e=2.10^{13}$ cm^{-3} /2/ can probably be explained by the fact that a regime similar to that described in the paper has not be achieved at such n_e-value.

Summary.

1. In Ohmically heated plasmas with high density the T_e-profile is peaked. That should lead to the current channel shrinkage. Electron heat conductivity K_e is decreased in the plasma core and is slightly changed at the periphery with $\bar{n}_e$-increase.

2. The energy content increase under ECRH shows no I_p-dependence when the P_{HF}-profile is narrower than the P_{OH}-profile. Also, the degradation in the total electron confinement time $\tau_{Ee}(a_L)$ is in a reasonable agreement with the Ohmic scaling $\tau_{Ee} \propto \langle T_e \rangle^{-0.5}$.

3. When K_e increases drastically under ECRH (in high density plasmas), it does not exceed, nevertheless, the value typical for ECRH in low density regime (when $Q_{ei} \ll Q_{OH}$).

4. The degradation in the global confinement time τ_E under ECRH can, to a great extent, depend on radial profiles of the power input to separate plasma component.

References.

/1/. Goldston R.J. Plasma Phys. and Contr. Fusion. 26, 87(1984) (Proc. of 11th Europ. Conf.)

/2/. Alikaev V.V. et al. In Plasma Phys. and Contr. Nucl. Fusion Res. 1984, IAEA, Vienna, 1985, v.1, p.419

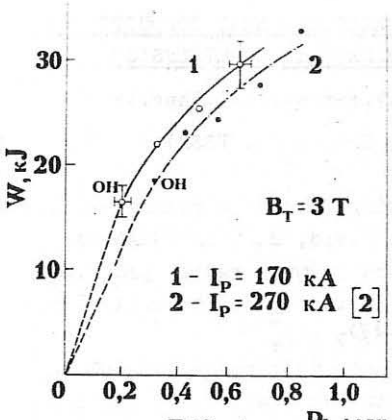

FIG. 1

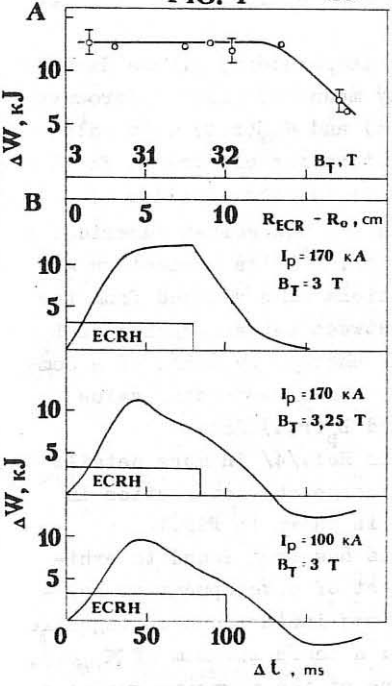

FIG. 3

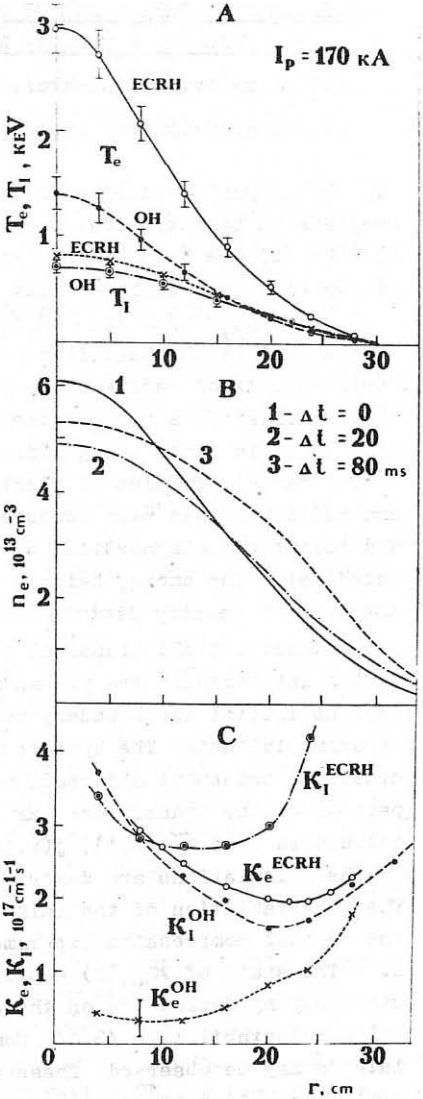

FIG. 2

TEMPERATURE DEPENDENCE OF THE ELECTRON HEAT CONDUCTIVITY IN TUMAN-2A, A TOKAMAK WITH MAGNETIC COMPRESSION

S.G.Kalmykov, S.I.Lashkul, Yu.V.Petrov, I.D.Shprits

(Physical-Technical Institute, Leningrad, USSR)

1. The experiments on ohmic heating (OH) of a plasma and its compression by a toroidal magnetic field, B_T, in TUMAN-2A (R = 40 cm, a_L = 8 cm) /1,2/ resulted in many radial profiles of the effective electron heat conductivity coefficient /3-5/,

$$\chi_{eff}(r) = W_{tr}(r) / (4\pi^2 R r \nabla T_e).$$

Here $W_{tr}(r)$ is the heat flux in electrons through the cylindric surface of radius r and length $2\pi R$ due to heat and particle diffusion, a power gained by the particle flux in a radial electric field being ignored.

The radial profiles of electron temperature, plasma density and radiation loss were measured by means of laser, microwave and bolometric diagnostics. $W_{tr}(r,t)$ and $\chi_{eff}(r,t)$ were calculated using the energy balance equation for electrons. To find the current density distribution, $j(r,t)$, the equation of poloidal magnetic field classical transport was solved numerically taking into account the plasma motion. All its parameters as well as initial and boundary conditions were deduced from the experimental data. The agreement between our assumption on B_p classical transport and reality was checked by means of a comparison of the transformer EMF and the corresponding value calculated from $\sigma(r,t)$, $j(r,t)$ and $B_p(r,t)$ data.

The calculations are described in Ref./4/ in more detail. The time variation of the main discharge characteristics in the typical compression experiment is shown in Fig.1.

2. The shape of $\chi_{eff}(r)$ - profiles has been found to exhibit a strong dependence on the extent of development of helical MHD instabilities /3,4/. Sometimes indications of magnetic islands may be observed. These are: a sharp maximum of $\chi_{eff}(r)$, $\chi_{eff}^{max} > 12 \times 10^{17} cm^{-1} s^{-1}$, at one of the magnetic surfaces with integer q-value (Fig.2a), a high amplitude of B_p oscillations with corresponding m=q, and, in some cases, a local fla-

ttening in $T_e(r)$-profile.

Another situation arises during magnetic de-compression (DC) when B_T decays by a factor 2 in 2 ms and a wide zone free of integer-q surfaces appears in the inner part of the plasma column (Fig.2b). Here τ_{eff} is very small, $\tau_{eff} < 2\times10^{17}\,cm^{-1}\cdot s^{-1}$, close to neoclassical value.

At last, an intermediate case is also realized in the experiment when the surfaces with integer q do exist in the plasma but the tearing modes turn out to be stable. Nevertheless the electron heat conductivity is anomalous, $\tau_{eff} = (4\div9)\times10^{17}\,cm^{-1}\cdot s^{-1}$, (Fig.2c). Such values of τ_{eff} are in Fig.2a out of the maximum or in Fig.2b in the external part of the plasma column where surfaces with q=3and4are localized. This range of τ_e -values is characteristic of tokamaks, typically τ_e varying little over the plasma cross section. The law $\tau_e \simeq 5\times10^{17}\,cm^{-1}\cdot s^{-1} \simeq$ const is known as "Alcator scaling" (see,e.g.,/6/). The anomaly may be due to a microturbulence /7,8/or a magnetic field ergodization /9/ near resonant surfaces. In the present paper we consider just the anomalous electron heat conductivity of the "Alcator scaling" type.

3. It is difficult to find the temperature dependence of τ_{eff}, basing on analysis of $\tau_{eff}(r)$ - profile (even when extremes mentioned in Section 2 are absent), because of strong changing not only T_e but also other parameters in the cross section. It is impossible to vary average $\langle T_e \rangle$ in an ohmic heated tokamak, not changing simultaneously I_p and other discharge features. To define $\tau_{eff}(T_e)$, we selected the values of τ_{eff} at r = 2 to 3 cm in OH as well as in the maximum of compression (C) and in the post-compression phase (PC) (see Fig.1). Here, we used the magnetic adiabatic heating as a currentless heating, a light impurity content being different in the different experimental runs. So, the temperature range in this fixed point was extended up to $100 < T_e < 300$ eV. At r = 2 to 3 cm, q = 1.5÷3, dq/dr was approximately the same in all considered cases, the extremes of $\tau_{eff}(r)$(see Section 2) were absent. At last, the error in τ_{eff} was minimum at this point, $\Delta\tau_{eff}/\tau_{eff} \leq 0.4$. τ_{eff} has been found not to

depend on n_e, B_T, Z_{eff}. τ_{eff} versus T_e is shown in Fig.3. One can see the dependence is weak, it may be approximated by a function $\tau_{eff}(T_e) \sim 1/T_e^{\alpha}$, $0 < \alpha < 1$. Another interpretation may be proposed: $\tau_{eff} \sim 1/T_e$ for $T_e < 200$ eV and $\tau_{eff} \simeq$ const for $T_e > 200$ eV.

4. There is not any difference between the values of τ_{eff} both for the ohmically heated plasma and for compressed one (see Fig.3). Apparently, the physics of the heat transport is the same in both states.

In spite of relatively low T_e and n_e in TUMAN-2A, the result obtained is in a good agreement with that of several large tokamaks: OH and NBI in PLT /10/, OH in FT /11/, OH and NBI (L- and H- modes) in D-III /12/. But it is in a sharp contrast with the ECRH data in T-10 /13/, where $\tau_{eff}(T_e) \sim T_e^{\alpha}$, $0.4 < \alpha < 1.1$. Perhaps, it means that in the ECRH - experiments τ_{eff} is defined by a cause which is characteristic of ECRH itself.

References :

1. M.I.Vil'dzhynas et al.. 10th Eur. Conf. on Contr. Fusion and Plasma Phys., Moscow, 1981, v.1, A-13.
2. S.G.Goncharov et al.. Ibid., v.2, p.172.
3. S.G.Kalmykov et al.. Pis'ma v JETF (JETP Lett.-USSR), 40 (1984), N°8, 334.
4. S.G.Goncharov et al.. Plasma Phys. and Contr. Nucl. Fusion Res. (Proc. of 10th Int. Conf., London, 1984), IAEA, Vienna, 1985, v.1, p.155.
5. S.G.Goncharov et al.. Fizika Plazmy (Plasma Phys.-USSR), 11 (1985), N°9.
6. Yu.N.Dnestrovskij, D.P.Kostomarov. Matematicheskoe Modelirovanie Plazmy (Mathematical Plasma Simulation - USSR), M., 1982.
7. N.V.Ivanov. Fizika Plazmy (Plasma Phys. - USSR), 9 (1983), N°4, 703.

8. Parail V.V., Pogutse O.P.. Pis'ma v JETF (JETP Lett.-USSR), 32, (1980), N°6, 408.
9. R.White. In: Handbook of Plasma Physics , v.1, North Holland Publ. Co., Netherlands, 1983.
10. Eubank H. et al.. Phys. Rev. Lett., 43 (1979),270.
11. Bartiromo R. et al.. Plasma Phys. and Contr. Nucl. Fusion Res. (Proc. of 8th Int. Conf., Brussel, 1980), IAEA, Vienna, 1981, v.1, p.43.
12. M.Nagami et al.. 11th Eur. Conf. on Contr. Fusion and Plasma Phys., Aachen,1983, part 1, p.115.
13. V.V.Alikaev et al.. Plasma Phys. and Contr. Nucl. Fusion Res.(Proc. of 10th Int. Conf., London, 1984), IAEA, Vienna, v.1, p.419.

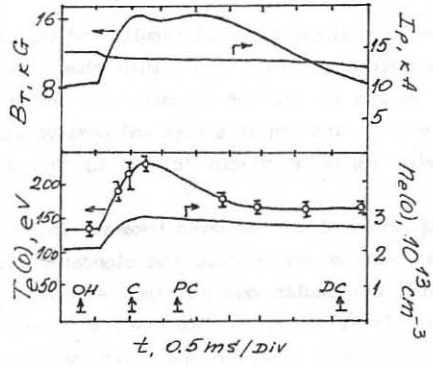

Fig. 1

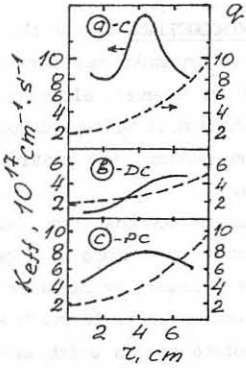

Fig. 2

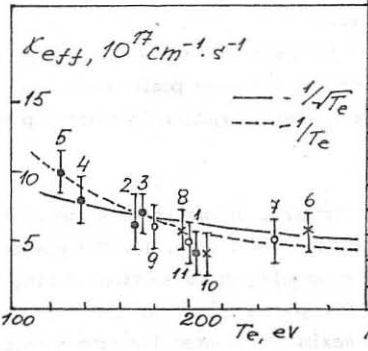

Fig. 3

Point number	Date of exper.	Z_{eff}	n_e (10^{13} см^3)	Phase of disch.	sign
1	Jan. 82	3.2-5	2.6	OH	●
2	— " —	3-4.5	2	OH	●
3	Apr. 83	1.8	1.6	OH	●
4	— • —	1.7	2	OH	●
5	Apr. 81	1.3	2	OH	●
6	May 83	4.1	2.2	C	×
7	— " —	3.3	1.8	PC	○
8	Apr. 81	2.2	2.7	C	×
9	— • —	2.2	2.5	PC	○
10	Apr. 83	2.1	2.4	C	×
11	— " —	2	2	PC	○

POSITIONAL STABILITY OF HIGHLY ELONGATED TOKAMAK PLASMA IN A CONDUCTING SHELL

F. Hofmann, F.B. Marcus and A.D. Turnbull

Centre de Recherches en Physique des Plasmas
Association Euratom - Confédération Suisse
Ecole Polytechnique Fédérale de Lausanne
21, Av. des Bains, CH-1007 Lausanne, Switzerland

I. INTRODUCTION. Recent theoretical and experimental results indicate that elongated tokamaks may have considerably higher beta limits than circular ones [1-4]. However, elongated tokamaks are subject to positional instabilities, which must be suppressed by a combination of active and passive stabilization systems, the passive elements being placed "close" to the plasma surface.

When we consider the startup phase of an elongated tokamak, this problem becomes even more difficult: Let us assume that the elongated plasma will be produced by starting with a circular one and then extending the cross-section until it reaches its final shape. In this case, there will be intermediate states which are positionally unstable and which cannot have conducting walls or passive coils everywhere close to the plasma, since room must be left for further expansion. It is clear that, under these circumstances, the startup phase will be critical.

The basic question which we wish to address in this paper is the following: Are there configurations which will ensure positional stability throughout the startup evolution, as the plasma elongation increases up to a value of four, for example.

II. STARTUP SCENARIO. We assume an axisymmetric plasma whose shape evolves from a circle to a vertical race-track with b/a = 4 (Fig. 1). The plasma is surrounded by a conducting shell with rectangular cross-section. During the startup phase, the plasma shape and its position within the shell are adjusted in such a way as to obtain the maximum wall-stabilization effect.

This implies that the shape will always be a race-track with straight lateral boundaries, and the plasma position will be asymmetric with respect to the midplane (Fig. 1). The equilibria shown here were computed with the FBT code [5], assuming $p' = c_p(\varphi+\ell\varphi^2)$, $TT' = c_T(\varphi+\ell\varphi^2)$, where $\varphi = (\psi-\psi_{lim})/(\psi_{axis}-\psi_{lim})$, $c_T/c_p = R_0^2\mu_0((1/\beta)-1)$, $\beta=0.3$ and $\ell = -0.5$. This gives fairly broad current profiles, which are superior for vertical stability, as will be shown below. The plasma current is assumed to increase with elongation such that q_ψ remains constant at the plasma-vacuum boundary ($q_\psi=2.1$).

In order to determine whether such a scenario is feasible, we analyze the axisymmetric stability of the race-track at four representative "snapshots" during its evolution (Fig. 1). We do not consider here the real-time transition from one equilibrium to the next. We assume that this happens slowly, so that all intermediate states can be considered as quasi-static equilibria. The resistive plasma evolution, as well as shape control problems and the effects of a non-ideal shell will be discussed elsewhere [6].

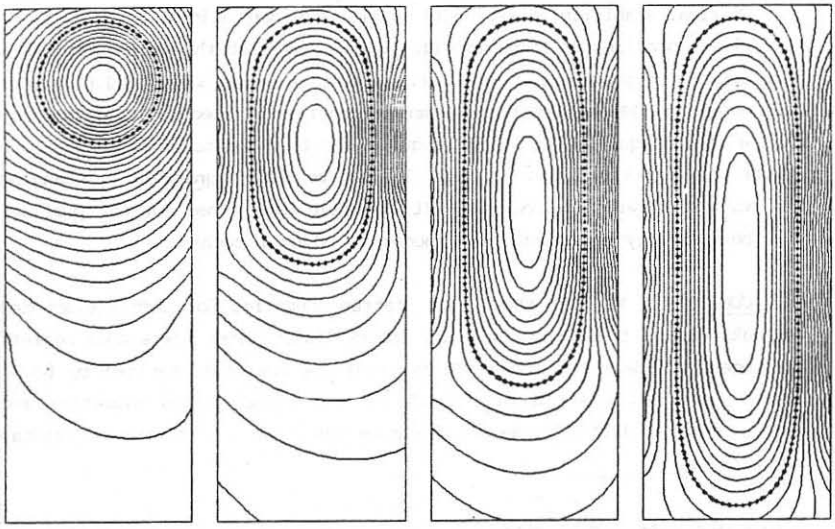

Fig.1.: Startup Scenario for Elongated Tokamak (k= b/a)

III. AXISYMMETRIC STABILITY. We compute the growth rate of the dominant vertical mode by using the FBTS code [7], which assumes an ideal MHD plasma within a perfectly conducting shell. The shell has no gaps so that both toroidal and poloidal image currents can flow freely. Plasma surface currents are excluded.

Figure 2 shows the growth rate as a function of the lateral plasma-wall distance for the four equilibria shown in Fig. 1. The parameter Δ is the distance between the plasma surface and the vertical walls (measured at the height of the magnetic axis) divided by the horizontal minor radius, a. The top-wall distance is assumed constant ($\Delta_{top}=0.22$ at $R=R_o$). Note that the growth rates are normalized by the Alfvén frequency, $\omega_A^2 = B_o^2/(\mu_o \rho_o R_o^2)$, and that negative values of ω^2 indicate stable oscillations whereas positive values imply unstable growth. We observe that for $\Delta \lesssim 0.32$, all four equilibria are stable. Furthermore, we note that the marginal points for k=3 and k=4 almost coincide. This is caused by the cancellation of a destabilizing effect (vertical elongation) and a stabilizing effect (closeness of the bottom wall) as one goes from k=3 to k=4.

Vertical stability is extremely sensitive to variations in the width of the current profile, as shown in Fig. 3. Here, we plot the growth rate as a function of the profile parameter, ℓ. We also show the normalized width, w, defined as the FWHM of the radial current profile, divided by 2a. It is seen that a stable equilibrium which is quite far from the marginal point, such as the one with k=3, ℓ=-0.5 in Fig. 3., can be driven unstable by changing the normalized width by only 7%. It is clear that broad current profiles will be crucially important for a successful startup scenario.

IV. CONCLUSION. We have shown that startup scenarios for highly elongated tokamaks can be found such that all intermediate states are stable against axisymmetric, ideal MHD modes. These scenarios are characterized by broad current profiles (FWHM about 80% of the horizontal plasma diameter) and close lateral walls (plasma-wall distance less than 25% of the horizontal minor radius).

Acknowledgements This work was partly supported by the Swiss National Science Foundation.

References

[1] F. Troyon et al., Plasma Physics 26A (1983) 209.

[2] A. Sykes et al., in Europhysics Conference Abstracts (Proc. 11th European Conf. on Controlled Fusion and Plasma Physics, Aachen 1983) Vol. 7D, Part II, p. 363.

[3] R.D. Stambaugh et al., in Plasma Physics and Controlled Nuclear Fusion Research (Proc. 10th Int. Conf. London 1984) paper IAEA-CN-44/A-IV-2-1.

[4] M. Okabayashi et al., ibid., paper IAEA-CN-44/A-IV-3.

[5] F. Hofmann, Lausanne Report INT 110/82.

[6] F. Hofmann, F.B. Marcus, S.C. Jardin, to be published.

[7] F. Hofmann, F.B. Marcus, A.D. Turnbull, Lausanne, Report LRP 266/85.

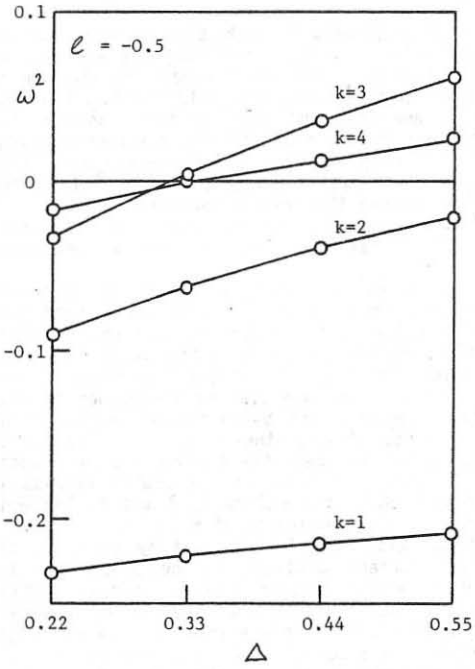

Fig.2. Normalized Growth Rate vs. Plasma-Wall Distance, Δ

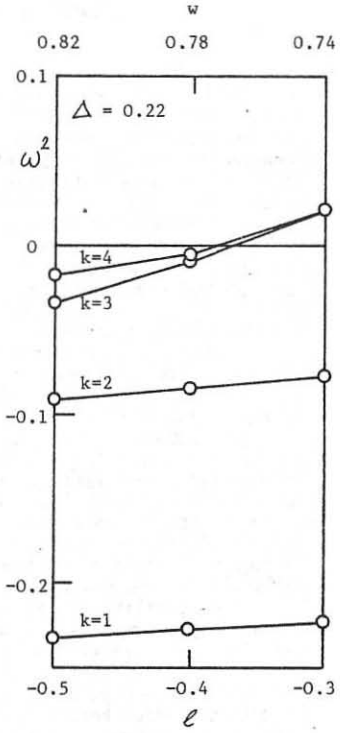

Fig.3. Normalized Growth Rate vs. Profile Parameter, ℓ

HIGH-BETA TOKAMAK STABILITY OF TOROIDAL PLASMAS WITH ELLIPTICAL AND D-SHAPED CROSS-SECTIONS

J.P. Goedbloed, G.M.D. Hogeweij, R. Kleibergen, J. Rem,
Association Euratom-FOM, FOM-Instituut voor Plasmafysica
Rijnhuizen, Nieuwegein, The Netherlands

R.M.O. Galvão
Laboratorio de Estudos Avançados, Centro Técnico Aerospacial
São José dos Campos, São Paulo 12200, Brazil

P.H. Sakanaka
Instituto de Física "Gleb Wataghin", Universidade Estadual de Campinas
Campinas, São Paulo 13100, Brazil

Global and local stability of high-beta tokamak plasmas with various current- and pressure profiles and with different cross-sections are studied with the numerical programme HBT [1]. A high-beta tokamak equilibrium is characterized by the shape of the cross-section, the value of $\varepsilon\beta_p$ (inverse aspect ratio times beta poloidal), and unit profiles for the quantity $\Gamma(\psi)$ (which reduces to the current density at $\varepsilon\beta_p = 0$) and the pressure gradient $\Pi(\psi)$. At the magnetic axis, $\psi = 0$ and $\Gamma(0) = \Pi(0) = 1$. The average beta $\langle\beta\rangle/\varepsilon$ and $\varepsilon\beta_p$ are related through $\varepsilon\beta_p = \eta(\langle\beta\rangle/\varepsilon)q^{*2}$. Here, $\eta \equiv S/\pi a^2 e^2$ (= 1 for a circle), is a geometric factor involving the area S and the elongation $e \equiv L/2\pi a$ of the cross-section, and q* represents the toroidal current "safety factor": $q^* = aLB_0/(\mu_0 R_0 I_\phi)$. The global stability is thus represented in a $\varepsilon\beta_p$ versus q* diagram.

In Ref. [2], we investigated the global stability of various equilibria with a circular cross-section. Stability studies of equilibria with broad current profiles where q_1/q_0 takes on values between 1.5 and 2.0 (q_1 = safety factor at the boundary, q_0 = safety factor on the magnetic axis) show that at large currents ($q^* \sim 1$-3) global stability is largely determined by the external kinks m = 2,3 and the internal modes m = 1,2. At low values of $\varepsilon\beta_p$, the external kinks lead to unstable regions just below integer values of q* (no stabilizing wall). At higher values of $\varepsilon\beta_p$, these regions (adjacent to q_1 = 1,2, etc.) widen and merge with the ones due to the internal modes (adjacent to the curves q_0 = 1, 2, etc.). This results in stable islands in the $\varepsilon\beta_p$ - q* plane along the q*-axis above the values 1, 2 and 3. The most stable plasmas are found for currents corresponding to $q^* \approx 2$.

The stability of the external kinks can be affected by changing the current-density profile. A smaller current gradient at the plasma surface leads to a decrease of the unstable regions. Having chosen a simple profile function $\Gamma(\psi)$, and keeping q* fixed, such a decrease of the current gradient also decreases the value of q_0. Thus, a change in the profile $\Gamma(\psi)$ such that the external modes become more stable is accompanied by a motion of the q_0 = 1 and q_0 = 2 curves (and also the adjacent regions of the internal modes) in the $\varepsilon\beta_p$-q* plane to lower values of the current, i.e. to higher values of q*. Consequently, the internal m=1 mode will affect the stable region near $q^* = 2$ when the curve $q_0 = 1$ has moved too far to the right. One might argue

that to limit this motion of the $q_0 = 1$ and 2 lines as much as possible, one should change the current gradient only near the plasma surface and keep the profile as flat as possible near the magnetic axis. However, this has the undesired effect of decreasing the shear near the magnetic axis, which causes the unstable regions of the internal modes to come down to much lower values of $\varepsilon\beta_p$. Therefore, it is better to combine a small current gradient near the plasma boundary with a sizeable shear near the magnetic axis. This leads to the following choice of the profile functions:

$$\Gamma(\psi) = (1-\psi^2)(1-\psi) + 4.5\psi^2(1-\psi)^2; \quad \Pi(\psi) = (1-\psi^2)(1+40\psi) \qquad (1)$$

which, for a circular plasma, give rise to a stable beta of $\langle\beta\rangle/\varepsilon = 0.082$ at $q^* = 1.97$.

For elliptical and D-shaped plasmas, the same current- and pressure profiles (1) also result in optimum values of beta. The main difference between an elliptical plasma with $b/a = 1.2$ and a circular one is that the first one permits larger currents: the entire stable region is shifted to lower values of q^* [optimum: $\langle\beta\rangle/\varepsilon = 0.11$, $\varepsilon\beta_p = 0.365$, $q^* = 1.83$] (Fig. 1).

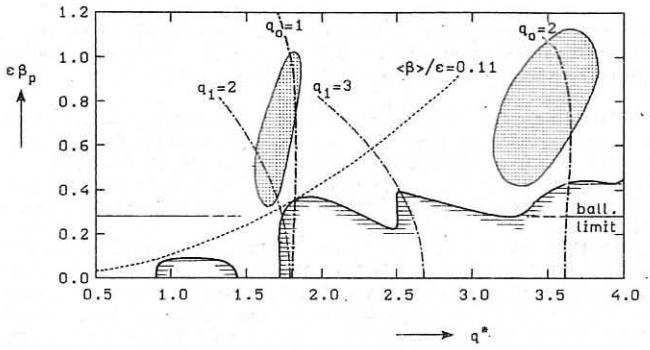

Fig. 1. Stability boundaries for the equilibrium corresponding to Eq. (1) in an elliptical cross-section ($b/a = 1.2$). The two shaded regions are unstable to the internal m=1,2 modes (wall on the plasma). The stable regions in the absence of a wall are situated on the shaded side of the thick lines. The dotted lines indicate the loci where q at the plasma surface is given by $q_1 = 2,3$; the dash-dotted lines are the loci where q on the magnetic axis is given by $q_0 = 1$ and 2.

In addition, the unstable regions for the internal m=1 and 2 modes widen as compared to those of the circle [3]. The stability of the D-shaped cross-section is very similar to that of the ellipse (Fig. 2). Also here the major effect is a shift of the lines of marginal stability to higher currents, thus permitting higher values of beta to be reached than for a circular plasma [$\langle\beta\rangle/\varepsilon = 0.11$, $\varepsilon\beta_p = 0.36$, $q^* = 1.84$]. The effect on the unstable regions of the internal modes is, however, just opposite of that of the ellipse. Here, the regions corresponding to the internal m=1 and 2 not only shrink, but also move up to higher $\varepsilon\beta_p$. It is precisely this aspect of the D-shape which for $b/a = 1.4$ and $c = 0.2$ results in a higher value of stable beta than obtained for the ellipse $b/a = 1.4$ [optimum of D-shape $b/a = 1.4$, $c = 0.2$: $\langle\beta\rangle/\varepsilon = 0.135$, $\varepsilon\beta_p = 0.40$, $q^* = 1.77$].

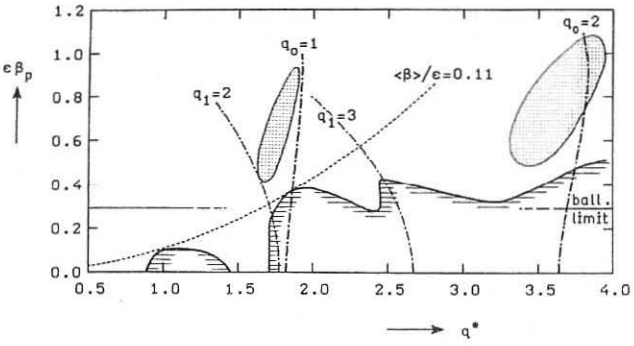

Fig. 2. Stability boundaries for the equilibrium corresponding to Eq. (1) in a D-shaped cross-section (b/a = 1.2, c = 0.1). Internally unstable and externally stable regions are indicated as in Fig. 1.

The ballooning stability boundary for a high-beta tokamak plasma consists of a simple limit in $\varepsilon\beta_p$: the plasma is unstable for $\varepsilon\beta_p$ surpassing a critical value which is independent of the value of q* (Ellipse b/a = 1.2: $\varepsilon\beta_p$ = 0.28; D-shape b/a = 1.2, c = 0.1: $\varepsilon\beta_p$ = 0.29). These limits show the well-known feature, viz. that the D-shape is more stable to ballooning modes than the ellipse.

The fact that the ballooning limits for the ellipse and the D-shape are lower than those set by the global modes raises the question whether the critical beta of these configurations is not determined by the ballooning modes. This is true for the configurations discussed above because these results were optimized only for stability of global modes, and not of ballooning modes. However, a simple change of the pressure profile makes it possible to improve upon the stability of the latter modes. By replacing $\Pi(\psi)$ of (1) by the expression:

$$\Pi(\psi) = [(1-\psi^2)(1+40\psi)]^{\nu_\pi}, \qquad \nu_\pi = 0.3 \qquad (2)$$

the ballooning limit for the D-shape (b/a = 1.2, c = 0.1) increases to $\varepsilon\beta_p$ = 0.38 whereas this limit was $\varepsilon\beta_p$ = 0.29 for ν_π = 1. This change in $\Pi(\psi)$ hardly affects the global stability, so that we reach the conclusion that, as far as the optimum stable beta is concerned, the limit in beta is set by the stability of the global modes only. The same conclusion holds for the circle and the D-shape b/a = 1.4, c = 0.2.

The profile functions $\Gamma(\psi)$ and $\Pi(\psi)$, that result in the optimum betas for the various cross-sections, originated from an analysis of the circular cross-section, where we had concluded that the equilibrium leading to an optimum beta should have q* ≈ 2 and $q_0 \approx 1$. With respect to optima for arbitrary values of q* (current), we obtained results from the following equilibrium:

$$\Gamma(\psi) = [(1-\psi^2)(1-\psi)+4.5\psi^2(1-\psi)^2]^{\nu_\Gamma}, \quad \Pi(\psi) = [(1-\psi^2)(1+40\psi)]^{0.3}. \qquad (3)$$

For ν_Γ = 1 this equilibrium corresponds to the ones discussed above, while for ν_Γ > 1 it yields equilibria with the line q_0 = 1 shifted towards higher values of q*. From the results for a number of equilibria (various

ν_T's) for the D-shaped (b/a = 1.2, c = 0.1) and for the circular cross-section, the following picture emerges. For q* in the neighbourhood of the optimum (ν_T = 1) the envelope of optimum $\langle\beta\rangle/\varepsilon$'s is determined by the stability of the global modes, while beyond the region where the external m=3 kink becomes unstable the envelope is formed by the ballooning limit and q_0 = 1. When this is plotted in a Troyon diagram ($\langle\beta\rangle/\varepsilon$ versus the toroidal current, or e/q*) it results into curves for the circular and for the D-shaped cross-section, below which stable equilibria belonging to (3) exist (Fig. 3).

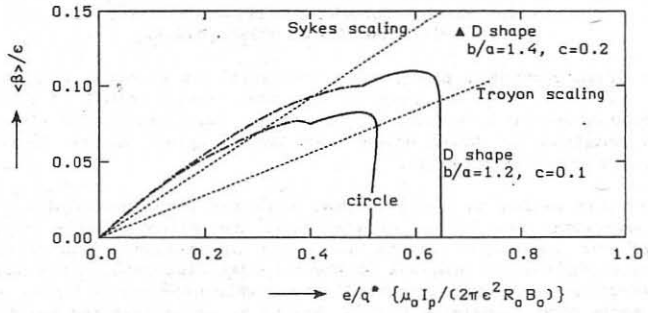

Fig. 3. Kink and ballooning stable betas as functions of the toroidal current for a circular and a D-shaped cross-section (b/a = 1.2, c = 0.1). The drawn curves indicate that the limit is set by the kink modes and the dash-dot curves indicate that the limit is set by the ballooning modes.

Clearly, for fixed plasma cross-section, the curve of optimum $\langle\beta\rangle/\varepsilon$ is not a simple straight line, as suggested by the Troyon and Sykes scaling laws

$$\langle\beta\rangle/\varepsilon = f\cdot\mu_0 R_0 I_\phi/(2\pi a^2 B_0), \quad f_T \equiv 0.14, \quad f_S \equiv 0.22 ,$$

but the optima obtained do fall within the range indicated by these laws.

Acknowledgement

This work was performed under the Euratom-FOM association agreement. It was supported financially by the "Stichting for Fundamenteel Onderzoek der Materie" (FOM), the "Nederlandse Organisatie voor Zuiver-Wetenschappelijk Onderzoek" (ZWO), Euratom, the "Fundaçao de Amparo à Pesquisa do Estado de São Paulo", the "Conselho Nacional de Desenvolvimento Cientifico e Technológico", and the "Comissão Nacional de Energia Nuclear" (Brazil).

References

[1] Galvão, R.M.O., Goedbloed, J.P., Rem, J., Sakanaka, P.H., Schep, T.J., Venema, M., 9th Int. Conf. on Plasma Phys. and Contr. Nucl. Fusion Res., Baltimore, September 1982 (IAEA, Vienna, 1983) Vol. III, p. 3.
[2] Goedbloed, J.P., Hogeweij, G.M.D., Kleibergen, R., Rem, J., Galvão, R.M.O. Sakanaka, P.H., 10th Int. Conf. on Plasma Phys. and Contr. Nucl. Fusion Res., London, September 1984 (IAEA, Vienna, 1985) Vol. II, p. 165.
[3] Manickam, I., Nucl. Fusion 24 (1984) 595.
[4] Troyon, F., Gruber, R., Saurenmann, H., Semenzato, S., Succi, S., 11th Eur. Conf. on Contr. Fusion and Plasma Phys., Aachen, September 1983; Plasma Phys. 26 (1984) 209.

High $\langle\beta_t\rangle$ Studies In The PBX Tokamak*

H. Takahashi, K. Bol, D. Buchenauer, P. Couture, R. Fonck, B. Grek, G. Gammel, W. Heidbrink, K. Ida, K. Itami, G. Jahns, R. Kaita, S. Kaye, H. Kugel, B. LeBlanc, K. McGuire, N. Ohyabu, M. Okabayashi, M. Reusch, G. Schmidt, S. Sesnic, F. Tenney+ and H. Yamada
Plasma Physics Laboratory, Princeton University
Princeton, N.J. 08544, U.S.A.

The PBX (Princeton Beta Experiment) tokamak[1] is a device with the ultimate aim of achieving high β operation in the second region of stability for ballooning modes by indenting the plasma on its inboard side ("bean shape"). Results obtained to date, which have been limited to the first stability region, are reported here [2].

The operating region is shown in Fig. 1 in terms of the poloidal β_p and the volume averaged toroidal $\langle\beta_t\rangle$ based upon the square of the toroidal field averaged over the plasma crosssection. The plasma boundary is defined here as the flux surface containing 95% of the poloidal flux between the magnetic axis and either the separatrix or the limiter, whichever comes first. A between-shot moments code calculates both β_p and $\langle\beta_t\rangle$, using measured poloidal fluxes, coil and plasma currents as constraints, and assuming a constant on-axis q value ($q_0 = 0.8$). If data from a recently implemented internal diamagnetic loop is used as an additional constraint to replace the q_0 assumption, values of $\langle\beta_t\rangle$ would be somewhat different. However, the new analysis has not yet been completed and all data reported here are based upon the constant q_0 method of $\langle\beta_t\rangle$ determination. The data set in Fig. 1 contains 659 discharges whose parameter ranges are summarized in the table. The operating region is a roughly triangular area in the β_p - $\langle\beta_t\rangle$ plane. The left-hand boundary of the triangle is set by the low current limit of operation. The lower boundary represents the limit of low q operation. The remaining boundary is the so-called β limit. Most high $\langle\beta_t\rangle$ discharges are near the confluence of the low q and β limits - a complicating factor for MHD study of the disruptive discharge termination.

The operating region is cast in a different form in Fig. 2: $\langle\beta_t\rangle$ is plotted against a "critical" value $\beta_c \equiv \mu_0 I_p/(a\langle B_t\rangle)$, where a is the plasma half-width at midplane and $\langle B_t\rangle$ is the toroidal field averaged over the plasma crosssection. Except for the choice of the averaged toroidal field, the critical β_c is identical to the parameter used by Troyon and Gruber[3], who derived a β limit, based upon the external kink instability in the absence of conducting shells, as $\langle\beta_t\rangle < C\beta_c$ with $C = (2.0 \sim 2.5)$. All data obtained in PBX to date fall below this limit with the higher choice of the coefficient. The beta limit for PBX, based upon the ballooning instability lies at a higher level[4] ($C = 2.8 \sim 3.1$). The low q limit is roughly a vertical line in Fig.2.

The PBX operation is still confined within the first region of stability, but its range in terms of $\langle\beta_t\rangle$ is extended greatly from that of its predecessor, PDX. In fact, the highest $\langle\beta_t\rangle$, 5.3% at an indentation of 0.19 and neutral beam injection power of 4.0MW, is, in absolute terms, a record value for major tokamaks. The increased current-carrying capacity of the plasma due to strong

+deceased

shaping - elongation and indentation, that leads to higher β_c, is responsible for the extension of the operating range. The equivalent cylindrical q value, $q_{cyl} \equiv 2\pi \langle a \rangle^2 B_t(0)/(\mu_0 R_p I_p)$, where R_p is the plasma major radius, $B_t(0)$ is the toroidal field at the geometrical axis and $\langle a \rangle$ is the radius of a circular plasma that would have the same crosssectional area as the indented plasma, reached as low as 1.0, whereas q_{edge} remained equal to or above 2.5 for indented plasmas. While indentation and elongation are closely coupled for PBX and their effect on the lowest achievable q_{cyl} is difficult to determine separately, no other major tokamak has attained this low value of q_{cyl}, even at elongations comparable to those of PBX. It is thus inferred that strong indentation also increases the current-carrying capacity.

Near the Troyon-Gruber limit, say, $\beta_n \equiv \langle \beta_t \rangle / \beta_c \geq 1.8$, the discharge either disrupts during the period of maximum beam power, or experiences (often abrupt) saturation in $\langle \beta_t \rangle$. Even within this restricted segment of the operating parameter space, a rich variety of MHD phenomena is observed, and no unique sequence of events appears to be ascribable to the disruptive termination of the discharge or $\langle \beta_t \rangle$ saturation. Studies of $\langle \beta_t \rangle$ saturation are further complicated, sometimes by transition into the H-mode often accompanied by impurity accumulation. The richness of MHD phenomena may in part reflect the fact that different segments of the operating region must be reached via different routes. For example, the high $\langle \beta_t \rangle$ ($\geq$ 4.0%, say) segment in Fig. 1 or 2 is also the high I_p (low q_{edge}) region, which can be reached in PBX only by rapidly ramping up I_p. These high dI_p/dt discharges have strong skin-effect, and are inferred to have a broad current profile needed to form strongly indented flux surfaces. These plasmas typically have a moderately high β_n (~2.0), low q_{edge} ($\leq$ 3.5), high dI_p/dt($\geq$ 1.5 Ma/sec), and a strong indentation ($\geq$ 0.18).

A high dI_p/dt discharge invariably has a series of sawteeth with an increasingly long period, and the disruption is preceded by what appears to be a long (~ 100 ms) sawtooth period. The level of MHD activities observed through Mirnov probes and soft X-ray detectors is generally low. In one subclass of these discharges, a typical sawtooth precursor precedes the disruption. In another, the precursor is distinctly different: little MHD activity is discernible on soft X-ray signals originating from the plasma center, and the Mirnov signal frequency is lower than one commensurate with central plasma rotation speed. Signals from a Mirnov coil and a neutron emission detector are shown in Fig. 3 for such a discharge. The disruption occurred just after the end of the data window at about 575 ms. There are a series of sawtooth relaxations, with an accompanying drop in neutron emission. A growing precursor oscillation is non-sawtooth-like and has a frequency around 8 kHz. The growth time just (a few cycles) before the disruption is about 120 μs, which is somewhere between the ideal MHD and resistive instability time scales. Throughout the operating region in Fig. 1 or 2, all MHD modes that have been examined are found to have a small toroidal mode number (mostly unity) and a small (2 ~ 4) poloidal mode numbers.

Fishbone activity is generally an order of magnitude lower in PBX than in PDX. For example, the discharge shown in Fig. 3 has the highest $\langle \beta_t \rangle$ obtained to date, but only one small fishbone burst is visible during the entire discharge. This reduction in fishbone activity is attributable in part to the fact that PBX is heated by two perpendicular and two parallel beams while PDX was heated by four perpendicular beams. Parallel beams contribute less to excitation of fishbone instability because of a broader spectrum of fast ion precession frequency.

*This work supported by the United States Department of Energy Contract No. DE-AC02-76-CHO-3073.

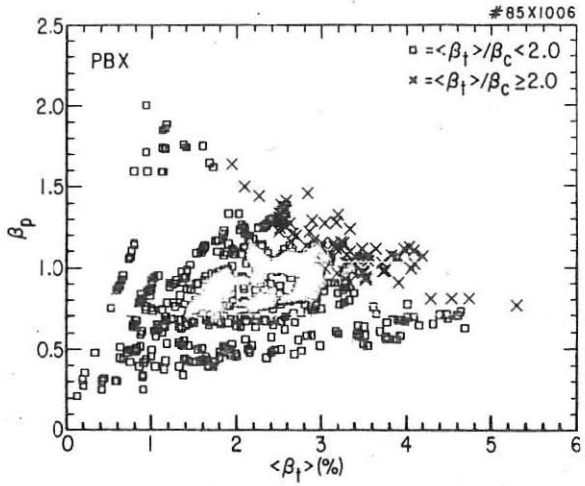

Fig. 1. Operating range of PBX in terms of the poloidal β_p and volume-averaged toroidal $\langle\beta_t\rangle$. The data points with the normalized β_n greater than 2.0 are identified by the symbol X.

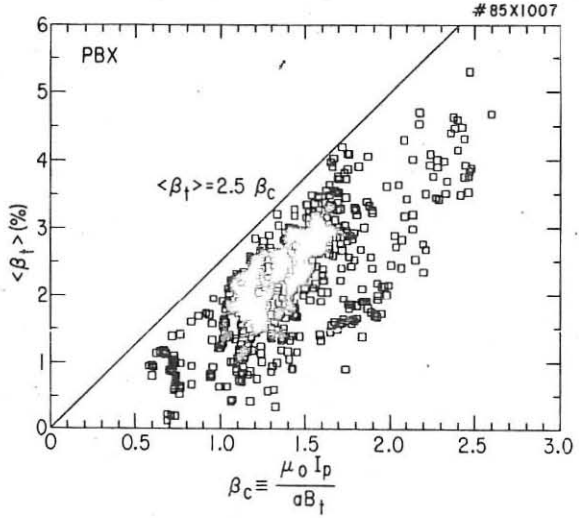

Fig. 2. Plot of the volume-averaged toroidal $\langle\beta_t\rangle$ vs. critical β_c.

Fig. 3. Signals from (a) Mirnov probe and (b) neutron detector in a discharge with broad current profile in PBX.

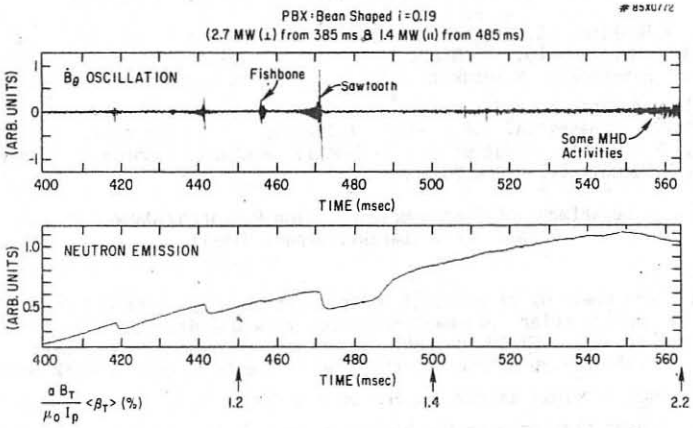

Table: Range of PBX Parameters

$B_t(0)$	0.7 - 1.4T	toroidal magnetic field at geometrical center
I_p	< 600 kA	plasma current
R_p	1.42 - 1.56 m	major radius
a_{mid}	0.29 - 0.41 m	midplane half-width
P_b	< 5.5 MW	injected neutral beam power
q_{edge}	> 2.5	edge q value (indented plasmas)
q_{cyl}	> 1.0	equivalent cylindrical q value
i	< 0.22	indentation
κ	< 1.86	elongation
δ	< 0.34	triangularity
$\langle \beta_t \rangle$	< 5.3%	volume-averaged toroidal β
$\beta_t(0)$	< 16.2%	on-axis toroidal β

References

1. M. Okabayashi et al, Plasma Physics and Controlled Nuclear Fusion Research 1984 (IAEA, Vienna, 1985), Vol. 1, 229
2. H. Takahashi et al, PPPL Report 2227, Plasma Physics Lab., Princeton University, Princeton, N.J., June 1985
3. F. Troyon and R. Gruber, Report LRP 239/84, Centre de Recherches en Physique des Plasmas, Assocaition Euratom-Confederation Suisse, Ecole Polytechnique Federale de Lausanne, 21, av. des Bains, CH-1007 Lausanne, Switzerland
F. Troyon, et al, Plasma Physics and Controlled Fusion 26 (1984) 209
4. A. Todd, Private Communications

High Beta and Confinement Studies in the JFT-2M Tokamak

T.Shoji, K.Hoshino, S.Kasai, T.Kawakami, H.Kawashima, M.Maeno, T.Matoba, T.Matsuda, H.Matsumoto, Y.Miura, M.Mori, K.Odajima, H.Ogawa, T.Ogawa, H.Ohtsuka, S.Sengoku, N.Suzuki, H.Tamai, Y.Tanaka, Y.Uesugi, S.Yamamoto, T.Yamamoto, T.Yamauchi, M.Hasegawa*, K.Ohta*, S.Takada**, I.Yanagisawa***, A.Funahashi, K.Hasegawa, A.Honda, I.Ishibori, T.Kashimura, Y.Kashiwa, M.Kazawa, K.Kikuchi, Y.Matsuzaki, K.Ohuchi, H.Okano, T.Shibata, T.Shibuya, T.Shiina, K.Suzuki, T.Tani, K.Yokoyama

Department of Thermonuclear Fusion Research, JAERI
Tokai, Naka, Ibaraki, Japan, 319-11

ABSTRACT

After the power up of poloidal power supplies, high beta and confinement studies of non-circular plasma (ellipticity $\kappa \leq 1.6$) without divertor are first done in the JFT-2M tokamak. The volume averaged toroidal beta limits have a similar q_ψ-dependence to that due to the n=1 external kink mode instability (q_ψ : flux safety factor at plasma boundary). It is demonstrated that the plasma shaping with the higher triangularity as well as ellipticity is effective in order to obtain a higher beta value. The energy confinement time in ICRF and/or NBI heating increases with the electron density, plasma current and ellipticity and decreases with the heating power.

APPARATUS

JFT-2M [1,2] plasma has a D-shaped configuration with R=1.31m and a x b = 0.35m x 0.53m minor cross section, maximum plasma current I_p of 550kA and maximum toroidal field B_t= 1.42T. The plasma boundary is determined by graphite limiters. ICRF power up to 1.8MW is launched with an array of three loop antennas from the high field side in the two-ion-hybrid heating regime. NBI power up to 1.5MW is injected from a co- and a counter-injectors with the injection angle of 38 degrees to the plasma axis.

NON-CIRCULAR PLASMA CONTROL AND LOW-q OPERATION

A positional instability of non-circular plasma is controlled by the hybrid control method using upper and lower vertical field coils. Observed growth rate of positional instability without the feedback control is 500/s at $\kappa \simeq 1.6$. This value is consistent with the calculation, which includes passive feedback effects of vacuum vessel and poloidal coils, and image current in an iron core. A variety of plasma shapes covering a wide range of ellipticity (κ=1.0-1.6) and triangularity (δ=0-0.6) are obtained. Especially, the triangularity can be widely changed at fixed ellipticity, to clarify the dependence of critical beta on the triangularity. Obtained minimum q_ψ is nearly 2 ($q_L \simeq 1.5$, $q_L = 5\, a^2\, B_t\, R^{-1}\, I_p^{-1}\, (1+\kappa^2)\, /\, 2$).

On leave from * Mitsubishi Electric Co., ** Mitsubishi Electric Computer Systems Tokyo Co., *** Mitsubishi Atomic Power Industries Inc..

ENERGY CONFINEMENT STUDIES

The energy confinement time for non-circular plasma is investigated in the wide parameter range with ICRF and/or NBI heating : B_t = 0.5 - 1.42T, I_p = 165 - 500kA, q_ψ = 2 - 5, κ = 1.0 - 1.6, $\bar{n}$ = (0.5/OH - 6/Heating) x 10^{13} cm^{-3}, $P_{RF} \leq 1.8$ MW, $P_{NBI} \leq 1.5$ MW. The beta value is determined by the magnetic field fitting method [3]. This value agrees with that by using the kinetic data of the circular plasma within 20% difference. As shown in Fig.1, gross energy confinement time increases with line-averaged electron density $\bar{n}$ in both ICRF and NBI heating cases ($\tau_{EG} \propto R\, I_p^2\, \beta_p / P_T$, $P_T = P_{OH} + P_{RF} + P_{NBI}$, where P_{RF} and P_{NBI} are injected powers). This dependence is different from that in L-mode experiments [4,5]. And also it increases with ellipticity (Fig.2(a)) and with plasma current I_p ($I_p^{0.55}$ at low power and $I_p^{0.9}$ at high power, Fig.2(b)), but decreases with total power P_T and is almost independent of toroidal field B_t. These dependences are expressed approximately in the following formula (Fig.3) :

$$\tau_{EG}^{2M} \simeq 20\, R^2(m)\, a(m)\, \bar{n}_{13}^{p}\, [I_p^q(MA) / P_T^r(MW)]\, (1+\kappa^2)/2 \quad (ms)$$

where $\bar{n}_{13} = \bar{n} / 10^{13}$ cm^{-3}, $p \simeq 1 \pm 0.2$, $q = 0.55 - 0.9$, $r \simeq 0.75 \pm 0.15$, and the dependence of τ_{EG} on R^2a is assumed from the neo-Alcator scaling.

HIGH BETA STUDIES

High beta studies of non-circular plasma are done by ICRF and/or NBI heating at high B_t ($\simeq$ 1.2T) and by NBI heating at low B_t (< 1T). Obtained beta values are : $\beta_t \simeq 2\%$ for B_t = 1.2T, $P_T \simeq$ 3MW, κ = 1.43 and $\beta_t \simeq 3\%$ for B_t = 0.65T, $P_T \simeq$ 1.6MW, κ = 1.43. These beta values are limited by confinement and total heating power. Dependences of critical beta on plasma shaping (especially triangularity) are, therefore, investigated at low B_t and small κ ($\leq$ 1.3). Experimental results indicate , as shown in Fig.4, that the dependence of the beta limit on q_ψ is similar to that due to the kink mode instability [6]. Although JFT-2M has a conducting wall of stainless steel of 2.5cm in thickness and 0.415m x 0.595m in radius, the kink mode is unstable for some current distribution [7]. The details are now being investigated. Also, Fig.4 shows that the plasma shaping with higher triangularity is effective in order to obtain a higher beta value, especially $q_\psi \simeq 2$.

ACKNOWLEDGEMENT

The authors are grateful to Drs. T.Takeda, S.Tokuda and T.Tsunematsu for their fruitful discussions on the beta limit and to Drs. S.Mori, Y.Iso, and M.Tanaka for their continuous encouragements.

REFERENCES

[1] SHOJI,T., et al.,in Controlled Fusion and Plasma Physics (Proc. 11th Europ. Conf. Aachen, 1983) ;vol.1 (1983) 55.
[2] MORI,M., et al.,in Plasma Physics and Controlled Nuclear Fusion Research (Proc. 10th. Int. Conf. London,1984), vol.1, IAEA, Vienna (1985) 445.
[3] SWAIN,D.W. and NEILSON,G.H., Nuclear Fusion 22 (1982) 1015.

[4] NEILSON,G.H., et al., Nuclear Fusion 23 (1983) 285.
[5] NAGAMI,M., et al., in Plasma Physics and Controlled Nuclear Fusion Research (Proc. 9th Int. Conf. Baltimore, 1982) vol.1, IAEA, Vienna (1983) 27.
[6] TUDA,T.,ibid. (Proc. 10th. Int. Conf. London. 1984) vol.2, IAEA, Vienna (1985) 173.
[7] TSUNEMATSU,T., et al.,in this conference, "Stability of external kink mode of tokamak".

FIGURE CAPTIONS

Fig.1 Dependence of gross energy confinement time on line-averaged electron density and total input power.

Fig.2(a) Gross energy confinement time versus ellipticity.
(b) Gross energy confinement time versus plasma current.

Fig.3 Gross energy confinement time scaling for JFT-2M tokamak.
τ_{EG}^{2M} (p=1,q=r= 0.75) : Scanned parameter ranges are B_t = 0.5-1.42 T, I_p = 165-500kA, q_ψ = 2-5, κ = 1.14-1.6, $\bar{n}$ = (0.5/OH -6/Heating)x10^{13} cm^{-3}, $P_{RF} \leq 1.8$MW, $P_{NBI} \leq 1.5$MW.

Fig.4 Critical beta limit dependence on safety factor q_ψ and triangularity δ. Solid lines correspond to the upper bounds of attainable β_t for δ = 0.4 and 0.2. Broken lines correspond to theoretical calculations for the kink instability.

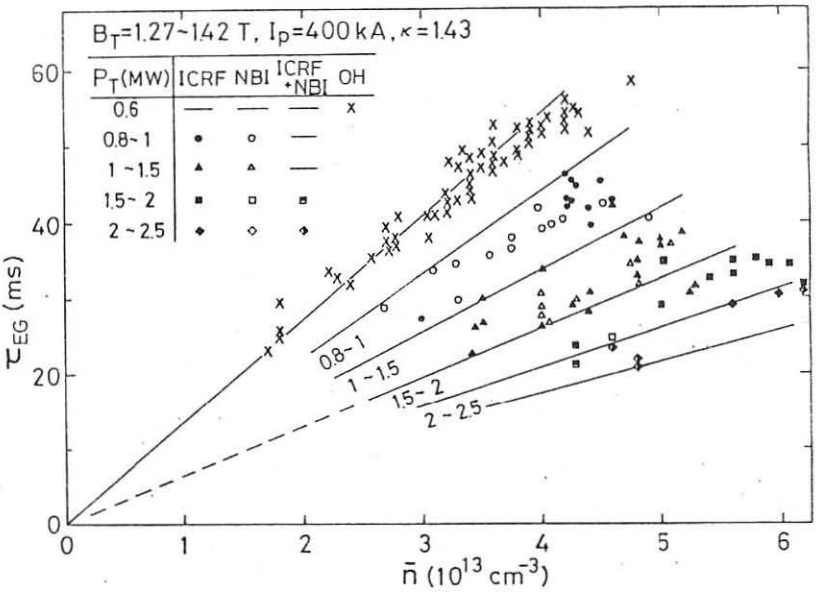

Fig. 1

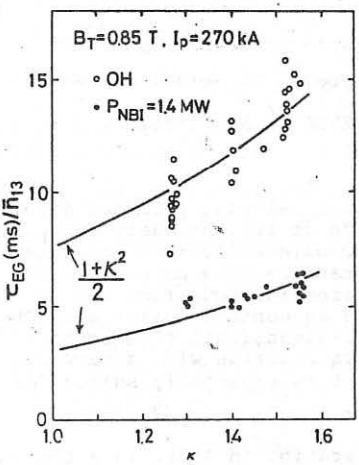

Fig. 2 (a)

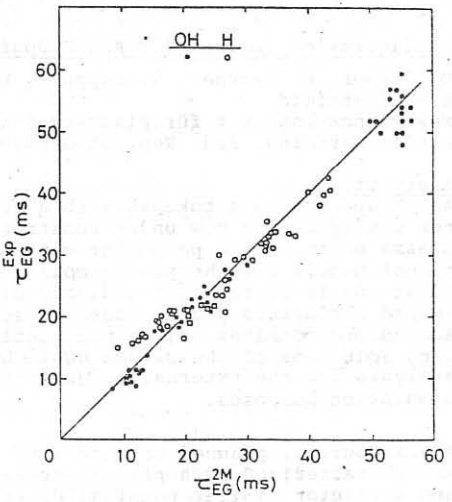

Fig. 3

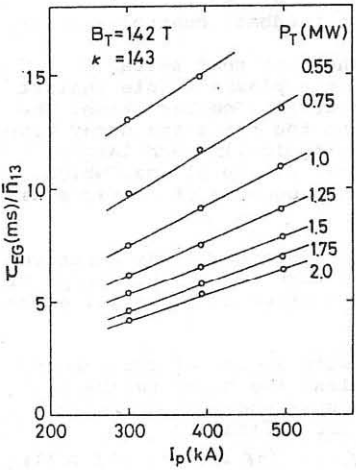

Fig. 2 (b)

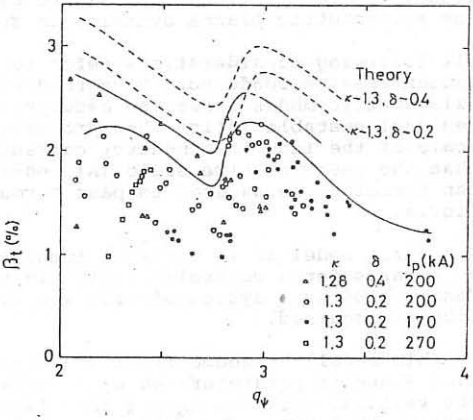

Fig. 4

Configuration Control for ASDEX Upgrade

O. Gruber, K. Lackner, G. Lappus*, H. Preis, U. Seidel, H. Woyke*, H.-P. Zehrfeld
Max-Planck-Institut für Plasmaphysik, EURATOM Association, D-8046 Garching, Fed. Rep. of Germany

Abstract
ASDEX Upgrade is a tokamak with a reactor relevant poloidal divertor configuration now under construction at IPP. As basis for plasma position and parameter control considerations two computational models for the plasma-coil interaction were developed. The first one is in terms of ordinary differential equations for lumped parameters and supposed to serve as control design aid. The second one combines self consistently 2-dimensional flux conserving solutions of the plasma equilibrium equation with a network analysis for the external conductors. It is especially suited for simulation purposes.

ASDEX Upgrade, planned to come into operation in 1988, is a tokamak characterized by a plasma current capability of 1.6 - 2 MA, and a reactor similar poloidal divertor configuration. To simulate in it, in addition to the plasma boundary physic and the plasma wall interaction also the configuration control problems of a fusion reactor, it has been designed with the poloidal field coils outside the toroidal ones and distant from the plasma. Due to this, and its strongly elongated plasma cross-section (b/a = 1.6 - 1.9), feedback control of position and shape of the plasma is a central issue. Two computational modes have been developed to describe the axisymmetric plasma dynamics in such feedback control studies.

All following considerations refer to the case that suitably chosen passive conductors have rendered the plasma stable against axisymmetric modes under the assumption of flux conservation. The residual unstable motion then proceeds on the resistive decay time scale of the induced conductor currents, typically much larger than the inertial time scale (Alfven-time) of the plasma, which can therefore be assumed to pass through sequences of static equilibria.

The first model is in terms of lumped parameters and was contrived as a basis for a controler design in the time domain where a plant description by a system of ordinary first order differential equation is required.

In this model the geometry of a plasma with a general cross-section shape is parameterized by 3 variables: the major radius R_c, the vertical position Z_c and the plasma cross-section area expressed by a mean minor radius a. They are defined by

$$\int_{F_p} R\,df = R_c \int_{F_p} df \qquad \int_{F_p} z\,df = Z_c \int_{F_p} df \qquad \int_{F_p} df = \pi a^2 \tag{1}$$

*TU München

With normalized coordintes $\tilde{x} = (R-R_c)/a$ and $\tilde{z} = (Z-Z_c)/a$ any distributed magnitude can be expressed by $v = v_c \cdot \tilde{v}(\tilde{x},\tilde{z})$. It is a basic assumption of the model to consider $\tilde{v}(\tilde{x},\tilde{z})$ as constant. In this case the standard definition of inductivity

$$L_{ik} = \frac{1}{J_i J_k} \int_{\tilde{F}_i} \psi_{ik} j_i \, dF \tag{2}$$

is consistent for both flux and energy considerations also for distributed currents and will be employed.

A detailed balance of the variations of all energy contributions of the system due to varying geometrical parameters finally reduces to

$$dW_{el} + dQ = dW_{pol} + dW_{tor} + dU_{th} \tag{3}$$

where $W_{pol,tor}$ is the total poloidal, toroidal magnetic field energy, U_{th} the thermal plasma energy, W_{el} the inductive part of the electric energy delivered by the toroidal current sources and Q the net plasma heating energy.

Applying the 1st law of thermodynamics equ. (3) becomes

$$dW_{el} = dW_{pol} + dW_{tor} - p\,dV \tag{4}$$

With the notations of (1) to (2) and the assumption of toroidal flux conservation in- and outside of the plasma the evaluation of the terms of (4) to the lowest order of the aspect ratio leads to 3 equilibrium equations:

$$\frac{1}{2} \sum_i \sum_k J_i J_k \frac{\partial L_{ik}}{\partial R_c} R_c = -2\pi p_c A_p R_c a^2 + W_T' \qquad \text{(a)}$$

$$\frac{1}{2} \sum_i \sum_k J_i J_k \frac{\partial L_{ik}}{\partial a} \frac{a}{2} = -2\pi p_c A_p R_c a^2 - W_T' \qquad \text{(b)} \tag{5}$$

$$\sum_i \sum_k J_i J_k \frac{\partial L_{ik}}{\partial z_c} = 0 \qquad \text{(c)}$$

where the sums have to be taken over all toroidal current circuits, $A_p = \int \tilde{p}\, d\tilde{f}$ and W_T' is an energy related to the plasma's diamagnetism.

Second variation of equ. (4) shows that in the usual regime ($a^2 A^2 \gg 1$, $\beta_t \ll 1$) transitions between equilibria under flux conservation in the plasma column are dominated by the high energy content of the toroidal field, which for time independent main coil currents enforces

$$\frac{a^2}{R_c} = const. \tag{6}$$

With it (5a) and (5b) can be combined to

$$\sum_i \sum_k J_i J_k \frac{dL_{ik}}{dR_c} = -8\pi p_c A_p a^2 = -\mu_0 J_p^2 \beta_{pol} \tag{7}$$

which is identical with Shafranow's formula for the applied equilibrium field.

The equations (5c), (6) and (7) are supplemented by an equation for the plasma's thermal behaviour which for adiabatic variations around a given equilibrium becomes

$$\beta_{pol} = \beta_{pol\,0} \left(\frac{J_{p0}}{J_p}\right)^2 \left(\frac{R_{c0}}{R_c}\right)^{2\varkappa - 1} \tag{8}$$

The model is finally completed by the flux equations for all poloidal field generating circuits. For the K-th of n circuits one obtains

$$U_K = R_K J_K + \sum_i \left(L_{iK} \dot{J}_i + J_i \left(\frac{dL_{iK}}{dR_c} \dot{R}_c + \frac{\partial L_{iK}}{\partial z_c} \dot{z}_c \right) \right) \qquad (9)$$

The formulation of the equations allow for the use of different models for the plasma current distribution and its variation: e.g. the superposition of volume and surface currents, or the representation by a sum of modes. Furthermore the model can be adjusted to two-dimensional solutions of the plasma equilibrium equation, by evaluating the expressions in (1) and (2) from an actually computed start equilibrium.

Given the nominal trajectories for all currents I_{no}, the plasma geometry and β_{po} a linearized version of the model equations (5c), (6), (7), (8) and (9) constitutes the plant representation required for a systematic controler design and for fast simulation.

For the application of the outlined model to ASDEX Upgrade the induced vessel currents were taken into account in terms of modes of the poloidal vessel current distribution. For this purpose the vessel was modeled by a system of 60 toroidal line currents linked by magnetic and ohmic (by the resistivity of the bellows) coupling. This surogate network was subjected to an eigenvalue analysis and the self and mutual inductivities of the resulting eigenmodes were calculated with the definition of equ. (2). Since the influence of the higher modes on the plasma position can be neglected the consideration was restricted to the two dipole and the two quadrupole moments.

The second, two-dimensional plasma model which will be applied is that of isentropic and flux conserving sequences of static MHD equilibria representing the plasma motion.

The corresponding computational procedure uses the fact that for given toroidal plasma current density j_T the poloidal magnetic flux of a free-boundary plasma configuration in an external conductor system can be written as

$$\psi(x,t) = \psi^*(x,t) + \frac{1}{4\pi^2} \iint_{\partial R} \frac{G(x,x')}{R'^2} \nabla' \psi^*(x',t) \cdot dS' + \mu_0 \sum_{k=1}^{N} G(x,x_k) I_k(t) \qquad (10)$$

$$R^2 \, div \frac{\nabla \psi^*}{R^2} = -\mu_0 R j_T \qquad (11)$$

$$I_k = I_k(U_1(x_1,t), \ldots U_n(x_n,t); U_e, R, \Omega) \qquad (12)$$

$$U_i(x_k,t) = -\iiint_{G(\psi_3,t)} G(x_k,x') \frac{\partial j_T(x',t)}{\partial t} d^3x' + \frac{1}{2\pi} \iint_{\partial G(\psi_3,t)} G(x_k,x') \frac{\partial \psi(x',t)}{\partial t} \frac{dS'}{|\nabla \psi|} \qquad (13)$$

$$G(x,x') = \frac{2}{k} (RR')^{1/2} \left\{ (1 - \tfrac{1}{2} k^2) K(k) - E(k) \right\} \qquad (14)$$

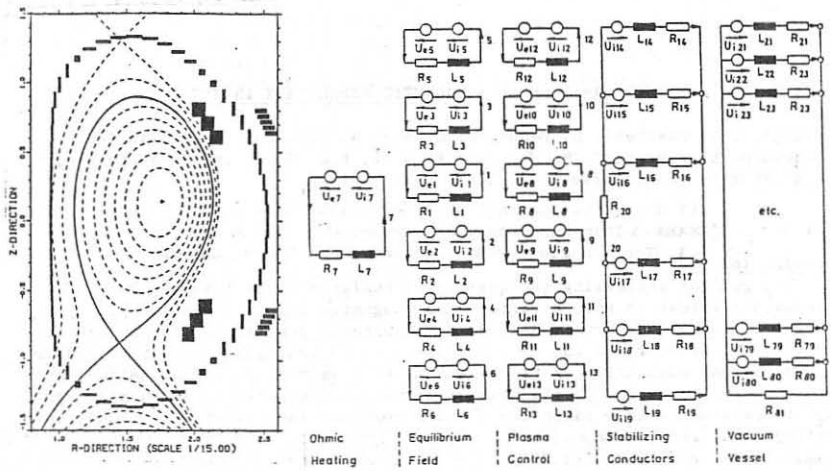

In (10) Ψ^* is the solution of the partial differential equation (11) satisfying the boundary condition $\Psi^*/\partial\mathbb{R} = 0$, where $\mathbb{R}$ is a rectangular part of the R-z plane enclosing the plasma region $\mathbb{G}$; G is the Green's function (14). The $I_k(t)$ ($k = 1, N$) represent the currents in passive and active external conductors and the $U_i(x_k,t)$ the corresponding induced voltages due to variations of plasma current density and plasma position. The currents I and the voltages U_i are related by the equations (12) which represent the electromagnetic interaction of plasma and conductor systems and are quasi-analytic solutions of corresponding circuit differential equations /1/. The U_e are current-controlling source voltages; R and L symbolize resistances and inductances of the tokamak electrical circuit (K and E are the complete elliptical integrals K and E with the modulus $k^2 = 4RR'/((R+R')^2 + (z+z')^2)$).

The system of equations must be closed adding the expression for j_T required by plasma equilibrium and flux and entropy conservation: $j_T = j_T(R, J_o(\Psi), p_o(\Psi))$, where $J_o(\Psi)$ and $p_o(\Psi)$ are poloidal current and pressure distributions in the plasma at an initial time /2/. The figure shows a typical ASDEX Upgrade separatrix-bounded initial plasma equilibrium and the corresponding equivalent circuit of the external conductor system which are subject of the model studies.

/1/ H. Preis, H.P. Zehrfeld,"Modelling of plasma dynamics in conducting shells", Proceedings 13th SOFT, Varese (Italy), 1984

/2/ F. Casci, A. Kaleck, H.P. Zehrfeld, "Equilibrium configuration and positional stability control for INTOR/NET". NET-Report No. 27, EUR _II 324/27, pp. II-1 - II-40.

THE FORMATION OF A MAGNETIC SEPARATRIX IN JET

A. Tanga, D.J. Campbell, B. Denne, A. Gibson, N. Gottardi, A. Kellman†, E. Lazzaro, K.F. Mast, G. McCracken*, P. Noll, F.C. Schüller, P. Stangeby*, D.D.R. Summers, A.J. Tagle, P.R. Thomas, M. Valisa

JET Joint Undertaking, Abingdon, Oxon, OX14 3EA, U.K.
*UKAEA Culham Laboratory, Abingdon, Oxon, OX14 3DB, U.K.
†G.A. Technologies, P.O. Box 85608, San Diego, Ca. USA

Introduction

The goal of increasing the quality of confinement in tokamaks has led to a renewed interest in the "divertor" and "magnetic limiter" configuration in which the plasma boundary is defined by a magnetic separatrix, detached from the material limiter and the vacuum vessel. Such a configuration may afford improved thermal insulation of the plasma as well as reduced contamination from impurities. The region at the plasma boundary may be able to sustain a high edge temperature with a large temperature gradient when substantial additional heating is applied. Such a so-called "H mode" shows a much reduced radial transport compared to the "L mode" (1,2,3). In this paper the initial results and the experimental observations on the formation of a magnetic separatrix in ohmic JET discharges are presented.

Analysis of the magnetic configuration

The transformation of a closed plasma boundary into one with a separatrix can be regarded as an extreme case of plasma shaping for which a particular mode of operation of the poloidal circuit is required. A poloidal cross section of the JET configuration is shown in Fig.1. The iron circuit, the equilibrium coil PF4 and the shaping doublet PF2 and PF3 are clearly shown. The field produced by the coils PF2-PF3 is largely quadrupolar and is suitable for the control of the plasma elongation. A field is also produced by the primary coil, especially when the primary carries its full current, due to the local saturation of the iron.

This field has a strong hexapolar component and changes the triangularity of the plasma. In practice, a stagnation point can be produced near the top-bottom of the vessel by cancelling the predominantly horizontal plasma poloidal field.

The relative contribution of the field produced by the coil PF2 and of the primary can be seen by plotting the horizontal field produced by the current in the coil PF2 in the top of the vessel for a case in which the current of the primary was large and a case in which the current of the primary was zero.

This effect is shown in Fig.2 in the upper and lower curve, respectively. The formation of a magnetic separatrix is possible, either by having a large current in the coil PF2, or at the end of a long plasma current pulse due to the effect of the field produced by the primary. The combination of these two fields makes possible the formation of a magnetic separatrix at large values of plasma current.

The magnetic diagnostic of the configuration is based on the equilibrium identification calculations performed with the JET code IDENT B suitably modified for accurate determination of the field null location. As reported elsewhere (4,5), the code solves an inverse equilibrium problem finding the free boundary solution of the Grad-Shafranov equation which fits best the magnetic measurements of flux and poloidal field. To locate the separatrix in the first approximation, an initial run of the code is made.

Using a spline interpolation routine the separatrix line is traced and its

intersection with the equatorial plane is taken as a new boundary position. The successive runs converge easily to the solution, if the initial case is not pathological. As a consequence, the relevant parameters of the flux and current distribution such as the safety factor at the magnetic axis, the value of poloidal beta and that of the internal inductance are determined, within the accuracy of the magnetic data (6).

Experimental results

The separatrix configuration has been maintained for several seconds on discharges with plasma currents of 1.5MA and 2.0MA. The value of the toroidal field was 2.6T, the line average density was $1.0.10^{19} m^{-3}$.

In the 1.5MA discharge shaping has been obtained by applying a pulse on the coils PF2-PF3 only, with nearly zero current in PF1. A plot of the poloidal flux contours is shown in Fig. 3.

The separatrix configuration for the discharges at 2.0MA plasma current has been obtained all along the final five seconds of a tokamak discharge lasting for twenty seconds, needed to bring the current in the primary coil to a high negative value. The poloidal flux plot is shown in Fig. 4.

The presence of the two null points located approximately 10-15cm inside the vessel is apparent. The plasma is well detached from both the limiter and the inner vessel. This was also confirmed by the absence of H_α emission from these surfaces. The high value of triangularity $\delta = 0.46$ for the discharge in Fig. 4 is a consequence of the hexapolar moment produced by the PF1 coil. The IR camera viewed a poloidal section of the vessel.

Areas of intersection of the plasma with the inconel protection plates were clearly visible. In Fig. 5, the intensity along the poloidal cross section of the vessel is shown. The intensity, within a window centred around the wavelength of 0.9μ, shows two maxima separated by 24cm which are in correspondence of the left and right intersection of the magnetic separatrix with the bottom of the vacuum vessel, in good agreement with the plot of the poloidal flux. The properties of the edge plasma during the 1.5MA experiments have been measured using an array of four Heat Flux/Langmuir probes as described in ref. (7). Three probes face the ion drift side and are located at distance 1,4,8cm from the array tip and one facing the electron drift direction is located 1cm from the array tip. The major radius position of the probe on the torus was $R_p = 3.252$m and the array was moved up-down in the vertical direction between $1.71 < Z < 1.76$, Z being the distance between the probe array tip and the equatorial plane of the machine.

Fig. 6 gives an example of the ion saturation current density (particle flux density) radial profile. As can be seen, the e-folding length on the electron-drift side $\lambda = 57$mm is about twice that on the ion drift side, $\lambda = 28$mm. The reasons for this difference are still under investigation. Measurements of radiated power have been performed by a multi-channel array bolometer camera, described elsewhere (8).

The signals along the viewing lines pointing to the regions of the X point were up to ten times larger than the average.

The generalised Abel inversion of the radial profile, excluding the channels affected by the enhanced radiation around the X points shows that, for the 1.5MA discharges, most of the radiated power comes from the outer regions of the plasma. The total radiated power can be described as the sum of the power which is radiated by the whole valome of the plasma ≅450kW and the power which is radiated in the regions of the X points ≅250kW. The total ohmic input power was 780kW.

A preliminary analysis of the spectral lines of the impurities shows that the nickel content of the discharge was very low and well below 0.1%, whilst the concentration of oxygen and carbon was of the order of 1%; both these values are comparable with the concentrations of an equivalent limiter JET

discharge.

References

1) F.L. Hinton et al, in Plasma Physics and Controlled Nuclear Fusion, Tenth Conference proc., London 12-19 Sep. 1984, IAEA Vienna 1985, vol.II p.3.
2) M. Okabayashi et al, ibid., vol.I p.229.
3) C.E. Singer et al., to be published in Nucl.Fus.
4) J. Blum, J. Le Foll, B. Theoris, JET Workshop on Magnetic Measurements Culham 1980.
5) M. Brusati et al, Comp. Phys. Rep. 7-8 345 (1984).
6) M. Brusati et al, Proc, Workshop on Diagnostics for Fusion Reactor Conditions, Varenna 1982 p.235.
7) P.C. Stangeby et al, this conference.
8) N. Gottardi, H. Krause, K.F. Mast, this conference.

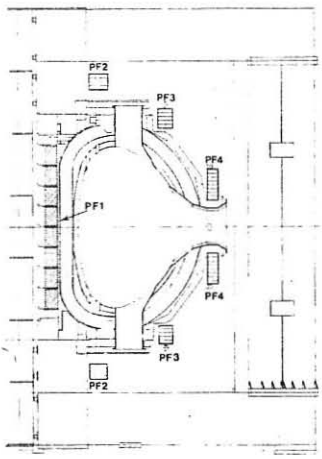

Fig. 1
Cross section of JET showing position of poloidal field coils (PF).

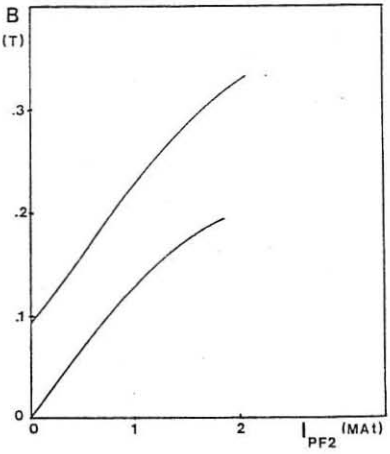

Fig. 2
Horizontal field produced by the PF2 coil current at the tip of the vessel (T). Upper curve is with a large primary current, lower curve is with zero primary current.

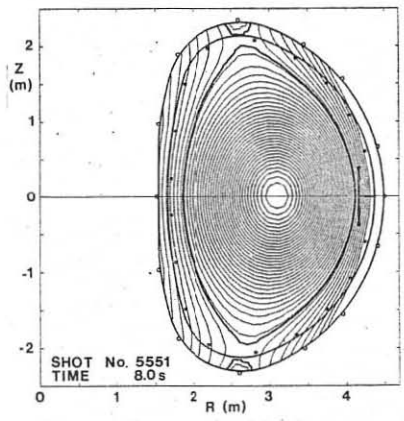

Fig. 3
Poloidal flux contours in the plasma: current 1.518MA, poloidal beta 0.26, internal inductance 1.29, plasma elongation 1.75.

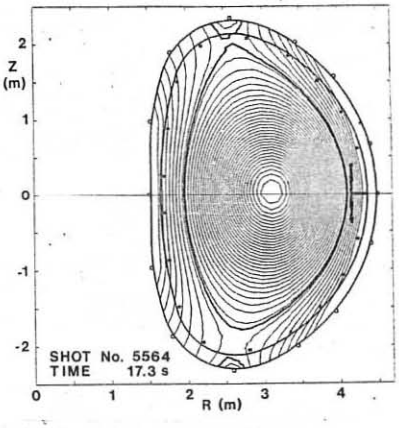

Fig. 4
Poloidal flux contours in the plasma: current 1.995MA, poloidal beta 0.09, internal inductance 1.4, plasma elongation 1.8.

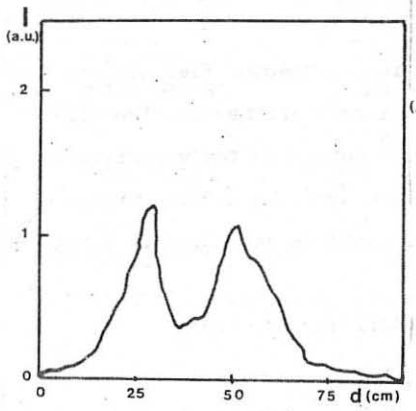

Fig. 5
Intensity of infrared emission along the protection plates as a function of the distance.

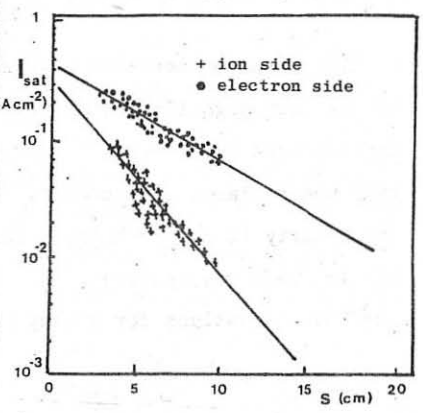

Fig. 6
Ion saturation current measured in the plasma scrape-off layer versus the distance from the plasma edge.

Vaporization Model of Pellet under Fusion Plasma Conditions

Ming lun Xue Xiao Li
Institute of Mechanics, Chinese Academy of Sciences,
Beijing, China

Abstract

A gas-dynamic model of pellet vaporization under fusion plasma conditions is analysed. It is proved that the bremsstrahlung radiation from the dense vaporized medium absorbed by pellet surface is the dominant energy source to vaporize the pellet while energy from heat conduction only plays an indirect effect.

To operate a contineous work fusion reactor fuel pellets inject into high temperature plasma core are needed. The size and injected velocity of the pellet depend on the vaporization rate under plasma environment. Since near the pellet surface the density is rather high, model based on gas- dynamic principles seems reasonable.

The basic equations for steady spherical flow are:

$$\rho u r^2 = G_T$$

$$\rho u \frac{du}{dr} = - \frac{dp}{dr}$$

$$\rho u \left(c_p \frac{dT}{dr} + u \frac{du}{dr} \right) = \frac{1}{r^2} \frac{d}{dr} \left(r^2 \lambda \frac{dT}{dr} \right) - \kappa \rho^2 T^{\frac{1}{2}}$$

$$p = \rho R T$$

here p, ρ, T, u, R, λ, c_p are notations of pressure, density, temperature, radial velocity, gas constant, heat conductivity and specific heat of the vaporized medium , the last term of energy equation is expressed as bremsstrahlung radiation, K is a constant.

The boundary conditions are r=a, $T = T_a$; $r \to \infty$, $T \to T_\infty$, a is the radius of the pellet.

The vaporization mass flow rate is determined by the energy absorbed by the pellet surface,

$$G = \frac{4\pi a^2}{L}\left[\left(\lambda \frac{dT}{dr}\right)_a + q_r\right]$$

here q_r is the radiation energy absorbed by the pellet and L is the latent heat of the pellet.

It is shown energy from heat conduction alone is far from enough to explain the experimental vaporization rate. To make an upper estimation, neglect the br. radiation and $u\frac{du}{dr}$ in the energy equation, the mass flow rate can be expressed as,

$$\frac{G}{a} = \int_{T_a}^{T_\infty} \frac{\lambda\, dT}{h - h_a + L}$$

here h is enthalpy, since $\lambda = cT^{5/2}$ for high temperature plasma,

$$\frac{G}{a} \approx \frac{c}{c_p} \cdot 0.4 \cdot T_\infty^{5/2}$$

and the life time of a pellet with initial radius a is,

$$\tau_p = \int_0^{\tau_p} dt = 0.4\, \frac{\rho_s c_p a^2}{c\, T_\infty^{5/2}}$$

with $T_\infty = 1{,}600$ ev, $a = 0.05$ cm, we get $\tau_p \sim 12.8$ s. which is nearly four orders of magnitude longer than the experimental life time $\tau_{p\,ex.} = 0.25$ ms .

Bremsstrahlung radiation from optical thin vaporized medium absorbed by the pellet surface can be expressed as,

$$q_r = \frac{\alpha_s}{4\pi a^2} \int_a^\infty K \rho^2 T^{\frac{1}{2}} \left[r^2 - r\left(r^2 - a^2\right)^{\frac{1}{2}}\right] dr$$

$$\approx \frac{\alpha_s K}{4} \int_a^\infty \rho^2 T^{\frac{1}{2}}\, dr \qquad \alpha_s \text{--absorptivity}$$

numerical calculations show the dominant part of g_r comes from dense vaporized medium around the pellet within the distance of several radius of the pellet, the vaporization mass flow rate based on the absorbed energy g_r fits well with the experimental data.

The distribution of thermodynamic quantities is shown in the following figures,

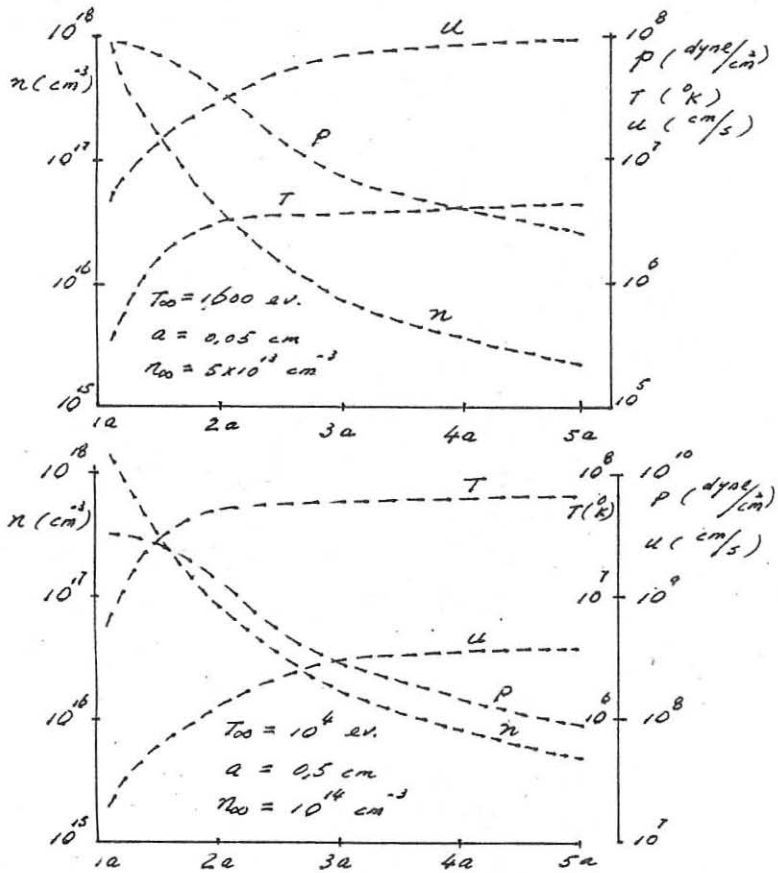

Conclusions:

1,High vaporization mass flow rate of pellet under fusion plasma conditions induces very high pressure at the pellet surface (10^{3} --10^{4} atm.).

2,Bremsstrahlung radiation from dense vaporized medium absorbed by the pellet surface is the dominant energy source for vaporization, while energy transport through heat conduction only plays an indirect effect.

3,Since β is very high near the pellet, flow pattern seems not to be influenced by the magnetic field.

4,Plasma heat conductivity is very high at high temperature, so temperature and supersonic velocity of the vaporized plasma are nearly constants after $r \sim 5a$.

References

1, Chang,C.T., Nuclear Fusion, vol.20,(1980) 859

2, Milora, S.L., J. of Fusion Energy, vol.1,(1981) 15

3, Parks,P.B., Nuclear Fusion, vol.20 (1980) 311

4, Chang,C.T., Physics of Fluids, vol.26 (1983) 805

Quasi Stationary D_2 Pellet Injection into ASDEX Divertor Discharges

G.Vlases*, M.Kaufmann, O.Gruber, G.Haas; Pellet Injection Team: R.S.Lang, K.Büchl, W.Sandmann; ASDEX Team
Max-Planck-Institut für Plasmaphysik, EURATOM Association, D-8046 Garching, Fed. Rep. of Germany

Introduction

We report on deuterium divertor discharges in ASDEX where the particle inventory is sustained entirely, after an initial gas fuelling phase, by the injection of a series of up to 80 frozen D_2 pellets, 1 mm in diameter and 1.2 mm long ($N_D \leq 4.5 \times 10^{19}$), at intervals ranging from 20 to 50 ms, and speeds to 720 m/s, by means of a centrifuge /1/. Investigations performed on Ohmic, NI, and ICRH heated discharges have shown that the most important parameter characterizing the discharges is the ratio of the pellet penetration depth, Δ, to the fall-off length for neutral particles in a gas fuelled case (typically 5 - 8 cm in ASDEX).

For shallow penetration, only minor differences, relative to gas fuelled shots, are observed. In contrast, with deep penetration (e.g. $\Delta \geq a/2$) the density profile is more peaked, and the temperature profile flattened, when compared with gas fuelled discharges at the same line integrated density, $\bar{n}_e$. The discussion here concentrates on these characteristic "deep fuelling discharges". Because of the limited pellet size and velocities presently available, these deep fuelling discharges are Ohmically heated with $T_e \leq 1$ keV. In the following paragraphs we discuss energy and particle confinement, aspects of recycling, and density limits.

Energy balance

Figures 1 and 2 show the time dependence of several plasma parameters for a representative deep penetration (20 cm), ohmically heated, pellet fuelled discharge (# 14669, q = 3.4, B = 2.2 T). In this case the density was first increased to $\bar{n}_e = 1 \times 10^{19}$ m^{-3} at 500 ms by a gas valve, which was then turned off. Pellets were injected at 35 ms intervals, beginning at 522 ms, causing the cycle-time-averaged density $(\bar{n}_e)_c$ to increase to 3×10^{19} m^{-3}. When a pellet enters, the temperature drops rapidly throughout the plasma /2/; the density peaks continuously within a given pellet cycle, and is more peaked for later cycles in the series. The neutron fluence drops and recovers, as T_i recovers.

We have analyzed individual pellet cycles, using both a transport code /3/ based on measured time-dependent T_e, n_e, and P_{rad} profiles, and global magnetic measurements, and cycle-averaged agreement is obtained. The results of such analyses for the 12th pellet cycle of shot 14669 are given in fig. 3. It can be seen that β_p increases throughout the cycle, and drops discontinuously at the time of injection of pellet # 13, indicating a non-adiabatic injection, with a loss of about 2 kJ plasma energy. Such a loss at

* University of Washington , Seattle. Work supported by US DOE/OFE.

each injection event constitutes a time-averaged loss of up to 100 kW which lowers the value of $(\tau_E)_{cycl} = (1/\Delta t)\int \tau_E dt$, from the 55 ms measured within the cycle, to about 45 ms averaged over the cycle + injection, in approximate agreement with the long-time-averaged (several cycle) global magnetics value. This should be compared with τ_E = 74 ms obtained in a gas fuelled comparison shot (# 14671) with the same time-averaged $\bar{n}_e(t)$ (see fig. 1).

The local transport analysis shows that within error bars, χ_e and χ_i are unchanged between the gas fuelled and pellet fuelled discharges: χ_e corresponds to the normal scaling observed in ASDEX /4/, while χ_i is one times neoclassical.

The analysis further reveals that three mechanisms are responsible for the reduction in total energy confinement seen in these deep fuelled, peaked discharges: (1) There is an enhanced convection of energy from the inner to outer plasma regions due to the cycle-averaged net outward particle flux Γ_p, which must equal the pellet fuelling rate. For the cycle discussed here, the convective power is about 150 kW at r = a/2. (2) There is increased radiation, consistent with the peaking of the density profile (P_{rad} increases from 106 kW (# 14671) to 150 kW (# 14669). (3) The non-globally-adiabatic pellet injection constitutes a time-averaged loss rate of about 100 kW for the quasi-steady phase of # 14669.

Particle Balance

For the deep penetration case described above, the equivalent particle supply rate is about 60 % of that required for the gas fuelled comparison shot (# 14671). The divertor plasma and neutral densities remain consistently below that of the comparison shot, reaching values of about 80 % and 50 % near the end of the 1.2 second injection phase.

The flux of particles leaving the plasma seems to fall rapidly after a first very short burst, resulting from the non-adiabatic injection, and starts to recover about 20 ms after injection. This suggests that an enhanced inward convection may be present early in the cycle. The effective particle confinement time, $\tau_{eff} = N/\dot{N}$, is about 130 ms at the beginning of the cycle and 100 ms at the end, during the quasi-stationary phase of shot # 14669. The time averaged true particle confinement times, estimated from the recycling flux and particle supply rate, are about 120 ms and 45 ms for the pellet and gas fuelled shots, respectively.

Plasma boundary and divertor

The plasma boundary density shows a sharp peak ($\Delta t \lesssim 5$ ms) immediately after injection, near the separatrix, which then is followed by a pronounced decrease of the density fall-off length, which recovers later in the cycle. The plasma density in the divertor likewise shows a sharp spike followed by a pronounced decay, and finally recovery (fig. 2): These observations are in qualitative agreement with the ASDEX edge-layer theory described in ref. /5/.

Density limit

A density limit in Ohmic pellet shots can be attained by increasing the $\bar{n}_e$ at the time injection begins, and/or by increasing the pellet injection frequency. The results from a limited number of such discharges are: (1) Peak densities 20 - 40 % higher than in

gas fuelled discharges at the same q(a) are obtained before discharges is accompanied by very strong central peaking of density and radiation ($n_{eo} \leq .8 \times 10^{20}$ at $q = 3.4$, $I_p = 310$ kA; $P_{rad}(o) = .35$ W/cm^3), and collapse of the central temperature. In contrast to the situation in gas fuelled density limit discharges /6,7/, strong and asymmetric radiation from the boundary is not observed and strong disruptions do not occur. Sometimes the discharge recovers to its predisturbance state. The observations are in line with the interpretation of the usual density limit as a boundary density limit. With pellet refuelling it is possible to decouple the central density from its boundary limit. The density limit in pellet fuelled NI discharges could only be reached by supplemental gas puffing. As expected, no characteristic differences from gas fuelled shots were found.

Conclusions

Deep penetration pellet fuelled ohmic discharges in ASDEX reach higher density limits and require a lower particle supply rate than gas fuelled discharges. The peaked profiles, along with slightly non-adiabatic injection events, however, lead to a degradation of energy confinement, caused by enhanced convection and radiation.

Acknowledgement

We wish to thank Drs. K.Lackner and F.Wagner for helpful discussions.

References

/1/ W.Amenda, R.S.Lang, J. Phys. E: Scient. Inst. (to be published)
/2/ G.Vlases, K.Büchl, D.Campbell, "Proc. 11th Europ. Conf. on Contr. Fus. Plasma Physics",Vol. 1, p. 127 (Aachen, 1983)
/3/ R.Hawryluk, in "Physics of Plasmas Close to Thermonuclear Conditions", Vol. 1, Varenna (1979) (EUR-FU-BRU/XII/476/80)
/4/ O.Gruber, "Proc. Invited Papers, Int. Conf. on Plasma Physics", Lausanne (1984), Vol. 1, p. 67
/5/ Y.Shimomura et al., Nucl. Fus. 23, 869 (1983)
/6/ H.Niedermeyer et al., these proceedings, paper # 195
/7/ J.Neuhauser et al., these proceedings, paper # 158.

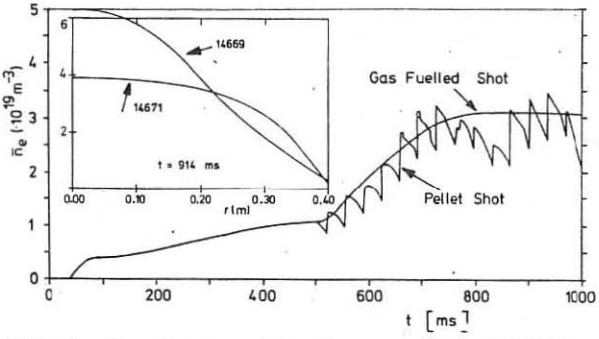

Fig. 1: Density vs. time for a pellet (14669) and a gas fuelled comparison (14671) shot. Gas valve closed at 500 ms for pellet shot. Inset shows $n_e(r)$ for both at 914 ms.

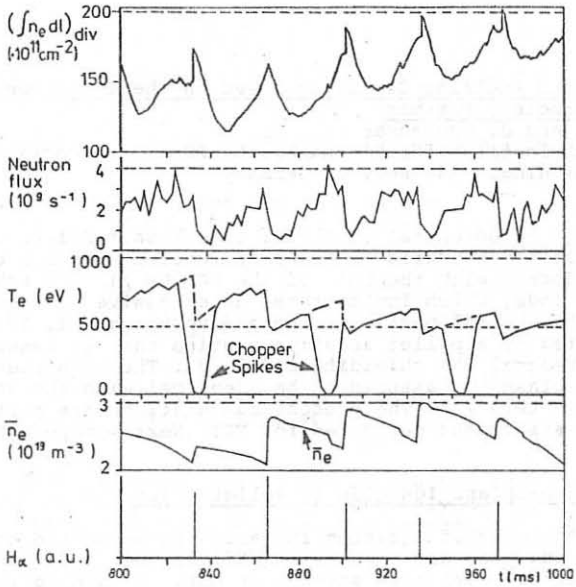

Fig. 2: Representative diagnostic traces, shot 14669. H_α light spikes indicate pellet injection times.

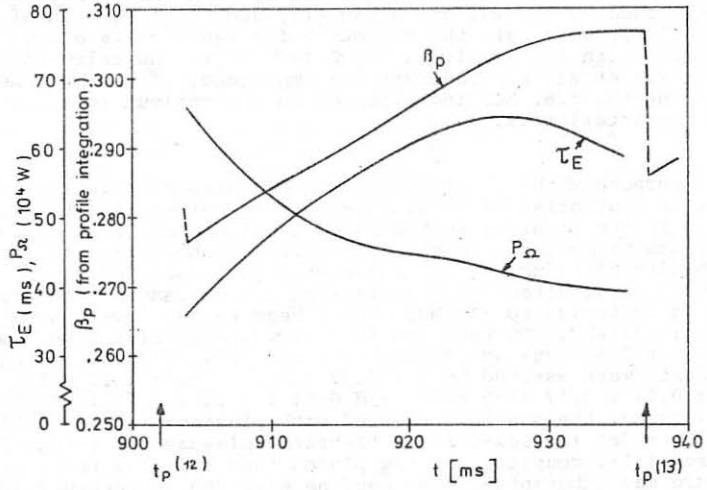

Fig. 3: Time dependence of β_p, τ_E, P_Ω within 12th pellet cycle, shot 14669. Note: τ_E is 48 ms when non-adiabatic injection is included. For gas comparison shot: β_p = .300, P_Ω = 300 kW, τ_E = 74 ms.

Ignition and Fuelling Scenarios Based on the Injection of Pellets in Thermonuclear Plasmas

L.Lengyel and J. Neuhauser
Max-Planck-Institut für Plasmaphysik, EURATOM Association,
D-8046 Garching, Fed. Rep. of Germany

Some of the potential of pellet injection for future fusion machines is demonstrated by means of reactor scenario calculations performed with the help of the BALDUR /1/ 1-D tokamak transport code, which incorporates an extensive Monte Carlo treatment of the neutral particles and a divertor model. The code is supplemented by a pellet ablation routine that is based on the so-called neutral gas shielding model /2/. The parameters of the recipient plasma are assumed to be identical with the standard INTOR parameters /3/. The present calculations are part of an extensive assessment performed for NET (Next European Torus) /4/.

Density Ramp-up and Ignition by Pellet Injection

Early analyses of ignition scenarios in NB-heated tokamaks (see, for example, Watkins et al. /5/, Holmes et al /6/, and Houlberg et al. /7/) have shown that optimum path to ignition in the n,T space always starts with a low-density high-temperature plasma state. The calculations of Watkins et al. show that, irrespective of the scaling laws assumed by them (Alcator-Intor, Coppi-Mazzucato, Ohkawa, and a radially dependent version of Alcator-Intor scaling), the minimum ß for ignition is always associated with low densities ($n_i \lesssim 10^{20}$ m^{-3}). The calculations of Houlberg et al. /7/ indicate the importance of the NB penetration depth, i.e. heating profile, on the optimum ignition power characteristics.

The purpose of the present ignition scenario calculations is to assess the potential of density ramp-up by pellet injection in planned fusion machines such as NET, based on the INTOR design and plasma parameters. Special attention has been paid to the possibility of reducing the beam energy envisaged for INTOR (175 keV) by simultaneously increasing the envisaged beam power (from 75 MW to 100 to 110 MW). Three beam energy levels were considered: 120 keV, 100 keV, and 80 keV, respectively). The respective power fractions associated with the 1/1, 1/2, and 1/3 energy components were assumed to be: 0.59 : 0.22 : 0.19 (120 keV), 0.62 : 0.21 : 0.17 (100 keV), and 0.64 : 0.20 : 0.16 (80 keV) /8/. In all cases, the scenario started with plasma in the so-called "hot ion mode" (in low-density NB-heated plasmas the energy is preferentially coupled into the plasma ions and thus the ion temperature may substantially exceed the electron temperature in the heat deposition zone). As soon as the minimum ß value necessary for ignition has been reached, a pellet of preselected size was injected into it, thus adiabatically ramping the plasma density up to

the value necessary for ignition (i.e. for a self-sustained alpha reaction rate). The values of β_{ign} and n_{ign} were previously determined from standard INTOR start-up phase calculations (E_{bi} = 175 keV, P_{bi} = 75 MW) with marginal ignition ($_{bi}$ = 4 s) and were found to be: β_{ign} = 2.5 and n ign 9.5 x 10^{19} m^{-3}, respectively. Details of these calculations can be found in /9/.

The pellet velocity assumed (approx. 2400 m/s after correction for the ellipticity of the plasma cross-section) corresponds to values not very far from the presently obtainable ones. The ablation rates yielded by the neutral gas shielding theory /2/ were used without corrections for possible magnetic shielding effects. Thus the actual pellet penetration depths may be larger under reactor conditions than those calculated here /4/. (This may again further relax the requirements on the NB and pellet injector systems.) Since the intense deuterium beams make the discharge rather tritum-lean in the reactor zone, only tritium pellets were used for ramp-up purposes.

It should be noted that the results of reactor scenario calculations such as those described here strongly depend on the scaling laws (transport models) used. The present calculations are limited to Alcator-Intor scaling, on which the standard INTOR and NET calculations are based.

The NB heat pulse data and pellet sizes required for ignition by means of density ramp-up via pellet injection can be summarized as follows:

Particle energy	Total beam current	Beam pulse duration	Pellet radius	Pellet injection time
120 keV	1.25 kA	2.16 s	0.37 cm	2.15 s
100 keV	1.40 kA	2.68 s	0.34 cm	2.67 s
80 keV	1.70 kA	3.00 s	2 x 0.29 cm	1 s 2.99 s

The pellet injection times shown are counted from the start of the beam pulse. In the first two cases considered, the starting plasma density was 4 x 10^{19} m^{-3}, while in the third case it was reduced to 1 x 10^{19} m^{-9}. Because of the rather large beam current associated with the 80 keV case and the corresponding rather tritium-lean discharge, it was found necessary to inject a tritium pellet already in the early discharge phase, thus ensuring an acceptable D-T mixture in the reaction zone to the end of the NB heating pulse.

In conclusion, the potential of density ramp-up in NB-heated plasmas by pellet injection may be summarized as follows:

a) The injection scenario can be started with plasma densities sufficiently low to ensure deep beam penetration, central particle deposition and thus peaked temperature and density profiles. Advantage may be taken of the hot ion mode in this case.

b) While in the case of density ramp-up by gas puffing the ramp-up time is finite and the beam may be blocked off at the plasma periphery before the heating pulse is off, density ramp-up by pellet injection is practically instantaneous and unimpaired beam penetration may be granted during the entire heating phase.

c) Pellet injection transports fresh fuel to the reaction zone on a time scale that is much shorter than the diffusion time characterizing the method with gas puffing. Hence the timing of the moment of density ramp-up with respect to the heat pulse is less complicated in the case of pellet injection than in the second case.

d) Transition from NB-driven fusion to self-sustained alpha particle production may be possible at lower beam energies and shorter beam pulses (with increased beam currents) than in the case of gas puffing.

Continuous Fuelling by Pellet Injection

In a series of calculations performed for NET, the optimum combinations of pellet sizes, pellet velocities, and pellet frequencies applicable to reactor fuelling were investigated by injecting a string of 10 pellets ("continuous" fuelling) into an already ignited standard INTOR plasma. Before and after pellet injection, the density was kept at a constant level by gas puffing. The same transport scaling laws were assumed here as in the case of the ignition scenarios (Alcator-Intor) with an addendum: a "soft beta limit" was applied to obtain steady-state burning conditions. Details of these calculations can be found in /9/ as well.

The results obtained have shown that the response of the recipient discharge to the injection of a continuous string of pellets, i.e. the change of the temperature and density distributions, the onset of favourable or unfavourable profiles and the resulting changes of the particle and energy confinement times are functions of the pellet mass-velocity-frequency combinations applied. Hence, for determining the optimum injection characteristics, systematic scanning of these parameters was performed on the basis of the following considerations: First, deep pellet penetration produces favourable density profiles, improves the confinement time, and increases the alpha production rate. Hence for a given velocity the pellet mass should be large enough to ensure deep penetration and yet small enough not to cause large-amplitude density fluctuations. Second, the pellet frequency required for continuous fuelling depends on the particle confine-

ment time associated with the modulated density and temperature profiles developing during continuous pellet fuelling. Care should be taken that the frequencies chosen and the respective injection periods are different from the characteristic response time associated with burn control ($\gtrsim 1$ s). Third, the particle exhaust flux should be large enough to ensure the rate required for helium pump-off.

In conclusion, reactor fuelling scenario calculations have shown, that fuelling by pellet injection at technically feasible pellet velocities is superior to fuelling by gas puffing alone: a) It produces favourable density and temperature profiles, thus increasing the particle and energy confinement times; b) it increases the central and average β_T values and may cause a substantial increase of the thermal alpha power production; c) the particle exhaust flux corresponding to pellet fuelling is somewhat reduced compared with edge fuelling but is still more than sufficient for effective helium pump-off.

This study is part of an analysis performed for NET on the basis of the EURATOM contract No. 138/83-11/NET. Useful discussions with K. Borrass of the NET Team are gratefully acknowledged.

References

/1/ D.E.Post et al., Rept. No. 33, PPPL, TFTR Physics Group, 1981.

/2/ P.B.Parks and R.J.Turnbull, Phys. Fluids 21 (1978) 1735.

/3/ INTOR, Phase One, IAEA, Vienna 1982.

/4/ L.L.Lengyel, Assessment of Pellet Injection for NET, IPP Repts. 1/231 to 1/233 (1984), and 1/236 (1985).

/5/ M.L.Watkins, T.E.Stringer, A.Gibson, et al., Pl. Phys. and Contr. Nucl. Fus. Res. (Proc. 8th Int. Conf. Brussels, 1980), IAEA, Vol. 1 (1981), 639.

/6/ J.A.Holmes, J.A.Rome, W.A.Houlberg, et al., Nucl. Fus. 20, (1980), 59.

/7/ W.A.Houlberg, S.E.Attenberger, and L.M.Hively, Nucl. Fus. 22 (1982), 935.

/8/ E.Speth, IPP Garching, privat communications.

/9/ Paper submitted to Nuclear Fusion; see also IPP Rept. 1/236 (1985).

A Theory of Marfes

T.E. Stringer

JET Joint Undertaking, Abingdon, Oxon. OX14 3EA, UK.

Introduction A marfe is a toroidally symmetric band of enhanced radiation sometimes observed in tokamaks. It is strongly localised near the plasma edge, typically has a poloidal width of about 30°, and always occurs on the inboard side. They were first reported on Alcator C[1].

Marfes have been attributed to a radiative thermal instability[1]. As is discussed later, a local decrease in temperature leads to a local increase in radiation cooling. This destabilising effect is opposed by parallel thermal conduction. Instability can occur only near the plasma edge where parallel thermal conductivity is low. A criterion for the onset of such an instability will be derived and its saturated state studied. Theoretical predictions are consistent with experiment.

Linear Analysis of the Radiative Thermal Instability The balance between radial conduction into the edge region, enhanced radiation from the cool region and parallel conduction of energy into the cool region, is described by the total energy conservation equation:

$$3\frac{\partial}{\partial t}(nT) = \frac{\partial}{\partial s}\left\{K_{\parallel}\frac{\partial T}{\partial s} - 5nTv_{\parallel}\right\} + \frac{1}{r}\frac{\partial}{\partial r}\left\{rK_{\perp}\frac{\partial T}{\partial r}\right\} - \sum_z nn_z L_z(T) \qquad (1)$$

where $T=T_e=T_i$, s denotes distance along a field line, $K_{\parallel}$ and $K_{\perp}$ are the thermal conductivities parallel and perpendicular to the magnetic field, n_z is an impurity density, $L_z(T)$ the radiation rate, and other notation is standard. Since marfes are observed to be toroidally symmetric, the temperature and density perturbation are assumed to be functions only of poloidal angle and radius, i.e. $\tilde{T}(r,\theta,t)=\tilde{T}(r)\cos m\theta \exp(\gamma t)$. To obtain a dispersion equation for γ, Eq.(1) is linearised and combined with the continuity equation and the parallel component of the fluid equation of motion. This gives:

$$\gamma\left[\gamma^2 + \frac{5}{3}C_s^2 k_{\parallel}^2\right] = -\frac{1}{3n}\left[K_{\parallel}k_{\parallel}^2 + \frac{K_{\perp}}{\Delta^2} + nn_z\frac{dL}{dT}\right]\left[\gamma^2 + C_s^2 k_{\parallel}^2\right] + \frac{4}{3}\frac{n_z L}{M}k_{\parallel}^2 \qquad (2)$$

where $C_s^2=2T/M$ and $k_{\parallel}^2=-\partial^2/\partial s^2=m^2B_\theta^2/r^2B_\phi^2$. In deriving this equation the perpendicular heat conduction term in Eq.(1) has been replaced by $-K_{\perp}\tilde{T}/\Delta^2$, where $\Delta\cong$ the radial half-width of the perturbation, and the fractional density perturbation of the impurity is assumed equal to that of the electrons. The

condition for instability is:

$$K_{\parallel}k_{\parallel}^2 + \frac{K_{\perp}}{\Delta^2} - \frac{2nn_z}{T} + nn_z\frac{dL}{dT} < 0 \qquad (3)$$

An equivalent criterion has been derived independently by J. Neuhauser[2].

Both the parallel and perpendicular heat conduction tend to inhibit the instability, the former is usually the more important. The third and fourth terms in Eq.(3) express the change in radiation due to density and temperature variation respectively. Density varies roughly inversely with temperature as plasma moves to maintain constant pressure along the magnetic field. The temperature variation in the radiation rate for carbon in coronal equilibrium is shown by the solid curve in Fig.1. However, impurity ions near the plasma edge are generally far from coronal equilibrium. A rough approximation to non-coronal radiation may be obtained by shifting the coronal radiation curve $L_c(T)$ to higher temperatures, i.e. $L(T_e)=L_c(\zeta T_e)$, where ζ can vary from 1 to 0.3 depending on how far the ionisation distribution differs from coronal[3]. The third term in Eq.(3) is always destabilising, while the fourth is destabilising for T_e larger than the maximum in $L(T_e)$. The two terms are comparable in magnitude.

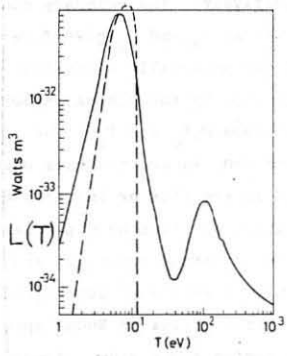

Fig.1 Coronal radiation rate for carbon (solid curve) and analytic model (dashed).

When applied to Alcator C with 1% carbon concentration and ζ=0.5, Eq.(3) predicts a critical edge density of $1.1\times10^{20}m^{-3}$ for marfe onset. This is close to that observed[1]. The measured Doppler broadening in the CIII line in JET suggests ζ=0.3. This gives a predicted critical edge density of $8\times10^{18}m^{-3}$ in JET which, although about twice that observed, is within the uncertainty in the present analysis.

The Saturated Instability This must satisfy the nonlinear steady state form of Eq.(1). An important nonlinear effect is the variation of parallel thermal conductivity with temperature, $K_{\parallel}\cong CT^{5/2}m^{-1}sec^{-1}$ To allow a simple analytic solution of Eq.(1) the following form is assumed for the radiation rate:

$$\begin{aligned} L(T) &= PT^{1/2} && \text{for } T<T_0 \\ &= bPT^2\,[T_1^{7/2}-T^{7/2}] && \text{for } T_0<T<T_1 \\ &= 0 \text{ for } T>T_1 \end{aligned}$$

where $T_1=T_0[(1+b)/b]^{2/7}$. The dashed line in Fig.1 illustrates this function for

T_0=6eV, b=0.1. The analytic solution should be at least qualitatively correct, and the scaling can be seen more clearly than in a numerical solution. Omitting the convective term, the solution of Eq.(1) is then

$$\begin{aligned} T^{7/2} &= A\cosh g\theta + H/g^2 && \text{for } \theta<\theta_0 \\ &= -B\cos(h\theta+\psi)+F/h^2 && \theta_0<\theta<\theta_1 \\ &= T_1^{7/2}+H(\theta-\theta_1)(2\pi-\theta_1-\theta)/2 && \theta>\theta_1 \end{aligned} \qquad (5)$$

where $g^2=uPT^2nn_z$, $u=7r^2B_\phi{}^2/2CB_\theta{}^2$, $H=uD$, h^2-bg^2, $F=h^2T_1^{7/2}-H$.

D=total conducted heat influx to the edge region/$8\pi^2rR\Delta$, where 2Δ is the radial width of the marfe. θ_0 and θ_1 are the angles at which $T=T_0$ and T_1 respectively. The boundary conditions $T(\theta_0)=T_0$, $T(\theta_1)=T_1$, and continuity of $\partial T^{7/2}/\partial\theta$ at θ_0 and θ_1 give five equations for the constants A,B,ψ,θ_0 and θ_1. Thus the poloidally asymmetric steady state, if one exists, is completely determined by the plasma parameters nT, n_z/n and D, and the radiation rate parameters P,T_0 and T_1. The steady state is arbitrarily taken to be centred around θ=0, in practice its poloidal location is determined by poloidal asymmetry in the flux or impurity drifts. Figure 2 shows the predicted temperature variation for Alcator C parameters, with carbon as the radiating impurity, and several values for nT. $D=2\times10^6$ w/m^3 corresponds to a total conduction influx of 200kW spread over an edge region 2.5cm wide. Asymmetric steady states become possible only when the maximum radiation rate (at T_{max} where L(T) has its maximum) exceeds the energy input. For the chosen parameters this is when $nT>2.1\times10^{20}$ eV/m^3. The steady state has a central region around θ=0 where $T<T_{max}$, such that radiation locally balances the energy input, and an outer region around $\theta=\pi$ where $T>T_{max}$ and radiation is less than the energy input. The surplus energy is conducted into an intermediate region where radiation is near its maximum, and locally exceeds the energy input. As nT increases, the strongly radiating intermediate region becomes narrower and moves to smaller θ until finally it reaches θ=0 and the inner region disappears. The experimental marfe illustrated in Reference 2 has $nT=2\times10^{21}$eV/m^3, the radiating region extends

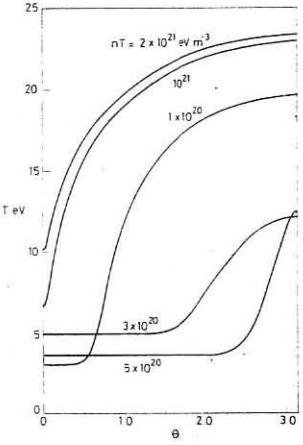

Fig.2 Stationary poloidally asymmetric temperature distributions for various nT.

poloidally over 30°, and the temperature varies poloidally by a factor of about 2 with an inverse variation in density. This is quite similar to the predicted variation in Fig.2 for the same nT value.

Acknowledgement The author is grateful to W. Engelhardt for pointing out the destabilising effect of density variation and other constructive criticism.

References

[1] LIPSCHULTZ, B. et al. Nucl. Fusion 24 (1984) 977.

[2] NEUHAUSER, J. Private communication.

[3] DNESTROVSKII, V. and PEREVERZEV, G. Nucl. Fus. 23 (1983) 633.

STOCHASTIC MOTION AND DIFFUSION OF ALPHA PARTICLES IN TOKAMAKS DUE TO TOROIDAL RIPPLE

V.Ya.Goloborod'ko, Ya.I.Kolesnichenko, V.A.Yavorskij

Institute for Nuclear Research, Ukrainian SSR
Academy of Sciences, Kiev, USSR

Abstract: The problem of the dynamic stochasticity of the trapped particle motion in tokamaks with the toroidal ripple is considered. It is shown that the stochasticity condition is strongly dependent on the magnetic moment and radial position of the particle. The ripple threshold for the alpha particle loss fraction is concluded to be smooth or even absent.

The toroidal field ripple of a tokamak may result in the prompt loss of alpha particles / 1 / as well as the alpha loss due to more complicated mechanisms / 2-4 /. The loss fraction of alphas in the presence of ripple is found numerically in Ref. / 5 / to be very large. On the other hand, the recent calculations / 6 / yield much more favourable results. It is clear that further study of the influence of the toroidal ripple on the behaviour of alphas is required. To do a step in this direction we consider the problem of stochastic motion of the particles and compare our results with those of Ref. / 2 / where studying of this problem was started.

We proceed from the equations of motion for the particle guiding center in the magnetic field $B=B_0(1-\epsilon\cos\theta-\delta\cos N\varphi)$ using the following values as coordinates:

$$J=\int\frac{\epsilon\,d\epsilon}{q}-\frac{v_{\parallel}}{\omega_B R}\,,\quad \Phi=\varphi-q\theta\,,\quad \varphi$$

Here $\epsilon=\rho/R$, ρ is the flux surface radius, θ and φ are the poloidal and toroidal angles, R is the major radius of the torus, q is the safety factor, N is the number of the field

coils, $V_{||}$ is the longitudinal particle velocity, $\omega_B = eB/(mc)$. One can show that most of the change in J occurs close to the turning points. It allows to construct a map describing the banana motion in a finite time step $\Delta t = \tau_b/2$, τ_b being the particle bounce period:

$$\bar{J} = J + \Delta J_m \left[\sin\alpha + \frac{1}{\sqrt{2}\gamma}\sin\left(2\alpha + \sigma\frac{3\pi}{4}\right)\right]$$
$$\bar{\alpha} = \alpha + \varphi_p(\bar{J}) + \bar{\sigma}\,\varphi_b(\bar{J}) \qquad (1)$$

Here $\alpha = N\varphi + \varphi_p + \sigma[\varphi_b - \gamma^{-1}\cos(N\varphi + \varphi_p + \sigma\varphi_b) - \frac{\pi}{4}]$; $\Delta J_m = 2(V_d/V)\sqrt{\pi\delta\gamma^{-1}}$, $\gamma = 2\epsilon\varkappa\sqrt{1-\varkappa^2}/(Nq\delta)$, V_d is the toroidal drift velocity of a particle, $\varkappa^2 = 1/2 + (\lambda-1)/(2\epsilon)$, $\lambda = V_\perp^2 B_0/(V^2 B)$, φ_b and φ_p are the increase of $N\varphi$ over Δt due to the particle motion along the field line and the toroidal precession, respectively, given by expressions

$$\varphi_b = 4Nq\sin^{-1}\varkappa$$
$$\varphi_p = 8\sqrt{2}\,\frac{NV_d}{V}\frac{\partial}{\partial J}\left\{q\sqrt{\epsilon}\left[E(\varkappa) - (1-\varkappa^2)K(\varkappa)\right]\right\}$$

$K(\varkappa)$ and $E(\varkappa)$ are the complete elliptic integrals of the first and second kind, $\sigma = \mathrm{sgn}(\sin\theta_t)$, $\theta_t = \theta(V_{||} = 0)$. The line over letters denotes that the corresponding value is taken in the subsequent half-period of oscillations. Eqs. (1) are valid for $\gamma > 1$ and obtained in the linear approximation in γ^{-1}. In the limit $\gamma^{-1} \to 0$ they transform to the Cohen's map / 7 /.

Eqs. (1) contain the resonant condition $\varphi_p(J_s) = \pi s$ with $s = 0, \pm 1, \pm 2, \ldots$ (i.e. $N\omega_p = s\,\omega_b$, ω_p and ω_b are the precession and bounce frequencies of a particle) which determines the resonant surfaces J_s. We linearize Eqs. (1) at $J = J_s$ and obtain:

$$\bar{P} = P + \mathcal{K}\left[\sin\alpha + \frac{1}{\sqrt{2}\gamma}\sin\left(2\alpha + \sigma\frac{3\pi}{4}\right)\right]$$
$$\bar{\alpha} = \alpha + K_\sigma\bar{P} + \beta_\sigma \qquad (2)$$

where

$$P=(J-J_s)(|\varphi_p'|+|\varphi_b'|)\,,\quad \varphi_{p,b}' \equiv d\varphi_{p,b}/dJ\Big|_{J=J_s}$$

$$\mathcal{K}=\Delta J_m\,(|\varphi_p'|+|\varphi_b'|)\,,\quad K_\delta=\frac{\varphi_p'+\varphi_b'}{|\varphi_p'|+|\varphi_b'|} \qquad (3)$$

$$\left.\begin{aligned}\beta_+ &= \pi s+\varphi_b\\ \beta_+ &+\beta_- = 0\end{aligned}\right\}\ \mathrm{mod}\ 2\pi$$

The parameters $\mathcal{K}$, K_δ, γ, β_+ determine the particle motion. When $\mathcal{K}$ exceeds some $\mathcal{K}_{cr}(K_\delta,\gamma,\beta_+)$ (that means $\delta > \delta_{cr}$) the motion becomes stochastic. However when $\mathcal{K} \simeq \mathcal{K}_{cr}$ the diffusion coefficient is close to zero and the fraction of particles involved into the diffusion process is small. Hence the dynamic stochasticity may result in the loss of the considerable fraction of the trapped alpha particles provided that $\mathcal{K} >> \mathcal{K}_{cr}$ only.

The finite γ^{-1} may strongly affect the particle motion decreasing $\mathcal{K}_{cr}$. It is seen from Fig.1 where dependence of $\mathcal{K}_{cr}$ on γ^{-1} for $K_\delta = 1$ and $\beta_+ = 0$ is presented. Note that the choice of parameters K_δ, β_+ is not unique, Fig.2 illustrates this (it is assumed $R/a = 4$, $V_d/V = 5\cdot 10^{-3}$, $\rho/a = 0.4$, $q = (1-0.5\,\rho^2/a^2)^{-1}$, a is the plasma radius, dotted lines indicate the resonant values of $2e^2$). Therefore a variety of the magnitudes for $\mathcal{K}_{cr}$ and the different functional expressions for the stochasticity condition $\mathcal{K} > \mathcal{K}_{cr}$ exist. For instance, this condition contains $|\varphi_p'|$ for $K_\delta = 1$ instead of $|\varphi_b'|$ for the case of Ref. / 2 /. The finite value of γ^{-1} weakly affects the particles with $K_\delta = \pm 1$.

It follows that when $\delta = \delta_{cr} = [(\pi N q/\epsilon)^{3/2}\rho_L\, dq/d\rho]^{-1}$ (ρ_L is the Larmor radius) found in Ref. / 2 / for the case of $\gamma^{-1} << 1$, $K_\delta = \pm 1$, $\theta_L = \frac{\pi}{2}$ only a very small fraction of alphas takes part in the diffusion and, moreover, it has a chance to be confined in a plasma due to transition of the particles to other resonant surface.

In general, because of a strong dependence of $\mathcal{K}_{cr}$ on the particle parameters the alpha particle loss fraction ν_α is not a sharp function of δ . Moreover, if we suppose that Fig.1 is valid for $\gamma^{-1} \to 1$ we conclude that the ripple threshold is absent. Note that this conclusion rather then introduction of the critical ripple is in agreement with the numerical calculations of $\nu_\alpha(\delta)$ in Ref. / 5 /.

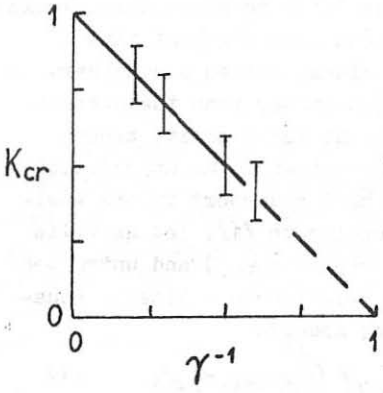

Fig.1

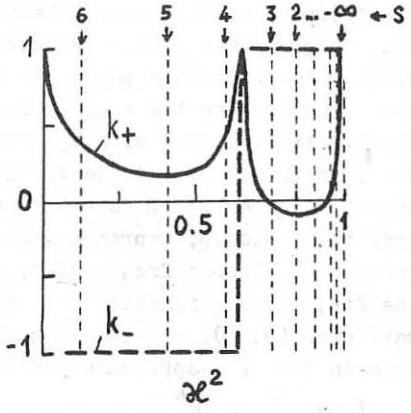

Fig.2

REFERENCES

1. V.S.Belikov, Ya.I.Kolesnichenko, V.A.Yavorskij. Fizika Plazmy, 3 (1977) 487.
2. R.J.Goldston, R.B.White, A.H.Boozer. Phys. Rev. Lett., 47 (1981) 647.
3. S.V.Putvinskij, V.V.Shurygin. Fizika Plazmy, 10 (1984) 933.
4. V.Ya.Goloborod'ko, V.A.Yavorskij. Nucl.Fusion, 24 (1984) 627.
5. K.Tani et al. Nucl. Fusion, 23 (1983) 657.
6. L.M.Hively. Nucl. Fusion, 24 (1984) 779.
7. V.V.Chirikov. In "Voprosy teorii plazmy", v.13 (1984) 3.

TO A THEORY OF ION HEAT CONDUCTION IN TOKAMAK

Yu.V.Gott, E.I.Yurchenko

I.V.Kurchatov Institute of Atomic Energy,
Moscow, USSR

The experiments on determination of an ion heat conduction coefficient, made on some tokamaks, show its value to be a few times higher than that calculated according to a standard neoclassical theory. In this paper it is shown that the heat fluxes rise, approaching the experimental values, due to a considerable contribution of ions with the energies higher than the thermal one into transport and due to an account for a finite banana width. The results of calculations are given in an approximational relationship, representing the heat transport in the whole range of collision frequencies. According to /1/, let us write the distribution functions for the trapped (f_t) and untrapped particles (f_u), obtained from the solution to a kinetic equation in the τ -approximation (Krook model):

$$f_t = \frac{1}{1-e^{-\gamma}} \int_{\psi-2\pi}^{\psi} \alpha_t F_M(z_*) \exp\left(\int_{\psi}^{\psi'} \alpha_t \, d\psi''\right) d\psi' \qquad (1)$$

$$f_u = \frac{1}{1-e^{-\gamma_u}} \int_{\theta-2\pi\sigma}^{\theta} \alpha_u F_M(z_u) \exp\left(\int_{\theta}^{\theta'} \alpha_u \, d\theta''\right) d\theta' \qquad (2)$$

where, F_M is the Maxwell function, θ is the poloidal angle,

$\varkappa \sin\psi = \sin\frac{\theta}{2}$; $\varkappa^2 = \frac{\omega(1+\varepsilon)-\mu B_0}{2\varepsilon\omega}$; $\varepsilon = r/R$;

$\omega = \frac{E-e\Phi}{T_i}$; $\gamma = \int_{2\pi} \alpha_t \, d\psi$; $\alpha_t = \frac{3\sqrt{2\pi}}{4} \frac{\beta(\omega)}{\omega^2} \frac{\gamma_*}{\sqrt{1-\varkappa^2\sin^2\psi}}$

$\gamma_u = \int_0 \alpha_u \, d\theta$; $\alpha_u = \frac{3\sqrt{2\pi}}{8} \sigma \frac{\beta(\omega)}{\omega^2} \frac{\gamma_*}{\sqrt{2\varkappa^2-\sin^2\theta/2}} \frac{1+\varepsilon-\varepsilon\varkappa^2}{\varkappa^2}$; $\sigma = \pm 1$;

$z_* = z_0 - \frac{\rho_4}{\sqrt{2}} \sqrt{2\varkappa^2}\cos\psi$; $z_u = z_0 - \sigma \frac{\rho_4}{\sqrt{2}} \sqrt{2\varkappa^2-\sin^2\theta/2}$;

z_0 is the motion integral /4/, $q = \frac{eB_0}{RB_T}$, ρ is the Larmor ion radius, $\gamma_* = \frac{\sqrt{2}\,Rq}{v_T \varepsilon^{3/2} \tau_i}$; $v_T = \sqrt{\frac{2T_i}{m_i}}$; $\tau_i = \frac{3\sqrt{m_i}\,T_i^{3/2}}{4\sqrt{2\pi}\, n Z_{eff} e^4 \ln\Lambda}$

Using the functions (1) and (2), one can calculate the flux of particles, Γ, and the heat flux q by standard method. Let us use the ambipolarity condition to exclude the electric field.

When $\Gamma_i = \Gamma_e \approx 0$, the ion heat flux, as the calculations show, is represented by a relationship:

$$\hat{Q} = \frac{Q}{Q_p} = \frac{0.36\,\nu_*}{1+0.8\,\nu_*^{3/4}}\left(1+\frac{1.2\varepsilon}{1+0.14\nu_*}\right)\Psi + \hat{Q}_{PS} \qquad (3)$$

where

$$Q_p = -\frac{3\sqrt{\pi}}{4}\,\frac{\rho^2 q\, v_T n}{R}\,\frac{dT_i}{dr} \qquad (4)$$

$$\Psi = 1 + \frac{0.3x^2}{1+x^4}\left(Z_T^{1/2}(1-0.01\nu_*^2) + Z_n\right) \qquad (5)$$

$$\hat{Q}_{PS} = 0.53\,\varepsilon^{3/2}(1.6 + 1/q^2)\,\nu_* \qquad (6)$$

is the Pfirsch-Schlüter flux

$x = 30\rho_0 q$; $\rho_0 = \rho(T_i(0))/a$; $Z_T = \left|\frac{d\ln T_i}{d(r/a)}\right|$; $Z_n = \left|\frac{d\ln n}{d(r/a)}\right|$

The thermal fluxes calculated in /3-5/ and those, by the relationship (3) in a standard neoclassical approximation $\hat{Q}_0$ when a finite banana width is not taken into account, i.e. at $\Psi \equiv 1$, are given in Fig.1. One can see that the results of calculations by a relationship (5) coincide with the data from /4,5/, which approximately twice exceed the results of /3/ often used.

The distribution functions (1) and (2) noticeably differ from the Maxwellian ones at the energies greater than thermal ones, when a finite width of the banana trajectories and a finite displacement of untrapped particles respective to magnetic surfaces are taken into account, and this results in a Ψ -times increase in thermal fluxes in comparison with the neoclassical ones.

The dependences Q/Q_0 on the frequency of collisions at a few values of ρ_0 are given in Fig.2. One can see that, with a rise in ρ_0, the flux rises, exceeding the flux $\hat{Q}_0$ four times at the maximum, and then it slowly decreases. The calculations have been done at $r/a = 0.7$; $\varepsilon = 0.2$ $T_i = T_0(1-(r/a)^2)^4$; $n = n_0(1-(r/a)^2)^2$. The experimental data on thermal fluxes in modern tokamaks are given in Figs. 1,2 as shaded areas. One can see that these results exceed the neoclassical ones. The account for a finite banana width, even at $\Gamma_e = 0$, allows to decrease a difference between the theory and the experiment.

Actually, the diffusive electron flux is anomalous. Therefore, the estimation of this anomality effect on the ion heat transfer is of interest. One can show that the thermal flux in this case is equal to:

$$\hat{Q}_{an} = \hat{Q} + y \Gamma_{an} \hat{T}_i \left(1 + \frac{0.6x^2}{1+0.6x^2}\right) \quad (7)$$

where $y = 1.31 \frac{1+0.77\sqrt{\nu_*}}{1+0.17\sqrt{\nu_*}}$ (8)

Let us assume the temperature distribution and ion density as: $T_i = T_0 (1-(r/a)^2)^{\alpha_T}$; $n = n_0 (1-(r/a)^2)^{\alpha_n}$ to estimate the radial electric field, emerging at anomalous electron transfer. Then,

$$\frac{\varphi(r)}{T_i(r)} = -\frac{\alpha_n}{\alpha_t} - (y - 3/2) + \Gamma_{an} \hat{T}_i \frac{0.37\nu_*}{1+1.34\nu_*}\left(1 + \frac{0.5x^2}{1+0.6x^2}\right) \quad (9)$$

From the equation (9) one can see that the potential is negative and of the order of $T_i(r)$ at $\Gamma_{an} = 0$. It decreases in its absolute value at anomalous electron transfer and can, in principle, change its sign. If one uses the Merezhkin-Mukhovatov scaling law in the calculations of Γ_{an} , the electric potential for, say, T-11 tokamak will drop by 20%, and the ion heat flux rises by 20% in comparison with the case, when $\Gamma_{an} = 0$. Star designates an experimental value of $\hat{Q}_{an}$ in Fig.3. One can see that there is a good agreement between the theoretical calculation and the experimental value of $\hat{Q}$.

References

1.L.M.Kovrizhnykh. Fizika plasmy, 1982, 8, 1105.
2.A.A.Galeev, R.Z.Sagdeev. In "Voprosy teorii plasmy", Moscow, Atomizdat, 1973, v.7, p.205.
3.D.F.Düchs at all. Nucl. Fus. 17, 565 (1977).
4.C.Bolton, A.A.Ware. Phys. Fluids, 26, 459 (1983).
5.F.L.Hinton, R.D.Hazeltine. Rev. mod. phys. 48, 239, (1976).

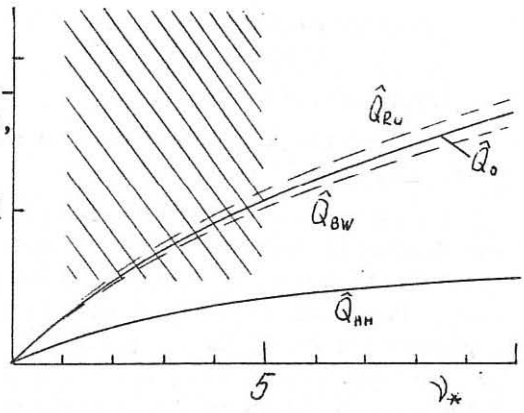

Fig.1 Heat fluxes vs. frequency of collisions in the neoclassical approximation: $\hat{Q}_o$ from Eq.(4), $\hat{Q}_{Ru}$ from /3/; $\hat{Q}_{BW}$ from /4/, $\hat{Q}_{HH}$ from /5/; ⫽ - expertimental data

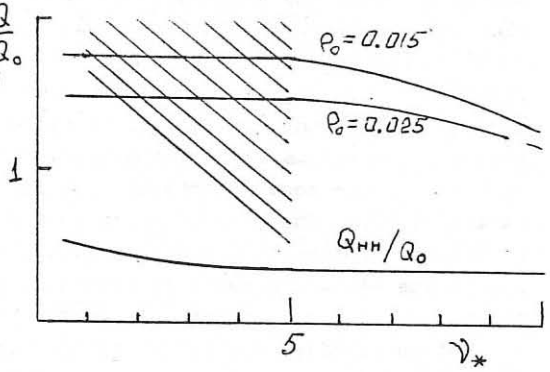

Fig.2 Heat fluxes vs. frequency of collisions at finite Larmor radii

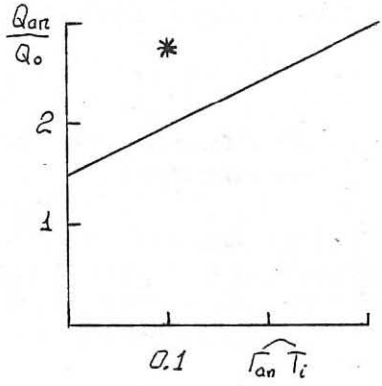

Fig.3 Ion heat flux vs. anomalous electron flux. (✱ is the experimental value of Q_{an}/Q_o from T-11 at ν_* =2)

STOCHASTIC MOTION OF PARTICLES AND ANOMALOUS HEAT CONDUCTION IN TOKAMAK

V.V.Parail, P.N.Yushmanov

I.V.Kurchatov Institute of Atomic Energy,
Moscow, USSR

The energy loss through an electron channel in tokamak has experimentally been shown to be anomalous. Theoretical studies of the mechanism of anomalous electron heat conduction have been mainly done until recently within the frames of a quasi-linear approximation /1-3/. In the paper /3/, it has been suggested to use the longitudinal Ohm's law for representing the coupling between oscillations in the electric and magnetic fields, that allows to bring the transport due to the electric and magnetic fluctuations together. An idea about saturation of the heat conduction coefficient in a strongly-nonlinear regime has also been suggested there. However, an actual use of a quasi-linear approximation in /3/ has not allowed to build up a selfconsistent theory for an anomalous transport in a non-linear regime ($v_\perp > v_F = \omega/k_\perp$), the most interesting one for the analysis of experimental results. The present paper is the first attempt at selfconsistent representing the anomalous electron transfer processes in the electromagnetic fluctuations of high amplitude with the account for a coupling between the potentials $\tilde{A}_\parallel$ and $\tilde{\varphi}$.

Let us consider the motion of electrons in the fluctuations of electric ($\vec{E}_\perp = -\vec{\nabla}_\perp \tilde{\varphi}$) and magnetic $\vec{B}_\perp = [\vec{e}_z \vec{\nabla} \tilde{A}_\parallel]$ fields. Let us analyze, first of all, the transversal drift motion:

$$\frac{d\vec{r}_\perp}{dt} = \frac{c[\vec{e}_z \vec{\nabla} \tilde{\varphi}]}{B_0} + \frac{v_\parallel \vec{B}_\perp}{B_0} . \qquad (I)$$

Let us use the reference frame with such a helicity which coincides with the helicity of an oscillation localized in the vicinity of r_0, $m = n q(r_0)$, and rewrite the equation (I) as a Hamiltonian, taking only unperturbed motion in the toroidal magnetic field of tokamak into account in $v_\parallel$ ($v_\parallel = v_{\parallel 0} + v_{\parallel \ell} \sin \omega_\ell t$, $\omega_\ell = v_{Te}\sqrt{\varepsilon}/qR$)

$$d\vec{r}_\perp / dt = [\vec{e}_z \vec{\nabla} H], \qquad (2)$$

where

$$H(r,\vartheta,t)= C\,\tilde{\varphi}(r,\vartheta,t)/B_0 + v_{\parallel}(t)\,(\tilde{A}_{\parallel}(r,\vartheta,t)+A_S(r))/B_0 .$$

The term with A_S represents the motion due to a change in the helicity of the field lines at deviation from the resonance surface. According to the frequency spectrum observed in oscillations, which is found to be considerably lower than the frequency of particle motion along the periodic orbit $\omega \lesssim 3\cdot10^5 \ll \omega_B \sim 2\cdot10^6$ /4/ , the main dependence on time in the Hamiltonian is included in $v_{\parallel}(t)$, the dependences of $\tilde{A}_{\parallel}$ and $\tilde{\varphi}$ on time can be neglected. In this case, the Hamiltonian for the drift motion of electron is expressed as:

$$H(r,\vartheta,t) = C\,\varphi(r,\vartheta)/B_0 + v_{\parallel}(t)\,A_{\parallel}(r,\vartheta)/B_0 . \qquad (3)$$

Without special analysis, from the form of Hamiltonian only, one can see that the motion of passing particles, for which $v_{\parallel}(t) = v_{\parallel 0}$, can be integrated and cannot result in a radial diffusion: they simply move along the equipotential lines,

$$C\varphi(r,\vartheta) + v_{\parallel 0}\,A_{\parallel}(r,\vartheta) = \text{const}$$

The trapped particles only, for which $v_{\parallel}(t) = v_{\parallel B}\sin\omega_B t$ only when $C\varphi \lesssim v_{\parallel} A$ can result in a radial diffusion, as the motion of electrons will occur along the lines at the level $\varphi(r,\vartheta)$ = const, when $C\varphi \gg v_{\parallel B} A_{\parallel}$. The nature of diffusion is qualitatively clear from the Hamiltonian representation (3). When $C\varphi \lesssim v_{\parallel B} A_{\parallel}$, particles move along the lines at a level averaged between φ and $A_{\parallel}$ The averaged lines are different at different instants of time. A characteristic space scale for the divergence of trajectories in case of relatively-low amplitudes is a translation for a time $1/\omega_B$; in case of high amplitudes, when the particles are able to pass many times along the equipotential for a time $1/\omega_B$, is a difference between the equipotentials φ and $A_{\parallel}$ As the amplitudes of oscillations observed in the experiments are rather high /4/, the second case is of a greater interest. Moreover, only in this case one can expect that the diffusion coefficients will not be dependent on the amplitude of oscil-

lations. One can assume that the oscillations with preset helicity $m = n\,q(r)$ are excited near the rational surface so that the potential can be represented as

$$\varphi(r,\vartheta,t) = \varphi(r)\exp(-i\omega t + im\vartheta + in\varphi). \qquad (4)$$

The coupling between $A_\parallel$ and φ is determined by Ohm's law which follows from the equation for a longitudinal motion of electrons

$$\frac{dv_\parallel}{dt} = \frac{e\vec{B}_0\vec{\nabla}\varphi}{m_e B_0} + \frac{e}{m_e c}\left(\frac{\partial A}{\partial t} + \frac{c}{B_0}[\vec{\nabla}\varphi\,\vec{\nabla}A_\parallel]\right). \qquad (5)$$

The first term in the right-hand side of the equation represents a change in $v_\parallel$ due to the electric field. Later, using (4), it is rewritten as

$$\frac{e}{m_e}\,\frac{K_\parallel(r)}{\omega}\,\frac{\partial\varphi}{\partial t}$$

In the oscillating fields of high amplitude ($\Omega \sim K_\perp v_\perp \gg \omega, K_\parallel v_\parallel$), the transversal motion of particles, as it has been shown above, is a motion within the closed cells. Therefore, in difference from a linear motion, particles cannot be displaced within the poloidal angle with respect to a wave at high level of oscillations. A phase of the wave at the trajectory oscillates fast around its average value $\varphi(t) = \varphi_0 \exp(-i\omega t + iz\sin\Omega t)$, where $z \lesssim 1$. From here one can see that the longitudinal thermal motion cannot affect the phase significantly at the trajectory and therefore cannot affect the coupling between $A_\parallel$ and φ. Taking this into account, let us transform the equation (5), assuming that the motion of particles is performed along the hydrodynamical trajectories

$$\frac{dv_\parallel}{dt} = \frac{e}{m_e c}\left(\frac{\partial}{\partial t} + \frac{c}{B_0}[\vec{e}_z\vec{\nabla}\varphi]\vec{\nabla}\right)\left(A_\parallel - \frac{K_\parallel c}{\omega}\varphi\right). \qquad (6)$$

It is easy to see that the operator $\partial/\partial t + c\,B_0^{-1}[\vec{e}_z\vec{\nabla}\varphi]\vec{\nabla}$ in the right-hand side of the equation is completely equivalent to the operator d/dt in the left-hand side of the equation, therefore the solution to Eq. (6) has a simple form:

$$v_\parallel = (e/m_e c)(A_\parallel - K_\parallel c\,\omega^{-1}\varphi).$$

Taking $j_\parallel = (4\pi)^{-1} c\,\Delta_\perp A_\parallel$ into account, the following dependence between $A_\parallel$ and φ follows from it:

$$\Delta_{\perp} A_{\parallel} = \frac{\omega_p^2}{c^2}\left(A_{\parallel} - \frac{K_{\parallel} c}{\omega}\varphi\right), \qquad (7)$$

which coincides with an equation derived from a linear Ohm's law for plasma without account for a thermal motion of electrons. From this equation one can see that s spatial scale of difference between the lines of the levels $A_{\parallel}$ and φ is c/ω_p .

Thus, the analysis of anomalous electron heat conduction in non-linear oscillations is reduced to the analysis of a drift motion for particles represented by the Hamiltonian (3) with the account for coupling (7). The results of numerical calculations for D in the dependence on the parameter $K_{\parallel} v_T/\omega$ and on the amplitude of oscillations (ratio of frequencies Ω/ω_B) is given in Figure. One can see that in the limit of a strong non-linearity of oscillations ($\Omega \gtrsim \omega_B \gg \omega$), the diffusion coefficient reaches an asymptotic value $D \approx 2\omega_B c^2/\omega_p^2$ and ceases to be dependent on the amplitude of fluctuations. With the account for the fact that only trapped particles take part in the diffusion, the electron heat conduction coefficient can be estimated as $\chi_e \approx 2\varepsilon c^2 v_{Te}/\omega_p^2 q R$.

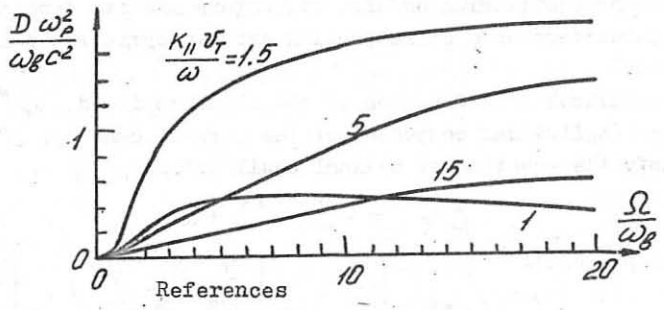

References

1. B.B.Kadomtsev, O.P.Pogutse. Plasma Phys. and Contr. Nucl. Fus. Res., IAEA, Vienna, 1979, v.1, p.649.
2. A.B.Rechester, M.N.Rosenbluth. Phys.Rev. Letters, 40(1978),38.
3. V.V.Parail, O.P.Pogutse. Pis'ma Zh. Ehksp. Teor. Fiz. 32 (1980) 458.
4. P.Liewer. A review of measurement of microturbulence in tokamaks and comparisions with theories of turbulence and anomalous transport. California Ins.of Techn., 1984.

NON-LINEAR DEVELOPMENT OF HELICAL MODES AND HELICAL EQUILIBRIUM IN TOKAMAK

Yu.N.Dnestrovskij
I.V.Kurchatov Institute of Atomic Energy, Moscow, USSR
D.P.Kostomarov, A.V.Pedorenko, A.M.Popov
M.V.Lomonosov Moscow State University, Moscow, USSR

Tokamak operation regimes with low $q_a = q(a) \geq 2$ need a careful plasma behaviour analysis within a range of linear instability for the external m/n=2 helical mode. It has been shown in /1/ that the development of instability at a non-linear stage can result in stabilized states of the plasma column at $q_0 = q(0) < 1$. These saturated states correspond either to a helical equilibrium or to a stationary convective motion. Possible long-wave solutions of the helical equilibrium equation in the plasma column are studied in a given paper by numerical methods. The purpose of this study is to find out when a bifurcation to a helical equilibrium occurs, its nature and its dependence on the parameters of a corresponding axially-symmetric plasma equilibrium.

A helical flux function of the magnetic field, $\psi^*(r,\theta)$ and a longitudinal component of the current density, $j(r,\theta)$, satisfy the equation of helical equilibrium:

$$\Delta\psi^* = -j(\psi^*) + 2$$

The dependences

$$j(\psi^*) = \begin{cases} j_0\left(1-\left(\dfrac{\psi^*-\psi_p^*}{\psi_0^*-\psi_p^*}\right)^\varkappa\right), & \psi^* < \psi_p^* \\ 0, & \psi^* > \psi_p^* \end{cases}$$

have been used for the current distribution. Here, ψ_0^* and ψ_p^* are the values of ψ^* at the magnetic axis and at the plasma boundary, respectively. The functions ψ^* and j in the equation are measured in $a^2 B_0 \alpha$ and $R B_0 \alpha/\mu_0$ so that

$$\vec{B} = B_0\left\{[\nabla\psi^*, \vec{e}_z] + \alpha r \vec{e}_\theta q + \vec{e}_z\right\}$$

Here, $\alpha^{-1} = mR_0/n$ is the lead of a helix B_0 is the longitudinal magnetic field. A parameter $\varkappa$ allows to vary the current distribution localization and, due to this, q_a/q_0. A quantity j_0 is found in the process of solution from the total current conservation condition

$$I_p = \int j(\psi^*)\, ds$$

The value of ψ_p^* is found from the necessity of passing the plasma boundary through two symmetric fixed points:

$$\psi_p^* = \psi^*\left(b, \pm \frac{\pi}{2}\right)$$

The second semiaxis of plasma ellipse, a and the ratio $k=b/a$ are found in the process of solution.

An ideally-conducting case of circular cross-section with the radius r_w, at which the boundary condition

$$\psi^*\Big|_{r_w} = 0$$

is imposed, has been located beyond the boundary Γ_p.

The calculated dependences of the ratio of semiaxes for an elliptical plasma cross-section in the helical equilibrium on the ratio I_p/S_p, where S_p is the plasma cross-section, are shown in Fig.1. A parameter of the curves is the ratio q_a/q_0 or the exponent of a power in the current distribution In these calculations, the case has been located at $r_w/b = 1.5$. The points of bifurcation for different current distributions correspond to the entrance to the linear instability zone at a reduction in the ratio I_p/S_p. At $q_a/q_0 = 1$ (uniform current), the curve on a plane shows that there are no helical equilibria to the left of the point I_p/S_p, corresponding to the boundary of linear stability. This corresponds to the results from /2/ and to the analytical dependence found there:

$$K \equiv b/a = -\left(1 - I_p/2S_p\right) + \sqrt{\left(1 - I_p/2S_p\right)^2 - 1}$$

The curve slightly slopes to the right for a uniform current, and it issues from the X-axis with an infinite derivative, that speaks about the subcritical bifurcation. In this case, the plasma evolution from an axially-symmetric equilibrium to a helical one should be of an "explosive" nature. In case of a

quasi-parabolic current, when $q_a/q_o=2$, a branch of equilibrium solutions with elliptical cross-sections appears at the entrance to the zone of linear instability with respect to a parameter I_p/S_p. This branch, outgoing from the bifurcation point, tends asymptotically to a straight line with $q_o=1$. Here a supercritical bifurcation takes place, and an evolutionary transition to a helical equilibrium should be of a "soft" nature. Such a behaviour is confirmed by the numerical integration of non-linear time-dependent equations /1,3/. The situation is drastically changed, when we transfer to the values of $q_a/q_o > 2$. In this case, the curve of equilibrium ellipticity has a maximum inside the instability range, and then the ellipticity is reduced in the vicinity of the boundary of the external mode instability area. This branch should continuously transit into helical equilibria with elliptic cross-sections, corresponding to the internal mode.

A surface of equilibrium solutions in a three-dimensional space (k, I_p/S_p, q_a/q_o) is given in Fig.2. I_p and S_p are conserved in the non-linear MHD-evolution. The parameter q_a/q_o, characterizing the current ditribution, is also slightly changed. Thus, an evolution of the cross-section should occur along a vertical line in the Figure. A line segment depicted as a dashed-dotted line corresponds to a non-linear evolution of the m=2 external helical mode considered in /1,3/. Intersection of a given straight line with a surface of helical solutions provides the values of ellipticity which can be obtained via the evolution of a non-stable, axially-symmetric equilibrium. Note that the helical equilibrium solutions with q_o slightly exceeding unity appear at a close location of the case, $\tau_w \lesssim 1.2\,\beta$. Such a tendency is seen from /4/, where the equilibria have been found without surface currents.

Thus, the presence of equilibrium helical configurations without surface currents, which can be obtained by the evolution of an unstable equilibrium at $q(o) \sim 1$ and at low $q(a) < 2$, is shown in the paper.

References

1. Yu.N.Dnestrovskij, D.P.Kostomarov, A.M.Popov, E.A.Shagirov, XI Eur. Conf. on Contr. Fusion and Plasma Phys., Aachen, 1983, II, p.173.
2. L.E.Zakharov, Fizika plasmy, 1981, No.1, p.1295.
3. R.B.White, D.A.Montichello, M.N.Rosenbluth, H.R.Strauss, B.B.Kadomtsev, Int. Conf. on Plasma Phys. and Contr. Nuclear Fusion Res. Tokyo, 1974, Vienna, IAEA, 1975, 1, p.495.
4. A.Sykes, J.A.Wesson, Int. Conf. on Plasma Phys. and Contr. Nucl. Fusion Res., Brussels, 1980, IAEA, CN-38/J-2-1.

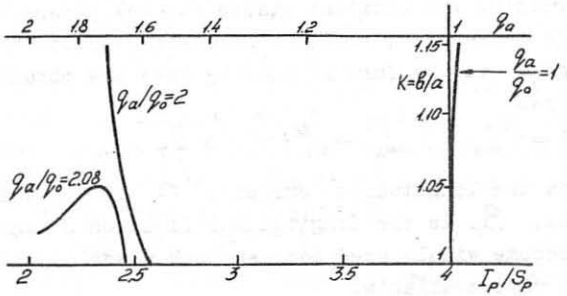

Fig. 1

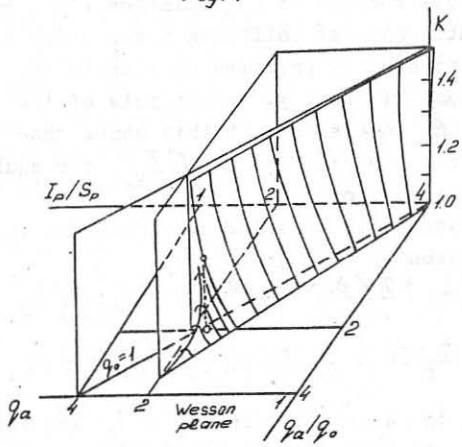

Fig. 2

AN SCALINGS FOR THE LIMITING β VALUES IN TOKAMAKS

L.M. Degtyarev, V.V. Drozdov, A.A. Martynov,
S.Yu. Medvedev

Keldysh Institute of Applied Mathematics
USSR Academy of Sciences, Moscow

1. In this paper numerical results of using the optimization procedure described in [1] , [2] are given. This procedure allows determining the limiting stable tokamak plasma equilibria in a wide range of equilibrium parameters. Fitting formulae for limiting β in the form of scaling laws are obtained. Simple scaling laws

$$\beta = C I_N \quad , \quad I_N = \mu_0 I_p / a B_T \quad , \tag{1.1}$$

where I_p is the longitudinal current, a is the small radius of a torus, B_T is the longitudinal field on a magnetic axis, have become widely used because such a scaling fits well experimental data available.

As for numerical results in [3] relation (1.1) was obtained for equilibria stable against ballooning modes only. A class of longitudinal current density profiles considered in [4] is limited by a two-parametric family. An analysis of the scaling laws for limiting β carried out in this paper shows considerable deviations from the scaling $\beta = C I_N$ for equilibria stable against all ideal modes.

2. The calculations given below were made for the plasma with the cross-section

$$\begin{aligned} r &= R + a\left[\cos\theta - \left(\frac{\gamma_1+\gamma_2}{2} + \frac{\gamma_1-\gamma_2}{2}\sin\theta\right)\sin^2\theta\right] \\ z &= a\sin\theta\left(\frac{k_1+k_2}{2} + \frac{k_1-k_2}{2}\sin\theta\right), \quad 0 \le \theta < 2\pi, \end{aligned} \tag{2.1}$$

where $A = R/a$ is the aspect ration; k_1 , k_2 are elongations and γ_1 , γ_2 triangularities of the upper ($z > 0$) and lower ($z < 0$) parts of the cross-section, respectively. Like in [1],

the limiting ballooning mode values of $\beta = \beta^{\infty}$ and limiting all ideal mode values of $\beta = \beta^{c}$ are found at the fixed safety factor $q(\Psi)$ to be determined from the forceless equilibrium configuration ($dp/d\Psi = 0$, p the plasma pressure) with the longitudinal current density

$$r j_{\varphi} = \left[1 - (1 - \Psi/\Psi_0)^{\varkappa}\right]^{\lambda} , \qquad (2.2)$$

$\Psi = \Psi_0$ and $\Psi = 0$ are the magnetic axis and boundary values; everywhere below $q(\Psi_0) = q_0 = 1.1$. For the fixed λ in (2.2) the plasma boundary safety factor q_s varies only with the parameter $\varkappa$. As a definition for β we use the relation

$$\beta = 2\mu_0 \int_{V_p} p\,dV \Big/ \int_{V_p} B_T^2\,dV \qquad (2.3)$$

It is assumed that a conducting wall is at infinity.

The results of calculating β^{∞} and β^{c} as the functions of normalized current I_N (1.1) for three different sets of plasma geometries (2.1) are given in Figs. 1 and 2. First of all we note the validity of the relation

$$\beta^{\infty}(\%) = C^{\infty} I_N \qquad (2.4)$$

where C^{∞} = 2.9 - 3.2 weakly depends on both the plasma geometry and the current density distribution (parameter λ).

The relation of type (2.4) for β^{c} is not fulfilled for all I_N , since the dispersion of β^{c}/I_N for a fixed geometry is rather great. Local maxima of β^{c} are reached when q_s is just above the integers 2,3,4... . Flatter distributions of the current density at the plasma edge (larger λ in (2.2)) lead to reducing the pits between these integers. Let us establish

$$\beta^{c} = C I_N \qquad (2.5)$$

just for such values of q_s , and determine an effect of plasma parameters upon the coefficient C . For $k \geq 1.5$, $\delta \sim 0.3$ the values in (2.5) weakly depend on k , which provides a certain universality of (2.5). The value of δ = 0.3 is close to an optimum: further increasing the triangularity δ results in reduction of β^{c} along with increasing β^{∞} . The value of C and its evolution with the aspect ratio are strongly influenced by the density distribution at the boundary (parameter λ). Spe-

Max-Planck-Institut für Plasmaphysik
8046 Garching bei München

cifically, for the D-shaped plasma ($\kappa \geq 1.5$, $\delta = 0.3$) with $\lambda = 1$, $q_s \geq 3$ the function $C(1/A)$ is nearly linear:

$$\beta^c \simeq \left(1.6 + \frac{3.2}{A}\right) I_N \qquad (2.6)$$

Most interesting values of $\lambda = 2$, $q_s \geq 3$ at the moderate I_N yield β^c close to maximal values (Fig. 1) which obey the scaling

$$\beta^c = \begin{cases} (3.0 \div 3.1)\, I_N, & A \leq 4 \\ (2.5 \div 2.6)\, I_N, & A \geq 5. \end{cases} \qquad (2.7)$$

For these parameters of the D-like cross-section the relation

$$I_N = \frac{\pi(1+\kappa^2)}{A}\left(\frac{1}{q_s} + 0.12 + \frac{0.3}{A^2}\right) \qquad (2.8)$$

is satisfied with good accuracy. Poor dependence of I_N on the current profile (parameter λ) and β observed gives us confidence to consider formula (2.8) applicable not only to the specific family (2.2) but also to a wide class of peaked current profiles in tokamaks. For the INTOR parameters [5] ($I_N \simeq 1.2$) the relations (2.6)-(2.8) yield $\beta^c = 3 \div 4\%$. For circular cross-section $\beta^c < \beta^\infty$ and $C < 2$ (Fig. 2), which results in $\beta^c = 2.5\%$ even for steep tori with A=2. The elongation and triangularity of cross-sections (k=1.6, $\delta = 0.3$) suppress the toroidal destabilization so that $\beta^c \simeq \beta^\infty = 9\%$ for A=2, $q_s \geq 3$, but $I_N \simeq 2.8$.

3. Let us compare the equilibria with asymmetric cross-sections and an initial symmetric configuration (A=4, k=1.6, δ =0.3, q_c =1.1, $\varkappa$ =2, λ =1, q_s =2.17) for the same values of q_c, $\varkappa$, λ and preserved values of $(\kappa_1+\kappa_2)/2$, $(\delta_1+\delta_2)/2$ (But q_s somewhat varies). The Table lists the values of β^∞, β^c, q_s for such equilibria.

κ_1	κ_2	δ_1	δ_2	β^∞	β^c	q_s
1.6	1.6	0.3	0.3	5.19	3.5	2.17
1.7	1.5	0.3	0.3	5.10	3.45	2.18
1.8	0.3	0.3	5.0	3.3	3.3	2.20
1.6	1.6	0.4	0.2	5.1	3.3	2.19
1.6	1.6	0.5	0.1	4.94	2.9	2.27
1.8	1.4	0.5	0.1	4.91	2.25	2.32
1.8	1.4	0.1	0.5	4.76	3.1	2.27

For asymmetric equilibria the β^∞ and β^c values are less than in the symmetric case. The smallest β^c takes place for configurations close to a real divertor one (see N 6 in the table).

REFERENCES

1. Degtyarev L.M. et al. - In: Proc Invited Papers of Intern. Conf. on Plasma Phys., Lausanne, 1984, v.1, p. 157. 2. Degtyarev L.M. et al. - In: Proc. of 10th Intern.Conf. on CFPP, London, 1984, IAEA-CN-44/E-III-2. 3. Sykes A., Turner M.F., Patel S. Proc. 11th Eur. Conf. CFPP, Aachen, 1983, v.2, p.363.

4. Troyon F. et al. - Plasma Phys. and Contr. Fus., 1984, v.26, p.209. 5. INTOR, Phase One. - Vienna: IAEA, 1982.

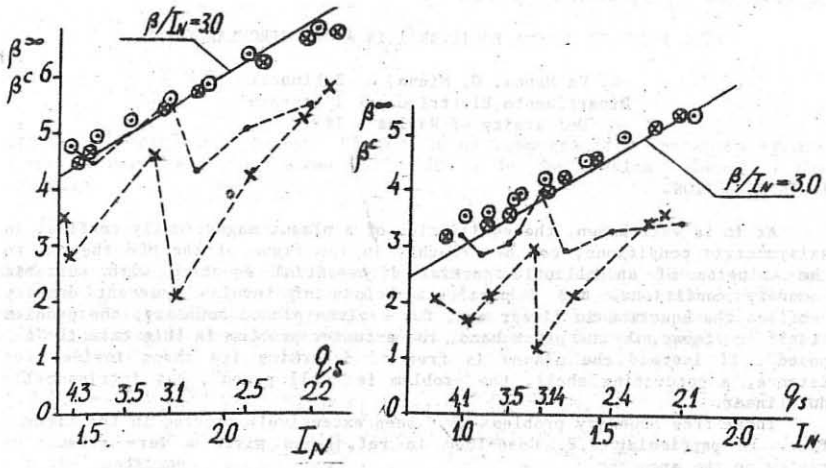

Fig. 1. β^{∞} and β^{c} as functions of normalized current I_N for plasma with D-shaped cross-section: k=1.6, δ = 0.3; (a) A=4, (b) A=3; ⊙ for β^{∞} and for β^{c} correspond to λ =2 in (2.2); ⊗ for β^{∞} and × for β^{c} correspond to λ = 1. The scale q_s is plotted by points β^{c} for λ = 2.

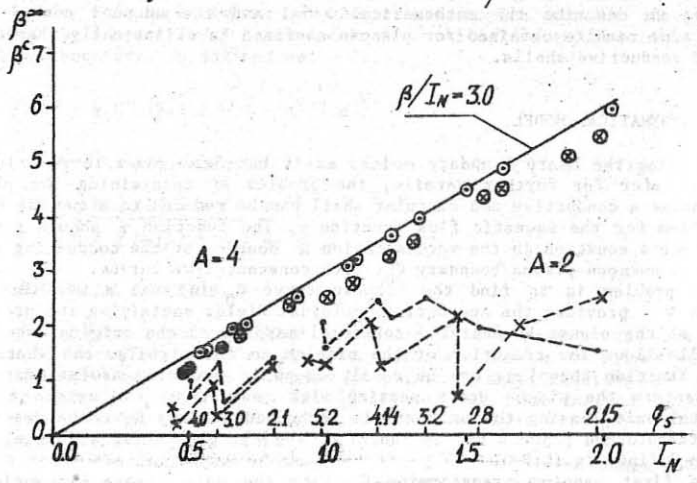

Fig. 2. β^{∞} and β^{c} as functions of I_N for the circular plasma.

FREE BOUNDARY PLASMA EQUILIBRIA IN A NON CIRCULAR SHELL

L. De Menna, G. Miano, G. Rubinacci
Dipartimento Elettrico per l'Energia
University of Naples - Italy

1. INTRODUCTION.

As it is well known, the equilibrium of a plasma magnetically confined in axisymmetric conditions, can be brought, in the frame of the MDH theory, to the solution of an elliptic partial differential equation with suitable boundary conditions. For a particular class of toroidal current density profiles the equation is linear and, for a given plasma boundary, the problem itself is linear. On the other hand, the exterior problem in this case is "ill posed". If instead the plasma is free of determing its shape inside, for istance, a conducting shell, the problem is "well posed", but intrinsecally non linear.

These free boundary problems have been extensively treated in the literature. In particular J.P. Goedbloed in ref. [1] has given a very exhaustive review on the argument.

In this paper the free boundary equilibrium of a sharp boundary high beta Tokamak with a conductive shell is solved, on the basis of the same integral equation for the poloidal magnetic field described in [1].

However a different method is used in order to obtain an analytical solution. In particular, the non linear functional describing the free boundary problem is expanded into a Volterra functional series, thus obtaining a hierarchy of linear integral equations, which can be solved analytically.

Here we describe the mathematical model and the adopted method and we give some results obtained for plasmas confined in elliptically shaped and D-shaped conductive shells.

2. THE MATHEMATICAL MODEL.

By using the sharp boundary model, as it has been shown in ref. [1], to which we refer for further details, the problem of determining the plasma shape inside a conductive non circular shell can be reduced to a two dimensional problem for the magnetic flux function ψ. The function ψ should satisfy the Laplace's equation in the vacuum region Ω bounded by the conducting shell C_1 and the unknown plasma boundary C_0, both constant flux curves.

The problem is to find the unknown curve C_0 in such a way that the solution ψ provides the appropriate poloidal field, satisfying the pressure balance at the plasma boundary. A conformal mapping of the original shape of the shell allows the reduction of the problem to the circular one where the Green's function thecnique can be easily adopetd. Another conformal mapping, which centers the plasma cross section with respect to the origin at the horizontal axis leaving the unit circle unchanged, allows C_0 to be described in the transformed plane ζ by the function $\rho = g(\theta)$, $g(\theta)$ being a unique value function defined in $(0, 2\pi)$.

The first mapping transforming C_1 into the unit circle C_1'(w-plane), and C_0 into C_0' leaving the origin unchanged can be written as:

$$z = \sum_{m=1}^{\infty} w^m a_m \qquad (2.1)$$

The other mapping is the Moebius transformation centering C_0' and leaving unchanged C_1':

$$w = \frac{\zeta + \delta}{1 + \delta \zeta} \qquad (2.2)$$

Letting $g(0)=g(\pi)= \gamma$, the pair (δ, γ) can be computed from the shift of the plasma center Δ and the plasma half-width a in the physical plane, by the condition:

$$z = \Delta \pm a \quad . \quad \leftarrow \quad \zeta = \pm \gamma \qquad (2.3)$$

Then the application of the Green's theorem to the double connected region between C_0' and C_1', using the Green's function for the unit circle and the appropriate boundary conditions for the flux function, leads to the following integral non-linear equation in the unknown function $g=g(\theta)$:

$$\int_0^{2\pi} G[g, \theta - \theta'] \, V[g, \theta', K^2, \delta, \gamma, a_1, \ldots, a_m] \, d\theta' = - \psi_1 \qquad (2.4)$$

with the condition:

$$g(0) = g(\pi) = \gamma \qquad (2.5)$$

Here

$$V = F \, h_0 \, (g^2 + \dot{g}^2)^{\frac{1}{2}} \qquad (2.6)$$

where h_0 is the scale factor of the transformation between the physical plane and the computational plane and F, proportional to the poloidal field at the plasma boundary, is defined as:

$$F = \{1 + \tfrac{1}{2} K^2 \, [Re(z) - \Delta - a] \, / \, a\}^{\frac{1}{2}} \qquad (2.7)$$

The parameter is proportional to the flux on C_1 while K^2 is defined as:

$$K^2 = 1 - \left[\frac{F \, [Re(z) = \Delta - a]}{F \, [Re(z) = \Delta + a]} \right]^2 \qquad (2.8)$$

3. THE ANALYTICAL SOLUTION.

The solution of the problem is obtained by expanding the non linear functional describing the free boundary problem into a Volterra functional series that gives rise to a hierarchy of linear integral equation.
This hierarchy of integral linear equations has been derived in ref. [2], where a description of the adopted method can be found with particular reference to a circular shaped wall.

To study the influence of the wall shape on the plasma shape and on the poloidal beta, walls slightly deformed from circular shape are considered. To

leading order in the wall distorsion the coefficients a_m of Eq.(2.1) can be related to the coefficients of the Fourier expansion of the wall contour:

$$r(\theta) = 1 + \Sigma_m \cos m\theta \tag{3.1}$$

by means of the following relationships, [3]:

$$\begin{aligned} a_1 &= 1 + \eta_0 \\ a_m &= \eta_{m-1} \qquad m > 1 \end{aligned} \tag{3.2}$$

Then, following ref.[2], the solution can be obtained by expanding $g(\theta)$, K^2 and ψ_1 in a power series of δ, η_0, η_1, ..., η_m, to leading order in η_m and neglecting cross-terms in δ and η_m, as:

$$\begin{aligned} g &= \Sigma_n g_c^{(n)} \delta^n + \Sigma_i g_{w,i} \eta_i \\ K^2 &= \Sigma_n \lambda_c^{(n)} \delta^n + \Sigma_i \lambda_{w,i} \eta_i \\ \psi_1 &= \Sigma_n \psi_c^{(n)} \delta^n + \Sigma_i \psi_{w,i} \eta_i \end{aligned} \tag{3.3}$$

In the limit $\delta=0$, $\eta_m=0$, for $m=0,1,\ldots$, the solution is easily found to be $g=\gamma$, $K^2=0$ and $\psi_1=-\gamma\ln\gamma$, therefore $g^{(0)}=\gamma$, $\lambda^{(0)}=0$ and $\psi^{(0)}=-\gamma\ln\gamma$. Now first inserting eqs. (3.3) into (2.4), next differentiating the resulting identity 1,2,...k times with respect to δ and once with respect to η_m for $m=0,1,\ldots$, and finally setting $\delta=0$, $\eta_m=0$, a hierarchy of Fredholm's linear integral equations of the second kind, with equal and symmetric nuclea is obtained. The nuclea of the hierarchy admit, as eigenfunctions, the sinus and cosinus functions. Then $g_c^{(n)}(\theta)$ and $g_{w,m}(\theta)$ can be expanded in Fourier series where only cosine therms are present because of the up-down symmetry of the configuration with respect to the equatorial plane. As consequence the solution of the hierarchy can be recursively found analytically.
Then $\lambda_c^{(n)}$, $\psi_c^{(n)}$, and $\lambda_{w,m}$, $\psi_{w,m}$ can be computed by imposing the constraints:

$$\begin{aligned} g_c^{(n)}(0) &= g_c^{(n)}(\pi) = 0 \\ g_{w,m}(0) &= g_{w,m}(\pi) = 0 \end{aligned} \tag{3.4}$$

4. RESULTS.

The following cases have been studied: circular wall, elliptical wall and D-shaped wall.

a) Circular wall. In this case $\eta_m=0$ for every m. To the third order in δ the solution is:

$$g_c(\theta) = \gamma + 3\delta^2\gamma^3\frac{1-\gamma^4}{1+3\gamma^4}(1-\cos 2\theta) + 4\delta^3\gamma^4\frac{1-\gamma^6}{1+2\gamma^6}(\cos 3\theta - \cos\theta) \tag{4.1}$$

while the poloidal beta, defined as $2p/\langle B_p\rangle^2$ to the first order in δ is given by: $a\varepsilon\beta_p \cong K^2/4 \cong 2\delta\gamma$. Here $\langle B_p\rangle$ is the poloidal magnetic field

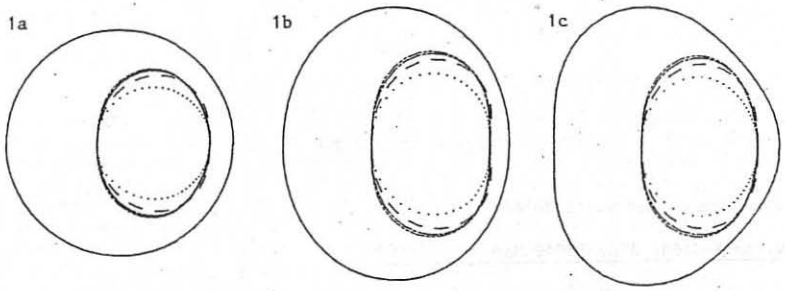

Fig.1. Plasma shapes to the different orders in δ: 1a circular, 1b elliptical and 1c D-shaped shell, respectively (...up to 1th order; - - - up to 2nd order; - - up to 3th order; - - up to 4th order; _____ numerical solution). a=.5 Δ=.3.

averaged on the plasma section.

b) Elliptical wall. In this case $\eta_0=-\eta_2=\lambda/2$ and $\eta_m=0$ for $m\neq 0$ and $m\neq 2$, where λ is the ellipticity. Let $g_E=g_C+\Delta g_E$, $K_E^2=K_C^2+\Delta K_E^2$, to the leading order in λ the solution is:

$$\Delta g_E(\theta) = 3/2\ \lambda\gamma^3\ \frac{1-\gamma^4}{1+2\gamma^4}\ (1-\cos 2\theta) \qquad (4.2)$$

By taking into account in the expansion (3.3) also the cross-therms $\delta\eta_m$ it can be shown that $\Delta K_E^2 \sim \delta\lambda$; hence the elongation of the wall increases the poloidal beta only if combined with a toroidal shift.

c) D-shaped wall. In this case to the leading order in λ and t: $\eta_0=-\eta_2=\lambda/2$ and $\eta_1=-\eta_3=-t/4$, where t is the triangularity. Let $g_D=g_C+\Delta g_D$, $K_D^2=K_C^2+\Delta K_D^2$. The solution is:

$$\Delta g_D(\theta) = 3/2\ \lambda\gamma^3\ \frac{1-\gamma^4}{1+2\gamma^4}\ (1-\cos 2\theta) + 1/2\ t\gamma^4\ \frac{1-\gamma^6}{1+2\gamma^6}\ (\cos 3\theta-\cos\theta) \qquad (4.3)$$

$$\Delta K_D^2 = \gamma t\left[2-4\gamma^4\frac{1-\gamma^6}{(1-\gamma^2)(1+2\gamma^6)}\right] \qquad (4.4)$$

Here again the ellipticity in ΔK_D^2 appears only in combination with the toroidal shift. The triangularity of the wall increases the poloidal beta also at $\delta=0$.

In Fig.(1a) we have plotted the plasma shapes at different orders in δ for the circular boundary case togheter with the numerical solution obtained by the method described in ref.[2]. In Figs.(1b) and (1c) we have shown the plasma shapes to leading order in λ and to different orders in δ for an elliptical and D-shaped case, respectively.

5. REFERENCES.

[1] J.P. Goedbloed, Phys. Fluids 25, (1982) 852.
[2] L. De Menna, G. Miano, G. Rubinacci, "Free Boundary Tokamak Equilibria" submitted for publication.
[3] V.I. Smirnov, "A Course of higher Mathematics", Vol.III part.II.

PREDICTION OF SAWTOOTH OSCILLATION PARAMETERS IN TOKAMAK DISCHARGES

A.G. Olivares and Mario Soler.

Div. de Fusión, JEN, 28040 Madrid (SPAIN)

I. Introduction.- A general method is presented for the prediction of sawtooth oscillations in Tokamak plasmas. The method relies on the assumption that localized perturbations resulting from violation of Suydam and Mercier conditions for stability suddenly activate reconnection at the m = 1, n = 1 magnetic island, thus causing the internal disruption. Appearance of the instability has been found in a systematic analysis of q profile evolution in cyclic disruptive regimes. The regimes were simulated by means of a perturbative transport code alternating with accurate solution of Kadomtsev's reconnecting model at each disruption, as explained in section II. Since no adjustable parameters are included in our predictions, very tight relations are established between physical quantities directly observed in experiments (such as temperature profiles, sawtooth amplitudes $\Delta Te/Te$, periods τ_s, inversion radii r_i) and unobservable parameters characterizing the plasma behaviour (heat transport coefficients, Z effective, resistivity). Some of the experimental possibilities opened by the method are outlined in section III. We finally discuss in section IV the extent to which our result can be considered as independent of the assumptions made in the method.

II. Prediction of cyclic sawtoothing regimes.- Sawtooth oscillations cyclically show two clearly distinct regimes: slow diffusion during the rise of the central temperature and fast disruption at its drop. We will briefly discuss our procedure to deal with each of these phases. Diffusion can be adequately studied by means of a transport code, while disruption is sufficiently described as a sudden reconnection of the magnetic surfaces with conservation of the magnetic flux, in the manner originally pictured by Kadomtsev.[1] A convenient transport code for the diffusive phase deals with perturbed $\widetilde{T}_{e,i} = T_{e,i} - T_{e,i}^{eq}$ rather than absolute temperatures $T_{e,i}$.[2] $T_{e,i}^{eq}$ represent the equilibrium temperature profiles if the sawtooth oscillations were suppressed. If the densities are considered stationary it is a simple matter to write general dimensionless equations advancing in time the perturbed $\widetilde{T}_{e,i}$ profiles originated by internal disruptions. These should be completed with evolution of the magnetic field after the perturbation

$$\frac{\partial B}{\partial t} = \frac{\partial}{\partial r} \frac{\eta}{r} \frac{\partial}{\partial r} rB \qquad (1)$$

where η is the electric resistivity. The current distribution J is immediately obtained from (1). In the transport equation for Te, besides the electron ion equilibration term $\eta J^2 - \eta^{eq} J^{eq2}$ should be kept, since both η and J appreciably change in sawtoothing regimes. The simplicity of this diffusive system makes it very convenient for analysis of a variety of regimes in different devices, since the main features affecting the sawtooth oscillations

are included, while other complicated processes can be considered to cancel when subtracting $T_{e,i} - T_{e,i}^{eq}$. We emphasize, however, that once the method to be now described is validated, full transport codes should be used for each particular device in order to obtain best results.

The disruptive phase requires the q profile to drop below 1 within a certain radius $0 < r < r_s$. Clearly accurate prediction of sawtoothing regimes calls for precise knowledge of the q profile evolution during a whole cycle, with a final disrupted profile equal to the initial one. In general finding profiles evolving with such property would be a hard problem. The striking stability of sawtoothing regimes which is also clearly manifest in experiments provides however an easy way out of the problem: sawtoothing immediately arrives at stationary regimes. When the period for disruption is adjusted to its experimental value, it is seen that the q profile evolution for cyclic regimes can be well described, close to the end of the cycle by the expression

$$q = 1 + \epsilon \frac{t_s - t}{t_s} + (\rho - \Delta)^2(\alpha + \beta\rho^2)(\rho^2 - \rho_s^2) \qquad (2)$$

where $\Delta \neq 0$ only for the largest devices,[3] α, β are of order 1, $\rho = r/a$ (a, minor radius) $\rho_s = r_s/a$, $\epsilon \ll 1$, and time units such that $t_s = 1$ is the sawtooth repetition time.

At $t = t_s$, $\dot{q} = 0$, $q = 1$ for $\rho = \Delta$. Suydam and Mercier's conditions for stability are violated. We assume that fast oscillations caused by this local stability greatly accelerate reconnection at $r = r_s$ and cause the disruption.[4] Adjusting the period is thus no longer necessary.

A large number of runs have been made with this method, using the approximately known transport coefficients, Z effective and "equilibrium" $T_{e,i}^{eq}$ profiles extrapolated from experimental data (about 10% higher at r = 0 than $T_{e,i}$ at the peak of the sawtooth). Sawteeth thus obtained are invariably in excellent agreement with those observed. Since no parameter fits are involved, the method can be turned around to predict transport coefficients if accurate transport codes are used for the sawtooth predictions.

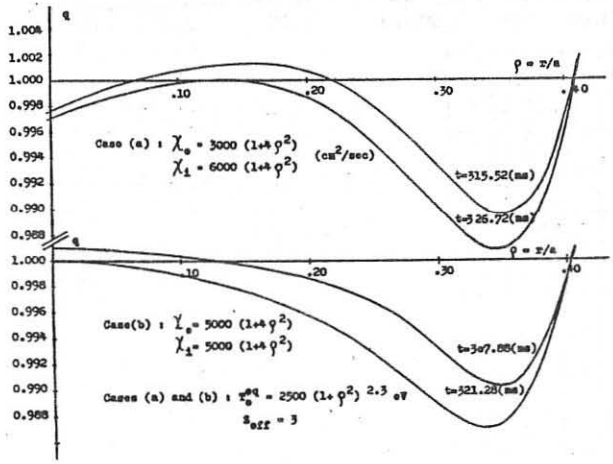

Fig. 1: q profile evolution for TFTR geometry and two different sets of transport coefficients producing t_s=80 ms, r_s=33.5 cm. For large devices where $\chi_i > \chi_e$ (case (a)) $\Delta \neq 0$ in eq(2). Small devices always follow the pattern shown in (b) ($\Delta = 0$).

III. Relation between sawtooth features and transport.- The extent to which sawtooth features depend on transport provides a measure of the method's interest for determining transport coefficients. It should be mentioned that temperature profiles are seen to be most influential in some sawtooth features such as location of r_I. Profiles depend on transport but on other phenomena as well. It is therefore useful to compare sawtooth regimes having the same profiles (T_e, T_i, n) but different χ_e, χ_i. We show for this purpose two different cases, (a), (b) of Fig. 2, corresponding to the same χ_i but with different χ_e. The sawtooth period, $\Delta T/T$ amplitude, central saturation, retardation and shape of the heat pulse are crearly shown to differ in both cases. Our third case (c) corresponds to the same χ_i, χ_e as (a) but lower Z effective. This produces longer periods as expected, since current penetration slows down, enhances $\Delta T/T$ because periods lasts longer, but does not change transport features such as retardation and shapes of heat pulses.

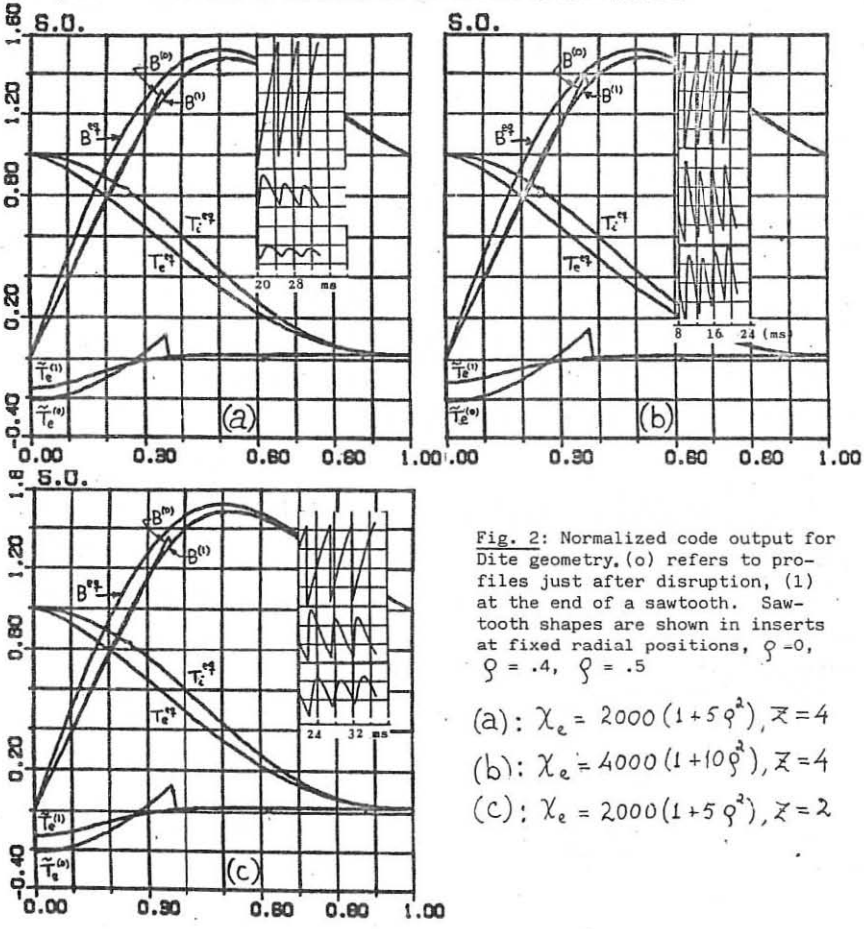

Fig. 2: Normalized code output for Dite geometry. (o) refers to profiles just after disruption, (1) at the end of a sawtooth. Sawtooth shapes are shown in inserts at fixed radial positions, ρ -0, ρ = .4, ρ = .5

(a): $\chi_e = 2000\,(1+5\rho^2)$, $Z=4$

(b): $\chi_e = 4000\,(1+10\rho^2)$, $Z=4$

(c): $\chi_e = 2000\,(1+5\rho^2)$, $Z=2$

IV. Model independent properties.- It is convenient to examine to what extent the relations obtained between observable data and physical parameters characterizing the discharge (χ_e, χ_i, Z and consequently η, q) depend on the particular model here proposed. In our view such relations are independent of the model, whose main merit is to provide excellent fits to actual sawteeth. Whether or not our explanation for the onset of disruption is correct, it provides the unique cyclic evolution of temperatures and current profiles for the given periods and inversion radii. We will therefore point out some outstanding properties observed in all computationally produced sawtoothing regimes, since in our opinion there can be little doubt that they are also realized in experiments.

One basic fact is that q is extremely flat in $0 < r < r_s$ and stays practically still. This is particularly true and particularly important in the large devices hot regimes. For these low resistivity cases, it is hard to imagine any other q diffussion pattern different from a minute change in the $0 < r < r_s$ region from one initial almost straight position above q = 1 to another just below. For they would involve such long periods as to make it impossible to fit the experimental data. On the other hand, the r_I inversion radius is shifted to large values, so for almost half of the plasma one has q=1. The current profile is consequently maintained practically stationary by the cyclic sawtoothing at a situation largely differing from equilibrium. Unless this is taken into account, there is little chance that resistivity and Z effective can be properly evaluated.

Another striking feature of sawtooth oscillations is the ease they show in changing from one regime to another. This in turn shows the great stability characterizing these regimes and the large damping with which they are arrived at. It also constitutes an added source of information, for it allows to follow the fast changes experienced by Tokamak plasmas for instance when subject to additional heating. Our numerical method clearly exhibits these same features. In fact, as mentioned above, it would be quite hard to find cyclic regimes if they did not set themselves spontaneously as observed in experiment.

Footnotes and References

1) B.B.Kadomtsev; Sov.J.Plasma Phys.,1 ,710 (1975)
2) A.G.Olivares and M.Soler,to be published
3) For $\Delta \neq 0$ cases, a situation more involved than Kadomtsev's simple reconection picture might be present as suggested by V.V.Parail,G.W.Pereversev, Sov.J.Plasma Phys.,6, 14 (1980).
4) Island uniform growth should thus be distinguished from disruption, in line with careful observations in TFR. See M.A.Dubois,A.L.Pecquet,C.Reverdin; Nucl.Fus,23 ,147 (1983)

ECE-Measurements on TEXTOR Tokamak during Ohmic and Ion Cyclotron Resonance Heating Experiments

G. Hrehuss* and G. Waidmann

Institut für Plasmaphysik der Kernforschungsanlage Jülich
Association EURATOM/KFA, P.O.B. 1913, D-5170 Jülich, FRG

*Central Research Institute of Physics, Budapest, Hungary

Abstract
A scanning radiometer for ECE measurements using 2nd harmonic X-mode is described and its calibration is explained. Fixed and swept frequency measurements were performed for electron temperature studies. Details concerning the sawthooth activity of TEXTOR are reported.

1. Introduction

The emission of electron cyclotron radiation (ECE) represents in tokamaks of sufficient density and temperature a means to study the electron temperature distribution in a large part of the plasma volume. A calibrated radiometer channel for a millimeter wavelength in the ECE spectrum is under proper plasma conditions an easy, continuous monitor of the electron temperature and also for well behaved plasma performance. Minor disruptions are immediately recognized and additional heating of the electrons is promptly detected. Heterodyne detection systems were chosen in TEXTOR because of its easy operation requirements and the very low system noise figures realised with modern solid state technology. The ECE receivers stand in the neighbourhood of megawatt rf-transmitters but no pick-up was found so far. The power received with a 30 dB directional horn antenna is so high that several radiometric channels can easily be supplied with the required ECE-power.

2. System Description

The ECE from TEXTOR is detected by heterodyne receiver systems. They are interfaced to a diagnostic data acquisition system as shown schematically in Fig. 1. The central part of the plasma is surveyed by a scanning radiometer covering a frequency range of 11 GHz from 113 to 102 GHz with a scan rate up to 100 Hz. A low system noise figure of 7 dB was realised using a varactor tuned Gunn oscillator and a Schottky barrier diode integrated into a frontend. A sensitivity of -78 dBm was found for an IF-bandwidth of 400 MHz yielding a radial resolution of ΔR = 1.5 cm. A 30 dB gain antenna mounted outside of the vessel on the low magnetic field side and an over-dimensional waveguide system transfer the ECE to the scanning receiver. A careful calibration over the broad frequency band was performed to take into account the damping properties of the various microwave components involved. A lock-in-technique was employed for calibration. The thermal radiation of an oven and the emission of the heated liner surface (T = 400°C) in the TEXTOR vessel were measured over the real optical path. The scanning ECE-data were then corrected with a frequency dependent sensitivity curve by a computer processing routine.

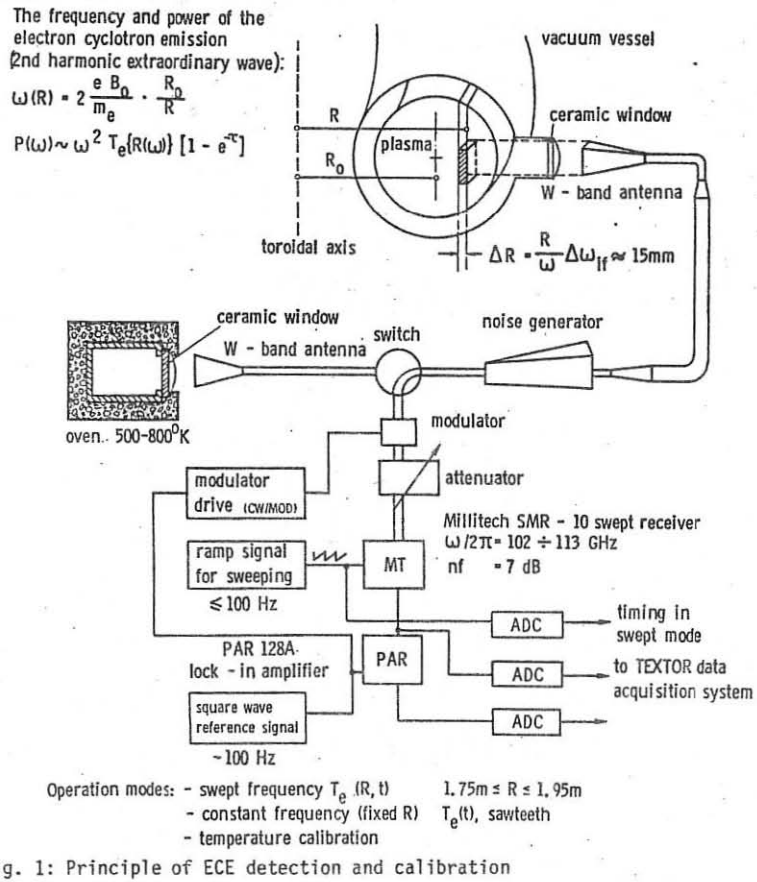

Fig. 1: Principle of ECE detection and calibration

For standard electron temperature monitoring a calibrated fixed frequency radiometer is installed. For a magnetic field of 2 Tesla on axis the central electron temperature is available. Z_{eff} on axis can be obtained if the safety factor q(0) on axis is provided.

3. Experimental Results

The temporal development of the electron temperature in the central part of a TEXTOR discharge is shown in Fig. 2. The step in the temperature around 1 sec is caused by an ion cyclotron resonance heating pulse which leads also to an electron temperature increase via a mode conversion process. The increase of the electron temperature at the end of the discharge is due to a density decrease in the current ramp-down phase. The ripple on the surface in the temperature diagram is generated by sawthooth activity

in the ECE. Since the scan frequency of the radiometer is lower than the sawtooth frequency the local temperature oscillations are scrambled over the surface. With fixed frequency operation of the radiometer the sawtoothing activity in the center of the discharge is demonstrated in Fig. 3. The slope of the sawteeth together with the local electron density n_{eo} allows an estimate of the local power deposition on the electrons: $\Delta Pe \cong n_{eo} \cdot \Delta Teo/\Delta t$. From the Ohmic input power on axis 20 to 50 % are calculated to be expelled from the central plasma by the internal disruption. A multiple of the Ohmic heating power is indicated by the drastic change in slope of the sawteeth when the ICRH is turned on.

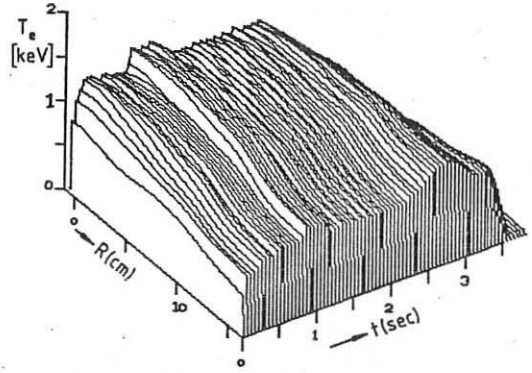

Fig. 2: Electron temperature distribution within the q=1 surface of TEXTOR

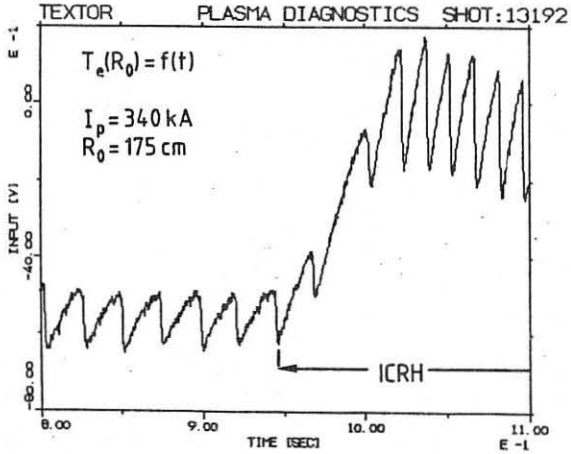

Fig. 3: Sawtooth activity before and during ICRH-heating

The internal disruptions and connected with it the emission of a temperature wave are shown in Fig. 4. For different shots the radiometer was set at different receiver frequencies and therefore different positions on the radius of the plasma. After crossing the q = 1 surface at R = 190,5 cm the sawteeth show a phase flip and an attenuation in amplitude.

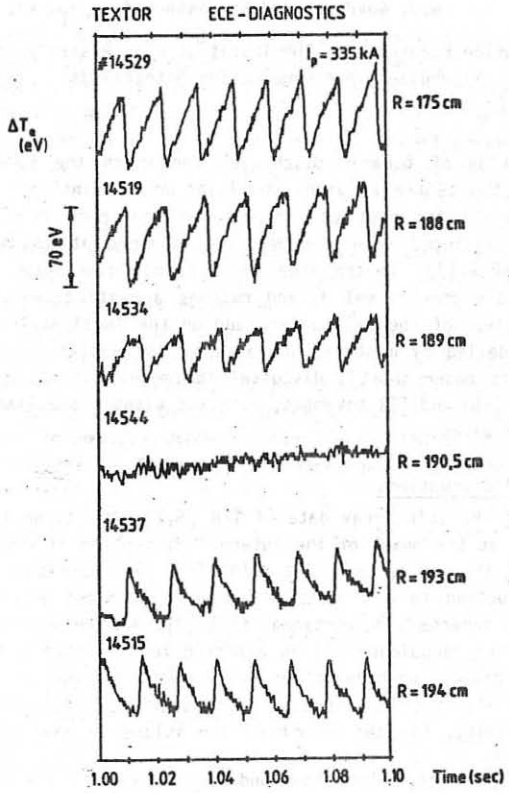

Fig. 4: Sawteeth observed at different radial positions of TEXTOR

Well behaved discharges show sawtoothing after a relaxation of the current density distribution at the end of the start-up phase and the establishment of a broad electron density profile. The disappearance of sawteeth indicates deformed peaked electron profiles which soon lead to a disruptive behaviour of the plasma. Discharges which do not exhibit sawteeth after the start-up show them occasionally (see poster) after a minor disruption which then has readjusted the density profile. Sawtoothing activity stops shortly before a density disruption occurs. Again peaked electron density profiles are observed. Strong m = 2 modes are then observed which possibly could interact with the internal mode activity.

SIMULATION OF TOKAMAK DISCHARGES WITH SAWTEETH

W.J. Goedheer and E. Westerhof

Association Euratom-FOM, FOM-Instituut voor Plasmafysica
Rijnhuizen, Nieuwegein, The Netherlands

Introduction

The simulation of tokamak discharges for which the safety factor q drops below 1 at the centre requires modelling of the internal disruptions, which are responsible for most of the outward transport from the central plasma. We have developed such a model and attached it to the 1D radial transport code ICARUS [1]. In the model an internal disruption is triggered when the resistively growing m=1 island reaches a critical value, δ_c, which depends on the radius of the q=1 surface and on the local shear. The disruption itself is modelled by a strong increase of the radial transport in the plasma centre. This paper shortly discusses the model and its application to discharges in the T-10 and TFR tokamaks, with and without auxiliary heating by electron cyclotron waves.

Model for internal disruptions

Analyses of the soft X-ray data of TFR [6,7] have shown that the size of the m=1 island at the onset of the internal disruption is some function of the local shear at the q=1 surface ($\hat{s} \equiv r_s(\partial q/\partial r)$) [2]. Ascribing the onset of the internal disruption to a transition to chaos predicts a critical island size, δ_c, which is inversely proportional to $\hat{s}$ [3]. Also ascribing the onset of the disruption to turbulence [4] is expected to give such a law. In order to have some flexibility, we have chosen $\delta_c/r_s = A\,\hat{s}^{-\alpha}$ in our simulations, where A and α are adjusted in accordance with available experimental data on the saw-tooth activity. For the growth of the island we have chosen the law for nonlinear evolution given by Dubois and Samain [4], $\delta^2(t) = \int_0^t 3\eta dt'$, where η is the resistivity and t the time elapsed since the previous disruption.

The disruption itself is modelled by an increase of the radial transport of particles and energy within and around the q=1 surface, typically by a factor of 50-500. This increment and the duration of the disruptive phase are chosen such, that the decrease in density and temperature at the centre is in accordance with the experiments. The resistivity is not enhanced in the disruptive phase, so the q-profile is not affected.

Simulations of T-10 discharges

Measurements of the electron-temperature profile in T-10 [5] have provided us detailed information on the behaviour of this profile during disruptive discharges, both in ohmically-heated plasmas and in plasmas with a substantial additional heating with electron-cyclotron waves at the fundamental harmonic. Furthermore, measurements of the evolution of the perturbation on the T_e-profile caused by the sawtooth activity have given information on the heat conductivity in the outer 10 cm of the plasma.

Adjustment of the critical island parameters to the sawtooth data of an ohmic discharge with $B_T = 3$ T, $I_p = 440$ kA, $n_e(0) \approx 9\times10^{19}$ m^{-3}, $T_e(0) \approx 1100$ eV yielded $A = 0.11$ and $\alpha = 2$. For the transport coefficients we took the χ_e deduced from the evolution of the temperature perturbation, $\chi_e = 0.3$ m^2 s^{-1} for $r \leq 15$ cm, $\chi_e = 0.3 + 9.7\times10^{-2}$ (r-15) m^2 s^{-1} for r up to 32.5 cm, the limiter radius. This χ_e is approximately 0.6 times the ALCATOR-INTOR value. The particle transport we took as $D_e = 0.35\ \chi_e$, while for the ion thermal transport we used the neo-classical value. The neo-classical resistivity described the current profile evolution.

Figure 1 shows the behaviour in time of the central electron temperature, as simulated and as measured. Figure 2 shows at which time, elapsed since the occurrence of a disruption, the temperature disturbance reaches its maximum at different radii outside the region where the fast redistribution has taken place. These data which are closely related to the electron thermal transport in the outer parts are also in agreement with experimental values.

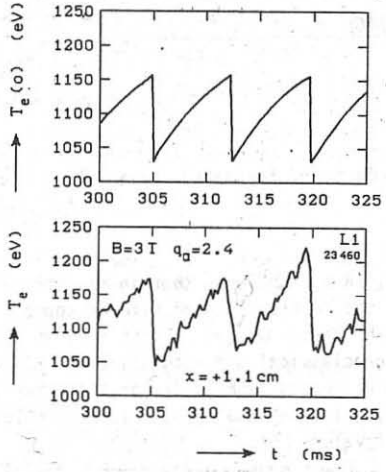

Fig. 1. Central temperature of T-10, ohmic phase, $B_T = 3$ T, $I_p = 440$ kA.

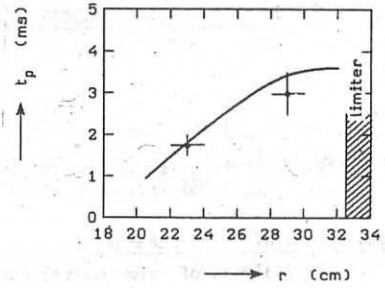

Fig. 2. Time of maximum perturbation outside region of fast redistribution.

With the same set of transport and disruption parameters, simulation of a discharge with a lower plasma current I_p = 350 kA, with the same B_T and $n_e(0)$, again yielded good agreement with experimental data, both in the ohmic phase and with additional heating with 400 kW of O-mode microwave power at the fundamental electron-cyclotron harmonic. Figure 3 shows the behaviour of the central temperature in both phases, as simulated and as measured.

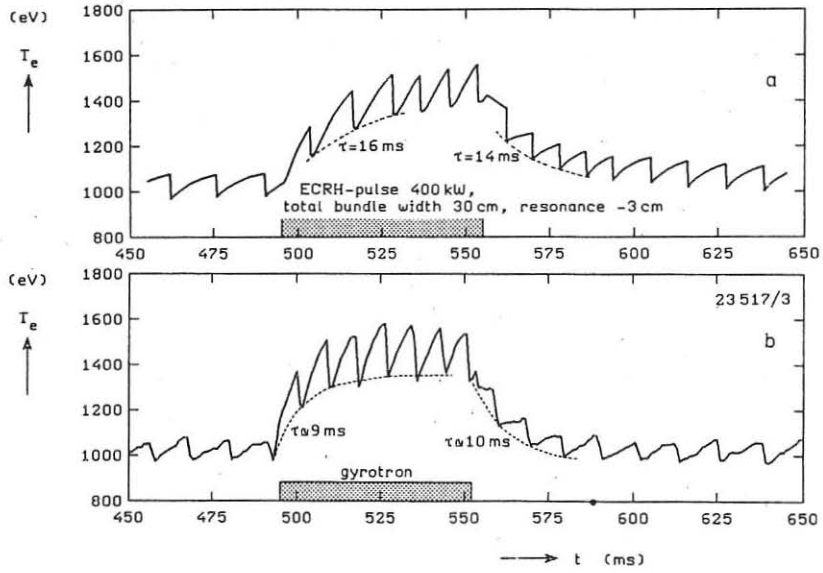

Fig. 3. Central temperature of T-10, ohmic and EC-heated. B_T = 3 T, I_p = 355 kA.

Simulations of TFR-discharges

An analysis of experimental data of TFR has shown us that in discharges with a toroidal magnetic field of 4 tesla, the critical island size is approximately $\delta_c/r_s = 0.011\ \hat{s}^{-2}$ [2]. Simulations of these discharges with $n_e\chi_e = (1.5+0.5\ r/a)10^{19} m^{-1}s^{-1}$, $D_e = 0.25\ \chi_e$, χ_i neoclassical and with Spitzers' resistivity yielded the sawteeth on $T_e(r)$ as presented in Fig. 4. For this discharge the plasma current was 300 kA, $T_e(0) \approx 1200$ eV and $n_e(0) \approx 1.7\times10^{20} m^{-3}$. The results closely agree with experimental values [6].

Also simulations of discharges at a lower magnetic field (2.1 tesla) with and without electron-cyclotron heating showed reasonable agreement with experiments.

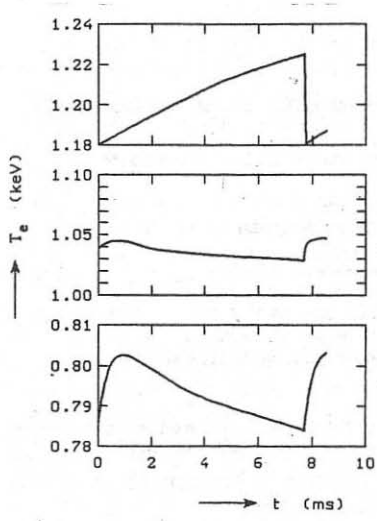

Fig. 4. Sawtooth of TFR at different radii, ohmic discharge with B_T = 4 T, I_p = 125 kA.

Conclusions

Prescribing the onset of an internal disruption when a resistively growing m=1 island reaches a critical value, $\delta_c/r_s = A\hat{s}^{-\alpha}$, which depends only on the shear on the q=1 surface, $\hat{s}$, yields simulations of tokamak discharges in agreement with experimental observations. Both discharges in T-10 and TFR can be simulated with $\delta_c/r_s \sim \hat{s}^{-2}$, the amplitude A being a factor of 10 different. This difference is to a large extent due to the fact that in TFR discharges the neoclassical correction on the resistivity was not taken into account, which gives higher values for q_0 and lower values for $\hat{s}$, while r_s is hardly affected.

Acknowledgements

The authors are indebted to Dr. M. Dubois (Fontenay-aux-Roses) for many discussions and for communicating unpublished TFR-data, to Dr. H.W. Piekaar and Dr. R.M.J. Sillen for their contributions to the analysis of the T-10 simulations and to Dr. M. Watkins and Dr. A.E.P.M. Abels-Van Maanen (JET) for making the ICARUS-code available.

This work was performed under the Euratom-FOM association agreement with financial support from ZWO and Euratom.

References

[1] Watkins, M. et al., in "Methods in Computational Physics" 16, Eds. J. Killeen et al., Academic Press, New York, 1976.
[2] Westerhof, E. and Goedheer, W.J., to be published.
[3] Lichtenberg, A.J., Nucl. Fusion 24 (1984) 1277.
[4] Dubois, M. and Samain, A., Nucl. Fusion 20 (1980) 1101.
[5] Sillen, R.M.J. et al., submitted to Nucl. Fusion.
[6] Dubois, M. et al., Nucl. Fusion 23 (1983) 147.
[7] Dubois, M. et al., Nucl. Fusion 20 (1980) 1355.

MAGNETIC ACTIVITY DURING INTERNAL DISRUPTIONS IN JET DISCHARGES

P.A. Duperrex*, R. Keller*+, M. Malacarne and A. Pochelon*+

JET Joint Undertaking
Abingdon, OX14 3EA, Great Britain

* on attachment from, + permanent address,
Centre de Recherches en Physique des Plasmas
Association Euratom - Confédération Suisse
Ecole Polytechnique Fédérale de Lausanne
21, Av. des Bains, CH-1007 Lausanne, Switzerland

Abstract. Two new types of magnetic activity have been measured by the internal magnetic coils on a very fast time scale during the thermal relaxation produced by the internal disruption. They indicate a propagation at a wave speed, in addition to the usual thermal diffusion pulse.

I. INTRODUCTION. JET is at present the largest magnetic confinement device. The parameters are $B_\phi < 3.45$ T, $I_p < 5$ MA, $R = 2.96$ m, $a = 1.25$ m, discharge elongation $b/a < 1.6$ and energy confinement time close to a second.

JET is equipped with 144 magnetic coils distributed in 8 equidistant poloidal planes with 18 coils in each octant. This permits both toroidal and poloidal mode determination. These coils measure the magnetic field component parallel to the vacuum vessel wall (i.e., that principally oriented in the b_θ direction). These coils are protected by a 2.5 mm thick inconel 600 tube which integrates $\dot{b}_\theta$ above 10 kHz. The signal is therefore proportional to $\dot{b}_\theta$ below 10 kHz, whereas above 10 kHz it is proportional to the magnetic field b_θ.

The other diagnostics used are electron cyclotron emission (ECE) in the Fabry-Perot mode, providing the electron temperature evolution on axis, various provisional soft X-ray diodes, viewing horizontally and tangentially through a central chord, the H_α light emission from the limiter, and a reflectometer signal measuring a constant density layer displacement.

II. FAST MAGNETIC PULSE. The first type of observed magnetic activity, which has been called the Gong-mode, takes the form of a fast $\dot{b}_\theta$ pulse, lasting typically 1 ms and having a toroidal mode number $n = 1$. Its transient resembles a strongly-damped ($Q \sim 1$-2) motion, with an oscillation frequency between 2-6 kHz (Fig. 1).

The arrival of the "Gong"-motion at the edge is much in advance of the heat pulse as indicated by the limiter H_α light emission (Fig. 2). It appears in perfect simultaneity with the internal disruption, as measured by

the ECE central electron temperature fall on axis, which has been acquired on the same ADC-unit, with a sampling frequency of up to 40 kHz. During the internal disruption, the electron temperature drop lasts typically 50-200 μsec. The $\dot{b}_\theta$ "Gong" signal measured at the edge sometimes even preceeds the explosive phase of the internal disruption, as exhibited by the rapid fall of T_e on axis. Thus $\dot{b}_\theta$ is capable of revealing the very first phases leading to the explosive process. The radial motion revealed by the reflectometer yields very similar information to the integrated $\dot{b}_\theta$ signal.

The toroidal mode number n, determined by using 4 low field side quasi-equatorial probes and integrating $\dot{b}_\theta$, yields clearly an n = 1 motion, n = 0 and n = 2 components being an order of magnitude smaller. The poloidal distribution is evolutive and strongly asymmetric: the pulse occurs first predominantly on the outside equatorial position (coil 1 and 18, Fig. 3), then progressively "invades" the other poloidal angles. The m-number is seen to evolve rapidly towards higher m's, with typically $3 \lesssim m \lesssim 5$, as determined by the number of poloidal periods. The strong low/high field side asymmetry is of the order of 5 to 10, even with the plasma closer to the probes located near the inner wall than to the probes at the outer wall. One should stress the essentially different character of the "Gong" oscillation compared to the periodically enhanced m = 2, n = 1 island activity at lower frequency sometimes observed around the sawtooth drop[2]. These two activities are often observed to coexist. The helicity of the deformation is measured to be of the same sign than that of the field lines.

The amplitude of the "Gong" motion increases with decreasing q_ψ. It also increases when the sawtooth amplitude is enhanced during rf-heating. Typical b_θ amplitudes are in the range of 10^{-4} Tesla.

The mode structure obviously strongly "remembers" the n = 1, m = -1 helical structure of the q = 1 surface, located close to the core, from where the motion presumably originates. The observation of the n = 1 toroidal mode number can obviously not be explained by an n = 0 rearrangement of the equilibrium. Furthermore, the n number cannot be modified by toroidal and non-circular shape coupling, consistent with the observation. On the contrary, the poloidal modes m are coupled which may explain the various m-number measured, depending on conditions. The very fast transmission from the core to the edge indicates a wave phenomenon. The observed helicity is characteristic of the n > 0 side of the spectrum where the stable MHD-modes are close to zero frequency, i.e. $n + m/q(r) \cong 0$, with n = 1, q > 0 and n and m of opposite sign. The radial propagation may either originate from the coupling of such a low frequency wave with a fast wave (kink), or may be due to a global MHD-wave[3]. More experimental and theoretical investigations are needed.

III. MAGNETIC BROADBAND ACTIVITY. The level of magnetic broadband turbulence has been shown to be strongly related to electron confinement time both in ohmic discharges[4] and in neutral beam-injected discharges[5].

The b_θ spectrum measured between 10 and 60 kHz shows a $f^{-2\pm0.5}$ depen-

dence, with typical levels of a few 10^{-8} Tesla $kHz^{-1/2}$ at 10 kHz. This level is not sensitive to the amplitude of the m = 2 n = 1 Mirnov activity, except at the very high predisruptive amplitudes, for which it dramatically increases.

After each internal disruption, the magnetic broadband activity (at 15 kHz) exhibits a periodic enhancement of more than a factor 2 in low q (q_ψ < 3) discharges, with a sharp rise less than half a millisecond after the internal disruption (Fig. 4). This increased activity is measured at the edge at a time before the heat pulse has reached the edge, as measured by the periodic H_α-light enhancements. We therefore conclude that confinement properties in the core and magnetic broadband activity are inversely related, and on time scales that seem to reveal a faster than a diffusive propagation.

IV. CONCLUSIONS. We have measured magnetic activity at the edge of the discharge related to the very central q = 1 internal disruption activity. The time scale indicates for both the described activities a wave rather than a solely diffusive propagation. The "Gong"-mode is characterised by n = 1, strong poloidal ballooning-like asymmetries, a step in b_θ with the main frequency component between 2-6 kHz, and the same sign of helicity as the field lines.

Acknowledgements. It is a pleasure to acknowledge stimulating disussions with Professor F. Troyon. L.C. de Kock and G. Tonetti and A.L. Stevens are gratefully achnowledged for making the magnetic measurement available, as well as D. Campbell, R. Gill, A. Hubbard and P.D. Morgan for diagnostics information, and T. Hellsten and K. Appert for valuable discussions.

References:

1. P.A. Duperrex, R. Keller, A. Pochelon and G. Tonetti, SSP Spring Meeting, March 1985, Helvetica Physica Acta 58, 4 (1985).
2. A.W. Morris and D.C. Robinson, private communication (1984).
3. K. Appert, J. Vaclavik and L. Villard, Phys. of Fluids 27 (1984) 432.
4. P.A. Duperrex et al., Phys. Lett. 106A (1984) 133, this Conf. Paper 97.
5. B.A. Carreras et al., Phys. Rev. Lett. 50 (1983) 503.

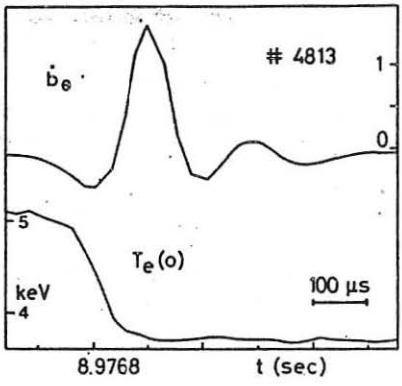

Fig. 1: The "Gong"-mode exhibited by the $\dot{b}_\theta$ signal at the time of the internal disruption, shown together with the central electron temperature drop (ECE)

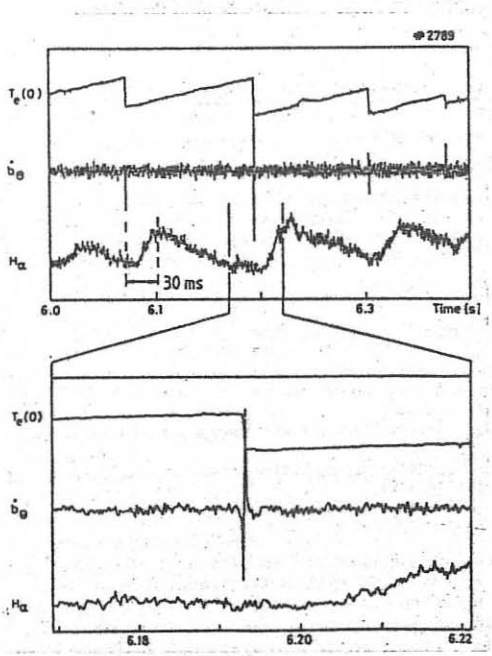

Fig. 2: The internal disruption on T_{eo} $\dot{b}_\theta$ and the heat pulse indicated by the limiter H_α light emission.

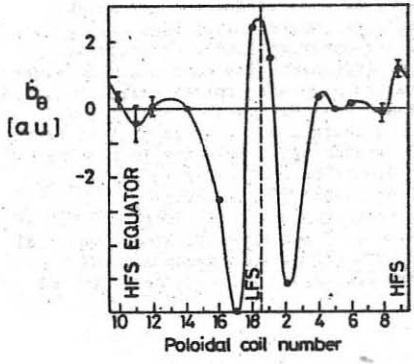

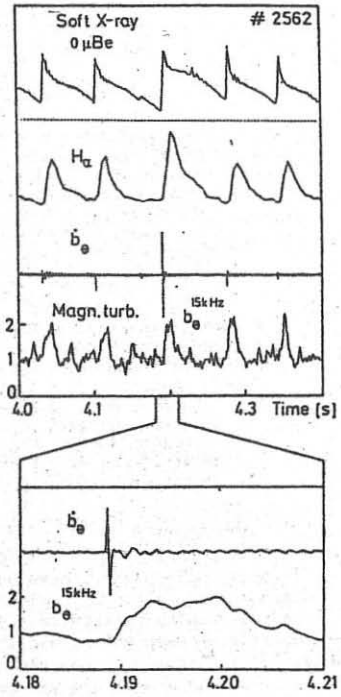

Fig. 4: The magnetic broadband turbulence pulse ($b_\theta^{15\,kHz}$), shown together with soft X-rays, limiter H_α and the "Gong"-mode as a time-marker of the internal disruption.

Fig. 3: A poloidal section of the "Gong"-mode, showing the strong asymmetry

ANALYSIS OF SAWTOOTH INSTABILITIES IN JET

D J Campbell, D V Bartlett, C Best, M Brusati, J P Christiansen, S Coda, J G Cordey, A E Costley, [X] G A Cottrell, L de Kock, P A Duperrex*, A Edwards, J A Fessey, D J Gambier[X], R D Gill, A Gondhalekar, C W Gowers, J Hugill[+], A Hubbard[o], J Jacquinot, O N Jarvis, S E Kissel, P P Lallia, E Lazzaro, P D Morgan, R M Niestadt[≠], J O'Rourke, Th Oyevaar[≠], H W Piekaar[≠], A Pochelon*, R Prentice, R T Ross, G Sadler, M F Stamp, T E Stringer, D Summers, G Tonetti*, B J D Tubbing[≠], M Valisa, P van Belle and J A Wesson,

JET JOINT UNDERTAKING, ABINGDON, OXON, OX14 3EA, UK

* On attachment from EURATOM-SUISSE Association, CRPP, CH-1007, Lausanne Switzerland.
X On attachment from EURATOM-CEA Association, Fontenay-aux-Roses, France
\+ On attachment from EURATOM-UKAEA Association, Culham Laboratory, Abingdon, Oxon, OX14 3DB, UK.
o On attachment from Imperial College of Science and Technology, University of London, London, UK.
≠ On attachment from EURATOM-FOM Association, Instituut voor Plasmafysica, Rynhuizen, Nieuwegein, The Netherlands.

1. INTRODUCTION

Sawtooth instabilities /1/, which are observed in virtually all JET 'flat-top' discharges, have been investigated with a wide range of diagnostics: electron cyclotron emission, neutron emission, soft x-ray diodes, density interferometry and reflectometry, H_α and impurity emission, magnetic pick-up coils, and limiter viewing camera. Aspects of sawtooth activity studied include the onset of sawteeth at early discharge times, MHD oscillations associated with sawteeth, sawtooth fall times, 'giant' (double) sawteeth, and the variation of sawtooth behaviour when additional heating (ICRH) is applied. It is found that sawtooth behaviour in JET is not satisfactorily described by conventional models /2/ of the sawtooth instability.

2. INSTRUMENTATION

Second harmonic, extraordinary mode ECE is used to determine the temporal evolution of the electron temperature in JET /3/. An absolutely calibrated Michelson interferometer measures the electron temperature profile with a scan time of 15 ms. A static Fabry-Perot interferometer and, more recently, a twelve channel grating polychromator /3/ provide high time resolution measurements of the variation of electron temperature at predetermined radii. Both instruments may be scanned across the plasma on a shot-to-shot basis. Ion temperature measurements are obtained from a neutron total yield monitor /3/.

A provisional 4-channel surface barrier diode array viewing just above and below the JET midplane provides measurements of soft x-ray emission. Density measurements are obtained from a seven-channel far-infrared interferometer, and a single channel 2-mm interferometer. Although the latter instrument measures the line integral of the electron density along a vertical chord, correlations of sawtooth measurements with the soft x-ray and ECE measurements reveal that it is a sensitive detector of sawtooth activity and

associated MHD oscillations. In addition, a microwave reflectometer monitors the variation of plasma density near the plasma edge.

Edge diagnostics available include H_α and impurity line emission, infrared thermography of the limiters, and magnetic pick-up coils.

3. SAWTOOTH ACTIVITY IN OHMIC DISCHARGES

Analysis of sawtooth behaviour in JET indicates that two distinct sawtooth regimes exist during ohmic discharges. During the current rise phase (which lasts several seconds), and during the current flat-top in discharges with high values of q_{cyl} ($\sim$10), sawteeth are generally preceeded by a growing odd m (presumably m=1) oscillation with a frequency in the range 0.1-1 kHz. At such times the electron temperature profile is very peaked and the sawtooth inversion radius may be only 10 cm. Figure 1(a) shows a striking example, measured by 2 mm interferometry, in which the MHD oscillation frequency decreases during successive sawteeth. The corresponding electron temperature profile is shown in Figure 1(b) (note that R_o = 2.96 m and a = 1.25 m).

During the current flat-top in most JET discharges, a second sawtooth regime is observed: sawtooth behaviour may be very irregular with 'single' and so-called 'giant' sawteeth /4/ occurring, apparently at random. The principal characteristic of this regime is that precursor oscillations are invariably absent, though successor oscillations are often observed. In addition, 'giant' sawteeth exhibit a partial sawtooth which i) does not penetrate to the plasma axis, ii) may occur on either the high-field or low-field side of the plasma axis, and iii) within the resolution of the diagnostics ($\lesssim$5 cm), has the same inversion radius as the full sawtooth. Figure 2 shows such a sawtooth measured by the twelve-channel ECE grating polychromator. Note that only every second channel is shown.

There are several possible explanations for the lack of precursor oscillations in this regime: there may be no magnetic island; an island may exist but be locked; there may be a very small rotating island which is beyond the resolution of the diagnostic instrumentation; or the growth time of the island may be so short that no significant rotation occurs before the disruption. These possibilities are currently under investigation, but it is clear that there is a discrepancy between these observations and the conventional picture of the sawtooth instability /2/. Similar discrepancies have been observed previously in TFR/5/.

A further aspect of sawtooth activity in JET not explained by the conventional model is the collapse time. Figure 3 shows a time interval of 1 ms around the collapse of central electron temperature. This observation was obtained from an ECE Fabry-Perot with signal bandwidth of 100 kHz and a sampling rate of 40 kHz. The electron temperature profiles obtained from the Michelson interferometer before and after the sawtooth collapse are also shown. It is clear that the collapse time is $\sim$100 μs. Typical sawtooth collapse times in JET lie in the range 100-200 μs, though a range of times of up to 1 ms have been observed within a single discharge. The model of the sawtooth collapse due to Kadomtsev /2/ predicts that

$$\tau_c \sim (\tau_R \tau^*)^{\frac{1}{2}} \qquad (1)$$

where τ_R is the resistive diffusion time, and τ^* the Alfven transit time in the helical magnetic field B* associated with the sawtooth. For the discharge parameters relevant to the case shown in Figure 3, and making the simplest assumptions about the development of B*, equation (1) gives $\tau_c \gtrsim 10$ ms.

4. SAWTOOTH ACTIVITY WITH ADDITIONAL HEATING

During additional heating experiments in JET, carried out with up to 5 MW of ICRH for periods of 1 - 3 seconds /3/, sawtooth activity exhibits the same

basic behaviour as in ohmic discharges, though with some modifications. The most striking of these is a substantial increase in sawtooth amplitude. Whereas the electron temperature fluctuation due to sawteeth in ohmic discharges is $\lesssim$ 15%, during ICRH the fluctuation on axis rises to 30 - 50% of the maximum electron temperature. By comparison, the ion temperature fluctuation shows a modest increase from $\lesssim$ 10% during ohmic heating, to 10 - 15% during ICRH (while the average ion temperature on axis may show a substantial increase of order 30%)

The sawtooth inversion radius increases slightly during ICRH, but this may simply reflect an acceleration of the gradual expansion of the inversion radius which occurs during the current flat-top. In addition, the sawtooth period increases slightly relative to the ohmic phase, but giant sawteeth with a period $\sim$ 300 ms have been observed. However, the details vary depending on the target plasma, heating mode, antenna coupling, and power level.

A remarkable feature of this heating regime is the observation at relatively low values of q_{cyl} (I_p = 4 MA, B_p = 3.4T, q_{cyl} = 3.3) of a large saturated MHD oscillation preceding the sawtooth collapse. This mode may exist in a saturated state for up to half the sawtooth period, with an amplitude $\gtrsim$ 30% of the sawtooth amplitude. An example of this phenomenon is shown in Figure 4. Correlation of soft x-ray and ECE signals indicate that this is an n = 1, m = 1 mode.

5. PLASMA DIAGNOSIS BY SAWTEETH

Analysis of the measured changes in temperature and density associated with sawteeth permits the determination of plasma parameters inaccessible to conventional diagnostic techniques. The use of the sawtooth heat pulse to investigate thermal diffusivity is well known /6/ and has been applied to JET plasmas /3/.

Measurements of sawtooth fluctuations in the line integrated density have been used, together with some modelling assumptions about the variation in the electron density profile, to investigate particle convection in the centre of the discharge. It is found that the fuelling of the core of the discharge, and restoration of the peaked density profile between sawteeth can be explained by the neoclassical pinch effect /7/, with pinch velocities in the range 5 - 10 x 10^{-2}m/s. The role of this effect in the buildup of the plasma density profile is still under investigation.

Study of the periodic electron and ion temperature variations during sawteeth allows the different components of the energy balance in the central region to be distinguished. Using an axial current derived from the condition that q = 1 on axis, ohmic heating during sawteeth can be derived. The mean rate of increase in the electron temperature during the sawtooth recovery phase then gives a measure of the central resistivity and hence of Z_{eff}. Thus, for a typical JET ohmic discharge, this yields Z_{eff} (o) = 5 compared with $\bar{Z}_{eff}$ = 4, derived from the neoclassical resistivity, and Z_{eff} = 3, calculated from visible Bremsstrahlung measurements.

REFERENCES

/1/ S von Goeler et al, Phys. Rev. Lett. 33 1201 (1974).
/2/ B B Kadomtsev, Sov. J. Pl. Phys. 1 389 (1975).
/3/ For additional details see papers 142 (B J D Tubbing et al), 185 (O N Jarvis et al), 186 (A E Costley et al) and the invited paper by J Jacquinot at this Conference.
/4/ W Pfeiffer, G A Technologies Report GA - A16994 (1983).
/5/ M A Dubois et al, Nucl. Fus. 23 147 (1983)
/6/ M Soler and J D Callen, Nucl. Fus. 19 703 (1979).
/7/ F L Hinton et al, Phys. Rev. Lett. 29 698 (1972).

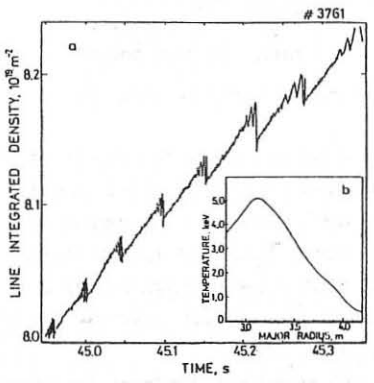

Figure 1: (a) Sawteeth density fluctuations measured by 2 mm interferometry during the rise phase of a JET discharge. (b) Temperature profile at this time measured by an ECE Michelson interferometer.

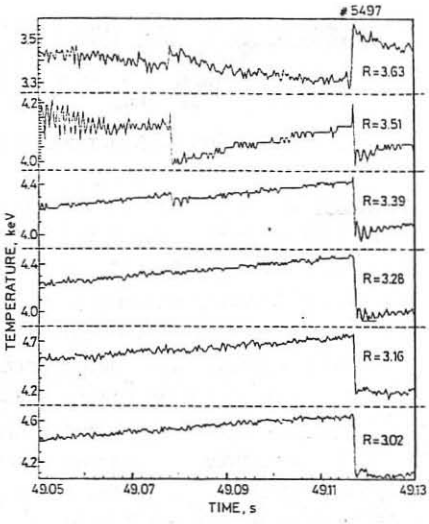

Figure 2: Partial and complete temperature sawteeth measured by an ECE grating polychromator.

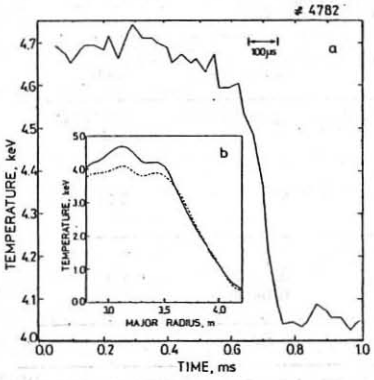

Figure 3: (a) A time interval of 1 ms around the collapse of a sawtooth measured by an ECE Fabry-Perot interferometer. (b) The temperature profiles measured before (solid lines) and after (dotted lines) the collapse, measured by an ECE Michelson interferometer.

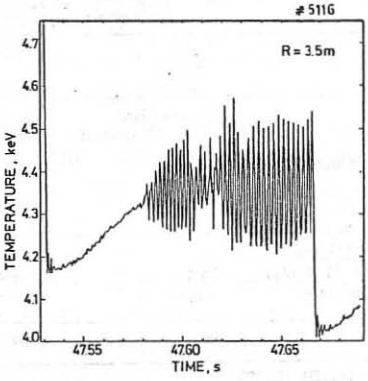

Figure 4: Sawtooth measured by an ECE Fabry Perot interferometer, during ICRH, showing large saturated MHD oscillation.

COMPOUND SAWTEETH AND HEAT PULSE PROPAGATION IN TFTR

K. McGuire, J.D.Callen* R.J. Colchin,**
P.C. Efthimion, E. Fredrickson, K. Hill, V. Paré,**
W. Park, N. Sauthoff, G. Taylor, R. White, H. Yamada.***

PLASMA PHYSICS LABORATORY, PRINCETON UNIVERSITY, PRINCETON, NEW JERSEY 08544 U.S.A.

ABSTRACT: A compound sawtooth in TFTR [1] is shown to consist of a subordinate relaxation, which typically does not affect the central electron temperature, but flattens T_e in an annulus around the magnetic axis, followed by a main relaxation, which reduces $T_e(0)$ but has a smaller inversion radius. The χ_e determined from heat pulse propagation in TFTR [2] usually exceeds that determined from background plasma power balance considerations by a factor ranging from 2 to 40.

SAWTOOTH ACTIVITY: Three types of sawtooth activity have been identified in TFTR: (1) simple or normal sawteeth, (2) small sawteeth and (3) compound sawteeth. Figure 1(a) shows simple sawteeth which are observed in TFTR plasmas with small minor radius (a < 60cm) and/or high q_a. The compound sawteeth shown in Fig. 1(c) are sometimes observed in bursts interspersed with small sawteeth (Fig. 1(b)). Table 1 lists some of characteristics for the three types of sawteeth in TFTR.

TABLE 1: TFTR SAWTOOTH SUMMARY

	SIMPLE/ NORMAL	SMALL	COMPOUND	
			SUBORDINATE	MAIN
r_1	Smallest(10cm)	Medium(20cm)	Largest(25cm)	Medium(20cm)
q	$q>4$ or 1st sawtooth	$q<4$	$q<4$	$q<4$
$\tau_{sk} = \mu_0 r_1^2/\eta$	~1.0sec	~2.0sec	~4.0sec	~2.7sec
Crash time(m/n=0/0)	0.1-0.5ms	0.1-0.5ms	N/A	0.03-1.0ms
m/n=1/1 PRECURSOR				
$\Delta\tilde{X}/X$ (m/n=1/1)	Large	Small	Small	Very small
Growth time	0.5ms	0.1ms	0.1ms	<0.1ms
m/n=3/2	no	no	maybe	no
m/n=1/1 SUCCESSOR				
$\Delta\tilde{X}/X$	Very small	Medium-Large	Large	Medium
Damping time	N/A	1ms	5-20ms	2-10ms
Mixing zone	$\sim 1.4\, r_{inv}$	$\sim 1.4\, r_{inv}$	$\sim 1.4\, r_{inv}$	$>2\, r_{inv}$
χ_{HP}/χ_{PB}	≥ 2	~2-20	~2-20	~4-40

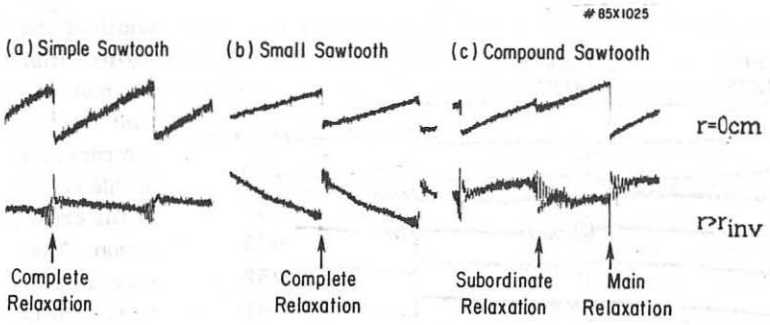

Figure 1. Sawteeth in TFTR. (80msec for each trace)

Simple tokamak sawtooth oscillations are a series of m/n=0/0 relaxations, each with an m/n=1/1 precursor mode. In contrast, compound sawteeth (observed in recent large tokamaks [3-6]) consist of a subordinate relaxation followed by a large (up to 20%) main relaxation with a smaller inversion radius. Compound sawteeth are commonly called "double sawteeth" because of their approximate double period in most cases. Compound sawteeth appear frequently in ohmically heated TFTR plasmas with high plasma current (I_p > 1.0 MA) and/or high density (n_e > 2.0 x 10^{19} m^{-3}). However, compound sawteeth do not always appear in these discharge regimes; instead, small sawteeth can be present. For these conditions, flat or slightly hollow current profiles form from the previous relaxation and evolve slowly between sawteeth because of the long skin time in the central region of the plasma. Thus, the compound sawteeth may be associated with relatively flat or hollow current profiles. Figure 2 shows that the main relaxation flattens the central temperature profile while the subordinate relaxation affects only the intermediate radii of the plasma. This suggests that the main relaxation is caused by a full reconnection, including the hot core at the center, while the subordinate relaxation does not affect the hot core. Because small and compound sawteeth are usually observed together, this suggests that a small or localized change of plasma parameters affects the characteristics of the sawtooth significantly. Small sawteeth are very similar to simple or normal sawteeth, except that the amplitude of the m/n=1/1 precursor is low and the m/n=1/1 successor oscillations are large. These observations suggest the presence of two q=1 surfaces.

Expanded views of one compound sawtooth are shown in Fig. 2. The m/n=1/1 precursor oscillation is seen to be small. This may imply that the

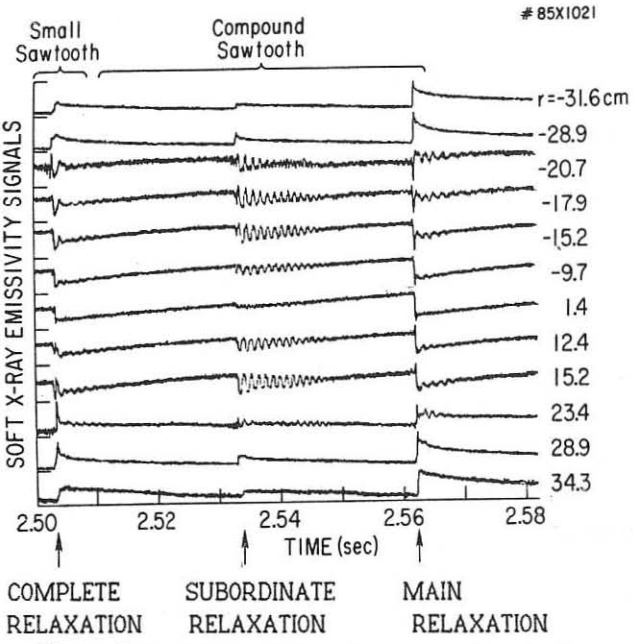

Figure 2. Detailed time history of a compound sawtooth.

width of the m/n=1/1 island is small or that the temperature profile is flat in the central region. The subordinate relaxation is not observed near the center and its inversion radius is larger (~25cm) than that of the main relaxation (18cm). The difference between these inversion radii is about 7cm, although it can be as large as 10cm. The outer inversion radius of the subordinate relaxation is always larger than that of the main relaxation.

The time evolution of the precursor mode is different from that of the simple sawtooth observed in earlier tokamaks; the main relaxation is associated with a small amplitude m=1 precursor mode, and the subordinate relaxation has an m=1 precursor with a larger amplitude m=1 successor.

HEAT PULSE PROPAGATION: The propagation of the sawtooth induced heat pulse is measured using a horizontally viewing soft x-ray array with about 5cm resolution at the tangency radius and with a fast ECE system which gives a T_e profile with about 5cm resolution every 4ms. The data are analysed using the time-to-peak method [7] as well as by a phase shift analysis based upon a Fourier expansion in time of the perturbed heat diffusion equation [2]. The solution of the resulting equation shows

that the phase shift of a given harmonic increases linearly with radius, with slope $d\theta/dr = (3n\omega/4\chi)$ where $\omega = 2\pi/t_{saw}$ and n is the harmonic. Analysis of the ECE and soft x-ray data using these techiques yields similar results.

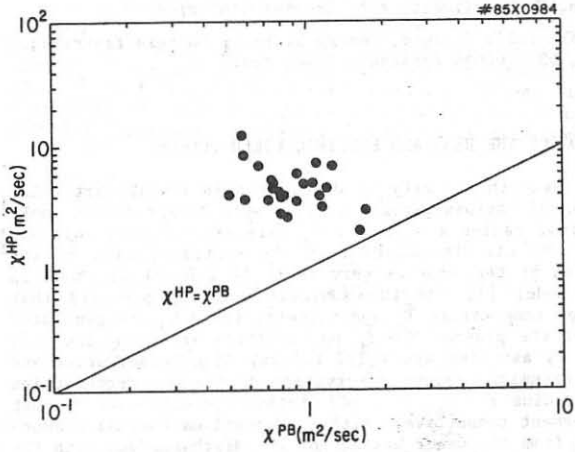

Figure 3. Comparison of χ^{HP} with χ^{PB} from TFTR.

Analytic and computer solutions of the electron heat diffusion equation have been used to clarify previous work, develop new methods for determining χ_e from phase analysis and pulse shape techniques, and make comparisons with the experimentally observed space-time evolution of T_e[2]. The sawtooth induced electron temperature perturbations are found to diffuse through the TFTR plasma at a rate (χ_e^{HP}) which is faster than that expected from the overall equilibrium electron heat transport (χ_e^{PB}), as shown in Figure 3. While extensive work has shown that the space-time evolution of the heat pulse is consistent with a diffusive process we do not have a viable model to explain why $\chi_e^{HP} \gg \chi_e^{PB}$. Resolution of this discrepancy could shed considerable light on the anomalous transport mechanisms operative in large tokamak plasmas such as TFTR.

This work was supported by D.O.E. Contract No. DE-AC02-76-CH0-3073.
*University of Wisconsin, Madison, WI. U.S.A.
**Oak Ridge National Laboratory, Oak Ridge, TN U.S.A.
***Permanent address: Dept. of Nuc. Eng., Univ. of Tokyo, Tokyo, Japan.

REFERENCES:
[1] Yamada, H., et al., PPPL report 2213(1985) to be published.
[2] Fredrickson, E., et al., to be published
[3] Pfeiffer, W., et al., GA Technologies Report GA-A16994 (1983)
[4] Thomas, P.R., et al., Proc. 10th Int. Conf. London, 1984, p.353
[5] Efthimion, P.C., et al., Proc. 10th Int. Conf. London 1984, p.29
[6] Kim, S.B., et al., Bull.Am.Phys. Soc. 29 (1984) 1395.
[7] Callen, J.D., et al., Phys. Rev. Lett. 38 (1977) 491.

ANALYSIS OF SAWTOOTH RELAXATIONS IN OHMIC AND RF HEATED DISCHARGES OF THE FT TOKAMAK

F. Alladio, G. Mazzitelli, A.A. Tuccillo, G. Vlad

Associazione EURATOM-ENEA sulla Fusione, Centro Ricerche Energia Frascati, C.P. 65 - 00044 Frascati, Rome, Italy

PROPAGATION OF THE HEAT AND ELECTRIC FIELD PULSES

The effect of the sawtooth activity is often felt in FT (in particular at low q_L) as modulation of various signals such as soft X-rays diodes looking up to 4/5 of the minor radius a = 20 cm, D_α emission and loop voltage. The time delay between the signals observed in the central region of the plasma and those observed at the edge is very short (1-2 msec) as shown in Fig. 1. The Kadomtsev model [1] for the sawtooth activity predicts that perturbations of electron temperature $\tilde{T}_e$ and magnetic field $\tilde{B}_\theta$ are generated in the central region of the plasma. The $\tilde{B}_\theta$ perturbation after the internal disruption is evaluated by assuming m/n = 1/1 helical flux conservation and the $\tilde{T}_e$ perturbation by assuming energy conservation during the reconnection up to the reconnection radius $r = r_\rho$. We study whether the diffusion of such perturbations is in agreement respectively with the anomalous thermal conductivity $\chi_e(r)$ as deduced from the power balance of the discharge and with the neoclassical electrical conductivity $\sigma_o(r) = \sigma(T_{eo})$ calculated from the steady state electron temperature profile $T_{eo}(r)$. We solve in cylindrical geometry the two linear decoupled diffusive equations

$$\frac{\partial^2}{\partial r^2}\tilde{T}_e(r,t) + \frac{1}{r}\frac{\partial}{\partial r}\tilde{T}_e(r,t) - \frac{3}{2}\frac{1}{\chi_e(r)}\frac{\partial}{\partial t}\tilde{T}_e(r,t) = 0 \qquad (1)$$

$$\frac{\partial^2}{\partial r^2}\tilde{B}_\theta(r,t) + \frac{1}{r}\frac{\partial}{\partial r}\tilde{B}_\theta(r,t) - \frac{\tilde{B}_\theta(r,t)}{r^2} - \mu_o\,\sigma_o(r)\frac{\partial}{\partial t}\tilde{B}_\theta(r,t) = 0 \qquad (2)$$

with boundary conditions

$$\tilde{T}_e(a,t) = 0, \quad \tilde{B}_\theta(a,t) = 0 \qquad (3)$$

and initial conditions $\tilde{T}_e(r,0)$, $\tilde{B}_\theta(r,0)$ as deduced from the Kadomtsev reconnection model. In Fig. 3 the calculated $\tilde{T}_e(r,t)$ evolution is shown for radii outside the reconnection region ($r > r_o$). The calculated time-delay at the edge is in remarkable agreement with the experimental results. If the thermal conductivity is multiplied by an arbitrary factor α $\chi_e(r)$ the agreement is still reasonable in the range $0.5 < \alpha < 2$. Also the calculated loop voltage time delay is in agreement within a factor 2 with the experimental observations. A more detailed comparison with the esperimental soft X-ray flux is shown in Fig. 4. We compute the SXR emission from a plasma contamined by Fe and O whose concentrations are deduced from spectroscopic measurements and match the resistive Z_{eff}. Bremsstrahlung, recombination and K and L lines radiation are taken into account assuming coronal equilibrium.

ELECTRIC FIELD PROFILE AT LOW q_L

At low q_L (~ 2.5) the electron temperature profile appears to be quite flat in the central region of the discharge, the sawtooth inversion radius is between 7 and 9 cm with a period τ_R between 3 and 9 msec, amplitudes $\Delta n_e/n_e \sim$ ~ 3% and $\Delta T_e(0)/T_e(0) \sim 15\%$. From the measured profiles, assuming $Z_{eff}(r) =$ = constant, the following parameters are obtained: q on magnetic axis $0.4 <$ $< q(0) < 0.7$, radius of $q = 1$ resonance $9 < r_s < 11$ cm, effective ion charge $1 < Z_{eff} < 1.5$. Such q(0) value is quite low and it is not very sensitive to neoclassical corrections for the resitivity neither to various attempts of peaking the $Z_{eff}(r)$ profile. So the main questionable point remains the assumed $T_e^{3/2}$ coupling between electron temperature and current density. In order to investigate such question we have solved the system of coupled non-linear diffusion equations for the perturbed quantities $\tilde{T}_e$ and $\tilde{B}_\theta$:

$$\frac{\partial^2}{\partial r^2}\tilde{T}_e(r,t) + \frac{1}{r}\frac{\partial}{\partial r}\tilde{T}_e(r,t) - \frac{3}{2}\frac{1}{\chi_e(r)}\frac{\partial}{\partial t}\tilde{T}_e(r,t) =$$

$$= -\frac{1}{n_e(r)\chi_e(r)}\left[\frac{J^2(r,t)}{(\sigma_o(r)+\tilde{\sigma}(r,t))} - \frac{J_o^2(r)}{\sigma_o(r)}\right] \qquad (4)$$

$$\frac{\partial^2}{\partial r^2}\tilde{B}_\theta(r,t) + \frac{1}{r}\frac{\partial}{\partial r}\tilde{B}_\theta(r,t) - \frac{\tilde{B}_\theta(r,t)}{r^2} - \mu_o\sigma_o(r)\frac{\partial}{\partial t}\tilde{B}_\theta(r,t) =$$

$$= \mu_o\tilde{\sigma}(r,t)\frac{\partial}{\partial t}\tilde{B}_\theta(r,t) + \mu_o\left[E(r,t)\frac{\partial}{\partial r}\sigma(r,t) - E_o\frac{\partial}{\partial r}\sigma_o(r)\right] \qquad (5)$$

where E_o is the steady state ($\tau_R \to \infty$) applied electric field, $J_o(r) = \sigma_o(r)E_o$ is the steady state current density, $\tilde{\sigma}(r,t)=\sigma(T_{eo}+\tilde{T}_e)-\sigma(T_{eo})=\sigma_o(r,t)-\sigma_o(r)$ is the perturbed electrical conductivity, $J(r,t)=J_o(r)+1/(\mu_o r)\partial(r\tilde{B}_\theta)/\partial r$ is the current density and $E(r,t)=J(r,t)/\sigma(r,t)$ is the electric field. The asymptotic solutions of Eqs (4), (5) with boundary conditions (3), has been derived by an iterative procedure in which the initial conditions $\tilde{T}_e(r,0)$, $\tilde{B}_\theta(r,0)$ are iteratively calculated from the Kadomtsev reconnection model after a given sawtooth repetition time $t = \tau_R$. In the case of low q_L discharges, the observed repetition time is imposed: the asymptotic solution for the current density profile is remarkably lower, in the central region, than the steady state $\tilde{T}_{eo}^{3/2}$ profile [2] (see Fig. 5). Consequently the time averaged electric field profile can not be considered uniform over the plasma cross section for the low q_L discharges in FT. This suggests that the real q in the center is at all times very near to q(0) = 1. On the other hand the electron temperature is able to recover during the sawtooth period as shown in Fig. 6.

SAWTOOTH REPETITION TIME FOR OHMIC AND RF HEATED DISCHARGES

The model of the coupled non-linear Eqs (4), (5) shows that two characteristic times are present in the relaxation of the current density profile: the shorter one is related via non-linear terms to the evolution of the temperature profile and the longer one is the resistive diffusion time for the decay of the initial condition $\tilde{B}_\theta(r,0)$. If the asymptotic solution of Eqs (4), (5) is searched prescribing a repetition time τ_R shorter than the first characteristic time the q value is greater than one in the centre inhibiting any further reconnection. After that $q(0) \leq 1$ appears in the centre and a

sudden variation of r_s is obtained increasing the imposed τ_R which is at the end followed by a much slower variation toward the steady-state ($\tau_R \to \infty$) [3]. Figure 7 and Figure 8 show this behaviour for two different ohmic discharges: in both cases it appears that the experimental repetition time is near the minimum τ_R that allows the reconnection. Using this self consistent argument it is possible to analyze the observed sudden increase of the sawtooth period when the LH heating is applied on a sawtoothing discharge (see Fig. 2). This sudden increase can be justified either by a sudden increase of the electrical conductivity of the discharge or by a sudden decrease of its thermal conductivity as soon as the RF wave is applied. A rough model in which these two quantities are multiplied by a factor constant over the radius, i.e. $\sigma_{RF}(r) = k_1\sigma(r)$ or $\chi_{eRF}(r)=\chi_e(r)/k_2$ has been used. An increase of the sawtooth period consistent with the experimental results is obtained respectively for values of $k_1 \cong 1.75$ or $k_2 \cong 4$.

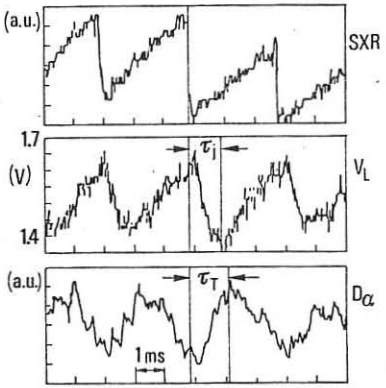

Fig. 1 - Experimental delay between central SXR sawtooth, loop voltage and D_α emission at the edge.

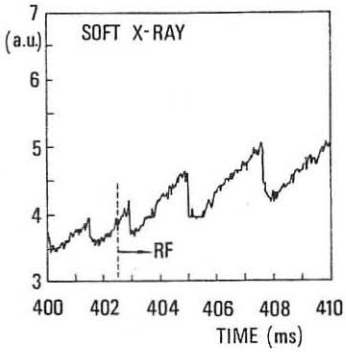

Fig. 2 - Increase of the sawtooth period when 300 kW of LH heating on applied.

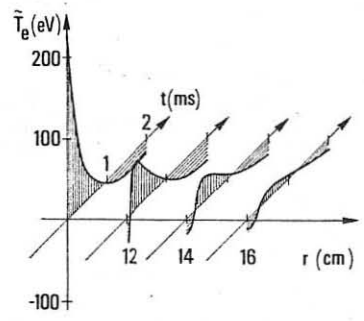

Fig. 3 - Calculated $\tilde{T}_e(r,t)$ evolution outside the reconnection radius $r=r_o$.

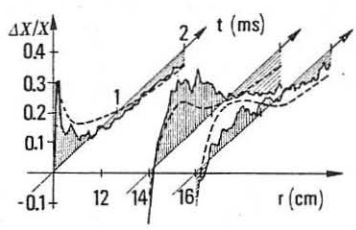

Fig. 4 - Comparison between experimental and calculated SXR emission.

Discharge parameters are B_T=38.3 kG, I_p=362 kA, $n_e(0)=7\times10^{13}$ cm^{-3}, $T_e(0)$=1080 eV, Z_{eff}=1.7, q_L=2.5, τ_R=2.2 msec.

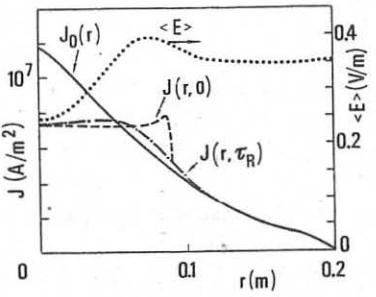

Fig. 5 - Typical low q_L discharge: steady state $J_o(r)$ profile, $J(r,t)$ profile excursion resulting from saw tooth activity and time averaged electric field $\langle E(r)\rangle$.

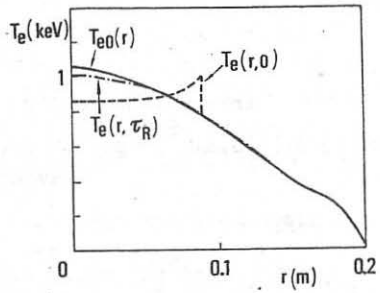

Fig. 6 - Typical low q_L discharge: steady state $T_{eo}(r)$ profile and $T_e(r,t)$ profile excursion resulting from sawtooth activity.

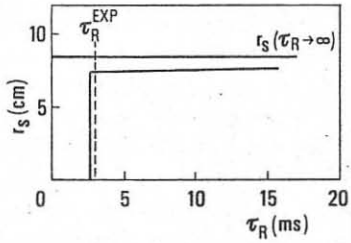

Fig. 7 - Calculated radius r_s of q=1 vs sawtooth repetition time τ_R for a low density discharge ($\bar{n}_e = 4.5\times10^{13}$ cm^{-3}).

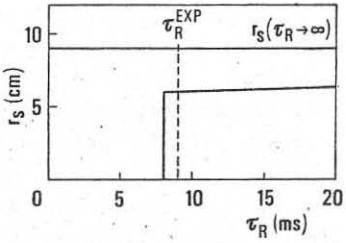

Fig. 8 - Calculated radius r_s of q=1 vs sawtooth repetition time τ_R for a high density discharge ($\bar{n}_e = 3\times10^{14}$ cm^{-3}).

REFERENCES

[1] B.B, Kadomtsev: Sov. J. Plasma Phys. 1 (1975) 389.
[2] F. De Luca, A. Jacchia: Nuovo Cimento Lett. 34 (1982) 395.
[3] Yu.N. Dnestrovskii, S.E. Lysenko, R. Smith: Sov. J. Plasma Phys. 3 (1977) 9.

Internal Disruption Study in T-10 Plasmas

Bobrovskii G.A., Esiptchuk Yu. V., Notkin G.E., Portnov D.V., Savrukhin P.V.

Kurchatov Institute of Atomic Energy, 123182, Moscow, USSR.

The study of internal disruption has been carried out since 1973 /1/, but its nature is not clear yet. ECRH provides new opportunities for such a study because it allows actively affect internal disruption. The main diagnostics used in this study on T-10 are X-ray imaging system with a slot aperture, Si(Li)-spectrometers and 2-channel superheterodyne EC-radiometer. The imaging system has a spatial resolution 1.5 cm and a time resolution 0.04 ms. The plasma parameters were I_p = 80÷600 kA, B_t = 1.5÷3.5 T, a_L = 17÷34 cm, $\bar{n}_e = (1.5 \div 6) \cdot 10^{13}$ cm^{-3}.

1. Internal disruption is known to be often accompanied by sinusoidal oscillations m=1, n=1 which should exhibit on the q=1 surface /1/. The phase analysis of signals from the detectors spread in poloidal and toroidal directions on T-10 indicates the m=1, n=1 structure too. A maximum in the relative amplitude of sinusoidal oscillations falls to a phase-reverse radius of sawteeth, r_s, on T-10, as well as in /1/. Hence, one can conclude that the r_s-surface coincides with the q=1 surface. Also, close to 1 is $q(r_s)$ calculated from the T_e-profile (see Fig.1).

2. Studies of sinusoidal oscillations which regularly accompanied internal disruptions led to the conclusion /1,2/ that internal disruption was the result of the m=1, n=1 mode growth. However, an irregularity in the emergence of sinusoidal oscillations in a series of internal disruptions is registered on T-10: the oscillations can accompany only some disruptions and have different amplitudes in different cases, they can continue or emerge after a disruption, can appear instead of a disruption. On the other hand, sinusoidal oscillations, as it has been shown in /1/ and confirmed on T-10, is a result of the m=1 mode rotation with a definite velocity, namely, that of the electron dia-

magnetic drift. Therefore, the irregular emergence of sinusoidal oscillations means most probably the absence of perturbation than the absence of rotation. The irregularity indicates that there is no connection between the m=1 mode and internal disruption, although they are often correlate with each other. The absence of connection contradicts the heuristic theories developed in /2,3/.

3. Coincidence between the r_s-surface and the q=1 surface means that the presence of the latter in the plasma column is the necessary condition for the development of internal disruption. However, this condition is not sufficient: time which is needed to suppress sawteeth at the ECRH start-up /4/ is conciderably shorter than their period, so that the q=1 surface should remain inside the plasma column. To find the sufficient condition a logarithmic gradient in T_e on the r_s-surface has been analyzed and it has been shown that it is equal to $(4.7 \pm 0.6).10^{-2}$ cm^{-1} just before disruption in all the regimes under study. Therefore, one can conclude that the fulfillment of this equality is the second necessary condition for the development of disruption. This condition is equivalent to the presence of a critical value of $d\ln(n_e T_e)/dr$ at r_s, as the n_e-gradient is close to 0 there. Satisfaction of both necessary conditions mentioned above could be considered as the sufficient condition for the development of disruption. However, some cases have been registered on T-10, when sawteeth were absent though both conditions were fulfilled.

4. During ECRH: a) sawteeth are suppressed when the resonance zone is displaced out of the r_s-surface /4/; b) sawteeth are excited in plasma with low $\bar{n}_e < \bar{n}_{e\,cr}$, at which they are absent at the Ohmic stage (Fig.2), in this case r_s is the same as that in plasmas with higher n_e at the Ohmic stage; c) "additional" internal disruption appear, their r_s being less than that of the "main" ones (Fig.3, see also Fig.1).

5. Study of dependence of the main characteristics of internal disruption, r_s and T, on plasma parameters has shown that: $r_s \sim 1/q_L$ (Fig.1), r_s does not depend on n_e and is not practically changed under ECRH at any position of the resonance zone; period T is proportional to $\bar{n}_e$ at $q_L < 3$, does not depend on n_e at $q_L > 3$, weakly depends on q_L at $\bar{n}_e$ = const, considerably changes under

ECRH. Comparison between the dependences of r_s and T on the plasma parameters points out the absence of the direct connection between these two values. This conclusion contradicts both the numerical simulation /5/ based on the model /2/ and the experimental results from TFR /6/.

6. Comparison between a quasi-stationary profile of T_e and the amplitude of T_e-change in sawteeth, measured by radiometer, shows that the reconnection is not complete at the moment of disruption within the r_s-surface, at $q_L \geqslant 4$. Probably, the full reconnection takes place in plasmas with $q_L \simeq 2$. The absence of the full reconnection at higher q_L is indicated also by the conservation of sinusoidal oscillations and of the peaked profile of X-ray intensity after disruption.

In summary, some results obtained yet in /1/ and explained in /2/ were confirmed on T-10, but some phenomena are in contradiction with the model /2/: a) the complete reconnection inside r_s does not occur at the time of disruption, at least with $q_L \geqslant 4$; b) there is no direct connection between internal disruption and m=1 mode and between r_s and T; c) presence of the q=1 surface in plasma is not sufficient for the internal disruption development; d) coexistence of disruptions with different r_s's is possible.

/1/. S. von Goeler et al. Phys. Rev. Lett. 33, 1201(1974)
/2/. B.B. Kadomtsev. Fizika Plasmy. 1, 710(1975)
/3/. M.A. Dubois et al. Nucl. Fusion. 23, 147 (1983)
/4/. T-10 Group. In 11th Europ. Conf. on Contr. Fusion and Plasma Phys., Aachen, 1982, part 1, p.283
/5/. Yu.N. Dnestrovskii et al. Fizika Plazmy. 3, 18 (1977)
/6/. TFR equipe. In Plasma Phys. and Contr. Nucl. Fusion Res. 1976, IAEA, Vienna, v.1, p.279

Figure Captions:

Fig.1. The dependence of x_s (●), of the q=1 radius (○) and of x_s for additional disruptions (△) on q_L (x_s are the chords of phase inversion). The curves are the $1/q_L$ dependence.

Fig.2. The regions of the internal disruption exictence (above the curves) in Ohmic phase (solid curve) and under ECRH.

Fig.3. The X-ray detector signal scopes under central ECRH. The additional disruption is shown. B_t = 3.04 T, q_L = 2.5.

FIG.1.

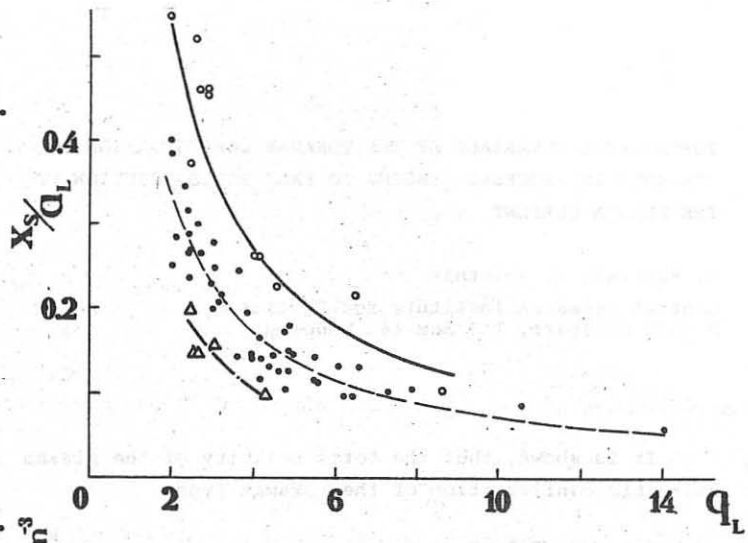

FIG.2.

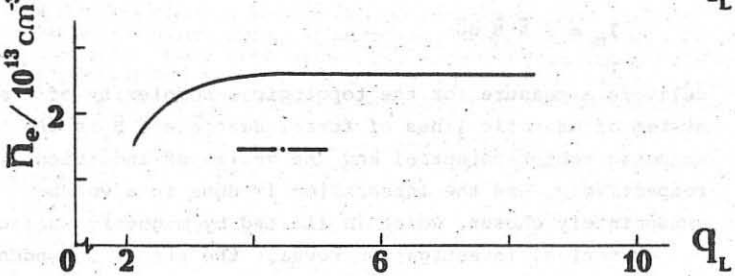

FIG.3.

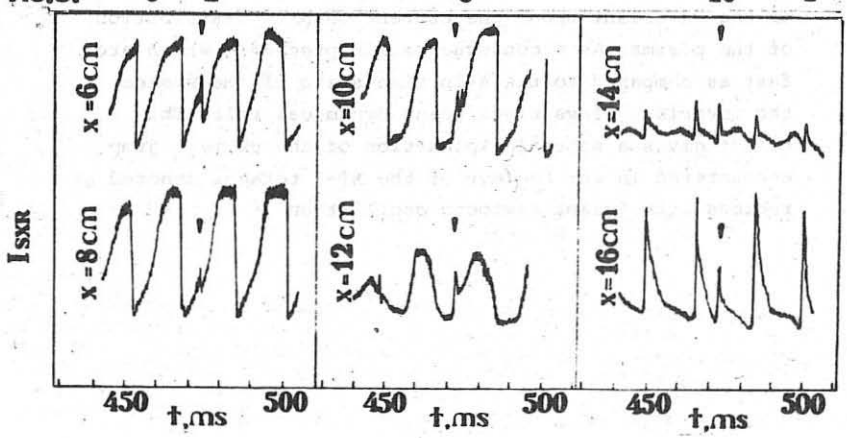

TOPOLOGICAL INVARIANT OF THE TOKAMAK CONFIGURATION AND ITS ROLE IN PROCESSE LEADING TO FAST REDISTRIBUTION OF THE PLASMA CURRENT

A. Montvai, S. Zoletnik
Central Research Institute for Physics
H-1525 Budapest, P.O.Box 49, Hungary

It is shown, that the total helicity of the plasma -magnetic configuration of the tokamak type:

$$I_m \propto \int \bar{A}\,\bar{B}\,d\bar{U}$$

delivers a measure for the topological complexity of the system of magnetic lines of force. Here $\bar{A}$ and $\bar{B}$ is the magnetic vector potential and the vector of induction respectively, and the integration is done in a volume apropriately chosen, which is limited by magnetic surfaces.

Numerical investigation reveals the strong dependence of the invariant upon the current density distribution of the plasma. As a consequence, in processes which are fast as compared to the skin time-scale of the system, the invariant plays significant dynamical role. This effect gives a natural explanation of the current jump encountered in the regimes of the MT-1 tokamak denoted as regimes with "giant sawtooth oscillation".

DENSITY LIMIT DISRUPTIONS IN JET

J. Wesson, C. Gowers, W. Han*, F. Mast#, F. Nave, M. Turner*, M. Watkins

JET Joint Undertaking, Abingdon, Oxon., OX14 3EA, UK
* Culham Laboratory, Abingdon, Oxon., OX14 3DB, UK
# On attachment from IPP, Garching.

Abstract

The experimental observations on density limit disruptions in JET are consistent with a model in which radiation losses lead to a strongly mhd unstable configuration.

Introduction

The operating regime in JET has a disruption density limit given approximately by

$$\left[\frac{\bar{n}}{10^{19}}\right] < 12\,\frac{B_T}{R_o q_c} \qquad \ldots (1)$$

where $\bar{n}$ is the mean electron density, B_T the toroidal magnetic field, R_o the major radius of the plasma and $q_c = 2AB_T/\mu_o IR_o$, A being the plasma area and I the plasma current. For a given value of plasma current the highest electron density is achieved at disruptions on the current fall, that is for currents lower than the peak current. Figure 1 shows a plot of such disruptions in the Hugill diagram.

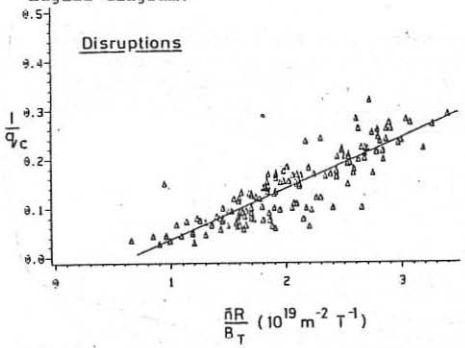

Fig 1: Hugill plot of density limit disruptions.

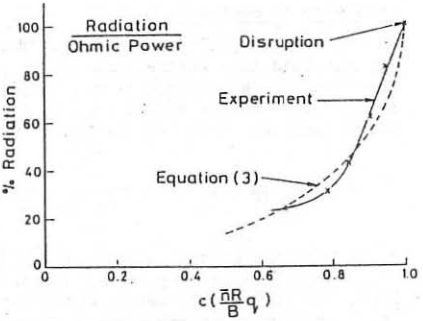

Fig 2: (Radiated power/ohmic power) against $(\bar{n}R/B)q$.

Radiation [1-7]

It is found that prior to density limit disruptions, the total radiation in the plasma increases, reaching a value ~ 100% of the input power at the time of disruption. This radiation comes mainly from the edge of the plasma. The relationship between this variation in radiated power and the quantity $\bar{n}Rq_c/B_T$ can be seen from a simple model. Inside the radiating layer the radiation losses are balanced by thermal conduction, and taking the layer to be thin

$$K \frac{d^2T}{dr^2} = R(T) f n_e^2$$

where K is the thermal conductivity, R(T) the radiation parameter and f the ratio of impurity ion density to electron density. Integration of this equation across the layer gives the radiated power as a fraction, ϕ, of the total plasma heating power.

$$\phi = 1 - \left[1 - \frac{8\pi^2 AKR_1 f n_e^2}{P^2}\right]^{\frac{1}{2}} \qquad \ldots (2)$$

where $R_1 = \int_o^\infty R\, dT$, P is the plasma heating power per unit length and A is the plasma area.

Now $2\pi R_o P = VI = V2AB_T/\mu_o R_o q_c$ where V is the loop voltage, and substitution into equation (2) gives the relationship between ϕ and $n_e R_o q_c / B_T$,

$$\phi = 1 - \left[1 - \alpha^2 \left[\frac{n_e R_o q_c}{B_T}\right]^2\right]^{\frac{1}{2}} \qquad \ldots (3)$$

where

$$\alpha^2 = 8\pi^4 K R_1 f (\mu_o R_o / V)^2 / A.$$

This relationship is complicated but it can be seen from equation (3) how the observed growth of the radiation fraction ϕ can occur as the disruption parameter $\bar{n} R_o q_c / B_T$ is increased. Figure 2 shows the result of a bolometer measurement of ϕ as a function of $\bar{n} R_o q_c / B_T$ during a particular discharge together with a normalised plot of equation (3) assuming α is a constant and that $n_e \propto \bar{n}$.

Stability to contraction

When $\phi = 1$ the plasma is thermally disconnected from the limiter. This may or may not lead to a contraction of the plasma. Some understanding of this question can be obtained from a simple model in which the plasma is taken to be circular and the radius, a_p, of the radiating layer is taken as the dependent parameter. Thus the energy balance equation may be written

$$\frac{d}{dt}(\pi a_p^2 \varepsilon) = I^2 R_p(a_p) + 2\pi \left[- c n_e(a_p) a_p - K \frac{T_R}{a - a_p} a_p\right] \qquad \ldots (4)$$

where ε is the average plasma energy density, I is the plasma current and R_p the plasma resistance per unit length. The second term gives the radiation loss, the linear dependence on n_e coming from the analysis outlined above, and the last term gives the thermal conduction loss from the layer, T_R being the temperature of the peak in the radiation parameter and a the radius of the limiter. Linearisation of equation (4) with constant I leads to the stability equation:

$$\gamma \tau_E = \tfrac{1}{2}\left[\frac{a_p}{R_p}\frac{dR_p}{da_p} - \phi\left[1 + \frac{a_p}{n_e}\frac{dn_e}{da_p}\right] - (1 - \phi)\frac{a}{a - a_p}\right].$$

where γ is the growth rate and τ_E is the energy confinement time.

It is seen that under normal circumstances, with ϕ well below unity, the last

term dominates because of the small denominator $a-a_p$. The plasma is then stable to contraction. However as ϕ approaches unity this term goes to zero. The plasma is then unstable to contraction if

$$-\frac{a_p}{n_e}\frac{dn_e}{da_p} > 1 - \frac{a_p}{R_p}\frac{dR_p}{da_p}$$

It is very difficult to determine this criterion theoretically because of the complexity of physics involved. However the experimental results indicate that both stable and unstable behaviour is possible. Figure 3 shows the contraction of the radiation layer observed before a disruption and Figure 4 shows the contraction of the electron temperature profile.

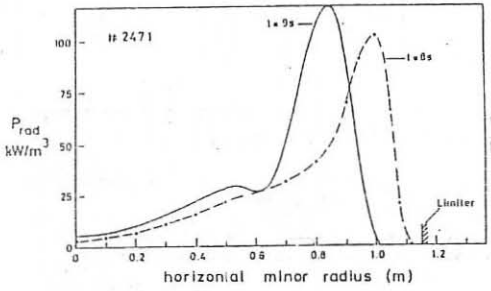

Fig 3: Radiated power against radius before disruption.

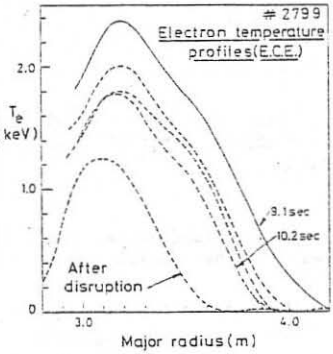

Fig 4: Electron temperature profiles

Disconnection and disruption

Contraction of the temperature profile leads to an increasingly unstable current profile and ultimately disruption can result [8]. The condition for 100% radiation as given by equation (3) is

$$\frac{n_e R}{B_T} = \frac{1}{\alpha}\frac{1}{q_c} \quad \ldots (5)$$

It is clear that the form of this relation is similar to that of the disruption boundary shown in Figure 1. However what is plotted in Figure 1 is the instant of disruption whereas condition (5) is the condition for 100% radiation. These must be separated in time by a time $\gamma^{-1} \sim \tau_E \sim$ 1sec. A consistent description requires therefore that there should be an event prior to the disruption which marks the onset of the contraction. A candidate for this is the onset of a hesitation in the density $\bar{n}(t)$, which is observed typically 1 second before the disruption as shown in Figure 5. In Figure 6 the hesitation onsets are plotted for discharges during a given period of operation.

In many discharges no disruption occurs and the time trajectory in the Hugill diagram follows the direction of the hesitation and disruption lines. It seems likely that these are cases where the 100% radiation limit is reached but where the plasma is stable to contraction.

Simulation

A computer calculation has been carried out to simulate the disruption model outlined above. The code uses the large aspect-ratio, circular approximation. Maxwell's equations are solved together with an energy transport equation including the effects of impurity radiation losses. The self-consistent quasi-linear tearing mode island growth and the effect of the m=1 mode are followed

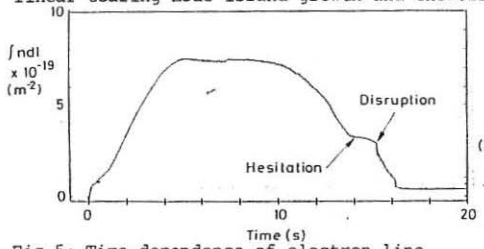

Fig 5: Time dependence of electron line density showing hesitation before disruption.

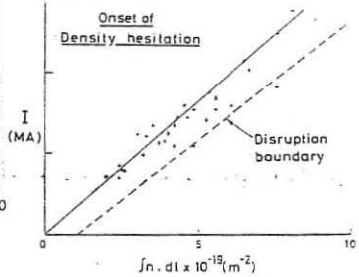

Fig 6: Hesitation onsets plotted in (I, ∫n dℓ) diagram.

in time. Figure 7 gives results from these calculations showing the inward movement of the radiating layer leading to a disruptively unstable current profile.

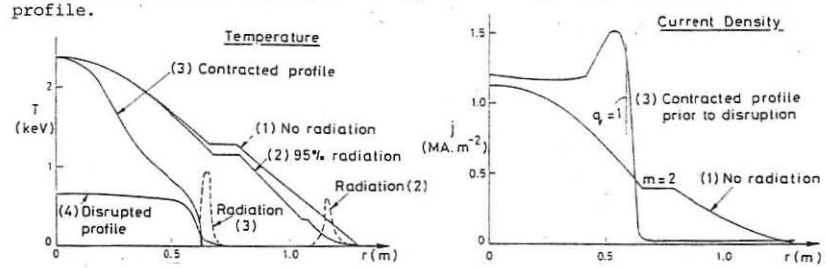

Fig 7: Plots of simulation results showing time development of the temperature and current density.

Acknowledgements

The authors would like to thank the ECE group in JET for Figure 4.

References

[1] Gibson, A., Nucl. Fusion, 16 (1976) 546.
[2] Rebut, P.H. and Green, B.J. in Plasma Physics and Controlled Nuclear Fusion Research (Proc. 6th Int. Conf. Berchtesgaden, 1976) 2, IAEA, Vienna (1977) 3.
[3] Gibson, A. and Watkins, M.L. in Controlled Fusion and Plasma Physics (Proc. 8th European Conf. Prague, 1977) 1 (1977) 31.
[4] Watkins, M.L., Physics Reports 37 (1978) 111.
[5] Igitkhanov, Yu.L. et al., Nucl. Fusion 18 (1978) 415.
[6] Ohyabu, N., Nucl. Fusion 9 (1979) 1491.
[7] Ashby, D.E.T.F. and Hughes, M.H., Nucl. Fusion 21 (1981) 911.
[8] Turner, M.F. and Wesson, J.A., Nucl. Fusion 22 (1982) 1069.

Experimental Observations of Disruptions in JET

F C Schüller, F Alladio[+], D Campbell, F Crisanti[+], L de Kock, H Krause[o], P Lomas, M Malacarne, F K Mast[o], M F F Nave, B Niestadt*, P Noll, H W Piekaar*, P R Thomas, J Thompson, G Tonneti[#], B Tubbing*, J Wesson

JET Joint Undertaking, Abingdon, Oxon OX14 3EA
[+]Euratom - ENEA Association, Frascati, Italy
[o]Euratom - IPP Association, Garching, Fed. Rep. Germany
*Euratom - FOM Association, Nieuwegein, The Netherlands
[#]Euratom - Suisse Association, Lausanne, Switzerland

1 Introduction

The main aim of JET is the study of plasmas in which α-particle heating is a significant part of the input power and this depends on reaching a value of the product $n_i T_i \tau_E > 5.10^{21} m^{-3} s^{-1}.keV$. With ohmic heating alone all 3 parameters are about a factor 3 too small. The maximum value of $\bar{n}$ reached up until now is $3.75\ 10^{19} m^{-3}$ and limited by the high density disruption. It has been shown elsewhere that additional heating brings this limit up with a factor 1.5 to 2 which is not enough. Moreover it is undesirable to induce a disruption at every pulse when heating is switched off. Study of high density disruptions is therefore a key issue for JET.

2 Disruption Database

A database has been developed in order to document the occurrence of disruptions. For every disruptive pulse 16 plasma quantities are stored at 3 moments in time:

a) the moment of energy quench is undistinguishable from the start of the current quench and is defined as the plasma current data point where after $dI/dt < -0.4I$;
b) one time slice preceding a) because often diagnostics are wiped off during the energy quench.
c) The start of the MHD-precursor (m=2/n=1) defined as the time slice in which the MHD-activity is twice as large as the average over the preceding second.

3 Operational Window

The database can be used for the construction of Hugill-diagrams. Fig. 1 gives as an example the 1984 disruptions in the $(1/q_\psi)$ - $(\bar{n}R/B)$ plane. Two categories can be observed:

a) disruptions connected to the rise phase or early flat-top: their probability is enhanced by increasing current ramp-rates [1] and shows a maximum around $q_\psi \cong 3.3$ although these disruptions may occur at any q-value.
b) high density disruptions. It is shown [2] that these disruptions occur when the radiative loss about equals the input power. Low Z radiation is dominant. The fact that also in JET these disruptions follow the well known diagonal in the Hugill diagram can be described by a simple model: assume that the input power is dissipated within the q=2 surface and the

radiative loss takes place outside this surface. When radiation is 100% of the input power a disruption will occur. If one takes the empirical dependence of the input power on B, q and dimensions and for the low-Z radiation the corona-model predictions for the second "helium-like" radiation peak one finds the following for JET:

$$\bar{n}R/B = 1.2 10^{20} \; B_t^{-3/4} \; q_\psi^{0.1} \; [(q_\psi - 2)\,(Z_{eff} - 1)]^{-\frac{1}{2}} \qquad (1)$$

Curves of this dependence for typical values of B_t and Z_{eff} are shown in the diagram. In 1985 the Murakami parameters obtained are about 20% higher than in 1984. The record value being 4.7 $10^{19} m^{-2} T^{-1}$ was obtained without disruption at low B_t=1.7T and q_ψ=3.2.

4 Precursors

On a timescale of about 1 sec before disruption noticeable changes in the plasma edge can be observed: changes in the recycling pattern, i.e. reduction at the limiter, increase at the wall, increase in low Z radiation, increase in $\beta_{pol}+\ell_i/s$. Often this leads to a development of a "marfe", sometimes to the development of a growing cool plasma mantle leading to a thermal collapse. On shorter timescales (100 to 500ms) an increase in MHD - activity mainly m=2/n=1 leads finally to a disruption in most cases with the mode locking to a "standing wave". this mode-lock occurs always in the same toroidal location. This preference can either be explained by a toroidal asymmetry in the poloidal field distribution or by the fact that the position control acts on magnetic signals from one toroidal location.

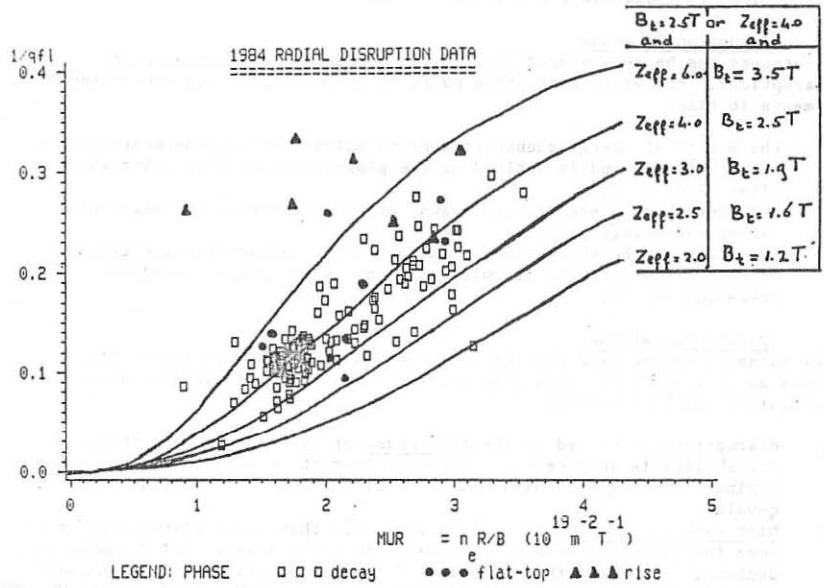

Fig. 1
Hugill diagram for 1984 disruptions. The drawn lines give the results of eq.(1) for a few combinations of toroidal field and Z_{eff}-values.

5 Energy quench

From fast e.c.e - measurements [3] the width of the magnetic island can be estimated as being the width of the shoulder in the Te-profile at the q=2 radius. A few ms before the final collapse the width starts to grow rapidly such that Te inside the q=2 surface decreases by several 100eV and outside increases with a similar amount. This time scale is in good agreement with the scaling law [4].

$$(\gamma)^{-1} \equiv \tau_\sigma^{3/5} \cdot \tau_{pol.Alfvén}^{2/5}$$

However the final collapse occurs on a much faster timescale: T_e drops over the whole cross-section to a flat profile of about 100eV within one data sampling time of 200μsec. The data suggests that this collapse occurs when the magnetic island has grown so far that it either touches the limiter or contacts the q=1 surface.

6 Current-quench

Depending on the magnitude of the energy quench and the plasma current level at disruption the subsequent current quench is "soft" (decay time around 300ms) if the position control circuitry is able to maintain control by ramping down the vertical field fast enough. If the power amplifier comes into saturation position control is lost and the current quench is much faster. Current quenches up to~180MA/s have been observed. Fig. 2 illustrates the difference between slow and fast current quenches by showing the magnetic surfaces as calculated from the magnetic diagnostics. In Fig. 3 the influence of the voltage capability of the position control power amplifier on the $\dot{I}$-value as function of the current value at the moment of

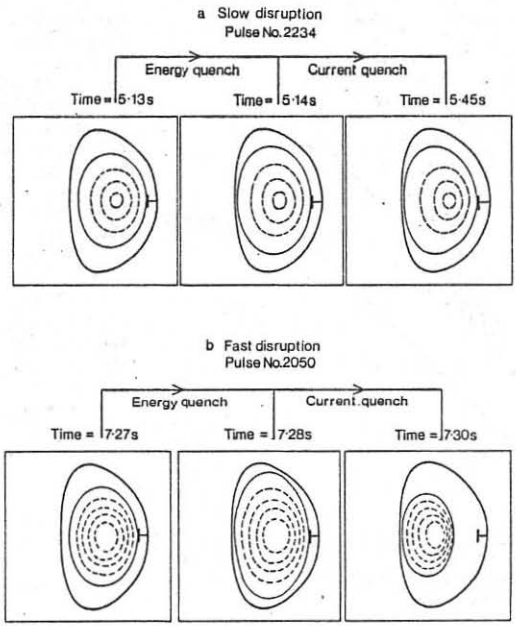

Fig. 2 Examples of a slow and a fast current quench. The magnetic surfaces are reconstructed from magnetics by the ODIN-code. Note the blow-up during the energy quench and the loss of position in the fast quench example
case a: I=1.5MA; $\dot{I}$=4MA/s
case b: I=1.9MA; $\dot{I}$=56MA/s
B_t=2.5T; q_{cyl}=4.8 for both.

disruption is shown. A high voltage capability (o) lowers I compared with a low capability (Δ). The ohmic driving voltage during the rise-phase is about 4 x larger than during the flat-top. Therefore the input power is higher which slows the current quench of rise-phase disruptions (x) down compared with quenches occurring in the flat-top or decay-phase. This again raises the chance that position control is maintained.

References

[1] F C Schüller et al. This conference.
[2] J Wesson et al. This conference.
[3] B Tubbing et al. This conference.
[4] J D Callen et al. IAEA 8th Int. Conf. Plasma Physics and Contr. Nucl. Fus. Brussels [1980].

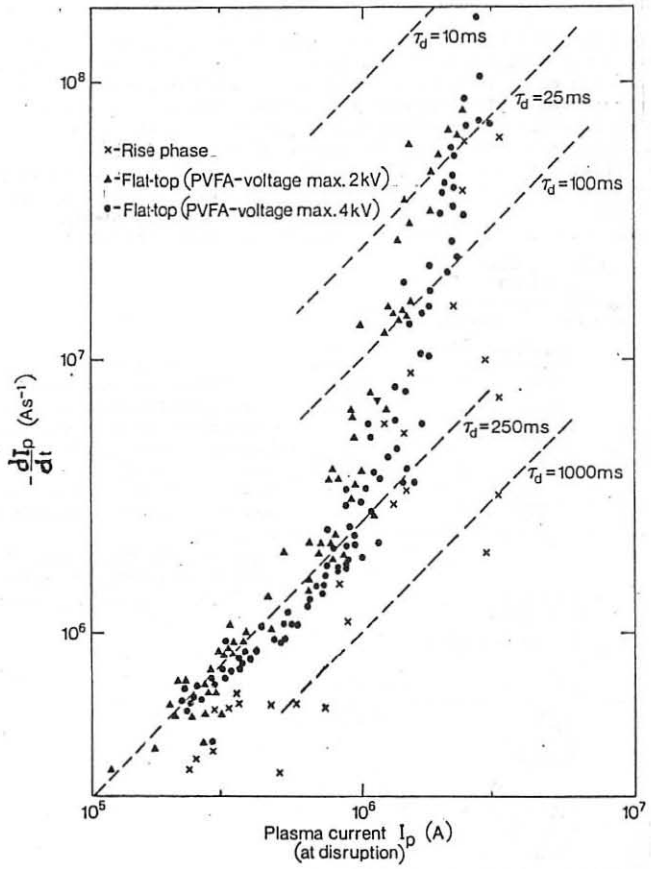

Fig. 3
The current quench rate as function of the current at disruption. As long as the position is controlled the decay rate is given by a time constant of about 250ms. Above 1MA this becomes difficult and the decay-rate is enhanced by the loss of position.

POLOIDALLY ASYMMETRIC EDGE PHENOMENA IN JET

J O'Rourke, D Campbell, B Denne, A Gondhalekar, N Gottardi, H Krause*, G Magyar, M Malacarne, F Mast*, P Morgan, M F Nave, F C Schüller, M Stamp, D Summers

JET Joint Undertaking, Abingdon, OX14 3EA, UK
* On attachment from IPP-Euratom Association, 8046 Garching, RFG

ABSTRACT
JET discharges near the density limit frequently form a region of high-density strongly radiating plasma localised at the plasma edge, on the small major radius side. A detailed description of such an event is presented. The onset of such an event coincides with a decrease in the kinetic energy content of the discharge. The asymmetric state initiates a transition of the discharge to a new poloidal symmetric state characterized by high edge radiation and decreased interaction with the limiters. The concomitant modifications of the density and energy dynamics of the discharge are observed.

INTRODUCTION

In this paper we present observations of the formation and evolution of regions of high density and enhanced radiation localised at the edge of JET plasmas, on the small major radius side. Similar events in ALCATOR C discharges [1] have been termed 'marfes' and the same designation is adopted here.

'Marfes' in JET occur near the density limit of the operating regime (see Figure 1). They have been observed to form during all phases of JET discharges: current rise, flat-top and decay. No correlation has been observed with details of vessel conditioning history. Beyond the general characteristics mentioned in the proceeding paragraph, 'marfes' exhibit a varied phenomenology. For consistency we shall concentrate in the following on a typical 'marfe' which occurred during pulse 3428. Important differences with observations of other 'marfes' in JET will be pointed out.

STRUCTURE

Figure 2 shows the position, in a poloidal plane, of the 34 chords of the bolometer arrays and the 7 vertical chords of the far infrared interferometer. These diagnostics are separated toroidally by 135°. Also shown is the plasma boundary (deduced from magnetic measurements) for pulse 3428 (at t=10 s).

Figure 3 shows the time evolution of the plasma current, the line integrated electron density along 3 interferometer chords, the poloidal β and the radial position of the inside plasma boundary at z=o. The radial position of the outside plasma boundary is at the limiter. At 10.1 seconds, the line integrated density on the innermost chord (R=1.883 m, 0.1 m inside the plasma boundary at z=o) rises by nearly 10^{19} m^{-2} in 300 msec. This event is clearly poloidally asymmetric (as no corresponding change occurs on the outer interferometer channels) and is not due to motion of the plasma boundary. Figure 4 shows the evolution of bolometric and spectroscopic signals.

Comparison of signals from single bolometers situated toroidally around the plasma confirms that the 'marfe' is axisymmetric. At its onset the 'marfe' is most pronounced on channels V12-V14, UH2-UH6 and LH1-LH4. By referring to Figure 2, one deduces that it is localised poloidally between Θ=145° and Θ=210°. Figure 5 (however taken from a different pulse) shows the relative increase in several spectral line intensities during a 'marfe' as a function of the ionization potential of the emitting ion. Probe measurements yield a temperature at the plasma boundary of about 50 eV. The enhancement of lines with ionization potentials of about 100 eV shows that the 'marfe' is situated within the plasma boundary. Localisation of the 'marfe' inside the plasma boundary permits us to interpret the line integrated density as a mean density in the 'marfe' of at least $1.2\times10^{19}m^{-3}$. The density at the centre of the discharge is $2\times10^{19}m^{-3}$. The line-integrated density through the 'marfe' location exhibits large (10%) modulations both prior to and during the 'marfe'.

DENSITY DYNAMICS AND TRANSITION TO A NEW POLOIDALLY SYMMETRIC STATE

The increase in poloidal β during the current decay is arrested when the marfe occurs (see Figure 3). The increase in the rate of loss of kinetic energy which this implies can be interpreted as due to the increased rate of loss of bulk plasma particles.

A horizontally viewing analyser in the mid-plane shows a large ($\sim$x2) enhancement of the neutral particle efflux at all measured energies (2-15 keV) during a 'marfe' (see S Corti et al, this conference). D_α light from the initial 'marfe' location is not monitored in this pulse, but as the 'marfe' spreads into the line of sight of vertically viewing D_α monitors, an increase in D_α light is observed. This supports the hypothesis that there is an increased source of neutrals at the wall.

The end of the 'marfe' usually coincides with a sudden increase in C III signal (Figure 4) and a burst of D_α light from the inner wall. The radiation asymmetry subsides by spreading poloidally beginning at about 10.5 sec. This is best seen on the vertical bolometer channels (Figure 4). At about 11.3 sec this asymmetry is no longer observed and the 'marfe' is terminated. The density asymmetry, evidenced by the innermost interferometer channel, subsides simultaneously with the radiation asymmetry.

The end of the 'marfe' coincides with an increase in the total radiated power, and a progressive shrinking of the radiating shell away from the plasma edge. The electron density profile also becomes increasingly peaked. Figures 6 and 7 compare the density and radiation profiles at 10 sec (before the 'marfe') and 12 sec (after the 'marfe').

The D_α and C_{III} light measured at the vessel wall continue to rise, while that at the limiter decreases, indicating that the wall is becoming a relatively more important source of electrons compared with the limiters. We refer to this as detachment from the limiters.

Taking as definition of the global particle confinement time, τ_p, the equation

$$\dot{N} = -\frac{N}{\tau_p} + \phi_\ell + \phi_\omega + \phi_g$$

where N is the total number of electrons, and ϕ_ℓ, ϕ_ω and ϕ_g are the limiter, wall and external fluxes, assuming that the wall flux is uniform everywhere, and accounting for the presence of impurities, we obtain τ_p = 0.60 sec before the 'marfe' and τ_p = 0.93 sec after. No attempt is made to estimate the

confinement time during the 'marfe', since the assumption of uniformity is not valid.

This change in plasma behaviour can be seen very clearly in the evolution of the discharge in the Hugill diagram (Figure 8). At the end of the 'marfe', the Murakami parameter begins to increase, and the discharge evolves towards the density limit.

Not all 'marfe' events lead to detachment of the plasma from the limiters, although this is often the case. Further elucidation of such a bifurcating process requires a more detailed knowledge of the parameters at the plasma edge.

CONCLUSION

In the 'marfe' state, a discharge is characterised by poor particle confinement. The end of a 'marfe' frequently signals the transition to a state of increased particle confinement and decreased interaction with the limiters.

[1] B Lipschultz, B La Bombard, E S Marmar, et al., Nuclear Fusion, Vol.24, No.8 (1984) 997.

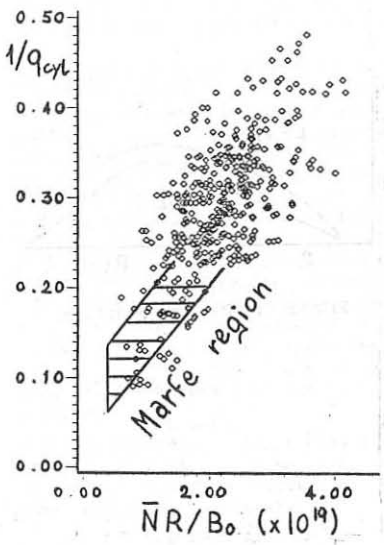

FIGURE 1: Marfes in JET operating regime.

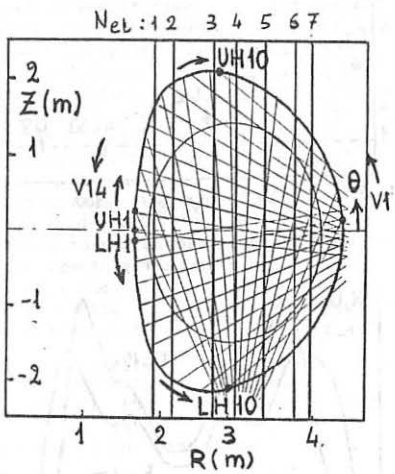

FIGURE 2: Layout of bolometer and interferometer arrays.

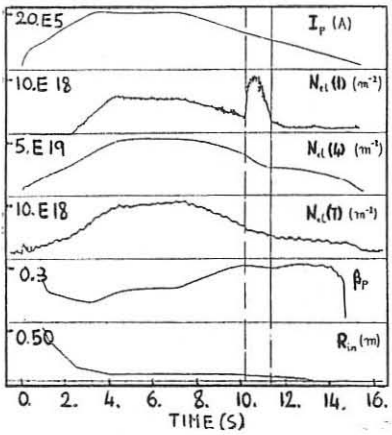

FIGURE 3: Evolution of JET pulse 3428.

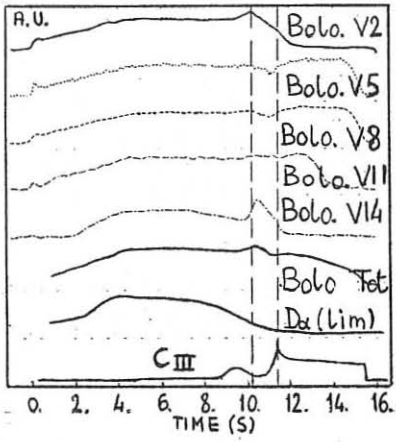

FIGURE 4: Some bolometric and spectroscopic signals.

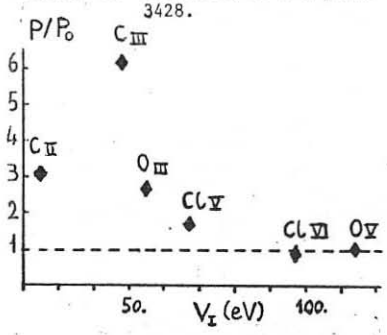

FIGURE 5: Enhancement factor for some impurity lines.

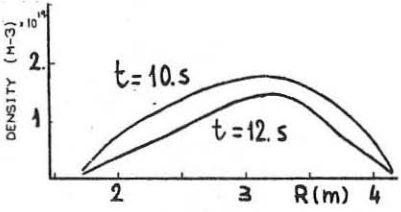

FIGURE 6: Density profiles.

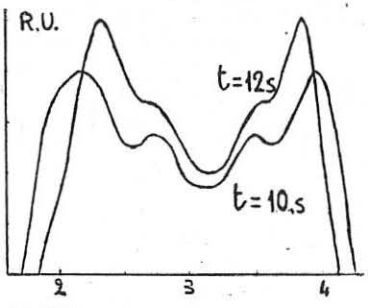

FIGURE 7: Bolometric profiles.

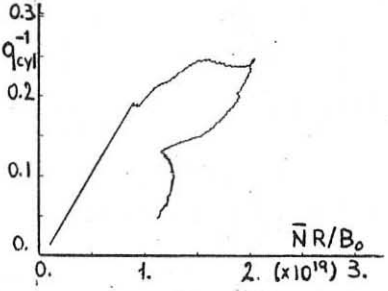

FIGURE 8: Hugill diagram evolution.

INVESTIGATIONS INTO THE DENSITY LIMIT OF THE TOKAMAK WITH OHMIC AND NEUTRAL BEAM HEATING

H. Niedermeyer, R. Bartiromo[1], G. Becker, H.S. Bosch, H. Brocken, A. Eberhagen, G. Fußmann, O. Gehre, J. Gernhardt, G. v. Gierke, A. Giuliana[1], E. Glock, O. Gruber, G. Haas, G. Janeschitz, F. Karger, M. Keilhacker, O. Klüber, M. Kornherr, P.B. Kotzé[2], K. Lackner, M. Lenoci[1], G. Lisitano, A. Mahdavi[3], H.-M. Mayer, K. McCormick, D. Meisel, V. Mertens, E. R. Müller, H. Murmann, W. Poschenrieder, H. Rapp, H. Röhr, F. Ryter[4], F. Schneider, G. Siller, P. Smeulders, F. Söldner, E. Speth, K. H. Steuer, G. Vlases[5], O. Vollmer, F. Wagner

Max-Planck-Institut für Plasmaphysik
EURATOM Association, D-8046 Garching

Introduction: In /1/ we showed that in ASDEX the disruption at the density limit in an Ohmic discharge at $q = 4.2$ ($q = 2\pi B_T a^2/\mu_o I_p R$) is preceded by the poloidally asymmetric formation of a cold high density plasma near the boundary ("marfe" /2/) and a shrinking of the current profile. In order to get an improved data base for an empirical density limit scaling and more insight into the phenomena involved we now extended our investigations to discharges in a large parameter range including neutral beam heating. Results from discharges with continuous pellet injection are reported in /3/.

The experimental method: After non-gettered divertor discharges had reached a current plateau and quasi-stationary conditions with sawtooth activity, the line averaged electron density was slowly increased by controlled gas puffing until a disruption was detected. When desired, neutral beam injection started simultaneously with the density increase. With injection, slow density ramp up was made possible by extending the heating pulses in time at the cost of power by firing our two beamlines one after the other. The reduced maximum beam power of 1.7 MW permits only L-type discharges.

Parameter scaling: Figure 1 shows Hugill-diagrams /4/ for Ohmically and beam heated discharges in hydrogen with a toroidal magnetic field B_T of 1.9 T (left) and various B_T-values between 1.3 T and 2.5 T (right). The data points represent peak values of $\bar{n}$ (electron density averaged along a horizontal chord in the midplane). Ohmic data show the well known linear dependence $\bar{n} \sim 1/q \sim I_p$ for high q-values and the bending off at q-values below about 3. Discharges with beam heating reach an appreciably higher $\bar{n}$ for all q-values.

While at the density limit $\bar{n}/B_T$ is fairly independent of B_T and only a function of q in the Ohmic case, we see in Fig. 1, that the maximum density reached in beam heated discharges is a more complicated function of B_T. At least at this power level $\bar{n}$ is also a function of the beam power.

---

[1] CNEN Frascati, Italy
[2] Nuclear Development Corp. of South Africa, Pretoria
[3] GA Technologies Inc., San Diego, USA
[4] CEN Grenoble, France
[5] University of Washington, Seattle

$\bar{n}\ R/B_T$ obviously being no scaling parameter for beam heated discharges we plot the maximum density as a function of the variables I_p and B_T (Fig. 2). We see again that $\bar{n}$ is proportional to I_p in Ohmic discharges for $q > 3$. The maximum of all the curves corresponds to $q = 2.7$. For beam heated discharges we still have an explicit variation of the density limit with I_p. A function proportional to the square root of I_p fits well all data points from discharges with $q > 3$.
In both cases the total heating power varies with the plasma current. The heating power shortly before the disruption varies roughly with the square root of I_p in Ohmic discharges, in beam heated discharges P_{OH} is only a small fraction of the total power, so that despite of a variation of P_{OH} with I_p the total power is constant within 10 % at fixed beam power.
The few data available for different beam powers are compatible with $\bar{n} \sim P^{\alpha}$, $\alpha = 0.3 \ldots 0.4$. This scaling applied to Ohmic discharges together with an assumed "intrinsic" I_p-scaling is too weak to explain the linear I_p scaling observed. If we assume a universal scaling law to be valid for all heating methods we have to postulate a more complicated power dependence.

Phenomena observed before the disruption: As one might already presume from the strong bend in the density limit curves we have to distinguish between low q and high q discharges, the boundary q value being about 2.7 in ASDEX. Typical signal traces from q=2.2 and q=4.7 discharges with Ohmic and beam heating are plotted in Fig. 3.

The Ohmic high-q discharge shows all signs of a growing marfe and shrinking current channel as described in /1/: increase of U_L and l_i, strong increase of radiation from low ionization states of low-Z impurities (CIII), reduced divertor loading (H_α!). The difference between the interferometer signals at half radius above and below midplane shows that the "marfe" is located below the midplane. This is also confirmed by space resolved bolometer measurements (not shown). Poloidally asymmetric radiation sources are not measured correctly by the bolometers. Nevertheless we can state that the power radiated from the marfe is substantial. Strongly growing MHD activity (probably $m = 2$, localized at the q=2 surface) sets in about 15 - 20 ms before the disruption.

With beam heating we observe the signs of a marfe mentioned above already at rather low densities. (See also shaded areas in Fig. 1). l_i measurements do not clearly indicate a shrinking of the current profile, but Thomson scattering measurements show a peaking of the T_e and n_e profiles well before the disruption. The power radiated from the marfe seems to be higher than in the Ohmic case but small compared to the total power. About 50 ms before the disruption the lower edge channels of the bolometer array (which see the region of the lower stagnation point) detect a strong increase of the radiation. This might indicate a stronger marfe or a dramatic change of the scrape-off plasma at the divertor entrance. We do, however, not observe a drop of the neutral gas density in the divertor chamber. The onset of MHD-activity is similar to the Ohmic case.

The behaviour of low q-discharges with Ohmic or NB-heating is completely different before the disruption compared to the high-q case: Nothing indicates a thermal instability at the plasma edge. Thomson scattering shows also in this case that T_e decreases all over the cross section when $\bar{n}$ is being increased, but there is no sign of a slow current shrinking. It seems that in low q-discharges an MHD instability not being triggered by a thermal instability leads to the disruption. Discharges at very low q-values do not even show the strongly increasing oscillations indicating rotating modes: the plasma simply disrupts.

Spurious density limits: In a few discharges, especially in deuterium one observes completely different phenomena leading to a density limit at lower values than given by the scaling described above.

Ohmic discharges in D_2 at low I_p showed an increase of the radiation from the plasma centre with increasing $\bar{n}$, then a stop of the sawtooth activity and finally a disruption at a rather low $\bar{n}$ value. Thomson scattering confirmed the radiational collapse from the centre: T_e-profiles flattened at the plasma centre or became even indented the outer part of the profiles staying unperturbed. The flat area expanded until it reached about half the plasma radius, then the discharge disrupted. This effect results from the higher content of metal impurities in D_2-discharges.

Other (beam-heated) discharges showed some kind of "density clamping" obviously caused by an increased mode activity. By strongly increased gas puffing it was possible to further increase $\bar{n}$, but we cannot exclude that the density limit would be higher, if we were able to avoid these modes.

We believe that limits of this kind can be overcome by improved discharge scenarios, wall conditioning or other choice of wall materials and excluded them from further discussions.

Conclusion: The increase of $\bar{n}$ beyond the density limit is finally prevented by MHD phenomena, probably an instability arising at the q=2 surface. But all our observations indicate that this is related to the power balance.

In high q-discharges the q=2 surface considered to be most sensitive is so distant to the boundary that it is not directly affected by the power losses at the edge. With increasing losses edge cooling does not simply flatten gradients at the edge, but leads to a thermal instability which causes a shrinking of the current channel and finally an MHD unstable situation.

In low-q discharges the q=2 surface is very close to the boundary. The zone of strong volume losses (ionization, charge exchange losses, low-Z radiation) overlaps with it. The discharge becomes MHD unstable before the boundary becomes thermally unstable.

A theoretical treatment of the problem suffers from the poor knowledge of particle transport. A simple model leads to the conclusion that the power lost only by refuelling is proportional to $D \cdot n^2$, D being the particle diffusion coefficient. Assuming a proper functional dependence of D on n, I_p, B_T and P we can explain any empirical density limit scaling by thermal effects. An increase of D with power would explain the weak increase of the density limit with power. Vice versa we might deduce the functional dependence of D from empirical density limit scaling laws.

References

/1/ H. Niedermeyer, et al., 11th Europ. Conf. on Contr. Fusion and Plasma Physics, Aachen 1983, p. 47
/2/ B. Lipschultz et al., Nucl. Fusion, Vol. 24, No. 8 (1984), p. 977
/3/ G. Vlases, et al., this conference
/4/ J. Hugill, Proc. 2nd Joint Grenoble-Varenna International Symposium, Como, 1980, p. 775.

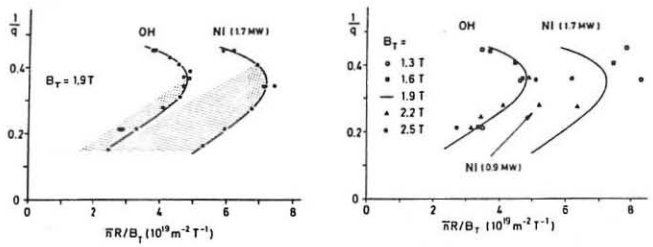

Fig. 1: Hugill diagrams for B_T = 1.9 T (left) and various B_T-values. Shaded area: appearance of marfes.

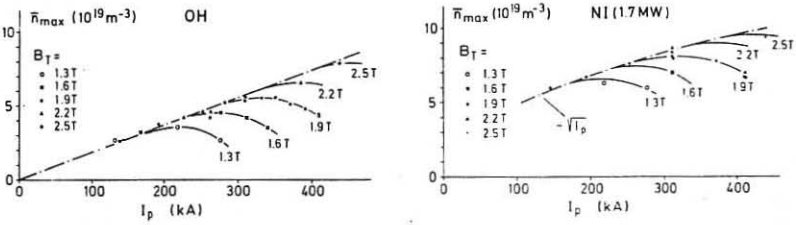

Fig. 2: Density limit as a function of I_p and B_T for Ohmic (left) and neutral beam heated discharges (right)

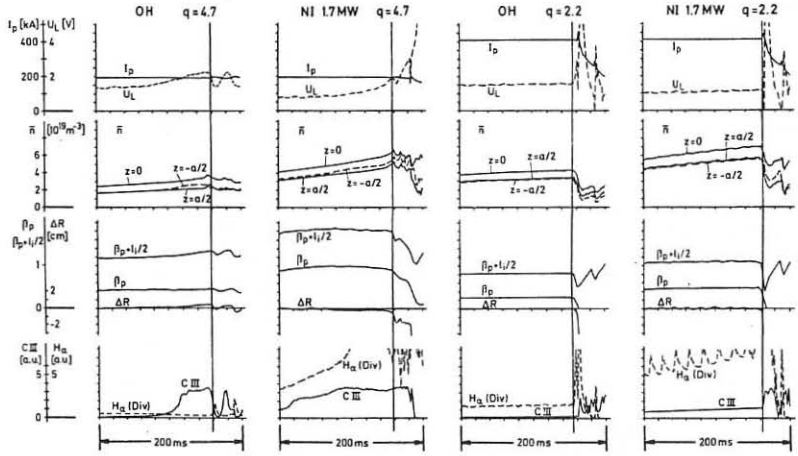

Fig. 3: Characteristic behaviour of different types of discharges in a short period before the density limit disruption (marked by vertical lines)

FAST DETERMINATION OF PLASMA PARAMETERS THROUGH FUNCTION PARAMETRIZATION

B.J. Braams*, W. Jilge, and P. Martin
Max-Planck-Institut für Plasmaphysik, EURATOM Association,
D-8046 Garching bei München, Fed. Rep. Germany.
*F.O.M. Instituut voor Plasmafysica,
Postbus 1207, 3430 BE Nieuwegein, The Netherlands.

Introduction. In the interpretation of tokamak diagnostics the amount of experimental information that is utilized is often not limited by the rate at which measurements can be made, but more by the rate at which the raw diagnostics can be interpreted. Clearly then, efficient methods of data analysis are highly desirable. A very efficient procedure, function parametrization, was developed by H. Wind (CERN) for the purpose of fast momentum determination from spark chamber data [1], [2]. Although this method had not previously been noticed outside the high energy physics field, it has a much wider range of applicability, and can be considered whenever many measurements are to be made with the same diagnostic setup. Its utility for tokamak physics applications, and in particular for the determination of characteristic equilibrium parameters from magnetic measurements, was proposed in [3], and is demonstrated in the present paper.

Function parametrization relies on an analysis of a large data set of simulated experiments, aiming to obtain an optimal representation of some simple functional form for intrinsic physical parameters of a system in terms of the values of the measurements. Statistical techniques for dimension reduction and multiple regression are used in the analysis. The resulting function may be chosen to involve only low-order polynomials in only a few linear combinations of the original measurements; this function can therefore be evaluated very rapidly, and needs only minimal hardware facilities.

Three steps have to be made for experimental data evaluation based on function parametrization. (1) A numerical model of the experiment is used to generate a data base of simulated states of the physical system, in which each state is represented by the values of the relevant physical parameters and of the associated measurements. (2) This data base is made the object of a statistical analysis, with the aim to provide a relatively simple function that expresses the physical parameters in terms of the measurements. (3) The resulting function is then employed for the fast interpretation of real measurements.

Determination of characteristic parameters of a magnetically confined plasma is a particularly indicated application. The MHD equilibrium model provides a well defined and generally accepted connection between the unknown intrinsic plasma parameters, the externally applied fields, and the magnetic measurements. Identification of the position and the profile of the plasma column is the basis for interpretation of practically all other diagnostics, and requires an efficient algorithm. Ultimate aim of our work is in fact on-line real-time analysis, with use of the derived information for feedback plasma control.

Mathematical description. A classical physical system is considered, of which P denotes a typical state. The system may have any number of degrees of freedom, but

interest will be restricted to a (partial) characterization by n intrinsic real parameters, represented collectively by a point $\mathbf{p} \in \mathbf{R}^n$. In the experimental situation $\mathbf{p}$ is to be estimated from the readings of m measurements, represented by a point $\mathbf{q} \in \mathbf{R}^m$.

The aim of the function parametrization is to obtain some relatively simple function $\mathbf{F} : \mathbf{R}^m \to \mathbf{R}^n$, such that for any state P the associated $\mathbf{p}(P)$ and $\mathbf{q}(P)$ satisfy $\mathbf{p} = \mathbf{F}(\mathbf{q}) + \mathbf{e}$ for a sufficiently small error term $\mathbf{e}$. The functional form of $\mathbf{F}$ may typically be chosen as a low-order polynomial in only a few linear combinations of the components of $\mathbf{q}$. The unknown coefficients in $\mathbf{F}$ are then determined by analysis of a data base containing the values of the parameters $\mathbf{p}_\alpha$ and of the measurements $\mathbf{q}_\alpha$ corresponding to N simulated states P_α $(1 \leq \alpha \leq N)$. This is a problem for which techniques from multivariate statistical analysis are appropriate.

Since the dimensionality m of the space of the measurements lies between several tens and several hundred in many cases, the dimensionality of the space of trial functions with which the parameters are to be fitted can be very large. A polynomial model of degree l in all variables, for instance, has $\sim m^l/l!$ degrees of freedom for each physical parameter. It is therefore desirable to first reduce the number of independent variables (the components of $\mathbf{q}$) by means of a transformation to a lower-dimensional space. A second, and also very important, aim for this transformation of variables must be to eliminate or reduce multicollinearity (near linear dependencies) between the data points, and thus to improve the conditioning of the regression problem. Multicollinearity is expected to be present whenever the number of measurements is much larger than the number of independently determinable physical parameters.

A common statistical technique to find a lower-dimensional space in which to represent the measurements is based on principal component analysis. From the N suitably scaled pseudo measurements, $\{\mathbf{q}_\alpha\}_{1 \leq \alpha \leq N}$, the sample mean, $\bar{\mathbf{q}} = N^{-1} \sum_\alpha \mathbf{q}_\alpha$, and the $m \times m$ sample dispersion matrix,

$$\boldsymbol{S} = \frac{1}{N} \sum_{\alpha=1}^{N} (\mathbf{q}_\alpha - \bar{\mathbf{q}})(\mathbf{q}_\alpha - \bar{\mathbf{q}})^T,$$

are calculated. $\boldsymbol{S}$ is symmetric and positive semi-definite. An eigenanalysis will yield m eigenvalues, $\lambda_1^2 \geq \ldots \geq \lambda_m^2 \geq 0$, with corresponding orthonormal eigenvectors $\mathbf{a}_1, \ldots, \mathbf{a}_m$. Any measurement vector $\mathbf{q}$ may be resolved along these eigenvectors to obtain a set of transformed measurements, $x_i = \mathbf{a}_i \cdot (\mathbf{q} - \bar{\mathbf{q}})$. The sample variance of the component x_i is given by λ_i. Now the assumption is made that the most significant information will be contained in those transformed measurements that show the largest variation over the simulated data, viz. in the components $(x_i)_{1 \leq i \leq s}$ where $s \leq m$, and preferably $s \ll m$. These s components are called the 'significant components', and the associated first s eigenvectors $\mathbf{a}_i$ are the 'significant variables'. The desired dimension reduction is thus achieved through the transformation $\mathbf{R}^m \to \mathbf{R}^s$ defined by $\mathbf{x} = \mathbf{A}^T \cdot (\mathbf{q} - \bar{\mathbf{q}})$, where $\mathbf{A}$ is the matrix that has columns $\mathbf{a}_i$ $(1 \leq i \leq s)$.

Having obtained the preliminary linear transformation $\mathbf{q} \to \mathbf{x}$ it is next necessary to face the task of fitting the, in general nonlinear, relation between $\mathbf{x}$ and $\mathbf{p}$. It is desired to find for each component p_j $(1 \leq j \leq n)$ a regression, $p_j = f_j(\mathbf{x}) + \epsilon_j$, to fit the data $(\mathbf{x}_\alpha, \mathbf{p}_\alpha)_{1 \leq \alpha \leq N}$. A polynomial model, of the form

$$p_j = \sum_{\mathbf{k}} c_{\mathbf{k}j} \cdot \prod_{i=1}^{s} \phi_{k_i}(x_i/r_i) + \epsilon_j, \tag{1}$$

is suitable. Here, the multi-index $\mathbf{k}$ has s components $k_1, \ldots, k_s$ in the nonnegative integers, the c_{kj} are the unknown regression coefficients, which are determined by a least-squares fitting procedure over the data base, $(\phi_\ell)_{\ell \geq 0}$ is some family of polynomials (Chebyshev, Hermite, Legendre, or monomials), r_i is a suitable scaling factor for the component x_i, and ϵ_j is the error term. An upper bound on some norm of $\mathbf{k}$ must be supplied in order to make the model finite, and in addition it is possible to employ with the above model some form of subset regression, the objective being to retain in the final expression only the terms which make a significant contribution to the goodness-of-fit.

Function parametrization thus leads to simple explicit approximations for the physical parameters in terms of the measurements. Although a significant effort may be involved in generating and analyzing the data base, the evaluation of the final function — and this is the operation that has to be performed many times — is almost trivial.

Application to magnetic data analysis. As an initial study we applied function parametrization to the determination of a limited set of characteristic equilibrium parameters for the ASDEX experiment, using only magnetic signals measured outside the plasma. The relevant measurements consist of three differential flux measurements, four field measurements, the current through the multipole shaping coils, and the plasma current. However, the plasma current can be scaled out of the problem, so that 8 independent measurements remain. The physical parameters to be determined include the position of the magnetic axis, the geometric center of the cross section, the current center, the horizontal and vertical minor radius, $\beta_p + l_i/2$, a normalized q-value at the separatrix, the flux difference between the separatrix and the vacuum vessel, the position of the lower and upper saddle points, and the point of intersection of the separatrix with each of the four divertor plates.

The data base was generated using the Garching equilibrium code [4], which has recently been much optimized, and computes an equilibrium on our 64×128 grid in ~ 0.6 sec on the Cray 1. The free parameters of the code were randomly varied in order to cover the operating regime of the ASDEX experiment in the divertor mode, and for each of the ~ 4000 calculated equilibria the corresponding magnetic measurements and physical parameters were recorded.

Results. A principal component analysis of the correlation matrix obtained from the simulated measurements gave the following sequence of eigenvalues: 3.67, 1.91, 1.39, 0.99, 2.01×10^{-2}, 1.12×10^{-2}, 1.90×10^{-3}, 8.93×10^{-4}. It thus appeared that 4 significant variables should be retained for the regression analysis. Of these four, the first two are even under up-down reflection of the equilibrium, and together already provide a measure of the radial position and of $\beta_p + l_i/2$. The third significant variable is odd under reflection, and is related to the vertical position of the plasma, and the fourth one (again even under reflection) is essentially the multipole current.

Further analysis showed that the measurement of the multipole current is of little overall importance, but is mainly relevant for the determination of the intersection of the separatrix with the divertor plates. After experimenting with various possible regression models we selected a model that is second order in the first three significant variables, and first order in the fourth: For each of the physical parameters p,

$$\begin{aligned} p = {} & c_0 + c_1 x_1 + c_2 x_2 + c_3 x_3 + c_4 x_4 + c_5 H_2(x_1) \\ & + c_6 x_1 x_2 + c_7 x_1 x_3 + c_8 H_2(x_2) + c_9 x_2 x_3 + c_{10} H_2(x_3) \end{aligned} \tag{2}$$

where $H_2(x) = (x^2 - 1)/\sqrt{2}$. In order to overcome a first-derivative discontinuity in the physics of the system, separate fits were used for the two cases when the separatrix x-point is located in the lower, resp. in the upper half plane. The results obtained with this model for some representative physical parameters are shown in the following Table.

parameter	aver	min	max	variance	δ ($\epsilon = 0.0$)	δ ($\epsilon = 0.1$)
r_{axis}	1.72	1.63	1.83	5.6×10^{-2}	2.2×10^{-3}	4.1×10^{-3}
r_{curr}	1.71	1.61	1.82	5.6×10^{-2}	3.1×10^{-4}	3.4×10^{-3}
z_{axis}	0	−0.10	0.10	5.4×10^{-2}	2.3×10^{-3}	5.8×10^{-3}
z_{curr}	0	−0.10	0.10	5.4×10^{-2}	2.5×10^{-3}	6.0×10^{-3}
a	0.367	0.290	0.463	3.0×10^{-2}	3.8×10^{-3}	6.2×10^{-3}
b	0.358	0.295	0.438	2.5×10^{-2}	1.9×10^{-3}	4.7×10^{-3}
$\beta_p + l_i/2$	1.79	0.56	3.43	0.63	1.2×10^{-2}	4.4×10^{-2}

For each of the parameters the Table shows first the average, minimum, and maximum values occurring in the data base, and the standard deviation about the average. The last two columns show the standard error, δ, of the model in Eq (2), first for exact measurements ($\epsilon = 0.0$), and then for measurements which have been randomly perturbed by a term coming from a normal distribution with average 0 and width equal to a fraction $\epsilon = 0.1$ of the variance of the measurements.

Conclusion. The application described above establishes function parametrization as a straightforward and effective way in which to obtain numerical approximations for a variety of characteristic equilibrium parameters in terms of the magnetic measurements. These approximations are not only extremely easy to evaluate, but are also more accurate than the analytic approximations that are now in common use. The procedure does not require very specific assumptions about the MHD equilibrium, and is also well suited to a consistent analysis of a system consisting of several different diagnostics. We expect that in the future function parametrization will have an important rôle both for on-line data analysis and for real-time plasma control.

Acknowledgements. The authors wish to acknowledge many valuable discussions with Dr. K. Lackner. This work was performed under the Euratom-IPP and Euratom-FOM association agreements with financial support from ZWO and Euratom.

References.

1. H. Wind, *Function Parametrization*, in "Proceedings of the 1972 CERN Computing and Data Processing School", CERN 72-21, 1972, pp. 53–106.
2. H. Wind, (a) *Principal Component Analysis and its Application to Track Finding*, (b) *Interpolation and Function Representation*, in "Formulae and Methods in Experimental Data Evaluation", Vol. 3, European Physical Society, Geneva, 1984.
3. B.J. Braams and K. Lackner, *A Proposed Method for Fast Determination of Plasma Parameters*, Report IPP 1/228, Max-Planck-Institut für Plasmaphysik, 1984.
4. K. Lackner, *Computation of Ideal MHD Equilibria*, Comput. Phys. Commun. **12** (1976), 33–44.

MHD EQUILIBRIUM DETERMINATION

B.J. Braams
F.O.M. Instituut voor Plasmafysica,
Postbus 1207, 3430 BE Nieuwegein, The Netherlands.
On attachment to Max-Planck-Institut für Plasmaphysik,
D-8046 Garching bei München, Fed. Rep. Germany.

Results from recent studies related to the numerical solution of the MHD equilibrium equations and to equilibrium determination from magnetic measurements are summarized. More details will be provided in [1] and [2].

MHD equilibrium calculations using multigrid. A code has been written to demonstrate the utility of the multigrid numerical method for the computation of axisymmetric ideal MHD equilibria. This code achieves optimal multigrid efficiency, and is several times faster than codes based on direct rapid elliptic solvers. A solution on a 128 × 128 grid is computed in $\simeq$ 120 milliseconds on the Cray 1.

Following up on this work, two other prospective applications have been investigated. The first of these is to the axisymmetric MHD equilibrium problem in the 'inverse coordinates' formulation, computing the Cartesian coordinates r and z as a function of ψ and ϑ, where ϑ is an angle-like variable. In previous work, ϑ has been defined either via orthogonality or through an equation for the Jacobian of the transformation. An analogy with grid generation through elliptic equations suggests instead to employ for ϑ the homogeneous equilibrium equation, $\Delta^* \vartheta = 0$. Then r and z are governed by a quasi-linear elliptic system that should be particularly suitable for multigrid treatment.

The other prospective application that was investigated is to three-dimensional equilibrium and evolution calculations. We attempted to construct a suitable distributive relaxation scheme, using local mode analysis as a guide. Our best point relaxation scheme will still be slowly converging for two classes of disturbances: the shear Alfvén and the slow magnetosonic modes, in both cases with the wavevector nearly transverse to the magnetic field. These are the lowest frequency ($\rightarrow 0$) modes in the MHD spectrum. We therefore do not yet have a method that can achieve full multigrid efficiency for 3-D equilibrium, but something has been learned. Distributive line relaxation along the magnetic field may improve the treatment of the troublesome modes; this emphasizes the need for an adaptive, flux-tied grid for 3-D MHD calculations. The proposed relaxation scheme may be suitable for ideal MHD evolution calculations when one wants to follow the low-frequency disturbances, while at the same time efficiently eliminating the faster time scales.

Higher order discretization for 2-D equilibrium. Conventional second order accurate discretization methods for the equilibrium equation, $\Delta^* \psi = f(r, \psi)$, are of the five point molecule form,

$$\begin{pmatrix} & * & \\ * & * & * \\ & * & \end{pmatrix} \psi = f.$$

Better methods are available for smooth f, in particular a fourth order accurate 'compact' discretization of the shape,

$$\begin{pmatrix} * & * & * \\ * & * & * \\ * & * & * \end{pmatrix} \psi = \begin{pmatrix} & * & \\ * & * & * \\ & * & \end{pmatrix} f.$$

Specifically: Consider a uniform rectangular mesh with spacing $\delta x = h$ and $\delta y = k$. Consider the natural splitting, $\Delta^* = \mathcal{L}_x + \mathcal{L}_y$, and define the second order accurate difference approximations $\mathcal{L}_x^h$ and $\mathcal{L}_y^k$ by,

$$[\mathcal{L}_x^h \psi](x,y) = \frac{1}{h^2}\Big(\frac{x}{x+h/2}\big(\psi(x+h,y) - \psi(x,y)\big) - \frac{x}{x-h/2}\big(\psi(x,y) - \psi(x-h,y)\big)\Big)$$

$$[\mathcal{L}_y^k \psi](x,y) = \frac{1}{k^2}\big(\psi(x,y+k) - 2\psi(x,y) + \psi(x,y-k)\big)$$

Then a fourth order discretization of $\Delta^* \psi = f$ is obtained from the identity,

$$\begin{aligned} &\Big[\mathcal{L}_x^h + \mathcal{L}_y^k + \frac{1}{12}(h^2+k^2)\mathcal{L}_x^h \mathcal{L}_y^k + O(h^4+k^4)\Big]\psi \\ &\qquad = \Big(1 + \frac{1}{12}h^2 \mathcal{L}_x^h + \frac{1}{12}k^2 \mathcal{L}_y^k\Big) f. \end{aligned} \tag{1}$$

A special treatment on the plasma–vacuum interface is required in order to take full advantage of the higher accuracy obtained for the interior equations.

Free field boundary conditions. For plasma in a given external field the proper boundary conditions for the equilibrium problem demand regularity at $r = 0$ and at ∞ for that part of the flux function that is due to currents in the plasma. On a finite computational domain, G, which must completely enclose the plasma, these conditions may be replaced by an integral equation relating ψ and $\partial\psi/\partial n$ on the boundary ∂G. This is a simplification of the method described in [3].

Let ψ_{ext} be the given external field, and define $\psi_{pl} = \psi - \psi_{ext}$. Let $K(\mathbf{r},\mathbf{r}')$ be the Green function for the problem in the infinite domain: $\Delta^* K = r'\delta(\mathbf{r}-\mathbf{r}')$, and K vanishes at ∞ and at $r = 0$. By application of Green's second identity one finds,

$$\mu_m^{-1} c(\mathbf{r}')\psi_{pl}(\mathbf{r}') + \oint_{\partial G} r^{-1}\mu_m^{-1}\psi_{pl}\frac{\partial K}{\partial n}\,ds = \oint_{\partial G} r^{-1}\mu_m^{-1} K \frac{\partial \psi_{pl}}{\partial n}\,ds, \tag{2^a}$$

and

$$\mu_m^{-1} c(\mathbf{r}')\psi(\mathbf{r}') + \oint_{\partial G} r^{-1}\mu_m^{-1}\psi\frac{\partial K}{\partial n}\,ds = \oint_{\partial G} r^{-1}\mu_m^{-1} K \frac{\partial \psi}{\partial n}\,ds + \mu_m^{-1}\psi_{ext}(\mathbf{r}'), \tag{2^b}$$

where

$$c(\mathbf{r}') = \begin{cases} 0, & \text{if } \mathbf{r}' \text{ is an interior point of } G, \\ \dfrac{\varphi(\mathbf{r}')}{2\pi}, & \text{if } \mathbf{r}' \in \partial G, \\ 1, & \text{if } \mathbf{r}' \text{ is an interior point of } G_e, \end{cases}$$

and where $\varphi(\mathbf{r}')$ is the exterior angle subtended by ∂G at the point $\mathbf{r}' \in \partial G$. Either Eq. ($2^a$) or Eq. ($2^b$), in each case restricted to $\mathbf{r}' \in \partial G$ may be used as the integral equation boundary condition connecting ψ and $\partial\psi/\partial n$ on ∂G.

Integral relations for current profile determination. The following family of integral relations [4] (with modified notation) relates moments of the current in G to the normal and tangential components of the poloidal magnetic field on ∂G.

$$\int_G \chi j_t \, dS = \frac{1}{\mu_0} \oint_{\partial G} (\xi B_n + \chi B_s) \, ds, \tag{3}$$

where χ is any solution to $\Delta^* \chi = 0$ in G, and $\nabla(r^{-1}\xi) = \nabla\chi \times \nabla\phi$. The polynomial solutions given in [4] are extended to all orders by defining, for $n > 1$,

$$\chi_n = \sum_{k=0}^{\lfloor n/2 \rfloor - 1} (-4)^{-k} \frac{(n-1)!/2}{k!\,(k+1)!\,(n-2k-2)!} r^{2k+2} z^{n-2k-2},$$

$$\xi_n = \sum_{k=0}^{\lceil n/2 \rceil - 1} (-4)^{-k} \frac{(n-1)!}{(k!)^2\,(n-2k-1)!} r^{2k+1} z^{n-2k-1},$$

as may be found by separation of variables in spherical (ρ, ϑ, ϕ) coordinates [2]. This family of solutions is incomplete for the study of tokamak configurations, not only because of the neglect of the negative power of ρ solutions, but also because the solutions involving conical functions of ϑ have been neglected. A complete family is more suitably obtained by separation of variables in cylindrical or in toroidal coordinates [2].

Current profile from flux surface geometry. Christiansen and Taylor [5] have discussed the possibility of determining the plasma current profile from purely geometric information about the magnetic surfaces. They conclude that for a toroidal configuration this determination is always possible, but the following simplified treatment shows their argument to be incorrect, and clarifies under which circumstances this method of current profile determination will be well-conditioned.

Assume that some function σ, known to be a flux-surface quantity, has been measured over the poloidal cross-section of the plasma. As

$$\begin{aligned} \Delta^* \sigma &= \frac{d\sigma}{d\psi} \Delta^* \psi + \frac{d^2\sigma}{d\psi^2} |\nabla\psi|^2 \\ &= -\frac{d\sigma}{d\psi} F \frac{dF}{d\psi} - \mu_0 \frac{d\sigma}{d\psi} \frac{dp}{d\psi} r^2 + \frac{d^2\sigma}{d\psi^2} |\nabla\sigma|^2 \Big/ \Big(\frac{d\sigma}{d\psi}\Big)^2, \end{aligned}$$

where p is the pressure and $F = rB_t$, it follows that,

$$\Delta^* \sigma = -\alpha - \beta r^2 - \gamma |\nabla\sigma|^2, \tag{4}$$

where α, β, and γ are flux surface quantities; specifically, $\alpha = \sigma' F F'$, $\beta = \mu_0 \sigma' p'$, and $\gamma = -\sigma''/(\sigma')^2$, where $'$ denotes $\partial/\partial\psi$. The representation of $\Delta^*\sigma$ in Eq. (4) is unique, and the functions α, β, and γ are determinable from knowledge of the function σ, provided that $|\nabla\sigma|^2$ is not, on any flux surface, linearly dependent on 1 and r^2. One may then consider ψ as a function of σ, and derive from $\gamma = -\sigma''/(\sigma')^2$ the differential equation,

$$\frac{d}{d\sigma} \ln\Big(\frac{d\psi}{d\sigma}\Big) = \gamma(\sigma). \tag{5}$$

With two integrations ψ is obtained as a function of σ, and therefore also as a function of (r,z). Of the two free constants arising from the integrations, one is determined by the total current, and the other is irrelevant.

Thus, except in a degenerate case, the current profile in a toroidal configuration can be determined from the flux surface geometry together with a measurement of the total plasma current. The procedure fails if $|\nabla\psi|^2 = c_1(\psi) + c_2(\psi)r^2$ over a range of values of ψ, for some two flux functions c_1 and c_2. That such equilibria exist is shown in [6] and [7]. If the degeneracy occurs only on isolated flux surfaces or only approximately then the procedure may still be feasible, but will be badly conditioned.

Integral relations for nonideal MHD. The following family of integral relations [4], valid for ideal MHD equilibrium, is well known,

$$\int_T \Big[p\nabla\cdot\mathbf{Q} + \frac{1}{2\mu_0}(B_t^2 - B_{t0}^2) r^2 \nabla\cdot(r^{-2}\mathbf{Q}) - \frac{1}{\mu_0}\mathbf{B}_p\cdot\Big(\nabla\mathbf{Q} - \frac{1}{2}(\nabla\cdot\mathbf{Q})I\Big)\cdot\mathbf{B}_p\Big]\,dV = \frac{1}{\mu_0}\oint_{\partial T}\Big[\frac{1}{2}B_p^2\,\mathbf{Q}\cdot\mathbf{n} - (\mathbf{Q}\cdot\mathbf{B}_p)(\mathbf{B}_p\cdot\mathbf{n})\Big]\,dA$$

where T is an axisymmetric toroidal region enclosing the plasma, p is the pressure, B_t (B_{t0}) is the (vacuum) toroidal magnetic field, $\mathbf{B}_p$ is the poloidal field, and $\mathbf{Q}$ is an arbitrary axisymmetric poloidal vector field. The corresponding relations valid in the presence of pressure anisotropy and plasma rotation are obtained by the simple substitutions [2],

$$\begin{aligned} p &\rightarrow \frac{1}{2}(p_\parallel + p_\perp + \rho v^2), \\ B_t^2 - B_{t0}^2 &\rightarrow \sigma B_t^2 - B_{t0}^2 - \mu_0\rho v_t^2, \\ B_p^2 &\rightarrow \sigma B_p^2 - \mu_0\rho v_p^2, \end{aligned}$$

where $\sigma = 1 + \mu_0(p_\perp - p_\parallel)/B^2$, and the other quantities have their usual meaning. This clarifies how anisotropy and rotation affect the determination of the characteristic plasma parameters β_I, μ_I, and l_i.

Acknowledgement. This work was performed under the Euratom-FOM and Euratom-IPP association agreements with financial support from ZWO and Euratom.

References.

1. B.J. Braams, *Multigrid and the Computation of MHD Equilibria*, Report IPP 5/3, Max-Planck-Institut für Plasmaphysik; in preparation.
2. B.J. Braams, *The Interpretation of Tokamak Magnetic Diagnostics: Status and Prospects*, Report IPP 5/2, Max-Planck-Institut für Plasmaphysik; in preparation.
3. K. Lackner, Comput. Phys. Commun. **12** (1976), 33–44.
4. L.E. Zakharov and V.D. Shafranov, Sov. Phys. Tech. Phys. **18** (1973), 151–156.
5. J.P. Christiansen and J.B. Taylor, Nucl. Fusion **22** (1982), 111–115.
6. D. Palumbo, Nuovo Cim. X **53B** (1968), 507–511.
7. C.M. Bishop and J.B. Taylor, *Toroidal Minimum-B and Related MHD Equilibria*, presented at the 1985 Sherwood theory conference.

ANALYSIS OF AXISYMMETRIC MHD EQUILIBRIA BY TOROIDAL MULTIPOLAR EXPANSION

F. Alladio, F. Crisanti, M. Marinucci

Associazione EURATOM-ENEA sulla Fusione, Centro Ricerche Energia Frascati, C.P. 65, 00044 Frascati, Rome, Italy

The Grad-Shafranov equation for the flux function ψ

$$\frac{\partial^2\psi}{\partial R^2} + \frac{\partial^2\psi}{\partial Z^2} - \frac{1}{R}\frac{\partial\psi}{\partial R} = \mathcal{L}\psi = -2\pi\mu_o R J_\phi(R,Z) \qquad (1)$$

can be solved in toroidal coordinates $(\theta,\tilde{\omega})$ [1] by using a decomposition in multipolar moments

$$\psi(\theta,\tilde{\omega}) = \frac{1}{\sqrt{ch\theta-cos\tilde{\omega}}} \sum_{m=0}^{\infty} \{[M_m^i(\theta)f_m(ch\theta) + M_m^e(\theta)g_m(ch\theta)]\cos(m\tilde{\omega})\} + C \qquad (2)$$

where the functions $f_m(ch\theta)$ and $g_m(ch\theta)$ are the Fock functions and C is a constant. The use of the Green's function method leads to define the internal and external multipolar moments $M_m^i(\theta)$ and $M_m^e(\theta)$ as integral expressions of the current density flowing in the plasma and in the external windings [1]. The plasma contribution to the multipolar expansion is specified by the equilibrium current density

$$J_\phi(R,\psi) = 2\pi R \frac{dP(\psi)}{d\psi} + \frac{\mu_o}{4\pi R}\frac{dI^2(\psi)}{d\psi} \qquad (3)$$

where a reasonable choice for $P(\psi)$ and $I^2(\psi)$ can be

$$P(\psi) = \begin{cases} \alpha\psi^\lambda; & \text{for } \psi > 0 \\ 0 \ ; & \text{for } \psi \leq 0 \end{cases} \qquad I^2(\psi) = \begin{cases} \alpha c\psi^\lambda; & \text{for } \psi > 0 \\ 0 \ ; & \text{for } \psi \leq 0 \end{cases} \qquad (4)$$

Equations 1-4, together with the constraint on the total plasma current (that is proportional to the sum of the internal multipolar moments [2]) and the assignment of boundary conditions (expressible in terms of the external multipolar moments) are the basis for the iterative scheme for our predictive equilibrium code. Fixed boundary plasma equilibrium problems can be solved by assigning the plasma contour and computing, during the iterative procedure, the necessary external multipolar expansion. On the other hand, for free boundary problems the external multipolar expansion is immediately evaluated from the current in the poloidal field system. In particular the fixed and the free boundary codes can be used in series to optimize the poloidal field system in order to obtain particular plasma configurations. The fixed boundary code provides the external multipolar expansion necessary for the given plasma shape; the unknown currents in the external windings that best fit such expansion can be, at this point, evaluated by solving a linear deter-

mined or overdetermined system. Finally the free boundary code can be used in order to check the result. In Fig. 1 an expanded boundary equilibrium, simulated for the future Frascati Tokamak FTU (at reduced plasma current performance), is shown.

The use of the fixed boundary code has allowed to obtain the internal multipolar expansion for a large set of plasma parameters: $0.05 \leq \beta_p \leq 2.5$; $0.3 \leq \ell i/2 \leq 1.3$; $2 \leq R/a \leq 4$; $1 \leq b/a \leq 1.5$ (where R/a is the aspect ratio and b/a is the elongation). For a given $\beta_p + \ell i/2$ the internal multipolar spectrum exhibits a clear variation as a function of β_p. If such variation is greater than the uncertainty on the moments produced by random errors on the measured fluxes and fields, separate measurements of β_p and $\ell i/2$ is possible (see Fig. 2) after a threshold value of $\beta_p + \ell i/2$. The analysis shows that the threshold in $\beta_p + \ell i/2$ is lower for smaller value of aspect ratio R/a; moreover the enhancement of the elongation b/a strongly and fastly lowers such threshold [3] (see Fig. 3). Intuitively that means that the information on the splitting of β_p and $\ell i/2$ is available only when the constant j_ϕ surfaces are sensibly detached from the isoflux surfaces.

This suggests a possible approach to a reconstructive equilibrium code that can be interfaced with experimental magnetic measurements. In a purely mathematical sense the equilibrium identification problem is not well posed, as the internal multipolar expansion M_m^1 has not an ordered correspondence with the two Taylor expansions of the analytical functions $p(\psi)$ and $I^2(\psi)$. On the other hand, when the experimental uncertainties are considered, it turns out that, at most, the first four terms (M_o^1 to M_3^1) can be measured; correspondingly the experimental results allow to restrict the functional dependance of $p(\psi)$ and $I^2(\psi)$ to

$$\begin{cases} p(\psi) = p_\alpha \psi^\alpha + p_\beta \psi^\beta \\ I^2(\psi) = I_\alpha \psi^\alpha + I_\beta \psi^\beta \end{cases} \qquad 1 < \alpha,\beta < 4 \ , \quad \alpha \neq \beta \tag{5}$$

The exponents α and β provide a degree of freedom that allows slight profile adjustments without large influence on averaged parameters such as β_p and $\ell i/2$. The identified equilibrium is solved by iteratively determining the coefficients p_α, p_β, I_α, I_β by means of a linear system having as known terms the m = 0,1,2 and 3 internal moments at the plasma boundary.

Examples of application of the reconstructive code are given in Figs. 4, 5 and 6 for three different JET shots [4]. Figure 4 shows steady state plasma; Fig. 5 reports the equilibrium behaviour during a major disruption; Fig. 6 shows a spontaneous expanded boundary configuration at low plasma current and high β_p.

REFERENCES

[1] F. Alladio, F. Crisanti, Proc. 11th Eur. Conf. on Controlled Fusion and Plasma Physics, (Aachen 1983), Vol. 2, p. 57

[2] G.N. Deshko, T.G. Kilovataya, Yu.K. Kuznetsov, V.N. Pyatov, I.V. Yasin, Nucl. Fusion 23 (1983) 1309

[3] L.L. Lao, H.St. John, R.D. Stambaugh, W.W. Pfeiffer, "Separation of β_p and ℓi in Tokamaks of non-circular cross-section" Report GA-A17611 (1984)

[4] G. Tonetti et al., " JET Magnetic Diagnostic" 26th Bullettin A.P.S., paper 5T17, Boston 1984.

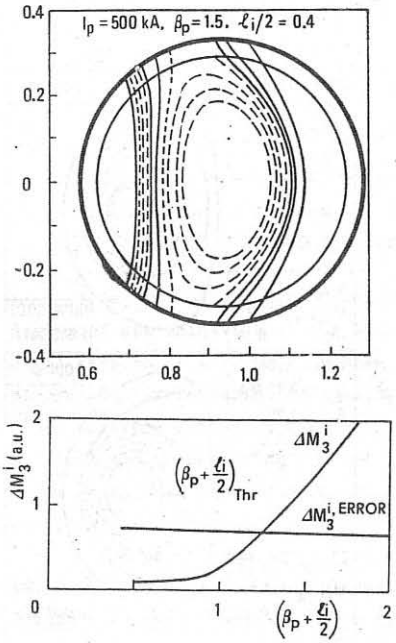

Fig. 2 - Behaviour of $\Delta M_3^{i,ERROR}$ (RMS deviation) with ± 1% signal perturbation and of β_p induced variation ΔM_3^i versus $(\beta_p + \ell i/2)$ for circular plasma with $R/a = 3$.

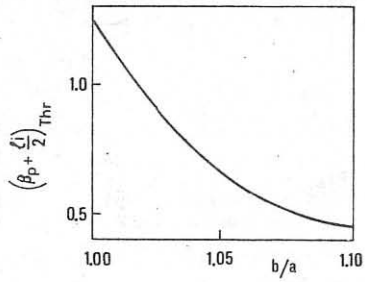

Fig. 3 - Variation of the threshold value of $\beta_p + \ell i/2$ for separability of β_p and $\ell i/2$ as a function of the elongation b/a for plasma aspect ratio R/a = = 3.0. Random pertubations of ± 1% on the measurements are assumed.

Fig. 1 - Simulated expanded boundary equilibrium for the future Frascati Tokamak (FTU).

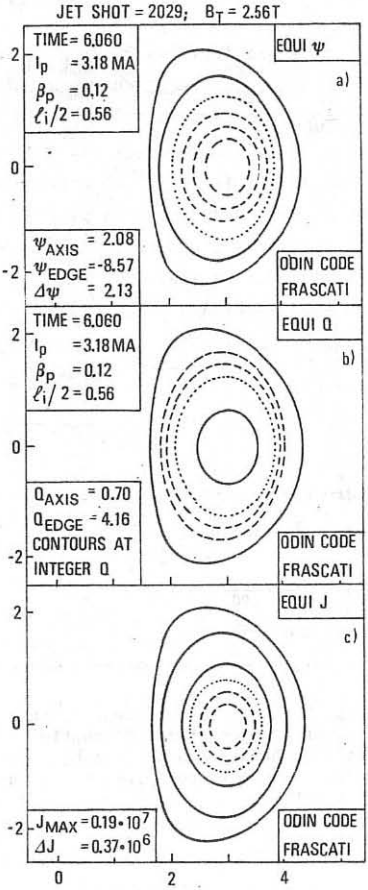

Fig. 4 - Equilibrium identification for a typical JET shot.

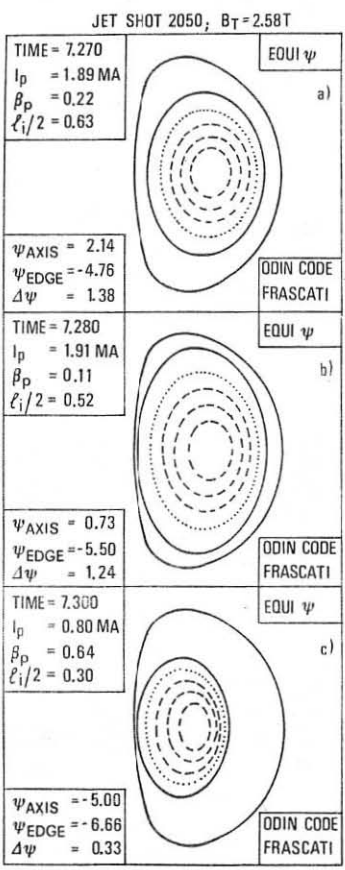

Fig. 5 - Equilibrium identification during a major plasma disruption in JET. a) before disruption; b) just after loop voltage spike; c) during current quench.

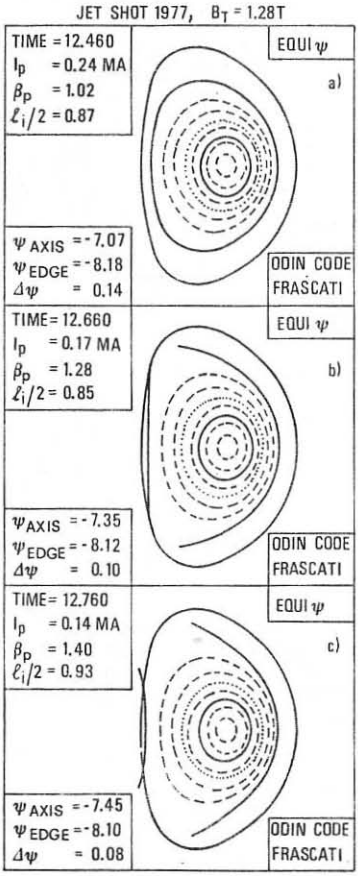

Fig. 6 - Equilibrium identification during spontaneous expanded boundary formation in a JET shot at low plasma current and high β_p.

COMPARATIVE STUDIES FOR THE NUMERICAL SIMULATION OF IMPURITY TRANSPORT IN TOKAMAK PLASMAS

F. Spineanu, M. Vlad
Institute of Physics and Technology of Radiation Devices
P.O.Box MG-7, Magurele, Bucharest, Romania

1. Despite of the considerable progress achived in obtaining low degree of contamination of the tokamak discharge, the impurity evolution still remains an important problem. It is especially connected with the cold plasma edge where radiative cooling dominates and the fast dynamics of various particle species influences the parameters of the whole plasma. The physical and mathematical aspects of the problem of impurity transport are examined in this work by means of a system of computer codes which solve the problem as described by various models, using different numerical methods.

The one dimensional model of the diffusion of a certain species of impurity ions in a hydrogen plasma, accompanied by ionization and recombination processes consists of the system of equations:

$$\frac{\partial n_k}{\partial t} + \frac{1}{r}\frac{\partial}{\partial r}(r\Phi_k) - n_e S_k n_{k-1} + n_e(\alpha_k + S_{k+1})n_k - n_e \alpha_{k+1} n_{k+1} = f_k \qquad (1)$$

where n_k is the density of the ions in the k^{th} stage of ionization, S_k and α_k are ionization and recombination rates and f_k is a source term. Φ_k is the diffusion flux having a general expression of the form:

$$\Phi_k = a \frac{\partial n_k}{\partial r} + b_k n_k \qquad (2)$$

which permits the inclusion of the neoclassical and of various anomalous contributions. In particular, we have introduced the diffusion flux containing the classical, Pfirsch-Schluter and banana-plateau terms and also taking into account the collisions with the impurity ions. Anomalous fluxes are introduced by suitable modifications of the functions a and b_k in (2). Additional loss of ions in the cold plasma edge and scrape off layer are simulated by the term $-n_k/\tau$, τ being an equivalent confinement time.

2. The system (1) was transformed into a matrix equation by three different discretisation procedures /1/, briefly described in the following:

-finite difference discretisation using a Cranck-Nicholson scheme, the

derivatives of a and b_k being determined numericaly;

-cubic spline representation of the unknown functions $n_k(r)$ and of their derivatives,the coefficient a and b_k being analytically differentiated;

-an integral formulation of the problem (Galerkin's method) in which the unknowns $n_k(r)$ are represented as a superposition of integrable functions("chateau").The integrals involving a and b_k are approximated with the average value on each interval of the radial mesh.

Having a large dimension (determined by the number of charge states multiplied by the number of points in the radial mesh),the algebraic system of equations was solved using two methods:

-an iterative procedure (conjugate gradient) which has the advantage of consisting only of matrix multiplication operations.(About 10 iterations are sufficient to obtain the result.)

-the Gaussian elimination adapted to the form of the matrix.

The codes allow the specification of the conditions at the plasma edge in two forms,i.e. by giving either the absolute values of the densities or the fluxes.Because in the quasi steady stage of the tokamak discharge the impurities can reach stationary profiles (which are solutions of (1) with $\partial n_k/\partial t = 0$),the codes are designed to solve,at option,this problem too.In general,the functions a and b_k depend on the impurity ion densities n_k determining the equations (1) to be nonlinear.An iterative procedure is used in the codes to deal with this nonlinearity for the stationary problem and a predictor-corrector algorithm for the evolution problem.

The three codes have been tested in various situations and their results compared.A very good agreement (within 1%) is obtained,but cubic spline method is recommanded because it has the advantage of giving accurate results even on discretisation meshes with small number of points. Consequently,a module which provides the adaptation of the necessary input plasma parameters was added to this spline code which was specially developed in order to be used in connection with any experimental data or plasma transport computer simulations /4/.

3.As an alternative to the system (1),the impurity problem can be treated by a less accurate but simpler and computationally more efficient method /3/.A diffusion equation for the total impurity density is solved and the population on the various charge states are distributed according

to the corona model.We have developed for this simplified model a code which can work both independently and coupled with a one dimensional full plasma transport code /2/.

4.The full model (1) requires initial and boundary conditions for each charge state impurity ion density.It is difficult to provide this set of data on a firm experimental basis,so that it is necessary to know the sensitivity of the solution $n_k(r,t)$ to variations of these parameters.

The initial profiles of impurity densities have a two-fold influence on the numerical simulations.First,due to the nonlinearity caused by the dependence of the functions a and b_k on the unknowns n_k,the iterative procedures may not converge both in the stationary and nonstationary cases. E.g.,for parameters of the early stage of a T-10 discharge (T_e=200eV, $n_e=5.\ 10^{13}$ at r=0),the corona equilibrium densities assumed at start for the stationary problem are modified in the iterations (in the highest charge states) by two orders of magnitude.Second,in the nonstationary case, the same initialisation leads to rapid changes following the start of the simulation.Many similar experiments support the conclusion that in the current rise stage of the discharge both the corona equilibrium and the stationary impurity ion profiles cannot be assumed.

The importance of the boundary conditions is a more complex problem, depending on their form (densities or fluxes at r=a) and on the expression of the diffusion flux.We have performed computations with various formulas for b_k and found that its radial dependence strongly determines the influence of the given boundary densities $n_k(a)$ /1/.For b_k (arising from purely neoclassical diffusion) having positive values at the plasma edge, the boundary condition influence is restricted to a narrow region near r=a. For $b_k=0$ or $b_k<0$ in the outer part of plasma,the influence is extended to the whole range and the necessity of choosing physically reasonable values is more stringent.For instance,the highest levels may appear to be radially uniform populated,with a density given by the boundary value even when corona equilibrium indicates that these levels are practically empty.The condition prescribed as boundary flux has always a strong influence on the solution.To a large extend this is connected with the model of neutral impurity behaviour.

5.A simple model of the neutral impurity component of the plasma consists of considering the flux of atoms radially penetrating from the

border with a constant velocity v_o, being ionized along their path. This implies the following expression for the neutral atom density:

$$n_o(r) = n_o(a)\ \exp\left(-\int_r^a n_e S_1\ dr/v_o\right) \qquad (3)$$

This model imposes serious restrictions on the range of the decisive parameter $n_o(a)$, due to the strong influence which the neutral atom profile has on the low ionization stage populations. The complicated physical problem was restated in another formulation involving the flux of neutral atoms.

Defining Φ_o as the flux emitted by a unit surface at the plasma edge in the unit solid angle in a certain direction, the total flux at a point $P(r,\theta,z=0)$ inside plasma is given by:

$$\vec{\Phi}(r,\theta) = \int_{-h}^{h} dz \int_{-\pi}^{\pi} a\ d\chi\ \vec{e}_{SP}\ \Phi_o/(l_{SP}^2 v_o(S,P))\ \exp\left(-\int_0^{l_{SP}} n_e S_1 dl'/v_o(S,P)\right) \qquad (4)$$

where $S(a,\chi,z)$ is the current point on the plasma surface in cylindrical coordinates, l_{SP} is the distance between S and P, $v_o(S,P)$ is the velocity of the neutrals leaving S in the direction of P, $\vec{e}_{SP}$ is the versor of this direction. The density n_o in P now depends on $\Phi_o(\chi,z;r,\theta)$ which was analytically modelled. Physically, Φ_o can be connected with the flux of particles impinging the wall or with a recycling process.

6. Various computations lead to the conclusion that the simplified impurity ion transport model described in paragraph 3. cannot accurately account for the low charge ion densities in the cases when an inward neutral atom flux must be considered. The full model (1) reveals important populations in these states when recycling (either constant or variable in time) was assumed. In general, even when the inward neutral flux is very small the results of the simplified model agree only qualitatively with those of the extended model (1). However, the effective charge obtained by the two simulations are not too different on the plateau of the discharge, indicating that the simplified model can be used in a full plasma transport code.

7. References

/1/ F.Spineanu, M.Vlad, I.I.Popescu, Report LOP-47-1984, ICEFIZ-Bucharest

/2/ F.Spineanu, M.Vlad, Rev.Roum.Phys. 30(6), 1985

/3/ P.H.Rutherford, Report MATT-1039, 1974

/4/ F.Spineanu, M.Vlad, I.I.Popescu, submitted to Comp.Phys.Comm.

/5/ S.P.Hirshman, D.J.Sigmar, Nucl.Fusion 21(9), 1981

NUMERICAL SIMULATION OF MHD EFFECTS ON TOKAMAK PLASMA CONFINEMENT

K. SHIMIZU, H. SHIRAI, T. HIRAYAMA, M. AZUMI, T. TAKIZUKA, K. TANI
Japan Atomic Energy Research Institute
Mukoyama, Naka-Machi, Naka-Gun, Ibaraki-Ken 311-02, Japan

Various kinds of MHD activities are observed in a tokamak discharge. These MHD activities deteriorate the plasma confinement and limit the operation region of plasma parameters. In the plasma center, m=1 modes excite sawtooth oscillations and flatten the temperature profile. High-frequency oscillations and fishbone oscillations for high beta operations enhance the high-energy-particle loss. Tearing mode activities produce magnetic island and may reduce the confinement. The contact of m/n=2/1 island with a limiter or the overlapping of m/n=2/1 island with m/n=3/2 island are considered to cause major disruptions.

The purpose of this paper is to clarify the operation region for joule heated plasma of JT-60 by using a tokamak transport code with MHD effects. In order to simulate the sawtooth oscillations, the model similar to that given by Waddel et al. [1] is incorporated into the tokamak code. When the safety factor at the plasma center q_0 is lower than unity, the magnetic island grows around the $q=1$ resonance surface, $r=r_s$, as $W_s=W_0\exp\int\gamma dt$, where γ is the linear growth rate including the diamagnetic effect. When the width of this island, W_s, becomes larger than r_s, the minor disruption occurs and the current density is mixed inside the critical radius on the basis of Kadomtsev model [2] as well as the flattening of the electron temperature.

The stability of m/n=2/1 and 3/2 tearing modes is examined by the

marginal mode equation. When the mode is unstable ($\Delta'(0)>0$), the saturated island width is estimated by using the non-linear Δ' analysis [3] ;

$$\Delta'(W_s) = (d\Psi/dr|_{r+} - d\Psi/dr|_{r-}) / \Psi(r_s) = 0$$

where Ψ is the eigenfunction of perturbed helical flux and $r\pm=r_s\pm W_s/2$.

The impurity transport equations [4] are solved by combining with the plasma transport in order to investigate the radiation cooling effect on the current density. These equations describe ionization, recombination and anomalous diffusion ($\Gamma_k = -D_A dn_k/dr + V_A n_k$ with $D_A=1\ m^2/s$ and $V_A/D_A=2r/a^2$) for each charge state k.

The calculations have been carried out by using the parameters of JT-60 as listed in Table 1. We adopt the Neo-Alcator scaling for the electron thermal conductivity, $\chi_e=4.4\times10^{20} r/R^2 n_e\ m^2/s$. At first, we investigate the possibility of the low-q operation ($q_a<3$). Figure 1 shows the dependence of the magnetic island width on the safety factor at the plasma surface, q_a, in the steady state with the volume-averaged density of $<n_e>=3.5\times10^{19}\ m^{-3}$. The m/n=2/1 island width is sensitive to the wall position $r=b$, especially for the low-q operation; for the case of $q_a=2.5$, the 2/1 island contacts with the limiter for $b/a>1.5$, while the mode is stable for $b/a=1.0$. In the following, we set the wall at $b/a=1.2$. The 2/1 island width is little changed in the range of $2.5<q_a<7$ and the 3/2 tearing mode is stable, as shown in the figure. The position of resonance surface of the 1/1 mode is also plotted in the same figure. The tearing mode stability in the low-q operation depends on the current rise rate dI_p/dt. Figure 2 shows the time evolution of magnetic islands during the current rise-up phase. The rapid increase of the plasma current ($dI_p/dt>0.75\ MA/s$) increases the current density gradient at the

resonance surface and leads the contact of the 2/1 island with the limiter. The disruption due to the rapid current rise can be prevented by the surface cooling by the gas-puffing, although the large gas-puffing ($d\langle n_e\rangle/dt > 2\times10^{19}$ $m^{-3}s^{-1}$ for $dI_p/dt=0.75$ MA/s) shrinks the current channel and again leads to the disruption due to the overlapping of 2/1 and 3/2 magnetic islands. These results indicate that the careful control of the current rise and the gas-puffing is required for the stable low-q operation.

We also study the dependence of the maximum plasma density on the plasma current. As the plasma density is increased with fixed impurity content and plasma current, the radiation loss increases almost proportionally to the square of the density. When the radiation loss becomes comparable to the joule heating power, the current channel starts to shrink. This shrink due to the surface radiation cooling destabilizes the tearing modes, and causes the overlapping of 2/1 and 3/2 magnetic islands. Figure 3 shows the critical density due to the disruption as the function of the plasma current for the oxygen impurity content of 1 % and 2 %. This result qualitatively agrees with experimental results and indicates the importance of the impurity control for the high density operation.

References

1] B.V. Waddel, G.L. Jhans, J.D. Callen, H.R. Hicks, ORNL/TM-5840 (1977).

2] B.B. Kadomtsev, Fizika Plazmy 1 (1975) 710.

3] B. Carreras, B.V. Waddel, H.R. Hicks, Nucl. Fusion 19 (1979) 1423.

4] T. Hirayama et al., GA-A17406 (1984).

Table 1 JT-60 parameters

major radius	R = 3.03	m
minor radius	a = 0.95	m
toloidal field	B_T = 4.5	T
total current	I_p = 2.7	MA

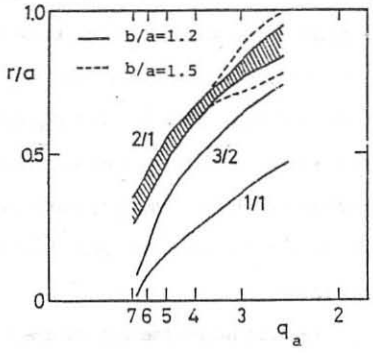

Fig. 1 Saturated island v.s. q_a.

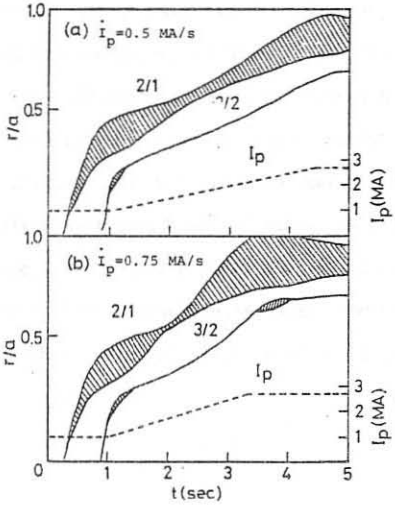

Fig. 2 Time evolution of island width for low-q operation.

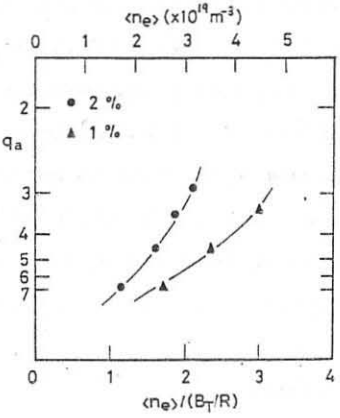

Fig. 3 Density limit caused by overlapping.

THREE-DIMENSIONAL CALCULATIONS OF THE TRANSPORT OF NEUTRAL HYDROGEN AND MOLECULAR IMPURITIES IN TFTR*

D. B. Heifetz, W. D. Langer, A. B. Ehrhardt
Plasma Physics Laboratory, Princeton University
Princeton, N. J. 08544

1. Motivation

Knowledge of the density and temperature of atoms and neutral molecules in TFTR is necessary for the interpretation of measurements of limiter heating, charge-exchange emission spectra, hydrogen line radiation, and residual gas analyzers, and estimation of getter pumping. It is also important in the modeling of the bulk plasma transport and energetic ion behavior, the generation and transport of impurities, and in determining the overall particle and power balances. Future modifications in machine design, such as, for example, its pumping system, will require understanding of neutral particle kinetics in TFTR.

Information about the spatial variation of neutral particle density and temperature in TFTR has been experimentally determined using two pressure gauges, four H_α detectors around the torus, and charge-exchange emission detectors. The edge neutral pressure is typically seen to drop below 10^{-7}-10^{-8} torr, which is the lower bound of the gauges' sensitivities. The H_α detector nearest the movable limiter usually sees 10-100 times the emission rate that is seen by the other three detectors. Particle flux measurement by the charge-exchange analyzers has not been absolutely calibrated.

In order to refine this very rough picture of neutral particle behavior, a multi-dimensional model of neutral particle transport has been applied to the TFTR geometry for a range of plasma parameters. Results from these calculations are presented here.

2. The Numerical Model

A three-dimensional Monte Carlo algorithm [1] was used in order to include the effects of asymmetric device geometry and neutral particle sources. Discharges modeled used the TFTR movable limiter. The model geometry included a complete three-dimensional torus containing a sector of a torus of the correct dimensions to simulate the movable limiter. While this was not a faithful representation of the device geometry, it does simulate the major geometric effects of the actual limiter.

The plasma characteristics remain fixed in the calculation. Profiles of plasma density and temperature were taken, where possible, from fits to experimental data. Three sources of neutral particles were included: those produced by plasma recycling of the limiter, reycling off the vacuum wall, and by recombination. Gas fueling is typically negligible in TFTR, with the overall particle confinement time longer in TFTR than the discharge time. No sources due to beam heating or pellet injection were included.

One uncertainty in the calculation is the relative strengths of the sources, in particular, the ratio of the ion current onto the limiter to the current onto the wall. Uncertainties also exist in the models for wall reflection and reaction rates for neutral/plasma interactions.

Reflection of ions and neutral particles off the limiter and first wall is not understood. We only have guidance from experimental measurements made under very different conditions. Thus a range of models for particle reflection was used in order to include this uncertainty in our results.

*Work supported by the U.S. DOE Contract No. DE-AC02-76-CHO-3073.

Some results proved to be very sensitive to the variation in models while others were relatively insensitive. Other aspects of the overall reflection model, such as wall pumping, and the rate of molecular desorption, were also varied so as to test the sensitivities of the results to the model used.

Neutral/plasma interactions are better known. Even so, some cross sections in some temperature ranges may not be known even to within a factor of two. Again the sensitivity of the results to these unknowns has been explored.

3. Calculated Neutral Hydrogen Distributions

As a sample case, we considered an ohmically heated deuterium plasma with a minor radius of 85 cm, $\langle n_e \rangle = 4.2 \times 10^{13}$ cm^{-3}, $Z_{eff} = 1$, $n_e = n_i$ (r=85 cm) $= 10^{13}$ cm^{-3}, $T_e = T_i = T$, $T(r=0) = 2.3$ keV, $T(r=85) = 75$ eV, and density and scrape-off lengths of 2 cm [2]. A confinement time of 200 ms was assumed, resulting in a current of 7.4×10^{21} D^+/sec onto the movable limiter. Based on past experience from PLT [3], the total ion current onto the first wall was taken to be a tenth of this limiter current.

The base case model for wall reflection assumed: (1) reflection coefficients for normal incidence, (2) rough walls (so the effective wall reflection coefficient was a power of that for smooth walls), (3) the walls were fully saturated with all D_2^0 desorbing at wall temperature, and (4) no getter pumping.

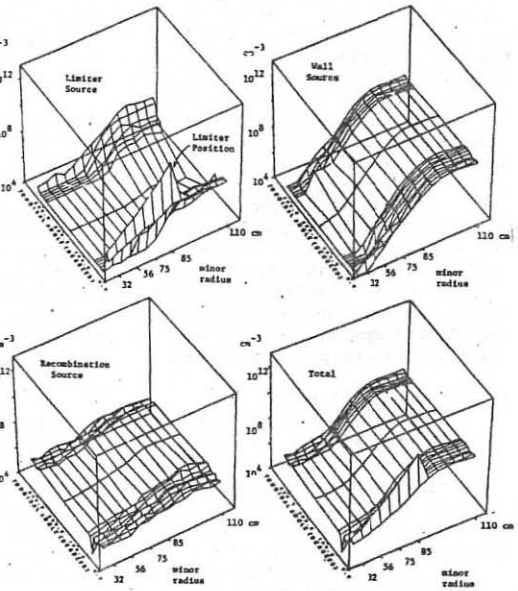

Fig. 1. D^0 densities averaged poloidally produced by each source, and the total density, computed for the TFTR base case.

The primary result of our calculation was the high degree of localization of the neutral particle population near the movable limiter. The poloidally averaged density of D^0 resulting from each source is shown in Fig. 1, along with the total D^0 density. Atoms in the outer 15 cm were due primarily to the first wall source. Those in the central 60-70 cm are from recombination, $e^- + H^+ \rightarrow H^0$. The effect of the asymmetric limiter source is apparent only very near the limiter where, however, the density of D_o was factor of 100 times greater than anywhere else. Note also that this peak in D_o density in front of the limiter extended to r < 40 cm. The D_2^0 density also shows a similar peak in front of the limiter face.

We note that this localization is a consequence of the mean free path length for atoms at the plasma edge (r=85 cm) being small compared to the

limiter dimensions (5-10 cm versus a limiter width of ~ 60 cm). Particles are trapped, with a highly ionizing plasma on one side, and a carbon limiter on the other, and few atoms reaching the edges of the limiters.

Other quantities which are functions of neutral densities also show large asymmetries. The radially and poloidally averaged D_α emission rate varied toroidally, peaking at the limiter position and dropping a factor of 100 15-20° toroidally away, and remained constant around the rest of the machine.

The particle and energy sources due to ionizing neutrals were also localized near the limiter. Almost 100% of the neutrals formed by the limiter source reionized within 10 cm of the limiter face. Preliminary results using the one-dimensional BALDUR [4] plasma transport code coupled with this detailed neutral transport model also showed a strong localization of neutral particle density near the face of the PDX scoop limiter [5], and a resulting flattened profile in the plasma density.

Gas pressure near the vacuum vessel wall was computed to be in the 10^{-10} - 10^{-9} torr range. This is below the sensitivity of the existing gauges on TFTR (~ 10^{-8} torr). This sensitivity will be lower during the next experimental series.

Neutral particle and energy fluxes peaked on the movable limiter in the area of plasma contact. The atomic particle flux there was 3-4 × 10^{18} cm^{-2} sec^{-1}, dropping to 2 × 10^{15} cm^{-2} sec^{-1} at the limiter ends. The toroidally averaged particle flux was roughly a constant 6 × 10^{14} cm^{-2} sec^{-1}. Contribution of the limiter source to the first wall flux was negligible. Particle flux fron this source peaked at 6 × 10^{13} cm^{-2} sec^{-1} at a point behind the limiter edge, at the same poloidal position as the plasma/limiter contact area, and dropped quickly in strength from there.

Thus when computing the removal rate of the TFTR getter system [6] only the flux of the first wall source is relevant. Assuming a 9% getter wall coverage and a 50% trapping efficiency, the getters would then remove approximately 3.4 × 10^{19} D^+/sec plus 5 × 10^{19} D^o/sec.

Some results proved more sensitive to the physical models assumed than others. One sensitive quantity was edge neutral pressure. By varying the wall reflection model (reducing roughness, using angularly dependent reflection coefficients and specular reflection, and introduing anomalous wall pumping) the D_2^o edge pressure due to the limiter source varied by factors of 10-100. Other quantities, such as central D^o density varied less. Such sensitivity studies will be systematically tabulated in future work.

A study of the effect of plasma rotation on neutral particle kinetics was also made using two plasmas. The first was a simplified beam heated plasma: 100% D^+, Z_{eff} = 1, $\langle n_e \rangle$ = 1.4 × 10^{13} cm^{-3}, $T_i(r=0)$ = 10 keV, and $T_e(r=0)$ = 6.9 keV, a 200 ms particle confinement time, and a wall source one-tenth the limiter source. Two cases were modeled, a stationary plasma, and one rotating with a velocity equal to the local sound speed.

Plots of the toroidal variation of the poloidally averaged D^o density are shown in Fig. 2. The effect of the plasma flow is dramatic, with the neutral density increasing in the rotating case over the stationary case at all radii up to 100 degrees toroidally on the downstream side.

A second, more realistic plasma, was modeled assuming Z_{eff} = 2.7, $\langle n_{H^+} \rangle$ = $\langle n_{D^+} \rangle$, a peak n_{D^+} at r=0 cm and a peak n_{H^+} at r=40 cm. The same qualitative behavior as in the D^+ plasma was seen, with little difference in the computed H^o versus D^o populations. In particular, charge-exchange emission spectra for H^o looked similar to that for D^o.

4. Neutral Methane Kinetics

It is important to understand the mechanism for the introduction of carbon and oxygen into the TFTR plasma. Substantial amounts of methane and water are detected by RGA's between discharges, and it must be assumed that carbon and oxygen may enter the plasma originally as part of these molecules.

A one-dimensional model for the transport of methane including the important dissociation processes is given in [7]. It was shown that the isotropic dissociative processes return roughly half of the produced carbon to the wall, with the remaining carbon atom pentrating further into the plasma than a carbon atom released directly from the wall.

The three-dimensional model of neutral transport will be applied to methane and carbon to improve and expand on the earlier calculations. The new calculation will enable us to follow transport both across and along the field lines. We can calculate not only the penetration of carbon into the plasma, but how much reaches a divertor or a pump. The energy distribution of the molecules and atoms in the plasma can be determined for use in impurity transport codes. New experimental information is available on the collisional processes involving the plasma with methane and its derivative radicals, and these will replace those used in the earlier calculations [7]. Finally, the radiative properties of carbon and the carbon bearing molecules will be included to calculate impurity radiative cooling at the edge.

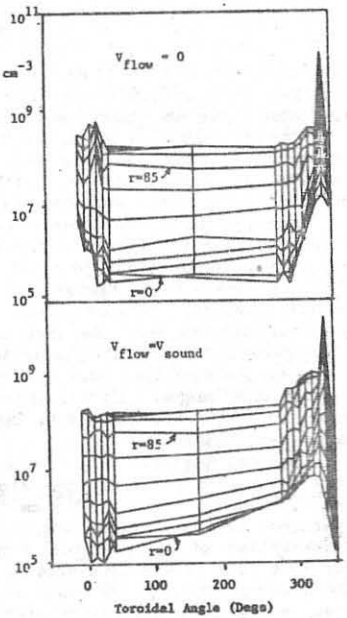

Fig. 2. Toroidal variation of the poloidally averaged D^{o} density beam heated TFTR plasma, for a stationary plasma ($V_{flow}=0$), and a rotating plasma with rotational velocities equal to the local sound speed ($V_{flow}=V_{sound}$).

References

[1] D. Heifetz, et al., J. Comput. Phys. 46 (1982) 309.
[2] R. Budny, private communication.
[3] D. Ruzic, et.al., Bull. Am. Phys. Soc. Vol. 29, No. 8 (1984) 1334.
[4] C. Singer, et al., to appear in Comput. Phys. Comms.
[5] R. Budny, et al., J. Nucl. Mater. 128-129 (1984) 425.
[6] J. Cecchi, et al., J. Nucl. Mater., 128-129 (1984) 1.
[7] W. Langer, J. Nucl. Fus., Vol. 22, No. 6 (1982).

CATI - A Code for Axisymmetric Motions of Plasma in Tokamaks with Iron-Core Transformer

P. Börner, A. Kaleck
Institut für Plasmaphysik der Kernforschungsanlage Jülich,
Association EURATOM-KFA, P.O.B. 1913, D-5170 Jülich

Introduction

The CATI-code is an extension of the CAT-code including the effects of an iron-core transformer. The CAT-code has been introduced in /1,2/. Both codes describe two-dimensional axisymmetric plasma motions on a time scale $\tau_{alfvén} << \tau << \tau_{diffusion}$, and include all external electric components treatable by an axisymmetric model. The above relations on the one hand ensure the plasma to be in equilibrium at every moment ($\nabla p = j \times B$) and on the other hand to behave as superconducting and isentropic. The codes are used as equilibrium codes for given external currents and for positional stability and positioning problems. While the CAT-code uses for the solution of Ampéres law a fast Buneman solver on a rectangular mesh, the CATI-code, to handle the complicated iron geometry, uses a POISSON-solver on a triangular mesh. To the TEXTOR device the code was applied to calculate self-consistent equilibria, study positional stability and to analyse the sensitivity of the Faraday-signal for the determination of the plasma current distribution.

Numerical Essentials of the Code

The presence of iron requires solving the elliptic equation $\nabla \times H = j(r)$ as a boundary value problem with regions of different permeability μ. We use the old "POISSON"- code from Cern /3/ which we improved by the ICCG-method /4/ to solve the linear problem on a 13000 point triangular mesh with 2.7 s on the CRAY-XMP. Since the iron transformer of TEXTOR goes only moderately into saturation, we fix the relative permeability as a known function in space, so we have to solve only the linear problem. At each iteration step of the CATI-code we need the flux functions $\psi_i(r)$ of all external currents and $\psi_p(r)$ of the plasma current. We make use of the superposition principle for solutions of Ampéres law, preproduce the ψ_i and so, at each iter-

ation step, only one solution of Ampères law for $\psi_p(r)$ is necessary. One iteration step requires 8 sec CRAY-XMP-time, and 5-7 iterations are necessary for one time step at an accuracy of 10^{-4}.
The vacuum vessel and the liner were represented by sin/cos (m θ) current distributions ($0 \leq m \leq 2$). Also prompt field penetration through the high-resistive bellows is taken into account /5/. With a non-selfconsistent model described in /5/ we predicted an almost circular cross section (deviation < 2 %). For a selfconsistent equilibrium Fig. 1 shows the poloidal flux pattern. We found maximal deviations from circular shape of 3 % for $\beta_{Pol} = 2$ and peaked current distributions.

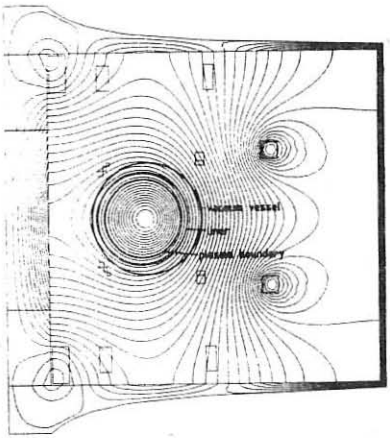

Fig. 1

Flux Pattern of a Self-consistent TEXTOR Equilibrium

In addition to the diamagnetic loop β_{Pol} can be determined from the vertical field. Since Shafranovs formula is no more valid for a compact torus surrounded by iron the CATI-code was used to determine β_{Pol} by the knowledge of the currents in the vertical field coils and in the feed-back coils. The simple formula contains a term corresponding to Shafranovs plasma inductance l_i which is a function of a current shaping factor, the latter is also being measured at TEXTOR /7/.

Positional Stability Calculations

The presence of iron can lead to positional instability in spite of the circular cross section of the TEXTOR plasma. Earlier approximations /5/ led to instability in both directions, but our more realistic CATI-code shows that only vertical displacements are unstable. This is because of the attractive forces of the lower and upper yokes and the unstable index of the vertical field which was necessary for the circular cross section in the iron environment. We studied the stabilization by the vacuum vessel and the liner. Using the model described in /5/ for the non-axisymmetric vessel with a time constant τ = 8 ms and a prompt field penetration of 50 %, we calculated the displacement of the plasma column after a step disturbance. For three cases - only liner is present - only vacuum vessel - both are present - Fig. 2 shows the vertical displacement as a function of time. In the two first cases we have a purely exponential behaviour

$$Z(t) = a\, e^{t/\tau} - b$$

with $\tau_{liner} \approx 3$ ms and $\tau_{vessel} \approx 30$ ms.

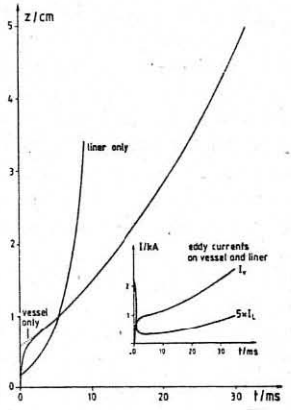

Fig. 2

Vertical Displacement of the Plasma Column after Step Disturbance with Eddy Currents on: Liner only, Vessel only, Liner and Vessel

The CATI-code as a Mean for Interpretation of Experimental Results

The use of the equilibrium code for β_{Pol}-determination was already mentioned. The Faraday-rotation measurements /6 / which serve to determine the plasma current distribution was also considered. Since the direct inversion of the data seems to be problematic statistical regression methods - described in /8/ - seem to be adequate. To study the sensitivity of the Faraday-signals with respect to different current distributions we introduced in the CATI-code the differential equation for the Faraday-rotation of a HCN-laser beam /9/. The normalized signals of two different equilibria are shown in Figs. 3 and 4. The shape of the two curves are very similar but the maximum-minimum values are good measures of the width of the current distribution. Since the measurements are very accurate ($\varepsilon < 3\ \%$) we hope to get much more information by applying the principle component analysis and further studies about error propagation. This work is in progress.

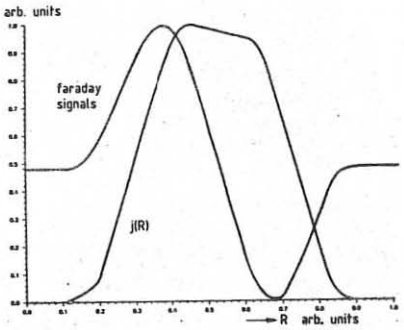

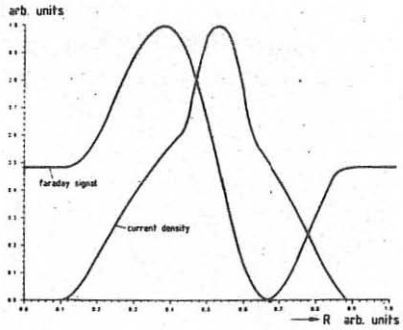

Figs. 3 and 4
Normalized Faraday-rotation Signals for Two Equilibria with the same Density Profile but Different Current Profiles

/1/ Casci, F., et al, Aachen, Sept. 1983 (B43)
/2/ Casci, F., et al, NET Report EUR XII 324/27
/3/ Winslow, A.M., J. of Comp. Phys. Vol. 1, No. 2, 1966 (149-172)
/4/ Kershaw, D.S., J. of Comp. Phys. Vol. 26, 1978 (43-65)
/5/ Kaleck, A., Proc. of the 12th SOFT, Jülich 1982 (1197-1201)
/6/ Soltwisch, H., Aachen, Sept. 1983 (C01)
/7/ Brüssau, W.D. et al., Bayreuth, April 1985 (P66)
/8/ Braams, B.J. et al, IPP 1/228, Sept. 1984
/9/ Segre, S.E., Plasma Physics, Vol. 20, 1978 (295-307)

LASER-INJECTED IMPURITY TRANSPORT IN OHMIC AND ICRF-HEATED TFR PLASMAS

TFR GROUP presented by B. Saoutic
Association EURATOM-CEA sur la Fusion
BP 6. 92260 Fontenay-aux-Roses (FRANCE)

1 Introduction:

Impurity transport phenomena in tokamak plasmas have received considerable attention in the last few years.This has generally shown that the impurity transport is anomalous(it needs a much larger diffusion coefficient than predicted by neo-classical theories).Experimental data used in these studies are almost always V.U.V line radiances,the utilisation of supplementary data from high resolution X-ray spectroscopy being quite recent.

Since the production of intrinsic impurities cannot be controlled at will, the best way to study impurity transport is by purposely injecting a selected impurity by laser blow-off technique.This has two distinct advantages.First,by controlling the amount of injected material,the target plasma is not perturbed.Secondly,the injection time can be selected in order to study a chosen phase of the discharge.In particular,by changing the injection time it is possible to verify if impurity transport is affected by supplementary heating. This is an important problem,since the general tendency in all devices is for the energy confinement time to decrease during supplementary heating. However,it is not clear if this applies also to the(impurity and base) ion particle confinement time.

Laser blow-off injection of impurities has already been used in TFR heated discharges [1],allowing the transport parameters to be evaluated(an anomalous expression for the impurity ion flux,characterized by a diffusion coefficient D_a and an inward convection velocity V_a,is used [2]).The only clear dependance of impurity behaviour on plasma parameters was an improved confinement with increasing mass of the base ions.

In this paper,we shall present new spectroscopic results obtained by injecting vanadium,with the aim of detecting if a difference of particle behaviour exists between ohmic and ICRF-heated plasmas.Section 2 will deal with strong resonance lines of Mg-,Na-,Be- and Li-like isoelectronic sequences,in the V.U.V. region.In section 3,we shall consider the w-line(resonance line of the He-like ions V XXII at 2.38Å),in the soft X-ray region.

The plasma conditions in all the laser blow-off V injection experiments described in this paper were:plasma current Ip=250-300 kA,toroidal magnetic field Bt=4.5 T,carbon limiter radius a=19 cm.The working gas was deuterium with an admixture of hydrogen(20%),in order to satisfy the condition of a central two-ion hybrid layer for ICRF-heating in the mode conversion regime [3].Typically, 100 ms ICRF pulses of 600-800 kW were applied at the Ip plateau,250 ms after the discharge beginning.

2 Numerical simulation of V.U.V. vanadium radiances:

Our impurity transport simulation code has been previously discussed [2,4]. The code considers independently the transport of any atomic species and gives

in cylindrical geometry the density of the ions of all charges as function of time and radius;line radiances and emissivities(data available from experiments)are also calculated.

As already discussed [2],the code uses "ad-hoc" boundary conditions:the incoming neutral atom flux Γ_0 at the limiter radius a is chosen,asfunction of time,in such a way as to correctly simulate the absolute radiances of peripheral ions(i.e.,V XII 355Å and V XIII 423Å).Note that the transport between the limiter radius and the shell where these two peripheral ions exists,mainly depends on D_a.It is then necessary to adjust Γ_0 for each D_a value.

Figure 1(top experiment,bottom simulation)shows the adjustment of the two peripheral lines in the case of V injection into ohmic plasmas,using $D_a=4000$ cm^2s^{-1} and $V_a=1200$ cms^{-1}.Once this is done,the subsequent step is to simulate the absolute radiances of central ions[1](V XX 159Å and V XXI 240Å).An example is given in table 1 and figure 2.We have first varied D_a between 2000 and 6000 cm^2s^{-1},keeping a constant value for the convection parameter $S=aV_a/2D_a=3$(first three columns of table 1).The peak radiance values agree with the experimental ones only for $D_a=4000$ cm^2s^{-1} and $V_a=1200$ cms^{-1}.Agreement on the peak radiance values can also be obtained with the other two D_a values but only by modifying the convection parameter(last two columns of table 1).However,as shown in figure 2 for the three cases of peak radiance adjustment(top experiment,bottom simulations after adjustment of Γ_0 for each D_a value:solid line $D_a=4000$ cm^2s^{-1} dashed line $D_a=2000$ cm^2s^{-1},dot-dashed line $D_a=6000$ cm^2s^{-1}),the time evolution only agrees with experimental data for $D_a=4000$ cm^2s^{-1} and $V_a=1200$ cms^{-1}.

During the same series of experiments,a similar comparison has been performed for V injection into ICRF-heated plasmas.The best agreement with experiments is again found for $D_a=4000$ cm^2s^{-1} and $V_a=1200$ cms^{-1}.It is therefore concluded that the penetration of the puff into the peripheral plasma and the transport coefficients(i.e.,the particle confinement time)are not affected by ICRF(even though the energy confinement time is reduced by ICRF supplementary heating [3,5]).

3 Numerical simulation of He-like w line radiance:

Contrary to the $\Delta n=0$ lines detected in the V.U.V. spectral region,the $\Delta n=1$ w line is sensitive to the electron temperature value through the excitation rate coefficient.It is therefore expected that the w line be saw-tooth modulated and this is indeed the case:its modulation can reach 40-50% of its peak value.

Simulations of the time evolution of the central w and V XXI 240Å ion line radiances have been performed for injection into ohmic and ICRF-heated plasmas.In this section we will present the most interesting case:injection of V just prior to the application of the ICRF pulse.Figure 3 shows(b and c,upper)the normalized w and V XXI line radiances.Time t=0 is the injection time, whereas the ICRF pulse is applied 20 ms later,at the time shown by the dashed vertical line.During the first 15 ms,we have only used the electron temperature $T_e(r)$ and density $n_e(r)$ profiles at the top of the saw-teeth(the reference soft X-ray and T_e signals are irregularly modulated during the transition phase that occurs in the first 5-10 ms following the V injection).We start to

consider the saw-tooth modulation on T_e and n_e, two saw-teeth before the beginning of the ICRF pulse. $T_e(r)$ is varied discontinuously following in detail the evolution given by the time-resolved $2\omega_{ce}$ channels (figure 3a: central channel), with six jumps during the recovery phase. The simulation results, shown at the bottom of figure 3b and 3c, show excellent agreement for both lines (the V XXI noise fluctuations are considerably larger than the small saw-tooth induced variations). Note that the simulation requires the same transport parameters ($D_a = 4000$ cm^2 s^{-1}, $V_a = 1200$ cms^{-1}) before and during the ICRF pulse, again showing that the impurity transport is not modified by the ICRF supplementary heating.

All these simulations imply no change of transport parameters during internal disruptions. It is worth recalling here two previously reported TFR results. In ohmic discharges, the modulation of central Mo ion emission was interpreted, as in this paper, as due only to the T_e saw-teeth [6]. On the other hand, in NBI-heated plasmas strong Ni XXV modulations could only be simulated by varying D_a and V_a at the disruption [4]. Attempts have been made to simulate the experimental data of figure 3 by modifying the transport coefficients at the disruption as reported in ref. [4], and also as reported in ref. [7] for giant inverted long-period saw-teeth in PLT during Al injection. In all cases, no situation giving agreement with the experiment could be obtained. It appears therefore that completely different saw-toothing regimes are possible in the same machine, depending on the experimental conditions.

4 Conclusion:

In this paper we have studied impurity transport in ohmic and ICRF-heated plasmas, using both V.U.V. and soft X-ray spectroscopy along with our impurity transport code. No difference has been observed in the two plasma heating situations in both amplitudes and time evolutions of the experimental radiances, both cases requiring the same transport parameters to be correctly simulated: impurity transport is not affected by ICRF supplementary heating. On the other hand, the same discharges have shown energy confinement degradation due to ICRF-heating [3,5], thus implying that impurity particle transport does not follow necessarily the same variations as energy transport.

The use of the saw-tooth modulated time resolved He-like w line radiance from X-ray crystal spectroscopy (beside giving an additional confirmation of the transport parameters deduced from V.U.V. spectroscopic radiances) has also allowed to show that, for both experimental conditions, the n_e and T_e modifications due to internal disruptions are sufficent to account for the experimental results.

Reference

[1] TFR GROUP, Phys. Letters 87A (1982) 169

[2] TFR GROUP, Nucl. Fusion 23 (1983) 559

[3] EQUIPE TFR, in Heating in Toroidal Plasmas (Proceed. 4th Intern. Conf., Rome, 1984), CCE: Brussels, 1 (1984) 277

[4] TFR GROUP, Report EUR-CEA-FC 1255 (Nucl. Fusion in press)

[5] EQUIPE TFR,in Plasma Physics and Controlled Nuclear Fusion(Proceed. 10th Intern. Conf.,London,1984),IAEA:Vienna,1(1985)103

[6] BRETON,C.,DE MICHELIS,C.,FINKENTHAL,M. and MATTIOLI,M.,Phys. Rev. Letters 41(1978)110

[7] COMPANT LA FONTAINE,A.,DUBOIS,M.,PECQUET,A.L.,BOYD,D.,CAVALLO,A.,et al, Plasma Phys. Contr. Fusion 27(1985)229

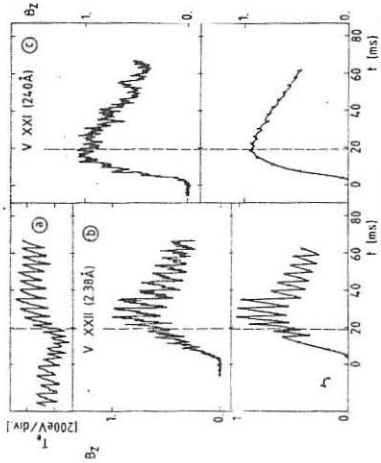

Fig.3

		EXP.	SIMULATION				
D_A [cm²/s]			2000	4000	6000	2000	6000
V_A [cm/s]			600	1200	1800	1200	1200
B_z [* 10^{15} ph/cm² s sr]	V XII 355Å	3.	3.1	2.9	3.	3.	3.
	V XIII 423Å	1.5	1.5	1.5	1.5	1.5	1.5
	V XX 159Å	1.	0.6	0.9	1.4	1.	0.9
	V XXI 240Å	0.8	0.5	0.8	1.2	0.9	0.8

Tab. 1

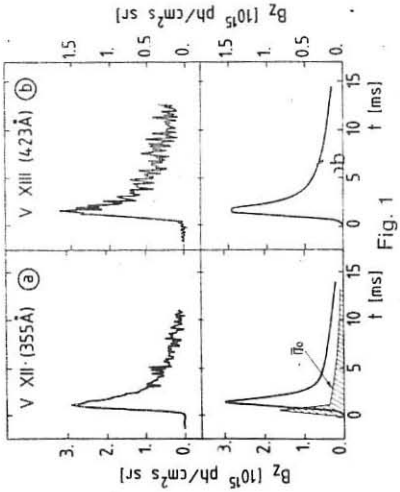

Fig. 1

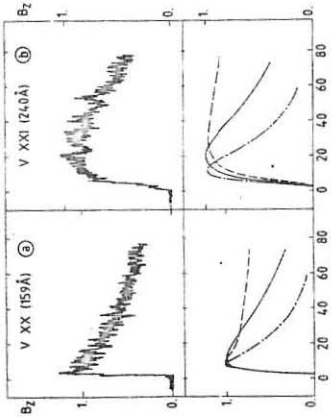

Fig. 2

IMPURITY BEHAVIOUR FOR VARIOUS AUXILIARY HEATING METHODS IN ASDEX

G. Fussmann, R. Bartiromo[1], G. Janeschitz, P.B. Kotzé[2], E. R. Müller, F. Söldner, H. S. Bosch, A. Eberhagen, O. Gehre, J. Gernhardt, G. v. Gierke, E. Glock, O. Gruber, G. Haas, F. Karger, M. Keilhacker, A. Kislyakov[3], O. Klüber, M. Kornherr, M. Lenoci[1], G. Lisitano, A. Mahdavi[4], H.-M. Mayer, K. McCormick, D. Meisel, V. Mertens, H. Murmann, H.Niedermeyer, W. Poschenrieder, H. Rapp, F. Ryter[5], J. Roth, F. Schneider, G. Siller, P. Smeulders, E. Speth, K. Steinmetz, K.-H. Steuer, O. Vollmer, F. Wagner and F. Wesner

Max-Planck-Institut für Plasmaphysik
EURATOM Association, D-8046 Garching

Introduction: Three different additional heating methods are being applied in the ASDEX divertor tokamak: neutral injection (NI), ion cyclotron heating (ICRH) at the 2nd harmonic of hydrogen, and lower hybrid heating (LH). In this paper we discuss the impurity behaviour observed for three heating scenarios. Applying all three methods in the same tokamak has the advantage of allowing a fair comparison of the concomitant impurity problems. Such a phenomenological comparison of the impurity levels has been made for the most important elements Fe, Ti, O, and C. A more profound judgement of the impurity problem, however, will have to distinguish between impurity production, penetration depth of the neutrals into the plasma boundary, and transport in the scrape-off and inner plasma regions. We are not yet in a position to identify the actual importance of these different causes, but some preliminary information was obtained from our measurements. Furthermore, the identification of the dominant production mechanisms is also a matter of crucial importance. We briefly address the problem of sputtering of wall material (Fe) by CX neutrals during NI and access the evidence for the preliminance of ion sputtering in the case of both HF-heating methods.

NI heating: Neutral injection has been applied in ASDEX up to a power level of 4.2 MW ($\Delta t \lesssim 0.4$ s, D^0 or H^0 with $E \leq 45$ keV). The impurity problems arising with this additional heating are in general tolerable ($P_{rad}/P_{tot} \leq 20$ %) with the exception of the cases where the quiescent H-mode had been realized. In this latter case a radiation collapse is observed ($P_{rad} \sim 3$ MW) which can be attributed to accumulation of iron /1/. Typical concentrations for the ohmic phase and the normal H-phase of NI ($P_{NI} = 2.8$ MW, $\bar{n}_e = 2.5 \times 10^{13}$ cm^{-3}, D_2) are in the range: O: 0.15 % (OH), 0.6 - 1 % (NI); Fe: 0.2×10^{-4} (OH), 1.2×10^{-4} (NI). Simulating the impurity behaviour with a time dependent transport code - using measured T_e and n_e profiles as input data - yield some information on the transport parameters and the impurity fluxes. For D_2 discharges we find $D \sim 4000$ cm^2/s for OH and the normal H-phase, and $D \sim 10^4$ cm^2/s for the L-phase of NI. In addition, a moderate inward drift velocity of $v_{in} = -2D\, r/a^2$ is indicated. The Fe fluxes increase for the above NI power level by a factor of 20 to $\Gamma_{Fe} = 3 \times 10^{13}$ cm^{-2} s^{-1} with respect to the OH phase. In order to estimate the influence of a change

[1]ENEA Frascati, Italy; [2]Nuclear Development Corp. of South Africa, Pretoria
[3]Ioffe Institute, Leningrad, USSR; [4]GA Technologies, San Diego, USA;
[5]CEN Grenoble, France

in penetration depth with the transition from OH → L → H the measured boundary profiles /2/ of n_e and T_e were properly taken into account in the transport calculations. For unchanged Fe fluxes we should thus expect a change of concentrations according to 1 (OH) → 0.3 (L) → 0.8 (H) for the three phases. It should be noted, however, that these ratios are actually tendency factors because of the sensitivity with regard to the exact position of the separatrix and the absolute values of T_e. The rather low screening efficiency during the H-phase results in particular from the low T_e and n_e values in the scrape-off.

To address the question of Fe production, discharges were performed in H_2, D_2, and He. An extended discussion of the ohmic phase of these experiments is given in /2/. The behaviour of two Fe line intensities as well as soft X ray and bolometer traces for the NI phase are depicted in Fig. 1 for the three different gas fillings (P_{NI} = 2.8 MW, L-phase, H^o, E = 45 keV). For similar densities (n_{eo} = 3.5, 3.3, 3.8 x 10^{13} cm^{-3}) the temperatures measured were T_{eo} = 1.25, 1.80, 1.55 keV in the case of H^+, D^+, He^{++} background ions, respectively. The iron concentrations $n_{Fe}(0)/n_e(0)$ in the corresponding cases were found to be 1.1 x 10^{-4}, 1.0 x 10^{-4}, and 2.4 x 10^{-4}. In particular, the high concentrations in the case of He are surprising in view of the low He^{++}-He^o CX cross-sections and the impossibility of producing high-energy neutrals in the core plasma via charge exchange with H^+ beam particles. Whether sufficient CX neutrals are still produced in the outer plasma regions - as is conjectured for the ohmic phase in /3/ - to explain our results needs further investigation.

ICRH heating: First attempts with ICRH revealed serious impurity problems. In comparison with NI much higher Fe concentrations were found even for lower heating powers. An example is shown in Fig. 2 where during the same discharge 900 kW of NI and 450 kW of ICRH power were launched into the torus. We ascertain a strong increase of the Fe intensities and a further rise of the main plasma radiation losses (bolometer) with ICRH, whereas the C III signals in the main chamber and in particular in the divertor are found to decrease. This decrease of the divertor radiation is indicative of reduced power flow into the divertor, consistent with the enhanced radiation losses from the main plasma (P_{rad}/P_{tot} = 20 % → 40 %). A considerable improvement - reduction of the power losses by up to a factor of 2 - was achieved by operating at toroidal field strengths where the ion cyclotron resonance layer coincides with the divertor entrance /3/: This observation suggests that the enhancement of the Fe fluxes is caused by up drifting suprathermal ions being produced in the resonance zone. In any case, an additional Fe production mechanism probably has to be postulated since the impurity levels are already substantially increased for marginal changes of CX-fluxes and ion temperatures.

The best heating results are obtained by combining ICRH with NI. There may be two reasons for the beneficial effect of NI: better coupling of the wave to the plasma due to pre-heating, and in addition thermal stabilization of the scrape-off, this being required to prevent deep penetration of the impurities owing to a decrease of temperature in this region. However, also with NI and under optimized ICRH conditions an overproportional increase of the radiation losses with the onset of ICRH is found. In Fig. 3 this behaviour is documented for three different power levels P_{ICRH} = 0.6, 1.8, and 2.45 MW, overlapping with NI heating at 1.75 MW. Adding the same power of 1.8 MW to NI is seen to increase the soft X-ray ($h\nu > 400$ eV) and Fe XVI intensities by a factor of 5 to 6. According to our transport code analysis this increase directly reflects the enhancement of the Fe fluxes since the T_e and n_e profile changes are small (T_{eo} = 1.34 → 1.57 keV) and the trans-

port parameters can be assumed to be effectively determined by NI heating (L-phase). Further confirmation of these assumptions is inferred from the OVIII signals shown in Fig. 3, which exhibit only a moderate and non-monotonic increase with ICRH power. For the cited case of $P_{NI} = P_{ICRH} = 1.8$ MW we obtain $n_{Fe}(0) = 3.1 \times 10^{10}$ cm^{-3} ($n_{Fe}(0)/n_e(0) = 7 \times 10^{-4}$) and a total flux of $\Phi_{Fe} = \Gamma_{Fe} \times 2.5 \times 10^5 cm^2 = 2.4 \times 10^{19}$ s^{-1}. This flux is to be compared with the stationary H^+ flux leaving the plasma, which, however, is not well known in the case of additional heating. Taking for reference the ohmic recycling flux $\Phi(H^0) \sim 2 \times 10^{21} s^{-1}$ as a lower limit /4/ and multiplying it by the maximum sputtering rate of 1 % (H^0 on SS), we obtain just the above Fe flux. Despite the rather large uncertainties, these considerations suggest that the outdrifting suprathermals are an appreciable fraction of the total ion flux.

LH heating: Apart from initial difficulties, caused by arcing at the grill antenna and neighbouring surfaces, no serious impurity problems generally occur with LH-heating. This statement, however, should be qualified by adding that so far only moderate powers ($\leq$0.7 MW) could be launched into the torus /5/. The impurity behaviour in the case of LH shows a pronounced trend with density. In Fig.4 a comparison between ohmic and LH heated plasmas (P_{LH} = 400kW, D_2, I_p = 300kA, B_o = 2.17T, $\bar{N}_{\parallel} = 4$, mode: $\pi 0\ \pi 0\ \pi$) is shown. Plotted in the figure are the increment of the radiation loss and the ratios of the Fe XVI, CIII and OVI line intensities as functions of $\bar{n}_e$. For $\bar{n}_e \leq 2 \times 10^{13}$ cm^{-3} the waves are coupled preferentially to suprathermal electrons. In this regime efficient plasma heating is found and the increase of radiation losses is small /5/. For higher densities coupling to the ions becomes predominant /6/. For this regime the production of badly confined suprathermal ions in the boundary region with characteristic tail energies of 3-4 keV was substantiated by CX diagnostics /7/. The corresponding fluxes increase with density up to $\bar{n}_e = 4.5 \times 10^{13} cm^{-3}$. It can be assumed that these particles cause the steep increase of iron above $\bar{n}_e = 2 \times 10^{13}$ cm^{-3}, as shown in Fig.4.

Summary: Impurity problems arising with auxiliary heating are mainly caused by metalic impurities (Fe and to some extent Ti and Cr being released from the wall of the plasma chamber. These impurities result in peaked radiation profiles (bolometer profile measurements) with non-negligible power losses in the plasma centre. The worst case is observed for the quiescent H-mode of NI, where improved confinement leads to impurity acucmulation. Apart from this exceptional case, the impurity concentrations found during NI are comparatively low. In respect of our He experiments, however, the Fe production mechanisms during NI are still uncertain. There are several indications that the increase of Fe concentration in the case of ICRH and LH can be attributed to enhanced Fe production caused by suprathermal ion sputtering. When the three heating methods are compared, ICRH is found to produce the highest Fe densities for the same power input. However, in this case too, the total power losses can be kept tolerable ($\leq$35 %) when combining ICRH with NI.

References

/1/ M. Keilhacker et al., Proc. 10th Int. Conf. on Plasma Physics and Contr. Nucl. Fus. Research, London (1984), IAEA-CN-44/A II-1
/2/ J. Roth et al., this conference
/3/ K. Steinmetz et al., this conference
/4/ G. Haas et al., J. Nuclear Materials 121 (1984), 151-156
/5/ F. Söldner et al., this conference
/6/ F. Leuterer et al., Proc. 10th Int. Conf. on Plasma Physics and Contr. Nucl. Fus. Research, London (1984), IAEA-CN-44/F-IV-3
/7/ D.Eckhartt et al., 4th Int. Symp. on Heating in Toroidal Plasmas, Rome (1984)

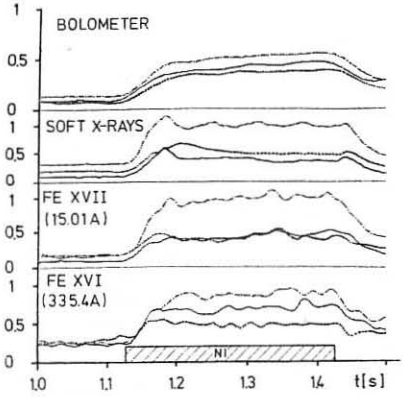

Fig. 1: Traces of bolometer, soft X-ray, and Fe line intensities during ohmic and NI phase (2.8 MW) for various filling gases: H_2 (solid), D_2 (dotted), and He (dashed-dotted).

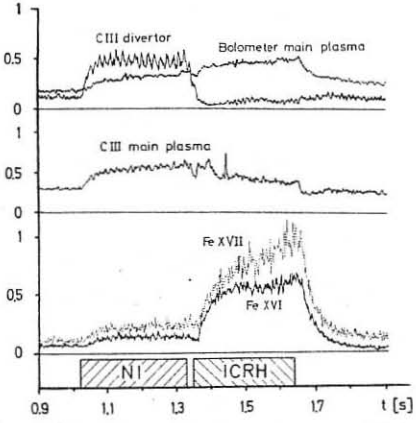

Fig. 2: Comparison between NI (900 kW) and ICRH (450 kW) heated plasmas. Plotted vs. time are radiation losses (bolometer), CIII and Fe line intensities from main plasma, and a CIII divertor signal.

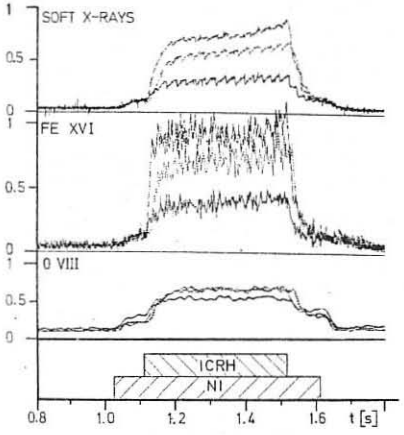

Fig. 3: Soft X-rays, Fe XVI (335 Å) and O VIII (19 Å) line intensities for combined NI (1.75 MW) and ICRH heating: P_{ICRH} = 0.6 (solid lines), 1.8 (dotted), and 2.45 MW (dashed-dotted).

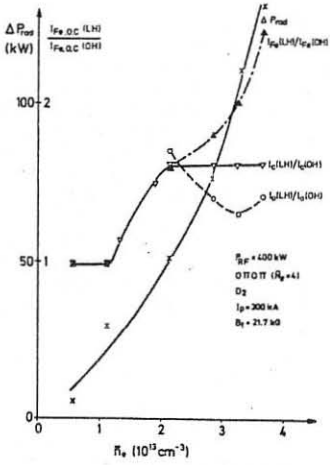

Fig. 4: Increase of radiation losses ΔP_{rad} vs. density for LH heating. Also shown are intensity ratios with respect to ohmic heating for Fe XVI, OVI and CIII emission.

MEASUREMENT OF THE CURRENT DISTRIBUTION IN ASDEX DURING LOWER HYBRID CURRENT DRIVE USING THE LI-BEAM/ZEEMAN EFFECT TECHNIQUE

K. McCormick, R. Bartiromo[1], H.S. Bosch, M. Brambilla, H. Derfler, A. Eberhagen, D. Eckhartt, G. Fussmann, O. Gehre, J. Gernhardt, G. v. Gierke, A. Giuliana[1], E. Glock, O. Gruber, G. Haas, M. Hesse[2], G. Janeschitz, F. Karger, M. Keilhacker, O. Klüber, M. Kornherr, P. B. Kotzé[3], M. Lenoci[1], F. Leuterer, G. Lisitano, H. M. Mayer, D. Meisel, V. Mertens, E. R. Müller, M. Münich, H. Murmann, H. Niedermeyer, W. Poschenrieder, H. Rapp, F. Ryter[2], K. H. Schmitter, F. Schneider, G. Siller, P. Smeulders, F. Söldner, K.H. Steuer, T. Vien, G. Vlases, F. Wagner, F. v. Woyna, M. Zouhar

Max-Planck-Institut für Plasmaphysik
EURATOM Association, D-8046 Garching

Abstract: Results are presented for an exploratory investigation into the behavior of the current density distribution during LH current drive. Indications are that the current profile broadens slightly, in contrast to a peaking of the electron temperature profile, thereby implying that the RF-driven current is not strictly coupled to Spitzer conductivity.

Diagnostic Description: The Zeeman technique /1/ yields the local pitch angle $\theta_p = \tan^{-1}(B_p/B_T)$ of the magnetic field lines, from which the safety factor $q(r)$ and poloidal field $B_p(r)$ can be determined. As illustrated in Fig. 1, a 60 keV/0.5 mA neutral Li beam /2/ is injected into the plasma for the length of the discharge. The collisionally excited Li resonance line radiation is gathered by a lens ($\Omega \sim 10^{-3}$ sr) from a volume (~1.5 x 1.5 cm) defined by the field stop image on the beam. The projection of θ_p in the plane perpendicular to the optical axis is measured by rejecting the spectrally shifted σ components of the Zeeman triplet with a Fabry-Perot interferometer, and then determining the azimuth (θ_p) of the remaining unshifted π component - which is polarized parallel to $\vec{B} = \vec{B}_p + \vec{B}_T$ - by a polarimeter /1/. A profile of $\theta_p(r,t)$ is gained by scanning the beam radially from shot to shot.

Experiment: In a double null diverted discharge (H_2, R ~ 169 cm, a ~ 39 cm, $B_T(R)$ ~ 21.2 kG, I_p = 292 kA, $\bar{n}_e \sim 7 \times 10^{12}$ cm^{-3}) 400 kW of RF power at 1.3

[1]ENEA Frascati, Italy; [2]CEN Grenoble, France
[3]Nuclear Development Corp. of South Africa, Pretoria,

GHz is injected, from t = 0.9 - 1.5 sec, into the plasma chamber via an 8-waveguide grill which is phased so that propagating waves are radiated ($\phi = 105^{o}$, $n_{\parallel}$ spectrum peaked at ~1.8). The plasma current is sustained during this time essentially entirely by the RF as evidenced by the concomitant drop of the loop voltage U_L to zero in Fig. 2. A further consequence is the increase in $\beta_p + l_i/2$ (calculated using the equilibrium vertical field) of ~ +0.079 between t = 0.9 and 1.45 secs. (OH, LH phases). The simultaneous change in $\beta_{p\perp}$ (not shown; measured by a diamagnetic loop) of ~+0.065 means, under the assumption that $\beta_p = \beta_{p\perp}$, that $\Delta l_i = l_i(LH) - l_i(OH) = +0.028$; i.e., the magnetic measurements taken alone indicate a peaking of the current profile. The electron temperature T_e is measured (perpendicular to $\vec{B}_T$) by a quasi-stationary Nd-YAG Thomson scattering system at 16 points over the vertical diameter. The two T_e traces at r = 0, 19 cm of Fig. 2 illustrate that electrons are heated preferentially in the plasma center, since the $T_e(r=19)$ curve remains constant at ~0.7 keV, whereas $T_e(0)$ goes from ~1.4 to ~2 keV.

Li-Beam Results: In Fig. 2 the experimentally measured θ_p - smoothed with a 10 ms time window - is given as a function of time for five radial points, the radius r being measured from the center of the outermost flux surface. The base lines for the $\theta_p(t)$ curves are determined by fitting the $\theta_p(r,t=0.9$ sec) profile to the value computed at the plasma edge (r=a) using the Shafranov formula for $B_p(a)$ in conjunction with $\theta_p(a) = \tan^{-1} B_p(a)/B_T$.

In the OH phase, although the I_p flat top is attained at 0.5 sec, the $\theta_p(t)$ signals for $r \leq 28.6$ cm do not reach their plateau values until t ~ 0.75sec, which is in qualitative agreement with the time behavior of $\beta_p + l_i/2$. Further, at t = 0.5 sec, $\theta_p(r = 10.7, 19.5)$ have only ~70 % of their plateau values, with this percentage increasing to ~90 % for r = 37 cm. The failure of $\theta_p(37)$ to follow I_p closely is presently not understood, since it would be expected for θ_p near the separatrix to be relatively free of thermal or skin effects. The very weak dependence of θ (-1.9) on I_p indicates that this point is near the magnetic axis.

Switching on the RF produces a significant change in θ_p only for θ_p (10.7), which exhibits a continuous decrease until towards the end of the pulse.

Discussion: Radial profiles of $\theta_p(r)$ for the OH and LH phases are presented in Figs. 3a and 3b respectively, along with the associated (cylindrical)

safety factor q curves. The vertical error bar of ± 3 mrad is approximately the peak-to-peak noise level of $\theta_p(t)$. For comparison, the θ_p and q profiles derived from $T_e(r)$ assuming Spitzer resistivity (current density $\propto T_e^{3/2}$) and a constant electric field over the radius are also plotted.

In Fig. 3a, although there are not enough measuring points to adequately describe q for r < 10.7 cm, the $q_{exp}(0)$ value of ~1.1 is consistent with the observed absence of sawteeth during the discharge. Moreover, there is surprisingly good agreement between the experimentally determined θ_p^{exp}, and the calculated $\theta_p^{Spitzer}$. The corresponding values of l_i are 1.18 and 1.16, respectively.

For the LH phase (Fig. 3b) there is a large difference between θ_p^{exp} and $\theta_p^{Spitzer}$ for r < 20 cm, which is reflected in l_i values of 1.15 and 1.23. $q_{exp}(0)$ is ~1.25 in contrast to a Spitzer q(0) of ~0.55. Comparison of $\theta_p^{exp}(LH)$ to $\theta_p^{exp}(OH)$ (note that for $\theta_p^{exp}(OH)$ only the points are plotted in Fig. 3b, and not a curve) reveals that current drive causes a flattening of the current distribution within r ~ 20 cm, leading to $\Delta l_i = -0.03$. This is in strong contrast to the behavior anticipated, were the current profile to continue to follow $T_e^{3/2}$, which peaks during the RF pulse due to strong central heating.

The disparity between the magnetically derived $\Delta l_i = +0.028$ (using $\beta_p = \beta_{p\perp}$) and the measured $\Delta l_i = -0.03$ suggests that $\beta_p(LH) > \beta_{p\perp}(LH)$, which would be compatible with an enhanced energy deposition by RF in the parallel electron component. In view of the uncertainties associated with the magnetic data for the small changes discussed here, no attempt at quantitatively estimating this additional parallel energy is made.

In summary, the Li-beam Zeeman diagnostic has been brought into operation on ASDEX and found - for the OH phase - to produce results in close agreement with those predicted by assuming Spitzer resistivity. During LH current drive, the current density profile appears to decouple from the bulk thermal electron population, as demonstrated by the decrease in $\theta_p^{exp}(r < 20)$ accompanied by an increase in T_e in the plasma center region.

References:

/1/ K. McCormick, M. Kick and J. Olivain, Proc., 8th Eur. Cont. on Controlled Fusion and Plasma Physics (Prague, 1977) 140

/2/ K. McCormick, et al., J. Nucl. Mater. 121 (1984) 48.

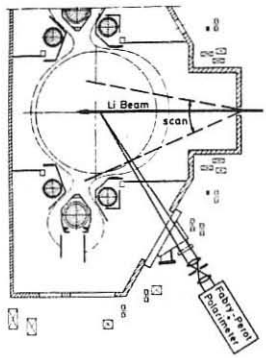

Fig. 1: Diagnostic setup on ASDEX.

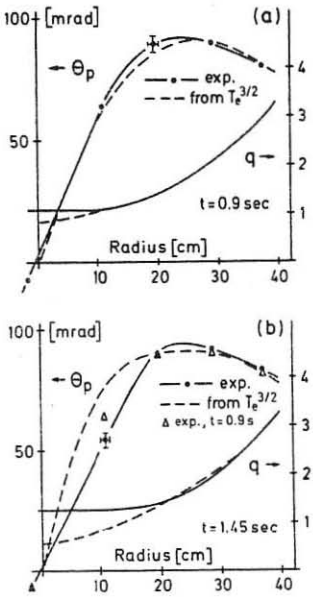

Fig. 3: Comparison between the directly measured Θ_p profiles and $\Theta_p(r)$ derived from $T_e^{3/2}$, and their associated q values for: (a) the OH phase, t = 0.9 sec, (b) during current drive, t = 1.45 sec, including the measured Θ_p (OH) points.

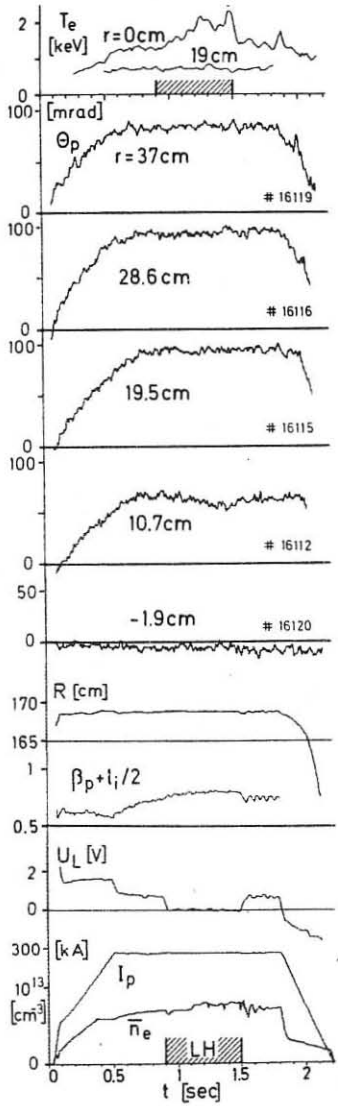

Fig. 2: Time behavior of T_e (r=0,19cm), Θ_p at five radial points, R, $\beta_p + l_i/2$, U_L, I_p and $\bar{n}_e$.

CHARGE EXCHANGE SPECTROSCOPY ON DITE

B.P. Duval*, S.J. Fielding, N.C. Hawkes, J. Hugill and N.J. Peacock

Culham Laboratory, Abingdon, Oxon, OX14 3DB, U.K.
(UKAEA/Euratom Fusion Association)

*Attached Clarendon Laboratory, Oxford

Introduction

Measurements of line emission from hydrogen-like carbon and oxygen impurity ions in DITE tokamak have been made during neutral injection of 25 keV hydrogen atoms at beam powers of up to 2 MW. Observations of the spectrum from oxygen encompass the Lyman series in the XUV region (1s-np, $n < 9$) and $\Delta n = 1$ transitions in the VUV and visible regions, and for carbon the visible and VUV. By investigating the possible decay routes of the impurity ions after excitation by the beam atoms it is intended to get a clear understanding of the effect of the plasma environment on the charge exchange (C/X) processes. At 25 keV the C/X process is nearly resonant, populating levels $n = \sim 2 - \sim 5$ and electron dipole decay selection rules dictate that the decay is via the $\Delta n = 1$ "Y-rast" route ($1 = n-1 \rightarrow n-2$) [1].

DITE [2] has 4 injection beam lines, each delivering up to 0.5 MW of 25 keV hydrogen neutrals. All observations were carried out at approximately the same toroidal position, intersecting one neutral beam (B-line). The X-ray and VUV spectrometers are described in an earlier paper [3]. The visible spectrometer was a conventional 1 m monochromator fitted with a photomultiplier (time response ~ 1 μs) coupled to the torus via a rotating mirror to give spatial profiles of visible light emission (scan time 2 ms).

Results

Fig.1 shows the time evolution of the $n = 3-2$ transition (102 Å) in OVIII. The signal closely follows the injector current with rise and fall times (< 0.1 ms) much faster than the OVII and OVIII ionisation times (0.4 ms, 1 ms respectively). Thus the rapid enhancement is identified as being solely due to prompt C/X excitation. Using theoretical C/X cross-sections [4,5] and a cascade model for the radiative decay, the oxygen concentration is estimated from the absolute signal intensity to be $\sim 1-2\%$ of the electron density, n_e. Similar results were obtained for the behaviour of the $n = 4-3$ (293 Å) transition in OVIII and low $\Delta n = 1$ transitions in CVI. No rapid enhancement was observed with the injection of any beam not directly crossing the spectrometer line of sight.

In contrast, the Lyman X-ray and visible transitions show no such time signature. For the X-ray observations (Fig.2) the slow enhancement in intensity did not depend significantly on which beam was injected into the plasma, and is explained by changes in the ionisation balance due to the C/X recombination process. Since the electrons decaying from n = 3-2 also decay through n = 2-1, some of the X-ray intensity must be due to prompt C/X since there is negligible direct C/X population into n = 2. With a better viewing position, and lower beam attenuation it is estimated that the $\Delta n = 1$ Lyman alpha (19 Å) transition will show a resolvable component from prompt C/X decay.

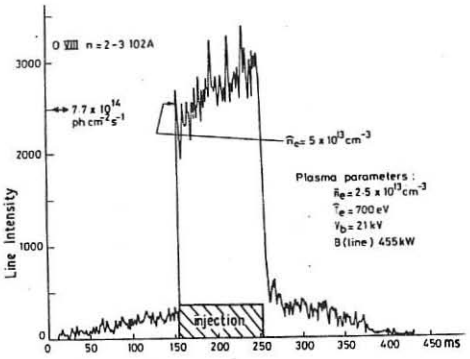

Fig.1 Time history of the line emission from OVIII, n = 3 → 2 (102 Å).

Spatially resolved measurements have been made of the n = 8-7 transition (5291 Å) in CVI. This line, like all other visible lines observed, does not show a clear C/X signature. However, from the difference between spatial scans with and without B-line injection, a C/X excited feature is revealed (Fig.3). This component of the line emission is clearly asymmetric about the toroidal axis (1.17 m) and localised to the beam-illuminated volume of the plasma.

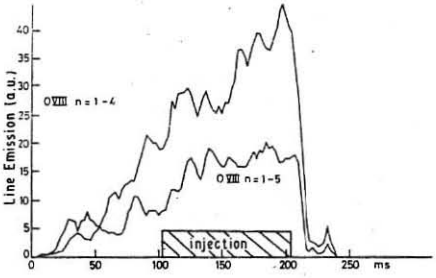

Fig.2 Time history of the line emission from OVIII, n = 4 → 1 (15.18 Å) and OVIII, n = 5 → 1 (14.82 Å).

The remaining line emission after subtraction of the C/X component can be Abel inverted to give the radial distribution shown in Fig.4. This is radiation not directly attributable to beam neutrals, and is ~ 10 times the magnitude of the C/X component. Neither C/X excitation of CVII by thermal neutrals nor radiative recombination excitation has a sufficiently large cross-section to account for the absolute intensity of the signal. Electron impact excitation of CVI ions, assuming a coronal

charge state distribution, would give rise to a signal of the wrong spatial form (Fig.4), and yields a carbon concentration which is at least a factor of 10 too large. However, if C/X recombination of CVII on thermal hydrogen ions is included in the ionisation balance, then electron impact excitation of CVI gives rise to a model line emission similar in spatial form and magnitude to the experimental data (Fig.4). The effect of impurity diffusion has been neglected in these computations, but it can be shown to be inadequate to explain the spatial form of the line emission.

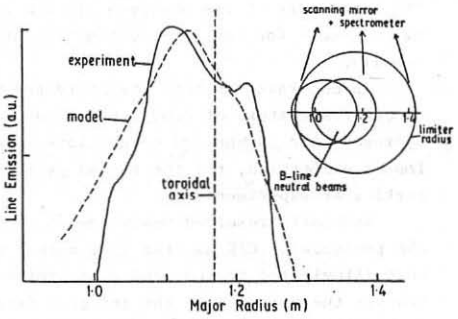

Fig.3 Spatially resolved line emission from CVI, n = 8 → 7 (5291 Å) obtained from the difference between scans with and without 0.4 MW of B-line injection. The insert shows the spectrometer viewing geometry.

The carbon concentration and charge state distribution estimated above have also been used to model the prompt C/X component, using the beam geometry defined in Fig.3, together with a reasonable approximation for the beam power profile (Gaussians of 1/e width 0.1 m, centred at 1.01 m and 1.11 m) and a beam attenuation code. The result is shown in Fig.3, where good agreement is obtained with the spatial form of the experimental data and the amplitudes agree to within a factor of 2.

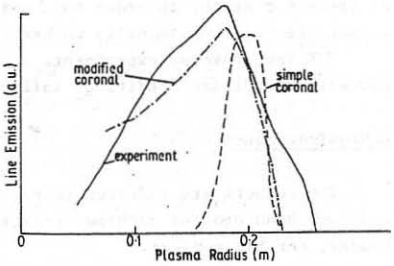

Fig.4 Spatially resolved line emission from CVI, n = 8 → 7 (5291 Å) after subtraction of the prompt C/X component of Fig.3, and Abel inversion.

Conclusions

The clear signature of prompt C/X excited radiation, a large increase in line emission with a rise-time determined by the injector switch-on time, has been observed in DITE for carbon and oxygen impurity lines in the spectral region 100-650 Å. These lines originate from

energy levels in the impurity ions most efficiently populated by C/X. The amplitudes of the observed signals are in agreement with model calculations for impurity concentrations of ~ 1% of the electron density.

In contrast, in both the X-ray and visible regions of the spectrum no clear signature of prompt C/X is observed. Line emission from hydrogen-like carbon and oxygen ions appears to be dominated by electron impact excitation, for the plasma parameters and viewing geometry of these particular experiments.

Spatially resolved measurements in the visible region have identified the presence of C/X excited line emission from carbon, localised to the beam illuminated region, and of approximately the expected magnitude. However the majority of the emission from these carbon lines comes from the peripheral regions of the plasma, outside the beam illuminated volume, and is interpreted as being due to electron impact excitation of CVI, whose distribution is determined by a modified coronal equilibrium, where recombination of CVII is dominated by C/X on thermal neutral hydrogen. Similar behaviour of visible carbon lines has been recently observed in ASDEX [6].

In the interpretation of the carbon visible line emission data, for both the C/X and electron impact excited components, it has been necessary to include statistical redistribution in the population of the sublevels of the n = 8 state, in order to obtain signals consistent with a reasonable value of impurity concentration (~ 1% n_e).

C/X spectroscopy experiments are continuing on DITE, with viewing geometry and plasma conditions tailored to optimise C/X line intensities.

Acknowledgements

The authors are indebted to the DITE operating team under R.W. Storey and R.E. Bradford for machine operation and to Dr J.W.M. Paul, the Group Leader, for his support.

References

[1] R.J. Fonck, D.S. Darrow et al. Phys. Rev. A.29, No.6 (1984).
[2] J.W.M. Paul in Plasma Physics and Controlled Nuclear Fusion Research. (Proc. 6th Int.Conf. Berchtesgaden,1976), IAEA, Vienna, Vol.2 (1977).
[3] B.P. Duval, et al. Nucl Inst. Method. July Issue (1985).
[4] R.K. Janev, et al. J.Phys. Chem. Ref. Data 12, No.4, 829 (1983).
[5] R.C. Isler, Proc. HIA Conf. Nucl. Inst. Method, 89 in press (1985).
[6] P. Carolan, et al. (1985). See proceedings of this conference.

INJECTED IMPURITY TRANSPORT STUDY IN THE T-10 PLASMA BY X-RAY AND VUV-SPECTROSCOPY

A.A.Bagdasarov, V.I.Bugarya, N.L.Vasin, V.A.Vershkov, A.N.Vertiporokh, V.V.Volkov, N.M.Gegechkory, S.A.Grashin, S.L.Efremov, V.A.Zhuravlev, I.V.Ivanov, N.V.Ivanov, Yu.Yu.Karzhavin, P.E.Kovrov, V.A.Krupin, A.B.Pimenov, V.F.Strizhov, V.M.Trukhin
I.V.Kurchatov Institute of Atomic Energy, Moscow, USSR

S.M.Egorov, B.V.Kuteev, V.Yu.Sergeev
M.I.Kalinin Polytechnical Institute, Leningrad, USSR

V.P.Belik
A.F.Ioffe Physico-Technical Institute, Academy of Sciences, USSR

On T-10 the transport study of impurities and main plasma have been continued in deuterium discharges with high $\bar{n}_e$ and low I_p, where either anomalously low impurity confinement (S-regimes) or enhanced one (B-regimes) had been observed [1].

A VUV-monochromator (150-1200 Å), scanning across the plasma column, has been added to a set of diagnostics [1].

Behaviour of injected impurities - K (pellet) and Ar - has been studied. Recycling of K has been evaluated experimentally to be less than 5-10%. The profiles of the main plasma parameters in both regimes (I_p=200kA, B_t=25kG) are given in Fig.1. In B-regime (solid line) the values of $T_e(0)$ and $T_i(0)$ are higher, the shape of $n_e(r)$ is more peaked, and $Z_{eff}(0)$ is 2-3 times higher. The influx of the main impurity, C, remains unchanged. The behaviour of the K^{+17} concentration in both regimes at r=0 and at r=8cm is shown in Fig.2 by points. In spite of the large difference in the dynamics of $n_{K^{+17}}$ in both regimes, the magnitudes and profiles are similar (Fig.3) at the decay phase (moments t_1 and t_2 in Fig.2). The line intensity of Ar^{+15} (352 Å) in a region X~a/2 (Fig.4) reaches a stationary level for 60 ms in both regimes (Ar injection at the 610thms). This time rises up to 200 ms in B-regime for a central zone, where this emission is determined by the recombination of Ar^{+16}. The amplitude and radius of saw-tooth oscillations r_s are the same in both regimes. A sharp rise of the confinement time for K and Ar ions at r=0 in B-regimes indicates the presence of enhanced confinement zone ($r \lesssim a/2$), which determines the integral impurity confinement

time τ_z.

The results of numerical simulation (using the impurity fluxes as $\Gamma_z = D_z \nabla n_z + V_z^p n_z$) are shown in Figs.2-4 by solid and dashed lines. The distributions of impurity diffusion coefficient D_z and pinching velocity V_z^p used in the numerical calculations for both regimes, are given in Fig.5. For the zone of enhanced confinement in B-regime the impurity transport parameters ($D_z \sim 500 \frac{cm^2}{s}$ and $V_z^p \sim 60 \frac{cm}{s}$) and ion thermal diffusivity χ_i are close to the neoclassical values. An experimental value of electron thermal diffusivity is anomalously low ($\chi_e \sim 600 \frac{cm^2}{s}$) for similar discharges [2]. However, the measurements of D_e and V_e^p for the main plasma by the technique, described in [1], in B-regime give $D_e = 4000 \frac{cm^2}{s}$, $V_e^p = 150 \frac{cm}{s}$ for $r \sim 10\text{-}15$ cm (Fig.6).

In S-regime, $D_z \sim 4000 \frac{cm^2}{s}$ and $V_z^p \sim 300 \frac{cm}{s}$, which exceed D_e and V_e^p of the main plasma almost five times. The use of D_e and V_e^p in the model [1] provides τ_z greater than the experimental one by an order of magnitude. Note that the experimental value $\chi_i \sim 10^4 \frac{cm^2}{s}$ corresponds to such high D_z in this regime.

Values of τ_z for the K^{+17} ion vs the parameter $\bar{n}_e/I_p^2$ in B- and S-regimes are shown in Fig.7. Three separate branches are differed by the intrinsic impurity (C, O) level. The branches "bb" and "b" belong to B-regime, the branch "s", to S-regime. Strong dependence of τ_z on the plasma contamination by impurities C and O is observed in the experiment. In order to find out whether τ_z depends on Z_{eff} [3] or on the radiation losses P^{rad}, neon (impurity with a higher radiation efficiency than that for C or O) has been added to S discharge to increase the bolometric signal up to its "bb" level. In spite of the fact that $Z_{eff}(0)$ has remained to be low (~ 2), the values of τ_z have increased up to their "bb" levels. This fact and inverse dependences τ_z and Z_{eff} on $\bar{n}_e/I_p^2$ (at a good correlation between P^{rad} and $\bar{n}_e/I_p$) can lead to consideration that the impurity radiation losses at the plasma periphery are the main factor affecting so high τ_z values.

A current rise up to 350-400 kA in B-discharges eliminates the zone of enhanced confinement, and τ_z decreases up to 30-50 ms. Large influx of Ne (close to disruption of discharges) is not capable of increasing τ_z. The role of saw-teeth does not seem to be decisive, as the considerable changes of the $r_s = 0\text{-}10$

cm, (with a variation of B_t) in "bb" discharges do not affect τ_z (Fig.7). It can be caused by a wider zone of enhanced confinement in "bb" discharges. The discharges with anomalously high τ_z ~250 ms (Fig.7) and 2-4 times greater impurity densities n_{k+17} have been obtained at high $\bar{n}_e/I_p^2$. Such discharges are observed at $q(a) \geq 3.5$ only and characterized by a decreased value of $T_e(0)$, peaked profiles of $n_e(r)$ and low levels of saw-teeth and m=2 mode. Transition into these regimes becomes difficult when plasma is more pure. Thus, for a branch "s", such a transition was observed at the "predisruptive" values of $\bar{n}_e/I_p^2$ only.

A rise of the impurity influx, a rise of $\bar{n}_e$ and a decrease of I_p, and a rise of $q(a)$, when $q(a) \geq 3-4$ can be considered as common reasons for decreasing the current density j at the plasma periphery. This is in agreement with the measured decrease of T_e at the plasma periphery and with an increase of the radius of localization for the m=2 mode at the transition from S- to B-regime. As a result of such changes, a rise of the gradient of j and the shear, that can be responsible for a decrease of the anomalous impurity transport, can take place within the region $r \leq a/2$. A gradual accumulation of impurities within a zone with $r \leq a/2$ makes j(r) more flat at the plasma column centre and supresses saw-teeth (the very effect is observed in B discharges with $q(a) \geq 3.5$). As a result, an additional accumulation of impurities takes place, and a rectangular profile of j(r) is formed. Both last effects are proportional to $Z_{eff}(0)$ [3] and capable to increase τ_z in the discharges with a narrow zone of enhanced confinement.

Thus, all transport coefficients are greatly different in B- and S-regimes. Heat and impurity transport approaches neoclassical values in central zone for B-regime. An appearance of this enhanced confinement zone may be connected with observed transformation of the current profile due to cooling of plasma periphery.

[1] A.A.Bagdasarov et al. X Int. Conf. on Plasma Phys. and Contr. Nucl. Fus., London, 1984, IAEA-CN-44/A-III-4.

[2] A.B.Berlizov et al. IX Int. Conf. on Plasma Phys. and Contr. Nucl. Fus., Baltimora, 1982, IAEA.

[3] E.S.Marmar et al. Nucl. Fus., 22 (1982) 1567.

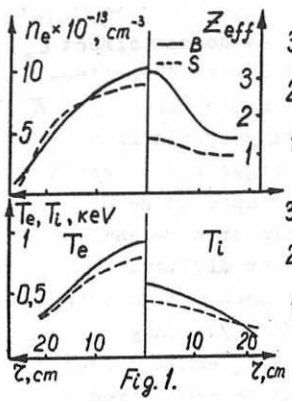

Fig. 1.

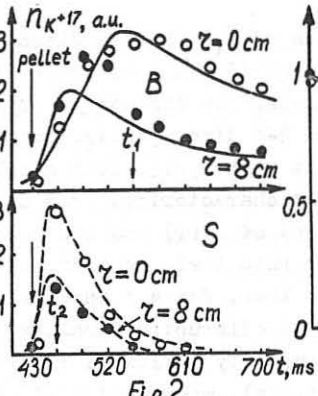

Fig. 2.

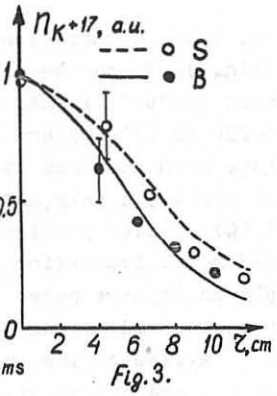

Fig. 3.

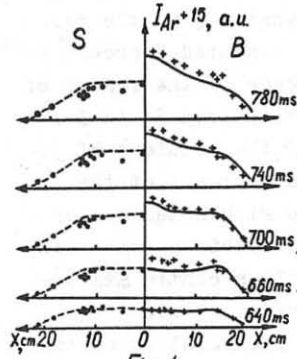

Fig. 4.

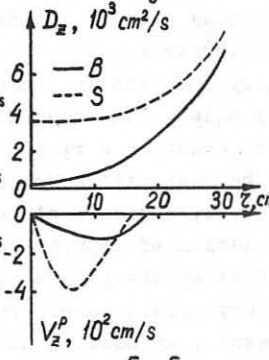

Fig. 5.

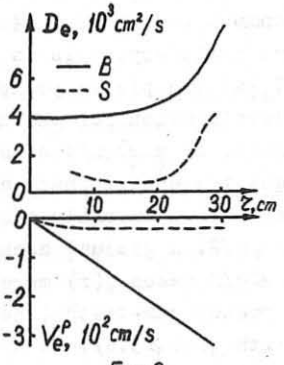

Fig. 6.

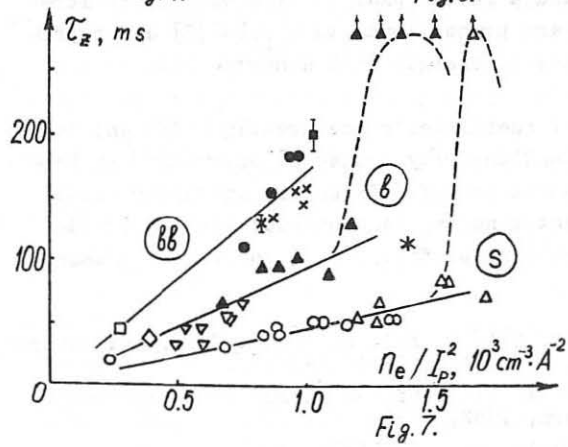

Fig. 7.

	I, кА	B_T, кГ	q(a)	$Z_{eff}(0)$
×	185	14	2,7	4 ÷ 5
●	185	20	3,8	
■	185	31	6,0	
□	360	31	3,0	
◇	230	16	1,9	3,5
✱	125	20	4,5	2 ÷ 3
▲	160	20	3,5	
▽	230	20	2,4	
△	160	22	4,1	1,2 ÷ 1,7
○	180	22	3,7	

PRELIMINARY MEASUREMENT OF THE BURN UP OF THE FUSION-PRODUCED TRITONS IN FT

E. Bittoni*, A. Fubini+, M. Haegi, E. Pedretti□, M. Pillon, A. Vannucci†

Associazione EURATOM-ENEA sulla Fusione, Centro Ricerche Energia Frascati, C.P. 65 - 00044 Frascati, Rome, Italy

ABSTRACT

The confinement of the 1 MeV triton produced by the (D,D) reaction in the FT Tokamak operated at a high magnetic field and in pure ohmic heating, is evaluated using threshold activation techniques.

The fundamental requirement for an ignition fusion device, is that the charged particles produced by the fusion reactions should be well confined in order to allow them the time to transfer their energy to the plasma and in this way to overcome the plasma energy losses. This paper is intended to give experimental information on triton slowdown and confinement processes. In deuterium plasma discharges, 1.01 MeV tritons are produced by the reaction D(d,p)T with a nearly equal probability as that for the 2.45 MeV neutrons.

According to the classic theory, the fast triton born on a contained trajectory, is slowed down to the plasma thermal energy mainly by the electron drag. The (D,T) cross section after thermalization is at least 10^3 times smaller than that during deceleration. Thus, because the deceleration time and the thermalized confinement time of the triton are comparable, the contribution of the cold tritons to the production of the 14 MeV neutrons is of the order of 10^{-3}. It can also be shown that the contribution to the 14 MeV neutrons, due to the bombardment of the deuterium adsorbed on the wall by the fast tritons escaping from the plasma, is negligible. Thus, the (D,T)/(D,D) neutron emission ratio can be related to the confinement factor f_c of the fast tritons during deceleration by:

$$N_{14\ MeV}/N_{2.5\ MeV} = f_c \langle P_{DT} \rangle$$

where $\langle P_{DT} \rangle$ is the average probability of fusion for the confined triton in the deuterium plasma. The classic confinement factor f_c is calculated as a function of the plasma current, assuming the current density profiles related to the 3/2 power of the measured electron temperature profiles, and taking into account the finite Larmor radius.

* ENEA, Centro di Calcolo, Via Mazzini, 40124 Bologna, Italy
+ ENEA, Dip. TIB, Div. Fisica Applicata, CRE Frascati, 00044 Frascati, Rome, Italy
□ ENEA, Dip. TIB, CRE Casaccia, Rome, Italy
† ENEA Student

Theoretical investigations [1] and numerical calculations, see Ref. in [2], have shown that the magnetic ripple leads to rapid loss of the fast particles which have banana-like trajectories. This is specially true for the FT device where the fast tritons on these trajectories are lost after a few hundred orbits, leaving only a few percent of their energy in the plasma [3]. In our calculation of f_c we have therefore considered all the banana orbits as unconfined.

The computation of $\langle P_{DT} \rangle$ is done by using a bidimensional Monte Carlo code [4]. Such a procedure is necessary because the fast triton have large radial excursions which require the integration of the density and the electron temperature along all the possible trajectories, weighted by the triton source function.

The measurement of the 2.5 and 14 MeV neutron flux has been made by the activation of respectively Indium and Copper samples [5]. While the measurement of the 2.5 MeV neutron flux is straightforward, that for the 14 MeV is more delicate because of the low flux ($\sim 10^3$ cm^{-2} sec^{-1}) of these neutrons in the high background of the 2.5 MeV neutrons and possible hard X-rays. The reaction $^{63}Cu(n,2n)\ ^{62}Cu$, which has a threshold of 10.9 MeV, has a fairly high cross section of 0.44 barn at 14 MeV, which permits, using samples of several hundreds grams, measurements on a single FT discharge. The ^{62}Cu decays into ^{62}Ni with a half-life of 9.73 min. by emitting a β^+. The subsequent 511 keV gamma rays have been measured by a high purity germanium spectrometer. Account has been taken of the activation by epithermal neutrons of ^{64}Cu emitting also a β^+ with a half life of 12.71 hours.

No hard X-rays are measured at high density discharges ($\bar{n}_e \gtrsim 10^{14}$ cm^{-3}) used for activation measurements. However, in order to confirm that the $^{63}Cu(\gamma,n)^{62}Cu$ does not contribute to the 14 MeV neutron counting, we have exposed for a few tens of shots aluminium samples to identical FT discharges, as the ^{24}Na produced by the $^{27}Al(n,\alpha)^{24}Na$ reaction cannot be obtained by photonuclear reaction. The impurity content of our samples has been checked by thermal neutron activation and has been found better than 10^{-5} for interfering elements.

The self absorption coefficient of the γ rays in the sample has been measured [5] and calculated [6] for our particular sample-germanium geometry.

The alteration of the 14 MeV neutron flux over the finite dimension of the sample, inserted into the massive structure of the FT toroidal coils and cryostat, has been calculated by means of the ANISN code in cylindrical geometry. Calculations, still under way, by means of a tridimensional numerical code will permit the study of toroidal geometry and non axisymmetric features like the windows and the samples themselves. As a first approximation we have found that the dominant effect is the attenuation of the 14 MeV neutron flux across the material, while the scattered neutrons due to the high threshold of the $^{63}Cu(n,2n)^{62}Cu$ have little effect.

Up to now we have analysed by means of activation about 20 shots with copper and 20 shots with aluminium. The magnetic field was $B_\phi = 80$ kG, the mean density about $\bar{n}_e \cong 2\times10^{14}$ cm^{-3}, and the plasma current $I_p = 450$-570 kA, no additional heating was used. We are convinced that, in order to obtain a fair understanding about the influence of the plasma parameters on the triton confinement, it is necessary to proceed to the calculation of the $N_{14}/N_{2.5}$ classic value using the particular measured profiles and the absolute value

for T_i, T_e and n_e for every single group of shots, and to monitor the MHD activities. These operations are currently underway; however, from preliminary calculations based on standard profiles for FT, the following assessments can be made:

- In our operating conditions, the hard X-rays did not alterate the copper activation measurement.

- The (D,D) cross section around 1 keV varies as: $\sigma_{DD} \propto T_i^6$. This dependence on T_i amplifies considerably the uncertainties on the 2.45 MeV neutron production and on the correlated 1.01 MeV triton source function.

- The preliminary results are:

I_A	$N_{14}/N_{2,5}$ measured	$N_{14}/N_{2,5}$ classic theory
450 kA	$1.8\pm1.1 \times 10^{-3}$	2.3×10^{-3}
510 kA	$2.7\pm1.6 \times 10^{-3}$	2.6×10^{-3}
570 kA	$2.9\pm1.7 \times 10^{-3}$	2.9×10^{-3}

It can be seen that within the standard total error, which has been calculated to be ± 60%, there is a substantial agreement between the measured and the classic ratio.

- The calculated cumulative probability of (D,T) reaction for the confined triton is plotted as a function of its energy in Fig. 1. Using this relation the previous statement can be expressed in the following way: the average triton, born on a confined orbit, is decelerated in the FT plasma to at least 300 keV, possibly down to full thermalization.

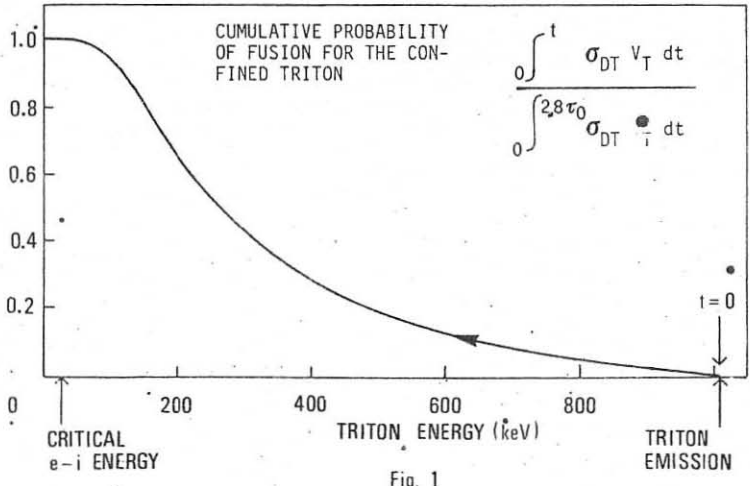

Fig. 1

- Keeping in mind the relatively large experimental uncertainties, the above result could be compared with that of PLT [7], operated at a magnetic field of 32 kG, heated by neutral injection and where the tritons were mainly produced by collision of the deuterium beam on the deuterium plasma. Using in the same way the relation of Fig. 1, their results, with identical absolute errors could be expressed as follows: the initially confined average triton is slowed down to 500-150 keV before being lost from the PLT plasma.

REFERENCES

[1] A.H. Boozer, Phys. Fluids 23 (1980) 238
R.J. Goldston and H.H. Towner, PPPL Report 16/37 (1980)
[2] E. Bittoni, M. Haegi, F. Santini, S.E. Segre, Nucl. Fusion 22 (1982) 1675
[3] E. Bittoni, M. Haegi, Proc. of 2nd Joint Grenoble-Varenna Int. Symp., Como (1980) vol. II , 1089
[4] E. Bittoni, M. Haegi, ENEA Report (1985) to be published
[5] A. Fubini, M. Haegi, M. Pillon, A. Vannucci, ENEA Report (1985) to be published
[6] B. Arcipiani, E. Pedretti, Atomkernenergie 35 (1980) 210
[7] W.W. Heidbrink, R.E. Chrien, J.D. Strachan, Nucl. Fusion 23 (1983) 917.

A TWELVE - CHANNEL GRATING POLYCHROMATOR FOR MEASUREMENT OF ELECTRON TEMPERATURE IN JET

B J D Tubbing*, E Barbian*, D J Campbell+, C A J Hugenholtz*, R M Niestadt*, Th Oyevaar*, H W Piekaar*

JET Joint Undertaking, Abingdon, Oxon, OX14 3EA
* on attachment from FOM Instituut voor Plasmafysica, 'Rijnhuizen', Nieuwegein, The Netherlands

1. INTRODUCTION

A twelve-channel grating spectrometer for electron cyclotron emission measurements has recently been installed and put into operation at JET. The first measurements have yielded a wealth of information in particular about sawtooth behaviour.

2. THE SPECTROMETER

The spectrometer measures the electron-temperature as a function of time at twelve radial positions along the line of sight of the antenna, using the second harmonic, extraordinary mode e.c.e. emission. It is a grating instrument of the conical diffraction type with twelve exit channels. A prototype is described in [1]. Rotation of the grating allows for shifting of the set of twelve radial positions on a shot to shot basis. The typical spatial range is of the order of 70 cm for a particular grating angle.

Plasma radiation is collected by one of the horizontal JET ECE antennae and transmitted to the spectrometer via an oversized (S band, 34x72 mm) waveguide system approximately 40 m long [2]. The spatial resolution perpendicular to the line of sight is about ±8 cm. The spatial resolution along the line of sight is about ±3 cm as determined by the spectrometers resolving power ($\sim$60).

The grating is used in first order. The spectrometer is also sensitive however to frequencies diffracted in higher grating orders. These frequencies are rejected by low-pass filters, consisting of unidirectional gratings mounted on S band waveguide bends. Two such filters in cascade provide sufficient suppression in the stop band [3].

A radiation chopper with a 95% duty-cycle is incorporated in the feeding waveguide in order to enable signals to be corrected for drift of the amplifiers.

The diffracted radiation in the exit waveguides of the spectrometer is detected by InSb detectors at liquid helium temperature. The electronic signals are amplified, a low-pass filter is applied and the signals are digitised. The maximum electronic bandwidth is 200 kHz, the maximun sampling rate is 1 MHz and there is 16 k words of memory installed for each channel. The noise of the system when expressed in plasma temperature, is about 30 eV r.m.s. at 10 kHz electrical bandwidth.

Calibration of the system is carried out by cross-calibration with the standard JET ECE Michelson interferometer [4].

3. A MAJOR DISRUPTION

The spectrometer has proved to be capable of following the rapid evolution of the temperature profile during major disruptions. An example is provided in Figure 1. The sampling time is 200 μs in this case. The centre of the discharge is approximately at 3.01 m and the limiter is at 4.174 m. Eleven channels cover the range of radii from 2.95 to 3.86 m. In the first stage of the disruption, the central temperature collapses. The effect of the rapid loss of confinement propagates inwards with a velocity of about 1 m/ms. The collapse of the central temperature is shown by the solid lines in the figure. From these successive profiles, it can be seen that the central temperature drops from about 1.7 keV to about 0.9 keV and that over 75% of the minor radius the temperature becomes nearly constant. Outside a radius of 3.7 m, the temperature increases by about 0.2 keV or 30%. Prior to this first phase of the disruption, the central region had a temperature gradient of about 2 keV/m, whereas at the end of this phase the gradient is almost zero. The collapse takes about 600 μs. For the next 400 μs the profile is stationary, existing in a second plateau stage. Then within 200 μs the central region reheats, while maintaining the flat profile; the temperature rises from 0.9 keV to 1.2 keV. This can be seen by comparing the profiles of Figure 1 (broken and solid lines). Finally, a second collapse occurs as shown by the broken line in Figure 1. Within 400 μs nearly all thermal energy is lost. The plasma current was observed to start decaying from this time onwards, going from 2.2 MA to zero in about 40 ms.

4. SAWTOOTH BEHAVIOUR IN THE INNER REGION

Sawtooth activity in JET, which is discussed in detail in [5], has been studied with the grating spectrometer. Figure 2 shows the temperature evolution at 5 different positions during part of a pulse. 2 MW of ICRH is applied at this time. The current centre is at 3.02 m major radius. The toroidal field is 2.0 T. The short straight lines in the traces are not real, but are interpolations across chopper spikes. The noise on the signals is the noise of the amplifiers and detectors.

The figure shows a common phenomenon: two normal and one partial sawtooth (47.45 sec) collapse, the partial one being followed by an oscillation which is probably m=1. The inversion radius at 0.5 m can clearly be distinguished. Comparing sawtooth amplitudes at different positions shows that the inversion radii for the normal and the partial sawteeth are equal to within 4 cm. Sometimes it was observed on other discharges that the partial sawtooth collapse affects the plasma only at major radii $R > R_o$. At radii $R < R_o$ the collapse is not seen and the temperature is affected only by the subsequent oscillation. The oscillation has it's largest amplitude at $R - R_o = 0.26$ m, well inside the inversion radius. It is remarkable that the oscillation on the inversion radius is very small: i.e. about 50 eV (2.5%).

5. SAWTOOTH BEHAVIOUR IN THE OUTER REGION

The sawtooth collapse perturbs the temperature profile by flattening it up to the so-called mixing radius, on a timescale of the order of 0.1 ms. On a much slower timescale the perturbation relaxes by a diffusive process with a heat conduction coefficient $\chi_e(r)$ [6] [7]. For radii outside the mixing radius this effect manifests itself as a heat-pulse propagating outwards. The delay time $t_D(r)$ between the collapse of the sawtooth and the time of the maximum of this pulse for a given minor radius r yields information about $\chi_e(r)$.

Figure 3 shows the temperature evolution for 5 different radial positions. These traces are obtained from the data by averaging over 10 sawteeth,

synchronising them by triggering on their fast edges. In addition digital filters are applied to reduce the noise, especially in the outer channels. The traces are recorded during application of 1.5 MW ICRH and similar traces were obtained for the ohmic phase.

The $t_p(r)$ values for both cases are shown in Figure 54. It is clear that the pulse propagation velocity is very similar for both cases, although the sawtooth amplitude is greatly enhanced by the ICRH. (Central ΔT_e = 500 eV for the ohmic phase and ΔT_e = 1500 eV during ICRH.) It is observed that the mixing radius shifts slightly outwards during the ICRH.

In order to derive χ_e from the measured $t_p(r)$ values a simulation program is used that numerically solves the diffusion equation, in a cylindrical geometry, for given density and initial temperature perturbation profiles. It is assumed that $\chi_e(r)$ is inversely proportional to the density profile n(r).

$$\chi(r)_e = \frac{\chi_{eo}\, n_o}{n(r)} \qquad n(r) = n_o (1 - 0.99(\tfrac{r}{a})^2)^{\frac{1}{2}}$$

where χ_{eo} and n_o are central values of χ_e and n. The line drawn in Figure 5.2 shows the $t_p(r)$ for a simulation with $\chi_{eo} = 1.5\ m^2/s$ $n_o = 2.9 \times 10^{19} m^{-3}$ and mixing radius $r_m = 0.66$ m.

Figure 5 shows the corresponding $\chi_e(r)$ in the relevant region of the plasma. The χ_e value is significantly larger than χ_e values obtained from transport codes [8].

ACKNOWLEDGEMENTS

We are indebted to Dr T E Stringer for his co-operation in the heat-pulse studies, to Dr D A Boyd for his analysis of the major disruption data, and to Dr D V Bartlett, Dr A E Costley and Dr S E Kissel for sharing the calibration data from the Michelson interferometer.

REFERENCES

[1] R M J Sillen, H W Piekaar, Th Oyevaar and W Werner, A F.I.R Grating Polychromator Using Conical Diffration as a Diagnostic Tool for E.C.E Plasma Measurements. Infrared Physics, 24, 6, 511 (1984).

[2] E A M Baker et al., Proc. 4th Int. Workshop on ECE and ECRH. Frascati (1984)

[3] E Barbian, D J Campbell and G de Zwart, to be published.

[4] A E Costley et al., Paper 186 this conference.

[5] D J Campbell et. al., Paper 182, this conference.

[6] G Jahns et al., Internal Disruptions in Tokamaks, Nucl. Fusion 18, 5 (1970).

[7] T Bell et al., Measurements of χ_e in ISX-B Beam-Heated Discharges by Heat-Pulse Propagation, Nucl. Fusion, 24, 8 (1984).

[8] M Brusati, J G Cordey, Paper 189, this conference

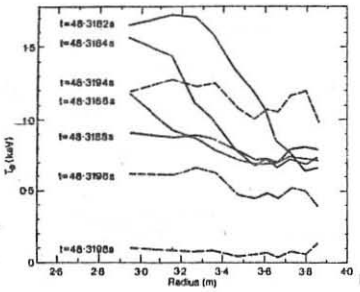

Fig. 1 Profiles during a disruption.

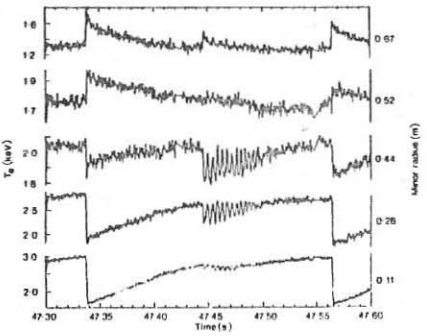

Fig. 2 Sawteeth inside the mixing radius

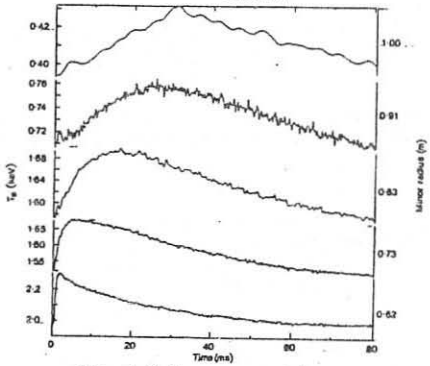

Fig. 3 Pulse propagation

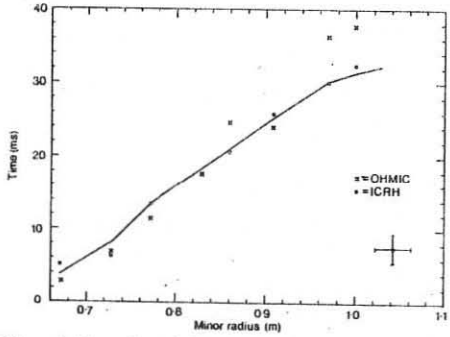

Fig. 4 The time delay values

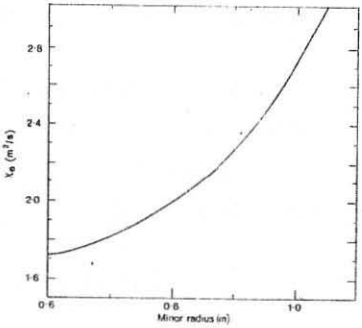

Fig. 5 Heat conductivity ceofficient

ANALYSIS OF NEUTRAL PARTICLES IN JET

S Corti, G Bracco*, M Brusati, A Gondhalekar, G Grosso+
F Hendriks°, S Segre*, V Zanza*

JET Joint Undertaking, Abingdon, Oxon OX14 3EA, UK

* on attachment from CENTRO RICERCHE ENERGIA, Euratom-ENEA Association Frascati, Italy
\+ on attachment from ISTITUTO FISICA DEL PLASMA, Euratom-CNR Association Milan, Italy
° Euratom Fellow

This paper describes features related with the analysis of neutral particles and the ion temperature in JET as measured with a passive Neutral Particle Analyser. Ten energies for two species (Hydrogen and Deuterium) are detected simultaneously so that the two energy spectra can be obtained at any time of a discharge.

An analysis code taking into account all the relevant processes, including recombination, is available. This code, using the measured neutral particle fluxes, the measured T_e and n_e profiles, taking the edge neutral density as a free parameter and assuming a T_i profile shape, allows to compute the neutral density profile and the maximum ion temperature along the line of sight. The ion and the electron densities are assumed equal throughout the calculation. The analyser used, one out of a final array of five, views a horizontal chord in the the equatorial plane of the torus at an angle of 10° with respect to a major radius /1/.

In Figure 1 typical results for a deuterium pulse are shown. The fitting of the experimental points in 1a shows a maximum ion temperature of 2.5 keV. The contribution to the neutral density due to recombination is shown in 1b while 1c and 1d show the radial location, along the line of sight, of the detected source functions. The importance of the recombination in obtaining information closer to the centre of the discharge should be noted.

Using the source function for each energy and the corresponding absolute measured flux it is in principle possible to determine an average ion temperature over the halfwidth of the source, obtaining thus ten points on the ion temperature profile. This has been done for a I=4 MA, B_T=3.4 T discharge and the resulting ion temperature profile is compared in Figure 2 with the one

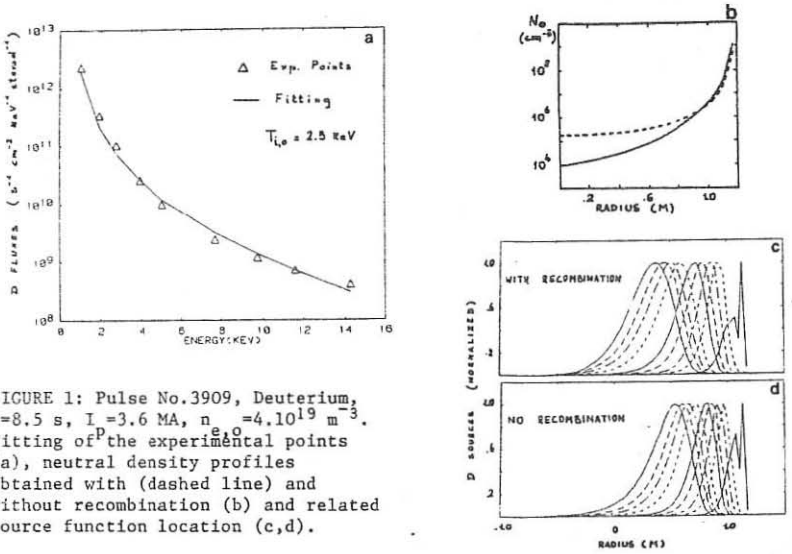

FIGURE 1: Pulse No.3909, Deuterium, t=8.5 s, I_p=3.6 MA, $n_{e,o}$=4.10^{19} m^{-3}. Fitting of the experimental points (a), neutral density profiles obtained with (dashed line) and without recombination (b) and related source function location (c,d).

obtained from transport analysis assuming an anomaly factor of 5 with respect to neoclassical ion conductivity. The horizontal error represents the halfwidth of the source function. The discrepancy between the profiles obtained in these two different ways requires further investigation, as it may be due either to departure of ion transport from the neoclassical functional dependence or to overestimating the electron temperature at the plasma edge.

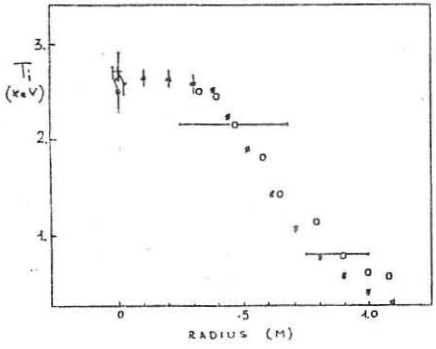

FIGURE 2: Comparison of T_i profiles from transport (*) and from local neutral sources (o) calculations. Experimental points are also shown: (+) Neutron Measurements, (•) NPA.

Some JET deuterium discharges following CH_4 carbonization, have comparable H and D concentrations due to H influx from the walls. Preliminary studies of the time behaviour of the ratio H/(H+D) at different plasma depths indicate that hydrogen reaches a stationary concentration profile in about 1s, possibly with signs of accumulation at the plasma centre.

At relatively high values of n/I, transient phenomena with strong poloidal asymmetry of the edge density and radiation (Marfes) have been observed /2/. During these events a marked enhancement of neutral particle fluxes at all energies is observed (Figure 3a).

Although the NPA is looking at the volume where marfes occur, it cannot detect particles from that zone (as shown in Figure 1c). The fact that the enhancement is observed on all channels is indicative of a modification of the neutral density beyond the zone directly affected by marfes. This is supported by a concomitant increase of the H_α measured along a vertical chord through the centre of the machine (Figure 3b).

The NPA diagnostic has been used extensively during ICRH (Ion Cyclotron Resonance Heating) studies both with He^3 and with H minority in deuterium using various types of antennae configurations (monopole, dipole, quadrupole). As an example, Figure 4a shows the ion temperature (obtained with a simple linear fitting of the measured spectra for $E \leq 2\ T_i$) when RF power is coupled through two antennae (1 MW on a quadrupole antenna between 6 and 8 seconds and 1.5 MW on a monopole between 7 and 9 seconds) for hydrogen minority heating.

Figures 4b and 4c show deuterium and hydrogen spectra.

It can be seen that the shape of the D spectra remains unchanged below 6 keV indicating that RF heating affects mainly the central ion temperature, causing probably a peaking of the profile.

The hydrogen spectra, having been corrected for background, show the appearance of an energetic tail above 7 keV with a slope corresponding to about 20 keV.

REFERENCES

/1/ G Bracco, S Corti, V Zanza et al - 'First Results from JET Neutral Particle Analyser' - JET Report JET-IR(84)04.

/2/ J O'Rourke et al - 'Poloidally Asymmetric Edge Phenomena in JET' - this conference.

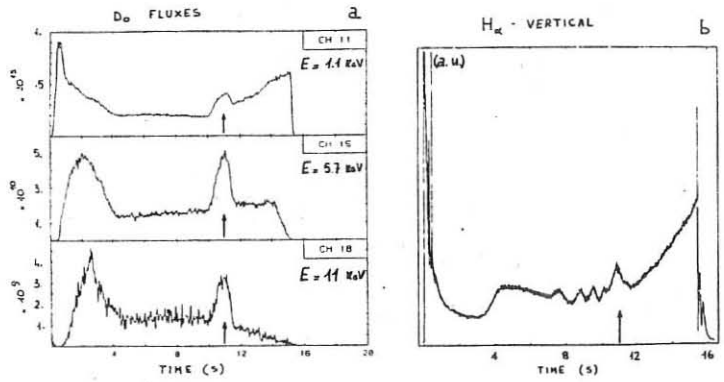

FIGURE 3: Neutral fluxes (a) and vertical H_α (b) measured during a plasma discharge showing the appearance of a Marfe around 11 s (pulse number 3428).

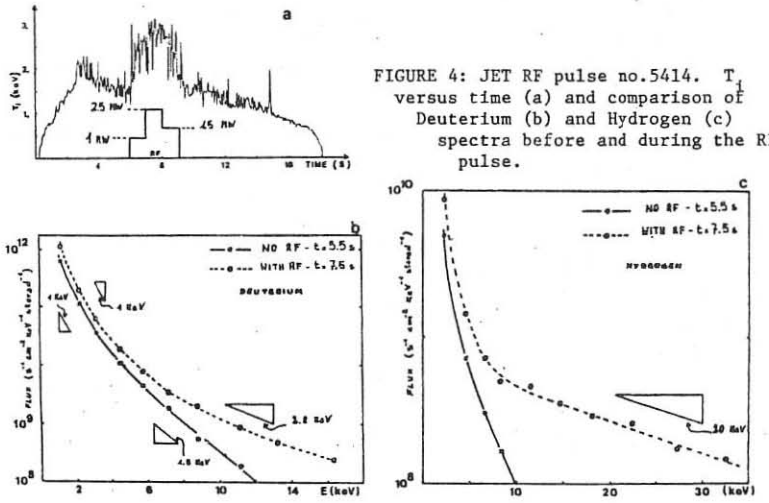

FIGURE 4: JET RF pulse no.5414. T_i versus time (a) and comparison of Deuterium (b) and Hydrogen (c) spectra before and during the RF pulse.

ION TEMPERATURE AND DENSITY MEASUREMENTS IN JET USING NEUTRON DIAGNOSTICS

O N Jarvis, G Gorini, M Hone, J Källne, V Merlo, G Sadler, P van Belle
JET Joint Undertaking, Abingdon, Oxon, OX14 3EA, UK

Introduction Two neutron diagnostic systems are in use on JET for determining the ion density and temperature for deuterium plasmas. The first comprises three sets of fission counters [1], each mounted on a separate magnet limb on the horizontal midplane of the machine, to measure the instantaneous neutron emission from the plasma. The second is a ^{3}He ionization chamber spectrometer[2] located in the well-shielded Roof Laboratory about 20 m above the midplane of the machine and viewing the plasma through a collimator (set in the floor of the Roof Laboratory) aligned with a vertical diagnostic port in the vacuum vessel.

The neutron emission is related to the volume integral over the plasma of the product $n_d^2 \langle\sigma v\rangle$, where n_d is the deuterium ion density and $\langle\sigma v\rangle$ is the plasma reactivity. For a Maxwellian plasma the reactivity varies with temperature as T_i^α, with $\alpha \sim 4.0$ for $T_i = 3$ keV. Thus, assuming that the spatial profiles of density and temperature for electrons, which are measured routinely, apply also to ions with only the scale factors differing, then the neutron emission measurements provide an estimate for the product of central parameters $\hat{n}_d^2 \hat{T}_i^\alpha$.

The ^{3}He chamber possesses excellent energy resolution (42 keV at 2.5 MeV) and is thus able to measure the thermal broadening of the thermonuclear neutrons, which should exhibit a nearly Gaussian energy spectrum [3] with fwhm = $82.5\sqrt{T_i}$, with T_i in keV. The primary result from the spectrometer is therefore a value for $\hat{T}_i$ which can be used in conjunction with the neutron emission measurements to determine $\hat{n}_d$.

Neutron Emission Each set of fission counters comprises a ^{235}U fission chamber and moderator, engineered to give a flat energy response, and a ^{238}U fission chamber which has a neutron energy threshold at about 1 MeV. Both counters operate simultaneously in pulse counting and current modes to provide coverage for neutron emission intensities from 10^{10} to 10^{22} neutrons/sec. Present yields from deuterium plasmas rarely exceed 10^{14} neutrons/sec.

The ^{235}U fission counters have been calibrated with both a ^{252}Cf radioisotope neutron source and a pulsed 14 MeV neutron tube by placing them, separately, at a large number of positions within the vacuum vessel. The vessel is effectively enclosed within the copper toroidal field coils and an iron support structure in which the voids are filled with high density borated concrete. This copper/iron/concrete blanket is about 40 cm thick and effectively inhibits neutron leakage from the vacuum vessel except through the various penetrations. Because of this blanket, it is clear that those neutron which reach a fission counter do so only after having scattered a few times from the material surrounding the vacuum vessel before leaving through the large diagnostic port closest to the counter and scattering in or near the port closure plate into the direction of the counter. We have found that the counter response as a function of source position is remarkably insensitive to

neutron energy and that the positional dependence is easy to model in terms of the toroidal co-ordinates. With the aid of this model, the total neutron emission from a deuterium plasma of known dimensions can be determined from the fission counter response to an absolute accuracy of ± 10%.

Figure 1 shows the time dependence of the central ion temperature $\hat{T}_i$ for discharge number 3050 as determined from the neutron emission measurements. The analysis incorporates two significant assumptions: (i) that the d-d fusion reactivity is an accurately known function of temperature, and (ii) that the deuterium ion density is half the electron density.

Neutron spectrometry In principle, analysis of the data obtained with the ^{3}He spectrometer is particularly straightforward: the neutron energy spectrum is assumed to be Gaussian in shape [3] so the measured detector response function is convoluted with a Gaussian neutron energy spectrum appropriate to a trial temperature T_i and a maximum likelihood optimization of T_i is performed to obtain the best fit with the measured pulse-height spectrum. In practice, entirely satisfactory fits have been obtained, but only after very careful measurements of the detector response function were made. It should be noted that it proved not to be acceptable to adopt the response function reported in the literature [4] for a ^{3}He spectrometer with identical specification to ours. The source of difficulty is not the determination of the fwhm of the full-energy peak in the counter (from the n + ^{3}He → p + t + 0.764 MeV reaction) but rather that of determining the precise shape of the apparently insignificant low-energy tail due to the wall-effect in the ionization chamber. The relative magnitude of this wall effect increases with neutron energy. It was also found that appreciably better counting statistics were required to determine T_i to a given accuracy than was predicted [5] on the basis of a simple Gaussian-shaped response function. This prediction connects the required accuracy ($\Delta T_i/T_i$), the spectrometer resolution (R), the width of the neutron spectrum (W) and the necessary total count in the measured neutron energy spectrum through

$$N = 2\,[T_i/\Delta T_i]^2\,[1 + R^2/W^2]^2$$

where it is assumed that R is known precisely and that both spectrometer response and neutron spectrum are Gaussian in form. For R = 42 keV, W = 143 keV (T_i = 3 keV), we should be able to ignore R^2/W^2 and to deduce that a 10% measurement requires only 200 counts. In practice we find we need at least 600 counts. This finding is also attributed, at least partially, to the low energy wall effect tail in the spectrometer resolution function; taking moments about the centroid of that portion of the repsonse function contributing to the measurement so as to obtain an "equivalent Gaussian" shows that R is comparable with W. Thus, we have found that the spectrometer wall effect is already very important and can be expected to become more so as ion temperatures rise and neutral beam heating with deuterium beams is introduced.

Of the many plasma discharges now analysed, one sequence of 3 MA discharges (numbers 3047 to 3052) is outstanding because of their very long plasma duration, with flat-tops extending over 8 seconds (see Figure 1). These discharges used ohmic heating only and the plasmas were formed under identical conditions. It has been observed that in a sequence of repeated discharges the total neutron emission per discharge has been reproduced to ± 1%, implying a very high order of reproducibility in the machine control elements. The

individual discharges in the selected sequence were analysed and flat-top temperatures in the range 2-3 keV have been deduced, but with only ± 20% accuracy. A considerably improved accuracy is achieved by summing the individual spectra to obtain 1000 counts in the peak, as shown in Fig. 2.

Analysis of the summed spectrum gives a time averaged ion temperature of 2.73 ± .18 keV. This result refers to the line-integrated neutron emission along a vertical chord and can be converted to the required central temperature by multiplying with the factor 1.08 ± .02 obtained from numerical studies on plasmas with density and temperature profiles similar to those on which the measurements were made. The short period temperature variations, such as those due to sawteeth, are not significant for ohmically heated plasmas as can be seen from the detailed time dependence in T_i measured by the fission counters (see Fig. 1).

Density fraction The mean value for the central ion temperature of 2.95 ± .21 keV obtained from the spectrometer is to be compared with the mean temperature of 2.64 keV derived from the fission counters on the assumption of a density ratio $\hat{n}_d/\hat{n}_e = 0.5$. Adoption of the spectrometer value permits the density fraction to be refined to $\hat{n}_d/\hat{n}_e = 0.47 \pm .08$ for the discharge sequence studied. The uncertainty quoted here is determined primarily by the temperature measurement but includes contributions for the absolute calibration of the fission counters and for the uncertainty in the basic d-d fusion cross-sections.

References

1. M T Swinhoe and O N Jarvis, Nucl.Instrum.Meth. in Physics Research 221 (1984) 460.

2. Jordan Valley, Emek Hayarden, Israel. Spectrometer type FNS-1.

3. H Brysk, Plasma Physics 15 (1973) 611.

4. W A Fisher, S H Chen, D Gwinn and R R Parker, Nucl.Instrum.Meth. in Physics Research 219 (1984) 179.

5. O N Jarvis in Diagnostics for Fusion Reactor Conditions, EUR 8351-EN, Vol. 1 (1984) 353

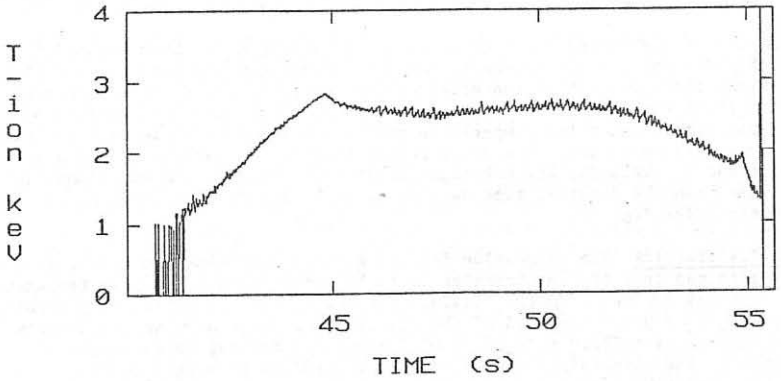

Figure 1 The central ion temperature determined from the neutron emission measurements for discharge number 3050, with a toroidal field of 3.4T and a plasma current of 3.6MA. The plasma is formed at time 40 seconds.

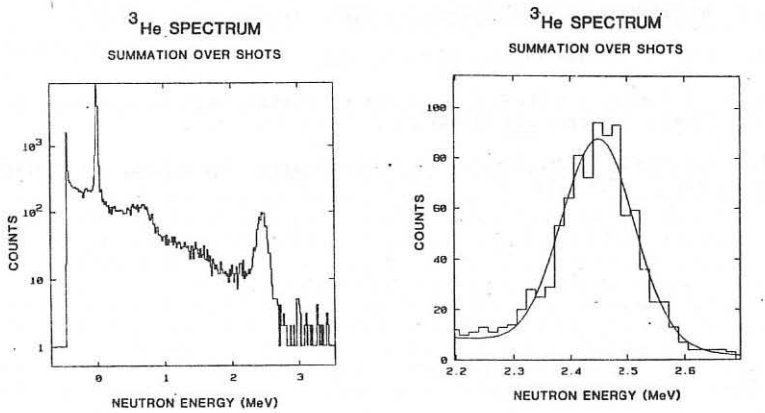

Figure 2 The pulse-height spectrum obtained with the ^{3}He ionization chamber for the sum of six discharges (numbers 3447 - 3052). Discharge numbers 3447-3052. Note that the thermal neutron peak (left picture) appears at a pulse-height equivalent to 764 keV. The excellent fit to the 2.5 MeV thermonuclear peak (right picture) substantiates the claim for a Maxwellian ion energy distribution.

ELECTRON TEMPERATURE MEASUREMENT ON JET

A E Costley, E.A.M. Baker†, M. Brusati, D V Bartlett, D J Campbell
G Decker+, M Gadeberg*, R D Gill, E Källne, S Kissel, P Nielsen,
D Pasini# and R Prentice

JET JOINT UNDERTAKING, ABINGDON, OXON, OX14 3EA, UK.

* On attachment from the Risø National Laboratory, Denmark
\+ Permanent address: University of Düsseldorf, West Germany
\# Permanent address: University of British Columbia, Vancouver, Canada.
† Permanent address: National Physical Laboratory, U.K.

1. INTRODUCTION

The electron temperature on JET is measured routinely using two independent diagnostics: a single point Thomson scattering system and a spatial scan electron cyclotron emission (ECE) system. In addition, some measurements of the electron temperature have been made with a preliminary soft x-ray pulse height analysis (PHA) system.

In this paper these three diagnostics are described. Results obtained with the diagnostics are presented and compared, and some examples of the use of the measurements in the study of plasma physics phenomena on JET are given.

2. THE SINGLE POINT THOMSON SCATTERING SYSTEM

The Thomson scattering system has the conventional 90° scattering geometry/1/. Light from a ruby laser (λ = 694.3 nm) illuminates the plasma along a vertical chord. The laser has two operating modes: a single pulse mode giving one 20J pulse during a JET discharge and a multipulse mode with lower energy and repetition rates up to 1Hz. The scattering volume (2 mm diameter by 50 mm length) can be chosen to at be one of seven discrete locations in the equatorial plane of the torus. The scattered light is collected by an array of large mirrors arranged as a double Newtonian telescope, and is transmitted to the spectrometer with F number of 10. The spectrometer consists of three prism spectrometers in series, the first two constituting a notch filter for the ruby wavelength. The scattered light is detected with ten photomultipliers fitted with GaAs photocathodes.

The laser and spectrometer are located outside the biological shield so the diagnostic will be compatible with the active phase of JET operation. Alignment systems employing HeNe laser beams keep the diagnostic aligned to the torus. The entire diagnostic is operated automatically through the JET computer system (CODAS).

Temperatures in the range 0.5 - 6 keV have been measured. The sensitivity of the diagnostic allows measurements at densities as low as $3 \times 10^{18} m^{-3}$. The temperatures are obtained by a conventional non-linear least squares fit of the data to tabulated theoretical spectra. The tabulated spectra are calculated using a complete relativistic analysis. The accuracy in the measurement is typically ± 10%.

3. THE SPATIAL SCAN ECE SYSTEM

The spatial scan ECE system has been designed to measure the spatial dependence of the electron temperature in the poloidal cross-section/2/. It is a flexible system; for example it has two operating modes. In the first, the spatial dependence of the electron temperature is measured along ten different chords in the plasma with moderate time resolution ($\lesssim$ 15 ms). In the second, the time dependence of the temperature at specific locations in the plasma is measured with a high time resolution ($\lesssim$ 20 μs).

The first element in the system is an antenna array mounted inside the torus vacuum vessel which views the plasma along 10 different chords in the poloidal cross-section. The radiation is transmitted through crystal quartz vacuum windows and then along oversized aluminium waveguide (S-band) to the measurement area outside the biological protection wall, where the spectrometer and detection systems are located. These consist of four low resolution rapid-scan Michelson interferometers, one high resolution rapid-scan Michelson interferometer and six rapid-scan Fabry Perot interferometers all fitted with liquid helium cooled indium antimonide detectors. The system is operated through CODAS and is compatible with the active phase of JET operation.

One of the 10 planned channels of the system has been operated routinely since the autumn of 1983. It is fitted with a low resolution Michelson interferometer and this is used to measure the ECE radiation emitted in the range 70 GHz $< f <$ 350 GHz. (typically $f_{ce} < f < 4f_{ce}$). The line of sight is 13 cm below the mid-plane and parallel to the major radius. From the emission measured around $f = 2f_{ce}$ the spatial profile of the electron temperature is obtained using the established frequency to space, and intensity to temperature transformations. In the analysis full account is taken of the internal magnetic fields in the plasma due to the plasma current. The spatial resolution in the measurement is $\sim$ 15 cm and the time resolution is $\sim$ 15 ms, and typically 320 temperature profiles are acquired on a JET discharge. The system is calibrated using large area black-body sources. The uncertainties in the measurement are such that the relative shape of the profile is obtained to an accuracy of ± 10% and the absolute level to ± 20%.

In addition measurements have been made of the time dependence of the temperature at specific locations in the plasma with one of the Fabry-Perot interferometers. In this case the time resolution is $\lesssim$ 20 μs and the sensitivity is such that temperature fluctuations of $<$ 5 eV can be measured. Further measurements of the time dependence of the electron temperature at specific radial locations have also been made with a 12 channel grating polychromator/3/.

4. THE SOFT X-RAY PHA SYSTEM

The preliminary PHA system measures the spectrum of the soft x-ray emission in the energy range 4 - 30 keV. The line of sight is defined by a

set of apertures and is along the major radius. The detector is a mercuric iodide detector/4/ and the plasma is viewed through a 200 μm beryllium window. A composite absorber of beryllium, aluminium and air is used to reduce the sensitivity of the system at low energies and to allow observation of the helium like nickel lines and the continuum emission at higher energies. Both the metal concentration and the electron temperature are extracted from the measurements. Since the measurement is a line of sight integral the analysis takes account of the radial variations of both the plasma temperature and density. The central electron temperature deduced from this analysis is found to be insensitive to profile effects. The accuracy of the measurement is typically ± 10%.

In recent experiments the diagnostic has been optimized for the determination of plasma impurity concentration by employing absorbers which restrict the energy range to 4 - 12 keV. Under these conditions the diagnostic is not so well suited to the measurement of the electron temperature and so the uncertainty in the determination of this parameter is higher.

5. RESULTS AND COMPARISONS

Temperatures measured by the Thomson scattering and ECE systems have been compared over a wide range of plasma conditions; 1 MA < I_p < 5 MA, 2T < B_T < 3.4T, 1 x $10^{19}m^{-3}$ < $n_e(o)$ < 5 x $10^{19}m^{-3}$, 0.5 keV < $T_e(o)$ < 6 keV, 2 < Z_{eff} < 5. For the bulk of the data (> 90%) agreement is obtained to within the stated uncertainties; frequently the measurements agree to within 10%. A more limited comparison has been made including results from the preliminary PHA system. Again agreement to within the stated uncertainties is usually obtained. The main conclusions to be drawn from these agreements are (i) that the diagnostics are operating correctly and (ii) that the plasma is thermal. This latter conclusion arises from the fact that these diagnostics are sensitive to different parts of the electron velocity distribution. Examples of the comparisons are shown in Figures 1 and 2.

Extensive use of the measurements has been made in studies of many plasma physics phenomena on JET: for example, measurements have been made of the time and space dependence of the electron temperature during sawteeth oscillations, Figure 3. Note the flattening of the profile after the disruption and the lack of precursor MHD oscillations/5/. Other phenomena studied with the diagnostics include energy confinement, MHD activity and disruptions. The measured temperature profiles (provided by the ECE system) have also been used in plasma optimization studies: it has been observed that the T_e profile shape at early times is important to subsequent plasma behaviour. An example is shown in Figure 4. More details of the comparisons, and further examples of the use of the measurements will be given in the poster presentation.

REFERENCES

/1/ P Nielsen, Proc, Course on Diagnostics for Fusion Reactor Conditions, Vol 1, Pages 225 - 259, Varenna, 1982.
/2/ A E Costley et al. Proc. 4th International Workshop on Electron Cyclotron Emission and Electron Cyclotron Resonance Heating, pages 1 - 10, Rome, 1984.
/3/ B J D Tubbing et al. paper 142, this conference.
/4/ A J Dabrowski et al. IEEE Trans. Nucl. Science NS-28, 536, 1981.
/5/ See also paper by D J Campbell et al, paper 182, this conference.

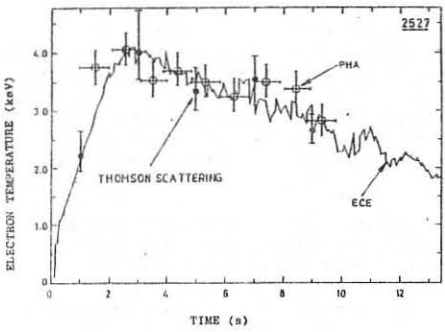

Fig 1: Electron temperature measured by Thomson scattering, ECE and soft x-ray (PHA) on a typical JET pulse, B_T=2.8T, I_p=2.2MA.

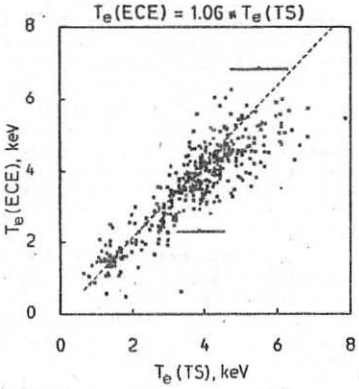

Fig 2: Electron temperature measured by ECE versus electron temperature measured by Thomson scattering. 415 independent measurements are included in the comparison. The slope of the best fit line is $T_e(ECE)=1.06T_e(TS)$.

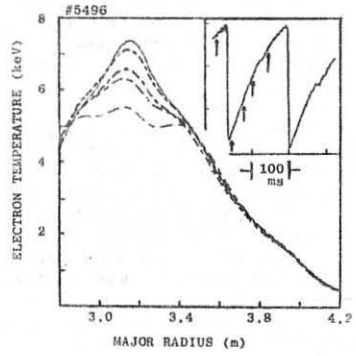

Fig 3: The time dependence of the electron temperature profile during a single sawtooth oscillation on a JET discharge (3.4T, 3.9MA) with 4MW of ICRH. Inset shows the time dependence of the electron temperature at R=3.1m. Measurements made with the ECE system.

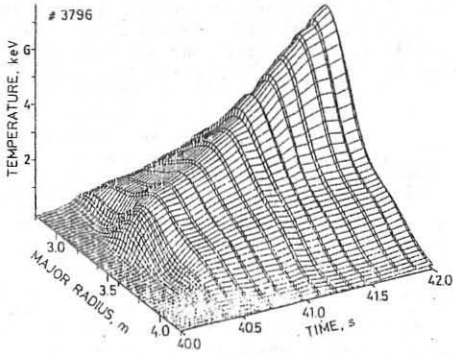

Fig 4: The time dependence of the electron temperature during the early phase of a standard JET discharge, B_T=3.4T, I_p=2.8MA.

Neutron Production during Deuterium Injection in Deuterium Plasmas in ASDEX

K. Hübner, R. Bätzner, H. Hinsch
Institut für Angewandte Physik, Universität Heidelberg, D-6900 Heidelberg

H. Rapp, H. Wurz and A. Eberhagen, O. Gehre, V. Mertens
ASDEX Team+, Neutral Injection Team+
Max-Planck-Institut für Plasmaphysik, EURATOM Association, D-8046 Garching

Measurements of neutron energy spectra and time dependent neutron rate are presented. They agree well with the results of a simple classical deuteron relaxation model. Determination of the plasma deuterium temperature seems possible from the energy spectra as well as from the neutron rate.

Energy spectra: The energy of neutrons produced by reactions between fast injected deuterons and plasma deuterons is shifted from 2.45 MeV towards higher energies for forward emission and towards lower energies for backward emission. On ASDEX with 45 keV injection energy, neutron energies of 2.70 and 2.24 MeV, respectively, are expected (broken lines in Fig. 1). Spectral measurements by means of nuclear emulsions along tangential lines of sight in the co- and counter direction of the injection beam show shifted peaks with maxima at 2.65 and 2.32 MeV (Fig. 1). Due to integration over a finite space angle of neutron emission the measured spectra cannot show the maximum energy shift.

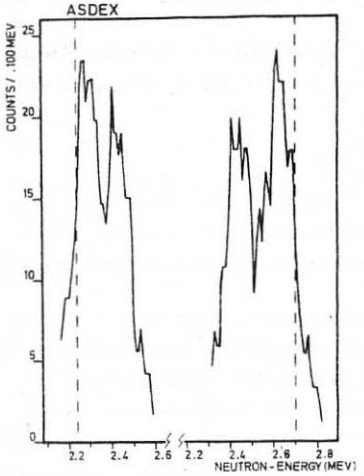

Fig.1 Neutron energy spectra

The 2.45 MeV line is caused by thermonuclear reactions in the bulk plasma. From its FWHM we obtain a deuteron temperature of 1.9 keV integrated over the observation volume and the injection time. Using the measured electron density profile $n_e(r)/n_e(0)$ for deuteron density and temperature profiles, $n_D(r)/n_D(0)$ and $T_i(r)/T_i(0)$, we calculate $T_i(0) = 2.0$ keV. This value is about 10 % above the

+The members of the ASDEX and NI teams are presented in the paper of F. Wagner et al., this conference.

central electron temperature. The error of the ion temperature determination is at least 20 % in this case.

Neutron rate, classical relaxation model: The energy of an injected fast deuteron with initial energy W_o decreases in a plasma as $W(t) = W_o \exp(-t/\tau_w)$. τ_w is the energy relaxation time. The number of neutrons Y_D produced by one fast deuteron during its relaxation is given by

$$Y_D = \int_o^{\tau} n_D \sigma \sqrt{\frac{2W}{m}}\, dt = (n_D/n) \int_{W(\tau)}^{W_o} \sqrt{\frac{2}{mW}}\, \sigma\, n\tau_w\, dW.$$

Here m is the mass of a deuteron, n the electron density, n_D the deuteron density and τ the confinement time of the fast deuteron. Due to the strong decrease of cross-section σ with energy the neutron production occurs mainly during the first half of the energy relaxation time, i.e. approximately 15 ms in ASDEX. For our plasma data the energy relaxation parameter $n\tau_W$ depends only on the electron temperature. Hence the neutron production by injected deuterons depends essentially on the electron temperature of the target plasma. On the other hand the cross-section σ is a function of the ion temperature. For temperatures in the region of some keV it may be approximated by

$$\sigma(W,T_i) = \sigma(W,0) + 1.16 \times 10^{-28}\sqrt{W} \cdot T_i \text{ barn (W and } T_i \text{ in keV)}.$$

The neutron rate is calculated by integrating the product of Y_D times the deposition profile for fast deuterons over the plasma volume.

Due to the lack of a direct measurement we assume that the deuteron density is a constant fraction of the electron density, the total neutron rate may then be expressed by

$$Q(T_i) = (n_D/n)\, Q_{inj}(0) \cdot (1+\gamma T_i) + (n_D/n)^2 Q_{therm}(T_i)$$

where Q_{therm} is the thermonuclear rate of the bulk plasma. Here both, Q_{inj} and Q_{therm} are calculated with the electron density profile. Using this relation one can get the bulk ion temperature from the total neutron rate.

Neutron rate, experimental results: The neutron rate measurements have been carried out with BF_3- and U-238 counters which have been calibrated independently by a Pu-238-B neutron source /1/ and by the nuclear emulsion technique. Figure 2 shows the measured neutron rate for the discharges to which the energy spectra of Fig.1 belong. The discharges are of the H-type /2/ with I_p = 420 kA, $\bar{n}_e = 4.9 \cdot 10^{13}$ cm^{-3} and P_{inj} = 1.85 MW at 45 kV. In Fig. 2 $Q(T_i)$ is calculated using the measured profiles of the electron temperature (ECE) and electron density (HCN interferometer), Z_{eff} as derived

from the loop voltage (for determination of n_D/n) and the deuteron depositon profile as computed by the FREYA code /3/. T_i was determined by the neutron spectra. The shadowed areas indicate the measurement errors. For $Q(T_i)$ they are mainly caused by some uncertainties in n_D/n. Within the limits of the errors all values agree well, thus indicating classical relaxation for the fast deuterons as assumed in the model.

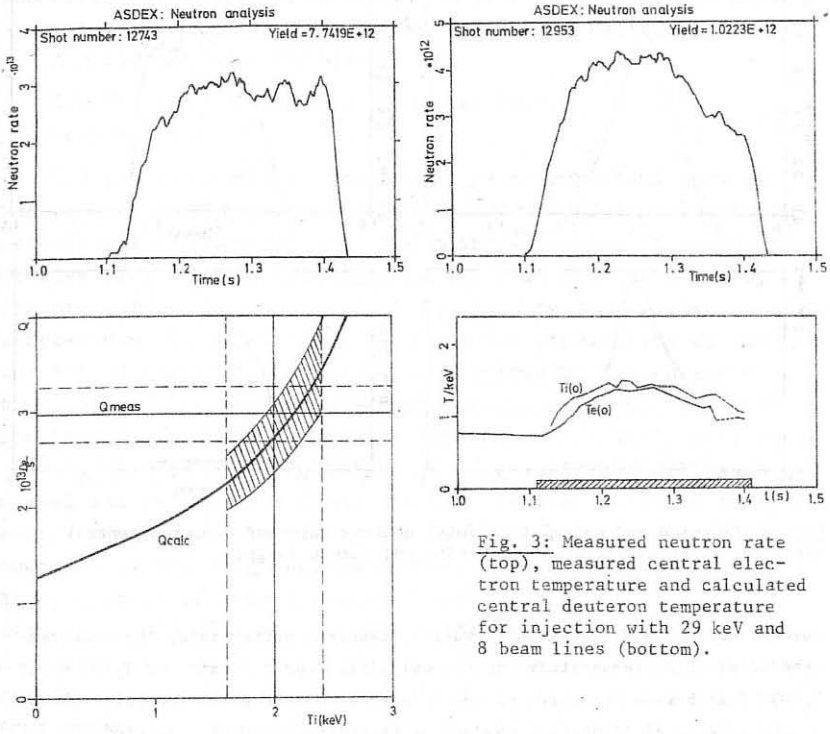

Fig. 3: Measured neutron rate (top), measured central electron temperature and calculated central deuteron temperature for injection with 29 keV and 8 beam lines (bottom).

Fig. 2: Measured neutron rate Q(t) (top), and calculated $Q(T_i)$ for $t = 1.25$ s for injection with $W_o = 45$ keV and 4 beam lines (bottom).

Next, results are presented for three other discharge types on ASDEX:

A) P_I=1.3 MW, 8 beam lines, W_o=29 keV, I_p=420 kA, $\bar{n}=6.3\times10^{13}cm^{-3}$, L-type

B) P_I=3.9 MW, 8 beam lines, W_o=45 keV, I_p=275 kA, $\bar{n}=4.4\times10^{13}cm^{-3}$, H-type

C) P_I=2.9 MW, 6 beam lines, W_o=45 keV, I_p=420 kA, $\bar{n}=4.9\times10^{13}cm^{-3}$, H-type

Figure 3 shows the measured neutron rate and central electron temperature

for case A. Further $T_i(0)$ is shown as calculated from the neutron rate. It is again about 10 % higher than the electron temperature, demonstrating the validity of the model also for low injection energies and L-type discharges.

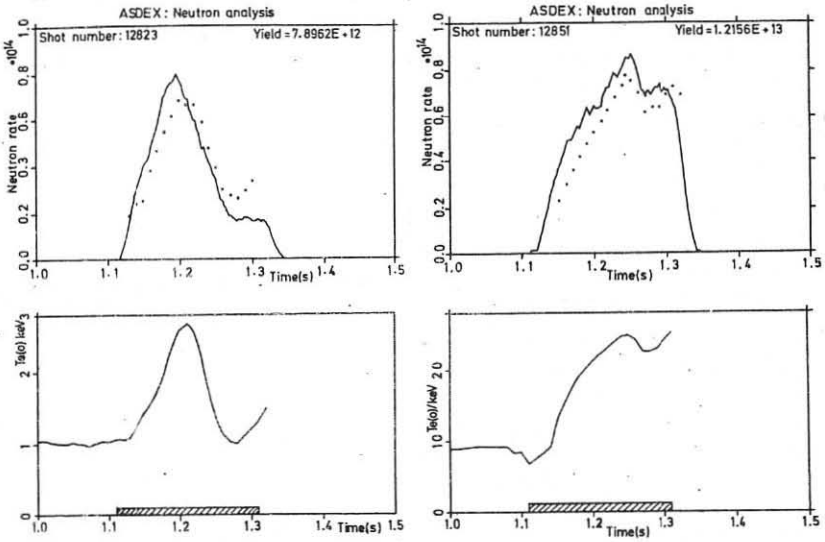

Fig. 4: Measured and calculated (dots) neutron rate and measured central electron temperature for case B (left) and case C (right).

For the cases B and C, Fig. 4 shows the measured neutron rate, the measured central electron temperature and the calculated neutron rate for $T_i(0) = 1.2\ T_e(0)$. Case B is a discharge of the burst-free H-type which typically shows a strong decrease of neutron production after about 100 ms injection. Our results for Q_{calc} demonstrate the dependence of neutron production on target electron temperature. In case C the electron temperature, and accordingly the neutron rate, remain nearly constant during injection.

Part of this work was supported by the Deutsche Forschungsgemeinschaft.

References

/1/ G. Assi, H. Rapp, IPP-Report III/70, March 1981
/2/ F. Wagner, et al., Phys. Rev. Letters 49 (19), November 1982
/3/ G.G. Lister, D.E. Post, R. Goldston, 3rd Symp. on Plasma Heating in Toroidal Devices, Varenna 1976.

ION TEMPERATURE MEASUREMENT BY CHARGE EXCHANGE IN THE PRESENCE OF CONVECTIVE ION TRANSFER IN TOKAMAK

E.L.Berezovsky, Yu.N.Dnestrovskij, S.L.Efremov, V.S.Zaveryaev, D.P.Kostomarov, A.A.Medvedev, M.V.Nesterova, A.B.Pimenov, A.P.Smirnov

I.V.Kurchatov Institute of Atomic Energy,
Moscow, USSR

The ion temperature measurement is an important part of the program on the plasma energy balance study in tokamaks. The corpuscular diagnostics with the charge-exchange atoms in its passive or active modification is the most developed one by the present time among the techniques of measuring the ion temperature. This method is based on the possibility of finding the ion distribution function over energy by the energy spectrum analysis for a flux of charge-exchanged atoms. The energy spectrum measurement is usually carried out in the energy range $E \approx (3 \div 8) T_i$. In this case, one is forced to assume a maxwellian nature of a local ion distribution function in this energy range for determining the temperature (mean energy). However, if the longitudinal magnetic field ripple is rather high, a group of locally-trapped particles drifting across the magnetic field will emerge. The drift velocity rises fast with a rise in the ion energy. For a long time it has been considered that the high energy particle enhancement occurs only in that section of the plasma column to which ions drift. In the opposite section, the ion distributions have been assumed to be not very sensitive to this drift.

However, as it has been shown in /1,2/, there is a mechanism, called as a "convective ion transfer", due to which drifting ions, trapped within the magnetic field ripples, can transit into a group of toroidally-trapped particles, trajectories of which extend over the whole plasma periphery, by collisions. Thus, the whole plasma periphery turns out to be enhanced by the high energy particles. The distribution function of passing

particles is involved into this process too. This distortion in the ion distribution function rises, when the plasma density n_e and the magnetic field B_t are reduced. Under these conditions, the term "ion temperature" includes only the mean energy of particles at this or that point in plasma without unambiguous union with the distribution function slope in difference from the maxwellized plasma.

The purpose of a given work is to find the necessary algorythm for choosing such an energy range in which the atomic charge exchange spectra slopes satisfactorily depict the mean ion energy at the hottest plasma region along a given observation line. It is natural that the extent of the particle energy spectra distortions is different for different plasma regions, and it depends on the discharge parameters. However, as this paper shows, the energy range of interest can be selected for a wide range of plasma parameters by a limited number of calculations.

On the basis of a model described in /2/, we have made the calculations of local distribution functions for trapped and passing ions and for the integral spectra of atoms outgoing from plasma along different chords as well. The calculations have been done for T-10 machine in the following range of parameters: $B_t = (1.5 \div 3.0)$T, $I_p = (200 \div 400)$kA, $n_e(0) = (3 \div 10) \cdot 10^{13}$ cm^{-3}, $a_L = (16 \div 32)$ cm. The calculated local distribution functions for separate regimes have been compared either with the ion distribution functions locally-measured by charge-exchange at an artificial target produced by the atomic beam or with the locally-measured mean ion energies by the Doppler broadening in the H_α spectral line emitted during the charge-exchange between the plasma ions and the diagnostic beam atoms /3/.

The calculated energy ranges for different chords are given in Fig.1 (a,b,c), with which one can find a mean ion energy at the hottest plasma region along a given chord. These ranges are given as a function of the parameter $n_e(0) \cdot B_t$ which determines the ion drift displacement.

The examples of integral spectra of charge-exchange atoms along different chords, $\rho = \frac{r}{a_L}$ (r is the impact para-

meter) are given in Fig.2. The ranges of energy for the ion temperature determination according to the calculations are shown.

The ion temperature profile, $T_i(r)$ as a result of the same procedure, is given in Fig.3. A dashed profile obtained with the slopes of high energy "tails" to the distribution functions is also given there. However, as calculations show, some corrections due to non-transparency of plasma for the charge--exchange atoms should be included into the result obtained. A final version of the ion temperature profile is given in Fig.3 as a dotted line. Comparing these data with the results of Doppler measurements given in the same Figure, one can make a conclusion about the possibility of finding the ion temperature profile from the atomic spectra due to charge exchange even under intense convective ion transfer.

References

1. E.L.Berezovsky et al. 10th Europ. Conf. on Control Fusion and Plasma Phys., Moscow, 1981, v.1, A-10.
2. E.L.Berezovsky et al., Nucl. Fusion, v.23 (1983), 1575.
3. E.L.Berezovsky et al., 3^{d} All-Union conference on high temperature plasma diagnostics, Dubna, 1983, 5.1.3 (In Russian).

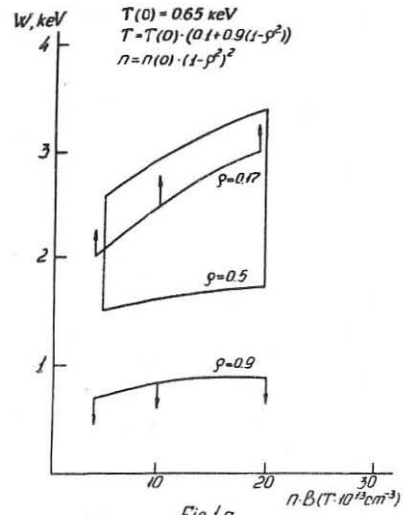

Fig 1a

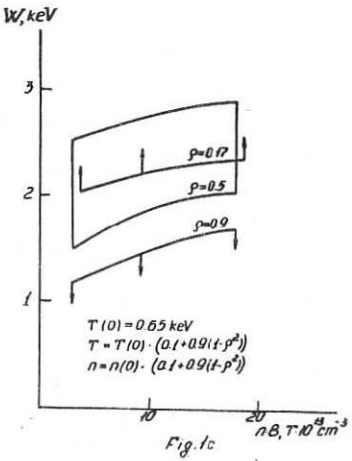

Fig. 1c

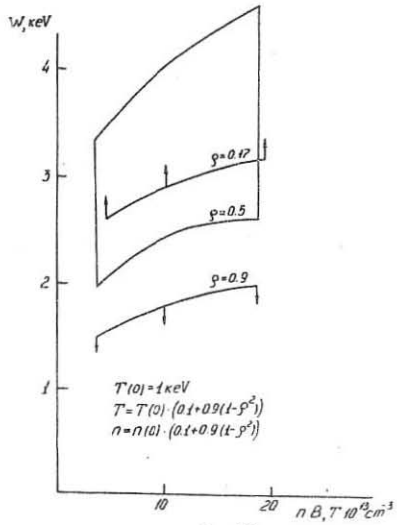

Fig 1b

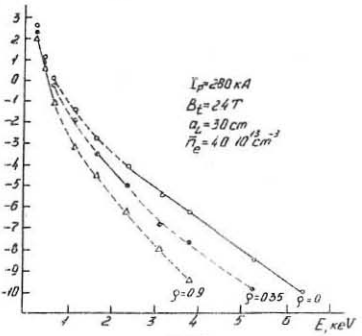

Fig 2

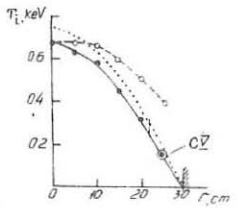

Fig 3

METHOD OF LOCAL EFFECTIVE ION CHARGE DETERMINATION IN TOKAMAK BY MEANS OF RESONANCE FLUORESCENCE

V.M.Barbotko, S.S.Bychkov, R.S.Ivanov and G.I.Stotsky
Institute of High Temperatures, USSR Academy of Sciences, Moscow, USSR

I. Introduction. In the magnetic confinement devices the last years the considerable efforts have been applied to the development of various laser diagnostic techniques due to high obtainable spatial resolution of measured plasma parameters.

In the present paper a new technique for the local measurement of the effective ion charge (Z_{eff}) is proposed. This resonance fluorescence technique is the integral modification of the method [1] and it is based on the determination of the homogeneous hydrogen spectral line width caused by the charged particle Stark broadening.

2. Principles of Z_{eff} measurement. In hot plasma the Stark broadening is caused by collisions of a radiative hydrogen atom with protons and impurity ions. At typical tokamak plasma parameters ($n_e \sim 10^{13}$ cm^{-3}, $T_i \geq 20$ ev) the collisional broadening is dominating for all charged particles. The collisional broadening width Γ may be written as follows [2] :

$$\Gamma = \frac{32}{3} n_e Z_{eff.} \langle v_p \rangle^{-1} \frac{\hbar^2}{m_o^2} \left(\ln \frac{\rho_\Phi}{\rho_o} + 0.215 \right) I(n,n'), \quad (1)$$

where $Z_{eff.} = \frac{\sum Z_i^2 N_i}{n_e}$, ρ_Φ is the Debye length, ρ_o is the Weisskopf radius, I(n,n') is the factor depending on the main quantum numbers of the radiative transition levels (for the transition from n = 3 to n = 2 I(n,n') = 27), $\langle v_p \rangle = \sqrt{\frac{8kT_i}{\pi m}}$ is the thermal proton velocity which is considered to be relative one between the excited hydrogen atoms and broadening ions. Summarising the contributions of plasma ions with different ion charge Z_i it is assumed that $\tilde{Z}_i = Z_{eff}$ due to the weak dependence of $\ln \frac{\rho_\Phi}{\rho_o}$ on Z_i. Thus the determination of Z_{eff} may be carried out from the measured value Γ when n_e and T_i are known independently.

The phenomenon of the radiative transition saturation caused by the narrow-band laser radiation was used for the determination of Γ . The observed fluorescent spectral profile is the convolution of the Doppler profile with the line profile induced by the strong laser field. The latter is dispersional in shape with half-width $\Gamma_B = \Gamma\sqrt{1+G}$ (the Bennet gap), where G is a saturation parameter of the transition [3] :

$$G = \left(\frac{p_{12}\mathcal{E}}{\hbar}\right)^2 \frac{1}{\Gamma}\left(1/\tilde{\gamma}_1 + 1/\tilde{\gamma}_2\right),$$

$\tilde{\gamma}_1$ and $\tilde{\gamma}_2$ are the population relaxation constants of the levels 1 and 2, p_{12} is the transition dipole moment, $\mathcal{E}$ is the laser-induced electric field. Thus the measurement of the observed fluorescent profile half-width at different saturation parameters enables the determination of the Doppler ($\Delta\lambda_D$) and the dispersion profile (Γ_B) half-widths. It should be noted that the fluorescent profile may be obtained by the wave-scanning of the narrow-band laser line in a set of successive reprodusible discharges.

When the laser radiation being nonmonochromatic the computer calculations of the fluorescent profile should be performed. The calculations of the probability $\langle W_{23} \rangle$ of a transition from n=2 to n = 3 levels were carried out at $\lambda_F = \lambda_0$ for different values of $\Delta\lambda_D$ and Γ when $\Delta\lambda_F$ was considered fixed at 0,1Å since such a laser spectral half-width has been used in our experiments (fig.1 and 2). The curve for monochromatic laser radiation is also shown here for the comparison (curve 4 in fig. 1).

3. Experiments in tokamak TV-1. The fluorescence experiment have been performed in tokamak TV-1 (r=23,5 cm, a_L=3,5 cm) with the help of flush-lamp pumped dye laser with the narrow spectral line (0,1 Å). The laser line was independently monitored crudely with monochromator SPM-2 ($\delta\lambda$ = 1 Å) and accurately with Fabry-Perot interferometer ($\delta\lambda$ =0,09 Å).

In a reproducible set of tokamak discharges the fluorescence intensity measurements were carried out while wave tuning of the dye laser against the H_α line center being successively changed. The typical H_α profiles at different values of G on plasma axis in the start of discharge (0,3 ms) and on current plateau are shown in fig. 3 and 4 respectively. The absorbtion

profile is observed to be broadened with laser power being increased. The dependences of $\Delta\lambda_D$ and Γ_β (fig. 5 and 6) on laser power density are obtained for one of the basic tokamak operation modes (I_p = 5 kA, B_T = 14 kG, U_L = 1,5÷2,5 v, n_e = $(2\div3)\cdot10^{13}$ cm^{-3}).

The mean value of $\Delta\lambda_D$ was found to be 0,5 Å that corresponded to $T_a \approx$ 1 ev. The mean Γ determined from the slope of the curve (fig. 5) was 0,08 Å. The calculation of Z_{eff} yields 3÷4 when $n_e(0) = 4{,}5\cdot10^{13}$ cm^{-3}, T_e = 100 ev, T_i = 30÷60 ev. The obtained density of atoms was $(4\div5)\cdot10^{9}$ cm^{-3}.

4. Discussion. The high saturation parameters at reasonable laser nonmonochromaticity should be achieved for the realisation of this method. The two limitations of method should be taken into account:

a) the nonlinear spectroscopy calculations may be considered valid only when the energy gap is much higher than the radiation/atom interaction energy;

b) the maximal power of the available dye lasers are limited.

In our experiments the obtained power density of 1÷2 kwt/cm^2 was sufficient for the saturation of the tokamak plasma, the interection energy of H_α transition with laser radiation being (4÷5) orders of the magnitude lower than the energy gap between the second and the third levels of a hydrogen atom. The up-to-date dye lasers may generate power as high as 100 kwt that is sufficient for the saturation of the Doppler profile at $T_a \sim$ 100 ev which is typical for the edge plasma in large tokamak machines.

5. References

1. Abramov V.A. and Lisitsa V.S. Sov.J.Plasma Phys. 3, No.4, 799, 1977.
2. Vainstein L.A., Sobel'man I.I. and Yukov E.A. Atom Exitation and Spectral Line Broadening (Moscow: Nauka, 1979).
3. Letokchov V.S. and Chebotaev V.P. Principles of the Nonlinear Laser Spectroscopy (Moscow: Nauka, 1975).

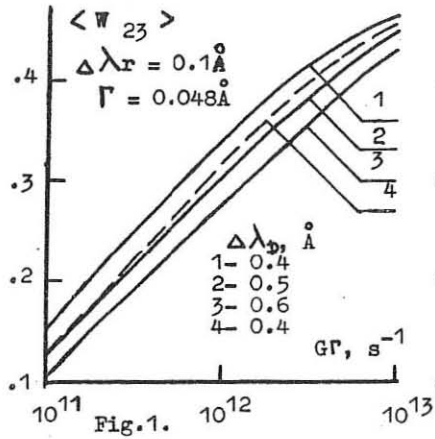

Fig.1.

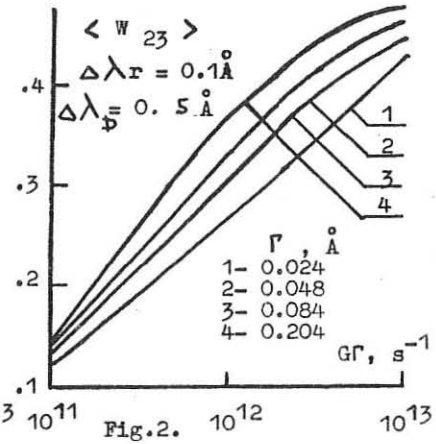

Fig.2.

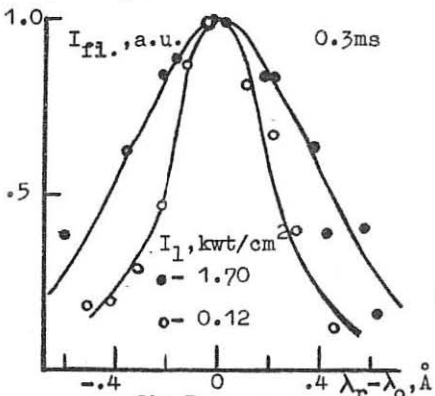

Fig.3.

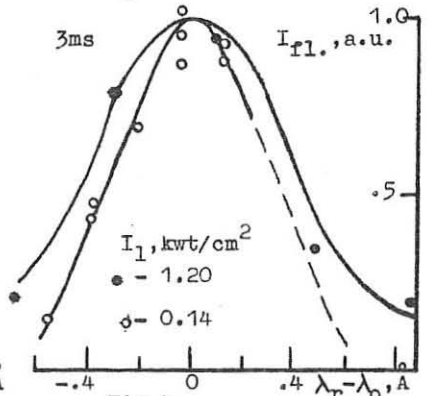

Fig.4.

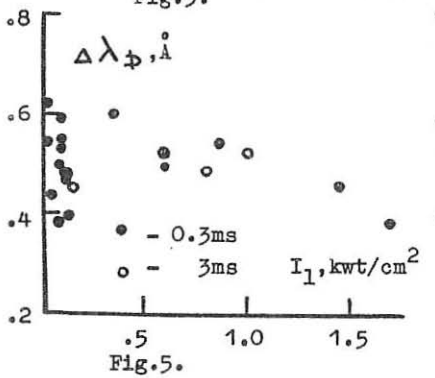

Fig.5.

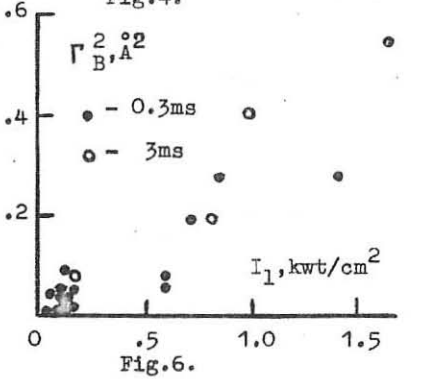

Fig.6.

DISTORTION OF THE MAXWELLIAN DISTRIBUTION IN INHOMOGENEOUS MAGNETIZED PLASMA

G.S.Irisov, P.N.Yushmanov

I.V.Kurchatov Institute of Atomic Energy,
Moscow, USSR

One of the methods of measuring the ion plasma temperature in tokamak is the measurement of fast atomic spectra formed as a result of charge exchange between the plasma ions and neutral atoms of the gas. The neutral atoms produced in the charge exchange of the ions with the energies $w \gg T_i$ are registered. The experiments have shown that the ion distribution function strongly differs from a maxwellian one in a range $w \gg T_i$, especially at the plasma column periphery /1,2/. The differences are expressed by a broadening in the temperature profile for an epithermal component in comparison with the main one and by the presence of a strong rise in the ion distribution function at high energies.

High energy part enrichment in the ion distribution function due to a finite transversal size of orbits is theoretically studied in the present paper. A cyclotron rotation as well as a drift motion in toroidal systems are considered. In comparison with the theoretical studies made previously, a kinetic equation for the ion distribution tail has been obtained by a regular technique of averaging over a fast oscillating variable /3/. Let us consider a situation close to the experimental one, when a transversal size of the orbits for thermal particles is considerably less than the size of an inhomogeneity in the system and, hence, the distribution function of thermal particles is close to the maxwellian one. Moreover, considering an epithermal range, we limit ourselves by not too high energies, $T_i \ll w \lesssim (m_i/m_e)^{1/3} T_e$, to be able not to take the collisions of ions with electrons into account.

Let us consider first the case of homogeneous magnetic field, when a deviation from the field line is provided by cyclotron rotation. Then, a kinetic equation for the ion distribution tail has a form:

$$\frac{df}{dt} = \frac{4\pi\lambda e^2 n}{m^2}\left\{\frac{1}{v}\frac{\partial}{\partial v}\left(f + \frac{T}{mv}\frac{\partial f}{\partial v}\right) + \frac{1}{2v^3}\left[\frac{1}{\sin\vartheta}\frac{\partial}{\partial\vartheta}\left(\sin\vartheta\frac{\partial f}{\partial\vartheta}\right) + \frac{1}{\sin^2\vartheta}\frac{\partial^2 f}{\partial\varphi^2}\right]\right\}, \quad (I)$$

where m is the ion mass, λ is the Coulomb logarithm, n and T are the ion density and temperature, depending on the coordinates. Let us make a transition to the integrals of motion in Eq. (I), $w = mv^2/2$, $r_0 = r - v\omega_B^{-1}\sin\vartheta\sin\varphi$ where ω_B is the cyclotron frequency, and, averaging Eq.(I) over the period of Larmor rotation, exclude a fast oscillating variable φ from the kinetic equation:

$$\frac{\partial}{\partial w}\left(f + T(r_0)\frac{\partial f}{\partial w}\right) + \frac{1}{4w\sin\vartheta}\frac{\partial}{\partial\vartheta}\left(\sin\vartheta\frac{\partial f}{\partial\vartheta}\right) + \frac{1+\cos^2\vartheta}{4m\omega_B^2}\frac{\partial^2 f}{\partial r_0^2} = 0. \quad (2)$$

In case of a toroidal magnetic field, let us use the same method and, for this purpose, make a transition to the variables in Eq.(I), which separate a fast oscillating variable α (poloidal angle) and the integrals of motion in the explicit form: $s = h\sin^2\vartheta$, $r_0 = r - h\omega_J^{-1}\sqrt{2w/m}\,(\cos\vartheta - h\varphi(s))$, where $h = 1 + \varepsilon\cos\alpha$, ω_J is the ion cyclotron rotation frequency in a field of the current. The function $\varphi(s)$ is introduced because $\oint\cos\vartheta\,d\alpha \neq 0$ for passing particles. After integration over the period of fast motion, the equation for a high energy part of the distribution function has a form:

$$\frac{\partial}{\partial w}\left(f + T(r_0)\frac{\partial f}{\partial w}\right) + \frac{1}{wJ_1}\frac{\partial}{\partial s}\left(sJ_3\frac{\partial f}{\partial s}\right) + \frac{s}{2m\omega_J^2}\frac{\partial}{\partial r_0}\left[\left(1 - \frac{J_2^2}{J_1 J_3}\right)\frac{\partial f}{\partial r_0}\right] = 0, \quad (3)$$

where $J_1 = \oint dl/\cos\vartheta$, $J_2 = \oint dl$, $J_3 = \oint h\cos\vartheta\,dl$, and $\varphi(s) = -\int J_2/2J_3\,ds$ is chosen from the continuity condition for a flux across the separatrix.

The equations (2), (3) are found to be too complicated for analytical solutions. Therefore, we shall consider only two limit cases: dominance of angular scattering and its insignificance. In the first case, f doesn't depend on ϑ (or s) and we can integrate the equation with respect to an angle; in the second case, one can simply discard the angular scattering operator. In both limit cases the equations (2), (3) become two-dimensional ones:

$$\frac{\partial}{\partial w}\left(f + T(r)\frac{\partial f}{\partial w}\right) + \frac{\partial}{\partial r}\left(D\frac{\partial f}{\partial r}\right) = 0. \quad (4)$$

The equation (4) for a high energy part of the ion distribution function in case of a toroidal magnetic field differs from an equation for a rectilinear magnetic field by a form of the coefficient D. For a case of the angular scattering dominance, these coefficients have a form $D_{TOR} = 0.49\sqrt{\varepsilon}/m\omega_J^2$ and $D = (3m\omega_B^2)^{-1}$; at a weak angular scattering

$$D^s_{TOR} = \frac{s}{2m\omega_J^2}\left(1 - \frac{\gamma_z^2}{\gamma_1\gamma_3}\right), \quad D^\vartheta = \frac{1+\cos^2\vartheta}{4m\omega_B^2}.$$

In case of a weak angular scattering, the coefficient D^ϑ in a homogenenous field almost does not depend on the angle ϑ ; but in a toroidal field, D^s_{TOR} is a very strong function of s , important in the region of trapped particles only (Fig.1). Note that the equation (4) averaged over s in the toroidal case coincides with the equation obtained in /4/ with the use of a neoclassical approach.

In spite of the simplifications made, the solution to Eq.(4) by the analytical method is impossible in the general case. Therefore, we limit ourselves by the consideration of a private case allowing an analytical solution and rather well corresponding to the experimental conditions, $T(r) = T_0(1 - r/a)$, D = const. Then, the equation (4) can be solved with the Laplace transform:

$$f(w,r) = \frac{n_0 a^{2/3}}{2^{3/2}\pi^{5/2} T_0^{7/6} D^{1/3}} \int_0^{T_0^{-1}} p^{-1/3}\xi^{-1/4} \exp\left\{-wp - \frac{2}{3}\xi^{2/3}\right\} dp, \qquad (5)$$

where $\xi = a^{2/3}(1-(1-r/a)T_0 p)/(D p T_0^2)^{1/3}$.

The most reliably-measured quantity in the experiment is a local temperature: $T_w = -[d\ln f/dw]^{-1}$. Therefore, later we shall pay attention to the behaviour of the very quantity. Using the saddle-point method and proceeding from the distribution (5), one obtains an equation for T_w:

$$\left(\frac{T_w}{T(r)} - 1\right)^{1/2} + \frac{1}{3}\left(\frac{T_w}{T(r)} - 1\right)^{3/2} = \frac{w}{w_c} \qquad (6)$$

where $w_c = a\sqrt{T_0/D}\,(1-r/a)^{3/2}$.

The dependence of local temperature on the radius and energy is

shown in Fig.2. T_w is preset by the expressions

$$T_w = T(\tau)\cdot(1+w^2/w_c^2) \quad \text{and} \quad T_w = T(\tau)\cdot(1+3\,(w/w_c)^{1/3})$$

for the limit cases, $w \ll w_c$ and $w \gg w_c$.

Let us compare the results obtained with the calculations for the distribution function, using the τ-approximation in the collision operator /5/. For comparison, let us use the large angular scattering limit ($D = 0.49\sqrt{\varepsilon}/m\omega_3^2$), which better corresponds to real conditions. Then, in a range $w \gg w_c$ according to /5,6/, the local temperature can be represented as:

$$T_w^* = T(\tau)\left[1 + 3\,\frac{\sqrt{\varepsilon}}{\omega_3}\sqrt{\frac{w}{m}}\left/\frac{d\ln T}{d\tau}\right.\right].$$

The ratio of local temperatures T_w^* and T_w (6) in the most interesting range $T_w \gtrsim T(\tau)$ is the product of three small parameters:

$$\frac{T_w^*}{T_w} = \varepsilon^{1/3}\left(\frac{T(\tau)}{w}\right)^{1/3}\left[\frac{1}{\omega_3}\sqrt{\frac{w}{m}}\left/\frac{d\ln T}{d\tau}\right.\right]^{1/3}$$

From this ratio one can see that the results /5,6/ represent the lower bound to a real effect.

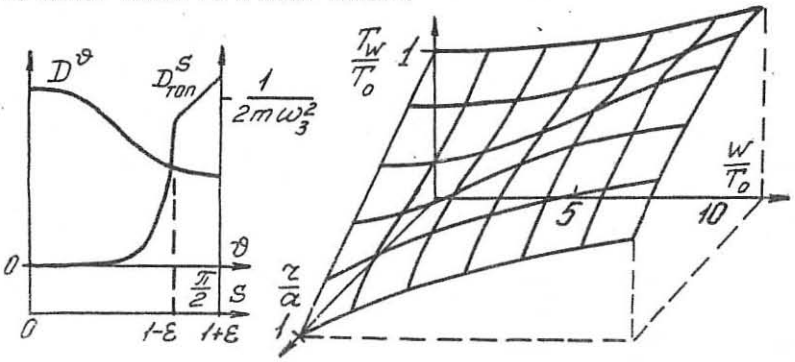

References

1.M.P.Petrov. Pis'ma J.Ehksp. Teor. Fiz., 17, 110, 1973.
2.V.S.Zaveryaev et al. Fizika plasmy, 4 (1978) 1205.
3.S.T.Belyaev. Plasma Physics and Controlled Fusion Problem (in Russian), Moscow, ed. AN SSSR, 1958, p. 50.
4.A.A.Ware. Phys. Fluids, 27 (1984) 1215.
5.L.M.Kovrizhnykh. Fizika plasmy, 5 (1982) 1105.
6.Yu.V.Gott, E.I.Yurchenko. DAN SSSR, 260 (1981) 1352.

INVESTIGATION OF CURRENT PROFILES IN THE TUMAN-3 TOKAMAK

S.P.Bondarenko, A.O.Kaminskij, Yu.K.Kuznetsov, V.N.Pyatov, I.V.Yasin

Institute of Physics and Technology, the Ukrainian Academy of Sciences, Kharkov 310108, USSR

V.E.Golant, M.P.Gryaznevich, S.V.Lebedev, N.V.Sakharov, K.G.Shakhovets

Ioffe Institute of Physics and Technology, the USSR Academy of Sciences, Leningrad, USSR

The plasma current density distribution is an important characteristic of the magnetic configuration of a tokamak. In our experiments in the Tuman-3 tokamak, the equilibrium distributions of the plasma current j_φ and pressure p were obtained from external magnetic measurements [1]. We measured poloidal fluxes $\bar{\psi}_1, \bar{\psi}_2$ along two contours L_1, L_2 encircling the plasma column in the meridian section, the total plasma current I_p, the total current in toroidal field coils F_e, and the change in the toroidal flux due to the plasma Φ_p. The signals from the magnetic sensors were digitized and processed by a computer.

The method of calculating the plasma current profile. To obtain the equations relating the external magnetic measurements to the local plasma parameters, we have used a model representation of the plasma current density j_φ: $j_\varphi(r,\psi) = a_p \frac{r}{R} f_p(\psi) + a_F \frac{R}{r} f_F(\psi)$, where R is the major radius of the torus; a_p, a_F are the normalization constants; f_p, f_F are the arbitrary functions of the poloidal flux ψ which satisfies the Grad-Shafranov equation [2]:

$$L(\psi) = r\,div(\nabla\psi/r^2) = -\frac{8\pi^2}{c} j_\varphi(r,\psi) \qquad (1)$$

with a boundary condition on the contour L_1:

$$\psi|_{L_1} = \bar{\psi}_1(\bar{x}), \qquad \bar{x} \in L_1 \qquad (2)$$

Using the Green function method, the solution of eqs.(1), (2) is written as

$$\psi(x) = \frac{8\pi^2}{c}\int_S G(x,y) j_\varphi(y)\, d\sigma_y - \int_{L_1} \vec{n}\,\nabla G(x,\bar{x})\bar{\psi}_1(\bar{x})/r(\bar{x})\, dl_{\bar{x}} \qquad (3)$$

where S is the region in the φ =const plane of the cylindrical

system of coordinates τ, φ, z and is bounded by the contour $L_1; x, y \in S$, $\vec{n}$ is the vector of the external normal to L_1; $G(x,y)$ is the Green function of the two-dimensional operator L which has an analytical representation [1] for a circular L_1 contour and can be calculated numerically [2] for an arbitrary L_1 shape. The constants a_p, a_F were related to $I_p = \int_S j_\varphi \, d\sigma$ and $\Phi_p = \frac{2}{c} \int_S F_p(t)/\tau \, d\sigma$ as

$$a_p = (I_p - a_F \int_S R/\tau f_F(t) d\sigma)/(\int_S \tau/R \, f_p(t) \, d\sigma) \qquad (4)$$

$$a_F = c R B_{\varphi 0} \Phi_p / (2(\psi_M - \psi_L) \int_S R/\tau \int_0^t f_F(t') dt' d\sigma) \qquad (5)$$

where $t = (\psi - \psi_L)/(\psi_M - \psi_L)$; ψ_L and ψ_M are the flux values on the plasma edge and on the magnetic axis, respectively; F_p is the poloidal plasma current, $B_{\varphi 0} = 2F_e/cR$. In eq.(5) we put $F_p \ll F_e$. The f_p, f_F functions were obtained from the minimum condition of the functional $\chi^2 = \sum_i \sigma^{-2}(\vec{x}_i)[\bar{\psi}_2(\vec{x}_i) - \psi_2(\vec{x}_i)]^2$ where $\bar{\psi}_2(\vec{x}_i)$ and $\psi_2(\vec{x}_i)$ are, respectively, the measured and calculated by eq.(3) poloidal flux values at point $\vec{x}_i$ of the L_2 contour; $\sigma(\vec{x}_i)$ is the standard deviation of the i-th measurement. The search for the minimum χ^2 was carried out using the set of the parabolas of the type $f_{p,F}(t) = \alpha_{p,F} t + (1 - \alpha_{p,F}) t^2$. To check the efficiency of the magnetic analysis technique presented above, we have performed numerical test computations. The test equilibrium j_φ profiles and the $\bar{\psi}_1$, $\bar{\psi}_2$, I_p, Φ_p, F_e values were generated using

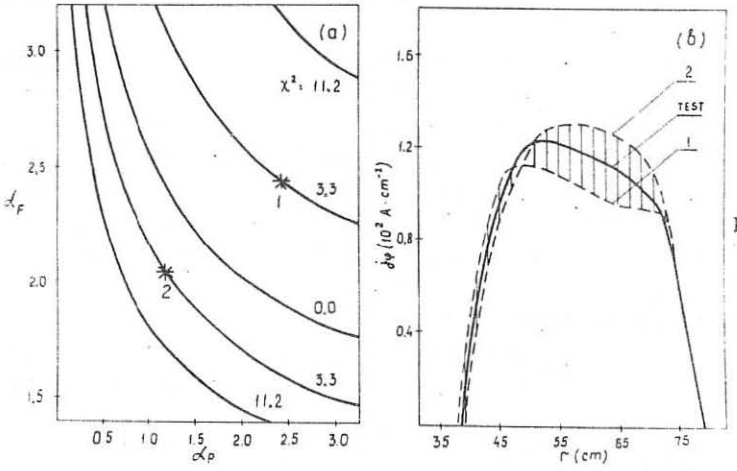

Fig. 1

the MHD code [3] that models the Tuman-3 coil/plasma system. Different types of equilibrium current profiles (peaked, flat and skinned) were reconstructed. Fig.1 exemplifies the result of the flat profile j_φ reconstruction. Along each χ^2 =const isoline (fig. 1a) we had one and the same j_φ profile which changed only in going from one isoline to another. The solid line in fig. 1b shows the test j_φ profile, and the shaded area shows the reconstructed j_φ profiles at $\chi^2 < \chi^2_s = 3.3$, χ^2_s corresponds to a random error ~ 5% in the $\bar{\psi}_1$, $\bar{\psi}_2$, I_p, F_e, Φ_p values.

Experimental results. Three discharges (see fig.2) were studied by means of the magnetic analysis. The first discharge (solid curve 1) corresponded to ohmic heating. In the second discharge (dahed curve 2) the ICR heating was applied (30 ms starting time, 7 ms pulse length). In the third discharge (dash-dotted curve 3) the plasma disruption occurred. Fig. 3 shows the reconstructed j_φ and p profiles in the z=0 plane together with the outermost magnetic surfaces for different times. It is seen that in the discharges considered parabolic p profiles and flat or skinned j_φ profiles were realized, except discharge 3, where the j_φ profile change and the current I_p disruption took place at $t \geq 37.6$ ms due to plasma column displacement to the limiter. The pressure P in the discharges varied with the I_p current value. In discharge 2, during the RF pulse the P value increased in spite of the I_p decrease.

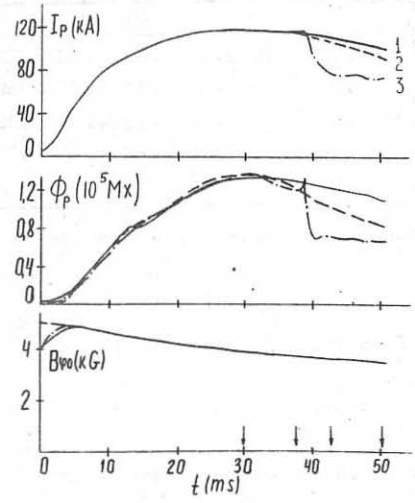

Fig. 2

The table given below lists the following parameters: the the safety factors on the plasma edge, q_L, and on the magnetic axis, q_M; the internal inductance l_i; the poloidal, β_p, and toroidal, β_T, betas.

The magnetic analysis results obtained have shown the existence of stable skinned ($q_M > 1$,

$q_L \lesssim 2$) and peaked ($q_M \lesssim 1$, $q_L \lesssim 3$) j_φ profiles.

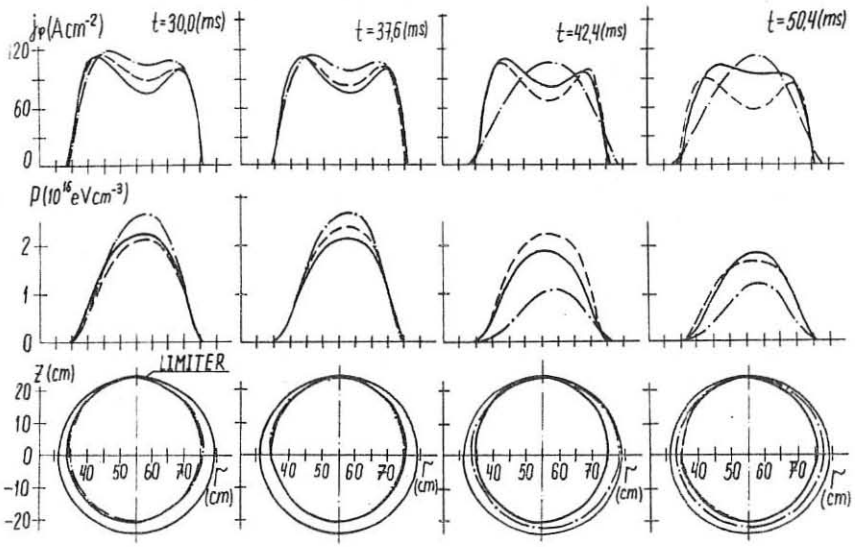

Fig. 3

Table

Time	30 ms			37.6 ms			42.4 ms			50.4 ms		
Disch.	1	2	3	1	2	3	1	2	3	1	2	3
q_L	1.75	1.81	1.73	1.68	1.68	1.66	1.76	1.75	2.8	1.74	1.88	2.72
q_M	1.45	1.33	1.14	1.46	1.34	1.13	1.35	1.59	0.86	1.11	1.71	0.94
ℓ_i	0.84	0.82	0.89	0.81	0.83	0.90	0.84	0.81	1.18	0.93	0.81	1.18
β_p	0.25	0.23	0.24	0.26	0.27	0.26	0.23	0.30	0.14	0.22	0.31	0.16
$\beta_T \cdot 10^{-2}$	1.57	1.37	1.60	1.64	1.76	1.83	1.35	1.74	0.55	1.42	1.53	0.69

The authors would like to thank V.D.Shafranov, V.S.Mukhovatov and L.E.Zakharov for useful discussions of this work.

References

1. Yu.K.Kuznetsov, V.N.Pyatov, I.V.Yasin. Preprint KhFTI 85-2, Moscow (1985).
2. L.E.Zakharov, V.D.Shafranov. In: Voprosy Teorii Plazmy, is.11, Ehnergoizdat, Moscow (1982).
3. M.P.Gryaznevich, T.G.Kilovataya, V.N.Pyatov, Fizika Plazmy 9 (1983) 715.

DETERMINATION OF THE FLUX OF THERMAL NEUTRAL PARTICLES FROM THE WALL OF A TOKAMAK BY PULSED GAS INJECTION

G. Bertschinger, D. Reiter and L. Könen
Institut für Plasmaphysik der Kernforschungsanlage Jülich GmbH,
Association EURATOM/KFA, P.O.B. 1913, D-5170 Jülich, FRG

Abstract
We demonstrate a new approach to determine the primary neutral particle source at the first wall of a tokamak. Using a modulated gas inlet, the neutral density in the plasma and therefore the flux of fast charge exchange neutrals is modulated. The flux increase due to the known amount of additional gas can then be compared with the flux caused by neutral particle release from the vessel wall. Geometrical differences of these two particle sources are taken into account by Monte Carlo code calculations.

Introduction

In fusion devices emission of fast neutral atoms is one channel of plasma-wall interaction. The flux of fast neutrals ejected by the plasma is proportional to the density of neutrals in the central region/1/. For small and medium size tokamaks the density of neutrals in the plasma center is proportional to the influx of neutral particles from the wall and the limiter. The usual way to determine the influx is to measure the absolute flux of fast atoms and to compare the results with transport code calculations.
In order to measure the primary sources of neutrals at the wall of TEXTOR we use a different approach, which was made possible by the development of a 3-dimensional transport code /2/. We compare the flux of fast neutrals caused by recycling at the wall with the flux caused by an additional particle source of known flux at the same distance from the plasma.
The ratio of the two fast fluxes is directly proportional to the ratio of the sources at the wall. For the same distribution of the source densities at the wall the factor of proportionality is exactly one, for different distributions the different geometry is taken into account by the transport code. The ratio of the fluxes is fairly insensitive to the plasma parameters at the plasma boundary and the details of the wall interaction of particles emitted by the plasma.

Experimental

The procedure was used to measure the sources of neutrals at the first wall of the TEXTOR-tokamak (major radius r_0 = 175 cm, minor radius a = 47 cm, central electron density $n_e(o) = 3 \times 10^{13}$ cm^{-3}). The plasma is concentrically surrounded by a liner with minor radius a_L = 55 cm. We use a limiter which is located in toroidal direction 110 degrees from the location of the neutral particle analyser, therefore recycling at the limiter has no influence on the measurement. The wall was carbonized /5/, raising the overall recycling coefficient close to one, i.e. the electron density remains constant or even rises slowly, although the main gas feed is switched off.
To increase the influx of neutrals to the plasma we use a gas injection system whose flow rate is measured. To avoid a large increase in plasma density and a disturbance of the plasma boundary the flow rate should be as small as possible. Lock-in techniques are used to discriminate against the wall fluxes. As the response time of a gas injection system decreases for low injection /3/ we had to speed up the system. We use a Piezo valve and a tube in the viscous flow range with minimum length ($\sim$ 45 cm). The tube has an exponentially increasing diameter. Compared to a cylindrical tube, the response time of the flow is 2.4 times faster.

The experimental arrangement is shown in fig. 1, the response of the gas feed system in fig. 2. The total gas inlet is measured by the decrease of the pressure in the buffer volume, the response time is measured by photon emission in the wavelength interval 5 nm $< \lambda <$ 20 nm, which is probably caused by charge exchange recombination of light impurities.
The minimum pulse width is 4 ms, the maximum frequency 60 Hz, for a Deuterium pulse with a gas feed rate of 3 mbl/s the rise time is 1,8 ms, the fall time constant is about 2,5 ms.
As the gas inlet system is connected opposite to the neutral particle analyzer, the response is not the same for the different energy channels. The channels with low energies are only weakly modulated, whereas the higher energy channels show a higher modulation (Fig. 3). Above 1,3 keV the modulation is approximately constant. This is caused by the different radial positions where the neutrals with different energies are born. The low energy particles come from the boundary plasma just in front of the analyzer, which is hardly influenced by the additional gas feed. The higher energy particles have their origin in the center of the plasma, where the modulation of neutral density is higher.

Comparison with code calculations

The distribution function of escaping neutrals without gas injection is used to determine the maximum ion temperature on the line of sight /1/. The profiles of electron temperature and density are taken from Abel-inverted interferometer data and Thomson scattering /4/. The distribution function is then compared to the 1 - D version of the Monte Carlo transport code, the flux density at the liner is chosen arbitrarily. Within experimental errors, the shape of the distribution function is reproduced (Fig. 4a). The same set of plasma parameters is then used to calculate the spectrum of escaping neutrals caused by the gas feed by means of the 3 - D version of the code (Fig.4b). Above 0.8 keV the spectrum is reproduced very well, for the lower energies the accuracy of both the measurement and the calculation decreases. The flux density of neutrals at the liner is now calculated to be $1,8 \times 10^{14}$ D_2 molecules/s cm^2, corresponding to $3,6 \times 10^{14}$ D atoms/s cm^2. Integrated over the liner surface, we get a total flux of 2×10^{20} D atoms/s.
The code gives us now the neutral densities in the plasma caused by the external sources (Fig. 4c,d). The neutral density in the plasma center is rather low, about 2×10^6 D atoms/cm^3. The Deuterium atom density in the plasma center caused by radiative recombination is about 2×10^5 D atoms/cm^3 and is neglected. Comparison of the profiles for the neutral densities and the effective source functions i.e. the production rate of neutrals by charge exchange multiplied with the probability to leave the plasma in the direction towards the neutral particle analyzer (Fig. 4e, f) shows clear differences for the two particle sources. Whereas the neutral density is strongly asymmetric for the gas inlet and symmetric for the liner source, the situation is different for the effective source function which is characteristic for the spectrum of emitted neutrals. Here the distribution is more asymmetric for the liner source then for the gas inlet.

References

/1/ F. Wagner, J. Vac. Sci. Technol., 20 1211(1982)
/2/ D. Reiter, Berichte der KFA-Jülich, JÜL-1947 August 1984)
/3/ K.M. Burrell, Rev. Sci. Instrum. 49 948 (1978)
/4/ H. Soltwisch et al., Plasma Physics 26 23(1984)
/5/ J. Winter et al., J. Nucl. Mat. 128+129, 841(1984)

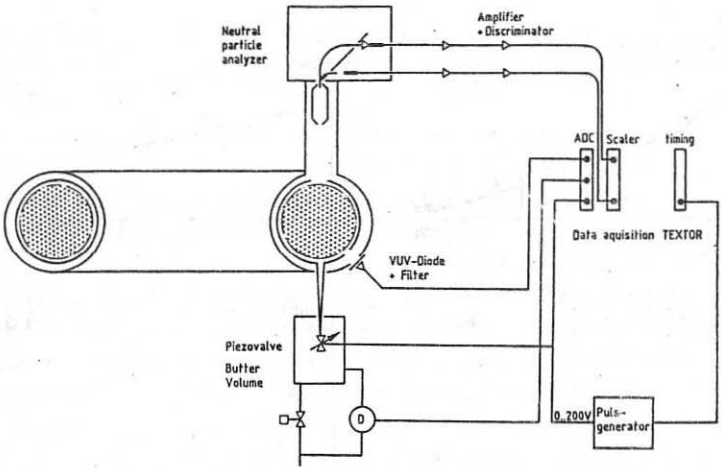

Fig. 1 Scheme of gas injection diagnostic

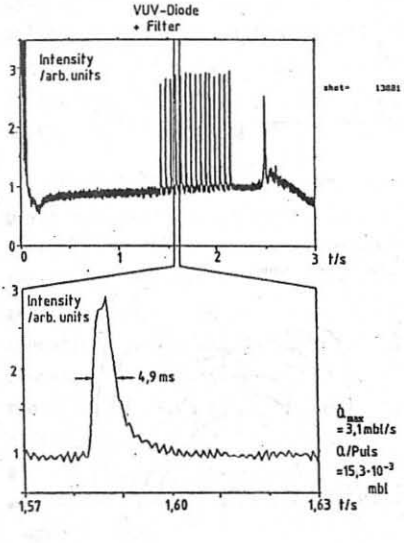

Fig. 2 Response of the gas injection system, gas feed starts at 1.43 s

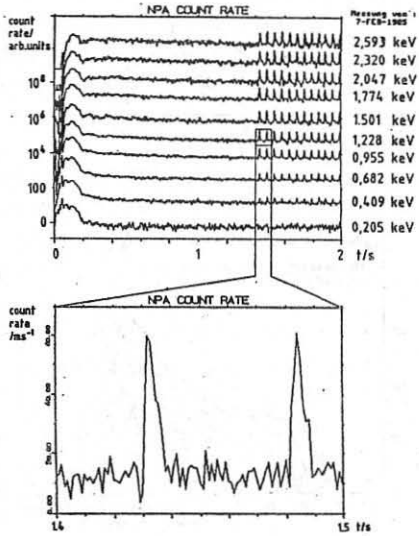

Fig. 3 Neutral particle spectra with modulated gas feed

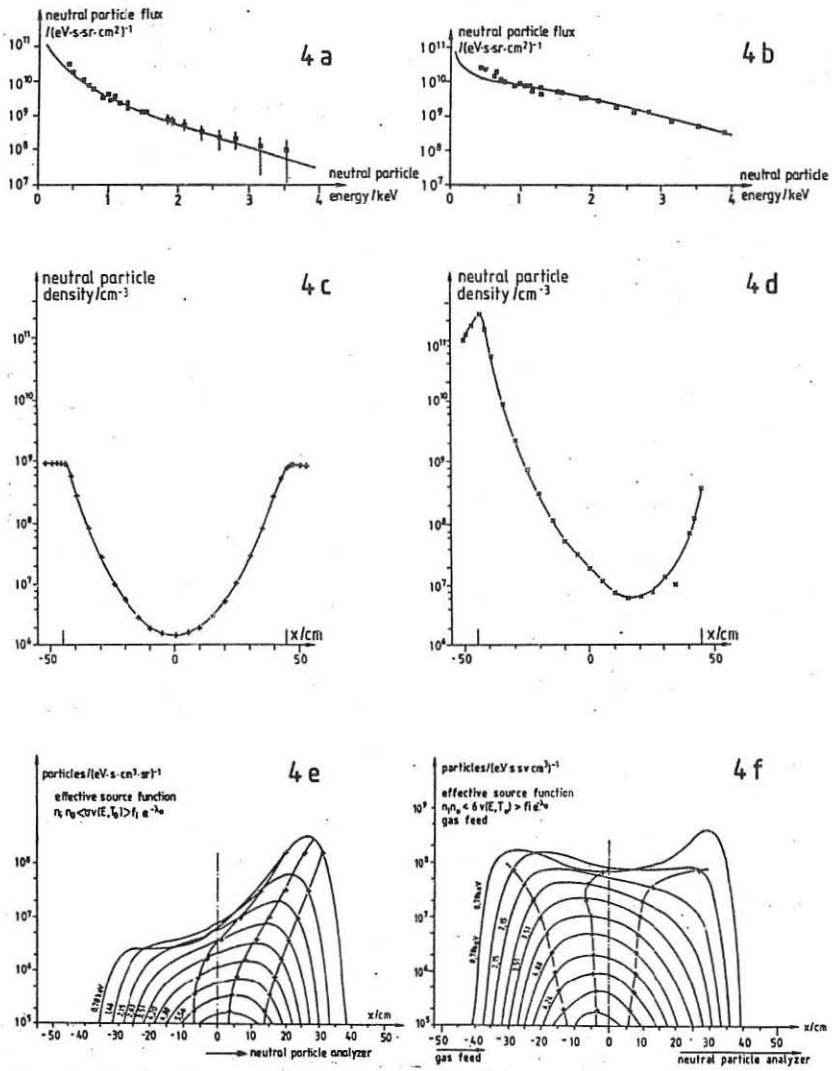

Fig. 4 Comparison of liner source (left) with gas feed (right)

liner
$Q = 3.6 \times 10^{14}$ D atoms/scm^2

gas feed
$Q = 1.52 \times 10^{20}$ D atoms/s

FLUCTUATION MEASUREMENTS ON THE RENTOR TOKAMAK,* R. L. Hickok, K. Saadatmand, and W. C. Jennings; Rensselaer Polytechnic Institute, Troy, New York 12181, U.S.A.

A heavy ion beam probe has been used to simultaneously measure the turbulent spectra of ϕ and $nF(T_e)$ fluctuations on the RENTOR tokamak. RENTOR is a small research tokamak whose pertinent parameters are: $R = 45$ cm, $a = \cong 10$ cm, $B_t \cong 0.4$ T, $I_{oh} \cong 15$kA, $n(0) \cong 5 \times 10^{12}$ /cm^3, $T_e(0) \cong 120$ ev, pulse length $\cong 10$ msec. The plasma was probed with a 20 keV Cs^+ beam and the energy and intensity of the Cs^{++} secondary ions created by electron impact ionization were measured. The energy difference between the primary and secondary ions is directly proportional to the space potential, ϕ, at the location where the secondary ions were created. The intensity of the secondary ion signal is proportional to $nF(T_e)$ where $F(T_e)$ is the effective cross-section for the ionization reaction. Spatial resolution is 3 dimensional with a sample volume that is approximately 0.1 cm^3. The shape of the sample volume is roughly cylindrical with a radius of 0.5 cm and a height of 0.1 cm. This sets a limit on the minimum wave length fluctuations that can be resolved. The location of the sample volume can be set at any predetermined location in the cross-section of the plasma by selecting the appropriate beam energy and injection angles.

The energy of the secondary ion beam is measured with a parallel plate electrostatic energy analyzer with split plate detectors. The system is set up so that when the space potential is zero, there is equal secondary ion current on the two split plates. If the potential is not zero, then one plate will receive more current than the other. In operation the signals from the two plates are digitized and stored in the computer. After the pulse, the data is processed to give the sum of the two split plate currents, s, which is proportional to $nF(T_e)$ and the difference which is proportional to ϕ. The digitizing rate is 1 MHz and the signals are analog filter at 250 kHz to prevent aliasing.

Typical auto power spectra for the sum and space potential fluctuations and the coherence and phase between the two signals are shown in Figure 1. The dashed lines indicate the 66% confidence intervals. These spectra were generated from a 2 msec time series starting 3 msec after plasma formation. Data was taken throughout the plasma pulse but

there was no significant variation of the fluctuation spectra with time. The amplitude of the fluctuations decreases slowly with time which reduces the coherence between the two signals late in the pulse.

Only one spatial location was observed on a given plasma pulse but measurements were carried out over the whole plasma cross-sections on succeeding pulses. To within the accuracy of the measurements, there was no variation in the fluctuation spectra with polodial angle. The orientation of the sample volume changes as the observation point is moved through the plasma. At some locations, the small characteristic dimension of the sample volume (0.1 cm) is oriented radially and at other locations it is essentially polodial. This did not cause a noticeable difference in the observed fluctuation spectra. The amplitude of the sum signal decreased with radius in such a manner that $\tilde{s}/\langle s \rangle$ remained constant. The amplitude of the space potential fluctuations showed very little radial dependence. Normalization of the space potential fluctuation amplitude to the electron temperature results in strong peaking at the outer edge of the plasma. This is due entirely to the decrease in electron temperature with radius. If on the other hand $\tilde{\phi}$ is normalized to the average value of the space potential $\langle \phi \rangle$, which is not a strong function of radius, then there is no apparent radial variation. It should be noted that the plasma radius for this set of measurements was approximately 7 cm and there were strong spatial gradients throughout the plasma.

Figure 1 shows that there is a weak low frequency ($\sim$30 kHz) coherent oscillation in the space potential (suspected to be a Mirnov oscillation) which is not present in the sum signal. This results in a reduction in the coherency between the two signals below 50 kHz and large uncertainty in determining the phase angle. Above 50 kHz, however, the coherency is approximately 0.65 and the phase angle is well defined. The phase difference is approximately -30° for all frequencies indicating that the intensity fluctuation lags the space potential. The fluctuation induced radial flux is given by

$$\Gamma = \frac{k_\theta \gamma \tilde{\phi} \tilde{s} \sin \alpha}{B} \tag{1}$$

where k_θ is the polodial wave number, γ is the coherency between the two signals and α is the phase difference.[1] Since only single point measurements were carried out, no information is available regarding the k spectra. We can, however, obtain an estimate of the lower limit of the flux by assuming that all fluctuations are m = 1 mode thereby replacing k_θ with 1/r. The flux represented by Eq. 1 is for the quantity s or $nF(T_e)$. For the conditions in RENTOR $F(T_e)$ is proportional to T_e, so that Eq. 1 gives the flux of nT_e. The present measurements do not permit separate evaluation of $\tilde{n}$ and $\tilde{T}_e$ but it is possible to consider some limiting conditions. If we assume that the fluctuations in the sum signal are entirely due to density fluctuations, then it is possible to evaluate an effective particle diffusion coefficient. This yields a diffusion coefficient of 4×10^4 cm^2 sec, which is about 4 orders of magnitude larger than neoclassical and is approximately equal to Bohm. If on the other hand we assume that the fluctuations are entirely due to temperature fluctuations then it is possible to evaluate an effective thermal conductivity coefficient. This assumption gives a conductive coefficient of $\sim 10^{17}$/cm sec which is about 3 orders of magnitude larger than neoclassical.

The present series of measurements clearly establish that the turbulent fluctuation spectra can cause particle or thermal transport that is orders of magnitude larger than neoclassical predictions. The lack of information on the k spectra and the inability to separately evaluate $\tilde{n}$ and $\tilde{T}_e$ prevent accurate quantitative evaluation of the enhanced particle diffusion and thermal conductive coefficients. A new series of experiments are being planned that will provide simultaneous multi-point measurements and also simultaneous measurements of both 2^+ and 3^+ secondary ions. This will permit evaluation of both the k and w spectra and separate evaluation of $\tilde{n}$ and $\tilde{T}_e$.

1. E. J. Powers, Nucl. Fusion 14, 749 (1974)

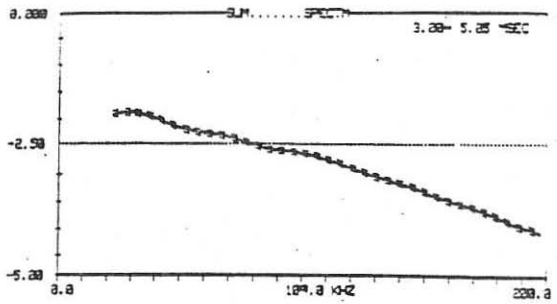

Fig. 1a. Auto power spectrum for the intensity fluctuations.

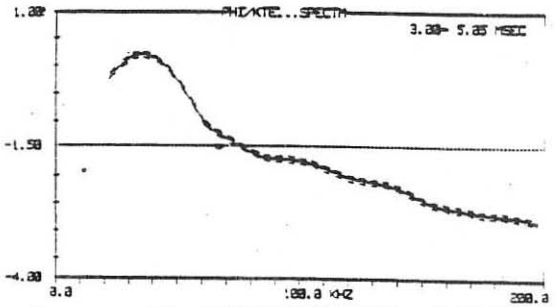

Fig. 1b. Auto power spectrum for the space potential fluctuations.

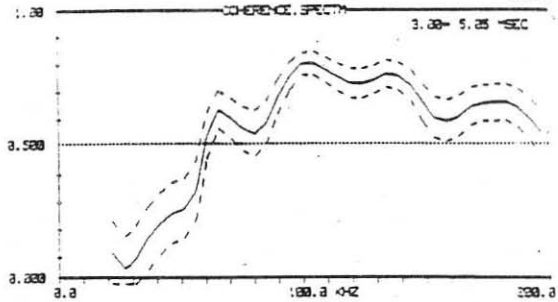

Fig. 1c. Conerence between the intensity and space potential fluctuations.

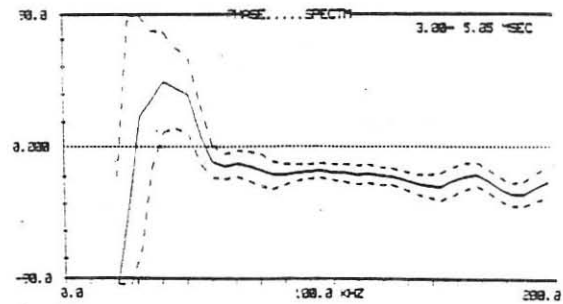

Fig. 1d. The pnase difference between the intensity and space potential fluctuations.

DENSITY FLUCTUATIONS MEASUREMENT ON FT TOKAMAK BY SMALL ANGLE CO_2 SCATTERING

P. De Simone, D. Frigione, F. Orsitto

Associazione EURATOM-ENEA sulla Fusione, Centro Ricerche Energia Frascati, C.P. 65 - 00044 Frascati, Rome, Italy

I. INTRODUCTION

The understanding of the loss mechanisms related to the anomalous transport in Tokamaks requires, among other, the study of density fluctuations with wavelengths much smaller than the plasma minor radius, usually denoted as microinstabilities [1]. Collective scattering of laser or microwave radiation is usually employed for such investigations [2,3].

Drift waves [1] are considered to be the most favourite candidate for explaining the anomalous energy and particle diffusion: these modes have frequency of about 100 kHz and wavelength of few millimiters for typical tokamak regimes. Many experiments [3] have found a strong activity in this range, indicating also that the observed fluctuations are to be described as a turbulence rather than as a superposition of linear modes.

In this paper we present the results obtained on FT (R=83 cm, a=20cm, B_T=40÷80 kG, T_e=1 keV, $n_e \sim 10^{14}$ cm^{-3}) by a small angle CO_2 (10.6 μm) scattering experiment: measured fluctuations have an average relative level of 1÷6%, wavelengths of 1÷5 mm and frequency spectra extending up to few hundred kilohertz.

II. RELEVANT SCATTERING THEORY

Figure 1 sketches a typical scattering experiment employing coherent detection: two gaussian beams, the incident and antenna beam, the latter obtained as a virtual image of the local oscillator, cross at their waists in a plasma described by a fluctuating electron density $\tilde{n}(r,t)$.

When propagating along the z axis each beam has the usual amplitude profile $u_{i,a}=\exp[-(x^2+y^2/w^2]$: taking account of the beam orientation shown in Fig. 1, the scattering volume is identified by the spatial weighting function

$$U(r) = u_i u_a = \exp\left[-\frac{2}{w^2}\left(x^2 + y^2 + \frac{\theta^2}{4} z^2\right)\right] \qquad (1)$$

The photocurrent power spectrum, due to the beating between the local oscillator and the radiation scattered along the antenna beam is given by

$$P(\omega) = \left(\frac{c}{4\pi} E_i E_a r_o \lambda_i R\right)^2 V[S_{u,T}(K_\Delta,\omega) + S_{u,T}(-K_\Delta,\omega)] \qquad (2)$$

where $E_{i,a}$ are the incident and antenna beam electric field amplitude, r_o the

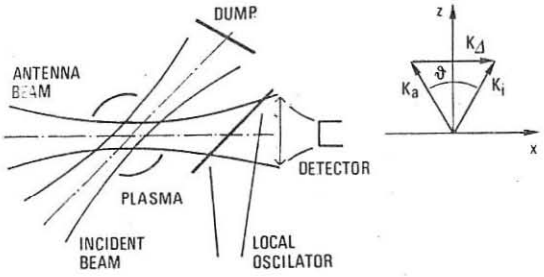

Fig. 1 - Schematic of a scattering experiment employing coherent detection.

classical electron radius, R the detector responsivity and λ the incident wavelength. $S_{u,T}(K;\omega)$ is the form factor relative to the volume $V = \int d^3r\, U(r)^2$ and time interval T, defined by

$$S_{u,T}(K,\omega)=|\tilde{n}_{u,T}(K,\omega)|^2/VT \tag{3}$$

where

$$\tilde{n}_{u,T}(K,\omega) = \int_T dt\, e^{-j\omega t} \int d^3r\, e^{-j\underline{k}\cdot\underline{r}}\, U(\underline{r})\, \tilde{n}(\underline{r},t) \tag{4}$$

Equation (2) shows that the measured quantity $P_s(\omega)$ gives directly the form factor or fluctuation spectral density at the $\underline{k}$-vector imposed by the scattering geometry. Furthermore, an integration of experimental points leads to the total fluctuation level defined as

$$\langle\tilde{n}^2\rangle = \frac{1}{VT} \int dt \int d^3r\, U^2(r)\, |\tilde{n}(r,t)|^2 = (2\pi)^{-4} \int d\omega \int d^3K\; S_{u,T}(K,\omega) \tag{5}$$

III. EXPERIMENTAL SET-UP

The output of a PL4 Edimburgh Instr. Ltd. Laser, working on TEM_{00} mode is focused by a concave mirror into the plasma with a beam waist ($1/e^2$ intensity point) of 5 mm and a total power of 1.5 W. Before entering the machine a portion of the beam is splitted and sent to the detector to form the local oscillator field (~ 100 mW). Apart from mirrors, which are copper made, any optical element is of Zinc Selenide, thus allowing the use of a He-Ne beam for the alignement procedure.

The receiver is composed by a SBRC Cu-Ge mixer working at 4.2 °K, followed by a low noise amplifier operating in the range 30-1600 kHz. The homodyne detection system for power spectrum measurement is completed by a HP spectrum analyser. A typical value for the scattered power is $P_S \sim 10^{-10}$ W/Hz at 100 kHz and 12 cm^{-1} while the detection system noise equivalent power is $NEP \sim 10^{-17}$ W/Hz. The signal to noise ratio is 40÷80 depending on the frequency resolution (30÷100 kHz). The scattering volume is vertically limited by the plasma size while horizontally has a diameter of 5 mm this corresponding to K resolution $\Delta K_{OR}=4$ cm^{-1} $\Delta K_{VER}=0.2$ cm^{-1}.

IV. RESULTS AND DISCUSSION

We have investigated the turbulent density spectrum in a K range 12÷60 cm^{-1} over the frequency interval 30÷1600 kHz, along a vertical chord posi-

tioned at 16 cm from the plasma center towards the external region (x/a=0.8). The frequency dependence of the form factor is shown in Fig. 2: experimental points are fitted with zero centered gaussian curves and normalized to their maximum. Data show a significant change of spectral widths when going from 12 to 24 cm^{-1}, while only differences within experimental errors are seen for different toroidal fields. In order to investigate the roll-off slope, we have reported the same data in a log-log scale: the high frequency points are fitted by lines representing a relationship $S(\omega) \sim \omega^{-n_\omega}$ with $n_\omega = 3 \div 4$.

Frequency integrated K spectrum, has been investigated over a wider K-range for 40 kG discharges (Fig. 3): a slope $n_k = 4.5$ is obtained for this shots. Both n_ω and n_k fall in the same range as already reported in literature, under many different plasma conditions [5-8]: such circumstance could be explained by the presence of a turbulence whose final state is independent from the driving mechanism. A dimensional analysis, similar to that made for

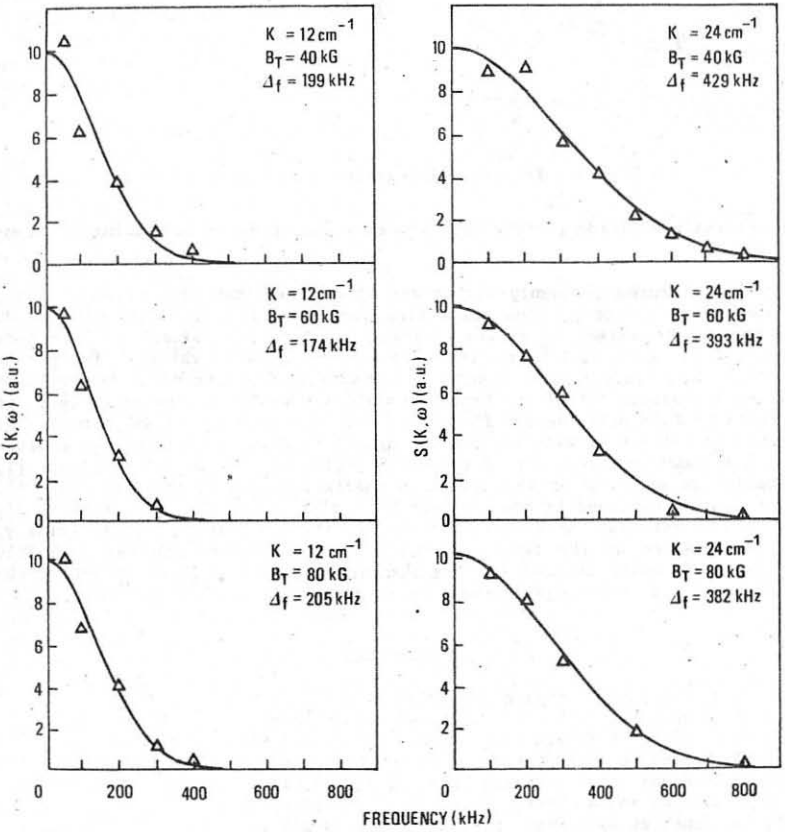

Fig. 2 - Form factor vs frequency Δf is taken at 1/e point.

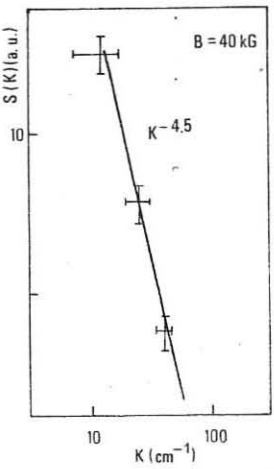

Fig. 3 - Frequency integrated form factor vs K.

uncompressible fluids gives a dipendence of the spectrum of the kind K^{-5}, ω^{-5} [8,9].

The measured frequency widths are about 3÷4 times the maximum value of diamagnetic frequency, thus indicating that spectral broadening is not due to the finite extention of the scattering volume. An estimate of the total fluctuation level $\langle \tilde{n}^2 \rangle^{1/2}/\langle n \rangle$ leads to the approximate value of few percent (1-6%). This calculation assumes a isotropic K-spectrum in the poloidal plane. A gaussian fit of the K-spectrum gives a width K=20 cm^{-1}: being L_n the density profile scale length (5 cm at $r/a=0.8$) one obtains $1/KL_n = 0.01$. This result is consistent with the scaling $\tilde{n}/n \sim 1/KL_n$ usually employed for evaluating the order of magnitude of the density fluctuations saturation level [1]. Finally, an estimate of the diffusion coefficient due to the microinstabilities may be obtained by the formula $D_\perp \sim \gamma/K^2$ where γ,K are, respectively, the growth rate and the K-vector of the density fluctuation [1]. Assuming γ,K to be measured by the frequency and K spectral widths one has $D_\perp = 3.7 \times 10^3$ cm^2/s which could account for the observed losses. It is worth noting that such number is to be regarded only as an order of magnitude estimate.

REFERENCES

[1] W.M. Tang, Nucl. Fusion 18 (1978) 1089
[2] E. Mazzucato, Phys. Rev. Lett. 48 (1982) 1828
[3] C.M. Surko, R.E. Slusher, Science 221 (1983) 817
[4] E. Holzhauer, J.H. Massig, Plasma Phys. 20 (1978) 867
[5] D.E. Evans et al., Plasma Phys. 25 (1983) 617
[6] TFR Group and A. Truc, Plasma Phys. 26 (1984) 1045
[7] A. Semet et al., Phys. Rev. Lett. 45 (1980) 445
[8] M. Okabayashi, V. Arunasalam, Nucl. Fus. 17/3 (1977) 497
[9] F.F. Chen, Phys. Rev. Lett. 15 (1965) 381.

STUDIES OF EDGE PHENOMENA IN JET WITH VISIBLE SPECTROSCOPY

P G Carolan*, M J Forrest*, N C Hawkes* and N J Peacock*
JET Joint Undertaking, Abingdon, Oxon OX14 3EA, UK
*Culham Laboratory, Abingdon, Oxon OX14 3DB, UK
(EURATOM/UKAEA Fusion Association)

INTRODUCTION

Visible spectroscopy affords an effective means of studying edge phenomena in JET, by monitoring the behaviour of lowly ionised or neutral states. Here we report on the following edge related topics. (a) effect of RF heating on minority species; (b) MARFES, and (c) Zeeman splitting of impurity lines.

The experimental arrangement is shown in Fig.1. Light from a tangential chord viewing a carbon limiter is coupled by 120 metres of high transmission 1 mm quartz fibre to a Czerny-Turner spectrometer. A calibrated Optical Multichannel Analyser (OMA) samples 16 nm increments of the output spectrum with a resolution of 0.03 nm and a variable time resolution (set to 196 ms). The available spectral range has been surveyed and the main impurities identified. Impurity atoms and ions of the usual impurities such as O, C, Cr with multiplets conveniently close to the Balmer Series are routinely monitored. The survey aspect of the diagnostic is particularly valuable however in detecting unexpected elements or unforeseen plasma or impurity behaviour.

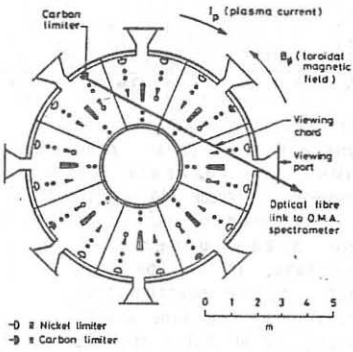

Fig.1 The tangential viewing optics arrangement in JET which obtains a clear view of the carbon limiter.

RESULTS

(a) Effect of RF Heating on the Plasma Edge

RF heating power on JET is coupled to the plasma by minority heating of H or ^{3}He. Extensive line shape studies have been made of the HeII 468.5 nm line before and during the RF heating pulses. Because there is a significant change in the HeII line shape during high power RF injection, it is possible to evaluate edge plasma heating for a wide range of launched powers and for the various antennae configurations. The analysis is based on a two gaussian best fit programme used after the observed spectral line has been deconvolved using the measured instrumental function. Figure 2a and 2b, show two gaussian fits for the 468.5 nm line before and during RF heating which combined a dipole 0.7 MW, and a monopole 1.75 MW into a 2.8 MA plasma. In each case the two gaussians represent a family of gaussians associated with a cold outer edge region and a hotter zone a few cm inside. The outer zone remains cold (80 eV) before and during RF, presumably because of the heat sink effect of

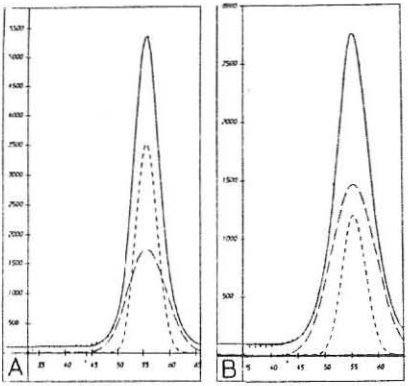

Fig.2 Two Gaussian fits on the HeII 468.5 nm line for (A) before the RF amd (B) during the heating pulse. The solid line is the sum of the two gaussians fitted on the data points while the long and short dashed curves are the 'hot' and 'cold' individual Gaussians components. The offset between the data curve and the two Gaussians has been added for clarity.

effect of the limiters. In contrast the 'hot' zone shows an increase of temperature from 244 eV to 310 eV. From inspection of the areas under the gaussians, it can be seen that before heating they are roughly the same whilst during the RF pulse the hot component is three times that ascribed to the cold edge.

The effect of RF power from the dipole (2.75MW) and then the monopole (2.64MW) antennae in the same plasma shot (3.4T 4MA) is shown in Fig.3. In this example the two gaussian fit reveals an outer layer around 100 eV before and during the pulse - the hotter inner layer remains around 400 eV until the monopole pulse is applied when it increases to ≈ 550eV. The dipole which was switched on 1 second earlier has little effect.

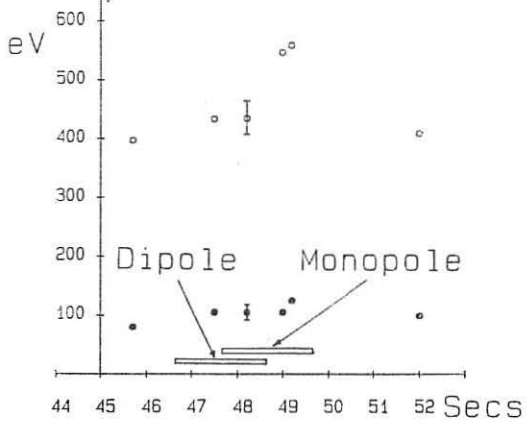

Fig.3 Variation of temperature in the outer edge (filled circles) and hotter inner zone (open circles) for times that span pre RF, dipole emission (D), monopole emission (M) and post RF.

Transport codes indicate that HeII would only exist for a few cm inside the plasma boundary, therefore our measurements show considerable increases in edge temperature for some antenna configuration. The evaluation of the effect of antenna geometry on edge heating is an ongoing study. The results described are for two RF heating experiments and are given to illustrate the value of line shape analysis to determine temperatures in an area normally difficult to diagnose.

(b) MARFES

A MARFE, first reported in Alcator[1] is currently conceived as a toroidally symmetric but poloidally asymmetric band of enhanced radiation - apparently peculiar to tokamaks. MARFE's in JET are characterised by rapid changes in the line emission from low ionisation states of low Z impurities, accompanied by an increase in the n_e and the bolometer signal on the inner edge of the plasma. These are discussed at length [2](this conference) the results in this section represent additional material.

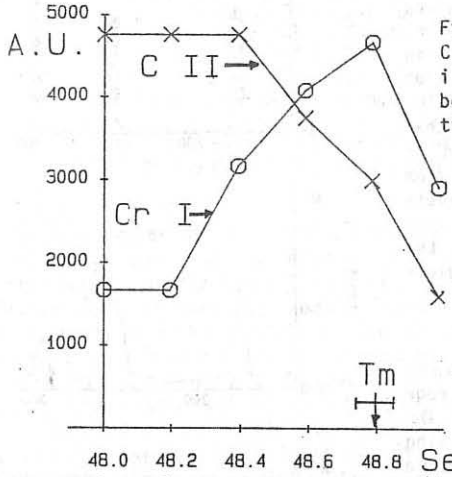

Fig.4 Time history of CII and CrI line intensities illustrating precursor behaviour relative to the MARFE time T_m.

The references[e.g.1] report no change in T_e or radiation in the central plasma or in the outer edge. Our findings are contrary to the latter, in that significant changes in the line emission from the plasma in close proximity to the limiter are observed. From comparisons with other lines of sight it has been determined that the tangential viewing chord employed is dominated by limiter rather than wall effects (see next section). Figure 4 shows a time sequence in 200 ms steps illustrating a characteristic drop in CII intensity. The MARFE time as detected by the inboard n_e interferometer channel is indicated. Within the limits of our timing accuracy ± 50 ms it appears that MARFES are signalled some 200 ms earlier by changes in the outer edge emission than by the inner edge interferometer channel. This effect is corroborated by a vertically viewing optical fibre, with photomultiplier detection, which show changes in H_α and CIII intensity some 50 ms after outer edge changes. There is also evidence that the drop in edge CII intensity is preceded by a two fold increase in the Cr influx by some 200 ms, but it is unlikely that this would have a significant effect on the plasma edge behaviour.

(c) Zeeman Splitting

To date Zeeman splitting of the spectral lines HI (6563), CII (5132.9, 5133.3, 5146, 5151, 6578 and 6583), CIII (4794, 4810 and 4819) and Cr I (4254, 4274 and 4289) has been observed[3] in the JET plasma. A representative time sequence of spectra is illustrated in Fig.5 for the CIII triplet at the

termination phase of a discharge. The observations are of particular importance in determining the sources of impurity influx since the location of the emitting regions can be determined from the magnitude of the splitting and the known toroidal field distribution. Localisation of the impurities has been determined at the limiters and at the inside plasma periphery both at the setting up and termination phases. The source of impurities which show Zeeman splitting depends on the initial time history of the plasma profile and the plasma excursions or expansion during termination. The Chlorine spectrum shown in Fig.5 located the influx region at the inner periphery thus showing that the plasma vessel, rather than the limiters, was contaminated at this time (these results were from a discharge which had relatively high Cl influx that was later substantially reduced with the consequent reduction to negligible levels of the line intensities.)

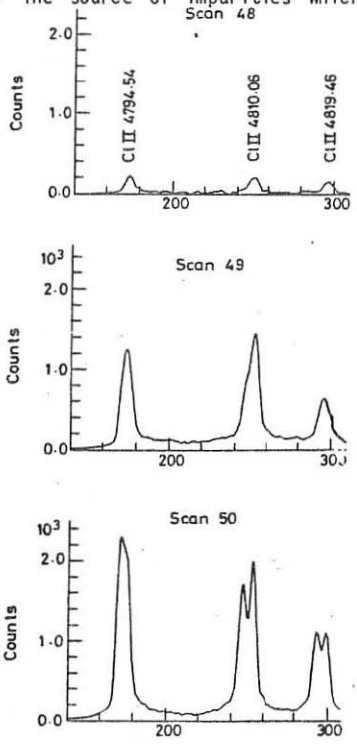

Fig.5 A time sequence in 196 ms increments for the Cl II triplet at the termination of the JET discharge. The Zeeman splitting on the third frame indicated the influx of Cl was from the inner wall.

CONCLUSIONS

Visible spectroscopic observations of the JET plasma edge shows significant heating in the edge vicinity during rf heating (for certain antenna configurations), they detect MARFE behaviour before changes in n_e are seen and the source of impurity influxes are localised from Zeeman splitting.

ACKNOWLEDGEMENTS

The authors wish to thank the whole JET operational team for their support, but in particular Drs K H Behringer, P D Morgan, M F Stamp and W W Engelhardt.

REFERENCES

1. B Lipschultz, B LaBombard et al, Nucl Fus 24 No.8 (1984) 997.
2. J O'Rourke et al Paper 190 this conference.
3. P G Carolan, M J Forrest, N J Peacock and D L Trotman, JET preprint JET-P(85)05, accepted for publication in Plasma Phys and Cont Fusion.

CHARGE EXCHANGE RECOMBINATION SPECTROSCOPY OF ASDEX

P G Carolan, B P Duval*, A R Field+, S J Fielding, N C Hawkes and N J Peacock
Culham Laboratory, Abingdon OX14 3DB, UK
(Euratom/UKAEA Fusion Association)

G Fussman, G Janeschitz and F Söldner
Max Planck Institut für Plasmaphysik
Euratom Association D-8046 Garching, Germany

K H Behringer
JET Joint Undertaking, Abingdon, Oxon, OX14, 3EA UK

*Attached Clarendon Laboratory, University of Oxford.
+Attached Royal Holloway College, University of London.

INTRODUCTION

In this paper we report on experiments and theoretical predictions relating to the spectroscopic observations of charge exchange (C/X) processes occurring between highly ionised impurities in the core of tokamak devices and high power beams of energetic neutral atoms. Our goals were to calibrate a Vacuum Ultraviolet (VUV) spectrometer and to show that fibre optically transmitted visible C/X radiation could be used to diagnose remotely tokamaks up to and including the crucial active phase. The diagnostic potential of these C/X lines has been emphasised in recent years, and has been recently reviewed (Fonck, 1984 and Isler, 1985). Our observations cover emission from hydrogenic ions in both the VUV and the visible, and we have developed a computer code to model the experimental data. This is based on calculated cross sections for charge exchange into the $[n,\ell]$ resolved quantum levels and the subsequent cascade radiative decay.

VISIBLE SPECTROSCOPY

A 1m Czerny-Turner visible spectrometer viewed the plasma via a quartz window as indicated in Figure 1. This line of sight observes the interaction of one injector beam with half the plasma cross section - a region where the beam attenuation is small (<20%). For survey work it was operated with a PARC Optical Multichannel Analyser (OMA). For faster time measurements a spectrometer fitted with a photomultiplier detector sampled at 100 μs intervals was used. The spectrometer was equipped with gratings of 1200 and 2160 lines/mm, giving dispersions of 0.2Å/OMA-pixel and 0.05 (second order) Å/OMA pixel respectively.

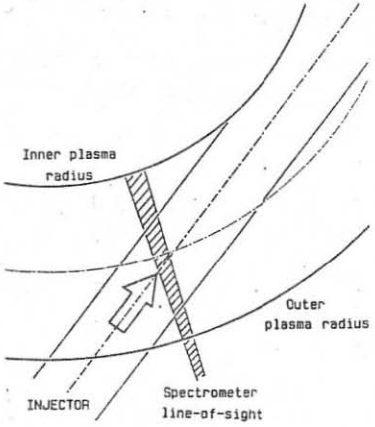

Fig.1 Arrangement of spectrometer line of sight intersecting injector beam.

C/X excited transitions were observed from Hydrogen-like Helium, Carbon, Oxygen, Fluorine, Sulphur and Chlorine. Several lines that bear the C/X signature of very rapid fall off of intensity with the end of injection are as yet unidentified. Figure 2 shows radiation from C, O, and S before and during injection. Of all the C/X lines only the C line was present before injection, but was much stronger during injection.

Least squares fitting a Gaussian to the C line gave ion temperatures of 250 eV before injection but during injection we measured ion temperatures of 750 eV from C and ~1.5 keV from O and S, the reason for this difference is not understood.

Observations of the Doppler shift of the C/X lines yielded bulk rotational velocities of 1-2 x 10^{+5} m/s in the co-injected (beam-driven) direction. In the case of the C line, its appearance before injection provided a convenient wavelength reference.

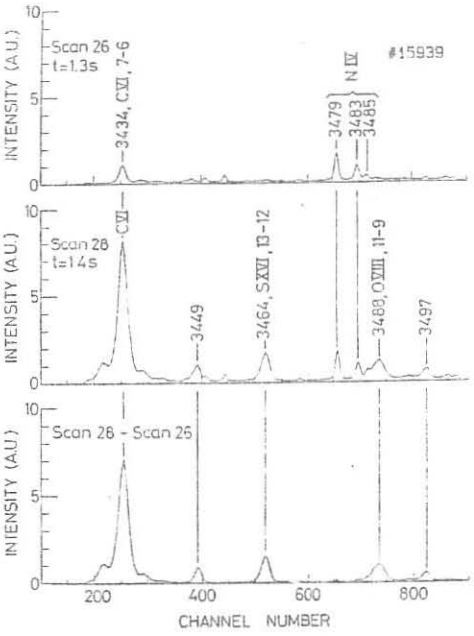

Fig.2 Visible spectrum 3400-3500Å, before injection (at 1.3s), during injection (at 1.4s) and the result of subtracting the spectrum at 1.3s from that at 1.4s (to remove all but the charge exchange features).

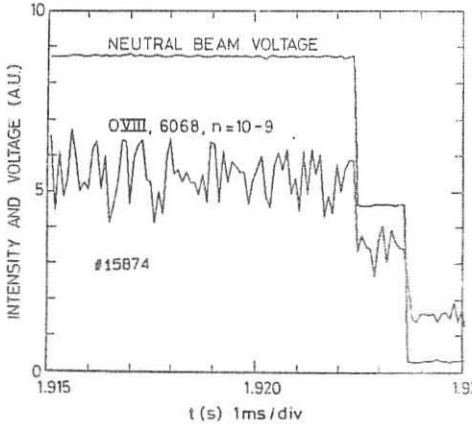

The time histories of the visible $\Delta n=1$ transitions of O and C were examined with the photomultiplier. Figure 3 shows the time history of the OVIII n=10-9 line at the end of injection. The double step in the figure is due to the two

Fig.3 OVIII n=10-9 C/X line intensity fall off at the end of injection. (Neutral Beam Voltage refers to the sum of the voltages across each of two sources in the beam line, and is equivalent to total beam current).

sources in the neutral beam switching off at slightly different times. The line intensity falls off rapidly with the switch off of the two sources. This drop in intensity is far faster than any changes in the ionisation balance, which would be expected to occur on a timescale of about 1 ms. The step change in intensity is a measure of the C/X contribution to the line intensity, since the C/X excitation process turns off on a timescale much shorter than 100 μs.

For the accurate calculation of C/X line intensities needed for calibration of the VUV instrument, it was necessary to measure the fraction of beam power at each energy. This was done (following Fielding, 1981) by injecting the beams into the torus, when filled with neutral gas, and observing the Doppler shifted components of H_α light corresponding to the different beam neutral velocities. This yielded a power ratio of 40%:40%:20% at energies E, E/2 and E/3 (where E is the primary beam energy component of 42keV).

VACUUM ULTRAVIOLET MEASUREMENTS

A vacuum ultraviolet spectrometer (Fonck, 1982) covering the wavelength range 100-1700Å (with modest resolution ~2Å) viewed the plasma radially, at the same position as the visible instrument in Figure 1. The spectrometer was equipped with a multichannel detector consisting of a microchannelplate intensifier coupled to an OMA of the same type as used on the visible spectrometer above.

The important C/X lines were identified by scanning the entire spectrum, which could be achieved once every 16 ms. Figure 4 shows half a survey spectrum during beam injection. This clearly illustrates the strong C/X lines, which have negligible intensity before and after injection.

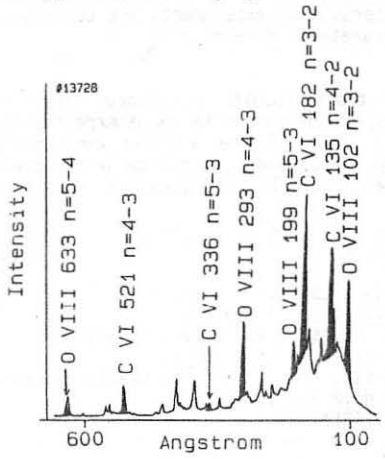

Fig.4 Portion of VUV spectrum showing the strong C/X lines.

The C/X line intensities could be recorded once every 1-2ms by restricting the detector to scan only specific parts of the spectrum. However the fall off time of the C/X line intensity at the end of injection was still detector limited. Previous observation of these lines in DITE (Duval, 1985) and observations of C/X lines in the visible (discussed earlier in this paper) give us confidence that the fall off time is actually less than 100μs. Despite the relatively poor temporal response of the detector, the time behaviour of these lines is seen to be markedly different from that of the resonance lines in the spectrum. This difference is due to the fact that the resonance lines apparently take many ionisation times to respond to the neutral beam switch-off, while the C/X line intensities change within one scan time of the detector.

The relative sensitivity of the spectrometer as a function of wavelength was derived using the theoretically modelled excitation cross sections of the C/X transitions, (Isler, 1985). (To this end Olson (1985, 1981) has calculated the C/X cross sections at 42 keV into $[n,\ell]$ levels up to n=12, and n=14 for Carbon and Oxygen respectively.) The results obtained were consistent with a spectrometer sensitivity calibration constructed piecemeal from line ratios observed in JET discharges, and with that of the prototype spectrometer, SPRED. The absolute sensitivity of the spectrometer was established at wavelengths above 1100Å by reference to a calibrated deuterium discharge lamp.

The spectrometer, now absolutely calibrated, was used to make two measurements of impurity concentrations. Firstly, the concentrations of Carbon and Oxygen were calculated using a code for beam decay and impurity excitation rates and the measured volume emissivities of the C/X transitions, this gave typical impurity levels of 2%. A second measurement of impurity concentration was made using a 1-D transport model (Denne, 1985) and line emission from lower ionisation states during the ohmic part of the discharge. The latter measurement gave a rather lower figure for the concentrations of the impurities (about half). It is to be expected that the impurity content of the plasma during injection should be higher than during the ohmic phase.

CONCLUSIONS

Our experiments in the VUV have borne out calculations of C/X line intensities for the 42 keV primary neutral energy of the ASDEX injectors, and enabled us to calibrate a VUV spectrometer. The time histories of the visible signals confirm them as being C/X in origin. Our efforts are now aimed at correlating the observed intensities in the visible ($n \gtrsim 8$) with the VUV measurements ($n \lesssim 5$). From the VUV data, the impurity concentrations have been measured, and the visible data has given ion temperatures and bulk plasma velocities. The results appear encouraging regarding the use of visible instruments to derive important plasma parameters which previously required the use of close-coupled vacuum spectrometers. Our experiments are continuing in order to increase confidence in the theoretical models.

ACKNOWLEDGEMENTS

The authors wish to acknowledge the valuable assistance given by M Keilhacker and the ASDEX and Neutral Injection groups in these experiments. We are indebted to R C Isler (ORNL) who did much of the original work on the codes, and to R E Olson (Missouri-Rolla) for computing the high n C/X cross sections. The enthusiastic encouragement of W W Engelhardt (JET) is gratefully acknowledged.

REFERENCES

B Denne et al, this Conference.
B P Duval et al, Nucl Inst Methd, July Issue (1985).
S J Fielding and D Stork, Nuclear Fusion 22 No.5 617 (1982).
R J Fonck, A T Ramsey, R V Yelle, Applied Optics 21 No.12 2115 (1982).
R J Fonck, D S Darrow, K P Jaehnig, Phys Rev. A 29 No.6 (1984).
R C Isler, Nucl Inst Methd July Issue (1985). Proc. Conf. HIA (1984) Oxford.
R C Isler, R A Langley, Applied Optics 24 No.2 254 (1985).
R E Olson, Phys Rev. A 24 No.4 1726-1733 (1981).
R E Olson, Private communication (1985).

OPTICALLY PUMPED FIR LASERS AND TOKAMAK INTERFEROMETRY

J.S. Bakos and Zsuzsa Sörlei

Central Research Institute for Physics
H-1525 Budapest, P.O.Box 49, Hungary

Heterodyne laser interferometers are usually used in plasma density measurements of tokamaks because of the reduced sensitivity against intensity and frequency instability [1]. The increased requirement for time resolution and the use of appropriate but as short as possible wavelength to avoid beam refraction gives emphasises to the application of optically pumped lasers [2].

Namely the intermediary frequency of the interferometer i.e. the beat frequency of two lasers can be as large as some megahertz decreasing the time of one measurement below one microsecond. Furthermore the wavelength of the lasers can be changed easily choosing another pumping line [3].

The typical set-up of the FIR laser system for the interferometry can be seen in Fig. 1.

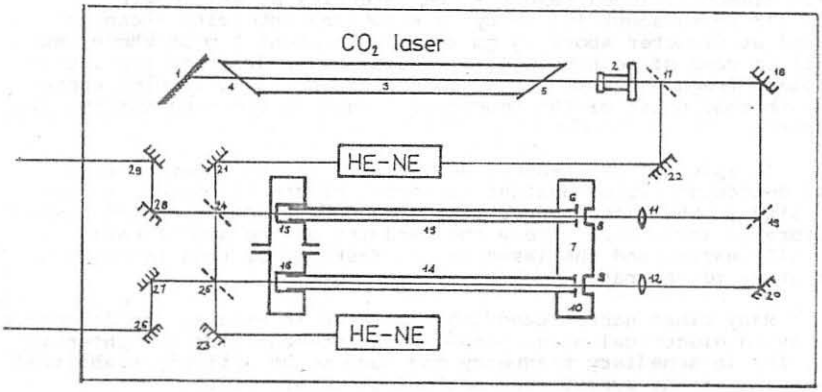

Fig. 1

Optically pumped FIR laser-system

1. Grating; 2. piezoceramy controlled output mirror; 3. discharge tube; 4,5. ZnSe Brewster windows; 6,10. gold-coated mirror with central hole; 7. vacuum chamber; 8,9. AR-coated ZnSe windows; 11,12. ZnSe lenses; 13,14. FIR cells; 15,16. FIR hybrid output mirror; 17. NaCl plate; 19. ZnSe beamsplitter; 18,20,21,22,23,26, 27,28,29. gold-coated folding mirrors; 24,25. mylar foils with dielectric coating for HeNe laser.

The cw CO_2 laser pumps the twin laser i.e. it pumps two FIR lasers. The difference between the frequencies of the two lasers is the intermediary frequency of the interferometer which is determined by the different lengths of the two resonators.

The molecular vapour in the cells in the FIR laser resonators is pumped longitudinally. The FIR beam emerges from the exit mirror which stops the pumping beam. For the most efficient pumping the interaction length has to be enlarged increasing the length of the cell. The best solution is the use of hybrid mirror reflecting the pumping beam and partially transmitting the FIR beam.

There is a trade off between two constructions of the hybrid mirror, namely between the capacitive mesh overcoated by multilayer dielectrics and the multilayer dielectric mirror overcoated by gold except the outcoupling center hole. The former gives more homogenous outcoupled beam without mode instability but worse reflexion at the pumping wavelength. The opposite is true for the last one. (Good result is observed - pure mode without instability and large intensity - for the mirror with hole of diameter 5 mm at 15 mm dia waveguide in case of methanol [4].) To have the largest mode volume consequently the largest intensity of the laser waveguide has to be used as the cell. There is a compromise in choosing the cell diameter because of the vibrational bottleneck and the waveguide loss.

The diffusion limited relaxation of the lower level determines the optimum pressure and therefore the intensity at definite cell diameter. (Good result - the intensity at wavelength λ = 118 μm is about 100 mW by 20 W pumping intensity - can be found at diameter about 15 mm and length about 1 m of the pyrex cell in case of methanol [4].) To avoid fast drift of the intermediary frequency symmetrical construction has to be used where the thermal drift of the resonator length is the same for the two lasers.

In spite of the reduced sensitivity of the interferometer and detection system against the drift of the frequency and intensity of the lasers invar stabilized construction of the resonators is advisable. Namely the bandwith of the amplification is usually narrow and the laser drifts fast out of this region and it stops to generate.

Many times narrow bandwith amplifier is used by the detectors to avoid electrical noise problems and to economise the intensity. The intermediary frequency may have to be actively stabilized in spite of the symmetrical mechanical construction.

The cw CO_2 pumping laser has to be of single mode with high output intensity and frequency tunable by grating and PZT transducer. The invar construction of the resonator and the stabilization of the working parameters (pressure, temperature, current, gas flow speed, etc.) is highly desirable. Namely the frequency of the FIR laser depends on the frequency of the pumping light

through the induced change of the index of refraction. Moreover the level of this dependence changes with the parameters of the FIR resonator [5].

Therefore the intermediary frequency also depends on the pumping offset. The up to date waveguide construction of the CO_2 laser gives already the same intensity as the common type laser but with far enlarged tuning range. Therefore the use of the waveguide laser is advisable to enlarge the frequency range of the FIR lasers too.

The lasers has to be set on rigid table so as to avoid vibrationally induced instabilities because of the feedback from the FIR lasers. The table can be made of granite where no difficulties arise because of eddy current induced by the time varying magnetic field of the tokamaks.

Among the different types of interferometers the Mach-Zender interferometers seems to be most advantegeous from the point of view of vibration compensation. But the experimental test on T-7 tokamak shows that occasional torsional vibrational motion destroys the vibrational compensation of the reference arm and the signal is half of that of the Michelson interferometer. Therefore the use of the Michelson type interferometer can be recommended. In case of large torsional vibration corner cube reflectors has to be used and the longitudinal vibration can be compensated by using second wavelength preferably in the visible region of the spectrum (λ=0.63 μm or λ=3.39 μm) of the HeNe Laser. In all the construction of the interferometers special care has to be given to avoid feedback problems (especially in the case of Michelson interferometer).

The detector of the FIR beam can be Li or Ga dopped germanium. The sensitivity of this detector is enough to use the FIR laser (100 mW intensity/cell) as the light source of the interferometer with just as many as nine chords.

The phase shift is usually measured digitally and the data acquisition is made by CAMAC system.

FIR laser and interferometer is constructed for the T-7 tokamak using the above described principles [4]. The results show that in case of large tokamaks inavitably two wavelength interferometer has to be used to avoid vibrational problems. The construction and the characteristics of the laser including the frequency stability and the intensity also is adequate for the density measurements also in many chords.

References

[1] D. Veron: Submillimeter Interferometry of High Density Plasmas
Infrared and Millimeter Waves
Edited by Kenneth J. Button
Academic Press 1979.

[2] S.M. Wolfe: Modulated Submillimeter Interferometer System for Plasma Density Measurements
Ph. D thesis MIT 1971

[3] Reviews of Infrared and Millimeter Waves
Editors K.J. Button, M. Inguscio, F. Strumia, Plenum Press New York, 1984.

[4] T.O. Ábrahám et al.: Heterodyne Submillimetric Laser Interferometer on T-7
3rd All-Union Conference of High Temperature Plasma-diagnostics, Dubna 1983.

[5] T.O. Ábrahám, J.S. Bakos, Zs. Sörlei, J. Tar: Frequency pulling in optically pumped FIR methanol laser
Infrared Physics Vol. 25. p. 77 1985.

A START-UP DISCHARGE PHASE IN A CASTOR TOKAMAK

Valovič M., Badalec J., Jakubka K., Kopecký V.,
Stöckel J., Žáček F.

Institute of Plasma Physics, Czechoslovak Academy of Sciences,
Pod vodárenskou věží 4, 182 11 Prague 8, Czechoslovakia

Abstract: It is shown experimentally, that during the inductive Tokamak breakdown strong overthermal plasma potential is generated. Simultaneously convective losses during the breakdown are measured. Mechanism of the losses and generation of electrostatic field is discussed.

Introduction: As is known, time delay between switching-on of the ohmic heating circuit and formation of the plasma with substantial density can be minimalized by a suitable external perpendicular magnetic field. During this time interval electron density rises due to avalanche ionization: $n_e \sim e^{\gamma t}$. Exponential rate is given by $\gamma = \beta - \tau^{-1}$, where lossless avalanche rate β is a known function [1] of reduced toroidal electric field E/n (n--filling atom density) and τ denotes loss time. During the avalanche a poloidal magnetic field is smaller than total perpendicular magnetic field $B_\perp$ (summ of external and stray fields). Several mechanisms of breakdown losses has been proposed. Geometrical electron losses [2] give $\tau = a/(v_D B_\perp / B_T)$, where $v_D = I_p/(\pi a^2 e n_e)$ is electron drift velocity, I_p - plasma current, a - plasma radius e-electron charge and B_T-toroidal magnetic field. Ambipolar toroidal drift for $B_\perp = v_D = 0$ leads to Bohm-like diffusion [3]. In the case $v_D = 0$, $B_\perp \neq 0$ and fully ionized plasma expression for τ is found in[4]. In [5] is considered breakdown between limiters as electrodes. Picture of the tokamak breakdown is not clear up to now. Present paper is a contribution to this problem.

Experiment: To investigate inductive breakdown we try to look simultaneously for losses and plasma potential. Measurements was performed on CASTOR tokamak with major radius R = 0.4m and plasma radius a = 85mm. Geometry of the experiment is shown on Fig.1. Net plasma current was measured by Rogowski coil inserted into

limiter shadow. Floating potential on the plasma edge was detected by a set of Langmuir probes. Toroidal magnetic field B_T=1.3T and filling hydrogen atom density $n=2.5\times10^{19}m^{-3}$ was held fixed. Dynamics of the breakdown for $B_\perp$= -1mT, vertically oriented, is shown on Fig. 2. Plasma current exponentially rises up to the breakdown value I_B, corresponding to the transition into the fully ionized plasma conductivity. During the exponential phase electron drift velocity changes slightly and so the plasma current is proportional to the electron density. Floating potentials U_{FL} rise to high values and then relaxe after formation of rotational transform. It indicates generation of perpendicular electrostatic field, antiparallel to the perpendicular magnetic field. Floating potential is large comparing with the probe sheath potential (electron temperature T_e= 10eV). Since peak value of electrostatic field is approximately the difference of the floating potentials of the opposite probes: $2aE_\perp = U_{FL}(1)-U_{FL}(2)$. Further, we changed perpendicular magnetic field both in vertical and horizontal directions in the interval $|B_\perp|$ = 0 - 2mT. Breakdown voltage rises with $|B_\perp|$ and is U_B= 20-36V. This interval corresponds to the electron drift velocity $v_D = (0.85\text{-}1.3)\times10^6$m/s and to the exponential rate $\beta = (0.95\text{-}1.5)\times10^5 s^{-1}$. On Fig. 3 is shown dependence of the electrostatic field, relative losses and breakdown current on $|B_\perp|$. A large scattering of points is caused by a space inhomogeneity and time modulation of magnetic field. Electrostatic field is proportional to $|B_\perp|$: $\vec{E}_\perp = -5\times10^3\vec{B}_\perp$[V/m, mT]. Losses λ are defined as the ratio of lost electrons to the all electrons born in the avalanche: $\lambda = 1 - \gamma/\beta$, where $\gamma = (1/I_p)\times(dI_p/dt)$. Losses are proportional to the magnetic field and reach more than 50%. Breakdown current is roughly independent on $B_\perp$. Corresponding electron density is $n_B = (1\text{-}2)\times10^{17}m^{-3}$.

Discussion: Observed electrostatic field is strongly overthermal $eE_\perp a \approx 60T_e$. Field is generated by a charge separation of electrons and ions (fixed). Velocities of gradient and centrifugal drifts are negligible and then plasma polarizes only due to directed flow of electrons along lines of force. Theoretically electrostatic field can rise up to the steady state value $E_\perp = B B_T/B_\perp$, when electron current vanishes. In experiment steady state is not reached because time of equilibration of space

charge $a/(v_D B_\perp/B_T) \approx 0.1$ms is comparable with the duration of the avalanche. Thus the value of electrostatic field in our experiment is about one half of value $ExB_T/B_\perp$.

Charge deficit is much more smaller than the relative losses:

$$\delta n_e/n_B \approx 2\varepsilon_0 E_\perp/(ea n_B) \approx 10^{-5} \ll \lambda$$

(ε_0 - vacuum permittivity), and then mechanism of individual escape of electrons [2] can not be accepted. Measured losses can be explained by $\vec{E} \times \vec{B}$ drift. If we assume homogeneous profiles for electrostatic field and electron density, the loss time is

$$\tau = (2/\pi) B_T a/E_\perp \approx 5 \times 10^{-5}\ s,$$

for $B_\perp = 1$mT. This value is in a good agreement with the time determined from the exponential rates: $\tau = (\beta\lambda)^{-1} = 2\times10^{-5}$s. It must be noted, that the rate of current rise γ may be partially affected by a "reverse" effect of electrostatic field.

Generally described mechanism can take place if the toroidal current exists but poloidal magnetic field does not yet prevail perpendicular one. Then it may appear in non-inductive current--rise experiments as well. Finally note that energy flow on the limiter is negligible during the breakdown (1kW comparing with 100 kW in the developed discharge in our experiment). But more danger rises from enhanced arcing probability due to the large plasma potential.

References:

[1] Buffa A. et al.: Phys. Rev. A3 (1971) 955

[2] Papoular R.: Nucl. Fusion 16(1976) 37
Prinzler H. et al.: Czech.J.Phys. B34(1984) 665

[3] Abramov V.A. et al.: Fizika Plazmy 1(1975) 536

[4] Parail V.V. et al.: in Plasma Phys. and Contr. Nucl. Fusion Res. (Proc. 10th Int. Conf. London 1984), Vol. 1, IAEA Vienna (1985) 605

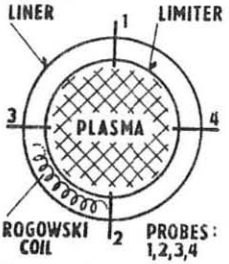

Fig.1: Geometry of the experiment.

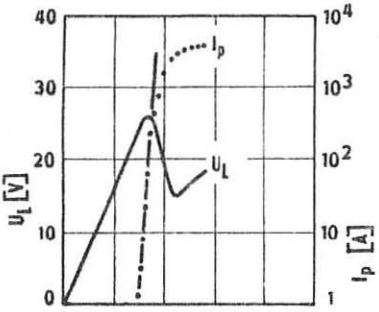

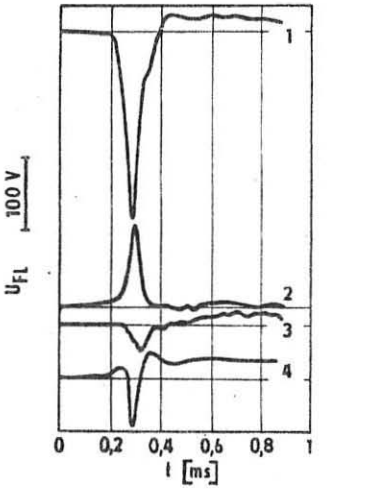

Fig.2: Temporal evolution of loop voltage U_L, plasma current I_p (logarithmic scale) and floating potentials U_{FL}. Numbers 1-4 refers to the probes on Fig.1 .

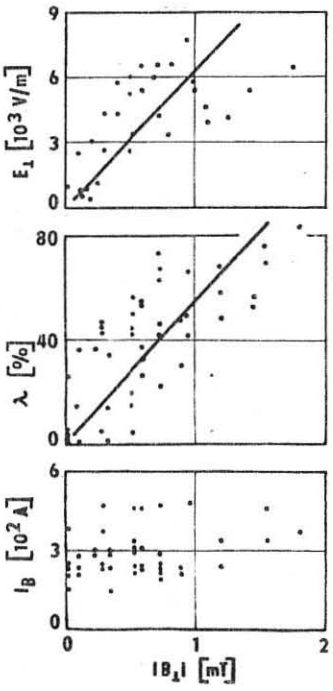

Fig.3: Dependence of electrostatic field, losses and breakdown current on perpendicular magnetic field.

Transport Analysis for Current Build-Up in ASDEX and JET

O. Gruber, K. Lackner, R. Wunderlich
Max-Planck-Institut für Plasmaphysik, EURATOM Association,
D-8046 Garching, Fed. Rep. of Germany

Abstract

Neoclassical resistivity describes the current penetration for MHD stable current ramp-up in ASDEX with $\dot{I} \leq 1$ MA/s showing monotonously increasing q(r) profiles during current rise. Simulations for JET yield the same current ramp rates, bute these can be increased by a factor of 3 if the current is ramped up together with the toroidal field.

1. Introduction

In a tokamak discharge MHD activity increases with increasing rate of current rise and finally disruptions occur. On the other hand, lowering the current ramp rates leads for large experiments like JET to current rise times amounting to a large fraction of the main field pulse duration.

Experiments on current ramp rates in ASDEX /1/ showed that for current rises below 1 MA/s MHD activity could be avoided. But too strong gas puffing during current rise leads also to hard disruptions of the high density limit type. In the present paper the current start up phase of ASDEX is analyzed, and optimum current build-up scenarios for JET are developed and simulated numerically with the 1d-Baldur transport code /2/.

2. Current Build-Up in ASDEX

In standard operation the plasma current I in ASDEX is ramped up in two stages. Up to a current between 50 and 100 kA the initial current rise is rapid with $1.5 < \dot{I} < 3$ MA/s, and then a much slower one follows with $\dot{I} \leq 1$ MA/s to reach 300 to 450 kA. Electron temperature T_e (ECE, Thomson scattering) and density n_e (HCN-interferometry) measurements show rather flat radial profiles at the beginning of the discharge peaking up towards the end of the current rise. Using the time development of these measured profiles together with the loop voltage, β_p and l_i the current ramp has been

simulated with the Baldur transport code and neoclassical resistivity. Anomalous electron thermal diffusivity in the form $\chi_e = \frac{3.4 \cdot 10^{15}\ B_t\ a/R}{n_e 0.8\ T_e\ q}$ [m²/s, T, m^{-3}, keV], a particle diffusion coefficient $D = 0.2\,\chi_e$ and an inward drift velocity $v = \frac{3r^2}{a^3} \cdot D$ are taken /3/. As impurities the species iron (produced by a sputtering model) and oxygen (influx is varied to get the measured Z_{eff} and the bolometrically measured radiation losses) are taken into account using a noncoronal diffusion model /4/. The simulations start typically 10 ms after the discharge has started with an I of 30 to 50 kA. The measured T_e and n_e profile evolutions are obtained as well as the onset time of sawtooth activity which is taken from the calculations as the time when $q(o) = 1$ is reached (see Fig. 1). No hollow $T_e(r)$ or toroidal current density $j(r)$ profiles are found and the $q(r)$ profiles are monotonously increasing towards the boundary. Increasing the current ramp rate above 1 MA/s after the first rapid rise yields skin currents and nonmonotonous q-profiles, which can be unstable to double tearing modes /5/.

The electron density rise is kept below $\dot{\bar{n}}_e = 1.5 \cdot 10^{20}\ m^{-3}\ s^{-1}$, but has to be even lower for dirty discharges. Increasing the density rise above that limit for $\dot{I} = 1$ MA/s leads to hollow density profiles in the simulations which seem to be vulnerable for density limit disruptions. Writing the density limit for low Z_{eff} ohmic discharges as

$\bar{n}_e \lesssim 1.25 \cdot 10^{20}\ B_t/(Rq_a^*) = 0.25 \cdot 10^{20}\ \frac{I}{b \cdot a}\ \frac{2K}{K^2+1}$ [m,T,MA] ($K = b/a$)

yields for ASDEX $\bar{n}_e \lesssim 1.5 \cdot 10^{20}\ I$ [m,MA] which is equal to the critical value during current rise.

3. Current Build-Up in JET

Simulations for JET ($a_{eff} = \sqrt{b \cdot a} = 1.6$ m, $R = 3$ m) with the same model as described above lead to a minimum current rise time of 3 sec for a current increase from 1.5 MA to 4.5 MA ($B_t = 3.1$ T) both with a constant density of $\bar{n}_e = 1.5 \cdot 10^{19}\ m^{-3}$ and with a density increase of $\dot{\bar{n}}_e = 0.25 \cdot 10^{20}\ \frac{\dot{I}}{ba}$ [m,MA,s] to avoid nonmonotonous q(r) profiles and hollow density profiles. High Z_{eff} (> 3) values with radiation losses up to 50 % of the ohmic input power allow only slightly higher ramp rates. q(o) values between 1.5 and 2 are obtained at the end of current rise. With longer rise times

($\dot{I} \leq 0.6$ MA/s) q(o) = 1 is reached during the ramp-up. Current ramp from 0.2 MA to 2.2 MA at 2.2 T need equal ramp rates (a_{eff} = 1.1 m), and with $\dot{I}$ = 0.67 MA/s q(o) = 1 is already reached during ramp-up after 1.8 sec in agreement with experimental results.

Efficient use of the JET main field pulse capabilities suggests to carry out the current build-up contemporary with the B_t-increase, which according to the scaling laws of the main field compression should eliminate the tendency for skin current formation keeping q at the plasma boundary fixed. Therefore main field compression at fixed toroidal radius has been included in the Baldur code by varying at the beginning of each time step plasma parameters in correspondence with the laws of adiabatic flux conserving compression followed-up by the solution of the diffusion equations.

Different combined B_t and I ramp-up scenarios have been investigated for JET parameters and Fig. 2 compares computed profiles after 1 sec rise time with and without ramping from 1.03 T to 3.1 T for I_p = 1.5MA → 4.5 MA, $\bar{n}_e = 1.5 \cdot 10^{19} \rightarrow 4.5 \cdot 10^{19}$ m^{-3}, R = 3.05 m, a_{eff} = 1.6 m and Z_{eff} = 1.5. Without B_t ramping q_a^* decreases from 9 to 3, whereas it is kept at q_a^* = 3 with B_t ramping. Current rise starts in both cases with the same T_e and n_e profiles. With B_t ramping monotonous q(r) profiles and peaked density profiles result, but the profiles obtained with a constant B_t would show strong MHD activity during ramp-up and with strong gas puffing (the case shown here) probably a density limit disruption.
Notice that also with peaked temperature profiles skin currents are possible during the start-up phase.

Due to the adiabatic compression of the poloidal flux with B_t ramp-up the toroidal current density in the plasma is increased by an amount depending on the relation between compression time and diffusion time. The resulting higher T_e-values lead to a lower resistive loop voltage, and less resistive flux is needed from the OH transformer which is clearly seen in the transport calculations. On the other hand, due to the increase of $\frac{l_i}{2}$ from 0.6 to 0.9 an appropriate flux change $I \cdot \Delta L$ has to be provided by the OH circuit which might counterbalance the flux gain seen in the transport

calculations. With the faster current penetration q(o) = 1 is reached earlier, and the corresponding onset of sawtoothing should help to suppress dangerous m = 2 MHD activity.

References

/1/ Karger, F., et al., 11th Europ. Conf. on Controlled Fusion and Plasma Physics, Aachen, 1983, Vol. 7D, Part I, p. 63.
/2/ Post, D.E., et al., PPPL Transport Group, TFTR Physics Group, Rep. 33 (1981).
/3/ Gruber, O., Proc. Invited Papers Int. Conf. on Plasma Physics, Lausanne (1984), Vol. I, p. 67.
/4/ Chodura, R., et al., 9th Conf. on Pl. Phys. and Contr. Nucl. Fus. Res., IAEA, Vienna (1982), Vol. I, p. 313.
/5/ Mahajam, S.M., Hazeltine, R.D., Nucl. Fusion 22 (1982) 1191.

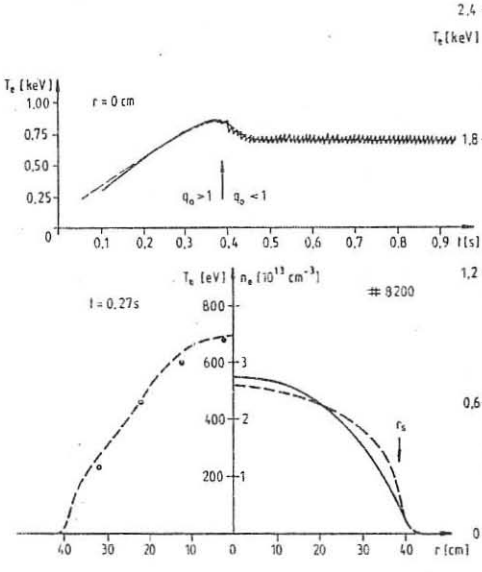

Fig. 1: T_e (r = 0 cm) vs. time and T_e and n_e profiles after current ramp-up at 0.27 s in ASDEX discharge # 8200
measured values: ——, •
calculated values: -----

The authors would like to thank A.Eberhagen and O.Gehre for the measurements.

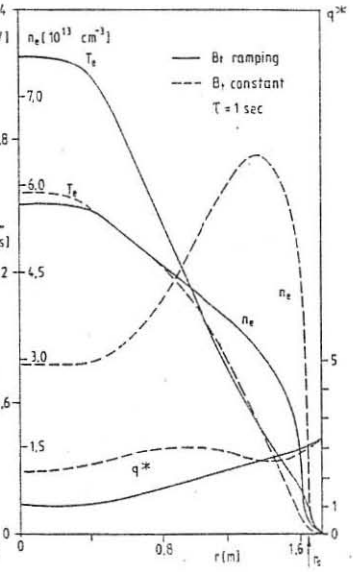

Fig. 2: Calculated $T_e(r)$, $n_e(r)$ and q(r) profiles after 1 sec current ramp-up in JET from 1.5 to 4.5 MA at constant B_t = 1.3 T (---) and with simultaneous B_t ramping from 1.03 to 3.1 T (——). Electron density increases from 1.5 to 4.5·10^{19} m^{-3} in 1 s.

VOLT-SECONDS CONSUMPTION OF JET DISCHARGES

P R Thomas, J P Christiansen and S Ejima†
JET Joint Undertaking, Abingdon, Oxon OX14 3EA, UK
†GA Technologies, San Diego, CA 92138, USA

Introduction

JET has been designed to contain plasmas where α-particle heating is a significant part of the power balance. To do this it must be capable of operation at high enough plasma current to trap the 3.5MeV α-particles and for long enough for them to slow down and impart their energy to the plasma. The full performance specification of the device was for 4.8MA plasma current. This has recently been exceeded, albeit with little flat-top. The behaviour of other limiter tokamaks with intense additional heating indicates that still higher current might be necessary to obtain the thermonuclear yield required for an observable level of α-particle heating. Therefore the volt-seconds consumption of JET discharges is of interest because it will, in part, determine the ability of the machine to meet its design goals. Also the performance of JET should guide the design of the next generation of machines such as INTOR and NET.

JET has operated at plasma currents in the range 1-5MA, toroidal fields 1.3-3.4T, elongation ratios 1.05-1.85 and mean densities $0.75\text{-}3.5\times10^{19}m^{-3}$. The minor radius was typically 1.16-1.22m corresponding to major radii 3.01-2.95m. Most discharges had the same start-up conditions and so were used to determine the dependence of the flux consumption on the flat-top plasma-parameters. A smaller selection of discharges, in which the break-down voltage and current ramp-rate were varied have been used to determine the sensitivity of the flux consumption to these parameters.

Volt-seconds Consumption at the End of the Flat-top

Two codes have been used to fit parameterisations of the plasma current density to the magnetic diagnostic signals. The internal inductance ℓ_i and β_I can be separated reliably when the elongation ratio is $\gtrsim$1.3. The FAST code[1] uses an analytic expression for the separation and is routinely used on all JET discharges of more than 1MA. ODIN[2] solves the Grad-Shafranov equation with a four parameter representation of the current distribution. It is only used for single time-slices of a small number of discharges. The results from both codes show that ℓ_i depends only on $q_{cyl}=2AB_T/\mu oI_pR$, where A is the poloidal cross-sectional area. Most of the points group together very tightly except for those with b/a<1.3, where the value of ℓ_i is not reliable. ℓ_i is well represented by

$$\ell_i \tilde{\sim} 0.9 + 0.05q_{cyl} \quad . \qquad (1)$$

The ODIN results yielded an estimate for the flux difference between the magnetic axis and the plasma surface. This was found to be related to the internal inductance by

$$\psi_i \tilde{\sim} \mu o\, I_p\, R\, (\ell_i/2 + 0.3) \qquad (2)$$

When equation (2) was compared with the volt-seconds consumed at the end of the flat-top, it was found that a simple model described the resistive consumption on axis,

$$\psi_r = V_\ell(0)t + \psi_{bd} \quad , \qquad (3)$$

where V_ℓ is the loop voltage on axis at time t near the end of the flat-top and ψ_{bd} is a "breakdown" loss. The flux swing measured at the plasma surface is compared with $\psi_i+\psi_r-\psi_{bd}$ in figure 1. The model for the resistive loss gave surprisingly good agreement with the data considering that $V_\ell(0)$ was taken constant and the current penetration was not complete in many of the high current, high field discharges. ψ_{bd} was found to be typically 1-3Wb. The points with the largest flux swings include 2MA discharges with a total pulse duration of 20 seconds to the end of the flat-top and a 5MA pulse with little flat-top.

Dependence on Breakdown Voltage and Current Ramp-rate

The dependence of the volt-seconds consumption on breakdown voltage has been determined by varying the premagnetisation current of the ohmic primary and measuring the total flux swing at the end of the flat-top of 2MA discharges. At breakdown the premagnetisation current is diverted through a resistor across the primary whose value determines the breakdown voltage and decay time. As a consequence, increasing the breakdown voltage with the resistance fixed also increased the plasma current ramp-rate. Therefore the flux consumption of a series of discharges with constant breakdown conditions and a varying ramp-rate was studied to separate the two effects.

The total flux-swing is plotted against breakdown voltage in Figure 2. The filling pressure was increased in proportion to the breakdown voltage. It may be seen that as the breakdown increased from 8 to 27 volts the flux consumed went up by 2.5Wb. Since the 2.5Wb loss corresponds to one third of the extra flux obtained by raising the premagnetisation current, this limits the plasma current that is achievable.

The effects of varying the current ramp-rate after breakdown are illustrated in Figure 3. The flux consumed at the end of the current rise and the end of the flat-top is plotted against ramp-rate. The flux is a decreasing function of ramp-rate at the end of the rise because of the drop in inductance and the reduced time for resistive dissipation. However at the end of the flat-top this difference has disappeared because the current has penetrated. The "path independence" of the flux consumption has been confirmed in other discharges where the current was increased half-way through the flat-top. We would conclude form this that the increased losses during the breakdown voltage scan occurred at breakdown and not in the current rise.

Summary and Conclusions

It has been found that the total flux consumption of a JET discharge is well represented by a simple model for the internal flux and resistive consumption on axis (see Figure 1). To a good approximation, the flux

consumed after current penetration is complete is independent of the current ramp-rate up to 2.0MA.s^{-1}. Lowering the breakdown voltage from 27 to 8 volts saved 2.5Wb.

Under normal operating conditions, only half the maximum magnetising current is used. A further increase of the magnetisation current does not raise the plasma current significantly because of the increased breakdown losses. The flux that is unavailable because of the extra losses and the limit on the maximum stable current ramp-rate amounts to some 8 Wb or 10 seconds flat-top at 5MA, 3.4T. Making use of this flux is now the main aim of the future development of the JET ohmic heating circuit. The success of the simple model for flux consumption encourages us to believe that 7MA operation is possible in JET with $\beta_p \sim 1$.

References

[1] M Brusati, J P Christiansen, J G Cordey, K Jarrett, E Lazzaro, R T Ross, Comp. Phys. Rep. 1 (1984) p345.

[2] By F Alladio and F Chrisanti, CRE-Associazione Euratom-ENEA, Frascati, Italy.

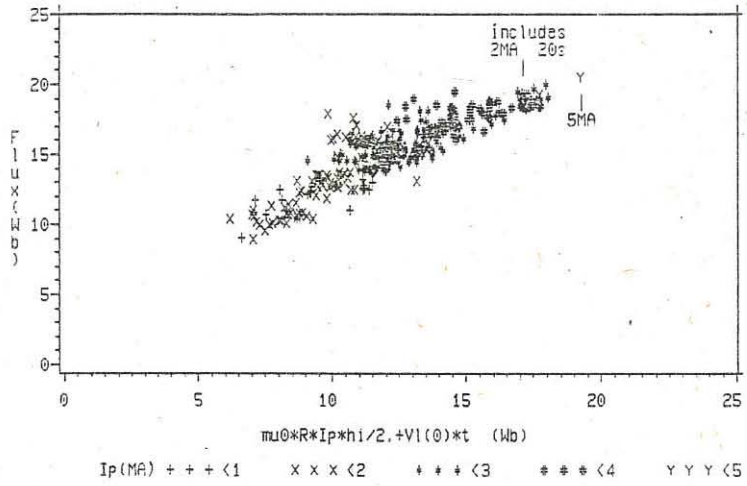

Figure 1
The flux swing measured at the plasma surface against the simple model given in equations 2 and 3. Points with different plasma currents are distinguished.

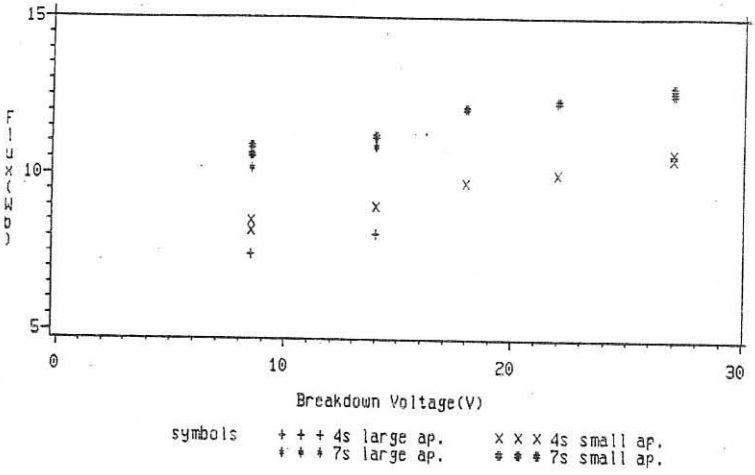

Figure 2
The surface flux swing against breakdown voltage for a series of 2.1MA, 2.6T, b/a=1.38 discharges. The measurement times were 4 and 7s after breakdown and the initial minor radius was either 0.8m (small) or 1.05m (large) minor radius. The filling pressure was increased with the breakdown voltage to keep $E/_p \sim 1.5 \times 10^4 V.m^{-1}mb^{-1}$.

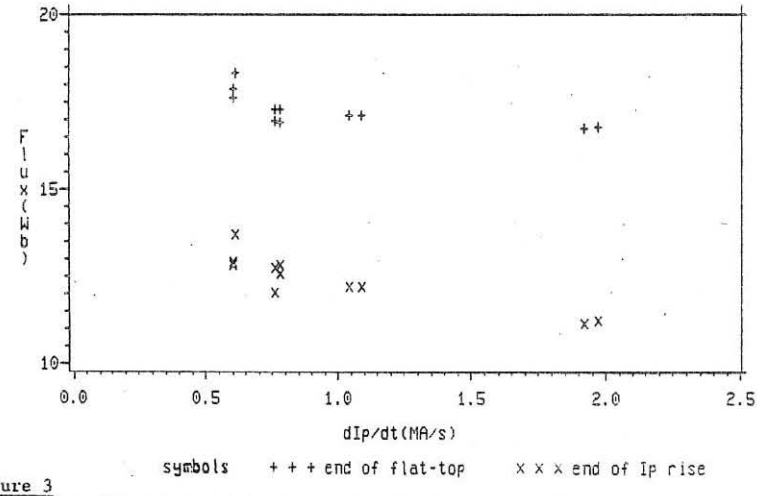

Figure 3
The surface flux-swing against current ramp-rate for discharges with I_p=2.6-2.8MA, a=1.16m and b/a≅1.37. The two sets of points correspond to the end of the current rise and the end of the flat-top.

Plasma Evolution and Skin-Effects in JET

F C Schüller, P R Thomas, A Kellman*, E Lazzaro, P Lomas,
H W Piekaar+, A Tanga
JET Joint Undertaking, Abingdon, Oxon OX14 3EA
*GA Technologies, La Jolla, Cal. USA
+Euratom-FOM Association, Nieuwegein, The Netherlands

Introduction

The evolution of a plasma pulse in JET can be described by defining a number of phases and transitions between them (TABLE I). In the following the experimental conditions for successful transitions will be given and it will be shown that skin current effects are important.

Breakdown/Townsend Phase

The only two necessary conditions to enter this phase are:

a) A poloidal field null should be somewhere in the vessel. This requires an accuracy of the vertical field control of $2 \cdot 10^{-3}$T.

b) $E_t/p > 5 \cdot 10^3$ Vm^{-1} $mbar^{-1}$

Whilst obtaining some breakdown is not difficult, the sustainment and transition to the next phase was not always successful. The usual predictions of the charged particle loss rate along magnetic field lines intersecting the vessel wall allows for JET a ratio of $B_\perp/B_t$ of 10^{-2}. In reality for sustainment it is found that the area within which $B_\perp/B_t < 10^{-3}$ must be a substantial fraction of the vessel cross-section. These requirements became even more stringent when the vessel was dirty. Lowering the prefill in order to raise E_t/p didn't help, but increasing E_t was very effective. This lead to the hypothesis that it was not the loss-rate which was too high but the ionisation-rates which were too low compared with expectations. It is a well known effect in gaseous discharges that inelastic electron-impurity collisions deplete the high energy tail of the electron velocity distribution thereby lowering the ionisation rate for a given E/p. The condition to reach the next phase can only phrased qualitatively:

c) the applied loop voltage should be large enough to ensure sufficient ionisation in the presence of impurities and the cross-sectional area within which $B_\perp/B_t < 10^{-3}$ should be at least substantial.

Cold Coulomb Collisions Phase In contrast with the preceding phase here it is the energy balance which controls the evolution since the plasma has to burn through the low Z radiation barrier. Only rarely does this phase fail to reach the next phase but the quality of the plasma can affect the success of further stages. Depending on wall conditions one can raise $\dot{I}$ from near to zero to 5MA/s by decreasing the prefill, increasing E_t, or increasing the aperture. However too large $\dot{I}$ leads to excessive MHD-activity, strongly hollow Te-profiles and extra impurity influx. Too low $\dot{I}$ costs V.sec. [1]. Emperically it is found that:

d) a successful end of the cold radiative phase is obtained by tuning prefill and initial aperture such that with given loop voltage the resulting $\dot{I}$ is between 2 and 3 MA/s.

Magnetic Field Diffusion Phase - Inward. In this phase the current ramp-rate has been varied under different conditions: constant/expanding aperture. constant/ramped toroidal field, low/high $\partial\bar{n}/\partial t$:

- with constant aperture and B_t current ramp-rates up to 1MA/s didn't show MHD-activity nor anomalous penetration [2]. Above 1MA/s some MHD can be observed but not enough pulses are available yet for extensive study. Scaling experiments in ASDEX [3] predicted MHD-activity and anomalous penetration from 0.8MA/s upwards and disruptions above 1.3MA/s.
- With expanding cross-section ramp-rates up to 2MA/s didn't show any MHD-activity. In these pulses q_a was kept close to constant. Similar effects could be obtained by simultaneous ramp of I and B_t. Both methods require some extra initial V.sec. because of low initial q_a, but the overall gain in flat-top duration is still positive.
- strong inward diffusion of particles has been observed which means a VxB-term in Ohm's Law of near equal magnitude to the applied E_t. Simultaneous ramp of n and I seems to facilitate simultaneous inward diffusion of particles and field.

e) strong gas introduction is beneficial but the density limit is somewhat lower than in later phases and should obviously be avoided.

Relaxation Phase. In this first part of the flat-top net inward particle diffusion stops and the VxB-term in Ohm's law becomes neglectable. Skin current effects die down on a timescale between 1 and 4 seconds: ℓ_i still increases; the sawtooth inversion radius continues to increase; the shaping coil current has to increase to keep the elongation constant. An increase and then decrease of MHD-activity is noticeable (see Fig. 1) if $\bar{n}$ was large in the preceding rise-phase. Seemingly the profile relaxes from one stable situation with skin-current to another stable one without skin current by passing through an unstable situation. Quite often this passage leads to a disruption just about 1 sec into the flat-top:

f) Ramp-rates above 1MA/s with constant B and aperture during the rise-phase enhances the chance of disruption in the early flat-top.

Stationary Phase: The confinement results obtained during this phase are described elsewhere [4]. Sometimes the relaxation took so much of the flat-top duration that no stationary state was reached.

Diffusive Decay Phase In this phase skin-effects as well as outward particle and energy diffusion are coupled:

- high values of $\Lambda=\beta_p+\ell_i/2>2$;
- sawteething goes on for seconds during current-decay;
- the density decreases proportional to I_p with no change in profile; as in the rise-phase this means that VxB is very important in Ohm's Law and for the magnetic field diffusion rate;
- close to the high density limit sometimes "marfes" occur i.e. strong poloidal asymmetries in density and radiation distribution. These change the density decay markedly and might initiate a high density disruption [5] See Fig. 1 at t=15.5.

Table I
Evolution of JET Pulses showing correspondence between control technical phases and physics processes.

Machine Control Phases	Physics Process Phases
t=0.0	t=0.0
Fast Rise: o no current feedback o Ohmic drive by $V=V_0\exp[-t/t_1]$ $6<V_0<30$; $0.2<t_1<0.85$s; $1<\dot{I}<5$MA/s o no density control before t=0.2 filling pressure 10^{-5}-10^{-4}mbH$_2$/D$_2$ o position control when I>100kA $0.4<a<1.0$ o mostly constant B_t $0.15<B_t<3.4$T sometimes $\dot{B}=0.5$T/s	Breakdown/Townsend Phase o ionisation by electron neutral collisions competes with particle loss along field lines o $I_p<100$kA; $\bar{n}<10^{18}$m^{-3}
	t=0.02-0.05
	Cold Coulomb Collision Phase: o low Z-radiation competes with ohmic input o $I_p<300$kA; $\bar{n}<10^{19}$m^{-3}; T<50eV
	t=0.1-0.3
	Magnetic Diffusion-Inward: o inward diffusion of B_{pol}, particles and energy o diffusion equation coupled: VxB not neglectable in Ohms Law o classical or anomalous skin diffusion
t=0.4-0.8	
Slow Rise: o current feedback requested $0.2<\dot{I}<2.0$MA/s o density feedback: $0.1<\dot{\bar{n}}<1.10^{19}$m^{-3}s^{-1} o position and shape feedback: expanding aperture a=0.8→1.2m o toroidal field normally constant: $1.3<B_t<3.4$T sometimes $\dot{B}=0.5$T/s	
t=2.5-6.0	t=2.5-6.0
	Relaxation Phase: o magnetic diffusion without strong driving terms
	t=(2.5-6)+(1-4)
Flat-top: control facilities identical to Slow Rise with appropriate control parameters kept constant	Stationary Phase o time-derivatives small in balance equations o at a high current this phase cannot be reached
t=8.0-20.0	t=8.0-20.0
Termination: o no current feedback Ohmic drive negative due to coil resistance: $-1.5<V<0$; $-1<\dot{I}<-0.3$MA/s o no density control: all gas feed stopped o full position and shape feedback o toroidal field decoy with	Diffusive Decay Phase o outward diffusion of B_p, n and T o again strong skin effect: o high $\Lambda=\beta_p+\ell_i/2>2$ o $n\propto I$ unless "marfes" o again VxB important o surplus particles pumped by wall?
t=12.0-25.0	t=12.0-25.0
End of Plasma: $I_p=0$	

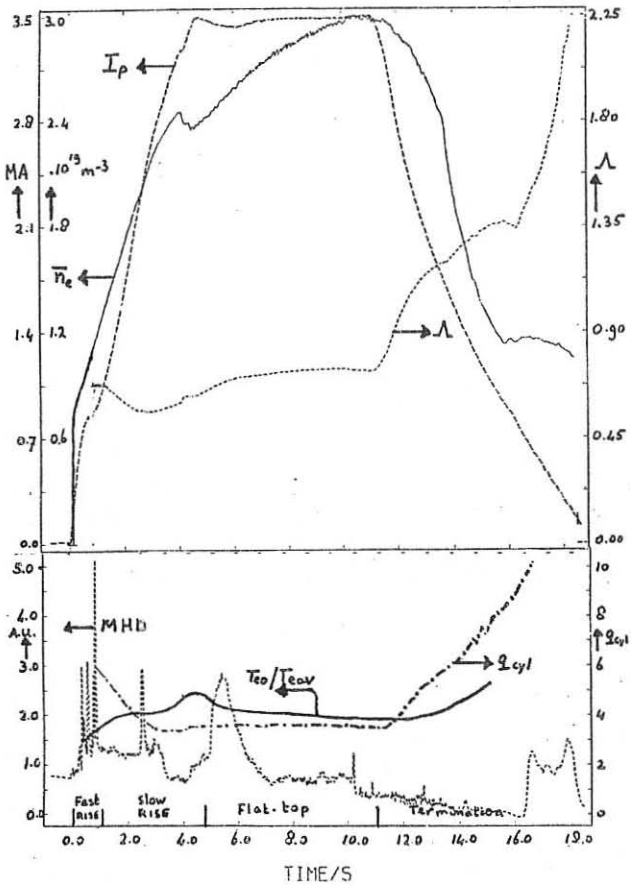

Fig.1. The evolution of pulse 5507:I(t) and $\bar{n}$(t) as given; B_t=3.4T; R=2.98m; a=1.20m; b/a=1.47; T_{eo} (t=10)=3.5KeV. Note the MHD-activity during: a)fast-rise; b)slow-rise when I>1.0MA/s; c)the relaxation phase; d)the termination phase when a "marfe" has spoiled the density decay.

References:

[1] P R Thomas et al. This conference.
[2] J P Christiansen et al. This conference.
[3] F Karger et al. Post Dead-line paper EPS Conference Aachen 1983.
[4] J G Cordey et al. This conference.
[5] J O'Rourke et al. This conference.

STUDIES OF THE BROADBAND MAGNETIC FLUCTUATIONS IN THE TCA TOKAMAK

M.L. Sawley, A. Pochelon and R. Keller
Centre de Recherches en Physique des Plasmas
Association Euratom - Confédération Suisse
Ecole Polytechnique Fédérale de Lausanne
21, Av. des Bains, CH-1007 Lausanne, Switzerland

There is at present a large interest in the study of microscopic fluctuations in an attempt to understand the observed anomalous transport in tokamak plasmas[1]. Recent preliminary investigations on several tokamaks have shown a strong relation between the level of broadband magnetic fluctuations at the plasma edge and the global confinement time. This has been demonstrated both in ohmic (TCA[2], JET[3]) and neutral beam heated (ISX-B[4], D-III[5]) discharges, the level of magnetic fluctuation decreasing with increasing confinement time. It is important to note that no such relation has been found for low temperature tokamaks[6,7].

To date there has not been a detailed study of how the fluctuation amplitude varies over the possible wide range of tokamak operational parameters. In the present paper we report on such a study, undertaken in the ohmic phase of TCA. The main TCA parameters are $R = 61$ cm, $a = 18$ cm, $B_\phi \leq 1.51$ T, $I_p \leq 175$ kA with a current flat-top of $\lesssim 150$ ms, yielding $\bar{n}_e \leq 10^{14}$ cm^{-3} and $T_e \leq 1$ keV. The fluctuating field is detected with wide bandwidth, triple (measuring $\tilde{b}_r$, $\tilde{b}_\theta$ and $\tilde{b}_\phi$) magnetic probes. The probes are placed in the shadow of the limiters, since internal measurements are not possible in TCA. The results described here were obtained from a probe situated in the equatorial plane. Spectral information of the broadband fluctuating field which is observed at frequencies above that of the Mirnov oscillations ($\sim$ 10 kHz) was obtained by passing the probe signal through a series of 8 adjacent half-octave passive bandpass filters, covering the frequency range of 40 - 660 kHz.

As has been observed on other tokamaks, it was found that b_r and b_θ are similar in amplitude. However, by careful alignment of the rotatable probe it was possible to determine that the fluctuating field is plane-polarized normal ($\pm 2^\circ$) to the toroidal direction. This result was found over the entire fluctuation spectrum for the wide range of $3.3 \leq q(a) \leq 7.3$ considered. Hence, we find that the broadband magnetic fluctuations are confined to a plane normal to the toroidal magnetic field and <u>not</u> to the total magnetic field at the probe position.

The fluctuating field has been measured over a large number (> 150) of

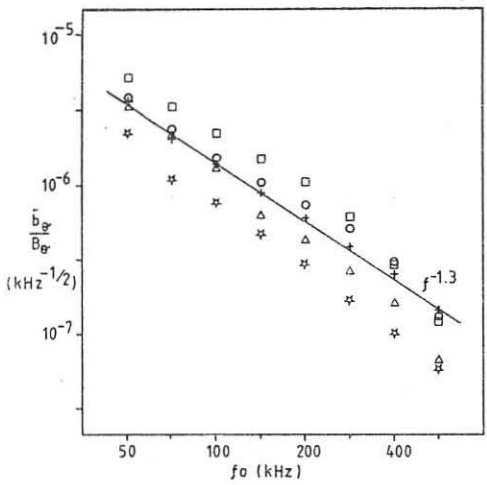

	B_ϕ (T)	q(a)	$\bar{n}_e$ (10^{13} cm^{-3})
△	1.16	3.1	2.5
+	1.16	3.1	1.5
○	1.16	5.5	1.5
□	0.78	5.5	1.5
✲	1.51	3.1	2.5

with $\dot{\bar{n}}_e$, $\dot{\bar{I}}_p$ = 0

Figure 1

tokamak discharges spanning the operational regime: B_ϕ = 0.78, 1.16, 1.51 T; 2.6 < q(a) < 15; and 6 x 10^{12} < $\bar{n}_e$ < 10^{14} cm^{-3}. Deuterium was used as the working gas. All discharges considered had a low level of mode activity with no discernible runaway population. As shown in Fig. 1, the rms value of $\tilde{b}_\theta/B_\theta$ varies as $f^{-1.3\pm0.3}$ over a wide range of operational parameters. Although somewhat different spectra have been measured for extreme values of $\bar{n}_e$ and q(a), taking a single band (that centred around 140 kHz, for example) as representative of the entire spectrum appears nevertheless justified.

Before determining the scaling of the fluctuation amplitude with the various parameters, it is important to gauge its dependence on the rate of change of those parameters that may vary during a tokamak discharge. In Fig. 2

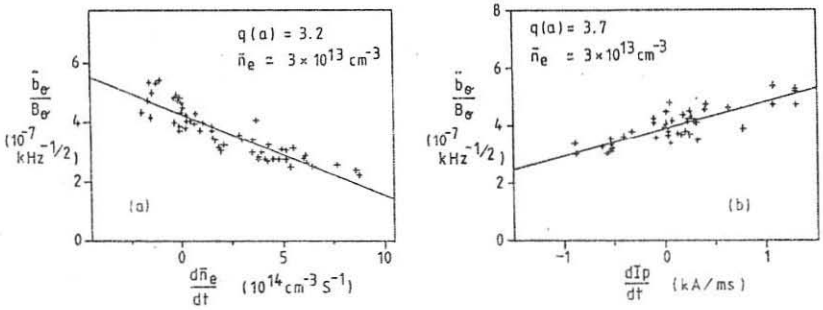

Figure 2

is plotted the rms value of $\tilde{b}_\theta(140\ \mathrm{kHz})/B_\theta$ as a function of (a) $d\bar{n}_e/dt$ and (b) dI_p/dt, keeping all the other parameters constant. It is seen that $\tilde{b}_\theta$ decreases with increasing $\bar{n}_e$ or decreasing I_p. This was found to be true for all values of $\bar{n}_e$ and I_p, although the change in $\tilde{b}_\theta/B_\theta$ with $\dot{\bar{n}}_e$, $\dot{I}_p$ is a function also of $\bar{n}_e$, I_p.

By considering only times in discharges for which $\dot{\bar{n}}_e$ and $\dot{I}_p$ were small, the dependence of the fluctuation amplitude on B_ϕ, I_p and $\bar{n}_e$ was determined. (This was achieved either by a regression analysis of the entire database, or by considering values for which two of these parameters were constant over a range of the third, yielding similar results.) As shown in Fig. 3, it was found that over the entire operational regime $\tilde{b}_\theta(140\ \mathrm{kHz})/B_\theta \propto (B_\phi \bar{n}_e^{1/2})^{-1}$. The normalized fluctuation amplitude, $\tilde{b}_\theta/B_\theta$, was found to depend only very weakly on the value of I_p. It should be noted, however, that the normalization for the fluctuation amplitude is not unique. The most appropriate normalization should, in principle, be determined by the theoretical model with which one is interpreting the experimental data.

It is interesting to note that for the TCA tokamak operating under identical conditions, the energy confinement time, $\tau_E^* = 1.5\ \bar{n}_e k[f_e T_e(o)+f_i T_i(o)]/P_{OH}$ with $f_e = 0.3$, $f_i = 0.5$ is proportional to $B_\phi \bar{n}_e^{1/2}$, as shown in Fig. 4. The reason for the weaker than linear dependence of τ_E^* on $\bar{n}_e$ is attributed to the fact that for the higher values of $\bar{n}_e$ considered in the present wide parametric study, ion neoclassical thermal conduction becomes an important loss channel[2]. The present scaling compares favourably with that determined by considering data from a number of ohmically heated tokamaks with circular plasma cross-section[8].

Comparing the above two experimentally determined scaling laws suggests that the normalized fluctuation amplitude $\tilde{b}_\theta/B_\theta$ scales inversely proportional to the energy confinement time. The present study thus extends the pre-

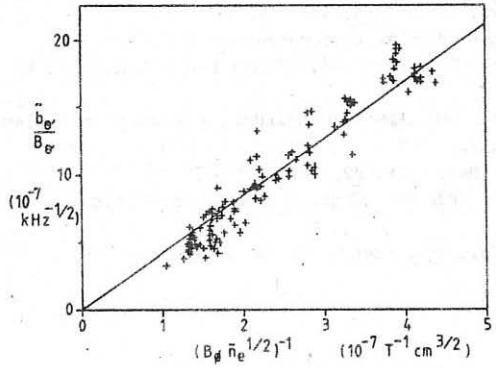

Figure 3

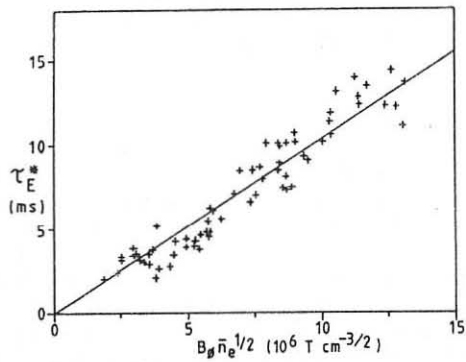

Figure 4

liminary results of magnetic fluctuation scaling obtained to date to a much wider range of tokamak operation, as well as quantifying the dependence on various plasma parameters. In addition, the important role played by the plasma geometry in determining the polarization of the magnetic fluctuations has been shown.

Acknowledgements: The authors gratefully acknowledge the efforts of P.A. Duperrex, Ph. Marmillod and W. Simm towards the present work. They also thank A. de Chambrier, B. Joye, J.B. Lister and J.-M. Moret for making available unpublished experimental data. This work received support from the Fonds National Suisse.

References:

[1] P.C. Liewer, Nucl. Fusion 25, 543 (1985).
[2] P.A. Duperrex et al., Phys. Lett. 106A, 133 (1984).
[3] P.A. Duperrex et al., Paper 98, this conference.
[4] M. Murakami et al., Proc. 10th Int. Conf. Plasma Phys. Controlled Nucl. Fusion, 1, 87 (1985).
[5] E.J. Strait et al., Proc. 11th EPS Conf. Controlled Fusion and Plasma Phys., Aachen, 1, 59 (1983).
[6] S.J. Zweben et al., Phys. Rev. Lett. 42, 1270 (1979).
[7] J.J. Ellis et al., Proc. 10th Int. Conf. Plasma Phys. Controlled Nucl. Fusion 1, 363 (1985).
[8] J. Hugill and J. Sheffield, Nucl. Fusion 18, 15 (1978).

CONNECTION BETWEEN LOW FREQUENCY TURBULENCE AND ELECTRON ENERGY CONFINEMENT IN TFR

TFR Group and A. TRUC*

ASSOCIATION EURATOM-CEA SUR LA FUSION
Département de Recherches sur la Fusion Contrôlée
Centre d'Etudes Nucléaires
Boite Postale n°6. 92260 FONTENAY-AUX-ROSES (FRANCE)

INTRODUCTION

Compared with the expected energy losses from Coulomb collisions, the electron energy losses are anomalously high. This anomaly, observed in ohmic discharges, is further enhanced during auxiliary heating experiments. In this paper, we shall examine plasma density fluctuations, considered as one aspect of the turbulence that could cause this energy deterioration and show an experimental relationship between the density fluctuations and the electron energy transport losses for plasmas with ohmic heating and auxiliary heating (either NBI or ICRF).

DESCRIPTION

Low frequency turbulence is measured with a small angle CO_2 laser scattering experiment with which, for a given wave vector $\vec{k}_\perp$, the frequency spectrum of the density fluctuations within a vertical cylindrical volume of the plasma (coinciding with a diameter in the reported experiments) is determined (1). The wave number and frequency ranges accessible with the optics, i.e. : $3\ cm^{-1} \leqslant |\vec{k}_\perp| \leqslant 45\ cm^{-1}$ and $10\ KHz \leqslant f \leqslant 2\ MHz$ cover the domain of the strongest fluctuations observed. We have verified that the form of the $\vec{k}_\perp$ spectrum obtained during ohmic discharges is not significantly changed with the addition of auxiliary heating. Thus, in order to characterise changes in the turbulence level, it suffices to follow only one $k_\perp$ component, which for the data reported here is $k_\perp = 6\ cm^{-1}$ (close to the spectrum maximum (2)). In all cases, the frequency integrated turbulence value will be given.

The transport losses are deduced from a OD code which describes the temporal evolution of the energy balance of five species of particles at the centre of the plasma (electrons, protons, deuterons, a fully ionized light impurity, and a heavy impurity). This code try to reproduce the temporal evolution of the observed signals (density, electron and ion temperatures, loop voltage, impurity brightness...). The unknown losses that one has to introduce are considered as heat transport losses P_T(2). For RF pulse experiments in mode conversion regime, the RF power is directly transferred to the electrons (it is estimated from the initial change of the slope of the T_{eo} signal) while during NBI heating, the power transferred to the electrons is not instantanecus and we rely on a code using a Monte Carlo calculation for evaluating P^e_{ad}.

In addition, we can make a separate estimate of the losses associated with any sawtooth activity present P_{ST} and by assuming that

$$P_T = P_{ST} + P_x$$

* Laboratoire PMI - Ecole Polytechnique - Palaiseau (FRANCE).

we are able to estimate the remaining losses P_x ; both P_T and P_x will be considered.

OHMIC AND NEUTRAL BEAM INJECTED PLASMAS

Here we compare the frequency integrated turbulence with the estimated P_T and P_x losses of a deuterium plasma (B_T = 41 kG, I_p = 240 kA, T_{eo} = 1.4 keV, T_{io} = 0.9 keV, $0.5.10^{14} < n_{eo} < 10^{14}$ cm^{-3}), both in the ohmic phase and during H° beam injection (W_c = 35 keV).

As shown in Fig. 1, the diameter integrated density fluctuation signal $<\delta n^2>$ (with an integration time constant of 2 ms) measured initially in the ohmic phase was constant, but increased with the onset of the NBI and saturated after typically 20 ms.

In our analysis we choose a quantity $<\delta n^2>/n_o^2$ considered as representative of the mean square relative density fluctuations $<(\delta n/n_o)^2>$ where the density increase during NBI ($\Delta n \sim 15$ %) has been taken into account. The proportionality between both qantities is valid if the density and the density fluctuations profiles do not vary and we shall assume that this is approximately the case.

For this set of experiments ($P_{NI} \sim 600$ kW of injected power). T_{io} increases by 200 eV whereas T_{eo} increases very little ($\Delta T_{eo} \sim 50$ eV), suggesting enhanced losses for the electrons. Fig. 2 shows the values of P_T and P_x for a number of Tokamak shots (each given a specific letter) plotted versus the measured values of $<\delta n^2>/n_o^2$. Here the small letters refer to ohmic phase measurements and the capital letters to NBI stationary phase measurements ; the letters with circles are the P_x values while those without are the P_T values. It is clear that both quantities increase with $<(\delta n/n)^2>$ In spite of the dispersion of the points we conclude that P_T and P_x vary almost linearly with the turbulence power. Moreover the fact that the NBI points align with the ohmic ones suggests a continuity in the process.

OHMIC AND ICRF PLASMAS

The results for ICRF heating in the mode conversion regime are shown in Fig. 3 . A constant RF power ($\sim$ 600 kW) is launched from the inside of the torus into deuterium plasma (B_T = 45 kG, I_p = 200 kA, T_{eo} = 1.5 keV T_{io} = 1 keV, n_{eo} = 1.10^{14} cm^{-3}) containing 20 % of hydrogen. As previously reported (3), the electron temperature suffers a rapid increase ($\tau \sim 10$ ms) and then saturates, after which it may remain at this constant level or decrease significantly. This behaviour explains the scatter of the ICRF points in Fig. 3 , whereas the ohmic ones vary weakly. Arabic numbers refer to measurements during the ohmic phase while those Roman nunbers were measured 20 ms after the beginning of the RF pulse ; as for NBI experiments a reasonably linear relationship between losses and turbulence is noticed, suggesting again a continuity in the losses process between the ohmic phase and the ICRF one. Moreover the fact that P_x values extrapolate closer to the origin suggests that this power loss is more directly related to the turbulence.

SUMMARY

The previous results for ohmic, NBI heated and ICRF heated plasmas can be summarized by computing the products $P_T^{-1} <(\delta n/n/)^2>$ and $P_x^{-1} <(\delta n/n)^2>$ respectively as a function of τ_T and τ_x (τ_T and τ_x are defined by $P_T = W_e / \tau_T$ and $P_x = W_e / \tau_x$, W_e is the electron plasma energy density). It is worth noting that $P_T^{-1} <(\delta n/n)^2>$ remains approximately constant (within a

standard derivation $\sigma = \pm 20\ \%$) when τ_T varies by a factor 4 and $P_x^{-1} < (\delta n/n)^2 >$ remains also constant ($\sigma = \pm 30\ \%$) when τ_x varies by a factor 9 for this set of experiments. We have estimated the value of W_e for these experiments and P^{-1} can be considered proportional to τ, thus showing as well that the electron confinement time is inversely proportional to the density fluctuations.

CONCLUSION

The experimental results show a close relationship between the turbulence, the transport losses and the electron confinement time. As there is a great difference between the ohmic, NBI and ICRF heating, the observed constancy in the product $P^{-1} < (\delta n/n)^2 >$ argues quite strongly that the turbulence to transport losses connection is a property of the plasma itself.

REFERENCES

(1) A. TRUC, J. OLIVAIN, D. GRESILLON, A. QUEMENEUR, F. GERVAIS
EUR-CEA Report 1135 (1981)

(2) TFR Group and A. TRUC
Plasma Physics and Controlled Fusion. 26 - n°9 1045 (1984)

(3) TFR Group and A. TRUC
Accepted for Publication in Plasma Physics and Controlled Fusion (1985)

This research is carried out in the frame of a general agreement between Association Euratom-CEA and PMI Laboratory of Ecole Polytechnique.

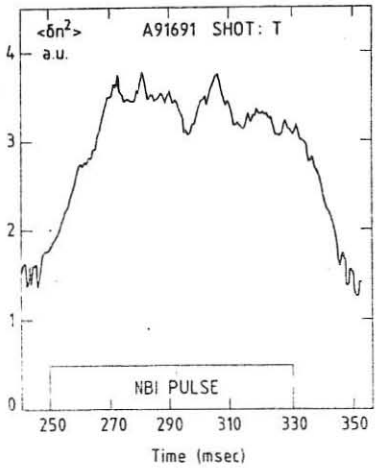

Fig. 1

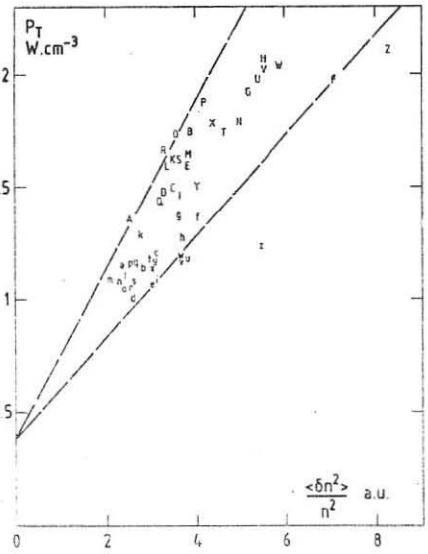

Fig. 2-a

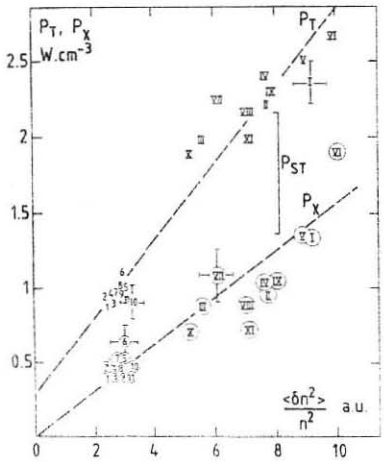

Fig. 3

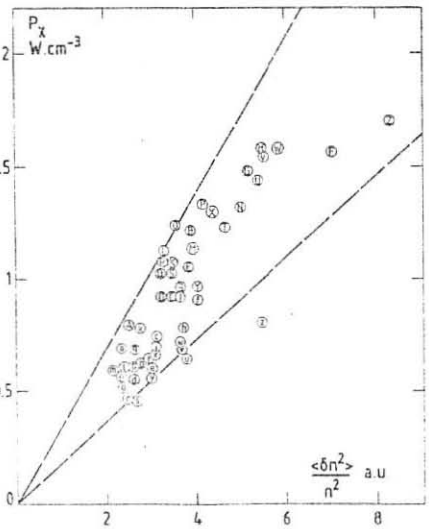

Fig. 2-b

"Poloidal Asymmetric Impurity Radiation in Asdex in the Presence of Neutral Injection"

W.Feneberg,M.Kornherr,P.Smeulders,R.Bartimoro[1],G.Becker,H.Bosch, H.Brocken, A.Eberhagen,G.Fussmann,O.Gehre,J.Gernhardt,G.v.Gierke,A.Giuliana[1] E.Glock,O.Gruber, G.Haas,G.Janeschitz,F.Karger,M.Keilhacker,O.Klüber,P.Kotzé[2], K.Lackner, M.Lenoci[1],G.Lisitano,H.Mayer,K.McCormick,D.Meisel,V.Mertens, E.Müller, H.Murmann,H.Niedermeyer,W.Poschenrieder,H.Rapp,H.Röhr,F.Ryter[3], F.Schneider, G.Siller,F.Söldner,E.Speth,K.Steuer,G.Vlases[4],O.Vollmer,F.Wagner.
Max-Planck-Institut für Plasmaphysik,EURATOM Association, D8046-Garching.

During high power neutral beam injection (NI) in Asdex large poloidal asymmetries in the impurity radiation are observed. Dependent on the confinement regime [1]vertical asymmetries are found in energy and particle fluxes in top and bottom divertors and are also measured in the main chamber by VUV-spectroscopy, by bolometer and ultra-soft-X-ray (USX-) pinhole cameras. These measurements are all performed in the vertical plane. Fig. 1 shows the asymmetric line-integrated flux profiles as seen by the USX-camera for low confinement L-regime and for the normal high confinement H-regime close to the $L \rightarrow H$ transition. In the latter regime the up/down asymmetry becomes even more pronounced, while the bottom part of the profile appears to be similar to the one in single-null discharges [2]. The asymmetry starts to appear about 50 msec after the start of NI.

By means of a second USX-camera mounted nearly on top of the divertor tokamak also horizontal asymmetries are detected, which become especially pronounced in the H-regime during high power NI (3.4 MWatt)

The asymmetries are also dependent on the type of H-regime, that can be established. Two types have been found : the normal H- and the H^*-regime, which are characterised by the appearance or non- appearance of the edge-localised mode (ELM). The ELM's have a strong effect on both vertical and horizontal asymmetries and seem to prevent the impurity accumulation, that normally takes place in the quiescant H^* discharges without ELM-activity. As a matter of fact the accumulation of impurities seems to be closely correlated to a contraction of the radiation in the poloidal plane towards the outside of the torus, as can be seen in fig. 2.

Changes in the asymmetries are seen to be related to the plasma confinement properties. A possible candidate, that might explain the behaviour of the horizontal asymmetry of the impurity spatial distribution, is a stong toroidal rotation due to the nearly parallel NI. The rotation can be expected to depend on the confinement of particles and energy and has been measured spectroscopicly to be $2.10^7 cm/s$, during a normal H- discharge, in agreement with angular velocities of observed tearing modes.

The magnitude of this rotation is largely sufficient to make the centrifugal force the dominant term in the momentum balance along the magnetic surfaces, yielding a poloidal impurity distribution , that in first order of $\epsilon = r/R$, the inverse aspect ratio, can be written as :

$$n_Z(\theta) = n_Z(\frac{\pi}{2}) \cdot (1 - \epsilon (\frac{v_\phi}{v_{Zt}})^2 \cos\theta) \qquad (1)$$

Here the poloidal angle θ increases clock-wise from torus inside to outside.v_{Zt} is the impurity thermal velocity and the remaining symbols are explained after eqno. 3.

If T_e and n_e are constant along the lines of force, then the measured emissivity would have a similar dependence on θ. The stuctures shown in fig 2. are obtained from the

data of the two USX-cameras limiting the number of possible Fourier components in the poloidal plane. The spatial distribution of the emissivity $I(r,\theta)$ has then the general form of:

$$I(r,\theta) = I_0(r) \cdot (1 + h(r)\cos\theta + v(r)\sin\theta + e(r)\cos 2\theta) \qquad (2)$$

with $h(r), v(r), e(r)$ being the horizontal, vertical and resp. elliptic variation of the relative emissivity [3].

Recent more complete calculations show the connection between impurity spatial asymmetries and the impurity accumulation.

These calculations are based on momentum equations in the collisional regime for the main plasma ions and impurities as given by Braginski [4]with the friction term proportional to the relative velocities only. This means, that temperature effects [5]are neglected and impurities are treated as test particles. The neutral beam is assumed to produce a rotation of the main plasma in toroidal and poloidal direction. In contrast to present theories [5,6]the dependence of poloidal asymmetries and of the perpendicular transport of impurities from the poloidal rotation has been widely investigated. Using an expansion into the inverse aspect ratio for a geometry of concentric magnetic surfaces one gets in first order of ϵ for the average perpendicular impurity flow $< v_{Z,r} >$, defined as the ratio of the radial flux $\Gamma_{Z,r}$ to the mean density $< n_Z >$, the result :

$$< v_{Z,r} >= \frac{\Gamma_{Z,r}}{< n_Z >} = \frac{cT}{eBrZ}\epsilon a_1(1 + \frac{m_Z v_\phi^2(r)}{2T}(1 - \frac{Zm_i}{m_Z} + 2(1-\delta)\frac{Rq}{a}\frac{cTL_i}{v_\phi(r)eBr})) \qquad (3)$$

$T = T_e = T_i = T_Z$ being the temperature, B the toroidal field, r the minor radius of the surface to be considered, Z the ionic charge, m_z, m_i the masses of impurities and main plasma ions, a the plasma radius, R the major radius, q the safety factor, $L_i = (r/p_i).(dp_i/dr)$ the dimensionless radial decay length of the ion pressure. The toroidal main plasma velocity is assumed to have a paraboloic profile : $v_\phi(r) = v_\phi^{(0)}(1 - (r/a)^2)$. The parameter of the poloidal rotation of the plasma ions δ is defined as $\delta = v_{i,\theta}^{(0)}/(L_i cT/eBr)$, where the poloidal rotation follows the relation $v_{i,\theta} = v_{i,\theta}^{(0)}(1 - \epsilon\cos\theta)^{-1}$. The last term in eqn. 3 shows the difference between co- $(v_\phi(r) > 0)$ and counter- $(v_\phi(r) < 0)$ injection, that originates from the difference in the toroidal rotation of impurities and the main plasma due to friction. The inertial term produces a large effect on the perpendicular transport of heavy impurities, the sign of which depends on the sine-Fourier component a_1 in the expansion $n_Z = n_Z^{(0)}(1 + \sum_{m=1}^{\infty}(a_m \sin m\theta + b_m \cos m\theta))$. The impurity distribution has been obtained from the continuity equation $\nabla_\theta n_z v_{z,\theta} = 0$, assuming a quasi steady state equilibrium with poloidal flow velocities much larger than the perpendicular ones : $v_{Z,\theta} \gg v_{Z,r}$. A solution is readily obtained, when the impurity distribution is assumed to be far away from accumulation ($(1/n_z)(dp_Z/dr) \ll (1/n_i)(dp_i/dr)$). This is shown in fig. 3 and 4. As expected one finds the impurities concentrating to the outside due the centrifugal force. Fig. 4 shows that even for co-injection a poloidal rotation of the size of the diamagnetic drift causes a strong inward flux in the same order of magnitude as observed in Asdex during the H^* confinement regime. On the other hand a much larger poloidal rotation seems to produce a very effective outward drift. The latter could well be used to control the impurity level in divertor and limiter tokamaks.

References:
[1]M.Keilhacker et al.,Plasma Phys.and Contr.Nucl.Fusion Research 1984 1 IAEA-CN-44
[2]F.Wagner et al.,Phys.Rev.Lett.**53**,15,1453 (1984)
[3]P.Smeulders, submitted to Nucl. Fusion
[4]S.I.Braginski,Rev.of Plasma Physics,Vol I,214
[5]K.Brau,S.Suckewer,S.K.Wong,Nucl.Fusion **23**,12, (1983)
[6]W.M.Stacey Jr.,D.J.Sigmar,Phys.Fluids **27**,8, (1984)

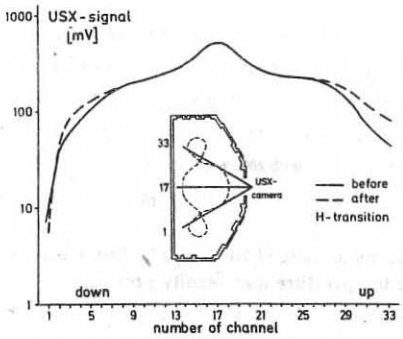

Fig.1 USX measurements in the vertical plane in mV versus diode number shortly before and after the $L \rightarrow H$ transition for a normal H-discharge. Three lines of sight are shown in the inserted Asdex cross-section.

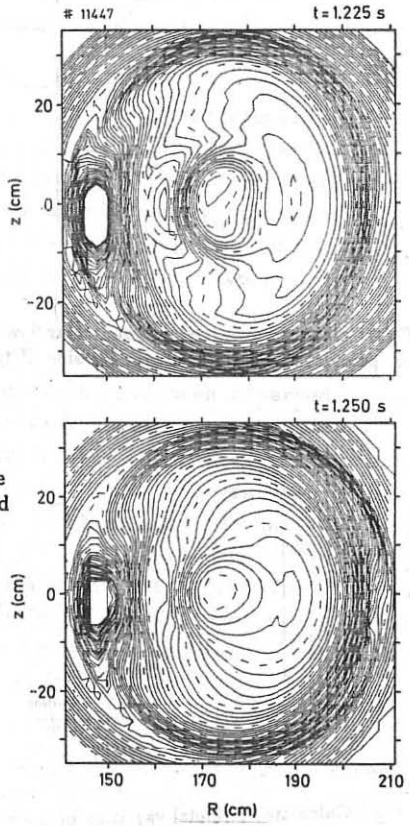

Fig:2 Iso-emissivity lines showing the plasma cross-section in USX light for maximum β (t=1.225 s) and later in time during the impurity accumulation phase (t=1.25 s) for a H^* discharge. $I(r=0)$ increases from 0.5 to 1.5 W/cm^3 during this time.

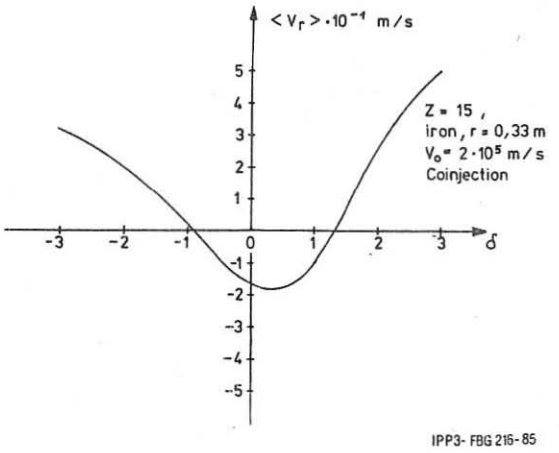

Fig.4 Calculated averaged perpendicular flow velocity in units of 10^{-1} m/s in Asdex versus the poloidal rotation parameter δ, using H-type temperature and density profiles.

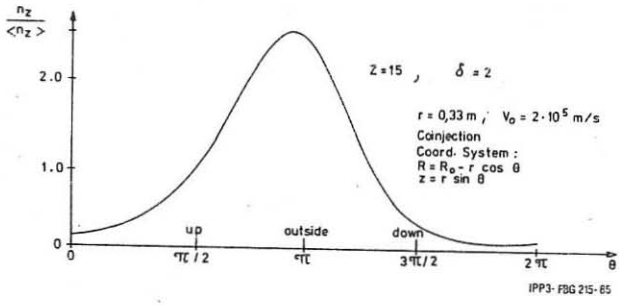

Fig.3 Calculated poloidal variation of the relative impurity density in Asdex.

[1] CNEN Frascati,Italy
[2] Nuclear Developement Corp. of South Africa, Pretoria
[3] CEN Grenoble, France
[4] University of Washington, Seattle

TURBULENCE-INDUCED PLASMA TRANSPORT IN TOKAMAK TV-1

V.P.Budaev, R.S.Ivanov

Institute for High Temperatures, Academy of Sciences,
Moscow, USSR

Abstract

In tokamak TV-1 density and the electric field fluctuations at a plasma edge as well as the fluctuation-induced radial cross-field transport of the charged particles have been investigated with the help of Langmuir probes. The significently high level of radial fluctuation-induced fluxes $\tilde{\Gamma} \sim 10^{16} \div 10^{18}$ cm^{-2}s^{-1} obtained, may easily explain the anamalous diffusivity of the tokamak edge plasma.

I. Introduction

The small-scale density fluctuations have been observed in many tokamak devices using the microwave scattering, the high-speed imaging or Langmuir probes [1,2]. The increased attention that was paid to the edge plasma fluctuations last years is stimulated by the attempts to explain the existence of the anamalous transport in tokamaks as well as by the search for the methods of the active control of the edge plasma transport properties. The edge plasma turbulence has been analized in many theoretical papers. Nevertheless due to the lack and incompleteness of the experimental data the nature of this turbulence is not proved yet.

II. Experimental details

The electric fluctuations of the edge plasma have been investigated in small tokamak TV-1 (R = 235 mm, a = 41 mm, B_T = 1.6 T, $T_e \sim 150 \div 200$ ev, $n_e = 3 \cdot 10^{13}$ cm^{-3}, I_p = 15 KA). The system of Langmuir probes could be inserted through the diagnostic port in the outer equatorial plane at toroidal angle of 90^o from the electron side of the full poloidal limiter. The cylindrical tips of the probes 1.3 mm in length and 0.6 mm in diameter were made of

tungsten. Plasma density and its fluctuations were determined from the single probe measurements of the ion saturation crurrent. The two other probes positioned nearby and poloidaly spaced were used for the measurements of the floating potential drop oscillations, which were considered as oscillations of poloidal electric field. The probe signals were simultaneously registered by the transient recorder DL-902 or by the digital oscilloscope T-468 and then transmitted to the personal computer HP-85 for the further processing and calculations. The turbulence-induced particle fluxes were derived from the simultaneous measurements of the density and poloidal electric field oscillation and their cross-correlating.

III. Results and Discussion

The measurements were performed in the geometrical shadow of the poloidal limiter ($0.83 \leqslant r/a \leqslant 1.0$) and somewhat deeper in the plasma bulk ($0.79 \leqslant r/a \leqslant 0.83$). On fig. 1 and 2 the radial profiles of the density fluctuation level $\langle \tilde{n} \rangle$ (the mean square root value) and the relative fluctuation level $\langle \tilde{n} \rangle / \langle n \rangle$ are presented. The poloidal electric field fluctuations increased up to the value of 40 - 50 v/cm with the probes being inserted deeper into the plasma. It should be noted that the high level of density and the electric field fluctuations at a plasma edge certainly does not mean the existance of such or even more intensive oscillations in the central zone of the discharge. On fig. 4 the results of change in double probe orientation against B_T direction is shown the suprising existance of sufficiently intensive oscillations of electric field $\tilde{E}_{\parallel} \sim 10$ v/cm along B_T should be carefuly examined and explained. The continuous frequency spectra of $\tilde{n}$ and $\tilde{E}_\rho$ (Fig.5) are typical for the turbulent state of plasma and spreaded widely up to several MHz, while the major part of these oscillation is below 100 KHz. The density and the poloidal electric field oscillations are partialy correlated (50%). The radial profile of the fluctuation-induced particle outflux $\tilde{\Gamma}_\perp = \int \tilde{n}(t)\tilde{v}_\perp (t)\, dt$, where $\tilde{v}_\perp = c\frac{\tilde{E}_\rho}{B}$ is the fluctuating drift velocity in the crossed $E_\rho \times B$ fields, is presented in fig. 6. The ubrupt rise of the fluctuation-induced particle flux in the narrow radial zone inward from the limiter-layer edge may be naturaly considered as a result of the non-zero flux divergence. Otherwise any of two

or three dimentional effects of the spatial flux redistribution should be involved for the explanation of this fenomenon. Nevertheless the local measurements by the H_α resonant fluorescence did not proved any rise of the neutral hydrogen density in this zone (the source of charged particles). The estimation of the effective cross-field diffusivity $D_\perp \sim \Gamma_\perp \frac{dn}{dr}$ easily yields the values of 10^4 $cm^2 s^{-1}$, that is very close to those obtained recently in tokamak CALTECH [1].

IV. References

1. Zweben S.J., Liwer P.C., Gould R.W. J.Nucl.Mat 111/112, 39, 1982.
2. Lewinson S.J. et al., Nucl.Fus., v. 24, 5, 1984.

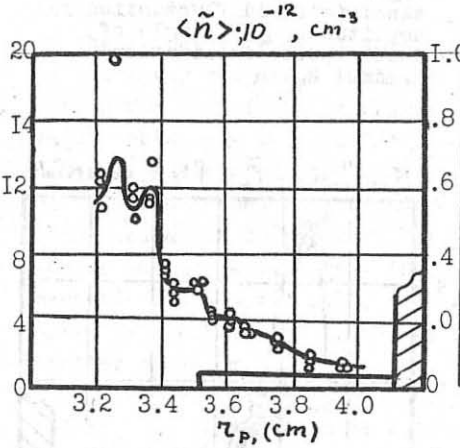

Fig. 1. Density fluctuation amplitude in deuterium via miner radius.

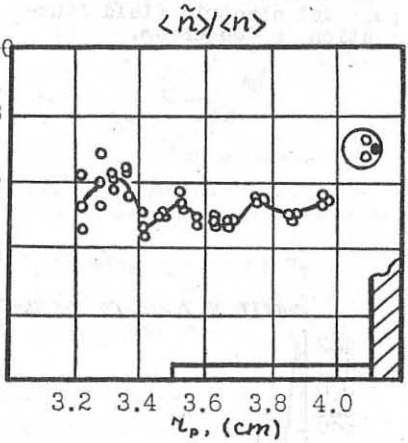

Fig. 2. Relative level of density fluctuations in deuterium via miner radius.

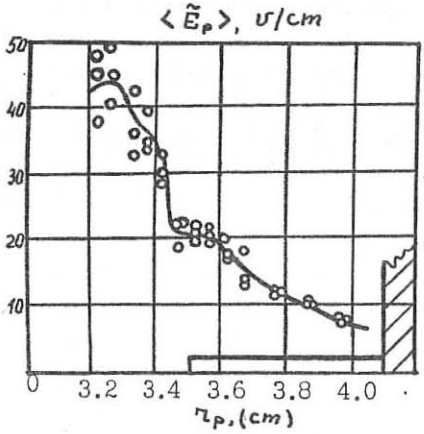

Fig. 3. Radial profile of poloidal electric field fluctuation in deuterium.

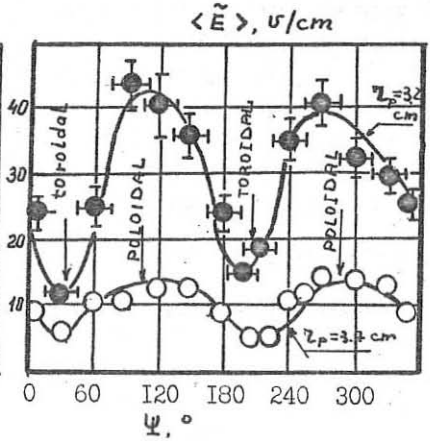

Fig. 4. Angle dependence of electric field fluctuation amplitude. Ψ is angle of double probe inclination against B_T.

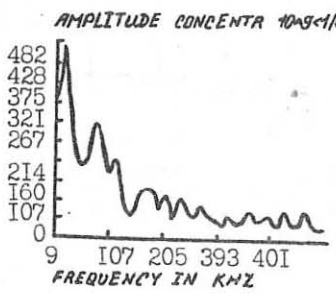

Fig. 5. Frequency spectrum of plasma density fluctuations.

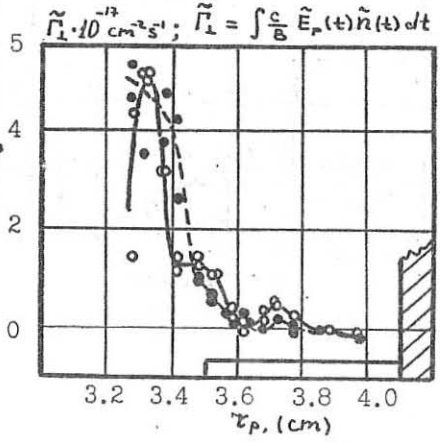

Fig. 6. Fluctuation-induced particle flux via small tokamak radius in hydrogen; O-B=1.32 T ● -B=1.6 T.

MHD-MODE m=2 SUPPRESSION BY ECRH HEATING IN TOKAMAK T - 10

A.A.Borshchegovskij, I.A.Popov, M.M.Stepanenko

I.V.Kurchatov Institute of Atomic Energy, Moscow, USSR.

A program on the study of phenomena related to ECRH /1/ has been carried out on T-10 for a long time. The studies on the ECRH effect on the m=2 mode intensity, when the ECRH zone is located near the resonance surface q=2, have been carried out. A position of the ECRH zone, designated as r_h in Fig.1, - a distance to the right or to the left from the plasma column centre - was presented by a magnitude of the toroidal magnetic field B_o. A radius of the resonance surface q=2 was calculated from the results of estimating the radial current density distribution profile on the basis of the temperature measurements by the X-ray radiation with due regard for the effective charge values obtained. The m/n=2/1 mode was registered with a set of magnetic probes located and connected as it is shown in Fig.1

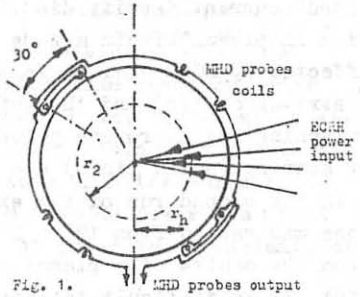

Fig. 1. Diagram of microwave power launching into the chamber and disposition of probes coils.

The measurements were made in the following regime of T-10: magnetic field B_o=25-34kG, plasma current I=230 kA, plasma density n_e=2.-4.5x10^{13}cm^{-3}, safety factor q=3-4, radius of the limiter r_L=28 cm.

In the first run of the experiments, a position of the ECRH zone r_h was varied from 14 to 21 cm toward the low-field side from the centre of the plasma cross-section, i.e."external" heating. An oscillogram of the m=2 mode signal envelope under "external" ECRH at the position of the ECRH zone inside the resonance surface r_2=14 cm is shown in Fig.2a. The same signal, at the position of the ECRH sone at r_h=20 cm, that corresponds to the plasma heating outside the radius r_2 of magnetic surface q=2, is shown in Fig.2b. One should note that a rise in the signal, when $r_h < r_2$ (Fig.2a), is proportional to the pro-

duct of the amplitude of oscillations and their frequency $A_2\,\omega_2$ and occurs mainly due to a rise in the frequency ω_2. When the ECRH zone is displaced into an external plasma region with respect to r_2, Fig.2b, the signal drops mainly due to the amplitude reduction. The experimental result from T-10 can be explained by the emergence of an equilibrium "flattened" current density distribution in plasma within a zone affected by ECRH near surfece q=2. The radial current density distribution j(r) and the safety factors q(r) at a time before switching the microwave pulse on (dashed line) and by the end of heating (solid lines) are given in Fig.3.

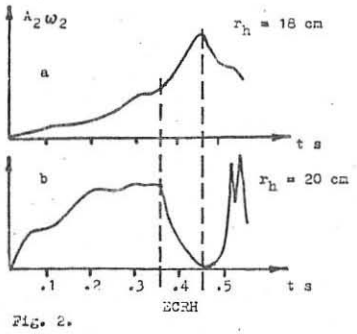

Fig. 2.

m=2 mode probes signal under heating inside the resonant surface q=2 (a) and outside it (b).

In the second run of the experiments, a position of the ECRH zone was varied from 12 to 22 cm towards the high-field side from the centre of a plasma cross-section, i.e."internal" heating. It is difficult to expect the pronounced effect of stabilization under "internal" heating, as the zone of microwave power deposition can be found extend due to refraction of the microwaves from the density gradients and due to the beam defocussing. The experimental results have shown that the stabilizing effect takes place even in that case. The m=2 mode signal behavior and a simultaneous variation in the frequency of oscillations ω_2 under heating of plasma in the zone r_h=-20.5 cm are shown in Fig.4. The specific feature of this regime is a steep rise in the frequency of oscillations of the m=2 mode at a simultaneous drop in the signal

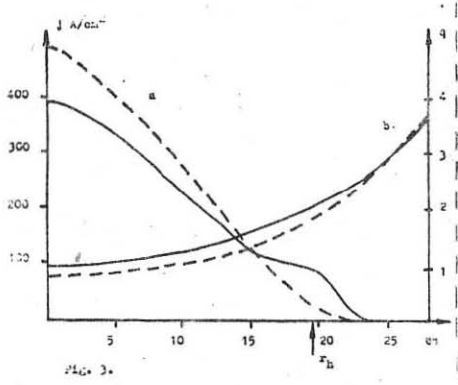

Fig. 3.

Current density profiles (a) and safety factor profiles (b) before (solid line) and during ECRH.

proportional to its frequency and amplitude $A_2\omega_2$. Such a shift in the frequency is typical for a case, when the supression of the oscillations occurs due to a change in the parameters of a system but not due to dissipative phenomena. The experimental data from both runs are shown in Fig.5. The position of the ECRH zone is layed off as abscissa, the logarithm of a ratio of the m=2 mode amplitude in the end of the ECRH pulse to its value before switching the ECRH power on under ohmic heating is layed off as ordinate. Under "internal" heating a decrease in the effitiency of suppressing the MHD-oscillations at the removal of the ECRH-zone from the surface q=2 was observed. As soon as the minimum of ECRH power was about 200 kW one can hope that this level of power is sufficient for mode m=2 stabilization.

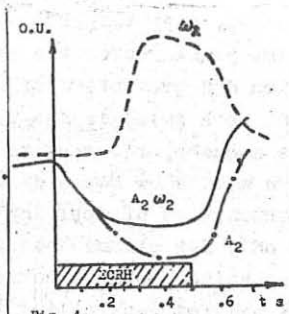

Fig. 4.

m=2 mode signal variation in time and separately frequences and amplitudes of the signal under "internal" heating, r_h=18 cm.

The use of ECRH has allowed to obtain some data on the possibility of preventing disruption. A drastic increase in the gas puffing gave a chance to increase the MHD activity of the m=2 mode, resulting in a number of minor disruptions (Fig.6). When the ECRH was on before puffing a gas and the conditions for stabilizing the m=2 mode were satisfied, there was no rise in the signal of this mode till the end of the microwave heating pulse Fig.6b. The disruptive instability was prevented even when the first minor disruption did not occur by the beginning of the microwave pulse. After a number of minor disruptions, which were characterized by the presence

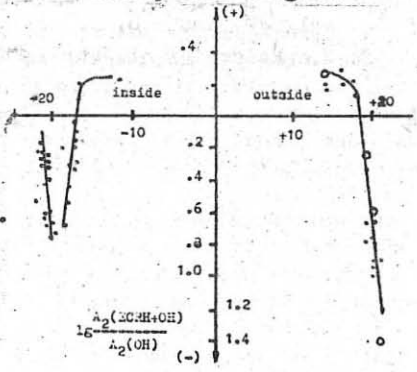

Fig. 5.

Relative changes of the amplitude of the mode m=2 on a logarithmic scale at variation in the ECRH zone position.

of steep, deep temperature drops in the plasma core, the stabilization and prevention of disruption, as a rule, is not possible.

As a whole, the results of a given work show how wide are the opportunities of applying ECRH not only for plasma heating but for shaping a stable current profile and for controlling the operation of tokamak regime. The experimental results confirm the theory /3/ which has shown the possibility of suppressing the MHD modes m/n=2/1 and m/n=3/2 by the electron temperature rise and, as a result, by the current density rise from an external side of the resonance surface q=2.

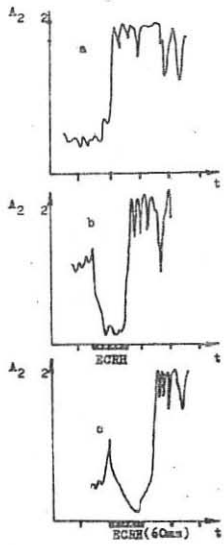

Fig.6
MHD-activity signals under ECRH affect on disruption.

References.

1. 10th Europ. Conf. on Contr. Futions and Pl. Phys., Moscow, 1981, v.2, p. 11.
2. V.V.Alikaev, M.M.Stepanenko. Pis'ma J. Exp. Teor. Fiz., vol. 40, issue 8, 327-329.
3. J.A.Holmes et al. Nucl. Fusion, 1979, 19, 1333.

FLUCTUATIONS AND LOSSES IN THE TOSCA TOKAMAK

A Howling*, A Coté*, E J Doyle≠, D E Evans and D C Robinson
Culham Laboratory, Abingdon OX14 3BD, UK
(Euratom/UKAEA Fusion Association)
*University of Oxford. ≠University College, Cork, Ireland

INTRODUCTION

Experiments have been performed on TOSCA (R = 30cm, $a_L \lesssim$ 8cm, B_ϕ = 0.5T, $I_p \sim$ 10kA, $\bar{n}_e$ = 0.5→2 x $10^{19}m^{-3}$) with double Langmuir probes, novel split limiters (in which the electron and ion drift sides can be insulated and independently monitored) and CO_2 laser scattering. Results and discussion are presented in two sections; the first refers to high frequency fluctuations (100→450 kHz), the second to measurements during large MHD activity (40→50 kHz). In each section, the nature of the fluctuations and their contribution to edge losses are considered.

1. HIGH FREQUENCY FLUCTUATIONS IN THE BOUNDARY PLASMA

Probes show $n \lesssim 10^{18}m^{-3}$ and $T_e \sim$ 10→15 eV ($r > a_L$), comparable with edge plasmas in many tokamaks. Scrape-off e-folding lengths are L_n = 1.3 cm and L_T = 4.0 cm. In the absence of strong MHD, $\tilde{n}/n \sim$ 0.4→0.8 and $\tilde{V}_f/T_e \sim$ 0.4→0.6 (V_f is the floating potential) whereas $\tilde{B}_\theta, r/B \lesssim 10^{-4}$. $\tilde{n}/n$ increases with minor radius but $\tilde{V}_f/T_e$ and $\tilde{B}_\theta$ have the opposite behaviour. The power spectra of $\tilde{n}$, $\tilde{V}_f$ show an f^{-p} dependence with $p \sim 2$; $p \sim 4$ for the $\tilde{B}_\theta$ spectra. The forms of the fluctuation power spectra are roughly independent of $\bar{n}_e$. Autocorrelation times are $\lesssim 5\mu s$ and coherence levels between different parameters are $\lesssim 0.5$ in the absence of MHD. Limiter and laser scattering measurements detect a top-bottom asymmetry in fluctuation magnitude of ~ 2 indicating some poloidal asymmetry. $\tilde{T}_e$ was estimated using a technique[1] not previously used on a tokamak, in which probe current fluctuations $\tilde{I}$ are analysed in terms of contributions from $\tilde{n}$, $\tilde{T}_e$ and voltage fluctuations. Measurements show $\tilde{T}_e/T_e \sim 1\% \ll \tilde{n}/n$ (isothermal fluctuations) above MHD frequencies (Fig 1(a)), therefore $\tilde{V}_f \sim \tilde{V}_p$ (plasma potential fluctuations) and $\tilde{I}_{sat} \propto \tilde{n}$.

Phase measurements of $\tilde{V}_f$ (probes) and $\tilde{n}_e$ (laser scattering) show $\underline{k}$ to be predominantly perpendicular to $\underline{B}$. Figure 2 shows a probe dispersion relation ($r < a_L$); the phase velocity V_{ph} agrees with the scattering results[2] and, after allowing for E_r, is in the direction and of the order of magnitude of the electron diamagnetic drift velocity. However, it was not possible here to distinguish between propagating waves and plasma rotation. For $r > a_L$, probes show that the direction is reversed; plasma potential profiles also indicate a reversal in E_r near the limiter radius suggesting that E_r/B drifts may be responsible.

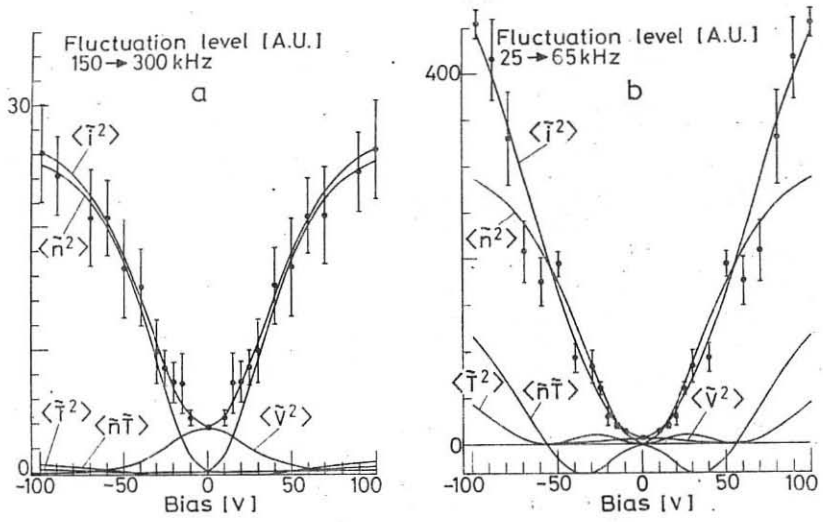

Figure 1 Non-linear least-squares fit to $\tilde{I}$ as a function of bias, (a) 150 → 300 kHz (b) 25 → 65 kHz

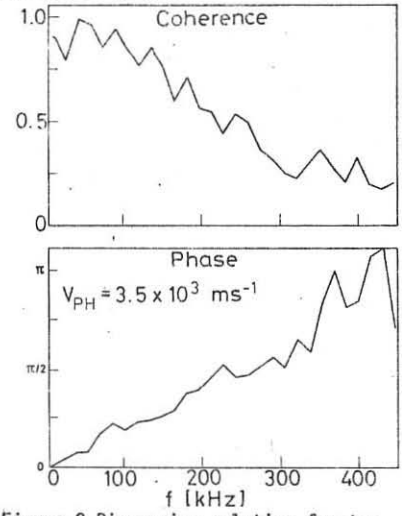

Figure 2 Dispersion relation for two $\tilde{V}_f$ probes, averaged over 8 shots

Fluctuation-induced particle loss due to $\langle \tilde{n}\tilde{v}_r \rangle$ convection (where $\tilde{v}_r = \tilde{E}_\theta/B = ik\tilde{V}_p/B$ in the electrostatic approximation) is estimated from the correlation between $\tilde{I}_{sat}$ and $\tilde{V}_f$ (valid for $T_e/T_e << 1$) and the measured k-value. Figure 3 presents the phase between $\tilde{I}_{sat}$ and $\tilde{V}_f$, and the frequency-resolved flux - results are similar to those on Pretext [3]. The integrated flux yields $D_\perp \sim 2.2 m^2 s^{-1}$ ($\chi_e \sim 3 m^2 s^{-1}$ from sawtooth propagation observations, consistent with $\tau_E \sim 0.3$ ms) at $r \sim a_L$ where $D_{BOHM} \sim 2 m^2 s^{-1}$. Uncertainties in probe calibration and poloidal asymmetry could introduce significant errors.

The scaling of $|\tilde{V}_f|$ and $|\tilde{n}_e|$ with $\bar{n}_e$ was investigated: probe measurements ($r \gtrsim a_L$) show $|\tilde{V}_f|$ and $|\tilde{n}/\bar{n}_e|$ are independent of $\bar{n}_e$, and laser scattering demonstrates only a weak inverse dependence for the latter. At $r=a_L$ we find $k_\perp \rho_s \sim 0.2$ and $\tilde{n}/n \sim 1/k_\perp L_n \sim 5\rho_s/L_n$, where ρ_s is the ion gyroradius evaluated at $\bar{T}_e$.

Experiments in which large biases (± 90V) are applied between limiters and vessel, or between ion and electron drift sides of the split limiters (thereby affecting current flow through the limiter sheaths) show no measurable influence on the level or spectrum of $\tilde{I}$ or $\tilde{V}_f$. Also, no discontinuity in fluctuation parameters is observed across the limiter radius. The aim of this series of experiments was to test the theory [4] that limiters may be in part the cause of edge fluctuations; the results seem to show that local mechanisms, rather than discontinuities due to the limiters, are responsible for the turbulent edge. The single marked effect was to change the mean level of V_f (as measured by probes toroidally near and far from the limiters): grounding the limiters to the vessel raised the probe potential by $3\bar{T}_e$ compared to when the limiters were floating.

The edge plasma of TOSCA is observed to be turbulent under all the conditions of an ohmically heated circular plasma investigated. The turbulent nature renders identification of specific mechanisms difficult, but the indication is that local effects are responsible for the large fluctuations. The low level of $\tilde{T}_e/T_e$ discriminates against the rippling and impurity driven rippling modes, but observations are not inconsistent with turbulent drift wave theory predictions. Convective losses are always outwards and of sufficient magnitude to account for the observed transport. However, if this is the primary loss mechanism, the relative insensitivity of $|\tilde{V}_f|$ and $|\tilde{n}/\bar{n}_e|$ to $\bar{n}_e$ in the outer regions means that subtle changes in coherence lengths, phase angles and wave-numbers must be involved. The radial profile and density-independence of $|\tilde{B}_\theta|$ suggest that magnetic fluctuations are not the cause of anomalous transport in the outer regions of TOSCA[5].

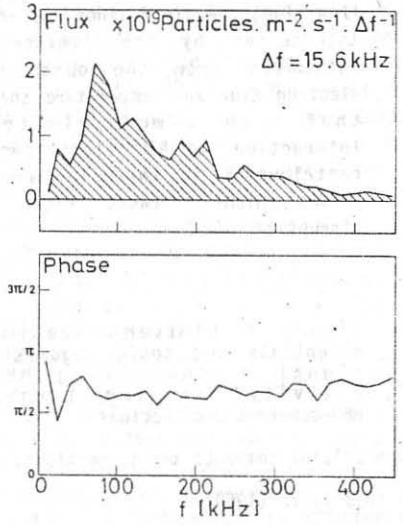

Figure 3 Phase between $\tilde{I}$ and $\tilde{V}_f$ and frequency-resolved flux, integrated flux = 1.7×10^{20} particles $m^{-2}s^{-1}$

2. EFFECTS OF STRONG MHD ACTIVITY

During strong m=2, n=1 activity ($\tilde{B}_\theta/B_\theta \sim 2\%$) large coherent unipolar oscillations in V_f are observed on a 3-limiter floating array (top, bottom and outer-midplane) for a well-centred discharge (Fig 4). Oscillatory electron currents of amplitude 10→15A flow when grounded to the vessel. Phase analysis is consistent with an m=3, n=1 mode (the toroidal dependence is deduced from a fourth limiter), with $q_L = 4 \rightarrow 4.5$. The frequency of this mode is the same as the m=2 mode, one interpretation is that the plasma is rotating toroidally as a rigid body (anti-parallel to the plasma current).

Laser scattering shows a strong $\tilde{n}$ correlation with MHD, as do $\tilde{T}$ and $\tilde{V}_f$ of probes provided that $r < a_L$: the MHD component becomes small on probe signals if $r > a_L$. Also, if any limiter is moved to a smaller radius, the oscillation in V_f is 'scraped-off' from the others, demonstrating that the effect is radially well-defined. Split limiter measurements demonstrate that the V_f oscillation occurs principally on the electron drift side. Probe current fluctuation analysis, Fig 1(b), shows that $\tilde{T}_e/T_e$ is large (comparable to $\tilde{n}/n$) at the MHD frequency, and is sufficient to account for the size of $\tilde{V}_f$ ($\Delta V_f \gtrsim 40V$ ie $\Delta T_e \gtrsim 15eV$ so that $T_{max}/T_{min} \gtrsim 2$).

These observations are commensurate with a rotating magnetic structure modulating a flux of hot (30→40 eV), current-carrying electrons which flow along the field lines and are intercepted by the limiters. Estimates from the observed electron flux and temperature show that such a mode/limiter interaction has a significant contribution to thermal energy losses which increases before a disruption.

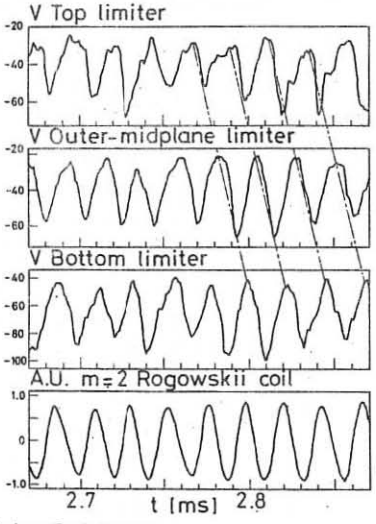

Figure 4 Limiter floating potentials and cos2θ Rogowskii signal during strong MHD activity, showing large, MHD-coherent oscillations

Acknowledgements

We wish to thank A W Morris for many helpful comments and suggestions.

References

[1] D C Robinson and M G Rusbridge, Pl Phys 11 73 (1969)
[2] D E Evans et al, Pl Phys 25 617 (1983)
[3] S J Levinson et al, Nucl Fus 24 527 (1984)
[4] R W Motley, Phys Rev A 24 2151 (1981)
[5] J J Ellis et al, Proc 10th IAEA Int Conf London 1 363 (1984)

OBSERVATION OF MULTIPLE HELICITY MODES ON JET+

P S Haynes*, A W Morris#, D C Robinson*
JET Joint Undertaking, Abingdon, Oxon, OX14 3EA, UK

*Culham Laboratory, (Euratom/UKAEA Fusion Association)
#Balliol College, University of Oxford
+Work performed under a Task Agreement between Culham and JET

Introduction Studies of the MHD activity on JET have revealed modes of more than one helicity. This is manifest in the existence of at least two toroidal mode numbers (n) or in the presence of current perturbations on more than one rational q surface for a single n. The fluctuations were measured with internal coils and external saddle loops, and earlier studies were reported[1]

Observations of modes with different n

Figure 1 shows a striking example of this phenomenon. The n=2 component has twice the frequency of the n=1, consistent with purely toroidal rotation at speeds up to 3.10^4m/s. The figure confirms that low amplitude eigenmodes have a single dominant n in the tight shaped plasmas on JET. The discharge was near the density limit and the plasma disrupted at 50.686s in the current decay, I_p = 1.1 MA, b/a = 1.35, q_ψ = 8. The n=2 component is triggered at a critical level of the n=1 (which increases from ~ .05% to ~ 0.08% B_θ ($\mu_o I/2\pi r$)) and saturation occurs with b(n=2) ~ 25% b(n=1). The two modes decay together. The frequency falls slowly and the maximum amplitude increases with time. Phase measurements indicate (m=2,n=1) and although (4,2) is suggested, toroidal effects on the phase and the temporal behaviour imply a distinct mode, (3,2). The relative phase is that expected from simple non-linear effects, ie the n=2 component has an O-point at the outboard O-point of the parent (2,1) island. In the final burst the n=2 saturates at ~ 0.03% B_θ whilst the n=1 part grows exponentially (τ_g ~ 10ms) until locking occurs at an amplitude ~ 0.7% B_θ. The field at locking is ~ 10G and this level is approximately the same for all disruptions in centred plasmas. The modulations are not directly correlated with the sawtooth, which has a period of ~ 30 ms continuing through most of the figure.

Not all cases are as in Fig 1 - often the n=1,2 components grow together, the ratio n=2:n=1 ~ 25%. This has been observed when a radiation dominated layer moves in from the limiter. The n=2 mode is then identified as m=3, with a larger out/in amplitude ratio (~ 3) than the n=1 (m=2) signal (~ 2). The (2,1) (3,2) islands are estimated to be similar in size, and overlap may occur before mode locking but contact with the limiter is not expected. Again the n=2 component saturates while the n=1 grows exponentially (τ_g ~ 10ms) until locking when the growth becomes approximately linear, and the electron temperature profile narrows and flattens before disruption.

n=2 signals have been observed when (m ~ 4, n=1) modes are excited in the final current rise and have $m \gtrsim 5$. Oscillations stimulated by the

appearance of a radiation dominated region at the edge of the plasma are also observed to have n=2 components; the principle mode being $m \gtrsim 3$, n=1.

Single n multiple helicity modes

Consideration of the resistive MHD equations leads to predictions of eigenfunctions of single n in toroidal or shaped plasmas. The effect of geometry is to give eigenmodes with current perturbations on all surfaces q=m/n for given n. The sign and magnitude at each surface depends upon the equilibrium. The result is monitored by the poloidal variation in phase and amplitude of the magnetic oscillations at the wall. The current perturbations are required to obtain the correct resonant radial field at each surface and hence the magnetic island sizes. Computations in JET geometry give distortion of the phase from $m\theta_{coil}$ and strong outward ballooning of the amplitude. The effect of other surfaces becomes unimportant when there is only one n=1 resonant surface in the plasma (ie low q) or the principal surface is very close to the coil (eg in the current rise).

Figure 2 shows the amplitude variation for three plasmas, all in the flat top and b, c shortly before disruption. Comparing (a), (c), the chief difference is the q, and for (c) there are thus many n=1 resonant surfaces present. The behaviour near coil 1 is consistent with the effect of ellipticity on local rotational transform, but the observed in/out ratio apparently requires perturbations of appropriate sign at other surfaces.

The phase plot for the examples of Fig 2 has slope m=2 (phase vs coil angle from R = 3.0m), and does not show the phase distortion observed for modes excited near the edge during the final current rise (for dI/dt large enough), which have an in/out amplitude ratio near to unity. The wall acts as a reasonable conductor at these frequencies ($\lesssim$ 1 KHz), but this increases the slope only slightly.

Discharges at low q

The increase in amplitude of $\tilde{b}$ with falling q[1] is still observed when mhd activity is present but discharges can be free from coherent modes, with $b_\tau/B_\theta < 3 \times 10^{-5}$ for $q_\psi \gtrsim 2.3$. No pronounced activity occurs at $q_\psi \sim 3$. Figure 3 shows a set of waveforms for a low q disruption on JET, in this case somewhat below the density limit extrapolated from higher q. The smoothed mhd signal is dominated by the fast oscillations at the sawteeth. The oscillatory period is very brief (~ 10ms). The growth in both oscillatory (with $\lesssim$ 25%n=2) and locked periods is approximately exponential with $\tau_g \sim$ 3ms. This should be compared with the linear growth after locking at higher q[1] before density limit disruptions. Just before disruption I_p = 3.3MA, q_ψ = 2.3, b/a = 1.4 The mode structure remains primarily m=2, n=1 and b_τ (n=1) reaches a maximum of 290G (6%B_θ) just before disruption but at ~ 2% additional structure appears on the b_τ signal. At this change (47.245s) the ece from the central region falls, not as in a normal sawtooth. The (2,1) island is predicted to overlap the limiter (the fields penetrate the wall on this timescale). The in-out amplitude ratio of the locked mode is close to unity similar to Fig 2(a). The energy quench as revealed by the central ece signal is rapid ($\lesssim$1ms).

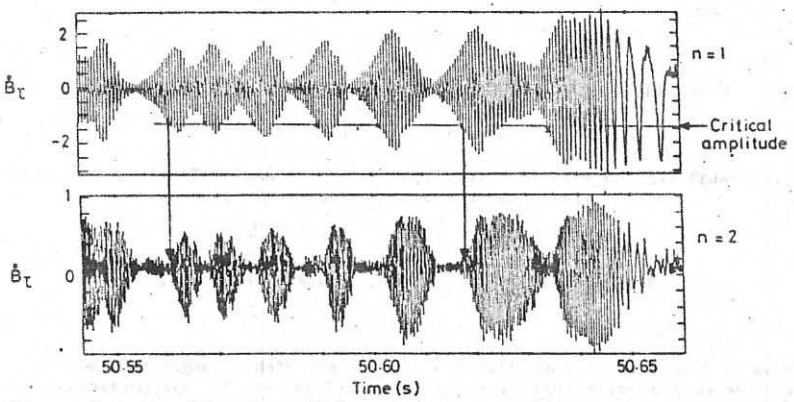

Figure 1 n=1 and 2 mode activity showing the onset of n=2 activity at a critical n=1 level

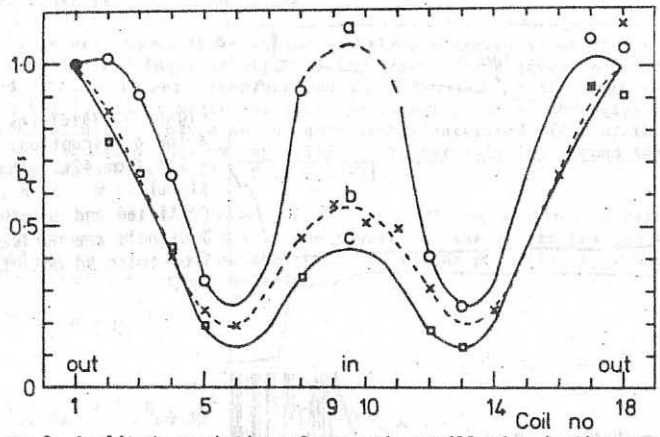

Figure 2. Amplitude variation of magnetic oscillation (m=2) around vessel (a) q_ψ = 2.7, b/a = 1.5;(b) q_ψ = 4.5 b/a = 1.2;(c) $q_\psi \sim 6$, b/a = 1.5.

Conclusions The observed poloidal variation in phase and amplitude of the MHD activity on JET with a single n is in qualitative agreement with theoretical predictions of tearing modes in non-circular toroidal geometry, which require the existence of currents on several resonant surfaces. MHD activity is accompanied by an n=2 mode and in some cases is triggered at a critical level of b_τ (n=1). Discharges with $q_\psi \gtrsim 2.3$ can be free from mhd activity. Disruptions at the density or q limit are associated with large m=2,n=1 perturbations which can grow rapidly but involve little n=2 activity.

Acknowledgement We would like to thank D Campbell for his assistance with the e.c.e diagnostic.

Ref [1] PR Thomas, JA Wesson et al, Proc IAEA Int Conf London, 1 353 (1984)

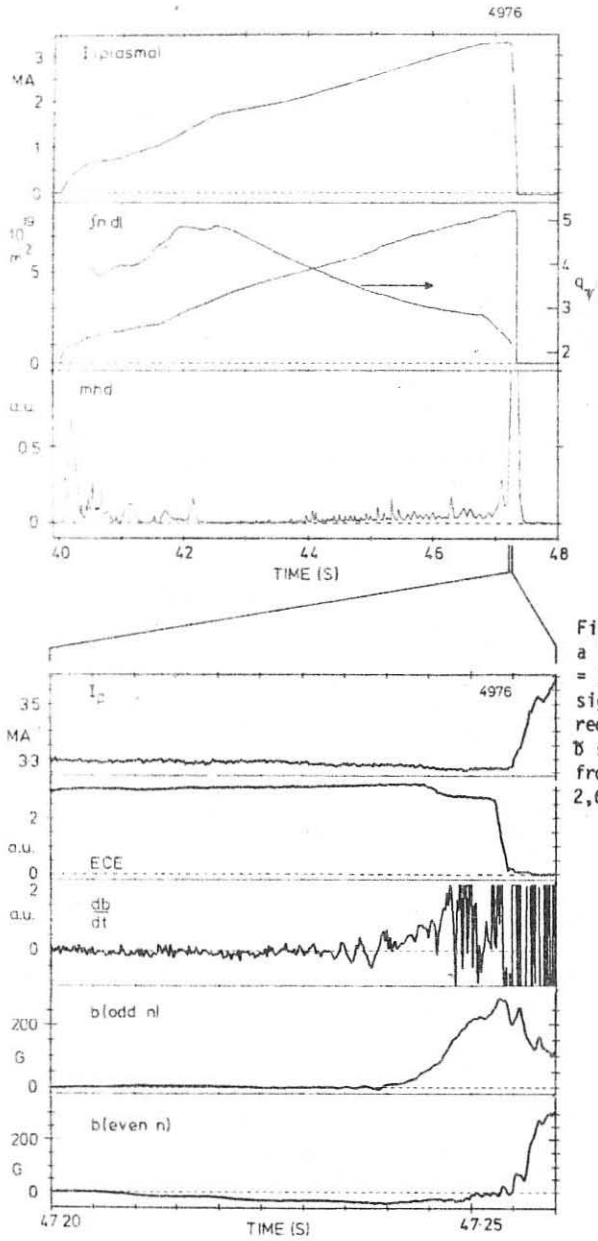

Figure 3. Waveforms for a low q disruption. b/a = 1.4 from 42s. The mhd signal is m ~ 2, n=1 rectified and smoothed. $\dot{B}$ signals are derived from coils in octants 2,6.

IDENTIFICATION OF MAGNETIC HELICAL PERTURBATION IN A TOKAMAK

F. Alladio, F. Crisanti

Associazione EURATOM-ENEA sulla Fusione, Centro Ricerce Energia Frascati, C.P. 65 - 00044 Frascati, Rome, Italy

E. Lazzaro

JET Joint Undertaking, Abingdon, Oxon, OX143EA, U.K.

A complete magnetic data analysis in tokamaks should comprehend an accurate reconstruction of the axysymmetric magnetic flux structure as well as information on the location, width and rotation of the most relevant island structures produced by resistive tearing modes. A computerised procedure is generally desirable and especially in conditions of non circular plasma and vessel cross sections such as JET.

It is well known that outside an island centered around the $q = m/n$ surface the true nonlinear solution of the tearing mode equation is well approximated by the linear eigenfunction characterised by the logarithmic slope jump $\Delta'(0)$ [1]; as a matter of fact the linear solution characterises so well the real situation that also the quasilinear saturated width of the island is usually calculated just by exploring the linear solution around the resonance until the condition $\Delta'(w) = 0$ is met [2].

For a cylindrical plasma of radius a, enclosed within a perfectly conducting vessel of radius $b > a$, the physics of the linear tearing mode is described by an equation for the perturbed vector potential $\tilde{A}_z$ and an equation for the perturbed current density $\tilde{J}_z$

$$\nabla^2 \tilde{A}_z = - \mu_o \tilde{J}_z \tag{1}$$

$$B_{oz} \frac{\partial \tilde{J}_z}{\partial z} + \frac{1}{r} B_{o\theta} \frac{\partial \tilde{J}_z}{\partial \theta} = - \tilde{B}_r \frac{\partial J_{oz}}{\partial r} \tag{2}$$

with boundary conditions

$$\tilde{A}_z \big|_b = 0; \quad \partial \tilde{A}_z / \partial r \big|_b = \tilde{B}_\theta \tag{3}$$

Considering a single mode helical perturbation of the form

$$\{\tilde{J}_z, \tilde{A}_z, \tilde{B}_r\} = \{\tilde{J}_m, \tilde{A}_m, \tilde{B}_{rm}\} \exp [i(m\theta - (n/R) z)] \tag{4}$$

neglecting the terms $O/(a^2/R^2)$, one obtains

$$\tilde{J}_m = \frac{ir \tilde{B}_{rm} (dJ_{oz}/dr)}{m B_{o\theta} [1-n/m\, q(r)]} \tag{5}$$

which is singular at the resonant radius $r = r_s$. It gives rise to the discontinuity

$$\Delta'(0) = \lim_{\varepsilon \to 0} \frac{r}{\tilde{A}_m} \frac{d\tilde{A}_m}{dr} \Big|_{r_s-\varepsilon}^{r_s+\varepsilon} \tag{6}$$

On the other hand such discontinuity can be generated by an equivalent singular surface current $J_z = J\,\delta(r-r_s)\exp[i(m\theta - (n/R)z)]$, provided that [3],

$$\Delta'(0) = \frac{\mu_o |J|}{\tilde{B}_{rm}(a)} \left[\frac{\tilde{B}_{rm}(a)}{\tilde{B}_{rm}(r_s)} \right] \tag{7}$$

So, the problem of determining the stability parameter $\Delta'(0)$ can be reduced, also in cases of a geometry more complex than the cylindrical one, to that of finding an equivalent surface current J located on the resonant surface such that the boundary conditions

$$\tilde{A}\big|_{\Gamma} = 0 \text{ and } \partial\tilde{A}/\partial\nu\big|_{\Gamma} = \tilde{B}_{\tau} \tag{8}$$

are met. Here Γ is the meridian contour of the perfectly conducting vessel and $\vec{\nu}$ and $\vec{\tau}$ are the normal and tangential directions to Γ.

For the JET case we take in full account the shape and toroidicity of the vacuum vessel as well as of the resonant surface, but neglect the helicity. From the condition (8) the identification of the equivalent surface current, described piecewise like J_k on the k-th toroidal scale of the resonant surface, can be accomplished by solving the linear induction system

$$\sum_{k\varepsilon S_q} M^q_{ik}\,\dot{J}_k + \sum_{j\varepsilon S_v} M^v_{ij}\,\dot{I}_j = 0 \tag{9}$$

where

M^v_{ij} is the mutual inductance of the j-th toroidal scale of the vessel with the i-th reference ring on the vessel contour.

M^q_{ik} is the mutual inductance of the k-th toroidal scale of the resonant surface with the i-th reference ring on the vessel contour.

J_k is the local surface current flowing in the k-th toroidal scale of the resonant surface and is the unknown.

I_j is the local surface current flowing in the j-th toroidal scale of the vessel and is provided by the $\tilde{B}_{pol}$ measurements, that are taken by coils adjacent to the inside of the vacuum vessel as

$$\dot{I} = \dot{\tilde{B}}_{pol}/\mu_o \quad [A/m\cdot sec] \tag{10}$$

The second physical measurement required for the $\Delta'(0)$ determination is (see Eq. (7)) the value of the radial fluctuating field at the plasma boundary. It can be calculated in an inductive form as

$$\dot{\tilde{B}}^i_r = \frac{1}{2\pi R_i} \frac{d}{dS_b} [M^{bv}_{ik}\,\dot{I}_k + M^{bq}_{ij}\,\dot{J}_j] \tag{11}$$

where S_b is the poloidal arclength of the plasma boundary, R_i is the major

radius of the i-th toroidal scale of the boundary, M_{ik}^{bv} is the mutual inductance between the i-th toroidal scale of the boundary and the k-th toroidal scale of the vessel, M_{ij}^{bq} is the mutual inductance between the i-th toroidal scale of the boundary and the j-th toroidal scale of the resonant surface. Figure 1 shows the equilibrium reconstruction [4] from magnetic data, with display of the q rational surfaces, during the large MHD activity of JET shot ≠ 2453 that terminated in a major disruption. The solution of Eqs (9) and (11), having as input the measured magnetic fluctuations at the time slice of the equilibrium reconstruction, leads to the evaluation of a fluctuating radial field with m = 2 symmetry at the plasma boundary as shown in Fig. 2 and, at the same time, to the evaluation of the distribution of the equivalent surface current on the q = 2 resonance, as shown in Fig. 3. From the maxima and minima of this latter waveform it is possible to locate the nodal and focal points of the magnetic island as shown in Fig. 4. To evaluate the corresponding island size a reduction of the reconstructed equilibrium profiles to a cylindrical approximation is required: a mapping conserving the q value seems the most suitable one. For every flux surface ψ, within which a current $I(\psi)$ flows and which is characterised by a $q(\psi)$ value, one can define an equivalent cylindrical radius and an equivalent cylindrical current density profile as

$$\rho = \sqrt{2\times10^{-7}\,\frac{q(\psi)\cdot R_{axis}\cdot I(\psi)}{B_{T\ axis}}}\,; \qquad J^{\circ}(\rho) = 5\times10^{6}\,B_{T\ axis}\,\frac{\left(2 - \frac{\rho}{q(\psi)}\,\frac{dq}{d\rho}\right)}{2\pi\,R_{axis}\,q} \tag{12}$$

The profile ρ, $J^{\circ}(\rho)$ is used to determine the tearing mode eigenfunction $\tilde{B}_r$ outside the resonant surface ($r > r_s$) with boundary condition

$$\frac{r}{\tilde{B}_r}\left.\frac{d\tilde{B}_r}{dr}\right|_a = \frac{(m-1) + (m+1)\,(b/a)^{2m}}{1 - (b/a)^{2m}} \tag{13}$$

The ratio b/a being the ratio of the poloidal arclengths S-vessel/S-boundary. Then the value of $\Delta'(0)$ associated to the surface current J (see Eq. (7)) and the radial field $\tilde{B}_r(a)$ is used to explore the eigenfunction inside the resonant surface ($r^{rm} < r_s$). The residual degree of freedom of the equilibrium identification [4] allows limited adjustments of the values of q(0), which are sufficient to obtain the correct behaviour $\sim r^{m-1}$ at r = 0.

A number of disruptive JET shots has been similarly analysed featuring a variety of q at the edge $4.5 < q(a) < 8.5$ and a variety of j-profile peaking parameter $4. < q(a)/q(0) < 9.$

In all the cases, given $\Delta'(0)$ measured from the magnetic fluctuations, it is possible to obtain the correct matching of the eigenfunction in r = 0 and therefore the correct evaluation of the island width. This shows that it is possible to obtain a consistency between the equilibrium magnetic identification and the magnetic fluctuations interpreted as due to resistive tearing modes. Furthermore the strong sensitivity to q(0) can help in the identification of its correct value, improving the equilibrium identification itself. The island sizes obtained are in the range $0.08 \leq w/a \leq 0.18$, corresponding to $1.6 \leq \Delta'(0) \leq 3.3$. The q(0) is found to vary between 0.87 and 1.21 with an adjustment $\Delta q(0) \cong \pm 0.1$ within the degree of freedom of the equilibrium reconstruction. Moreover the sensitivity of other bulk parameters (β_p and ℓi) to such adjustment are negligible ($\Delta\beta_p \cong \pm 0.02$, $\Delta\ell i \cong \pm 0.05$).

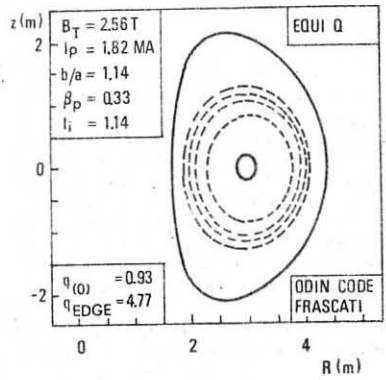

Fig. 1 Identification of equilibrium with display of q = 1,2,3,4 surface and plasma boundary during large MHD activity.

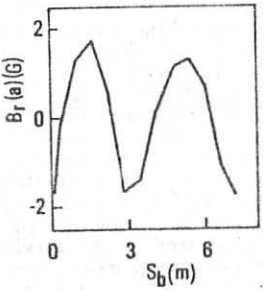

Fig. 2 Radial magnetic field perturbation $\tilde{B}_r$ (a) at the plasma surface.

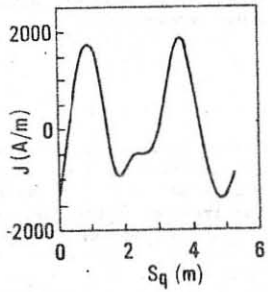

Fig. 3 Equivalent surface current density on the q=2 surface.

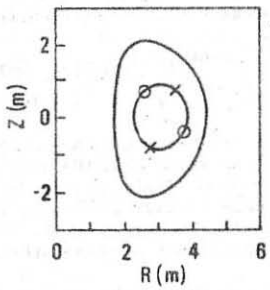

Fig. 4 Nodal and focal points of the q=2 magnetic island.

REFERENCES

[1] H.P. Furth, J. Killeen, M.N. Rosenbluth, Phys. Fluids 6 (1963) 459.
[2] M.F. Turner, J.A. Wesson, Nucl. Fusion 22 (1982) 1069.
[3] T. Jensen, M. Chu, J. Plasma Phys. 24 (1980) 229.
[4] F. Alladio, F. Crisanti, M. Marinucci, paper 275 this Conference.

EXTRAPOLATION OF BUNDLE DIVERTOR RESULTS TO A REACTOR OF INTOR/NET SIZE

P J Harbour and P C Johnson
Culham Laboratory, Abingdon, Oxon, OX14 3DB, UK
(Euratom/UKAEA Fusion Association)

1. Introduction

Following a review [1] of present knowledge of tokamak discharges with a bundle divertor, the results have been extrapolated to assess the potential of a bundle divertor for a reactor of INTOR/NET size, with emphasis on compositional control and exhaust. Our present knowledge is based on experiments with the DITE bundle divertor [1,2,3] and on the results of modelling. In extrapolating the DITE performance to a reactor the aim must be twofold, firstly, to operate with good confinement at low-q in order to achieve high beta, and secondly to take steps to achieve efficient energy exhaust and to handle the power that flows into the divertor.

2. The Approach to Achieving Stable Discharges at Low-q

In the DITE experiment it was found that diverted discharges with good confinement are obtained but only with the safety factor $q \gtrsim 3$ at the separatrix, when mhd activity is not significant. These discharges have confinement times as good as or better than those of limiter discharges. At low values of $q(q_{sep} \lesssim 3)$ stationary islands are formed due to mhd interaction (at m=2 and m=3) with the divertor field and confinement is seriously degraded, by a factor of about 2. Attempts to suppress or circumvent this q-limit have been unsuccessful.

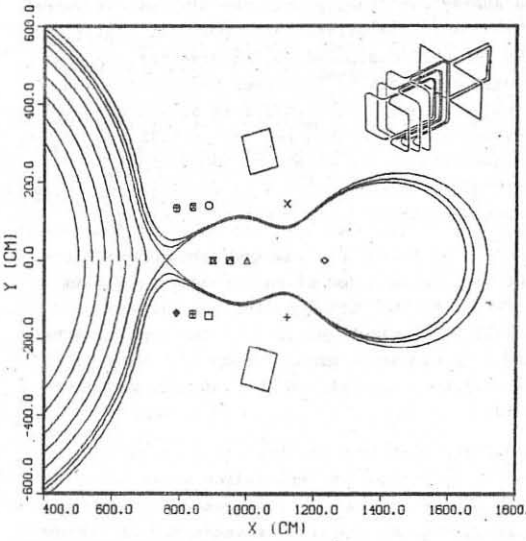

Fig.1 Cascade bundle divertor with flux expansion coils. An isometric view is shown in the inset [7].

It might be possible to design saddle coils which effectively cancel the interaction between the divertor and tokamak equilibrium fields but it is not yet clear how to do this, nor is it clear whether this would only work at one radius, e.g. where q=2. A complementary approach is to select a configuration with low ripple in the toroidal field. In the DITE Mk.II divertor the ripple on axis, $\Delta B_T/B_T \approx 2.6\%$.

The bundle divertor offering the lowest ripple ($\lesssim$ 0.2% on axis for NET), the least current and the smallest physical size, and providing adequate space (0.6m) for shielding, is the staged T-shaped or cascade bundle divertor [4]. Using a commercially available Nb_3Sn cable and a shield of tungsten and borated water, a lifetime $\gtrsim$ 5MW yr m^{-2} is predicted and the current density is no more than 3.5kW cm^{-2}: good flux surfaces are also predicted, with minimum formation of magnetic islands [4]. One arrangement of cascade plus T-shaped divertor is shown in Fig.1 in plan view, clarified in the inset. This divertor also features a very high flux expansion, with magnetic mirror ratios $R_u \approx 2$ on the upstream side of the throat and $R_d \approx 50$–100 on the downstream side. Whether it is possible to obtain stable operation at low-q would require an experimental demonstration, possibly incorporating two such bundle divertors with low-ripple and saddle coils to reduce the effective perturbation to the equilibrium field.

3. Power Handling if Efficient Energy Exhaust is Achieved

Very efficient energy exhaust has been achieved in DITE with about 70% efficiency in ohmic discharges without gas feed: otherwise efficiencies are 10% to 25% in beam heated discharges independent of gas feed, and only a few percent in ohmic discharges with gas feed. Most of the exhaust is concentrated in a layer of high temperature plasma with a heat flux of 100MW m^{-2} and a particle flux of 10^{24} $m^{-2}s^{-1}$. This layer is small, both poloidally and radially in agreement with predictions from both fluid and kinetic models. Most of the energy not flowing into the divertor is found on walls and limiters, possibly due to the existence of poloidal regions of the scrape-off layer which are not well connected to the divertor; another cause might be a change in radial transport ($\kappa_\perp^e$) between beam-heated and ohmic discharges. Improved energy exhaust might therefore be achieved by allowing more space for the scrape-off layer than the 5cm in DITE and/or by eliminating regions of poor connection to the divertor. This might be achieved with the divertor of Fig.1, its stagnation axis (B=0) being concave to the plasma rather than convex, and/or by using a second divertor.

If efficient power exhaust is achieved in a reactor, the power flux density at the divertor throat will be an order of magnitude larger than with a poloidal divertor, ~ 2GW m^{-2} in NET with 80MW into one divertor. A high downstream mirror ratio will be required and if $R_d \gtrsim 20$, the (parallel) power flux density at the target should be no greater than in a poloidal divertor and will require the target to be inclined at a similar glancing angle of incidence to the field.

With such a high expansion, the heat flux at the throat is so much larger than at the target that it is limited by the maximum electron flux through the throat, where the transport is locally collisionless, although collisional elsewhere. High recycling is predicted in the divertor and so the net electron flux is negligibly small. The divertor plasma becomes cold

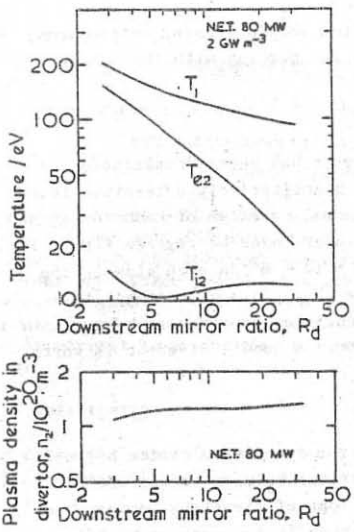

Fig.2 Plasma exhaust conditions predicted for NET. T_i is the separatrix temperature, T_{e2}, T_{i2} are the electron and ion temperatures and n_2 is the density in the divertor.

and dense [1] but the scrape-off layer is much hotter, and drives the heat-flux through the thermal barrier at the throat. Predicted plasma parameters in the scrape-off layer and divertor of NET are shown in Fig.2. The plasma temperature in the divertor becomes acceptably low (T_e ~ 20-30eV) if R_d is in the range 30-20. The scrape-off temperature is about 100eV and the density in the divertor is about 10^{14}m^{-2}. These values are all similar to those predicted for a poloidal divertor for INTOR [5]. The electron heat-flux limited mode of divertor operation has apparently not been achieved in DITE where R_d is too small (~ 2 to 4).

4. Compositional Control

No systematic experimental studies of helium or impurity control have been carried out in DITE, but in diverted discharges, heavy impurities are insignificant and there is ~ 0.5-1.5% of light impurities (mainly C and O), with low radiation loss (25-40%, mostly from the boundary) and low Z_{eff} (~ 1.5 to 2.5). Using theoretical arguments [1] it is predicted that impurity and helium ions are well retained in bundle divertors by the magnetic mirror forces: electrostatic forces also help retention under the low recycling conditions of DITE; apart from around the throat region, they are insignificant under reactor conditions. In the throat there are two competing effects. Electrostatic forces tend to oppose retention, but these may be more than compensated by frictional forces due to the high plasma velocity in the restricted area of the throat.

As far as helium pumping is concerned, the plasma conditions we have predicted for the bundle divertor are so similar to those predicted for the

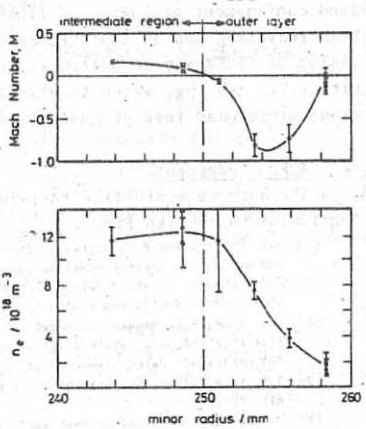

Fig.3 Radial profiles of Mach number and density in the scrape-off layer near the DITE divertor entrance [6].

poloidal divertor that the pumping of helium should present no problems, especially allowing for the better access for pumping with the bundle divertor.

5. Fuelling and Reverse Flow

Fuelling of DITE via the bundle divertor has been demonstrated and, uniquely, reverse flow of plasma has been quantitatively determined in the outer scrape-off layer. Figure 3 shows radial profiles of Mach number and density in the scrape-off layer, with an outer layer of reverse flow. The area of this layer is estimated [6] to be $\approx 10^{-3}$ m^2 on each side of the divertor, with a peak flux of $\approx 2\times10^{20}$ ion s^{-1}. This corresponds to a change in $\bar{n}$ of 1×10^{19} s^{-1} in 40ms, but impurities appeared to be retained in the divertor. The fuelling of a reactor from a bundle divertor is worth further study.

6. Conclusion

Selecting a divertor for the NET reactor requires a choice between a large number of unknowns. Provided that it can be made to operate at low q, the bundle divertor may be able to handle most of the plasma power, and it may be easier to pump but it may take up space in the reactor building normally required for access to maintain the reactor and there are various unknowns which will have to be resolved by experiment. If progress is to be made in making a choice of divertor, an engineering design study will be required to optimise the use of space for the bundle divertor and for access for maintenance and a new experiment is required, with or or two divertors similar to that of Fig.1. It is necessary to provide a demonstration of good confinement at low q, of flux-limited electron energy transport with high recycling and of impurity control under these conditions. Either TEXTOR or ASDEX may be suitable, each having the possibility of high power with r.f. heating, which is also important in investigating any divertor-induced loss of confinement of fast particles.

7. Acknowledgement

The authors would like to thank Dr T.F. Yang for discussions and for permission to publish Fig.1.

[1] P.J. Harbour and P.C. Johnson, "The bundle divertor: compositional control and exhaust in tokamak experiments and the NET reactor", to be published.

[2] P.C. Johnson, et al. Paper IAEA-CN-44/A-IV-4 at 10th Int. Conf. on Plasma Phys. Contr. Fusion Res., London, UK, September 1984 (IAEA, Vienna, 1985).

[3] K.B. Axon, N.C. Hawkes, J. Hugill et al. "Effect of the non-axisymmetric fields of the DITE bundle divertor on magnetic topology, and instabilities and rotation" Paper presented at this conference.

[4] T.F. Yang, et al. "In search of optimised bundle divertors", PFC/JA-81-4, MIT 1981.

[5] M.F.A. Harrison, P.J. Harbour and E.S. Hotston, Nucl.Tech/Fusion 3 (1983) 432.

[6] P.J. Harbour, P.C. Johnson, G. Proudfoot, et al., J. Nucl. Mat. 128 & 129 (1984) 359-367.

[7] T.F. Yang, personal communication, 1985.

RESISTIVITY AND FIELD DIFFUSION IN JET

J.P. Christiansen, D.J. Campbell, J.G. Cordey, S. Ejima*, E. Lazzaro

JET Joint Undertaking, Abingdon, Oxon., OX14 3EA, UK.

* General Atomic Co., San Diego, USA.

Abstract: Studies have been made of parallel plasma resistivity and magnetic field diffusion in JET discharges. In these discharges plasma elongation, plasma current and toroidal field are varied. The first study includes comparisons of Spitzer resistivity and neoclassical resistivity derived from several diagnostic measurements during the flat top of the current waveform. In the second study field diffusion is followed for discharges in which the plasma current is programmed to rise from one flat top to another flat top level.

1. Resistivity and Z_{eff}

The following expressions are used to define the Spitzer resistivity $\eta_{\parallel}^{0}$ and the neoclassical resistivity $\eta_{\parallel}^{*}$ in terms of Z_{eff} and electron temperature T_e:

$$\eta_{\parallel}^{0} = \frac{m_e^{1/2} e^2}{3 \varepsilon_0^2 \pi^{3/2}} Z_{eff}\, \alpha(Z_{eff}) \frac{\ln \Lambda_{ei}}{T_e^{3/2}} \qquad \ldots (1)$$

$$\eta_{\parallel}^{*} = g\, \eta_{\parallel}^{0}, \qquad \ldots (2)$$

where [1] $$\alpha(Z_{eff}) = 0.29 + 0.46/(1.08 + Z_{eff}), \qquad \ldots (3)$$

and $$g = (1 - f_T/(1 + \xi\, \nu_*))^{-1}, \qquad \ldots (4)$$

f_T, ξ and ν_* being given in [2]. Ohms Law is integrated over the plasma cross section as

$$I_\phi = \int E_\phi / \eta_{\parallel}\, da, \qquad \ldots (5)$$

where I_ϕ is the plasma current and E_ϕ the toroidal electric field.

Assuming a uniform Z_{eff} we can determine two estimates of Z_{eff} from (5) using for $\eta_{\parallel}$ either (1) or (2). These values of Z_{eff} are referred to as Z_{Spi} and Z_{Neo} respectively. A third estimate of Z_{eff} is found from visible Bremsstrahlung data collected from a vertical sight line. This estimate referred to as Z_{Vis} is evaluated from

$$Z_{Vis} = C\, B_v \left(\int n_e^2\, g_{ff}\, T_e^{-1/2}\, dl\right)^{-1} \qquad \ldots (6)$$

where C is a constant, B_v the brightness and the integration taken along the viewing line. The variation of the Gaunt factor g_{ff} with T_e is accounted for and typically varies from 4.5 in the centre to 1.5 at the edge. ECE electron temperature data is used [3] and the density profile is matched to data from a single sight line interferometer.

2. Comparison of Estimates of Z_{eff}

From studies of 600 JET discharges it is found that Z_{Neo}, the value of Z_{eff} derived from (5) using neoclassical resistivity (2) is a factor 0.8-1.2 times Z_{Vis} given by (6). The values of Z_{Spi} are larger than Z_{Vis} by a factor 1.5-3. Figure 1 shows Z_{Neo} and Z_{Spi} plotted against Z_{Vis}; each point in Figure 1 represents a JET discharge value calculated 1 second before the end of the current flat top. The difference between Z_{Neo} and Z_{Spi} is approximately a factor 2 and is mostly due to electron trapping in a tight torus, i.e. the term f_T in (4) is typically 0.5 and ν_* is usually below 0.1. However, some JET discharges also included amongst the points in Figure 1 have low values of field-current with T_e in the range 1-1.5keV. For such discharges ν_* is of order 0.2-0.5 and the reduced effect from trapping yields a ratio Z_{Spi}/Z_{Neo} of order 1.5. The dependence of resistivity upon ν_* is apparent from Figure 1 and shows up as a smaller spread in the Z_{Neo} values for a given Z_{Vis} than it does for the corresponding values of Z_{Spi}.

3. Field Diffusion

In three JET discharges the plasma current has been programmed to rise from one flat top level of 1MA to a second flat top level of 2MA. During this current rise phase lasting 2 seconds the plasma shape is approximately constant. Parallel resistivity is studied both during the current rise phase and during the subsequent penetration phase at 2MA. A sequence of MHD equilibria [5] are calculated from magnetic pickup coil and flux loop data. The internal inductance ℓ_i calculated for these equilibria falls from 1.6 to 1.05 during the current rise as shown in Figure 2. Approximately 1.4 seconds after the end of the rise phase the current is fully penetrated and ℓ_i has increased to its final value of 1.25. The period of 1.4 seconds is marked in Figure 3 as the time taken for the loop voltage on the plasma surface to approach the loop voltage on axis. From the calculated flux function ψ, current density J_ϕ and electric field $E_\phi = -\partial\psi/\partial t$ we form the ratio $\eta_M = E_\phi/J_\phi$ as a function of space and time. The ratio η_M is then compared with space-time dependent values of $\eta_{||}^0$ and $\eta_{||}^*$ as given by Eqs.(1) and (2). The latter values are calculated from ECE temperature profiles and $Z_{eff} = Z_{Vis}$ is assumed. Figure 4 shows the ratios $\eta_M/\eta_{||}^0$ and $\eta_M/\eta_{||}^*$ against major radius at a particular time during the current rise. The vertical bars indicate the time variation of these ratios.

4. Discussion

Both studies show that the resistivity inferred from Z_{Vis} or determined from MHD equilibria is within a factor 0.85-1.15 equal to the neoclassical value given by (2) and higher by a factor 1.4-2.6 than the Spitzer value given by (1). This applies to plasmas in a steady state and plasmas with applied external electric fields. The variations from discharge to discharge in Z_{Neo}/Z_{Vis} (Figure 1) are due to experimental errors in T_e(10%) [3], errors on the n_e profile assumption used in (6) as well as unknown variations in impurity contents, e.g. metal vs carbon; the Gaunt factor g_{ff} used assumes an atomic Z^2 in the range 4-9. The variations with time of the ratio $\eta_M/\eta_{||}^*$ (Figure 4) are mainly subject to errors in T_e and errors arising from the equilibrium fit to the magnetic data: errors on current density J. We conclude that the parallel resistivity in JET is close to neoclassical especially, since the ratio $\eta_M/\eta_{||}^0$ (Figure 4) clearly exhibits the lack of trapping effects. This result should be compared with a Doublet III study [5] in which trapping was found to be far less dominant.

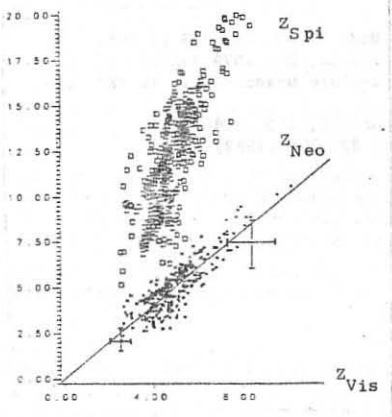

Fig 1: Estimates of Z_{eff} calculated using (1) □ and (2) * versus Z_{eff} from (6). Each point represents a flat top value from a JET discharge.

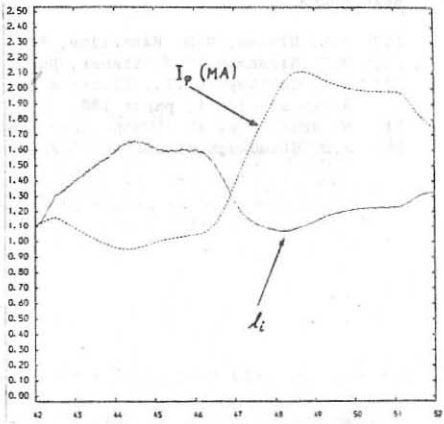

Fig 2: Internal inductance ℓ_i and plasma current I_ϕ in MA as functions of time for shot 4896.

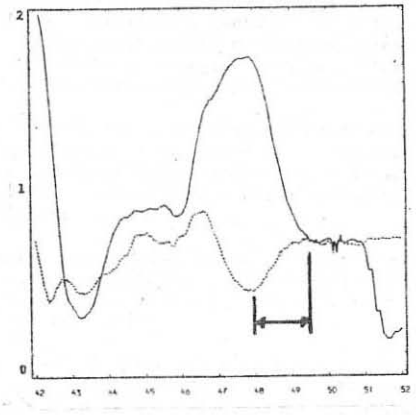

Fig 3: Loop voltages on plasma surface (solid line) and on axis (dashed line) versus time for shot 4896.

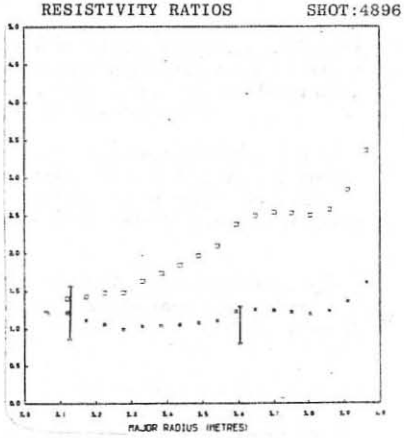

Fig 4: The ratios $\eta_M/\eta_{||}^*$ (asterisks) and $\eta_M/\eta_{||}^\circ$ (squares) versus minor radius at 47 sec. The vertical bars indicate time variations during current ramp.

References

[1] F.L. Hinton, R.D. Hazeltine, Rev. Mod. Phys., 48, 239 (1976).
[2] S.P. Hirshman, D.J. Sigmar, Nucl. Fusion, 21, 1079 (1981).
[3] A.E. Costley et al., Electron Temperature Measurements in JET, EPS, Budapest (1985), paper 186.
[4] M. Brusati et al., Comp. Phys. Reports 1, 345 (1984).
[5] R.D. Stambaugh et al., Nucl. Fusion, 22, 395 (1982).

THE TRANSIENT BEHAVIOUR OF THE BETA LIMIT IN ASDEX

G. v. Gierke, M. Keilhacker, R. Bartiromo[1], G. Becker, H.S. Bosch, A. Eberhagen, G. Fußmann, O.Gehre, J. Gernhardt, E. Glock, O. Gruber, G. Haas, G. Janeschitz, F. Karger, O. Klüber, M. Kornherr, P.B. Kotzé[2], K. Lackner, M. Lenoci[1], G. Lisitano, H.-M. Mayer, K. McCormick, D. Meisel, V. Mertens, E.R. Müller, H. Murmann, H. Niedermeyer, W. Poschenrieder, H. Rapp, F. Ryter[3], F. Schneider, C. Siller, P. Smeulders, F. Söldner, E. Speth, K.-H. Steuer, O. Vollmer and F. Wagner

Max-Planck-Institut für Plasmaphysik
EURATOM Association, D-8046 Garching

Introduction

In a previous paper /1/ it was shown that the ß limit in ASDEX follows a law $ß_{max} = C \cdot I/(a \cdot B)$ (%,MA,m,T) with $C \simeq 3.5$ for $ß^{equ}$ (ß from equilibrium measurements) and $C \simeq 2.8$ for $ß^{dia}$ (ß from a diamagnetic loop), in agreement with theoretical predictions /2/. It was also pointed out that ß - at constant neutral beam power - cannot be kept at that maximum value but decreases to a lower value. It was speculated that this decay in ß corresponds to a resistive adjustment of the current density distribution to the less favourable broad H-mode temperature profiles.

In the following we discuss this transient behaviour of the ß limit and show that in ASDEX H-discharges the stationary ß limit (for $ß^{dia}$) lies about 20 - 30 % below the maximum value.

Qualitative description of a ß limit discharge

Although important aspects of the ß limit are still not understood, we have by now at least a good qualitative picture of an H-discharge close to the ß limit. Not surprisingly, this behaviour is closely connected to the transport and profile developments characteristic of the H-phase.

We discuss the main phases of an H-mode ß limit discharge with the aid of Fig. 1, which shows $ß_p^{dia}$ and D_α signals together with $\dot{B}$ data from 7 outer and one inner Mirnov coils (1a) and radial profiles of electron pressure $n_e \cdot T_e$ obtained from a recently commissioned 60 Hz Nd-YAG laser scattering diagnostic (1b):

During the L-phase, which is relatively long in this particular shot, the pressure profile peaks. The $\dot{B}$ signals first show a continuous and then a bursting mode with mode numbers n = 1, m = 3 and a frequency rising from 28 to 43 kHz /3/.

At t = 1.27 s the L/H-transition occurs and the MHD modes stop (probably due to q(o) becoming larger than 1). The most distinctive feature at the H-transition is an instantaneous steepening of the pressure profile at the plasma edge leading to a "pedestal" in the profile (Fig. 1b). This confirms our previous findings /5/ that the H-mode is an edge phenomenon which, as a

[1] CNEN Frascati, Italy
[2] Nuclear Develoment Corp. of South Africa, Pretoria
[3] CEN Grenoble, France

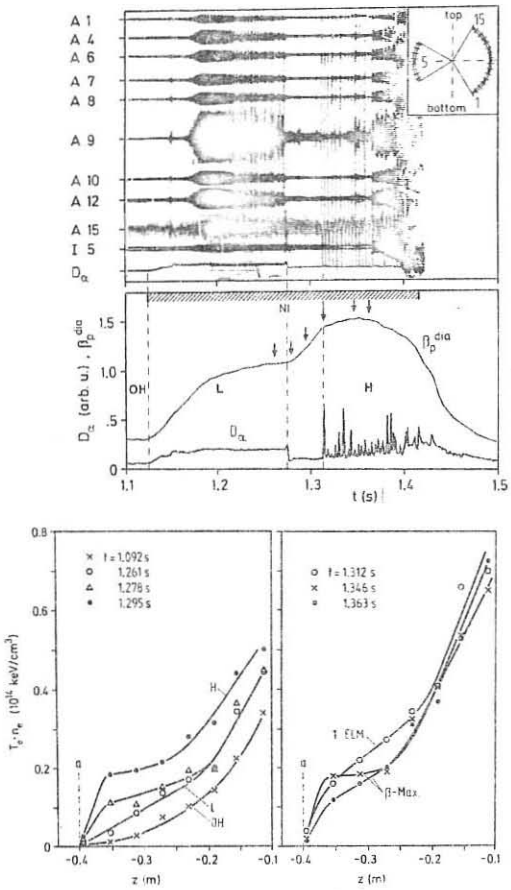

Fig. 1: $\dot{B}$ (from 7 outer and 1 inner Mirnov coils), β_p^{dia} and D_α signals (Fig. 1a) together with profiles of electron pressure $T_e \cdot n_e$ at characteristic times (Fig. 1b) of an H-mode β limit discharge (I = 310 kA, $\bar{n}_e$ = 3.4 x 10^{13} cm^{-3}, P_{NI} = 3.5 MW).

result of high edge T_e and strong shear in the separatrix vicinity, suppresses the anomalous transport prevailing in this region. The resulting pressure gradient, assuming $T_e = T_i$, corresponds, to a very good approximation, to the theoretical limit for ballooning modes /4/

$$-\frac{dp}{dr} \leq 0.3 \frac{B^2 r}{\mu_o R q^3} \frac{dq}{dr} \quad \text{yielding} \quad -\frac{dp}{dr}\Big|_{r=a} \leq 0.6 \frac{B^2}{\mu_o R q a^2} \quad \text{for } q = q_a \left(\frac{r}{a}\right)^2.$$

After the H-transition, with its formation of a transport barrier at the plasma edge, the plasma energy rises again by increasing the pressure in the plasma interior. As the pressure gradients there approach the ballooning limit (possibly even only locally), the outflux of energy increases. Since the pressure gradient at the plasma edge is already at its marginal stability limit, the edge layer becomes unstable, expelling particles and energy from the plasma periphery (so-called edge localized modes, ELM's

/1/). Such a situation is reached in shot 15520 at t = 1.31 s, when the first and largest ELM occurs and the rate of increase of ß is substantially reduced. This picture also explains the absence of ELM's in the burst-free H-discharges described in /1/: The large radiation losses (from iron) encountered in these discharges (which were produced rather close to the SS limiters) transport enough energy out of the plasma in a non-conductive way that the ballooning limit is not exceeded.

Since the critical ß for ballooning modes is highest for peaked current density distributions, whereas the H-mode is characterized by flat T_e and conductivity profiles, it is reasonable to assume that the maximum ß-value during a ß limit discharge corresponds to relatively peaked profiles frozen in from the OH and L-phases and that the observed slow decay in ß (20 % in 200 ms, c.f. Fig. 2) reflects the resistive adjustment to the H-mode profiles. There are, however, strong indications (changes in the plasma inductance, loop voltage) that during the high-ß phase additional currents in the plasma centre (which are compensated by induced currents) lead to an enhanced peaking of the current density distribution capable of relaxing on a much shorter time scale, thus explaining the first, much faster ß-decay (in 20-50 ms) observed at high power input (c.f. Fig. 2d,e). These transient currents seem to be connected with neutral injection (positive effect only with co-injection, larger effect for D^0 than for H^0-injection), and could be produced partly by the circulating fast ions, but to a larger extent by the beam induced plasma rotation. The increasing ß might also lead to such currents. The decrease in ß is accompanied by increased MHD activity and later by a growing m = 2, n = 1 tearing mode with f = 16.3 → 10 kHz /3/ (Fig. 1a).

Transient and stationary beta limit

To compare discharges with different parameters we normalize with $ß_{max}$ = 2.8 · I/(a · B) (Troyon limit). This also defines the maximum energy content for a tokamak plasma (with elongation b/a) W_{max} = 0.33 b·R·B·I.

Figure 2 shows maximum normalized ß-values $ß/ß_{max}$ and corresponding plasma energies W obtained in a B-scan at constant beam power P_{NI} = 3.5 MW and for two plasma currents I = 311 and 370 kA. The observed linear increase of $ß/ß_{max}$ with P/B for $ß/ß_{max} < 1$ reflects the fact that for a given heating power $P = P_{OH} + P_{NI,abs}$ (and assuming $\tau_E = f \cdot I$)

$$ß/ß_{max} \sim \frac{f\,P}{b\,R\,B}$$

holds /1/ (independent of I, as also found experimentally). At large enough heating power P/B the ß-limit can clearly be seen.

As shown by the $ß_p^{dia}$ and D_α signals of Fig. 2a-f there is a clear correlation between the maximum normalized ß values $ß/ß_{max}$, the time behaviour of the ß-decay (accompanied by a characteristic feature of the D_α spikes) and the level to which ß decays: Starting at low power input P/B (Fig. 2a), we have $ß/ß_{max} \simeq 0.7$ resulting in an H-phase with no ELM's. With increasing relative power (Fig. 2b), the maximum ß is almost constant yielding a stationary ß limit $ß_{stat} = 0.8 \cdot ß_{max}$. Increasing P/B still further (Figs. 2c-f) leads to $ß/ß_{max} \simeq 1.0$, followed by first a continuous and then, for higher P/B, a two-phase ß-decay resulting in lower stationary ß values than case 2b. At high power a disruption sets in, at first during the ß decay (Fig.2 e), but then moving forward in time with increasing P/B (Fig. 2f), until it finally occurs already during the ß rise (disruptive ß limit; not

shown here). Thus it seems that in ASDEX H-discharges, the stationary ß limit depends on an exact tailoring of the power input to the diffusive and resistive time scales.

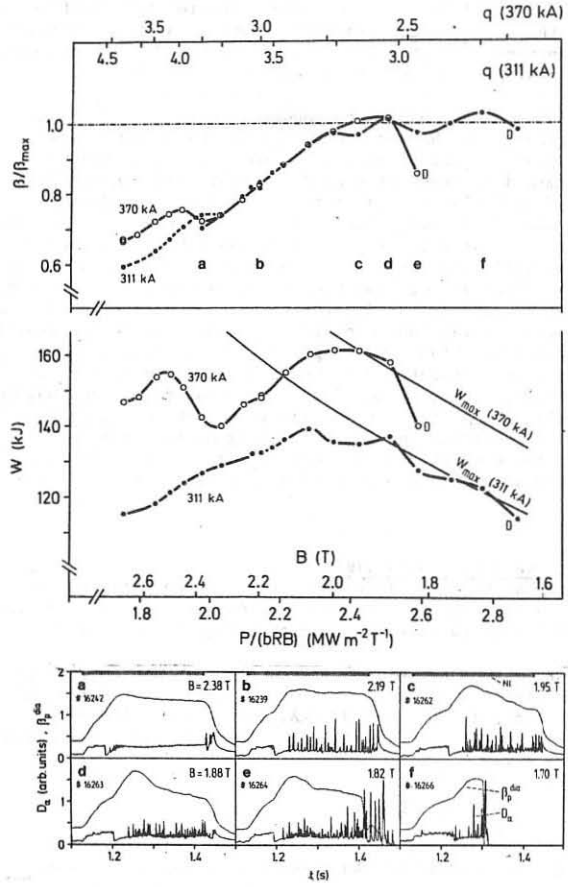

Fig. 2: Maximum normalized ß values $ß/ß_{max}$ and corresponding plasma energies W obtained in a B-scan at constant power $P = P_{OH} + P_{NI,abs} = 3.15$ MW for I = 311 and 370 kA together with $ß_p^{dia}$ and D_α signals (a-f) typical of certain $ß/ß_{max}$ values.

References:

/1/ M. Keilhacker et al., Plasma Phys. and Contr. Nucl. Fus. Res. 1984, Vol. 1, IAEA, Vienna 1985, 71
/2/ F. Troyon et al., Plasma Phys. and Contr. Fus. 26 (1984) 209.
/3/ R. Stambaugh et al., Report IPP III/103 (1985)
/4/ J.W. Connor et al., Phys. Rev. Lett. 40 (1978) 396
/5/ F. Wagner et al., Phys. Rev. Lett. 53 (1984) 1453.

CONFINEMENT STUDIES ON ASDEX IN THE INTERMEDIATE REGION FROM OHMIC TO NEUTRAL INJECTION SCALING

F. Wagner, O. Gruber, R. Bartiromo[1], G. Becker, H.S. Bosch, A. Eberhagen, G. Fußmann, O. Gehre, J. Gernhardt, G. v. Gierke E. Glock, G. Haas, G. Janeschitz, F. Karger, M. Keilhacker, A. Kislyakov[2], O. Klüber, M. Kornherr, P.B. Kotzé[3], K. Lackner, M. Lenoci[1], G. Lisitano, H.-M. Mayer, K. McCormick, D. Meisel, V. Mertens, E.R. Müller, H. Murmann, H. Niedermeyer, W. Poschenrieder, H. Rapp, H. Riedler, F. Ryter[4], J. Roth, F. Schneider, G. Siller, P. Smeulders, F. Söldner, E. Speth, K. Steinmetz, K.-H. Steuer, and O. Vollmer

Max-Planck-Institut für Plasmaphysik
EURATOM Association, D-8046 Garching

Abstract: The scaling of the global energy confinement time with density and plasma current is studied in the intermediate region from Ohmic to neutral injection L-scaling with beam power $P_{NI} \sim (1 - 3) \times P_{OH}$. A gradual transition from Ohmic to neutral injection L-scaling is found. The results can be described by quadratically adding the Ohmic- and L-scaling characteristics indicating that the L-scaling may be the continuation of Ohmic scaling towards higher power and that non-local properties determine the transport.

Introduction: The global energy confinement time τ_E of Ohmic (OH) discharges increases linearly with density at low density and saturates towards higher densities /1/. In the linear range, τ_E increases with safety factor q_a while it decreases with q_a in the saturation region /2/. In neutral injection (NI) heated L-discharges with degraded global confinement, τ_E does not show any density dependence but increases linearly with plasma current I_p in the limit $P_{NI} \gg P_{OH}$ /3/.

Results: Figure 1 and 2 summarize the scaling results obtained in ASDEX in the transition regime $P_{NI} \sim P_{OH}$. Plotted is τ_E (deduced from a carefully compensated diamagnetic loop) versus density (Fig. 1a, b for a D^+ and Fig. 2 for an H^+ plasma) for low and high q_a and versus plasma current (Fig. 1c, d) for low and high density. The injection isotope is hydrogen.

---

[1] CNEN Frascati, Italy
[2] Ioffe Institute, Leningrad, USSR
[3] Nuclear Development Corp. of South Africa, Pretoria
[4] CEN Grenoble, France

Ohmic phase: The data of Fig. 1a, b and Fig. 2 show both the linear region where $\tau_E \propto \bar{n}_e$ and the saturation region where τ_E is rather independent of density. The comparison of low- and high-q_a-cases of Fig. 1a and b confirms the previously reported fact that the confinement improves with q_a in the linear range but decreases with it in the saturation range /2/. A comparison of the results shown in Fig. 1a and 2 reveals that the Ohmic τ_E-values are about the same in the linear range but differ in the saturation regime with $\tau_E^D/\tau_E^H = 1.3 - 1.5$. The result that the isotope mass affects τ_E only in the saturation regime may clarify the conflicting observations: Those tokamaks which operate predominantly in the linear range (small minor radius or low B_T/R_o) do not observe an isotope effect while clean divertor tokamaks which can run at high density and generally operate in the saturation region do.

Neutral injection phase: The net effect of NI is a general decrease of τ_E with beam power (L-regime). At low density, however, the τ_E-values with one NI-source are comparable to (or even above) the Ohmic values and at high density they seem to continue the variation of the Ohmic data towards higher densities (see Fig. 1a). This deviant behavior at the edges of the density range may be attributed to the ion confinement: At low density, in the limit of $T_i \gg T_e$, τ_E approaches $\tau_{ei} \cdot P_i/P_{NI}$ (τ_{ei} is the electron-ion euqilibration time, and P_i/P_{NI} is the beam power fraction directly transferred to the ions). Decisive beam contributions to β_p at low density enhancing τ_E can be ruled out. At high density, the confinement is determined by neoclassical ion heat conduction, which does not seem to degrade with beam heating /4/. The density dependence of τ_E vanishes gradually with beam power. At $P_{NI} = 0.45$ MW, the linear and saturation regions are still discernible, and the maximum in τ_E is shifted to higher density. At $P_{NI} = 1.32$ MW there is still a slight density dependence. The increased power, however, has enhanced the electron transport to such an extent that the ion transport does not play any role in the given density range and the OH τ_E-values are no longer attained (Fig. 1a). At high q_a (low plasma current), NI causes a loss of density dependence even at low beam power (Fig. 1b). This is partly due to the small density window accessible at high q_a. On the other hand, the q_a-enhancement of the OH values in the linear density range is easily offset because NI confinement favors high current. This is also shown by the current scaling of high density discharges (Fig. 1d) while the high current τ_E-values are hardly affected at low density (Fig. 1c). Both the low and high density runs show the gradual transition into the linear I_p-scaling with NI.

Discussion: The degradation in confinement occurs both in the low density linear region but is more pronounced in the saturation region. The local transport analysis in the insulation zone, the density fall-off length in the scrape-off layer and the rise of the electron energy density in the plasma center after a sawtooth event indicate enhanced transport with NI over the whole plasma cross-section. It appears that the plasma is forced to locally adjust its transport properties.

It has been observed before /5/ that the electron temperature (and consequently the current density j) shows a remarkable profile conservation (termed profile consistency /6/) during beam heating. This property applies also to the density scans of Fig. 1a: The central electron temperature varies by a factor of 3 from 0.55 keV (high density, OH) to 1.8 keV (low density P_{NI} = 1.32 MW) while the T_e profile parameter $\alpha(T_e = T_{eo}\ (1-\rho^2)^\alpha)$ scatters between 1.1 and 1.5. It appears that Ohmic heating conditions which link power deposition and the j-profile (Ohmic constraint) give rise to an optimal j-profile (e.g. due to the stability condition of macroscopic modes) yielding low transport. With the independent power deposition profiles of neutral injection, the plasma maintains the optimal current density profile by changing its transport properties. Peaked deposition causes a general rise in the thermal diffusivity χ_e but low beam energy, off-axis deposition yields a remarkable reduction of χ_e in the plasma core /7/.

The possible dependence of χ_e not only on local parameters but also on a global consistency condition encouraged Goldston to quadratically add the Ohmic $\bar{n}_e q_a^{1/2}$-scaling and the NI I_p-scaling which yielded a heuristic description of the saturation region of Ohmic confinement /5/. We have analyzed the scaling results presented here according to $\tau_E^{-2} = (\tau_E^{OH})^{-2} + (\tau_E^{NI})^{-2}$ (equ. 1) with $\tau_E^{OH} = C_1\ \bar{n}_e\ q_a^{0.5}$ and $\tau_E^{NI} = C_2\ I_p\ P_{NI}^{-0.6}$. The coefficients C_1 and C_2 are obtained from fitting the OH-curve of Fig. 1a; the power dependence of τ_E^{NI} is chosen according to the L-regime scaling at low beam power /3/. The dashed lines in Fig. 1a-d represent the calculated values putting experimental data of $\bar{n}_e$, I_p and the total OH and NI power into relation (1). Good agreement is found which indicates that non-local conditions (like profile effects) may affect confinement and that the L-regime of beam heated plasmas is the continuation of an OH scaling porperty to larger heating power. On the other hand, the saturation region of OH ASDEX plasmas can be explained by neoclassical ion transport /8/. The observed isotope dependence, however, which is common to both the OH saturation region and the L-scaling does not agree with neoclassical ion transport. It has to be tested whether the

different scaling relations can be reconciled incorporating the ion transport in the form $\tau_E^{-1} = (\tau_E^{OH})^{-1} + (\tau_{Ei}^{NI})^{-1} + (\tau_E^{NI})^{-1}$

References

/1/ Klüber, O., and Murmann, H.D., IPP III/72, Garching 1982
/2/ Ejima, S., et al., Nucl. Fus. 22 (1985) 1627
/3/ Stäbler, A., Wagner, F., et al., Proc. 4th Symp. on Heating on Toroidal Plasmas, Rome 1984, Vol. 1, p. 3
/4/ Becker, G., Nucl. Fusion 24 (1984) 1364
/5/ Goldston, R., Plasma Phys. and Contr. Nucl. Fusion 26 (1984) 87
/6/ Coppi, B., Comments Plasma Phys. Contr. Fusion 5 (1980) 201
/7/ Speth, E., et al., this conference
/8/ Gruber, O., Proc. Int. Conf. on Plasma Phys. Lausanne (1984), p. 67.

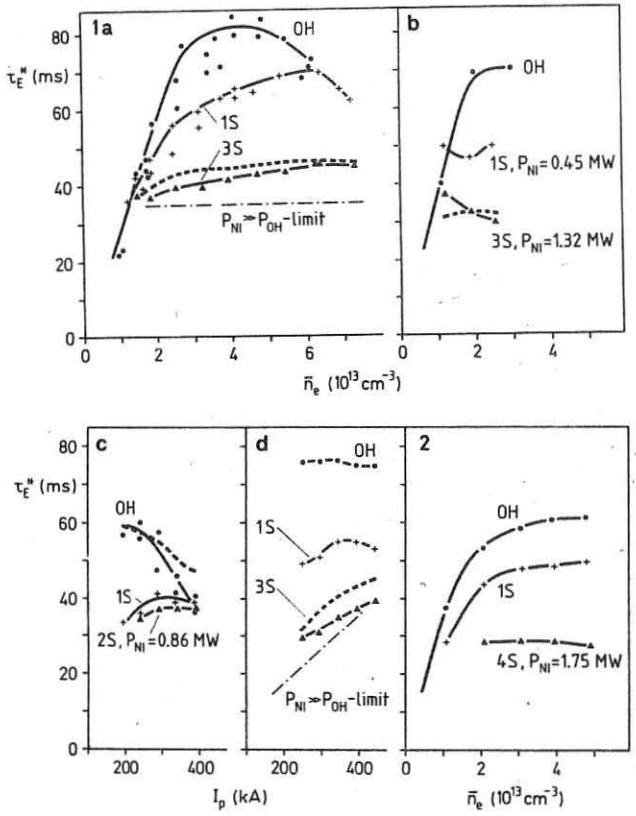

Fig. 1: Density and current scaling of the global energy confinement time of deuterium discharges. S = number of NI-sources
a) I_p = 0.4 MA, B_T = 2.2 T, q_a = 2.6; (b) I_p = 0.25 MA, q_a = 4.2;
c) $\bar{n}_e$ = 1.7 · 10^{13} cm^{-3}, B_T = 2.2 T; (d) $\bar{n}_e$ = 3.3 · 10^{13} cm^{-3}.

Fig. 2: Density scaling of hydrogen discharges. I_p = 0.4 MA, B_T = 2.2 T.

Formation of Detached Plasmas in TFTR

J.D. Strachan, F.P. Boody, C. Bush[+], B. Grek,
R.J. Hawryluk, D. Heifetz, H.W. Hendel[++], K.W. Hill,
D.W. Johnson, A.T. Ramsey, S. Sesnic, J.F. Schivell,
M. Shimada[*], G. Taylor, and M.C. Zarnstorff

Princeton University, Plasma Physics Laboratory
Princeton, New Jersey 08544

Many experiments indicate that tokamak plasma behaviour is influenced by the plasma edge region and some TFTR experiments have been motivated by this including those which remove the influence of the limiter by sudden vertical or horizontal movement [1] of the plasma column. In the experiment reported here, the plasma is detached from the limiter by reducing the plasma current while simultaneously injecting cold neutral deuterium gas. This paper documents one example of these detached plasmas but does not represent an exhaustive study of the phenomenon.

So far, the detached state has always been preceeded by a MARFE [2]. Somehow the decaying plasma current and intense gas puffing helps to evolve the plasma from the MARFE into the detached condition. For the discharge in Fig. 1, the plasma is attached to the limiter when the current is 1.2 MA. The current was purposely reduced at a rate of .3 MA/sec and a MARFE formed at about 2 sec. The plasma density (as viewed horizontally through the plasma by a microwave interferometer) decreased rapidly causing (through the density feedback system) a large gas injection rate of 40 Torr-ℓ/sec of D_2 during the MARFE. Separation of the plasma edge from the limiter seemed to start during the MARFE and increased as long as the current was being reduced (Fig. 2). When the current was held constant (e.g. after 3 sec in Fig. 1), then a 55 cm plasma remained detached from the 83 cm limiter (fig. 3) for the subsequent duration of the discharge (2 seconds).

Evidence that the plasma had actually detached from the plasma comes from the lack of observable density, electron temperature, or plasma radiation (Fig. 3) in the 20 cm wide region inside of the limiter radius. Some cold plasma might exist in the 20 cm in front of the limiter since for plasmas with T_e < 50 eV the Thomson Scattering System is not a good measure of density. Perhaps of more importance than the actual detachment is simply the formation of the highly radiating boundary which was thermally stable.

As expected by the lack of limiter or vessel contact, the impurity levels were low. The soft X-ray spectrum (Fig. 4) indicated no measurable high Z impurity peaks, and the inferred Z_{eff} from the continuum enhancement (due to low Z impurities such as Carbon and Oxygen) was about 1.5. The neoclassical resistivity Z_{eff} was 2.0. The visible bremsstrahlung Z_{eff} levels were ≈ 2 but it is possible that this may be enhanced by molecular hydrogen radiaton which could be a feature of such plasmas. Readings of the residual gas analyzer taken 1 sec after the discharge indicated that the CO and methane peaks were an order of magnitude lower than for plasmas with limiter contact. All the radiation comes from the plasma edge (Fig. 2,3)

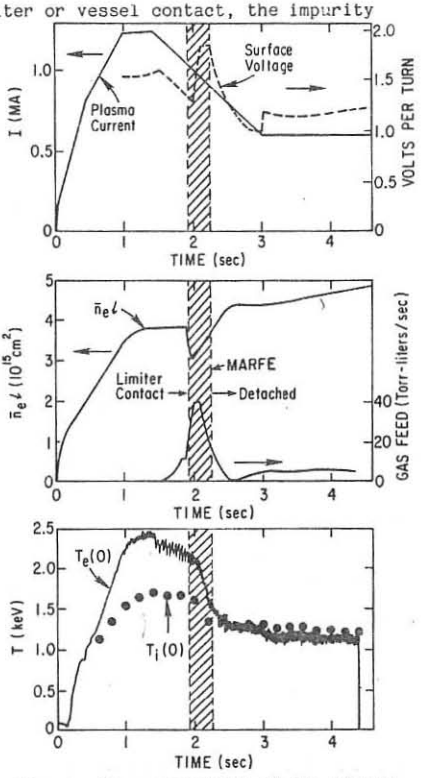

Fig. 1 Time evolution of the plasma current, I, surface voltage, line integal density, gas feed and central electron and ion temperature from the neutron emission for a detached plasma. $T_i(o) \approx T_e(o)$ in this detached plasma.

and it is more toroidally and poloidally symmetric than in limiter discharges. The gross energy confinement time is about 250 msec which is as high a confinement time as was achieved for TFTR a=55 cm limiter plasmas having similar conditions [3]. The density is 50% higher than was achieved with those limiter plasmas. All of the ohmic power eventually appeared as radiation with the bolometer actually measuring slightly more power than the ohmic input [which is probably a calibration uncertainty in the bolometer signals]. Analysis of the energy balance indicates that the plasma is near the ion dominated regime; ion conduction losses in the range of 2 → 5 Chang-Hinton values were the dominant energy transport mechanism to the radiating plasma boundary.

Several interesting ideas exist about the detached plasmas:

1) Can the plasma current be increased once the plasma is detached in order to form 2 MA plasmas with low impurity levels?

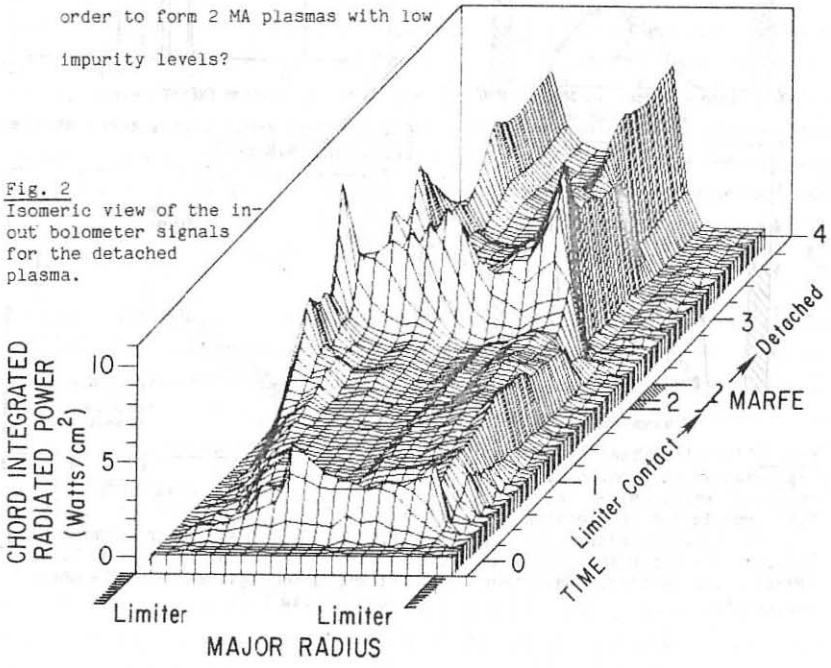

Fig. 2
Isomeric view of the in-out bolometer signals for the detached plasma.

2) Does a gas blanket [4] exist which shields the plasma from the vessel?

3) Is the detached state actually a poloidally symmetric MARFE?

4) How do auxilary heating and compression influence the detached plasma?

The support of D.M. Meade and the TFTR operations group and K.M. Young and the TFTR diagnostics group is gratefully acknowledged.
Work Supported by U.S. DoE Contract No. DE-AC02-76-CHO-3073.

+ ORNL, Oak Ridge, Tennessee, ++ RCA David Sarnoff Research Center, Princeton, New Jersey
* JAERI, Tokyo, Japan

[1] G.D. Tait et al., Plasma Physics and Contr. Nucl. Fusion Research 1984, Vol. I, 141 (IAEA, Vienna, 1985).
[2] B. Lipschultz et al., Nucl. Fus. 24, 977 (1984).
[3] P.C. Efthimion et al., Plasma Physics and Contr. Nucl. Fusion Research 1984, Vol. I, 29 (IAEA, Vienna, 1985).
[4] B. Lehnert, Plasma Physics for Thermonuclear Fusion Reactors, 307 (ed. G. Casini, CEC, 1979).

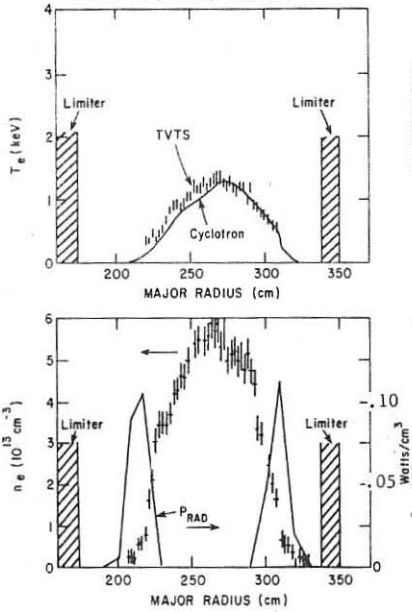

Fig. 3 Electron temperature profiles (as measured by Thomson Scattering and cyclotron emission) and electron density profile for the detached plasma. The Abel inverted radiation power profile is shown with $n_e(r)$. Radiation levels $\leq$ .02 watts/cm^3 have been suppressed.

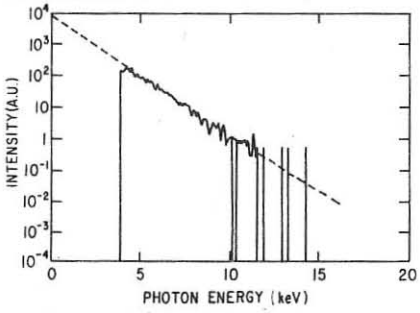

Fig. 4 Soft X-ray signal taken at the TVTS time (4.8 sec).

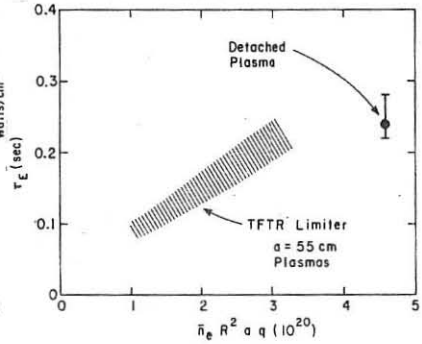

Fig. 5 Total energy confinement time forthe detached plasma at the TVTS time plotted against the TFTR ohmic scaling law [3].

ION BEHAVIOR IN TFTR DURING OHMIC AND NEUTRAL BEAM OPERATION†

S.S. Medley, M. Bitter, A.C. England*, E. Fredrickson, S. von Goeler, R.J. Goldston, G.W. Hammett, R.J. Hawryluk, H.W. Hendel**, K.W. Hill, R. Kaita, S.M. Kaye, K. McGuire, D.M. Meade, M. Murakami*, E.B. Nieschmidt***, A.L. Roquemore, S.D. Scott, J.D. Strachan, G.D. Tait, C.E. Thomas*, K-L. Wong, K.M. Young, and M.C. Zarnstorff

Plasma Physics Laboratory, Princeton University
Princeton, New Jersey 08544 USA

ABSTRACT - Ion temperature measurements for ohmically heated and neutral-beam heated plasmas are discussed. For ohmic plasmas an empirical scaling expression for the central ion temperature is obtained by regression analysis of data from TFTR and other tokamaks. For neutral-beam heating of target plasmas with $\bar{n}_e \gtrsim 2 \times 10^{19}$ m^{-3}, the observed ion heating efficiency is $\xi_i = \Delta T_i(0)\ \bar{n}_e/P_{abs} = 1.5 \times 10^{19}$ keV m^{-3} MW^{-1}. Measurements of toroidal rotation velocity and fast-ion energy distributions are also reported.

INTRODUCTION - The central ion temperature (T_i) in TFTR was obtained from measurements of the Doppler broadening of the Ti XXI Kα line, the total neutron emission, and the neutral energy distribution measured by passive charge exchange (cx). For deuterium ohmic and $H^0 \rightarrow D^+$ beam-heated plasmas, ion temperatures are provided by all three methods. For neutral beam heating with $D^0 \rightarrow H^+$, the Ti XXI Kα Doppler broadening and the mass-resolved charge exchange diagnostics were used while for $D^0 \rightarrow D^+$ only the Ti XXI Kα Doppler broadening technique remained viable for measurement of the ion temperature.

RESULTS - For ohmic discharges, a data base of TFTR ion temperatures was combined with other tokamak data in a regression analysis to yield an empirical scaling relation for the central ion temperature as shown in Fig. 1, $T_i \propto I_p^{0.42}\ B_T^{0.42}\ R^{0.70}\ \bar{n}_e^{-0.13}\ a^{-0.33}\ A^{-0.25}$, where A is the atomic mass. For the TFTR data, the chord-measured Ti XXI Kα Doppler broadening measurements of the T_i were used. Reasonable agreement is noted between measured and scaled values of T_i for order of magnitude variations in most of the data base parameters listed in Fig. 1.

Neutral beam heating experiments [1,2] ($D^0 \rightarrow H^+$ and $D^0 \rightarrow D^+$) were performed at deuterium beam powers up to 6.3 MW and injection energy up to 80 keV. An example of the ion heating results is shown in Fig. 2 for a scan in beam power with constant line average density ($\bar{n}_e = 4.5 \times 10^{19}$ m^{-3}) existing at the end

of the beam injection period. From this plot and other data not shown, the observed ion heating efficiency is $\xi_i = \Delta T_i(0)\ \bar{n}_e/P_{abs} = 1.5 \pm 0.2$ (10^{19} keV $m^{-3}MW^{-1}$). The heating efficiency obtained in TFTR is roughly consistent with the PLT value ($\xi_i \simeq 4$) [3] if one assumes that the local energy transport coefficients are independent of plasma size ($\xi_i \propto 1/R$).

For $D^0 \rightarrow H^+$ beam heating experiments at low plasma target density ($\bar{n}_e \lesssim 1.2 \times 10^{19}$ m^{-3}), the impurity T_i measured by the Kα Doppler broadening diagnostic ($T_i > 10$ keV) significantly exceeds the hydrogen species T_i measured by charge exchange ($T_{icx} < 6.5$ keV). At these low densities, the differential coupling of beam power to the various ion species can produce impurity ion temperatures which exceed the central T_i of the hydrogen ions by up to 30% [3]. The expected chordal cx energy spectrum is simulated numerically to treat the effects of: (1) plasma opacity and the radially varying neutral density; (2) a neoclassical-like ion temperature profile; and (3) depletion of the central thermal ion density by fast ions and impurities. There is also a small correction to the Doppler broadening T_i measurement due to profile effects. In some cases, application of these corrections to the diagnostic measurements yields T_i values that are consistent with the expected impurity-hydrogen temperature difference. In other cases, it is difficult to obtain agreement without invoking a hollow $n_H(r)$ profile during $D^0 \rightarrow H^+$ heating, or damping of toroidal rotational energy into the impurities. Toroidal rotation velocities up to 6×10^5 m/s were observed by measurement of the Doppler shift of the Ti XXI Kα line. Extensions in theoretical analysis and transport modeling may be necessary for satisfactory understanding of this 'energetic ion' regime.

Fast neutral spectra were measured for a wide range of neutral beam injection experiments by a tangentially viewing charge exchange analyzer. Shown in Fig. 3 is the tangential fast neutral spectra resulting from injection of 80 keV neutral beams until t = 2.500 s, followed by adiabatic major-radius compression (compression ratio C = 1.38). Immediately after compression, fast ions are observed up to 150 keV, consistent with the maximum C^2 acceleration predicted for ions moving exactly along the magnetic field. The predictions of a Fokker-Planck simulation (dashed curves) incorporating classical slowing down and magnetic compression are in good agreement with the measured charge exchange spectra (solid curves). Due to the rapid change of local neutral density following compression, the measured and calculated distributions are normalized in amplitude for each energy spectrum in Fig. 3.

DISCUSSION - Since the observed Kα line emission arises predominantly from the plasma core, the correction to the chord-measured ion temperature for radial variation of the T_i is typically small ($\lesssim$ 8%). Broadening of the resonance line due to dielectronic satellites is negligible when the electron temperature exceeds 1.3 keV. The correction to the T_{icx} for plasma opacity was examined both by comparison of the data with the other T_i measurements and by the numerical simulation of the charge exchange chordal measurements. In ohmic plasmas, agreement was observed in the scaling of the correction factor with increasing line-integral density, but the numerically-predicted opacity factor on T_i was consistently larger by ~ 15%. The typical charge exchange opacity correction ranged from $\leq$ 15% at $\int n_e d\ell \lesssim 2 \times 10^{19}$ m^{-2} up to ~ 60% for $\int n_e d\ell \simeq 6 \times 10^{19}$ m^{-2}. After correction, the passive T_{icx} is in agreement with the neutron emission and Ti XXI Kα Doppler broadening T_i results to within ±15% under plasma conditions which permit simultaneous application of these diagnostics.

During neutral beam injection, additional corrections to the T_i measurements with the Ti XXI Kα Doppler broadening must be addressed. The horizontally viewing sightline for the Ti XXI Kα diagnostic is offset by an angle of 22° relative to the centerline of the machine to provide measurements of the toroidal rotation velocity using the Doppler shift of the Ti XXI Kα line. Modeling of the Ti XXI Kα line profile distortion due to shear in the toroidal rotation velocity shows only a minor effect on the Ti measurement (< 10%). The correction is small primarily because the Ti XXI Kα line emission is core-dominated.

Acknowledgments - The authors wish to acknowledge the dedicated efforts of the TFTR neutral beam group, the facilities operations staff, and the computer division in support of these experiments.

†Research supported by U.S. Dept. of Energy Contract No. DE-AC02-76-CHO-3073.
* Oak Ridge National Laboratory, Oak Ridge TN USA
** RCA David Sarnoff Research Center, Princeton, NJ USA
*** Idaho National Engineering Laboratory, EG&G, Idaho, USA

[1] H.P. Eubank, et al., "Proceedings of the Tenth International Conference on Plasma Physics and Controlled Nuclear Fusion Research," London, UK, 1984. (IAEA, Vienna, Austria, 1985) Vol. I, p. 303-318.
[2] M. Murakami et al., Sixth Topical Meeting on the Technology of Fusion Energy, San Francisco, 1985. Accepted for publication in Fusion Technology, July 1985.
[3] H.P. Eubank, et al., "Proceedings of the Seventh International Conference on Plasma Physics and Controlled Nuclear Fusion Research," Innsbruck, Austria, 1978. (IAEA, Vienna, Austria, 1979) Vol. I, p. 167-197.

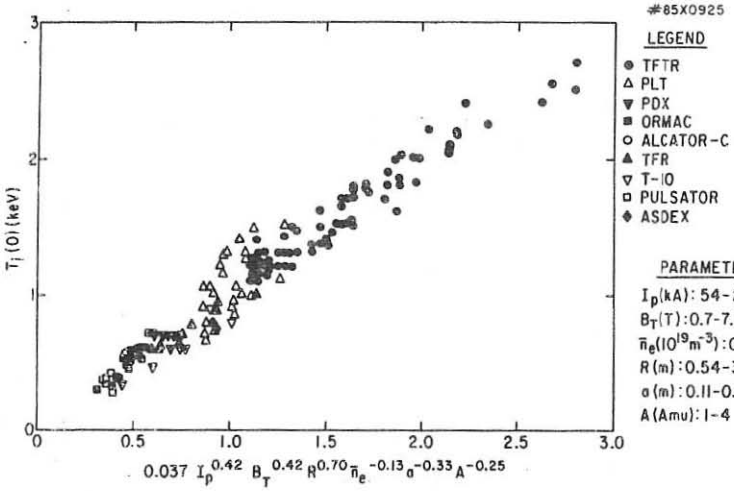

Fig. 1 T_i regression analysis for ohmic plasmas.

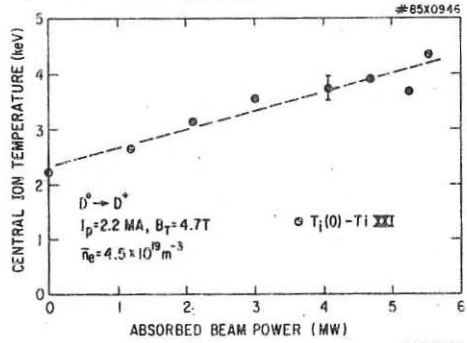

Fig. 2 Ion heating with beam injection on TFTR.

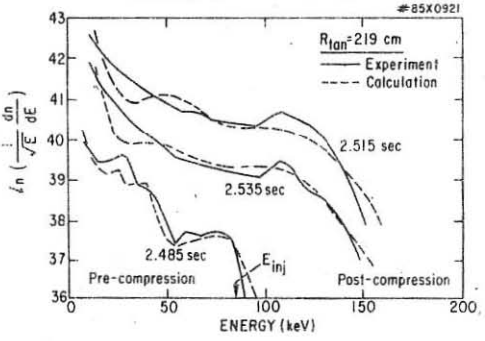

Fig. 3 Fast-ion energy distributions during adiabatic compression.

ON LIMIT β IN A TOKAMAK WITH STRONG FIELD AND WITH ADIABATIC PLASMA COMPRESSION

L.M.Degtyarev, S.Yu.Medvedev
M.V.Keldysh Institute of Applied Mathematics,
Academy of Sciences, USSR
S.V.Putvinskij, V.A.Chuyanov
I.V.Kurchatov Institute of Atomic Energy,Moscow, USSR

A knowledge of plasma behaviour in the range of thermonuclear parameters is necessary to design the fusion tokamak-reactor. At present there are no reliable experimental data on limit β and energy confinement times in plasma with thermonuclear temperatures. The transition to a regime in which a powerful source of additional heating-thermonuclear reactions - appears can result in some new physical phenomena unpredicted beforehand. It seems to be expedient to study these phenomena at special facilities, where the use of a strong magnetic field allows to reduce their scale and power consumption. An experiment of such a type based on a tokamak with strong field and with adiabatic plasma compression was suggested in [1,2,3] . The combined adiabatic plasma compression along the minor radius (compression coefficient C_a = 2.5) first and then along the major radius (compression coefficient C_R= 2.5) is suggested as the main technique of heating. An anxiliary plasma heating by neutral injection and ICRH with the total power P≈2 MW is used before adiabatic compression.

The cross-section of a vacuum chamber and the positions of plasma at different stages of adiabatic compression are shown in Fig.1. A change in the major and minor radii of the plasma column in the process of compression and a quantity

$$\beta = 2\mu_0 \int p dV / \int B_T^2 dV,$$

where, B_T is the toroidal field, p is the plasma pressure, integration is made over the plasma volume, are shown in Fig.2. Under compression along the minor radius, β drops as $P/B^2 \sim B^{-1/3}$, and it rises again under compression along the major radius. In case of a combined compression, $\beta = \beta_0 C_R^{4/3} \cdot C_a^{-1/3}$.

The main goal of the experiment is to obtain and to study a plasma in which the fusion power exceeds the power of losses. It seems to be important to obtain plasma with maximum β at a fi-

nite compressed stage, as $Q \sim n^2 \sim \beta^2$ at a given finite-stage temperature $T = 7$ keV. A value of β can be limited not only by the stability condition at a finite compressed stage but by that at all intermediate stages of the equilibrium evolution under compression. Not only internal plasma parameters but the disposition of a conducting wall respective to the plasma edge are changed at the plasma column displacement.

The results of the calculations on limit β respective to the ballooning and ideal kink modes for tokamak with a strong magnetic field and with adiabatic plasma compression are given. It has been considered that the development of hydromagnetic instabilities should rapidly rearrange the plasma pressure profile; therefore, the pressure profile has been optimized in the calculations of limit β . A two-stage optimization of the equilibrium configuration has been used, an optimization of the pressure profile respective to the stability against the low scale ballooning modes [4] has been done at the first stage. The equilibrium obtained has been used at the second stage of optimization. At this stage, the stability against external kink modes $n = 1,2...$ has been verified. If the equilibrium optimized with respect to the ballooning modes has been found to be unstable, the distribution $p(\Psi)$ has been varied to reach stability against all the modes.

In the calculations of stability, the proper displacements and increments in the linear problem have been determined by the variational principle. In calculations it has been considered that $q=1.1$ at the axis and q_s at the boundary has been changed due to a variation in the current profile.

A solid line in Fig.3 shows the limit β at different stages of the plasma column compression. A dashed line in the same figure shows the limit β, when the vacuum chamber is absent, a dotted line shows the limit β for ballooning modes. One can see that the presence of a close conducting wall at the external contour of the torus stabilizes the kink modes at the initial non-compressed state, the stability is determined by the ballooning modes. After the compression along the minor radius, the wall is remoted from the plasma surface and, practically, does not affect its stability. After the compression along the major

radius, the plasma column approaches the wall again, but the wall is located at the internal contour in this case, and its stabilizing role is not great. This results in that the limit betas at a finite stage are provided by kink modes, and the β - values are found to be 1.5 - times lower than those for the ballooning modes. A change in β under combined plasma compression in tokamak with a strong field and with adiabatic compression is shown in Fig.3 as an illustration. One can see that the limitation on β is imposed at a final stage after all compressions. In order to reach limit β at a final stage, one should have a plasma with $\beta \approx 1\%$ before compression. This value is considerably lower than the plasma stability limit at the initial stage. The result given in Fig.3 has been obtained for $q_s=2.24$, and it is not changed qualitatively at a variation in q_s. Note that the finite values $\beta = 2\%$ correspond to β at the axis equal 6 %.

REFERENCES

[1]-V.F.Demichev, V.A.Chuyanov, Preprint IAE-3222, 1979.

[2]-E.A.Azizov, Yu.A.Alekseev, N.N.Brevnov et al. Atomnaya energia, v.52, N 2, p.108, 1982.

[3]-E.A.Azizov, Yu.A.Alekseev, H.H.Brevnov, et al., Plasma Physics and Controlled Nuclear Fusion Research 1980, v.11, p.599, IAEA, Vienna, 1981.

[4]-P.N. Vabishchevich, L.M.Degtyarev, S.Yu.Medvedev, Fizika Plasmy, v.9, p.163, 1983.

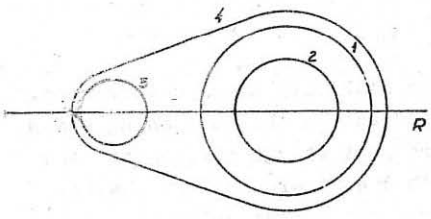

Fig 1

Fig.1. Conducting vacuum chamber (4) and the positions of plasma under combined compression. 1 -before compression, 2 - after compression along the minor radius, 3 - after compression along the major radius.

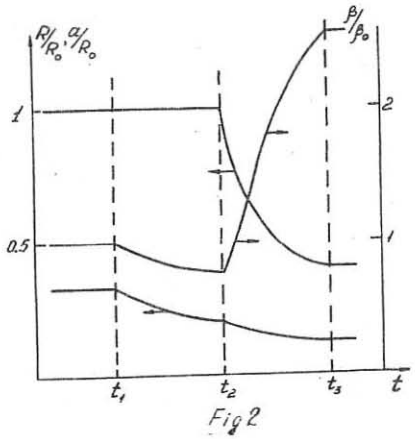

Fig 2

Fig.2. Changes in R, a, and in β under plasma compression.
$t_1 < t < t_2$ - compression along the minor radius,
$t_2 < t < t_3$ - compression along the major radius.

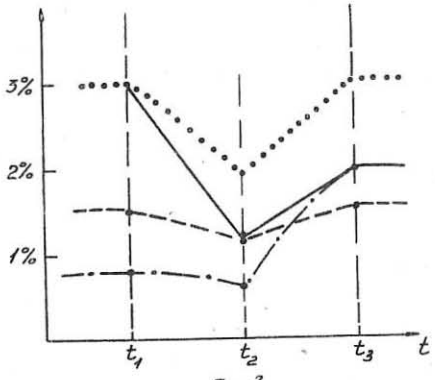

Fig 3

Fig.3. Limit for hydromagnetic stability under compression.
.... - limit β with respect to the ballooning modes,
—— - limit β with respect to the ballooning and kink modes with due regard for the chamber,
---- - limit β with respect to the ballooning and kink modes without regard for the chamber,
-.-. - actual change in β under adiabatic compression.

Electron density profile dependence on plasma parameters on T - 10.

Vasin N.L., Kurchatov Institute of Atomic Energy, Moscow

The electron density profiles across the plasma column, $N_e(r)$, on T-10 were measured in a wide range of the discharge parameters /1,2,3/ . However, the different initial conditions (conditioning of the chamber, material of the limiter, radius of the limiter) did not allow to come to the dependencies of $n_e(r)$ on the discharge parameters.

The studies of $N_e(r)$ vs. plasma parameters on T-10 were done within a wide range of parameters at the same r_L and under identical conditioning of the chamber.

As these studies were made simultaneously with the experiments on electron heat conduction described in /3/, we used the same regime identification. One additional regime, not included into /3/, was added.

I. Diagnostics, regimes.

The electron density distribution was determined by a phase shift in the electromagnetic wave passing through plasma with a multichannel quasi-optical interferometer . The total error in the measurement along any chord was 0.25 radian and it did not depend on the absolute value of a phase shift measured.

The specific feature of a given experiment was that the ICRH-antenna was placed in the same cross section of the torus, where the density measurements were made. That antenna (Fig.1) occupied 1/3 of the chamber circumference, that reduced the number of diagnostic channels from 8 to 6.

A standard set of diagnostics for T-10 was used to measure other plasma parameters. All the regimes were divided into six groups. The main parameters of those regimes are given in Table I based on the results from /3/, where the same symbols are used.

II. Results of the measurements.

The main experimental data were obtained at simultaneous diagnostics through six channels. The impact parameters in diag-

nostics were (see Fig.1) -30,-21,-12,-3,6,15 cm.For each group of regimes the data obtained in 20-30 shots were processed.

The results of the experimental data processing for a stationary stage of the discharge have shown that a change of the absolute phase shift in time makes an analysis of the profile evolution difficult. Therefore, such an analysis is made in the more convenient normalized form. Here and later, the normalization by a phase shift along the chord X=-3cm is used. Such an analysis of the phase measurements has shown that the profile shape is well conserved for all the six regime groups, as it is shown for one of the regimes in Fig.2a(b). This result allows to perform the processing for the same instant of time and, if necessary, to normalize the result by a phase shift along the central chord.

A shape of the phase profile, $\varphi(r)$, is also well conserved from shot to shot in each group, that allows us to introduce the idea of averaged profile for a group.

The averaging has been made over the normalized values to provide an easy control over the profile configuration reproducibility. An illustration of a given procedure for a few shots is given in Fig.3. In the processing of the whole train of pulses, it has been found out that an average quadratic error of non-reproducibility along any of the chords is less than the errors in the phase measurements (i.e. less than 0.25rad/$\phi_{(x)}$).

The experiments were partly repeated without the ICRH-antenna to obtain an information on the second gradient area of the density profile. The normalized phase profiles well coincide with those obtained previously along six chords.

The data on the phase measurements in six groups of shots are given in Fig.4. The phase renormalization by a maximum in the curve approximating the experimental points is made in this Figure.

A dependence of the $\varphi(r)$-profile on the safety factor at the limiter, q_L, is well seen in Fig.4. From the comparison between the $\varphi(r)$-profiles obtained and the data given in Table I, one can see that the profile configuration mainly depends on q_L, and does not depend on such parameters as: plasma current, I_p, longi-

tudinal field, H_z, and average density, N_e. However, it is valid with the assumption that the similar $N_e(r)$ correspond to the same configuration of $\varphi(r)$; that is, strictly speaking, not always true.

The fact that the profile configuration at a stationary stage does not depend on the current configuration preevolution (or that is the same on q_L). I(p) in two discharges with q_L=7 obtained in different manner are given in Fig.4.

The results of the $N_e(r)$-processing are shown in a normalized form in Fig.5 for the moments of time pointed by arrows. One can see that these profiles coincide, except of the plasma column displacement along the major radius.

A preliminary processing of the experimental data allows to find out some qualitative dependencies in the $\varphi(r)$-behaviour on the discharge parameters and, in this way, to exclude the possible errors related to the solution of an inverse problem reproduction of $N_e(r)$ by the phase measurements.

The data obtained on the density profile are well approximated by a polynomial of the form: $N_e(r)=N_o(1-(\frac{r}{r_d})^{\alpha_k})^b$. This approximation is made in the polar coordinates, i.e. without account of the displacement of internal magnetic surfaces. The results of such an approximation are given in Table I.

III. Brief conclusions.

1. The profile configuration is conserved at a stationary stage of the discharge.
2. The density profile depends on the safety factor at the limiter and the greater is q_L, the steeper is the profile (see Fig.5).
3. The density profile is determined by the position of a limiter and such a large heterogenity as the ICRH-antenna does not distort it.
4. The electron density profile does not depend on the technique of shaping the current, it depends on q_L only under the same initial conditions.

Table I.

	I	II	III	IV	V	VI
I_p	435-440	435-440	240	240	580	380
H_z^p/k /	30	30	16	30	30	30
α	4	4	4	2	2	6
b	2	2	2	3/2	3/2	2

r_0(cm)	37	37	37	37	39	37

References.

1.Berlizov A.B., Bobrovskij G.A.,Vasin N.L. et al.First results from the T-10 Tokamak.6th Intern.Conf.on Plasma Phys.and Contr. Nuclear Fusion Research,Berchtesgaden,1976,vI,p.3-17.

2.Berlizov A.B.,Bugarya V.I.,Buzankin V.V.et al.Low-q discharge in the T-10 Tokamak.,Pasma Phys.and Contr.Nucl.Fusion Research, Proc.8th Int.Conf.,Brussels,1980,vI,IAEA(1981)23-24.

3.Berlizov A.B.,Bobrovkij G.A.,Vasin N.L. et al.Transport coefficient measurements on T-10.Proc.of 9th Int.Conf.on Plasma Phys. and Contr.Nucl.Fusion Research,Baltimore,1982.

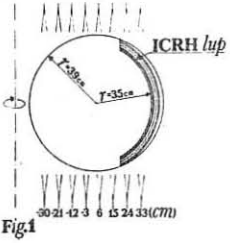

Fig.1

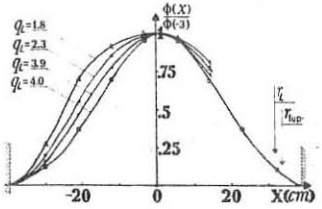

Fig.4

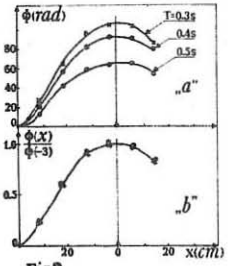

Fig.2

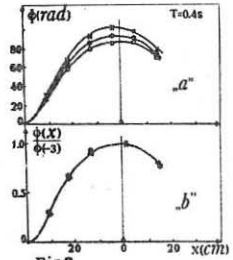

Fig.3

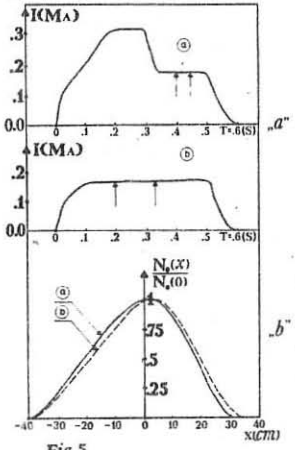

Fig.5

PLASMA CURRENT DENSITY SHAPING AT THE INITIAL STAGE OF DISCHARGE ON T-10

V.A.Gulyaev, B.S.Levkov, G.E.Notkin;
I.V.Kurchatov Institute of Atomic Energy, Moscow, USSR

An increase in the plasma current in tokamak and the regimes with a low safety factor q at the limiter ($q_L \sim 2$) are prevented by the development of the so-called disruptive instability. The leading role of helical perturbations in the development of a given instability, in which the m/n = 2/1 mode is a decisive one, is universally adopted.

The experiments on T-10 show that the modes with m/n = 4/1, 5/1, etc., do not result in the disruptive instability, perturbing insignificantly the plasma column. The m/n = 3/1 mode by itself does not induce the current disruption, but it can serve as a triggering pulse for developing the m/n = 2/1 mode. It is necessary to profile the plasma current density in such a way that it would be sufficiently peaked at a stage of the breakdown and current rise to exclude the development of the m/n =3/1 mode and, at the same time, rather wide to exclude an excessive development of the m/n = 2/1 mode.

As it follows from the experiments, it can be obtained by shaping the plasma current density profile with a gas puffing regulation.

For the program of a plasma current change at the initial stage of discharge (breakdown $\frac{dI_p}{dt} \approx 5 \div 10$ MA/sec, plasma current rise with a constant rate $\frac{dI_p}{dt} \approx 1$ MA/sec), the problem is reduced to a proper choice of an initial gas pressure in the chamber at a breakdown in plasma ($P_{\quad}$) and to that of a gas puffing at the current rise stage (see /1/). For a given current rise rate $\frac{dI_p}{dt}$ (determining a rate of the current channel expansion due to the skin-effect), one should choose such a gas puffing (determining a rate of the current channel radius decrease due to a cooling of the periphery) at which the current channel expansion will provide a constant q at the current channel boundary. In this case, the most sensitive parameter of the current density profile is an amplitude of the m/n = 2/1 mode.

A problem of the proper gas inflow choice at a stage of the current rise under varying vacuum conditions is especially difficult in the presence of a sorbing graphite limiter. It has been solved with a feed-back control system (FCS), using the m/n = = 2/1 mode amplitude as a controlled value and the gas puffing as a control action (see /2/). The system has been reliably operated up to 1,7 MA/sec.

An analysis of the MHD-activity at a breakdown shows that a picture of the current density profile shaping is true even at $\frac{dI_p}{dt} \approx 5 \div 10$ MA/sec. In this case, the gas flow to the plasma column boundary is determined by an initial pressure Pin.

If P_{in} exceeds a certain value, the discharge with high amplitude of the m/n = 2/1 modewill be observed from the very beginning, that will be resulted in the current disruption, in spite of the fact, that FCS completely cuts-off the gas puffing. If P_{in} is lower than a certain critical value, MHD-activity will manifest itself from the very beginning as separate frequent bursts with rising amplitudes (the m/n = 2/1, 3/1, 4/1 and higher modes are observed in these bursts), FCS will not be able to prevent the m/n = 3/1 mode development, and this will also be resulted in the plasma current disruption. I.e. as soon as the MHD-instability regime starts at the beginning of the plasma discharge, the second mode FCS is not able to interrupt its development. A proper choice of the initial pressure, P_{in}, is difficult because of a lack of information on the saturation of the liner walls and limiter with the working gas and with impurities, as the gas puffing into plasma at a breakdown is mainly determined by two components:

$$P_{in} = P_{in_V} + P_{WL} \quad ,$$

where, P_{in_V} is the pressure produced by an initial (preliminary) gas puffing through the valve; P_{WL} is the pressure produced by a gas puffing from the walls and from the limiter at a break-down.

Thus, there is a necessity in the diagnosis of a limiter condition and in that of the tokamak chamber walls before the discharge as well as the necessity in providing initial pressure (before discharge) P_{in_V} dependent on that condition.

For solving this problem on T-10, a preliminary discharge with a special diagnostic capacitor bank is performed before

the main discharge in plasma, at a low initial diagnostic gas puffing. The power of radiation losses from plasma (W_p) at a break-down serves as an indicator of the wall and limiter condition. A radiation loss signal from a pyroelectric sensor depends on the pressure of a gas entering plasma (see /3/), at a break-down of the gas. The general gas condition of the chamber is determined by a peak of the signal from the sensor during the diagnostic discharge. As a height of the diagnostic signal peak from the sensor (for a given volume and at a given break-down voltage) in an operating range is directly proportional to P_{WL} (without taking account of the diagnostic gas pressure) and the peak signal from the sensor in the main discharge is directly proportional to P_{in}, one can approximately write:

$$U_p = \frac{1}{k_1}\left[P_{inv} + k_2 U_{pd}\right] \quad ,$$

where, U_p is the peak signal from the radiation loss sensor at the main break-down in plasma; U_{pd} is the peak signal from the radiation loss sensor at the diagnostic discharge; k_1, k_2 are the dimensional proportionality factors.

Proceeding from this, a preliminary gas puffing is made according to:

$$P_{inv} = K_1(K_2 - K_3 U_{pd}) \quad ,$$ where, K_1, K_2, K_3 are the dimensional transfer coefficients, to stabilize U_p at its rated value, $U_p = U_{p\ rated} = const$.

The algorythm described was realized in the feedforward control system based on radiation losses from plasma at a break-down. A larger preliminary gas inflow is made at a less saturation of the walls and the limiter with a working gas and with impurities (at a lower U_{pd}), a smaller one, at a greater saturation (at a higher U_{pd}).

Thus, with some approximation one can write:

$$U_p = \frac{1}{k_1}\left[K_1(K_2 - K_3 U_{pd}) + k_2 U_{pd}\right] .$$

The oscillogram of two typical discharges with radiation loss feedforward system in operation is shown in Fig.1. Here are the discharges No 36425 and No 36426. I_p = 340 kA, B_z = = 25 kOe.

The switching of a given system on decreases about two times the spread between the limit radiation loss peaks respective to their average value at the break-downs.

The MHD-second mode feedback system and the radiation loss feedforward system were in operation at $\frac{dI_p}{dt} \leq 1{,}7$ MA/sec, B_z = = 15 ÷ 30 kOe, Ip = 100 ÷ 560 kA, q_L = 2,9 ÷ 1,8. A number of stable discharges noticeably rises with given systems in operation.

The results of the work done can be summarized in the following way:

- a possibility of shaping the plasma current density profile at the current rise stage via the control over the second MHD-mode with a gas puffing has been shown;
- a diagnostics to determine the saturation of the walls and the limiter with the working gas and with the impurities before discharge has been developed;
- a possibility of controlling the radiation losses from plasma at a break-down with a gas puffing has been shown;
- the plasma discharge stability has been raised.

REFERENCES:

1. Notkin G.E. Fizika plasmy, 1985, v.11, issue 1, pp. 62-67
2. Gulyaev V.A. et. al. Proc. of the 3d All-Union Conf. on Engineering Problems in Fusion Reactors , Leningrad, 1984, June.
3. Vertiporokh A.N. et. al. Fizika Plasmy, 1980, v.6, p.14.

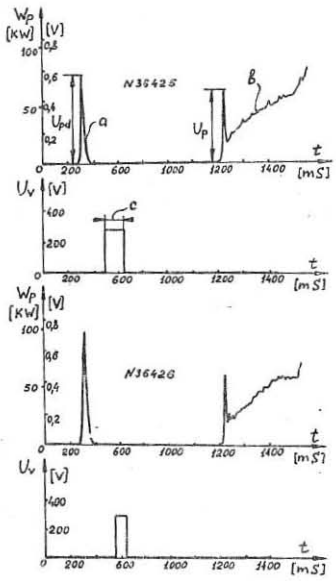

Fig.1. Oscillogram of the discharges with radiation loss feedforward control system in operation.

U_V is the voltage to the gas puffing valve;

a is the signal from a sensor during the diagnostic discharge;

b is the signal from a sensor during the operating (main) discharge in plasma;

c is the duration of a control voltage to the preliminary gas puffing valve

LOCAL PARTICLE BALANCE IN A TOKAMAK WITH MAGNETIC COMPRESSION - TUMAN-2A

V.I.Gladushchak, V.A.Ipatov, S.G.Kalmykov, S.I.Lashkul, Yu.V.Petrov, G.T.Razdobarin, I.D.Shprits

(Physical-Technical Institute, Leningrad, USSR)

1. Absolutely calibrated measurements of the spectral line intensities for impurity ions (C and O) and neutral hydrogen (H°) have been performed during ohmic heating (OH) and compression (C) in the tokamak TUMAN-2A (see, e.g., Ref. /1/ and another our paper at this Conference). Two devices were used. The H_α intensity was measured by a polychromator /2/ scanning the plasma cross section. Usually, it was used in the Thomson scattering measurements.

The absolute calibration of the VUV - monochromator ($500 < \lambda < 3000$ Å) was made by comparing a part of the spectrum ($1000 < \lambda < 1800$ Å) with the bolometer signal of which the corresponding spectrum part was separated by means of LiF and quartz filters. The monochromator did not scan the cross section, and shapes of the radial profiles of H° and ion emission were taken from /3-4/. But this uncertainty has been shown not to deteriorate the further results strongly.

Based on spectroscopical measurements, atom and ion density calculations were made using data from /5/.

The hydrogen puffing was performed in two locations along the torus: near the polychromator or near the monochromator, the toroidal angle 60° being between these points.

2. The non-uniformities of H_α radiation were observed in both toroidal and poloidal direction, the first of them being due to the puffing. The poloidal asymmetry was rather expressed during OH. The maximum of the radiation was at the side where locally trapped ions drifted to. A symmetrization of the H_α intensity space distribution occured during the compression. Perhaps, the asymmetry was caused by the recycling poloidal non-uniformity. In the further treatment, the H_α intensity was averaged over both coordinate angles.

The puffing itself has been found to play a little role in the particle balance as compared with the recycling (less than 20 %). However, the hydrogen recycling intensity depends on puffing power and varies during the discharge. The shape of $n_{H^o}(r)$ - profile turns out to be close to that obtained by the charge-exchange diagnostics in TUMAN-2A /3/. The measurements carried out by both spectroscopic devices yield coincidental values of n_{H^o}. But, they are almost by the order of magnitude greater than those obtained in /3/.

3. The specific powers of electron sources due to ionization of H°, C and O-ions (I_{H^o}, I_C, I_O, respectively, $I_e = I_{H^o} + I_C + I_O$) are plotted versus r in Fig.1. One can see that at $Z_{eff} > 3$ the ionization of impurities becomes the main electron source in the inner parts of the plasma column.

The fluxes of the different ions were calculated from the ion density radial profiles using ionization equilibrium equations (see, e.g., Ref. /6/). After subtracting neoclassical pinch influx, the values of the anomalous transport fluxes and then the radial profiles of the anomalous diffusion coefficient for ions, $D_i^A(r)$, were computed. The plasma diffusion effective coefficient, D_{eff}, was calculated using the electron balance equation,

$$\int_0^r I_e(r)\, r\, dr - \frac{\partial}{\partial t}\int_0^r n_e(r)\, r\, dr = r\, \mathcal{D}_{eff} |\nabla n_e| .$$

In Fig.2, $D_O^A{}^{+6}(r)$ for the most abundant ion O^{+6} is compared with $D_{eff}(r)$ (in D_{eff} the neoclassical part is negligible). They are seen to be close.

$D_{eff}(r)$ - profiles at the different plasma densities are presented in Fig.3. D_{eff} seems to follow the "Alcator scaling" (see, e.g., /6/) like the anomalous electron heat conductivity, $D_{eff} \sim 1/n_e$.

In previous our papers (see,e.g., /1/) we dealt with an effective electron heat conductivity coefficient: $\varkappa_{eff} = \varkappa + (5 n_e \mathcal{D}_{eff} \nabla \ln n_e)/(2 \nabla \ln T_e)$. In Fig.4 $\varkappa_{eff}$ and $(5 n_e \mathcal{D}_{eff} \nabla \ln n_e)/(2 \nabla \ln T_e)$ are compared. Their radial profiles are similar, the heat transport with particles makes 30÷70%

of the whole heat flux. Fig.4b demonstrates a case when the magnetic island with m = 5 arises and develops during the compression (see Ref. /1/, case B). In $\chi_{eff}(r)$ it reveals itself by a pronounced maximum. The similar maximum occurs also in the radial distribution of $(5n_e D_{eff} \nabla \ln n_e)/(2 \nabla \ln T_e)$.

4. Conclusion. The method of a VUV - monochromator absolute calibration using a bolometer is developed. In discharges with $Z_{eff} > 3$, the impurity electron sources play dominant role in the internal parts of the plasma column. In the anomalous transport regime (like "Alcator scaling" transport), the anomalous diffusion coefficients of ions are close to those of the whole plasma; the density dependence of the diffusion coefficient is the same as for the heat conductivity, $D_{eff} \sim 1/n_e$; about half the heat flux is transported with the flux of particles. Appearance of the magnetic islands increases the particle transport approximately as well as heat one.

References:

1. S.G.Goncharov et al.. Plasma Phys. and Contr. Nucl. Fusion Res. (Proc. of 10th Int. Conf., London, 1984), IAEA, Vienna, 1985, v.1, p.155.
2. V.K.Gusev et al.. Fizika Plazmy (Plasma Phys. - USSR), 4 (1978), N°2, 269.
3. V.V.Afrosimov et al.. Ibid., 5 (1979), N°4, 753.
4. S.G.Goncharov et al.. Ibid., 8 (1982), N°5, 1013.
5. V.I.Ghervids et al.. In: Voprosy teorii plazmy (Problems of Plasma Theory - USSR), v.12, M., 1982, p.156.
6. Yu.N.Dnestrovskij, D.P.Kostomarov. Matematicheskoe modelirovanie plazmy (Mathematical Plasma Simulation - USSR), M., 1982.

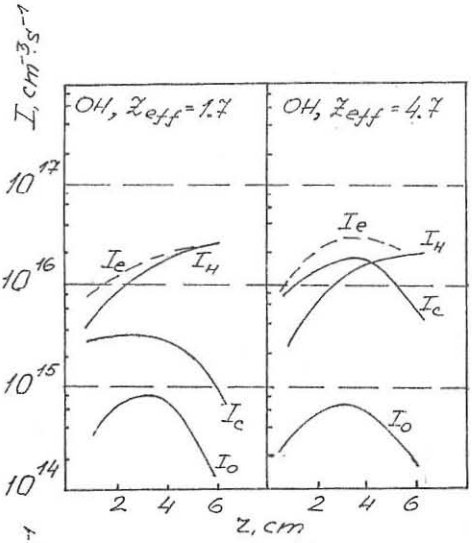

Fig. 1

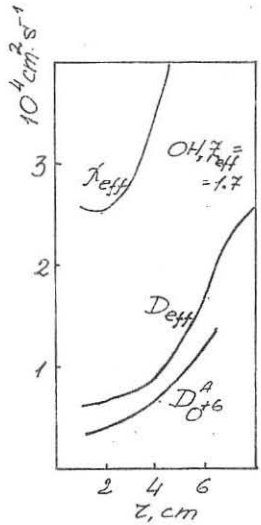

Fig. 2

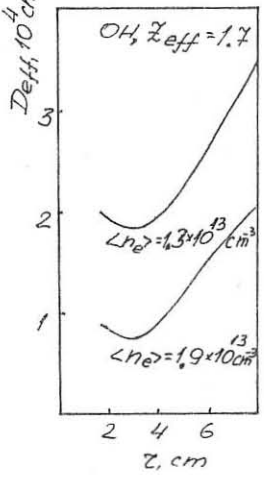

Fig. 3

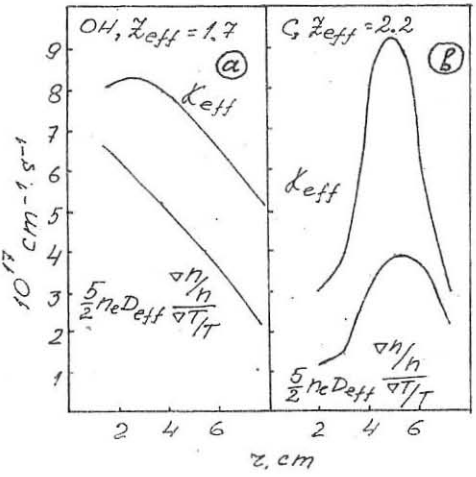

Fig. 4

EXPERIMENTS ON R-COMPRESSION AND ICR HEATING IN TOKAMAK "TUMAN-3"

Askinasi L.G.,Golant V.E.,Goncharov S.G.,Gryaznevich M.P.,
Gusev V.K.,Dyachenko V.V.,Izvozchikov A.B.,Krikunov S.V.,
Lebedev S.V.,Lipin B.M.,Pavlov I.P.,Razdobarin G.T.,
Rozhdestvenskij V.V.,Sakharov N.V.,Khalilov M.A.,
Chernyshev F.V.,Shakhovetz K.G.,Shcherbinin O.N.,
*Bender S.E.,*Litunovskij R.N.,*Minyaev O.A.,*Teplov P.P.

A.F.Ioffe Physico-Technical Institute,Leningrad,USSR
*D.V.Efremov Institute for Electrophysical Equipment,Leningrad

The previous experiments carried out on "Tuman-3"/1,2/ and "Tuman-2"/3/ have demonstrated high efficiency of the magnetic compression technique for plasma heating in tokamaks. However the experiments on ATC/4/ and TFTR/5/ as well as the experiments on combined R- and a-compression on "Tuman-3"/6/ showed decreasing energy and particle life time owing to compression along the major radius. The first part of this paper gives preliminary results of the strong R-compression ($R_o/R_c \approx 1.5$) on tokamak Tuman3.

A serious disadvantage of the Tuman -3 experiments is the low plasma parameters in the Ohmic heating. That is why the ICRF heating was used as an additional heating method at the precompressed stage of the discharge. The first results of this experiment is presented in the second part of the paper.

I. R-compression. The Ohmic stage used in the experiments had the following parameters: R_o= 0.63 m, B_t=1.0 T, I_p= 45 kA, $\bar{n}_e$= $1 \times 10^{13} cm^{-3}$. The smaller radius of the plasma torus was limited by two horisontal rail limiters with a 0.26m distance between them. The electron temperature measured by soft X-ray technique was equal to 200-300 eV before compression. The ion temperature by CX-diagnostics was equal to 150 eV.

The plasma column was shifted to the radius R_c=0.45 m in the stationary phase of the discharge 20 msec after the beginning by means of the special program in the control system of the plasma equilibrium and the discharge of the additional capacity bank on

the control field winding. The compression time was not larger than 5 msec. Typical discharge oscillogramms are shown in Fig.1. The current axis displacement was 18-20 cm. It is worth noting that the system used for feeding the transformer for Ohmic heating did not permit to increase the plasma current according to poloidal flux conservation requirement, that means $I_c = I_o R_o/R_c$. So some experiments were carried out with not sufficiently large current increase during the compression. In the rest of the experiments an additional capacitor maintaining the loop voltage was used for higher plasma current.

Fig.2 shows the chord density measurments versus the major radius position in the initial stage (curve 1) and in the shifted column (curve 2). After the displacement a fast decrease of density takes place which indicates the particle life time deterioration. The ion heating after the compression is close to the adiabatic law. But the ion temperature decreased rapidly in the postcompression stage. Fig.3 shows the time dependence of the ion temperature for various analyser inclination angles. Also the scheme of the measurments is presented which gives the opportunity to determine the distance between the plasma column axis and the line of observation before and after the displacement.

An essential question is how the recycling influences plasma parameters at fast removal of plasma column from the limiters. In our experiments it was possible to carry out the compression both with rail limiters and without them. In the last case the velocity of plasma removal from the limiter is much higher. None the less there was no difference in plasma behaviour in these two cases.

II. ICRF heating. For ICRF heating experiments an all-metal antenna of TFR type was installed through a horisontal port of the chamber at the low field side. The width of the RF current conductor was 45 mm and poloidal angle of the antenna was 70°. The experiments were conducted on deuterium-hydrogen mixture. For operating frequency 8 MHz the hydrogen resonance layer was placed near the plasma center at $B_t = 0.52$ T. The RF power input was 100-150 kW and pulse duration was 10 msec.

During the RF pulse the loop voltage and plasma density increased on 20-30% and 50-80% respectively. The proton energy spectrum

was distorted strongly due to appearence of high energy particles up to 10 keV. Fig.4 shows the increase of deuterium and hydrogen temperatures as a function of relative hydrogen concentration calculated from maxwellian parts of the energy spectra. The initial plasma parameters for the case were the following: T_{io}= 120 eV, $\bar{n}_e$= 2x10^{13}cm^{-3}, B_t= 0.45 T. The CX spectra for B_t=0.6 T are presented in Fig.5. It is seen that the heating efficiency increased with magnetic field and plasma density.

Sharp dependance on plasma parameters was found for electron heating. The maximum increase of T_e was registered at B_t=0.6T and n_p/n_e=20%, when the ion-ion hybrid resonance was placed near the axis. Fig.6 shows the T_e distribution measured by Thomson scattering. It is interesting to note that the electron heating was obtained by exiting the FMS waves from the LF side of the torus. It can be explained by comparatively narrow evanescence region in our experimental condition. At present much attention is paid to increase the RF power input. The utilisation of RF heating before the compression will give the opportunity to rise the adiabatic compression efficiency.

REFERENCES

/1/ Vorob'ev G.M.,Golant V.E. et al. Fizika plasmy,9,(1983),105

/2/ Golant V.E.,Goncharov S.G. et al.Proc.of the 11-th Europ.Conf. on Contr.Fusion and Plasma Phys.,Aachen,1983,v.1,p.107

/3/ Gusev V.K,Ipatov V.A. et al. 7th Europ.Conf. on Contr.Fusion and Plasma Phys.,Lousanna,1975,v.1,p.4

/4/ Daughney C.C.,Bol K. Nucl.Fusion,17 (1977),367

/5/ Tait L. et al. 10th Int.Conf. on Plasma Phys. and Contr.Fusion London,1984,IAEA-CN-44/a-III-1

/6/ Bender S.E.,Golant V.E. et al. 11th Europ.Conf. on Contr.Fus. and Plasma Phys.,Aachen,1983,v.1,p.111

/7/ Askinasi L.G.,Golant V.E. et al. Pis'ma v JTF,11 (1985),315

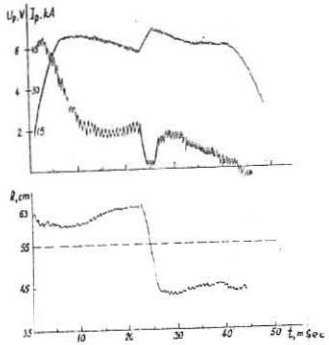

Fig. 1

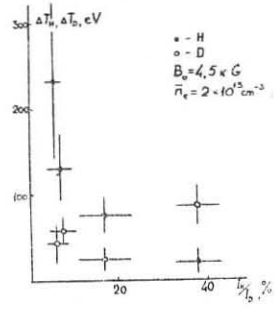

Fig. 4

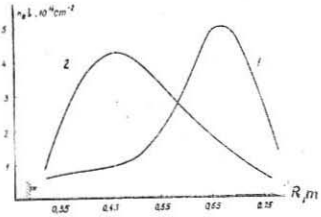

Fig. 2

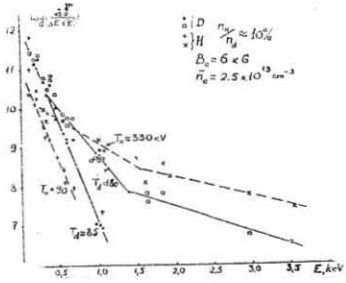

Fig. 5

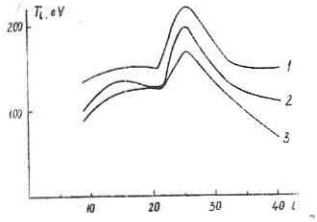

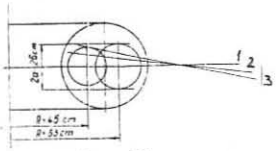

Fig. 3

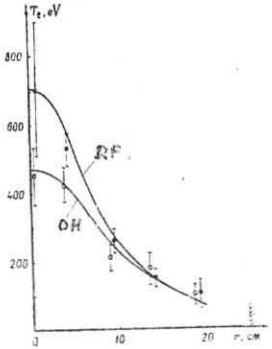

Fig. 6

DIFFICULTIES WITH THE ESTABLISHING OF "GAS BLANKETS" AT THE BORDER OF MAGNETICALLY CONFINED PLASMAS

A. Sestero

Associazione EURATOM-ENEA sulla Fusione, Centro Ricerche Energia Frascati, C.P. 65 - 00044 Frascati, Rome, Italy

A. Nocentini

NET Team, c/o Institut für Plasmaphysik, Garching

ABSTRACT

The possibility of establishing a "gas blanket" at the border of a magnetically confined plasma is investigated with the help of an appropriate one-dimensional transport code. The results obtained suggest the conclusion that gas blanket features cannot in general be steadily maintained, not even under the form provided by the suitably weakened, "generalized" definition of gas blanket which is discussed in the paper.

THE TRANSPORT MODEL

A border plasma layer, within which the transport of energy by neutrals is more conspicuous than the transport of energy by ions and electrons, for the sake of convenience will be here said to constitute a generalized gas blanket. In the present paper the possibility of occurrence of such border plasma conditions is investigated. We consider the following set ot transport equations:

$$\begin{aligned}
&\frac{\partial N_i}{\partial t} + \frac{1}{r}\frac{\partial}{\partial r}(r\,\Gamma_i) = S_i \\
&\frac{\partial N_n}{\partial t} + \frac{1}{r}\frac{\partial}{\partial r}(r\,\Gamma_n) = S_n \\
&\frac{3}{2}\frac{\partial}{\partial t}(N_e\,T_e) + \frac{1}{r}\frac{\partial}{\partial r}(r\,Q_e) = W_e \\
&\frac{3}{2}\frac{\partial}{\partial t}[(N_i+N_n)\,T_i] + \frac{1}{r}\frac{\partial}{\partial r}[r(Q_i+Q_n)] = W_i+W_n
\end{aligned} \qquad (1)$$

where - with obvious meaning of the indices "e" (for electrons), "i" (for ions), and "n" (for neutrals) - the N's are particle densities, the Γ's are particle fluxes in the radial direction, the S's are particle sources, the T's are temperatures, the Q's are energy fluxes in the radial direction (with Q_e not including the latent heat of ionization), the W's are energy sources, and where one has, furthermore, $S_e = S_i$ (charge conservation), $N_e = N_i$ (charge

neutrality), $\Gamma_e = \Gamma_i$ (ambipolarity of charged particle fluxes), $S_i + S_n = 0$ (particle conservation), and $T_n = T_i$ (strong collisional coupling between neutrals and ions).

The transport fluxes associated with the charged particle species - namely, the quantities $\Gamma_i (=\Gamma_e)$, Q_i and Q_e - are calculated according to the theory of transport in highly collisional toroidal plasmas due to F. Engelmann and A. Nocentini [1] (as appropriate for the very low temperature border plasmas which are here being considered).

The transport fluxes Γ_n and Q_n associated with the neutral species are given the following expressions:

$$\Gamma_n = - \frac{1}{M_n N_i \langle\sigma v\rangle_{chex}} \frac{d(N_n T_n)}{dr}$$

$$Q_n = - 2 \frac{N_n T_n}{M_n (N_i \langle\sigma v\rangle_{chex} + N_n \langle\sigma v\rangle_{n-n})} \frac{dT_n}{dr} + \frac{5}{2} T_n \Gamma_n \qquad (2)$$

where M_n is the mass of the neutral particles, $\langle\sigma v\rangle_{chex}$ is the rate parameter for charge exchange (which is the dominant process in the ion-neutral interaction), and $\langle\sigma v\rangle_{n-n}$ is the rate parameter for elastic neutral-neutral collision (which is the dominant process in the neutral-neutral interaction). For $\langle\sigma v\rangle_{chex}$ use is made of the expression given in [2], and for $\langle\sigma v\rangle_{n-n}$ the hard-sphere formula is employed.

The source terms on the right-hand side of Eqs (1) are specified to have the following expressions:

$$\begin{aligned} S_i &= - S_n = N_e (N_n \langle\sigma v\rangle_{ion} - N_i \langle\sigma v\rangle_{rec}) \\ W_e &= W_{coll} - W_{rad} - S_i E_{ion} \\ W_i + W_n &= - W_{coll} \end{aligned} \qquad (3)$$

where $\langle\sigma v\rangle_{ion}$ and $\langle\sigma v\rangle_{rec}$ are respectively the ionization and recombination rate parameters, W_{coll} is the rate of collisional energy transfer from ions to electrons, W_{rad} is the total radiation loss (due to Bremsstrahlung, recombination radiation, and line radiation), and E_{ion} is the ionization energy from the ground state (13.6 eV for hydrogen). For $\langle\sigma v\rangle_{ion}$ use is made of the expression given in [2], and for $\langle\sigma v\rangle_{rec}$ of the expression given in [3]; for W_{coll} the familiar Spitzer value has been introduced; finally, for the important radiation loss term W_{rad} reference has been made to the rather detailed calculations carried out in [4].

Numerical solutions of the above defined set of transport equations have been obtained with the help of a suitably modified version of a transport code originally written by G. Cenacchi and A. Taroni of the ENEA Computing Centre in Bologna. The runs have been typically started off from profiles assigned so as to be consistent with coronal equilibrium.

RESULTS AND CONCLUSION

The example which is illustrated in the figures is referring to a magnetically confined hydrogen plasma, with discharge parameters that are proper

of the device "Frascati Tokamak Upgrade" (FTU) currently under construction. Such parameters are: plasma major radius R = 0.9 m, plasma minor radius a = = 0.3 m, toroidal magnetic field (on axis) B_T = 8 T, toroidal plasma current I_p = 1.6 MA. A radial domain has been considered which ranges from r = 28.6 cm to the limiter-defined plasma border at r = 30 cm. Furthermore, the following numerical values have been assigned on the cold side (wall side): common temperature $T_i(=T_e=T_n)$ = 1.34 eV, total heat flux $Q_i+Q_e+Q_n$ = 10 W cm^{-2}, and total flux of heavy particles $\Gamma_i+\Gamma_n$ = 0. The total density of heavy particles has been instead prescribed on the warm side (plasma side) to have the value N_i+N_n = 7.5×10^{14} cm^{-3}. Such value is just below the critical value beyond which the border plasma would become thermally unstable because of excessive energy losses.

A glance at the figures shows clearly which pattern of evolution the system is adjusting to. The profiles move markedly away from the coronal equilibrium configuration which was set up as initial condition, with the ion density expanding significantly toward the wall (see Fig. 1). As a consequence, the favourable gas blanket properties of the coronal equilibrium solution tend to disappear (also with reference to the weaker "generalized gas blanket" requirements), as disclosed by the fact that the domain over which in Fig. 2a the upper and lower curves are coming to coalesce disappears altoghether in Fig. 2b (with the neutrals' heat flux turning actually negative everywhere but on the very border of the graph). It seems that the main reason for such a negative result is to be traced to the fact that the recombination coefficient has a rather weak dependence on the temperature, so that the rate of recombination remains very sluggish even at the fairly low border temperatures that we have imposed. Hence, even a small inflow of ions from the neighbouring warmer regions (driven by the gradient of the ion partial pressure) can easily build up the ion density near the wall to values well beyond coronal equilibrium - which in turn, through the charge-exchange interaction, is markedly depressing the neutrals' thermal transport efficiency, thus eventually bringing about the disappearance of those generalized gas blanket properties one was instead hopeful to preserve.

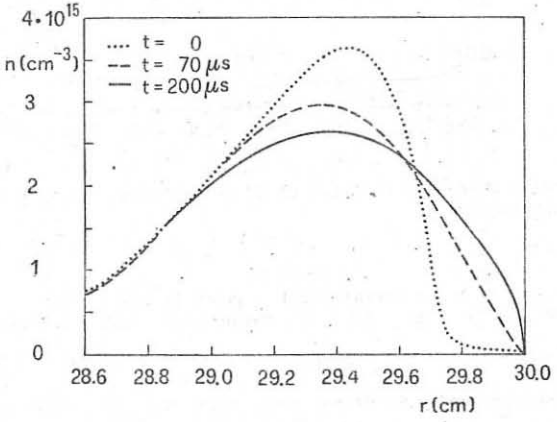

Fig. 1 Evolution of the profile of $N_i(=N_e)$.

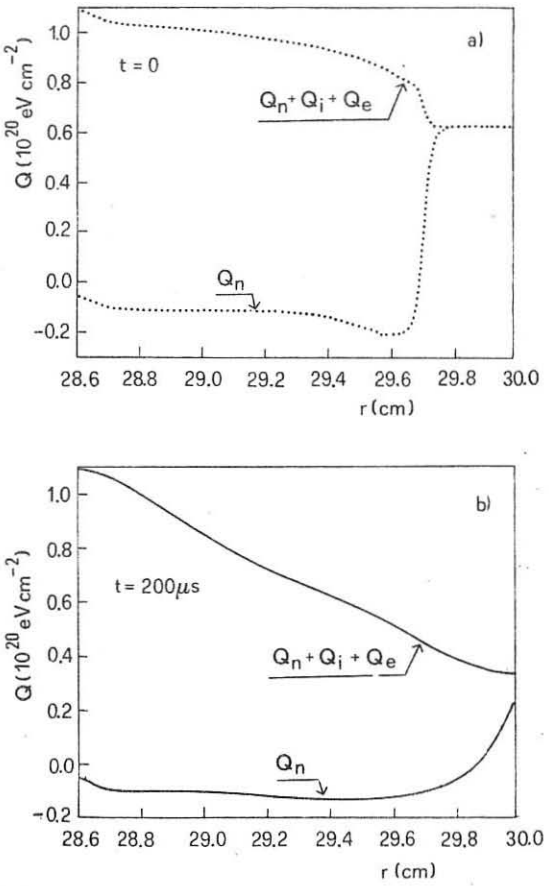

Fig. 2 Evolution of the profiles of Q_n (lower curves) and $Q_n + Q_i + Q_e$ (upper curves).

REFERENCES

[1] F. Engelmann and A. Nocentini, Nucl. Fusion 16 (1976) 694
[2] D.F. Düchs, D.E. Post and P.H. Rutherford, Nucl. Fusion 17 (1977) 565
[3] Yu.N. Dnestrovskii, S.E. Lysenko and A.I. Kislyakov, Nucl. Fusion 19 (1979) 293
[4] R.W.P. McWhirter and A.G. Hearn, Proc. Phys. Soc. 82 (1963) 641

EFFECT OF THE NON-AXISYMMETRIC FIELDS OF THE DITE BUNDLE DIVERTOR ON MAGNETIC TOPOLOGY, MHD INSTABILITIES AND ROTATION

K.B. Axon, N.C. Hawkes, J. Hugill, P.C. Johnson,
W. Millar, N.J. Peacock and J. Pritchard

Culham Laboratory, Abingdon, Oxon. OX14 3DB, U.K.
(Euratom/UKAEA Fusion Association)

The Bundle Divertor

The unique, localised toroidal field bundle divertor installed on DITE is described in detail elsewhere [1,2]. For the present experiments we used the Mark II version of this device [3] at $2T < B_T < 2.6T$ with stagnation point on the median plane at major radius, $R_s = 1.53$ m. The field modulation at the toroidal axis, R = 1.17m is ± 2.5%. This results in an approximate separatrix minor radius, $a_s = 0.21$m compared with the limiter radius, $a_L = 0.26$m.

Magnetic Topology

The structure of the magnetic field has been studied by integration along field lines. The bundle divertor field is simply added to the field of a model axisymmetric equilibrium. Evidently, this procedure is not self-consistent. Indeed, we have no model 3-D equilibria for diverted discharges. However, an axisymmetric poloidal field should be a reasonable approximation for discharges with a well-compressed current channel, since the deviation of the magnetic axis from circular form is small.

The results of these computations for a particular case is shown as a Poincaré plot in Fig.1. The field topology is complex. Near the rational surfaces, where q = m/n in the axisymmetric case (m = 2,3,5; n = 1,2), there are 2m/n islands with widths ~ 10-15% of the minor radius. Between the island chains there are some well-closed magnetic surfaces. However, the field structure near the separatrix is ergodic.

In spite of the considerable destruction of magnetic surfaces shown in Fig.1, the energy confinement in diverted discharges can be at least as good as that in nominally axisymmetric non-diverted discharges [4].

MHD Instabilities

The character of mhd instabilities in diverted discharges is conveniently discussed with reference to the safety factor at the separatrix,

defined by $q_s = 2\pi a_s^2 B_T / \mu_o R I_p$.

At $q_s > 3$ diverted discharges behave similarly to non-diverted discharges. In the absence of strong Mirnov oscillations the sawtooth instability is usually observed. However, it is affected by the divertor fields, even when the discharge is resting on the inner limiter and divertor action is absent. The period is shorter and more irregular than in non-diverted discharges, as shown in Fig.2, and the inversion radius is smaller. The central SXR intensity also rises with time (faster than $\bar{n}_e^2$) possibly indicating impurity accumulation on axis.

Sawteeth are not observed when Mirnov coils at the discharge periphery detect mhd modes with $\tilde{B}_p/B_p \gtrsim 0.4\%$. The largest mode usually has poloidal mode number, m = 2. However, when q_s is reduced towards 3 by increasing the plasma current or moving the discharge towards the divertor null point, a substantial mode with m = 3 is excited. This is invariably coupled to the m = 2 mode, the coupling point being on the outside near the median plane ($\theta \approx 0$). The modes interfere constructively on the outside and destructively on the inside of the torus, producing a large 'ballooning' effect by which the presence of the m = 3 mode can be detected.

Provided the m = 3 mode remains small, the modes continue to rotate in diverted discharges. However, the presence of a large m = 3 mode is associated with locking of the coupled modes to the divertor field. This occurs in a slip-stick fashion, as illustrated in Fig.2. It is accompanied by a marked decrease in particle and energy confinement [4]. Assuming the Mirnov oscillations are due to independent tearing modes, their amplitude and phase at the time of locking imply island widths of ~ 40 mm and ~ 30 mm for the m = 2 and m = 3 modes respectively, with X-points near $\theta = 0$ at the position of the divertor.

At $q_s \lesssim 3$ a series of minor disruptions always occurs, originating in the outer regions of the discharge. It is assumed that the growth of the locked and coupled m = 2, m = 3 modes is responsible for this. The confinement characteristics are further degraded and plasma arrives in the scrape-off layer and divertor chamber in a series of bursts, as shown in Fig.3, reminiscent of the edge relaxation phenomenon in H-mode discharges [5].

Plasma Rotation

Measurements of plasma rotation were made in diverted and non-diverted discharges in the following conditions: $B_T = 2.6$T, $I_p = 100$kA, $\bar{n}_e$ (max) = $4\text{-}5 \times 10^{19}$ m^{-3} with tangential neutral beam injection at a power ~ 2MW.

There was no observable, low-m mode or sawtooth activity in either case ($q_s \sim 5$). The toroidal rotation speed was measured from the Doppler shift of the $\lambda = 592$Å line of FeXIX and the $\lambda = 633$Å line of OVIII, observed with a tangentially-viewing grating spectrometer fitted with a multichannel detector [6].

In non-diverted discharges, rotation speeds of $1.5 - 2.0 \times 10^5$ ms^{-1} near the axis and $\lesssim 2 \times 10^4$ ms^{-1} near the periphery are reached, yielding a momentum confinement time of $\sim$ 22ms. In diverted discharges, although the values of density and β are almost the same, the central rotation speed drops by an order of magnitude to $\lesssim 2 \times 10^4$ ms^{-1}. It is thought that the modulation of the toroidal field strength by the bundle divertor (ripple) is the main cause of this result [7].

Conclusions

Although the bundle divertor apparently produces considerable destruction of magnetic surfaces, energy confinement in diverted discharges is unimpaired. Momentum confinement, however, is strongly reduced; an effect which is ascribed to field ripple rather than enhanced transport. The effect on internal mhd modes is small but an m = 3 mode localised near the divertor separatrix locks to the divertor field. Its stability is also worsened, so that stable operation at $q_s < 3$ is not achieved.

Acknowledgements

We acknowledge the continuing support of the DITE Group Leader, Dr J.W.M. Paul. Mr S. Bygrave was responsible for part of the Mirnov coil analysis. Messrs J. Allen, S.J. Fielding and G. Proudfoot supplied the data for Fig.3.

References:

[1] P.E. Stott, C.M. Wilson and A. Gibson, Nucl. Fusion 17 (1977) 481.
[2] K.B. Axon, et al. Culham Laboratory Report, CLM-R235 (1983).
[3] K.B. Axon, et al. in Plasma Physics and Controlled Nuclear Fusion Research (Proc. 9th Int. Conf., Baltimore, 1982), Vol.III p.201 (1983).
[4] P.C. Johnson, et al. in Plasma Physics and Controlled Nuclear Fusion Research (Proc. 10th Int. Conf., London, 1984), Vol.I p.239 (1984).
[5] M. Keilhacker, et al. ibid. Vol.I p.71 (1984).
[6] N.C. Hawkes and N.J. Peacock, submitted to Nuclear Fusion (1985).
[7] K.T. Tsang and E.A. Frieman, Physics of Fluids 19 (1976) 747.

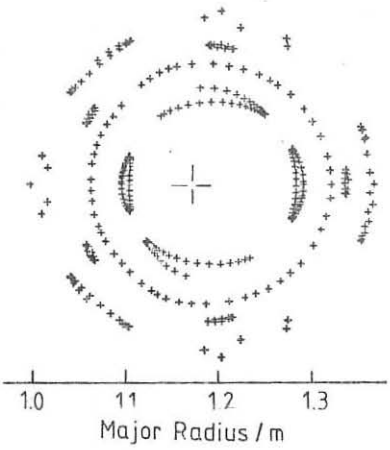

Fig.1. Intersection of magnetic field lines with r, θ plane at 180° toroidally from bundle divertor for q_s = 3.8.

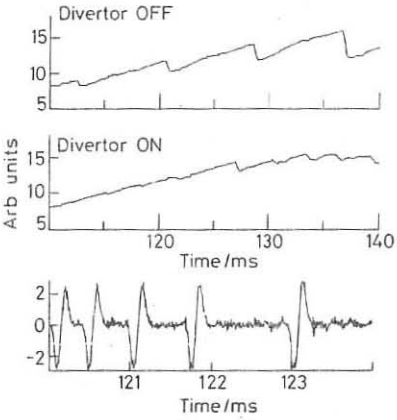

Fig.2. Top and centre: central chord SXR diode signals without and with divertor field. Bottom: Mirnov coil signal showing locking of coupled m = 2,3 mode.

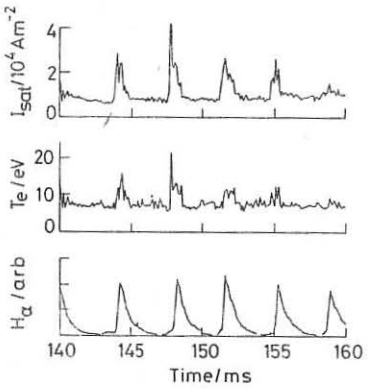

Fig.3 Measurements in divertor chamber during minor disruptions at $q_s \lesssim 3$. Top and centre: I_{sat} and T_e from Langmuir probe. Bottom H_α intensity.

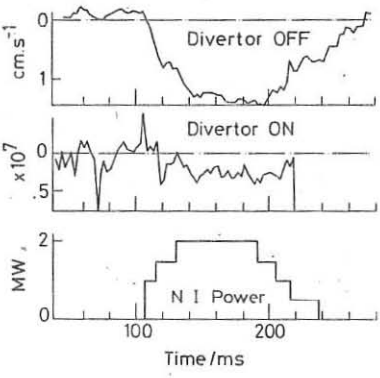

Fig.4 Toroidal velocity from Doppler shift of impurity line radiation during beam injection, with divertor off and on.

MHD Characteristics of JT-60 Plasmas

JT-60 Team*

Japan Atomic Energy Research Institue
Naka-machi, Naka-gun, Ibaraki 311-02, Japan

INTRODUCTION

JT-60 is a large tokamak with a compact poloidal divertor /1/. The first phase of experiments on ohmically heated plasmas was carried out from April to June in 1985. Stable divertor discharges with currents up to 1.6 MA were achieved. The divertor function as established in smaller-size tokamaks /2,3/ was confirmed with the outer divertor separatrix and the crammed divertor chamber of JT-60. The radiative power loss from main plasma was reduced to about a quarter of ohmic input power.

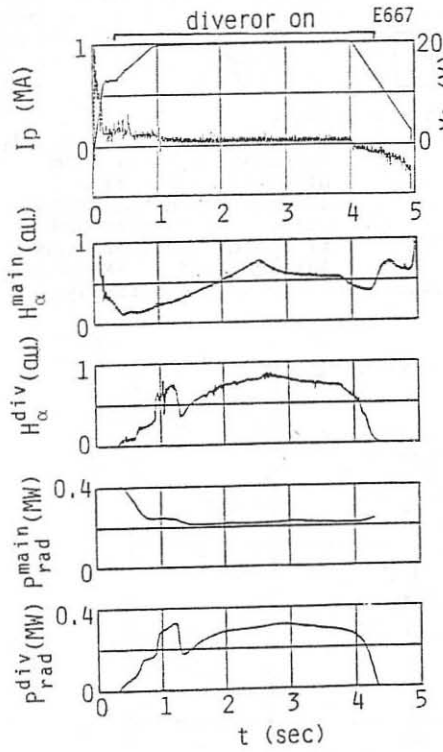

Fig. 1. Waveforms of a divertor discharge.

DIVERTOR DISCHARGE

In a divertor discharge, the plasma was started in the limiter configuration and the divertor coils were excited from the plasma current ramp up phase. The divertor configuration was verified by a magnetic fitting code based on MHD equilibrium calculation. Experimental observations of the transition from the limiter to divertor configuration are as follows; H_α emission and radiation power appear in the divertor region (Fig. 1), TV image shows disappearance of the interaction of plasma with limiters, H_α emission from main plasma decreases by a factor of more than two, rise of soft X-ray emission with time is suppressed, line integrated electron density decreases

when gas puffing is kept constant, radiative power loss from main plasma is reduced, and the radiation profile deduced by a 4-ch bolometer array changes from peaked to flat or hollow.

Figure 2 shows a discharge in which divertor is activated during the current flat top of a limiter discharge. The decay time of the radiation, which is related to the confinement time of impurities, is a few hundreds milli-sec for the central chord.

It is of interest to explore the possibility of remote cooling to alleviate heat load on divertor plates. The radiative power loss and H_α emission from the divertor region increase with electron density of main plasma as shown in Fig. 3. The radia-

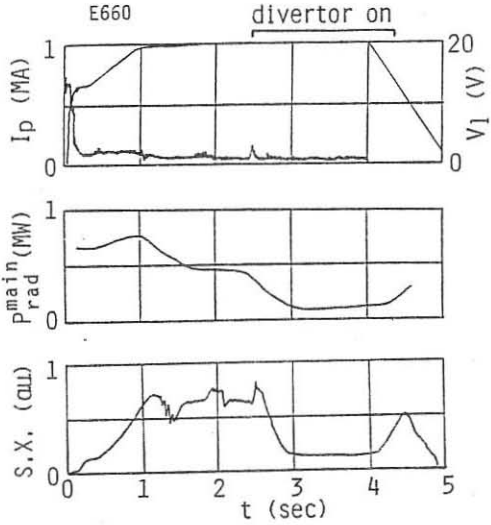

Fig. 2.
Time evolution of radiation power and soft X-ray diode with 20-μm Be foil signal when divertor is activated at the second half of a discharge.

Fig. 3.
Radiation power (○,△) and H_α emission (●,▲) from divertor region as a function of electron density. The circles and triangles represent those for 1-MA and 1.5-MA discharges, respectively.

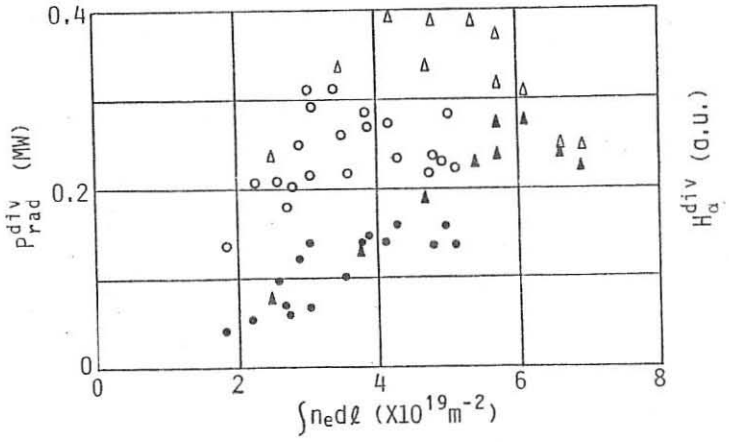

tion power is raised as the ohmic input power is increased. The divertor plasma radiates up to 0.4 MW, which exceeds the radiative power loss from main plasma.

MHD ACTIVITY

At the current flat top, no sawtooth oscillation was detected in soft X-ray diode traces in the divertor discharges even with an effective safety factor near the separatrix down to 3; we use the effective q-value which is defined by the analytic formula /4/,

$$q_{eff} = \frac{2\pi}{\mu_0}\frac{a^2}{R}\frac{B_t}{I_p}\{\,1 + (\frac{a}{R})^2(\,1 + \Lambda^2/\,2\,)\,\}$$

where a and R are minor and major radius, respectively, and $\Lambda = \beta_p + \ell i/2$. The MHD equilibrium analysis indicates that broad current profile is formed in the divertor discharges since the internal inductance is about unity. Therefore the safety factor at the magnetic axis is not reduced to unity. On the other hand, the soft X-ray diode traces start sawtoothing after plasma current reaches its flat top with q-value above 4 in the limiter discharges.

During the current ramp up phase, bursts of H_α emission and radiation power in the divertor region were observed as seen in Figs. 1 and 4. The bursts are triggered when the effective q-value falls on around integer values. The burst in Fig. 1 occurs at $q_{eff} \sim 5$ and those in Fig. 4 occur at $q_{eff} \sim 5{,}4$. The step increase at earlier period corresponds to $q_{eff} \sim 7{,}6$. Kink-like modes are excited at those periods when the rate of current rise is high. The spikes in the H_α signal in Fig. 4 are due to the mode. It should be noted that the burst lasts longer than the

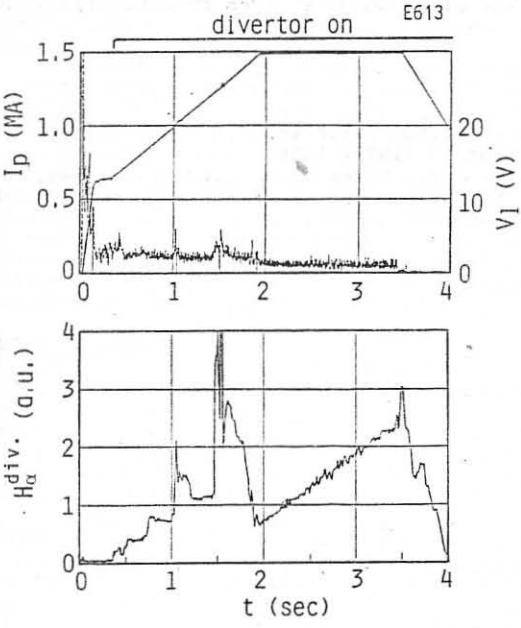

Fig. 4.
Divertor discharge in which kink-like modes and H_α bursts in the divertor region are excited.

mode and that even when any noticeable activities are not observed in the main plasma, pedestal-like increase appears as in Fig. 1. No change in the equilibrium configuration was found. Nonetheless the particle flux and heat flux to the divertor are enhanced when the plasma edge crosses the rational surface.

The kink-like modes during the current ramp up phase are more unstable in the divertor discharge than in the limiter discharge. The activities in the one-turn loop voltage which takes the form of humps with negative spikes (Fig. 4) are larger in the divertor configuration. The difference may arise from different current profile between divertor and limiter configurations. Sharp boundary may be formed in the divertor discharge. The activities during the current rise, however, do not affect on the plasma parameters at the current flat top period.

CONCLUSIONS

Divertor discharges in JT-60 were examined by radiation measurements. The divertor plasma radiates a few hundreds kilowatt, which is comparable to the radiative power loss from main plasma. Broad current profile with $q_o > 1$ is formed at the current flat top in the divertor configuration. Bursts of H_α emission and radiative power loss in the divertor region were observed during the current ramp up phase.

*List of the members of the JT-60 team is given in ref. /1/.
Presented by S. Tsuji.

REFERENCES

/1/ Yoshikawa, M., et al., Invited paper in this conference.
/2/ DIVA GROUP, Nucl. Fusion 18 (1978) 1619.
/3/ Shimada, M., et al., J. Nucl. Mater. 128 & 129 (1984) 340.
/4/ Todd, T.N., in Proc. Second European Tokamak Programme Workshop, Sault-Les-Chartreux (1983).

SPECTROSCOPIC MEASUREMENTS OF THE IMPURITY CONTENT OF JET PLASMAS WITH OHMIC AND RF HEATING

B Denne, K H Behringer, W Engelhardt, R D Gill, N C Hawkes[+], E Källne[o], H Krause*, G Magyar, M Mansfield, K F Mast*, C De Michelis[o], P D Morgan, D Pasini†, N J Peacock[+], H P Summers

JET Joint Undertaking, Abingdon, Oxon OX14 3EA, UK
+ EURATOM-UKAEA Association, Culham Laboratory, Abingdon, Oxon OX14 3DB, UK
* EURATOM-IPP Association, IPP Garching, Federal Republic of Germany
o EURATOM-CEA Association, Fontenay-Aux-Roses, France
† Stipendiary of the Natural Sciences and Engineering Research Council of Canada

INTRODUCTION

Knowledge of the impurity concentrations in the JET plasmas is based mainly on the analysis of resonance line intensities in the VUV, with additional information coming from measurements of soft x-ray spectra.

The plasma impurity content is monitored routinely by a McPherson Model 251 VUV broadband spectrometer, covering the wavelength range 100-1700 Å by means of two interchangeable gratings and equipped with a multi-channel detector. The spectrometer views a horizontal central chord in the torus midplane. Up to 128 spectra are recorded during a plasma discharge, allowing the study of the time evolutions of various spectral line intensities.

A relative calibration of the spectrometer sensitivity has been obtained by studying transitions between charge-exchange populated, excited levels in C VI and O VIII during neutral beam injection on the ASDEX tokamak. The absolute sensitivity is derived from the H_α-L_β branching ratio using a special H_α monitor along the same line-of-sight.

The soft x-ray spectra over the range 4-30 keV are recorded by a HgI_2 detector viewing the plasma in the horizontal mid-plane through Al, Be and air absorbers. The detector has an energy resolution of 0.6 keV at 6 keV, which is sufficient to separate the groups of He-like metal impurities in the plasma. The spectra show both continuous emission and the characteristic K-lines of Ni and Cr. The latter are used to calculate the nickel concentrations in the centre of the plasma.

METHOD OF ANALYSIS

A transport code is used for the interpretation of JET VUV line intensities. It solves, in cylindrical co-ordinates, the coupled set of continuity equations for the individual ionisation stages, taking into account ionisation, recombination and diffusion processes. The code predicts the radial distribution of ground state densities and emission shells, line-of-sight integrals of selected lines and local as well as global radiation losses caused by line emission.

The ionisation rate coefficients are calculated as proposed by Lotz /1/. For Na-like ions, correction factors for inner-shell ionisation have been evaluated and implemented in the code. The Burgess formula /2/ is used for the dielectronic recombination rates, taking into account modifications by Merts et al /3/ and a density dependence according to Post et al /4/. The

resonance line excitation rates required are mostly found in the literature for light impurity ions, otherwise the $\bar{g}$ approximation is used. For the actual analyses, T_e profiles from the ECE diagnostic were used. Electron density profiles were taken from the multi-channel DCN interferometer. The conditions at the plasma edge were estimated from Langmuir probe measurements in the scrape-off layer.

The impurity ion fluxes are described by an anomalous diffusion coefficient D and a convective term $V_D = - 2Dr/a^2$, leading to moderately-peaked profiles for the total impurity ion densities. The analyses of several accidental injections of iron and nickel into the JET plasmas resulted in diffusion coefficients of 0.6-1.0 m^2/s, as found in many other tokamaks. $D = 0.6\ m^2/s$ is used in the code.

Several ionisation stages of important impurities have been investigated routinely, in order to check the consistency of the analysis method. For ions with metastable levels, the population of these has been assessed by measuring the intensities of transitions within the metastable spin system. The number densities in the metastable levels have been added to the ground state densities. Results calculated from different ionisation stages of the same element are consistent to within about a factor of two. The total radiated power, calculated from the measured impurity concentrations, agrees well with the bolometer measurements. Z_{eff} values, derived from the spectroscopic analyses, are usually within ± 1 of the Z_{eff} results obtained from visible bremsstrahlung. The remaining difference is probably due to uncertainties in the light impurity levels, which are obtained from the plasma edge.

Nickel concentrations have been evaluated from the x-ray spectra during 4 s of the flat tops of the plasma pulses, using theoretical excitation rates for the four main lines in Ni XXVII and using the electron temperatures as obtained from the high energy tail. Coronal ionisation equilibrium is assumed to predict the total nickel concentration. The respective results agree with those of VUV spectroscopy within the mutual error limits, although the results from the x-ray spectra have a tendency to be somewhat lower.

RESULTS

The main impurities in JET are C (2-3%), O (1-4%), Cl and metals (a few tenths of a percent).

Nickel is the most important metal impurity. In addition, chromium and some iron are observed. Ni and Cr are the main constituents of the Inconel vessel wall, and the Faraday shields of the ICRH antennae are made of Ni. During glow discharge cleaning and also normal tokamak operation these metals are deposited on to the graphite limiters, which thus become the main source of the metal impurities.

Studies of the general impurity behaviour for a variety of ohmic plasmas have shown that the concentrations of light impurities are fairly insensitive to plasma current and electron density, but increase with electron density close to the density limit. Chlorine shows a similar behaviour. The metal impurities are especially prominent in low-density plasmas. They increase with plasma current, but decrease with electron density, particularly steeply near the density limit.

Carbonisation of the vacuum vessel walls has been carried out on several occasions. The purpose of the carbonisations has been to assess the influence of an all-carbon wall on plasma behaviour and metal impurities; also to remove oxygen and chlorine.

Spectroscopically, the carbonisation brought about a large reduction in metals. This is consistent with the observation of hollow bolometric radial profiles and an appreciable decrease in radiated power from the plasma centre. Generally, the total radiated power decreased to about 50% of the ohmic input

power after carbonisation, to be compared with typically ∿ 70% radiated power before carbonisation. Both figures hold for low and intermediate electron densities.

After carbonisation oxygen and chlorine are somewhat reduced.

The effect of carbonisation on the impurity line intensities is shown in Fig.1 for three selected lines: Ni XXV 117.93Å, O V 629.73Å and C IV 312.43Å. All the points plotted are for plasmas with B_T=3.4 T, I_p=2.8 MA and $\bar{n}_e$=2.3-2.6x10^{19} m^{-3}. The vertical dashed line between shots #4202 and #4228 indicates where carbonisation took place (6 hours of glow discharge cleaning in deuterium doped with 12% methane). A drastic decrease in the Ni-signal is seen immediately after carbonisation. However, within the following 20-25 shots, the Ni-signal recovers to the level before carbonisation. This behaviour is consistently observed for heavy carbonisations. However, after a recent, much heavier carbonisation (48 hours of glow discharge cleaning in deuterium doped with 17% methane) the reduction in nickel persisted for approximately 2 weeks of operation (∿ 200 shots).

Analysis of the plasma impurity content before carbonisation (shot #4186) and immediately after (#4228), reveals a practically unchanged carbon concentration (2.3% → 2.5%), a slight decrease in oxygen content (1.4% → 1.2%), a factor of 2.5 decrease in chlorine (0.1% → 0.04%) and a factor of 4-5 decrease in nickel concentration (0.09% → 0.02%).

During 1985, ICRH experiments have started on JET/5/. The maximum power available from the RF-generators was 6 MW (3 MW per antenna) of which up to 80% was coupled to the plasma.

Figure 2 shows the relative increase of radiated power, line-integrated electron density and two impurity line signals (C IV 384.1Å and Ni XXV 117.93Å) as a function of RF-power coupled to the plasma. ^{3}He minority heating was used with B_T = 3.4 T and I_p = 4 MA.

The radiated power increases linearly with RF-power. The fraction of the total input power lost by radiation is ∿ 50% both before and during RF. The increase in line-integrated electron density, $\bar{n}_e\ell$, is approximately constant above 2 MW of RF power. The C IV and Ni XXV line intensities (corrected for the density increase during RF by dividing by $\bar{n}_e\ell$) indicate that there is no appreciable increase in impurity concentrations during ICRH, within the RF power range investigated. It should be pointed out, that since the electron density profile changes during RF in the sense that the edge density increases (flatter profile), correcting the line intensities to the local change in n_e rather than $\bar{n}_e\ell$ would have the effect of increasing the Ni XXV points somewhat and decreasing the C IV points. The Z_{eff}, as measured from the visible bremsstrahlung, does not change significantly during RF.

Analysis of the impurity concentrations before and during ICRH for one of the pulses with 5 MW RF-power gives the following results: the carbon and oxygen concentrations do not change (3% C and 0.8% O), also the chlorine concentration stays constant (0.06%) while the metal concentration increases slightly during RF. The metal concentration obtained from the VUV is in good agreement with that obtained from the soft x-ray measurements.

REFERENCES

/1/ W Lotz, Lab.Reports IPP 1/62 (1967) and IPP 1/76 (1968), Garching, Germany.

/2/ A Burgess, Astrophys.J. 141, 1588 (1968).

/3/ A L Merts, R D Cowan, N H Magee, Los Alamos Scientific Laboratory Report LA-6220-MS (1976).

/4/ D E Post, R V Jensen, C B Tarter, W H Grasberger, W A Lokke, Atomic Data and Nuclear Data Tables 20, 397 (1977).

/5/ J Jacquinot, invited paper, this conference.

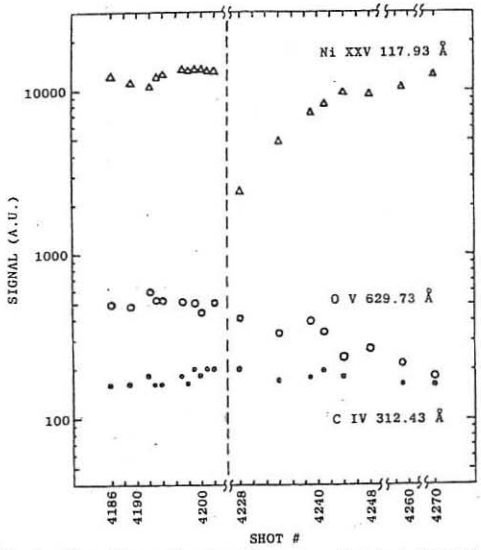

FIGURE 1 The effect of wall carbonisation on selected impurity line intensities.

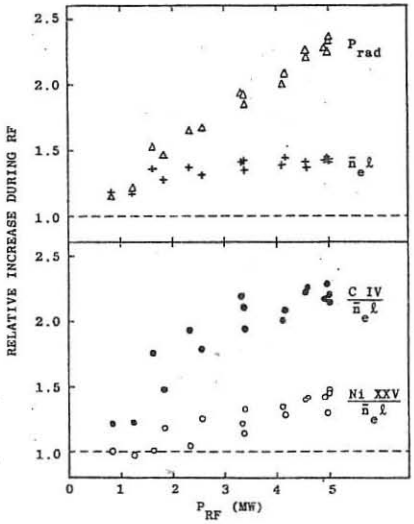

FIGURE 2 Relative increase in radiated power, line-integrated electron density and C IV and Ni XXV line intensities during ICRH, as a function of RF power.

B

stellarators

70 GHz ECRH EXPERIMENTS ON THE W VII-A STELLARATOR

V. Erckmann, G. Janzen, W. Kasparek, G.A. Müller, P.G. Schüller, K. Schwörer, M. Thumm, R. Wilhelm

Institut für Plasmaforschung, Universität Stuttgart, Stuttgart, F.R.G.

G. Cattanei, D. Dorst, A. Elsner, G. Grieger, P. Grigull, H. Hacker, H.J. Hartfuß, H. Jäckel, R. Jaenicke, J. Junker, M. Kick, H. Kroiss, G. Kuehner, H. Maaßberg, C. Mahn, S. Marlier, G. Müller, W. Ohlendorf, F. Rau, H. Renner, H. Ringler, F. Sardei, M. Tutter, A. Weller, H. Wobig, E. Würsching, M. Zippe

Max-Planck-Institut für Plasmaphysik, EURATOM-Association, Garching, F.R.G.

1. Introduction

In continuation of ECRH experiments at 28 GHz /1/ a new 70 GHz/200 kW/100 ms RF system was put into operation on the Garching W VII-A stellarator. According to the increased frequency this new system has given access to remarkably improved plasma parameters: The plasma density regime could be extended to values well above $10^{19} m^{-3}$ now allowing combined ECRH and NBI operation. Simultaneously electron temperatures above 2 keV were achieved due to the enhanced plasma confinement at the larger magnetic field (B_{res} = 2.5 Tesla). As before the stellarator plasma could be built up from a neutral gas background of deuterium or helium.

In the following paragraphs the heating results for various kinds of EC wave irradiation (unpolarized and linearly polarized O-mode irradiation at the fundamental frequency and X-mode irradiation at the second harmonic frequency) will be reported. Specific problems like impurity release, fast particle generation, and RF related current drive will be discussed, too.

2. Plasma heating for various kinds of EC-wave irradiation

In a first step of the 70 GHz experiments the gyrotron radiation (mainly TE_{02} mode) was launched into the equatorial plane of the torus from the low-field side. The incident wave with $\bar{k} \perp \bar{B}$ corresponds to a 50%/50% O/X-mode mixture, where the X-mode content is reflected at the X-mode cutoff layer at the outer plasma edge.

In a second step the RF power was transformed into the almost linearly polarized HE_{11} mode with the help of specific mode converters. Mode purity was conserved by using optimized overmoded RF components /2/. The resulting low aperture wave was irradiated in O-mode orientation ($\bar{E} \parallel \bar{B}$, $\bar{k} \perp \bar{B}$) for fundamental, and in X-mode orientation ($\bar{E} \perp \bar{B}$, $\bar{k} \perp \bar{B}$) for harmonic ($\omega_{RF} = 2 \cdot \omega_{ce}$) heating. Again the plasma was irradiated from the low-field side. A tiltable mirror (± 10°) was mounted to the opposite inner torus wall allowing current drive experiments by oblique reflection of the non-absorbed power fraction. The incident power and thus the beam absorption could be analysed by five RF pickup antennas installed in the mirror.

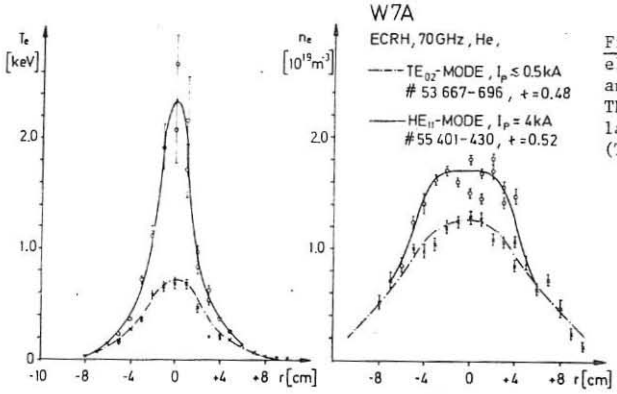

Fig. 1: Profiles of electron temperature and density for TE_{02}- and HE_{11}-mode launching. (Thomson scattering).

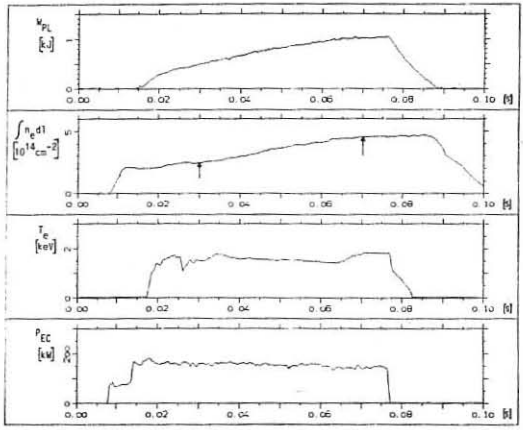

Fig. 2: Temporal development of the plasma energy content W_{PL}, line integrated density $n_e dl$, electron temperature (soft-X) T_e and incident RF-power P_{EC}

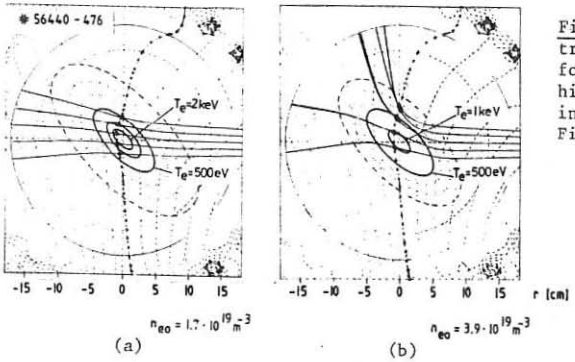

Fig. 3: Calculated ray traces (ordinary mode) for the low (a) and high density case (b), indicated by arrows in Fig. 2.

With the transition from unpolarized to advanced, polarized O-mode irradiation a substantial improvement of the resulting plasma parameters has been achieved. This is illustrated in Fig. 1 with temperature and density profiles for both kinds of irradiation. In this example of low density operation (n_{eo} = 0.3 $n_{e,crit}$) the central electron temperature could be doubled by using the polarized beam. Increasing the plasma density towards the cutoff value ($n_{e,crit}$ = 6.25 x $10^{19}m^{-3}$) generation of a hot plasma failed for the unpolarized irradiation, whereas T_e remained above 1 keV (e.g. at n_{eo} = $4 \cdot 10^{19}m^{-3}$) in the case of polarized wave launching. Fig. 2 gives an example of the temporal development of density ramp-up (by gas puffing), plasma energy, electron temperature (soft x-ray signal), and the RF pulse. At two moments, specified in the figure, a cross sectional view of the plasma together with the calculated patterns of rays is given in Figs. 3a and b. From these figures one recognizes that refractional effects and, therefore, access to the central plasma core become critical for the high density operation (n_{eo} = 0.7 · $n_{e,crit}$, Fig. 3b). The measured attenuation of the rays (signals of the diagnostic antennas) agreed in all cases quite well with the calculated relativistic absorption according to linear theory.

Further data for the cases of wave heating at the fundamental frequency are summarized in Table I:

Mode	T_{eo} [keV]	n_{eo} [$10^{19}m^{-3}$]	W_p [kJ]	τ_E [ms]	P_{inc} [kW]	Mode content O/X	η [%]
TE_{02}	1.1	0.8	0.2	4.0	170	50:50	30±10
HE_{11}	2.3	1.8	0.5	4.3	175	90:10	65±10
	1.1	4.0	1.1	9.7	175	90:10	65±10

Tab. I: Heating results for two different kinds of wave launching ($\omega_{RF} = \omega_{ce}$)

According to Table I the heating efficiency $\eta = P_{abs}/P_{inc}$ – as determined by power modulation techniques /1/ – is strongly improved in the case of polarized HE_{11} wave irradiation. The relatively large X-mode content of about 10% in the HE_{11} beam can be attributed to a meanwhile identified asymmetric mode content of the 70 GHz gyrotron emission. The missing power fraction in absorption of 35%, even with the advanced HE_{11}-irradiation, is consistent with the small size of the hot and "dark" plasma core in combination with the ray refraction. A further important conclusion is that the power fraction which is not absorbed as O-mode in the first pass, essentially does not contribute to bulk plasma heating. This is explained by a loss of direction and polarization of the primary wave due to multiple wall reflections and subsequent effective surface absorption via oblique X- or R-waves. As a consequence high quality of the incident beam (divergence, polarization) and good absorption (electron temperature, plasma size) are goals for O-mode fundamental heating.

In the first experiments with X-mode irradiation at the cyclotron harmonic frequency ($\omega_{RF}=2\cdot\omega_{ce}$ with B_{res} = 1.25 Tesla) immediate breakdown and plasma build-up was achieved, too. The resulting temperature and density profiles (with T_{eo} = 0.8 keV and n_{eo} = $2.5 \cdot 10^{19}m^{-3}$) were rather broad according to the enlarged absorptivity at $\omega=2\omega_{ce}$. The heating efficiency was determined to η = (80 ± 10)% .

3. Impurity radiation, fast particle production and current drive

The typical radiation losses for the 70 GHz heated stellarator plasmas were around 40 kW. According to the spatially resolved bolometric radiation measurements the major fraction of radiation is emitted from the outer region (i.e. $r > 2/3\ a$) and is attributed to atomic processes in this zone. In the inner part of the plasma the radiated power remains at about 30 mW/cm^3. A few discharges with additional OH-current showed an increase of Z_{eff} by up to 25% during the ECRH pulse.

The RF generated fast electron population was analyzed by ECE measurements in perpendicularly and parallel oriented observation direction to the major radius. In the low density regime ($n_{eo} \approx 1$ to $2 \cdot 10^{19} m^{-3}$) a small fraction $n_e/n_{eo} \approx 10^{-3}$ with an energy of 10 keV was found. Operation at higher densities ($n_{eo} \approx 3\text{-}4 \cdot 10^{19} m^{-3}$) showed no suprathermal electrons.

Toroidal plasma currents in the range of 0.5 to 1 kA were observed for all kinds of wave irradiation. The following mechanisms were identified to contribute to the measured current: Co- and counterstreaming fast electrons of different confinement as a main mechanism for current generation at low densities /1/ and as a mechanism of minor importance at higher densities ($n_e \geq 10^{19} m^{-3}$). Because of the increased pressure gradients in the present experiments the pressure driven (bootstrap) current obviously gives the major contribution to the toroidal current. In addition the radial shift of the plasma in the helical field due to finite β contributes to the total current. A directly driven RF-current could be generated by reflection of the non-absorbed incident wave fraction at an oblique angle from the high-field side. By choosing different oblique angles the non RF driven currents could be compensated or even overcompensated.

4. Conclusions

Build-up and heating of a stellarator plasma to reasonable parameters was achieved by polarized and well focussed EC wave irradiation (170 kW, 100 ms) for both cases: first harmonic ordinary mode irradiation (T_{eo}=2.3 keV, $n_{eo}=1.8 \cdot 10^{19} m^{-3}$) and second harmonic extraordinary mode irradiation (T_{eo}=0.8 keV, $n_{eo}=2.5 \cdot 10^{19} m^{-3}$). The impurity radiation remained at low level and the relative fraction of suprathermal electrons was found to be negligible ($\leq 10^{-3}$). Besides direct RF-current drive at slightly oblique angles, plasma induced currents were observed and mainly attributed to the pressure gradient (bootstrap current) or to the toroidal plasma shift.

References

/1/ Wilhelm, R., V. Erckmann, G. Janzen, W. Kasparek, G. Müller, E. Räuchle, P.G. Schüller, K. Schwörer, M. Thumm, W VII-A Team, Plasma Phys. and Controlled Fusion, 26, 1433 (1984)

/2/ Thumm, M., V. Erckmann, G. Janzen, G. Müller, P.G. Schüller, R. Wilhelm, Proc. 4th Int. Symposium on Heating in Toroidal Plasmas, Rome, 1984, Vol. II, p. 1461.

Ambipolar Electric Fields and Transport

H. Maaßberg, W VII-A Team*), NI Team*)

Max-Planck-Institut für Plasmaphysik
EURATOM-Association, D-8046 Garching
Federal Republic of Germany

ECRH Group*)
Institut für Plasmaforschung der Universität Stuttgart
D-7000 Stuttgart
Federal Republic of Germany

I. Introduction

In the W VII-A Stellarator with large aspect ratio (A = 20), very small helical field ripple and nearly perpendicular neutral beam injection (NI) heating, radial electric fields have strong influence on the confinement properties. From Doppler shift measurements of impurity lines, a large poloidal plasma rotation ($v_{EXB} \sim 10 - 30$ km/s) was derived which is associated with the NI heating power and with strong pressure gradients. The large ambipolar electric fields, which reduce significantly the deviations of particle orbits from the magnetic surfaces, lead to an increased heating efficiency of the NI /1/ and to an improved particle confinement ($\tau_p \sim 100$ ms). Also in ECR heated discharges (f_{ECRH} = 70 GHz) poloidal plasma rotation ($v_{EXB} \sim 10$ km/s) was found at higher plasma densities ($n_e \sim 5 \times 10^{13}$ cm^{-3}).

The influence of the ambipolar electric fields on transport in the plateau regime is described within neoclassical theory by a simple model. Based on this model, the ambipolar electric fields are calculated for an ECR heated discharge. The influence of these fields for reducing the heat conduction of the thermal ion component in NI discharges as well as the impurity transport is briefly discussed.

II. Model of transport in the plateau regime

For simplicity, we assume an axisymmetric magnetic field model and use the Krook collision term. The stationary drift kinetic equation

$$(\underline{v}_{\parallel} + \underline{v}_D) \cdot \underline{\nabla} f = - \nu (f - f^{Max}) \qquad (1)$$

is linearized with the ansatz $f = f^{Max} + f_1$, and only the ambipolar potential $\Phi(r)$ is taken into account for calculating the drift velocity $\underline{v}_D = \underline{v}_{EXB} + \underline{v}_{\nabla B}$. The solution of eq. (1) is well known /2/:

---

*) see paper W VII-A Team, NI Team, ECRH Team "Influence of the Magnetic Configuration on Plasma Behaviour in the WENDELSTEIN VII-A Stellarator", this conference

$$f_1 = \frac{v_{th}}{\iota\omega_c} \cdot \frac{\nu^* \sin\theta - (c_\parallel + \eta)\cos\theta}{(c_\parallel + \eta)^2 + \nu^{*2}} \cdot (c_\parallel^2 + \tfrac{4}{2} c_\perp^2) \cdot \left[\frac{n'}{n} + \frac{q\Phi'}{T} + (c^2 - \tfrac{2}{2}) \frac{T'}{T} \right] f^{Max} \qquad (2)$$

with $c = v/v_{th}$, rotational transform ι, collisionality $\nu^* = R\nu/\iota v_{th}$ and the poloidal drift parameter $\eta = R\Phi'/\iota r B_0 v_{th}$, all other quantities have the usual meaning. The radial fluxes are averaged over the magnetic surfaces and the particle flux Γ and the heat flux Q are given by:

$$\begin{aligned} \Gamma &= - n \left\{ D_n \left(\frac{n'}{n} + \frac{q\Phi'}{T} \right) + D_T \frac{T'}{T} \right\} \\ Q &= - nT \left\{ \chi_n \left(\frac{n'}{n} + \frac{q\Phi'}{T} \right) + \chi_T \frac{T'}{T} \right\} \end{aligned} \qquad (3)$$

with the transport coefficients: $\left(\alpha = \frac{V_{th}^3}{2\iota R \omega_c^2} \right)$

$$D_n = \alpha(1/2\ G_0 + G_2 + G_4) \qquad (4a)$$

$$D_T = \alpha(3/4\ G_0 + G_2 + 1/2\ G_4 + G_6)$$

$$\chi_n = \alpha(3/2\ G_0 + 5/2\ G_2 + 2\ G_4 + G_6) \qquad (4b)$$

$$\chi_T = \alpha(15/4\ G_0 + 21/4\ G_2 + 7/2\ G_4 + 3/2\ G_6 + G_8).$$

The function $G_m\ (\eta + i\nu^*)$ is the Hilbert integral transform of the moments of the Gaussian:

$$G_m\ (\eta + i\nu^*) = \frac{1}{\sqrt{\pi}}\ Im \left\{ \int_{-\infty}^{\infty} \frac{x^m\ e^{-x^2}}{x - (\eta + i\nu^*)}\ dx \right\}.$$

For small values $\eta \ll 1$ and $\nu^* \ll 1$, the transport coefficients in eq. (4) become constant, whereas for large values $\eta \gg 1$ or $\nu^* \gg 1$, the transport coefficients are proportional to $\nu^*/(\eta^2 + \nu^{*2})$. Due to the large aspect ratio of W VII-A, the poloidal drift parameter $\eta \propto A/\iota$ is much greater than in usual tokamaks.

The model outlined above is restricted to the Plateau regime. For most of the W VII-A discharges, the electrons as well as the thermal ions are within the Plateau regime, whereas impurities are close to or within the Pfirsch-Schlüter regime. Thus, for investigating the impurity transport, the model had been generalized. A 1st order density correction $n_1(r,\theta)$ in the collision term and small nonambipolar potentials $\Phi_1(r,\theta)$ had been included in the linearisation of the drift kinetic equation (1). The densities $n_{1\alpha}$ for all particles species α (= e,i,z) are calculated by means of the parallel force balance equation with the Braginskii friction term with parallel velocities $V_{\parallel\alpha}(r,\theta)$ estimated from the continuity equation. The 1st order potential Φ_1 is determined by the quasi-neutrality condition $\sum q_\alpha \cdot n_{1\alpha} = 0$. For doing this, the full linear equation system (for all species α) is solved yielding the fluxes Γ_α and Q_α depending on the ambipolar field Φ'. Neglecting impurities, the parallel force balance equation can be replaced by the generalized Ohm's law yielding an analytical expression for Φ_1 which drive the Pfirsch-Schlüter diffusion.

The high energetic ions of the NI (up to 27 keV) with small parallel velocities have large deviations from magnetic surfaces and can be lossed directly (~10 cm plasma radius in W VII-A). Neoclassical theory is based on the assumption of distribution functions close to Maxwellians, this includes that the step size of the transport process is very small compared with the radial plasma size. The beneficial effect of strong ambipolar electric field on the confinement of these ions had been demonstrated by Monte Carlo simulations /1/, however, this effect cannot be described by neoclassical theory. Thus, we are restricted to the estimation of the thermal loss fluxes.

The ambipolar electric fields are calculated from the condition of ambipolarity of the particle fluxes $\Sigma q_k \Gamma_k = 0$. Fits to experimental data are used for the density and temperature profiles.

III. ECR heated discharges

Strong poloidal plasma rotation was observed in ECR heated discharges (2.5 T; 70 GHz; $P_{RF} \sim 160$ kW) with higher plasma densities ($n_e \sim 5 \times 10^{13}$ cm^{-3}). The profiles in Fig. 1 are fits to n_e and T_e data measured by Thomson scattering and to T_i measured by CX analysis and by Doppler broadening of the C^{4+} impurity line. For these profiles, the ambipolar electric field has been calculated (Fig. 2), experimental data for E_r at 2 radii are derived from the Doppler shift measurements. These values are calculated from the poloidal rotation velocity where the diamagnetic drift velocity of the C^{4+} ions is included, v_{dia} was estimated assuming a corona model. This procedure yields a lower limit for the radial electric fields.

In Fig. 3, the ion heat conduction coefficient χ_T (comp. eq. 4) is shown. In these ECRH discharges, however, the ion heat conduction has only small influence, since the ion energy balance is dominated by collisional ion heating and CX losses.

IV. NI heated discharges

In discharges heated by neutral beam injection the measured poloidal plasma rotation was significantly larger than the calculated one for thermal plasmas. Monte Carlo simulations indicate that the ambipolar electric fields are driven by the fast ions of the NI slowing down distribution. The electric fields derived from the measurements lead to a very strong reduction of the ion heat conduction. For the high ion temperatures ($T_i \sim 1$ keV), the ion energy balance is mainly determined by collisional heating of the NI slowing down, the collisional cooling by the electrons ($T_e < T_i$) and the reduced ion heat conduction /3/.

V. Conclusions

In the plateau regime the transport coefficients can be strongly reduced by poloidal plasma rotation which is driven by ambipolar electric fields. This effect becomes important with large aspect ratio and low rotational transform and is confirmed in the W VII-A Stellarator. For Maxwellian plasma distributions, the measured rotation is in agreement with theoretical predictions based on neoclassical theory. Furthermore, calculations indicate a reduced impurity transport due to the poloidal plasma rotation.

References

/1/ F.P. Penningsfeld et al., Computation of Fast Ion Confinement by Electric Fields in W VII-A Stellarator, paper No. 210, this conference

/2/ T.E. Stringer, International School of Plasma Physics (1971); Course on Instabilities and Confinement in Toroidal Plasmas, p. 109

/3/ W VII-A Team et al., Plasma Confinement and the Effect of Rotational Transform in the WENDELSTEIN VII-A Stellarator, IAEA-CN-44/DI1, London 1984

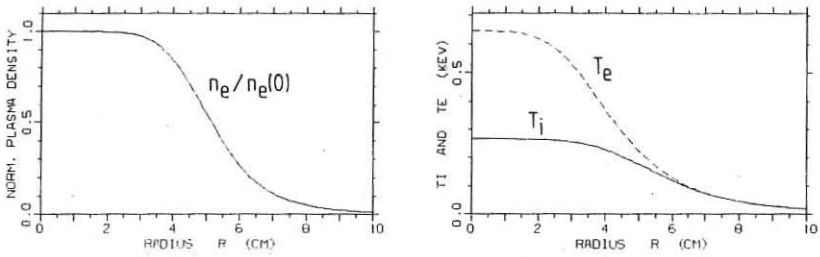

Fig. 1: Density and temperature profiles of an ECRH discharge (2.5 T, 70 GHz) used for the calculations.

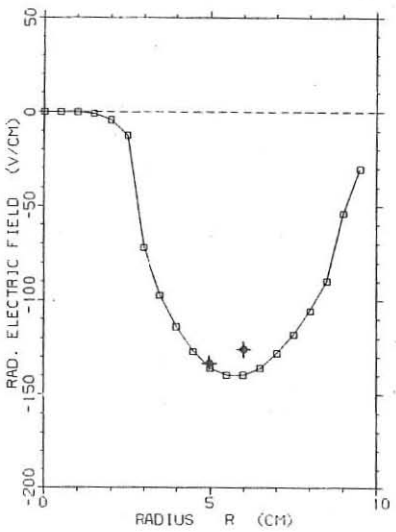

Fig. 2: Ambipolar electric fields calculated by means of $T_e = T_i$.

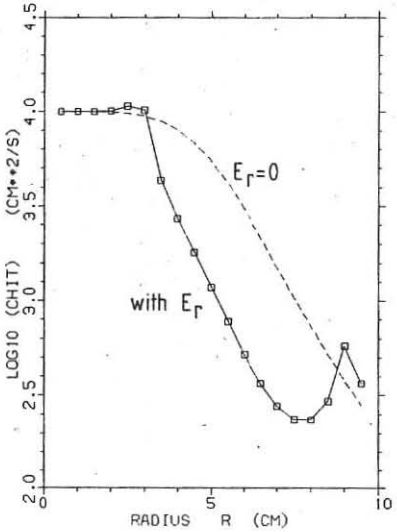

Fig. 3: Ion heat conduction coefficient χ_T with the ambipolar electric fields of Fig. 2.

Influence of the Magnetic Configuration on Plasma Behaviour in the WENDELSTEIN VII-A Stellarator

W VII-A Team*), NI Team**)
Max-Planck-Institut für Plasmaphysik
EURATOM-Association, D-8046 Garching
Federal Republic of Germany

ECRH Group***)
Institut für Plasmaforschung der Universität Stuttgart
D-7000 Stuttgart
Federal Republic of Germany

Currentless discharges have been studied in a wide range of plasma parameters in the shearless W VII-A Stellarator (helical windings $l = 2$, $m = 5$; rotational transform $0 < \iota < 0.7$ with $[\iota(a) - \iota(o)]/\iota(o) = \Delta\iota/\iota(o) < 1$ %). For plasma build-up and plasma heating two different heating methods have been used: Neutral beam injection at a power level of $P_N \simeq 1$ MW and electron cyclotron resonance heating (ECRH) at 28 GHz and recently at 70 GHz with $P_{RF} \simeq 200$ kW for $\Delta t = 100$ ms.

Favourable properties for stability and confinement have been demonstrated for currentless operation in W VII-A /1/. The confinement shows a strong dependence on the rotational transform ι. Resonances with reduced containment are observed to be associated with low order rational values of $\iota(a) = m/n$; e.g. 1/2, 1/3, 2/3... where $\iota(a)$ is the total rotational transform at the plasma edge. Residual currents I_p, which may be generated by the heating mechanism itself or by plasma pressure anisotropy, contribute to the external vacuum transform ι_o with $\iota_p \sim I_p/B$. In addition modifications in the ι-profile are predicted from MHD-equilibrium codes even for moderate plasma pressures with $\beta(o) \leq 10^{-2}$ /2/. The position of resonant magnetic surfaces throughout the entire plasma and the extension of islands connected with these resonant surfaces, which are expected to influence the confinement, have been modified by internal parameters: current density distribution and plasma pressure. Within the experimental limitations it has been tried to separate some of these effects.

It has been found, that even moderate shear can reduce the deterioration by rational values of the transform. In order to maintain stationary discharges the total rotational transform $\iota(a)$ at the plasma edge has to be controlled carefully.

---

*) G. Cattanei, D. Dorst, A. Elsner, V. Erckmann, G. Grieger, P. Grigull, H. Hacker, H.J. Hartfuß, H. Jäckel, R. Jaenicke, J. Junker, M. Kick, H. Kroiss, G. Kuehner, H. Maaßberg, C. Mahn, S. Marlier, G. Müller, W. Ohlendorf, F. Rau, H. Renner, H. Ringler, F. Sardei, M. Tutter, A. Weller, H. Wobig, E. Würsching, M. Zippe
**) K. Freudenberger, W. Ott, F.-P. Penningsfeld, E. Speth
***) G. Janzen, W. Kasparek, G. Müller, P.G. Schüller, K. Schwörer, M. Thumm, R. Wilhelm

Operating the new VARIAN 70 GHz gyrotron at W VII-A (plasma radius $a \leq 0.1$ m) plasma parameters with density $n_{eo} \leq 5 \times 10^{13}$ cm^{-3} (cutoff density $n = 6.3 \times 10^{13}$ cm^{-3}), temperatures $T_e \geq 1$ keV, $T_i \simeq 250$ eV and energy replacement time $\tau_E = 10$ ms are achieved at 2.5 T main field /3/. Further heating of the plasma by neutral injection up to densities $n_{eo} \geq 10^{14}$ cm^{-3} has been possible.

In this parameter range the effect of ι and shear has been investigated

1. Shearless configuration at low plasma current and low ß

To explore the confinement as close as possible to the shearless vacuum configuration of W VII-A, discharge conditions with low plasma current and low plasma pressure have been chosen. In Fig. 1 the energy content W is shown as a function of the rotational transform $\iota(a)$ at the plasma edge. All data have been taken from stationary ECRH discharges at 70 GHz, varying the external transform shot by shot. The density was kept around $n_{eo} \simeq 10^{13}$ cm^{-3}, which limits the averaged ß to $< 2 \times 10^{-4}$.

During the RF-pulse a plasma current I_p builds up to $I_p \leq 0.5$ kA at a constant rate of increase. This current contributes to the total transform only with $\Delta\iota_p \leq 0.008$.

Optimum confinement is found close to the main resonances $\iota = 1/3, 1/2, 2/3$, where the density of low order rational numbers is smaller.

Similar experiments with 28 GHz at 1 T /4/ have shown the same behaviour however the regions of good confinement extend over a wider iota range, are not as narrow. It is believed, that this is due to the shear caused by the higher ß and the larger contribution of the plasma current ($\iota_p \sim I_p/B$), which was also 0.5 kA in the 1 T case. In both cases fluctuations in the power supply contribute also with $\tilde{\iota}/\iota = 0.01$ and may smear out some fine structure.

2. Shear by plasma current I_p

In a next step shear has been added by inducing plasma currents up to $I_p = +4$ kA with a small loop voltage $U_L < 0.5$ V. With ß still being small, $< 2 \times 10^{-4}$, the current density profile is determined by the temperature profile and results in a "tokamak-like" shear with $\Delta\iota/\iota < 0.5$. For these low currents the ohmic heating power P_{OH} (2 kW) is negligible and current driven instabilities have not been detected.

In Fig. 2 the energy content W vs the edge value of the transform $\iota(a)$ is given around $\iota = 1/2$. The shear is increased with increasing plasma current. At $I_p = 4$ kA the associated shear seems already sufficient to reduce the influence of the rational values of the transform. Even with the $\iota = 1/2$ surface at the plasma boundary the energy content is only slightly reduced.

The contribution of the plasma current to the transform is given by the relation $\iota_p = 0.016\, I_p$, with I_p /kA/ for a toroidal field of $B_o = 2.5$ T and a plasma radius $a = 0.1$ m.

3. Shear by plasma pressure

Even for central ß values of $ß(o) < 10^{-2}$ /2/ the MHD equilibrium codes predict a significant modification of the entire ι-profile depending on the pressure

profile. In addition nonhomogeneous current density distributions contribute to the shear.

No direct measurements of a particular ι-profile are possible, however with increasing β a study of the confinement as a function of the edge value of the transform indicates the influence of plasma pressure.

With 70 GHz ECRH and combined heating with NI, central β values of $\beta(o) \simeq (2 - 3)\,\overline{\beta}$, with $\overline{\beta} \leq 2 \times 10^{-3}$, have been obtained. In Fig. 3 the energy content W has been plotted vs ι around $\iota = 1/2$ for small plasma current $I_p \leq 0.5$ kA. By control of the density the plasma pressure could be varied during ECRH. In combination with NI the density is increased to $n_{eo} \simeq 10^{14}$ cm^{-3}. The particle influx from NI and good particle confinement leads to a linearly growing density within the pulse. The RF power has therefore to be switched off, when the cutoff density in the central part of the plasma is exceeded. Stable plasma containment can be achieved within a relatively extended range of ι even for low plasma current, if β is sufficiently large. For the maximum β the correlated $\Delta\iota/\iota$ is expected to be 0.2.

Because pressure profile, current density and transport are linked together a proper adjustment of the external parameters during the build up phase is critical to achieve optimum confinement. Thus for particular values of ι no high β discharges can be obtained in contrast to the case with I_p and low β.

4. Conclusion

The experiments in W VII-A tend to confirm, that the effect of resonances at rational values of the rotational transform is due to island formation and subsequent plasma convection. Small perturbing fields can lead to extended islands at resonant surfaces. Convection becomes particularly important, if such islands are localized at the low temperature edge. By moderate shear, either by nonhomogeneous current density distribution or by sufficiently high plasma pressure the deterioration by such resonances can be reduced in the otherwise shearless W VII-A configuration. The time variation of current and the plasma pressure determine the optimal ι-range. Therefore a careful adjustment of external parameters is necessary.

In a next step W VII-A will be operated with variable shear $\Delta\iota/\iota = + 0.2$ already for the vacuum configuration. The two different helical winding systems will be supplied with unbalanced currents for this in a torsatron like mode . The position of resonant surfaces in the entire plasma and the extension of islands depending on shear are then controlled by external parameters.

REFERENCES

/1/ W VII-A Team, NI Group, Plasma Phys. and Contr. Fusion (Proc. 9th Int. Conf. Baltimore 1982) Vol. 2, IAEA Vienna (1983), p. 241.

/2/ J. Kisslinger, H. Wobig, 12th Europ. Conf. and Plasma Physics Budapest 1985, paper 144.

/3/ ECRH Group, W VII-A Team ,12th Europ. Conf. and Plasma Physics Budapest 1985, paper 117.

/4/ W VII-A Team, NI Group, Plasma Phys. Contr. Nucl. Fusion (Proc. 10th Int. Conf. London 1984) Vol. 2, IAEA Vienna 1985, p. 371.

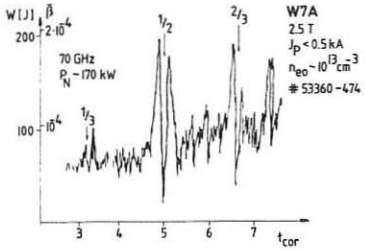

Fig. 1: Plasma energy content versus rotational transform ι. 70 GHz ECRH at 2.5 T main field. Low plasma current $I_p \leq 0.5$ kA.

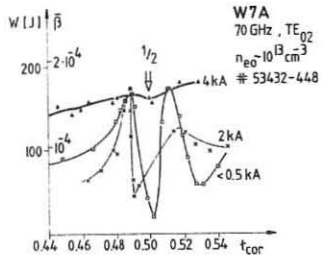

Fig. 2: Plasma energy content versus ι for different plasma currents I_p close to $\iota = 1/2$. I_p controlled by $|U_L| < 0.5$ V. Low pressure: $\bar{\beta} < 2 \times 10^{-4}$, 70 GHz ECRH at 2.5 T.

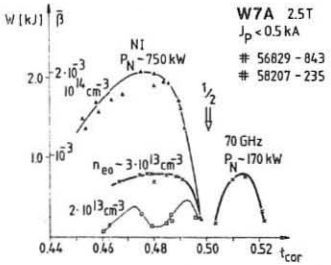

Fig. 3: Influence of plasma pressure: Energy content W versus rotational transform. Low current: $I_p \leq 0.5$ kA. 70 GHz ECRH: $P_{IN}/P_N = 0.6$ NI H_2 : $P_{IN}/P_N = 0.4$ Plasma density varied.

COMPUTATION OF FAST ION CONFINEMENT BY ELECTRIC FIELDS IN THE W VII A STELLARATOR

F.P.Penningsfeld, W.Ott and E.Speth

Max-Planck-Institut für Plasmaphysik
EURATOM-Association, D-8046 Garching

Abstract: The confinement of fast injected ions in W VII-A is strongly affected by the presence of radial electric fields. The neutral beam deposition code ODIN so far had been valid for the treatment of small electric fields ($|E| < 100$ V/cm) and therefore had to be revised to cover large electric fields as well. The accuracy achieved for typical cases has been estimated by using a perturbation method.
It is shown that the new version of ODIN gives correct results within an error of $\pm$ 10 % for the total heating efficiency and $\pm$ 20 % for the power deposition profiles up to 5.0 kV radial electric potential. The observed heating efficiency for co and counter injection $\eta \approx 0.35$ is very well represented by code results for a potential of 2.0 kV with negligeable influence of its radial dependence.

Introduction: At the beginning of NBI experiments on W VII-A a heating efficiency was found experimentally that was higher than predicted by the numerical simulations /1/. An explanation of this fact was the occurrence of a radial electric field confirmed by the observation of a fast poloidal plasma rotation /2/ which was not considered in the numerical calculations. The beneficial effect of an electric field on η was then confirmed qualitatively by ODIN calculations /3/. However, for large electric fields the quantitative results showed a number of inconsistencies, which required a revision of the code. The subsequent improvements and an investigation of the resulting accuracy are described in the first part of this paper. In the second part the new version is used to recalculate the heating efficiency for W VII-A and to demonstrate the influence of the electric field on the orbit of single particles. The results are in qualitative accordance with a bounce averaged Monte-Carlo simulation /4/.

I. Revision of the neutral beam heating code ODIN:

The improvements that become necessary in order to include large electric fields are: energy conservation, time step control and a more careful modelling of the electric field.

I.1 Energy conservation: For a correct energy balance for each injected particle in the presence of electric fields the potential energy $q_b \cdot \Phi$ of an ion at every point of the trajectory has to be calculated to conserve the total energy

$$E_{tot} = 1/2\ m_b v_b^2 + q_b \Phi(r) = \text{const.}$$

The term $q_b \Phi$ previously not included may be neglected only for $q_b \Phi \ll E_b$.

I.2 Timestep control: The ExB-drift causes an additional poloidal velocity exceeding the ∇B and curvature drift of the fast ions for $|E| > 135$ V/cm at W VII-A conditions. The dynamic adaptation of the iteration time step of

the orbit calculation has been corrected for this fast drift component. For runs with $|E| > 500$ V/cm the time step parameter itself must be reduced accordingly to avoid numerical errors underestimating the heating efficiency and the power deposited locally in the region of high electric fields.

I.3 Model of the electric field: The physical constraint is that the electric equipotential surfaces Φ = const. have to be identical with the magnetic flux surfaces Ψ = const. of the configuration used. Otherwise a poloidal field component E_ϑ is generated which causes an unrealistic radial particle drift. For numerical reasons central ellipses are used in ODIN to fit the magnetic configuration computed from a Dommaschk field representation /5/. As seen from Fig. 1a this is a good approximation for $r/a < 0.3$ only. But the position of the best fitted flux surface can be varied by the application of an additional vertical magnetic field $0 < B_V < 50$ Gauss (Fig. 1b,c).

I.4 Error estimation for the code results: To estimate the errors induced by the electric field model, firstly the position of the best fitted magnetic surfaces was varied by varying B_V for parabolic potentials

$$\Phi = \Phi_a (r/r_a)^2 \quad \text{with } 1 \leq \Phi_a \leq 7 \text{ kV}.$$

In this way the erroneous poloidal field components $E_\vartheta(r/a)$ introduced by the misfitting of the flux surfaces is changed in a wide range. In the worst case (i.e. $B_V = 0$) the misfitting of the outermost flux surfaces is greatest where $|E_\vartheta|$ reaches its maximum also resulting in the highest E_ϑ-component there. It shows up (e.g. in Fig. 2 for 3.0 kV) that the code results are not sensitive to that variation indicating that $|E_\vartheta(r/a)| < |E_{\vartheta,crit}(r/a)|$ in these cases, $|E_{\vartheta,crit}|$ being the limit, where the erroneous field component starts to influence beam deposition. To get a number for $|E_{\vartheta,crit}(r/a)|$ the elliptical equipotential surfaces were perturbed by changing their half axes $\alpha \to \varepsilon\alpha$, $\beta \to \beta/\varepsilon$ in order to generate an artificial poloidal component $E_\vartheta(r/a)$. Figure 3a shows the global results for different potentials Φ. Admitting an error of $\pm$ 10 % for η, a critical field value $|E_{\vartheta,crit}|$ can be deduced depending on Φ. The corresponding deposition profiles for 3.0 kV are plotted in Fig. 3b. Since the two methods should give consistent results one concludes that the code is not sensitive to E_ϑ-components in the outer plasma region but to poloidal electric fields at $r/a = 0.5$. This is in accordance with the fact that this region is most frequented by the heating particles. In Fig. 5 the estimated critical poloidal field at $r/a = 0.5$ is given as a function of Φ_α together with the value occurring in ODIN for the worst case (i.e. $B_V = 0$). We conclude that the global and local ODIN results are correct within an error of 10 % and 20 %, respectively, if $|E_\vartheta| < |E_{\vartheta,crit}|$ at $r/a = 0.5$, i.e. $\Phi_\alpha < 5$ kV for a parabolic potential.

II. Application of the revised code for W VII A

II.1 Heating efficiency: In Fig. 5a,b the recalculated $\eta(\Phi)$ for co resp. counter injection are given assuming parabolic potentials. The observed direction of the plasma rotation excludes negative Φ_α shown here for completeness. The experimental value $\eta \simeq 0.35$ for co and counter injection is very well represented by code results for $\Phi_\alpha = (2.1 \pm 0.3)$ kV. This also holds for an electric field $E(r) \propto \nabla p$ as seen from Fig. 5c.

II.2 Particle tracing method: The influence of the electric field on the ion orbits can be made visible by plotting the intersection points of the trajectories of a set of test particles with a given poloidal plane. The behaviour of the orbits for ions starting in the z = 0 plane at different radii

R may be quantified by the area F(R) in the poloidal plane which surrounds these intersection points. In Fig. 6 an example for this confinement parameter F(R) for fast co-injected ions is shown. With increasing positive potential, the zone of good confinement, i.e. the minimum of F(R) is shifted towards the plasma center resulting in a more efficient trapping of the injected ions. For small negative potentials $-1.0 \lesssim \Phi_\alpha \lesssim -0.5$ kV no confinement is found corresponding to the poloidal drift resonance were the ExB-drift and the rotational transform drift for the fast ions cancel each other. Higher negative potentials would improve the confinement again beginning with ions starting at $R < R_0$ caused by the counterwise poloidal rotation which then again is dominated by the electric field.

References

/1/ W VII-A Team and Neutral Injection Team, Proc. 8th IAEA Conf. on Plasma Physics and Contr.Nucl. Fusion Research, Brussels 1980, Vol.I,p. 185

/2/ W VII-A Team and Neutral Injection Team, Proc. 2nd Joint Grenoble-Varenna, Int. Symp. on Heating in Tor. Plasmas, 1980, Vol. II, p. 789

/3/ W VII-A Team and Neutral Injection Team, Proc. 9th IAEA Conf. on Plasma Physics and Contr.Nucl. Fusion Research, Baltimore, 1982, Vol.II,p.241

/4/ Maaßberg H., 1984, Proc. 5th Int.Workshop on Stellarators, Ringberg, FRG, Vol.II, P.507

/5/ Dommaschk, W., 1978, IPP-Report 0/38.

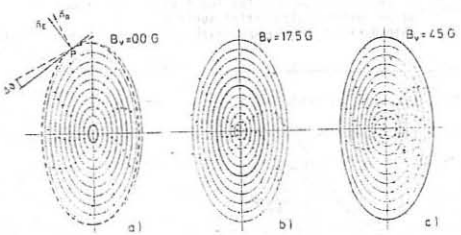

Fig.1: Equipotential surfaces used in ODIN for various vertical magnetic field components B_V plotted in the ϑ = 18°plane. The position of the best fitted flux surface is indicated by a fat line.
$\vec{n}_B$: normal to the flux surface at a given point P
$\vec{n}_E$: used direction for the electric field $\vec{E}$ at this point.

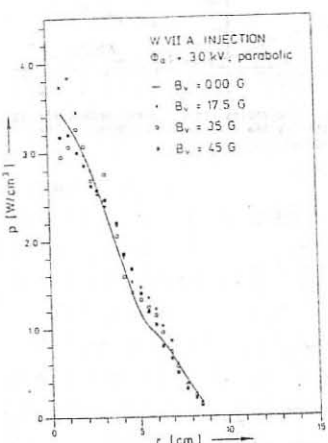

Fig.2: Power deposition profiles for different vertical magnetic fields B_V.

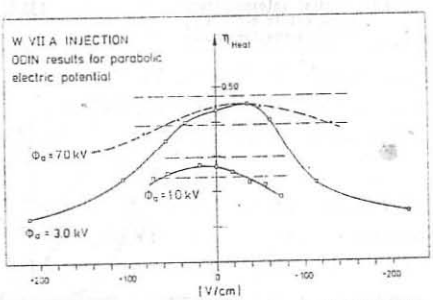

Maximum poloidal field component $E_{\vartheta,MAX}$ for $r/a = 1.0$ $(0 \leq \vartheta \leq 90°)$

Fig.3a: Heating efficiency as a function of $E_{\vartheta,max}$ for perturbed equipotential surfaces

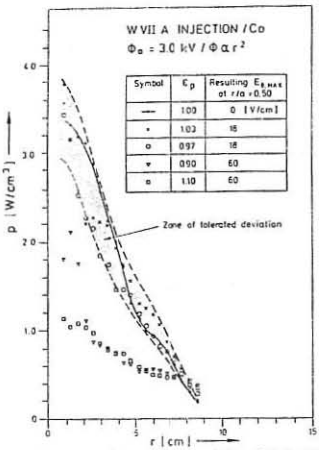

Fig.3b: Power deposition profiles for a set of perturbed equipotential surfaces with Φ_a = 3.0 kV (parabolic)

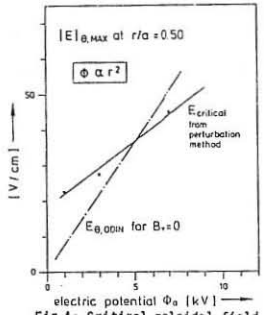

Fig.4: Critical poloidal field component as derived by the perturbation method

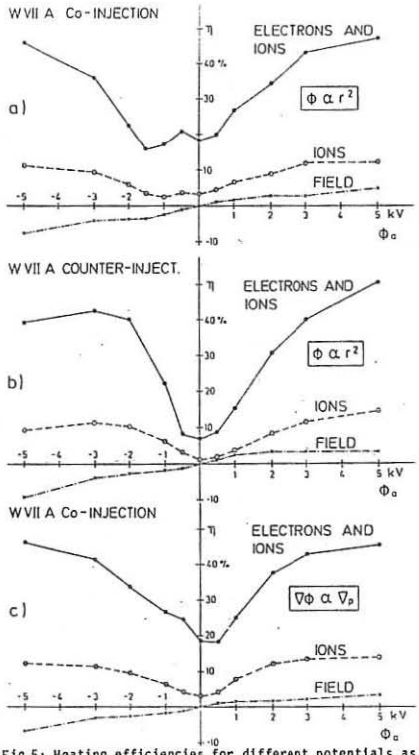

Fig.5: Heating efficiencies for different potentials as calculated by the new version of ODIN for shot Nr. 38000 at 180 ms

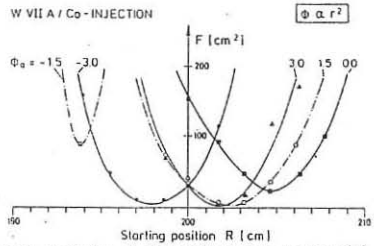

Fig.6: Variation of the confinement parameter F(R) with the strength Φ_a of a parabolic potential

NBI AND ECR HEATING EXPERIMENTS OF THE HELIOTRON E DEVICE

K.Uo, A.Iiyoshi, T.Obiki, O.Motojima, S.Morimoto, M.Wakatani, M.Sato, S.Sudo, F.Sano, K.Kondo, K.Hanatani, T.Mutoh, H.Zushi, H.Kaneko, S. Besshou, M. Nakasuga, T.Mizuuchi, H.Okada, Y.Takeiri, I.Ohtake , J.E.Rice*

Plasma Physics Laboratory,
Kyoto University
Gokasho, Uji, Kyoto, Japan

ABSTRACT Recent results of the neutral beam injection heating (NBI) and the electron cyclotron resonance heating (ECR) experiments of the Heliotron E current-less plasmas are reported. The current-less heliotron plasma with the high electron temperature is produced by ECR heating. To increase the ion temperature and density, NBI heating is applied. We have installed three NBI beam lines with the maximum power of 3.0MW. The results of the high-power heating experiments at 1.9Tesla, and high beta experiments at 0.98Tesla are reported.

Recent results of the neutral beam injection heating (NBI) and the electron cyclotron resonance heating (ECR) experiments of the Heliotron E current-less plasmas are reported [1]. The current-less heliotron plasma is produced by ECR heating using maximum three gyrotrons (53.2GHz, 200kW/tube). To increase electron and ion temperatures and density, the high-power NBI heating is used [2]. We have installed three NBI beam lines with the maximum power of 3.0MW (25kV).

The current-less plasma is produced by ECR heating, which is a very effective heating method to obtain the high electron temperature [3]. We have carried out the ECRH experiments using three gyrotrons simultaneously and obtained the maximum electron

* Plasma Fusion Center, Massachusetts Institute of Technology, Cambridge, USA

temperature is 2.5keV at the electron density of $0.4 \times 10^{13} cm^{-3}$. This is shown in Fig. 1. In order to increase the central electron temperature, the focused micro-wave injection method using Vlasov antenna was investigated. In this case, the optimum magnetic field is slightly higher than that of TE02 mode injection which has a broad injection pattern [3]. Heating rate, as far as measuring the central electron temperature, is improved by about 30% comparing with the case of TE02 mode. The collisionality is in the collision-less regime. The transport analysis on the ECRH plasma is reported in another paper of this conference [4]. The ECRH experiment will continue increasing the number of gyrotrons operated at the same time. The impurity transport process of the ECRH plasma is investigated injecting Si atoms by the laser blow-off method. The diffusion coefficient (D) is a function of the electron density. The impurity confinement time is a positive function of the density, which is shown in Fig. 2. The typical value is $D=2000 cm^2/sec$ ($\overline{N}_e=1.0 \times 10^{13} cm^{-3}$). The impurity transport is dominated by the anomaly process.

Since the necessary density for the NBI experiment is more than $2.0 \times 10^{13} cm^{-3}$, it is increased with the gas puffing and the hydrogen pellet injection. The ion temperature is increased by the additional NBI power to more than 1.0keV [1],[2],[5]. Due to the pellet injection [1], line averaged density is increased to more than $1.3 \times 10^{14} cm^{-3}$. In Fig. 3, the typical time traces of the plasma parameters during pellet injection experiments are shown. The electron density is effectively increased. Although, both the electron and ion temperatures decrease at the beginning, they increase again to the original values during 20msec. The radiation from plasma does not change so much, and this means that impurity level of the plasma is low. The plasma energy increases after pellet injection. The maximum $\overline{N}_e \tau_{E-NET}$ value reached $5.0 \times 10^{12} cm^{-3} sec$. The impurity confinement time of the high density plasma is much longer than that of ECRH plasma [6]. The impurities injected by the laser blow-off method are rapidly transported to the central region of the plasma and does not diffuse out for more than 0.1sec, which is the longest duration of the high density plasma produced by NBI. By reducing the

magnetic field down to 0.94Tesla and using second harmonic resonance of the microwaves in order to produce a target plasma, a high beta plasma is obtained by NBI. Maximum central beta value obtained is 3.5%. It is the most important subject to analyze the limiting mechanisms of maximum beta value obtained experimentally. Theoretical approach to this subject is also in progress. It is made clear that the MHD beta limit is strongly related with the pressure gradient at $\iota=1$ ($r/a_p=0.7$) surface. Therefore, the flat pressure profile is effective to suppress MHD activities and to obtain high-beta plasmas. At present, the energy balance of the high-beta plasma is dominated by the radiation, which is shown in Fig. 4. Study on the impurity concentration and the plasma-wall-interaction is recognized as another important experimental subject. The structure of the divertor layer and mechanisms of plasma-wall-interaction are now in progress. We have started the experiment using an in-situ surface station and the data-base increases for the discharge cleaning process and Ti gettering procedure.

REFERENCES

[1] K. Uo, A. Iiyoshi, T. Obiki, O. Motojima, S. Morimoto, et al., in Plasma Physics and Controlled Nuclear Fusion Research, 1984 (Proceedings 10th International Conference, London, 1984), IAEA-CN-44/D-I-2

[2] K. Uo, A. Iiyoshi, T. Obiki, O. Motojima, S. Morimoto, et al., Nuclear Fusion 24 (1984) 1551

[3] A. Iiyoshi, O. Motojima, M. Sato, T. Mutoh, S. Sudo, et al., in Plasma Physics and Controlled Nuclear Fusion Research, 1984 (Proceeding of 10th International Conference, London, 1984), 1 (1985 IAEA Vienna) 453

[4] O. Motojima, H. Zushi, S. Sudo, K. Kaneko, F. Sano, et al., This conference, titled by "Study on the Transport and Energy Balance of the Heliotron E Plasma".

[5] F. Sano, T. Obiki, O. Motojima, A. Sasaki, K. Hanatani, et al., Nuclear Fusion 24 (1984) 1103

[6] J. E. Rice, J. L. Terry, E. S. Marmar, O. Motojima, H. Kaneko, Nuclear Fusion 24 (1984) 1205

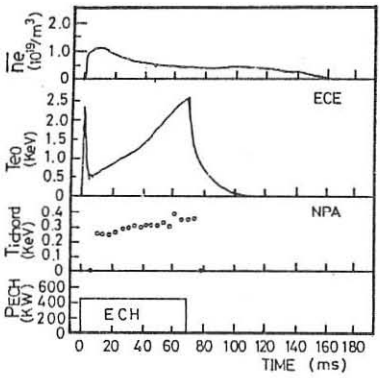

Fig. 1 Parameter Traces of ECRH Plasma

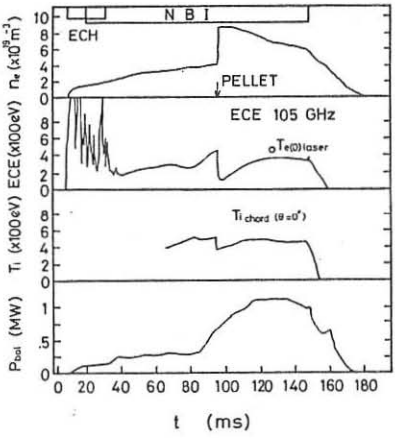

Fig. 3 Parameter Traces of Pellet Injection Experiment

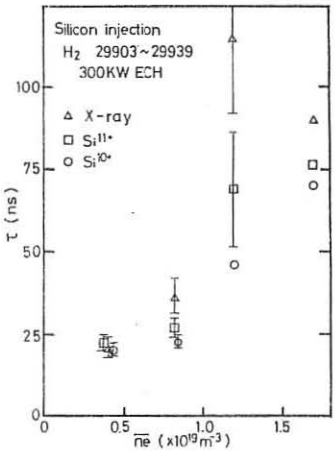

Fig. 2 Impurity Confinement Time in the Function of Electron Density

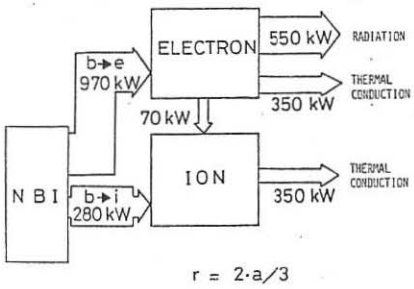

Fig. 4 Energy Balance of High Beta Plasma

STUDY OF THE TRANSPORT AND ENERGY BALANCE OF HELIOTRON E PLASMAS

O.Motojima, H.Zushi, S.Sudo, K.Kaneko, F.Sano, M.Sato, S.Besshou, T.Mizuuchi, T.Mutoh, K.Kondo, H.Okada, I.Ohtake, Y.Takeiri, T.Obiki, A.Iiyoshi, and K.Uo

Plasma Physics Laboratory, Kyoto University
Gokasho, Uji, Kyoto, Japan

ABSTRACT Transport processes and energy balance of Heliotron E plasmas are studied. To obtain the confinement scaling of the Heliotron E device, we have been accumulating various data sets of plasma parameters measured during the last three years. We especially concentrated our interests on the current-less plasmas produced by electron cyclotron resonance heating (ECRH). The electron energy transport coefficients are evaluated by a one-dimensional transport code and compared with neoclassical predictions. The effects of the plasma current on the transport are discussed.

Transport processes and energy balance of Heliotron E plasmas are studied. The plasmas are produced by feed-back controlled OH heating (OH, 3V•sec) or electron cyclotron resonance heating (ECRH), and heated additionally by neutral beam injection (NBI,three beam lines) in order to increase the ion temperature further. In previous studies, we have suggested (1) drift-scaling of the electron energy confinement time of OH plasmas [1], (2) neoclassical-close electron confinement in the central region of ECRH plasmas [2], (3) the density dependence of energy confinement time in NBI plasmas [3], and (4) neoclassical-close ion confinement [4]. In order to proceed with the study of transport and energy balance, we have accumulated data sets of OH, ECRH and NBI plasmas in the last three years. Improvements of diagnostics and power up-grading of the heating systems have been achieved for this purpose. The major diagnostics used for the transport

analysis are a multi-channel laser Thomson scattering system (10-ch's), an electron-cyclotron-emission measurement system, a neutral particle energy analyzer, a bolometer array (7-ch's), and a vacuum-ultra-violet spectrometer. We developed a one-dimensional-transport-analysis code. The input profile data are the following: (1) electron and ion temperatures, (2) the electron density, (3) the radiated power, (4) Z_{eff}, (5) deposition of the input power and (6) the neutral particle density. Three dimensional NBI-beam-deposition is modelled using a monte-carlo-method [5], which takes into account the real three dimensional configuration of the Heliotron E device. We calculate the neutral particle density in the plasma from the measured flux of the charge-exchanged neutral particles.

In this paper, we have concentrated our interests on the analysis of OH and ECRH plasmas to make clear the effect of the plasma current on the confinement. The density range investigated is from $1.0\times10^{13}cm^{-3}$ to $3\times10^{13}cm^{-3}$. For OH plasmas, typical heat conductivity coefficients at half radius are $5000cm^2/sec$ for I_{oh}=21.9kA and $40000cm^2/sec$ for I_{oh}=47.5kA (B=1.7Tesla). The heat conductivity increases linearly with the drift parameter, which is the ratio of the electron drift velocity and the electron thermal velocity, $\xi=V_d/_{th}$. The result is shown in Fig. 1. In 1980, we produced primarily OH plasmas and carried out the global confinement analysis for various parameter ranges. The typical electron energy confinement time has a dependence on the drift parameter [1]. Our present analysis directly suggested the drift scaling from the view point of the local electron heat conductivity.

ECRH is the most conventional and effective method to produce a current-less plasma with the high electron temperature. We have first demonstrated this in the current-less toroidal facilities [6]. To analyze the transport of ECRH plasmas, the microwave power deposition profile should be evaluated accurately. It is possible to evaluate this according to the following equation, $P_{dep}(r)=N_e(r)T_e(r)V_p/\tau_e(r)$, where V_p is a plasma volume. For this purpose we measured the decay time of the electron cyclotron emission just after the cutoff of the ECRH power, and determined

the local decay time of the electron temperature ($\tau_e(r)$). Radiation losses could be neglected. Since the microwave injection mode is TE02 and has a broad wave pattern, the obtained data suggests a very broad absorption profile, which is shown in Fig. 2. The microwave power is changed from 160kW to 320kW in our data base. The typical heat conductivity coefficients at the half radius are 3000cm^2/sec for 160kW and 5000cm^2/sec for 320kW (1.9Tesla). The radial dependence of the electron heat conductivity of the former is shown in Fig. 3. It increases with increasing radius. The enhancement factor from the neoclassical prediction is less than ten in the central region. However, it increases toward the outside. At the boundary, the anomalous processes should be taken into account to explain the transport of ECRH plasmas.

The ion confinement is well expressed by the neoclassical predictions for both OH and ECRH plasmas.

REFERENCES

[1] T. Mutoh, O. Motojima, S. Sudo, K. Kondo, Y. Ijiri, et al., IEEE Transactions on Plasma Science PS-11 (1983) 238

[2] A. Iiyoshi, M. Sato, O. Motojima, T. Mutoh, S. Sudo, et al., Physical Review Letters 48 (1982) 745

[3] K. Uo, A. Iiyoshi, T. Obiki, O. Motojima, S. Morimoto, et al., Nuclear Fusion 24 (1984) 1551

[4] F. Sano, T. Obiki, O. Motojima, A. Sasaki, K. Hanatani, Nuclear Fusion 24 (1984) 1103

[5] K. Uo, A. Iiyoshi, T. Obiki, O. Motojima, S. Morimoto, et al., in Plasma Physics and Controlled Nuclear Fusion Research 1982 (Proceedings 9th International Conference, Baltimore 1982), IAEA, Baltimore (1982) IAEA-CN-41/L-5

[6] Joint US-EURATOM Report, "Stellarators, Status and future Directions"

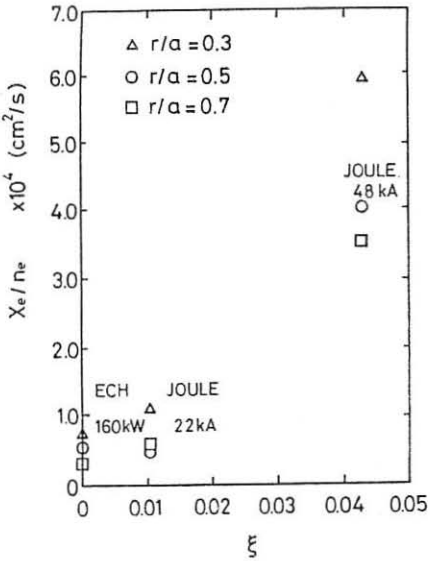

Fig. 1 Local Electron Heat Conductivity in the Function of Drift Parameter

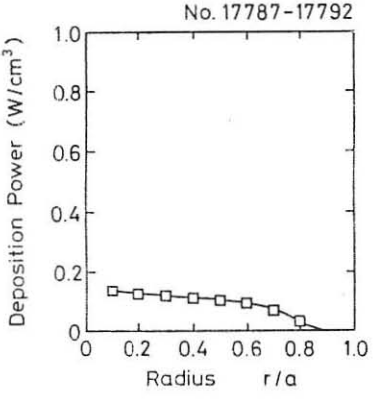

Fig. 2 Micro-Wave Deposition Profile

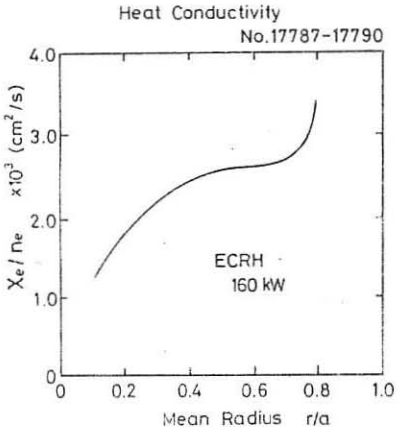

Fig. 3 Profile of the Electron Heat Conductivity

Effect of Wall Stabilisation on Free Boundary $m = 2$ Modes in Toroidal $\ell = 2$ Stellarators with Small Shear

F. Herrnegger
Max-Planck-Institut für Plasmaphysik,
EURATOM Association, D-8046 Garching

J.L. Johnson*
Plasma Physics Laboratory,
Princeton University,
Princeton, N.J.08544/USA

1. Introduction.

It has been shown[1] that results on the normalized eigenvalues $(\gamma R_T/v_A)^2$ of unstable fixed boundary $m = 2$ modes in straight $\ell = 2$ stellarator configurations with vanishing longitudinal net current computed with the asymptotic STEP code[2] (based on the stellarator expansion and averaging) are in good agreement with results obtained with the HERA helically symmetric eigenvalue code[3] and the BETA 3D code[4]. In the present paper the asymptotic STEP code has been applied to investigate free-boundary $m = 2, n = 1$ modes in $\ell = 2$ stellarator configurations with vanishing longitudinal net current. The $\ell = 2$ configurations were selected so that the rotational transform ι (twist) is in the range $0.36 < \iota_{ax} < 0.58$, where the $m = 2, n = 1$ mode is resonant: $k_{res} \approx mh\iota_p$, $\iota_p = \iota/M$, M is the number of equilibrium field periods of length L_p, $ha = 2\pi/L_p$, a is the minor radius of the free plasma boundary, b is the minor radius of the conducting wall, ka the wave number of the unstable mode, m its poloidal node number, n the longitudinal mode number, $v_A = (B_0^2/\rho_0)^{\frac{1}{2}}$ the Alfvén velocity, and B_0 the main magnetic field; the shear $(\iota_b - \iota_{ax})/\iota_b$ is typically 0.2.

2. Model.

The $\ell = 2$ configuration consists of $M = 5$ field periods of length L_p/a which is continuously bent into a torus with torus curvature $\epsilon = a/R_T$. If the toroidal curvature is $\epsilon = 0.13$, the configuration is a closed toroidal system with $ha = M\epsilon$. The vacuum magnetic field is given in a pseudo-cylindrical coordinate system (r, θ, z) by $\vec{B} = B_0[\vec{e}_z + \frac{\delta}{h}\nabla I_2(hr)\sin(2\theta - hz)]$, where the Bessel function $I_2(hr)$ is a solution of the Laplace equation in a straight system (Bessel model); δ describes the helical $\ell = 2$ field amplitude giving a twist ι_{ax} on magnetic axis of $\iota_{ax} = M\delta^2/16$ (asymptotic value). The pressure profile $p = p_0(1 - \bar{\Psi})$ is approximately parabolic in the minor radius r of the flux surfaces (Ψ is the poloidal flux

[1] F. Herrnegger and J.L. Johnson, 11th Int.Conf.Num.Simulation of Plasmas, 25-27 June 1985

[2] G. Anania and J.L. Johnson, Phys.Fluids 26 (1983) 3070; D. Lortz and J. Nührenberg, Z.Naturforsch.36a (1981) 317

[3] R. Gruber, S. Semenzato, F. Troyon, T. Tsunematsu, W. Kerner, P. Merkel, and W. Schneider, Comput.Phys.Comm.24 (1981) 363

[4] F. Bauer, O. Betancourt, and P. Garabedian, Magnetohydrodynamic Equilibrium and Stability of Stellarators (Springer Verlag New York, 1984); O. Betancourt, R. Gruber, F. Herrnegger, P. Merkel, J.Nührenberg, and F. Troyon, J.Comput.Physics 52 (1983) 187

*On loan from Westinghouse Research and Development Center, Pittsburgh, PA.

inside a magnetic surface). In all cases one wave length of the instability fits onto $M = 5$ field periods: $k = h/M$. A rather small average $\langle\beta\rangle \approx \beta_0/2 \approx 0.8\%$ is chosen so that the change of the ι-profile in the toroidal configurations with zero net current is small (e.g. for $\delta = 1.2$ the twist varies in the range $0.45 \leq \iota(r) \leq 0.55$ for $\epsilon = 0$ and $0.46 \leq \iota(r) \leq 0.53$ for $\epsilon = 0.13$). The $\iota(r)$-profile is approximately a parabolic function of r. No additional vertical field is applied ($B_v = 0$).

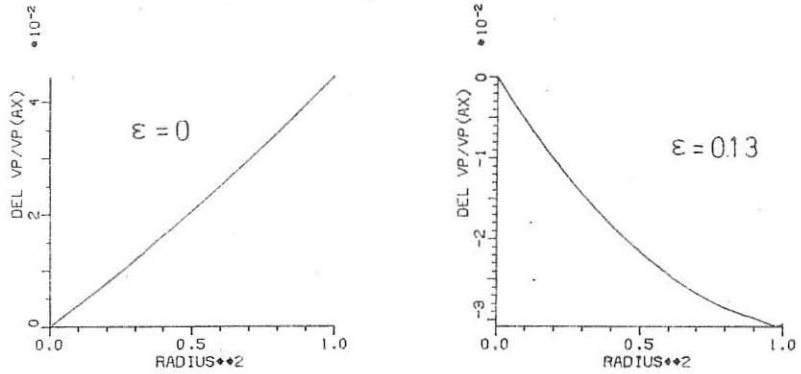

Fig.1. Normalized specific volume as function of r^2 for $\epsilon = 0, 0.13$.

The normalized specific volume $(V_b' - V_{ax}')/V_{ax}'$ as function of r^2 is plotted in Fig.1 for $\epsilon = 0,\ 0.13$. A rather deep magnetic well ($V'' < 0$) is created at $\epsilon = 0.13$ for $\langle\beta\rangle = 0.8\%$ which affects the stability of the configuration. The corresponding vacuum field has a magnetic hill ($V'' > 0$). Applying an additional vertical field ($B_V > 0$ causes a radially inward shift of the plasma column) the magnetic well can be diminished and therefore the stability properties are changed.

3. Results.

Using the STEP code it is shown that in toroidal $\ell = 2$ stellarators the resonant free boundary $m = 2$ mode can be stabilized by a conducting wall being close enough even for those $\ell = 2$ configurations where the twist at the plasma boundary is $\iota = 0.5$ being resonant to that mode. In straight $\ell = 2$ configurations there is no wall stabilization effect on that resonant $m = 2$ mode. Introducing toroidal curvature creates a magnetic well at finite β and the $m = 2$ fixed-boundary mode is completely stabilized. The absolute eigenvalue of the free-boundary $m = 2$ mode is diminished as well. These results are shown in Figs.2 - 5 where the eigenvalues of $m = 2, n = 1$ free-boundary and fixed-boundary modes are plotted as function of the twist ι_{ax} on axis for various positions b/a of the conducting wall. Figure 2 shows the results for the straight $\ell = 2$ configurations ($\epsilon = 0$). At $0.44 < \iota_{ax} < 0.52$ one observes a stabilizing effect due to the wall scaling approximately like $(a/b)^4$ with the inverse wall distance. At $\iota_{ax} \approx 0.408$ the corresponding twist value at the free-boundary is $\iota_b = 0.50$ which is resonant to the $m = 2, n = 1$ mode, no stabilizing effect due to the wall can be observed. Increasing the curvature to $\epsilon = 0.065$ (Fig.3) the resonance phenomenon

is less distinct and obviously a stabilizing effect due to the wall is observed even at a wall position of $b/a = 1.2$.

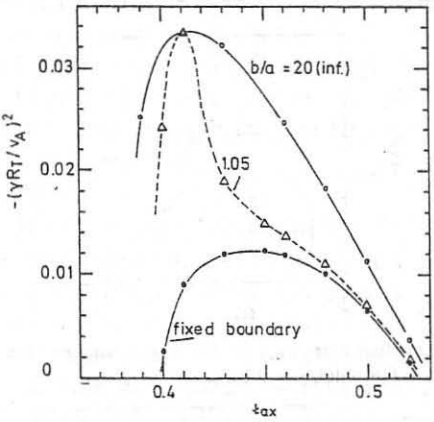

Fig.2. Normalized eigenvalues versus ξ_{ax} for the free-boundary ($b/a = 1.05, 1.20, \infty$) and the fixed-boundary mode (straight, $\epsilon = 0$).

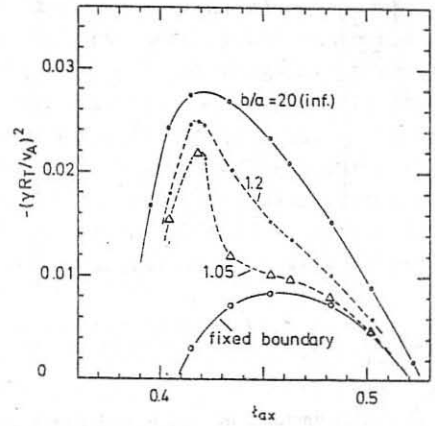

Fig.3. Normalized eigenvalues versus ξ_{ax} for the free-boundary ($b/a = 1.05, 1.20, \infty$) and the fixed-boundary mode (toroidal, $\epsilon = 0.065$).

The wall stabilization effect on the free-boundary mode depending on the wall distance b/a is even more obvious at $\epsilon = 0.13$ (Fig.4). In this case the fixed-boundary mode could

not be found. The left edge of the eigenvalue curves is shifted to higher ι_{ax}-values as ϵ is increased. Figure 5 shows the maxima of the eigenvalue curves as function of the torus curvature ϵ for the free-boundary mode at various wall distances [$b/a = 20$ (infinity) and 1.2] and the fixed-boundary modes. The eigenvalues scale approximately like ϵ^2.

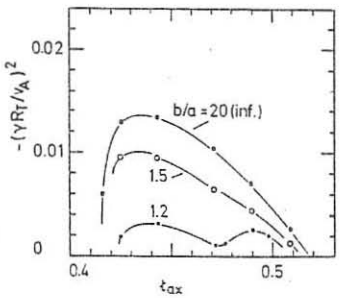

Fig.4. Normalized eigenvalues versus ι_{ax} for the free-boundary ($b/a = 1.20, 1.50, \infty$) and the fixed-boundary mode (toroidal, $\epsilon = 0.13$).

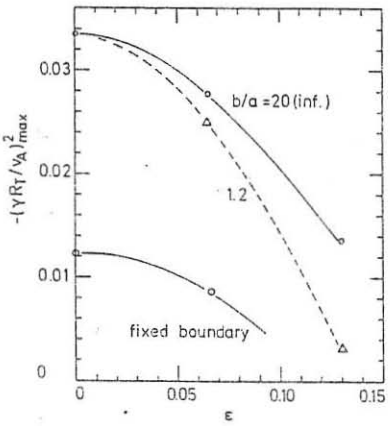

Fig.5. Scaling of the maxima of the eigenvalue curves as function of toroidal curvature $\epsilon(\epsilon_{max} = 0.13)$.

According to this model weakly unstable $m = 2, n = 1$ free-boundary modes can be stabilized by a conducting wall in a toroidal $\ell = 2$ configuration (e.g. for $\langle\beta\rangle \approx 0.8\%$ the wall position is about $b/a \approx 1.1$ to stabilize this mode).

MEASUREMENT OF ELECTRON CYCLOTRON RADIATION SPECTRUM(ECR) IN THE L-2 STELLARATOR BY FAST-SCANNING FOURIER-SPECTROMETER

Akulina D.K., Lazarev V.B.[+], Lapshin V.I.[++], Leonov V.N.[++], Fedorenko S.I.[+], Fedyanin O.I.

General Physics Institute, USSR Academy of Sciences

+ Kurchatov Institute of Atomic Energy

++ Lebedev Physical Institute, USSR Academy of Sciences

Moscow, USSR

1. Introduction

The measurements of ECR radiation in the L-2 stellarator with superheterodyne radiometer had been performed earlier/1/, but narrow range of frequency scan did not permit to obtain total spectra that offered difficuties in interpreting experimental data. For the L-2, fast-scanning Fourier spectrometer in the spectral range 30-200 GHz with ~3GHz spectral resolution has been designed. The L-2 magnetic field has radial component B_r achieving ~ 20% of total field modulus at a plasma border, that results in Faraday rotation of polarization plane of electric field of radiated wave. Hence, the optical scheme permitting simultaneous registration of two orthogonal polarizations was chosen. In the Fourier-spectrometer the polarizing interferometer with 4 screw-reflecting axisymmetric rotating mirrors is used /2,3/. The InSb-cooled detector has sensitivity corresponding to ~ 20 eV at $2f_{He}$ = 70 GHz. The antenna of radiometer is located on the torus external side, the resulting resolution near plasma center being 2,5cm. The time needed to record one interferogramm is about ~ 2msec. Detailed description of the spectrometer is given in /2,3/

2. Experiment

The spectrum measurements have been made in ohmically heated discharges with the parameters: magnetic field strength B(0)= 1-1,4 tesla, plasma current I_p=14-18kA, plasma density $\bar{n}_e = 5.10^{12} - 3.10^{13} cm^{-3}$, electron temperature T_e=300-600eV, pulse duration ~ 30-40 msec. Several interferogramms of plasma radiation have been recorded during one pulse as well as the total ECR intensity and integrated X-ray signal. Fig.1,2 shows the main discharge parameters. The spectra and the value of total intensity were observed

Fig1.
$\bar{n}_e$-is average electron density.
I_{ECE}-is total intensity in "thermal" regimes.

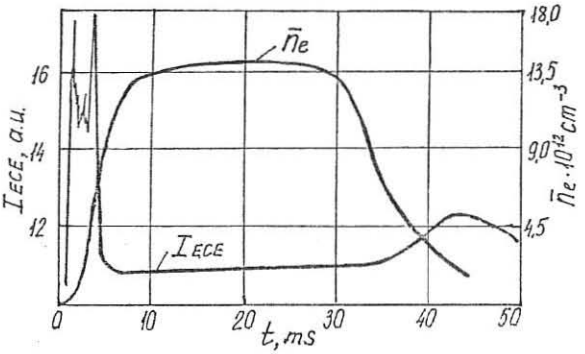

Fig.2
I_p-is plasma current,
B-is magnetic field strength on the axis,
U_L-is loop voltage.

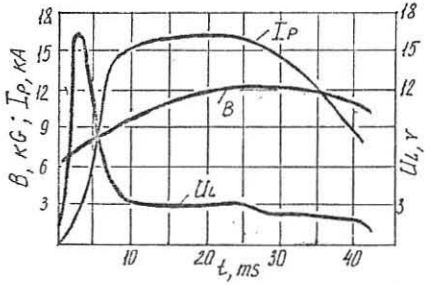

Fig,3
ECE spectra in "thermal" regimes.

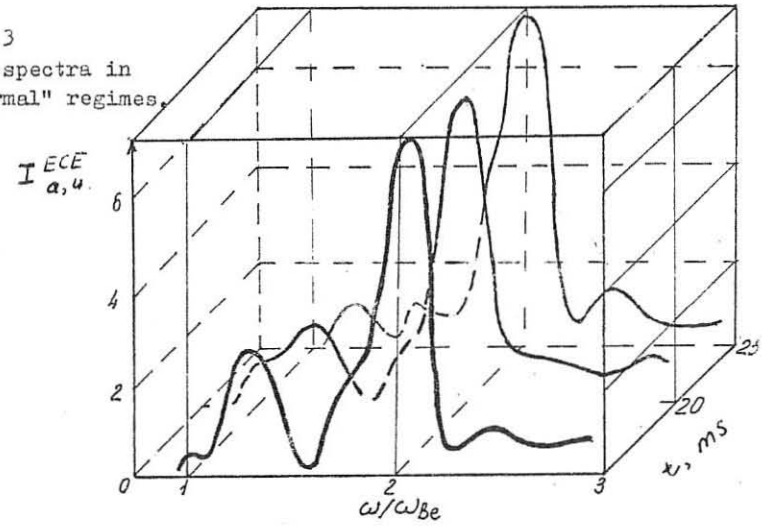

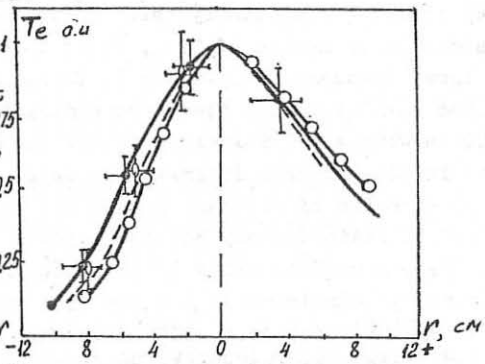

Fig.4
Electron temperature T_e distribution at different times.
(-)-15msec,(++)-20msec,
(-0-)-25 msec.
(+)-laser scattering data,

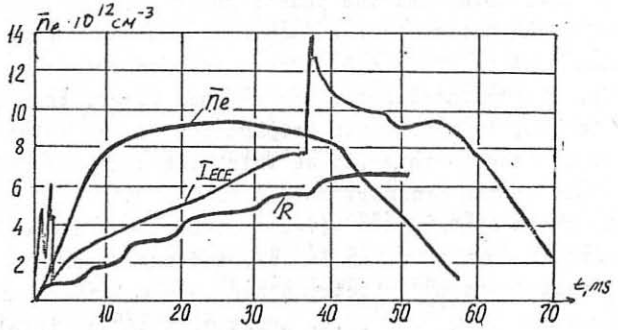

Fig.5
$\bar{n}_e$-is average electron density, I_{ECE}-is total intensity, R-is integrated X-ray signal in "runaway"regimes.

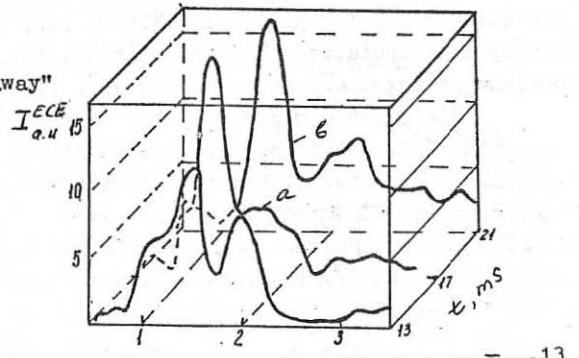

Fig.6
ECE spectra in "runaway" regimes.
a- at t=17msec.
b- at t=21msec.

to depend on plasma density. When plasma density exceeds $\bar{n}_e \geq 10^{13}$ cm^{-3}, the maxima of spectra correspond to frequency of the second cyclotron harmonic $2f_{He}$ in the plasma center (Fig.3). This is so-called "thermal"regimes. The $T_e(r)$ inferred from the spectra and its comperison with Tomson scettering data is given in Fig.4, showing fairly good agreement. When $n_e < 10^{13}$cm^{-3}, the I_{ECE}

X-ray increase essentially (see Fig1, $t > 35$ msec, Fig.5). In addition to maxima of $2f_{He}$, there is another one shifted to the lower frequency (Fig.6 a,b). These spectra are typical for regimes with "runaway" electrons and have been observed in many machines with similar regimes /4,5/. To be noted is the peculiarity in ECE integral intensity curve $I_{ECE}(t)$ at t=37 msec, observed in a series of discharges with the same parameters. This "burst" of radiation may be explained by "fan-like" instability /4/. The experiments allow to estimate the energy and density of "runaway" electrons /6 /. Since the experimentally observed frequency shift is about 20GHz, the energy of electron is 130-200 keV. Note that the peak's shift is very sensitive to discharge organization in the machine and may be essentially smaller than that in Fig.6 a,b. Moreover, when frequency equal to ~ 20 GHz, the radiated frequency becomes lower, than the upper hybrid one, that prevents propagation of the extraordinary mode towards the reciever, so we think the measured radiation to be mainly in the ordinary mode, because both Faraday rotation and the ratio $I_n^{ord} / I_n^{extra} = (v/c)^2$ at E=200keV are essential values. Using the method given in /6/, and experimental data, the density of "runaway" electrons has been estimated and found to be equal to $5.10^{10} cm^{-3}$, i.e. about 0,5% of the total plasma density,

The authors deeply appreciate Blokh M.A., Nakladov A.N., for the help in computations of data, Shpigel I.S, for useful discussions, and Azizov E.A., Solomonovich A.E. for support.

R e f e r e n c e s

1. Akulina D.K., Khol'nov Yu. Fizika plazmy ,1978,4,p.1015
2. Akulina A.,Kiktev A.,Lazarev V.,Lapshin V.,Leonov V.,Fedyanin O. Preprint FIAN N°1964,1982,Moscow
3.Akulina D.,Lazarev V.,LapshinV., Leonov V.,Fedorenko S., Fedyanin O . Pribory i tekhnika experimenta ,1985, N° 4
4. Campbell D., Eberhagen A.,Kissel S.,Nucl.Fusion, 1984, v.24,N°3
5.Brossier P. Nucl.Fusion ,1978,v.18,p.1069-1080
6. Celata C.,Boyd D. Nucl. Fusion ,1978,v,18,N°5

A NUMERICAL SIMULATION OF EXPERIMENTS ON ELECTRON CYCLOTRON PREIONIZATION AND PLASMA HEATING IN L-2 STELLARATOR

A.A.Fraiman, O.B.Smolyakova, and E.V.Suvorov

Institute of Applied Physics, Academy of Sciences of the USSR
46 Uljanov Street, 603600 Gorky, USSR

In order to investigate the electron cyclotron heating of a plasma in L-2 stellarator, numerical simulation of the wave propagation and absorption has been performed, including a ray-tracing technique and the calculation of cyclotron absorption and distribution of energy deposition over magnetic surfaces.

The analytical expressions in toroidal coordinates for plasma density, electron temperature and magnetic field take into account the characteristic features specific of L-2 stellarator, in particular, the presence of toroidal and helical harmonics of the magnetic field, the ellipticity of the plasma column cross-section and its screw structure. Figure 1 shows the lines of a constant magnetic field intensity and the model "separatrix" used in the calculations for the cross-section of launching the HF power in the experiments 1 . Parabolic radial distribution was assumed, both of them being zero at the separatrix.

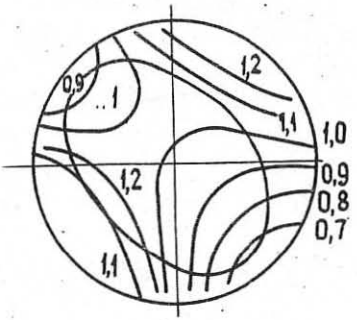

Fig.1.

The equations for ray trajectories were integrated in the parametric form

$$\frac{d\xi_\kappa}{dt} = \frac{\partial G}{\partial \eta_\kappa}, \quad \frac{d\eta_\kappa}{dt} = -\frac{\partial G}{\partial \xi_\kappa}$$

Here ξ_κ are the toroidal coordinates, η_κ are the components of the phase gradient, the hamiltonian G is taken in the form

$G = \frac{c^2 h^2}{\omega^2} - n_\pm^2$, where C is the velocity of light, ω is the wave frequency, $n_\pm^2$ are the squared refractive indices of the ordinary and extraordinary waves depending on plasma density, magnetic field intensity, and direction of the wave propagation.

The variation in the optical depth τ along the ray trajectory was calculated by a radiation transfer equation

$$\frac{d\tau}{dt} = 2\,\frac{\omega}{c}\,\varkappa\,\cos\theta$$

where $\varkappa$ is the imaginary part of the refractive index, and θ is the angle between the wave vector $\vec{\eta}$ and the group velocity.

The rate of energy deposition between the neighbouring magnetic surfaces was computed with a discrete step Δr over a small radius r :

$$P(r, r+\Delta r) = \sum_i \rho_i \exp(-\tau(r)) \cdot (1 - \exp(-\tau(r+\Delta r) + \tau(r)))$$

where ρ_i is the "weight" of the i-th ray in the whole radiation beam.

Now we shall discuss in more detail the results of numerical simulation of the experiments [1] , which showed effective electron heating (up to $T_e = 350 \div 450$ eV at plasma densities $\bar{N} = 4 \div 6 \cdot 10^{12} cm^{-3}$) in the regimes with a "slow" plasma density increase (Fig.2), while no detectable heating was observed in the regimes with a "fast" density increase (dashed lines in Fig.2).

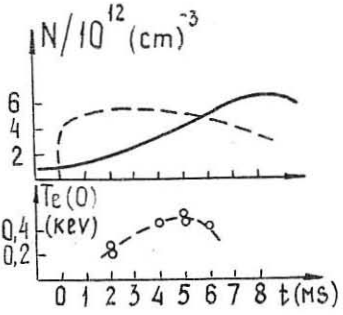

Fig.2.

The Gaussian beam of extraordinary waves used in the experiments was approximated by a set of 49 rays with the appropriate angular divergence of $\pm 6°$ and the intensity distribution over the transverse aperture provided e^2 times decrease at the distance of ± 2.5cm from the centre of the aperture.

In Fig.3 the energy deposition profiles are presented for experimental plasma parameters at different moments of time (for a resonant magnetic field at the magnetic axis) in the regime of slow density increase: b) $\bar{N} = 2 \cdot 10^{12} cm^{-3}$, $T_e = 190$ eV;

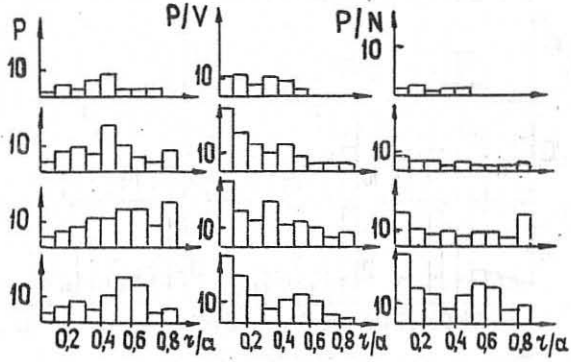

Fig.3.

c) $\bar{N} = 4 \cdot 10^{12} cm^{-3}$, $T_e = 430$ eV; d) $\bar{N} = 6 \cdot 10^{12} cm^{-3}$, $T_e = 350$ eV. Besides, the point a) is added: a) $\bar{N} = 1 \cdot 10^{12} cm^{-3}$, for which the temperature is unknown and assumed to be 100 eV. The first group of diagrams, $P(r)$, shows the radial distribution of energy deposition between two neighbouring magnetic surfaces (the scale of ordinates is 10 units to 4.3 kW). The second group, $P/V(r)$, is for the radial distribution of electromagnetic power absorbed in a unit volume (10 units to 22 W/cm^3) and the third one, $P/N(r)$, is for the radial distribution of power per one particle (10 units to 750 eV/mc). All scales are referred to the total launched power of 100 kW used in the experiments. The summary efficiency of one-pass absorption attains 40% at $\bar{N} = 1 \div 2 \cdot 10^{12} cm^{-3}$, decreases to 33% at $\bar{N} = 4 \cdot 10^{12} cm^{-3}$ and drops sharply (down to 14%) at $\bar{N} = 6 \cdot 10^{12} cm^{-3}$. The radial distribution profile both per unit volume and per one particle has its maximum in the centre as a rule.

The energy deposition profiles for the same densities as in Fig.3 but for low electron temperature (75 eV) are presented in Fig.4 illustrating a heating regime with fast increase in plasma density. The total heating efficiency is much lower (5% at

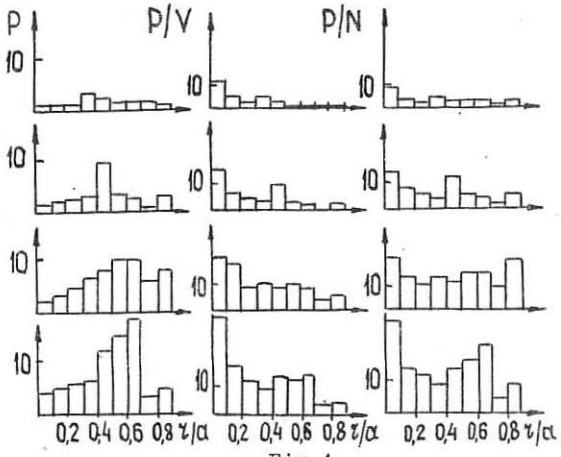

Fig.4.

$\bar{N} = 6 \cdot 10^{12} cm^{-3}$) in this case.

Such a difference in heating in the two regimes is caused by specific features of cyclotron absorption of the extraordinary wave at the first harmonic [2]. For a fixed value of the angle of propagation α, there exists an optimum relation between the plasma density N and the electron temperature T_e which provides maximum absorption: $\frac{\omega_p^2}{\omega_H^2} \approx \sqrt{\frac{T_e}{mc^2}} \cos\alpha$ (ω_p, ω_H are the plasma and the cyclotron frequencies, respectively, and mc^2 is the rest energy of the electron). Regimes of slow electron density increase that show a rather high heating efficiency in experiments are more close to the optimum one.

Thus, the results of numerical simulation within one-pass cyclotron absorption of extraordinary waves make it possible to explain the characteristic features of the experiment such as resonant dependence of the heating efficiency on the magnetic field intensity, steep decrease in efficiency at the end of the r.f. pulse, peaked electron temperature profile, as well as the absence of detectable heating in regimes with fast rise of plasma density. The total calculated efficiency is close to that obtained experimentally.

References

1. E.D.Andryukhina et al., Pis'ma v ZhETF, 40, 9, 377 (1984).
2. V.V.Alikaev et al., RF Plasma Heating, p.6 (1983), Gorky.

COMPARISON OF EXPERIMENTAL RESULTS AND NUMERICAL SIMULATIONS ON ECR PRODUCTION AND HEATING OF CURRENTLESS PLASMA IN THE L-2 STELLARATOR

E.D.Andryukhina, G.M.Batanov, M.S.Berezhetskii, M.A.Blokh, G.S.Voronov, N.P.Donskaya, K.S.Dyabilin, N.F.Larionova, S.V.Kladov, L.M.Kovrizhnykh, L.V.Kolik, A.I.Meshcheryakov, A.V.Novikova, S.N.Popov, A.V.Sapozhnikov, K.A.Sarksyan, I.S.Sbitnikova, V.N.Sukhodolskii, A.D.Smirnova, A.E.Petrov, O.I.Fedyanin, Yu.V.Kholnov, M.G.Shats, I.S.Spigel
Institute of General Physics, Academy of Sciences of the USSR, Moscow, USSR

E.F.Gippius, B.N.Illyukhin, V.N.Kolesnikov, A.V.Paramonov
P.N.Lebedev Physical Institute, Academy of Sciences of the USSR, Moscow, USSR

A.G.Litvak, O.B.Smolyakova, E.V.Suvorov, A.A.Fraiman
Institute of Applied Physics, Academy of Sciences of the USSR, Gorki, USSR

Experiments on production and heating of currentless plasma in the L-2 stellarator by electron cyclotron resonance waves were carried out in 1984 and reported in [1,2]. In contrast to analogous experiments in other machines [3,4] we have used linearly polarized microwave radiation with electric field component perpendicular to the L-2 magnetic field(X polarization). The Gaussian microwave beam was launched into the vacuum vessel through a vertical port, this being equivalent to launching from the strong field side due to specifics of the L-2 magnetic structure.Under conditions close to experimental ones, numerically calculated were the beam trajectories, cyclotron absorption along these trajectories, profiles of energy deposition.Ray-tracing was done for 49 rays within the Gaussian beam.Plasma energy balance was calculated within the framework of the neoclassical theory [5]. In this paper the result of experiments and calculations are qualitatively compared.

In experiments we have observed two significantly different regimes of heating.The first regime is characterized by slow growth of electron density during the heating pulse, provided that preliminary ionization $\bar{n}_e = 0.1\text{-}1,10^{12}$ cm^{-3} was applied (see Fig.1b). In this case the central electron temperature $T_e(0)$ continuously grows up to 400-600 eV and then slightly decreases (Fig. 1.c). In the second regime no preionization was used and the density rapidly increased in 200-300 s but the temperature was never higher than 60 eV. In calculations it was

of importance to reveal whether one-pass absorption of the X waves can provide the experimentally observed phenomena and the obtained heating efficiency about 40%.

According to numerical simulations, the integral coefficient of cyclotron absorption of X waves is about 40% in one pass, provided that the resonance condition $\omega_o = \omega_{He}$ is fulfilled at the plasma center and the parameters are as in the first regime. Thus, the calculated heating efficiency is close to experimental one. The numerical results are due to presence of an extended region of homogeneous magnetic field where the resonance conditions are satisfied along a ray (solid lines in the trajectories in Figs.2a,2b). Moreover, because of the beam refraction both at the boundary and inside the plasma, the rays deflect from the perpendicular to magnetic field, thus providing higher heating efficiency. During the heating pulse, in the first regime the calculated efficiency decreases from 40% down to 13% thus explaining the observed decrease of T_e (Fig. 1d). If in calculations the density behaviour is taken as in the second regime, the heating efficiency is never higher than 5% and does not provide heating. This difference in heating efficiencies is also seen experimentally in measurements of microwave power passing through the vessel. The oscillogramms in Fig.1e show that the ratios of power on the non-effective and effective heating in the beginning and an the end of the heating pulse are about 10 and 3 respectively. This figures well agree with calculated efficiences.

The calculated profile of microwave power absorption is shown in Fig.3. Up to 70% of power is seen to be deposited within the central region ($r/a \leq 0.5$). Using this profile, the plasma energy balance was numerically simulated by the neoclassical theory. Both the maximum T_e and the $T_e(r)$ profile obtained thereby are close to experimental ones, the transport in the center being neoclassical but an anomalous electron thermal conductivity being needed at the periphery (see Fig.4).

Moreover, plasma heating by extraordinary waves is expected to result in appearance of superthermal anisotropic electron velocities at least at densities low enough not cause maxwellization. Actually, this phenomenon was observed in experiments, al-

beit indirectly. Namely, in the initial stage of heating, X-ray radiation is harder than expected from temperature measurements (Fig.1f) and the energy contents determined from $n_e(r)$ and $T_e(r)$ profiles and from diamagnetic measurements differ, while at higher densities these discrepancies disappear.

Concludingly, the comparison of experimental and numerical results indicates that the phenomena observed can be explained by one-pass cyclotron absorption of the extraordinary waves with regard for neoclassical transport.

Références:

1. E.D. Andryuchina et al. X Conf. IAEA, London, 1984 CN-44/d-1-4

2. E.D. Andryuchina et.al. Pis'ma v ZhETF 40, 377, 1984
3. Uo K. et al. X Eur. Conf. on Contr. Fusion and Pl.Phys. 1981, Moscow, 1, E-1
4. Wilhelm R. et al. Pl. Phys. and Contr. Fusion 1984, 26, 1A, 259
5. Kovrizhnich L.M. Pl. Phys. and Contr. Fusion 1981, 26, 1A, 195

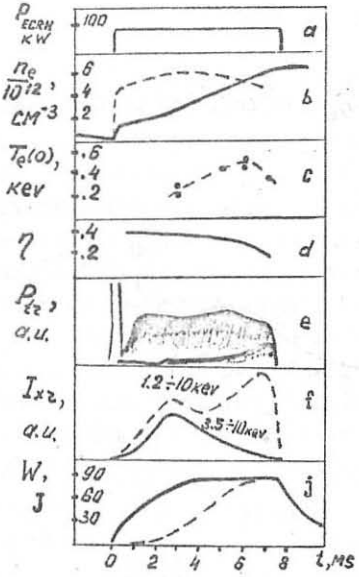

Fig.1. Plasma parameters is time, $B = B_{res}$, $P_0 = 90$ kW
a) UHF pulse envelope b) average electron density along the central chord $n_e(t)$ c) electron temperature at the center (laser scattering ($T_e(t)$) d) calculated absorption coefficient (η) e) passed UHF-power envelope I without heating II with heating
f) X-ray radiatinn intensity along the central chord
j) plasma energy I - from diamagnetic signal
2 - $4\pi^2 R \int [T_e(r) + T_i(r)] r n(r) dr$

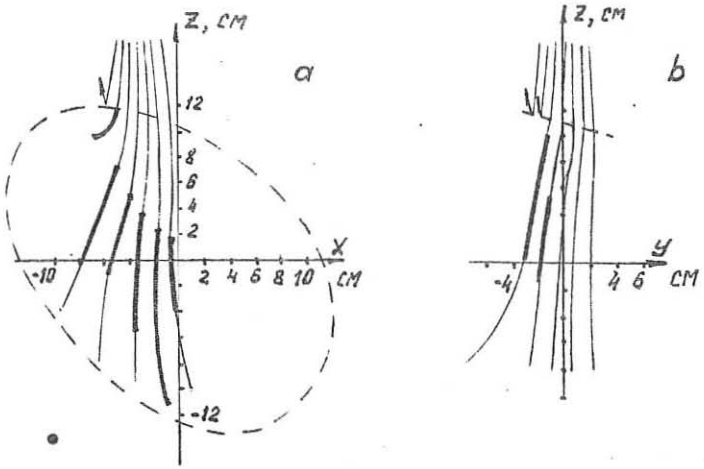

Fig.2. Calculated beam trajectories $\bar{n}_e = 4 \cdot 10^{12}\,cm^{-3}$, $B = B_{zes}$, $T_e(0) = 430\,ev$

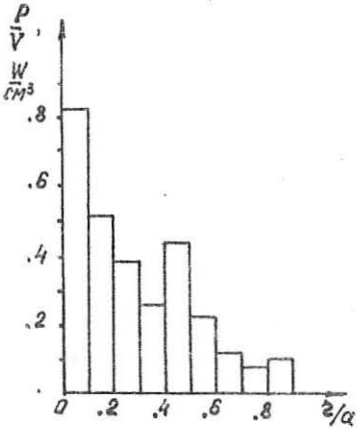

Fig.3. Calculated radial profile for absorbed UHF energy $\bar{n}_e = 4 \cdot 10^{12}\,cm^{-3}$, $B = B_{zes}$, $T_e(0) = 430$ ev.

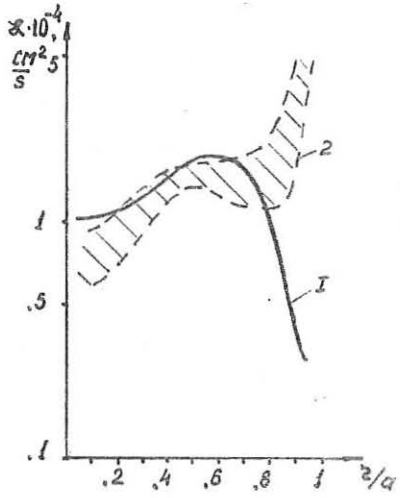

Fig.4. Radial profile of thermal conductivity coefficient
I neoclassical
2 with allowance for experimental radial distributions.

SPECTROSCOPIC STUDIES OF IMPURITIES DURING ECR PLASMA HEATING IN THE L-2 STELLARATOR

M.A.Blokh, G.S.Voronov, N.P.Donskaya, S.V.Kladov, N.F.Larionova, A.D.Smirnova, I.S.Spigel
Institute of General Physics, Academy of Sciences of the USSR, Moscow, USSR

E.F.Gippius, B.I.Ilyukhin, V.N.Kolesnikov, A.V.Paramonov
P.N.Lebedev Physical Institute, Academy of Sciences of the USSR, Moscow, USSR

The experiments on electron cyclotron heating of current-less plasma in the L-2 stellarator were carried out in 1984[1]. In that, the main impurity ions - oxygen, carbon and iron - were spectroscopically studied. In the range of VUV, spatial distributions of absolute intensities of OIV-OVI, CIV, FeXV resonance lines were measured using a LHT-30 monochromator absolutely calibrated at the S-60 synchrotron [2]. For measurements in the UV range a VMS-1 monochromator was used.

In order to recover the local intensities I(r) from the chord brightness profiles B(x) we have used the code which takes account of the ellipticity of magnetic surfaces in the L-2 stellarator [3]. Solid lines in Figs.1a-1c show the radial profiles of line intensities obtained thereby, the numbers at

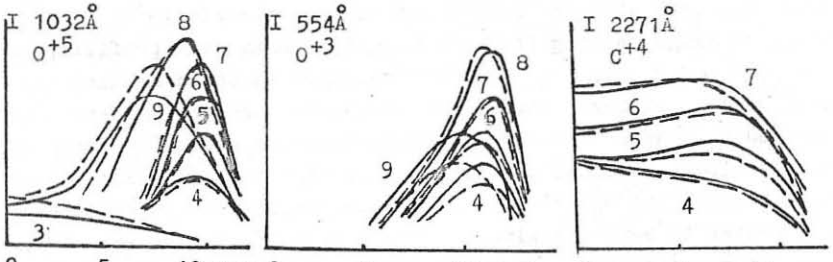

Fig.1a Fig.1b Fig.1c

curves mean milliseconds from the heating pulse start-up. Both the shapes and absolute intensities are seen to change strongly in time. This fact allows to reveal the dynamics of a series of plasma parameters during the heating pulse, provided the measurements are backed up by proper numerical simulations which, in our case, were based upon a model including the processes of transport, ionization, recombination and charge-exchange. In calculations we have used the profiles of electron density measured by 8-channel laser interferometer with $\lambda = 337\mu$. The time dependence of n_e is shown in Fig.2. As seen in Fig.3 the shape of $n_e(r)$ profiles stays practically constant in time. The electron temperature was measured by Thomson scattering, the time dependence of $T_e(0)$ being given in Fig.2. The Thomson scattering data for r=1 and 4 cm are very reproducible, while at low electron densities (at early time and at plasma periphery) no reliable Thomson scattering data could be obtained. That is why a complete temporal and spatial distribution could only be found using simulations with checking the results to the available values of T_e.

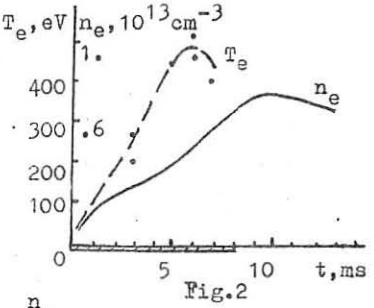

Fig.2

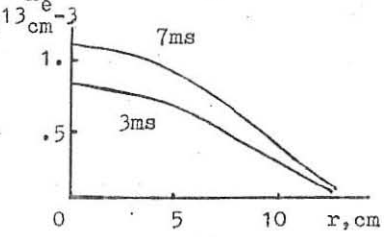

Fig.3

Similar simulations of impurities have been already carried out earlier for stationary phase of ohmic heating [4] with use of experimental profiles of $n_e(r)$ and $T_e(r)$. The impurity transport in ohmic heating was found strongly anomalous, since the observed fluxes were much greater than neoclassical ones. For ohmic heating with various densities the profiles of the anomalous diffusion coefficient $D_{an}(r)$ were fitted to satisfy the experiments and proved to have a maximum in the plasma center, to increase with plasma density, and not to depend on the ion's charge and

type. In the case of currentless plasma the role of neoclassical transport is of much greater importance. The cause is that in the L-2 stellarator the central value of rotational transform is $\iota(0) \simeq 1$ in presence of plasma current and $\iota(0) \simeq 0.2$ in vacuum or in currentless plasma, while in the Pfirsch-Schlütter regime of collisionality, which is characteristic of our experimental conditions, the impurity flux is proportional to $1/\iota^2$.

According to numerical simulations, the neoclassical impurity flux in the ECRH case is comparable with experimentally observed flux. Because of this, no anomalous transport was included into calculations done for ECRH. Resultingly, the number of fitting parameters could be reduced, so that the experimental data on ion lines intensities of oxygen and carbon $I_z(r,t)$ were used to reveal the fluxes of corresponding neutral impurities from the walls $\Gamma_o(t)$ and the electron temperature profiles $T_e(r,t)$.

The best agreement of experimental profiles $I(r,t)$ of all lines involved was obtained for the temperature profiles shown in Fig.4. In Fig.5 the simulated time dependences of OIV-OVI and CIV brightnesses $B(t)$ (dashed) are shown together with experimental ones (solid). To be noted is that although the absolute scale of oxygen ion concentration is fitted by the single parameter of neutral flux from the wall, the simulation correctly describes the relative brightnesses of lines corresponding to different ionization states. The dashed lines in Fig.2 depict the calculated profiles of corresponding lines. It is seen that the obtained $T_e(r)$

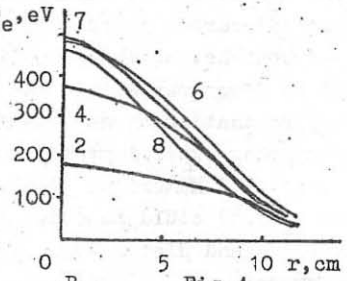

Fig.4

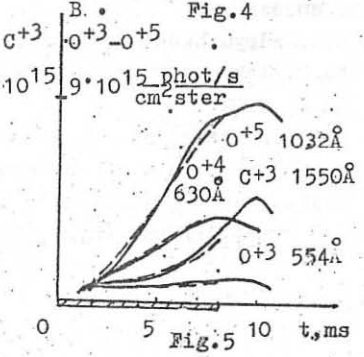

Fig.5

profiles satisfactorily simulate the behavior of impurities. Moreover, it means that the calculated neoclassical fluxes are close to experimental ones.

Fig.6 shows the corridor of $T_e(r)$ profiles inferred from the spectroscopic data with regard for their accuracy. Here t=6 ms when the electron temperature is maximum. The profiles well agree with the Thomson scattering values at r=1 and 4 cm which are also given in Fig.6.

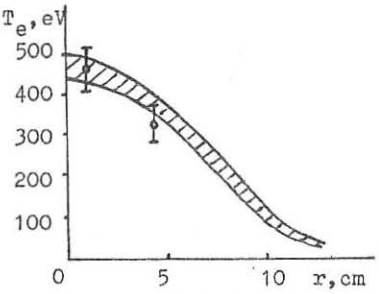

Fig.6

These data were then used to calculate the total plasma energy, the obtained value 85 J being in accord with that determined from diamagnetic measurements (78 J).

Thus, the spectroscopic measurements and corresponding numerical simulations for ECR heating in the L-2 stellarator indicated almost the same amount of oxygen and carbon to reside in plasma as in ohmic heating, but in contrast to ohmic heating, transport of impurity ions could be described within the framework of the neoclassical theory so that no anomalous transport needed being introduced.

Comparing experimentally measured line intensities of several ions with numerical simulations, the time and space profiles $T_e(r,t)$ could be determined which well agree with Thomson scattering and diamagnetic measurements.

References:

1. E.D.Andryukhina et al. Pis'ma ZhETF, 40, No.9, 377-379 (1984)
2. Yu.M.Aleksandrov et al. Kratkie soobshch. po fiz., 1981, No.3, 21-26
3. E.F.Gippius et al. Fizika plazmy, 9, No.3, 502-508 (1983)
4. M.A.Blokh et al. 11-th Europ.Conf. Contr. Fusion and Plasma Phys., Aachen, 1983, v.1, C23, p.215
5. TFR group. Plasma Phys., 20, No.8, 735-747 (1978)

PLASMA PRODUCTION AND CONFINEMENT IN A TOROIDAL HELIAC

S.M.Hamberger, L.E.Sharp, S.X.Shi, B.D.Blackwell

Australian National University, Canberra, Australia

The heliac configuration first proposed by Princeton (1) uses appropriately arranged circular coils to produce stellarator fields with helical axes and whose magnetic surfaces can have high transform, low shear, and significant mean magnetic well. We report here the first experimental evidence of their existence through direct observation of plasma produced and confined in such a heliac, which approximates to the first Princeton reference design. (2)

The apparatus (Fig.1) contains 24 two-turn toroidal coils, of mean radius 6.25 cm, equally spaced toroidally but with their centres displaced 2.5 cm radially from their mean position on the minor axis (R_o = 18.75 cm) so as to lie on the helix $\theta = 3\phi + 0.1 \sin\theta$. A 4-turn poloidal ring is located inside the toroidal coils at $R = R_o$, and the magnetic configuration completed by single-turn vertical field coils. The coil assembly is located inside a cylindrical stainless steel vacuum vessel. The coils are connected in series with facilities for fine adjustment to the vertical field and energized via a transformer from a capacitor bank. The magnetic field pulses have intensities up to 0.4 T and duration ~ 40 ms.

Fig.1

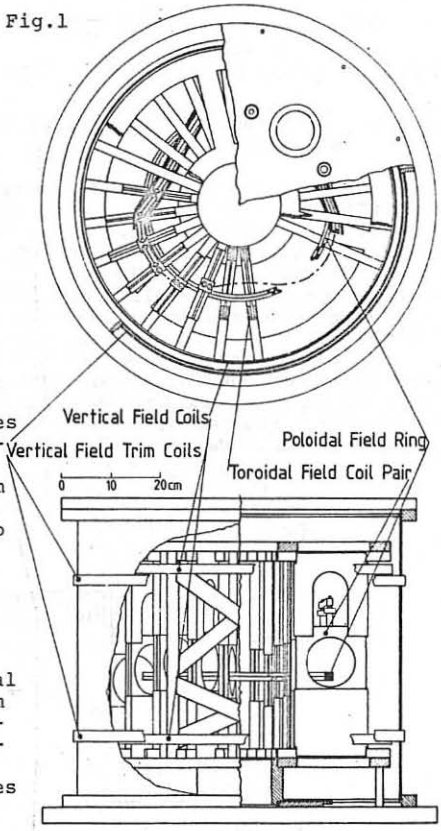

The resulting magnetic surfaces, which rotate three times about the poloidal ring, have bean-shaped cross-section as shown in Fig.2. The rotational transform (Fig.3) increases from $\iota(0) = 1.19$ on the helical magnetic axis to 1.35 at the outermost available closed surface. The magnetic well depth increases

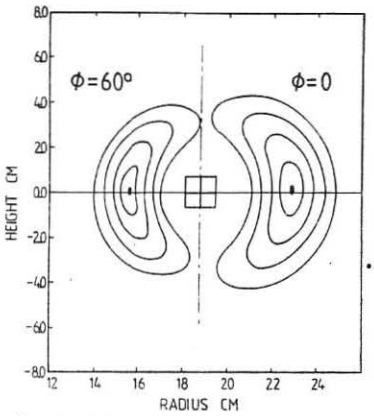

Fig.2. Computed Flux Surfaces

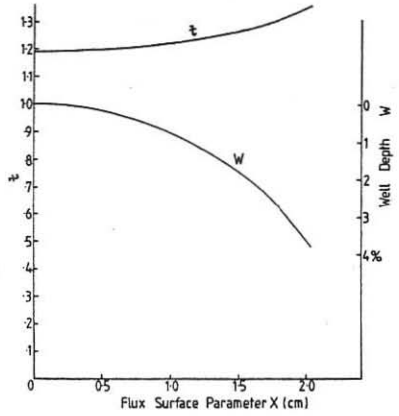

Fig.3. Rotational Transform and Well

smoothly from the axis to ~ 4% at the outside surface, whose mean radius is 3.1 cm.

Plasma is produced at gas pressures between 10^{-5} and 5×10^{-4} torr (Ar, He, H_2) by breakdown induced by superimposing a small r.f. current (~ 100 AT at 100-300 kHz) upon the normal poloidal ring current (~ 16,000 AT) so as to provide an oscillatory electric field (≤ 30 V/turn). The discharge persists as long as the r.f. is applied and the magnetic field exceeds 30 mT. Diagnostics include several single and double electrostatic probes, a 2 mm double pass interferometer and light emission. Typical waveforms are shown in Fig.4. At low pressures results are highly reproducible, and good probe characteristics can be obtained provided the probes are carefully cleaned, so enabling good density and temperature profiles to be obtained along several chords. Values of $\int n_e dl$ obtained in this way agree well

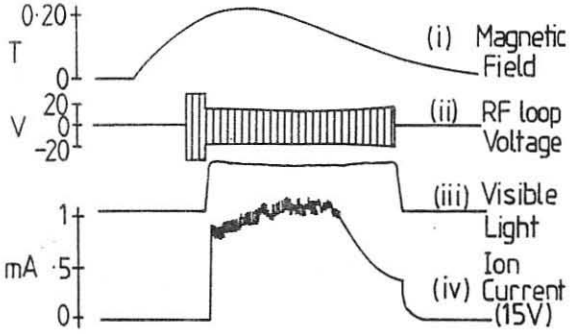

Fig.4. Typical Waveforms for Ar at 1.5×10^{-4} torr.

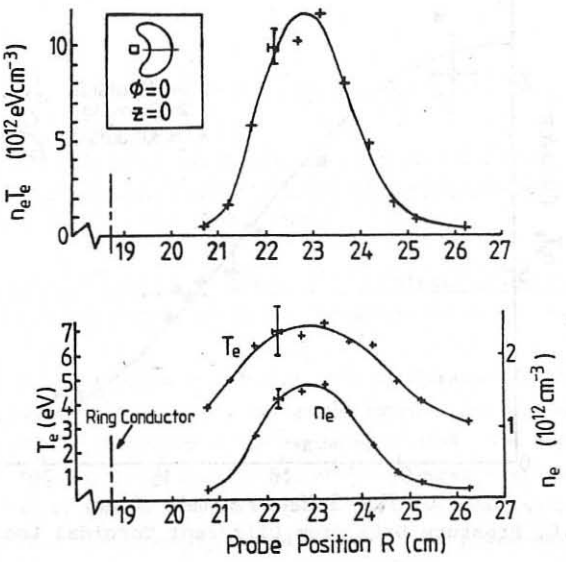

Fig.5. Radial Variation of n_e, T_e and Electron Pressure

with that from interferometry. Essentially fully ionized argon plasma with densities $n_e \leq 1.5 \times 10^{12}$ cm^{-3}, $T_e \sim 5 - 10$ eV are readily obtained using only ~ 100 W r.f. power. We find no detectable power input to the plasma from the time-varying magnetic field.

By moving double Langmuir probes along various chords located in different phases of the helical configurations the plasma density and temperature can be sampled on the various surfaces. Fig.5 shows typical profiles of n_e, T_e and pressure along a horizontal probe path (shown inset). By computation based on the actual current distribution in the coils, each probe position can be ascribed to a given magnetic surface (since $\beta \leq 10^{-4}$ and no significant plasma current flows vacuum calculations are sufficiently accurate for this). We find that the plasma pressure, taken as n_eT_e, has everywhere the same profile when plotted as a function of the flux surface. This is shown in Fig.5 where the parameter X is used as the sole position coordinate, showing the local pressure depends only on the flux surface. To obtain this simple relationship requires the position of the magnetic axis to be calculated to high accuracy (~ 1 mm) using the measured vertical field coil current.

For the conditions of Fig.5, the electron mean free path ~ 100 cm, significantly longer than the respective toroidal and helical curvature connection lengths of ~10 cm and 17 cm, so that the magnetic surfaces are well sampled by the electrons, i.e. the plasma would be in an intermediate diffusion regime.

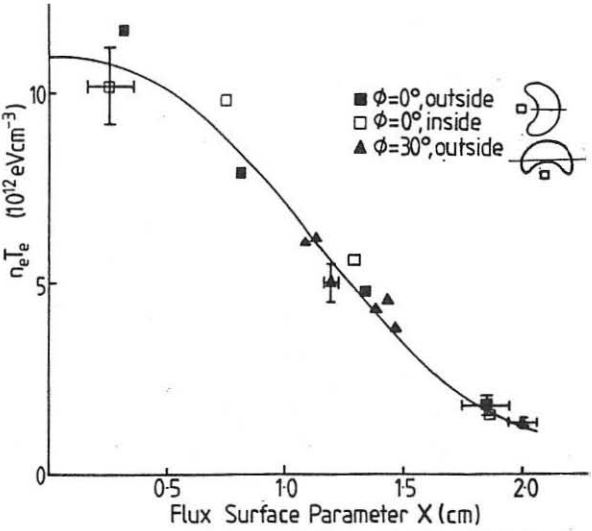

Fig.6. Pressure Data from Different Toroidal Locations.

Finally, we can estimate an approximate lower limit for energy confinement time, from the conditions $n_e \sim 1.5 \times 10^{12}$ cm^{-3}, $T_e \sim 5$ eV, vol = 4.10^3 cm^3, Pi < 100 W, as $\tau_E \sim 70$ μs. This, which includes inelastic losses, is considerably longer than both neo-Alcator scaling (~ 1 μs) and Bohm diffusion (~ 10 μs), and suggests good confinement properties.

References

(1) BOOZER,A.H., CHU,T-K., DEWAR,R.L., FURTH,H.P., et al. in Plasma Physics and Controlled Fusion Research (Proc. 9th Int. Conf., Baltimore 1982) Vol.III IAEA, Vienna (1983) 129; YOSHIKAWA,S., Nuclear Fusion Vol.23 (1983) 667.

(2) Proceedings of the IAEA Technical Committee Meeting on Plasma Confinement and Heating in Stellarators, 1984. CEC, Brussels (1984).

PHYSICS ISSUES IN THE DESIGN OF TJ-II

A. Perea, J.L. Alvarez Rivas, J. Botija, J.R. Cepero, J.A. Fábregas, J. Guasp, A. López Fraguas, R. Martín, A. Pérez Navarro, A. Pueblas, E. Rodriguez Solano
Junta de Energía Nuclear, JEN, Madrid, Spain.

B.A. Carreras, K.K. Chipley, T.C. Hender, T.C. Jernigan, J.F. Lyon, B.E. Nelson
Oak Ridge National Laboratory, Oak Ridge, Tennessee, U.S.A.

TJ-II is a medium size helical axis stellarator ("Heliac") |1| to be built at the JEN site in Spain. Design and construction of TJ-II is planned for 1985-1988, with startup at the beginning of 1989. The main physics properties of the Flexible Heliac |2| magnetic configuration chosen for TJ-II are described in an accompanying paper |3|. This paper deals with physics considerations in the engineering design of TJ-II: the plasma-wall separation, sensitivity to magnetic field errors, and plasma access considerations.

The TJ-II Flexible Heliac coil configuration is shown in Figure 1. The four field period (M=4) system has 32 circular TF coils linked by two central conductors (a circular conductor and an l=1 winding). The centers of the TF coils follow a helical path around the central circular coil in phase with the helical path of the l=1 winding. This coil configuration produces bean-shaped magnetic flux surfaces which rotate around the central circular coil in the same manner as the TF coils, as shown in Fig. 2. The TJ-II parameters are: R_o= 1.5 m, TF coil radius = 0.4 m, swing radius of TF coils=0.28 m, and swing radius of l = 1 winding = 0.07 m. The two VF coils are located at R = 2.25 m, z = $\pm$ 0.56 m. The coil currents (TF $\triangleq$ 230 kA, VF $\triangleq$ 100 kA, central circular $\triangleq$ 300 kA and l = 1 $\triangleq$ 300 kA) are chosen to give control over plasma size, rotational transform, and to some extent shear, over a wide range of values at B = 1T (pulse length 0.5 s).

Figure 2 illustrates the proximity of the TJ-II flux surfaces to the l = 1 winding and to the TF coils. These distances are shown in Fig. 3 for values of rotational transform ι_o = 0.96, 1.52 and 2.12 assuming a 3.5 cm

radius for the l = 1 winding (square cross section and 10 kA/cm^2 assumed) and an 8 cm radial thickness for the TF coil (5 kA/cm^2 assumed). These distances can be increased by using thinner TF coils, non-circular TF coils (Fig. 2), higher current density in the central windings, or more cross section poloidal elongation of the l = 1 winding. As Figure 3 shows, for a reasonable plasma-to-conductor spacing, the limiting factor is the distance to the l = 1 winding. For the same value of transform, increasing the poloidal extent of the l = 1 winding requires more current (95 kA, 135 kA and 215 kA at ι_0 = 1.46 for radial winding thicknesses of 7 cm, 4 cm and 2.5 cm, respectively) so the winding cross sectional area increases. For square or D-shaped TF coils, the total central coil currents remain unchanged but a larger fraction is needed in the circular coil.

Since the TJ-II magnetic configuration has high rotational transform and low shear, it is sensitive to small magnetic field errors arising from coil misalignments, especially those that break the basic 4-fold symmetry arising from the toroidal periodicity. The most dangerous resonant perturbations are those with low toroidal mode numbers (n) for various poloidal mode numbers (m). For ι values between 1 and 2.7, the most dangerous non-symmetry breaking (4-fold symmetric) perturbations (in order of decreasing importance) have m/n values of 4/2, 4/3, 8/3, 4/4, 8/5 and 12/5. Typically, for symmetry-preserving distortions such as "squaring" of the central conductors, deformations of 1-3 cm can produce serious deterioration of the magnetic surfaces. For symmetry-breaking perturbations (e.g., a horizontal shift or tilt of the central conductors with respect to the TF coils), the most dangerous errors (in order of decreasing importance) for ι between 1 and 2.7 are those with m/n values of 1/1, 2/1, 3/2, 5/2, 4/3, 5/3, 7/3, 8/3, 5/4, 7/4, 9/4, 6/5, 7/5, 8/5, 9/5, 11/5, 12/5, 13/5 and 14/5. When the rotational transform falls at these resonances, coil displacements of 1-3 mm significantly perturb the flux surfaces. In all cases, however, a relatively small change in the central coil currents moves the magnetic configuration away from the resonante ι value and restores flux surface quality, as shown in Figure 4.

The TJ-II coil configuration has a significant impact on the vacuum vessel geometry and on the access for plasma diagnostics and heating. One design option is a large cylindrical vacuum vessel containing all but the VF coils. Alternatively, if the vacuum vessel is interior to the TF coils, the

total vacuum wall area is reduced, but device assembly is more difficult. For both design options sufficient access exists for quasi-tangential NBI. Increasing the number of TF coils per period has little effect on flux surface quality but increases the depth of the magnetic well and decreases the access distance between coils (well depths of 1.3%, 2.4%, 3.3% and 3.8%, and maximum intercoil distances of 50 cm, 36 cm, 27 cm and 21 cm are obtained for 6, 8, 10 and 12 coils per period, respectively).

Further engineering studies show that forces and heating remain within acceptable ranges.

ACKNOWLEDGEMENTS

This work was funded by a grant from the U.S.-Spain Joint Committee on Cooperation in Science and Technology. H. Wobig and colleagues at IPP Garching made useful contributions to this study.

References:

|1|.- Yoshikawa, S., Nucl. Fusion 23 (1983), 667.
|2|.- Harris, J., et al., ORNL/TM-9504 (1984).
|3|.- Guasp, J. et al., "Physics Studies for the TJ-II Device" in this Conf.

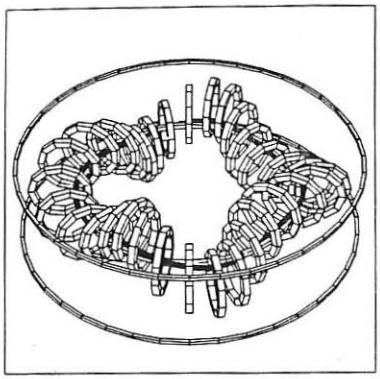

Fig. 1.
The TJ-II Flexible Heliac coil configuration.

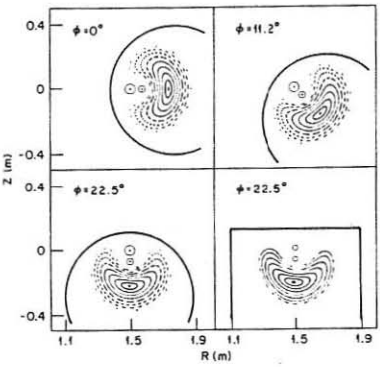

Fig. 2.
Flux surfaces at toroidal angles ϕ = 0°, 11.25° and 22.5° for circular TF coils and at ϕ = 22.5° for square TF coils.

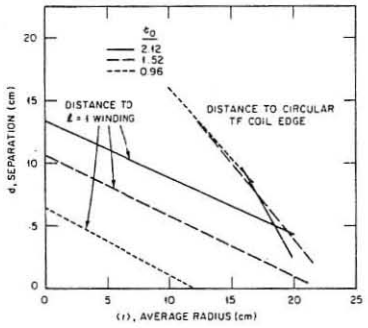

Fig. 3.
Separation between edge of TJ-II coils and flux surface vs average radius of flux surface for three different rotational transform values.

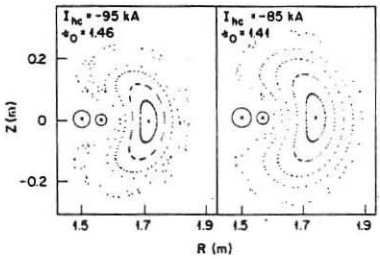

Fig. 4.
Small change in ℓ = 1 current restores magnetic surfaces broken by 2.5-mm offset of central conductor.

HELICON, A NEW HELICAL AXIS STELLARATOR

J. Guasp and J.A. Fábregas.

Div. de Fusión, JEN, Madrid.

Helical magnetic axis stellarators have retained lately some attention in reason of the theoretically alleged high equilibrium β limits, up to 20% |1, 2, 3|. In consequence some practical configurations have been proposed recently |1, 4, 5|, the Helicon has emerged as a lateral result of one of them: the TJ-II Flexible Heliac |5|.

The Helicon device consists in an l = 1 helical coil of 4, 8 or 12 periods that creates the toroidal magnetic field and produces the magnetic axis helicity. This coil is wrapped around a central structure, the hard - core, formed by two more coils: a circular one, 1 m radius, placed at the - helix center and another l = 1 helical coil, of lesser radius, 7 cm, wrapped too around the circular one with the same period than the outer helical coil, but shifted half a period. Two additional circular vertical field coils - compensate the vertical fields produced by the whole structure and allow - changes in the magnetic axis position. Fig. 1 shows a 4 period device. The minor radius of the outer helical coil is 42.5 cm and average toroidal magnetic field is 1 T. that means a 1.2 MA current in this coil.

In this way the Helicon differs from a Flexible Heliac only in - the replacement of the many (32 or 36) toroidal field coils by a single - helical coil, minimizing the total number of coils. From another point of - view the Helicon can be considered too as an l = 1 low period torsatron with two "pusher" coils just placed at the device center.

In our study, by similitude with the TJ-II device, we have considered only the four, eight and twelve period cases but nothing precludes other choices.

For the four period case we have found good magnetic surfaces for a wide range of currents in the hard core. The resulting magnetic surfaces are shown at Fig. 2, in this particular case they exhibit a triangular shape with a 3-cornered separatrix as a consequence of the closeness of the 1/3 rational surface to the plasma border, where the rotational transform by - period is 0.32, current in the central circular coil is 450 KA and in the - inner helical one - 150 KA.

The rotational transform profile shows a total variation ("shear") of about 8.3%, greater than in a flexible Heliac, for an average plasma radius of 16 cm. No magnetic well, but rather a steep magnetic hill, 11.6% - height, appears. A considerable toroidal effect is visible too at Fig. 2, - this effect can be attenuated, but not suppressed, by shifting slightly outwards the magnetic axis position decreasing the vertical field coil current intensities. Magnetic hill height can be decreased too by the same procedure but in no case a magnetic well can be achieved for the 4-period Helicon. For this particular case the usual rough estimate for the equilibrium β limit

|1| ammounts to 22.4%, a very high value that should need confirmation by 3-D equilibrium analysis yet to be done.

The scans done varying the currents passing by the coils show, as in the Flexible Heliac case, a considerable flexibility, that is, a wide range of rotational transforms values can be attained within the same structure by changing only the electrical currents. This effect appears in Fig. 3 where the value of the rotational transform at magnetic axis is shown for several values of the total current I_T, where $I_T = I_h + I_c$ is the addition of the helical current I_h and the circular one I_c, and is plotted versus I_h/I_T: the ratio between the helical coil current I_h and the total one I_T. The values spanned by $\iota(0)$ range from about 0.99 (I_T = 200 KA, I_h/I_T = -0.8) up to 1.82 (I_T = 550 KA, I_h/I_T = -0.3), a lesser span than in the Flexible Heliac |5|, but a very wide one.

The eight period case has been studied too, good magnetic surfaces have been found for a wide range of currents allowing a variation of the rotational transform at axis from 2.4 to 4.45, high values that suggest a very large equilibrium β limit. In addition slight magnetic wells can be attained (about 2% in depth). These properties give a great interest to this particular configuration.

Another very different kind of magnetic surfaces can be found in this N = 8 case, surfaces that do not circle around the hard core when advancing along the torus, surfaces that instead remain ever at the same side of the core, just like in an l = 1 torsatron with "pusher" coils. An example of this kind of surfaces is shown at Fig. 4, they are obtained for I_c=200 KA, I_h = -20 KA with the magnetic axis placed at 1.50 m plasma average radius is about 12 cm. Rotational transform is remarkably flat and very high 6.72 at axis, a high magnetic hill (9%) is present too.

Finally the twelve period case has been studied too, for this case we have found only torsatron-like magnetic surfaces, achieving lower rotational transform values, plasma average radius of 14.5 cm and a slight magnetic hills. These low t values should give lower β equilibrium limits than in the N = 4 and N = 8 cases.

The absence of heliac-like surfaces in this N = 12 case can be contrasted with the absence of torsatron-like ones in the N = 4 helicon. In fact the torsatron-like surfaces are shrinked to negligeable size, crashed against the outer coil borders in the N = 4 case. The opposite happens in the N = 12 case where the heliac-like surfaces are crashed against the central coils.

REFERENCES:

|1| Yoshikawa, S. Nucl. Fus. 23, No. 5 (1983), 667

|2| Boozer, A.H., Chu,T.K., et al. in Plasma Physics and Controlled Nuclear Fusion Research (Proc. 9th Int. Conf. Baltimore, 1982) Vol. 3, IAEA Viena (1983) 129

|3| Nuhrenberg, J. in Proc. 4th Int. Stellarator Workshop, Cape May, 1982, Vol. 1 Princeton (1982) 298

|4| Hamberger, S.M., Sharp, L.E. in Proc. 5th Int. Stellarator Workshop Schloss Ringberg, 1984, Vol. 2, EUR 9618 EN (1984) 75.

|5| J. Guasp et al. "Physics studies for TJ-II". This same conference.

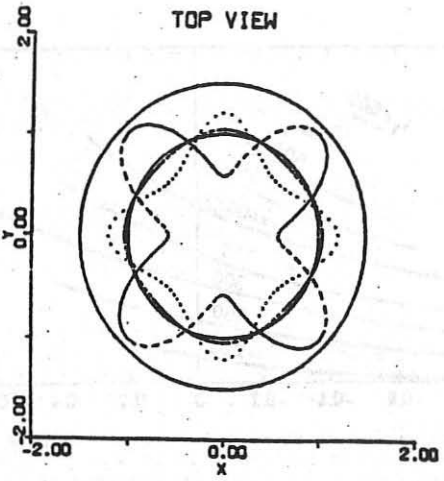

Fig. 1

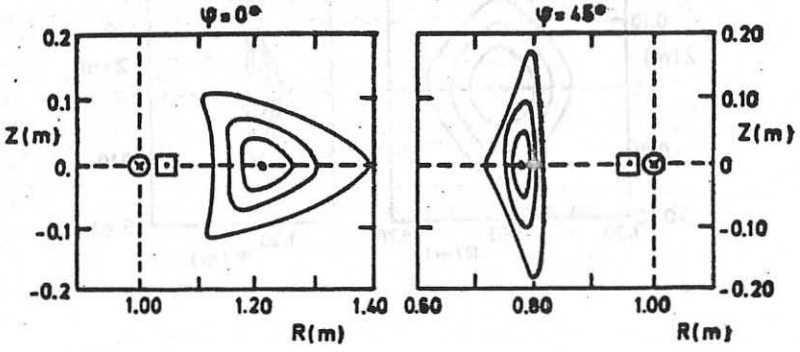

Fig. 2

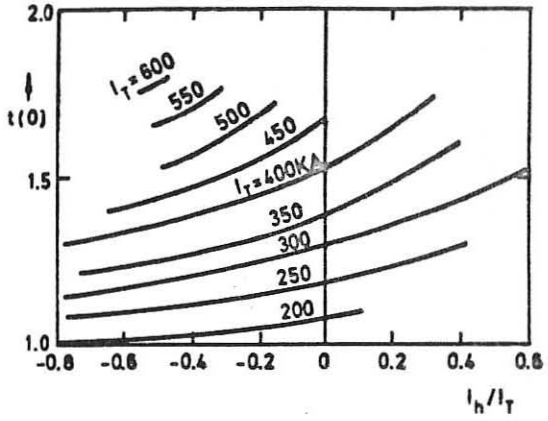
2.0
1.5
1.0
t(0)
I_T=600
550
500
450
I_T=400KA
350
300
250
200
-0.8
-0.6
-0.4
-0.2
0
0.2
0.4
0.6
I_h/I_T

Fig. 3

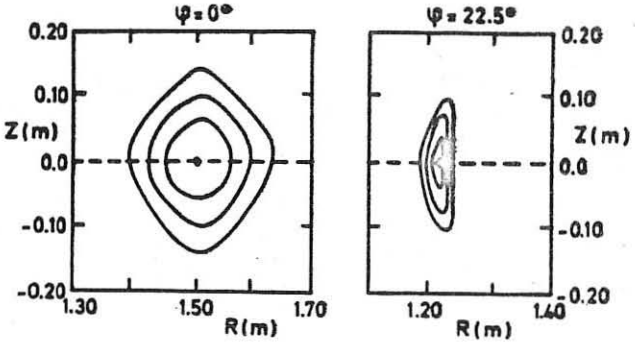
φ=0°
φ=22.5°
0.20
0.10
0.0
-0.10
-0.20
Z(m)
1.30
1.50
1.70
R(m)
1.20
1.40

Fig. 4

PHYSICS STUDIES FOR THE TJ-II DEVICE

J. Guasp, J.L. Alvarez Rivas, J.A. Fábregas, J.A. López Fraguas, A.P. Navarro, A. Perea, E.R. Solano.

Junta de Energía Nuclear (JEN) Madrid, Spain.

J.L. Cantrell, B.A. Carreras, J.H. Harris, T.C. Hender, H.R. Hicks, T.C. Jernigan, V.E. Lynch, J.F. Lyon, J.A. Rome.

Oak Ridge National Laboratory, Oak Ridge, Tennessee, U.S.A.

TJ-II is a medium size helical axis stellarator, to be built at JEN (Spain). The Flexible Heliac |1| has been chosen from a range of alternatives, (l = 2, l = 1 torsatrons, etc) |2 - 3| as the best suited to the Spanish Fusion Program objectives and constraints.

The Flexible Heliac is similar to the conventional Heliac |4| but an additional l = 1 winding has been added to the central conductor structure (Fig. 1) to provide indepent control of the rotational transform (ι_o) over a wide range and to some extend of shear |5|. The configuration adopted as a reference case has four field periods (M = 4), a 1.5 m major radius and a toroidal field coil radius of 0.40 m. The centres of the 32 TF coils are wound on a helix of 28 cm radius and the l = 1 central conductor describes a coincident helix of 7 cm radius. In addition to these coils a pair of vertical coils are required to centre the plasma.

The l = 1 winding gives the device its most characteristic property: flexibility, the capability to attain a wide range of magnetic configurations. In Fig. 2, lines of constant rotational transform per field period (ι_o/M) are shown for some of the achievable range of hardcore currents (I_{cc} = circular coil current, I_{hc} = helical current); the range of ι_o/M values extends over the wide range from 0.2 to 0.8. The magnetic surfaces corresponding to several of the ι_o/M values are shown in Fig. 3. High central conductor currents (particularly I_{hc}) push the plasma off the central conductor structure. Thus following contours of constant ι_o (Fig.2), the larger plasmas occur at the higher currents, with average radii of up to 25 cm being typical. Above some radius larger plasmas are, however, less bean shaped and thus have shallower magnetic wells. Fig. 4 shows this for the ι_o/M = 0.38 contour. The magnetic well depth is also a function of the ι_o value. At low ι_o the wells are very shallow (Typically 0.5%), whereas at high ι_o the wells are much deeper (Typically 6%).

The usual ι profile is very flat with most of the shear at the plasma edge. Some control over the shear can be obtained by providing the l = 1 coil with two independent current feeds such that the centroid of the helical current distribution can be radially shifted. Fig. 5 shows, by powering only the inner turns (r_{cc} = 5.25 cm) or the outer turns (r_{cc}=8.75 cm) of the l = 1 winding, how the shear can be changed from markedly positive to negative. This double control capability on ι profile allows the explora-

tion of an extremely wide range of configurations by changing only the coil currents without any mechanical modifications to the device.

Preliminary studies have been made of 3D equilibria in the TJ-II device. Previous studies for other heliacs have indicated the importance of fine scale control over the ι and shear, to avoid low order resonances where the β limit is very low. Equilibrium studies for TJ-II with both the NEAR code |6| and BETA code|7| have shown that good equilibria exists up to at least β_0 = 8%. By further refinements to the numerics and to the ι ranges studied, it appears probable that this value can be extended. Fig. 8 shows a β_0 = 5% TJ-II equilibrium with ι_0 = 1.46, computed with the NEAR code. So far only the Mercier stability of these equilibria has been studied; in the helically symmetric limit the results of Ref. |8| indicate very favorable stability properties for heliacs. The Mercier results from the BETA code for the TJ-II equilibria studied show stability in all cases.

Initial collisionless orbit calculations show confinement properties similar to the ATF device and a very strong beneficial influence from modest radial electric fields. The effect of the magnetic field ripple is under investigation. The ripple can be significantly reduced near the magnetic axis by toroidally modulating the toroidal field coil currents.

In conclusion, physics studies for TJ-II are in an advanced phase and show that TJ-II has a very wide flexibility, and good magnetic well properties with promising equilibrium and stability β limits. These studies will continue to optimize the TJ-II configuration and to provide information for the design of the device.

ACKNOWLEDGMENTS

We should like to thank F. Bauer, O. Betancourt, and P. Garabedian for providing us with a copy of the NYU BETA code. This work was funded by the US-Spain Committee for Scientific and Technological Cooperation.

REFERENCES:

|1| Harris, J., et al. ORNL/TM-9504 (1984)

|2| Navarro, A.P., et al. in Proc. 5th Intl. Stellarator Workshop Schloss Ringberg, 1982, Vol2, EUR-9618 EN (1984), 563.

|3| Alvarez Rivas, J.L., et al., Bull. Am. Phys. Soc. 29 (1984), 1273.

|4| Yoshikawa, S., Nucl. Fusion 23 (1983), 667.

|5| Perea, A. "Physics Issues in the Design of TJ-II" in this Conference

|6| Hender, T.C. et al., ORNL/TM-9239.

|7| Bauer, F., et al., "Magnetohydrocynamic Equilibrium and Stability of Stellarators " Springer Verlag, New York.

|8| Monticello, et al., Phys. Fluids 27, 1248 (1984).

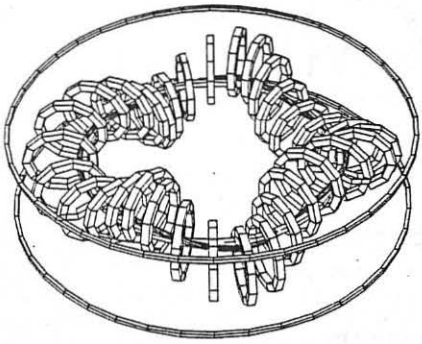

Fig. 1 Coil set for the TJ-II flexible heliac

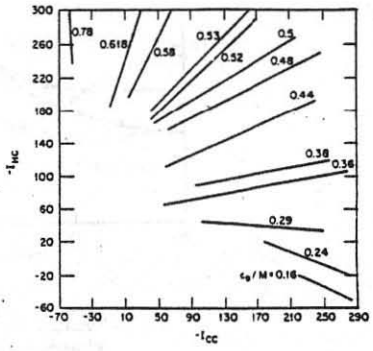

Fig. 2 Contours of ϵ_0/M, showing very wide flexibility which can be achieved by varying central conductor currents

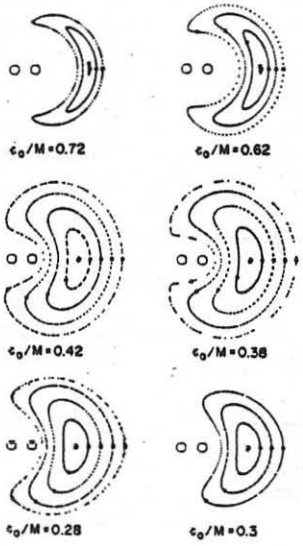

Fig. 3 Flux surfaces for various (ϵ_0/M)

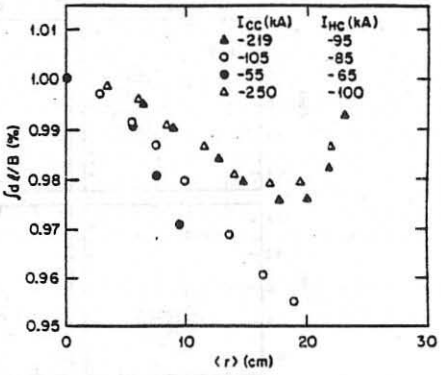

Fig. 4 Variation in magnetic well with current for fixed $\epsilon_0/M = 0.38$

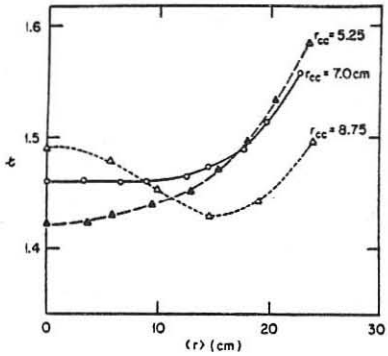

Fig. 5 Variation in ι which can be achieved by shifting the centroid of the 1 = 1 current

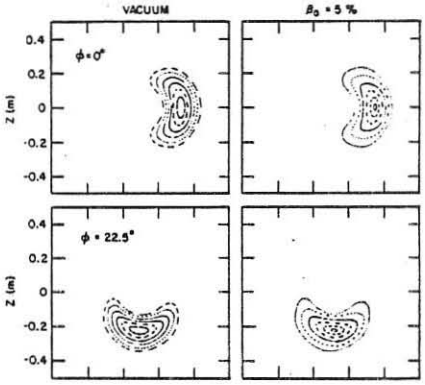

Fig. 6 Vacuum and β_o = 5% equilibrium flux surfaces for ι_o/M = 0.38 configuration

Ballooning Modes in 3D Finite-β Stellarators

J. NÜHRENBERG, R. ZILLE

Max-Planck-Institut für Plasmaphysik,
EURATOM Association, D-8046 Garching

The evaluation of Mercier[1] and resistive interchange[2] modes is followed up by generalizing the JMC code, which evaluates the current density from 3D equilibria as the basic quantity for the investigation of localized instabilities, in order to consider ballooning modes[3] in general 3D equilibria. (Previous work[4] was restricted to low-β approximations.) To this end, Boozer's coordinates[5] are constructed from the equilibria because they may conveniently be used to analyze the ballooning equation. A form of the Mercier criterion is used which is valid on field lines with rational twist. A typical field line of this type in a stellarator with five periods (such as W VII-AS) would have, for example, $\iota_T = 2/5$, where ι_T is the total twist, so that localized $m = 5, n = 2$ modes are considered. The analysis of such modes should not be plagued by existence problems of the equilibrium associated with ι_p (twist per period) being rational of much higher order (2/25 in the above example). The ballooning equation is cast in a form which avoids numerically dangerous cancellations and shows, explicitly, the order with respect to β of the various terms. Thus, the principal stabilizing terms (magnetic well diminished by its diamagnetic part and shear) and destabilizing terms (square of the parallel current density and unfavourable contributions from the field line curvature) are clearly borne out. Moreover, this form of the ballooning equation readily yields the asymptotic behaviour (for large arguments) which recovers the Mercier criterion in an analogous form. This feature not only facilitates testing of the code but may also be used to obtain the ballooning stability condition by asymptotic matching. Results are presented for tokamaks (as test cases) and 3D stellarators such as ATF and W VII-AS.

In Boozer's coordinates s, θ, ϕ, where s is the flux label and θ, ϕ are poloidal and toroidal angle-like variables, respectively, the local shear σ can be written in the following form

$$\begin{aligned}\sigma &= |\nabla s|^{-4}(\nabla s \times \vec{B}) \cdot \vec{\nabla} \times (\nabla s \times \vec{B}) \\ &= F_T^2 \iota'/\sqrt{g} + \vec{B} \cdot \nabla (I g_{\theta s}/\sqrt{g}|\nabla s|^2 - J g_{\phi s}/\sqrt{g}|\nabla s|^2)\end{aligned}$$

[1] Mercier, C., in Plasma Physics and Contr. Nucl.Fusion Res.1961, Nucl.Fus.1962, Suppl.2, IAEA, Vienna (1962) 801; R. Großmann, F. Herrnegger, J. Nührenberg, Proc.Sherwood Theory Conf., Arlington 1983, 1S21

[2] J. Nührenberg, R. Großmann, Proc.Sherwood Theory Conf., Incline Village 1984, 2R6; 5th Int.Workshop on Stellarators, Schloß Ringberg 1984, Comm.EC, EUR 9618 EN, I, 339

[3] D. Correa-Restrepo, Z.Naturforsch.**33a** (1978) 789

[4] H.L. Berk, M.N. Rosenbluth, J.L. Shohet, Phys.Fluids **26** (1983) 2616; W.A. Cooper, T.C. Hender, Plasma Phys.and Contr.Fus. **26** (1984) 921

[5] A. Boozer, Phys.Fluids **23** (1980) 904

Here, all functions are normalized to one field period of the equilibrium; F_T, J toroidal flux and current, F_P, I poloidal flux and current, $\iota_p = F_P'/F_T'$, $' = d/ds$, $p'V' = I'F_T' + J'F_P'$, $\sqrt{g}B^2 = -F_T'I - F_P'J$. The ballooning equation can then be reduced to the following equation for F (which indicates instability if F vanishes twice)

$$\frac{d}{d\phi}\left\{a^{-1}[1+(\bar{\sigma}\phi+\tilde{\sigma})^2]\frac{dF}{d\phi}\right\} + (\bar{D}\phi+\tilde{D})F = 0$$

Here, ϕ is used as the variable along the field lines and the coefficients a^{-1}, $\bar{\sigma}$, $\tilde{\sigma}$, $\bar{D}$, $\tilde{D}$ have to be used as function of this variable,

$$\begin{aligned}
a &= \sqrt{g}|\nabla s|^2 \\
\bar{\sigma} &= -F_T'\iota'|\nabla s|^2/B \\
\tilde{\sigma} &= (Ig_{\theta S} - Jg_{\phi S})/\sqrt{g}B \\
\bar{D} &= p'\iota' F_T'^{-1}(IB^{-2}{}_{,\theta} - JB^{-2}{}_{,\phi}) \\
\tilde{D} &= [\sqrt{g}p'^2/B^2 - p'\sqrt{g}_{,S} - p'B^{-2}(IF_T'' + JF_P'') + p'\sqrt{g}\vec{B}\cdot\nabla(\tilde{\beta}B^2)]/F_T'^2
\end{aligned}$$

Here, $\tilde{\beta}$ is the periodic part of the function β in the covariant representation of $\vec{B}$ ($\vec{B} = \nabla\chi + \beta\nabla s$). $\tilde{\beta}$, $\bar{D}$, and $\tilde{D}$ can be reduced as follows

$$\begin{aligned}
\tilde{\beta} &= -(F_T'g_{\phi S} + F_P'g_{\theta S})/\sqrt{g} \\
\sqrt{g}\vec{B}\cdot\nabla\tilde{\beta} &= p'(\sqrt{g} - V') \\
\bar{D} &= -F_T'^{-1}\iota'\sqrt{g}\vec{B}\cdot\nabla X, \qquad X = j_{\|}/B \\
-p'B^{-2}(IF_T'' + JF_P'') &= \sqrt{g}V'^{-1}[I'F_T'' + J'F_P'' + \iota' F_T'^2(I'J - J'I)/(IF_T' + JF_P')]
\end{aligned}$$

Thus, $\bar{\sigma}$ represents the stabilizing influence of the shear, $\tilde{D}$ (for stellarators with vanishing net toroidal current) mainly the stabilizing influence of an outwardly increasing B^2 diminished by the diamagnetic effect, $\bar{D}$ the terms connected with $j_{\|}$ and with the shear known from Mercier's criterion. In accordance with the explicit resemblance of this form of the ballooning equation with Mercier's criterion, the well-known asymptotic analysis, $F \propto \phi^\nu + F_1\phi^{\nu-1} + \ldots$, readily recovers that criterion in the form of the indicial equation

$$\nu = -.5 \pm [(.5 - \langle a\mathcal{D}/\bar{\sigma}^2\rangle)^2 - \langle a/\bar{\sigma}^2\rangle(\langle a\mathcal{D}^2/\bar{\sigma}^2\rangle + \langle\tilde{D}\rangle - \langle\mathcal{D}\rangle)]^{\frac{1}{2}}$$

where $\mathcal{D} = \int D d\phi = \iota' X$. This equation may also be used to obtain a partial test of four of the five coefficients of the ballooning equation which is solved in the following way. Relatively low order rational toroidal twist numbers are considered and the contracted variable $\bar{\phi} = N^{-1}m_i^{-1}\phi$ is used where $\iota_T = \frac{n_i}{m_i}$, N number of field periods. The coefficients of the ballooning equation are periodic in $\bar{\phi}$, so that the above averages $\langle\ \rangle$ are well defined. Stellarator equilibria of the usual symmetry are considered, so that it is possible to consider ballooning modes symmetric with respect to $\bar{\phi}$. Thus, $F(0) = 1, (dF/d\phi)(0) = 0$ is used and a ballooning instability is found if $F = 0$ for $\bar{\phi} > 0$.

The 3D equilibrium code used so far is BETA[1]; the JMC evaluation code only uses the flux invariants and the geometry of the equilibrium obtained, reconstructs the remainder of the equilibrium information, constructs Boozer's coordinates and obtains the coefficients of the ballooning equation. By way of example, Fig.1 shows a, $\tilde{D}$ for W VII-AS for $\iota_T = \frac{2}{5}$, note the three different scales: the equilibrium period, the poloidal period, and the period of the closed field line. All results shown are obtained with finite but reasonably fine meshes – the choices being guided by the experience in extrapolating Mercier's criterion – and are being complemented by extrapolation studies; Fourier convergence problems typical of magnetic coordinates also need further study.

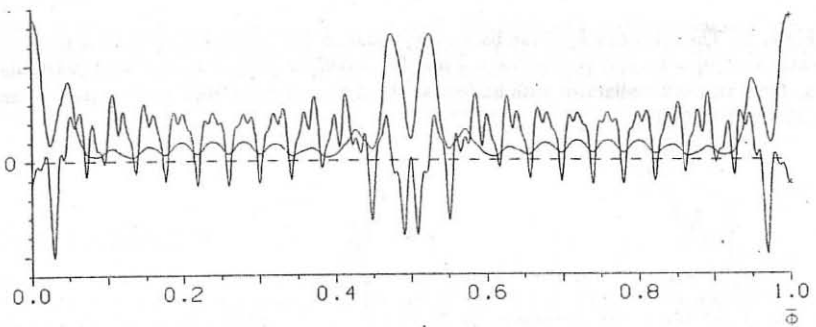

Fig.1. The coefficients a (+) and $\tilde{D}$ (×) for a W VII-AS equilibrium with $\iota_T = \frac{2}{5}$ and $\langle\beta\rangle = 0.028$.

Test results have been obtained for axisymmetric equilibria and a simple unstable $\ell = 2$ stellarator. Figure 2a shows F for $\iota_T = \frac{2}{3}$ in a standard circular tokamak at $\langle\beta\rangle = 0.02$; 0.03, below and above the ballooning stability boundary. Figure 2b shows F for $\iota_T = \frac{2}{5}$ in an $\ell = 2$ stellarator with five periods. Since for this twist value and a purely elliptic boundary no vacuum magnetic well is present, instability is seen at all β values and the ballooning character ($F = 0$ at $\bar{\phi} < n_\iota^{-1}$) prevails for $\langle\beta\rangle > 0.002$.
Results for W VII-AS and ATF are shown in Fig.3. The common feature is that the instabilities found are of the Mercier type, i.e. driven by the parallel current density ($\langle aD^2/\bar{\sigma}^2\rangle$) and occurring in the asymptotic range. Apparently, in these cases ballooning instability proper occurs at larger β-values than Mercier instability (in contrast to the tokamak situation). It will be interesting to see whether this behaviour persists in configurations in which Mercier instability occurs at higher β-values. In this connection we mention an $\ell = 1$, 2, 3 equilibrium encountered in the search for stable medium-β stellarators. The equilibrium shown in Fig.4 is Mercier stable at $\langle\beta\rangle = 0.05$. Ballooning stability results for this configuration are being obtained.

[1]F. Bauer, O. Betancourt, and P. Garabedian Magnetohydrodynamic Equilibrium and Stability of Stellarators (Springer, New York, 1984

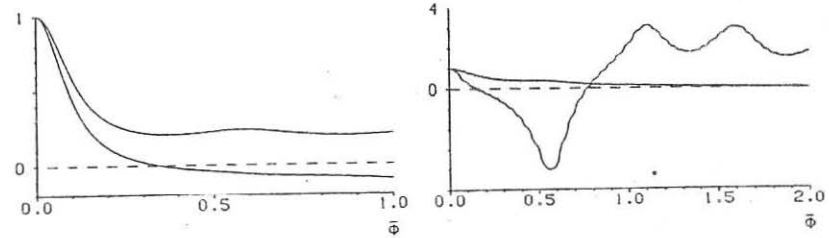

Fig.2. a. The solutions F of the ballooning equation for a circular tokamak with aspect ratio 3, $\iota_T(0) = 1, \iota_T(1) = \frac{1}{3}$ for $\iota_T = \frac{2}{3}$ and $\langle\beta\rangle = 0.02$ (stable) and $\langle\beta\rangle = 0.03$ (unstable). b. F for an $\ell = 2$ stellarator with half-axes ratio 2, aspect ratio 7.5, 5 periods, $\iota_T = \frac{2}{5}$ and $\langle\beta\rangle = 0.0012; 0.01$.

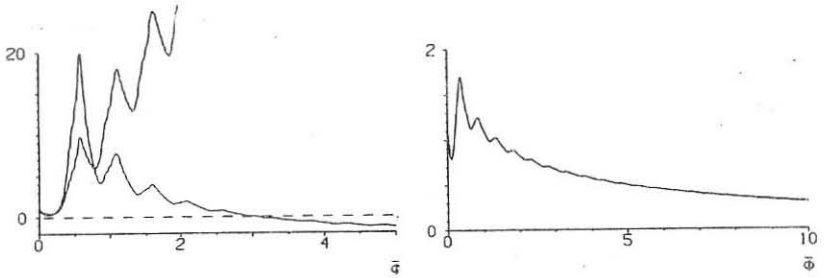

Fig.3. a. F for W VII-AS equilibria with $\langle\beta\rangle = 0.014$ (stable) and 0.028 (unstable) for $\iota_T = \frac{2}{5}$. b. F for an ATF equilibrium (standard flux-conserving case) with $\langle\beta\rangle = 0.033$ for $\iota_T = \frac{2}{3}$. This case is weakly Mercier unstable; $F = 0$ at $\bar{\phi} \approx 100$.

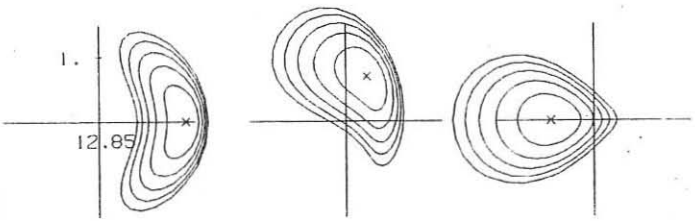

Fig.4. Flux surfaces of an $\ell = 1, 2, 3$ equilibrium which is stable with respect to Mercier and resistive interchange modes at $\langle\beta\rangle = 0.05$.

On Conventional and Modular Heliacs

E. Harmeyer, J. Kisslinger, F. Rau, H. Wobig

Max-Planck-Institut für Plasmaphysik, EURATOM-Association
D-8046 Garching

Abstract

For conventional and modular Heliacs with 4...8 field periods vacuum field properties, guiding center trajectories, and (for specific cases) 3D-Monte-Carlo computations of a particle diffusion coefficient are evaluated numerically. Although less flexible in their parameter range, modular Heliacs avoid an interlinked coil system, and thus are more reactor relevant than conventional systems.

Heliac Configurations

Among Stellarators, the Heliacs are characterized by a helically shaped magnetic axis, by a specific indentation of the outer flux surfaces, and by a reasonably low aspect ratio. The Heliac offers prospects for stable plasmas at comparatively large values of ß, due to its large rotational transform and magnetic well /1/.

Magnetic fields of conventional Heliacs are produced /1/ by a system of planar toroidal field coils arranged helically around a center current ring, and using an appropriate vertical field. Their rotational transform increases with the number of field periods and with the ratio of the helical to the major radius of the coil arrangement. A magnetic well can be obtained. The parameter range can be extended e.g. by a further helical conductor close to the center current ring /2/.

Heliac configurations can also be realized by modular coil systems. They avoid the interlinked arrangement of the conventional Heliac coils. As compared to planar noncircular coils /3/, nonplanar (twisted) coils are preferred since they allow a larger distance between the coils and the last magnetic surface, and also provide for a deeper magnetic well /4/. An analytic winding law for twisted coils is described in /5/.

In Heliacs with equally spaced toroidal field coils a comparatively large modulation of the magnetic field strength along the magnetic axis arises. It can be reduced considerably by different coil currents, or by proper arrangement of the coils in the toroidal direction. By the latter method, simultaneously, at outer flux surfaces broad minima of mod B can extend helically along the field period /4/.

Reference Cases

The present paper is concerned with a study of conventional and modular systems of m = 4...8 field periods. The magnetic properties of vacuum fields are obtained by numerical computations. Typical values of the rotational transform per field period are ι_m = 0.3...0.4; the shear is small, but a magnetic well can be ensured in many cases.

As examples for the various configurations studied, Fig. 1 and 2 show in the left part the coil arrangements and in the right half flux surfaces of the vacuum magnetic field, for a conventional Heliac with 4 field periods, and a reactor-sized modular system with 5 field periods, respectively. Some characteristic data are listed in the inserts. For the conventional Heliac the plane circular TF coils are tilted and placed at different toroidal distances. The vertical field coils are not shown. Note the close distance between the center ring and the last magnetic surface. In the reactor sized modular configuration, a distance D = 1.8 m is chosen between the last magnetic surface of Fig. 2 and the coils, such as to allow sufficient space for blanket and shield.

Magnetic field properties of conventional and modular Heliacs of 4 and 8 field periods are listed in Table I. For the cases with 8 field periods the major radii and the coil aspect ratios are twice those of the systems with m = 4.

Table I: Heliac Reference Configurations

		Conventional		Modular		
field periods	m	4	8	4	8	
av. major radius	R_o	1	2	2	4	m
av. minor radius	r	13.5	15.1	28.7	27.3	cm
rotational transform						
axis		1.18	2.78	1.63	3.32	
edge		1.29	3.03	1.53	3.24	
magnetic well	V"	-2.0	-0.8	0.9	-0.7	%

As a figure of merit for comparison of the different configurations we use the quantity

$$J^* = \langle \frac{B_o^2}{B^2} \cdot (1 + \frac{j_\parallel^2}{j_\perp^2}) \rangle$$

where B_o is a reference field and $\langle \ldots \rangle$ denotes the average on a magnetic surface. J* is a measure for the Pfirsch-Schlüter-currents, and also enters the stability criterion of resistive interchange modes /7/. Small J* is favourable for interchange stability. This number is about 11 for a standard ℓ = 2 Stellarator like WENDELSTEIN VII-A and can decrease to J* $\simeq$ 2 in the 8-period Heliac.

Low Pfirsch-Schlüter currents lead to a small Shafranov shift and high values of the equilibrium ß. Using the BETA-code /8/, a finite-ß equilibrium in a 5-period modular Heliac was calculated. At $\langle ß \rangle$ = 5.3 % a small Shafranov shift of 10 - 20 % of the plasma radius occurred /9/.

Fig. 1: CONVENTIONAL HELIAC

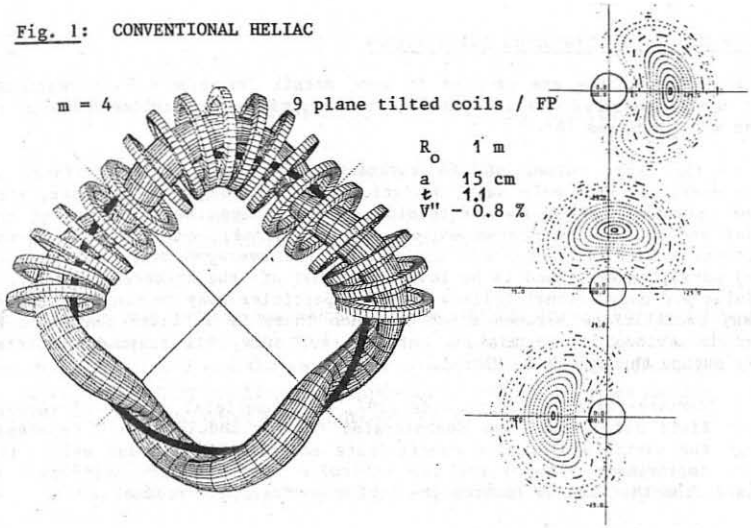

Fig. 2: MODULAR HELIAC

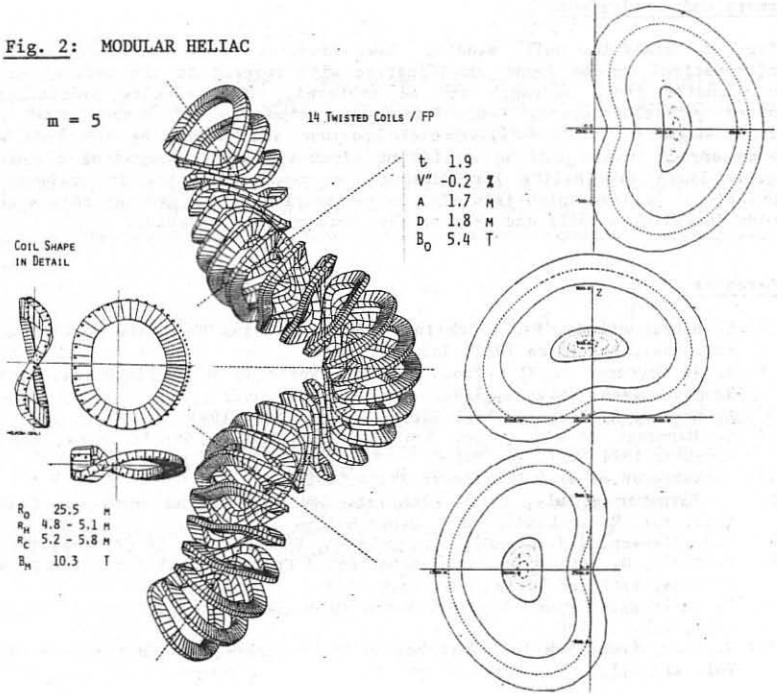

Particle Orbits and Transport Calculations

Guiding center orbits are studied in more detail for a m = 8 conventional Heliac with reduced field modulation, in comparison to earlier results of modular m = 5 systems /6/.

Due to the large values of the rotational transform, drift surfaces of passing particles show only small deviations from the magnetic surfaces, with maximum (minimum) offset in the toroidal planes where the direction of the toroidal and helical curvatures are opposite (parallel), respectively. In the configuration with reduced field modulation, the averaged drift velocity of trapped particles was found to be lower than that of the standard case. Both, in modular and conventional Heliacs, trapped particles stay on confined orbits for many oscillations between mirrors. Since there is a finite chance to be trapped in a local field minimum between two coils, all trapped particles finally escape through this channel.

Using a 3D-Monte-Carlo transport code /10/, the beneficial effect of reduced magnetic field modulation was demonstrated /6/ for modular m = 5 systems. Although the particle diffusion coefficients exceeded the plateau value, the relative improvement between the two otherwise nearly equal configurations increased from the plateau towards the long mean-free-path regime.

Summary and Conclusions

Using an analytic coil winding law, modular coil sets for Heliac configurations can be found. Optimization with respect to the modulation of the magnetic field strength can be achieved, thus reducing neoclassical trapped particle losses. Comparing field properties of conventional and modular Heliacs with m = 4...8 field periods and increasing the coil and plasma aspect ratios with m, so far no clear preference regarding m can be stated. Large flexibility for varying the parameter range is present in conventional heliacs which is useful in an experiment. The modular coil system avoids interlinked coils and thus appears more reactor relevant.

References

/1/ A. Boozer et al., Proc. 9th Int. Conf. on Plasma Phys. and Contr. Nucl. Fus. Res., Baltimore 1982, Vol. III, 129

/2/ B. A. Carreras et al., Proc. 5th Int. Workshop on Stellarators, Schloß Ringberg 1984, Vol. II, 729

/3/ A. Reiman, A. Boozer, Phys. Fluids 26 (11) Nov. 1983

/4/ E. Harmeyer et al., Proc. 5th Int. Workshop on Stellarators, Schloß Ringberg 1984, Vol. II, 749

/5/ E. Harmeyer et al., IPP report 2/274, 1985

/6/ E. Harmeyer et al., Proc. 10th Int. Conf. on Plasma Phys. and Contr. Nucl. Fus. Res., London 1984, paper H-II-4

/7/ A.H. Glasser, J.M. Greene, J.L. Johnson, Phys. Fluids 18 (7) July 1975

/8/ F. Bauer, O. Betancourt, P. Garabedian, A Computational Method in Plasma Physics, Springer Verlag, New York 1978

/9/ F. Herrnegger, Proc. 5th Int. Workshop on Stellarators, Schloß Ringberg 1984, Vol. I, 401

/10/ W. Lotz, Proc. 5th Int. Workshop on Stellarators, Schloß Ringberg 1984, Vol. II, 493

STELLARATOR EQUILIBRIUM BY LOW-BETA-EXPANSION

J. Kisslinger, H. Wobig

Max-Planck-Institut fuer Plasmaphysik
EURATOM ASSOCIATION, D-8046 Garching

Abstract

A numerical code is developed which calculates a Stellarator equilibrium following the low beta expansion as proposed by L. Spitzer /1/. In every iteration step the plasma currents are calculated and the resulting magnetic field is obtained from Biot-Savart's law. Since no boundary conditions are imposed, the method describes the free boundary equilibrium. Results are given for Wendelstein VII-A .

Low-beta expansion

In the ideal MHD-model of toroidal plasma equilibrium the scalar pressure p and the magnetic field $\vec{B}$ are calculated from

$$0 = -\nabla p + \vec{j} \times \vec{B} \quad ; \quad \nabla \times \vec{B} = \vec{j} \tag{1}$$

Several codes have been developed to solve these equations in three dimensions/2//3//4/. In all these codes boundary conditions are imposed on the last magnetic surface. In a steady state plasma, however , a conducting wall is only effective on a time scale short compared with the resistive diffusion time. Therefore a conducting wall is only effective for MHD-stability . The AJW-code /5/ calculates the Stellarator equilibrium in axisymmetric approximation, this method includes the free boundary equilibrium.

The iterative process proposed by L. Spitzer tries to solve the system (1) in the following way:

$$\left\{ \begin{array}{ccc} & 0 = -\nabla p + \vec{j}_{n+1} \times \vec{B}_n & \\ \nabla \cdot \vec{j}_{n+1} = 0 & \nabla \times \vec{B}_{n+1} = \vec{j}_{n+1} & \nabla \cdot \vec{B}_{n+1} = 0 \end{array} \right\} \tag{2}$$

$$n = 1, 2, \ldots$$

there is neither a prove that this iteration process converges nor is the topology of magnetic surfaces preserved. As pointed out by A. Boozer /6/ magnetic islands and field line ergodisation may occur. Nonetheless an attempt is made to calculate $\vec{B}$ from the system (2). The plasma current $\vec{j}_{n+1} = p'(\psi) \quad \nabla\nu \times \nabla\psi$ is calculated on the magnetic surface ψ = const. of the nth-iteration step. We only calculate $\vec{j}_{n+1}$ on magnetic surfaces without islands and ergodisation thus representing a pressure profile with $p' = 0$ in the island region. The stream function ν is calculated from

$$\vec{B}_n \cdot \nabla\nu = 1 \tag{3}$$

The constant of integration is chosen such that the current lines ν = const. are poloidally closed curves, thus representing a net current free Stellarator. In figure 1 this system of

equilibrium currents on a magnetic surface of W VII-A is shown. Figure 1 exhibits one period of a magnetic surface, horizontal axis being the toroidal coordinate and the vertical axis being the poloidal coordinate.

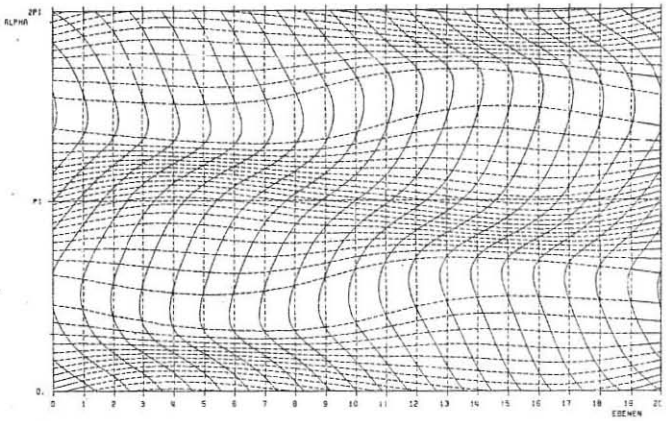

Fig. 1: Plasma currents on a magnetic surface of W VII-A (solid lines).

The typical S-shape of the plasma currents (solid curves) is caused by the Pfirsch-Schlueter currents $j_{\parallel}$ giving rise to the Shafranov shift. For calculating the magnetic field the continuum of these plasma currents is replaced by a finite set of current filaments $\nu =$ const with all filaments on a magnetic surface carrying the same plasma current. Since the current is proportional to the pressure gradient the radial current distribution is fixed by the pressure profile. Every current filament is discretized into a maximum of 64 straight elements and the field $\vec{B}^{*}_{n+1}$ at a point $\vec{x}$ added up over all current filaments following Biot - Savart's law. The element crossing $\vec{x}$ is omitted thus avoiding the divergence of $\vec{B}$ at $\vec{x}$. With the help of a relaxation parameter α the next iteration step $\vec{B}_{n+1} = \alpha \vec{B}^{*}_{n+1} + (1-\alpha)\vec{B}_n$ is defined. By field line integration the surfaces of $\vec{B}_{n+1}$ are found and the procedure is continued. The points $\vec{x}$ are chosen on the magnetic surfaces of $\vec{B}_n$. If the procedure converges - i.e. if the surfaces of $\vec{B}_n$ and $\vec{B}_{n+1}$ approach each other - the result is independent of the the parameter α.

As a practical measure of convergence the profile of the rotational transform ι is used. In applying the code to W VII-A it was found that after 10 iterations the Shafranov - shift and the shape of the magnetic surfaces saturate. About 20 - 30 iterations are necessary to make the error in ι less than 10^{-3}. The plasma currents lead to a modification of the profile of the rotational transform. In W VII-A the transform increases at the magnetic axis and decreases at the edge thus giving rise to an appreciable amount of shear.

In figure 2a the modification of the transform with increasing β is shown. For comparison figure 2b shows the result of the AJW-code (see also ref. /7/). The maximum shear at $\beta(0) = 1.5\%$ is $\delta\iota/\iota = 20\%$.

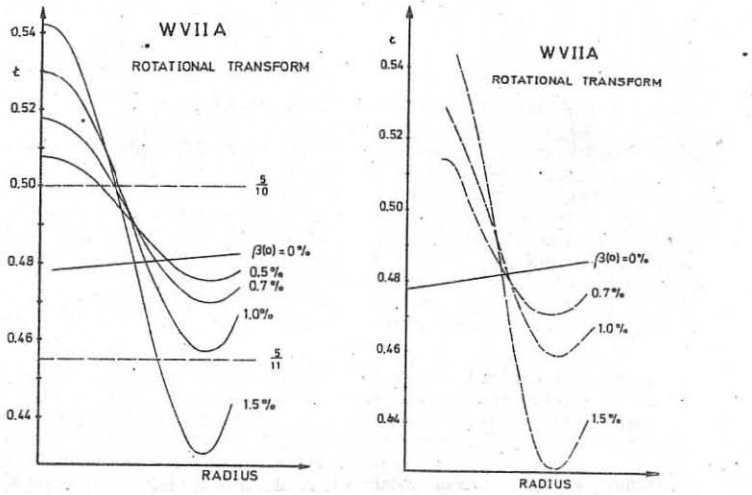

Fig. 2b (right): ι-profile of W VII-A as a function of plasma pressure. 2a(left): ι-profile W VII-A from AJW-code.

In order to improve the convergence the relaxation parameter α can be changed during the iteration. Convergence depends on the β -value chosen. At low β fewer iteration steps suffice, whereas at higher values ($\beta(0) > 1.5\%$ in W VII-A) the iteration process collapses due to island formation. It is not yet clear wether this is an indication of a real β -limit or wether numerical errors determine this limit.

Magnetic surfaces. The magnetic surfaces of W VII-A are shown in figure 3. The peak value of β is 1.5% in this case. As can be seen the Shafranov shift varies with toroidal angle, the maximum shift arises in the plane of the horizontal ellipse. At $\beta = 1.5\%$ ergodisation of magnetic surfaces begins to appear, calculation of plasma currents, however, averages over this fine structure and a further increase does not occur during the iteration process. At $\beta = 2\%$ island formation and ergodisation limit the iterative process and an equilibrium cannot be found. Island formation predominantly arises around $\iota = 5/10, 5/11, 5/12...$ with 10, 11, 12, ... islands. In a system with stronger shear and more field periods around the torus a reduction of this effect is expected. As an excample Heliotron E has been investigated. Heliotron E has a strong shear and 19 field periods. Here equilibria with $\beta(0) = 5\%$ can be calculated without serious island formation.

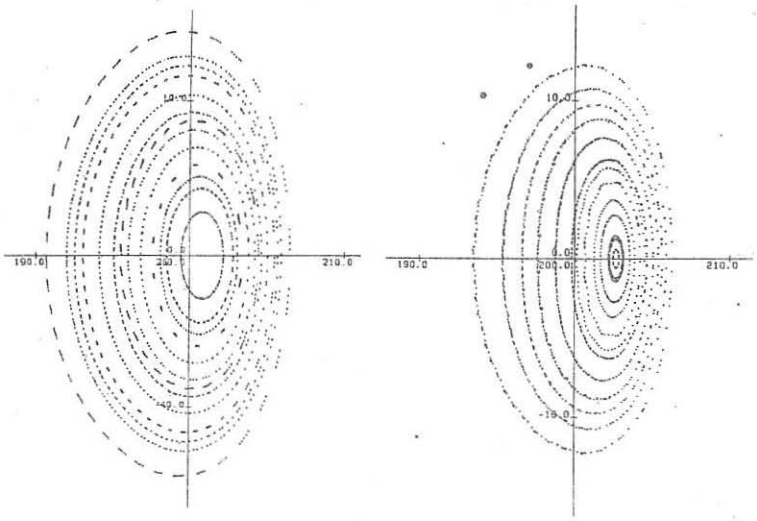

Fig. 3: Magnetic surfaces of Wendelstein VII A at finite β. left: $\beta(0) = 0.5\%$ right: $\beta(0) = 1.5\%$

Conclusions. The low-β iterative process permits to calculate 3-dimensional Stellarator equilibria with a free boundary. At sufficiently low β convergence can be achieved. Depending on the specific configuration (number of field periods, shear) ergodisation and island formation on magnetic surfaces determine the maximum β. So far it cannot be decided whether this break-up of surfaces is due to numerical errors or due to a physical effect. Other effects like rotational transform, magnetic well and Shafranov shift can be calculated with an accuracy sufficient for practical purposes.

References

/1/ L. Spitzer, Phys. Fluids 1958, Vol. 1 p.253 - 264
/2/ R.Chodura, A. Schlueter, J. Comput. Phys. 41 (1981) 68
/3/ F. Bauer ,O.Betancourt, P.Garabedian, A Computational Method in Plasma Physics, Springer Verlag, New York
/4/ T.C.Hender, B.A.Carreras, L.Garcia, J.A.Rome, V.E.Lynch, ORNL-report ORNL/TM 9239
/5/ G.Anania, J.L.Johnson, K.E.Weimer, Phys. Fluids 26,2210 (1983)
/6/ A. Boozer, Phys. Fluids 27 (8) Aug. 1984
/7/ F.Herrnegger, Proc. of the IAEA Techn. Com. Meeting on Plasma Confinement and Heating in Stellarators. Sept. 1984 EUR 9618 Vol.I p.401

IMPROVEMENT OF MAGNETIC SURFACES OF HELICAL AXIS TORSATRON

S.Nagao, S.Miyajima, M.Fujii, T.Saito and H.Katsumori
Engineering School, Chubu University, Kasugai, 487 Japan

Y.Abe and M.Fujiwara
Institute of Plasma Physics, Nagoya University, Nagoya, 464 Japan

ABSTRACT The improvement of magnetic surfaces of torsatron type stellarator with a closed helical magnetic axis (HAT), which was proposed previously (Ref. 1), are studied, since in the examples of magnetic surfaces there the radius of axial helix was rather small and so the stable confinement of high beta plasma seems to be difficult, though the aspect ratio of plasma column was so small as to be less than 8 even in the case of period number n = 9. Thus the method to improve such magnetic surfaces of HAT has been considered from the fundamental viewpoint of coil engineering upon the theoretical base. It was clarified that the compatibility of magnetic well and positive shear of field lines is not so easy to be realized in the framework of HAT, though the other characteristics of magnetic surfaces were improved to a great extent.

INTRODUCTION Recently it has become well known that the stellarator with a planar magnetic axis of appropriate period number, for example n = 6 of ATF-1, can have the compatibility of magnetic well and shear of filed lines in its configuration and however the interaction of toroidal curvature effect with the plasma pressure might destroy the helical symmetry of the system and so the beta value may be limited less than ten percent. On the other hand, in the helical axis stellarator system the toroidal curvature effect is rather small and the helical symmetry may be improved by the plasma pressure. Thus the plasma self-stabilization can be expected to achieve a high beta confinement. However in such helical axis stellarators, there are some technical difficulties: the helical axis of large radius makes the device manufacturing too complicated and the plasma aspect ratio becomes too large to be a candidate of fusion reactor in future.

Then it was proposed in the previous report to fabricate a helical axis stellarator by torsatron method. It is technically important that the device HAT as a whole is of the type of a simple torus and the plasma column only rotates helically insides, occupying the half of its circular cross section of torus, while the other half space of the cross section is left to be used for divertor region.

SURFACE CURRENT OF FIELD CONFIGURATION AND HAT COILS It is easy to show that the surface current K, given by Biot-Savart law to produce one of the best magnetic surfaces Ψ, considered in the linear helix approximation (Ref.2), consists of three components in Mercier coordinate system (ρ, ω, s),as follows,

$$K_{\omega} = (I / h) , K_{u1} = - (\kappa\rho\, I / h) \quad \text{and} \qquad (1)$$

$$K_{u2} = | \nabla \Psi | ,$$

where $h = 1 - k\rho\cos\theta$, $\theta = \omega - \kappa s$, $\vec{u} = (h\vec{e}_s + \kappa\rho\,\vec{e}_{\omega})/ g$ and

$$g = h^2 + (\kappa\rho)^2$$

I is axial field and k and κ are curvature and torsion of axial helix. K_{ω} component is solenoidal current on the circular surface around the axis but has to be approximated by a helical coil current, in torsatron type system, with pitch angle as large as possible. It is noticeable that K_{u1} is necessary to produce axial field I as well as K_{ω}. K_{u2} component to shape the magnetic surface can be approximated fairely well by several auxiliary helical coil currents in the vicinity of the outer most magnetic surface. Fig. 1 shows these surface current K_{u1} and K_{u2} as a function of azimuthal angle θ.

Thus it is obvious that the auxiliary helical coils to shape the magnetic surface should be located approximately at angles θ = 0 , 68 , 135 and or 180 respectively. However these locations are in Mercier coordinate system and so these coordinates must be transformed into rectangular system in order to compute the magnetic surface or for their manufacturing. Fig. 2 shows the change og the azimuthal angle in the rectangular system ϕ, which corresponds to θ above mentioned, as function of distance from the axis ρ. The location for each auxiliary helical coil in the case of a closed helical axis is determined refering to Fig. 2.

MODIFICATION OF HELICAL AXIS IN TOROIDAL SYSTEM In the toroidal system with a closed helical axis, it is well known that the axis can have many variations for example, as given by parameters (α, β,ε and ε') in its expression,

$$r = R\,(\,1 - \varepsilon \cos \omega_{\sigma}\,), \qquad z = \varepsilon' R \sin \omega \quad , \tag{2}$$

$$\omega_{\sigma} = n\,\phi + \alpha \sin n\,\phi + \beta \sin 2n\,\phi + \ldots$$

The first aim of survey of these parameters is to recover the helical symmetry, lost partly by the toroidality and to have the aspect ratio as small as possible. The second is to reduce the plasma column shift by its pressure and to have the beta value as large as possible.

As for the recovery of helical symmetry, it was shown in Ref. 3 that the additional non-symmetric terms of magnetic surface function $\Delta\Psi$ becomes minimum when

α is nearly equal to $-2.5\,h\varepsilon R / n$.

and moreover when the swing of the magnetic surface has to be in the same phase to the modulation of axis. In Fig. 3 is shown an example of the surface, which has the smallest aspect ration in the present survey of 7.0 in the case of period number n = 7. The measured value of α from the figure is 0.2, while the relation above mentioned gives the value of 0.19. The large shear (ι_{σ}= 0.9 to $\iota_{\mathscr{g}}$ = 1.5) and very high magnetic hill of 15 % to the great regret may also be another evidence of the recovery of helical symmetry.

Equ.(2) can also be used for the survey of axial parameters to deduce the plasma column shift by its pressure and to have a high beta plasma equilibrium. Fig. 4 shows the shift of column with circular cross section, given by Shafranov, as function of α. Here it is interesting to notice that the value of α which gives the minimum column shift, is nearly equal to gives minimum variation of the axial torsion along the torus and the integral of the torsion over one period nearly equal to π.

Thus to increase the rotational tranform on the axis ι_{σ} , another helical coil is added on the opposite to the main toroidal field coil. The positive current on this coil increases the ellipticity of the magnetic surface and so increases the transform on the axis.

Fig. 5 and Fig. 6 show the magnetic surfaces with same ellipticity but with different values of α. In the former α is 0.15, where the rotational transform varies from 1.5 on the axis to 2.0 on the outermost surface and in the latter case, it varies from 1.9 to 2.5 for the sake of negative value of α (= -0.4), which is nearly equal to the value of constant torsion and its integral being π.

Unfortunately, both examples of magnetic surface could not have well configuration but magnetic hill of more than 10 %.

FORMATION OF MAGNETIC WELL In the parameter survey carried out so far, the magnetic well configurations are realized only in the vicinity of the helical axis or in the cases of very large aspect ratio. It seems that the main reason for the failure may be the replacement of toroidal surface current K_{u1} in Equ. (1) by the main helical coil current. Further investigation is needed to continue in this direction.

CONCLUSION The toroidal field configuration with a closed helical magnetic axis is shown to be realized by the torsatron type helical coils, where the plasma column aspect ratio is in the range from 7 to 8 and rotational transtransform from 1.9 on the axis to 2.4 on the outermost surface.

However it is needed to continue the investigation to have the compatibility of magnetic well and shear of field lines further.

REFERENCE (1) N.Sasaki, Y.Abe, S.Nagao et al.: 11-th Europ. Conf. Controlled Fusion & P.P., Aachen,5-9 Sept. 1983, Contr. Papers P-1 p.233 (2) L.S.Solovev and V.D.Shafranov : Reviews of Plasma Phys., vol. 5 (3) S.Nagao et al. 7-th Symp. Eng. Prob. Fusion Res. M-17 Knoxville, 25-28 Oct. 1977.

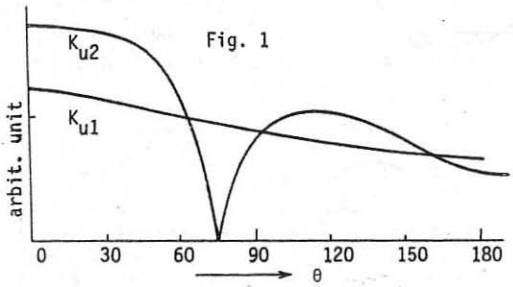

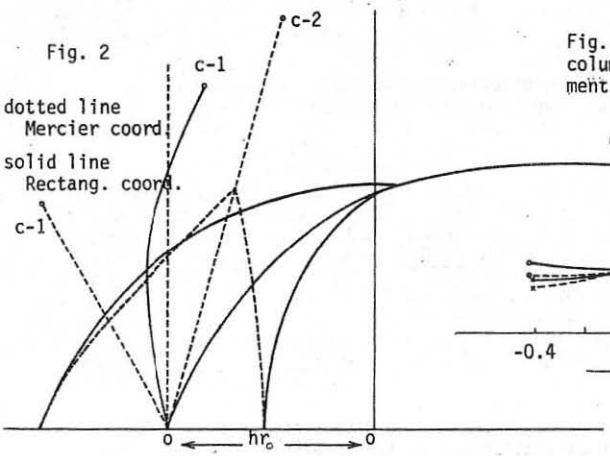

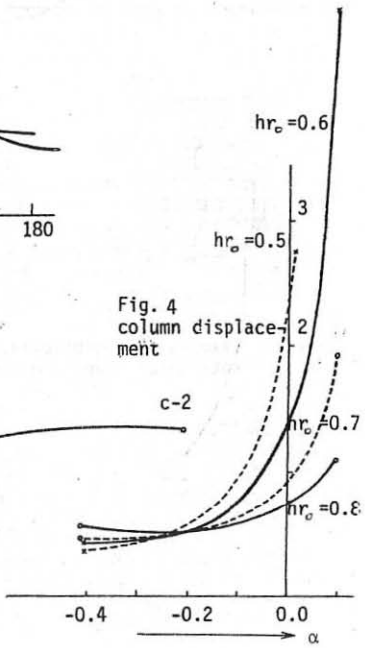

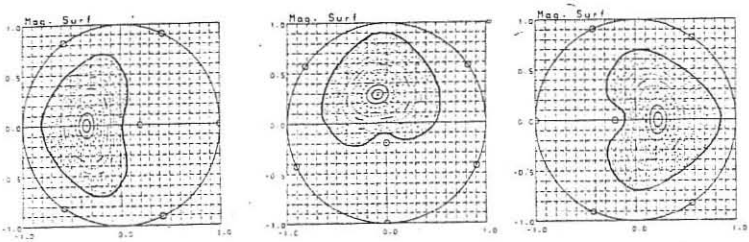

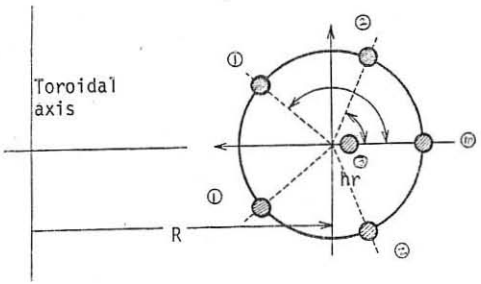

Fig.3 Helical coil position and example of magnetic surface with smallest aspect ratio (=7)

m: main coil with I

1: aux. coil with 0.2 I

2: aux. coil with -0.2 I

3: aux. coil with 0.2 I

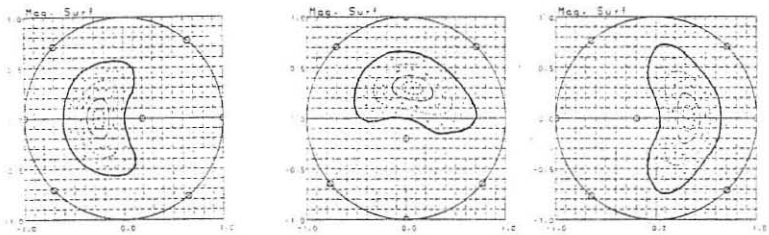

Fig. 5 Example of magnetic surface with positive α = 0.15 rotational transform from 1.5 to 2.0

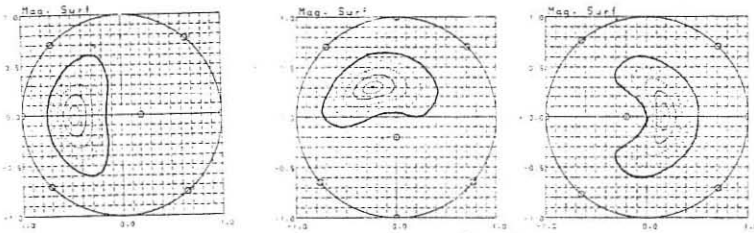

Fig. 6 Example of magnetic surface with negative α = -0.4 rotational transform from 1.9 to 2.5

Ripple Transport At Low Collisionality In Stellarators*

C.D. Beidler, W.N.G. Hitchon, H.E. Mynick† and J.L. Shohet

Torsatron/Stellarator Laboratory
University of Wisconsin
Madison, Wisconsin 53706 USA

In a non-axisymmetric device such as a stellarator, particles with low velocity parallel to the magnetic field may become ripple trapped between successive local maxima of the field. These trapped particles may drift unidirectionally for considerable periods of time, taking a substantial radial step. The transport associated with this radial step is generally thought to be the most serious loss mechanism at low collision frequencies in stellarators.

Predictions of transport rates have been largely based upon analytic solutions of the Fokker-Planck equation. To obtain these solutions various authors have found it necessary to make a number of simplifying assumptions. In this paper we heuristically derive a modification to the diffusion coefficient in a range of collision frequencies first examined by Galeev and Sagdeev.[1] We then present results of several numerical simulations which confirm the new scaling and are largely free of any simplifying assumptions.

We apply the term "low collisionality" to situations where the frequency of bouncing in a local ripple well, ω_b, is larger than the frequency of collisional detrapping from the well, ν_{eff}. For such cases, the adiabatic invariant associated with the bounce motion, J, is well conserved, where

$$J = \oint m v_{\parallel} \, d\ell \qquad (1)$$

Since ions and electrons have unequal diffusion rates in this regime, an ambipolar electric field must be set up to equalize the loss rates. The presence of the electric field (assumed to be radial in this work) leads to a poloidal $\vec{E} \times \vec{B}$ drift with frequency $\Omega_E = E/rB$, limiting the radial excursion of ripple trapped particles off a flux surface to $\Delta r \approx v_d/\Omega_E$, where v_d is the grad-B drift velocity.

In the range of collision frequencies where $\nu_{eff} \approx \Omega_E$, Galeev and Sagdeev solved a bounce-averaged Fokker-Plank equation for the ripple trapped population under the assumptions that the lowest order distribution function is Maxwellian and that the perturbed part of the distribution function must go to zero at the interface between the trapped and untrapped populations since untrapped particles are assumed to have a Maxwellian distribution function and continuity of the distribution function is required. The ordering scheme employed gives rise to a boundary layer at this interface. The boundary layer dominates the transport yielding a diffusion coefficient which scales as the collision frequency raised to the 1/2 power. This result is obtained heuristically by arguing that the fraction of particles involved in the diffusion process is the fraction in the boundary layer, $f \approx \sqrt{\nu/\Omega_E}$, the characteristic step size of the process is $\Delta r \approx v_d/\Omega_E$, and the characteristic time step is $\tau \approx \pi/\Omega_E$. Then

$$D \approx f(\Delta r)^2/\tau = \sqrt{\nu}\, v_d^{\,2}/\pi\Omega_E^{\,3/2} \qquad (2)$$

However, in part of the region where this result is expected to hold, the width of the Galeev-Sagdeev boundary layer, $\sqrt{\nu/\Omega_E}$, is comparable with or

exceeds the width of the ripple trapped region, $\sqrt{2\varepsilon_h}$, where ε_h is the magnitude of the helical modulation of the magnetic field. It is obvious that the fraction of particles involved cannot exceed the fraction which is helicly trapped. Substituting $f \approx \sqrt{2\varepsilon_h}$ for this region, we obtain

$$D \approx \sqrt{2\varepsilon_h}\, v_d^2/\pi\Omega_E \tag{3}$$

which is independent of collision frequency.

Numerical Simulations

In this section we give a brief description of four different numerical simulations which confirm the scaling of Eq. (3), and agree very well with each other.

The first is a bounce-averaged Monte Carlo computer simulation which has been described elsewhere[2] but which will briefly be summarized here. Particles which are ripple trapped in a local helical well are characterized by $0 \leq k^2 \leq 1$, where

$$k^2 = \frac{\kappa/\mu - B_{min}}{B_{max} - B_{min}} \tag{4}$$

where $\kappa = mv^2/2$, $\mu = mv_\perp^2/2B$, and B_{min} (B_{max}) is the local minimum (maximum) value of the magnetic field. Given the model stellarator field

$$B = B_o(1 + \varepsilon_t \cos\theta - \varepsilon_h \cos(\ell\theta + p\phi)) \tag{5}$$

symbols having their usual meanings, and assuming that the toroidal variation of the magnetic field within one field period is negligibly small with respect to the helical modulation, we obtain

$$k^2 = \frac{\kappa/\mu B_o - 1 - \varepsilon_t \cos\theta + \varepsilon_h}{2\varepsilon_h} \tag{6}$$

Particles with $0 < k^2 < 1$ are followed by iteratively conserving their bounce action, J,

$$J = J_o\, \varepsilon_h^{1/2}\, \frac{4}{\pi}\left[E(k) - (1-k^2)\, K(k)\right] \tag{7}$$

where J_o is a constant of the collisionless motion and K and E are the complete elliptic integrals of the first and second kind. Particles with $k^2 > 1$ are assumed to stream along field lines at constant radius (flux-coordinate representation). This choice eliminates certain diffusion mechanisms such as banana diffusion but is consistent with wishing to examine the diffusion rates due to ripple effects only. Discretized versions of the Lorentz collision operator are used at each time step, simulating the randomization of the particle's parallel velocity due to collisions.

The second is a guiding-center simulation wherein particle orbits are described by solving the drift equations numerically in flux coordinates. Particles with $k^2 > k_T^2$ are allowed to stream along field lines at constant radius. Typically $k_T^2 \approx 1.20$, allowing for the possibility of "collisionless" trapping events.

Third is a "hybrid" simulation, which combines the computational speed of a bounce-averaged treatment for ripple trapped particles with the more complete description of the motion provided by guiding-center equations near a detrapping/retrapping event. In this formulation we solve for k^2 using Eq. (4), where B_{max} is now the magnitude of the magnetic field at the lower of the two adjacent maxima. This expressly recognizes the fact that the toroidal variation in B is important, in general, even over a single ripple period. We are also left with a helical well which is not prefectly symmetric. In order to continue to use an equation for J which contains complete elliptic integrals, a symmetric "effective" well is constructed, in close analogy to that which is often used in rippled tokamak theory. The following constraints are used in its construction.

1. The magnitude of the effective magnetic field attains the same minimum value as that of the actual magnetic field.
2. The magnitude of the effective magnetic field attains the same maximum value as the lower of the two adjacent local maxima of the actual magnetic field.
3. The magnitude of the effective magnetic field equals that of the actual magnetic field at the point in phase space at which the simulation changes from a bounce-averaged treatment to integrating guiding-center equations.

The effective magnetic field becomes

$$B_{eff} = \frac{B_{max} + B_{min}}{2} + \frac{B_{max} - B_{min}}{2} \cos\left\{\frac{2\pi(\phi-\phi_o)}{\phi_1+\phi_2-2\phi_o}\right\} \tag{8}$$

where

$$2\phi_o = \frac{\pi(\phi_1-\phi_2)}{\pi-\cos^{-1}(2k_L^2-1)} + \phi_1 + \phi_2 \tag{9}$$

ϕ_1 and ϕ_2 are the two local values of ϕ which satisfy

$$B = B_{eff} = B_{min} + k_L^2(B_{max}-B_{min}) \tag{10}$$

and k_L^2 is the point in phase space, expressed in terms of k^2, at which the change is made from a bounce averaged formalism to guiding-center equations. Using this effective well we obtain the adiabatic invariant

$$J = J_o \left(\frac{B_{max}-B_{min}}{2B_o}\right)^{1/2} \frac{(\phi_1+\phi_2-2\phi_o)}{2\pi} \frac{4}{\pi} \{E(k) - (1-k^2)\, K(k)\} \tag{11}$$

The "hybrid" simulation is typically 3 to 15 times faster than its guiding center counterpart which is already much faster than a "full" guiding center treatment since it uses $k_T^2 \approx 1.2$.

The final simulation is a numerical solution of the bounce-averaged Fokker-Planck equation which is described elsewhere.[3]

In figure 1, numerical results are given for the guiding-center, "hybrid" and Fokker-Planck simulations for the stellarator configuration of reference 1 (numerical results for the bounce-averaged formalism may also be found in reference 1). In the central portion of the figure there is indeed a flat region as predicted by eq. 3 and a region scaling as $\sqrt{\nu}$, as expected from eq. 2. Further to the left, at the lowest collision frequencies, the data shows the ν scaling predicted by several authors.[1,4]

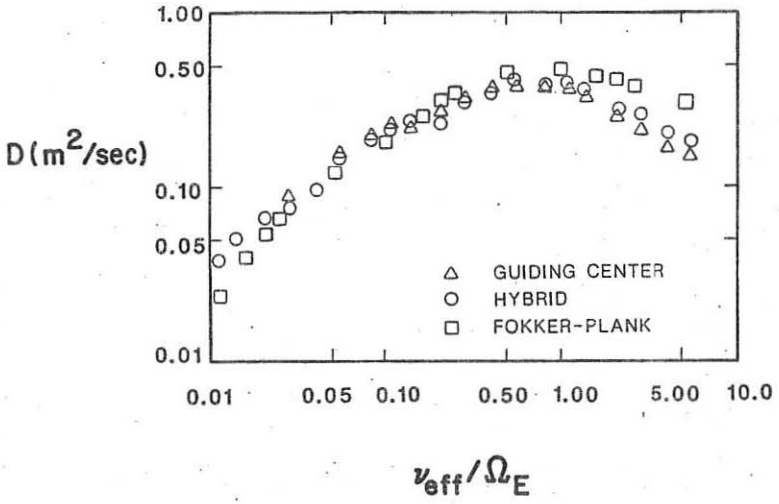

* Work supported under US Department of Energy Contract No. DE-AC02-84ER53166, the National Science Foundation under Grant No. ECS-8206027 and Oak Ridge National Laboratory under Contract No. 19X-27434C.
† Work supported under US Department of Energy Contract No. DE-AC02-76-CHO-3073, Princeton University, Princeton Plasma Laboratory, Princeton, NJ 08544 USA

References

1. Galeev, A.A. and Sagdeev, R. Z., Reviews of Plasma Physics, vol. 7, (1975), (Consultants Bureau, New York).

2. Hitchon, W.N.G., Beidler, C.D., Mynick, H.E. and Shohet, J.L., Nuclear Fusion, 25, (1985) 105.

3. Mynick, H.E. and Hitchon, W.N.G., "A Bounce-Averaged Fokker-Planck Code For Stellarator Transport", PPPL 2235

4. Mynick, H.E., Phys. Fluids, 26, (1983) 2609.

Magnetic Field Structure and ECR Plasmas In IMS*

D.T. Anderson, F.S.B. Anderson, R.P. Doerner,
P.H. Probert, J.L. Shohet and J.N. Talmadge
Torsatron/Stellarator Laboratory
University of Wisconsin-Madison
Madison, WI 53706 USA

Introduction

The Interchangeable Module Stellarator (IMS)[1] at the University of Wisconsin-Madison has been designed to provide an initial evaluation of the modular stellarator concept. The device approximates the magnetic parameters of the Proto-Cleo Stellarator[2]: R=40 cm, $\bar{a}$=4 cm, ℓ=3, 7 field periods $t \sim .6(\frac{r}{a})^2$. The modularization of the magnets is a natural consequence of employing the Proto-Cleo helical winding parameters in the 'ultimate stellarator'[3] approach to derive the coil set.

Investigations to be reported here have concentrated on the physically attained magnetic field structure, magnetic topology unique to the IMS configuration, and ECR plasma studies.

Vacuum Magnetic Surfaces

A large portion of the design effort for IMS went into ensuring that the magnetic surface structure would be free from large scale defects. Verification of the predicted magnetic structure was accomplished using a 400 μ-ampere electron beam to map the drift surfaces. The electron gun was moved radially in steps of four millimeters and complete 2-D scans taken for each of 7 launch positions. The magnetic axis was verified to be close to the correct position by a small collection plate on the back-side of the electron gun. Figure 1 shows the rotational transform profile obtained from the measured data along with the predicted transform obtained from field line tracing using filamentary coil models. The experimental transforms were evaluated by extrapolating toroidal transits to passes that resulted in an integral number of poloidal revolutions, so that drifts away and toward the flux surfaces would be averaged out. The curves in Figure 1 are in agreement to within experimental accuracies. No large island structures were observed, which would be evidenced as flat spots in the transform profile, with ι being constant over the island width.

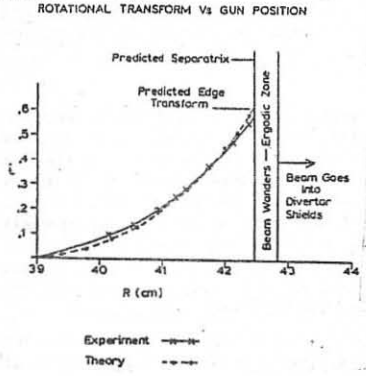

Figure 1

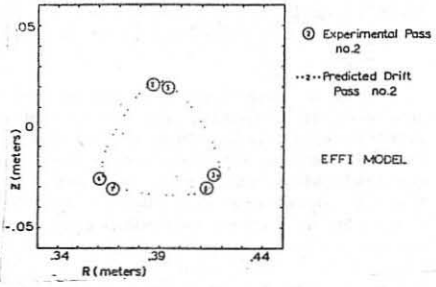

Figure 2

Phase stabilization of the electron beam as performed in other mapping experiments[4] was not possible in IMS due to the lack of an insulating toroidal break. Significant beam spreading occured after five or six toroidal passes, although the beam was easily detectable for between 10 to 20 passes. To corroborate the results presented so far, a guiding-center code was used to calculate the electron trajectories in the IMS fields and predict each toroidal pass location of the beam. Figure 2 shows a comparison of the predicted and detected pass locations for one surface. The excellent agreement seen in the Figure could only be obtained if a distributed current (finite-size) conductor model was used for the computations.

IMS has been predicted to have a series of discrete bundle divertors.[5] These structures have been examined using the electron beam techniques and with ECR-produced plasmas.

Modular Bundle Divertors

Field lines within the magnetic separatrix are presumably confined for an infinite number of transits. Lines of force sufficiently external to the separatrix quickly pass out of the toroidal shell of the magnet coils through the gaps between conductors. In the intermediate region, just outside the separatrix, field lines are confined for varying numbers of transits, some of which can be quite large. Some of the particles which make it sufficiently far outside of the separatrix can free-stream along the diverted field lines [mirror ratio along the diverted lines $\sim$ 1.4 - 1.6]. A simple field line model[5] based upon these considerations predicts a series of discrete modular bundle divertors in IMS.

This structure has been confirmed in IMS by both electron beam data and ECR plasma studies. Stainless steel shields are attached to, and electrically isolated from, the coil support rings in the locations of the diverted field lines. A search for the separatrix and study of the divertor structure was performed using the electron beam. The gun was moved radially outward in steps of 1 mm from inside the 'ideal' separatrix. For beam launch positions internal to the separatrix, the detected first pass location moved in an orderly fashion in concert with the predicted rotational transform profile with no detectable electron current to the shields. Just external to the predicted separatrix, the detected beam location lost its orderly progression with very low detected shield current for about 4 mm [indicated as "beam wanders" on Figure 1]. As the gun was moved further out, the electron current to the shields increased steadily until, at 1.2 cm external to the separatrix, virtually all of the beam current was collected on the shields.

ECR Plasmas

Plasmas have been created in IMS using electron cyclotron resonant breakdown of a neutral gas background with up to a 10 ms pulse of 3 kW 7.28 GHz microwaves. Most of the discussion to follow is based upon waves launched in the extraordinary mode in a vertical direction. Preliminary results using an o-mode antenna showed no significant differences. Typical parameters are (H_2): $T_e \sim 8$-12 eV with a hotter non-thermal component at higher microwave powers, $T_i \sim 6$-7 eV, $N_e \sim 1$-3 x 10^{11} cm^{-3} and particle confinement times of .8 - 1.2 ms at B_o = 2.6 kG. These plasmas have been used for further study of the bundle divertors and investigations of the breakdown process and confinement.

Two dimensional probe scans of electron and ion saturation current have been performed in the two easily accessible divertor regions and at two different minor radii using the ECR plasmas. The scans at the two

minor radii show a focusing of the diverted plasma as it approaches the coil minor radius. Figure 3 shows a comparison of the experimental divertor width (of the 50% contour) with the predicted width from a simple field line model. Experimental widths are approximately a factor of two larger than predicted by the simple model. Contour plots of the scans show the electron saturation has a more peaked distribution than the ion saturation across the divertor region. Virtually all of the plasma outside of the separatrix in IMS is located within these bundle divertors.

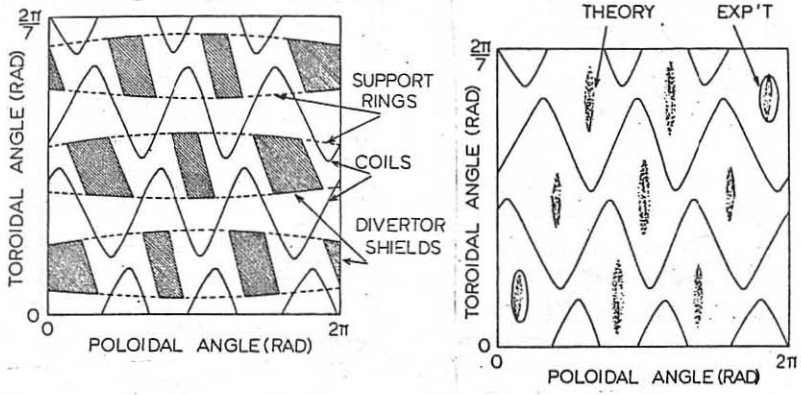

Figure 3

As part of the characterization of IMS ECR plasmas, an investigation into the breakdown process has been performed. The density build-up during the breakdown process is assumed to be given by the particle balance equation:

$$\frac{\partial N_e}{\partial t} = N_e N_o S_H - \frac{N_e}{\tau_c}$$

where τ_c is the particle confinement time, N_o is the neutral density, and S_H is the ionization rate coefficient. Scalings of time-delay from the onset of the microwaves to plasma formation, as a function of the neutral pressure, allow estimates of the confinement time of the breakdown electrons of between 50 and 100 μsec with an inverse scaling with applied microwave power.

Discharges have been formed using both hydrogen and argon gas backgrounds. Hydrogen plasmas showed hollow density and temperature profiles as inferred from Langmuir probes and gridded energy analyzers independent over a reasonable range (2.3 kG < B_o < 3.0 kG) of the toroidal field strength. Ion saturation current profiles in Argon did not show the hollow structure. A higher energy 'spike' in electron energy (> 100 eV) just prior to the overall density buildup was observed in both gases.

Due to field strength and machine size, the hot electrons formed by the ECR (with large $V_\perp$) should be poorly contained. An emissive probe was used to determine space potentials and associated electric fields set up by the expected loss of electrons. Figure 4 shows a comparison of the plasma potential contours for hydrogen and argon ECR plasmas, along with a representative magnetic surface at this toroidal angle. The contours appear to match the surface shape more closely in the argon plasmas. The

direction of the resulting electric field is opposite for the two cases, with hydrogen having a radially outward electric field in the center and argon having a radially inward electric field; the space potentials are positive for both cases but the central potential gradients are opposite in sign. More detailed experiments and quantitative analysis are currently underway to see if ECH induced convective cells are dominating the transport in IMS ECR plasmas.

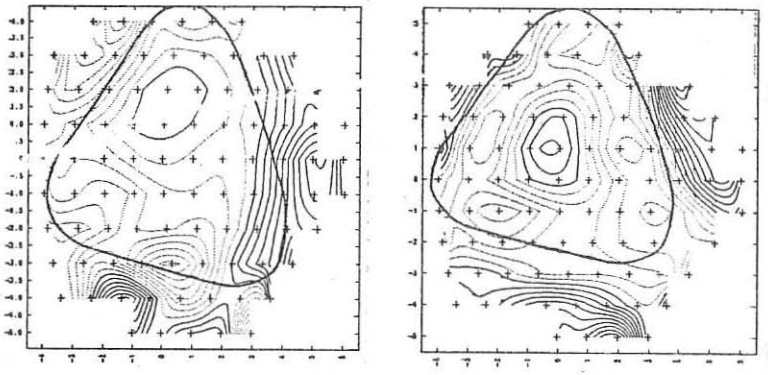

Hydrogen Argon

Figure 4

* Work supported by the US Department of Energy under Contract No. DE-AC02-84ER53166, by the National Science Foundation under Grant No. ECS-82-06027, and Oak Ridge National Laboratory Contract No. 19X-27434C.

References

1. D.T. Anderson, J.A. Derr and J.L. Shohet, IEEE Transactions on Plasma Science, PS-9, (1981).

2. R.A.E. Bolton, C.R.J. Hoffmann, D.J. Lees, S.S. Medley, et al., Phys. Fluids, 14, 1566 (1971).

3. D.T. Anderson, J.D. Callen, J.A. Derr, J.H. Harris, et al., Plasma Physics and Controlled Nuclear Fusion Research, Brussels, 1, 793 (1980).

4. R.M. Sinclair, J.C. Hosea, G.V. Sheffield, Review of Scientific Instruments, 39, 1569 (1968).

5. J.A. Derr and J.L. Shohet, IEEE Transactions on Plasma Science, PS-9, (1981).

COLLECTIVE PHENOMENA IN ECR WAVE-PLASMA INTERACTION IN SATURN STELLARATOR

M.P. Vasil'ev, A.E. Kulaga, I.E. Kuleshov, N.F. Perepelkin, V.S. Vojtsenya, A.Yu. Voloshko, S.I. Solodovchenko, and A.F. Shtan'

Kharkov Institute of Physics and Technology, Ukrainian SSR Academy of Sciences, 310108 Kharkov, USSR

The UHF wave absorption in a stationary ECR discharge plasma was studied in the l=3 stellarator SATURN (R=35 cm, a=8.7 cm). The vacuum chamber was fed as a multimode cavity by a 3 cm magnetron (P_o=13 w). Under the local resonance $\omega_o=\omega_{ce}(r) \gg \omega_{pe}$ the plasma with $\bar{n}_e=10^{10}-10^{11}$ cm^{-3}, $\bar{T}_e \lesssim 10$ eV, and $\bar{T}_i=0.1-1$ eV, and the 10 % ionization degree was confined within closed magnetic surfaces of mean radius $\bar{r}$=5.5 cm and ι_r=0.25 at $H_{ce}(r=0)$=3.35 kOe (D_2, He or Ar gas pressure $p=10^{-6}+10^{-4}$ Torr).

The measurements revealed the complicated nature of gas ionization during ECR plasma creation in the stellarator. Due to transformation of the extraordinary electromagnetic pumping wave f_o near the upper hybrid resonance $f_o=f_h=\sqrt{f_{ce}^2+f_{pe}^2}$ (as was indicated in previous experiments by the mixing of two UHF waves observed in generation of the beating frequency $\Delta\omega=\omega_{ce}^{(1)}-\omega_{ce}^{(2)}\approx 0\div 2\omega_{pi}$ [1]), subsequent absorption of the plasma wave is found to occur near the resonance $f_o \equiv f_{ce}$. The wave absorption is accompanied by electron acceleration and turbulent plasma heating in the vicinity of the resonance zone owing to exciting parametric electron cyclotron and ion sonic instabilities.

The ECR absorption zone in the stellarator is shown to lead to the radial distributions of the plasma temperature, density and accelerated particle flux being nonsymmetric about the ECR zone. The plasma density in the lower magnetic field behind the cyclotron zone is twice as large as that inside the torus before the cyclotron zone, the radial distribution of the electron temperature being reverse. The inhomogeneous distributions of the ion saturation current through the probe in the horizon-

tal (x) and vertical (y) planes are shown in fig.1 for different spatial positions of the cyclotron resonance zone indicated by arrows. Fig.2 represents the distributions of the signals for two pressures (solid line: 1.5×10^{-5}Torr Ar; dash line: 7×10^{-6}Torr Ar). E_f^2 denotes the intensity of the electron cyclotron wave, $\bar{j}_i$ the ion saturation current, E_ω^2 the noise intensity near f_{pi}, E_Ω^2 the amplitude of the plasma wave (f_0') modulated by frequencies near $\Omega \sim f_{pi}$, and f_Ω is the frequency of plasma wave modulation showing the plasma oscillations to be strongly localized near the ECR zone. The spectrum of the UHF radiation from the plasma is characterized by considerable attenuation (by a factor of 100) of the pumping signal due to the plasma absorption, by the satellites occurring at frequencies $f_0 \pm 2f_{pi}$, and by the asymmetric epithermal wings of the nonstationary UHF radiation with brightness temperature $T_{br} \sim (10^2\text{-}10^3)\bar{T}_e$ and far extending thermal wings with $T_{br}=\bar{T}_e=10$ eV. The epithermal UHF radiation corresponding to the red and violet wings of the spectrum (fig.3) is found to be the cyclotron UHF radiation of accelerated electrons corresponding to the regions of the lower and higher fields near the ECR zone.

The distribution of the UHF oscillation intensity in space and frequency obtained with a probe (fig.4) is indicative of the spectrum broadening and the epithermal UHF oscillations strongly localized in space ($\frac{\Delta r}{r} \simeq 0.05$) and corresponding to the wings of the spectrum. Also shown are the distributions of the standing pumping wave field ($f_0=9.4$ GHz; dash line) in the discharge chamber without the plasma and of the "residual" radiation in the presence of the plasma (solid line). The plasma noise spectra near the frequencies $f_{pi}=8$ MHz (fig.5) observed in the ECR zone by means of an electric probe, E_ω, as well as by the modulation of UHF oscillations, E_Ω, demonstrate saturation of the intensity of oscillations and excitation of the combination harmonics as the UHF power, P_0, of the pumping wave increases. Different nature of the spectra $E_\Omega(f)$ and $E_\omega(f)$ can be explained by the fact that the technique applied only permitted us to measure either a short-wave ($\Delta\omega \sim \frac{\omega_{pi}}{2}$, $k\rho_e \sim 1$) or a long-wave ($\Delta\omega \sim \frac{\omega_{pi}}{20}$, $k\rho_e \ll 1$) branch of plasma ion oscillations.

The two-temperature distribution of the electron energy has

been observed in the plasma with a multigrid analyzer (fig.6). The electron temperature T_e in the narrow ECR layer (1 to 2 mm) is about 5 or 6 times the average temperature in the rest of the plasma and reaches 50 eV, with the average plasma cloumn temperature being T_e 10 eV. The temperature of the hot "tail" and intensity of hard X-radiation from the target in the plasma, P_γ, are seen to decrease with the increasing gas pressure (highest energy of accelerated electrons $\mathcal{E}_e \sim 5$ keV). As a result, the intensity of the epithermal UHF radiation decreases at the wings of the UHF spectrum while the ion noise level, E^2_ω, increases markedly in the plasma.

Conclusions: 1. The gas breakdown and maintenance of the stationary ECR discharge in the stellarator turned out to be only possible in the presence of the cyclotron resonance in the space limited by the separatrix. The efficiency of the UHF wave absorption by the plasma is about 90%. Optimum conditions of plasma accumulation in the stellarator are created by placing the ECR zone at half-radius inside the torus.

2. The cyclotron absorption region crossing the magnetic surfaces in the stellarator is likely to cause trapping the accelerated electrons in the lower toroidal magnetic field adjacent to the ECR zone. Therefore the nonuniform radial distribution of macroscopic plasma parameters due to the presence of the absorption zone may result from violating the conditions of plasma pressure equalization at the magnetic surfaces with the ECR heating source localized on the magnetic surfaces.

3. The energy distribution of particles and spectra of plasma oscillations allow one to suggest, along with linear transformation of the electromagnetic wave in the region of the upper hybrid resonance, the turbulent electron cyclotron mechanism of wave absorption and plasma heating in the vicinity of the ECR zone owing to exciting the parametric instability when the oscillator velocities of electrons exceed threshold velocities $\tilde{u} \sim 10^2 v_{Te} > \tilde{u}_{thr} = \sqrt{\frac{m_i}{m_e}}\,\frac{v_{Te}\,\omega_{pe}}{\omega_{ce}}$ in the case of the pumping wave decay $\omega_o = \omega'_{ce} + \omega_s(\kappa)$ [2].

1. A.S.Bakaj et al. Fizika Plazmy (Russ),1976,2,issue 4, p.696.
2. D.G.Lominadze, Cyclotron waves in plasma (Russ),Tbilisi,1975.

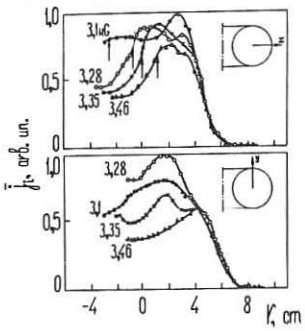

Fig.1

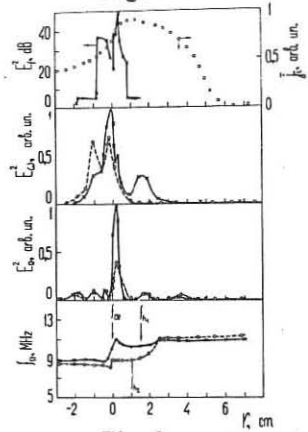

Fig.2

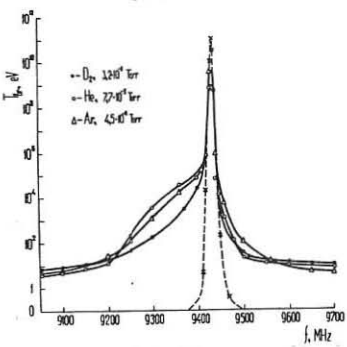

Fig.3

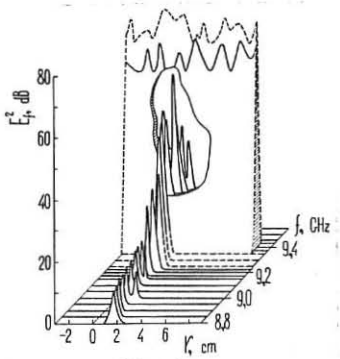

Fig.4

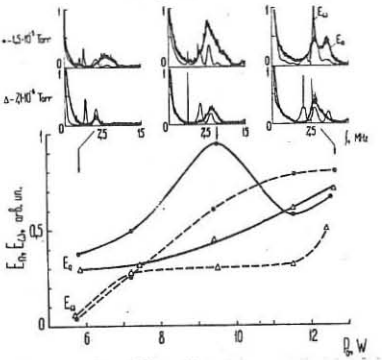

Fig.5

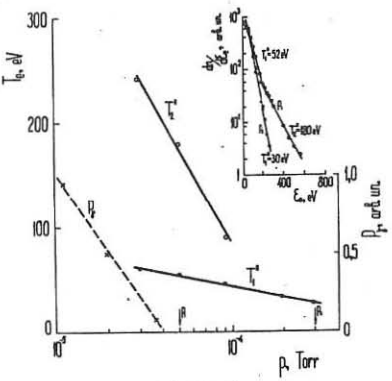

Fig.6

FEATURES OF LOWER HYBRID HEATING IN STELLARATORS

D.L. Grekov and V.E. D'yakov

Kharkov Institute of Physics and Technology, Ukrainian SSR Academy of Sciences, 310108 Kharkov, USSR

In recent years a series of lower hybrid (LH) heating and current drive experiments has been successfully carried out on tokamaks.

LH heating studies were also performed on stellarators [1,2]. This type of magnetic traps is characterized by complicated geometry of magnetic surfaces, the plasma and the confining magnetic field inhomogeneity being of three-dimensional nature. Therefore one may expect the LH wave propagation and absorption to differ essentially from predictions of the one-dimensional model. It is, however, impossible to obtain the electromagnetic field distribution in LH heating in stellarators by means of analytic methods. On the other hand, in present-day devices the scale of plasma inhomogeneity exceeds greatly the length of LH waves in the plasma. This allows the ray tracing method to be applied to derive important information on peculiar propagation and absorption of LH waves in stellarators.

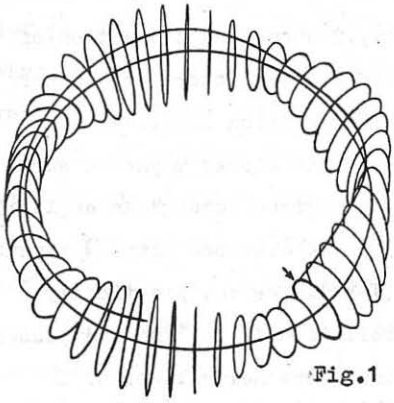

Fig.1

The paper presents calcula-

tions of the LH wave propagation (fig.1) and absorption for a stellarator with URAGAN 2M parameters [3]: l=2 and m=2 helical windings, radius of helical coils = 45 cm, elliptic plasma column major axis = 34 cm and minor axis = 17cm, R_0=170 cm, ι (0)= 0.2, B_0=2.8 T, $n_0=2\times10^{13}cm^{-3}$, and T_0=0.5÷2 keV. The electron Landau damping (ELD) and ion stochastic heating (ISH) were taken into account. The ray equations were solved numerically

$$\frac{dx^i}{d\tau}=\frac{\partial\omega}{\partial\kappa_i},\qquad \frac{d\kappa_i}{d\tau}=-\frac{\partial\omega}{\partial x^i},$$

where variables x^i are the toroidal coordinates (r is the minor radius and ϑ,ζ are the angles measured along the minor and major circumferences of the torus, respectively), κ_i are the components of the wave vector canonically conjugate to x^i and related to the frequency ω by a dispersion equation of the 6th degree, and τ is the time along the ray. Consideration was given to the excitation of the slow mode (SM) in the frequency range $\omega_{LH}(0)<\omega<2\omega_{LH}(0)$, with $\omega_{LH}(0)=\omega_{pi}(0)/(1+\omega_{pe}^2(0)/\omega_{ce}^2(0))^{-1/2}$.

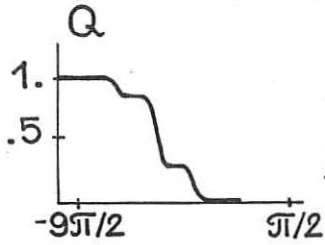

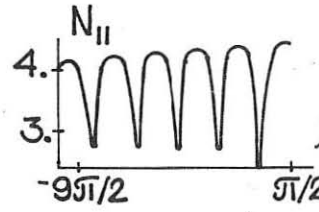

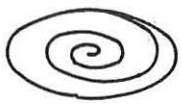

Fig.2

Fig.2 shows the projection of the ray trajectory on a minor cross section relative to the last closed magnetic surface turned through an angle $m\zeta$, $N_\parallel$ and absorbed power Q versus $(\vartheta-m\zeta)$. The ray practically follows a field line and passes under the helical coils. In this situation the helical mag-

netic field oscillates causing oscillations of the wave vector components. Unlike tokamaks, in stellarators the toroidal inhomogeneity of the longitudinal magnetic field is almost insignificant. The maximum values of the parallel and perpendicular refractive indices are found in the vicinity of the minor axis of the elliptic plasma column ($\vartheta=\pi/2$) therefore both ELD and ISH are observed near the minor axis.

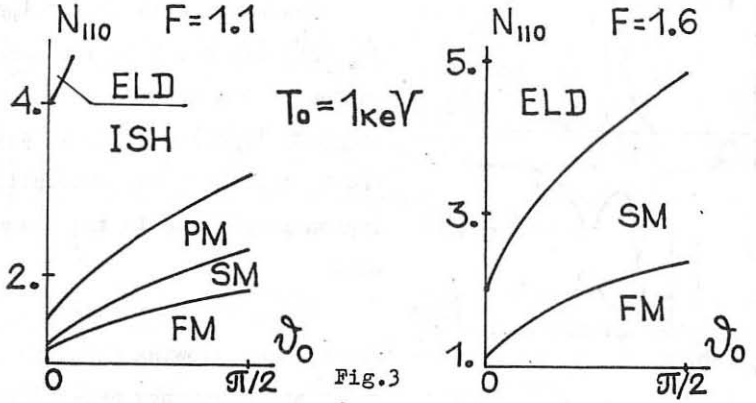

Fig.3

The features of the SM propagation and absorption are strongly dependent on the input point with respect to the major elliptic axis ϑ_0 and the initial slowing down $N_{\parallel 0}, F=\omega/\omega_{LH}(0)$, whereas the dependence on N_{ϑ_0} and the plasma density profile is rather weak. (See fig.3 where FM: SM conversion into a fast mode, Q=0; SM: SM reaches the center and propagates to the plasma edge, Q< 0.1; PM: SM conversion into the plasma mode (PM)). As distinct from tokamaks, the temperature profile does practically not influence the SM propagation.

In stellarators as well as in tokamaks there are three regimes of absorption depending on n_0 or ω. When ϑ_0 is fixed, do-

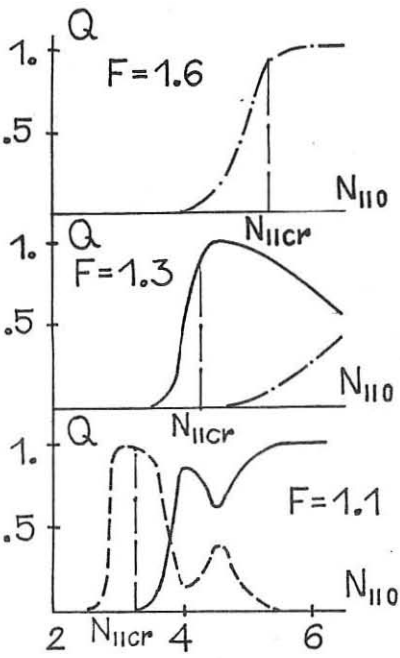

Fig.4

mination of any absorption mechanism (conversion into PM, ISH or ELD) is conditioned by F, $N_{\parallel 0}$, and T_0. Fig.4 represents Q vs $N_{\parallel 0}$ for $\vartheta_0 = \pi/2$ and $T_0 = 1$ keV: (- -) conversion into PM, (——) ISH, and (-.-.) ELD.

The waves with $N_{\parallel cr} < N_{\parallel 0} < N_{\parallel cr} + \Delta N_{\parallel 0}$ are completely absorbed in the plasma core. Here $N_{\parallel cr} = N_{\parallel cr}(F, T_0, \vartheta_0)$ and $\Delta N_{\parallel 0} \sim 1$. As $N_{\parallel 0}$ and T_0 increase, the absorption region is shifted to the plasma edge.

Thus, a proper choice of the initial slowing down, input point and frequency permits efficient heating of plasma ions or electrons in stellarators.

REFERENCES

1. F. Solder, P. Brouquet, M. Durvaux et al. Proc. 9th Eur.Conf. Contr.Fus.and Plasma Phys., Oxford, 1979, Contr.papers, p.5.
2. K. Ohkubo, S. Takamura and JIPP T-II Group. in: Heating in Toroidal Plasmas. Proc.3rd Varenna-Grenoble Int.Symp.,1982, 2, p.543.
3. E.P. Velikhov and V.D. Ryutov. Voprosy Atomnoj Nauki i Tekhniki, ser. Nuclear Fusion, issue 1(18) 1985, p.3.

STRUCTURE OF ICRF WAVES IN A PLASMA WITH HELICAL SYMMETRY

A. Fukuyama, N. Okazaki, A. Goto, S.-I. Itoh† and K. Itoh*

Department of Electronics, Okayama University, Okayama 700, JAPAN
†Institute For Fusion Theory, Hiroshima University, Hiroshima 730, JAPAN
*Japan Atomic Energy Research Institute, Tokai, Ibaraki 319-11, JAPAN

Abstract In order to study the propagation and absorption of ICRF waves in stellarator/Heliotron devices, the full Maxwell equation is numerically solved in a straight helical configuration. A cold plasma model is used to obtain the conductivity tensor. Two-ion hybrid resonance heating by fast wave is studied. For Heliotron-E grade plasmas, the wave can propagate into the central region of plasma and the antenna loading resistance is high.

The model we use is the straight $\ell=2$ Heliotron configuration. The helical corodinates (X,Y,Z) is defined as $X = x\cos zh + y\sin zh$, $Y = -x\sin zh + y\cos zh$ and $Z = z$, where (x,y,z) are the Cartesian coordinates. The pitch length L_p is defined by $L_p = 2\pi/h$. The magnetic flux function $\psi(X,Y,Z)$ is given as[1)]

$$\psi(X,Y,Z) = B_0 h \{ X^2 + Y^2 - 2h\rho K_2'(2h\rho)(X^2 - Y^2) \} /2 \qquad (1)$$

assuming that the plasma is thin. In Eq.(1), K_2 is the modified Bessel function, B_0 is the magnetic field at the axis, ρ is the minor radius of the helical coils and the X-axis is taken in the short axis of the crosssection. The density distribution is given as $n(X,Y) = (n_0-n_s)(1-\psi/\psi_b) + n_s$ $(\psi<\psi_b)$, where ψ_b is the boundary value of ψ.

The wave equation is given as

$$\nabla\times\nabla\times\vec{E} - \frac{\omega^2}{c^2}\mathbf{K}\cdot\vec{E} = i\omega\mu_0\vec{J}_{ext} \qquad (2)$$

where ω is the angular frequency of the wave, $\vec{J}_{ext}$ is the current on the antenna. $\mathbf{K}$ is evaluated by the cold plasma approximation[2)]. The equation (2) is used to study the two-ion hybrid resonance heating. The plasma is consist of electron, majority ion (D^+) and

minority ion (H^+). The cold plasma model can describe the effects of hybrid resonance and cut-off by introducing the effective collision ν. We approximate the wall to be highly conductive, i.e., the tangential component of $\vec{E}$ vanishes on the wall. Due to the helical symmetry, all quantities are Fourier decomposed as $F(X,Y,Z) = \Sigma_{k_z} F(X,Y,k_z)\exp(ik_z Z - i\omega t)$ and each k_z-component can be treated separately. The power absorption rate $P(X,Y)$ is calculated as $P = \omega\varepsilon_0 \mathrm{Im}[\vec{E}^* \cdot \mathbf{K} \cdot \vec{E}]$.

We study the fast wave excitation from the high field side. The rf current flows on the XY plane as is shown in Fig.1, i.e., $\vec{J}_{ext} = \{J^X(X,Y,k_z),\ J^Y(X,Y,k_z),\ 0\}$. We choose $|J_{ext}| = 1$ to calculate the antenna impedance. The current is approximated to be constant along the loop, because the quarter of the wave length is longer than the arc length of the antenna.

The standard parameters are $L_p = 1.45$m, $R = 2.1$m, minor radius $= 0.14 \times 0.28$m, average minor radius $a = 0.22$m, $B_0 = 1.8$T, $\omega/2\pi = 26.5$ MHz, $n_{e0} = 4\times10^{19}/m^3$, proton ratio $\eta = n_H/n_e = 0.1$. For these parameters, the mode conversion layer extends to the centor of the plasma column. The scrape-off density is chosen as $n_s/n_0 = 10^{-2}$ and $\nu/\omega = 10^{-2}$.

The figure 1 shows the contours of the electric field ($\mathrm{Re}E_x$, $\mathrm{Im}E_x$, $\mathrm{Re}E_y$, $\mathrm{Im}E_y$) and $P(X,Y)$ on the minor crosssection for $k_z L_p = 4\pi$. The antenna impedance is $Z = 0.085 - 1.38i$ (Ωm). The amplitude of the fast wave is strong in the plasma column and $P(\vec{r})$ is localized in the central region of the plasma. The phase of the electric field is taken with respect to the antenna current. The resistive damping in the scrape off plasma also occurs owing to the strong reactive field near the antenna. The standing wave component is large, because the wave length of the fast wave is comparable to the minor radius.

The energy deposition profile is affected by changing the hybrid-resonance surface position and/or the thickness of the evanescent layer. The figure 2 shows $P(X,Y)$ for $\eta = 0.2$ and 0.3 (other parameters are the same as Fig.1). Comparing to Fig.1, we find that the peaks of P move to the peripheral region, indicating that the wave does not penetrate in the central region of the plasma. This is because that the hybrid resonance layer moves to the high field side as η increases. The thickness of the evanes-

cent layer also increases, preventing the penetration of the rf wave to the high density region.

The figure 3 shows the k_z dependence of the loading resistance. The loading resistance becomes small for short wave length modes. For very large values of $|k_z|$, the evanescent layer at the plasma periphery becomes thick and the wave propagation is prohibited.[3] The peaks in Fig.3 are due to cavity resonances with various poloidal mode numbers. Writing the poloidal mode number m, the resonance condition is found to be

$$(k_z - mh)^2 + \bar{k}_r^2 + m^2/a^2 = \omega^2/v_A^2 \qquad (3)$$

where v_A is the average Alfven velocity and $\bar{k}_r$ is the effective radial wave number, the minimum value of which is estimated as $\pi/2a$ ($m=\pm1$) and π/a ($m\neq\pm1$). The m=1 component has a finite value of $|E|$ at the axis and wave energy can be deposited at the axis. The in-phase antenna excites odd-modes, m = 1,3 and the out-phase antenna excites even-modes, m = 0,2 and 4. The poloidal mode number of the resonance is denoted on the peaks of P in Fig.3.

In summary, analysis is performed for the model plasma of Heliotron-E, using this newly developed code.[4] The coupling of the fast wave to the helical plasma is found to be as good as to tokamak plasmas. We find that the wave can propagate into the central region of the plasma when the evanescent layer at the periphery is thin. The deposition profile is controlled by changing the location of the two-ion hybrid resonance surface.

References

[1] A. I. Morozov and L. S. Solov'ev, in Reviews of Plasma Physics (ed. M. A. Leontovich, Consultants Bureau, 1966) Vol.2, p42.

[2] T. H. Stix, The Theory of Plasma Waves (McGraw-Hill, New York 1962).

[3] K. Itoh, S.-I. Itoh and A. Fukuyama, Nucl. Fusion 24 (1984) 13.

[4] A. Fukuyama, N. Okazaki, A. Goto, S.-I. Itoh and K. Itoh, "ICRF Waves in Helical Plasmas" paper in preparation.

Computations are performed by use of the ACOS-1000 computer of the Okayama University. Work partially supported by Grant-in-Aid for Scientific Research and Grant-in-Aid for Fusion Research of MoE Japan.

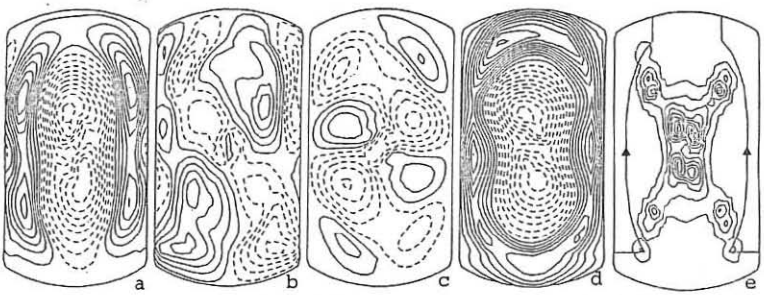

Fig.1 Contours of ReE_x (a), ImE_x (b), ReE_y (c), ImE_y (d) and P (e). Differences between two successive contour lines are 0.79V/m for (a) and (b), 0.71V/m for (c) and (d) and $P_{max}/10$ for (e). Arrows on the antenna loop indicates current direction of the in-phase excitation cases.

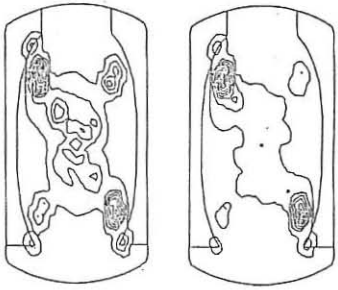

Fig.2 Contours of P for η= 0.2 (left) and 0.3 (right). Parameters are the same as Fig.1.

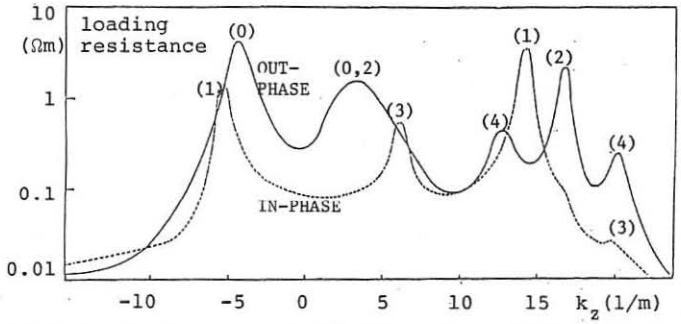

Fig.3 Loading resistance as a function of k_z. Solid line for out-phase excitation case and dashed line for in-phase excitation case. Number in ( ) denotes the poloidal mode number of the cavity resonance.

DETERMINATION THE PLASMA-PRESSURE ANISOTROPY IN STELLARATORS

E.D. Andryukhina, I.S. Danilkin, K.S. Dyabilin, O.I. Fedyanin
General Physics Institute USSR Academy of Sciences, Moscow, USSR

I. Plasma equilibrium in the case of anisotropic pressure.

The relation between equilibrium plasma currents and plasma pressure may be obtained, according to the ideal MHD model. Let us suppose that the pressure is anisotropic and the pressure tensor $\hat{P}$ is as usually, given by the relationship

$$\hat{P} = P_\perp \hat{I} + (P_\parallel - P_\perp)\hat{H}, \qquad (1)$$

where $\hat{I}$ is the unit tensor, $\hat{H}$ is the tensor composed from the components of the field unit vector $\vec{h} = \vec{B}/B$, $\|H\|_{i,k} = h_i \cdot h_k$.

The equilibrium equation can thus be written as following

$$c^{-1}[\vec{j}\,\vec{B}] = \operatorname{div}\hat{P}. \qquad (2)$$

Using the conditions $\operatorname{div}\vec{B} = 0$, $\operatorname{div}\vec{j} = 0$, the Maxwell equations $\vec{j} = \frac{c}{4\pi}\operatorname{rot}\vec{B}$ and neglecting the terms of order $\beta^2 \left(\beta = \frac{8\pi p}{B^2}\right)$, we obtain from (2)

$$\vec{j}_\perp \simeq c[\vec{B}\nabla_\perp P_\perp]/B^2; \quad \vec{j}_\parallel = \vec{B}\cdot J, \quad \vec{B}\nabla J \simeq -c\frac{[\vec{B}\nabla \ell_n B^2]}{B^2}\cdot\nabla\left(\frac{P_\perp + P_\parallel}{2}\right). \qquad (3)$$

Here the value $j_\parallel$ is expressed in inexplicit form in terms of scalar function J. Using the results from Ref./2/ both toroidal flux and radial magnetic-field components due to equilibrium currents may be derived in the form

$$\Phi_\parallel = -B_0 \int_0^a \frac{\beta_\perp}{2}\cdot 2\pi r\,dr \quad ; \quad B_r = -\frac{B_0}{2}\cdot\frac{\sin\theta}{r_0^2}\int_a^\alpha r^2 \frac{1}{\iota(r)}\frac{\partial}{\partial r}\left(\frac{\beta_\perp + \beta_\parallel}{2}\right) dr, \qquad (4)$$

where α is the plasma radius, r_0 and θ are the radius and poloidal angle of the observation point, B_0 is the toroidal magnetic field, ι is the rotational transform. Thus, the expression for toroidal flux includes the transverse pressure $\beta_\perp = P_\perp/(B_0^2/8\pi)$ while the radial magnetic-field components are determined by the "average" plasma pressure $(\beta_\perp + \beta_\parallel)/2 = (P_\perp + P_\parallel)/2 \times 8\pi/B_0^2$. Note whereas the toroidal magnetic flux is determined from the total transverse plasma pressure only the ra-

dial magnetic field depends on the pressure and $\iota(r)$ profiles. But this dependence appears to be relatively weak. Thus, in the case of ι = const (stellarator W-VIIA) B_r does not depend on the plasma pressure profiles and in the case of L-2 ($\iota(r) = 0.185 + 0.2\left(\frac{r}{a}\right)^2 + 0.42\left(\frac{r}{a}\right)^4$) in a wide profiles range $P(r) = P_0\left(1 - \frac{r^2}{a^2}\right)^n$ at $2 \leq n \leq 4$ the field amplitude changes by 25% only (supposing the plasma energy the same)

II. Results of measurements.

The experiments were carried out on the L-2 stellarator (l=2, the major radius R=100 cm, mean plasma radius a=11.5 cm, the radius of the vacuum chamber r_0 = 17.5 cm, B_0 = 1.0-1.1T). Currentless plasma is heated at the fundamental harmonic electron cyclotron frequency by the extraordinary -polarized electromagnetic wave launched from the strong magnetic field side (λ = 1 cm, $\omega = \omega_{ce}$, $\vec{E} \perp \vec{B}$, P = 60-80 kW). During the microwave UHF pulse (ΔT_{HF} = 8 ms) plasma density grows from n_e = (0.2-1) 10^{12} cm^{-3} up to n_e = (6.7) $10^{12} cm^{-3}$, electron temperature at the center reaches 0.5-0.6 keV and $T_i(0) \simeq$ 60 eV.

The toroidal flux is determined by cnnventional diamagnetic measurements [3]. The radial magnetic field was measured by two flat multiturn coils being connected in series which were put on the chamber surface at the distance of a half-period of the helical field from each other; it allows to compensate the signal from the stellarator magnetic field and to double up the useful signal.

Fig.1 shows the evolution of plasma parameters during the microwave pulse, and the value of the thermal plasma energy determined by

$$W_T = \frac{3}{2} \int dV \left(n_e T_e + n_i T_i\right),$$

W_T - is seen to increase monotonously all over the pulse duration. On the other hand, the measurements show that the behaviour of transverse energy (diamagnetic signal) differs noticeably from that of W_T : diamagnetic signal grows rapidly at the initial stage of heating and then changes slightly. Figs 2a,b show the evolution of transverse and longitudinal pressure $\langle P_\perp \rangle$ and $\langle P_\parallel \rangle$, (averaged over the plasma cross-section) obtained experimentally according to the above method. The figures illustrate the presence of a strong anisotropy at $t \leq 4 ms$ and the

consequent pressure isotropization. It gives also two typical cases which show that the rations $\langle P_\perp \rangle$ and $\langle P_\parallel \rangle$ during HF pulse and the time of isotropization may slightly vary, that is due to the peculiarities of the applyed heating technique, behaviour of particle density, etc.

As a rule, when plasma density grows slowly at the initial stage of heating, the main fraction of plasma energy is contained in the transverse component. For all the above cases Figs 2e,d show the total (solid curves) and the thermal (dashed curves) energy, derived, respectively, as

$$W = [\langle P_\perp \rangle + 0.5 \langle P_\parallel \rangle] \cdot V, \qquad (5)$$
$$W_T = \frac{3}{2} \langle P_\parallel \rangle \cdot V,$$

here V is the plasma volume.

The considered data illustrate the possbilities to measure anisotropic plasma pressure by the proposed technique. Our measurements show that energy estimation on the basis of diamagnetic measurements only, for example, or on the basis of T_e, obtained from laser measurements is not always valid. It might appear that the thermal energy contributes only a small fraction from the total energy.

References

1. W.N.G.Hitchon.Nuclear Fusion.1983, V.23, N3,p.383.
2. I.S.Danilkin. Fizika plasmy. 1978,V.4,N5,p.1033.
3. E.D.Andryukhina,O.I.Fedyanin.Fizika plasmy.1977,V.3,N4,p.792.
4. E.D.Andryukhina,L.N.Agapov,G.M.Batanov et al. Pisma v ZhETF. 1984,V.40,N9,p.377.

Fig.1

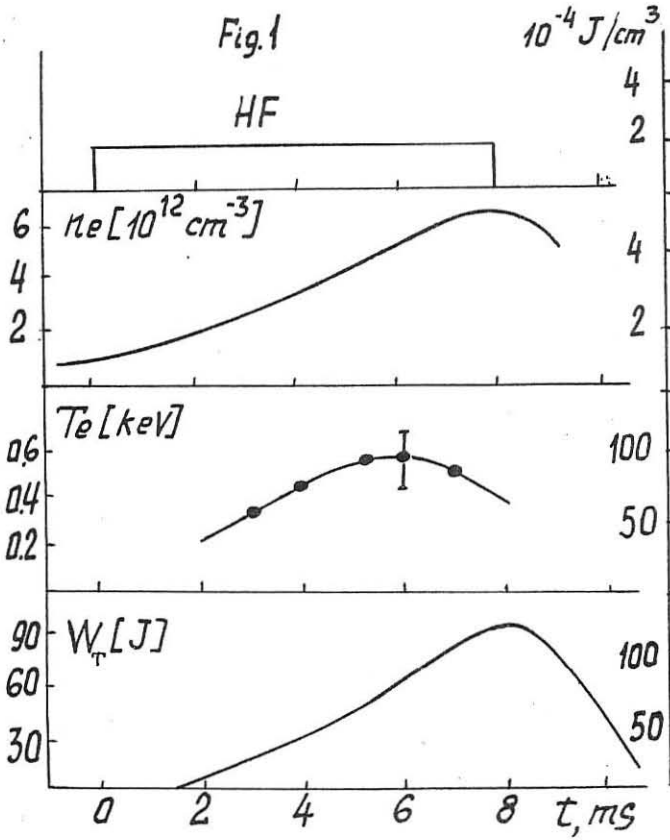
HF
ne [10^12 cm^-3]
6
4
2
Te [keV]
0.6
0.4
0.2
W⊥ [J]
90
60
30
0
2
4
6
8
t, ms

Fig.2

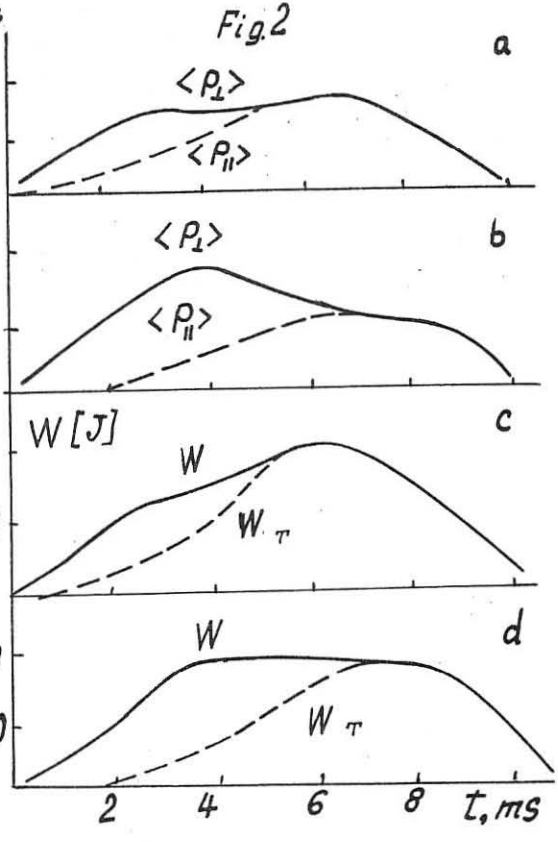
10^-4 J/cm^3
a
<P⊥>
<P∥>
4
2
b
<P⊥>
<P∥>
4
2
c
W [J]
W
W⊤
100
50
d
W
W⊤
100
50
2
4
6
8
t, ms

STABILITY OF HIGH BETA PLASMAS WITH HELICAL MAGNETIC AXIS

M. Mond
Department of Mechanical Engineering
Ben-Gurion University of the Negev
Beer Sheva, Israel

Recently, there has been a growing interest in configurations with a helical magnetic axis. Numerical, as well as analytical calculations, indicate that such configurations demonstrate favorable stability properties due to the large magnetic well created by the large helical curvature.[1,2] Based on the assumption of low plasma pressure, no stability limits on beta (the ratio of the plasma pressure to the magnetic field pressure) were found. It is the purpose of this work to extend the stability analysis of systems with a helical magnetic axis to high beta regimes. This is done by investigating the normal modes of the system. The main results of the present work are: (i) the reduction of the system of partial differential equations of the normal mode analysis to a second order ordinary differential equation, and (ii) the demonstration of the importance of the existence of a magnetic well even for high beta regimes.

As a first step towards obtaining the cited results, a coordinate system is introduced which is attached to the helical magnetic axis. Thus, s is defined as the arclength along the helical axis while r and θ are the polar coordinates in the plane which is perpendicular to the magnetic axis at a given s. Next, it is assumed that the physical quantities do not depend on s. As a result, a flux function $\psi(r,\theta)$ can be defined such that ψ = const form a set of nested surfaces. The special structure of the normal modes makes it worthwhile to introduce a new coordinate system (ψ,θ,s) instead of (r,θ,s).

The new coordinate system is not orthogonal, hence, both the covariant and contravariant basis vectors are defined and the metric tensors and the Jacobian of the transformation are calculated.

After setting up the geometry, the magnetohydrodynamics (MHD) equations are investigated in order to obtain the structure of the equilibrium magnetic field and plasma with helical symmetry ($\partial/\partial s = 0$). In addition, the rotatational transform is defined and is assumed to be a constant.

Next, the equilibrium is perturbed. As a result of the helical symmetry, the perturbed quantities can be expanded in terms of plane waves of the form $f(\psi,\theta)\exp[i(\omega t+ks)]$. The perturbation is considered to be small, hence, only first order terms in the perturbation are retained in the MHD equation. This linearization results in a set of seven partial differential equations for the perturbed magnetic field, velocity and pressure. These normal mode equations are investigated in order to find a solution for small ω and large ψ derivatives. Such a class of modes is admissible due to the absence of shear. Otherwise, localized modes have to be investigated. It turns out that the normal modes in shearless configurations lie mainly within the flux surfaces.

Using a technique developed by Pao,[3] the perturbed quantities are expanded in powers of ω. The expanded perturbations are, in turn, inserted into the

seven linear differential equations and solved order by order. As a result, the set of seven partial differential equations is reduced to the following second order ordinary differential equation.

$$\omega^2 \Lambda a_0'' + k^2 \Delta a_0 = 0 \tag{1}$$

where a_0 is the amplitude of the velocity component perpendicular to the magnetic surfaces, Λ is a positive definite quantity and

$$\Delta = (u' + \frac{P'}{\rho a^2})u' \tag{2}$$

where u' is the second derivative of the volume enclosed by a flux surface with respect to ψ.

Multiplying eq. (1) by a_0 and integrating over the whole range of ψ indicate that the sign of Δ and hence the sign of u' play an important role in determining the stability properties of high beta plasmas. Thus, $\Delta \geq 0$ is a necessary condition for stability and $u' < 0$ (a magnetic well) is sufficient for $\Delta \geq 0$. More detailed information about the unstable modes, as well as the stable oscillations, can be obtained by solving the eigenvalue equation (1).

References

1. M. Mond, Phys. Fluids, 26, 3327 (1983).

2. S. Yoshikawa, presented at the Fourth International Stellarator Workshop, Cape May, New Jersey, 1982, Vol. II, p. 1.

3. Y.P. Pao, Phys. Fluids, 18, 1192 (1975).

IDEAL MAGNETOHYDRODYNAMIC EQUILIBRIUM AND STABILITY STUDIES OF A TOROIDAL SYSTEM WITH ARBITRARY HELICAL FIELDS

GERHARD BERGE,[a] WON HO CHOE[b] AND J.P.FREIDBERG[b]

a) Department of Applied Mathematics, University of Bergen, Bergen, NORWAY.

b) Plasma Fusion Center, Massachusetts Institute of Technology, Cambridge, MA 02139 USA

Abstract

A sharp boundary calculation for configurations with arbitrary helical fields as well as a vertical field is presented. Critical β-limits are obtained for equilibrium and stability of global modes.

I.INTRODUCTION

This work is primarily motivated by the promising aspects of the stellarator configuration. Recent results suggest that a toroidal device with helical fields may have some advantages compared to axisymmetric devices, i.e., tokamaks, with regard to controlling disruptions. In this context one could think of two classes of systems: (a) pure stellarators (no ohmic heating current), or (b) a hybrid system which could either be a stellarator with an ohmic heating current or a tokamak with superimposed helical windings. The present work is a generalization of previous work[1] which was restricted to one type of helical field (one ℓ-number, ℓ being the poloidal multipolarity) and no vertical field. We have now been able to generalize this to include any combination of helical fields and also an arbitrary vertical field (which is essential for having an average magnetic well). This applies both to the equilibrium and the stability analysis.

The study is restricted to the surface current model, where we assume all the current to be flowing in a thin sheath forming the boundary between plasma and vacuum. From previous experience we know that such a model gives a reasonable description of the equilibrium and the stability properties of the global modes in such systems.

The main part of this work is analytic, and we resort to numerical solutions only at the final step both in the equilibrium and the stability analyses.

The equilibrium is established by the Princeton stellarator expansion in the inverse aspect ratio (ε). We can solve for the critical β for any net current, including the pure stellarator case with zero current.

The stability part is based upon the MHD-energy principle. We are able to write this in a concise form suitable for numerical evaluation.

We discuss critical β-limits from equilibrium and stability for systems with different combinations of helical fields.

II.EQUILIBRIUM

We consider the equilibrium and stability of a toroidal stellarator/tokamak hybrid as described by the sharp boundary surface current model. At this point we are particularly interested in the pure stellarator (no net current). The geometry is the usual one, we have the cylindrical coordinates (R,ϕ,z) are related to toroidal coordinates by $R = R_0 + r\cos\theta$, $Z = r\sin\theta$, $\phi = -z/R_0$. The fields are written as

$$\underline{B}_{plasma} = B_i \underline{b}, \quad B_{vacuum} = B_o(\underline{b} + \hat{\underline{b}}) \cdot b \equiv R_o/R \, \underline{e}_z + 1/h \, \nabla(\psi + \chi), \tag{1}$$

where h is the helical wavenumber and ψ and χ represent the helical and vertical fields respectively. The inverse aspect ratio is $a/R_o \equiv \varepsilon$ where a is the average plasma radius. Our expansion parameter is δ, the measure of the amplitudes of the helical fields, and the following ordering is assumed, $\varepsilon \approx \delta^2 \approx 1/N \approx \beta$, where $\beta = p/\frac{1}{2} B_0^2$ (p is plasma pressure) and $N = hR_o$, the number of helical periods.

We introduce new variables by $x = hr$, $s = hz$, and take the plasma surface to be given by $x = x(\theta,s)$. Solving the problem order by order in δ we write

$$\begin{aligned}
&\psi = \psi_1 + \psi_2 \ , \quad \chi = \chi_2 + \cdots \ , \\
&\hat{\underline{b}} = 1/h \, \nabla\{\psi_2(x,\theta) + \psi_3(x,\theta,s)\} + O(\delta^4) \\
&\psi_1 = 1/2 \, \hat{\psi}_1 e^{is} + \text{c.c.} \ , \quad x_1 = i/2 \, \hat{x}_1 e^{is} + \text{c.c.} \\
&\psi_3 = 1/2i \, \hat{\psi}_3 e^{is} + \text{c.c.} \ , \quad \chi_2 = 1/2 \, \hat{\chi}_2 e^{i\theta} + \text{c.c.} \\
&d/dn \equiv \partial/\partial x_0 - \dot{x}_0/x_0^2 \, \partial/\partial\theta \ , \quad d/d\theta \equiv \partial/\partial\theta + \dot{x}_0 \partial/\partial x_0 \ , \quad \dot{x}_0 = dx_0/d\theta
\end{aligned} \tag{2}$$

We define the following important quantity

$$F \equiv \nabla\hat{\psi}_1^* \times \nabla\hat{\psi}_1 \cdot e_z + 2(\hat{\chi}_2 - \hat{\chi}_2^*) = F(\theta, x_0) \tag{3}$$

where * means complex conjugate (c.c.), and the solution to the problem can be written as

$$dF/d\theta = 0, \ (\text{determines } x_0(\theta)) \quad \hat{x}_1 = -d\hat{\psi}_1/dn \ , \quad d\psi_2/dn = 0$$

$$1/2i \, d/dn(\hat{\psi}_3 e^{is}) + \text{c.c.} = 1/x_0 \, d/d\theta(x_1/x_0 \, \partial\psi_2/\partial\theta), \quad b^2 + 2\iota_h b - \beta/\varepsilon \, (w + \lambda) = 0 \tag{4}$$

$$b = 1/\varepsilon x_0 Q_0 \, d\psi_2/d\theta \ , \quad Q_0 = \sqrt{1 + \dot{x}_0^2/x_0^2}$$

$$\underline{\iota_h} = 1/4\varepsilon \, \nabla F$$

$$\iota_h = |\underline{\iota_h}| \, \text{sgn}(F_x) \qquad \text{helical transform}$$

$$w = 1/2\varepsilon \, |\nabla\psi_1|^2 + 2x_0/x_{av} \cos\theta \qquad \text{(magnetic "well")}$$

λ is a constant related to net current.

From Eq.(4) we notice that b is determined by a quadratic equation and this equation has two solutions. However, the stellarator case with no net current is obtained only from one of these solutions which we shall discuss here. We also notice that unless β/ε is below a certain value there is no solution, this condition for solution determines the critical equilibrium β-limit. The problem is solved numerically by first integrating $dF/d\theta = 0$ to find the surface, and then determine λ and the critical β for a given net current. The results for different configurations are shown in Figs. (1 - 4).

III. STABILITY ANALYSIS

We investigate the stability of this configuration by means of the Energy

Principle [3]. From previous experience the surface current model provides a reasonable description of long wavelength instabilities. A simplifying feature of the analysis follows from the fact that in minimizing δW the most unstable modes comes out to be incompressible to leading order i.e. $\nabla\cdot\underline{\xi}_0 = 0$ with $\underline{\xi}_0$ the leading order plasma displacement. In particular, the determination of δW ultimately requires a minimization, only with respect to a single scalar quantity, $\underline{n}\cdot\underline{\xi}$ evaluated on the plasma surface.

For the surface current model, the potential energy δW is conveniently written as a plasma-, surface- and vacuum-contribution

$$\delta W = \delta W_p + \delta W_s + \delta W_v$$

$$\delta W_p = \frac{1}{2}\int_p |B_1|^2 dr \quad , \quad \delta W_s = \frac{1}{2}\int_s |\xi|^2 n\cdot\Big[\nabla(p + B^2/2)\Big] ds \quad \delta W_v = \frac{1}{2}\int_v |\hat{B}_1|^2 dr \qquad (5)$$

The simplified expression for δW_p, reflect the fact that the most unstable modes are almost incompressible, B_1 and $\hat{B}_1$ are the perturbation in the magnetic fields in the plasma and vacuum respectively, $\xi(\theta,z) \equiv \underline{n}\cdot\underline{\xi}|_{r_p}$ is the normal component of plasma displacement evaluated on the plasma surface ($r = r_p$) The notation [A] denotes the jump in A from vacuum to plasma, where

$$\underline{n} = \underline{n}_s/|n_s| \quad , \quad \underline{n}_s = \underline{e}_r - 1/r_p\ \partial r_p/\partial\theta\ \underline{e}_\theta - R_0/R\ \partial r_p/\partial z\ \underline{e}_z$$

We then note that $\nabla\times\underline{B} = 0$ in both the plasma and vacuum region and $\underline{n}\cdot\underline{B}|_{r_p} = 0$. Consequently we can write $\underline{n}\cdot\nabla(p + B^2/2) = -\underline{B}\cdot(\underline{B}\cdot\nabla)\underline{n}$. This term can be evaluated and substituted into δW_s. The result is

$$\delta W_s = \frac{1}{2}\int d\theta ds|\xi|^2\ r_p R/hR_0\Big\{[B_\theta^2]/r_p\ \{1 - r_p\ \partial/\partial\theta(1/r_p^2\ \partial r_p/\partial\theta)\}$$

$$-2[B_\theta B_z]\partial/\partial\theta\ \{R_0/r_p R\ \partial r_p/\partial z\} \qquad (6)$$

$$-[B_z^2]\{\partial/\partial z(R_0^2/R^2\ \partial r_p/\partial z) - 1/r_p R\ \partial/\partial\theta(r_p\sin\theta)\}\Big\}$$

We now substitute the expanded form of the equilibrium and the perturbation into the expression for δW_s. The first non-vanishing terms are of order δ^4 and can be written as

$$\delta W_s/2\pi R_0 = A\int_0^1 |\xi|^2\Big\{b\nabla\cdot\underline{\iota_h} - g(x_0)/x_0 Q_0^3\ [b^2 + 2\iota_h b] - \beta/2\varepsilon\ dw/d\hat{n}\Big\}dv, \qquad (7)$$

$$A = \frac{1}{2}\varepsilon^2 B_0^2\ C\ , \quad C = \text{circumference of plasma boundary}$$

$$\underline{\iota_h} = 1/4\varepsilon\ \nabla F\ , \quad \iota_h = |\underline{\iota_h}|\,\mathrm{sgn}F_{x_0} \qquad (\iota_h \text{ helical transform})$$

$$w = 1/2\varepsilon\ |\nabla\psi_1|^2 + 2x_0/x_{av}\cos\theta \qquad \text{(magnetic "well")}$$

$$b^2 + 2\iota_h b + \beta/\varepsilon\ (w + \lambda) = 0 \qquad \text{(determines b for given current } (\lambda))$$

$$g(x_0) = 1 + 2\ \dot{x}_0^2/x_0^2 - \ddot{x}_0/x_0\ , \quad Q_0 = \sqrt{1 + \dot{x}_0^2/x_0^2}\ , \quad \dot{x}_0 = dx_0/d\theta$$

$$d\theta/dv = C/x_0 Q_0 \quad , \quad 0 \le v < 1 \qquad \text{(v archlength variable)}$$

We can write $B_1 = \nabla V$, $\hat{B}_1 = \nabla \hat{V}$, with $\nabla^2 V = 0$ and $\nabla^2 \hat{V} = 0$.

We require V regular at the origin and $\hat{V}$ regular at infinity (no conducting walls). Under these conditions, the plasma and vacuum terms can be converted to surface integrals in the usual way, using the boundary conditions and analytic minimization we obtain

$$\delta W_p/2\pi R_0 = A/C \int_0^1 \left\{-i\, d/dv(\xi \iota_h) + k_T \xi\right\} V^*(v)dv$$

$$\delta W_v/2\pi R_0 = -A/C \int_0^1 \left\{-i\, d/dv[\xi(\iota_h + b)] + k_T \xi\right\} \hat{V}^*(v)dv$$

Here k_T is the toroidal mode number. We use a Greens function in order to determine V^* and $\hat{V}^*$, and use truncated Fourier expansions in v to represent all physical quantities. The perturbation $\xi(v)$ is represented as a vector in Fourier space and δW can be conveniently written in matrix form $\delta W \approx \xi^* \cdot W \cdot \xi$. Minimizing this form numerically and computing the equilibrium β as described earlier. We may desplay the results in diagrams. A few results are shown in Fig. 1-4, here C_ℓ are basically the helical transform due to the single helicity field of order ℓ and B_v is the vertical field.

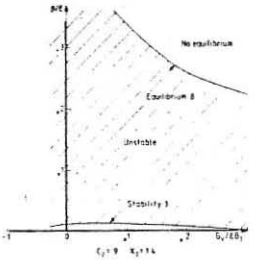

Fig.1

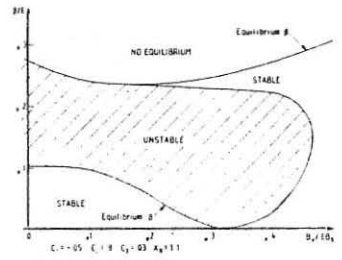

Fig.3

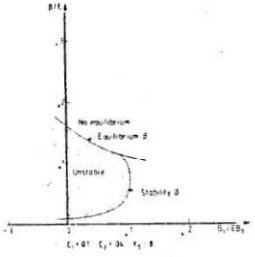

Fig.2

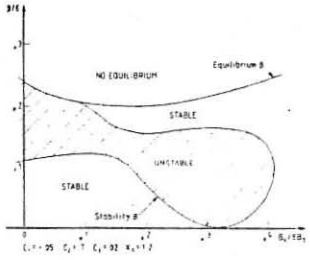

Fig.4

References

[1] D. Sherwell, J.P.Freidberg and G. Berge, Phys. Fluids 25, 1370 (1982).
[2] J.P. Freidberg, W.Grossman, F.A. Haas, Phys. Fluids 19, 1599 (1976).
[3] I.B. Bernstein et. al., Proc. R. Soc. London A 244, 17 (1958)

EFFECT OF ECH AND ICH ON AMBIPOLAR POTENTIAL FORMATION IN NAGOYA BUMPY TORUS

T. Shoji, M. Fujiwara, M. Hosokawa, T. Kamimura,
H. Ikegami, H. Iguchi, S. Kishimoto, K. Takasugi,
Y. Takita, C. Takahashi, F. Tsuboi, T. Tsuchidate
Institute of Plasma Physics, Nagoya University, Nagoya 464, Japan

Introduction

In nonaxisymmetric devices like bumpy tori and stellarators, diffusion coefficeints of ions and electrons are not automatically equal, so that an ambipolar field develops to maintain charge neutrality. Resultant $E_r \times B$ drift motion plays an essential role on both mobility and diffusion processes especially in a low collisionality regime, so the plasma confinement is profoundly influenced by the ambipolar potential profile. The present paper is devoted to give the results of the experimental study on the ambipolar potential formation in the wide range of the ratio T_i/T_e by introducing electron cyclotron heating (ECH) and ion cyclotron heating power.

ECH plasma

The Nagoya Bumpy Torus (NBT-1M) is consisted of 24 mirror sectors (mirror ratio 2.4 on the axis, B_{max} at midplane axis, 1T) connected toroidally with the major radius, 1.4 m and the minor radius at midplane, 0.1 m (Fig.1). The averaged density of plasmas is maintained at 0.5-1 x 10^{12} cm^{-3} by ECH (18 GHz, 45 kW, cw) and can be raised up to 1 x 10^{13} cm^{-3} by the RF plasma discharge with using Nagoya Type III coils (7 MHz, 400 kW, 10 msec). In standard ECH operation (T-mode), hot electron rings ($\sim$ 200 keV) are produced at the second harmonics cyclotron resonance region and stabilize the core plasma ($T_e \lesssim 50$ eV, $T_i \lesssim 15$ eV). Inside the hot electron rings, the negative potential well consisting of concentric equipotential surfaces is formed as shown in Fig.2. In this ECH mode ($T_e > T_i$) the potential well become deep as the electron temperature is raised by lowering the ambient gas pressure (P_μ = const) (Fig. 3). The particle confinement time in the steady state operation in this mode is found to increase as the potential well develops ($\tau_p \sim$ few msec). The confinement time in this configuration can not be explained simply by the

neoclassical transport theory[1] because the ion temperature is found to be too small ($\lesssim$ 15 eV) to get ions over the potential barrier ($\sim$ 120 V) within such a confinement time.

Ion heated plasma

In order to study the ambipolar potential formation in the region, where $T_i > T_e$, ICH has been applied to the ECH plasma. In the single antenna heating experiment,[2] efficient ion heating has been observed near the antenna cavity in the range of ion cyclotron frequency (Fig.4). For the potential study, many antennas (12 half turn antennas) are used to heat both toroidally passing and mirror trapped ions more uniformly around the torus. Increase in ion temperature by the application of RF power causes the substantial change in ambipolar potential profile. In Fig.5, examples of the change in the ambipolar potential profile by applying the RF at 9 MHz (B_0 = 4 kG), where slow wave mode is contributed to ion heating, are shown. The positive potential hill is observed as T_i is greater than T_e in this experiment. Such a change in the potential profile is also observed for the heating at 17 MHz (higher harmonics resonance heating), so that it appears that those change in the ambipolar potential is related to the increase in ion temperature, and not to the heating configuration of the wave. The increment of the center potential by the ion heating is proportional to the increase in the ion temperature as shown in Fig.6.

Conventional neoclassical theory[1] predicts that the potential well become deeper to confine the high energy ions when ions are heated, so that the present theory is contradictory to the experimental results. In the experiment, when $T_e > T_i$ (ECH plasma), the electrostatic potential is well shaped, and when $T_e < T_i$ (ion heated plasma), that is hill shaped (Fig.7). Confinement study of plasmas related those potential profiles is now underway.

References

(1) E. F. Jaeger, et al., Phys. Rev. Lett. 40 (1978) 866.
D. E. Hastings and T. Kamimura, Nucl. Fusion 24 (1984) 473.
(2) T. Shoji et al., Proc. 4th Int. Symp. on Heating in Toroidal Plasmas, Rome (1984) 412.

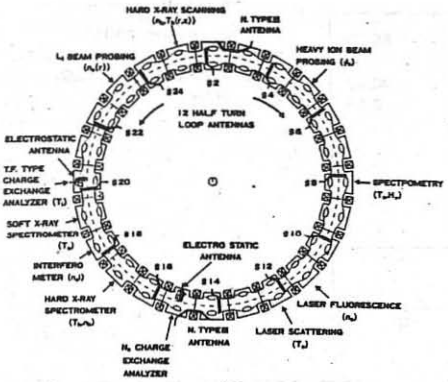

Fig.1
Arrangement of antennas and diagnostics in NBT-1M.

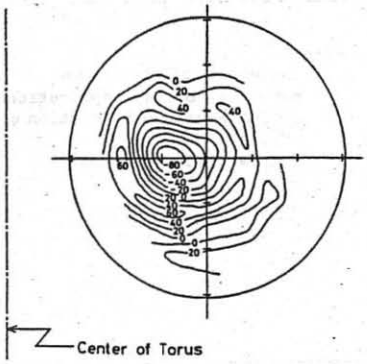

Fig.2
Equi-potential contour lines in ECH plasma measured by heavy ion beam probe (B_o = 4KG, P_{H2} = 1.4 x 10^{-5}torr).

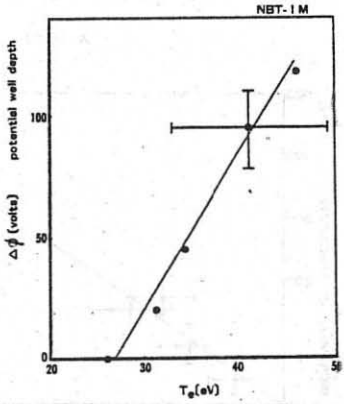

Fig.3
Depth of negative potential well as a function of T_e by changing P_{H2} (P_μ = 30KW, f_μ = 18GHz).

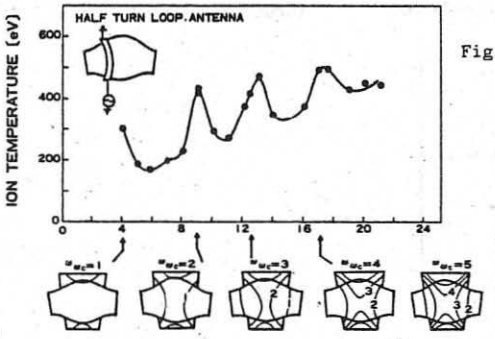

Fig.4
Ion temperature versus frequency applied to the half turn antenna (near the mirror throat).
The magnetic field strength at midplane axis B_o = 4KG, averaged density N_e = 6 x 10^{11} cm^{-3} and input RF power P_{rf} = 500W.

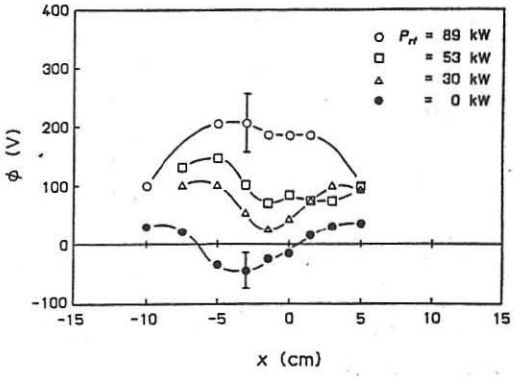

Fig.5
Change in the radial potential profiles by ICH. (f_{rf} = 9MHz, B_o = 4KG. $P_\mu \simeq$ 30KW)

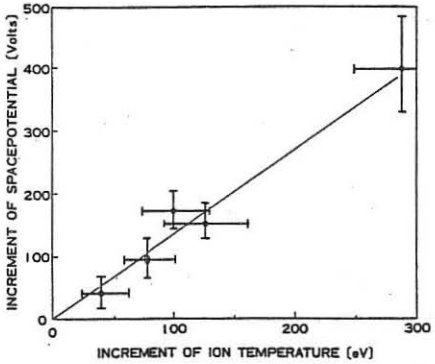

Fig.6
Increment of the center potential by the application of ICH power as a function of ΔT_i.
(f_{rf} = 9MHz, B_o = 4KG)

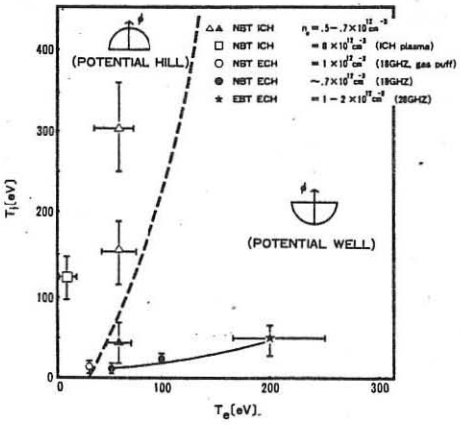

Fig.7
Ambipolar potential profiles in T_e - T_i space obtained in various ECH and ICH bumpy torus operations.

C

mirrors

Streaming Instabilities in Tandem Mirror Thermal Barriers

T. Kammash and G. Zavala
University of Michigan
Ann Arbor, Mich. 48109
USA

Abstract. Thermal barriers are utilized in Tandem Mirror Plasma confinement devices in order to insulate the electrons in the central cell from those in the plugs. A depression in the electrostatic potential is created along the field line from local density minima that are maintained by some ion pumping in the barrier region. The presence of such a depression and the appropriate magnetic structure, however, allows a group of ions to pass from the central cell into the barrier region, traverse this region and then get reflected back into the central cell by the high potential hill that exists at the outer edge of the barrier. As a result of this counter streaming motion electrostatic and electromagnetic instabilities could arise which could adversely affect the function of the barrier.

The Tandem Mirror Plasma Confinement scheme was orginally proposed [1,2] to alleviate the seriously low Q (ratio of fusion power to injected power) values associated with the standard mirror machine. The concept of thermal barriers was subsequently introduced into Tandem Mirror Confinement[3] for the purpose of insulating the electrons in the plug from those in the central cell in order to allow the ion density in the central cell (n_c) to substantially exceed the ion density in the plug (n). Because the peak magnetic field as well as the injection power in the plugs scales with the plug ion density while the fusion power is determined by the ion density in the central cell it is clear why a large would be desirable.

The creation of a thermal barrier requires that the ions in that region be pumped out in order to form a depression in the electrostatic potential which in turn serves as a barrier for central cell electrons attempting to freely move into the plug region. This potential depression along with the magnetic structure in the region, however, allows a group of ions from the central cell to pass through the barrier and be reflected back by the potential hill that exists on the plug side of the barrier. Such a group of "passing ions" stream through the thermal barrier and back into the central cell with a velocity which depends, among other things on the barrier mirror ratio and the potential well. In addition to the passing ions there are ions that become trapped in the barrier region but their density is expected to be sufficiently small especially if adequate pumping is maintained. The effectiveness of the barrier is assessed by its ability to maintain the potential depression which in turn depends on the ability to keep the trapped ions pumped out. Any phenomenon that may disrupt this process could detract from the function and the usefulness of the barrier and ultimately result in an unfavorable energy balance for the system.

In this paper we examine the micro-instabilities which may arise as a result of the passing ions streaming through the barrier region. In order to deduce the dispersion equation for the modes of interest it is necessary that we first calculate the number density of the passing ions (n_p) as well as their streaming velocity (V_s). Although the total (passing plus trapped) ion density in the barrier (n_b) can be expressed by

$$n_b = n_c \exp\left[-\varphi_b / T_{ec}\right] \tag{1}$$

where φ_b is the depth of the potential well in the barrier and T_{ec} is the temperature of the central cell electrons, the properties of the passing ions need be determined from their distribution function. If we denote by F_c the ion distribution in the central cell, and by F_b the ion distribution in the barrier then by conservation of flux we can write

$$\frac{1}{R} V_{\parallel} F_b(V_{\perp b}, V_{\parallel}) \, dV_{\perp b} \, dV_{\parallel} = V_{\parallel c} F_c(V_{\perp}, V_{\parallel c}) \, dV_{\perp} \, dV_{\parallel c} \tag{2}$$

where $R = B_b / B_c$. Furthermore, if we choose F_c to be Maxwellian, i.e.,

$$F_c(V_{\perp}, V_{\parallel c}) = \sqrt{\frac{2}{\pi}} \, n_c \left(\frac{m_i}{T_{ic}}\right)^{3/2} V_{\perp} \, e^{-\frac{m_i}{2T_{ic}}\left(V_{\perp}^2 + V_{\parallel c}^2\right)} \tag{3}$$

and utilize the conservations of mangetic moment and energy, then it can readily be shown that

$$F_b(V_{\perp b}, V_{\parallel}) = \sqrt{\frac{2}{\pi}} \, n_c \left(\frac{m_i}{T_{ic}}\right)^{3/2} e^{\frac{e\varphi_b}{T_{ic}}} V_{\perp b} \, e^{-\frac{m_i}{2T_{ic}}\left(V_{\perp b}^2 + V_{\parallel}^2\right)} \tag{4}$$

where m_i and T_{ic} are the ion mass and the ion temperature in the central cell respectively. At this point it is convenient to calculate the rate at which the Maxwellian ions in the central cell cross a plane in one direction i.e., neglecting the return flow; that is given by

$$J_M = \frac{n_c}{2\sqrt{\pi}} \left(\frac{2T_{ic}}{m_i}\right)^{1/2} \tag{5}$$

The number density of the passing ions (n_p) is obtained by integrating Eq. (3) over velocity space. The result is

$$n_p = n_c \, e^{\frac{e\varphi_b}{T_{ic}}} \left\{ \left[1 - \Phi\left(\sqrt{\frac{e\varphi_b}{T_{ic}}}\right) \right] - \left(\frac{R_c - R}{R_c}\right) e^{\left(\frac{R}{R_c - R}\right)\left(\frac{e\varphi_b}{T_{ic}}\right)} \right. \tag{6}$$

$$\left. \times \left[1 - \Phi\left(\sqrt{\left(\frac{R_c}{R_c - R}\right)\left(\frac{e\varphi_b}{T_{ic}}\right)} \right) \right] \right\}$$

where $R_c = B_{mb} / B_c$ and $\Phi(x)$ is the familiar error function. The flow current of these particles can be calculated by multiplying Eq. (4) by V_z and integrating over the same velocity limits used in Eq. (6). The result is

$$J_p = \frac{1}{2\sqrt{\pi}} \left(\frac{R}{R_c}\right) n_c \left(\frac{2T_{ic}}{m_i}\right)^{1/2} = \frac{R}{R_c} J_M \tag{7}$$

If, however, the passing ions had a pure Maxwellian distribution then in place of Eq. (7) we would obtain

$$J_{pM} = \frac{n_p}{2\sqrt{\pi}} \left(\frac{2T_{ic}}{m_i}\right)^{1/2} = \frac{n_p}{n_c} J_M \tag{8}$$

We now utilize Eqs. (7) and (8) to deduce an expression for the streaming velocity V_s. Noting that $\frac{1}{2} n_p$ would participate it is reasonable to define V_s by

$$V_s = \frac{2}{n_p} \left[J_p - J_{pM} \right] = 2 \frac{J_M}{n_p} \left[\frac{R}{R_c} - \frac{n_p}{n_c} \right] \tag{9}$$

which, upon substituting from Eq. (6), becomes

$$V_s = \frac{2 J_M}{n_p} \left\{ \frac{R}{R_c} + \left(\frac{R_c - R}{R_c}\right)^{1/2} \left[1 - \Phi\left(\sqrt{\left(\frac{R_c}{R_c - R}\right)\left(\frac{e\varphi_b}{T_{ic}}\right)} \right) \right] \times \right.$$
$$\left. \times e^{\left(\frac{R_c}{R_c - R}\right)\left(\frac{e\varphi_b}{T_{ic}}\right)} - \left[1 - \Phi\left(\sqrt{\frac{e\varphi_b}{T_{ic}}} \right) \right] e^{\frac{e\varphi_b}{T_{ic}}} \right\} \tag{10}$$

For $e\varphi_b / T_{ic} \gg 1$ Eqs. (6) and (10) reduce to

$$\frac{n_p}{n_c} = \frac{1}{\sqrt{\pi}} \frac{R}{R_c} \sqrt{\frac{T_{ic}}{e\varphi_b}} = \frac{1}{\sqrt{\pi} R_b} \sqrt{\frac{T_{ic}}{e\varphi_b}} \tag{11}$$

$$V_s = \sqrt{2} \left(\frac{e\varphi_b}{m_i}\right)^{1/2} \tag{12}$$

where $R_b = B_{mb} / B_b$ is the mirror ratio of the barrier magnetic field.

The above results will now be used to investigate the stability of electrostatic and electromagnetic oscillations propagating along the magnetic field that might be induced by the passing ions in the barrier region. For analytical convenience we will represent the passing ion distribution by a modified version of Eq. (4) that explicitly reflects the streaming aspect namely

$$F_p(\underline{v}) = 2 \left(\frac{m_i}{2\pi T_{ic}}\right)^{3/2} n_p \left[exp - \frac{m_i}{2T_{ic}} \left(\underline{v} - V_s \underline{e}_z \right)^2 + \right.$$

$$+ \exp - \frac{m_i}{2T_i} \left(\frac{v}{} + V_s \hat{\xi}_a \right)^2 \Bigg] \qquad (13)$$

where $\hat{\xi}_a$ is a unit vector along the magnetic field. The dispersion equation for electrostatic modes with a propagation vector $\underset{\sim}{k} = k_a$ is given by

$$1 + \frac{2\omega_{pe}^2}{k^2 v_{the}^2} \left[1 + \zeta_e Z(\zeta_e) \right] + \frac{4\omega_{pp}^2}{k^2 v_{thp}^2} \left[(\zeta_p - v) Z(\zeta_p - v) \right. \qquad (14)$$

$$\left. + (\zeta_p + v) Z(\zeta_p + v) \right] = 0$$

where ω_{pe} and ω_{pp} are the plasma frequency of the electrons and passing ions respectively, and

$$v = V_s / V_{thp} \quad , \quad \zeta_p = \frac{\omega}{k} \sqrt{\frac{m_i}{2T_i}} \quad , \quad Z(\zeta) = \frac{1}{\sqrt{\pi}} \int_{-\infty}^{+\infty} \frac{dx\, e^{-x^2}}{x - \zeta} \qquad (15)$$

with the latter being the familiar plasma dispersion function. Because of space limitation we shall focus our attention on the stability of these modes in a relatively cold plasma and the resulting dispersion equation is the standard two stream one or

$$1 = \frac{\omega_{pe}^2}{\omega^2} + \frac{\omega_{pp}^2}{2} \left[\frac{1}{(\omega - kV_s)^2} + \frac{1}{(\omega + kV_s)^2} \right] \qquad (16)$$

which yields an instability condition given by

$$kV_s < \omega_{pe} \left\{ 1 + \left[\frac{m_e}{2m_i} \frac{1}{k_b^2} \left(\frac{T_i}{e\varphi_b} \right) \right]^{1/3} \right\}^{3/2} \qquad (17)$$

In obtaining the above result use was made of Eqs. (11) and (12) which are applicable in the cold plasma limit. We note that (17) is difficult to satisfy for large barrier potential since the left-hand side decreases with $e\varphi_b$, except of course for very large wavelengths which can be excluded by careful design. It appears, therefore, that barriers with deep potential wells which are desirable for insulating plug electrons from central cell electrons tend to be stable against the electrostatic streaming instability. For electromagnetic modes propagating along the field, however, it can be shown that the condition for instability regardless of the beta value, is given by

$$V_s > V_A \sim \frac{B}{\sqrt{n_p}} \sim (e\varphi_b)^{1/4} \qquad (18)$$

which can be readily satisfied for large $e\varphi_b$ since V_s is proportional to $(e\varphi_b)^{1/2}$. This could have serious consequence since the quasilinear diffusion in velocity space resulting from this instability could destroy the function of the barrier.

1. G. I. Dimov, V. V. Zakaidakov, and M. E. Kishinevsky, Sov. J. Plasma Phys. 2, 326 (1976)
2. T. K. Fowler and B. G. Logan, Comments Plasma Phys. Controlled Fusion 2, 167 (1977)
3. D. E. Baldwin and B. G. Logan, Phys. Rev. Letters 43, 1318 (1979)

ICRF Field Solutions in Axisymmetric Mirror Plasmas

M. W. Phillips and A. M. M. Todd
Grumman Aerospace Corporation
105 College Road East
Princeton, N. J. 08540, U.S.A.

The results of a numerical code designed to calculate the three-dimensional structure of ICRF fields in axisymmetric mirrors are presented. The code solves the electromagnetic wave equation using a cold plasma dispersion relation with a small collision frequency to simulate absorption. The purpose of the calculation is to examine how ICRF wave structure and propagation is effected by the axial variation of the magnetic field in a mirror for various antenna designs. In the code the wave equation is solved in flux coordinates using a finite difference method. Field solutions for a typical antenna array in a simple mirror will be shown.

Introduction

A knowledge of the three-dimensional wave structure of ICRF fields in mirrors is important for understanding how waves propagate and are absorbed in mirror experiments. The global field structure of RF fields in mirrors can be of particular importance in determining the possibility of RF stabilization due to pondermotive forces of mirror plasmas such as recent experiments in Phaedrus suggest[1]. This paper describes a code developed to calculate ICRF fields in axisymmetric mirror geometry such as the central cell of a tandem mirror and in RF test stands that use a mirror magnetic field. Previous calculations in mirrors looked at the case where there was no axial variation of equilibrium quantities[2]. Such an approximation is useful when considering a long mirror such as the central cell of a tandem mirror where there are no resonances in the vicinity of the antenna. In a short mirror cell, or in cases where the antenna is located near a resonance, or when the variation of the magnetic field in the axial direction is significant, it is important to include the effects of the axial variation of equilibrium quantitites in the calculation.

The code solves the electromagnetic wave equation using a simple dielectric cold plasma dielectric tensor in a flux type geometry. An antenna structure is specified using filimentary straight and curved segments on which the currents are given. Equilibrium quantities are assumed specified on a 2-D grid so that axial and radial variation is allowed. The problem is solved using generalized coordinates with the coordinate system being specified by the equilibrium grid. The component of the electric field parallel to B can be optionally included in the calculation. Both a finite element and a finite difference method were tried for solving the wave equation. In this paper we discuss the results from the finite difference code.

Basic Equations

The fields are found by solving the wave equation:

$$\nabla\times(\nabla\times E) - k^2\, K\cdot E = i\omega\mu_0 J_{ext},$$

where $k=\omega/c$, K is the cold plasma dielectric tensor[3] with a small amount of collision frequency added to simulate absorbtion and J_{ext} is current density due to the antenna.

The wave equation is solved in a flux type coordinate system (ψ,ϕ,χ). The coordinate ψ is some function of the poloidal flux, ϕ is the poloidal angle coordinate, and χ is some measure along field lines. The exact specification of ψ and χ is left open since it may be desirable to concentrate the grid around certain regions. Given $r(\psi,\chi)$ and $z(\psi,\chi)$ mapped from an equilibrium the Jacobian and metric relations can be calculated.

The dielectric tensor, K, is typically given in a local orthogonal coordinate system oriented along the magnetic field. Hence a transformation from local orthogonal coordinates, (x,y,z) to equilibrium flux coordinates (ψ,ϕ,χ) is needed.

Numerical Solution

The fields from the current source are solved in free space by a Green's function method. The antenna structure is modeled using straight and curved current segments. The current and the phase are given at a particular point on each segment. The fields are solved over the region of interest and are then Fourier analyzed. Subsequent calculations deal with one Fourier component at a time. This reduces the remaining problem to 2-D which simplifies things somewhat.

The electric field is solved inside the plasma using a finite difference method. The 3 components of the wave equation can be written in the form

$$\sum_{k=1}^{3}\Bigg\{\sum_{m=1}^{3}\sum_{n=1}^{3}\frac{\partial}{\partial e_m}\frac{\partial}{\partial e_n}E_k(\nabla e_l\times\nabla e_n)\cdot(\nabla e_m\times\nabla e_k)$$

$$+\sum_{m=1}^{3}\frac{\partial}{\partial e_m}E_k\sum_{n=1}^{3}\frac{1}{J}\frac{\partial}{\partial e_n}\left[J(\nabla e_l\times\nabla e_n)\cdot(\nabla e_m\times\nabla e_k)\right]$$

$$-k^2\,\nabla e_l\cdot K\cdot\nabla e_k\,E_k\Bigg\} = 0 \quad \text{for } l = 1,\ 2,\ 3\ .$$

Here e_i, are defined as $e_1=\psi$, $e_2=\phi$, $e_3=\chi$. In the vacuum K = I. The partial derivatives can then be cast in finite difference form to give the finite difference equations.

Since all components of the electric field are being solved the resulting matrix can be quite large. The structure of the matrix is typical of those resulting from 2-D partial differential equations - block tridagonal with each block in turn block tridiagonal. The matrix is solved by direct LU decomposition using a method that minimizes matrix storage. Only the main diagonal block of the LU decomposed matrix is stored -either in memory, if there is enough room, or on disk if there is not. This keeps storage space for solving the matrix at a minimum so that the largest possible spatial resolution can be achieved. A partial pivoting scheme was tried by found unnecessary for most cases. The original matrix is not overwritten so that the residual can be calculated and the method iterated. This gives a clearer handle on the accuracy of the solution. Typically only 2 iterations are needed to achieve a relative error of $\| x_i - x_{i-1} \| / \| x_i \| < 1.0 \times 10^{-9}$ where x_i is a vector containing all three components of the electric field on an 41 x 81 equilibrium grid. However, if parameters are such that the solution is close to a normal mode of the system more iterations are required to achieve this accuracy.

Results

Figs. 1 and 2 show the results of typical calculations. These calculations were performed on a 41 x 81 grid solving for all components of the electric field. An axisymmetric loop antenna was used and a conducting wall was assumed on the edge of the grid. A density profile of the form $n(r,z) = n(\psi)\, g(\psi,x)$ was used where $n(\psi) = n_o e^{-\alpha\psi}$ and $g(\psi,\chi) = (1 - B(\psi,\chi)/B_{max})^{1/2} + n2$. The constants were chosen so that $n_{peak} = 5.0 \times 10^{18}$ $n_{end}/n_{peak} = 0.1$, $n_{wall}/n_{peak} = 0.01$. The mirror ratio was 4.4. The parameters were choosen to nominally model the central cell of the Phaedrus tandem mirror when run in an axisymmetric mode. In Fig. 1 $\omega = 1.5\ \Omega_{ci\ min}$ so that the fundamental resonance occurs at $z = 0.3$ m. This location can be seen in Fig. 1(a) where E^+ is zero. Fig. 1(b) shows E^- and Fig. 1(c) shows $E_\parallel$. As indicated by theory $E_\parallel$ is much smaller than E^- and E^+. Without looking too much at the variation of the fields the ratio of E^-/E^+ is also roughly what one would expect from slab geometry.

Fig. 2 shows E^+ and E^- for the case where $\omega = 0.9\ \Omega_{ci\ min}$ so that the fundamental resonance does not occur in the plasma. A comparison of Fig. 1 and Fig. 2 shows that the presence of the fundamental resonance in the plasma has a big effect on the structure of the electric field. The pondermotive potential of the ICRF electric field has been hypothesized as one mechanism for stabilizing axisymmetric mirror configurations. Experiments in Phaedrus have shown that a dramatic change in stability occurs at the point $\omega = \Omega_{ci\ min}$. This effect might be accounted for by a change in structure of the electric field when going from the case $\omega < \Omega_{ci\ min}$ to $\omega > \Omega_{ci\ min}$, as in Figs. 1 and 2. This will be the topic of future study.

References

[1] J. R. Ferron, N. Hershkowitz, R. A. Breun, Phys. Rev. Lett., 51, 1955 (1983).

[2] B. D. McVey, et al., MIT Plasma Fusion Center Report, PFC/JA-82-16 (1982).

[3] T. H. Stix; "The Theory of Plasma Waves", McGraw-Hill, U.S.A. (1962).

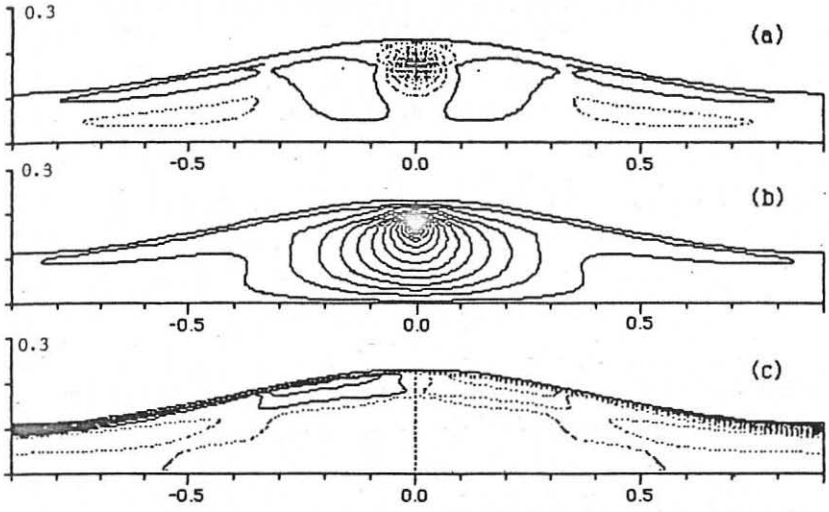

Fig. 1 (a) Contours of E^+, (b) Contours of E^-, (c) Contours of $E_{\parallel}$ for $\omega/\Omega_{ci\ min} = 1.5$, $n0 = 5.0\times10^{18}$ #/m3, $B_{min} = 0.086$T $B_{max}=0.384$ T, $\omega = 12.5\times10^{6}$ rad/sec.

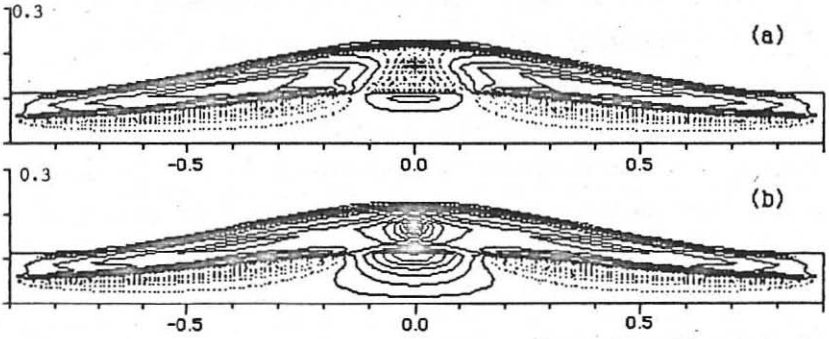

Fig. 2 (a) Contours of E^+, (b) Contours of E^-, for $\omega/\Omega_{ci\ min} = 0.9$, $n0 = 5.0\times10^{18}$ #/m3, $B_{min} = 0.086$T $B_{max}=0.384$ T, $\omega = 7.5\times10^{6}$ rad/sec.

Sloshing Ion Distribution Produced by ICRH in an Axisymmetric Mirror-Cusp Device, RFC-XX-M

R. Kumazawa, K. Adati, T. Aoki, H. Fujita, K. Hattori, S. Hidekuma, T. Kawamoto, K. Nishimura, S. Okamura, Y. Okubo, T. Sato, T. Hatori, H.R. Garner*, H.D. Price*

Institute of Plasma Physics, Nagoya University
Chikusa-ku, Nagoya 464, Japan

* GA Techonologies, Inc., San Diego, California 92138, USA

Abstract: A sloshing ion distribution has been found at the central mirror plasma produced by an ion cyclotron resonance heating (ICRH) in RFC-XX-M. This sloshing ion distribution has been certified by the measurement of the axial density profile and the pitch angle distribution of ions.

RFC-XX-M is an MHD stable, completely axisymmetric device with radio frequency (RF) plugging. The central mirror is connected to two cusps. The distance between the two field-null point is 3 m. The magnetic field strength is 2.1 T at the line cusp and 3.9 T at the point cusp in full operation. The central mirror radio is 2.8 and the magnetic field strength is 0.35 T at the midplane. A rotating type-III antenna installed at the mirror throat is excited by two 0.4 MW rf oscillators ($\omega/2\pi$ = 7 MHz) as shown in Fig. 1.

The plasma is produced by the left-handed rotation mode through the type-III antenna at the mirror. The plasma parameters are as follows: the plasma density, $n = 6 \times 10^{12}$ cm^{-3}, the electron temperature, T_e = 30 eV, the ion temperature by a

diamagnetic loop, $T_{i\perp}$ = 500 eV, ICRH power, P_{rf} = 200 kW and a hydrogen gas puffing rate, Γ = 30 torr·ℓ/sec. The left-handed rotation mode of an ion cyclotron wave (ICW) excited by the type-III antenna damps at a magnetic beach in the mirror field. Ions are heated perpendicularly to the magnetic field there. When a particle confinement time of ion is much shorter than an ion-ion scattering time (τ_{ii}) by Coulomb collissions, ions concentrate in a narrow pitch angle in the ion velocity space. In this plasma, a neutral density (n_a) is measured by a laser fluorescence method and n_a is 2×10^{10} cm^{-3}. The charge exchange time (τ_{cx}) is much shorter than τ_{ii}, therefore the sloshing ion distribution is expected.

The plasma density is measured for the various positions in the mirror when the magnetic field strength is 70 % of full operation (we refer as 0.7 PU.) as shown in Fig. 1. The densities are as follows: $n_{cc} = 6 \times 10^{12}$ cm^{-3} at the midplane (Z = 0 cm, B_{cc} = 0.25T), $n_{om} = 8 \times 10^{12}$ cm^{-3} at the off-midplane (Z = 42 cm, B_{om}/B_{cc} = 1.9) and $n_{th} = 4 \times 10^{12}$ cm^{-3} at the mirror throat (Z = 77 cm, B_{th}/B_{cc} = 2.8). In this experiment, the cyclotron reasonant point locates at Z = 42 cm and the peak density position agrees with this point. A density ratio of n_{om} and n_{cc} is measured for various magnetic field strength from 0.6 PU to 1.0 PU as shown in Fig. 2. The density ratio is largest in the case of 0.7 PU. The density peak of the sloshing ion distribution moves towards the midplane side with the cyclotron resonant point when increasing the magnetic field strength. The density ratio decreases to about a half beyond 0.75 PU as expected.

The pitch angle distribution of the ion has been measured by

a fast neutral particle analyzer (FNP). This anlayzer aims at Z = 28 cm with an angle of 80° ($\theta_{FNP} = 80^0$) to the magnetic axis as shown in Fig. 1. The ion energy distribution measurement has been done where we fiarly adjust the plasma density, the ion temperature and the hydrogen gas puffing rate to the same by changing the magnetic field strength from 0.6 PU to 1.0 PU. Figure 3 shows the results measured in 0.4 keV < E_i < 5 keV where E_i is ion energy. The ion temperature in the small pitch angle (in this case, $\Delta\theta = 3^0$) becomes largest to be about 0.9 keV at 0.95 PU. The total number of ions which has a pitch angle, $\theta = \theta_{FNP}$ at Z = 28 cm can be calculated by integrating the ion energy distribution ($\int f(E_i,\theta)dE_i$). It also has a peak value at 0.95 PU as shown in Fig. 3. The ion is produced perpendiculary to the magnetic axis at the cycltron resonant point, Z = 30 cm in the case of 0.95 PU. The pitch angle of the ion coincides with θ_{FNP} at Z = 28 cm.

The pitch angle distribution of ion in the midplane can be calculated from the data of Fig. 3 as shown in Fig. 4, assuming that the shape of the pitch angle distribution does not change for vairous magnetic field strength. The ion temperature and the density in loss cone are deduced by measuring the ion temperature of the cusp plasma by a time of flight type neutral particle analyzer and the mirror throat density, respectively. The full half width of the pitch angle is about ten degrees. The average ion temperature faily agrees with that from the diamagnetic loop signal, therefore these ions must be a great majority.

The sloshing ion distribution produced by ICRH at the central mirror in RFC-XX-M can be certified from these experimental results.

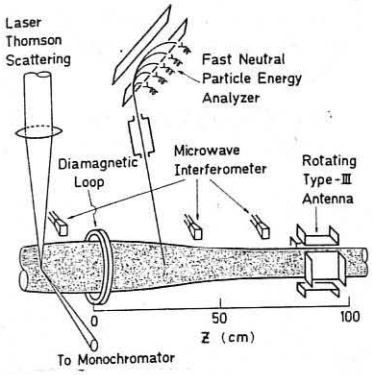

Fig.1 Schematic drawing of diagnostics and Rotating type-III antenna on RFC-XX-M

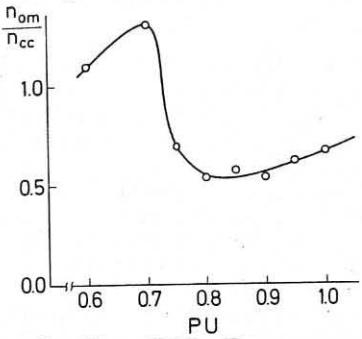

Fig.2 Dependence of the density ratio of the off midplane (n_{om}) and the midplane (n_{cc}) on the magnetic field strength.

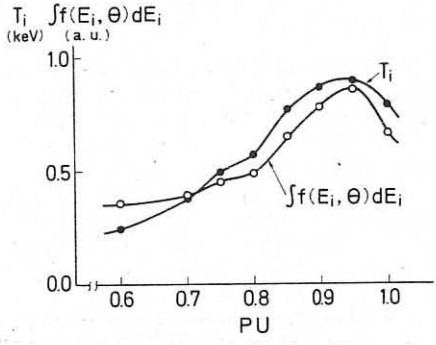

Fig.3 Dependence of the ion temperature and the ion number, $\int f(E_i,\theta)dE_i$ on the magnetic field strength.

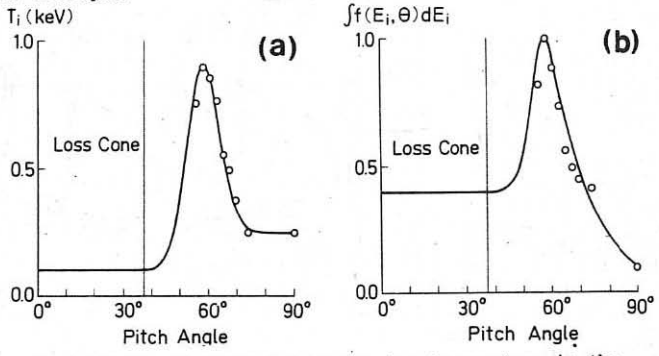

Fig.4 (a) The distribution of the ion temperature in the pitch angle space.
(b) The distribution of the ion number, $\int f(E_i,\theta)dE_i$ in the pitch angle space.

MAGNETIC FOCUSING OF 80 kJ MICROSECOND ELECTRON BEAM FOR PLASMA HEATING IN SOLENOIDS

V.V.Chikunov, B.A.Knyazev, V.S.Koidan, S.V.Lebedev, M.A.Shcheglov, S.G.Voropajev

Institute of Nuclear Physics,
630090 Novosibirsk, USSR

ABSTRACT: Experiments have been performed on magnetic focusing of an intense microsecond relativistic electron beam. The beam is generated in a high-voltage quasi-planar diode (E_{max}=0.8 MeV, I_{max}=40 kA, τ=5 μsec, $\varnothing$=18 cm). The total energy of the initial beam is 80 kJ. The beam is magnetically-focused by longitudinal injection into a magnetic mirror with the mirror ratio equal to 20. The gas pressure in the focusing chamber is varied from 10^{-5} to 1 Torr. The compressed beam with a 4 cm diameter, 70 kJ energy content, and current density up to 3 kA/cm² in the center of the mirror was obtained.

INTRODUCTION. High-power microsecond relativistic electron beams (REB) which have a current density of at least 2—3 kA/cm² can be used for effective plasma heating in open traps /1/. It may be possible to produced such a beam in a planar or foil-less high-voltage diode at a low current density, with subsequent focusing in a magnetic mirror /2/.

Experiments on magnetic focusing high-power REBs had previously been made with short pulse beams (about 50 nsec) /3,4/. The total beam energies in these experiments were not too high. As one might expect, an increasing the pulse duration by two orders of magnitude can qualitatively change the picture of beam focusing and transport.

In this paper we present the experimental results on magnetic focusing of an intense microsecond REB from U-1 accelerator /5/.

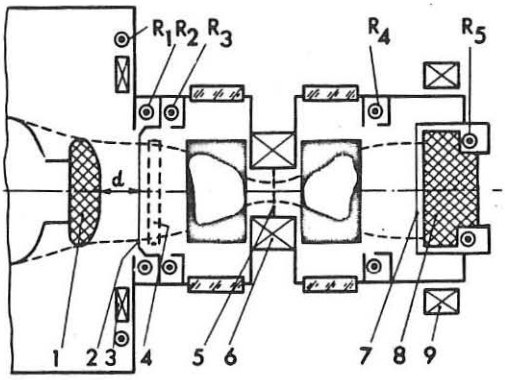

Fig.1. Experimental set-up. The gas glow induced by a REB was observed by means of an image-convertor tube (Δt = .5 μsec). 1: carbon cathode of 18 cm diam.; 2: anode foil; 3, 6, 9: magnetic field coils, dotted curves are magnetic field lines; 4: removable stainless steel collector; 5: 50 μm Ti foil (only in the certain test shots); 7: Al foil; 8: carbon calorimeter; $R_1 - R_5$: Rogowsky coils.

EXPERIMENT. Figure 1 shows a cross-sectional view of the experimental apparatus. The high-voltage pulse from a LC generator is applied to a 18 cm diameter carbon cathode (1). The beam is generated in a quasi-planar diode with a thin foil anode (2). The electron energy is determined by the applied

voltage prior to the moment at which the diode is shorted by the plasma /5/. The maximum current density of the beam does not exceed 0.2 kA/cm^2. The diode voltage U and beam current I_2 are shown in the oscillograms Fig.2A. These traces were obtained with a thick stainless still collector (4) placed 1 cm behind an anode foil («collector mode of operation»). The pulse duration is determined by the time necessary to fill the diode with plasma produced at the electrodes[1].

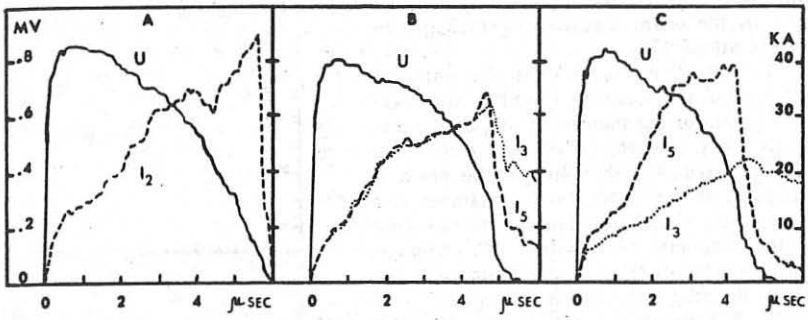

Fig.2. Oscillograms. Foil 2 is aluminized mylar. U: diode voltage; I_i: currents recorded by Rogowsky coils R_i. Diode gap d is 8.5 cm. Oscillograms A were recorded in the «collector mode of operation», while B and C were recorded in the «focusing mode of operation». $p = 1.2 \cdot 10^{-5}$ Torr background gas (B); $p = 6 \cdot 10^{-2}$ Torr Ar (C).

In the focusing experiments, the collector is absent and the beam passes through the anode foil into a gas-filled stainless-steel chamber. Unlike the previous experiments with a 50 kJ beam /6/, the acrilic plastic windows into the chamber were covered with metallic screens. The longitudinal magnetic field increases from 0.5 T in the accelerator diode to 10 T in the central coil (6). The mirror ratio is twenty. The total energy Q of the beam passing through the mirror is measured by a carbon calorimeter (8) situated in an evacuated chamber separated from the focusing chamber by a diaphragm of a thin Al foil. The magnetic field in this region is about 0.5 T. The distance between the foils (2) and (7) is 52 cm. The gas pressure in the focusing chamber is varied from 10^{-5} Torr (background pressure) to 1 Torr of argon.

The Rogowsky coils R_2 and R_5 measure, correspondingly, I_2, the current of the beam injected into the focusing chamber, and I_5, the current of the beam leaving the chamber. The coils R_3 and R_4 record the net current, i.e. the REB current plus the return plasma current, in the left, I_3, and right, I_4, sections of the focusing chamber. In the course of the experiments, the beam diameter is determined from the holes which are made in the foils (2), (5)[2] and (7), as well as from the microphotometric analysis of photographs (see Fig.1) obtained by means of an image-converter tube /6/. In the beam focusing experiments, the anode-cathode distance is 8.5 cm. A 10 μm aluminized mylar foil with a 0.5 μm layer of Al serves as an anode.

[1] After the diode is shorted the current I_2 is the arc current.
[2] A titanium foil (5) of 50 μm thick was used only for the certain test shots.

RESULTS AND DISCUSSION. The main results of the experiments are the following (see Figures 2 and 3) :

1. An intense microsecond REB from a high-voltage diode may be effectively magnetically focused. The total energy of the beam from U-1 accelerator which passes through the mirror varies from 45 to 70 kJ when the gas pressure in the chamber is varied within the range from 10^{-5} to 1 Torr (Fig.3A). The pulse duration is almost constant also (Fig.3B). The total energy of the initial beam («collector mode of operation») is 80 kJ. Consequently, the efficiency of the beam transporting through the mirror attain 85%.

2. The REB currents at the entrance and exit of the focusing chamber are equal ($I_2=I_5$) up to the moment at which the diode becomes shorted, i.e. there are no transverse losses. The diameter of the beam is 18 cm at the entrance to the chamber and is inversely proportional to the square root of the magnetic field within the chamber. The diameter reaches a minimum of 4 cm where the magnetic field is strongest.

3. The beam current in the focusing chamber is higher then the critical vacuum current (about 10 kA in our case). This implies that the beam creates a plasma which, in turn, neutralizes the space sharge of the beam. At a certain moment, the return current I_{ret} equal to I_5-I_3[3)] appears in the plasma (see Figs. 2C and 3C). This return current appears if the gas pressure is higher then 10^{-4} Torr, and delay of its appearance becomes less when the gas pressure is increased.

4. When the beam is passed through the mirror («focusing mode operation») the operation of the diode markedly changes in comparison with its operation in the «collector mode». First, the beam current decreases, and the voltage increases. Second, the shorting of the diode occurs earlier (see Fig. 2).

These phenomena are probably related to the fact that some of the beam electrons are reflected from the magnetic mirror and that they oscillate through the anode foil. These oscillating electrons lead to an increase in the rate of energy deposition in the anode foil, which results in the earlier ex-

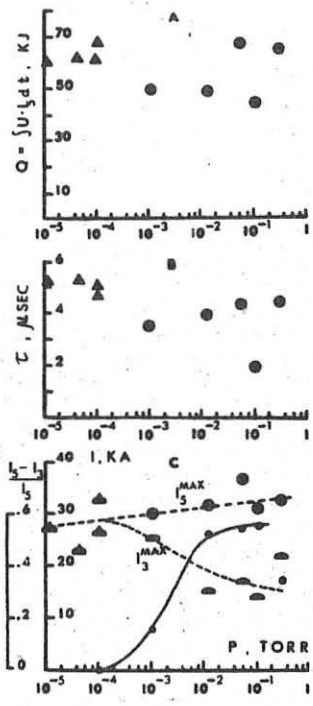

Fig.3. The total energy (A) and the pulse duration (B) of the beam passing through the mirror as functions of the gas pressure in the focusing chamber: triangles—background gas in the chamber; circles—the chamber is filled with Ar. C—the beam current I_5 and the net current I_3 measured before the shorting; solid curve is $(I_5-I_3)/I_5$.

[3)] The currents I_3 and I_4 are always the same.

plosion of the foil. With a mirror ratio of 20, the magnetic mirror reflects the electrons which have a pitch-angle exceeding 13° at the entry to the focusing chamber.

The pitch-angles of the beam electrons are determined mainly by scattering in the foil (θ_f) and by the sharp change in the direction of the magnetic field line in the entrance to the chamber when there exist a return current (θ_{rc}). Both a decrease of the diode voltage and an increase of the return current lead to the growth of electron pitch-angles. Fig.2 shows that these circumstances give rise to an increase in pitch-angles by the end of the pulse. For the shot in the Fig.2C the pitch-angle θ_{rc} of the electrons in the beam boundary reaches 5° and the angular scattering in the mylar foil $(\overline{\theta_f^2})^{1/2}$ is about 3°. If the beam current density becomes high the collective beam-plasma interaction may serve as an additional source of angular spread $(\overline{\theta_{bp}^2})^{1/2}$ /7/.

To investigate the effect of the reflected electrons on the time at which the diode becomes shorted, we replaced the mylar anode foil by thick aluminium foils. The substitution of the anode foil lead to a growth of the angular width $(\overline{\theta_f^2})^{1/2}$. The diode shorted in 3 μsec if the anode foils was 10 μm thick and in 0.5 μsec for a 30 μm foil.

CONCLUSION. The results of our work demonstrate the feasibility of effective magnetic focusing of a microsecond REB generated in a quasi-planar diode. The focused-beam parameters obtained (maximum total energy 70 kJ, diameter 4 cm, current density 3 kA/cm^2) enable this beam to be used for plasma heating experiments in open traps.

ACKNOWLEDGEMENT. The authors are indebted very much to D.D.Ryutov for helpful comments and discussion.

REFERENCES

/1/ V.S. Koidan, E.P. Kruglyakov, D.D. Ryutov.—Proc. 4-th Internat. Topical Conf. on High-Power Electron and Ion Beam Research and Technology, Palaiseau, v.2, p.531 (1981).
/2/ D.D. Ryutov.—Problems of atomic science and technology, Ser. Thermonuclear Fusion. Issue 1—2, Kurchatov Institute, Moscow, p.96 (1978).—in Russian.
/3/ P.E. Bolduc, E.L. Patterson.—J. Appl. Phys., v. 43, p.4006 (1972).
/4/ C. Stallings, J. Benford, K. Childers.—Plasma Physics, v.18, p.317 (1976).
/5/ S.G. Voropajev, V.S. Koidan, S.V. Lebedev, V.S. Nikolaev, V.V. Chikunov, M.A. Shcheglov.—Doklady Akad. Nauk SSSR (Soviet Physics Doklady), v. 276, p.111 (1984).
/6/ V.V. Chikunov, B.A. Knyazev, V.S. Koidan, V.V. Konyukhov, S.V. Lebedev, K.I. Mekler, M.A. Shcheglov, S.G. Voropajev.—Laser and Particle Beams, v. 5, N 3 (1985).
/7/ A.V. Arzhannikov, V.S. Koidan, S.L. Sinitsky.—Proc. 16-th Internat. Conf. on Phen. in Ionized Gases, Dusseldorf, 1983, p.348.

STABILITY OF A STEADY STATE IN OPEN TRAPS WITH NEUTRAL INJECTION

V.V.Mirnov

Institute of Nuclear Physics, Novosibirsk 90, USSR

A new class of low frequency instabilities in mirror machines is considered. The steady state is assumed to be maintained by the equilibrium between neutral beam injection and losses through the ends of the system. The instability is driven by the imbalance between the rate of fast ion losses and the neutral trapping rate. This imbalance is caused by the plasma density perturbation.

In open traps with neutral injection, steady states can exist where the Coulomb losses through the ends of the system are compensated by neutral beam ionization. The ionization rate is proportional to the first power of the density and the loss rate is proportional to the second. Thus if the density goes above the steady state value the loss rate increases faster than the trapping rate making the system stable.

Besides this "rough" mechanism of stabilization there exist kinetic effects which can significantly affect the stability. These result from the fact that the ions entering the system have relatively high energy while those leaving are relatively slow. If the density goes up, the increase in the ionization rate will be compensated for by a change in the loss rate which is delayed by the time necessary for a particle to diffuse from the injection velocity to the loss boundary. This delay can intensify the density perturbation and promote the instability. The purpose of this paper is to show that this time delay effect can cause the steady state to be unstable.

Let us consider a mirror machine in which a monoenergetic neutral beam with velocity v_1 is injected perpendicular to the magnetic field. The beam density N inside the machine is assumed to be fixed and independent of the plasma parameters. The rate of ionization per unit volume is $\dot{n} = n(\nu_i + \nu_{cx})$, where $\nu_i = N\langle v\sigma_i\rangle$ is the frequency of electron impact and $\nu_{cx} = N\langle v\sigma_{cx}\rangle$ is the charge exchange frequency. Via the factor $\langle v\sigma_i\rangle$, ν_i depends on the electron temperature T_e, while ν_{cx} is considered to be constant.

The choice of the physical model is determined by the requirement that the stability analysis involve only relatively simple analytical considerations. We will analyse the situation where T_e is small enough ($T_e \ll T^* = m_i v_1^2/2\,(m_e/m_i)^{1/3}$), that the fast ions drag on the electrons without appreciable angular scattering. If we neglect the small term that describes the angular scattering and the term with the second derivative with respect to v (which is of higher order in T_e/T^*) the ion kinetic equation can be presented as follows [1]:

$$\frac{\partial F}{\partial t} = \nu' n \frac{\partial}{\partial v}(vF) + n(\nu_i + \nu_{cx})\delta(v - v_1) - \nu_{cx} F \qquad (1)$$

where $\nu = \text{const}\cdot n T_e^{-3/2}$, $\nu' = \partial\nu/\partial n = \text{const}\cdot T_e^{-3/2}$ is introduced to share the dependences of ν on n and T_e, and $F(v,t)$ is the usual distribution function averaged over the angles and multiplied by the factor v^2:

$$F(v,t) = 2\pi v^2 \int f(v,\theta,t)\sin\theta\, d\theta$$

If angular scattering is negligibly small, the primary loss mechanism is caused by the ambipolar potential which pushes ions out of the mirror when their velocities fall below a

certain threshold $V_0 \ll V_1$. This effect can be taken into account by condition:

$$F(v, t) \equiv 0 \qquad v < v_0 \tag{2}$$

Formally, eq. (1) has no continuous solutions equal to zero at both $V = V_0$ and $V = \infty$. Thus it is used only for $V > V_0$ with the single boundary condition $F(\infty) = 0$. The solution for $V < V_0$ is given independently by (2). Then the density can be found as the integral:

$$n(t) = \int_{V_0}^{\infty} F(v, t)\, dv \tag{3}$$

The eqs. (1),(3) form a closed system of equations that describes the time evolution of the density. The value of T_e on which ν_i and ν' depend is determined by the electron energy balance. This balance is taken into account phenomenologically by introducing some unspecified dependence $T_e = T_e(n)$. The form of this function strongly depends on the mechanism of the electron losses. Since a wide range of physical conditions are possible we consider the general case of the arbitrary functions $\nu_i(n) = \nu_i[T_e(n)]$, $\nu'(n) = \nu'[T_e(n)]$ and present the marginal stability conditions in terms of the parameters ν_i / ν_{cx} , $d\nu_i / dn$, $d\nu'/dn$, evaluated at the steady state point.

We first consider the equations for steady state. If we drop the time derivative in (1), then the steady state distribution function can easily be found and after calculating (3) one gets the equation for the steady state values n :

$$n = \left(\frac{\nu_i(n) + \nu_{cx}}{\nu'(n)}\right)\left(\frac{1 - e^{-\Lambda\alpha(n)}}{\alpha(n)}\right) \tag{4}$$

where $\alpha(n) = \nu_{cx} / \nu' n$, $\Lambda = \ln(V_1 / V_0)$.

For the stability analysis, the density perturbation $\delta n(t)$

and the distribution function perturbation $\delta F(v, t)$ are introduced. The functions $\nu_i(n)$ and $\nu'(n)$ are linearized at the steady state point and the time dependence is chosen to be $e^{\gamma t}$. Finding $\delta F(v)$ from the linearized equation (1) and carring out the integration (3), one can get the dispersion relation:

$$\Gamma^2 - a\Gamma = \frac{1 - e^{-\Gamma b}}{e^b - 1}\left[(a - c)\Gamma - (1 + c)\right] \qquad (5)$$

where the values of the dimensionless parameters $b = \ln(1 + \nu_{cx}/\nu_i)$, $a = e^{-b} d \ln \nu_i / d \ln n$, $c = d \ln \nu' / d \ln n$ are taken at the steady state point given by (4), $\Gamma = \gamma / \nu_{cx}$.

Since we allow for arbitrary functions $\nu_i(n)$, and $\nu'(n)$ a situation can exist in which the instability results not from the time delay effect but from the "rough" mechanism mentioned above. To distinguish these two sources of instability, let us consider the slow perturbation with $\Gamma \to 0$ when the time delay effect is obviously of no importance. Taking this limit in (5), an inequality can be obtained that corresponds to those steady states which are stable with respect to the "rough" instabilities:

$$a < (1 + c)\, b / (e^b - 1) \qquad (6)$$

It is easy to show that within the scope of (6) there exist instabilities which have an oscillatory character and are caused by the time delay effect. Assuming that $\Gamma = i\pi / b$ in (5), the real and imaginary parts of (5) are:

$$a = 2c / (e^b + 1) \;, \quad c = \left[\pi^2 (e^b - 1) / 2b^2\right] - 1 \qquad (7)$$

If one takes for example $b = 1.3$ then eq. (7) gives $a = 2.9$, $c = 6.8$ and this set of parameters satisfies the inequality (6). It is clear that in the vicinity of this state there are solutions (5) with $\mathrm{Re}\,\Gamma > 0$.

1. Braginsky S.I., Voprosy teorii plazmy, 1, (1963), p. 185.

MHD - STABLE CONFINEMENT OF ROTATING PLASMA IN AN AXISYMMETRICAL OPEN TRAP

Botcharov V.N., Breizman B.N., Kiselev A.V., Konstantinov S.G., Kudryavtsev A.M., Myskin O.K., Panasyuk V.M., Tsel'nik F.A., Zavadsky N.A.

Institute of Nuclear Physics, 630090, Novosibirsk, USSR

An open trap with a rotating plasma was proposed in [1] as an improvement on the mirror machine: the centrifugal force in such a device decreases longitudinal losses. The main argument against the trap was a prediction that the plasma would be centrifugally MHD- unstable if the density decreased along the radius ($dn/dr < 0$) [2].

Later it was found [3,4] that the condition $dn/dr < 0$, though natural for a trap, is not necessary. With inhomogeneous rotation speed V and plasma temperature T (both decrease to zero at the outer border) the case $dn/dr > 0$ is also possible for the trap. It is shown in [5] that MHD - stable profile of the desired shape exist for n and V in a cold rotating plasma. Thus, if $dn/dr > 0$, centrifugal instability turns into centrifugal stabilization and this can be used in an axisymmetrical trap to suppress flute instability due to the curvature of the magnetic force lines. Although centrifugal stabilization is most naturally applied to such traps, it may be considered as a general way to MHD - stabilize a plasma (like, for example, min - B stabilization). It should be noted, in particular, that according to [3,4], stabilization in long traps is also possible when the rotation velocity is much smaller than the thermal ion velocity. Even a natural ambipolar electric field will be sufficient when the trap is long enough.

The above considerations change the problems associated with an experimental study of traps with rotating plasma. Before it was difficult to achieve stability because of the rotation [6], now the rotation itself is considered to be a means of suppressing MHD-instability.

The goal of the experiments on the SVIPP device is to obtain and to study centrifugal stabilization. In this simple mirror machine, plasma is created inside a plasma shell which is a transition layer between the rotating plasma and the wall [7]. The rotation is driven by radial electric field which is projected to the midplane from the end electrodes by longitudinal conductivity.

The plots in fig. 1 show that a stationary density profile $n(r)$ with $dn/dr > 0$ is achieved when an electrical potential is applied to the end electrodes with the plasma shell being switched on. Immediate conclusion about the stability of this configuration by energy life time τ measurements is difficult

due to masking processes (charge exchange, electrode discharge) decreasing τ up to 0,1 ms. It was therefore to identify the losses initiated by the instability only. For this purpose, a low density component of high energy electrons (tens of keV) was generated in the plasma by ECRH [8]. The decay time of this component after the ECRH was switched off was assumed to be equal to the plasma life time caused by instability, since the fast electrons move along the radius at approximately the same speed as the main plasma due to the low frequency flute instability. The loss cone scattering time for the hot electrons is long enough so that longitudinal losses are negligible. It can be seen from the oscillograms (Fig. 2) that after the ECRH was switched off, the characteristic decay time of the additional diamagnetism and hard X-ray flux was about 5-7 ms, implying that the plasma was MHD - stable. Turning off the shell destroys the stable conditions. In Fig. 2, this moment corresponds to the fast drop of the diamagnetic signals (of both, the main plasma and fast electrons) and to the burst of X-ray emission from the probe located near outer border of the plasma. A rapid increase in the current on the inner ring of the end electrodes after turning-off shell indicates that the plasma is filling the region near the axis. It can be seen from the light emission that the plasma flux towards the axis is azimuthally inhomogeneous. The transition to an unstable state occurs 20-30 μs after the shell is turned off, that is during a time less than the plasma energy life time. Therefore the stability observed can not be explained either by end short-circuit or the stabilizing effect of fast electrons, since the influence of these two factors can not be directly eliminated by turning-off the shell. These processes correspond to what can be expected when centrifugal stabilization takes place.

To increase the energy life time it is necessary to remove the residual gas from the plasma volume. For this purpose, one has to increase V and T. To do this in dense plasma is rather difficult. According to [9] the main obstacle here is the plasma-wall interaction which is inavoilable since electrode discharge is presently the only way of creating a rotating plasma in the experiments. In the new device SVIPP-M, plasma rotation will be obtained by injecting fast neutrals [10]. This avoids evaporation and sputtering of the end electrodes, even at a high level of input power. The scheme of injection chosen for these experiments allows control of the profile V(r) which is useful in the experiments on stability.

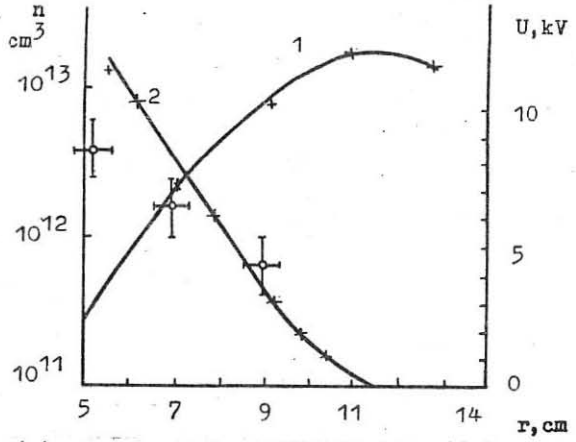

Fig. 1 1-n(r); 2-potential profile in the midplane: + calculated by projecting the potentials of the end electrodes along the field lines, °-measured by He° beam charge exchange [11]. Magnetic field-8kG, mirror ratio -3, distance between mirrors - 1m.

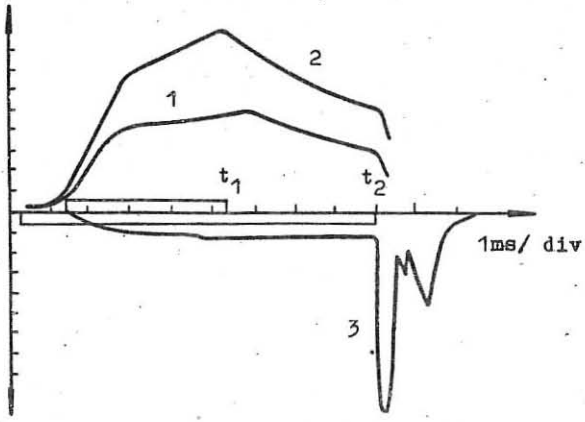

Fig. 2 1-plasma diamagnetism; 2 - plasma diamagnetism with ECRH switched on; 3-X-ray emission from the probe. At the moment t_1 ECRH is switched off. At the moment t_2 the shell is switched off.

References

1 Boyer, K., Hammel, J.E., Longmire, C.L., Nagle, L., Ride, F.L., and Riesenfeld, W.B.: Proc. of the 2nd Intern. Conf. on Peaceful Uses of Atomic Energy. Geneva 1958, Report No 2383.

2 Vedenov, A.A., Velikhov, E.P., Sagdeev, R.Z. U.F.N., 1961, 73, 701.

3 Panasyuk, V.M., Tsel'nik, F.A., Fizika Plazmy 1975, 1, 522.

4 Lehnert, B., Phys. Scripta, 1976, 13, 317.

5 Breizman, B.N., Tsel'nik, F.A., Fizika Plazmy, 1983, 9, 1157.

6 Konstantinov, S.G., Myskin, O.K., Sorokin, A.F., Tsel'nik, F.A., J. Techn. Phys., 1971, No 12, 2527.

7 Botcharov, V.N., Konstantinov, S.G., Kudryavtsev, A.M., Myskin, O.K., Panasyuk, V.M., Tsel'nik, F.A., Proc. of the 11th European Conf. on Controlled Fusion and Plasma Physics, Aachen, 1983, D19.

8 Agapov, L.N., Bogdanov, S.D., Botcharov, V.N., Vlasov, S.N., Zavadsky, N.A., Kiselev, A.V., Konstantinov, S.G., Kudryavtsev, A.M., Kurbatov, V.I., Myskin, O.K., Panasyuk, V.M., Pankratova, T.B., Petrov, S.P., Tsel'nik, F.A., Voprosy Atomnoi Nauki i Tekhniki, 1985, "Termojad. Sintez", 4, 17.

9 Botcharov, V.N., Konstantinov, S.G., Kudryavtsev, A.M., Myskin, O.K., Panasyuk, V.N., Tsel'nik, F.A., Fizika Plazmy, 1978, 4, 488.

10 Breizman, B.N., Tsel'nik, F.A., Fizika Plazmy, 1985, 11, 776.

11 Botcharov, V.N., Konstantinov, S.G., Kudryavtsev, A.M., Myskin, O.K., Panasyuk, V.M., Tsel'nik, F.A., Proc. of the 11th European Conf. on Controlled Fusion and Plasma Physics, Aachen, 1983, D18.

INVESTIGATION OF LOW-FREQUENCY PLASMA FLUCTUATION IN THE HER DEVICE

Ren Zhaoxing, Chen Shixian, Huang Chaosong, Fang Yude,
Wang Zhaoshen, Zhang Guangqiu, Wan Baonian
Institute of Plasma Physics, Academia Sinica
P.O.Box 26, Hefei, Anhui, China

1. INTRODUCTION

The investigation of the hot electron plasma fluctuation may provide new insights into important issues in the tandem mirror. The low-frequency fluctuation have been found in the EBT(1) with hot electron ring(E-ring), but where the plasma is toroidal and only the effect of neutral pressure is considered.

In this paper, we report the experiment in which the normalized amplitude of fluctuations and their correlations are studed more systematically under different mirror operations.

2. EXPERIMENTAL APPARATUS

The experiment was performed in the HER device which is a simple mirror. The axial magnetic field strenth Bo is 4 KG-5 KG at the midplane, the mirror ratio R is 2.2. The radius of cavity and length of mirror to mirror are 12.5 cm and 38 cm, respectively. The plasma is produced and heated by microwave that is applied at the electron cyclotron harmonic frequency. The microwave power Pu is about 15 KW at 20.5 GHz. The hot electron ring are created in the second harmonic electron cyclotron resonance region at the midplane. The radial position of the ring are adjusted by the magnetic field strength. At constant Pu, the C-, T-, and M- modes of operation are controlled by changing the background neutral pressure Po.

The hot electron parameters were diagnosed by hard X-ray, diamagnetic loop at the midplane, and by receivers viewing ECE along mirror axies.

3. EXPERIMENT AND RESULTS

In our experiment, the fluctuation signals were taken from a set of Langmuire probes at midplane which measure ion saturation current and from a multichannel spectrometer which views H_α radiations that come from plasmas located at different radial positions. One of the probes is radially movable, and the other two are at r=11 cm which are fixed.

To understand the nature of these fluctuations and the effects of E-ring on them, we investigated the behaviours of normalized fluctuation level $\Delta I/Io$, defined as the ratio of fluctuation's

variance to its mean value under different operating conditions. At the same time, the behaviours of various fluctuation's auto-power spectra, cross-power spectra, coherence spectra were also studed. These spectra were obtained by digital time series analysis techniques. The experimental results are summerized as follows.

3.1 Fluctuation vs neutral pressure Po

Fig.1 shows the $\Delta I/Io$ as function of Po. Note that the results are similar with that from EBT experiment. In the figure, the measured diamagnetic signal amplitude, $\Delta\phi$, was also plotted.

Three different operating modes of the mirror can by identified: M-mode(Po<1.2E-5 torr) characterized by higher $\Delta\phi$ and higher $\Delta I/Io$; T-mode(Po=1.2E-5~1.9E-5 torr) characterized by higher $\Delta\phi$ and lower $\Delta I/Io$; C-mode(Po>1.9E-5 torr) characterized by lower $\Delta\phi$ and higher $\Delta I/Io$.

Fig.2 shows the coherence spectra between two fluctuation signals under different Po. The signals are taken from two fixed Langmuire probes. It can be seen that there are fluctuations at 54 KHz, 80 KHz,etc. Their coherent amplitude is greatly reduced when the mirror is run into T-mode state.

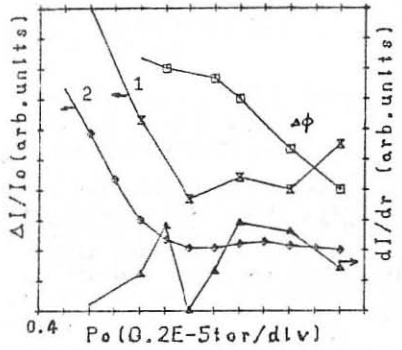

Fig.1 Po dependences of the fixed probe's $\Delta I/Io(1)$, $H\alpha$'$\Delta I/Io$, diamagnetic amplitude $\Delta\phi$, and related density gradient dI/dr at r=4 cm.

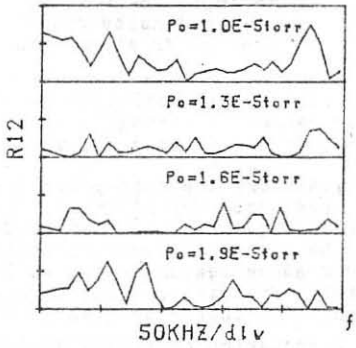

Fig.2 The coherence spectrum profiles of the two fixed probes are at the various neutral pressures.

3.2 Fluctuation vs field strengh Bo

We measured $\Delta I/Io$ and $\Delta\phi$ as function of Bo. Fig.3 is the measured result which shows that as Bo increases from 4 KG to 5 KG, probes' and $H\alpha$'$\Delta I/Io$ decreases, in contrast, $\Delta\phi$ increases. But the further increase of Bo results in a quite interesting situation where $\Delta\phi$ begins to drop, $H\alpha$'$\Delta I/Io$ increases and the probes' $\Delta I/Io$ keeps its low level. This phenomenon could be explained by the increase of E-ring radius duo to the increase of Bo, which was confirmed by a test where we set the movable probe at

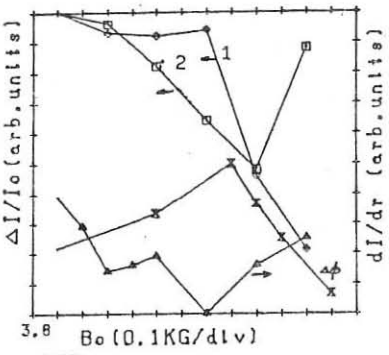

Fig.3 Bo dependences of the fixed probe's ΔI/Io(1), Hγ'ΔI/Io(2), diamagnetic amplitude $\Delta\phi$, and related density gradient dI/dr at r=4 cm.

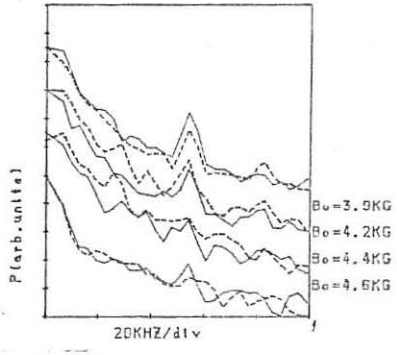

Fig.4 The auto-power spectra profiles of the two fixed probes are at various magnetic field strengths.

different radial positions and measured the corresponding hard X-ray radiation strength. The test results show that as Bo increases from 4 KG to 5 KG, the radius of E-ring increases from 8.5 cm to 10 cm.

Fig.4 shows the auto-power spectra of two fixed probes under different Bo. For lower Bo, the spectra exhibit those characteristic fraquencies as that in C-T and M-T transitions. For higher Bo, the coherent levels of these fluctuations are reduced also.

From above measurements, it is clear that as long as Po or Bo deviates from its optimal value, the fluctuations with these characteristic frequencies will be excited.

3.3 Fluctuation vs radial position

The spectral analysis shows that the correlations between signals taken from different two radial positions are quite different, which reveal the spatial dependence of coherence. The measured results are tabulated as follows:

Signal 1	Signal 2	Coherence degree
r<3 cm. H_α's	r>3 cm. H_γ's	weak
r<3 cm. H_β's	probe's	weak
r=r1>3 cm. H_α's	r=r2>3 cm. H_γ's	strong
r>3 cm. H_α's	probe's	strong

It was also noted that the magnitude of ΔI/Io at r=4 cm region was usually about 40% higher than that at neighbouring regions. As plasma relative density measurement indicated, at r=4 cm region the plasma has steeper density gradient. This implies that the fluctuations are intimataly related to plasma density gradient, (see Fig.1 and Fig.3), or in other words, the fluctuations are driven by the density gradient in nature.

These results show that the plasma low frequency fluctuations are strongly affected by E-ring. The fact was further supported by the test using movable probe. As the probe moved toward the E-ring from its outer edge, the 10 GHz ECE signal decreased gradually indicating the diminishing of E-ring (see Fig.5b), and the $\Delta I/Io$ gradually increased (see Fig.5a). When E-ring was disappeared completely, the $\Delta I/Io$ of H_α's from r=4 cm was 4 times greater than the neighbour's,(In contrast, at this time, the plasma density gradient was lower than before, but the average density of the plasma center is also lower than the normal value, and the density of the plasma edge is higher than the normal value, which suggests increasing of the plasma radial diffusion.)

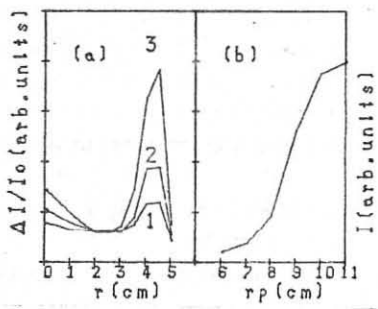

Fig.5 (a) H_α $\Delta I/Io$ vs.r, where curves 1,2, and 3, corresponds to movable probe positions r_p=11, 9, and 7 cm,respectively. (b) ECE amplitude vs.r_p.

The experiments show yet that the fluctuation at 1 KHz has above nature also, but it is affected by the E-ring slighter than that at 54 KHz.

4. DISCUSSION

From our experimental observations, several conclusions can be drawn.

The fluctuation at frequency 1 KHz, 54 KHz, and 80 KHz are closely related to plasma density gradient, so they are considered to be drift waves (1) or flute mode driven by plasma density gradient.

The high beta E-ring has the effect to reduce the fluctuation amplitude. As mentioned before, when E-ring is formed under optimal operating condition, the fluctuation is obviously suppressed, and when the E-ring is destroyed by a movable probe, an annular region with strong fluctuations appears. As an exception, in the case of low neutral pressure, some higher frequency fluctuations are excited, and the high beta E-ring is less effective in suppressing the fluctuations. In our experiments, there is the stabilizing effect of line-tying on the fluctuation, but it is not enough to stabilize plasma completely.

It was identified that in our case, the major driving source of fluctuations is located at r=4 cm region within the E-ring.

ACKNOWLEDGEMENTS

We wish to thank Yang Size, Zhang Shuqing, Tao Deyin, Chen Xiangren and Ying Zhuxu for help in experiment, Wang Zhenmin for work in perforiming hard X-ray measurement. We would also like to acknowleadge the continuing encouragement of professor Huo Yuping and professor Qiu Lijian.

REFERENCES (1) KOMORI,A., Nucl. Fusion 24 (1984) 1173.

PROPAGATION OF ICRF WAVES IN AN AXISYMMETRIC MIRROR PLASMA

A. Goto, A. Fukuyama and Y. Furutani

Department of Electronics, Okayama University
Okayama 700, JAPAN

In mirror devices a number of possible applications of the ICRF waves have been proposed in addition to the heating: plasma production, stabilization of MHD activities and control of a velocity distribution function. Previous analyses of ICRF wave in a mirror geometry have limited themselves to a one-dimensional analysis in the radial or axial direction. In this paper, we numerically study the propagation structure of the ICRF waves excited by an antenna, using an axisymmetric mirror plasma model, in which the magnetic field and the density are non-uniform in both the axial and radial directions. Using a cold plasma approximation, we solve the full Maxwell equation and obtain the spatial profile of the wave field and the power deposition and the loading impedance of the antenna.

In order to describe the wave propagation in the axisymmetric plasma, we use the cylindrical coordinates (r,ϕ,z) and solve the Maxwell equation as a stationary boundary value problem. The wave equation for an electric field $\vec{E}$ oscillating with angular frequency ω is given by

$$\vec{\nabla} \times \vec{\nabla} \times \vec{E} - \frac{\omega^2}{c^2} \overleftrightarrow{\varepsilon} \cdot \vec{E} = i \omega \mu_0 \vec{J}_A \,. \qquad (1)$$

We employ the cold plasma approximation to derive the dielectric tensor $\overleftrightarrow{\varepsilon}$ and introduce the effective collision frequency ν. In our axisymmetric model, we can expand the electromagnetic field in the Fourier series with respect to ϕ and write $\vec{E}(r,\phi,z) = \vec{E}(r,z) \exp(im\phi)$ where m is the mode number in the ϕ-direction.

The boundary condition which $\vec{E}$ must satisfy on the symmetric axis ($r = 0$) is derived from the finiteness of the induced magnetic field as $E_\phi - imE_r = 0$ and $mE_z = 0$, and the tangential component of $\vec{E}$ vanishes on a perfectly conducting wall. We numerically solve eq.(1) by the finite element method with triangular linear elements.[1]

Our plasma model with length $2z_M$ in the axial direction and radius a at $z = 0$ is surrounded by a perfectly conducting wall. The static magnetic field is given by $(0, -\partial\Psi/r\partial z, \partial\Psi/r\partial r)$ in terms of a magnetic flux function

$$\Psi(r,z) = \frac{1}{4}(1+R_M) B_0 r^2 + \frac{1}{4}(1-R_M) B_0 r^2 \cos\frac{\pi z}{z_M} [\, 1 + \frac{1}{4}\xi^2 + \frac{1}{12}\xi^4] \quad (2)$$

where R_M is the mirror ratio, B_0 is the magnetic field strength at $r = z = 0$ and ξ is $\pi r/2z_M$. We assume that the plasma density is constant along the magnetic lines of force, such that $n(r,z) = (n_0 - n_s)[1 - \Psi(r,z)/\Psi(a,0)] + n_s$; see Fig.1. ICRF waves are excited by a loop current $\vec{J}_A$ in the ϕ-direction.

Wave propagation in a plasma has different characteristics according to a mode number m. Typical example of the $m = 1$ mode is shown in Fig.2, where contours of Im E_r, Im E_ϕ and the density of the absorbed power, together with the Poynting vectors, are illustrated. The plasma is a hydrogen plasma and the parameters are listed thus: $R_M = 3$, $B_0 = 1.0$ T, $z_M = 0.6$ m, $a = 0.36$ m, $n_0 = 3\times10^{19}m^{-3}$, $n_s = 3\times10^{17}m^{-3}$, $\omega/2\pi = 18.24$ MHz, $\nu/\omega = 0.01$. The location of the antenna is marked by +, while the broken line indicates the ion cyclotron resonance (ICR). The antenna excites both the slow wave which is absorbed near the ICR of the antenna side and the fast wave which can propagate in the whole plasma. The fast wave is reflected at the wall ($z=-z_M$) and is partially mode-converted to the slow wave, which is absorbed near the ICR of the anti-antenna side.

An example of the $m = -1$ mode is shown in Fig.3. Parameters are the same as in Fig.2. Since the slow wave is mainly excited, the wave field is concentrated in the high-field-side of the ICR. As we approach the ICR surface, both parallel and perpendicular components of the wave number increase. This implies that a usual one-dimensional analysis does no longer work.

Fig. 4 depicts the dependence on B_0 of the loading resistance for the modes m = 1 and -1. In Figs.4 and 5, we use a deuterium plasma, $\omega/2\pi$= 18 MHz and other parameters are same as Fig. 2. In the case of m = 1, cavity resonance due to the global standing wave formation of the fast wave causes the several peaks of the loading resistance, in addition to the strong absorption of the slow wave at the ICR. Although the fast wave is propagative for all magnetic field intensity, the Alfven wavelength becomes longer as B_0 increases and it becomes harder to excite the fast wave when the half wavelength approaches the system length. In the case of m = -1, if the ICR locates in the low-field-side of the antenna, the slow wave is excited and immediately absorbed at the ICR without reflection. Sharp peaks in weak B_0 are due to the spatial resonance of the fast wave.

The relation between the central density n_0 and the loading resistance is shown in Fig.5 for m = 1, 0 and -1. In a low-density case, absorption is enhanced for the m = -1 mode, while, as the density exceeds $7 \times 10^{19} m^{-3}$, absorption of the m = 1 mode becomes stronger. In a low-density plasma, the fast wave has the wavelength longer than the system length and is hardly excited. The slow wave, however, can be excited and absorption becomes strong even for the low-density. Therefore, loading resistance of the m = -1 mode which easily couples with the slow wave becomes large. Absorption of the m = 0 mode turns out to be small, in comparison with other modes.

The cases of the two-ion hybrid resonance, the axially periodic boundary condition and the axially nonuniform density profile are also studied. [2]

Computations are carried out by ACOS-1000 of the Okayama University. Work partially supported by the Grant-in-Aid for Scientific Research of the Ministry of Education in Japan.

References

[1] A. Fukuyama, A. Goto, S.-I. Itoh and K. Itoh: "Finite Element Analysis of ICRF Waves in a Noncircular Tokamak", paper in preparation.

[2] A. Goto, A. Fukuyama and Y. Furutani: paper in preparation.

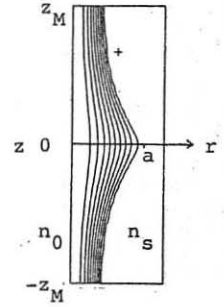

Fig. 1 density profile

Fig. 2 m = 1

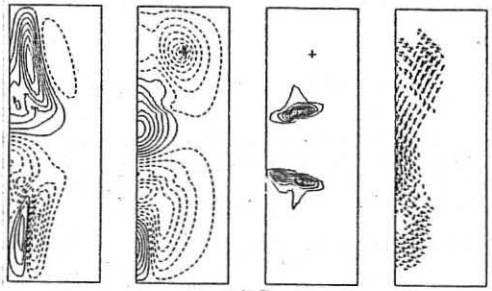

Fig. 3 m = -1

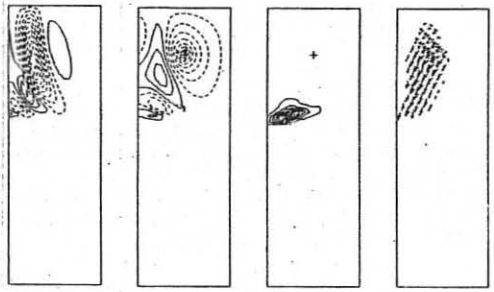

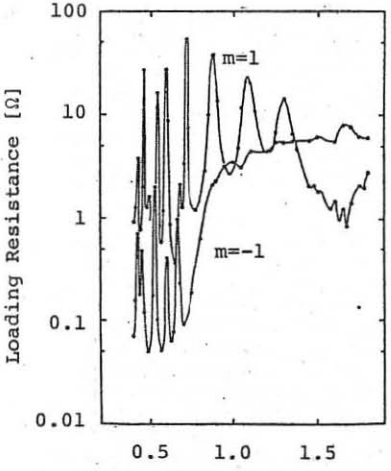

Fig. 4

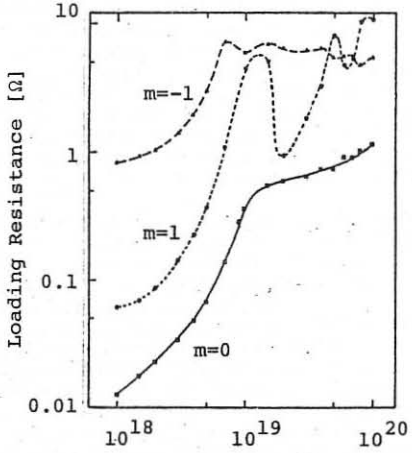

Fig. 5

PLASMA CONFINEMENT IN THE AXISYMMETRIZED TANDEM MIRROR GAMMA 10

A. Mase, S. Adachi, T. Cho, M. Ichimura, M. Inutake, K. Ishii,
A. Itakura, T. Kariya, I. Katanuma, Y. Kiwamoto, T. Kondo,
Y. Kusama, S. Miyoshi, Y. Nakashima, T. Saito, K. Sawada,
N. Yamaguchi, and K. Yatsu

Plasma Research Center, University of Tsukuba, Ibaraki 305, Japan

ABSTRACT: Plug potentials with thermal barrier have been confirmed in the axisymmetrized tandem mirror GAMMA 10. Strong end plugging has been achieved with central cell electron density higher than that of plug/barrier region. The ratio of plug electron temperature to central cell one is in the range of 3-5. Axial confinement time is two orders of magnitude better than mirror confinement time without plugging and agrees well with Pastukhov formula.

INTRODUCTION: In tandem mirror, thermal barrier concept is one of the critical issues under investigation /1,2/ since it allows the generation of higher electrostatic confining potentials to increase central cell ion confinement. Another improvement is to attain axisymmetric confinement of central cell ions for reducing radial losses due to non-axisymmetric configuration /3/. GAMMA 10 /2/ is under operation with an effective axisymmetric configuration. In this paper, recent thermal barrier experiments on GAMMA 10 is reported.

EXPERIMENTAL RESULTS: GAMMA 10 consists of a central cell, anchor cells, and axisymmetric end mirror cells. The anchor cells are minimum-B mirrors to suppress MHD instabilities. Plug and thermal barrier are produced in the axisymmetric mirror. Axial distribution of the magnetic field strength is shown in top of Fig.2. End plugging experiments are carried out by a combination of neutral beams and gyrotrons. Neutral beams are injected into each anchor (35kV 70A) to produce hot ions for MHD stability and into end cells (20kV 60A) to creat sloshing ions for plug/barrier formation. Two 28 GHz, 100 kW gyrotrons are used to generate mirror-confined hot electrons that produce the thermal barrier potential depression ($\omega=2\omega_{ce}$) and warm electrons for positive potential peak ($\omega=\omega_{ce}$) that confines central cell ions. In recent experiments, central cell plasmas are heated with 200 kW of ion cyclotron resonance frequency (ICRF) power.

When the plug ECRH is applied, significant decrease of end loss current and simultaneous increase of central cell line density are observed as shown in Fig.1 together with time sequence of the shot. Central cell potential ϕ_e and barrier potential depression ϕ_b are measured by using Au-neutral beam probes /4/, and plug potentials ϕ_p at both ends are obtained by end loss ion analyzers. The results of axial potential profile is plotted in Fig.2 together with density and electron temperature profiles measured by 2nd harmonic electron cyclotron emission and the soft X-ray absorption method. Electrostatic confinement ($\phi_p>\phi_e$) without having the plug density n_p above the central cell density n_c has been observed as long as n_p is larger than the barrier density n_b during the end plugging. The plug electron temperarure T_{ep} is larger than central cell one T_{ec}. The results are consistent with the

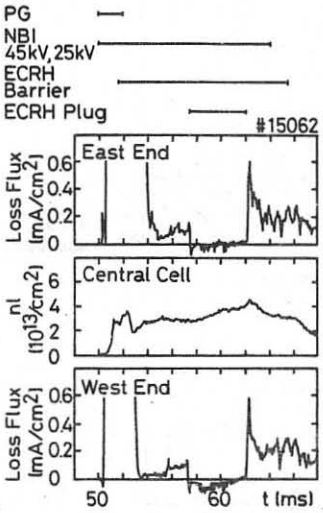

Fig.1. Time history of end loss flux and central cell line density.

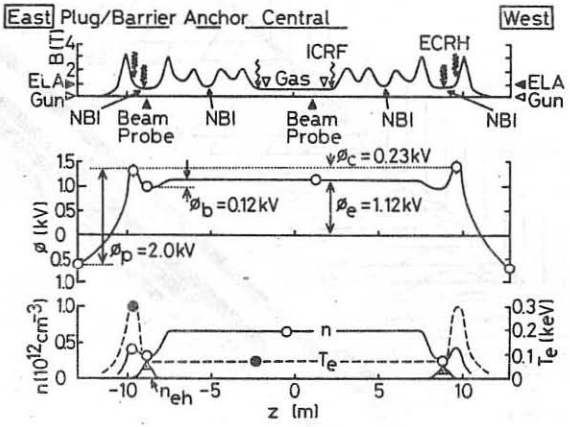

Fig.2. Axial distribution of magnetic field strength (top), potential (middle), and electron density and temperature (bottom).

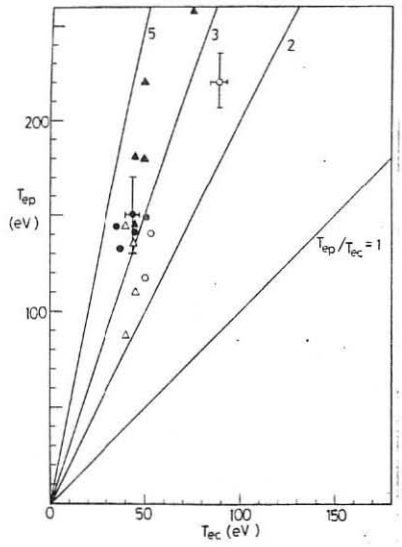

Fig.3. T_{ep} versus T_{ec} for strong end plugging case (▲ ●) and weak plugging case (△ ○).

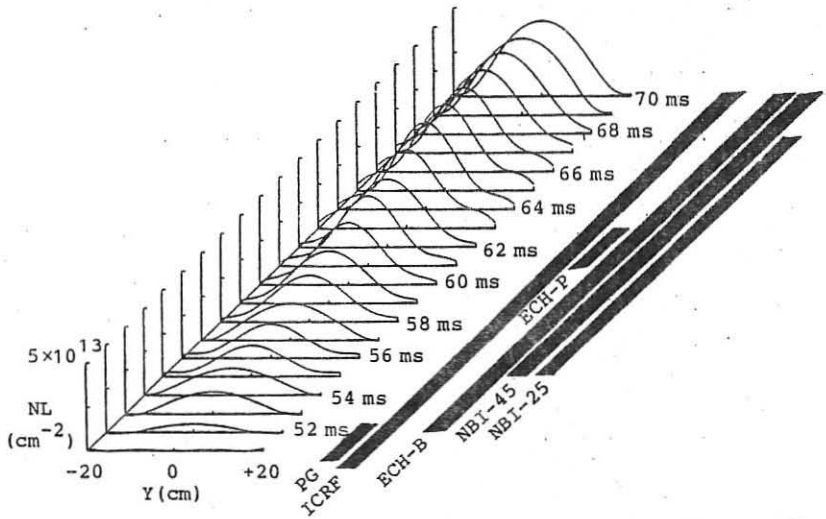

Fig.4. Time development of central cell line density profile.

predictions of thermal barrier theory, and the values are in good agreement with modified Boltzmann law /5/.

Axial particle confinement time is defined as

$$\tau_{//} = e \int_V n(r,z)\, dV \,/\, \int_S \Gamma_{//}(r)\, dS$$

where e is the ion charge, $\int n(r,z)dV$ is the total number of ions in the confinement region, and $\int \Gamma_{//}(r)dS$ is the total end loss current to both ends. The radial profiles of density and end loss current are measured with a scanning microwave interferometer and movable end loss analyzers. The value of $\tau_{//}$ thus obtained lies in the range of 50-500 msec depending on confining potential $\phi_c=\phi_p-\phi_e$, in good agreement with theoretically predicted scaling law /6/. The non-ambipolar confinement time $\tau_\perp^{NA}$ has been studied with end-plates forced to be grounded to the machine wall for diagnostic reasons to measure net axial current as a measure of non-ambipolar radial losses. Empirical scaling of $\tau_\perp^{NA}(\text{msec}) \sim 20\phi_e^{-1}(\text{kV})$ so far obtained may reflect effects of magnetic axisymmetrization.

Having successfully measured the confining potential with thermal barrier, we have focussed on enhancing the central cell plasma parameters using ICRF heating recently. We have observed to date the strong plugging at the central cell density $n_c \cong 3\times10^{12}$ cm^{-3}. and ion temperature $T_{ic} \cong 1$ keV. Figure 3 shows T_{ep} versus T_{ec} during the plug ECRH is applied. The ratio T_{ep}/T_{ec} is in the range of 3-5 for the strong plugging case, otherwise less than 3. We also observe the relation $n_c > n_p > n_b$, typically the ratio $n_c/n_p \cong 2$. When the ratio n_p/n_b decreases, such as due to ionization of neutral gas and collisional filling of central cell cold ions in the barrier region, the potential differences among the plug, barrier and central cell decreases resulting in the increase of end losses and decrease of $T_{ep}/T_{ec}(\lesssim 3)$. The time development of the central cell line density profile is shown in Fig.4. The peak density increases and the profiles do not change during the plug ECRH is applied, which may also suggest that the radial transport is not so effective in GAMMA 10 confinement even when strong end plugging is achieved.

REFERENCES:

/1/ T. C. Simonen et al., in Plasma Physics and Controlled Nuclear Fusion Research (Proc. 10th Int. Conf. London, 1984), Vol.2, IAEA, Vienna (1985) 255.

/2/ T. Cho et al., in Plasma Physics and Controlled Nuclear Fusion Research (Proc. 10th Int. Conf. London, 1984), Vol.2, IAEA, Vienna (1985) 275.

/3/ D. D. Ryutov and G. V. Stupakov, Fiz. Plazmy 4 (1978) 50; Sov. J. Plasma Phys. 4 (1978) 278.

/4/ K. Ishii, Z. Yamashita, A. Mase, and S. Miyoshi, Rev. Sci. Instrum. 56 (1985) 1053.

/5/ R. H. Cohen, I. B. Bernstein, J. J. Doring, and G. Rowlands, Nucl. Fusion 20 (1980) 1421.

/6/ T. D. Rognlien and T. A. Cutler, Nucl. Fusion 20 (1980) 1003.

D

compact tori and pinches

A FAST DENSE PLASMA FOCUS SYSTEM EMPLOYING REB TECHNOLOGY

A.SINMAN
Ankara Nuclear Research and Training Center,
Electron Physics Laboratory, Ankara-Turkey

S.SINMAN
Middle East Technical University, Electrical and
Electronic Engineering Department, Plasma
Engineering Laboratory, Ankara-Turkey

ABSTRACT

A comparison for electrical and plasma characteristics of two different type of fast Dense Plasma Focus (DPF) systems driven by a fast and low impedance (Z_o =1 ohm) Pulse Forming Line (PFL); and by a High Quality (HQ) Fast Capacitor Bank (FCB) have been done. By the numerical example given, in the fast DPF system driven by PFL, it has been observed that the energy deposition efficiency on pinched plasma is higher. Without any changing on the condition of computational experiments, according to the numerical results obtained by the driving methods of PFL and FCB-HQ, energies of 706.88 J and 462.08J have been respectively deposited on the pinched plasma. Moreover by the PFL driving method, the density and temperature values in the ranges of n_e= $5x10^{17}$- $2.5x10^{18}cm^{-3}$and T_e= 1.76 - 8.82 keV whereas by the method of FCB-HQ the values in the ranges of n_e= $5x10^{17}$- $10^{18}cm^{-3}$ and T_e= 2.88 - 5.76 keV have been found.

INTRODUCTION

As it is known, the evolution of a DPF occurs in three phases such as breakdown, acceleration and collapse phases. Particularly in the collapse phase, because of anomalous resistivity, the focus current falls down /1/ and so the energy transfer to focused plasma does not be sufficiently.

In conventional systems, controlling the velocity of plasma sheath and accelerator geometries /2/, syncronization between the collapse phase and the plasma current maximum may be obtained. Thus the energy efficiency may relatively enlarged. To grow up the current efficiency in the collapse phase, usage of high voltage fast capacitor bank with high impedance is a modern solution /4/.

Utilizing the possibilities of Relativistic Electron Beam (REB) technology /3/, combination of a REB generator with a DPF is also an other interesting alternative /5/.

The conceptual design of this new submitting focus cofiguration is based on REB technology. In DPF instead of a high impedance fast capacitor bank, the utilization of PFL combined with a Tesla resonant transformer was proposed /5/. Here the accelerator of fast DPF is the termination of PFL. By this method, in the case of DPF impedance is equal or greater then the impedance of PFL, because of the anomalous resistivity occured, the

reduction on focus current during collapse phase is being minimum. Thus the efficiency of deposition energy will increase. In addition, time varying non-linear impedance variations in the fast DPF are less effecting on the voltage-current characteristics of DPF.

MODEL

The mathematical model is in a dynamical character. By means of the algorithm consisted of tree parts; time varying focus impedance and anomalous resistivity in either FCB-HQ and PFL systems have been simulated.

This simulation have been done by the modification of sin(x)/x function. To determine the time variation of focus impedance; the factors such as the time shifting, time conversion, amplitude scaling factors and initial phase constant have been also added to this function.

By the aid of the theories about transmission line, signal and wave shaping, the algorithm of numerical model has been developed using a series depending only on reflection coefficient of transmission line /6/ and taking into attention of DPF physics.

In the algorithm used for FCB-HQ driving method, the energy dissipation mechanism on a time dependent loading resistor have also been taken into cosideration.

At the end of each sampling time (7.2 - 21.6 ns), calculating the energy used, after the comparison of the energy levels by the former bank energy, the initial value of charging voltage of PFL or capacitor bank voltage for the next step have been found.

Besides changing the distribution of anomalous resistiviy in time, it has been possible to investigate the behaviour of weak or intense compression phases.

COMPUTATIONAL RESULTS

Generally due to the initial operating voltage is 1 MV, in either FCB-HQ or PFL methods, it has been assumed that at a typical DPF system, to a rather high electric fields such as 250 kV/cm may be arrived. For this reason the formative time lag has been taken equal to sampling duration of 7.2 ns.

The results obtained from FCB-HQ driving method are shown in Fig.1. These variations are partly characterizing the conventional capacitor bank discharge. In the intense compression mode the rise time is 18 ns and pinch duration is 14.4 ns.

Whereas in PFL mode these values are found as 10.8 ns and 32.4 ns respectively. As shown in Fig.2., in PFL mode a negative resistance properties between 60 - 80 ns are observed. In this duration, the values of focus impedance are being smaller than the characteristic impedance of PFL and after 75 ns from the breakdown phase, changing this property, it is transformed into positive resistance condition.

During the maximum compression of 40 ns, the pinch current ratio of 274 kA(PFL)/178 kA(FCB-HQ) = 1.53 has been found.

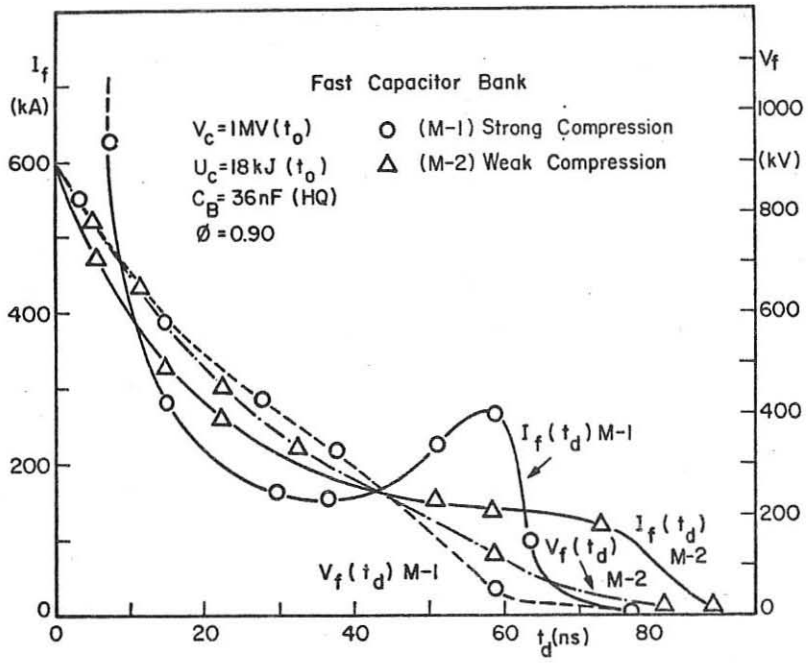

Fig.1. A typical result from computational experiment for FCB-HQ driven method (sampling time is 7.2 ns).

CONCLUSIONS

Using a rather simple mathematical technique, a DPF system driven by FCB-HQ or PFL has been simulated. It is possible to change the system parameters in the computational experiment. According to the results obtained, DPF system performance in PFL driving method is better. In this content, the reflection of MHD properties into electrical characteristics has been observed. In practice, the selected values may be realized by the modern REB technology. Thus the computational experimental results are mostly in realistic sizes.

An another important matter is neutron efficiency. Whereas as it is known, the neutron efficiency Y_N is a function of pinched focus current I_f by approximately $Y_N \doteq I_f^4$. Here the important point is how this discussed method act on the pinch phase of DPF. Therefore no other investigation on neutron efficiency has been carried out separetely.

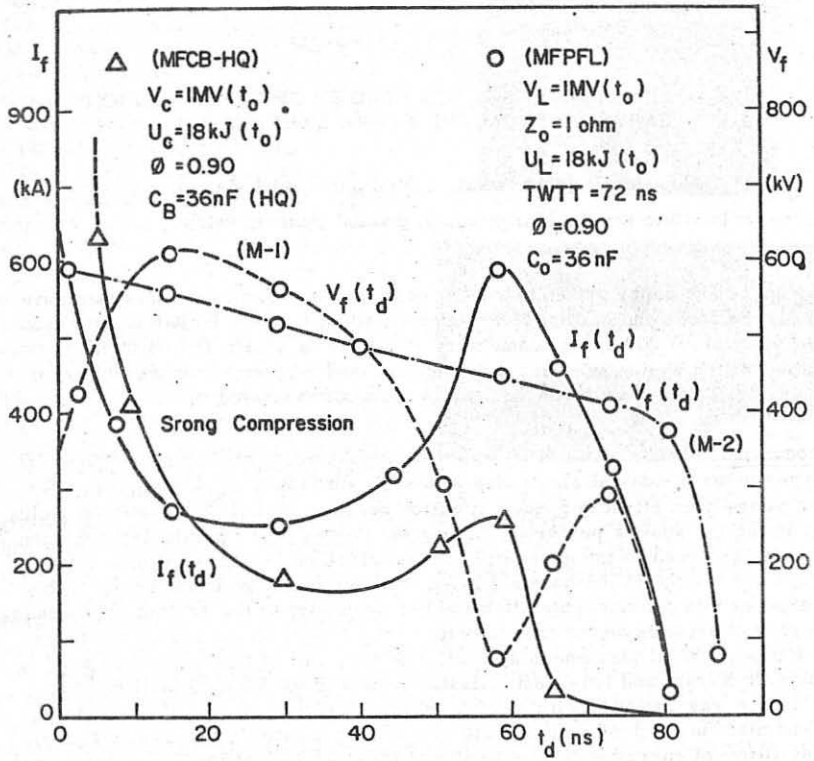

Fig.2. Time evolution and comparison of FCB-HQ and PFL driven methods (sampling time is 7.2 ns).

REFERENCES

/1/ Griem,H.R., and Lovberg,R.H., Plasma Physics, New-York, Academic Press Part A, Ch.,6., Part B, Chs, 11 and 15(1971).
/2/ Sinman,S. and Sinman,A., XVI Int. Conf. on Phenomena in Ionized Gases, Düsseldorf, Cont. Papers, Vol.2(1983)252.
/3/ Boscolo,I., et al., Rev. Sci. Instrum., Vol.48(1977)747.
/4/ Decker,G., et al., Phys. Fluids 26(1983)571.
/5/ Sinman,S., and Sinman,A., 1984 Int. Conf. on Plasma Physics, Lausanne June 27-July 3, 1984, Proc. Cont. Papers Vol.1 P12-18/165.
/6/ Sinman,S., and Sinman,A.,Fusion Energy-1981, Spring College on Fusion Energy Trieste, 26 May-19 June 1981, IAEA-SMR-82 (1982)269.

SPACE- AND TIME-RESOLVED STUDIES OF X-RAY AND ION EMISSION FROM THE PF-360 EXPERIMENT

M. Sadowski, L. Jakubowski, E. Rydygier and J. Żebrowski
Institute for Nuclear Studies, 05-400 Swierk, Poland

Abstract: The paper presents recent results of research on a fine structure of a plasma focus and on that of ion beams emitted by the PF-360 facility operated up to about 200 kJ. A filamentary structure of a soft /0.8-3.0 keV/ X-ray emitting region has been investigated, and a spike structure of fast /80 keV - 1.0 MeV/ deuteron beams has been corroborated.

Introduction. Plasma focus /PF/ experiments basing on high-current pulse discharges between coaxial electrodes with a low-pressure D_2-filling, have for many years been attracting much attention because of their high neutron yields [1]. In the PF studies performed during the recent years particular attention has been deserved to the generation of fast electron beams, hard and soft X-rays and energetic ion beams [2-7]. With an increase in the scale of the PF experiments considerable attention has been paid to the scaling of the emission characteristics and to the analysis of the experimental conditions under which new physical phenomena appear. The main aim of this paper has been to study soft X-ray and ion-beam emission from a large PF-360 facility [8]. The device was equipped with neutron optimized electrodes /hollow anode of 100 mm diameter and coaxial cathode of 150 mm diameter/, and it was operated at different energy levels up to about 200 kJ/38 kV, at the filling pressures of 2-14 torr D_2.

X-ray measurements. To investigate a structure of a pinch column, use was made of three vacuum pinhole cameras equipped with thin Be-filters and X-ray films. Most observations have been performed almost perpendicular to the z-axis at different azimuthal angles. The space-resolved measurements of soft /$<$1 keV/ X-radiation, which have been carried out under various experimental conditions up to about 200 kJ, demonstrate the appearance of a filamentary structure /see Fig.1/. And interesting feature of the PF-360 facility has been a quasi-spherical bulge of a pinch column /Fig.1/. This bulge could be a result of the reflection of current sheaths, provided that they are formed in different origins. In contrary to the observations with the Poseidon facility [9], the X-ray pinhole pictures from the PF-360 show in most cases a single axial filament only [8]. In some cases, however, there have been observed several quasi-axial filaments /see Fig.1/.

Since X-rays are absorbed partially by the working gas and a Be-filter, one can estimate that the minimum energy of the X-rays registered has been about

800 eV. The maximum energy of the X-radiation corresponding to the axial filaments was certainly below 3 keV, since no picture has been obtained on the second emulsion layer of the double-sheath X-ray film with a 180-μm-thick mylar base.

In order to study chronology of events revealing themselves in a filamentary X-ray pinhole picture, use was made of small /3 mm in diameter/ NE-102A plastic scintillators placed on the end plane of the pinhole camera. Those detectors were observed through fibre glass light-pipes by fast Philips XP2020 photomultipliers coupled with a two-beam pulse oscilloscope. Soft X-rays transmitted through 0.2 mm pinhole and 10-μm Be-filter could be registered in spite of an intense neutron and hard X-ray background, due to the application of thin scintillators and appropriate shielding of the detection system.

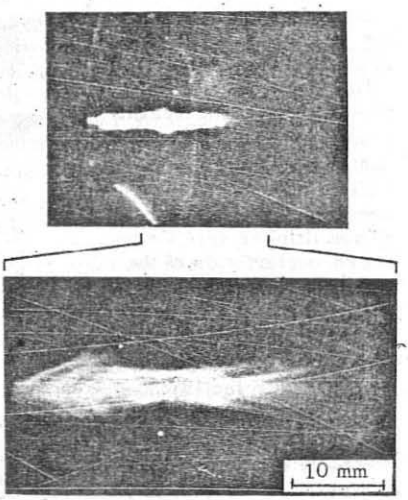

Fig.1. X-ray pinhole picture of an inner electrode edge and a pinch column; /below/ a part of the pinch showing quasi-axial filaments /11 torr D_2, 170 kJ/.

To enable simultaneous time-integrated and time-resolved measurements to be performed, the scintillators have been positioned behind small holes punched in the X-ray film at different places of an enlarged pinch image. In any of measuring channels there have been observed usually 2 or 3 distinct X-ray pulses /see Fig.2/. A time shift of the pulses registered in a given channel was 80-200 ns, while the corresponding pulses in different channels have been shifted by 20-40 ns in spite of a previous synchronization. For discharges with a higher neutron yield the X-ray pulses were stronger and more numerous. The X-ray signals described can correspond to the main compression phases and/or to the creation of the filaments and their rotation around the z-axis. The identification of individual filaments required a higher space- and time-resolving power that that achieved in the experiment described. Some efforts to study the dynamics of the filamention have already been undertaken.

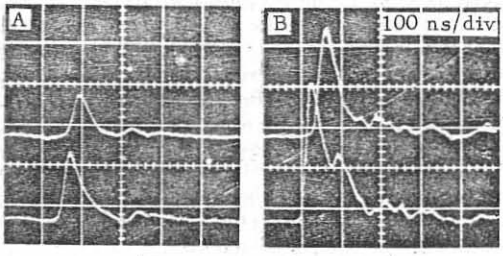

Fig.2. Soft X-ray signals from 2 small scintillators located in different places of a pinch column image /12 torr D_2, 170 kJ/, /A/ $Y_n = 8.6 \times 10^9$, /B/ $Y_n = 2.3 \times 10^{10}$.

Ion measurements. The ion studies at the PF-360 facility have included time-integrated angular measurements with SSNT detectors and ion pinhole cameras, as well as time-resolved measurements with scintillator-photomultiplier sets. General characteristics of the ion emission from the PF-360 device have been reported previously [8]. In comparison with other large />100 kJ/ PF facilities, where some 10^{15} deuterons/stereoradian were observed [4], the ion emission from a PF-360 run at 170 kJ has been lower, reaching only some 10^{13} d/sr />80 keV/. Therefore, the neutron optimized electrodes were not the best ones with regard to the ion emission. In concordance with the results obtained in the Poseidon experiment [10] it was observed that the maximum energy of deuteron beams from the PF-360 device is lower than that for medium-scale /<100 kJ/ PF facilities and it amounts to about 1 MeV only.

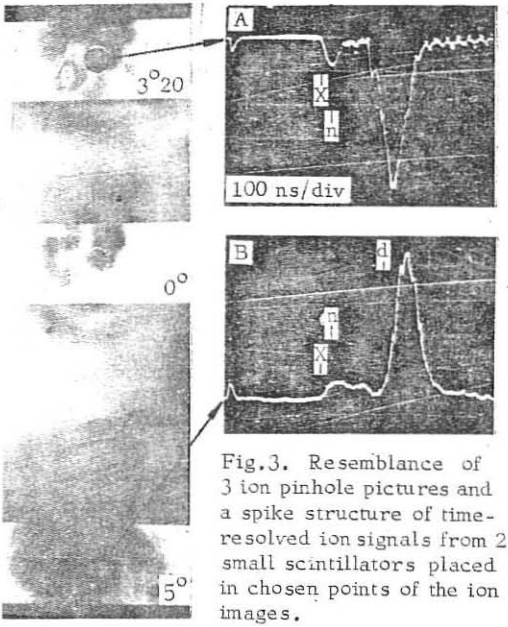

Fig.3. Resemblance of 3 ion pinhole pictures and a spike structure of time-resolved ion signals from 2 small scintillators placed in chosen points of the ion images.

Since among numerous low-energy />40 keV/ ions beams emitted from the PF-360 there have been revealed bunches of high-energy />80 keV/ deuterons [8], the recent ion measurements have been aimed at those energetic beams. To investigate their intensity and divergence, use was made of a multi-pinhole ion camera with CN films. Most attention has been paid to the pinholes looking at 0°, 3°20', and 5° in relation to the z-axis. Ion pinhole pictures taken under different experimental conditions, have confirmed [11] that the high-energy deuteron bunches are emitted within a narrow cone to the axis. A comparison of ion pictures obtained with closely-spaced pinholes has shown that a divergence of those bunches is often below 8°. To make possible simultaneous time-integrated and time-resolved ion measurements in selected points of the ion images there have been placed small NE-102A plastic scintillators coated with a light-tight Al-layer. Those detectors, located behind small holes drilled in the CN films, have been coupled with Philips 56 TVP photomultipliers and a fast oscilloscope. For a rough energy analysis, additional Al-filters have been placed in front of the CN films /brighter stripes in Fig.3/. Time-resolved ion signals from selected points of the pinhole images have revealed a spike structure of the ion emission. A FWHM value of individual spikes is

estimated to be <10 ns, while a FWHM value of the deuteron bunch detected in the center of the pinhole image, is usually about 80 ns. The ion signals registered by different detectors can be shifted by 0-100 ns. Since the quasi-axial high-energy deuteron bunches are hardly influenced by a magnetic field of a pinch column, their time characteristics deliver straight information when the ion micro-sources appear. These informations are of importance for the verification of new theoretical models [12,13] as well as for possible applications of high-energy ions.

Conclusions. A comparison of time-integrated and time resolved X-ray measurements, as performed with the Poseidon [9] and PF-360 facilities, suggest that the filamentation of a pinch column is a general feature of PF-discharges when a pinch current is high enough. This statement remains in a good agreement with new theoretical models [12,13] . For the first time presented here two-channel time- and space-resolved X-ray measurements, performed with scintillators placed on the enlarged image of a pinch column, shown that the time scale of the filamentation ranges from 20 to 200 ns.

Simultaneous time-integrated and time-resolved ion measurements, as performed for the first time with scintillators placed in selected points of different ion-pinhole pictures, corroborate a spike structure of high-energy deuteron bunches. They also show that the angular divergence of the bunches is usually below 8°, while a time jitter of those can be up to 80 ns. A nature of these high-energy ion bunches requires still more detailed investigation from the point of view of the verification of new theoretical models [12,13] as well as of possible applications in physics and technology.

References

1. H. Schmidt, Atomkernenergie-Kerntechnik 36 /1980/ 161.
2. Ch. Maisonnier et al., 3rd Int. Top. Conf. /Novosibirsk 1979/.
3. M. Sadowski et al., Phys. Lett. 83A /1981/ 435.
4. L. Bertalot et al., 10th Europ. Conf. CFPP /Moscow 1981/.
5. W. Stygar et al., Nucl. Fusion 22 /1982/ 1161.
6. A. Mozer et al., J. Appl. Phys. 53 /1982/ 2959.
7. T. Yamamoto et al., Jpn. J. Appl. Phys. 23 /1984/ 242.
8. A. Jerzykiewicz et al., 10th Int. Conf. PPCN /London 1984/.
9. M. Sadowski et al., Phys. Lett. 105A /1984/ 117.
10. H. Herold et. al., 9th Int. Conf. PPCN /Baltimore 1982/.
11. M. Sadowski et al., 3rd Int. Workshop PFR /Stuttgart 1983/.
12. A. Hayd et al., Uni. Stattgart Report IPF-84-4 /1984/.
13. A. Korbi et al., 4 th Int. Workshop PFR /Warsaw 1985/.

FUSION REACTION MECHANISMS IN THE PLASMA FOCUS POSEIDON

U. Jäger, W. Piermayer, H. Herold, H.J. Kaeppeler, H. Schmidt, R. Schmidt, M. Shakhatre, A. Shyam

Institut für Plasmaforschung, Stuttgart, Fed. Rep. of Germany

The plasma focus Poseidon (280 kJ, 60 kV) exhibits two phases of strong suprathermal neutron production: the pinch phase (quiet phase) from maximum compression till m = 0 instability onset and the subsequent instability phase.

For an analysis of the mechanisms leading to the neutron production in both phases a new model, the "Gyrating Particle Model" (GPM), was developed. In the GPM the trajectories of fast deuterons in the time varying focus structures are determined by a ray-tracing code. The profiles $n_e(r,z,t)$ and $T_e(r,z,t)$ for both phases are taken from measurements /1/ in a somewhat schematized form (rotational symmetry, two m = 0 constrictions only). The deuteron acceleration process is not treated, i.e. arbitrary initial distribution functions of the deuterons are taken at the beginning of each phase. Elastic collisions and fusion collisions of the fast deuterons with the thermal background plasma are treated with the help of Monte Carlo methods. Other reaction mechanisms, such as beam-beam or thermal production, are neglected. The trajectories of the reaction protons in the focus $\vec{B}$-field are traced up to measuring positions outside of the focus pinch. Thus, measurable quantities such as time resolved, time integrated, spatial angular and particularly, spectral resolved distributions of reaction protons (and neutrons) are obtained. They can be compared with experimental results.

In the experiments, methods developed in the past /2/ for the investigation of energy spectra and source structures of the reaction protons with etchable CR39 and PM355 films were applied. These time-integrated measurements were supplemented by neutron (Y_n; dY_n/dt) and fast deuteron ($d^2Y_d/dE,d\Omega$) measurements.

The validity of the GPM was tested by several methods. Generally,it turned out that best agreement is achieved when initial quasi-temperature distributions of the fast deuterons with T_I^* of 20 to 100 keV and slightly forward directed initial angular distributions are chosen. The deuteron source may be a point source. This is demonstrated in Fig. 1 by comparison with an experimentally obtained proton source structure. In Fig. 2, a measured angular distribution is compared with calculated distributions. The calculated curves are very sensitive against the choice of the plasma current amplitude. Thus, pinch currents can be determined.

Fig. 3 shows two series of measured and calculated proton spectra taken in different directions $0 \leq \theta \leq 180°$. The proton spectra were measured with a 54 step foil-spectrometer which has an energy resolution of 50 to 70 keV. Fig. 3a is typical for an average neutron yield from Poseidon of $8 \cdot 10^{10}$ and a T_I^* of 40 keV, whereas Fig. 4b shows a "poor" shot with distinctly lower T_I^* of 15 keV. The T_I^* were evaluated from the best fit of theoretical curves. It is remarkable that the number of fast deuterons needed to explain the observed proton yield is about the same in both discharges.

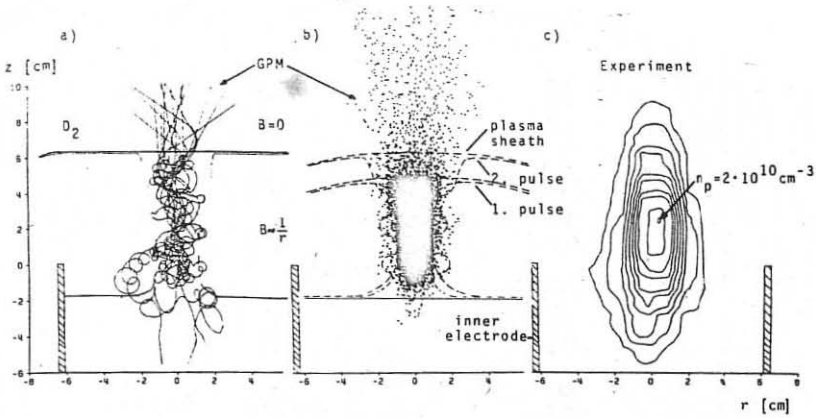

Fig. 1: Geometry of the POSEIDON–Plasma (280 kJ, 60 kV)

a) Trajectories of fast deuterons (E_d=100 keV) from a point source at t=0, r = 0.2cm, z = 0 cm, calculated with the gyrating particle model. (I_p=800 kA; $n_e=8\cdot10^{18}cm^{-3}$; T_e=0.6 keV).

b) Simulation of D–D–reactions with a quasi thermal fast deuteron distribution of T_I^*=80 keV and isotropic emission from a point source.

c) Reaction proton source measured with a CR–39 detector behind a pinhole. Spatial resolution: 5 mm. (p=8 mbar; total proton yield: $Y_p=7.4\cdot10^{10}$; maximum proton density: $2\cdot10^{10}cm^{-3}$).

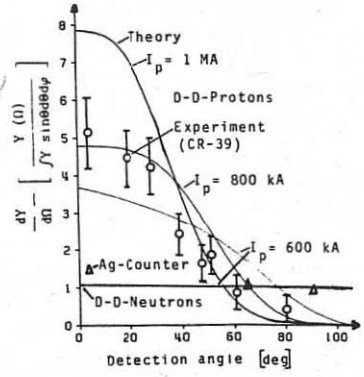

Fig. 2
Angular distribution of reaction protons distorted by the azimutal magnetic field. The reaction neutrons are measured at 3 angles. The theoretical curves are calculated for isotropic deuteron emission and T_I^*=80 keV.

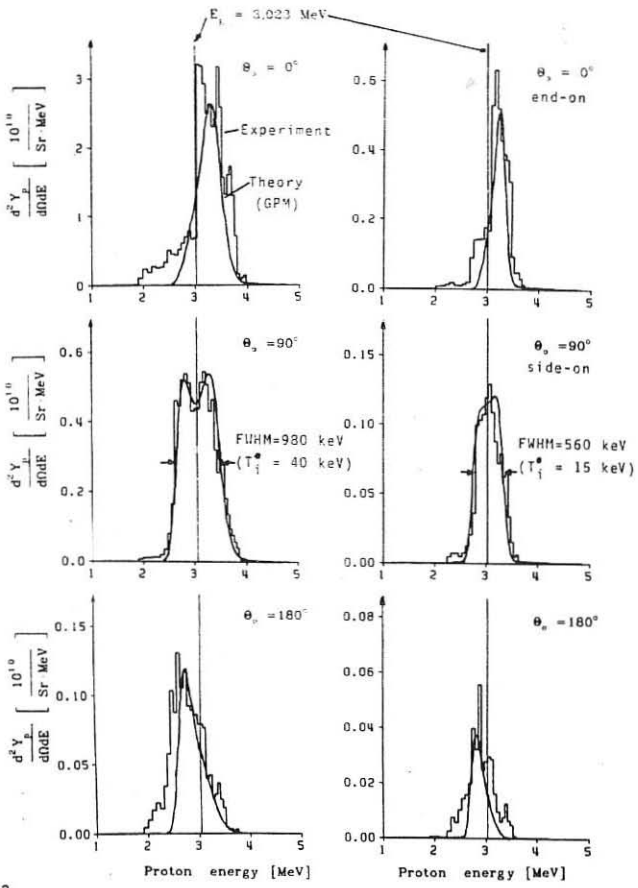

Fig. 3:

Two series of proton spectra at a filling pressure of p=11 mbar D_2, on POSEIDON (280 kJ, 60 kV). The given directions are reconstructed from the detection directions assuming a pinch current of 800 kA.

3a) Total proton yield: $Y_p=6.3\cdot10^{10}$; The parameters of the theoretical curves are: $T_i^*=40$ keV; number of fast deuterons: $N_b=6.8\cdot10^{16}$; anisotropy factor $A_d=4$ (slightly forward directed).

3b) $Y_p=5.4\cdot10^{9}$; theoretical parameters: $T_i^*=15$ keV; $N_b=8\cdot10^{16}$; $A_d=10$.

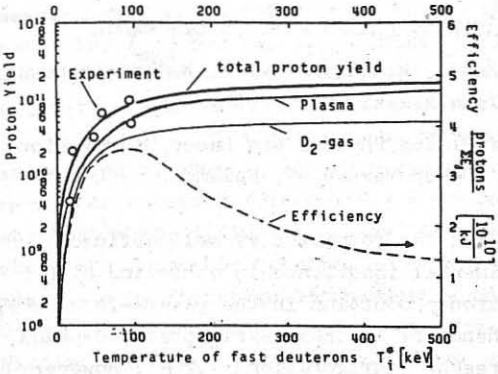

Fig. 4:

Calculated total proton yield of the Poseidon focus obtained with the GPM-Code. Parameters: Number of fast deuterons: $N_b = 8 \cdot 10^{16}$ isotropic emission and $I_p = 800$ kA. Efficiency is the number of reaction protons related to the total energy of the quasi thermal fast deuteron distribution. For the experiments T_i^* is evaluated from the reaction proton spectra.

Quantitative results of more discharges are summarized in Fig. 4. The calculations with the GPM were done for Poseidon conditions. The number of deuterons N_b was kept constant but T_i^* was varied. The fusion production in the D_2 gas and in the plasma are plotted separately. The experimental yields agree quite well for $N_b = 8 \cdot 10^{16}$ and demonstrate that high yields have to do with a high T_i^* of the fast deuterons. Regarding the energy efficiency (number of reaction-protons/total energy in the fast deuterons) the focus works at about optimum conditions. The efficiency decreases at higher T_i^* because the length of the deuteron trajectories in the focus $\vec{B}$-field and the fusion cross-section increase only slightly above $T_i^* = 100$ keV.

Conclusions:

Various quantitative agreements between theory and measurements show that a generalized beam target model, the GPM, describes well the neutron production process for reasonable basic data. They are: The fast deuterons have a quasi-temperature of 10 to 100 keV. About 10^{17} fast deuterons (up to 1% of the deuterons in the pinch) with an energy content of ≈ 10% of the thermal plasma energy are needed to explain the observed neutron or proton yield of up to 10^{11}. The reacting fast deuterons are trapped in the magnetic field of the focus for about 50 ns. The main effect which causes the high fusion efficiency is the lengthening of the deuteron paths in the pinch structure and in the surrounding gas by gyro-motion. The path lengths in the plasma amount to an equivalent of about 2 to 4 pinch lengths. For the instability phase, the application of the GPM is not free of doubt because there may exist high local n_i and long-lasting trapping in turbulence cells.

References:

/1/ H. Herold et al: Proc. 10th Int. Conf. PPCNFR, London 1984, Vol. 2, 579.

/2/ U. Jäger, L. Bertalot, H. Herold: Rev. Sci. Instr. 56, 77, 1985.

INFLUENCE OF INSULATOR ON PLASMA - FOCUS DISCHARGE

M.Borowiecki, S.Czekaj, S.Denus, W.Koziarkiewicz, W.Skrzeczanowski
R.Socha, K.Tomaszewski, M.Zadrożny

S.Kaliski Institute of Plasma Physics and Laser Microfusion
P.O.Box 49, 00-908 Warsaw 49, Poland

An uniform breakdown and the formation of well defined current sheath are of fundamental importance in achieving high energy compression and neutron production in the plasma-focus /PF/ discharge. The course of phenomena in these early phases depends on insulator-electrodes /breech/ configuration [1,2] . However, the knowledge of these processes is still insufficient and hence we have been taking up the study of the early phases of the PF discharge [3,4] . The paper presents the results of experimental

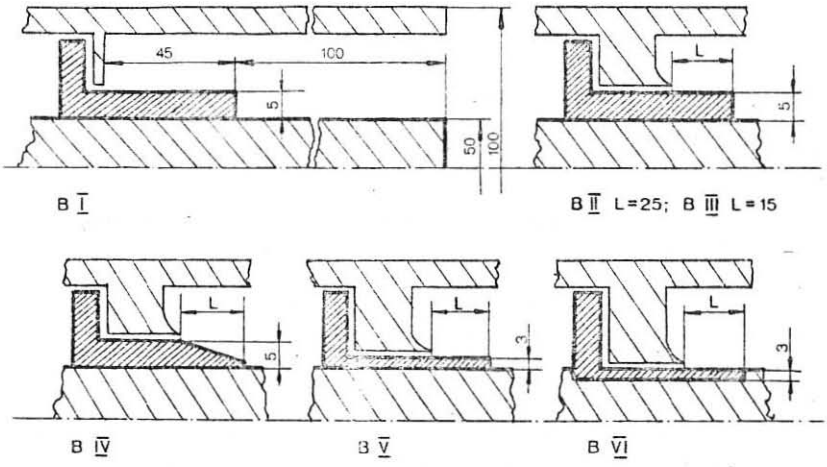

Fig.1. Breech configuration schemes
BI - typical, BII and BIII-typical with edge insert /EI/,
BIV- conically ended with EI, BV-thin-walled with EI,
BVI-plunged into the central electrode with EI

investigations concerning the influence of the insulator separating both electrodes upon the discharge in the PF device. The measurements were performed on the PF-20 device /$E_0 \approx 13$ kJ, $U_0 = 35$kV, p=1-4 Tr, $I_{max} \approx 300$ kA, $T_{1/4} = 2{,}5$ /us/ with a number of diagnostic methods like fast frame photography, magnetic probes, silver activation counters as well as standard ones.

Six types of alumina insulators differing in length, diameter and a kind of shaping of their edges near the central electrode have been examined /Fig.1/. Fig.2 presents the ICC photographs which show the diffuse breakdown in a whole interelectrode area above the insulator occurred in a very initial phase of the plasma-focus discharge independently on the insulator type used. Then, /after 0,1 to 0,15 /us/, this breakdown modified into the gliding discharge along the insulator surface, that was accompanied by the radial one occuring directly between the electrodes near the insulator face. While shortening the insulator the gliding discharge along its surface intensified whereas the radial

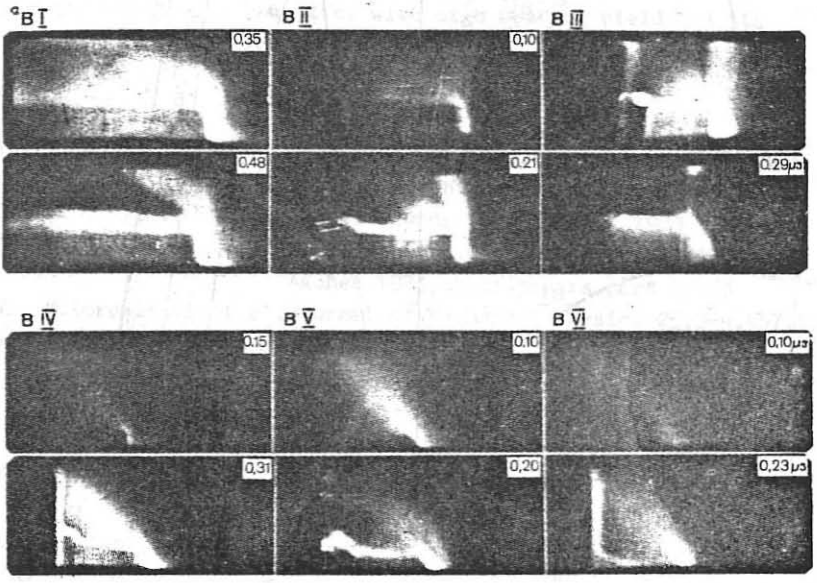

Fig.2. Side-on ICC Photographs of the breakdown phase /only area above insulator is visible; t=0 -the discharge beginning/

one weakened and deviated towards the cathode plate, thus missing its classic character /compare BI or BII with BVI in Fig.2/. As a result some increase of the current flowing in the plasma during its axial acceleration determined with a magnetic probe and hence a considerable rise of neutron yield in the final stage of the discharge/ according to scaling law $Y_n \sim I_{pl}^4$ [5] / were measured. The results of these measurements are presented in

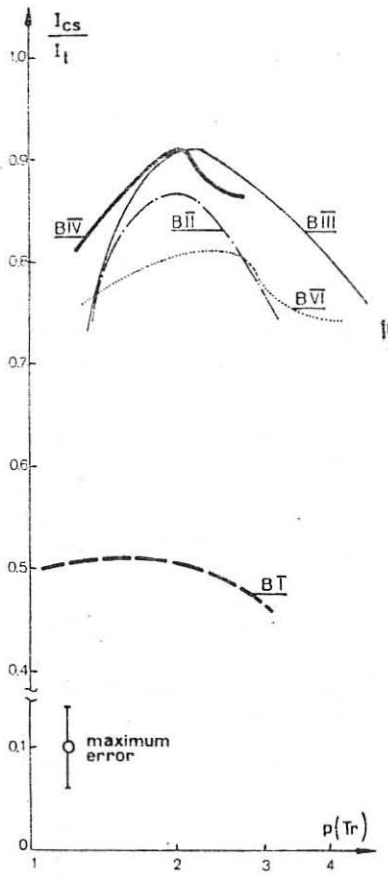

Fig.3. Plasma current to total current ratio vs the filling pressure

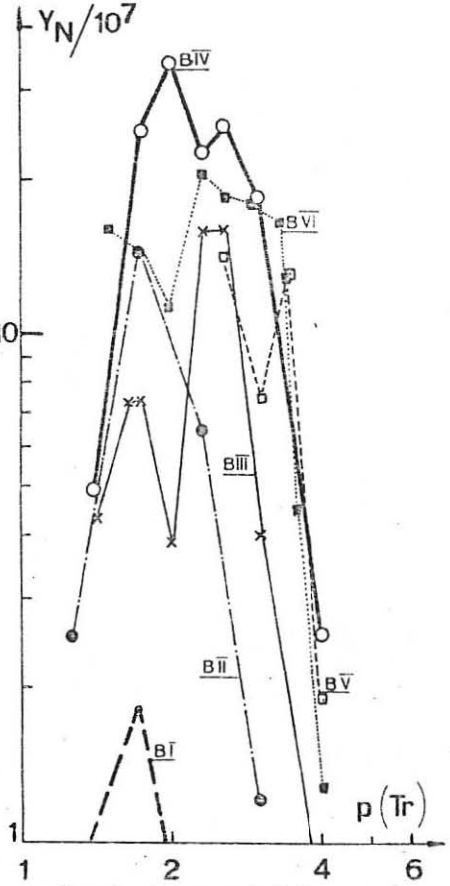

Fig.4. Average total neutron yield vs the filling pressure

TABLE-Current sheath parameters for the optimum filling pressure

Kind of configuration	BI	BII	BIII	BIV	BV	BVI
Maximum current density [kA/cm^2]	10	14	17	22	no data	16
Thickness [cm]	2,0	1,8	1,8	1,8	avail-able	2,1

Figs 3 and 4. On the other hand, when the insulators of different shape /BIII, BIV, BVI/ were applied, no essential changes of the plasma current value /Fig.3/ were observed although the current sheath structure / thickness and current density/ varied considerably /see table/ what also influenced the neutron yield to a quite an extent /Fig.4/.

On the basis of our results one can state that the conically ended configuration BIV provides operation of the PF-20 device with the best efficiency i.e. with high neutron yield and its good repeatability from shot to shot.

REFERENCES

1. C.Maissonier et al,Proc.VIth Int.Conf.Plasma Phys.Contr.Nucl. Fus.Res.Berchtesgaden,1976,vol.III,447
2. G.Decker et al,Physics of Fluids 26 /2/, 571, 1983
3. M.Borowiecki et al Proc.11th Eur.Conf.Contr.Fus.Plasma Phys. Aachen,1983,contr.papers,part I,543
4. M.Borowiecki et al,Journal of Technical Physics 25,3-4,457,1984
5. T.Oppenlander et al,Plasma Physics,19, 1075,1977

THE STUDY OF PLASMA DYNAMICS IN THE PF-300 DEVICE BY MEANS OF LASER DIAGNOSTICS

S.Czekaj, S.Denus, A.Kasperczuk, R.Miklaszewski, M.Paduch
T.Pisarczyk, Z.Wereszczyński

S.Kaliski Institute of Plasma Physics and Laser Microfusion
p.o.box 49, 00-908 Warsaw 49, POLAND

The investigations were carried out for deuterium pressures within the range of 2-12 Torr, and for energy of capacitor bank of 112-171 kJoules. Two types of pipe electrodes were installed with different diameter of the external electrode, reported as type A /15 cm diam./and type B /22.5 cm diam./, with no significant differences in the course of phenomenon.

The main diagnostic methods were four-frame shadowgraphy and interferometry, with the exposure time of each frame equal to about 2ns. The time interval between succesive frames was 50 ns. Thus, the subject of this paper is limited to the dynamics of the plasma in the PF-300 device.

The summary of the characteristic features of this dynamics is shown in Fig.1, where the time sequence of interferograms illustrating essential phases of the PF phenomenon is presented / the time t = 0 is the moment of maximum compression /.

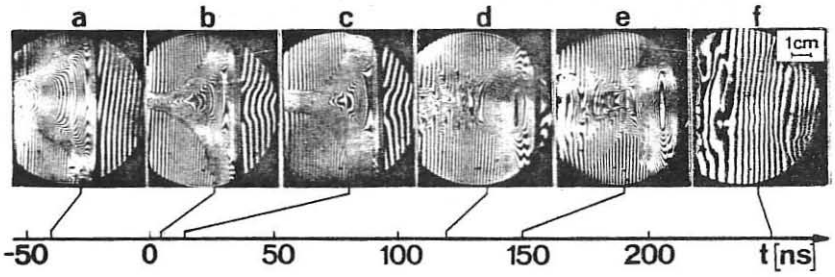

Fig.1. Time sequence of interferograms for p_o = 3 Torr.

1. Collapse phase.

It starts at t= -500ns and lasts to the moment when the plasma sheath achieves the axis. From sequences of the shadowgrams the time variations of the radial velocity V_r of the plasma sheath was determined for both types of the electrodes /Fig.2/.

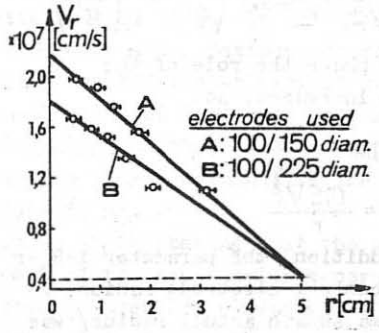

Fig.2 Radial plasma sheath velocity during collapse phase.

It was found that the initial value of velocity V_r is equal to the half value of axial velocity near the edge of central electrode. It is in agreement with shock wave theory and earlier investigations performed on PF-150 device [1].

The characteristic feature of the PF-300 device is strong magnetohydrodynamic activity during collapse phase. The development of the MHD instability of mode m=0 starts after the beginning of this phase /at the radius of 4.0-4.5 cm/ and saturated forms of this instability are visible even in pinch phase /Fig.3/.

Simple theoretical analysis based on the assumption that the plasma sheath forms a strong shock wave shows the best conditions for the development of this instability occur just for the radius equal to about 4 cm.

Starting from [2,3]:

$$\gamma_{max} \sim \left(\frac{g^2 \varrho}{\eta}\right)^{1/3},$$

$$\lambda_{max} \sim \left(\frac{\eta^2}{g \varrho^2}\right)^{1/3}$$

p_o=9Tr D_2

t= -30 ns

Fig.3. MHD instability of the plasma sheath during the collapse phase.

where: g - acceleration of the plasma sheath;
ϱ - plasma density
$\eta \sim T^{5/2}$ plasma viscosity

and assuming that ϱ=const /what is approximatiely true for the collapse phase/, it follows that:

$$T \sim p \sim V_r^2, \quad \gamma_{max} \sim \left(\frac{g^2}{T^{5/2}}\right)^{1/3} \sim \left(\frac{g^2}{V_r^5}\right)^{1/3}, \quad \lambda_{max} \sim \left(\frac{T^5}{g}\right)^{1/3} \sim \left(\frac{V_r^{10}}{g}\right)^{1/3}$$

For the final stage of the collapse phase the role of the magnetic force in acceleration term increases, so:

$$g = g_k + g_m, \quad g_k = \frac{dV_r}{dt}, \quad g_m = \frac{B_\theta^2}{4\pi\varrho r},$$

$$\varrho V_r^2 = \frac{B_\theta^2}{8\pi}, \quad g_m = \frac{0.5 V_r^2}{r}$$

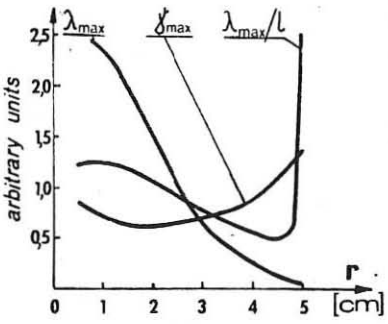

Fig.4 Results of computation for MHD instability characteristic parameters.

In addition, the parameter $l=R_o-r$ /R_o-central electrode radius, r-plasma sheath actual radius/ was defined and it is proportional to the sector length of the sheath available for instability development. The dependence of parameters characterizing MHD instability γ_{max}, λ_{max}, $\frac{\lambda_{max}}{l}$ is presented in Fig.4. It is clear considering the above dependence why the secondary MHD instabilities on flat sectors of the plasma sheath were not observed in later moments.

2. Formation and disintegration of the plasma column.

The minimum radius of the plasma column /r=0.25-0.7 cm/in the moment of maximum compression depends on the thickness of the plasma sheath in the final stage of the collapse phase. The thicker plasma sheath the greater is the plasma column radius.

Substantial correlation between the minimum radius of the plasma column and the neutron yield was observed /Fig.5/.

After the plasma column achieves its minimum radius the expansion phase begins and the radius of the column grows up and is even three times as much as its initial value. In this stage /30-100ns after maximum compression/ the MHD instability of mode m=0 developes and leads to disintegration of the plasma column. So the plasma column lifetime is 150-300 ns.

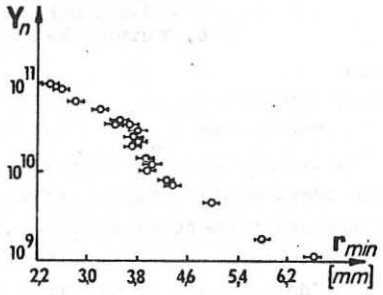

Fig.5 Correlation between the minimum radius of the plasma column and the neutron yield.

It is worth stating that the main part of the neutrons is generated from low density plasma after disintegration of the plasma column. This fact confirms important role of mechanisms leading to disintegration of the plasma column especially MHD instabilities.

1. S.Czekaj et al. in Controlled Fusion and Plasma Physics /Proc. 11th Europ.Conf.Aachen, 1983/ Part 1 /1983/469
2. Dyatchenko, V.F., Imshennik, V.S. in Voprosy Teorii Plazmy Moskva, Atomizdat 1974, V8, p 166.
3. Wilhelm, H.E. in Beitrage aus der Plasma Phys., 1/63.

Experimental Studies in Dense Plasma Focus

M. Yokoyama, Y. Yamada, Y. Yamamoto,
Y. Kitagawa and M. Yamanaka
Institute of Laser Engineering,
Osaka University,
2-6, Yamada-Oka, Suita, Osaka 565, Japan

I. Introduction

The plasma focus is not only very suitable device for detailed studies of fundamental plasma physics, but also one of the complementary fusion device between low-β Tokamak and high compression inertial fusion.

The ions, such as protons and deuterons, produced by a plasma focus device, are accelerated to above MeV, although the device is operated at low charging voltage below 100 kV. On the other hand, it remains difficult to explain the production mechanism of overall neutron yields emitted from a Mather-type device only by a thermonuclear fusion reaction. So, we must investigate high energy deuterons and their contribution to the neutron yield to clarify the neutron production mechanism.[1)]

II. Experimental Arrangement and Method

Our plasma focus device has a Mather geometry consisting of an anode of 5 cm diameter copper and a cathode of 12 copper rods distributed uniformly over a diameter of 10 cm. The device was operated at 30 kV - 18 kJ using a deuterium or a D_2-^{3}He gas mixture. Maximum current was 640 kA.

High energy deuterons were measured by nuclear activation techniques. The target used in the measurement, consisting of two hemicircular materials (aluminum and carbon), determined a mean energy of deuterons from $^{13}N/^{28}Al$ ratio.

We obtained the ion temperature and the kinetic energy from D-D/D-^{3}He yield ratio by using equimolecular D_2-^{3}He mixture. The $D(d,n)^3He$ reaction yield was determined from the neutron yield measured by a silver activation counter. While, the $^3He(d,p)^4He$ reaction yield was determined by an analysis of γ-decay spectrum induced by $^{63}Cu(p,n)^{63}Zn$ reaction (the threshold is 4.21 MeV). Such a mixture gas method was reported by Gullickson et al. in detail.[2)]

We obtained the electron density profile by the three-frame double exposed holographic interferometry (10 ns between each exposures) using a ruby laser (6943Å, pulse width of 2 ns). Deuteron sources were imaged on Kodak CN 85 films through the side-on and end-on ion pinhole cameras.

Moreover, we used a neutron time of flight detector to obtain the maximum neutron yield of 1.2×10^9 in 60 ns and a silicon PIN (250 μm thick) detector to determine the ion generation time, which agrees with the 10 ns pulse duration of hard x-rays. The spatial distribution of neutron emission was also measured by neutron pinhole camara consisting of a paraffin pinhole and a detector.[3)]

The experiments were compared between low (1.5 Torr) and high (4-5 Torr) pressure regimes, because the deuteron beam intensity is highest at 1.5 Torr, while the neutron yield is most at 5 Torr.

III. Results and Discussions

From the ratio of the activated products ^{13}N and ^{28}Al obtained from the target we obtained the mean deuteron energies as 1.5 MeV at 1.5 Torr and 1.4 MeV at 5 Torr, which shows that the mean energy depends weakly on the filling pressure, though the beam intensity is very sensitive to it. No activation of copper was observed, which indicates that the deuterons above 4 MeV is very few.

From the time sequence of the holographic interferogram at 1.5 Torr, it is found that the plasma sheath, after accelerated toward the center of anode and compressed, forms a pinched column (at -10 ns), and then the column is disintegrated at 1 mm ahead of anode tip (at 0 ns), resulting in a plasma diode formation. At this time both hard x-rays and high energy deuterons are emitted. After 10 ns, the anode plasma expands toward the plasma cathode. The dense plasma pinch phase, which exists in the high pressure regime, was not observed in the low pressure regime. Superposing a side-on pinhole image of deuteron (< 400 keV) at 1.5 Torr on the optical holographic image leads us to that the deuterons are generated at the pinched column disintegration point. The source dimension of the deuterons was 8 mm radially and 6 mm axially.

To study the correlation between neutrons and energetic

deuterons, we measured the deuteron temperature and kinetic energy by using a D_2-^3He mixture gas, where the pressure dependence of the neutron yields was same as in the pure deuterium gas. The results are listed on Table I, where we estimated the deuteron temperature T_i from a pure thermonuclear model and the deuteron kinetic energy E_d from a pure beam-target model. Ti = 11 keV at 1.5 Torr is much higher than the neutron time of flight value (3 keV), which implies that the thermonuclear model is not available at the low pressure.

Tabel I. Ion temperature T_i and deuteron kinetic energy E_d. The second column is an equiatomic case, whose data are not so different from the equimolecular case (the first column).

D_2+^3He	D-D neutrons / D-^3H_e protons	T_i (Thermonuclear Model)	E_d (Beam-Acceleration Model)
4 Torr (1:1)	14	5.0keV	42keV
4 Torr (1:2)	13	5.2keV	43keV
1.5 Torr (1:1)	3	11 keV	74keV

In low pressure regime, optical and ion pinhole images indicate that the deuterons are produced by the plasma diode. This plasma diode plays the role of an opening switch interrupting the current with very short rise-time, which may induce a high accelerating voltage across the plasma diode.

We estimate the accelerating voltage V_p described by

$$V_p = V - L\dot{I},$$

where V is the voltage across the electrodes, L is the inductance in the discharge and I is the discharge current. The inductance is assumed to be constant ($\sim$ 40 nH in our device) during the interruption. We assume ΔI, equal to a three quarter of the total current, to be 480 kA dropping off in 5 ns, determined from the hard x-ray emission time, yielding

$$V_p \simeq - L\Delta I/\Delta t = 3.8 \text{ MV}.$$

This voltage is consistent with observed deuteron energy.

The plasma diode was formed above anode surface, but the dense pinch was not formed in this regime. This suggests the possibility of the current interruption due to the enhancement of radiative loss caused by the high-z impurities such as a tantalum from the anode tip.

We estimate the neutron yield using a pure beam-target model as

$$Y_b = n_d \, n \, \sigma \, v \, ALt,$$

where n_d and n are the deuteron beam and target densities, σ is a reaction cross section, v is the beam velocity, A and L are the target plasma cross section and length, and t is the production duration. For 74 keV deuterons into a cold gas target of 1.5 Torr, $\sigma = 10^{-26}$ cm^2, $v = 2.7 \times 10^8$ cm$\cdot$s^{-1}, $n_d \simeq 8.8 \times 10^{16}$ cm^{-3} from experimental results, $A \simeq \pi \times 10^{-2}$ cm^2, $t \simeq 60$ ns, and $L = vt = 16$ cm, which agrees with the neutron pinhole camera measurement. The neutron yield is then 5.1×10^8. Since the measured average neutron yield was 7.0×10^8, the neutron production mechanism at the low pressure is explained by the beam-target model. Note that not the deuterons above 330 keV but the deuterons $\lesssim$ 74 keV contribute to the neutron yield.

In high pressure regime, the angular distribution at high pressure is different from the distribution at low pressure, suggesting that the deuterons at high pressure are not produced by a simple beam acceleration mechanism. Table I suggests that the thermonuclear reaction also contributes to the neutron-yield in this regime.

References

1) M. Yokoyama, Y. Yamamoto, A. Kisoda, Y. Yamada, Y. Kitagawa, M. Yamanaka and C. Yamanaka : 11th European Conference on Controlled Fusion and Plasma Physics (Aachen, 1983) 024.

2) R.L. Gullickson, J.S. Luce and H.L. Sahlin : J. Appl. Phys. 48, 3718 (1977).

3) Y. Yamamoto, A. Kisoda, A. Yamada, H. Niki, Y. Kitagawa, M. Yamanaka, M. Yokoyama and C. Yamanaka : Japanese J. Appl. Physics 23. 1410, (1984).

EXPERIMENTS WITH A PLASMA FOCUS DEVICE POWERED BY MAGNETIC FLUX-COMPRESSION GENERATORS

I.Ursu, M.Ivaşcu, D.Cotruţă, C.Dumitrescu-Zoiţa, A.Ludu, N.Mandache, B.Novac, V.Zâmbrcanu, V.Zoiţa

Central Institute of Physics, P.O.Box MG-7, Măgurele, Bucharest, R-76900, ROMANIA

Extension of the plasma focus (PF) operation in the 10 MA current range by means of capacitive energy storage is impeded by serious technological and economic limitations. Most of these problems can be solved or obviated if inductive storage is employed. Within this class of energy storage, of particular interest is the use of energy produced by magnetic flux-compression generators (MFCG) /1/. The characteristics of these devices, combined with suitable switching techniques, qualify them for proof-of-principle experiments in which the reactor potential of the PF device could be assessed.

This paper reports the first results of a series of experiments aimed at establishing the conditions for optimum coupling between MFCG's and a PF discharge chamber and of producing fusion relevant plasmas in the IPF-5X10 PF device which uses MFCG's as power supply.

In the IPF-5X10 device (whose equivalent electric circuit is presented in Fig.1) the electromagnetic energy is produced by a two-stage current amplifier consisting of two, series-connected MFCG's. The initial current (1.5-1.8 kA) is produced by a small condenser bank of 6.3 kJ energy stored at 4.4 kV. The first stage of the amplifier is a helical type generator whose coil is made from copper wires of increasing diameter, wound in 15 separate sections, each having different values for the turn spacing and number of paralleled wires. This generator, with 1 mH initial inductance, has an experimental current amplification in the range 100-150 for a 1.5 μH load. The second stage is another helical generator whose variable-pitch

coil is machined from a copper tube. It has 1.5 μH initial inductance and an experimental current amplification in the range 7-10 for a constant 100 nH load.

The electromagnetic energy produced in the current amplifier is transferred to the discharge chamber by means of high current opening and closing switches. The opening switch (OS) uses 24 or 32 exploding copper wires of (0.4-0.5) mm diameter and 90 mm length, connected in parallel. The switch voltage (U_s) can be modified from one experiment to another by changing the number of dielectric foils in the closing switch (CS).

The discharge chamber uses the Mather /2/ configuration for the coaxial, stainless-steel electrodes. The hollow anode is of 100 mm diameter and an active length of 145 mm, while the squirrel-cage cathode has a diameter of 150 mm. The insulator between the two electrodes is made of pyrex glass and has a length of 50 mm. The working gas (deuterium) pressure is (1-3) torr. Discharge chamber conditioning has been done on the IPF-3/50 PF device /3/ before each experiment and consisted in carrying out a few discharges, until the maximum neutron yield was obtained. The discharge chamber was afterwards sealed and transferred to the IPF-5X10 experimental site, where it was evacuated and refilled (a few minutes before the experiment) with the working gas at the appropriate pressure.

The plasma evolution in the coaxial accelerator has been simulated by a numerical code in which the plasma sheath dynamics (described by the coaxial accelerator inductance L_a) was coupled to the operation of both the flux-compression generators and the high current switches. The simulation of the second stage MFCG operation has used time-dependent generator inductance (L_2) and resistance (R_2). The physical evolution of the exploding wire opening switch has been simulated by taking into account the liquid, vapour and plasma states of copper. This numerical code has been used for the IPF-5X10 device to establish the optimum combinations for various sets of the working parameters : initial current for the second amplifier stage, switching time, switch voltage, plasma current rise-time, working gas pressure.

Plasma evolution and parameters of the device have been determined by the following diagnostics methods : Rogowski belts (RB), capacitive voltage divider (VD), X-ray detectors, magnetic probes, neutron activation counters, scintillator-photomultiplier neutron detectors.

The IPF-5X10 experimental site provides the necessary conditions such that the high current switches and the discharge chamber are protected from the shock produced by the MFCG's operation. A replaceble parallel plate transmission line was used to connect the output of the current amplifier second stage to the input of the opening switch.

The time evolution of the electrical parameters in a typical experiment are presented in Fig.2 (I_A= current in the amplifier circuit), Fig.3 (U_s= switch voltage) and Fig.4 (I_p = plasma current). Plasmas have been produced and studied in the IPF-5X10 device for currents up to about 400 kA. When using deuterium as working gas, neutron yields up to 5×10^8/discharge have been obtained. Since these yields are similar to those obtained, at the same currents, when using the discharge chamber in optimized conditions on the IPF-3/50 device, they indicate a proper energy transfer to the plasma in the IPF-5X10 device. As shown by Fig.2 (where it can be seen that the amplifier current is still rising after switch operation) the current capabilities of the device are much higher, so that experiments in the 1 MA range are being prepared.

REFERENCES

/1/ Fowler, C.M. et al., Proc. 2nd Int.Conf.Energy Storage, Compression and Switching, Venice, (1978)

/2/ Mather, J.W., Methods Exp.Phys., 9B, 187, Academic Press, (1971)

/3/ Cebanu, A. et al., Plasma Phys.& Controlled Nucl.Fus.Res., IAEA (1981), vol.2, p.197

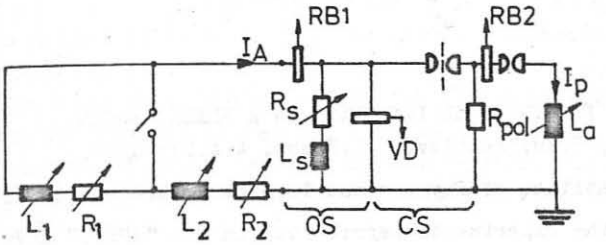

Fig.1.
IPF-5X10 device equivalent electric circuit

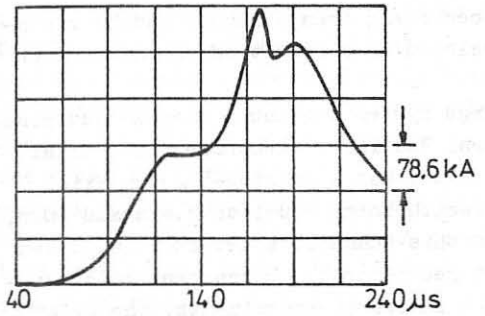

Fig.2.
Current I_A in the amplifier circuit

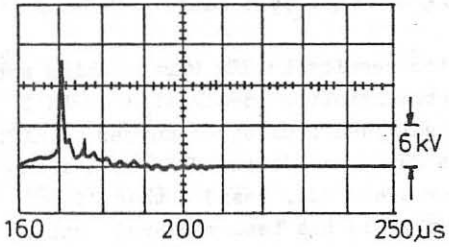

Fig.3.
Switch voltage U_s

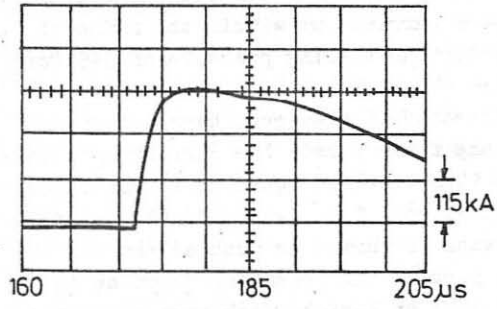

Fig.4.
Plasma current I_p

FORMATION OF ELECTRON AND ION BEAMS IN A PLASMA FOCUS.

R.G.Salukvadze, E.Yu.Khautiev, V.I.Kraus, A.A.Batenyuk.

I.N.Vekua Institute of Physics and Technology, Sukhumi, USSR.

The goal of the experiments carried out in the "KPF-3" device (40kV, 250kJ) was to study parameters of electron and ion beams (EB and IB) both by recording them directly and by observing hard x-rays (HXR) developed as a result of EB interaction with various targets.

Fig.1 shows the discharge system schematic diagram and positions for diagnostic sensors. The inner electrode in a coaxial discharge system (D=16cm, l=24cm) has a passing-through axial channel, its diameter and length being equal to 1,4cm and 40cm, respectively. At the end of this channel, a detector is placed with a low-resistance shunt recording the EB current which propagates along the axis. In a number of experiments, the axial channel at the entrance was stoppered by copper plates, 0,5-1mm in thickness.

The EB-collector interaction results in HXR bursts which are recorded by a high-current photomultiplier (designated as PH I in Fig.1) with a scintillator shielded from other sources of HXR. A similar sensor designated as PH 2 records the HXR which arise at the end surface of the inner electrode. Besides that, for every shot, the overall neutron yield has been measured, while a magnetic analyzer with a photomultiplier /I/ recorded IB.

The experiments have been carried out within the range of stored energy (W=30-100kJ) for the filling pressure of 3-5 Torr D_2. The main results are:

1. The traces of the detector of electrons have a complex structure (Fig.2a); after the first burst, the current drop follows which lasts for 10ns; then it rises again up to the value which is close to the original one. The overall duration of EB is nearly 100ns which is twice or thrice as much as the HXR duration (Fig.2b). The final part of the repeating EB pulse is smoother and is not accompanied by X-rays which fact indicates

that this component of the beam is of low energy. When the beam is passed through the limiter on entering the drift space and the grids under floating potential are used in the detector of electrons, the low-energy tail of the beam becomes cut off and the EB duration is reduced to that of HXR (Fig.3a,b). The peak (60-70kA) current of the main component of the beam is also reduced down to 30-40kA. Durations of individual EB pulses often do not exceed 10ns.

It should be noted that at the moment of pause in electron current, the PH I signal is, in a number of cases, kept at a fairly high level. This may be due to the fact that with the EB density decreased, there is a simultaneous increase in the energy of the beam particles. Thus, the bremsstrahlung from the target surface undergoes the decrease in its intensity while, on the other hand, there is the increase in the radiation fraction passing through the collector and the detector walls, as well as in the scintillator light output on absorbing harder quanta. The ions accelerated due to the collective processes evolved as a result of beam-background plasma interactions /2/ , can also influence on the EB pulse shape.

The current measured is smaller than the real current. The EB current value at the detector collector is in a marked extent defined by the conditions of its transporting into the drift space. For example, according to the thermal physics data for the inner electrode end ablation the beam current value exceeds 100kA when the beam energy is $\geq$ 1 kJ.

2. When compared, the PH I and PH 2 data show that both simultaneous and different-structured pulses are observed (Fig.3b.c). The PH 2 signal is longer in duration. The ratio of signal amplitudes undergoes shot-to-shot variation within a broad range which indicates that there are various radial distributions of the beam current, in particular, there is a possibility of forming hollow beams with relatively large diameters. HXR signals consist both of single pulses nearly 10ns in halfwidth and several pulses of various durations with the total formation time up to 50ns. Reappearing bursts of radiation shifted by 50-80ns with respect to the first one are also observed.

3. The HXR intensity time-integrated distribution at the inner

electrode end is judged of by pin-hole camera photoes, the camera being placed at the angle of 30° to the axis. When the axial channel is stoppered by a copper plate the EB is well-focused close to the discharge chamber axis and has lateral dimensions of ≈ 8mm (Fig.4a). Due to the beam action, an aperture appears at the central part of the plate. As a result of this effect, the discharge current becomes redistributed along the radius due to the fact that near the end, the current layer has lost its cylindricity. Individual regions of current fibers in a noncylindrical part are variously oriented with respect to the axis. Therefore, the electron beams generated in some of these regions can be variously directed. Lateral dimensions of the HXR emission zone start to grow and there appear several local regions corresponding to EB generated in various fibers (Fig.4b). More intense bursts of HXR arisen at the inner electrode end are usually observed in discharges where the neutron yield approaches to the value which corresponds to the well known scaling.

4. IB measurements indicate several pulses of ions of various energies over the range of 0.1-1.5MeV /1/. Durations of ion pulses are fairly well correlated with electron pulse durations. Ion spectra intensities also increase while the neutron yield approaches its scaling value corresponding to the consumed energy of the current supply. This method was fairly efficient in recording relatively high-energy ions with $\mathcal{E} \gtrsim 100$keV. However, a considerable number of 30-40keV electrons available (defined by pinhole pictures in HXR) can serve as an indirect evidence for the fact that PF generates a sizable amount of low-energy ions.

5. The results obtained evidence that the EB and IB current values and their energy spectra vary in characteristic times which are an order of magnitude less than the total duration of the whole process of their formation.

Analyzing these results together with previous ones, a conclusion can be drawn that plasma ions and electrons become accelerated in electric fields generated in fibers, the current shell breaking against them. A strong Langmuir turbulence develops in these fibers, then an anomalous resistance takes place and strong electric fields begin to appear. Under these conditions, a fraction of the discharge current starts to be transported as EB and IB of

various energies corresponding to the potential difference in various areas of current fibers. As a result of this process, the electron beam gives rise to HXR, while the ions interacting with the focus plasma generate the neutrons. A longer duration of the neutron-generating process in comparison with the ion pulse duration, can be due to the capturing of the low-energy ions by the focus self-magnetic field.

REFERENCES.

1. Khautiev E.Yu. et al. Fizika Plazmy, 11, N3, 1985, p.281-287.
2. Plyutto A.A. et al. Atomnaya Energia, v.27, N 5, 1969, p.148.

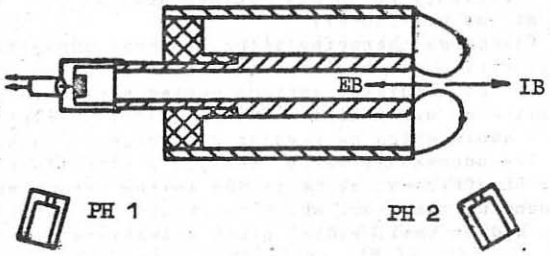

FIG.1

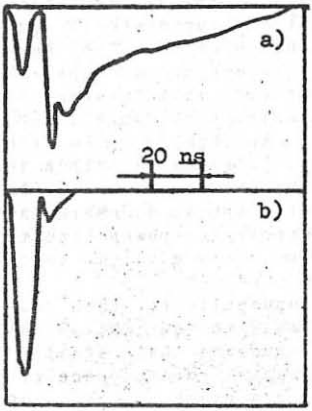

FIG.2

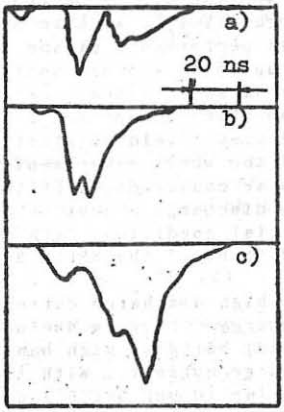

FIG.3

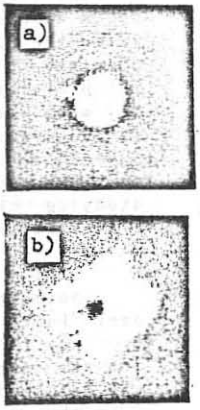

FIG.4

300 KV PLASMA FOCUS SPEED2: FIRST RESULTS FROM 3 MA DISCHARGES

W.KIES, C.VAN CALKER, G.DECKER, M.MÄLZIG, G.ZIETHEN
PHYSIKALISCHES INSTITUT I, UNIVERSITÄT DÜSSELDORF
FEDERAL REPUBLIC OF GERMANY

SUMMARY

Based on a high impedance driver concept the high voltage (300 kV) plasma focus SPEED 2 has been realized capable of driving more than 3 MA into a fast (400 ns) deuterium discharge. The optimization procedure with respect to neutron efficiency up to now yielded several 10^{11} neutrons per shot at 100 kJ (230 kV).

Discharge characteristics (pinch dynamics, anomalous resistivity) can be influenced by the energy input per unit area of the insulator surface during sheath formation. There exists an upper limit of this quantity (approximately 100 J/cm^2) above which no regular discharge is possible.

The uncommonly large reaction proton fluence anisotropy (>15) of efficient shots is due to the strong magnetic field surrounding the pinch which is caused by large pinch currents and/or small radial pinch dimensions.

300 KV PLASMA FOCUS SPEED 2

Encouraged by favourable results of our high impedance driver SPEED 1 /1/ and challenged by the promising pinch current (I_p) scaling of the neutron yield (Y) of deuterium focus discharges ($Y \sim I_p^4$) we have built and successfully operated the high performance plasma focus SPEED2. The bank consists of up to 40 storage units interconnected by parallel plate transmission lines. Each storage unit (6-stage 50 kV marx generator) comprises 6 capacitors (0.62 µF, 21 nH) and 3 pressurized field distortion sparkgaps. The 120 sparkgaps of the whole experiment are triggerable within 10 ns. The modular construction of the bank renders possible studying the discharge behaviour of the 400 ns discharge at different initial conditions with respect to power input. Maximum conditions of the SPEED 2 device are given in table 1.

Note the high discharge current unusually for this modest bank energy. This is due not only to low initial inductance (15 nH) but also high bank impedance that stabilizes the discharge current. With the bank-load impedance ratio being similar to our SPEED 1 device a pinch current of more than 2 MA is expected.

TABLE 1
Maximum experimental data of the plasmafocus SPEED 2

Energy	180 kJ	
Voltage	300 kV	
Bank impedance	70 mOhm	
Initial current rise	>20 TA/s	
Current rise time	400 ns	
Discharge current	4 MA	
Pinch current	>2 MA	(expected)
Neutron yield per shot	$>10^{12}$	(expected)

STATUS:

The optimization procedure of SPEED 2 started from the well known operating regime of SPEED 1 (20 kJ) with 10 storage units successively reaching a maximum neutron yield of $3*10^{11}$ neutrons per shot at 185 kV/70 kJ and 35 storage units. Meanwhile the full bank (40 storage units) is operated at 230 kV/100 kJ with discharge currents up to 3 MA. Though record yields of several 10^{11} neutrons per shot have been measured, indicating pinch currents of about 1.5 MA, optimum conditions have not yet been established.

PLASMA SHEATH FORMATION AND COMPRESSION

The power input during plasma sheath formation (within 100 ns) is more than 100 GW. This means that an energy of more than 10 kJ can be fed into the forming sheath which exceeds the energy input of conventional low voltage and slow devices of equal energy by more than 2 orders of magnitude. Discharge initiation under these initial conditions causes (i) fast sheath formation and (ii) thin and highly conducting plasma sheaths /2/.

Energy input W_i during sheath formation is proportional to accelerator voltage U_i, current rise $\dot{I}_i$, and the formation time T squared:

$$W_i = U_i \dot{I}_i T^2 \qquad (1)$$

The energy W_s needed to form a plasma sheath (ionization and heating to several eV) near the insulator surface depends on sheath volume, namely surface area A_s, sheath thickness d_s, and deuterium filling density n

$$W_s \sim A_s d_s n \qquad (2)$$

Setting both energies equal formation time becomes

$$T \sim (A_s d_s n / U_i \dot{I}_i)^{1/2} \qquad (3)$$

Since measurements of SPEED1 discharges have shown $\dot{I}_i = U_i / L_i$

and $d_s \sim n^{-1}$, formation time becomes density independent:

$$T \sim (A_s L_i)^{1/2} / U_i \qquad (4)$$

This expression implies that the sheath formation time can be reduced by maximum voltage, minimum insulator surface and inductance. However, there is an upper limit of U_i that is critical for spoke formation and an upper limit of energy input per unit area of insulator surface of about 100 J/cm^2, above which no well defined sheath is formed (electric signal evidence). Since L_i is closely related to the insulator dimensions for short accelerators $L_i \sim l_s / r_s$, $A_s \sim r_s l_s$ the formation time $T \sim l_s / U_i$ seems to depend on insulator length and voltage at ignition only. The strong influence of energy input on discharge behaviour is demonstrated by the waveforms of accelerator voltage and current derivative at sheath compression (see figure 1).

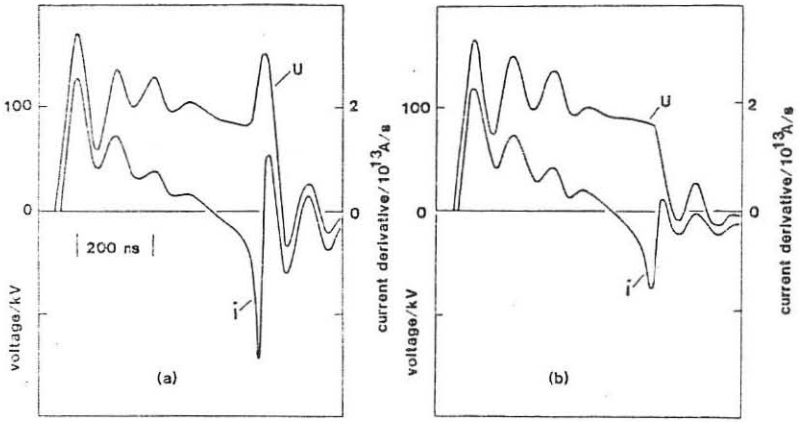

FIG. 1: Waveforms of voltage and current derivative

The energy input for a given insulator geometry well below the upper limit given above results in the waveforms (figure 1a) marked by steep spikes of current derivative and voltage at pinch time the latter of which is due to anomalous resistivity. Reaching the energy limit per unit area the waveforms of figure 1b develop. The spike of the current derivative is reduced indicating reduced pinch dynamics. No voltage spike is to be seen which is due to suppressed anomalous resistivity at pinch time. It seems likely that the increased energy input is for the benefit of sheath temperature and hence conductivity. This behaviour visualizes the strong influence of initial conditions on pinch dynamics .

REACTION PROTON FLUENCE AND SPECTRA

The neutron yield is measured with silver activation counters that are calibrated by proton fluence measurements using special proton spectrometers /3/ with PM 355 films. Figure 2 shows two (side-on and end-on) examples of proton spectra.

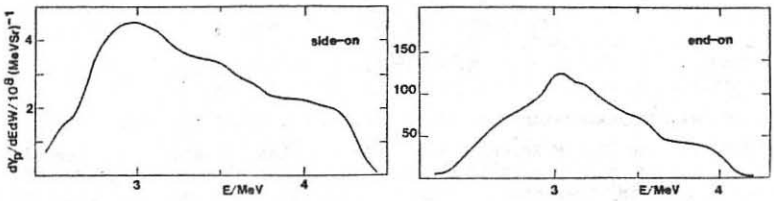

FIG. 2: Reaction proton spectra

The width of the side-on spectrum (>500 keV) indicates relatively high center of mass energy of the reacting deuterons in side-on direction. No marked energy anisotropy (E_{ymax} end-on/E_{ymax} side-on >1), typical for spectra of conventional focus devices, is measured. Most important is the striking fluence anisotropy (fluence end-on/fluence side-on)that can be more than 15 in efficient shots. This fluence anisotropy varies from shot to shot depending on discharge behaviour and fusion yield, and together with enhanced neutron fluence anisotropy Y_{eo}/Y_{so} >2 indicates that the magnetic field compressing the pinched plasma must be unusually strong. This is due to small radial dimensions of the pinch and/or large pinch currents.

Unfortunately, the pinch current is hardly measurable by traditional probe techniques. Therefore, a subnanosecond Schlieren-technique will be used to determine pinch dimensions and computer simulations of electric signals hopefully allow to evaluate the pinch current in comparing these signals with the measured ones.

References:

/1/G.Decker,W.Kies,G.Pross,J.Rybach; 4th IEEE Pulsed Power Conf.,Albuquerque 1983

/2/ G.Decker,W.Kies,G.Pross; Phys.Fluids 26(2), p571 (1983)

/3/C.van Calker,G.Decker,W.Kies,J.Rybach subm. for publ. Phys.Lett.(1985)

RESULTS FROM THE LOS ALAMOS RFP EXPERIMENTS*.

P. G. Weber, D. A. Baker, C. J. Buchenauer, L. C. Burkhardt,
T. E. Cayton, J. N. DiMarco, J. N. Downing, R. M. Erickson,
P. R. Forman, R. F. Gribble, A. Haberstich, R. B. Howell,
J. C. Ingraham, S. Masamune#, R. S. Massey, G. Miller,
C. P. Munson, J. A. Phillips, M. M. Pickrell, K. F. Schoenberg,
A. E. Schofield, R. G. Watt, D. M. Weldon and G. A. Wurden.

Los Alamos National Laboratory, MS F639, Los Alamos, NM 87545, USA.

ABSTRACT. The ZT-40M Reversed Field Pinch at Los Alamos has operated with flat topped currents up to 400 kA. Scaling of plasma parameters with discharge current is presented. Pulsed discharge cleaning was used to condition the Inconel vacuum vessel: significant effects on the electron density, temperature and impurity levels were observed. Z_{eff} has been determined spectroscopically; operation at higher densities at a given current yields lower impurity fractions. Limiter experiments in ZT-40M, including recent experience with toroidal rail limiters are reported. Finally, the ZT-P device (a prototype for the next generation of RFPs at LANL) has operated at current densities of up to > 4 MA m^{-2}; first results are presented.

INTRODUCTION. The ZT-40M RFP[1] (R=1.14 m, a=0.2 m) has an Inconel vacuum vessel, and is generally operated without limiters. Discharges are established on a millisecond timescale, and sustained for times (27 ms) much longer than the classical resistive diffusion time for the reversed toroidal magnetic field. This implies the existence of a 'dynamo' mechanism[2] which serves to maintain the RFP configuration. The plasma equilibrium is controlled by active feedback applied to correct the plasma position at the poloidal gap in the aluminum shell which surrounds the vacuum vessel. Diagnostics include interferometry, Thomson scattering, bolometry, spectroscopy (X-ray through visible), Faraday rotation , edge probes, time of flight particle energy analysis and external magnetics.

CONFINEMENT STUDIES. ZT-40M was operated with flat topped currents in the range 60 to 400 kA to ascertain the dependence of plasma properties on the plasma current. Pulsed discharge cleaning was used to condition the vacuum vessel walls, leading to higher electron densities and lower electron temperatures than would otherwise be achieved. By varying the number of PDC pulses between plasma discharges the electron density could be varied by a factor of three, with the profiles becoming broader at the higher densities. In the normal I_ϕ/N_e operating range, ($2\text{-}7.5 \times 10^{-14}$ a.m, with $N_e = \pi a^2 n_e$), the central electron temperature measured by Thomson scattering varied inversely with the electron density, implying constant electron poloidal beta. Ion temperatures were determined from Doppler broadening of impurity lines (C V, N VI, O VII), from a time-of-flight neutral spectrometer and from analysis of deposition profiles in edge probes. The spectroscopic data indicated $T_i > T_e$, with T_i at r/a ~0.75 being roughly two-thirds of the on-axis value, a similar ratio to that seen in the electron temperatures. The neutral particle diagnostics also detected hot ions, but the

interpretation is complicated by neutral density and ion temperature profile effects; numerical modeling of these effects is in progress.

The plasma poloidal beta, derived from the line average electron density, central electron temperature and the assumption of $T_i = T_e$, was constant for ZT-40M from 60 to 400 kA. For resistivity varying as $Z_{eff}\, T_e^{-1.5}$ and constant beta, the energy confinement time scaling is expected to be:

$$\tau_{Ee} \propto I_\phi^{1.5} \; (I_\phi/N_e)^{1.5} \; a^2 \; Z_{eff}^{-1}$$

The Lawson parameter should then scale as:

$$n\,\tau_{Ee} \propto I_\phi^{2.5} \; (I_\phi/N_e)^{0.5} \; Z_{eff}^{-1}$$

The data to support this scaling are plotted in Fig. 1. Also shown are the extrapolations to the proposed 2-4 MA ZT-H experiment.

Z_{eff} MEASUREMENTS. Z_{eff} has been measured in ZT-40M, using the continuum emission at 671 nm, a region free of line radiation[3]. The Z_{eff} obtained is comparable in magnitude to the resistive anomaly factors computed by comparing the experimentally estimated value of the on axis resistivity to the Z=1 Spitzer value. The parametric dependence of Z_{eff} is also the same as the resistive anomaly factor, namely, Z_{eff} increases rapidly with decreasing electron density at a given plasma current. This is illustrated in Fig. 2, for currents of 120 and 240 kA, with Z_{eff} evaluated during the current flat-top at 5 ms. The Z_{eff} database is presently too small to determine a more global scaling of Z_{eff} with plasma current.

The total resistive anomaly factor is, of course, due to both the Z_{eff} and to non-ohmic dissipation by fluctuations and the 'dynamo' mechanism. The contribution of the fluctuations to the anomalous resistivity has been estimated[4], the effect of fluctuations is generally small compared to the Z_{eff} contributions.

PLASMA WALL INTERACTIONS The Z_{eff} data, together with observations of impurities and total radiated power show that metal impurities play an important role in the operation of ZT-40M without limiters. Thus experiments have been performed to examine the effects of wall conditioning and limiters on the RFP.

Pulsed discharge cleaning (20-30 kA, <2 ms duration, "stabilized pinch" shots at 0.5-1 Hz) can be used to condition the Inconel vacuum vessel, both overnight and between normal plasma shots. Electron densities of 9×10^{19} m^{-3} and electron temperatures of > 5 eV are typical of PDC pulses. The PDC has several beneficial effects on plasma discharges, specifically elimination of the rapid density pumpout seen at the start of discharges without PDC, and hence higher operating densities, resulting in lower I_ϕ/N_e, and, as seen above, lower Z_{eff}. Also, measurements of D_α emission show that the particle confinement time is improved with PDC. Plasma wall interactions, as monitored spectroscopically, are also reduced after PDC. These results are not valid if the wall temperature is elevated. When, for example, the liner temperature was increased to 80° C, the particle recycling rate was increased by a factor two, and there was increased oxygen contamination of the discharge. The resistivity increased, and energy confinement was degraded.

ZT-40M has also been operated with limiters to reduce the plasma wall interaction. Several materials and limiter types have been used, including mushrooms, various rail limiters and tiles at selected locations, as well as graphite poloidal ring limiters[5].

In one experiment the mushroom limiter was used as a probe to gauge the effectiveness of several other limiters. A poloidal, segmented graphite limiter located 90° toroidally from the mushroom reduced the power to the

probe by 28 % at a major radius equivalent to the liner bellows. Tiles located close to the probe provided only small additional reductions in power load. This resulted in operation using four poloidal rings at the locations of most severe magnetic field errors; however, the scrape-off length was short compared to the connection length between the limiters in the predominantly poloidal edge magnetic field of the RFP. Toroidal rail limiters should be more effective: hence two complete graphite toroidal rail limiters were recently installed at $\pm \pi/4$ with respect to the outer midplane of ZT-40M. An RFP was established with these rails, but could not be maintained on long timescales. Currents in the rails generated net vertical magnetic fields which interfered with equilibrium control, and plasma interactions with the graphite raised the plasma carbon impurity level from < 0.1 % to 3-4 %. The graphite rails can hold large quantities of deuterium[6], so that recycling from the rails caused the electron density to be much larger than usual at a given plasma current. This high electron density, combined with 3-4 % concentrations of both carbon and oxygen is sufficient to radiate most of the ohmic power input: the electron temperature was clamped at 20-30 eV, these being the temperatures of highest radiation efficiency for low-Z impurities. The measured radiated fraction after formation always exceeded 46 %. Changing the fill gas to helium showed the importance of hydrogen recycling: seventy discharges were required to achieve 90 % helium content in the plasma, compared to six discharges in the absence of the graphite rails. Breakdown limitations at low pressures of helium, coupled with the equilibrium difficulties mentioned above, also prevented formation of lower density, hotter plasmas in helium. The rails have now been removed, and plans call for a stainless steel liner with full graphite armor to be installed at the beginning of 1986. The graphite armor will be an extension of the poloidal ring limiter technology, which has been successfully applied in ZT-40M.

ZT-P. A new RFP, named ZT-P (R=0.451 m, a=0.068 m) has been commissioned as a prototype for the proposed 2-4 MA ZT-H (R=2.15 m, a=0.4 m) experiment. ZT-P is an air core RFP with intrinsically low field errors; for example, the radial component of the $n > 12$ spatial ripple of the magnetic field is less than 0.3 % of the field at the reversal surface, so that island overlap is avoided for the large-n modes seen in several RFPs. The ZT-P torus assembly is readily replaced, allowing studies of various first wall and shell systems. Currently, a stainless steel vacuum vessel with 24 graphite poloidal ring limiters is used. The device will also explore the boundary conditions (conducting shell, etc.) required for RFP operation, and will develop a data base for compact reactor relevant current densities ($j_\phi > 5 \text{MA m}^{-2}$). To date, ZT-P has operated as an RFP with currents up to 60 kA ($> 4 \text{ MA m}^{-2}$), with temperatures estimated spectroscopically and from the resistivity to exceed 70 eV for currents greater than 20 kA. The RFP configuration is maintained for <0.5 ms, without the power crowbar being applied. Discharge optimization is in progress, with an emphasis on trimming currents in the equilibrium windings to achieve proper plasma centering. Active feedback systems for the plasma position are in preparation. Device conditioning is taking place simultaneously, with many thousands of pulses of PDC and a thousand plasma shots to date continuing to lead to lower resistance values. Additional diagnostics, particularly Thomson scattering and CO_2 laser interferometry are in preparation.

* Work supported by the U. S. Department of Energy.

Permanent Address: Kyoto Institute of Technology, Kyoto, Japan.

REFERENCES.

1. R. S. Massey, R. G. Watt, P. G. Weber, G. A. Wurden, et al, Fusion Technology, to be published (1985).
2. R. W. Moses, Proc. 1984 Int. Conf. on Plasma Physics, Lausanne, Vol I, p455 (1984).
3. P. G. Weber, submitted to Physics of Fluids (1985).
4. K. F. Schoenberg, R. W. Moses and R. L. Hagenson, Phys. Fluids 27, 1671 (1984).
5. J. N. Downing, C. J. Buchenauer, J. C. Ingraham, R. A. Krakowski, J. A. Phillips and R. G. Watt, J. Nucl. Materials, 128 and 129, 517 (1984).
6. B. L. Doyle, W. R. Wampler, D. K. Bryce and S. T. Picraux, J. Nucl. Materials, 93 and 94, 551 (1980).

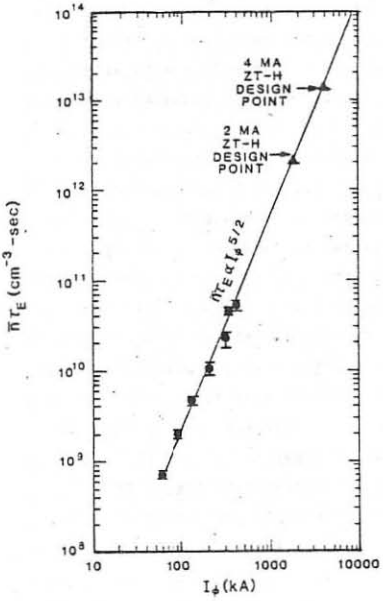

Fig. 1. Scaling of the Lawson parameter with I_ϕ in ZT-40M, with extrapolation to the ZT-H design points.

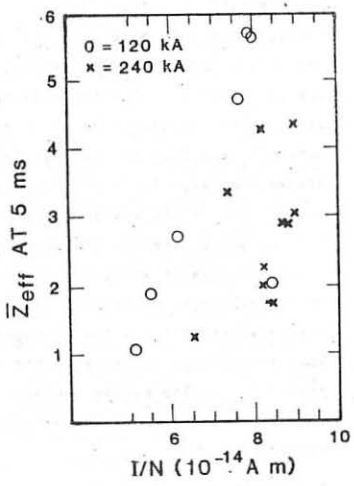

Fig. 2. Z_{eff} measured at the 5 ms time in ZT-40M shots as a function of I/N.

CONDITIONS FOR CONFINEMENT AND POSITIONAL STABILITY OF A Z-PINCH IN HIGH ORDER MULTIPOLE AND CUSP FIELDS

C. Wahlberg

Uppsala University, Department of Technology, Box 534, S-751 21 Uppsala, Sweden

Abstract. Conditions for the existence of equilibria and their positional stability are investigated for a generalized N-conductor Extrap configuration in the approximation N >> 1.

1. Introduction. The Extrap scheme /1/ consists of a pure z-pinch (no axial magnetic field) immersed in an octupole field, produced by four external current-carrying conductors. Alternatively, eight conductors with alternating current directions might be used (cusp)/2/. The experimentally observed stability of Extrap /3/, in particular the absence of unstable long external m = 1 kink modes, is not fully understood, but recent numerical /4/ and analytical /5/ investigations have shown that the following two factors are of importance: (i) the absence of a quadrupole component (i.e. elongation) of the equilibrium, in order to preserve the degeneracy of the m = 1 mode /5/, and (ii) an appropriate shape of the current profile close to the plasma boundary. In particular, Dalhed and Hellsten /4/ found that the growth rate of the axisymmetric m = 1 mode could be reduced to an essentially marginal level by choosing $j = 0$ and $dj/d\Psi = 0$ at the plasma boundary.

In the present work, conditions for the existence of equilibria and their positional stability (axisymmetric m = 1 mode) are investigated for a generalized N-conductor configuration in the approximation N >> 1. This approach clearly illustrates the important role played by the current profile close to the plasma boundary and the presence of the separatrix, and complements earlier investigations /5,6/ based on a small plasma size approximation.

2. Equilibrium. We use the integral equation formulation of the equilibrium problem, described in Ref. /6/, to calculate the form $r = R(R_o, \varphi)$ of the flux surfaces. R_o is a Lagrangian coordinate labelling the flux surfaces and can be chosen quite arbitrarily. A convenient choice however, which we will use here, is to take R_o equal to the average radius of the flux surface. With the normalization $j \to jI_p/2\pi R_p^2$ (I_p is the total plasma current and R_p the average plasma radius), $\Psi \to \Psi\mu_o I_p/2\pi$, $R \to RR_p$ and $R_o \to R_o R_p$, the equation for $R(R_o, \varphi)$ assumes the form

$$\frac{1}{2\pi}\int_0^{2\pi} d\varphi' \Big\{ \int_0^{R_o} dR_o' j(R_o') R' \frac{\partial R'}{\partial R_o'} \Big[\ln R R_p - \sum_{n=1}^{\infty} \frac{1}{n} \Big(\frac{R'}{R}\Big)^n \cos n(\varphi' - \varphi) \Big]$$

$$+ \int_{R_o}^{1} dR_o' j(R_o') R' \frac{dR'}{\partial R_o'} \Big[\ln R' R_p - \sum_{n=1}^{\infty} \frac{1}{n} \Big(\frac{R}{R'}\Big)^n \cos n(\varphi' - \varphi) \Big] \Big\}$$

$$- \frac{\lambda}{N} \sum_{n=1}^{\infty} \frac{1}{n} \varepsilon^{n-1} R^{nN} \cos nN\varphi = -\Psi(R_o) \qquad (1)$$

where

$$\lambda = (N I_C / I_P)\, \varepsilon \quad \text{and} \quad \varepsilon = (R_P / R_C)^N \qquad (2a,b)$$

I_C denotes the current in each external conductor, R_C the distance from the center of the plasma to the conductors and the notation R' stands for $R(R_o', \varphi')$. Eq. (1) is valid for the multipole type of external field, but is readily modified (omitting the even terms in the last sum /2/) for the cusp. It is to be noted that eq. (1) gives an <u>exact</u> formulation of the equilibrium problem with scalar pressure, and does not require for instance "almost circular" equilibria.

We now consider the limit $N \to \infty$. First we notice that in order for ε to remain finite the plasma radius must be scaled as $R_P = R_C(1 - \alpha/N)$, with $\alpha = O(1)$. Similarly, by inspection of the external field term it is seen that the ordering of R must be chosen as $R = R_o + R_1/N$, with $\langle R_1 \rangle = 0$. Furthermore, it is convenient to introduce the streching transformation $R_o = 1 + \xi/N$, with $-\infty < \xi \leq 0$, which magnifies the outermost $O(1/N)$ part of the plasma boundary. It can be shown that if the amount of current in this boundary layer is not larger than $O(1/N)$ (i.e. essentially bounded current density) only the total current contributes to the plasma part of Ψ, with the leading order φ-dependent part given by $(\xi + R_1)/N$. Clearly, λ must then be chosen as an $O(1)$ quantity in order for the external field to have any significant influence on the equilibrium. Writing $\Psi = \Psi_o + \Psi_1/N$, the $O(1/N)$ component of eq. (1) thus becomes

$$\xi + R_1(\xi,\theta) + (\lambda/2\varepsilon) \ln (1 + \eta^2 - 2\eta \cos\theta) = -\Psi_1(\xi) \qquad (3)$$

where $\eta = \varepsilon \exp[\xi + R_1(\xi,\theta)]$ and $\theta = N\varphi$. For the cusp the ln - term should be replaced by $(\lambda/4\varepsilon) \ln [(1 + \eta^2 - 2\eta\cos\theta)/(1 + \eta^2 + 2\eta\cos\theta)]$. Now, eq. (3) is very easy to solve numerically. (Note that $\Psi_1(\xi)$ will be determined

by the condition $\langle R_1(\xi,\theta)\rangle = 0$). Furthermore, for ε and λ both $\ll 1$ an approximate solution is found to be given by

$$R_1(\xi,\theta) = \lambda e^{\xi}\cos\theta + \ldots, \quad \Psi_1(\xi) = -\xi + \frac{1}{2}\lambda^2 e^{2\xi} + \ldots \qquad (4a,b)$$

However, by examining the equation for the plasma boundary, i.e. $R_1(0,\theta)$, it is easily seen (e.g. in the limit $\varepsilon \to 0$, where eq. (3) reduces to $R_1 - \lambda \exp(R_1)\cos\theta = \text{const.}$) that solutions can be obtained only for not too large values of $|\lambda|$. λ_{max} and λ_{min} are in Fig. 1 shown as functions of ε. The solid and dashed curves correspond, respectively, to the multipole and cusp type of external field. The physical origin of the $|\lambda|$ - limit above is that, for a given ε, the separatrix coincides with the plasma boundary at a sufficiently large current ratio NI_c/I_p. Thus, by plotting the solutions $R_1(0,N\varphi)$ of eq. (3) at the critical λ-values we obtain the form of the separatrix. Fig. 2 illustrates a few separatrices for the $N = 4$ multipole corresponding to various values of the current ratio. (The cusp case is not shown, but these curves look very similar to the ones in $\lambda > 0$ multipole case).

Apparently, the parameter λ gives a measure of the noncircularity of the plasma, and we see that a significant difference between the parallel currents ($\lambda > 0$) and anti-parallel currents ($\lambda < 0$) cases is that an appreciably larger noncircularity of the plasma is possible in the latter case.

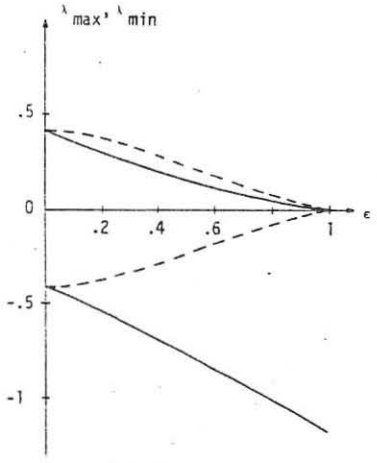

Fig. 1

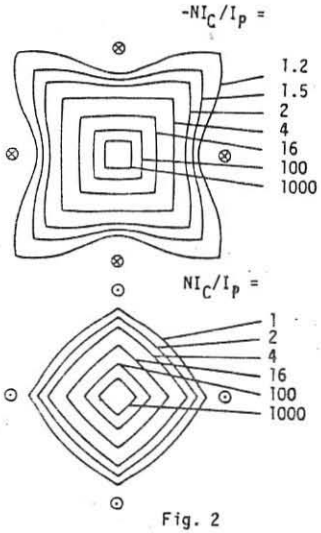

Fig. 2

3. Stability. In order to find out the positional stability of the equilibria above, we calculate the eigenvalue ω^2 for the axisymmetric, incompressible m = 1 eigenmode by solving /5/

$$\omega^2 \Delta\phi + \bar{B} \cdot \nabla [\Delta g + j'(\Psi) g] = 0, \quad \Delta\chi = 0 \qquad (5a,b)$$

inside and outside, respectively, of the plasma, together with the boundary conditions

$$\Lambda = 0, \quad \omega^2 \nabla\Psi \cdot \nabla\phi + \bar{B} \cdot \nabla (jg + \nabla\Psi \cdot \nabla\Lambda) = 0 \qquad (6a,b)$$

where $\Lambda = g - \chi$, $g = \bar{B} \cdot \nabla\phi$, $\bar{B} = -\hat{z} \times \nabla\phi$, $\bar{\xi} = -\hat{z} \times \nabla\phi$ ($\bar{\xi}$ = plasma displacement and $\hat{z}\chi$ is the vacuum vector potential. Unfortunately, this problem is very difficult even in the $N \to \infty$ limit, and some further simplification is necessary. For instance, adopting the small ε and λ approximation (4a,b), ω^2 can be obtained in terms of an expansion in powers of λ^2. Omitting the details, we obtain in the limit $N \to \infty$ and to leading order in λ :

$$\omega^2 = -2\lambda^2 \int_{-\infty}^{0} e^{2\xi} j(\xi)\, d\xi + \ldots \qquad (7)$$

For $j(\xi) = \text{const.} = j_0$ this gives $\omega^2 = -j_0\lambda^2$ which, when compared to the finite N expression /5/ $\omega^2 = -j_0\lambda^2(N-1)/(N-2)$ gives some indication of the size of the error in the infinite N approximation. Clearly, if $j(\xi) > 0$ everywhere, the plasma is unstable for any current profile. However, due to the presence of the exp (2ξ) factor in the integrand we see that the growth rate can be reduced to a very low level if the current density vanishes, or is very small in the outermost 1/2N boundary layer of the plasma. This result verifies, and adds some new physical insight to the numerical observations by Dalhed and Hellsten /4/.

References

1. Lehnert, B (1982) Unconventional Approaches to Fusion (B. Brunelli and G. G. Leotta, eds.) p. 135. Plenum Press, New York.
2. Bonnevier, B. (1982) Royal Inst. Tech., Stockholm, Rep. TRITA-PFU-82-10.
3. Drake, J.R. (1984) Plasma Physics and Controlled Fusion, 26, 387.
4. Dalhed, H.E. and Hellsten, T. (1982) Proc. Int. Conf. on Plasma Physics, Göteborg, Sweden, p. 361.
5. Brynolf, J., Ring, R. and Wahlberg, C. (1985) (to be published).
6. Wahlberg, C., Arora, A.K. and Ring, R. (1984) Plasma Physics and Controlled Fusion, 26, 1261.

RFP CONFINEMENT STUDIES IN ETA-BETA II

Alper† ,A., Antoni,V., Bassan,M., Buffa,A., Costa,S., Flor,G., Giudicotti,L., Innocente*,P., Martini,S., Merlin,D., Ortolani,S., Paccagnella,R., Puiatti,M.E., Scarin,P.

Istituto Gas Ionizzati del C.N.R. - Padova (Italy)
(Associazione Euratom-CNR)

† Culham Laboratory Euratom-UKAEA Association * Student

INTRODUCTION Density, temperature and impurity radial profiles have been measured for the first time in ETA-BETA II (a=.125 m, R=.65 m) for pulses with current flat-top $\lesssim$2 ms and I_ϕ= 100-200 kA [1]. These measurements are correlated with those of magnetic field profiles to obtain the values of β, χ and τ_E. The observed transport is discussed in terms of diffusion in a stochastic magnetic field. Temperature measurements extending at late times show that T_e steadily increases throughout the discharge along with the resistivity anomaly factor.

RESULTS Chord integrated density profiles have been measured by a 6-chord interferometer (λ=3.4μm) in various discharge conditions. The Abel-inverted profiles are seen to depend on both field and gas programming. In fig.1a,b,c profile evolutions are given for: a typical active crowbar discharge (1a), a high density dicharge obtained with gas puffing (1b), a passive crowbar shot (1c). During the current rise phase (not shown) the profile varies from hollow to flat and then becomes peaked; subsequently the radial dependence does not vary considerably, whereas, when the current is well sustained (fig.1 a), the average shift increases up to 2-3 cm outward. The radial dependence is typically not far from parabolic for normal discharges, but it can be flatter or more peaked, depending mainly on gas programming (e.g. fig.1b).

The temperature and density profiles have been measured by a multipoint Thomson scattering system [2] at $I_\phi \simeq$150kA. In fig.2a,b the results are reported at four times during flat-top. The temperature profiles also seem to be approximately parabolic or more

peaked. The outward shift is in fairly good agreement with the interferometer data.

From the measured F and Θ and from previous magnetic field profile measurements [3] the radial distribution of B_θ and B_ϕ can be inferred. From these data, assuming $T_e=T_i$, the following typical values for the confinement parameters are found : $\beta(0)\gtrsim 5\%$, $\langle\beta\rangle \gtrsim 6\%$, $\beta_\theta \gtrsim 9\%$, $D \gtrsim 60\ m^2s^{-1}$, $\tau_E \gtrsim 70\ \mu s$, $\chi \gtrsim 5\cdot 10^{21} m^{-1}s^{-1}$.

Most of the power spectrum of the magnetic fluctuations is at low frequencies (∿10kHz) and is interpreted as MHD activity. The dominant poloidal components are m=0,m=1 and the intensity is maximum near the surface where $B_\phi=0$. In spite of the low fluctuation amplitude (b/B∿1%), field line computations show that this results in a wide stochastic region with a magnetic diffusion coefficient $D_m = 2\cdot 10^{-5}$m. The related electron diffusion coefficient has been estimated as $D \sim D_m v_{th}^e = 60 m^2 s^{-1}$ in agreement with the experimental one. These values of the trasport coefficients are also consistent with the radial distribution of oxygen impurities [4].

The time evolution of the peak electron temperature as measured by Thomson scattering agrees well with data obtained by a Si(Li) PHA system [5] as shown in fig.3. The steady increase in Te throughout the pulse is associated to the density decrease so that the highest β_θ are actually obtained early when I/N is lower. Indeed a fit of data at various currents gives $\beta_\theta \propto I/N^{-.25\ \pm .05}$, as shown in fig.4. The resistivity anomaly factor on axis, Z^*_{eff}, increases with time up to 10-15. These high values of Z^*_{eff} may partly be due to the decrease in plasma density and associated increase of impurity percentage. Indeed with the spectroscopically estimated absolute density of impurities (OVI $\lesssim 2.10^{18} m^{-3}$, FeIX $\lesssim 10^{16} m^{-3}$, ClVIII $\lesssim 5\cdot 10^{17} m^{-3}$, CV $\lesssim 5\cdot 10^{17} m^{-3}$), at electron densities of $\sim 2\cdot 10^{19}\ m^{-3}$ one can account for values of Zeff as high as 4. An additional factor of about 2 could be due to profile sustainment effects [3], yet it would not completely justify the highest experimental Z^*_{eff}. This probably implies a loss of validity of the Coulomb collision model. Non-collisional phenomena are in fact likely to become important when I/N, and therefore the streaming parameter $\xi \propto (I/N)T^{-1/2}$, becomes large. Indeed high frequency fluctuations

increase rapidly in correspondence with the decrease of plasma density and the increase in ξ (fig.5) and $Z^{\star}_{eff}$ is found to be a linear function of ξ (fig.6).

CONCLUSIONS A first set of measurements of density, temperature and impurity profiles has been made on ETA-BETA II. Both density and temperature are rather peaked, and outward shifted. The values of β, χ and τ_E have been derived and are consistent with previous estimates [3]. Temperature measurements have been extended at late times of the pulse showing that the electron temperature continues to increase beyond 200 eV. However the relatively high temperatures obtained during the last part of the pulse are associated with high values of I/N and ξ and correspondingly large ($\geq$10) resistivity anomaly factors.

REFERENCES

[1] Antoni,V., Buffa,A., et al., 10th Int. Conf. Plasma Phys. and Contr. Nucl. Fus. Res., London (1984), vol.2, p.487
[2] Bassan,M., Buffa,A., Giudicotti,L., V APS Top. Conf. on High Temp. Plasma Diagn., Tahoe (1984), to be published
[3] Ortolani,S., in Next 20 Years in Plasma Phys., Trieste (1984)
[4] Gabellieri,L., Ortolani,S., et al., paper 28 this conference
[5] Alper,B., Carolan,P., et al., paper 343 this conference

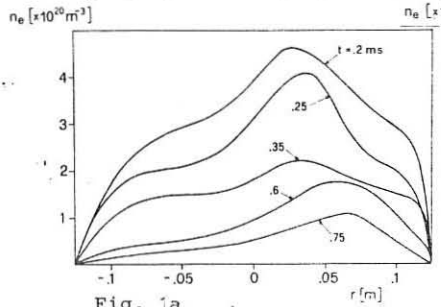

Fig. 1a

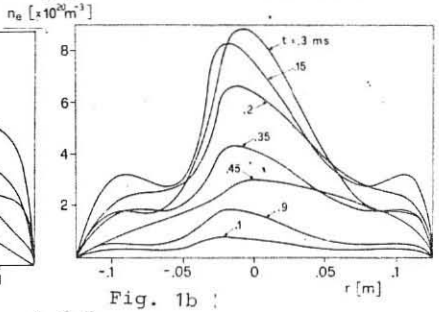

Fig. 1b

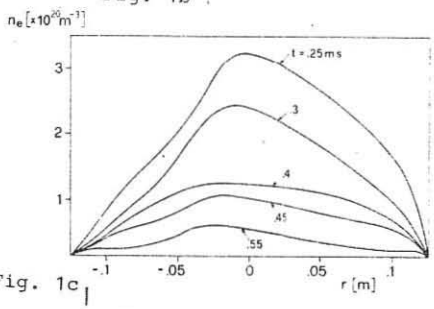

Fig. 1c

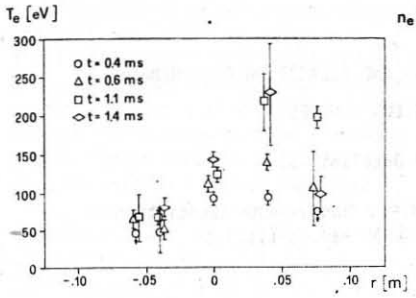

Fig. 2a

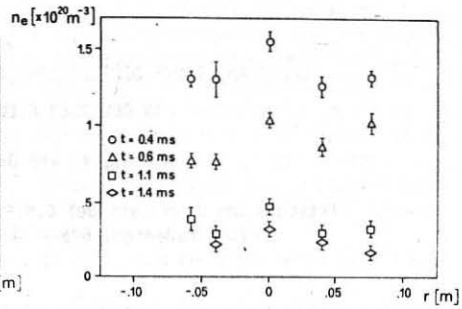

Fig. 2b

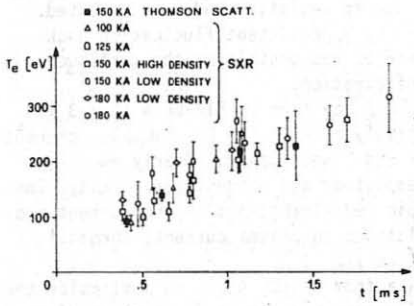

Fig. 3

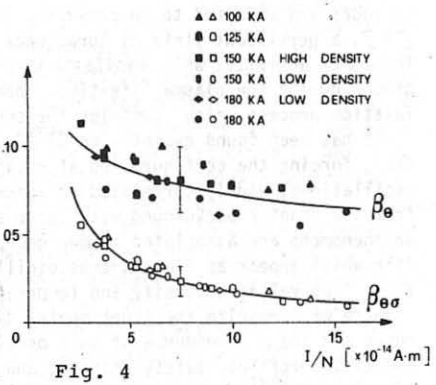

Fig. 4

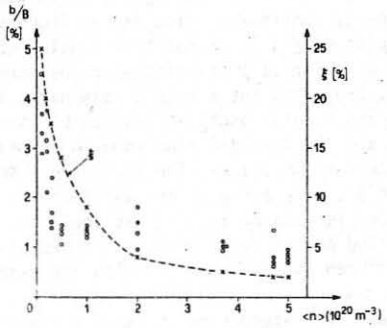

Fig. 5

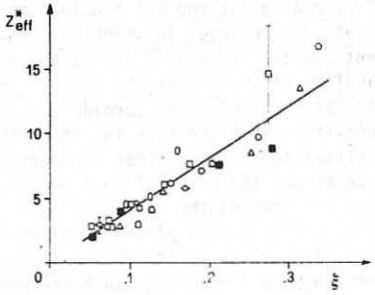

Fig. 6

LARGE AMPLITUDE OSCILLATIONS AND RELAXATION PHENOMENA IN REVERSED FIELD PINCHES

Antoni, V. and Ortolani, S.

Istituto Gas Ionizzati del C.N.R., Euratom-CNR Association
Via Gradenigo, 6/a - 35131 Padova (Italy)

INTRODUCTION The Reversed Field Pinch is a low q(q<1) configuration and therefore from the MHD stability viewpoint many simultaneous ideal and resistive modes are expected to be possible. In particular, as suggested by Kadomtsev [1], a persistent state of turbulence due to resistive modes is expected. This MHD activity, which manifests itself by a persistent fluctuation background during the plasma life-time, should be responsible of the continuous relaxation process which sustains the configuration.

It has been found recently on ZT-40 [2] and then on ETA-BETA II [3] that, forcing the configuration at relatively high Θ ($\Theta = B_{\theta w}/\langle B_\phi \rangle$), coherent oscillations, widely correlated in space and time, appear, clearly emerging from the chaotic background with large amplitude and evident periodicity. These phenomena are associated to macroscopic redistributions in the current profile which appear as simultaneous oscillations on plasma current, toroidal flux, loop voltage, density and temperature [2, 3].

Here we summarize the experimental data from ETA-BETA II, in particular the onset and the Θ dependence of such oscillations are reported. Relating, through the field profiles, safety factor q and Θ, the results are discussed in terms of a lower limit on the on axis q, analogous to the Tokamak case.

EXPERIMENTAL OBSERVATIONS For RFP configurations increasing the pinch parameter Θ it is found a decrease of the energy confinement time and an increase of plasma resistance and fluctuation amplitude [3]. It has been considered a set of discharges in which the Θ value is forced sustaining both the current and the toroidal field at the wall. Expanding for a high Θ discharge the waveform of the signals (Fig. 1), large and regular oscillations can be observed. In particular the toroidal current and the toroidal flux show an opposite behaviour: when the flux increases the current decreases. The amplitude of such oscillations shows a clear dependence on Θ : increasing Θ the amplitude increases and the onset of such oscillations is located at $\Theta \simeq 2$ as shown in Fig. 2. Tracing the discharge path, during one of such events in the F-Θ plane ($F = B_{\phi w}/\langle B_\phi \rangle$), the plasma oscillates between two extreme Θ: a slow increase of Θ($\Delta t \gtrsim 100$ μs) is followed by a faster recovery ($\Delta t < 50$ μs) of the initial Θ. In terms of field profiles, such process has been interpreted as large redistribution of current in the central region [3].

DISCUSSION As shown above, experimentally it is possible to drive discharges well beyond the theoretical Θ limit ($\Theta < 1.6$) predicted by Taylor's theory [4]. To explain this deviation it is necessary to assume μ-profiles (where $\mu = J_{\parallel}/B$) not uniform but more adherent to realistic configurations. These have been discussed in terms of a μ and pressure model by which the measured field distributions for non sustained discharges have been well reproduced [5]. The main results of these analysis is a saturation of the on axis μ with increasing Θ. A new parameter Θ_0 has been introduced as $\Theta_0 = \mu(o)a/2$ and it has been found an upper limit on Θ_0 for such discharges as $\Theta_0 < 2$. Remembering that the on axis safety factor is related to $\mu(o)$ through $q(o) = 2/(R\mu(o)) = a/(R\Theta_0)$, the upper limit on Θ_0 can be interpreted as a lower limit on $q(o)$ as $q(o) > a/(2R)$ [5].

In this context the high Θ discharges analysed have been obtained forcing with external currents the configuration. To simulate the measured F and Θ the assumed μ profiles are shown in Fig. 3. In particular it has been found that, to justify the experimental Θ ($\Theta > 3$) and F ($F < -1$) it is necessary to consider peaked profiles of μ (i.e. of current) in the central region. It is interesting to observe that increasing Θ the profiles become more peaked and as a direct consequence also Θ_0 increases. On the other hand from experimental data the onset of coherent oscillations appears to be located at $\Theta \cong 2$ which corresponds to $\Theta_0 > 3/2$. So the process looks like an oscillation on Θ_0 which is externally forced beyond $\Theta_0 = 2$ and then is restored by a relaxation process.

A possible interpretation is that during the first phase, when Θ increases, the natural peaking tendency of the current density due to diffusion dominates. The main effect on the q profile is of lowering the on axis q, as shown in Fig. 4 for various Θ. This new field distribution is characterized by a higher $\nabla J_{\parallel}$ and β [3] and then the present MHD instabilities, whose resonant surfaces are also pushed inside the plasma, are reinforced and can act so to redistribute the current profile. Indeed the recovery of the initial value of q(o) is experimentally associated to a large increase on the fluctuation amplitude at the edge which suggests an intense MHD activity (in particular a mode $m = 0$, $n < 6$ has been identified) (Fig. 5).

CONCLUSIONS For sustained RFP discharges on ETA-BETA II it has been found that beyond $\Theta = 2$ large oscillations take place in the plasma deteriorating the energy confinement. This has been interpreted as an upper limit on Θ_0 which can be discussed, in analogy to Tokamak case, as a limit on the current density on axis or as a lower limit on q(o). The sustainement of the discharge can be seen as the balance of the counteracting actions of diffusion and MHD instabilities. Forcing the configuration at high Θ allows this process to become more evident and related oscillations to emerge from the natural turbulent background of RFP discharges. A q(o) lower limit as $q(o) > 2/3\,(a/R)$ is thus suggested for RFP in analogy to the $q(o) > 1$ limit for Tokamaks.

REFERENCES

[1] KADOMTSEV, B.B., Plasma Physics and Controlled Nuclear Fusion Research (Proc. 6th Int. Conf. Berchtesgaden, 1976), Vol. I, IAEA, Vienna (1977) 555.

[2] WATT, R.G., and NEBEL, R.A., Phys. Fluids 26 (1983) 1168.

[3] ANTONI, V., and ORTOLANI, S., Istituto Gas Ionizzati del C.N.R., Padova, I.G.I. Report 85/03, 1985.

[4] TAYLOR, J.B., Phys. Rev. Lett. 33 (1974) 1139.

[5] ORTOLANI, S., "Stationary RFP Profiles" in Next Twenty Years in Plasma Physics, ICTP Trieste 1984.

Fig. 1

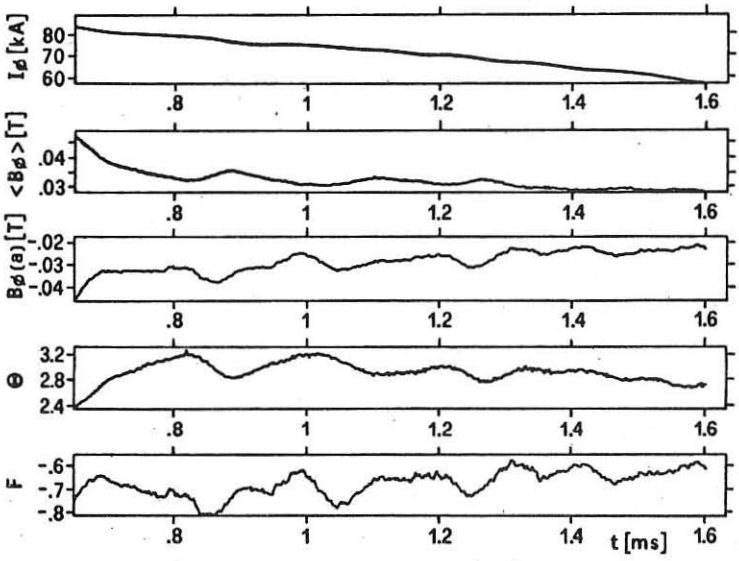

Fig. 2-a

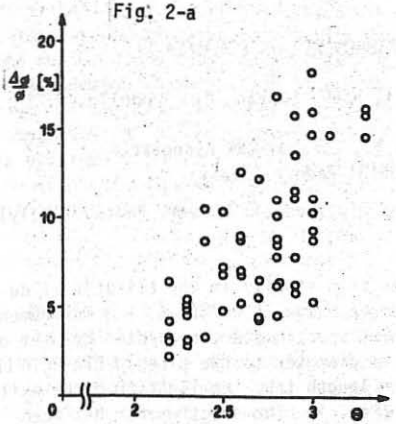

Fig. 2-b

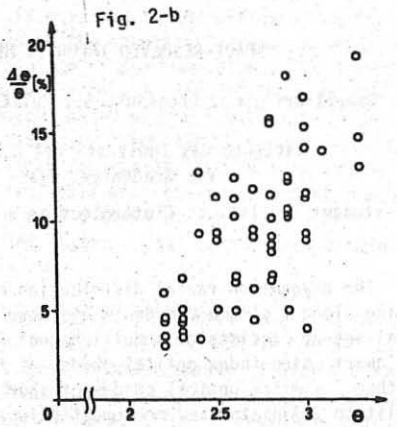

Fig. 3

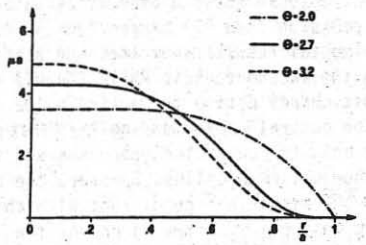

Fig. 4

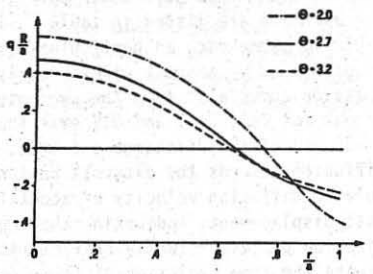

Fig. 5

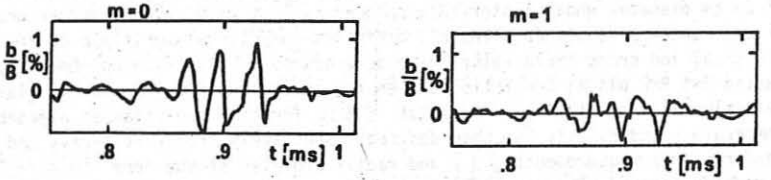

SPACE-RESOLVED IMPURITY MEASUREMENTS ON ETA-BETA II

Gabellieri+, L., Ortolani, S., Puiatti, M.E., Scarin, P., Tondello, G.*

Istituto Gas Ionizzati del C.N.R., Euratom-CNR Association
Via Gradenigo, 6/a - 35131 Padova (Italy)

+ student - * Ist. di Elettrotecnica e di Elettronica, Univer. Padova (Italy)

The oxygen ion radial distribution has been studied in the ETA-BETA II device along 7 plasma chords in the wavelength range 2900-7000 Å. The instrumental set-up consists of a multichannel Ebert spectrometer, connected by a set of 7 quartz step-index optical guides of 1 mm diameter to the pipes of ETA-BETA II; other 7 similar optical guides of shorter length take the light from the exit slit to 7 miniaturized photomultipliers (Fig. 1). The spectrometer has been absolutely calibrated by a tungsten lamp in the range 3500-7000 Å; at shorter wavelengths the calibration has been transferred from a 1-m Czerny-Turner spectrometer.

Measurements have been made of OII, OIII, OIV, OV lines. Only one weak OVI line at 3434 Å has been observed. The most intense and isolated lines observed for each ion are listed in table I. The emission from all oxygen ions is not radially symmetric; in particular, experimental results show that the plasma is displaced by about 1 cm externally in the vacuum vessel. While the OII emission comes also from the two outermost chords during the entire pulse length ($\sim$1 ms), OIII and OIV emit from the central region during the first part ($\sim$100 μs) of the discharge and then, due both to ionization processes and to diffusion towards the external region, show hollow profiles. However, the calculated diffusion velocity of about $10^2 \div 10^3$ m/s is not consistent with this fast displacement, indicating that during this phase of the discharge the ionization processes (whose characteristic times are of the order of $\sim$10 μs) dominate the time evolution of these ions. OV emits from about the whole plasma diameter also during the flat-top phase of the discharge, while in the time interval during which the OVI line may be measured ($\sim$200 ÷ 300 μs after the current start), its emission profile is peaked in the central region.

The experimental results have been interpreted by a one-dimensional transport model [1] assuming that the plasma has a circular cross section column of 23 cm diameter whose center is displaced by 1 cm with respect to the geometrical center of the vacuum vessel. Diffusion coefficients multiple of the classical ion cross field values have been assumed. Infact for an ohmically heated Z=1 RFP plasma the ratio between the observed diffusion and the classical value is a constant if $\beta_\theta \sim$ const [2]. The time evolution of electron temperature and density has been deduced respectively from soft X-rays and interferometric measurements [3] and radial profiles of the form $1 - (r/a)^4$ have been assumed. The atom influx rises the oxygen density up to $\sim 10^{18}$ m^{-3} during the first 200 μs and then a 100% recycling maintains the total oxygen

density constant in time. A fairly good simulation of the experimental chordal distribution of the various oxygen ions is obtained if the diffusion coefficients exceed by about an order of magnitude the classical values. Examples of the measured and computed chordal distribution of the line intensities of the lowest and highest ionization stages is shown in Fig. 2. Also the time evolution of the lines measured from the central chord of the spectrometer when compared with the corresponding calculated curves show that a good agreement is obtained if $D = 10 \div 30\ D_{class}$; an example for the OV line is show in Fig. 3. The absolute value of the line intensities agree with the experimental results within a factor of 3 if $D = 30\ D_{class}$ and with a total oxygen content of $\sim 10^{18}\ m^{-3}$. The radial distribution of the oxygen line emission each normalized to its maximum are shown in Fig. 4.

The absolute value of the diffusion coefficient is in this case $\gtrsim 10^2\ m^2 s^{-1}$, and corresponds to a particle confinement time $\tau_p = (\Delta x)^2/D \cong 50\ \mu s$ for OVII. This value of τ_p is consistent with soft X-rays measurements of OVII resonance line emission, whose value has been found $\cong 10^2$ times lower than the coronal equilibrium one [3]. Infact a simple zero-dimensional time dependent calculation [4] shows that the measured OVII emission is consistent with a particle loss characteristic time in the range $10 \div 50\ \mu s$; this is shown in Fig. 5 where the computed OVII ion population is drawn versus time for various values of the particle confinement time, τ_p.

CONCLUSION: the experimental spatial distribution of the oxygen ion emission has been measured by a 7 chord visible spectrometer and it has been interpreted by a one-dimensional time dependent transport model. A good agreement has been obtained with diffusion coefficients exceeding by about an order of magnitude the classical ion cross field values, corresponding to an oxygen impurity confinement time of about 50 μs.

TABLE I

ION	WAVELENGTH (Å)	TRANSITION
OII	4253.98	$3d'\ ^2G - 4f'\ ^2H^0$
OIII	3734.8	$3s\ ^5P - 3p\ ^5D^0$
OIV	3071.6	$3s\ ^2S - 3p\ ^2P^0$
OV	5606.5	$3p\ ^3P^0 - 3d\ ^3D$
OVI	3434.0	$6h - 7i$

REFERENCES

[1] TFR GROUP, Nuclear Fusion 22, 1173 (1982).

[2] ORTOLANI, S., "Stationary RFP profiles" in Next Twenty Years in Plasma Physics, ICTP Trieste 1984.

[3] ALPER, B., et al., "Soft X-ray measurements on ETA-BETA II, this conference, paper 343.

[4] COSTA, S., et al., University of Padova Report, UPee 75/06 (1975).

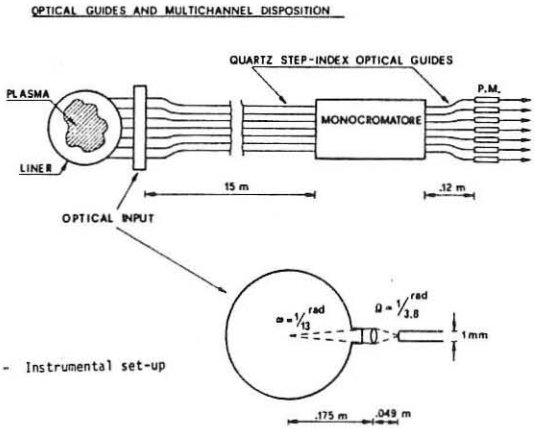

Fig. 1 - Instrumental set-up

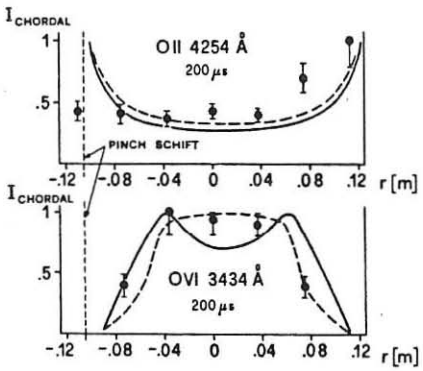

Fig. 2 - Experimental and computed chordal distribution of OII and OVI line intensities with $D = D_{class}$ (———) and $D = 10\,D_{class}$ (------)

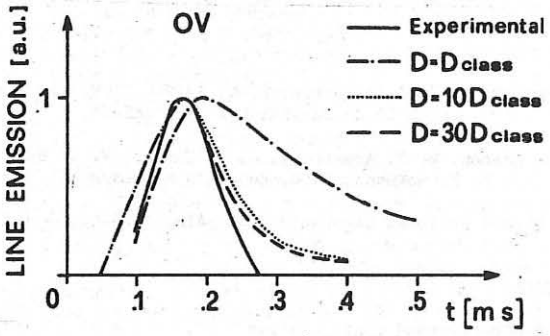

Fig. 3 - Experimental and computed time evolution of OV line intensity

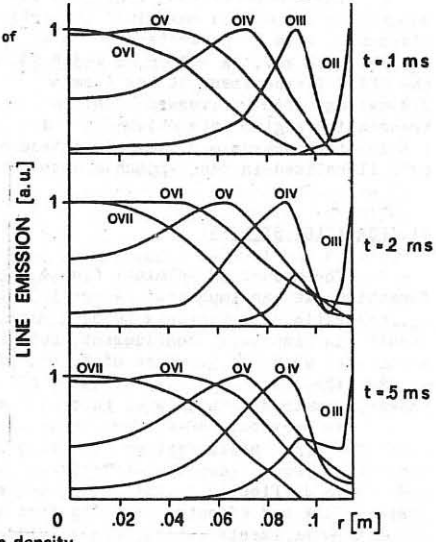

Fig. 4 - Radial distribution of the oxygen lines emission with $D = 30\,D_{class}$

Fig. 5 - Computed time evolution of the OVII ion population with different particle loss characteristic time

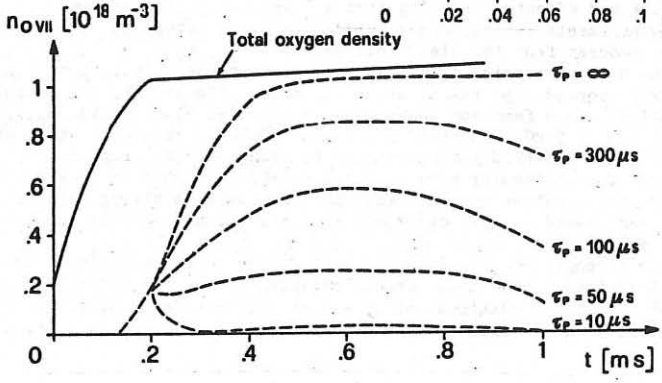

FIELD-REVERSED CONFIGURATION FORMATION, TRANSLATION, AND CONFINEMENT STUDIES ON THE FRX-C/T EXPERIMENT*

R. E. Siemon, W. T. Armstrong, R. E. Chrien, W. N. Hugrass, K. F. McKenna, D. J. Rej, and M. Tuszewski

Los Alamos National Laboratory, Los Alamos, N.M., 87545, USA

I. INTRODUCTION:

The field-reversed configuration (FRC) is a high β (>50%), prolate compact toroid plasma contained primarily by poloidal magnetic fields. FRC plasmas with parameters, $\bar{n} = (1\text{-}5)\times10^{15}\text{cm}^{-3}$, $T_i = 0.1\text{-}0.8$ keV, $T_e = 0.1\text{-}0.2$ keV, $R \simeq 7$ cm, $B = 5\text{-}8$ kG, lifetimes $\lesssim 300$ μs, are studied on the FRX-C/T experiment at Los Alamos.[1] FRX-C/T consists of a 0.5-m-diam., 2.0-m-long field-reversed θ-pinch coil, and a 0.4-m-diam., 5-m-long translation region into which FRC's are launched, translated, and trapped. A 5-20 mtorr pressure D_2 fill is introduced into the device by either a gas puff (localized in the θ-pinch source) or static fill system.

II. FORMATION STUDIES:

The amount of poloidal flux Φ_p trapped in an FRC at the time of formation is an important factor in determining the separatrix radius (or x_s, the ratio of separatrix to coil radii). Increased x_s is expected to result in improved confinement, but also to result in degraded stability associated with the increase of $\bar{s}$, the approximate number of ion gyroradii across the minor radius of the FRC. Thus an important issue for FRC research is to determine what governs the maximum Φ_p or x_s value.

In previous FRX-C experiments an oscillating θ-pinch current was used for gas preionization to trap reversed flux. In that method the ionization process depends strongly on the reversed bias field level B_b, and it is difficult to distinguish between effects caused by the amount of trapped flux and effects resulting from a change in preionization. In the present experiments a z-current discharge was added to decouple the ionization process from the bias field level.

The main conclusion from this work is that the limitations in B_b previously observed in FRX-C are not much affected by the method of preionization. As a function of pressure a critical bias field B_{crit} is observed (about 0.8 kG at 5 mtorr and about 1.6 kG at 20 mtorr) above which the FRC displays a marked deterioration in confinement properties. The details of the difficulty have not been established, but it appears to be associated with a rather sudden transition from weak to strong axial shocks and the associated axial dynamics as have been reported in earlier experiments.[2]

The strength of the axial contraction can be characterized by the minimum transient separatrix length relative to the separatrix diameter, $\varepsilon_m = \ell_s/2r_s$. For conditions of $p = 5$ mtorr, toroidal electric field $E_\theta = 0.4$ kV/cm, and final crowbarred field $B_c = 7$ kG, ε_m is observed to

vary from 5 to 1.5 as the B_b increases from 0.6 to 1.3 kG. The observations are in reasonable agreement with the values predicted by an analytic model[3] for formation, which takes into account the relevant shock physics as well as heating by compression and resistive dissipation. The observed B_{crit} corresponds approximately to $\varepsilon_m \approx 3$.

Above B_{crit} (or below $\varepsilon_m \approx 3$) the measured energy and poloidal flux confinement times are reduced from 100-200 μs to values of 10-20 μs. No discontinuities in any observable plasma parameter are noted as the bias field approaches B_{crit}. Some discharges with apparently the same formation histories have drastically different confinement after formation. One can speculate that either the internal or the external tilt modes could grow rapidly during the axial dynamics because of increased FRC magnetization and decreased FRC aspect ratio. Alternatively, with axial shock velocities close to the sound speeds at high bias field, one could argue that the axial shock strengths coupled to some asymmetries resulting from an earlier phase of the formation could be responsible for the observed deterioration in confinement.

III. STABILIZATION OF THE n=2 MODE ON TRANSLATED FRC's:

Until recently, FRX-C/T discharges have been always terminated by a rotational n=2 instability that appears between 60 and 120 μs after formation. This mode has been suppressed on several experiments[4-6] by the application of weak multipole fields. Moreover, stabilization by helical quadrupole fields on the NUCTE-II device was found to be more effective in that a five times smaller field is necessary than with straight quadrupoles.[5] The stabilizing properties of both straight and helical quadrupoles on translated FRC's have been investigated recently on FRX-C/T.

The details of the FRC translation process have been already reported.[1] In summary, FRC's formed at $B_b < B_{crit}$ have been launched out of the source with the use of a slightly conical θ-pinch coil. These plasmas have been efficiently translated into, and trapped inside, the adjacent translation region. The dc quadrupole fields are generated only in the translation region by coils located outside the vacuum chamber. The plasmas are observed to enter this region with negligible losses and to exclude the multipole fields.

Suppression of the n=2 distortion by the straight quadrupole fields is illustrated in Fig. 1a in which the maximum, peak-to-peak modulation in time of the line integral density $\Delta\int ndr$ (normalized to the mean value $\int ndr$) caused by this instability is plotted against the quadrupole coil current I_q. Each data point is from a separate discharge. The translated plasma parameters are: $\bar{n} \approx 0.8\times10^{15}cm^{-3}$, $T_e+T_i \approx 0.45$ keV, and $x_s \approx 0.6$. The threshold current needed for complete stabilization is 6 kA. The corresponding maximum B_θ-field at the separatrix in the presence of plasma is calculated to be 0.25 kG, a value that is approximate equal to 6% of the external poloidal field. As was found from straight quadrupole stabilization experiments performed on stationary FRC's in the FRX-C/T source,[4] this threshold field is about four times smaller than the theoretical threshold B_{th} predicted by Ishimura.[5]

Experiments have also been performed using a helical quadrupole coil wound with pitch $\alpha = 6.1$ radian/m. FRC trapping in the translation region is aided by an axial retarding force which results from the interaction of the moving plasma with the helical field. Suppression of the n=2 mode is shown in Fig. 1b. These data have been obtained for the same plasma parameters as those obtained with straight quadrupoles. The

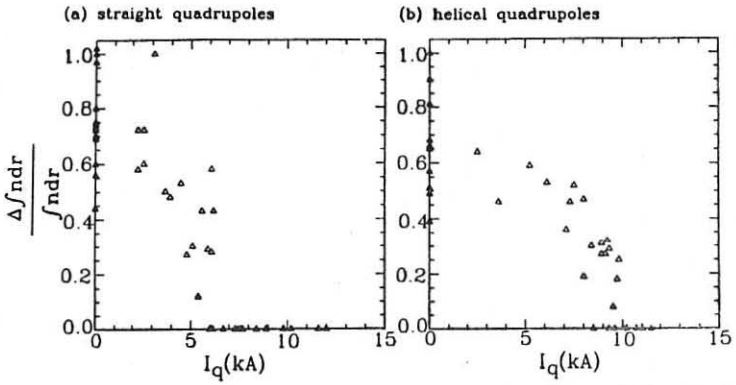

Fig. 1: Suppression of the n=2 distortion in the line integral density by the application of (a) straight and (b) helical quadrupole fields.

threshold helical current and maximum B_θ-field at the separatrix are 9.5 kA and 0.27 kG, respectively.

The observation on FRX-C/T that comparable field strengths of helical and straight quadrupoles are necessary for stability is quite different from that on NUCTE-II. A noteworthy difference is the tighter pitch (relative to the coil radius r_c) used on FRX-C/T. The product αr_c is 1.2 on FRX-C//T, compared with 0.4 on NUCTE-II.

The straight quadrupole field decreases the path length along B-lines between the plasma separatrix and the vacuum chamber wall; moreover, resistive diffusion of this field inside the FRC tends to destroy the closed flux surfaces. Consequently, one might expect a degradation in plasma confinement caused by this field. The helical field, on the other hand, does not tend to enhance plasma-wall interactions; furthermore, resistive diffusion of this field can still preserve closed magnetic surfaces,[7] thereby maintaining confinement. We plan to examine these expectations by assessing the confinement with quadrupoles on FRX-C/T.

IV. CONFINEMENT:

The energy, particle, and flux confinement of translated FRC's without quadrupole fields has been assessed. The results are summarized in this section.

ENERGY AND PARTICLE CONFINEMENT:

The dynamics of the translation process do not degrade the confinement. In some cases, even an improvement (up to 40%) in the confinement parameter $n\tau_E$ is obtained over that found on non-translated plasmas with the same temperature. For example, with a 5 mtorr puff fill, one obtains $\tau_E \approx 100$ μs at $\bar{n} \approx 1.0\times10^{15}$ cm^{-3} and $T = T_e+T_i \approx 0.7$ keV. Bolometric measurements indicate that impurity radiation does not contribute appreciably to the global energy loss.[1] The dominant contribution to τ_E is particle convection which can account in general for at least one-half of the total loss. The particle confinement times,

τ_N = 100 - 200 μs, indicate anomalous transport and they are usually within a factor of two of those predicted from the lower-hybrid-drift (LHD) instability.[8] The observed empirical scaling,[1]

$$\tau_N \propto x_s^{1.4} \ell_s^{0.2} n_M^{0.5} T^{0.4} ,$$

however, differs from the LHD theory by weaker dependences on x_s and ℓ_s, and a more favorable dependence on T. It is also consistent with data obtained on the TRX-1 experiment.[6]

POLOIDAL FLUX CONFINEMENT:

An anomalous poloidal flux loss is observed with typical flux confinement times, τ_ϕ = 100 - 200 μs. The observed empirical scaling,

$$\tau_\phi \propto x_s^{2.0} \ell_s^{-1.0} n_M^{0.2} T^{0.2} ,$$

indicates a much weaker dependence on T than expected from classical theory (assuming T_e/T = constant). The inverse relationship between τ_ϕ and the separatrix length ℓ_s, while intriguing, is not understood at this time.

TRANSLATION THROUGH A STATIC FILL:

A puff gas injection system was developed for FRX-C/T in order to reduce the charge exchange losses downstream that could be appreciable if a static D_2 fill were used. However, FRC translation experiments with a static fill resulted in surprisingly good confinement. From the side-on interferometry data, almost complete ionization of the 5 mtorr fill occurs before the FRC arrives downstream. This ionization is attributed to a precursor open field line plasma.

Because of this significant ionization of the static fill, the energy and flux confinement properties (τ_E = 70 - 100 μs, τ_ϕ = 170 - 200 μs) are as good as (if not better than) with puff fill. The particle confinement time has not been determined because the decay of the particle inventory N is possibly influenced by refueling as the FRC moves through the background ionized gas. Values of -N/(dN/dt) increase from 100 - 200 μs with puff fill to 200 - 400 μs with static fill. The decrease in the particle inventory decay rate may be explained either by an increase in τ_N and/or by refueling. An improvement in τ_N is conceivable because the large density gradient near the separatrix could be reduced by the substantial open field line plasma.

*This research is performed under the auspices of the U. S. D. O. E.

REFERENCES:

1. R. E. Siemon, et al., in Plasma Physics and Controlled Fusion Research 1984 (IAEA, Vienna, 1985) Vol. II, p. 511.
2. H. A. B. Bodin, et al., Nucl. Fus. Suppl. Part 2, 521 (1962).
3. L. C. Steinhauer, Phys. Fluids 26, 254 (1983).
4. R. E. Siemon, et al., submitted to Fusion Technology (1985).
5. M. Tanjyo, et al., op. cit. Ref. 1, p. 523.
6. A. L. Hoffman, et al., op. cit. Ref. 1, p. 601.
7. H. P. Furth and C. Ludescher, Fizika Plazmy 11, 5 (1985).
8. M. Tuszewski and R. K. Linford, Phys. Fluids 25, 765 (1982).

SPICA II: A HIGH-BETA EXPERIMENT WITH ELONGATED PLASMA CROSS-SECTION

SPICA II Team: C. Bobeldijk, J.A. Hoekzema, J. Lok, A.F.G. van der Meer
D. Oepts and A.A.M. Oomens
Association Euratom-FOM, FOM-Instituut voor Plasmafysica
Rijnhuizen, Nieuwegein, The Netherlands

Abstract

SPICA II is a toroidal screw-pinch device with a minor cross-section of race-track shape, constructed to study high-beta plasmas. A short description of the device is given, together with some of the results obtained in the test period. From the initial operation with plasmas it is observed that discharges showing good implosion and having a broad current-density profile can be produced in a wide range of filling pressures. More detailed measurements at 1 Pa are presented.

Introduction

The screw-pinch configuration is created by exposing a magnetized plasma column to fast rising toroidal and poloidal magnetic fields. This results in an implosion during which the bulk of the plasma and the bias magnetic field are swept up together, and the plasma is heated. Outside the main column a low-density plasma is left behind. Force-free currents in this dilute plasma conserve the pitch, q_{wall}, of the helical field as it moves inwards. Programming of a constant q_{wall} during current rise results in an outer region, where q is uniform in space. Previous screw-pinch experiments showed that for a circular cross-section stable discharges up to β = 15% (averaged over the main column) are possible and that the maximum value of β can be increased by elongation. In general, there is a fair agreement with theoretical models [1].

These results led to the design of SPICA II, with the objective to investigate the stability properties and the loss processes of a high-beta plasma [2]. The machine parameters and the design values for the plasma are listed in Table I. Plasma operation started in the summer of 1984. The machine time since then was severely limited by an accidental breakdown of the insulation between a primary coil and the shell and by a breakdown of a pumping port, causing a collapse of the quartz vacuum vessel.

TABLE I. DESIGN PARAMETERS OF SPICA II.

Major radius (quartz torus)	R : 0.45 m	Filling pressure p_o	: ≥ 0.2 Pa
Minor radius	r : 0.15 m	Electron density n_e	: 1-10×10^{21} m^{-3}
Height	h : 0.7 m	Electron temperature T_e	: 150-300 eV
Minor cross-section	race-track	Pressure ratio β_{peak}	: > 0.2
Toroidal field (max)	B_{tor}: 1.3 T	Volume compression	: > 10
Primary tor. current (max)	I_{tor}: 2 MA	Plasma elongation	: ~ 4
Rise time	: 11.3 μs	Eccentricity	: < 0.03 m
Bias field	B_o : 0.16 T	Safety factor q_{wall}	: 0.7 - 3
Flat-top duration	: ~ 1 ms	Plasma current I_{pl}	: ≤ 0.8 MA

Short description and test results

The load assembly of SPICA II consists of a quartz vacuum vessel, surrounded by a 40 mm thick aluminium shell, acting as the toroidal field coil, and four one-turn windings to induce the plasma current. Both field components rise simultaneously in 11.3 µs and can be actively crowbarred. The connection between the load assembly and the capacitor banks is made by plane-parallel plate systems. The circuit diagrams for the toroidal field and current are shown in Fig. 1. In order to distribute the current evenly along the circumference tuneable impedances have been inserted in the flange for the toroidal field coil [3]. Only slight adjustments were necessary. All banks in this circuit are tested up to the maximum operational voltages. As can be seen from Fig. 2, a current with a nearly flat top of 1 ms duration can be obtained. Pre-assembly tests showed that one of the primary coils for the toroidal current needed to be redesigned. In the meantime, operation at 70% of the design value for the current is possible. Tests of the circuit up to the 70%-limit were successful, with frequencies and current values in accordance with the design values. A base pressure below 1×10^{-5} Pa is achieved in the quartz discharge chamber after a few days pumping. The residual gas consists mainly of water vapour.

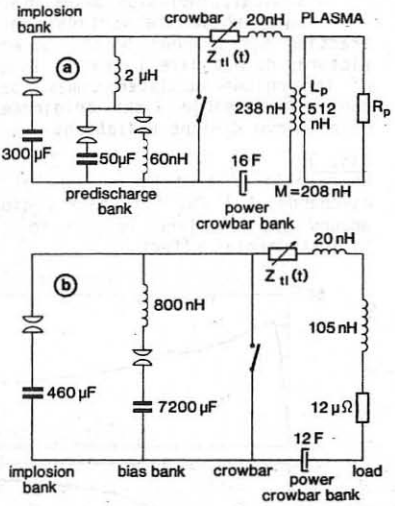

Fig. 1. Basic diagram of the electric circuit for the toroidal current (a) and toroidal field (b). $Z_{tl}(t)$ stands for the time-varying impedance of the transmission line. The maximum charging voltages are 45 kV for the implosion and predischarge banks, 5 kV for the bias bank, and 360 V for the crowbar banks.

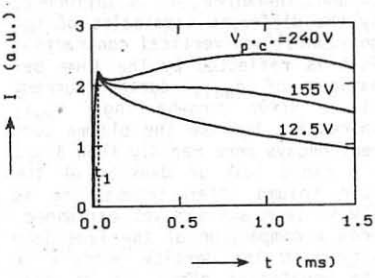

Fig. 2. Total poloidal current in the load for different charging voltages of the power crowbar bank. The voltage on the implosion bank is 25 kV.

Plasma operation

The first experiments showed that discharges can be produced in the pressure regime (p_0: 0.2-2 Pa), where high β-values and temperatures are expected (see also [2]). The pre-ionization system consists, apart from the predischarge bank of Fig. 1, of a capacitively-coupled high-frequency circuit and of four UV flash tubes. The latter two components are essential in achieving breakdown at low p_0. In all discharges investigated thus far, the values of the toroidal current (up to 500 kA) and of the toroidal inductance (300 nH) indicate that a broad current distribution is produced. The value of

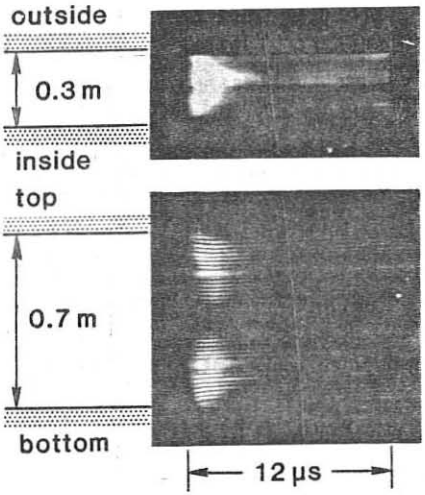

Some results of a passively crowbarred discharge are shown in Figs. 4 and 5. From this discharge and similar ones, the following observations are made. The value of the plasma inductance is strongly coupled to the shape of the plasma column. Therefore, it is influenced by the different timescales of the horizontal and vertical contraction. This is reflected by the time behaviour of q_{wall} during current rise. After crowbarring, q_{wall} increases, because the plasma current decays more rapidly than B_{tor}.

A rapid loss of density of the main column after crowbarring is always seen and not yet explained. From a comparison of the line density with the density profile in the equatorial plane, it is concluded that the density in the outer region is $\sim 3\times10^{20}$ m^{-3}, which is 10% of the density in the main column.

Fig. 4.
Results of a crowbarred discharge with p_0 = 1 Pa, B_0 = 0.08 T, B_{tor} = 1 T. From top to bottom: the plasma current, q_{wall}, and the line densities in vertical and in horizontal direction.

q_{wall} can be varied from 0.7-3. A preliminary investigation of the error fields in the neighbourhood of the gap shows that these fields are smaller than a few percent of the poloidal field at the wall. From streak pictures (a specimen is given in Fig. 3) and line-density measurements, it is deduced that the, mainly horizontal, implosion takes place in ~ 2 µs, while the vertical contraction takes about 10 µs. Streak pictures do not give a correct image of the column at later times, because the visible light originates mainly from H_α-line radiation.

Fig. 3.
An example of a streak picture of a discharge at 1 Pa. (The dark region around the midplane is due to an instrumental effect.)

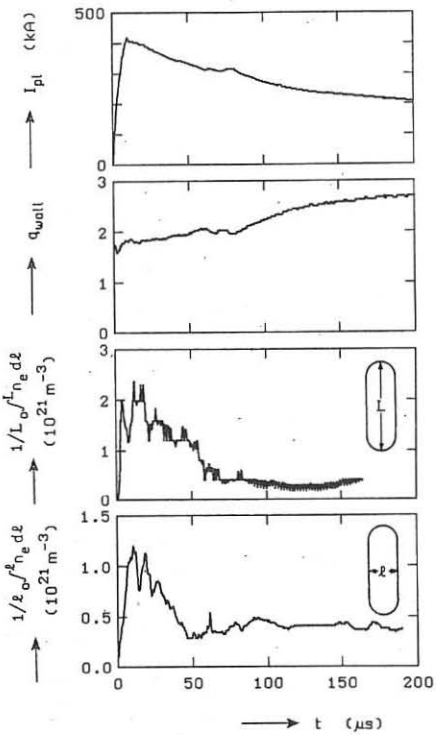

Combining this with the line density in vertical direction yields a volume compression of about 10, and an elongation of the central column of 4.5, in accordance with the design values. The observed value of the eccentricity (0.02 m) is consistent with model calculations for a plasma column with β = 0.1, surrounded by force-free currents. From the profiles of Fig. 5 a β of 0.08 is calculated, in contrast to β = 0.3 as expected for the initial conditions of this discharge. The relatively low β may be explained by a penetration of toroidal field prior to the implosion, because of too low a degree of pre-ionization (≈20%). Attempts are being made to raise the ionization degree.

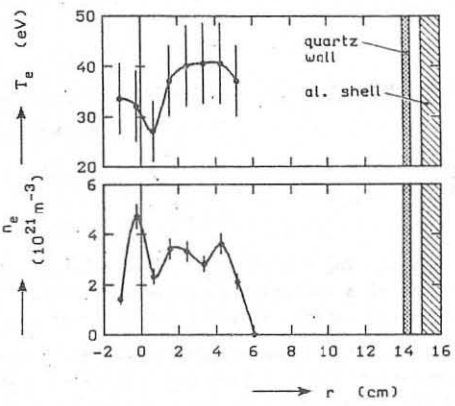

Fig. 5.
T_e- and n_e-profile in the equatorial plane at t = 10 μs as measured by Thomson scattering, for the same discharge as in Fig. 4. Each point represents the average value over a radial distance of 9 mm.

Acknowledgements

The authors wish to express their gratitude for the skillful operation of the machine by P.J. Busch, G. van Dijk, B.J.J. Grobben, W. Kooijman, W.J. Mastop, B.J.H. Meddens, P.H.M. Smeets and C.S. Vos, and for their assistance in diagnostics and data handling.

This work was performed under the Euratom-FOM association agreement with financial support from ZWO and Euratom.

References

[1] Bobeldijk C. et al., Nucl. Instrum. Methods 207 (1983) 49.
[2] SPICA II Team, Nucl. Instrum. Methods 207 (1983) 61.
[3] Hoekzema, J.A., Proc. 11th Symp. on Fusion Technology, Oxford (1980) p. 421.

NON LINEAR BOUNDARY EQUATIONS AT A THIN ANISOTROPICALLY CONDUCTING WALL (LINER)

G.F. Nalesso

Istituto di Elettrotecnica e di Elettronica - Università di Padova - Via Gradenigo 6/A - 35131 PADOVA (Italy) .

Abstract - The effect of a thin anisotropically conducting wall on the stability of a resistive fluid is considered. The boundary conditions at the liner for a non linear resistive MHD model of the fluid are discussed and derived.

Results of the effect of the finite conductivity of the liner on the linear stability of a Reversed Field Pinch plasma with the expected parameters of the Padova RFX experiment are shown as an example.

Assuming an infinitely long cylindrical surface of radius r_o, poloidal conductivity σ_θ and axial conductivity σ_z, surrounding a conducting fluid of conductivity $\sigma_p(r)$, a suitable set of boundary equations for a non linear resistive MHD stability analysis can be derived as follow.

Let us write with the superscript (0) the quantities at the inside of the surface and with (1) those outside the same surface. The solution of Maxwell's equations in the outside region (vacuum) can be obtained in terms of the Laplace and Fourier transforms of the axial component of the electric field and magnetic induction at the wall

$$E_z^{(1)}(r,m,k,s) = E_z^{(1)}(r_o,m,k,s)\,\frac{K_m(kr)}{K_m(kr_o)} \tag{1}$$

$$E_\theta^{(1)}(r,m,k,s) = \frac{m}{kr}\,E_z^{(1)}(r,m,k,s) - \frac{s}{k}\,\frac{K_m'(kr)}{K_m(kr_o)}\,B_z^{(1)}(r,m,k,s) \tag{2}$$

$$E_r^{(1)}(r,m,k,s) = \frac{i}{k}\left[s\,\frac{m}{kr}\,B_z^{(1)}(r,m,k,s) - \frac{\partial}{\partial r}\,(E_z^{(1)}(r,m,k,s))\right] \tag{3}$$

$$B_z^{(1)}(r,m,k,s) = B_z^{(1)}(r_o,m,k,s)\,\frac{K_m(kr)}{K_m(kr_o)} \tag{4}$$

$$B_\theta^{(1)}(r,m,k,s) = \frac{m}{kr}\,B_z^{(1)}(r,m,k,s) \tag{5}$$

$$B_r^{(1)}(r,m,k,s) = -i\,\frac{K_m'(kr)}{K_m(kr_o)}\,B_z^{(1)}(r,m,k,s) \tag{6}$$

$r > r_o$; K_m are modified Bessel functions.

We will assume now that, across the conducting liner, the tangential components of the electric field are continuous

$$\bar{n} \times \left[\!\left[\bar{E} \right]\!\right] = 0 \tag{7}$$

The jump in the tangential components of the magnetic induction is proportional to the surface currents flowing in the surface

$$n \times \left[\!\left[\bar{B} \right]\!\right] = \mu_o \bar{J} \tag{8}$$

while the normal component of the magnetic induction will still be continuous

$$\bar{n} \cdot \left[\!\left[\bar{B} \right]\!\right] = 0 \tag{9}$$

(see for instance reference /1/).

We have than

$$E_\theta^{(1)}(r_o) = E_\theta^{(0)}(r_o) = E_\theta(r_o) \tag{10}$$

$$E_z^{(1)}(r_o) = E_z^{(0)}(r_o) = E_z(r_o) \tag{11}$$

$$B_\theta^{(1)}(r_o) - B_\theta^{(0)}(r_o) = \mu_o j_z = \mu_o \sigma_z E_z(r_o) \tag{12}$$

$$B_z^{(1)}(r_o) - B_z^{(0)}(r_o) = -\mu_o j_\theta = -\mu_o \sigma_\theta E_\theta(r_o) \tag{13}$$

$$B_r^{(1)}(r_o) = B_r^{(0)}(r_o) = B_r(r_o) \tag{14}$$

From these equations we can express $B_z^{(1)}(r_o,m,k,s)$ in the form

$$B_z^{(1)}(r_o,m,k,s) = \frac{(\frac{\sigma_z}{\sigma_\theta}) B_z^{(0)}(r_o,m,k,s) + (\frac{m}{kr_o}) B_\theta^{(0)}(r_o,m,k,s)}{(\frac{\sigma_z}{\sigma_\theta}) + (\frac{m}{kr_o})^2 - s(\frac{\mu_o \sigma_z}{k}) \frac{K'_m(kr_o)}{K_m(kr_o)}} \tag{15}$$

and finally

$$B_z^{(1)}(r_o,m,k,t) = \int_0^t \left[(\frac{\sigma_z}{\sigma_\theta}) B_z^{(0)}(r_o,m,k,(t-\tau)) + (\frac{m}{kr_o}) B_\theta^{(0)}(r_o,m,k,(t-\tau)) \right] \cdot f(\tau) d\tau \tag{16}$$

where

$$f(t) = -\frac{K_m(kr_o)}{(\frac{\mu_o \sigma_z}{k}) K'_m(kr_o)} \exp\left[\frac{K_m(kr_o)}{K'_m(kr_o)} t / (\frac{\mu_o \sigma_z}{k}) \right] \tag{17}$$

and now $B_z^{(1)}(r_o,m,k,t)$ represents the Fourier transform of $B_z^{(1)}(r_o,\theta,z,t)$. We

have then, as a consequence

$$E_z(r_o,m,k,t) = \frac{1}{\mu_o \sigma_z}\left[\left(\frac{m}{kr_o}\right)B_z^{(1)}(r_o,m,k,t) - B_\theta^{(0)}(r_o,m,k,t)\right] \tag{18}$$

$$E_\theta(r_o,m,k,t) = \frac{1}{\mu_o \sigma_\theta}\left[B_z^{(0)}(r_o,m,k,t) - B_z^{(1)}(r_o,m,k,t)\right] \tag{19}$$

$$B_r(r_o,m,k,t) = -i\frac{K'_m(kr_o)}{K_m(kr_o)}B_z^{(1)}(r_o,m,k,t) \tag{20}$$

so that we see that the Fourier transforms of the above field components at the wall can be expressed (via convolution integrals in time) as a function of the Fourier transform of the two components of the magnetic induction at the inner wall $B_\theta^{(0)}(r_o,m,k,t)$ and $B_z^{(0)}(r_o,m,k,t)$.

Let us assume now that the plasma limited by the liner is described by the usual set of non linear MHD resistive equations /2/.

If we consider the Fourier transform (in the poloidal (discrete F.T.) and axial directions) and intend that everytime a product of two functions which are frequency (m or k) dependent appears, it must be considered as a convolution product (in the (m,k) space), we can derive the following set of boundary equations (i.e. equations valid at the wall $r=r_o$!). Assuming a rigid wall and no mass flow to it (i.e. $(\partial\rho/\partial t)_{r=r_o} = 0$) we get

$$\bar{v}(r_o,m,k,t) = 0 \tag{21}$$

$$\nabla\cdot(\rho\bar{v})\Big|_{r=r_o} = 0 \tag{22}$$

at the wall $r=r_o$.

From Ohm's law $\bar{j} = \sigma_p(\bar{E} + \bar{v}\times\bar{B})$ we can derive

$$\frac{1}{\mu_o \sigma_p(r_o)}(\nabla\times\bar{B})_\theta = \frac{1}{\mu_o\sigma_\theta}\left(B_z^{(0)}(r_o,m,k,t) - B_z^{(1)}(r_o,m,k,t)\right) + v_z(r_o,m,k,t)B_r(r_o,m,k,t) \tag{23}$$

$$\frac{1}{\mu_o \sigma_p(r_o)}(\nabla\times\bar{B})_z = \frac{1}{\mu_o\sigma_z}\left[\left(\frac{m}{kr_o}\right)B_z^{(1)}(r_o,m,k,t) - B_\theta^{(0)}(r_o,m,k,t)\right] - v_\theta(r_o,m,k,t)B_r(r_o,m,k,t) \tag{24}$$

From the momentum equation, for an inviscid fluid we can derive easily an equation for the radial component of the curl of $\rho(d\bar{v}/dt)$

$$\left[\nabla\times\left(\rho\frac{d\bar{v}}{dt}\right)\right]_r = \frac{1}{\mu_o}\left[(\bar{B}\cdot\nabla)(\nabla\times\bar{B}) - ((\nabla\times\bar{B})\cdot\nabla)\bar{B}\right]_r \tag{25}$$

Equations (21), (22), (23), (24), (25), plus (16), (20) and $\nabla \cdot \bar{B} = 0$ form a set of eight equation in the eight $(\rho, v_r, v_\theta, v_z, B_r, B_\theta^{(0)}, B_z^{(0)}, B_z^{(1)})$ Fourier transforms of the above quantities at the wall.

Moreover it is a self consistent set, because the interaction of the fluid with the external region, via the electromagnetic field has self-consistently taken into account. Furthermore it is easy to verify that in the limit $\sigma_\theta, \sigma_z \to \infty$ the standard boundary conditions at an ideally conducting wall are recovered /3/.

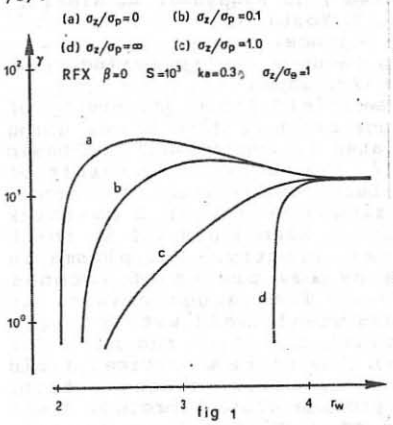

fig 1

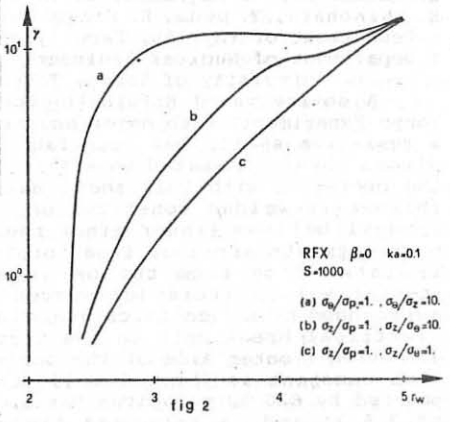

fig 2

The linearized version of the above set of equations has been used as boundary conditions in a 1-D numerical linear resistive code /4/. The results for a RFP type configuration with the expected plasma parameters of RFX (now in construction in Padova) are shown in figures 1 and 2. The equilibrium magnetic field configuration is the one discussed in /5/ with the pitch function given by $P(r) = 2(1 - r^2/8 - r^4/192)$. In figure 1 the reduced growth rate (τ_R/t_{ins}) is plotted for varicus values of the ratio wall to plasma diffusion time, as a function of the wall position. In figure 2 an example of the liner anisotropy is shown. Curve (a) which is more suitable for realistic liners $(\sigma_\theta/\sigma_z \sim 10)$ emphasizes the ineffectiveness of this liner to stabilise long wavelength modes.

References

/1/ Ramo S., Whinnery J.R., Van Duzer T.: "Fields and waves in communication electronics", J. Wiley and Sons, New York (1965).

/2/ Braginskii S.I.: "Reviews of Plasma Physics", I, 205-311 (New York: Consultants Bureau, 1965).

/3/ Nalesso G.F.: "MHD stability of a resistive fluid limited by a non ideal boundary" to be published in The Physics of Fluids.

/4/ Dibiase J., Killeen J., Journ. of Computat. Physics, 24, 158-185 (1977).

/5/ Robinson D.C., Nuclear Fusion 18, n. 7, 939-953 (1978).

Effects of Bias Toroidal Field and Filling Pressure on the Performance of the Reversed Field Pinch Device REPUTE-1

H. Toyama, N. Asakura, K. Hattori*, N. Inoue*, S. Ishida*, S. Matsuzuka, K. Miyamoto, J. Morikawa*, Y. Nagayama, H. Nihei*, S. Shinohara, Y. Ueda, K. Yamagishi, Z. Yoshida*
Department of Physics, Faculty of Science,
* Department of Nuclear Engineering, Faculty of Engineering,
University of Tokyo, Tokyo 113, Japan

A device named REPUTE-1(Reversed-Field Pinch University of Tokyo Experiment) with major and minor radii of 82 / 20 cm, using a resistive shell, has been fabricated to investigate the basic plasma physics related to RFP./1,2/ The preliminary result of the operation with this shell has been reported./3/ The vacuum chamber is welded construction using a series of 1 mm thick Inconel bellows (inner minor radius : 22cm) and 2.4 mm thick port segments arranged in a toroidal geometry. The plasma is isolated 2 cm from the bellows by 127 pieces of Inconel (tentative) limiters (demountable). The vacuum chamber is surrounded by a 1 cm thick stainless steel shell with a single electrical break both in the toroidal direction and poloidal direction (outer side of the torus). The shell's vertical field time constant is 1 ms. The 54 toroidal coils of single turn, powered by 820 kJ capacitor banks, provide a bias toroidal field of 2.5 kG and a reversed field of 1 kG for four reverse times:0.75, 1.5, 3, and 6 ms. The plasma current is driven by an iron-core transformer of 12 or 24 turns with a flux swing of 1.6 V sec. With the 1.5 ms risetime, ZT-40M has a critical pressure, below which the pinch no longer reverses. As the initial bias field is increased, the critical filling pressure increases./4/ The RFP experiments with slow risetimes have been carried out mostly in the matched mode and less attention has been paid to the plasma properties of the unmatched mode, because HBTX1A experiments have shown that volts-seconds input to the plasma normalized by the plasma current, the pinch parameter and the major radius has a minimum when the reversal is matched./5/ Even though aided-reversal mode is possible in the REPUTE-1, the following programing of B_ϕ field is found optimum; the bias field is forced to be zero in the case of no plasma. The spontaneous reversal of the toroidal field occurs when the plasma current flows. In this paper, therefore, we report the characteristics of the RFP plasma in the current level of 200kA, varying the bias toroidal field with this B_ϕ programming. The OH primary current is initiated at the time when the toroidal field power circuit starts to reverse the field. The risetime of the OH primary current and the reverse time of the B_ϕ field are 0.75 ms in these experiments. Piezoelectric valves are used for gas puffing. Filling gas pressure is controlled by changing the duration of valve opening, typically 15 - 50 ms with two valves. Valves are opened 500 ms before OH start in these experiments. An electron gun of 1 kV, 1 A is used for preionization. A discharge is initiated 50 μs after the start of OH primary current. The

breakdown voltage is 400 - 500 V. The initial plasma configuration is a tokamak mode. Figure 1 shows the time evolution of the plasma current and the toroidal flux inside the plasma column, the strength of the bias toroidal field B_ϕ being the parameter. When B_ϕ is high(2.3 kG), the initial toroidal flux(2.8 x 10^{-2} Wb) decreases in time to 1.6 x10^{-2} Wb at 0.5 ms; the start of RFP formation. The plasma current becomes maximum of 216 kA at 0.7 ms. The loop voltage is 135 V; therefore, the plasma resistance is 0.63 mΩ . The toroidal flux remains nearly constant after the current peak. In the case of the intermediate bias field(1.1 kG), the initial toroidal flux (1.4 x 10^{-2}Wb) remains nearly constant; so called matched mode. The plasma current is smaller than that of the high bias field. When the bias toroidal field is reduced further(0.7 kG), the toroidal flux increases from the initial value of 9 x 10^{-3} Wb to 1.3 x10^{-2} Wb at the RFP formation phase. The plasma current becomes smaller in this case. Plasma properties of three cases are summarized in Table 1. Figure 2 shows the common F-θ trajectory with the curve of the Bessel Function Model ,where F and θ are defined as the surface averaged toroidal and poloidal magnetic field at the plasma boundary, divided by volume averaged toroidal field inside the plasma column, respectively. The RFP state is set up at 0.5 ms after OH primary current starts in the case of high bias field(2.3 kG). The discharge stays at θ value of 2.0 at the flat-topped current portion (0.7 - 1.0 ms). The RFP formation is set up earlier and θ value at the flat-topped current portion is a little lower in the case of lower bias field (around 1.8 in the matched mode), even though each path to the RFP state is almost the same in three cases; the reason for the lower θ value is due to the lower plasma current. When the toroidal flux increases in the low bias case, θ decreases to 1.6. As the plasma current decreases in the termination phase, θ decreases and the reversal state is destroyed. Figure 3 shows the operation window in the filling pressure and the bias toroidal field. When the filling pressure is too low, the toroidal flux decreases monotonically in time and the RFP is not formed, as in the 1.5 ms risetime case of the ZT-40M/4/; the symbol x in the operation window designates this situation. At high filling pressure, the conductivity temperature decreases and O V is not burnt through. The symbol△ designates this situation. As the bias toroidal field is increased, the operation window for good RFP shifts to higher filling pressure and the window becomes narrow. The initial line-averaged density measured vertically by CO_2 interferometer corresponds nearly to the filling pressure. The density decreases in time gradually; for example, from 2.5 x 10^{14} cm^{-3} (initial)to 1.5 x 10^{14} cm^{-3} (at the time of the current peak) in the case of 4 mTorr filling pressure. The value of I/N at the flat-topped current portion is 1.1 X 10^{-14} A m.

In conclusion, the toroidal flux is reduced to almost the same value at the current flat portion independent of the initial bias field. The higher bias field makes better RFP plasma parameters, such as lower resistivity and higher flat-topped plasma current, even though the pinch parameter θ is higher. The reason is considered as the better plasma properties in the tokamak phase with higher toroidal field.

Table 1 Plasma Parameters	○	△	X
Bias toroidal field (kG)	2.3	1.1	0.7
RFP formation time (ms)	0.5	0.4	0.3
Plasma current (kA)	216	185	172
Plasma resistance (mΩ)	0.63	1.0	1.2
averaged density($10^{13}cm^{-3}$)	15.0	3.0	5.0
Pinch parameter	2.0	1.8	1.9
I/N (10^{-14} A m)	1.1	4.9	2.7

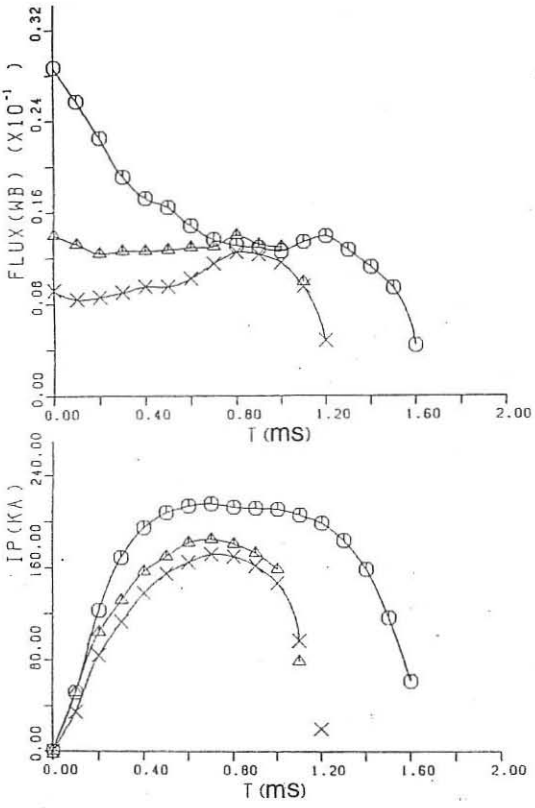

Fig. 1 Time evolution of plasma current (bottom) and toroidal flux (top), bias toroidal field being the parameter; ○: 2.3 kG, △: 1.1 kG, X : 0.7 kG.

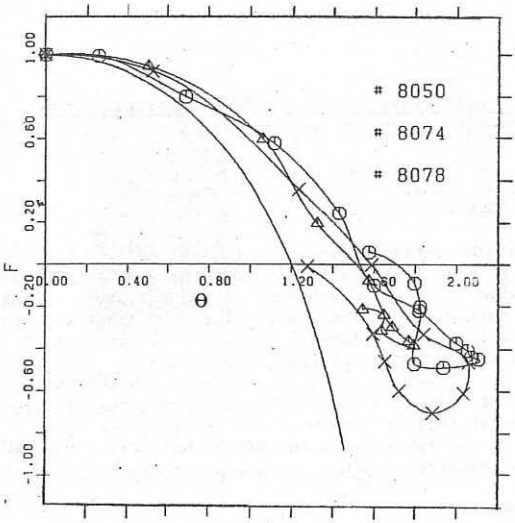

Fig. 2
Trajectories in F-θ diagram, bias toroidal field being the parameter;
○ : 2.3 kG,
△ : 1.1 kG,
X : 0.7 kG.

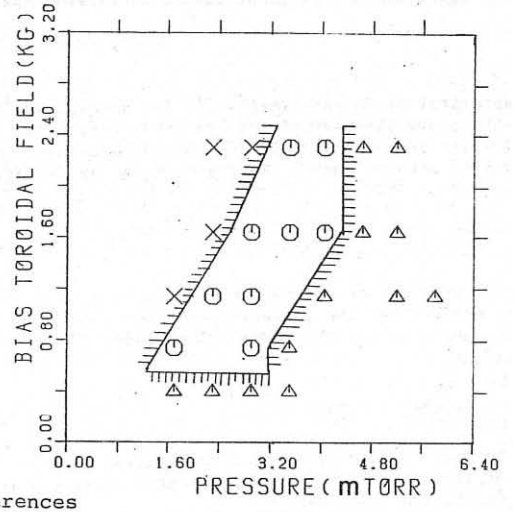

Fig. 3
Operation window in filling pressure and bias toroidal field;
○ : good RFP,
X : No RFP,
△ : bad RFP with heavy radiation loss.

References
/1/ T. Watanabe et al., 13th Symp. on Fus. Tech.1,741(1984).
/2/ Y. Ishigaki et al., ibid. 1,899(1984).
/3/ Z. Yoshida et al., Plas.Phys.& Cont.Nucl.Fus.Res.2,467(1985)
/4/ D. A. Baker et al., ibid. 1, 587 (1983).
/5/ H. A. B. Bodin et al. , ibid. 1,641 (1983).

Application of the Scaling Laws to the REXIMPLO Spherical Pinch Machine: Experimental Results

E. Panarella and V. Guty
National Research Council of Canada
Ottawa, Canada K1A 0R6

ABSTRACT: The spherical pinch configuration is characterized by a hot, dense plasma in the center of a sphere, plasma which is contained and compressed by spherical shock waves created by strong discharges at the periphery of the metal vessel. The recent derivation of the scaling laws for spherical pinches has provided new directions to the experimental program: 1) the central plasma seems to be able to approach the required temperature for satisfying the 1st scaling law, mainly because, at the high gas pressures that we are dealing with, of the order of several atmospheres, the plasma resistivity is at variance from the classical Spitzer's formula and in agreement with Braginskii's formula, and 2) the spherically imploding shock waves can be controlled to maintain the required symmetry for uniform compression of the central plasma.

High speed plasma flow visualization as well as other diagnostic techniques indicate that the central plasma and the imploding shocks are creating conditions of fusion interest in their approach to satisfying the Lawson criterion.

1. Introduction

The scaling laws for spherical pinch experiments [1] are quite clear in their prescriptions for creating a plasma satisfying the Lawson criterion for breakeven. The first scaling law states that a plasma should be created in the center of a spherical vessel with an energy density E_e/M_e so as to satisfy the following relation:

$$\frac{E_e}{M_e} \geq 1.86 \times 10^8 \text{ J/g} \qquad (1)$$

where E_e is the energy (in J) deposited in the central plasma of mass M_e (in g). The second scaling laws states that the following relation should be satisfied in order to contain and compress the central plasma for a time sufficiently long for breakeven:

$$\rho_o R\left(\frac{E_s}{M_s}\right)^{\frac{1}{2}} \geq 1.96 \times 10^6 \qquad (2)$$

where ρ_o (in $g.m^{-3}$) is the initial density of a deuterium-tritium mixture filling a spherical vessel of radius R(m), E_s(J) is the energy deposited in the spherical shell, and M_s(g) is the shell mass.

In recent times our work has been mainly confined to verifying if the first scaling law can be experimentally satisfied. However, we have also dedicated some attention to a preliminary investigation of the verification of the second scaling law.

The experimental results and some analysis are reported in the following sections.

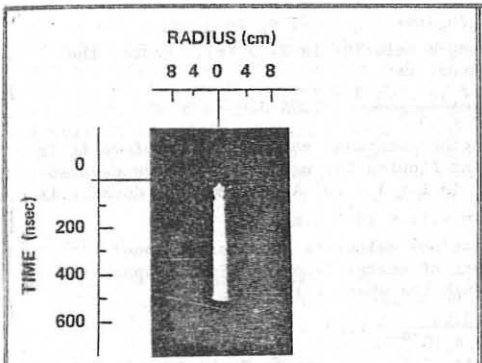

GAS: HYDROGEN

PRESSURE: 120 psi (~ 8.2 Atm)

ENERGY OF CONDENSER BANK: 726J

VELOCITY OF SHOCK FRONT: 5.38×10^7 cm/sec

kT ~ 2250 eV

FIG. 1

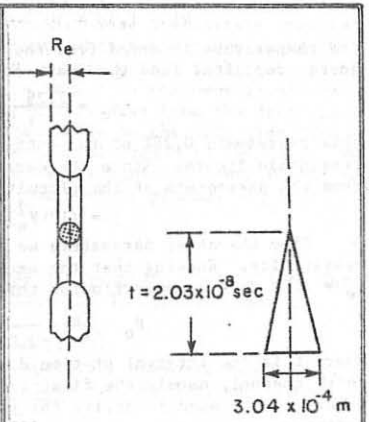

FIG. 2

2. First scaling law

The first scaling law summarizes the requirement that the central plasma should be heated to a temperature of not less than 2.58 KeV. In an attempt to verifying if such temperature can be approached in a high density gas by the deposition of electrical energy through a spark, we have discharged in hydrogen at ~8.2 atm a small condenser bank of 726J between two electrodes separated by a distance of 0.5 cm. A streak photograph of the spark development is shown in Fig. 1. It appears that the shock velocity, for the first 20 nsec of the discharge, is $\sim 5.38 \times 10^7$ cm.sec^{-1} which corresponds to a temperature of 2.25 KeV, according to the relation:

$$kT(KeV) = 7.76 \times 10^{-12} V_s^2 \ (m) \qquad (3)$$

This is an unusually high temperature for a spark. In order to see if it can be justified on the basis of the classical Spitzer's resistivity formula or Braginskii's formula, we have carried out the following calculations, assuming that the hot channel volume of the spark is a small sphere in the center space between the two electrodes (Fig. 2) and that its radius R_e increases vs. time as indicated in the same figure and as derived from the streak photograph of fig. 1. The calculations yield:

Average radius of the spark channel $R_e = 1.52 \times 10^{-4}$ m

Average volume of the spark channel $V_e = \frac{4}{3} \pi R_e^3 = 1.47 \times 10^{-11}$ m^3

Gas density (at 8.2 atm) $\rho_o = 8.49 \times 10^2$ g/m^3

Mass $M_e = V_e \cdot \rho_o = 1.25 \times 10^{-8}$ g

The relation between specific energy E_e/M_e and temperature kT in the spark channel is:

$$kT = 1.38 \times 10^{-8}(E_e/M_e)\text{KeV} \quad (E_e \text{ in J; } M_e \text{ in g})$$

The temperature inferred from the shock velocity is 2.25 KeV. Hence, the energy deposited into the spark channel is:

$$E_e = \frac{2.25 \times 1.25 \times 10^{-8}}{1.38 \times 10^{-8}} = 2.04 \text{ J}$$

This represents 0.28% of the total condenser bank energy and therefore it is a reasonable figure. Since the current flowing through the spark, as deduced from the parameters of the circuit, is $I = 3 \times 10^4$ A, the current density is

$$j = (I/\pi R_c^2) = 4.11 \times 10^{11} \text{ A.m}^{-2}$$

From the above parameters we can now calculate the spark channel resistivity. Knowing that the amount of energy deposited in the spark is $E_e = 2.04$ J, the power flowing through the spark is:

$$P_e = \frac{E_e}{t} = \frac{2.04}{2.03 \times 10^{-8}} = 1.00 \times 10^8 \text{ W}$$

where t is the interval of time during which the energy E_e is deposited in the spark channel, namely the first 20 nsec of the discharge. (Incidentally, this figure can be used to derive the voltage V_s across the central part of the spark:

$$V_s = \frac{P_e}{I} = \frac{1.00 \times 10^8}{3 \times 10^4} = 3.3 \times 10^3 \text{ V}$$

This figure is clearly consistent with the actual voltage V = 20 KV applied across the whole length of the spark gap).

We can now calculate the power per unit volume:

$$P = \frac{P_e}{V_e} = \frac{1.00 \times 10^8}{1.47 \times 10^{-11}} = 6.81 \times 10^{18} \text{ W.m}^{-3}$$

from which the spark resistivity is:

$$\eta = \frac{P}{j^2} = \frac{6.81 \times 10^{18}}{(4.11 \times 10^{11})^2} = 4.02 \times 10^{-5} \text{ ohm.m}$$

This resistivity is very close to the value provided by Braginskii [2]:

$$\eta = 4.5 \times 10^{-5} \text{ ohm.m}$$

and at variance from the Spitzer's resistivity [3]:

$$\eta = 3.3 \times 10^{-8} \, T^{-3/2} \text{ ohm.m (T in KeV)}$$
$$= 3.3 \times 10^{-8} \, (2.25)^{-3/2} = 9.78 \times 10^{-9} \text{ ohm.m}$$

In conclusion, it seems that the temperature of the spark, as derived from the shock velocity in the first 20 nsec of the discharge, can be justified with the Braginskii's formula for the spark resistivity, but not with the Spitzer's formula, which differs by about four orders of magnitude from the former.

3. Second scaling law

The prescription of the second scaling law (2) is that the working pressure of the gas within the spherical vessel has to be of the order of several atmospheres, if the range of radii of the vessel should remain unchanged at between 2 and 10 cm and the energy density deposited in the peripheral shell should also remain unaltered at $\sim 10^8$ J/g. To this end, we have recently built a high pressure cylindrical discharge vessel and are proceeding with some initial experimental tests in such cylindrical geometry. The peripheral energy deposition is obtained by means of resistive discharges, as schematically shown in Fig. 3. In detail, the geometrical configuration of the electrical circuit consists of two semicircular discharges in which the

sparks are arranged in series, as shown in Fig. 4. Some preliminary results are shown in Figs. 5 and 6. Figure 5 shows that, when the peripheral sparks from the discharge circuit on the left side have more energy than those on the right side, the imploding shock waves from the left push the central plasma to the right. On the other hand, when the peripheral sparks from the discharge circuit on the right side have more energy than those on the left side, the imploding shock waves from the right push the central plasma to the left. We are attempting now to equalize the two energy deppositions -left and right- in order to have a symmetric pinching action on the central plasma.

References

[1] E. Panarella and P. Savic, J. Fus. Energy 3, 199 (1983); Proc. 11th Eur. Conf. on Contr. Fus. and Plasma Phys., Sept. 1983, Vol. 7D, Part 1, p. 565.

[2] S.I. Braginskii, Sov. Phys. JETP 34, 1068 (1958).

[3] C.H. Watson-Munro, Properties of high temperature plasmas, in An Introduction to Discharge and Plasma Physics, S.C. Haydon, ed. (The University of New England, 1964) p. 425.

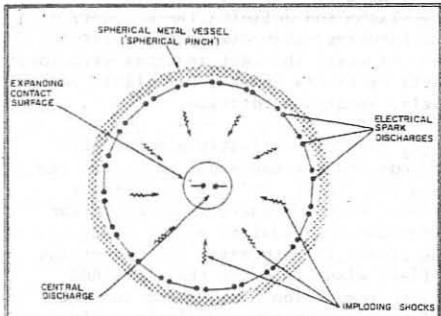

SPHERICAL PINCH APPARATUS FOR PLASMA FORMATION AND HEATING

FIG. 3

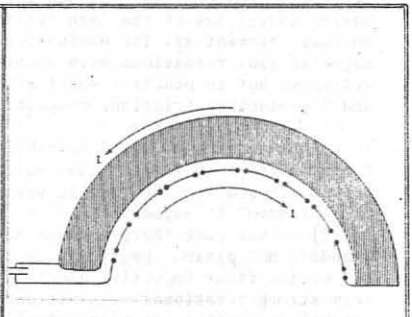

FIG. 4

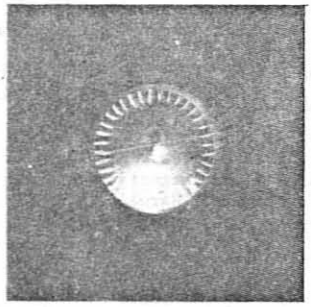

FIG. 5

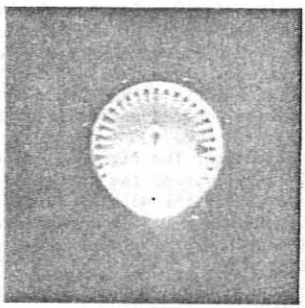

FIG. 6

CURRENT AND FIELD SELF-REVERSALS IN TOROIDAL PINCHES

E.A. Witalis, Res. Inst. of Nat. Defence, Box 27322, S-102 54 Stockholm, Sweden

Abstract: Magnetically induced plasma rotation is described and used together with early experimental results to explain self-reversals of poloidal current and toroidal field.

Theory: The basic fluid equations for plasma mass and charge transports,

$$\rho_m \frac{d\underline{V}}{dt} = \rho_e \underline{E} + \underline{j} \times \underline{B} - \underline{\nabla} \cdot \underline{\underline{P}} \quad \text{and} \quad \underline{j}/\sigma = \underline{E} + \underline{V} \times \underline{B} - \frac{1}{en_e} (\underline{j} \times \underline{B} - \underline{\nabla} \cdot \underline{\underline{P}}_e)$$

can, without simplifications, be combined to yield, [1]

$$\frac{d}{dt} \int \underline{B} \cdot d\underline{S} = - \frac{d}{dt} \oint \frac{\rho_m}{en_e} \underline{V} \cdot d\underline{s} + \oint \left[\frac{\rho_e}{en_e} \underline{E} - \frac{1}{en_e} \underline{\nabla} \cdot (\underline{\underline{P}} - \underline{\underline{P}}_e) - \frac{\underline{j}}{\sigma} \right] \cdot d\underline{s} \qquad (1)$$

The integrals refer to a closed loop, length element $d\underline{s}$, attached to the moving mass frame of the high density plasma and defining the boundary of a surface, element $d\underline{S}$. The dominating convective derivative terms relate magnetic flux variations with rotation of mass. The last integral describes wellknown but in practice small effects by excess charge, baroclinic vector and ion-electron friction, respectively, upon such rotation.

In a foot-note on p. 272 Braginskii [2] derives a slightly simpler differential form of (1) and then points out its gas dynamic limit, i.e. the Kelvin circulation theorem, as well as its "ideal" MHD theory limit of mass "frozen" to magnetic lines of force. However, there is no attention in [2] to the fact that, because of the quasi-neutrality $\rho_e/en_e \ll 1$, standard MHD plasma theory denies the capability expressed in (1) for the LHS moving frame inductive electric field alone to drive the first RHS term strong rotational mass motion. Upon inspection Eq. (1) and the Braginskii derivation are found, implicitely, to concern the plasma ionic species motion. The proof of their general validity [3] requires attention to the important but long overlooked fact that quasi-neutrality in a magnetized plasma in sustained by non-central particle interaction forces. The usual equality between external torque and angular momentum rate of change simply becomes incorrect!

Quasi-neutrality is thus the key physical property in proving Eq. (1), not an argument against it, [3]. In addition, the early Lighthill criticisms [4] of MHD plasma theory are found to be correct [5], and theoretical justification is obtained for various "ion Vlasov fluid" plasma models having kinetic or MHD fluid dynamic ions but with the electrons just as a massless, charge-neutralizing background.

Application. The figures, copied from [6], illustrate a representative case of stages during the current rise time up to a weak magnetic field self-reversal in the Mark IV torus of the CTR division at Harwell in 1960. Minor diameter 2a = 0.31 m, aspect ratio a/R = 1/4. Note how the initial field is retained at the conducting wall. By writing the pinch channel pressure balance as

$$- \frac{dp}{dr} = \frac{r}{R} i_\phi B_\phi [m(r) - n(r)], \quad m = RB_\theta / rB_\phi, \quad n = Ri_\theta / ri_\phi \qquad (2)$$

and applying a no-corrections slide rule analysis to the Fig. 1 data the turn number distributions of the helical magnetic lines of force (m) and current paths (n) were obtained as seen by Figs. (2)-(4). (The inverse of m(a) was later assigned excessive importance in toroidal discharge theory under names like "safety factor" and q-value.) Force-freeness, n=m, is seen to be a rather poor approximation. In contrast, "ideal" MHD theory leading to a Bessel function description [7] is good but only for the dense channel core region. Outside, a lower density and diffuse boundary region with $\lambda_i/a \approx 1$, $\lambda_i^2 = m_i/\mu_0 e^2 n_i$ exists where Eq.(1) replaces "ideal" or resistive MHD theory. (A small ion collisionless skin depth, $\lambda_i/a \ll 1$, is the general criterion for neglecting the Hall term i.e. for using classical MHD theory, [3].)

The pronounced minima of B_ϕ shown in Fig. 1 imply by the Maxwell equation curl $\underline{B} = \mu_0 \underline{j}$ a reversal there of the poloidal current density. Explanations based on direct or elaborated single-fluid MHD theory do not seem possible, [8]. This is seen here as expected as Eq.(1), instead, is valid. Consider a poloidally directed, moving, circular loop of radius r, initially r_{in}. An integration of the dominating convective derivative terms in Eq. (1) yields

$$C_0(r_{in}) = \Psi_\phi(r) + \frac{m_i}{e} 2\pi r V_{i\theta}, \quad \frac{m_i}{e} 2\pi r V_{i\theta} = \lambda_i^2 \mu_0 j_{\theta i} 2\pi r = -\lambda_i^2 \frac{\partial B}{\partial r} i\phi \; 2\pi r \qquad (3)$$

C_0 is the approximately conserved canonical angular momentum, Ψ_ϕ is its field part consisting of the enclosed toroidal magnetic flux, $m_i = \rho_m/n_e$ is the effective ion mass, $V_{i\theta}$ is the ion poloidal velocity, $j_{\theta i}$ is the associated current density creating a field variation $-\mu_0^{-1} \partial B_{i\phi}/\partial r$. Eq. (3) states that an increase of the field part Ψ_ϕ is accompanied by a decrease in the matter part, however, the latter also creates magnetic effects (except in the dense core region where by $\lambda_i \approx 0$ "ideal" MHD is reproduced as a limit). Thus, at the minima, $j_{e\theta} + j_{i\theta} = 0$, i.e. the fluxamplifying poloidal part of the helical electronic current distribution is cancelled by the opposed ionic current carried by the matter part of the conserved canonical angular momentum.

A helical path with n turns encompasses the magnetic flux $n\Psi_\phi - \Psi_\theta$. Note the signs. The self-inductive electric field $E_{\phi\theta}$ directed along this current path, when referring to a "toroidal unit" length a/R of the plasma channel, is given by the induction law

$$E_{\phi\theta} = -\frac{d}{dt}\left[\Psi_\phi(na/R - \Psi_\theta a/\Psi_\phi R)\right] = -\frac{d}{dt}\left[\Psi_\phi(na/R-\theta)\right] \qquad (4)$$

where the flux ratio term is well approximated by the usual pinch parameter $\theta = B_\theta(a,t)/B_i(t=0) = \mu_0 I_\phi/2\pi a B_i$. θ crudely accounts for the metal vessel toroidal flux conservation and it linearly increases from zero with $I_\phi(t)$. In contrast, na/R slowly increases from an initially indeterminate value of order unity. Thus, at a certain θ-value there will occur a reversal of the plasma channel self-inductive electric field so as to

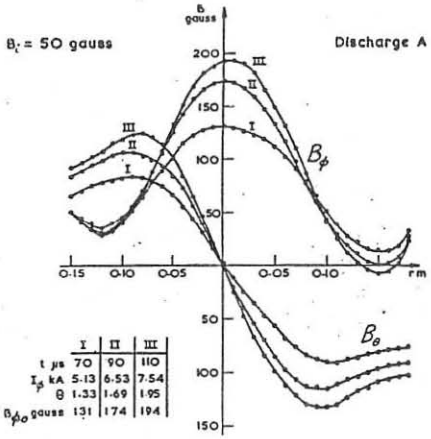

	I	II	III
t μs	70	90	110
I_ϕ kA	5·13	6·53	7·54
θ	1·33	1·69	1·95
$B_{\phi a}$ gauss	131	174	194

Fig. 1

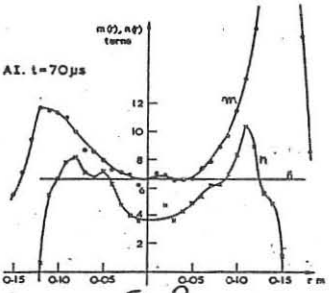

Fig. 2

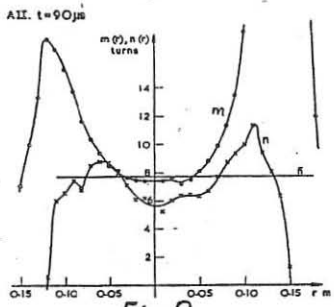

Fig. 3

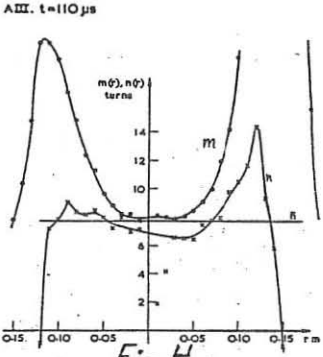

Fig. 4

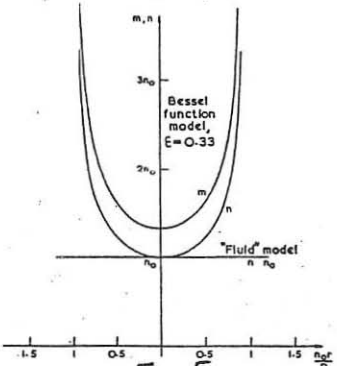

Fig. 5

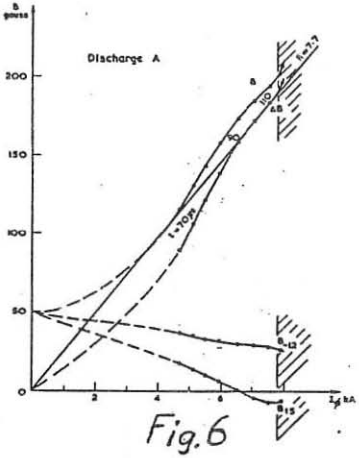

Fig. 6

make it no longer oppose but contribute to the external current driving flux swing field. The observed outcome, emphasized in [6], was a saturation for the average current turn number $\bar{n}$, referred in [6] to as a "rigid" current configuration, see Fig. 6, and the occurrence of the wellknown unsymmetry in the helical current distribution, described in [6] as a helical "notch" but later in MHD theory usually called an "m = 1 kink instability", [7]. These phenomena required θ-values of about 1.2 whereas actual toroidal field reversal was not reached until $\theta = 1.8$, [6].

Strong toroidal field reversal is usually taken, and correctly so, to be associated with complicated rearrangements of current and field distributions within the plasma channel, [7]. Lack of space prevents suggestions here of how the moving frame inductive field Eq. (4) couples to rotational plasma mass motions driven by inductive electric fields, as expressed by Eq. (1).

In the present work attention has been given to moving frame fields and moving current paths rather than the moving magnetic lines of force in usual MHD theory. (Electromagnetic theory offers no unique definition of the motion of a line of force.) An extention of this treatment is given in [5] where a magnetized plasma in fluid formulation is mathematically described as an assembly of moving, deformable, resistive, magnetically and mechanically interacting current tubes, each with its identity retained during their motion.

References

[1] E.A. Witalis, Phys. Rev. A 24, 2758 (1981).

[2] S.I. Braginskii in Reviews of Plasma Physics, ed. Leontovich, Consultants Bureau, vol. I, p. 205, 1965.

[3] E.A. Witalis, Z. Naturf. 38a, 625, 949 (1983).

[4] M.J. Lighthill, Phil. Trans. Roy. Soc. 252a, 397 (1960).

[5] E.A. Witalis, "A Further Look at Some Early Criticisms of Magneto-Hydrodynamic Plasma Theory", FOA Report D20105-A1, Oct. 1984, to be publ.

[6] E.A. Witalis, "Toroidal Discharge Configurations Obtained from Magnetic Probe Measurements", Culham Lab. Report, CLM-R7 (1961).

[7] H.A.B. Bodin and A.A. Newton, Nucl. Fusion 20, 1255 (1980)

[8] S.C. Prager and L. Turner, Phys. Fluids, 28, 1155 (1985).

DENSITY STUDIES IN HBTX1A REVERSED FIELD PINCH

D.E. Evans, D.P. Storey*, and P.D. Wilcock

Culham Laboratory, Abingdon, Oxon. OX14 3DB England
(EURATOM/UKAEA Fusion Association)

* University of Hull, UK

1. Introduction

A single-channel, double-pass, CO_2-laser phase-quadrature interferometer in the configuration of Jacobson and Call [1] has been used to measure $\bar{n}_e$, the plasma electron density averaged across a vertical minor diameter ($\sim$ 0.5 m) of HBTX1A reversed field pinch plasmas [2].

2. The Interferometer

The layout of the interferometer is illustrated schematically in Figure 1. The 10.6 μm gaussian beam from the CW laser, L, is directed onto a germanium acousto-optic modulator or Bragg cell, B, where it is diffracted as though by a moving grating. The zeroth order proceeds to a CdHgTe photovoltaic detector, D, while the first order, displaced from the incident beam 77 mrad in angle and 40 MHz in frequency, traverses the plasma and encounters a corner cube, C, which returns it back on itself to the modulator. Use of a corner cube as opposed to a simple mirror confers relative immunity to small refractive bending of the probe beam by the plasma. Rotating the modulator to the Bragg angle simultaneously maximizes radiation in the first order, and directs the reflected portion along the zeroth order path onto the detector. There, provided the path difference 2·BC between the beams is less than the laser's coherence length, the zeroth and first orders mix, generating a beat signal that appears as a voltage at an IF of 40 MHz.

Some radiation reflcted by the corner cube inevitably returns to the laser via the Bragg cell, but the interferometer and the laser are nevertheless decoupled because two passes through the modulator produce an 80 MHz frequency shift, moving the frequency of the returning beam well outside the laser gain profile.

Since the phase but not the amplitude of the IF signal carries the electron density information, the detector output is amplified by an automatic gain compression amplifier to 5V for any input greater than a few mV.

Vibration is negligible, at least for the first few ms of the plasma discharges, and the electrical noise level is such that a fringe shift of 0.001, corresponding to a change in density $\Delta\bar{n}_e = 1\times10^{17}\ m^{-3}$, can be detected.

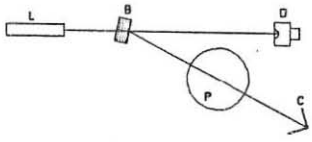

Figure 1 Schematic of the interferometer. L the laser, B Bragg cell, D detector, P plasma, C the corner cube reflector.

3. Plasma Density

Time-resolved density profiles, shown accompanied by a trace of toroidal current I_ϕ in Figure 2, exhibit a rapid rise to a maximum, followed by a decrease by a factor of about 5 to a level that persists or falls only slowly during the period of sustained field reversal, until a fairly abrupt termination occurs when current ceases to flow. Peak density $\hat{n}_e$ is proportional to the gas filling pressure p_o, and increases monotonically with peak current $\hat{I}_\phi$, as shown in Figure 3. The density at current peak however is quite independent of current and depends only on filling pressure (Figure 4). Once sustained reversed field has been established, filling pressure seems to have lost all influence, and density is then proportional to the prevailing current as can be seen in Figure 5. That is, during sustainment the density adjusts itself in such a way as to keep I_ϕ/N constant, where N is the number of electrons per metre around the torus. Assuming a parabolic density profile and plasma radius a = 0.245 m, $I_\phi/N = 1.3 \times 10^{-13}$ amp m in these discharges.

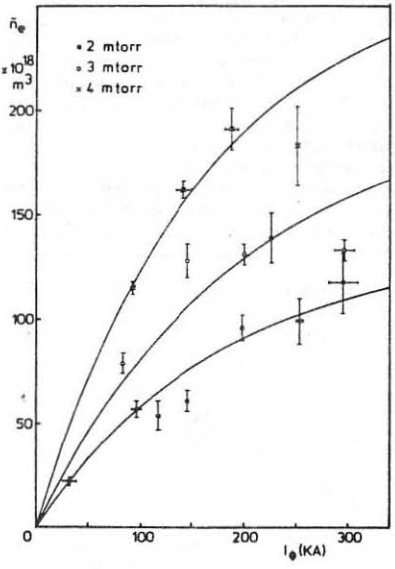

Figure 3 Peak density as a function of peak current.

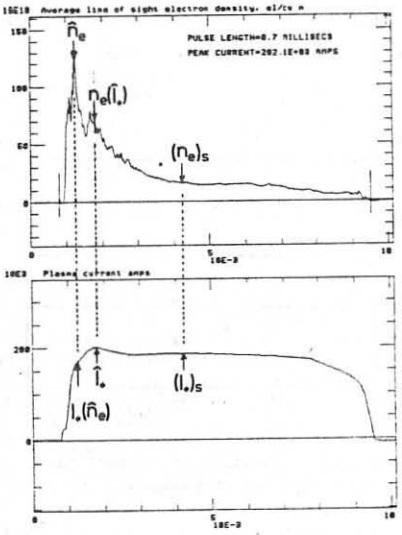

Figure 2: Upper trace: line-integrated density (m^{-3}) as a function of time; Lower trace: plasma toroidal current

4. Fluctuations

The noise level due to electrical sources, but excluding mechanical vibration, appears during the first ms of the density trace in Figure 2 before the plasma discharge begins. Expansion of the diagram reveals that this consists of digital steps of 0.0005 fringes amplitude, consistent with the 10-bit dynamic range of the ADC. The oscillations to be seen during the sustainment phase have excursions of 0.0025 fringes or more, and can be attributed to real fluctuations in line-averaged density $\Delta\bar{n}_e \cong 0.5 \times 10^{18}$ m^{-3}, corresponding to

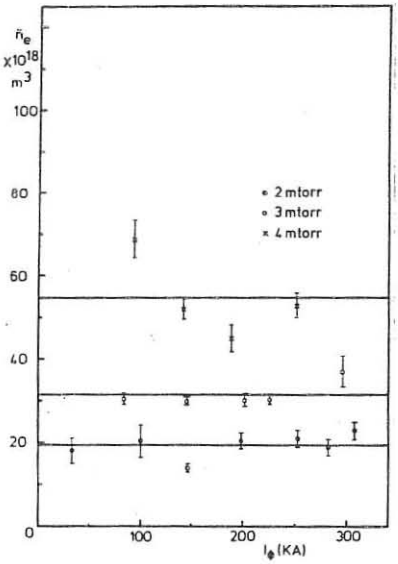

Figure 4 Density at current peak as a function of peak current.

column headed $(T_{eo}/T_{\sigma o})^{1.5}$. With the caveat that radial distributions for neither density nor temperature are actually known for this plasma, we adopt a parabolic density profile and a quasi-flat temperature distribution, as well as equal ion and electron temperatures to calculate the estimates of poloidal beta, β_θ , and energy confinement time τ_E , presented in the TABLE.

a relative line-averaged fluctuation level $\Delta\bar{n}_e/\bar{n}_e \sim 2.5$ % . Larger fluctuations can be seen during termination, and still larger during the setting-up phase but none of these have the character of sawtooth oscillations. The power spectrum of the sustainment phase fluctuations is maximum between 10-20 kHz, and falls towards higher frequencies according to a ν^{-4} law.

5. Derived Parameters

Combining density results with temperatures measured by Thomson scattering (which agree with SiLi detector x-ray data), and with resistivity, η, calculated on the basis of magnetic helicity balance [3] from measured values of the pinch parameter Θ, the reversal parameter F, and plasma resistance = loop volts/$I_\phi \sim 250\ \mu\Omega$, and assuming a quasi-flat temperature radial distribution, leads to derived parameters characterizing the sustainment phase of the pinch. These are summarized in the accompanying TABLE.

The conductivity temperature on axis $T_{\sigma o}$, is calculated assuming axial resistivity (which is the global value quoted divided by 1.45 for vertical field B_v off and by 1.3 for B_v on) is Spitzer-Härm for ion charge Z = 1. The striking discrepancy between the temperatures measured directly and those deduced from resistivity is presented in terms of an implied effective ion charge in the

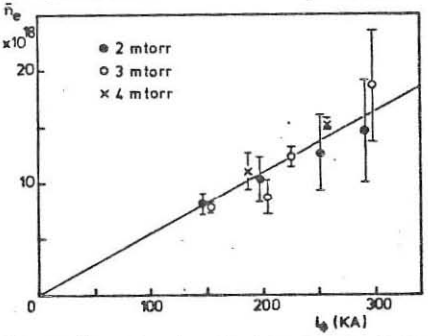

Figure 5 Density during sustained field reversal as a function of prevailing current.

TABLE

I_ϕ (kA)	$\bar{n}_e$ (m^{-3})	T_{eo} (eV)	η ($\mu\Omega m$)	$T_{\sigma o}$ (eV)	$(T_{eo}/T_{\sigma o})^{1.5}$	β_θ (%)	τ_E (μs)
B_v off							
200	1.25×10^{19}	250	5.8	29	25	6.3	95
B_v on							
200	0.9×10^{19}	345	4.4	34	32	7.6	115
300	2.2×10^{19}	400	2.0	59	18	9.6	145

6. Conclusions

A simply configured 10 μm wavelength interferometer has been used to trace the history of plasma density in typical RFP discharges in HBTX1A. During the setting-up phase, the plasma appears to lose all memory of the initial gas-filling pressure, and adjusts itself so that during the sustained reversal, the value of $I_\phi/N = 1.3 \times 10^{-13}$ amp metres is maintained. Line-integrated density fluctuations of a few percent are observed throughout sustainment, and anomalously high resistivity, corresponding to a discrepancy between conductivity temperatures and those measured directly, can be expressed as an effective ion charge often considerably greater than 10. This contrasts with the much lower values of Z_{eff} measured spectroscopically.

[1] A.R. Jacobson and D.R. Call Rev. Sci. Instrum. 49 318 (1978)

[2] P.G. Carolan et al. Proc. 10th International Conference on Plasma Physics and Controlled Nuclear Fusion Research London 1984 Vol II p. 449

[3] K.F. Schoenberg, R.W. Moses, Jr., and R.L. Hagenson Physics of Fluids 27 1671 (1984)

CHARGED PARTICLE MOTION IN A CYLINDRICALLY SYMMETRIC Z-PINCH

G. Eriksson
Uppsala University, Department of Technology, Box 534, S-751 21
Uppsala, Sweden

Abstract: An account of charged particle motion in a cylindrically symmetric Z-pinch, without axial magnetic field, is given. General rigid drift equilibria are considered.

1. Introduction

Recent Z-pinch experiments [1,2,3], showing remarkable stability, have called for a more detailed understanding of Z-pinch physics. Although it is one of the oldest configurations no general study of particle orbits seems to exist. (The different orbit types in relativistic motion have, however, been classified by Gratreau [4]). In the following only a brief outline of the subject can be presented. The details are to be found in [5].

2. The normalized Hamiltonian

In a rigid drift equilibrium, where the axial macroscopic drift velocities of electrons and ions are constants, the ion Hamiltonian in a system S can, after normalization with e, m_i, $v_{ith} \equiv (T_i/m_i)^{1/2}$, and r_o (the pinch radius), be written

$$H = p_r^2/2 + U(r|p_\theta, p_z) \ , \qquad (1)$$

where the effective potential

$$U(r|p_\theta, p_z) = p_\theta^2/(2r^2) + [p_z + \alpha(r)/\lambda_i]^2/2 + \alpha(r). \qquad (2)$$

Here, $\lambda_i \equiv U_s/v_{ith}$, where U_s is the axial velocity of S relative S_o, the system where $\Phi(r) = 0$. The function $\alpha(r) \propto A_z(r)$ contains the radial dependence of $A_z(r)$. In the special case of the Bennett equilibrium, where the electron and ion distributions are drifting Maxwellians, we have $\alpha(r) = 2\ln(1+r^2)$. (1) and (2) show that the problem is one-dimensional, and that $\lambda \equiv \lambda_i$, which is a measure of the ratio between electrostatic and magnetic forces, is the important parameter.

3. The number of minima in U

If U(r) for a given particle has only one minimum it simplifies the orbit analysis considerably. By examining the sign of U''(r) at the radii where U'(r) = 0 one can show that if

$$\alpha''(r)/\alpha'(r) = A_z''(r)/A_z'(r) > -3/r \qquad (3)$$

then there exists only one minimum in U(r) for all values of p_θ and p_z, i.e. for all particles. The corresponding radius we call $r_g(p_\theta, p_z)$. Condition (3) is equivalent to $j_z(r) > -\bar{j}_z(r)$, where $\bar{j}_z(r)$ is the average current density inside the radius r.

4. Classification of orbit types

Provided (3) is fulfilled the orbits with $p_\theta \neq 0$ can be classified according to Fig. 1. (The special case $p_\theta = 0$ must be treated separately, see [5].)

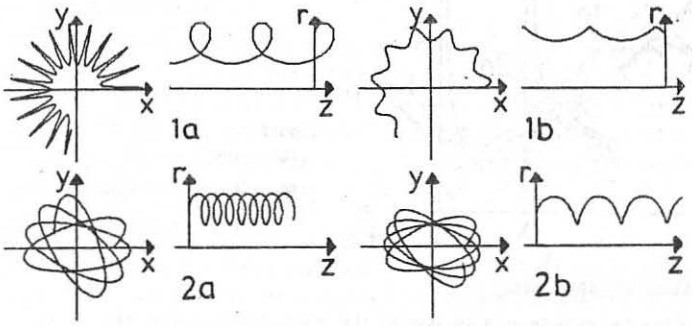

Fig. 1. Orbit types for $p_\theta \neq 0$.

Whether the orbit is of type 1 or 2 is determined by the curvature in the poloidal plane.

$$\begin{cases} \text{Type 1 if } E > E_c(p_\theta, p_z) \text{ and } p_z < -\lambda \\ \text{Type 2 if } E < E_c(p_\theta, p_z) \text{ or } p_z > -\lambda \,. \end{cases} \qquad (4)$$

$$E_c(p_\theta, p_z) = p_\theta^2/(2r_c^2) - \lambda p_z - \lambda^2/2 \,, \qquad (5)$$

and $r_c(p_z)$ is defined by

$$p_z + \lambda + \alpha(r_c)/\lambda = 0. \qquad (6)$$

Types a and b differ in that a-orbits have loops in the z-r plane and b-orbits have not.

$$\begin{cases} \text{Type a if } E > E_\ell(p_\theta, p_z) \text{ and } p_z < 0 \\ \text{Type b if } E < E_\ell(p_\theta, p_z) \text{ or } p_z > 0. \end{cases} \qquad (7)$$

$$E_\ell(p_\theta, p_z) = p_\theta^2/(2r_\ell^2) - \lambda p_z \,, \qquad (8)$$

and $r_\ell(p_z)$ is defined by

$$p_z + \alpha(r_\ell)/\lambda = 0. \qquad (9)$$

Furthermore E is limited from below by the fact that $p_r^2(r_g)$ must be positive,

$$E > E_{min}(p_\theta, p_z) \equiv U(r_g(p_\theta, p_z)|p_\theta, p_z) \ . \qquad (10)$$

Fixing $p_\theta \neq 0$, conditions (4), (7) and (10) are conveniently displayed in a p_z- E diagram. (Fig. 2).

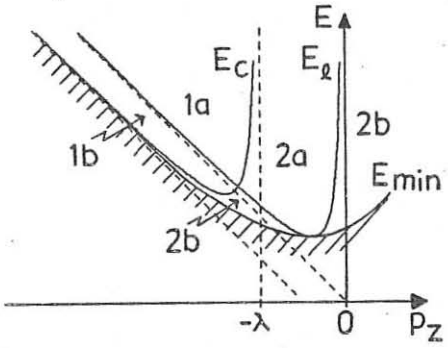

Fig. 2.
Orbit type diagram. $\alpha(r) = 2\ln(1+r^2)$, $\lambda = 1$, $p_\theta = 1/2$.

5. Distribution of orbit types

A p_z- E diagram can also be used to display the orbit type criteria for particles at a given fixed radius r. The curves E_c and E_ℓ are the same, but (10) is replaced by $E > U(r|p_\theta, p_z)$. ($p_r^2(r)$ must be positive). In Fig. 3 an example is shown, where the condition for small gyroradii, $E < p_z^2/2$, $p_z < 0$, is also included. The cross roughly represents thermal values of p_z and E.

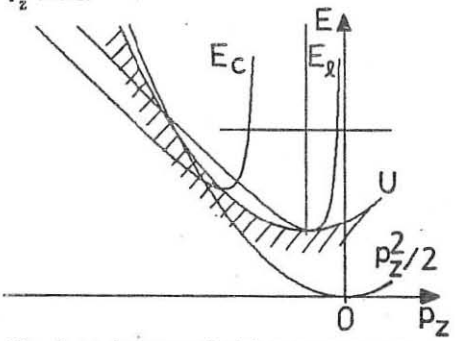

Fig. 3.
Orbit type diagram with r = 1/2.
$\alpha(r)=2\ln(1+r^2)$, $\lambda=1$, $p_\theta=1/2$.

Fig. 3 can be compared with a computer calculated distribution of orbit types, see Fig. 4. Positions and velocities are sampled according to the Bennett equilibrium distribution function.

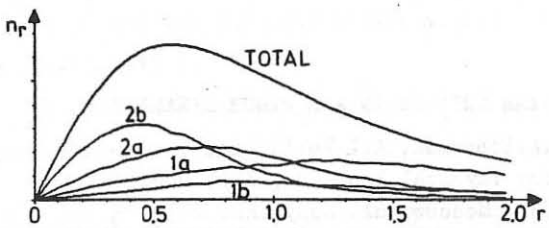

Fig. 4. The one-dimensional density $n_r(r)$ of different orbit types. $\alpha(r) = 2\ln(1+r^2)$, $\lambda=1$.

6. $\lambda \ll 1$ (Gyroorbits)

Here, U(r) can be expanded around r_g, and a measure, ζ, of the deviation from harmonic r-motion for typical particles is introduced. For $\lambda < \alpha(1/2)/2 \sim 0.2$ one gets $\zeta \sim \lambda$ which is the usual gyro ordering. In the range $0.2 < \lambda < 1$, however, two terms in $U'''(r_g)$ tend to cancel, and we find $\zeta \sim \lambda^{1/2}/3$. This means that even for $\lambda \lesssim 1$ the radial motion is approximately harmonic.

7. Constant current density

The first term in the Taylor expansion of $\alpha(r) = 2\ln(1+r^2)$ around r=0 is $\alpha_o(r) = 2r^2$, corresponding to a constant current density. Exact solutions of the equations of motion, with $\alpha(r) = 2r^2$ and arbitrary λ, can be obtained [5]. Unfortunately, elliptic functions and integrals must be used, and the dependence on the constants of motion is implicit and very complicated. In the limiting case $\lambda \gg 1$, however, explicit solutions can be obtained using canonical perturbation theory. It is found that up to $O(1/\lambda)$ the projections of the orbits onto the poloidal plane are stationary ellipses extending all over the pinch cross section. If $O(1/\lambda^2)$ terms are included the ellipse starts to rotate around the axis with angular rotation velocity $\dot{\Psi}_1 = -p_\theta/(2\lambda^2)$. However, the neglected terms in the Taylor expansion of $\alpha(r)$ also cause the ellipse to rotate, but with angular velocity $\dot{\Psi}_2 \approx p_\theta/4$. Hence $|\dot{\Psi}_1/\dot{\Psi}_2| \approx |-2/\lambda^2| \ll 1$, and the latter effect usually dominates.

References

[1] Linford, R.K., Sherwood, A.R., Hammel, J.E., in Unconventional Approaches to Fusion (Brunelli, B., Leotta, G.G., eds), Plenum Press, New York (1982) 463.

[2] Lehnert, B., ibid., 135.

[3] Haines, M.G., in Physica Scripta (Proc. Int. Conference on Plasma Physics, Göteborg, 1982) 380.

[4] Gratreau, P., Phys. Fluids 21 (1978) 1302.

[5] Eriksson, G., Uppsala Univ., Rep. UPTEC (1985).

SELF-SIMILAR MOTIONS IN A Z PINCH DYNAMICS

M.A.Liberman, A.L.Velikovich
Institute for Physical Problems, A.S. U.S.S.R.
117334 Moscow, ul. Kosygina, 2

New self-similar solutions of ideal MHD equations, which describe essentially nonuniform compression of a plasma in a cylindrical Z pinch geometry, are presented. They include collapse of shock waves and cavities, converging to the pinch axis, reflection of the shock wave from the axis, an inverse Z pinch flow, etc. In most of the solutions a concentrated current on the pinch axis is present, which can be interpreted as a current line penetrated into a weakly ionized plasma when the main current was switched on, a result of previous stages of plasma compression, or simply as a current via a central electrode, if there is one.

All the flow variables are assumed to be functions of $\xi = r/R(t)$ and time t, R(t) being the time-dependent length scale of the problem. Introducing the dimensionless compression ratio $a(t) = R(t)/R(t_0)$, we choose the self-similarity ansatz in the form:

$$u(r,t) = \dot{R}(t)\,\xi\,U(\xi)\,, \quad n(r,t) = n_0 a(t)^{2\chi}\,N(\xi)\,,$$

$$T(r,t) = T_0 a(t)^{-2\lambda}\,\Theta(\xi)\,, \quad H(r,t) = H_0 a(t)^{\chi-\lambda}\,B(\xi)\,, \qquad (1)$$

$$R(t) = R(t_0)\left|t/t_0\right|^{\alpha},$$

where u is the plasma radial velocity, H is the azimuthal magnetic field, n_0, T_0 and H_0 are normalization constants,

λ and χ are the two independent self-similarity exponents ($\alpha = 1/(\lambda + 1)$).

Passing into new variables S and A, related to sonic and Alfvén characteristic velocities, respectively,

$$S = \gamma\Theta/\xi^2(1 - U) , \qquad A = B^2/\xi^2 N(1 - U) , \tag{2}$$

reduces the system of four ordinary differential equations for $U(\xi)$, $N(\xi)$, $\Theta(\xi)$, $B(\xi)$ to an autonomous dynamic system in a 3D phase space (U, S, A), $\eta = \log(\xi)$ being the independent variable. The fourth equation is replaced by an integral, expressing $N(\xi)$ via $S(\xi)$, $U(\xi)$ and ξ, which is obtained exactly as in gasdynamics [1]. The self-similar solutions are represented by the trajectories of the dynamic system. To be physically meaningful, these trajectories should not intersect the characteristic plane

$$U + S + A = 1 \tag{3}$$

in nonsingular points of the dynamic system. Since the singular points, where the intersection is allowed, form a 1D manifold on the plane (3), here the spectrum of eigenvalues (λ , χ) is continuous - in contrast to gasdynamics, where the singular points on the line $U + S = 1$ are isolated, and the corresponding spectra - discrete [1-3].

The self-similar profiles are shown in Figs. 1-4. Fig. 1 represents a collapse of a cavity - or, which is the same, of a hollow plasma liner - on the current-carrying axis (here $\lambda = 0.1$, $\chi = -0.4$). Fig. 2 describes the same flow for $t > 0$, when the reflected shock wave propagates into the converging plasma. Figs. 3, 4, plotted for $\lambda = 0.25$, $\chi = 0$, correspond to

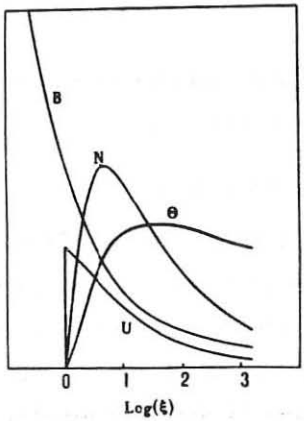

Fig. 1

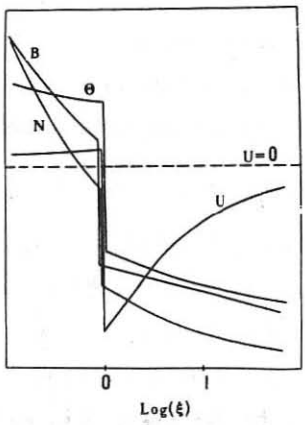

Fig. 2

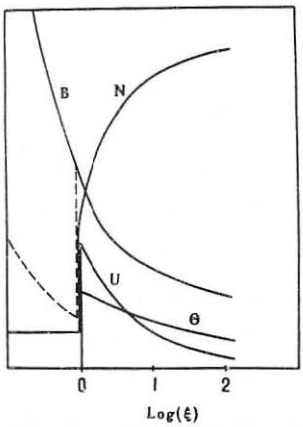

Fig. 3

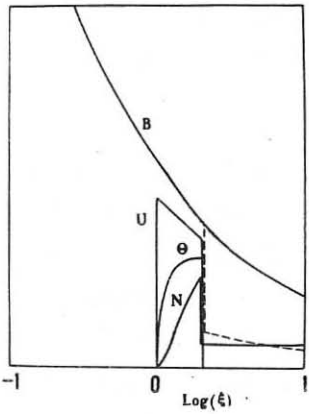

Fig. 4

parts of the same trajectory in the (U, S, A) phase space; Fig. 3 describes a converging ionizing shock wave ($t < 0$, collapse at $t = 0$), Fig. 4 - an inverse Z pinch flow, ionizing

the nonperturbed gas ($t > 0$). Here solid and dashed profiles $B(\xi)$ correspond to the gasdynamic and MHD limiting regimes of propagation of ionizing shock waves in magnetic field, respectively [4].

At the moment of collapse $t = 0$ the flow variables have the power-law profiles. Of course, the self-similar solutions must give integrable at $r = 0$ densities of mass, energy and current (this is so if $\gamma + 1 > 0$ and $\gamma - \lambda + 1 > 0$). To prevent the divergence of total mass and energy per unit length and current at $r \to \infty$, one should explicitly incorporate into the solution the current sheath on the plasma-vacuum interface. Then the current carried by the plasma $I_p(t)$ is finite, its time dependence being different from the power-law one, governing the current on the axis $I_0(t)$. They are both shown in Fig. 5 for the conditions of Fig. 1 (the scales of $I_p(t)$ and $I_0(t)$ are different).

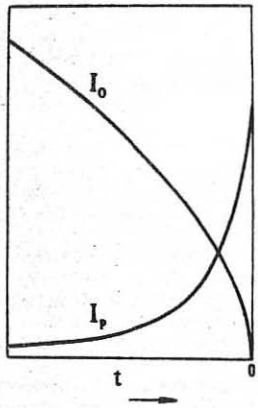

Fig. 5

References:

1. J.Meyer-ter-Vehn and C.Schalk, Z. Naturforsch. 37a, 955 (1982).
2. G.Guderley, Luftfahrtforschung 19, 302 (1942).
3. K.V.Brushlinski and Ya.M.Kazhdan, Uspekhi Mat. Nauk 18, 2 (1963).
4. M.A.Liberman and A.L.Velikovich, Phys. Reports 84, No. 1 (1982).

Equilibrium of Reversed Field Pinch with Iron Core

N. Asakura, N. Inoue*, K. Miyamoto, Y. Nagayama, S. Shinohara,
H. Toyama, Y. Ueda, Z. Yoshida*

Department of Physics, Fuculty of Science,
University of Tokyo, Hongo 7-3-1, Bunkyo-ku, Tokyo 113, Japan

*Department of Nuclear Engineering, Faculty of Engineering
University of Tokyo, Hongo 7-3-1, Bunkyo-ku, Tokyo 113, Japan

1. INTRODUCTION

The reversed-field-pinch (RFP) plasma has been maintained in the equilibrium by a thick conducting shell. However, the vertical magnetic field generated by the external coils must be applied to obtain the plasma equilibrium longer than the skin time of the shell.

In this paper, the RFP equilibrium is calculated to design the REPUTE-1 RFP device which has an iron core and a thin conducting shell. REPUTE-1 is designed to drive the plasma current of 400kA with the duration of more than the skin time of the shell (R/a = 82/20cm). The equilibrium field is maintained by vertical field coils rather than a conducting shell which has the skin time of 1 ms.

The Grad-Shafranov equation is used to obtain the toroidal axi-symmetric equilibrium with an iron core. The non-linear effect of the magnetic permeability of the iron core , which is a function of the magnetic field, is calculated by means of Finite Element Method. The poloidal field and the pressure profile are assumed as the form of the simple function of poloidal magnetic flux.

We can get the suitable profile of the decay index ($N \equiv -(R/B_Z)(\partial B_Z/\partial R)$) by changing poloidal coil positions and the current distribution. Here, B_Z is the externally applied vertical magnetic field. The RFP equilibrium profiles of the magnetic field and the plasma current density are calculated with parameters of β_{ax} and I_p (β_{ax} up to 30%, and I_p up to 500kA). These results are compared with the experimental ones obtained by the magnetic measurements in REPUTE-1, and we have fairly good agreement between them .

2. RFP EQUILIBRIUM CALCULATION CODE WITH IRON CORE

This RFP equilibrium calculation code consists of two programs, i.e., ICCODE and ECODE /1/.

In the ICCODE, the effect of the iron core is obtained by the following procedure. From the relations $\vec{B} = \mu \vec{H} = \nabla \times \vec{A}$ and $\nabla \times \vec{H} = \vec{j}$, where $\mu(R,Z,B)$ is the magnetic permeability and $B = |\vec{B}|$, we have the following equation in the cylindlical coordinates (R,ϕ,Z),

$$\nabla \cdot [\frac{1}{\mu R} \nabla (R \cdot A(R,Z))] = - \quad j(R,Z) \quad . \qquad (1)$$

Here, A(R,Z) and j(R,Z) are ϕ-components of $\vec{A}$, $\vec{j}$, respectively, and R·A(R,Z) corresponds to the poloidal magnetic flux $\psi(R,Z)$. The regions of vacuum, plasma and iron core are divided into the different size of triangular elements, and $\psi(R,Z)$ is assumed to vary linearly over each vertex of trianguler elements (Finite Element Method) /2/. The partial differential equation (1) is re-written as a finite-differential equation, where the plasma current density and the external coil currents are assumed to be constant in each triangular element.

Once these currents are given, this non-linear finite-differential equation is solved by the SOR method, and the poloidal magnetic flux is obtained. For the boundary condition, ψ is taken to be constant at the external surface of the iron core, where the iron core is assumed to be the axi-symmetric form with the same magnetic resistance as actual one (see Fig. 1).

We calculate $\psi_1(R,Z)$ and $\psi_0(R,Z)$ for the case with the iron-core($\mu = \mu(B)$ in the region of the iron core and $\mu = \mu_0$ in other regions) and without the iron core ($\mu = \mu_0$ in all regions), respectively. The effect of the iron core is defined as

$$\psi_{IC}(R,Z) = \psi_1(R,Z) - \psi_0(R,Z) \quad , \tag{2}$$

at each triangle vertex.

In the ECODE, the axi-symmetric equilibrium of the toroidal plasma is obtained. This equilibrium is described by following Grad-Shafranov equation for the poloidal magnetic flux ψ in the cylindrical coordinates (R,ϕ,Z).

$$\frac{\partial^2\psi}{\partial R^2} - \frac{1}{R}\frac{\partial\psi}{\partial R} + \frac{\partial^2\psi}{\partial Z^2} = -\mu_0 R\left[RP'(\psi) + \frac{\mu_0}{(2\pi)^2} I(\psi)I'(\psi)\right] \tag{3}$$

$$\equiv -\mu_0 R j_\phi$$

$$\vec{j} = j_\phi \vec{\phi} + \frac{1}{2\pi R}\nabla I(\psi) \times \vec{\phi} \tag{4}$$

Here, j_ϕ is the toroidal component of plasma current density $\vec{j}$. The notations $I(\psi)$ and $P(\psi)$ are poloidal current flux and pressure, respectively, which are arbitrary functions of ψ. $\vec{\phi}$ is the unit vector of ϕ direction.

To simplify the problem, we choose /3/ /4/

$$I'(\psi) = \alpha_0[1-(\psi/\psi_a)^n] \quad , \tag{5}$$

and

$$P(\psi) = P_0[1-(\psi/\psi_a)^{l_1}]^{l_2} \quad . \tag{6}$$

Here, α_0 and P_0 are constants. We take that $\psi = \psi_a$ on the plasma surface, and $\psi = 0$ at the magnetic axis. By choosing eqs. (5) and (6) with $n > 0$ and $l_2 > 1$, the plasma current density $\vec{j}$ becomes zero on the surface of plasma. The plasma configuration of this model with $I(\psi) = \alpha_0$ and $P_0 = 0$, corresponds to the Taylor's Bessel function model (BFM) /5/.

In order to obtain the poloidal magnetic flux ψ at the point of (R,Z), we re-write the eq. (3) as the following integral equation

$$\psi_c(R,Z) = L\left(j_\phi(R',Z') + j_{ex}(R',Z') \right) \quad . \tag{7}$$

Here, the operater $L(f)$ is defined as

$$L(f) \equiv \mu_0 R\int\frac{1}{\pi k}\sqrt{\frac{R'}{R}}\left[\left(1-\frac{k^2}{2}\right)K(k) - E(k)\right] f \, dR'dZ' \, ,$$

$$k^2 = \frac{4RR'}{(R+R')^2+(Z-Z')^2} \quad .$$

$j_\phi(R',Z')$ and $j_{ex}(R',Z')$ are the plasma current density and the external coil current at the point of (R',Z'), respectively. K(k) and E(k) are the first and the second kind of complete elliptic function.

For computation, an initial approximating j_ϕ and j_{ex} must be given at each mesh point. We consider the following iteration: Applying the plasma current density j_ϕ and the external coil currents j_{ex} to the eq. (7), the poloidal magnetic flux produced ψ_C by the currents is calculated. The poloidal magnetic flux ψ_{IC} of the iron core is given by the eq. (2) in the ICCODE. The total poloidal magnetic flux ψ is the sum of these poloidal magnetic flux. Substituting this value of ψ into eq. (4), we have the plasma current density j_ϕ. After the convergence of this iteration, the equilibrium plasma current density, magnetic field and pressure profile are obtained.

Using these two codes with an iterated process, equilibrium configuration of RFP plasma is derived.

3. RESULTS

Figure 1 shows the poloidal magnetic flux surfaces calculated numerically by this RFP equilibrium code. The iron core and the poloidal coil system of REPUTE-1 is also presented. In this case, plasma current I_p is 400kA, total ohmic heating coil current I_{oh} is 410kA and vertical field coil current I_v is 7 kA. The numbers of turn of vertical field coils are 10, 6,-2,-2,-4,-8 from the inner side to the outer side on the upper half plane. Negative value of the number indicates the opposite direction to the plasma current. The limiter position of REPUTE-1 (which has 20cm in minor radius) is indicated by a broken line.

We change the positions and the current distribution of the ohmic heating coil and vertical field coils under the following two constraints. One is zero ampere-turn of total vertical coil currents, and the other is to keep these coils away from the top, bottom and outer side ports of the torus. We can minimize the leakage flux by winding the ohmic heating coil around the central column of the iron core, and minimize the distortion of the equilibrium field in the plasma region by arranging the ohmic heating coil and the vertical field coils as the case shown in Fig. 1.

The poloidal magnetic flux near the plasma is shown in Fig. 2. The equilibrium RFP plasma with almost circular surface is obtained, and the toroidal shift Δ, which is defined as the displacement between the magnetic axis and the center of the poloidal magnetic flux ψ_a of the plasma surface, is observed.

Figure 3 shows the vertical magnetic field (B_Z) and decay index (N) profile in the median plane of Z = 0. Numerical results with the iron core (solid lines) and without the iron core (broken lines), and experimental results(circles) are represented. Here, B_Z is defined as total vertical magnetic field subtracted by the poloidal magnetic field produced by plasma current. We find that the stable condition for decay index (from 0 to 3/2) /6/ is satisfied in the plasma region.

Numerical results of $B_\phi(R)$ and $B_\theta(R)$ in the case of n = 8 and 14 in eq. (5) and $l_1 = l_2 = 2$ in eq. (6) are shown in Fig. 4. Here, the values of I_p, I_{oh}, I_v and β_{ax} are taken to be 150kA, 150kA, 3.0kA and 10%, respectively, which are corresponding to the experimental ones. These results are consistent with the observed ones as is shown in Fig. 4 (circles).

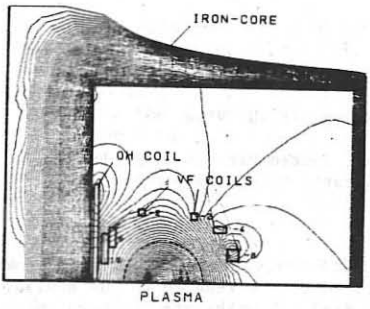

Fig. 1 Poloidal magnetic surfaces obtained by computational calculation; The cross section of the iron core and poloidal coils is shown in the case of REPUTE-1. In this case, I_p = 400kA, I_{oh} = 410kA, and I_v ≅ 7kA. Each number of turn of the coil is shown beside it.

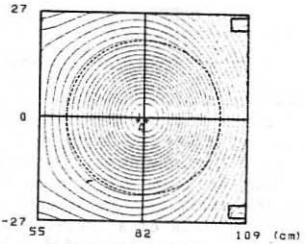

Fig. 2 Poloidal magnetic surfaces near the plasma; A broken line shows the limiter position of REPUTE-1. The value of n in eq. (3) is 4, l_1 and l_2 in eq. (4) are 2, and βax is 10%. represents the toroidal shift.

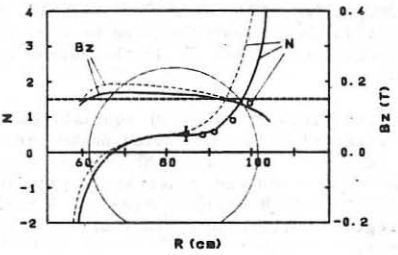

Fig. 3 Vertical magnetic field (B_z) and decay index (N); The computational results with an iron core (solid lines), and without an iron core (broken lines), and decay index obtained by the magnetic probe measurements (circles) are shown.

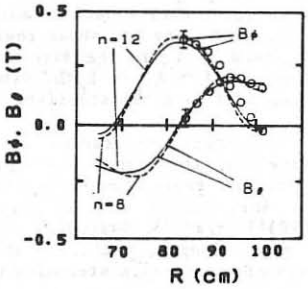

Fig. 4 $B\phi$ and $B\theta$ profiles obtained bythecomputational calculations (solid: n = 8 and broken line: n = 12), and the magnetic probe measurements (circles).

REFERENCES
/1/ Z. Yoshida, M. Kikuchi, M. Mori, K. Miyata, K. Okano, M. Nakanishi T. Kobata, N. Inoue and T. Uchida : Japan J. Appl. Phys. 20, 2389 (1981)
/2/ A.M. Winslow : Journal of Computational Physics 2, 149 (1967).
/3/ Y. Kondoh : Nucl. Fus. 22, 1372 (1982).
/4/ Y. Nagayama : Japan J. Appl. Phys. 24, 585 (1985).
/5/ J. B.Taylor : Phys. Rev. Lett. 33, 1139 (1974).
/6/ V.S. Mukhovatov and V.D. Shafranov : Nucl. Fus. 11, 605 (1971).

CURRENT DRIVEN DRIFT WAVES IN REVERSED FIELD PINCHES

S. Briguglio, F. Romanelli, G. Vlad

Associazione EURATOM-ENEA sulla Fusione, Centro Ricerche Energia Frascati, C.P. 65 - 00044 Frascati, Rome, Italy

The study of the current driven drift waves stability in slab geometry in the presence of a sheared magnetic field may be reduced to the analysis of the eigenmodes equation $[d^2/dx^2 + Q(x)]\,\Phi(x) = 0$ with outgoing wave boundary conditions for large $|x|$ [1]. In the limit $b = (k_y^2 a_i^2) << 1$

$$Q(x) = \frac{1}{a_i^2}\left[\lambda + \frac{x^2}{x_i^2} - \frac{\eta}{1+\eta}\,\frac{\omega_o - k_{//}u - \omega_{*e}}{\omega_o}\,\frac{x_e}{|x|}\,Z\left(\frac{x_e}{|x|} - \frac{x}{|x|}\,\xi\right)\right]$$

where $\omega_o = \omega_{*e}\,\eta(1-b)/(\eta+b)$, ξ is the electron streaming parameter, $\eta = T_i/T_e$, $x_i/x = \omega_o/k_{//}v_{thi}$, $\lambda = (1-\omega/\omega_o)(\eta+b)/(1+\eta)$, and elsewhere standard notation has been adopted.

We solve this equation using the matched asymptotic expansion technique and distinguishing two shear regimes: $\theta = L_s/L_n (m_e\,\eta/M_i)^{1/3}\, b^{2/3}\,(1-b)/(\eta+b) << 1$ and $\theta >> 1$. In the first regime it is found that the wave becomes unstable when $\xi > \xi_{cr} \sim L_n/L_s$ with a growth rate $\gamma \cong \omega_{*e}\,\xi$. In the second regime we find marginal stability ($\gamma = 0$).

Applying these results to a Reversed Field Pinch (RFP) equilibrium we observe that the high value typically attained by the streaming parameter in the external region causes instability in an annulus around the reversal surface. This can be seen in Fig. 1, where the adopted equilibrium profiles ($n=n(0)[1-(r/a)^2]^2$, $T=T(0)[1-(r/a)^3]$, $B_\phi = B(0)J_0(2.8\ r/a)$, $B_\theta = B(0)J_1(2.8\ r/a)$) are shown along with the instability regions corresponding to four different values of the on-axis streaming parameter.

The perturbation is then predicted to propagate in the direction $-\phi$ (that is, in the electron diamagnetic drift direction). Both the localization and the propagation direction of the perturbation are in agreement with the results of density fluctuations measurements performed on ZT-40M using interferometric signal correlation techniques [2]. With reference to the case of this device we assume $T(0)=150$ eV, $n(0)=8\times10^{13}$ cm^{-3}, $a=20$ cm and $I=120$ kA. Then the phase velocity predicted for the current driven modes in the unstable region is $|v_\phi| = |\omega_o/k_y| \cong 2.5\times10^4$ m sec^{-1}, and also this value seems to be in reasonable agreement with the measurements quoted in Ref. [2].

It is also interesting to note that, increasing $\xi(0)$ (i.e., for constant temperature, increasing the ratio I/N, N being the linear density) the unstable region expands towards the magnetic axis involving increasingly hotter and denser plasma domains. This fact seems to give a possible explanation of the observed confinement degradation in ETA-BETA II as I/N exceeds the value $1\div2\times10^{-14}$ A m [3]. The dependence of the unstable region width on I/N might

also explain the existence of the drift threshold observed in the analysis of the ZT-40M discharges termination [2].

We can estimate the ion flux associated with the above considered instability assuming the saturation amplitude to be reached when $|k_x \tilde{n}| \cong n/L_n$ (where $\tilde{n}$ is the fluctuating part of the density). As is well known, this assumption allows one to estimate the cross field diffusion coefficient $D_\perp$ as being of the order of $\gamma/k_x^2 \cong \gamma/k_y^2$. Referring to the case of ZT-40M, we find the value $\Gamma_i = |-D_\perp \nabla n| \cong 5\times10^{21}$ m^{-2} sec^{-1}, for the ion flux, which is consistent with the value deduced from the measurements; The magnitude, cross-field nature and localization of this flux make it presumably adeguate to support the dynamo model worked out in Ref. [4] by A.R. Jacobson.

These arguments suggest that current driven drift waves may play a fundamental role in the RFP dynamics. To support this suggestion we will show how the assumption that the transport in a RFP is dominated by these modes allows us to obtain a scaling law for the temperature in remarkable agreement with the experimental results.

Our hypothesis, here, is that the pressure profile in a RFP is determined by the stability against MHD modes and that, concerning the transport, one can identify an internal region with high thermal conductivity (hence rather flat temperature profile) and an external region dominated by radiation, these two domains being connected by a high pressure gradient region dominated by current driven mode turbolence. Then it is possible to estimate the energy confinement time (which in RFP's seems to be very close to the particle confinement time) as $\tau_E \cong r_{rev}^2/(\gamma/k_y^2) \cong r_{rev}^2/(\omega_{*e}\xi/k_y^2)$, where r_{rev} is the radius of the reversal surface. On the other hand the balance between losses and ohmic heating gives

$$RI^2 = \frac{3 \langle n\, T \rangle V}{\tau_E}$$

where R is the plasma resistance and V is the plasma volume and here $\langle\ \rangle$ indicates the volume average. Assuming that the resistivity is given by the classical Spitzer expression, we can eliminate τ_E and obtain for the average temperature

$$\langle T(eV) \rangle \cong 1.41\times10^{-3}\ Z_{eff}^{2/7}\ I^{6/7}\ a^{-2/7} \quad \text{(MKS units)} \tag{1}$$

where the numerical coefficient has been evaluated assuming $k_y a_i(0) = 0.25$, and the quoted equilibrium profiles.

In Fig. 2 the electron temperature values obtained in ZT-40M are presented versus the plasma current [5]. Two curves corresponding to the scaling law given in Eq. (1) for $Z_{eff}=1$, and $Z_{eff}=6$ are also shown for comparison.

In Fig. 3 an analogous comparison is performed for ETA-BETA II, plotting the on-axis temperature values [6] versus $Z_{eff}^{2/7}\ I^{6/7}$. A roughly linear scaling of T vs. I has been obtained also on other RFP devices [7].

The authors are indebted to Dr. S. Martini for making them acquainted with the experimental results shown in Fig. 3.

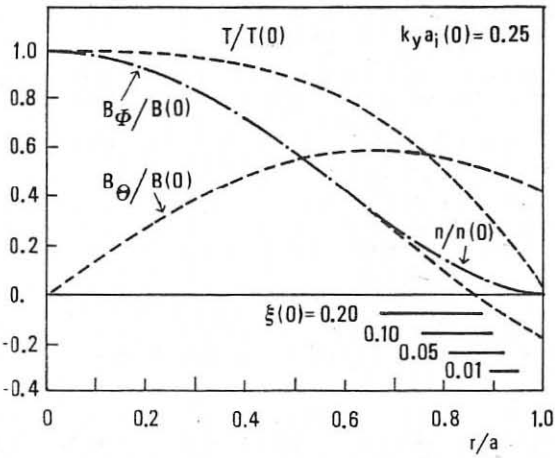

Fig. 1 Density, temperature and magnetic field profiles. The extension of the instability region for different values of the streaming parameter on axis $\xi(0)$ is shown. Here $k_y a_i(0) = 0.25$.

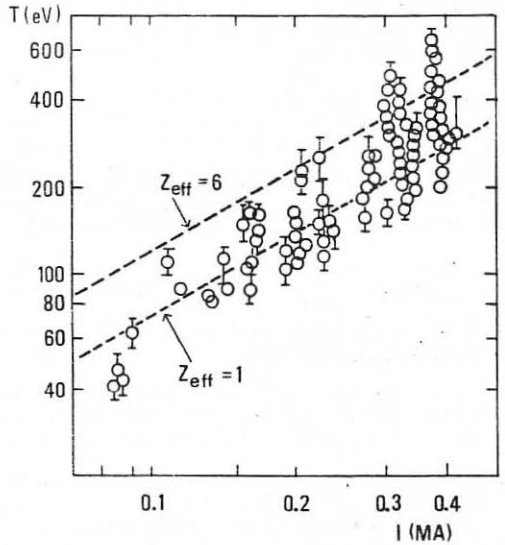

Fig. 2 On axis electron temperature vs plasma current for ZT-40M. The two dashed lines refer to the scaling law of Eq. (1) for $Z_{eff} = 1$ and $Z_{eff} = 6$.

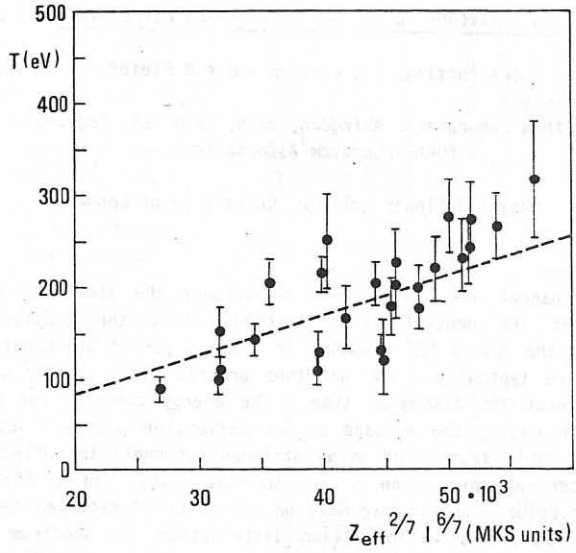

Fig. 3 On-axis electron temperature vs $Z_{eff}^{2/7} I^{6/7}$ for ETA-BETA II. The dashed line is the scaling law of Eq. (1).

REFERENCES

[1] M.N. Rosenbluth, C.S. Liu, Phys. Fluids 15 (1972) 1801
[2] A.R. Jacobson, M.G. Rusbridge, L.C. Burkhardt, J. Appl. Phys. 55 (1984) 125
A.R. Jacobson, Plasma Phys. 24 (1982) 1111
A.R. Jacobson, P.R. Forman, Appl. Phys. Lett. 41 (1982) 520
[3] A. Buffa, S. Costa, R. De Angelis, L. Giudicotti, C.W. Gowers, G. Malesani, G.F. Nalesso, S. Ortolani, P. Scarin, M.R.C. Watts, Proc. 8th Int. Conf. on Plasma Phys. and Controlled Nuclear Fusion Research (Brussels 1980), IAEA, Vienna 2 (1981) 275
[4] A.R. Jacobson, Phys. Fluids 27 (1984) 7
[5] D.A. Baker, C.J. Buchenauer, L.C. Burkhardt, E.J. Caramana, J.N. Dimarco, et al., "Experimental and Theoretical Studies on the ZT-40M Reversed Field Pinch" Proc. 10th Int. Conf. on Plamsa Phys. and Controlled Nuclear Fusion Research (London 1984), paper D-II-2
[6] B. Alper, P.G. Carolan, S. Martini, S. Ortolani, "Soft X-rays Measurements on Eta-Beta II" this Conference
[7] S. Ortolani, G. Rostagni, Nucl. Instrum. Methods 207 (1983) 35.

ION BEHAVIOUR IN THE HBTX1A REVERSED FIELD PINCH

C A Bunting, P G Carolan and A R Field*

Culham Laboratory, Abingdon, Oxon, OX14 3DB, England
(UKAEA/Euratom Association)

*Royal Holloway College, University of London

INTRODUCTION

A five channel NPA [1] is used to measure the time resolved energy distribution of the neutral atoms emitted, along the equatorial minor diameter, from the HBTX1A [2] plasma. In a 20 μs period the counts observed per channel were typically ~ 200 and thus provide statistically significant spectra throughout the discharge time. The energy coverage can be readily extended by increasing the voltage of the deflection plates. This has the additional desirable feature of using different channels to collect neutrals of the same central energy, on a shot to shot basis, and so highlight the influence particular channels may have on the observed detailed temporal and spectral behaviour. For a Maxwellian distribution the spectrum takes the form:-

$$dN/dE \propto n_i \, n_o < \sigma_{cx} \, v > E^{1/2} \exp(-E/T_i)/T_i^{3/2}$$

where dN is the neutral flux in an energy width dE, n_i is the ion density, n_o the neutral density, σ_{cx} is the charge exchange cross section, v is the ion velocity and E is the ion energy.

RESULTS

The energy distribution of the neutral particle emission (200 eV- 2keV) has been measured, at 20 μs intervals, for various plasma currents between 100 kA and 300 kA and in the filling pressure range of 1.5-6 mtorr deuterium.

The temporal variation and the associated power spectra of the relative neutral flux, at two energies (530 eV and 1920 eV), are shown in Fig 1 (200 kA and 3 mtorr). The initial peak in the channels occuring at plasma breakdown time is followed by a decrease to relatively low values during the initial plasma current rise (~ 0.7 ms). Following the peak current time there is a similar temporal behaviour in the various channels. There is, for example, a clear cross channel correlation, probably due to variations in the background neutral density, which would directly affect the flux in the individual channels in an identical fashion (cf Eqn above). Fluctuations in the electron density, and presumably the ion density, as observed with a CO_2 interferometer, are much lower [3]. We can observe from the power spectra

that they do not possess any ordered structure in either channel. Altering the instrumental energy dispersion, to encompass selected energies, but in different detector channels, reproduces much the same features, hence showing that the observed behaviour is not channel specific. The apparently random fluctuations are consistent with ions close to thermalisation. (However, this is only a necessary condition for thermalisation and not a sufficient one, since, for example, the fluctuations of the charge exchange neutral flux from different regions along the line of sight may have temporal structure which gets smeared out. To resolve this difficulty a simultaneous multichord system, or a localised measurement, is required.) Assuming that the high energy ions are components of a Maxwellian distribution, the average derived T_i from the high energy tail is about 280 eV. This is much higher than the few eV expected from electron-ion collisions. There is therefore an additional ion heating mechanism with a power greatly exceeding electron collisional heating. The required long collisional thermalisation time (eg ~ 1.5 ms for ion energies at 500 eV) suggests that there is also a non-collisional thermalisation process or that the ions are established close to a Maxwellian distribution by the heating mechanism.

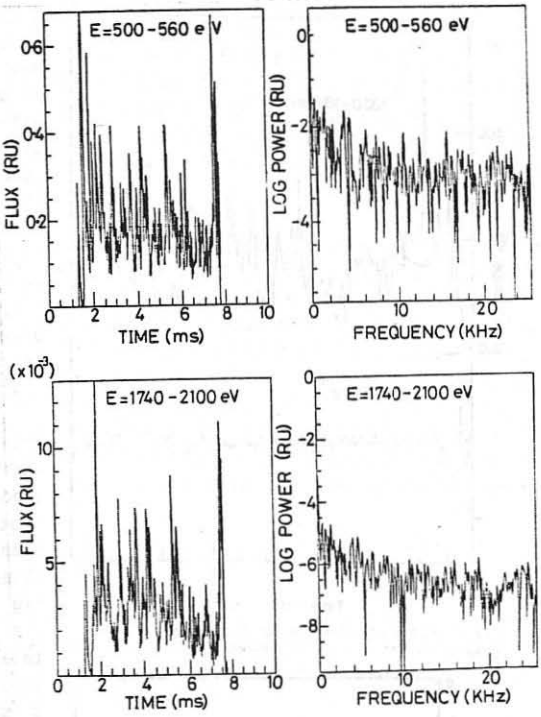

Fig 1 Variation of neutral flux and associated power spectra from two energy channels

The effect of the total flux variations may be removed, leaving those which are more temperature dependent, by simply taking the slope of ln dN/dE $E^{-1/2}$ against E for a few selected energy channels. The results of such an exercise are displayed in Fig 2 for the lower (380-538 eV) and higher (1.3-1.9 keV) energy neutrals. These results again show what appear to be random

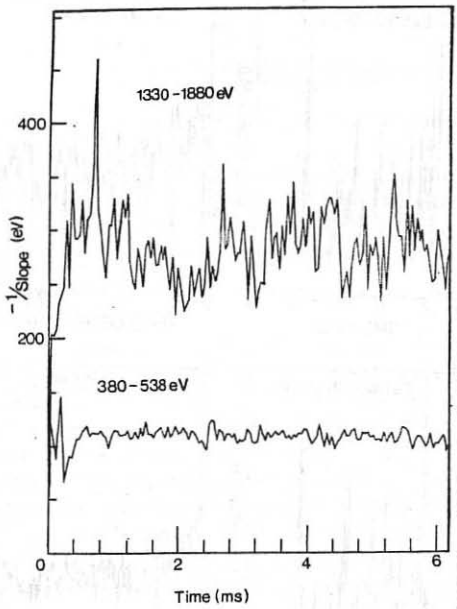

Fig 2 Plots of -1/slope of ln ($dN/dE\ E^{-1/2}$) Vs time

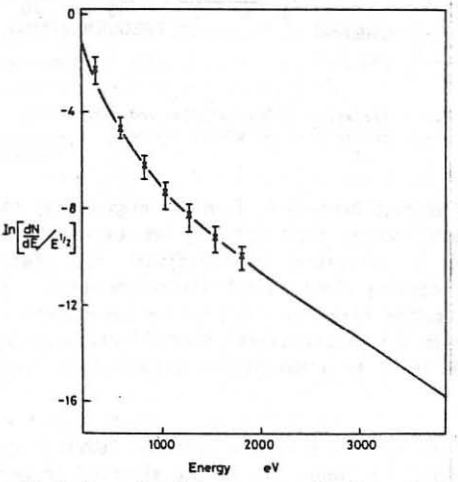

Fig 3 Comparisen between measured and computed neutral energy spectrum. The fit corresponds to $T_i(eV) = 400\ (1-(r/a)^2)$

fluctuations, as expected for ions close to thermal equilibrium. (A 40 μs time bin is used in the analyses to avoid effects associated with the different time delays (several μsec) suffered by the neutrals in the flight line from the plasma to the detectors). This exercise also allows us to monitor how the high energy slope varies with time and so obtain an estimate of the temporal behaviour of T_i.

We also use a Monte-Carlo treatment [4] to simulate the various processes involved in producing the final detected neutral energy spectrum. A comparison between computed and observed spectra is displayed in Fig 3. The error bars shown are due to shot-to-shot variation in total flux. The statistical error bars are much smaller for a single shot. The derived distribution is almost parabolic with a peak $T_i \sim 400$ eV which is about 30% larger than that obtained from the high energy slope taken between 1 keV and 2 keV. Thus the T_i temporal variation shown in the upper trace of Fig 2 may be considered only in representing relative changes in the central T_i. The behaviour of both traces shows no systematic change with time in associated T_i's and thereby indicating that there is little change in the peak or distribution of the ion temperature during the discharge. The higher fluctuations at the upper energy range are partly

statistical but may also indicate transient local heating or departures from a Maxwellian distribution. For example, the fluctuations in both energy ranges show some correlation with the neutral flux, the significance of which awaits further analysis. The approximate constancy of T_i is in contrast to $T_e(t)$ which steadily increases during a discharge [2]. Estimates of the total neutral flux emitted by the plasma show that the associated power loss is insignificant (<< 1%).

In assessing the dependence of the central ion temperature with I_p and filling pressure, ρ, we generally use the neutral energy spectrum obtained from a relatively long period (1.6 ms) following peak current time. (This improves the statistics when looking for weak trends but it may mask, or give undue weighting, to transient effects.) We find that at low ρ (1.5-2 mtorr) T_i appears to be independent of current (100-300 kA) and as ρ is increased there is a significant drop in T_i at lower currents (eg at 4 mtorr, T_i decreases by ~ 10% at 200 kA and by ~ 50% at 150 kA). Since the ratio, ξ, of the electron drift to sound speed exceeds unity for our discharges ion heating by micro-instabilities may play a dominant role (eg ion acoustic, which depends on ξ and T_i/T_e).

CONCLUSIONS

The ions are heated and, apparently, thermalised by non collisional processes. Assuming thermalistion, peak ion temperatures of about 400 eV are obtained for a range of currents (100-300 kA) at 2 mtorr. Neutral flux power losses from the plasma are insignificant (<<1% of total).

REFERENCES

[1] C A Bunting, P G Carolan and A R Field: APS 5th Top Conf High Temp Plasma Diagnostics (Lake Tahoe, 1984) K15; Rev Sci Inst 56 (1985) 1103

[2] P G Carolan et al: 10th Int Conf on Plasma Physics and Controlled Nuclear Fusion Research (London, 1984), Vol II, p449

[3] D E Evans, D P Storey and P D Wilcock: this conference, paper 132

[4] M Hughes and D E Post: J of Comp Phys, 28 (1978) 43

SOFT X-RAY MEASUREMENTS ON ETA-BETA II

B Alper, P G Carolan

Culham Laboratory, Abingdon, Oxon, OX14 3DB, England
(Euratom/UKAEA Fusion Association)

S Martini, S Ortolani

Istituto Gas Ionizzati del CNR
Via Gradenigo 6/a - 35131 Padova, Italy
(Associazione Euratom - CNR)

ABSTRACT

Soft X-ray pulse-height measurements were carried out on ETA BETA II at plasma currents between 100 kA and 180 kA, throughout the ~ 2 ms flat top. Electron temperatures rise steadily from ~ 100 eV soon after current peak to well over 200 eV towards the end of the discharge at all currents. The resistance anomaly factor rises over the same period from below 3 to as high as 15 in some cases and this increase displays a universal dependence on I/N. The poloidal beta β_θ is found to vary little over a wide range of plasma parameters but falls slightly with increasing I/N. Intensities of OVII line emissions indicate values well below the level expected at coronal equilibrium suggesting a rapid recycling of oxygen impurities throughout the duration of the discharge.

INTRODUCTION

Using a soft X-ray pulse height (Si(Li)) detector, the electron temperature (T_e) has been measured throughout the current sustainment phase of power-crowbarred discharges on ETA-BETA II RFP, (R=0.65 m, a=0.125 m). The Si(Li) detector system was developed on HBTX1A at Culham [1] for the relatively short pulse lengths, < 8 ms, and for temperatures 100 eV-500 eV which characterise present RFP machines. A sampling ADC is used to record, via CAMAC, the waveform output of the main amplifier. This permits off-line analysis of individual pulse shapes and leads to improved rejection of pulse pile-up and of electronic noise than is possible with conventional MCA techniques. Simultaneous measurements of electron density were made using a multichord He-Ne (λ=3.4 μm) interferometer.

RESULTS

Measurements of T_e, averaged over several discharges, were carried out at nominal values of toroidal current, I_ϕ, of 100 kA, 125 kA, 150 kA and 180 kA.

The filling density was scaled with current in order to operate as close as possible to optimum conditions in terms of I/N by keeping $I/N_o \sim 10^{-14}$ A.m [2], where N_o is the initial line density. Two sets of measurements were made at 150 kA and 180 kA with somewhat different electron density behaviour and are referred to as 'high' and 'low' (density) samples in the figures.

The values of T_e determined from the continuum soft X-ray spectra are shown for all data in Fig 1. At all currents, temperatures are found to rise steadily, and at a similar rate, from ~100 eV soon after current peak to well over 200 eV later in the discharge. Previous measurements of T_e, made during the first part of the discharge by Thomson scattering [3], showed the same trend but with absolute values somewhat lower.

In Fig 1 there is no apparent dependence of T_e on I_ϕ, though linear scaling is often quoted for RFP devices. Only when evaluated at constant I/N is a linear dependence found from these measurements. The scaling factor, assuming T_e=Const.I, is found to rise with I/N from 0.71 eV/kA at $I/N = 3.10^{-14}$ A.m to 1.12 eV/kA at $I/N = 6.10^{-14}$ A.m and to over 2 eV/kA at the highest values of I/N measured. For comparison, the scaling previously obtained by Thomson scattering at current peak and therefore low I/N, [2], corresponded to a value of 0.5 eV/kA.

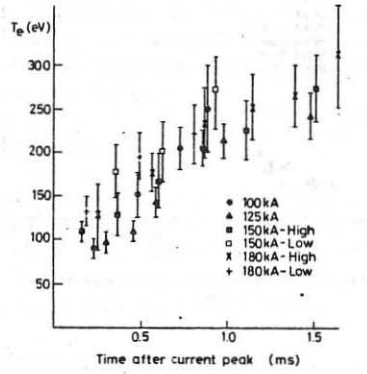

Fig 1 Variation of electron temperature with time

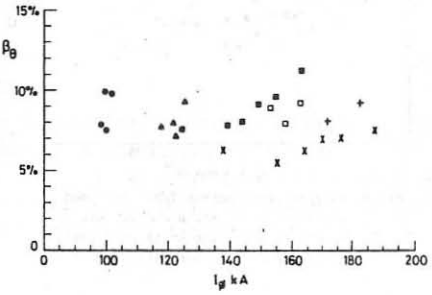

Fig 2 Poloidal beta versus plasma current

A better understanding of the observed relationship between T_e, I_ϕ and n_e behaviour is obtained if we consider poloidal beta ($\beta_\theta \propto T.N/I^2$). Recent theories of RFP plasmas [4] predict that β_θ should be constant over a wide range of conditions. Values of β_θ, calculated for all data assuming $T_e=T_i$, with parabolic temperature profiles and using the electron density measurements, are displayed in Fig 2 plotted against the corresponding values of I_ϕ. It can be seen that β_θ is approximately constant with an average value

of 8% and with no dependence on I_ϕ. When plotted in Fig 3 against I/N there is a trend for β_θ to drop with increasing I/N ($\beta_\theta \sim (I/N)^{-1/4}$) suggesting that the higher values are obtained at the higher densities present earlier in the discharge, though it should be emphasised that a constant temperature profile is assumed throughout.

The observation that β_θ is independent of most macroscopic parameters of the RFP discharge is highlighted when calculations were performed for additional discharges at 100 kA and 125 kA when a quadrant of the toroidal field circuit was not making electrical contact. Though discharges were of short duration with a rapid drop in density, the resulting values of β_θ also shown in Fig 3 display the same properties.

The resistance anomaly factor (Z^*_{eff}), defined as the ratio of the experimental resistivity on axis [2] to that calculated using the Spitzer formula with the measured value of T_e, is shown in Fig 4 for all data as a function of I/N. Values of Z^*_{eff} are seen to rise from ~3 for the earliest measurements (low I/N) to ~15 at the end of the current flat top (high I/N). The increase in Z^*_{eff} with I/N is the same for all currents.

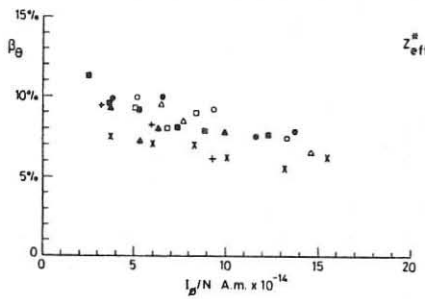

Fig 3 Poloidal beta versus I/N. Included are data at 100 kA, o and 125 kA, Δ, where a quadrant of the toroidal field circuit was not making contact

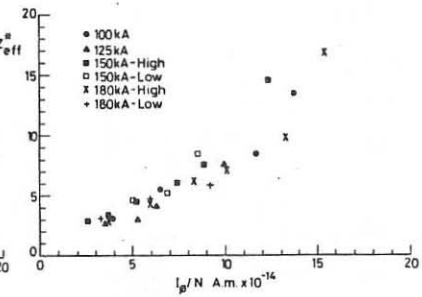

Fig 4 Dependence of the resistance anomaly factor on I/N.

It is possible that this marked rise in Z^*_{eff} represents a corresponding rise in the effective ion charge Z_{eff} through the release and subsequent ionisation of heavy ions in the plasma. (A similar rise in Z^*_{eff} has been observed in HBTX1A discharges [5].) However, to achieve Z_{eff} values as high as 15 for these discharges would require plasmas consisting of almost pure iron, for example. No supporting evidence for this effect has come from spectroscopic measurements. The absence of any major increase in impurity concentration is also indicated by values the X-ray anomaly factor ζ (the ratio of the measured intensity of the continuum spectrum to that calculated for a pure hydrogen

plasma). During the discharge ζ remains approximately constant, in marked contrast to the rapid increase in Z^*_{eff}.

Various models of the RFP (eg the dynamo mechanism) do suggest anomalous values of the resistivity (eg [2]) but the values predicted are in general ~2. Higher values of Z^*_{eff} could be obtained assuming unrealistic profiles with large values of J almost up to the plasma boundary where values of T_e are low. At high values of I/N the streaming parameter ($v_d / v_{th,e}$) has risen to over 0.3 which suggests that the Spitzer formula may not be valid in this region and that micro-instabilities could effect the observed values of resistivity. The absence of any electron runaway phenomena in the Si(Li) data, particularly later in the discharge when the electrons are expected to be essentially collisionless, also points to the presence of other than coulomb collisional mechanisms for electron momentum loss.

Some evidence for OVII emission has been obtained from the Si(Li) data at 125 kA, at X-ray energies down to 500 eV. A sharp rise in the soft X-ray flux observed below 800 eV can be explained by OVII line emissions (~ 571 eV). The intensity fitted to this spectrum is nearly two orders of magnitude below that expected from 1%-2% oxygen at coronal equilibrium. The observed emissions from OVII can be explained if the impurity ions are far from coronal equilibrium due to low electron densities and to continuous fast particle diffusion and recycling at a rate of ~ 10^{22} m^{-3} s^{-1}. Short impurity confinement times would add to the difficulty of explaining the high Z_{eff}, discussed above.

CONCLUSIONS

The measured rise of T_e throughout the current sustainment phase of RFP discharges on ETA-BETA II is matched by a corresponding fall in electron density such that a constant value of β_θ is maintained. The resistance anomaly factor is found to rise rapidly with I/N. This rise appears difficult to explain by impurities - at least not in a simple fashion.

REFERENCES

[1] B Alper & P G Carolan: Culham Laboratory report, in preparation.

[2] V Antoni et al: Istituto Gas Ionizzati Report, Padua IGI/03, May 1983

[3] V Antoni et al: Plas. Phys. and Cont. Nucl. Fus. Res., Vol 2, IAEA Vienna (1985) 487

[4] J W Connor, J B Taylor: Physics of Fluids, 27, 11 (1984) pp 2676-2681

[5] P G Carolan et al: Plas. Phys. and Cont. Nucl. Fus. Res., Vol 2, IAEA Vienna (1985) 449

A COMPACT TOROID FORMED BY MULTI MAGNETIZED T-TUBES*

S. SINMAN
Middle East Technical University, Electrical Engineering Department, Plasma Engineering Laboratory, Ankara-Turkey

A. SINMAN
Ankara Nuclear Research and Training Center, Electron Physics Laboratory, Ankara-Turkey

In recent years, the spheromak and Field Reversed Configurations (FRC) which are two different types of compact tori have extensively been investigated. The spheromak configuration itself has successfully been generated by three types of formation schemes such as (i) the magnetized co-axial gun, (ii) the field-reversed θ pinch with center column Z discharge and (iii) electrodeless quasi static scheme (Princeton Proto S-1 Spheromak).

As it is well known, one of the classical plasma guns is T-shaped pressure driven shock tube. Besides its simple structure, T-tube is a system with a lover impurity because of it contains minumum surface-volume rate but on the other side with a disadvantage of decreasing blast shock wave in time.

In the new spheromak production scheme presenting in this study, a T-tube developed as a plasma injector is used.

The modified T-tube consists of the complex magnetic field, the self-preionizer, the gas puffer and a rather short (10-20 cm) horizontal leg. The complex magnetic field on the leg combines with a thin iron cored cusp and octopole fields.

By this injector, a dense and warm plasma ring ($n_e = 10^{17}$ cm^{-3}, T_e = 5 - 15 eV and H or D gas pressures in the range of 20 - 50 mTorr) is pushed in a cylindrical flux conserver with an aspect ratio of 75%. The plasma ring is parallel to the vertical plane of the conserver. This ring establishs the toroidal field of the spheromak. For a symmetrical and stable toroidal field, four T-injectors take place around the conserver in 90^0 aparts. The poloidal field of the spheromak is formed by the FRC. The thin cusped field assists to shut in plasma ring and the octopole confines the ring stable. The FRC coils (equilibrium field coil system) are settled down to outside of the conserver.

After the application of FR field, four T-injectors are fired. A short duration of 3 - 5 μs later, the magnetic mirror ratio of FRC system is rised up with respect to inital value. Thus the formation of spheromak is completed. This system submitting with two T-injectors of 3 kJ each is under construction.

According to the theoretical results, for the electron density and temperature of this spheromak plasma in the range of 10^{16} - 10^{17} cm^{-3} and 10 - 20 eV and in the case of successive operation for two T-injectors, the plasma life time 100 - 200 μs are expected.

(*) Research is sponsored by the Division of Research and Laboratories, IAEA Vienna, under contract 3823/RB with the Turkish Atomic Energy Council.

LOCAL DRIFT PARAMETER, j/n_e AND RESISTIVITY ANOMALY MEASUREMENTS IN CTX SPHEROMAKS

H.W. Hoida, Cris W. Barnes, I. Henins, T.R. Jarboe
G. Marklin, C.J. Buchenauer, and S.O. Knox

Los Alamos National Laboratory
Los Alamos, New Mexico USA 87545

INTRODUCTION - In a spheromak, the magnetic fields confining the plasma are generated primarily by internal currents rather than external coils. In order to provide information on the possible existence of current-driven microinstabilities, localized measurements of the ratio of the drift velocity of the electrons generating the internal current to the thermal velocity, $V_d/V_{th} \propto j/n_e/T_e$ (known as the drift or streaming parameter), and j/n_e ($\propto V_d$) are needed. These microinstabilities are in some theories associated with an increase in the resistivity anomaly factor ($\eta/\eta_{Spitzer}$). We present results on local measurements (at the magnetic axis) of the values of V_d/V_{th} and $\eta/\eta_{Spitzer}$ by combining data from the spatially-resolved diagnostics employed on the CTX spheromak experiment, coupled with current density profile information inferred from surface current measurements and zero pressure equilibrium calculations. The values of V_d/V_{th} and j/n_e appear to be correlated with local variations in $\eta/\eta_{Spitzer}$, and can be changed by varying the plasma density. Data sets are presented for three values of n_e.

Spheromaks are generated in CTX by a coaxial helicity source.[1] The spheromaks are formed in a mesh flux conserver (MFC)[2] which has a major radius of 67 cm and a depth of 62 cm. A square current pulse is applied to the source electrodes, with the current amplitude typically 250 kA and the pulse duration 850 μs. The spheromak disconnects from the source at the end of the current pulse. The peak of the spheromak toroidal current is ~550 kA.

MEASUREMENTS AND ANALYSIS - The measurements shown in this paper are concerned only with the decaying portion of the discharge (after the spheromak has disconnected from the source). The areal electron density profile is measured with a six-beam multichord interferometer. This profile is then inverted using a simple subtraction algorithm assuming toroidal symmetry and uniform density over the annuli formed between adjacent beam impact parameters to yield the electron density profile. The electron temperature is measured with a space-resolved Thomson scattering apparatus. Due to experimental modifications limiting the field of view, the temperature is measured only near the magnetic axis at radii between 35 cm and 55 cm. The temperature is averaged over this "core" and also shot-to-shot. The current density profile is inferred from surface currents measured by Rogowski loops in the MFC, combined with calculations from a numerical model of the zero-pressure equilibrium in an ideal flux conserver.[3] The measured and the calculated surface currents are then compared to determine the surface current density profile in the spheromak, the poloidal flux, and the radius of the magnetic axis.

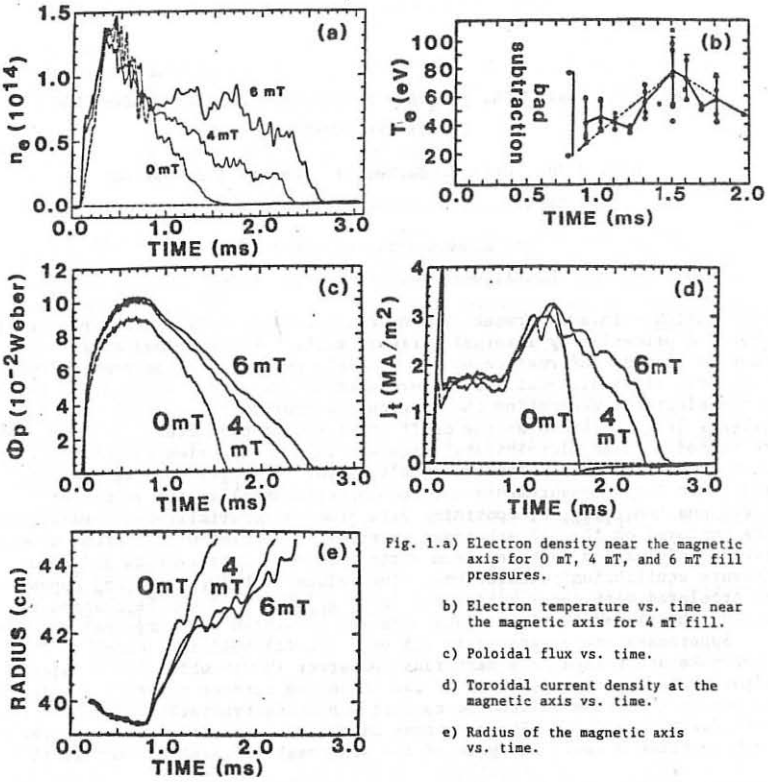

Fig. 1.a) Electron density near the magnetic axis for 0 mT, 4 mT, and 6 mT fill pressures.

b) Electron temperature vs. time near the magnetic axis for 4 mT fill.

c) Poloidal flux vs. time.

d) Toroidal current density at the magnetic axis vs. time.

e) Radius of the magnetic axis vs. time.

The drift parameter at the magnetic axis is determined from the local electron density, temperature, and current density. The local resistivity is determined from $\partial\Phi_p/\partial t$ (where Φ_p is the spheromak poloidal flux), the current density, and the radius of the magnetic axis. The local $\eta_{Spitzer}$ is determined from the measured temperature.

RESULTS - The background fill pressure determines the operating electron density of the spheromak after the helicity source is turned off. The electron density in turn affects the other plasma parameters. Figure 1 shows graphs of the measured values near the magnetic axis of n_e and j_t for 0 mT, 4 mT, and 6 mT fills. The radius of the magnetic axis is plotted in Fig. 1.e. The electron temperature for 4 mT fill is plotted in Fig. 1.b., the temperature for 6 mT fill is ~28 eV, and that for 0 mT and $t \geq 1.2$ ms is undetermined due to the low density. The results of calculations of the drift parameter and resistivity anomaly for two cases are shown in Fig. 2.a. (4 mT and 6 mT fills). Figure 2.b. shows the resistivity anomaly vs. j/n_e for the same data. For the 0 mT fill, we have calculated $\eta_{Spitzer}$ assuming the same temperature as the 4 mT fill. The results are plotted in Fig. 2.c. along with the data of Fig. 2.b. for scale.

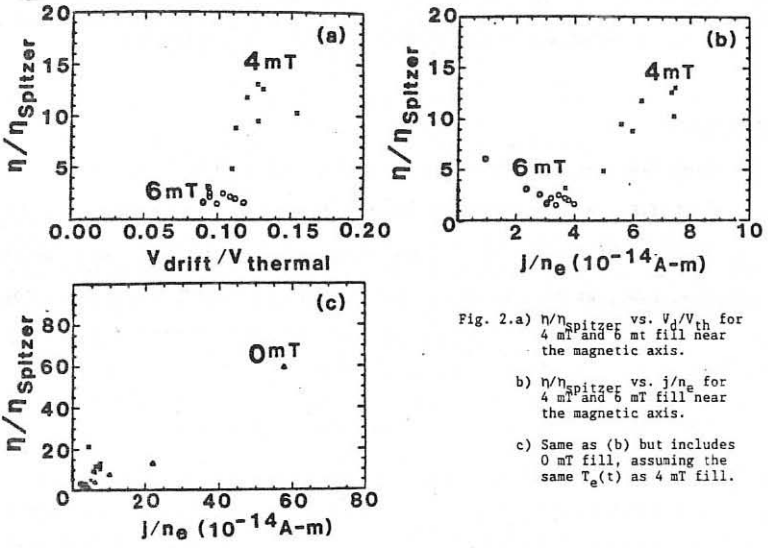

Fig. 2.a) $\eta/\eta_{spitzer}$ vs. V_d/V_{th} for 4 mT and 6 mt fill near the magnetic axis.

b) $\eta/\eta_{spitzer}$ vs. j/n_e for 4 mT and 6 mT fill near the magnetic axis.

c) Same as (b) but includes 0 mT fill, assuming the same $T_e(t)$ as 4 mT fill.

Previous studies of the resistivity have been done in decaying spheromaks in a 0.4 m radius MFC under conditions similar to the present 4 mT operation.[4] The global $\eta/\eta_{Spitzer}$ times Z_{eff} was found to be in the range of 5-6.

DISCUSSION - The initial plasma density (for a specific combination of electrodes and bank configuration) increases with increasing source current. Although the resulting plasma current may be higher, so is the electron density, and the initial operating range on j/n_e and V_d/V_{th} is restricted. During the decaying portion of the discharge several aspects of the plasma behavior are dominated by the level of the background fill. The fill pressure plus the particle recycling time determines the operating density in the decay phase and, to some extent, the electron temperature. The background fill appears to affect the plasma by changing V_d/V_{th}, which in turn affects the resistivity anomaly and limits the lifetime of the discharge. Thus for high fill pressures (6 mT) the plasma density is high resulting in a low anomaly factor, but the temperature is cold resulting in near classical resistivity. For higher fill pressures (> 6 mT) the plasma is colder still and although the resistivity is near classical the lifetime is decreased. The longest lifetimes are at 6 mT fill. For a moderate fill (4 mT) the temperature is higher, but V_d/V_{th} increases as does the resistivity anomaly resulting in a slightly shorter discharge. The highest temperatures are achieved at 4 mT. For no fill, we cannot measure the temperature for late times (we presume it to be higher) but j/n_e is seen to increase dramatically as does the resistivity resulting in a shorter yet discharge. Thus it appears that the lifetime of the spheromak during the decay becomes limited by enhanced resistivity associated with the parameter V_d/V_{th} or j/n_e when we try to increase j/n_e to heat the plasma.

Hotter spheromak temperatures are needed to determine differences in the effect of V_d/V_{th} and j/n_e on $\eta/\eta_{Spitzer}$. We will continue to investigate the spatial influence of V_d/V_{th} and j/n_e on the resistivity anomaly and also their influence on the energy and particle confinement.

REFERENCES

1. Jarboe, T.R., et al., Phys. Rev. Lett. 51, 39 (1983).

2. Jarboe, T.R., et al., Phys. Fluids 27, 13 (1982).

3. Knox, S.O., et al., LA-UR-85-2045 (submitted to Phys. Rev. Lett. 1985).

4. Barnes, C.W., et al., LA-UR-84-3667, (submitted to Nuclear Fusion, 1985).

A FIELD REVERSED CONFIGURATION GENERATED BY MEANS OF A ROTATING MAGNETIC FIELD

I.R. Jones and A. Knight
School of Physical Sciences
The Flinders University of South Australia
Bedford Park, S.A. 5042, Australia

Abstract

Results from a cylindrical rotating field experiment show that a Field Reversed Configuration can be produced and maintained using the rotating magnetic field technique of driving plasma currents. In the experiment reported here a plasma current of 1.2 kAmps was driven for 40 msec without any apparent instabilities. The lifetime of the configuration appeared to be limited only by the duration of the r.f. current pulse used to produce the rotating field.

Introduction

Theoretical models [1], [2] show that provided the angular frequency, ω, of an applied transverse rotating magnetic field, B_ω, lies between the ion and electron cyclotron frequencies (ω_{ci}, ω_{ce}; calculated with reference to the amplitude of the rotating field) and provided the electron-ion momentum transfer collision frequency is much less than the electron cyclotron frequency, then the magnetic field can penetrate a cylindrical plasma column and entrain the electrons so as to produce a steady azimuthal current. This azimuthal current generates an axial magnetic field component, $B_e(r)$ whose direction depends upon the sense of rotation of the rotating field. For the experiment described in this paper, $B_e(r)$ must be in the opposite direction to an initially applied steady axial magnetic field B_a in order to achieve magnetic confinement. It follows that if the driven current is sufficiently large, the axial field will be reversed.

The total magnetic field, therefore, has three components; (1) an applied d.c. axial bias field, B_a, (2) an applied transverse r.f. rotating field B_ω which drives a steady azimuthal plasma current thus producing (3) a d.c. axial field $B_e(r)$ which reverses the applied field B_a. The total magnetic field lines (steady plus rotating) at any instant of time are open. However the steady part of the total field is closed. The resulting plasma/field configuration can equally well be termed a Reversed Field Configuration or a Prolate Rotamak.

Description of experiment

A schematic diagram of the experimental apparatus is shown in Fig. 1.

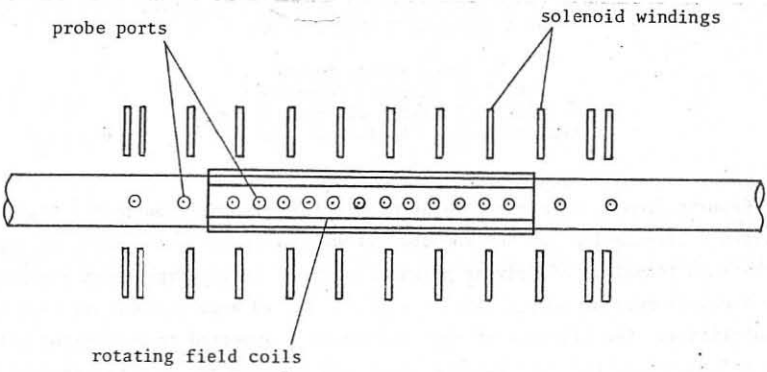

Fig. 1. Schematic diagram of experimental apparatus

The discharge vessel was a 10 cm diameter pyrex glass tube, 1.5 m in length. Two orthogonal dipole coils were wound over the central 50 cm. These were fed with r.f. current pulses of the same frequency but dephased by 90° to produce the transverse rotating magnetic field. The frequency of the r.f. pulse was 1.0 MHz and its duration was 40 msec. A solenoid generated a steady axial bias field over a 1.0 m length of the discharge vessel. The amplitude of this field could be varied continuously from zero up to a maximum of approximately 100 Gauss and it lasted for 50 msec. The two applied fields produced by these external coil structures are illustrated in Fig. 2.

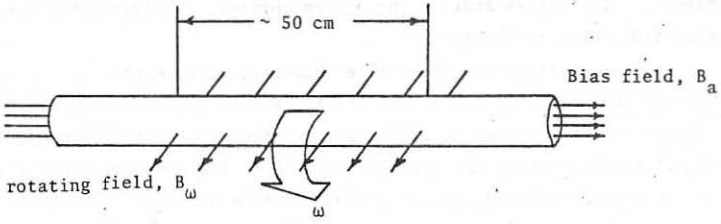

Fig. 2. The applied fields produced by the coil structures of fig. 1.

A small glass tube (5.0 mm o.d.) could be inserted across the diameter of the vessel at any of sixteen axial positions. A Hall-effect magnetic probe could be inserted into this tube to provide measurements of the total axial magnetic field.

Results

For the discharges reported in this paper the working gas was Argon at a filling pressure of 2m Torr. Fig. 3 shows the total axial field as a function of time with the probe located at r = 0, z = 0 (at the centre of the rotating field coil structure).

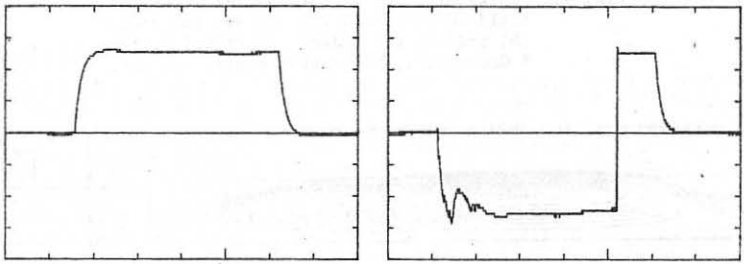

Fig. 3. Measured axial field as a function of time
(a) when no rotating field is applied and
(b) when rotating field is applied.
(Vertical scale: 10 Gauss/div.,
horizontal scale: 10 msec/div.)

Application of the rotating field drives sufficient current to reverse the applied bias field of 25 Gauss. By traversing the magnetic probe across diameters of the discharge vessel at many z-positions it was possible to obtain radial profiles typified by those shown in Fig. 4.

The axial field is observed to be reversed at the centre of the rotating field region. Towards the ends of this region, however, the field is weakened but is not reversed. The poloidal flux contours shown in Fig. 5. were obtained by numerical integration of these magnetic field measurements. It can be seen from Fig. 5 that a reversed field configuration was produced over an axial length of ~ 30 cm with the separatrix lying at the vessel wall. The configuration appears to be stable and its lifetime is only limited by the duration of the r.f. current pulse used to produce the rotating field.

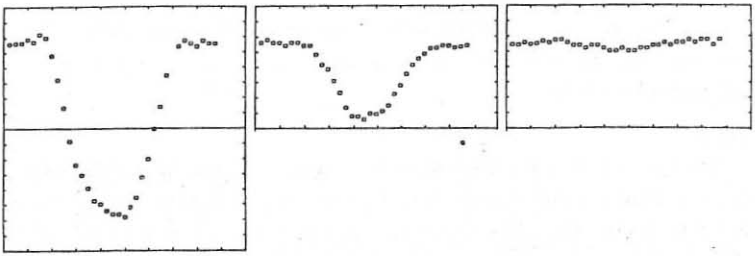

(a) (b) (c)

Fig. 4. Radial profiles of total axial magnetic field 20 msec into r.f. pulse; (a) z=0, (b) z=20cm, (c) z=40cm. (Vertical scale: 5 Gauss/div., horizontal scale: 2cm/div.

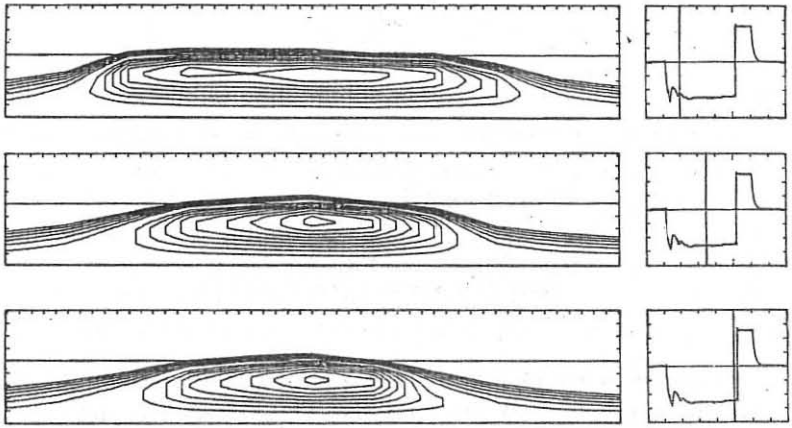

Fig. 5. Measured poloidal flux contours at three times during the discharge. Diagrams at right indicate the times at which the contours were measured.
Top trace: t = 10 msec after application of the rotating field, middle trace: t = 25 msec, bottom trace: t = 40 msec (contour spacing = 1×10^{-7} Webers).

References

[1] Jones, I.R. and Hugrass, W.N., 1981 J. Plasma Phys. 26, 441.

[2] Hugrass, W.N. 1982 J. Plasma Phys. 28, 369.

LONG DURATION ROTAMAK EXPERIMENTS

I.R. Jones and H. Kirolous
The Flinders University of South Australia
Bedford Park, S.A. 5042, Australia

Abstract

The toroidal plasma current in a compact torus configuration can be generated using a transverse rotating magnetic field. The results obtained in a moderately high powered, long duration Rotamak experiment are presented. An oblate compact torus configuration was generated and sustained for the duration of the rotating field pulse.

Introduction

The current drive technique using a rotating magnetic field of appropriate amplitude and rotational frequency is well established.[1-4] The Rotamak is a compact torus device in which a rotating magnetic field is used to maintain the toroidal plasma current.[5],[6] An additional externally generated poloidal field (the 'vertical field') is required to keep the plasma in equilibrium. The amount and duration of the toroidal plasma current depends mainly on the power and duration of the r.f. pulses which are used to generate the applied rotating field. The moderately high power and long duration Rotamak experiments described in this paper are the logical successors of two previous studies which used r.f. pulses of high power and short duration (2MW, 80 μsec)[7] and pulses of low power and long duration (6 KW, 10 msec).[8]

Experimental Apparatus

The rotating magnetic field was generated by feeding two r.f. current pulses of the same amplitude and frequency, but dephased by 90°, through a pair of orthogonally oriented Helmholtz coils located on the outside of the 10 litre spherical pyrex discharge vessel. The current pulses were generated using two high power (~ 80 KW) Class C power amplifiers. The vertical field required for equilibrium was generated via a pair of coils located on the z-axis. A schematic diagram of a Rotamak device is shown in Fig. (1).

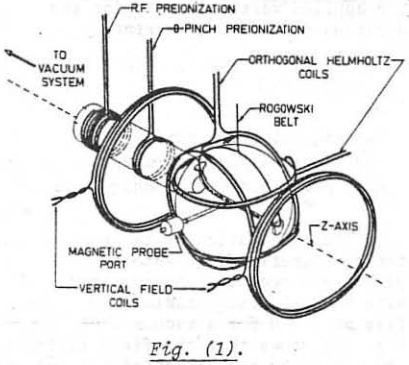

Fig. (1).
Schematic diagram of a Rotamak device

Twenty one retractable magnetic probe guides allowed the axial component of the total steady magnetic field $B_z(r,z)$ to be measured at a matrix of points lying in a poloidal cross section of the discharge vessel and along the z- axis. The filling gas was preionized using coils wrapped around the tube leading to the vacuum system.

Diagnostics

A Hall probe was used to measure the axial (z) component of the steady poloidal magnetic field. The Hall signal was filtered, digitized and stored to be used to construct the poloidal flux contours. A conventional magnetic probe was used to measure the rotating field at number of positions to monitor the field penetration into the plasma. The total driven plasma current I_θ was measured by means of a Rogowski belt threaded through the central axis glass tube and around a semicircular section of the discharge vessel. An 8 mm microwave interferometer was utilized to obtain the average electron number density across a diameter of the discharge vessel. The power delivered to the plasma was recorded using a set of voltage and current probes.

Experimental results

The results presented in this paper were obtained for one particular set of initial conditions. The filling pressure was 1.5 mTorr of Hydrogen. The amplitude of the vertical field (at r=0, z=0) was 23 gauss. The 40 KW r.f. output power from each amplifier produced a 27 gauss rotating field (at r=0, z=0) for 40 msec duration and rotational frequency of 1 MHz. Fig. (2) shows the oscillograms for I_{rf}, $B_V(0,0)$ (in the absence of plasma), I_θ and $B_z(0,0)$. A toroidal plasma current of 1080 Amps was driven and the associated poloidal field reversed the applied vertical field for the duration of the r.f. current pulse.

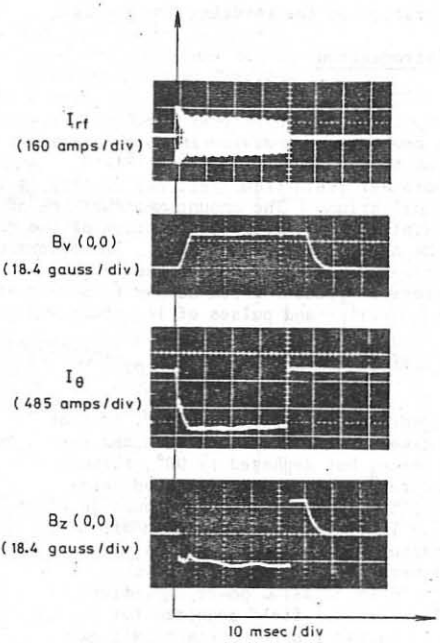

Fig. (2).

I_{rf}, $B_v(0,0)$, I_θ and $B_z(0,0)$ oscillograms for moderately high power Rotamak discharge

The penetration of the rotating magnetic field into the plasma was measured and compared with the calculated radial profile at z = 0 for a vacuum shot. Fig. (3) shows that the field failed to perfectly penetrate the interior of the plasma by the action of the induced r.f. poloidal screening current. Nevertheless, the penetration appeared to be better than that expected on the basis of the classical skin effect.

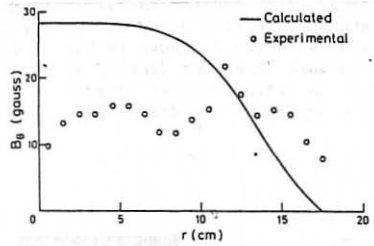

Fig. (3).

Penetration of rotating field into plasma

The radial profiles of $B_z(r)$ at twenty-one z-positions and at 1024 selected times (separated by 100 μsec) were measured. The poloidal flux function defined as

$$\psi(r,z,t) = 2\pi \int_0^r r' B_z(r',z,t)\, dr' ,$$

was obtained by numerical integration. The excellent reproducibility of the Rotamak discharges (e.g. two I_θ traces have been overlayed in Fig. (2)) allowed the data needed to plot the poloidal flux contours to be collected from 735 separate shots. The plots in Fig. (4) show that an oblate compact torus configuration was maintained, in an apparently stable manner, for the duration of the rotating magnetic field. Fig. (5) shows the time evolution of the separatrix (R_{sep}), magnetic axis (R_{ma}) and neutral point (Z_{np}) during the r.f. pulse duration.

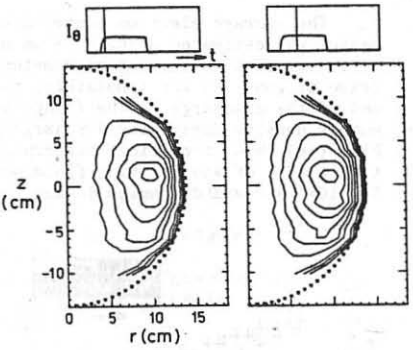

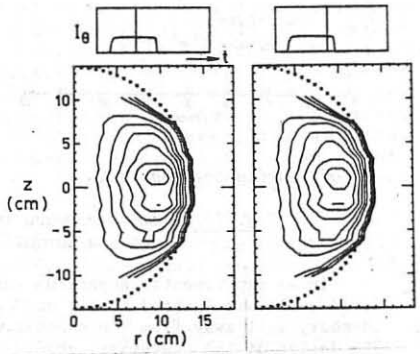

Fig. (4). Poloidal flux contours (Contour spacing $\pi \times 10^{-6}$ weber)

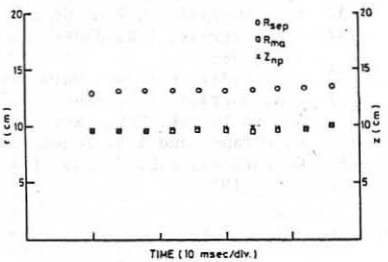

Fig. (5). Plasma position

The average electron number density across a diameter of the discharge vessel was estimated using an 8 mm microwave interferometer. Since the interpretation of the interferometer output during the plasma formation phase (rise of density) was impossible, the fringes were counted backwards from the end of the discharge. The fringe pattern and the slow decay in the electron number density during the discharge period (40 msec) is shown in Fig. (6a). Fig. (6b) shows the fringe pattern and the fall in number density at the termination of the rotating field pulse. An average number density of 5×10^{18} m^{-3} was estimated during the main period of the discharge.

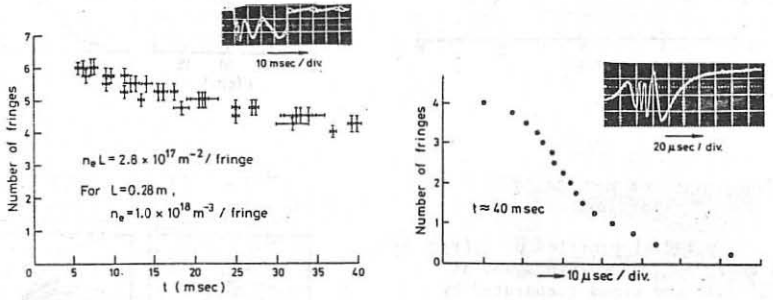

(a) during the discharge *(b) at the end of the discharge*

Fig. (6). 8mm microwave interferometer fringe pattern and the variation of electron number density.

In an experimental apparatus currently being constructed the rotating field coils are located within an 80 cm diameter stainless steel discharge chamber, well away from the chamber walls in order to minimize eddy currents. The design of the new vessel should ensure that plasma equilibria which sit well away from the vessel wall can be studied.

References

/1/ H.A. Blevin and P.C. Thonemann, Nucl. Fusion Suppl. part I, p.55 (1962).
/2/ I.R. Jones and W.N. Hugrass, J. Plasma Phys. 26, 441 (1981).
/3/ W.N. Hugrass and R.C. Grimm, J. Plasma Phys. 26, 455 (1981).
/4/ W.N. Hugrass, I.R. Jones and M.G.R. Phillips, J. Plasma Phys. 26, 465 (1981).
/5/ I.R. Jones, Flinders University Report No. FUPH-R-151, (1979).
/6/ W.N. Hugrass, I.R. Jones, K.F. McKenna, M.G.R. Phillips, R.G. Storer and H. Tuczek, Phys. Rev. Lett. 44, 1676 (1980).
/7/ G. Durance and I.R. Jones, Submitted to Phys. Fluids (1984).
/8/ G. Durance, B.L. Jessup, I.R. Jones and J. Tendys, Phys. Rev. Lett. 48, 1252 (1982).

Generation of Double Toroids of the Spheromak-Type in the Heidelberg Spheromak Experiment

H.Bruhns, C. Allgeier, G. Raupp, J. Steiger, A. Weichelt
Institut für Angewandte Physik II der Universität
Albert-Überle-Str. 3-5, D-6900 HEIDELBERG 1
Germany (FRG)

The study of spheromaks has proved the exceptional internal stability of this configuration in low temperature plasmas. Exceptions are the low number n modes. Issues of major concern for the future perspective of spheromaks are - apart from the study of hotter plasmas - the merging of toroids, the formation efficiency and to explore the possibility to translate the plasma. This latter option is impeded by the extreme liability of the spheromak to n=1 modes which requires the use of conducting walls or (passive) coils close to the separatrix of the plasma. However, the applicability of coils is unlikely to be compatible with a plasma translation scheme, while a close-up wall is a serious problem if hot plasmas are envisaged.

A possible method to maintain stability of the plasma against tilt and shift modes has been proposed /1/. This method consists in the formation of axially connected doubly toroidal configurations. Such plasmas are made up of two spheromak-like toroids which are interlinked by a common outer flux-shell and might have the additional advantage of enhancing the formation efficiency in a theta-z-pinch scenario. Fig. 1 depicts such a double toroid in an idealized fashion. Note that there are closed field-lines encircling around each toroid separately as well as linking them. Schematically, the coil arrangement for the generation of this poloidal configuration is sketched. Not shown are the electrodes for the axial current which is needed for the toroidal magnetic field component.

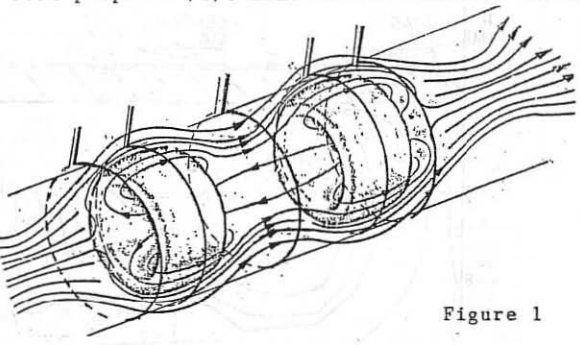

Figure 1

The purpose of this paper is to report on initial experiments to realize such structures.

We have equipped the HSE-device /1,2/ with an additional central coil and a correspondent capacitor bank and circuitry with an energy content of a total of 15 kJ. Also, the location of the main field and bias field coils have been adapted in order to allow for the simultaneous generation of a toroid on either side of the symmetry plane of the device. Both toroids should have a (separatrix) length-to-radius ratio of about 2 or less. The plasma- and bank parameters chosen are similar to the ones of single toroid investigations /2/.

The formation scenario is similar to the one of single toroids (i.e. conventional spheromaks), except that shortly before or after the onset of the mainfield bank the central bank is switched. This leads - depending on the time constant of this circuit - to a more or less rapid central intersection of the axially elongated toroid which is formed initially. A study of H_β stark broadening shows an initial increase of density near the symmetry axis which is connected with the axial current, subsequently, the density maximum is found near the magnetic axis. This is similar to paraxial observations made in single toroids.

Fig. 2 shows a plot of the poloidal flux in a r-z plane at t=15 usec i.e. in the first part of the stable phase. Two separate toroids, which are interlinked by a common flux shell, can be distinguished. With the present diagnostics, it was possible to measure the three orthogonal magnetic field components at radii up to only 10 cm while the inner radius of the vessel is 15 cm. For convenience, at larger radii the flux surfaces are extrapolated in the left hand part of the graph in an approximate fashion. Axially the plot extends to the separatrix. The main bank coils are located at larger z-positions.

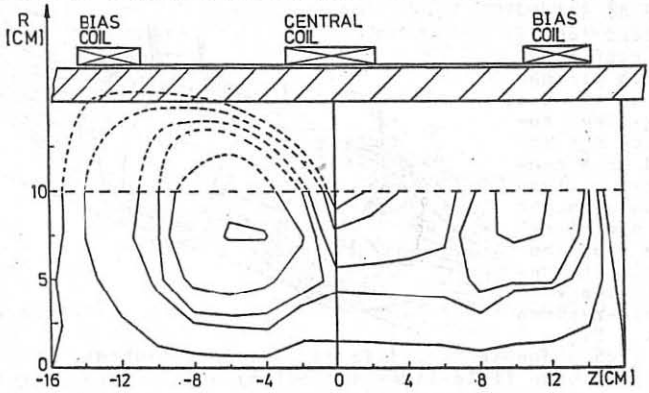

Figure 2

Experimentally, we can adjust the connecting flux shell by varying the time constant and/or the amplitude of the central bank appropriately. Thus it is possible to maintain the 'flux-

bridge' between the two toroids up to about 15 to 20 usec. Also, it is possible to cut this connecting shell apart at some fraction of that time. Fig. 3a shows the time history in the symmetry point of the whole configuration for a gentle operation of the central bank which yields a relatively stable configuration as long as the flux-bridge exists. Note that this time is much longer than a single toroid would exist without additional stabilizing means. By inspection of fig. 4a (which shows the radial profiles of the axial field in the center of one of the axially connected tori) it is evident that a stable state exists.If we increase the charging voltage of the central bank (or delay the crowbar) then the flux-bridge is cut apart soon after the field reversed configuration has been established (fig. 3b). In this case the radial profiles of the axial field in the center of one of the toroids clearly show a shift instability (fig. 4b).

We conclude from our investigations that it is possible to enhance the stable lifetime of a spheromak-like field reversed configuration by forming the plasma into a double toroid structure. We assume this to be due to the aligning effect of the mutual interaction of the magnetic moments of the two toroids. This should compensate the adverse action between the magnetic moments of the two toroids and the external field which causes the tendency to perform a n=1 deformation. Also, (in terms of field-curvature or index) we have individually almost spherical or slightly oblate toroids which combined, however, appear elongated with respect to the external field. Hence, separa-

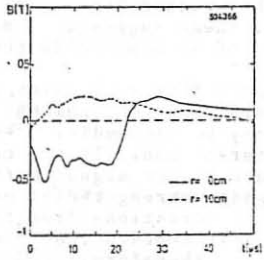

Figure 3a

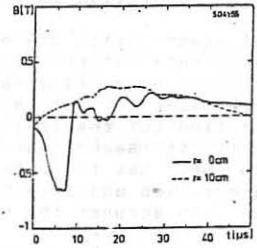

Figure 3b

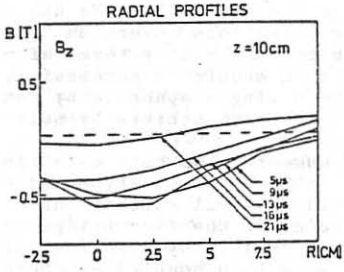

Figure 4a

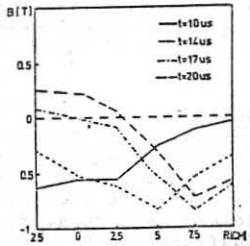

Figure 4b

tely they should be tilt-stable while combined shift stable. Of course, these suggestions are crude and are presented only in the absence of an applicable theory.

Although a flux-plot gives good insight into the structure of the configuration, it relies on the assumption of axisymmetry and hence may be misleading. We find good symmetry around the point of intersection. In the centers of the toroids, however, the structure of the magnetic field is much more complex. Especially, one finds strong radial components of the magnetic field which indicate deviations from the axisymmetric state . Also, from figure 2 it appears that the toroids are of quite different flux-content. Therefore, an issue of further investigations will be the symmetry of the configuration. We think however that the basic interpretation is unaffected by these precautions.

Several other topics are of concern. We like here to mention that the amplitude of the central field which is needed to separate the two toroids is much smaller than one would expect from pressure balance. This is consistent with early observations of a reconnection (or tearing) instability in the PS- experiment /3/. In fact, it seems that with the central bank the reconnection process only has to be triggered. A complete interpretation of the generation and interaction of the two toroids certainly has to take into account the mass-dynamics of the plasma as well.

To further study these reconnection and merging processes /4/, we are in the course of equipping the HSE-device with two sets of figure eight coils. We use the same type as in the single toroid investigations (version 2) /2/. This might allow us to maintain the toroids stably even after the loss of the common flux-shell. If this should be successful, we could make the toroids coalesce into a single spheroid by removal of the central magnetic barrier which we can achieve by suitably programming the central coil.

In summary, we have established a double toroidal configuration of the spheromak-type and have shown that the stable period of field reversal exceeds that obtained with a corresponding single toroid. If the flux bridge between the toroids is destroyed, they decay rapidly by a shift-instability. - The formation efficiency is more than doubled as conpared with the single toroid formation case. We obtain a magnetic energy of more than 600 Joules as compared to 250 Joules in the conventional spheromak-scheme although the energy-input is slightly less in the double toroid case.

References

/1/ H. Bruhns et al., Proc. 6th. Symp. on the Physics of Compact Toroids, Princeton 1984, p. 25 (Princeton, PPPL 1985)
/2/ H. Bruhns et al. this conference
/3/ H. Bruhns et al. Phys. Fluids 24, 1336 (1981)
/4/ Reiman, A., Phys. Fluids 25, 1885 (1982)
Shafranov, V.D., Nucl. Fusion 19,187 (1979)

This work is supported by the Deutsche Forschungsgemeinschaft

Studies of Single Toroids in the Heidelberg Spheromak Experiment

H.Bruhns, C. Allgeier, G. Böckle, G. Raupp, J. Steiger,
A. Weichelt, G. Wintermeyer
Institut für Angewandte Physik II der Universität
Albert-Überle-Str. 3-5, D-6900 HEIDELBERG 1
Germany (FRG)

The spheromak /1/ belongs to the class of compact toroidal plasmas (CT's). Interest in this configuration with both poloidal and toroidal fields of approximately equal amplitude has increased since it was shown that the plasma can be created with various schemes. This is because the resulting near-minimum energy state is quite independent from the detailed history of formation due to the subsequent relaxation /2/.

In this paper we shall present initial results from the HSE-device for the formation of conventional spheromaks with a low-temperature plasma.

The Heidelberg Spheromak Experiment (HSE) utilizes the combined theta- and z-pinch formation method /3/, hence belongs to the same class of experiments as the Maryland PS-devices. The dielectric cylindrical vacuum vessel has an inner diameter of 30 cm and a length of 1 m. Three separate capacitor banks with a total of 95 kJ are switched to the experiment to generate the plasma (after suitable hf-preionization). Two banks energize solenoidal coils to produce a configuration akin to the field reversed theta-pinch, i.e. providing a poloidal magnetic field structure. The third bank is switched to axial electrodes and generates an annular z-pinch just before the axial magnetic field is reversed. The pinch current closes inside the plasma and establishes the toroidal field component of the configuration which then relaxes towards the spheromak state. We report here on experiments in the 20 to 45 kJ range of stored energy. The standard filling pressure corresponds to 2.10^{15} cm^{-3}; formation is possible down to 2.10^{14} cm^{-3} with the present preionization scheme.

Due to the dielectric walls and the simple vacuum system the experiment operates in a temperature regime still accessible to magnetic probe diagnostics which is performed with various probes and allows one to obtain simultaneously a complete radial scan with one shot. Other diagnostics include spectroscopy in the visible, Thomson scattering for the measurement of n_e, T_e, and radiation energy and power loss measurements.

The formation of the spheromak plasma in the present set-up pro-

ceeds on a time scale considerably slower than in the PS-experiments with a half period of the axial current of 18 usec and a quarter period of the field reversing solenoidal field (theta-pinch) of 30 usec. As the magnetic fields range around .3 to .8 tesla, the typical Alfvén radial transit time $t_A \ll 1$ usec and hence the formation can be considered as slow or 'inductive' rather than pinch-like.

The axial current initially passes through the plasma in a broad channel: a rather flat current density is found up to r = 8 cm. When the axial current reaches its maximum (about 180 kA), this channel has narrowed to 2.5 cm. 67 kA are flowing within this channel, 165 kA within a radius of 10 cm. At the same time the axial field on axis has increased to values of .6 to 1 tesla - typically 4 ... 8 times the bias level; at low bias amplitudes enhancements of a factor of 10 to 20 or even more are observed. Also the absolute amplitude may be larger. This increase is accompanied by a decrease of the axial field at large radii. Shots without field reversing main field show that during this phase the total axial flux through the vacuum vessel increases by a factor of 1.3 to 3 depending on the ratio of bias field to axial current amplitude. Hence a strong field amplification by the axial current takes place. If the bias field is too weak, kink-like disturbances are observed which are not prominent at standard conditions. To invoke flux amplification in addition to compression is consistent with the slow time scale although (axial) spectroscopic observations give indications of an increase of density near the symmetry axis during the relevant period. If this happens in the central region where the toroid is to form, then either significant heating or a rapid axial mass flow has to be assumed since 5 to 8 microseconds later the Stark-broadening corresponds to about fill density.

Without additional stabilizing means the toroids undergo a rapid decay. While the rotation of the two-dimensional magnetic field vector in the r-z plane could be interpreted as a pure tilt, inspection of the three dimensional vector, however, shows a more complex motion than can be attributed to a single n=1 mode (fig 1: the magnetic field vector at the symmetry center of the whole device points from the origin to the tip of the B_r-arrows for the different times. There is a non-symmetric motion already during formation. The final decay starts at t= 10 us. The inverse decay time corresponds to the same order of magnitude as the calculated growth rates of the n=1 modes /4/. These studies are performed for nearly spherical toroids.

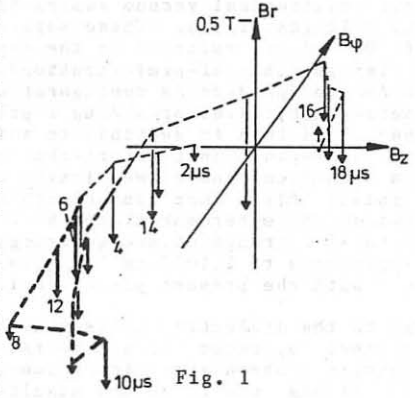

Fig. 1

As has been done in the Princeton and Maryland experiments, passive figure-eight coils /5/ have been inserted into the discharge vessel. Attempts, to stabilize the plasma by coils external to the vessel showed as in the PS-experiments no improvement, hence line tying seems to be important. We use two types of figure-eight coils: (1) a basket-like device with a radius of 12 cm, enclosing the plasma almost completely; (2) a version which cylindrically encompasses like a belt the plasma in the mid-plane with an inner radius of 14 cm i.e. close to the wall. Axially this coil structure extends 7 cm in both directions. There is no part of the coils extending to smaller radii. This version is similar to the one used in Maryland /7/. However, only half of the areas are used, hence the contact to the plasma should be reduced even more.

The first version yields stable plasmas for about 20 to 30 usec, where, as usual, times is counted from onset of field reversal at the outermost probe position (10 cm). The magnetic field profiles are well matched in shape by a force-free cylindrical model both in radial and in axial direction (fig. 2 shows the axial dependence of the poloidal and toroidal fields, fig. 3 a plot of the magnetic vector in the r-z-plane. Note that only above the dotted line in the figure measurements have been done, below the corresponding upper part is mirrored). Even in the case of initial deviation from symmetry the profiles are still very similar: toroids with stationary tilt-angles in the 10 to 25 degree range and displacements of a few cm with respect to the symmetry center of the device). Slight asymmetries in the orientation of the figure-eight coils already produce pronounced deviations from symmetry in the toroid. Temperatures around 5 eV have been determined spectroscopically. The decay of the magnetic field in the symmetry center is almost exponential (fig.5, dashed curve, r=0). In some shots also a linear decay is observed for some period as suggested by Auerbach /6/. In these cases, however, we know that the toroid is not complete-

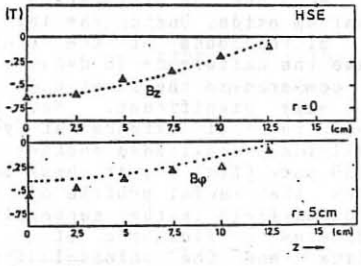

Figure 2

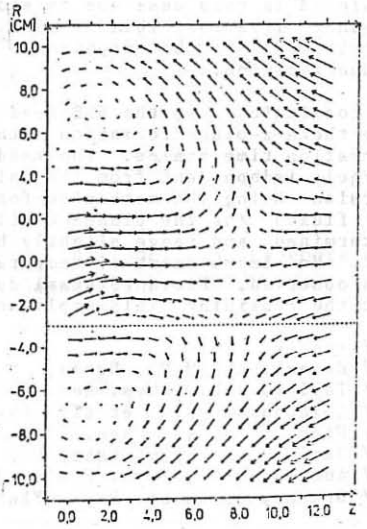

Figure 3

ly axisymmetrically located in the vacuum vessel, hence comparison with his model is difficult.

With the second version of figure-eight coils plasma temperatures of 15 to 20 eV are measured by ruby-scattering at r=6, z=7 cm, i.e. near the magnetic axis (fig. 4, solid curve. Note also the transient strong increase in density there). The improvement as compared to the first coil version is attributed to the reduced influx of impurities both due to the optimized shape and to the improved technique of insulation by aluminum oxide. During the initial 20 microseconds of the stable phase the difference in decay-time as compared to the first case is not very significant. But the field reversal extends at very small field amplitudes another 15 to 30 usec (fig. 5). At these late times the radial profile of the toroidal field in the centerplane indicates a flux-hole of 5 cm radius and the poloidal field shows a broad flat maximum. No scan in the r-z plane has yet been achieved in this case due to shot-to-shot irreproducibilities which we believe to be dependent on probe location.

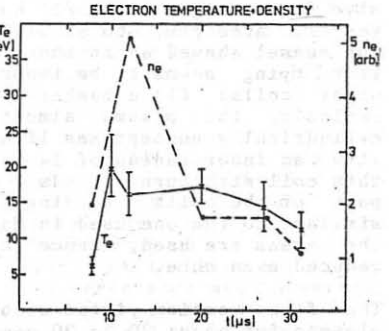

Figure 4

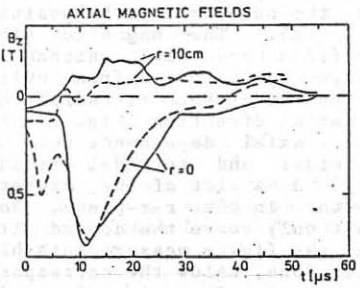

Figure 5

In conclusion, in the HSE device it has been demonstrated, that the theta-z-pinch formation method can be extended to even longer formation time scales. The resultant poloidal flux amplitude is largely independent from the initial axial bias level, flux conversion being the mechanism for establishing the required ratio of fluxes for the plasma equilibrium. Temperatures have been determined and range slightly higher than in the PS-experiments /7/. No improvement of temperature with decreasing fill density was observed. Field reversal duration extends up to 50 - 60 usec but the remaining field amplitudes are very small.

References

/1/ Rosenbluth, M.N., Bussac, M.N., Nucl. Fusion 19, 489 (1979)
/2/ Taylor, J.B., Phys. Rev. Lett. 33, 1139 (1974)
/3/ Goldenbaum, G.C. et al., Phys. Rev. Letters 44, 393 (1980)
/4/ Finn, J. et al. Phys. Fluids 24, 1336 (1981)
/5/ Jardin,S., Christensen, U., Nucl. Fusion 21, 1665 (1981)
/6/ Auerbach, S., Phys. Fluids 25, 1108 (1982)
/7/ Bruhns, H. et al. Phys. Fluids 26, 1616 (1983)

This work was supported by the Deutsche Forschungsgemeinschaft

Turbulent transfer rate of the magnetic field in a spheromak

Á,Ág, G.Németh
Central Research Institute for Physics
H-1525 Budapest P.O.Box 49. Hungary

Introduction

Using the method of D.Montgomery and others ([1], [2]and that of Biskamp and Walter [3]) the transfer rate of the magnetic field, investigated and is applied for a spheromak plasma.

The heating and the confinement of a spheromak plasma is possible by the method of Hugrass, Tuczek and others [4]: the "rotamak-concept", where the toroidal current is generated by a rotating magnetic field. This method (and the other ones too) induce perturbations decaying because of ohmic losses and other factors. In the initial phase the influence of the Hall effect is also important. The quasi-stationary character of the rotamak creates a long living background of perturbations with high wave numbers: the turbulent region. The stochastic field influences the "ground state" by nonlinear terms.

Supposing the force-free case and a quiescent plasma the MHD equations can be reduced to a system where only the magnetic field appears.

$$\frac{\partial \vec{B}}{\partial t} = a_1 \nabla^2 \vec{B} - a_2 \nabla \times [(\nabla \times \vec{B}) \times \vec{B}] \qquad (1)$$

Here $a_1 = c^2/4\pi\sigma$; $a_2 = c/4\pi n_e e$ (2)

We expend (2) into a series of angular functions, Legendre functions ($P_n^m(\cos\vartheta)$ and spherical Bessel functions ($j_n(k_{nq}r)$),

$$\vec{B}(\vec{r},t) = \sum_{nmq} \vec{B}_{nmq} \qquad (3)$$

$$\vec{B}_{nmq} = \vec{r} \times \nabla \psi_{nmq} + (1/k_{nq}) \nabla \times (\vec{r} \times \nabla \psi_{nmq}) \qquad (4)$$

$$\psi_{nmq} = (\alpha_{nmq}(t) \cos m\varphi + \beta_{nmq}(t) \sin m\varphi) j_n(k_{nq} r) P_n^m(\cos\vartheta) \qquad (5)$$

where α, β (t) are time dependent coefficients. The force-free condition yields

$$\nabla \times \vec{B}_{nmq} = k_{nq} \vec{B}_{nmq} \qquad (6)$$

If at the plasma boundary (r=a) the magnetic field is tangential, $k_{nq}=\lambda_{nq}/a$, where λ_{nq} is the q-th root of the j_n function.

A model of radial turbulence, i.e. where will be investigated the perturbations are axially symmetrical (m=0), supposing that the poloidal dependence is weak (n=1). For the evolution of (1) see Ág, Páris, Németh [5].

Interaction between the turbulent and the ground state

Supposing a separation between the small q-value region and the higher ones (f.ex. q=$\mathcal{O}$(1) and q=$\mathcal{O}$(10)) the equation (1), is transformed after a tedions algebra to

$$\dot{\alpha}_{10q}'' + \nu_{1q}'' \alpha_{10q}'' = -D_{10q}'' \Big\{ \sum_{q_1 q_1'} Q_1(q_1 q_1')\big(\alpha_{111}\beta_{11q}' - \alpha_{11q}'\beta_{111}\big) + \sum_{q_1} Q_1(q_1 1)\big(\alpha_{11q}\beta_{111} - \alpha_{111}\beta_{11q}\big) + \sum_{q q_1'} Q_1(q_1 q_1')\big(\alpha_{11q}\beta_{11q_1'} - \alpha_{11q_1'}\beta_{11q}\big)\Big\}$$

$$\dot{\alpha}_{11q}'' + \nu_{1q}'' \alpha_{11q}'' = -D_{11q}'' \Big\{ \sum_{q q_1'} -Q_2(q_1 q_1')\big(\alpha_{10q}\alpha_{11q_1'} + \alpha_{11q}\alpha_{10q_1'}\big) + Q_2(q q_1')\alpha_{10q}\alpha_{11q_1'} + Q_4\alpha_{10q}\beta_{11q_1'}\Big\} \qquad (7)$$

$$\dot{\beta}_{11q}'' + \nu_{1q}''\beta_{11q}'' = -D_{11q}'' \Big\{ \sum_{q q_1'} Q_2(q q_1')\big(\alpha_{10q}\beta_{11q_1'} + \alpha_{10q_1'}\beta_{11q}\big) - Q_2(q q_1')\alpha_{10q}\beta_{11q_1'} + Q_4\alpha_{10q}\alpha_{11q_1'}\Big\}$$

Here the functions $Q_i(q,q')$ are determined numerically, having the order of 10^{-2}-10^{-3} if q=q' and 10^{-4}-10^{-6} if q, q'-s are different.

Using the method of [1], [2] and [3] the stochastic field split into two parts: one originating from the stochastic evolution and to another resulting from the reaction of the long-wavelength part. Assuming a possibility of averaging upon the short-wavelength spectrum, we get

$$\dot{\alpha}_{101} + \nu_{11}\alpha_{101} = -\alpha_{101}\sum_{q_r} D_{101}\, A_0(q_r)\left(\frac{\langle \alpha_{11q_r}^{02}\rangle}{\nu_{1q_r}} + \frac{\langle \beta_{11q_r}^{02}\rangle}{\nu_{1q_r}}\right);$$

$$\dot{\alpha}_{111} + \nu_{11}\alpha_{111} = -\alpha_{111}\sum_{q_r}\left\{D_{11q_r}A_{11}(q_r)\frac{\langle \alpha_{10q_r}^{02}\rangle}{\nu_{1q_r}} - D_{10q_r}A_{12}(q_r)\frac{\langle \beta_{11q_r}^{02}\rangle}{\nu_{1q_r}}\right\} +$$

$$+\beta_{111}\sum_{q_r}\left\{D_{11q_r}B_{11}(q_r)\frac{\langle \alpha_{10q_r}^{02}\rangle}{\nu_{1q_r}} - D_{10q_r}B_{12}(q_r)\frac{\langle \alpha_{11q_r}^{02}\rangle}{\nu_{1q_r}}\right\};$$

$$\dot{\beta}_{111} + \nu_{11}\beta_{111} = -\beta_{111}\sum_q \left\{ D_{11q} B_{21}(q_1) \frac{\langle \alpha^{02}_{10q} \rangle}{\nu_{10q}} + D_{10q} B_{22}(q_1) \frac{\langle \alpha^{02}_{11q} \rangle}{\nu_{11q}} \right\} + \quad (8)$$

$$+ \alpha_{111}\sum_q \left\{ D_{11q} A_{21}(q_1) \frac{\langle \alpha^{02}_{10q} \rangle}{\nu_{10q}} + D_{10q} A_{22}(q_1) \frac{\langle \beta^{02}_{11q} \rangle}{\nu_{11q}} \right\}$$

D_{nmq} are proportional to a_2.

The functions A_{ij}, B_{ij} are determined numerically, these are combinations of the Q_i-functions, having values of the order of 10^{-2}, see for details [6]. The damping is a tensor, depending on the turbulent energy.

From the non-linear terms we can evaluate a turbulent rate, which means a damping first of all. For the mode of the "ground-state spheromak" (α_{101}), α^0_{11q}, α^0_{11q} being in the region of q_1=10, $A_0 \approx 10^{-2}$, and if about 10 modes are taken into account, the ratio of the damping coefficients is round the order of

$$\sigma \left\{ \frac{\nu \text{ ohmic}}{\nu \text{ nonlinear}} \right\} \cong 2$$

with a turbulent intensity of 10^6 CGS. This is the normal cascade process.

For the higher order terms (α_{111}, β_{111}) the damping is not so simple and there is a possibility of enhancement too (inverse cascade), depending on the shape of the turbulent energy spectrum.

References

[1] D.Montgomery, T.Hatori, Plasma Phys.Contr.Fusion 26,717(1984)

[2] D.Montgomery, H.Chen, Plasma Phys.Contr.Fusion 26,1199(1984)

[3] D.Biskamp, H.Welter Phys.Lett. 96A,25(1983)

[4] W.N.Hugrass, I.R.Jones, K.F.McKenna, M.G.R.Phillips, R.G.Storer, H.Tuczek, Phys.Rev.Lett. 44,1676(1980)

[5] Á.Ág, Gy.Páris, G.Méneth Plasma Phys.Contr.Fusion 26,959(1984)

[6] Á.Ág, G.Németh, to be published in KFKI Preprint.